COMPREHENSIVE CHIROPTICAL SPECTROSCOPY

Volume 1

COMPREHENSIVE CHIROPTICAL SPECTROSCOPY

Volume 1

Instrumentation, Methodologies, and Theoretical Simulations

Edited by

Nina Berova
Prasad L. Polavarapu
Koji Nakanishi
Robert W. Woody

WILEY

A JOHN WILEY & SONS, INC., PUBLICATION

Copyright © 2012 by John Wiley & Sons, Inc. All rights reserved

Published by John Wiley & Sons, Inc., Hoboken, New Jersey
Published simultaneously in Canada

No part of this publication may be reproduced, stored in a retrieval system, or transmitted in any form or by any means, electronic, mechanical, photocopying, recording, scanning, or otherwise, except as permitted under Section 107 or 108 of the 1976 United States Copyright Act, without either the prior written permission of the Publisher, or authorization through payment of the appropriate per-copy fee to the Copyright Clearance Center, Inc., 222 Rosewood Drive, Danvers, MA 01923, (978) 750–8400, fax (978) 750–4470, or on the web at www.copyright.com. Requests to the Publisher for permission should be addressed to the Permissions Department, John Wiley & Sons, Inc., 111 River Street, Hoboken, NJ 07030, (201) 748–6011, fax (201) 748–6008, or online at http://www.wiley.com/go/permission.

Limit of Liability/Disclaimer of Warranty: While the publisher and author have used their best efforts in preparing this book, they make no representations or warranties with respect to the accuracy or completeness of the contents of this book and specifically disclaim any implied warranties of merchantability or fitness for a particular purpose. No warranty may be created or extended by sales representatives or written sales materials. The advice and strategies contained herein may not be suitable for your situation. You should consult with a professional where appropriate. Neither the publisher nor author shall be liable for any loss of profit or any other commercial damages, including but not limited to special, incidental, consequential, or other damages.

For general information on our other products and services or for technical support, please contact our Customer Care Department within the United States at (800) 762–2974, outside the United States at (317) 572–3993 or fax (317) 572–4002.

Wiley also publishes its books in a variety of electronic formats. Some content that appears in print may not be available in electronic formats. For more information about Wiley products, visit our web site at www.wiley.com.

Library of Congress Cataloging-in-Publication Data:

Library of Congress Cataloging-in-Publication Data
Advances in chiroptical methods/edited by Nina Berova . . . [et al.].
p. cm.
Includes index.
ISBN 978-0-470-64135-4 (hardback : set)—ISBN 978-1-118-01293-2 (v. 1)—ISBN 978-1-118-01292-5 (v. 2)
1. Chirality. 2. Spectrum analysis. 3. Circular dichroism. I. Berova, Nina.
QP517.C57A384 2012
541.7–dc23

2011021418

Printed in the United States of America

10 9 8 7 6 5 4 3 2 1

CONTENTS

PREFACE

Chirality is a phenomenon that is manifested throughout the natural world, ranging from fundamental particles through the realm of molecules and biological organisms to spiral galaxies. Thus, chirality is of interest to physicists, chemists, biologists, and astronomers. Chiroptical spectroscopy utilizes the differential response of chiral objects to circularly polarized electromagnetic radiation. Applications of chiroptical spectroscopy are widespread in chemistry, biochemistry, biology, and physics. It is indispensable for stereochemical elucidation of organic and inorganic molecules. Nearly all biomolecules and natural products are chiral, as are the majority of drugs. This has led to crucial applications of chiroptical spectroscopy ranging from the study of protein folding to characterization of small molecules, pharmaceuticals, and nucleic acids.

The first chiroptical phenomenon to be observed was optical rotation (OR) and its wavelength dependence, namely, optical rotatory dispersion (ORD), in the early nineteenth century. Circular dichroism associated with electronic transitions (ECD), currently the most widely used chiroptical method, was discovered in the mid-nineteenth century, and its relationship to ORD and absorption was elucidated at the end of the nineteenth century. Circularly polarized luminescence (CPL) from chiral crystals was observed in the 1940s. The introduction of commercial instrumentation for measuring ORD in the 1950s and ECD in the 1960s led to a rapid expansion of applications of these forms of chiroptical spectroscopy to various branches of science, and especially to organic and inorganic chemistry and to biochemistry.

Until the 1970s, chiroptical spectroscopy was confined to the study of electronic transitions, but vibrational transitions became accessible with the development of vibrational circular dichroism (VCD) and Raman optical activity (ROA). Other major extensions of chiroptical spectroscopy include differential ionization of chiral molecules by circularly polarized light (photoelectron CD), measurement of optical activity in the X-ray region, magnetochiral dichroism, and nonlinear forms of chiroptical spectroscopy.

The theory of chiroptical spectroscopy also goes back many years, but has recently made spectacular advances. Classical theories of optical activity were formulated in the early twentieth century, and the quantum mechanical theory of optical rotation was described in 1929. Approximate formulations of the quantum mechanical models were developed in the 1930s and more extensively with the growth of experimental ORD and ECD studies, starting in the late 1950s. The quantum mechanical methods for calculations of chiroptical spectroscopic properties reached a mature stage in the 1980s and 1990s. *Ab initio* calculations of VCD, ECD, ORD, and ROA have proven highly successful and are now widely used for small and medium-sized molecules.

Many books have been published on ORD, ECD, and VCD/ROA. The present two volumes are the first comprehensive treatise covering the whole field of chiroptical spectroscopy. Volume 1 covers the instrumentation, methodologies, and theoretical simulations for different chiroptical spectroscopic methods. In addition to an extensive

treatment of ECD, VCD, and ROA, this volume includes chapters on ORD, CPL, photoelectron CD, X-ray-detected CD, magnetochiral dichroism, and nonlinear chiroptical spectroscopy. Chapters on the related techniques of linear dichroism, chiroptical imaging of crystals and electro-optic absorption, which sometimes supplement chiroptical interpretations, are also included. The coverage of theoretical methods is also extensive, including simulation of ECD, ORD, VCD, and ROA spectra of molecules ranging from small molecules to macromolecules. Volume 2 describes applications of ECD, VCD, and ROA in the stereochemical analysis of organic and inorganic compounds and to biomolecules such as natural products, proteins, and nucleic acids. The roles of chiroptical methods in the study of drug mechanisms and drug discovery are described.

Thus, this work is unique in presenting an extensive coverage of the instrumentation and techniques of chiroptical spectroscopy, theoretical methods and simulation of chiroptical spectra, and applications of chiroptical spectroscopy in inorganic and organic chemistry, biochemistry, and drug discovery. In each of these areas, leading experts have provided the background needed for beginners, such as undergraduates and graduate students, and a state-of-the-art treatment for active researchers in academia and industry.

We are grateful to the contributors to these two volumes who kindly accepted our invitations to contribute and who have met the challenges of presenting accessible, up-to-date treatments of their assigned topics in a timely fashion.

Nina Berova
Prasad L. Polavarapu
Koji Nakanishi
Robert W. Woody

CONTRIBUTORS

Sergio Abbate, Department of Biomedical Sciences and Biotechnologies, University of Brescia, Brescia, Italy *and* CNISM (Consorzio Nazionale Interuniversitario per le Scienze Fisiche della Materia), Rome, Italy

Jochen Autschbach, Department of Chemistry, University at Buffalo, The State University of New York, Buffalo, New York, USA

Evert Jan Baerends, Division of Theoretical Chemistry, Faculty FEW/Chemistry, VU University, Amsterdam, The Netherlands *and* WCU Program, Department of Chemistry, Pohang University of Science and Technology, Pohang, South Korea

Nina Berova, Department of Chemistry, Columbia University, New York, New York, USA

Christian Brouder, Institute of Mineralogy and Physics of Condensed Media, Universities of Paris VI-VII, Paris, France

Ettore Castiglioni, Jasco Corporation, Tokyo, Japan *and* Department of Biomedical Sciences and Biotechnologies, University of Brescia, Brescia, Italy

Eefei Chen, Department of Chemistry and Biochemistry, University of California, Santa Cruz, California, USA

Minhaeng Cho, Department of Chemistry, Korea University, Seoul, South Korea *and* Korea Basic Science Institute, Seoul, South Korea

T. Daniel Crawford, Department of Chemistry, Virginia Tech, Blacksburg, Virginia, USA

Lorenzo Di Bari, Department of Chemistry and Industrial Chemistry, University of Pisa, Pisa, Italy

Peer Fischer, Max-Planck-Institute for Intelligent Systems, Stuttgart, Germany

Joerg Fleischhauer, Institute of Organic Chemistry, RWTH Aachen University, Aachen, Germany

John Freudenthal, Department of Chemistry and Molecular Design Institute, New York University, New York, New York, USA

Lars Goerigk, Institute of Theoretical Organic Chemistry and Organic Chemistry, University of Muenster, Muenster, Germany *and* School of Chemistry, The University of Sydney, Sydney, New South Wales, Australia

Robert A. Goldbeck, Department of Chemistry and Biochemistry, University of California, Santa Cruz, California, USA

Jose Goulon, European Synchrotron Radiation Facility, Grenoble, France

Stefan Grimme, Institute of Theoretical Organic Chemistry and Organic Chemistry, University of Muenster, Muenster, Germany

Takunori Harada, Department of Life Sciences, Graduate School of Arts and Sciences, The University of Tokyo, Tokyo, Japan

Werner Hug, Department of Chemistry, University of Fribourg, Fribourg, Switzerland

Bart Kahr, Department of Chemistry and Molecular Design Institute, New York University, New York, New York, USA

Werner Kaminsky, Department of Chemistry, University of Washington, Seattle, Washington, USA

David S. Kliger, Department of Chemistry and Biochemistry, University of California, Santa Cruz, California, USA

Holger Kruse, Institute of Theoretical Organic Chemistry and Organic Chemistry, University of Muenster, Muenster, Germany

Hans-Georg Kuball, Department of Chemistry—Physical Chemistry, Technical University of Kaiserslautern, Kaiserslautern, Germany

Reiko Kuroda, Department of Life Sciences, Graduate School of Arts and Sciences, The University of Tokyo, Tokyo, Japan

Giovanna Longhi, Department of Biomedical Sciences and Biotechnologies, University of Brescia, Brescia, Italy *and* CNISM Consorzio Nazionale Interuniversitario per le Scienze Fisiche della Materia, Rome, Italy

Gilles Muller, Department of Chemistry, San José State University, San José, California, USA

Laurence A. Nafie, Department of Chemistry, Syracuse University, Syracuse, New York, USA

Koji Nakanishi, Department of Chemistry, Columbia University, New York, New York, USA

Valentin Paul Nicu, Division of Theoretical Chemistry, Faculty FEW/Chemistry, VU University, Amsterdam, The Netherlands

Magdalena Pecul, Faculty of Chemistry, University of Warsaw, Warszawa, Poland

Prasad L. Polavarapu, Department of Chemistry, Vanderbilt University, Nashville, Tennessee, USA

Ivan Powis, School of Chemistry, University of Nottingham, Nottingham, United Kingdom

Gerhard Raabe, Institute of Organic Chemistry, RWTH Aachen University, Aachen, Germany

Hanju Rhee, Seoul Center, Korea Basic Science Institute, Seoul, South Korea

James P. Riehl, Department of Chemistry, University of Minnesota, Duluth, Minnesota, USA

G. L. J. A. Rikken, National Laboratory of Intense Magnetic Fields, Toulouse, France

Alison Rodger, Warwick Centre for Analytical Science and Department of Chemistry, University of Warwick, Coventry, United Kingdom

Andrei Rogalev, European Synchrotron Radiation Laboratory, Grenoble, France

Kenneth Ruud, Centre for Theoretical and Computational Chemistry, Department of Chemistry, University of Tromsø, Tromsø, Norway

Piero Salvadori, Department of Chemistry and Industrial Chemistry, University of Pisa, Pisa, Italy

Matthias Stolte, Institute of Organic Chemistry, University of Würzburg, Würzburg, Germany

John C. Sutherland, Department of Physics, East Carolina University, Greenville, North Carolina, USA *and* Biology Department, Brookhaven National Laboratory, Upton, New York, USA

Patrick H. Vaccaro, Department of Chemistry, Yale University, New Haven, Connecticut, USA

Georges H. Wagnière, Institute of Physical Chemistry, University of Zürich, Zürich, Switzerland

Hong-fei Wang, Environmental Molecular Science Laboratory, Pacific Northwest National Laboratory, Richland, Washington, USA

Robert W. Woody, Department of Biochemistry and Molecular Biology, Colorado State University, Fort Collins, Colorado, USA

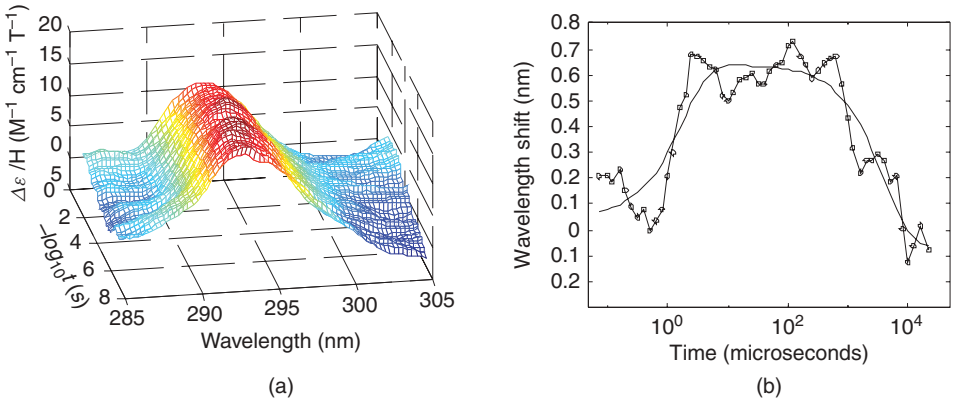

Figure 7.10. An early step in the R → T quaternary transition of hemoglobin detected by TRMCD spectroscopy of the tryptophan bands after photolysis of the CO complex. (a) Near-UV TRMCD spectra collected at delay times ranging from 63 ns to 25 ms after photolysis. (b) A plot of the near-UV Trp band position versus time shows a red shift at 2 μs that corresponds to formation of a Trp–Asp hydrogen bond between the two dimers of the Hb tetramer. (Adapted from reference 52 with permission from the American Chemical Society. See page 198 for text discussion.

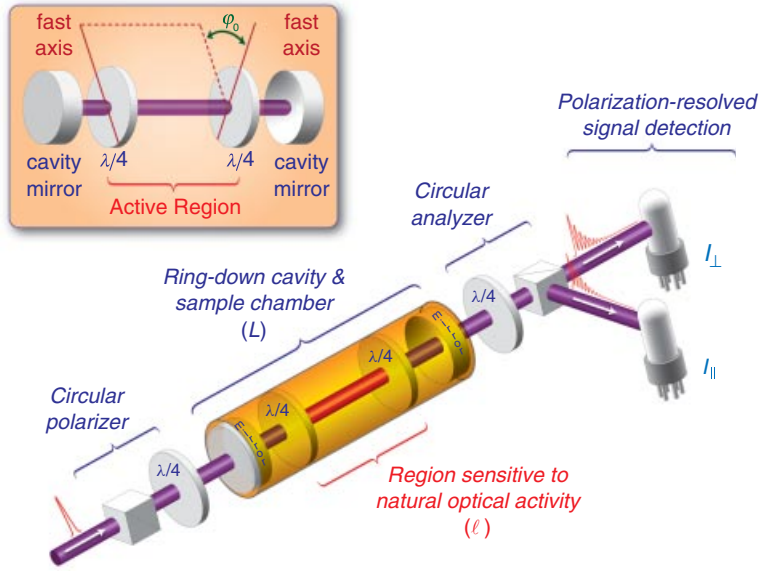

Figure 11.2. Schematic diagram of CRDP apparatus. Pulsed laser radiation traverses a circular polarizer consisting of a tandem calcite prism and quarter-wave plate ($\lambda/4$) before being coupled into a high-finesse linear cavity of length L. Matched intracavity $\lambda/4$ retardation plates are aligned to produce a stable linearly polarized field over the intervening region of length ℓ, thereby making this portion of the apparatus sensitive to the accruing effects of natural optical activity. Emerging light is imaged onto two identical detectors that separately monitor temporal profiles for the two linear components (parallel and perpendicular) generated by a circular polarization analyzer. The inset depicts the arrangement of cavity optics, highlighting the relative offset, φ_0, purposely introduced between the fast axes of intracavity waveplates so as to resolve the sign of measured specific rotation. See pages 292–293 for text discussion.

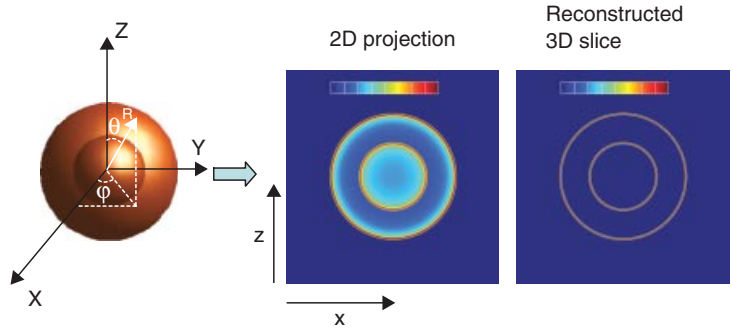

Figure 15.2. The photofragment imaging technique. A 3-D angular distribution of emitted electrons and their projection onto a 2-D imaging detector. Mathematical inversion of the projection recovers a slice through the 3-D distribution along with the energy and angular distribution functions. See page 415 for text discussion.

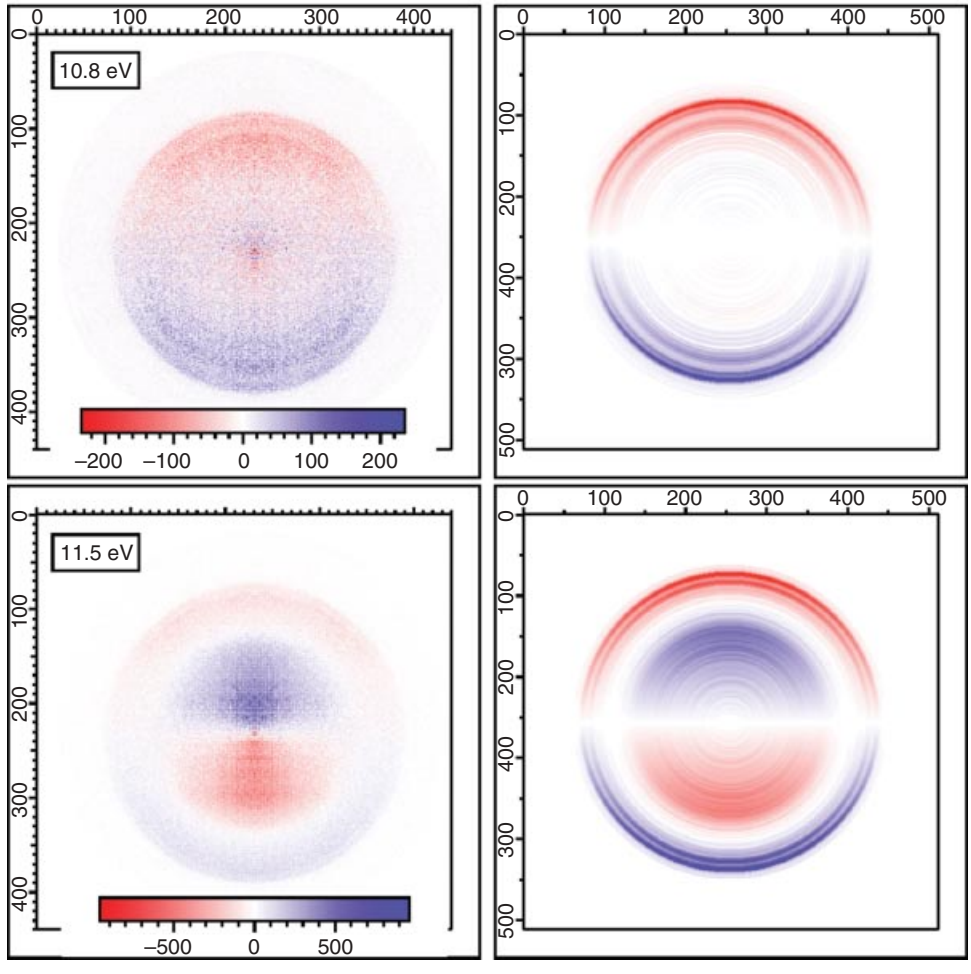

Figure 15.3. VMI images showing PECD in (*S*)-methyloxirane, with pseudo-color mapped intensities and **X, Y** axes that are marked in detector pixel units. The photon beam propagates vertically upwards, parallel to the image plane in these recordings. Left column: unprocessed 2-D photoelectron dichroism image (left CPL–right CPL). Right column: after treatment with pBaseX algorithm. See page 417–418 for text discussion.

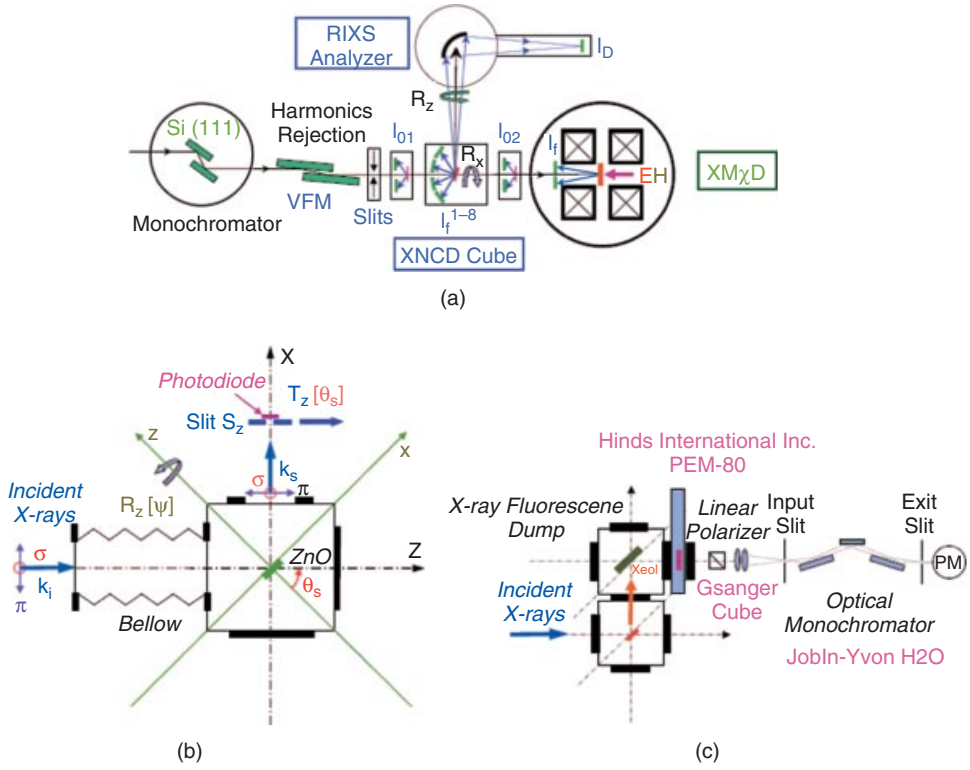

Figure 17.2. (a) Configuration in use for XNCD or XM χ D experiments. In XNCD experiments, gyrotropic crystals can be freely rotated around the direction of the incident X-ray beam (rotation R_χ). Beamline ID12 is equipped with a UHV-compatible RIXS analyzer that can be rotated around the vertical axis (Z) to select a given linear polarization. (b) Reflectometer adapted to measure the vector part of OA in zincite. (c) CP-XEOL detection; the combination of a photoelastic modulator (PEM) and a Gsänger linear polarizer made it possible to resolve the right/left-handed polarizations of the luminescence. See pages 466–467 for text discussion.

Figure 18.21. A mechanical film stretcher with oppositely threaded screws to ensure even stretching of the film. See page 515 for text discussion.

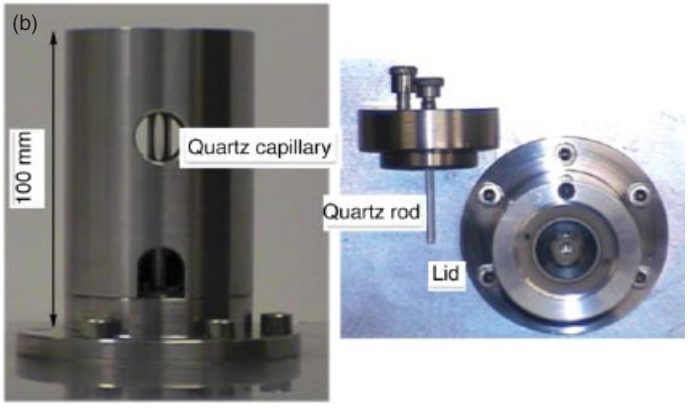

Figure 18.23. (a) Large-volume (2–3 mL) inner rotating cylinder Couette flow cell with 500-μm annular gap [6]. (b) Microvolume (25–60 μL) outer rotating [56, 57] Couette flow cell showing the outer quartz capillary (3-mm inner diameter) and inner quartz rod (2.5-mm outer diameter) which, when assembled, results in an annular gap of 250 μm. See page 516 for text discussion.

PART I

INTRODUCTION

1

ON THE INTERACTION OF LIGHT WITH MOLECULES: PATHWAYS TO THE THEORETICAL INTERPRETATION OF CHIROPTICAL PHENOMENA

Georges H. Wagnière

1.1. A BRIEF HISTORICAL RETROSPECTIVE

1.1.1. On the Nature of Light

The ancient Greek philosophers, such as Pythagoras and his disciples, later also Euclid, gave early speculations on the nature of light. Yet the fundamental question, what light really is, has been systematically approached only following the birth of modern astronomy in the fifteenth and sixteenth century. The developing manufacture of lenses and of other optical components for technical purposes undoubtedly stimulated this scientific endeavor.

The lasting foundations of a modern theory of light were, however, not laid before the second half of the seventeenth century. While Isaac Newton (1642–1727), after discovering the spectral resolution of white light, tended to consider it as made up of particles, Christiaan Huygens (1629–1695) attributed to it a wave nature and thereby succeeded in explaining reflection and refraction. Significant advances in the understanding of light were accomplished in the nineteenth century. Augustin Fresnel (1788–1827) extended the theory of Huygens to explain diffraction, thereby affirming the apparent superiority of the wave model. However, a satisfying deeper explanation of the nature of the oscillating medium was still missing.

Not before the development of a theory of electricity and magnetism was a significant next step made forward. Jean-Baptiste Biot (1774–1862) not only made important contributions to the understanding of the relation between an electric current and a magnetic field—the Biot–Savart law—but also discovered the rotation of the plane of linearly

Comprehensive Chiroptical Spectroscopy, Volume 1: Instrumentation, Methodologies, and Theoretical Simulations, First Edition. Edited by N. Berova, P. L. Polavarapu, K. Nakanishi, and R. W. Woody.
© 2012 John Wiley & Sons, Inc. Published 2012 by John Wiley & Sons, Inc.

polarized light in "optically active" liquids, such as sugar solutions. Michael Faraday (1791–1867) discovered both (a) the electromagnetic law of induction and (b) the effect named after him, namely, that a magnetic field could cause optical rotation in a material medium. James Clerk Maxwell (1831–1879) subsequently succeeded in mathematically unifying the laws of electricity and magnetism. From Maxwell's equations (see Section 1.2.1) one may directly derive an electromagnetic wave equation that has proven to be an excellent description of the properties of light and its propagation. Light then appears as a *transverse wave*, with an *electric* and a *magnetic* field component perpendicular to each other and to the direction of propagation.

Unexpectedly, and in spite of the success of the classical wave theory, the concept of a particle nature of light, dormant for about two centuries, resurfaced at the beginning of the twentieth century. In order to satisfactorily interpret the law of blackbody radiation, Max Planck (1858–1947) was led to assume that an electromagnetic field inside a cavity, and in thermal equilibrium with it, behaves as a collection of harmonic oscillators, the energy of which is quantized. From the photoelectric effect, Albert Einstein (1879–1955) concluded that radiation is absorbed by an atom in the form of quanta of energy proportional to its frequency, $E = h\nu$, where the quantity h is Planck's constant. Thus the concept of the *photon* was born. The particle-wave duality, not only for light, but also for matter, became a cornerstone of the quantum mechanics that then soon developed.

Assuming a formal analogy between the radiation oscillators and the quantum mechanical harmonic oscillator, P. A. M. Dirac (1902–1984) initiated an algebra of photon states. The radiation field is consequently represented as a many-photon system, each photon acting as a harmonic oscillator of given frequency. State changes of the radiation field are then described by photon creation and annihilation operators. However, even in this quantized frame, the electromagnetic picture derived from the classical description is essentially maintained. Considering a classical ray of light, one may, according to how the electric and magnetic field oscillate in space and time, speak of *linear, circular*, or *elliptic polarization*. The concept of *polarization* may also be attributed to a *single photon*. Beth's experiment in 1936 revealed that circularly polarized light carries angular momentum, and that this angular momentum corresponds to a *spin of the photon* of $\pm 1\hbar$, depending on if the photon is *left* or *right* circularly polarized.

In our aim to describe chiroptical phenomena of molecules, we ask ourselves to what extent the quantization of the radiation field must be taken into account. Is it for our purposes sufficient to describe the electromagnetic field classically, or is it also necessary to explicitly consider this field quantization? A fact taught in elementary quantum mechanics courses is that the quantum mechanical harmonic oscillator for increasing quantum numbers behaves more and more like a classical oscillator. Similarly, the radiation field at high quantum numbers, corresponding to a high photon density, behaves more and more classically as the intensity grows.

One of Albert Einstein's numerous seminal contributions to modern physics was to recognize that *absorption* of light by matter obviously can only be electromagnetic field-induced, but that there are two kinds of *emission, spontaneous* and *induced*. Spontaneous emission occurs even in the absence of external radiation. It may be pictured as an excitation of the vacuum state of the electromagnetic field by the atom or molecule. Its detailed interpretation indeed requires field quantization. In absorption and induced emission, on the other hand, one must assume a certain external light intensity to be present, and therefore the classical description is admissible. This is indeed the point of view that we shall adopt.

The particular practical significance of *induced emission* only became apparent in the middle of the last century and led to the development of *masers and lasers*. Some of the chiroptical phenomena that we shall briefly consider in the following sections indeed require the use of lasers. We shall treat these effects in the frame of the so-called semiclassical radiation theory [1–6].

1.1.2. Quantum Chemistry in Its Early Stages

For the understanding of the atomic and molecular spectra, measured at higher and higher resolution in the late nineteenth and early twentieth century, it became clear that only a quantum mechanical description of matter would be satisfactory. This also initiated the special field of *quantum chemistry*. Even the simplest molecule, that of hydrogen, already poses some difficult problems, however. In the calculation of Heitler and London [7], a solution of the Schrödinger equation for the electrons is sought, while a priori keeping the nuclei fixed. A systematic investigation of the *separability* of *electronic* and *nuclear motion* was worked out by Born and Oppenheimer [8]. They showed that due to the mass difference between electrons and nuclei, the molecular Schrödinger equation may be approximately separated into an equation for the electrons at different fixed nuclear positions, and an equation for the vibrations of the nuclei in the potential energy surfaces that are derived from the solutions of the electronic equation. Finally, there is the rotation of the molecule as a whole to be considered, approximated by a three-dimensional rotator, or top, of appropriate symmetry. Consequently, the overall molecular wavefunction may then be represented as a product:

$$\Psi_{\text{molec}} = \Phi_{\text{el}} X_{\text{vib}} \Theta_{\text{rot}},$$

and the energy E can be expressed as a sum. A molecular change of state is correspondingly written as

$$\Delta E_{\text{molec}} = \Delta E_{\text{el}} + \Delta E_{\text{vib}} + \Delta E_{\text{rot}},$$

with ΔE_{el} usually on the order of 10^4–10^5 cm^{-1}, $\Delta E_{\text{vib}} \approx 10^2$–$10^3$ cm^{-1}, $\Delta E_{\text{rot}} \approx 10^{-1}$–$10^1$ cm^{-1}.

It was soon recognized that the solution of the electronic equation alone already is a formidable task, the main difficulty being the electron–electron interaction. A general and rigorously justifiable procedure was then developed, consisting of several steps. (a) Calculate a set of orthonormalized molecular one-electron functions—for instance, *molecular orbitals* (MO) as linear combinations of *atomic orbitals* (LCAO)—by solving a simplified electronic Schrödinger equation that neglects electron–electron interaction. Multiply each MO with an appropriate spin function. Assign the electrons individually to these *spin orbitals*, respecting the *Pauli exclusion principle*. (b) Such an assignment was given the name *configuration*. An electron configuration is thus described as a product of the occupied one-electron molecular spin orbitals. Because electrons are fermions, these products must be antisymmetric with respect to the interchange of any two electrons. Therefore, the many-electron functions are to be *antisymmetrized* and may be written in the form of *Slater determinants*. Every Slater determinant thus represents an *electron configuration*. The solution of the many-electron Schrödinger equation is performed on the basis of these antisymmetrized configurational functions and is termed *configuration interaction* (CI). The electronic wavefunctions finally so obtained consequently present themselves as linear combinations of such Slater determinants.

It soon became obvious that the solution of these quantum mechanical electronic eigenvalue problems was heavily dependent on the availability of computational facilities. In general, the development of quantum chemistry closely parallels the development of the computer.

From the beginning, great effort was spent to optimize the molecular one-electron functions. This allowed calculations that were tractable, and the results could be pictured visually, which appealed to the structural thinking of the chemists. The 1930s saw the birth of the concept of *hybridization* [9], by which the occurrence of particular three-dimensional molecular geometries could be convincingly interpreted. The electronic properties of the important class of planar conjugated unsaturated hydrocarbons were described in the frame of the *Hückel theory* for π electrons [10]. These π-MOs are linear combinations of atomic p_z functions, the axes of which are perpendicular to the molecular plane. An attempt to extend the Hückel one-electron theory to nonplanar, three-dimensional molecules using a basis of s, p_x, p_y, p_z, and eventually d functions proved highly successful in spite of its limitations [11]. As an immediate and important application, it provided a computational background for the derivation of the symmetry rules for the stereochemically important electrocyclic reactions [12, 13].

The Hartree–Fock method, first formulated for atoms in the 1930s, attempts to optimize the one-electron functions by including the electron interaction as far as possible in a self-consistent manner at the one-electron level, thereby reducing the need for configuration interaction [14, 15]. A similar *self-consistent field* (SCF) method for molecules was developed in the 1950s [16].

However, the SCF method in no ways fully eliminates the need for configuration interaction, in particular also in the calculation of electronically excited states. The still limited computational resources of the 1950s and 1960s imposed severe restrictions on the possibilities to perform many-electron SCF-CI calculations. Great effort was therefore spent to reduce computational labor by adopting simplifications in the numerical evaluation of the many intermediate quantities appearing in a calculation—in particular, the two-electron repulsion and exchange integrals, as well as the integrals describing the interaction of the electrons with the positive atomic cores. This led to a number of *semiempirical* many-electron methods, such as the PPP and CNDO methods [17, 18] and modifications thereof, which were applied, with variable success, not only to the calculation of long-wavelength absorption, but also that of *circular dichroism* (CD) spectra.

As computational efficiency and speed increased, quantum chemical calculations became more accurate, and the semiempirical procedures gradually have given way to *ab initio* methods, in which all quantities are calculated as exactly as possible from their analytic expression. If in the 1960s and 1970s one was satisfied to perform CI calculations with perhaps 10^2 configurations, nowadays a routine molecular many-electron calculation may include on the order of 10^6 configurations. *Ab initio* methods have since also been refined, to increase their efficiency and to reduce computer time, by more sophisticated procedures, such as multiconfiguration SCF methods, the coupled cluster methods, and variants thereof. More recently, the Density Functional Theory (DFT) has been successfully used for a wide range of quantum chemical problems, due to its relatively easy applicability to large molecular systems.

1.1.3. Early Interpretations of Chiroptical Properties

Optical rotation, or *optical rotatory dispersion* (ORD), is a consequence of the fact that in an optically active medium the index of refraction is different for left (L) and right

(R) circularly polarized light. Inside absorption bands we encounter *anomalous* rotatory dispersion accompanied by *circular dichroism* (CD). While ORD is responsible for the rotation of linearly polarized light, CD transforms linearly polarized incident light into elliptically polarized light. In measuring this ellipticity, care had to be taken to distinguish between the ellipticity itself and the concomitant rotation of the polarization ellipse [19]. Technical advances in the manufacture of optical components and in phase-sensitive detection made it later possible to measure the difference of the absorption coefficient, $\Delta\varepsilon(\mathrm{CD}) = \varepsilon_\mathrm{L} - \varepsilon_\mathrm{R}$, directly. The first commercial *circular dichrographs* operating in this fashion became available in the 1960s. CD spectroscopy then developed into a subfield of absorption spectroscopy.

From a historic point of view, it seems somewhat paradoxical that the first attempts to interpret optical activity quantum mechanically coincided more or less with the elaboration of purely classical models, essentially based on coupled oscillators. We shall, however, leave the classical models entirely to history and concentrate on the quantum mechanical approach.

It was first shown by Rosenfeld that a direct connection could be established between the quantum mechanical states of a molecule and its optical activity [20]. In particular, the circular dichroism $\Delta\varepsilon(a \rightarrow b)$ for the transition from a molecular state a to a state b is proportional to the *rotatory strength*, which in principle is calculable:

$$\Delta\varepsilon(a \rightarrow b) \sim \mathrm{Im}\langle a|\boldsymbol{\mu}|b\rangle \cdot \langle b|\mathbf{m}|a\rangle. \tag{1.1}$$

$\langle a|\boldsymbol{\mu}|b\rangle$ represents the electric dipole transition moment and $\langle b|\mathbf{m}|a\rangle$ the magnetic dipole transition moment, of which we take the imaginary part (Im), which is real. As is taught in elementary courses, the total absorption coefficient is proportional to the *dipole strength*:

$$\varepsilon(a \rightarrow b) \sim \langle a|\boldsymbol{\mu}|b\rangle \cdot \langle b|\boldsymbol{\mu}|a\rangle, \tag{1.2}$$

in which only the electric dipole operator occurs.

Yet, as mentioned, the main problem in computing these quantities consists in obtaining molecular wavefunctions of sufficient quality. The calculation of molecular spectra, in particular of chiroptical spectra, necessarily and evidently depended on the general development of quantum chemical calculations, briefly summarized in the previous section. The unavailability of accurate wavefunctions stimulated the search for symmetry rules and for simplified models. These efforts initially went into two directions. One was the so-called *polarizability theory* of optical activity, the other was the *one-electron model*.

In the polarizability theory, pioneered by Kirkwood [21], the molecule is subdivided into pairs of optically anisotropic groups. The interaction between the groups is assumed to be essentially electrostatic, exchange effects being important only within the individual groups. The optical activity tensor is calculated from the radiation-induced electric and magnetic transition moments within the groups. The calculated optical activity of the composite system may then approximately be reduced to purely electric quantities that can be directliy related to the electric polarizability tensor of the groups, averages of which can be experimentally determined. The polarizability theory developed into what is now commonly called the *quantum mechanical coupled oscillator*, or *exciton model*, which has found wide application in the interpretation of the optical activity of organic and inorganic dimers and polymers.

An important concern was whether a potential exists which makes a single electron optically active and which leads to an analytically solvable Schrödinger equation. Such

a model was found in the asymmetrically perturbed three-dimensional harmonic oscillator. The model shows well how transitions that are purely electric dipole-allowed in the unperturbed, achiral case obtain a magnetic dipole-allowed component through the asymmetric perturbation; and similarly, transitions that originally are purely magnetic dipole-allowed obtain an electric dipole increment [22, 23], leading to nonvanishing rotatory strengths.

ORD and CD began in the 1950s and 1960s to be routinely applied in stereochemistry. Just as for ordinary dispersion and absorption, it was experimentally verified that ORD and CD are *Kronig–Kramers transforms* of each other. If one knows the ORD spectrum over a wide spectral range, the CD spectrum may be deduced and vice versa. On the practical level, CD became the method of choice, because one could better determine the contributions of individual transitions.

Chiroptical methods complemented crystallographic structure determinations of biopolymers, as well as those of metal–organic complexes. Here the theoretical procedure of choice was the coupled-oscillator or *exciton model* [24–30]. On the other hand, in the study of local effects, in particular the investigation of the stereochemical surroundings of particular substituents, a one-electron approach suggested itself. This then led to the so-called *sector rules* [31–33].

The various semiempirical SCF-MO-CI methods mentioned in the previous section have been widely applied to calculate CD spectra. They proved to be successful, for instance, for the interpretation of the chiroptical properties of chromophores that are inherently dissymmetric and cannot be subdivided into subgroups, such as the helicenes, and where neither the coupled-oscillator model nor the sector rules are typically applicable [34]. In other instances, they agreed satisfactorily with the exciton model [35] or with the sector rules [36]. As we shall see in the following chapters of this volume, the modern interpretation of electronic optical activity is based on a combined application of traditional models and of *ab initio* calculations.

Due to particular experimental challenges and some theoretical hurdles, the study of *vibrational optical activity* (VOA) has followed a path of its own [37–42]. Besides *vibrational* CD, *circular differential Raman scattering* (ROA) has proven to be a method of great potential. An interesting and particular aspect of VOA is the possibility to measure and interpret optical activity induced by isotopic substitution. The computation of vibrational rotatory strengths is not trivial, as for the calculation of the magnetic transition moments, *non-Born–Oppenheimer vibronic contributions* must be considered [37, 38].

With the advent of quantum mechanics, it was quickly recognized that the existence of mirror-image forms for one and the same molecule raises some fundamental questions. If only electrostatic interactions exist between the electrons and nuclei within an isolated molecule, if only electromagnetic forces manifest themselves, then the molecular Schrödinger equation must be *invariant* with respect to *spatial reflection*—that is, with respect to the *parity operation*. It is therefore not conceivable that solutions of such a parity-even equation may be chiral. For chiral molecules, the enantiomeric solution must be equally admissible. In other words, a chiral molecular wavefunction cannot describe a stationary state. This situation, called *Hund's paradox* [43], is actually not of great practical significance. The higher and broader the potential barrier between the potential energy minima of the enantiomers, the slower the inversion frequency. While H_2O_2, with a very low barrier, inverts within about 10^{-12} s, alanine, with a very high barrier needs on the order of 1000 years. A high inversion barrier implies quasi-stability. However, the

question is not always trivial, why under given circumstances a particular chiral molecule occurs, and not its enantiomer.

Within the last decades, interest has focused on the question as to what extent the influence of the *parity-violating weak nuclear forces* on atoms and molecules is detectable. Weak optical activity is indeed measurable in heavy atoms [44]. These parity-violating forces should also affect the spectroscopy and dynamics of molecules [45–47]. They might have played a role in preferentially stabilizing one enantiomer as opposed to the other in evolutionary processes, such as the development of *biological homochirality*.

1.2. ELEMENTS OF THE SEMICLASSICAL THEORY

After the foregoing initial historic excursion, we shall now attempt to briefly summarize the basic elements of the semiclassical theory of the interaction of light with molecules.

1.2.1. The Classical Description of Light

For a medium without free charges and without free currents, Maxwell's equations, in the system of Gauss–CGS units, are written as

$$\boldsymbol{\nabla} \times \mathbf{E} = -(1/c)(\partial/\partial t)\mathbf{B}, \qquad \boldsymbol{\nabla} \cdot \mathbf{B} = 0, \tag{1.3a}$$

$$\boldsymbol{\nabla} \times \mathbf{H} = (1/c)(\partial/\partial t)\mathbf{D}, \qquad \boldsymbol{\nabla} \cdot \mathbf{D} = 0, \tag{1.3b}$$

with

$$\mathbf{D} = \mathbf{E} + 4\pi\mathbf{P} \qquad \text{and} \qquad \mathbf{B} = \mathbf{H} + 4\pi\mathbf{M}, \tag{1.4a,b}$$

where $\mathbf{E}$ denotes the electric field, $\mathbf{D}$ the electric displacement, $\mathbf{H}$ the magnetic field, and $\mathbf{B}$ the magnetic induction. Inserting Eqs. (1.4a,b) into (1.3a,b), taking the curl of (1.3a,b) followed by some elementary vector manipulations, and considering the fact that $\boldsymbol{\nabla} \cdot \mathbf{E} = 0$ and that $\boldsymbol{\nabla} \cdot \mathbf{H} = 0$, one obtains the wave equation for an electrically and magnetically *polarizable* medium:

$$\Delta\mathbf{E} = (1/c^2)(\partial^2/\partial t^2)(\mathbf{E} + 4\pi\mathbf{P}) + (4\pi/c)(\partial/\partial \mathrm{t})(\boldsymbol{\nabla} \times \mathbf{M}), \tag{1.5a}$$

$$\Delta\mathbf{H} = (1/c^2)(\partial^2/\partial t^2)(\mathbf{H} + 4\pi\mathbf{M}) - (4\pi/c)(\partial/\partial \mathrm{t})(\boldsymbol{\nabla} \times \mathbf{P}); \tag{1.5b}$$

the vector quantities $\mathbf{P}$ and $\mathbf{M}$ represent the *induced electric* and *magnetic polarization*, respectively. We now define a plane wave, propagating in z direction and oscillating in x, y directions, as a solution of the above equations:

$$\mathbf{E}(z,t) = \mathbf{E}_{-}(z,t) + \mathbf{E}_{+}(z,t), \tag{1.6a}$$

$$\mathbf{H}(z,t) = \mathbf{H}_{-}(z,t) + \mathbf{H}_{+}(z,t). \tag{1.6b}$$

For the x components, say, of the field quantities we write in more detail:

$$E_{\mathrm{x}^-} = E^0_{\mathrm{x}^-} \exp(-i\varphi_{\mathrm{x}}), \qquad E_{\mathrm{x}+} = E^0_{\mathrm{x}+} \exp(+i\varphi_{\mathrm{x}}), \tag{1.7a}$$

$$H_{\mathrm{x}^-} = H^0_{\mathrm{x}^-} \exp(-i\varphi_{\mathrm{y}}), \qquad H_{\mathrm{x}+} = H^0_{\mathrm{x}+} \exp(+i\varphi_{\mathrm{y}}), \tag{1.7b}$$

with

$$\varphi_{\mathrm{x}} = \omega(t - (n_{\mathrm{x}}/c)z), \qquad \varphi_{\mathrm{y}} = \omega(t - (n_{\mathrm{y}}/c)z). \tag{1.8}$$

The quantities n_x and n_y are defined as the *index of refraction* for a wave with electric field oscillating in x and y directions, respectively. In what follows, we shall assume the medium in which the wave propagates to be isotropic, and thus $n_x = n_y \equiv n$. We now establish a relationship between the index of refraction n, which is optically measurable, and the quantities **P** and **M**, which represent material quantities that may be traced back to molecular susceptibilities. The particular property of an *optically active* medium is that **P** depends not only on **E**, but also on **B**; and **M** depends not only on **B**, but also on **E**. We assume the molecules in the medium to interact with the incident vacuum field, for which $\mathbf{B} = \mathbf{H}$. Considering the x components of the electromagnetic vectors, the *constitutive relations* thus read:

$$P_{x^-} = \alpha E_{x^-} + \beta i H_{x^-} \qquad \text{and} \qquad M_{x^-} = -\beta i E_{x^-} + \gamma H_{x^-}. \tag{1.9a,b}$$

The quantities α, β, and γ represent the isotropically averaged *electric polarizability* tensor, the *optical activity* tensor, and the *magnetic susceptibility* tensor, respectively. These quantities are defined to be real and will be derived in Section 1.2.3. The imaginary unit is denoted by i. Introducing (1.9a,b) and (1.7a,b) into (1.5a,b) and making use of (1.3a,b), we find, after some straightforward but rather tedious algebra, the following relations between E_{x^-} and H_{x^-}:

$$E_{x^-}(n^2 - \varepsilon\mu - 16\pi^2\beta^2) - H_{x^-}(8\pi i\beta\mu) = 0, \tag{1.10a}$$

$$E_{x^-}(8\pi i\beta\varepsilon) + H_{x^-}(n^2 - \varepsilon\mu - 16\pi^2\beta^2) = 0. \tag{1.10b}$$

In these relations we have introduced the *dielectric constant*, defined as $\varepsilon = 1 + 4\pi\alpha$, and the *magnetic permeability*, $\mu = 1 + 4\pi\gamma$. Similar equations of course also hold for the y components. The above two coupled equations for E_{x^-} and H_{x^-} have nontrivial solutions if the determinant of the coefficients (in brackets) vanishes. This condition then gives us an equation for the refractive index n in terms of the electromagnetic quantities:

$$n^2 - \varepsilon\mu - 16\pi^2\beta^2 = \pm 8\pi\beta\sqrt{\varepsilon\mu}. \tag{1.11a}$$

Therefrom follows

$$n = \sqrt{\varepsilon\mu} \pm 4\pi\beta. \tag{1.11b}$$

Introducing these solutions into (1.10a,b), we find

$$\frac{E_{x^-}}{H_{x^-}} = \pm i\frac{\sqrt{\mu}}{\sqrt{\varepsilon}}. \tag{1.12}$$

Such conditions can only be obeyed by *circularly polarized light*, as indicated here for the *left* (L) and the *right* (R) circular polarizations (c.p.):

$$\mathbf{E}_L = (e_0/2)((+\mathbf{i} + i\mathbf{j})\exp(-i\varphi) + (+\mathbf{i} - i\mathbf{j})\exp(+i\varphi)), \tag{1.13a}$$

$$\mathbf{H}_L = (h_0/2)((-i\mathbf{i} + \mathbf{j})\exp(-i\varphi) + (+i\mathbf{i} + \mathbf{j})\exp(+i\varphi)), \tag{1.13b}$$

$$\mathbf{E}_R = (e_0/2)((+\mathbf{i} - i\mathbf{j})\exp(-i\varphi) + (+\mathbf{i} + i\mathbf{j})\exp(+i\varphi)), \tag{1.14a}$$

$$\mathbf{H}_R = (h_0/2)((+i\mathbf{i} + \mathbf{j})\exp(-i\varphi) + (-i\mathbf{i} + \mathbf{j})\exp(+i\varphi)), \tag{1.14b}$$

where **i** and **j** represent unit vectors in x and y direction, respectively. From the above equations, we notice that the (+) sign in (1.12) pertains to a *left* c.p. wave, while the (−) sign refers to a *right* c.p. wave. Going back to (1.11b), we may then find

$$n_{\mathrm{L}} = \sqrt{\varepsilon\mu} + 4\pi\beta, \qquad n_{\mathrm{R}} = \sqrt{\varepsilon\mu} - 4\pi\beta; \tag{1.15a}$$

and for an *achiral racemic* mixture

$$n = (1/2)(n_{\mathrm{L}} + n_{\mathrm{R}}) = \sqrt{\varepsilon\mu}. \tag{1.15b}$$

These relations were already derived in 1937 by Condon [48, 49]. The quantities e_0 and h_0 are constant field amplitudes fulfilling the condition $\sqrt{\varepsilon}e_0 = \sqrt{\mu}h_0$.

1.2.2. Elements of Perturbation Theory

We start with the simplest assumptions, considering a molecule to be initially in its ground state $\Psi_a^{(0)}$ $(\mathbf{r}, t)$. Under the influence of the radiation field, we subsequently describe the system by the wavefunction:

$$\Psi_a(\mathbf{r}, t) = \Psi_a^{(0)} + \lambda\Psi_a^{(1)} + \lambda^2\Psi_a^{(2)} + \cdots. \tag{1.16}$$

The effect of the radiation is represented as a *harmonic perturbation*, the exact form of which will be treated in detail in the next section. However, for the sake of generality, we consider the incident light to contain more than one, say two, frequencies, ω_1 and ω_2:

$$\begin{aligned} \mathcal{H} &= \mathcal{H}^{(0)} + \lambda\mathcal{H}^{(1)}; \\ \mathcal{H}^{(1)}(\mathbf{r}, t) &= {}^1\mathcal{H}^-(\mathbf{r})\exp(-i\omega_1 t) + {}^1\mathcal{H}^+(\mathbf{r})\exp(+i\omega_1 t) \\ &\quad + {}^2\mathcal{H}^-(\mathbf{r})\exp(-i\omega_2 t) + {}^2\mathcal{H}^+(\mathbf{r})\exp(+i\omega_2 t). \end{aligned} \tag{1.17}$$

Introducing (1.16) into the time-dependent Schrödinger equation,

$$(\mathcal{H}^{(0)} + \lambda\mathcal{H}^{(1)})\Psi = i\hbar\partial\Psi/\partial t,$$

and equating coefficients of like powers of λ leads to an infinite sequence of coupled equations:

$$\begin{aligned} (\mathcal{H}^{(0)} - i\hbar(\partial/\partial t))\Psi_a^{(0)} &= 0, \\ (\mathcal{H}^{(0)} - i\hbar(\partial/\partial t))\Psi^{(1)} &= -\mathcal{H}^{(1)}\Psi_a^{(0)}, \\ (\mathcal{H}^{(0)} - i\hbar(\partial/\partial t))\Psi^{(2)} &= -\mathcal{H}^{(1)}\Psi_a^{(1)}, \\ &\ldots, \text{etc.} \end{aligned} \tag{1.18}$$

Considering only *steady-state solutions* [50, 51] for the hamiltonian (1.17), the first-order term in (1.16) will oscillate with the basic frequencies ω_1 and ω_2, and the higher-order terms will oscillate as sums or differences thereof. In this sense, one then may write

$$\Psi_a{}^{(0)}(\mathbf{r}, t) = \psi_a{}^{(0)}(\mathbf{r})\exp(-i\omega_a t), \tag{1.19a}$$

$$\Psi_a{}^{(1)}(\mathbf{r},t) = \{{}^1\psi_a{}^{(1)}{}_{(-1)} \exp(-i\omega_1 t) + {}^1\psi_a{}^{(1)}{}_{(+1)} \exp(+i\omega_1 t) + {}^2\psi_a{}^{(1)}{}_{(-1)} \exp(-i\omega_2 t) + {}^2\psi_a{}^{(1)}{}_{(+1)} \exp(+i\omega_2 t)\} \exp(-i\omega_a t). \quad (1.19b)$$

The functions denoted by ψ depend only on space variables; for instance,

$${}^1\psi_a{}^{(1)}{}_{(-1)} \equiv {}^1\psi_a{}^{(1)}{}_{(-1)}(\mathbf{r}), \text{etc.}$$

In the next higher order of the expansion we have

$$\begin{aligned}
&\Psi_a{}^{(2)}(\mathbf{r},t) = \\
&\{{}^1\psi_a{}^{(2)}{}_{(-2)} \exp(-i2\omega_1 t) + {}^1\psi_a{}^{(2)}{}_{(+0)} + {}^1\psi_a{}^{(2)}{}_{(+2)} \exp(+i2\omega_1 t) \\
&+ {}^2\psi_a{}^{(2)}{}_{(-2)} \exp(-i2\omega_2 t) + {}^2\psi_a{}^{(2)}{}_{(+0)} + {}^2\psi_a{}^{(2)}{}_{(+2)} \exp(+i2\omega_2 t) \\
&+ {}^{1,2}\psi_a{}^{(2)}{}_{(-1,-1)} \exp(-i(\omega_1+\omega_2)t) + {}^{1,2}\psi_a{}^{(2)}{}_{(-1,+1)} \exp(-i(\omega_1-\omega_2)t) \\
&+ {}^{1,2}\psi_a{}^{(2)}{}_{(+1,-1)} \exp(+i(\omega_1-\omega_2)t) + {}^{1,2}\psi_a{}^{(2)}{}_{(+1,+1)} \exp(+i(\omega_1+\omega_2)t)\} \exp(-i\omega_a t).
\end{aligned} \quad (1.19c)$$

In order to assess the quantities appearing in (1.19b,c), we proceed according to the well-known method of variation of constants, expanding in terms of eigenfunctions of $\mathcal{H}^{(0)}$:

$$\begin{aligned}
\Psi_a{}^{(0)}(\mathbf{r},t) &= \sum_k a_k{}^{(0)}(t)\psi_k{}^{(0)}(\mathbf{r}) \exp(-i\omega_k t), \\
\Psi_a{}^{(1)}(\mathbf{r},t) &= \sum_k a_k{}^{(1)}(t)\psi_k{}^{(0)}(\mathbf{r}) \exp(-i\omega_k t), \\
\Psi_a{}^{(2)}(\mathbf{r},t) &= \sum_k a_k{}^{(2)}(t)\psi_k{}^{(0)}(\mathbf{r}) \exp(-i\omega_k t), \\
&\ldots, \text{etc.}
\end{aligned} \quad (1.20)$$

Introducing (1.20) into (1.18), setting $a_k{}^{(0)} = \delta_{ka}$, the coefficients $a_k{}^{(1)}, a_k{}^{(2)}, \ldots$, are determined, according to elementary time-dependent perturbation theory, by successive integrations over the time t. However, we perform *indefinite integrations*, setting the constants of integration equal to zero. Thereby we avoid incipient terms and keep only *steady-state terms*. The expressions so obtained are compared with (1.19b,c) equating coefficients of like powers of exp (it).

In this way we find

$${}^1\psi^{(1)}_{a(-1)} = -\sum_k \frac{{}^1\mathcal{H}^-_{ka}}{\hbar(\omega_{ka}-\omega_1)}\psi^{(0)}_k, \quad (1.21a)$$

$${}^1\psi^{(1)}_{a(+1)} = -\sum_k \frac{{}^1\mathcal{H}^+_{ka}}{\hbar(\omega_{ka}+\omega_1)}\psi^{(0)}_k; \quad (1.21b)$$

and to second order we obtain

$${}^1\psi^{(2)}_{a(-2)} = \sum_k \sum_l \frac{{}^1\mathcal{H}^-_{la}\ {}^1\mathcal{H}^-_{kl}}{\hbar^2(\omega_{la}-\omega_1)(\omega_{ka}-2\omega_1)}\psi^{(0)}_k, \quad (1.22a)$$

$$ {}^1\psi^{(2)}_{a(0)} = \sum_k \sum_l \left\{ \frac{{}^1\mathcal{H}^+_{la}\,{}^1\mathcal{H}^-_{kl}}{\hbar^2(\omega_{la}+\omega_1)\omega_{ka}} + \frac{{}^1\mathcal{H}^-_{la}\,{}^1\mathcal{H}^+_{kl}}{\hbar^2(\omega_{la}-\omega_1)\omega_{ka}} \right\} \psi^{(0)}_k, \tag{1.22b} $$

$$ {}^1\psi^{(2)}_{a(+2)} = \sum_k \sum_l \frac{{}^1\mathcal{H}^+_{la}\,{}^1\mathcal{H}^+_{kl}}{\hbar^2(\omega_{la}+\omega_1)(\omega_{ka}+2\omega_1)} \psi^{(0)}_k. \tag{1.22c} $$

with corresponding additional expressions for the frequency ω_2 and for the combinations of ω_1 and ω_2.

The reader will notice that until now we have assumed the molecule to be initially in the state ${\Psi_a}^{(0)}(\mathbf{r},t) \equiv |a\rangle$ with certainty. However, the initial condition may be that the molecule is in state $|a\rangle$ only with a probability $p_a < 1$ and that it may also be in other states $|k\rangle$ with probabilities p_k such that the sum of all probabilities $\sum_k p_k = 1$. To describe such a situation, it is convenient to introduce the *density operator*, or *density matrix* ρ:

$$ \rho = \sum_k p_k |k\rangle\langle k|. \tag{1.23a} $$

It is then relatively straightforward to show, in analogy to (1.18), that the time evolution is given by the commutator $i\hbar(\partial\rho/\partial t) = [\mathcal{H}, \rho]$, to which a *damping, or relaxation, term* may be added. Thereby we may describe, besides damping due to absorption and induced emission, also incoherent effects, such as spontaneous emission and population changes induced by collisions and thermal fluctuations [52, 53]:

$$ i\hbar(\partial\rho/\partial t) = [(\mathcal{H}^{(0)} + \lambda\mathcal{H}^{(1)}), \rho] + i\hbar(\partial\rho/\partial t)_{\text{relax}}. \tag{1.23b} $$

The influence of damping will, however, not be further pursued here. We will consider radiation-induced absorption/emission processes in forthcoming sections.

1.2.3. The Interaction with the Radiation

The Hamiltonian for the interaction of a molecule with the electromagnetic radiation field does not explicitly contain the electric and magnetic light vectors, but rather the *vector potential* $\mathbf{A}$. The relation to the field vectors is (in the Coulomb gauge) given by

$$ \mathbf{E} = -(1/\mathrm{c})\partial\mathbf{A}/\partial t, \qquad \mathbf{B} = \boldsymbol{\nabla} \times \mathbf{A}. \tag{1.24} $$

For a single particle (electron) and disregarding electrostatic potentials, the Hamiltonian reads

$$ \mathcal{H} = (1/2m_e)(\mathbf{p} - (e/c)\mathbf{A}(\mathbf{r},t))^2. \tag{1.25a} $$

Multiplying out this expression and taking into account the fact that $\mathbf{p}\cdot\mathbf{A} = 0$, because of the *tansversality condition*, we obtain

$$ \mathcal{H} = (1/2m_e)(\mathbf{p}^2 - (2e/c)\mathbf{A}\cdot\mathbf{p} + (e^2/c^2)\mathbf{A}^2). \tag{1.25b} $$

The $\mathbf{A}^2$ term may be, for our purposes, conditionally neglected [54, 55], so that the effective interaction becomes (e, the electronic charge, m_e the mass of the electron)

$$\mathcal{H}_{\text{int}} = (-e/m_e c)\mathbf{A} \cdot \mathbf{p}. \tag{1.26}$$

We now assume $\mathbf{A}(\mathbf{r}, t)$ to be of the form

$$\mathbf{A}(\mathbf{r}, t) = \mathbf{A}^0{}_- \exp(-i\varphi) + \mathbf{A}^0{}_+ \exp(+i\varphi); \tag{1.27a}$$

with $\varphi = (\omega t - kz), k = 2\pi/\lambda$, and λ is the wavelength. Because the second term in (1.27a) is simply the complex conjugate of the first, we focus on the $\mathbf{A}_-$ term only. Thus,

$$\mathbf{A}^0{}_- \exp(-i\varphi) = \mathbf{i}A^0{}_{x^-} \exp(-i\varphi) + \mathbf{j}A^0{}_{y^-} \exp(-i\varphi). \tag{1.27b}$$

From (1.24) we obtain

$$\mathbf{E}^0{}_- \exp(-i\varphi) = \mathbf{i}(i\omega/c)A^0{}_{x^-} \exp(-i\varphi) + \mathbf{j}(i\omega/c)A^0{}_{y^-} \exp(-i\varphi), \tag{1.28a}$$

$$\mathbf{B}^0{}_- \exp(-i\varphi) = \mathbf{i}(-ik)A^0{}_{y^-} \exp(-i\varphi) + \mathbf{j}(+ik)A^0{}_{x^-} \exp(-i\varphi). \tag{1.28b}$$

We keep for convenience the time t constant, and we assume the wavelength λ to be much larger than z within the region where the particle is located (dimension of the molecule). This *long- wavelength approximation* allows us to expand exp $(-ikz)$ into a fast converging series [4]:

$$\mathcal{H}_{\text{int}} = (-e/m_e c)\mathbf{A}^0{}_- \cdot (\mathbf{p} + ikz\,\mathbf{p} - \ldots) = \mathcal{H}_{\text{int.1}} + \mathcal{H}_{\text{int.2}}, \tag{1.29a}$$

$$\mathcal{H}_{\text{int.1}} = (-e/m_e c)(A^0{}_{x^-} p_x + A^0{}_{y^-} p_y), \tag{1.29b}$$

$$\mathcal{H}_{\text{int.2}} = (-eik/m_e c)(A^0{}_{x^-} z p_x + A^0{}_{y^-} z p_y). \tag{1.29c}$$

In (1.29c) we make use of the identity,

$$zp_x = \frac{1}{2}(zp_x + xp_z) + \frac{1}{2}(zp_x - xp_z), \tag{1.30a}$$

$$zp_y = \frac{1}{2}(zp_y + yp_z) + \frac{1}{2}(zp_y - yp_z), \tag{1.30b}$$

and consider the following equalities, derivable from commutation relations:

$$\langle a|p_x|b\rangle = im_e\omega_{ab}\langle a|x|b\rangle, \tag{1.31a}$$

$$\langle a|zp_x + xp_z|b\rangle = im_e\omega_{ab}\langle a|zx|b\rangle; \tag{1.31b}$$

with $|a\rangle$, $|b\rangle$, being eigenfunctions of $\mathcal{H}^{(0)}$, $\omega_{ab} = \omega_a - \omega_b$.

Furthermore, we notice that $(zp_x - xp_z) = l_y$, $(zp_y - yp_z) = -l_x$, the components of the *angular momentum operator*.

Combining (1.31a) with (1.29b) we write

$$\langle a|\mathcal{H}_{\text{int.1}}|b\rangle = (-ei\omega_{ab}/c)(A^0{}_{x^-}\langle a|x|b\rangle + A^0{}_{y^-}\langle a|y|b\rangle). \tag{1.32a}$$

Comparing with (1.28a), we obtain the *electric field–electric dipole interaction*:

$$\langle a|\mathcal{H}_{\text{int.1}}|b\rangle = (-e)(E^0{}_{x^-}\langle a|x|b\rangle + E^0{}_{y^-}\langle a|y|b\rangle). \tag{1.32b}$$

Proceeding similarly, combining (1.31b) with (1.29c), we find

$$\begin{aligned}\langle a|\mathcal{H}_{\text{int.2,1}}|b\rangle &= (ek\omega_{ab}/2c)(A^0{}_{x^-}\langle a|zx|b\rangle + A^0{}_{y^-}\langle a|zy|b\rangle)\\ &= (-e/2)((\partial E_{x^-}(z)/\partial z)_0\langle a|zx|b\rangle + (\partial E_{y^-}(z)/\partial z)_0\langle a|zy|b\rangle),\end{aligned} \tag{1.33}$$

which represents the *electric field gradient–electric quadrupole interaction*. Finally, we derive the *magnetic dipole–magnetic field (magnetic induction) interaction*. One also starts from (1.29c). We now focus on the second terms on the right-hand side of Eqs. (1.30a,b), which, as already mentioned above, represent components of the angular momentum operator. We recall that the magnetic induction **B** is related to the vector potential **A** as shown in (1.24). We thus obtain

$$\begin{aligned}\langle a|\mathcal{H}_{\text{int.2,2}}|b\rangle &= (-eik/2m_ec)(A^0{}_{x^-}\langle a|l_y|b\rangle - A^0{}_{y^-}\langle a|l_x|b\rangle)\\ &= (-e/2m_ec)(B_{x^-}l_x + B_{y^-}l_y).\end{aligned} \tag{1.34}$$

Generalizing to an arbitrary coordinate system and reintroducing the time dependence, we may write in general the following:

$$\mathcal{H}_{\text{int.}} \equiv \mathcal{H}^{(1)}(\mathbf{r}=0;t) = -\boldsymbol{\mu}\cdot\mathbf{E}(t) - \mathbf{m}\cdot\mathbf{B}(t) - \mathbf{Q}:\boldsymbol{\nabla}\mathbf{E}(t) + \cdots. \tag{1.35}$$

Here the field quantities $\mathbf{E}(t)$ and $\mathbf{B}(t)$ no longer depend on spatial variables. They adopt spatially fixed values at the *origin of the multipole expansion*:

$$\mathbf{E}(t) = \mathbf{E}^0{}_-\exp(-i\omega t) + \mathbf{E}^0{}_+\exp(+i\omega t); \tag{1.36a}$$

$$\mathbf{B}(t) = \mathbf{B}^0{}_-\exp(-i\omega t) + \mathbf{B}^0{}_+\exp(+i\omega t). \tag{1.36b}$$

The electric field gradient is similarly understood to be taken at the same origin: $\boldsymbol{\nabla}\mathbf{E} \equiv \boldsymbol{\nabla}_\mathbf{0}\mathbf{E}$. From now on, however, we simplify our notation: $\mathbf{E}^0{}_- \equiv \mathbf{E}_-, \mathbf{B}^0{}_- \equiv \mathbf{B}_-$, and so on. The *electric dipole operator* $\boldsymbol{\mu}$ and the *magnetic dipole operator* $\mathbf{m}$ are, respectively, given by

$$\boldsymbol{\mu} = e\mathbf{r}, \qquad \mathbf{m} = (e/2m_ec)\mathbf{l}, \tag{1.37}$$

where $\mathbf{r}$ designates the position operator and $\mathbf{l}$ represents the angular momentum operator. The *electric quadrupole term* may be written $(e/2)$ $(\mathbf{rr}:\boldsymbol{\nabla}\mathbf{E})$ or, equivalently,

$$(e/2)\mathbf{r}\cdot(\mathbf{r}\cdot\boldsymbol{\nabla})\mathbf{E}. \tag{1.38}$$

Before proceeding to the detailed study of optical phenomena, we briefly return to the $\mathbf{A}^2$ term that we had neglected. This term is important in very high magnetic fields when diamagnetic effects become strong. It does not appear to significantly alter the multipole expansion as given in (1.35), which is generally accepted as a basis for the interpretation of optical phenomena in atoms and molecules. However, the problem is not trivial, and the interested reader is referred to the pertinent literature [54, 55].

1.2.4. The Induced Electric Polarization

Phenomena such as light scattering and refraction [39, 56, 57] depend mainly on the light-induced electric polarization **P**, as already indicated in Section 1.2.1. Here it is defined as a *macroscopic quantity*, with the dimensions of a dipole moment per unit volume. It may be considered as the average contribution of an individual molecule times the concentration of these molecules in the sample. Our immediate aim, therefore, is to calculate the radiation-induced electric dipole moment in a single molecule in a particular state, usually assumed to be the ground state a. We will denote this *molecular quantity* by $\mathbf{p}_a{}^{(n)}(\ldots)$. The index (n) stands for the order of the effect, and inside the parentheses $(\ldots)$ we indicate the optical process that gives rise to that particular contribution to the polarization. We may in general write [see Eq. (1.16) in Section 1.2.2]

$$\mathbf{p}_a \equiv \mathbf{p} = \langle \Psi_a(\mathbf{r},t)\ |\boldsymbol{\mu}|\ \Psi_a(\mathbf{r},t)\rangle. \tag{1.39}$$

The wave function in (1.39) is calculated as described in Eqs. (2.17)–(2.20). For ordinary Rayleigh scattering we thus find

$$\begin{aligned}\mathbf{p}^{(1)}(\omega;-\omega) &= \langle \psi_a{}^{(0)}|\boldsymbol{\mu}|\psi_a{}^{(1)}_{(-1)}\rangle + \langle \psi_a{}^{(1)}_{(+1)}|\boldsymbol{\mu}|\psi_a{}^{(0)}\rangle \\ &= \sum_k \left\{ \frac{\langle a|\boldsymbol{\mu}|k\rangle(\langle k|\boldsymbol{\mu}|a\rangle \cdot \mathbf{E}_-)}{\hbar(\omega_{ka}-\omega)} + \frac{(\langle a|\boldsymbol{\mu}|k\rangle \cdot \mathbf{E}_-)\langle k|\boldsymbol{\mu}|a\rangle}{\hbar(\omega_{ka}+\omega)} \right\}. \end{aligned} \tag{1.40}$$

The quantity $\mathbf{p}^{(1)}(\omega;-\omega)$ is to be read as follows: It is the first-order electric dipole response of the molecule to an incoming photon of frequency $(-\omega)$, giving rise to a scattered photon of frequency $(+\omega)$. The negative frequency $(-\omega)$ is to be formally interpreted as the loss of a photon of energy $\hbar\omega$ by the radiation field and the concomitant uptake by the molecule. Correspondingly, $(+\omega)$ means the reverse. The choice of the absolute signs is a matter of definition; the relative signs are to be considered.

A general classification of linear and nonlinear effects is represented in Figure 1.1. The reader will immediately recognize that the nonlinear, higher-order contributions lead to a growing variety of quantum mechanical terms, especially if several frequencies are involved. Assuming pure electric dipole interactions of the molecule with the radiation field, we find for *sum frequency generation* (SFG), for instance, the following:

$$\mathbf{p}^{(2)}(\omega_1+\omega_2;-\omega_1,-\omega_2) = \sum_k \sum_l \frac{\langle a|\boldsymbol{\mu}|l\rangle(\langle l|\boldsymbol{\mu}|k\rangle \cdot {}^2\mathbf{E}_-)(\langle k|\boldsymbol{\mu}|a\rangle \cdot {}^1\mathbf{E}_-)}{\hbar^2(\omega_{la}-\omega_1-\omega_2)(\omega_{ka}-\omega_1)} + \cdots \tag{1.41}$$

plus five similar terms. Figure 1.2 shows the $3! = 6$ possible permutations. As a next example, we consider a *Raman-type four-wave mixing* effect with incident frequencies $-\omega_1, +\omega_2$, and $-\omega_3$ and resulting frequency $(+\omega_1-\omega_2+\omega_3)$:

$$\begin{aligned}&\mathbf{p}^{(3)}(\omega_1-\omega_2+\omega_3;-\omega_1,+\omega_2,-\omega_3) \\ &\quad= \sum_k \sum_l \sum_m \frac{\langle a|\boldsymbol{\mu}|m\rangle(\langle m|\boldsymbol{\mu}|l\rangle \cdot {}^3\mathbf{E}_-)(\langle l|\boldsymbol{\mu}|k\rangle \cdot {}^2\mathbf{E}_+)(\langle k|\boldsymbol{\mu}|a\rangle \cdot {}^1\mathbf{E}_-)}{\hbar^3(\omega_{ma}-\omega_1+\omega_2-\omega_3)(\omega_{la}-\omega_1+\omega_2)(\omega_{ka}-\omega_1)} + \cdots. \end{aligned} \tag{1.42}$$

There are 23 additional similar terms in (1.42), $4! = 24$ in all. Here we have limited ourselves exclusively to considering *electric dipole interactions* with the radiation field.

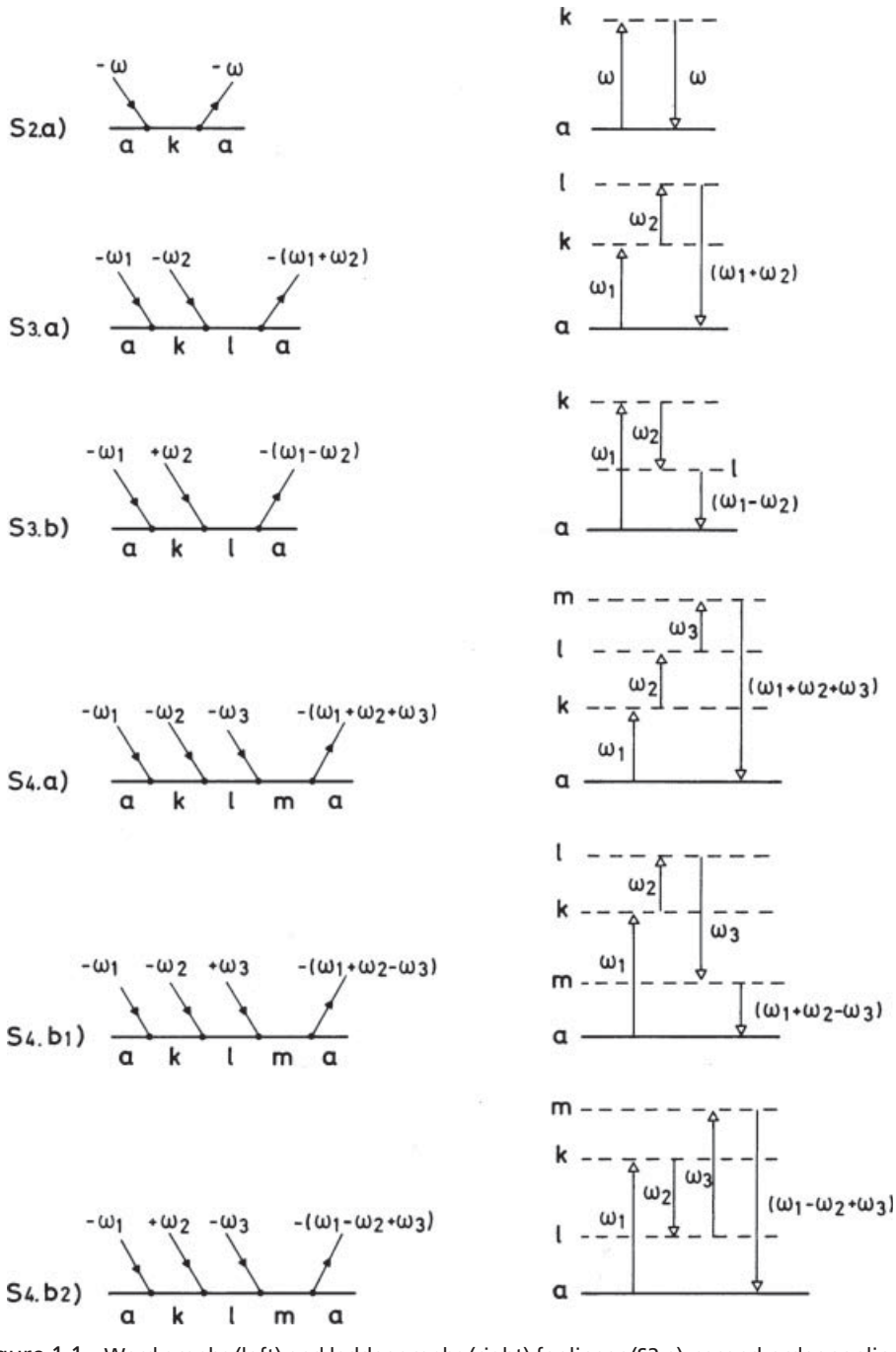

Figure 1.1. Ward graphs (left) and ladder graphs (right) for linear (S2.a), second-order nonlinear (S3.a, S3.b), and third-order nonlinear (S4.a, S4.b1, S4.b2) elastic scattering (S) processes. The broken horizontal lines in the ladder graphs represent virtual, nonstationary states of the molecular system. (Reproduced with permission, from reference 57.)

$$\mathbf{p}^{(2)}(\omega_1+\omega_2;\ -\omega_1,\ -\omega_2) =$$

$$\sum_k \sum_\ell \frac{\mu_{a\ell}\,{}^2\mathcal{H}^-_{\ell k}\,{}^1\mathcal{H}^-_{ka}}{\hbar^2(\omega_{\ell a}-\omega_1-\omega_2)(\omega_{ka}-\omega_1)}$$

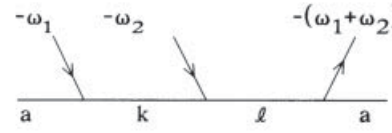

$$+\sum_k \sum_\ell \frac{\mu_{a\ell}\,{}^1\mathcal{H}^-_{\ell k}\,{}^2\mathcal{H}^-_{ka}}{\hbar^2(\omega_{\ell a}-\omega_1-\omega_2)(\omega_{ka}-\omega_2)}$$

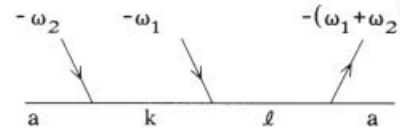

$$+\sum_k \sum_\ell \frac{{}^2\mathcal{H}^-_{a\ell}\,\mu_{\ell k}\,{}^1\mathcal{H}^-_{ka}}{\hbar^2(\omega_{\ell a}+\omega_2)(\omega_{ka}-\omega_1)}$$

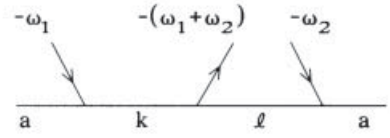

$$+\sum_k \sum_\ell \frac{{}^1\mathcal{H}^-_{a\ell}\,\mu_{\ell k}\,{}^2\mathcal{H}^-_{ka}}{\hbar^2(\omega_{\ell a}+\omega_1)(\omega_{ka}-\omega_2)}$$

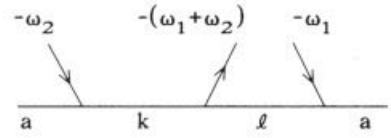

$$+\sum_k \sum_\ell \frac{{}^2\mathcal{H}^-_{a\ell}\,{}^1\mathcal{H}^-_{\ell k}\,\mu_{ka}}{\hbar^2(\omega_{\ell a}+\omega_2)(\omega_{ka}+\omega_1+\omega_2)}$$

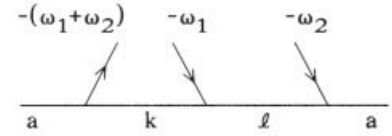

$$+\sum_k \sum_\ell \frac{{}^1\mathcal{H}^-_{a\ell}\,{}^2\mathcal{H}^-_{\ell k}\,\mu_{ka}}{\hbar^2(\omega_{\ell a}+\omega_1)(\omega_{ka}+\omega_1+\omega_2)}$$

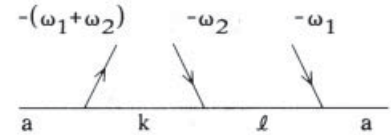

Figure 1.2. To every permutation of vertices in a graph corresponds a quantum mechanical term. Here is the example of sum frequency generation. (Reproduced with permission, from reference 57.)

1.2.5. The Evaluation of Rotational Averages

Optical measurements are often performed on media in which the individual molecules are randomly oriented, such as in liquids or gases. This requires the orientation-dependent quantities that we have derived above to be spatially averaged. Mathematically, this corresponds to the averaging of Cartesian tensors [57–59]. While the energy denominators in (1.40)–(1.42) are scalar quantities, independent of orientational effects, the numerators are, in general, tensors of rank $(n+1)$ for a polarization $\mathbf{p}^{(n)}(\ldots)$. We will briefly exemplify this averaging procedure with the expressions obtained in the previous section, starting with (1.40). We formally define $\langle a|\boldsymbol{\mu}|k\rangle \equiv \boldsymbol{\mu}_{ak}$ and $\langle k|\boldsymbol{\mu}|a\rangle \equiv \boldsymbol{\mu}_{ka}$.

The average is

$$\langle \boldsymbol{\mu}_{ak}(\boldsymbol{\mu}_{ka}\cdot\mathbf{E}_-)\rangle = (1/3)(\boldsymbol{\mu}_{ak}\cdot\boldsymbol{\mu}_{ka})\mathbf{E}_- . \tag{1.43a}$$

The spatially averaged induced polarization $\langle \mathbf{p}^{(1)}(\omega;-\omega)\rangle$ may thus be written in the form

$$\langle \mathbf{p}^{(1)}(\omega;-\omega)\rangle = \chi^{(1)}(\omega;-\omega)\mathbf{E}_- , \tag{1.43b}$$

where $\chi^{(1)}(\omega;-\omega)$ is a *scalar susceptibility* calculated in the *molecular reference frame*, and $\mathbf{E}_-$ is a *vectorial field part* defined in the *laboratory frame*. The reader will recognize that $\chi^{(1)}(\omega;-\omega)$ is just the averaged molecular *electric polarizability*, and that $N\chi^{(1)}(\omega;-\omega)=\alpha$, where N is the number of molecules per unit volume, and α represents the *macroscopic electric polarizability* [see Section 1.2.1, Eq. (1.9a)].

We presently proceed to the second order, to sum frequency generation, represented by (1.41). We formally define $\langle a|\boldsymbol{\mu}|l\rangle \equiv \boldsymbol{\mu}_{al}$, and so on. The average of the numerator is

$$\langle \boldsymbol{\mu}_{al}(\boldsymbol{\mu}_{lk}\cdot{}^2\mathbf{E}_-)(\boldsymbol{\mu}_{ka}\cdot{}^1\mathbf{E}_-)\rangle = (1/6)(\boldsymbol{\mu}_{al}\cdot\boldsymbol{\mu}_{lk}\times\boldsymbol{\mu}_{ka})({}^2\mathbf{E}_-\times{}^1\mathbf{E}_-). \tag{1.44a}$$

Similar expressions may be obtained for all six terms. The spatially averaged induced electric polarization $\langle \mathbf{p}^{(2)}\omega_1+\omega_2;-\omega_1,-\omega_2)\rangle$ can thus be written in the form

$$\langle \mathbf{p}^{(2)}(\omega_1+\omega_2;-\omega_1,-\omega_2)\rangle = \chi^{(2)}(\omega_1+\omega_2;-\omega_1,-\omega_2)({}^2\mathbf{E}_-\times{}^1\mathbf{E}_-). \tag{1.44b}$$

From (1.44a) we notice that $\chi^{(2)}(\omega_1+\omega_2;-\omega_1,-\omega_2)$ is not a scalar but instead a *pseudoscalar*. As a product of three polar vectors, it is *odd* with respect to space inversion—that is, with respect to the *parity operation*. It thus only fails to vanish in noncentrosymmetric media. Liquids (or gases) can only be *noncentrosymmetric* if they are *chiral*. In a racemic mixture there is no sum (or difference) frequency generation. In the special case that $\omega_1=\omega_2$ and ${}^2\mathbf{E}_-={}^1\mathbf{E}_-$, then $\langle \mathbf{p}^{(2)}(\omega_1+\omega_2;-\omega_1,-\omega_2)\rangle = \langle \mathbf{p}^{(2)}(2\omega;-\omega,-\omega)\rangle = 0$. In liquids, even in chiral ones, there is neither coherent second harmonic generation [60] nor optical rectification.

Finally, we return to the four wave mixing effect considered in (1.42). We define $\langle a|\boldsymbol{\mu}|m\rangle \equiv \boldsymbol{\mu}_{am}$, $\langle m|\boldsymbol{\mu}|l\rangle \equiv \boldsymbol{\mu}_{ml}$, and so on. The average of the numerator is

$$\begin{aligned}
&\langle \boldsymbol{\mu}_{am}(\boldsymbol{\mu}_{ml}\cdot{}^3\mathbf{E}_-)(\boldsymbol{\mu}_{lk}\cdot{}^2\mathbf{E}_+)(\boldsymbol{\mu}_{ka}\cdot{}^1\mathbf{E}_-)\rangle \\
&\quad = \{+(2/15)(\boldsymbol{\mu}_{am}\cdot\boldsymbol{\mu}_{ml})(\boldsymbol{\mu}_{lk}\cdot\boldsymbol{\mu}_{ka}) \\
&\qquad -(1/30)(\boldsymbol{\mu}_{am}\cdot\boldsymbol{\mu}_{lk})(\boldsymbol{\mu}_{ml}\cdot\boldsymbol{\mu}_{ka})-(1/30)(\boldsymbol{\mu}_{am}\cdot\boldsymbol{\mu}_{ka})(\boldsymbol{\mu}_{ml}\cdot\boldsymbol{\mu}_{lk})\}{}^3\mathbf{E}_-({}^2\mathbf{E}_+\cdot{}^1\mathbf{E}_-)
\end{aligned}$$

$$
\begin{aligned}
&+\{-(1/30)(\boldsymbol{\mu}_{am}\cdot\boldsymbol{\mu}_{ml})(\boldsymbol{\mu}_{lk}\cdot\boldsymbol{\mu}_{ka})\\
&+(2/15)(\boldsymbol{\mu}_{am}\cdot\boldsymbol{\mu}_{lk})(\boldsymbol{\mu}_{ml}\cdot\boldsymbol{\mu}_{ka})-(1/30)(\boldsymbol{\mu}_{am}\cdot\boldsymbol{\mu}_{ka})(\boldsymbol{\mu}_{ml}\cdot\boldsymbol{\mu}_{lk})\}{}^{2}\mathbf{E}_{+}({}^{3}\mathbf{E}_{-}\cdot{}^{1}\mathbf{E}_{-})\\
&+\{-(1/30)(\boldsymbol{\mu}_{am}\cdot\boldsymbol{\mu}_{ml})(\boldsymbol{\mu}_{lk}\cdot\boldsymbol{\mu}_{ka})\\
&-(1/30)(\boldsymbol{\mu}_{am}\cdot\boldsymbol{\mu}_{lk})(\boldsymbol{\mu}_{ml}\cdot\boldsymbol{\mu}_{ka})+(2/15)(\boldsymbol{\mu}_{am}\cdot\boldsymbol{\mu}_{ka})(\boldsymbol{\mu}_{ml}\cdot\boldsymbol{\mu}_{lk})\}{}^{1}\mathbf{E}_{-}({}^{3}\mathbf{E}_{-}\cdot{}^{2}\mathbf{E}_{+}).
\end{aligned}
\tag{1.45}
$$

Every one of the three terms in this sum consists of a scalar molecular part times a vectorial field part.

1.2.6. Transition from an Initial State to a Final State

The reader will notice that until now we have neglected damping effects. By introducing imaginary damping terms in the frequency denominators of the expressions for the induced polarizations, one obtains complex susceptibilities. The real parts of the susceptibilities then represent *dispersion effects*, the imaginary parts *absorptions*. Here we shall, for simplicity, not follow this procedure, but rather return to elementary perturbation theory (Section 1.2.2). There we assume a situation where one of the frequencies of the radiation field, $\omega_1, \omega_2, \ldots$, or a sum or difference thereof, is equal to the frequency of a given molecular transition, say between states a and b: $\omega_{ba} = \omega_b - \omega_a$.

As we have just seen, in the case of *scattering and refraction*, the quantity of interest is the induced polarization $\mathbf{p}_a$. This quantity may be formally viewed as the expectation value, or matrix element, of a *polarization operator* between the same initial and final state a. In the case of a *transition* from a to b induced by the radiation, the quantity of interest may be represented by the matrix element of a *transition operator* $R^{(n)}$ between initial and final state [57]. In the case of a one-photon transition in the electric dipole approximation, this quantity is the transition moment:

$$
\langle b|R^{(1)}(-\omega)|a\rangle = \langle b|-\boldsymbol{\mu}\cdot\mathbf{E}_{-}|a\rangle. \tag{1.46}
$$

The *transition probability per unit time* is proportional to the absolute value squared:

$$
\begin{aligned}
w^{(1)}(a\rightarrow b;\omega) &= (2\pi/\hbar^2)\mid\langle b|R^{(1)}(-\omega)|a\rangle\mid^2\delta(\omega_{ba}-\omega)\\
&= (2\pi/\hbar^2)\mid\langle b|-\boldsymbol{\mu}\cdot\mathbf{E}_{-}|a\rangle\mid^2\delta(\omega_{ba}-\omega)\\
&= (2\pi/\hbar^2)\langle b|-\boldsymbol{\mu}\cdot\mathbf{E}_{-}|a\rangle\langle a|-\boldsymbol{\mu}\cdot\mathbf{E}_{+}|b\rangle\ \delta(\omega_{ba}-\omega).
\end{aligned}
\tag{1.47}
$$

The resonance condition is marked by the delta function $\delta(\omega_{ba}-\omega)$. This relation (1.47) is also called the "Fermi golden rule."

For *two-photon absorption*, one similarly obtains

$$
\begin{aligned}
&\langle b|R^{(2)}(-\omega_1,-\omega_2)|a\rangle\\
&\quad=-\sum_k\frac{\langle b|\boldsymbol{\mu}\cdot{}^{2}\mathbf{E}_{-}|k\rangle\langle k|\boldsymbol{\mu}\cdot{}^{1}\mathbf{E}_{-}|a\rangle}{\hbar(\omega_{ka}-\omega_1)}-\sum_k\frac{\langle b|\boldsymbol{\mu}\cdot{}^{1}\mathbf{E}_{-}|k\rangle\langle k|\boldsymbol{\mu}\cdot{}^{2}\mathbf{E}_{-}|a\rangle}{\hbar(\omega_{ka}-\omega_2)}.
\end{aligned}
\tag{1.48}
$$

The two-photon transition probability per unit time then reads

$$
w^{(2)}(a\rightarrow b;\omega_1,\omega_2) = (2\pi/\hbar^2)\mid\langle b|R^{(2)}(-\omega_1,-\omega_2)|a\rangle\mid^2\delta(\omega_{ba}-\omega_1-\omega_2). \tag{1.49}
$$

In the *Raman effect* we encounter absorption of a photon $-\omega_1$ immediately followed by emission of a photon $+\omega_2$. The Raman transition operator $R^{(2)}(-\omega_1, +\omega_2)$ is obtained from the operator for two-photon absorption by replacing in the numerators of (1.48) ${}^2\mathbf{E}_-$ by ${}^2\mathbf{E}_+$, and in the denominator $-\omega_2$ by $+\omega_2$. Consequently,

$$w^{(2)}(a \to b; \omega_1, -\omega_2) = (2\pi/\hbar^2) \mid \langle b|R^{(2)}(-\omega_1, +\omega_2)|a\rangle \mid^2 \delta(\omega_{ba} - \omega_1 + \omega_2). \quad (1.50)$$

The interested reader may want to write out expressions (1.49) and (1.50) in detail, following the outlined procedure. We shall return to them in the Section 1.3.4. on two-photon optical activity and on Raman optical activity.

1.3. CHIROPTICAL PHENOMENA

1.3.1. Natural Optical Activity: CD and ORD

We begin by going back to Section 1.2.1 and we recall that in an optically active medium the induced macroscopic electric polarization **P** depends not only on the interaction with the electric field vector of the radiation **E**, but also on the magnetic field vector **H** [Eq. (1.9a,b)]. At the molecular level, we consider the Hamiltonian in the long-wavelength approximation [Eq. (1.35)]. In the previous sections we had only considered the electric dipole–electric field term: $-\boldsymbol{\mu} \cdot \mathbf{E}$. At present, we must indeed take into account both the magnetic dipole–magnetic induction contribution to the Hamiltonian, as well as the electric quadrupole–electric field gradient term. We notice that the electric dipole operator $\boldsymbol{\mu}$ is *odd* with respect to the *parity operation P*, the magnetic dipole operator **m** is *even*, and so is the electric quadrupole operator **Q**. From this symmetry point of view, we must take both additional terms in the Hamiltonian into consideration.

For practical reasons we will presently start out by considering *circular dichroism*. As one may immediately conclude, the transition probability per unit time for a naturally optically active transition $a \to b$ is then given by

$$\begin{aligned} w^{(1)}(a \to b; \omega) = (2\pi/\hbar^2)(&\langle b|\boldsymbol{\mu} \cdot \mathbf{E}_-|a\rangle\langle a|\boldsymbol{\mu} \cdot \mathbf{E}_+|b\rangle \\ &+ \langle b|\boldsymbol{\mu} \cdot \mathbf{E}_-|a\rangle\langle a|\ \mathbf{m} \cdot \mathbf{B}_+|b\rangle + \langle b|\mathbf{m} \cdot \mathbf{B}_-|a\rangle\langle a|\boldsymbol{\mu} \cdot \mathbf{E}_+|b\rangle \\ &+ \langle b|\boldsymbol{\mu} \cdot \mathbf{E}_-|a\rangle\langle a|\ \mathbf{Q} : \boldsymbol{\nabla}\mathbf{E}_+|b\rangle + \langle b|\mathbf{Q} : \nabla\mathbf{E}_-|a\rangle\langle a|\boldsymbol{\mu} \cdot \mathbf{E}_+|b\rangle \\ &+ \text{higher terms})\delta(\omega_{ba} - \omega). \end{aligned} \quad (1.51)$$

The first term in Eq. (1.51), the pure electric dipole term, is usually dominant. The second and third terms, mixed electric dipole–magnetic dipole factors, will be seen to be responsible for CD in chiral fluids. As we shall now show, the electric dipole–electric quadrupole contributions, terms 4 and 5 in (1.51), average to zero in an isotropic medium; for instance,

$$\langle b|\boldsymbol{\mu} \cdot \mathbf{E}_-|a\rangle\langle a|\ \mathbf{Q} : \nabla\mathbf{E}_+|b\rangle = (e^2/2)\langle b|\mathbf{r} \cdot \mathbf{E}_-|a\rangle\langle a|\mathbf{r} \cdot (\mathbf{r} \cdot \boldsymbol{\nabla})\mathbf{E}_+|b\rangle. \quad (1.52a)$$

In this expression we identify molecule-fixed and space-fixed vector quantities. In the process of isotropic averaging, following Section 1.2.5, we note that the vector operator

∇ behaves as an ordinary space-fixed vector. Following Eq. (1.44a), we thus find for the averaged quantity and from simple vector calculus the following:

$$(e^2/12)(\langle b|\mathbf{r}|a\rangle \cdot \langle a|\mathbf{r} \times \mathbf{r}|b\rangle)(\mathbf{E}_- \cdot \nabla \times E_+) = 0. \tag{1.52b}$$

After space-averaging, the two electric dipole–magnetic dipole terms in (1.51) survive, however, and we obtain the following for their contribution to $w^{(1)}(a \to b; \omega)$:

$$(2\pi/3\hbar^2)\langle a|\boldsymbol{\mu}|b\rangle \cdot \langle b|\mathbf{m}'|a\rangle i(\mathbf{E}_+ \cdot \mathbf{B}_- - \mathbf{E}_- \cdot \mathbf{B}_+)\delta(\omega_{ba} - \omega). \tag{1.53}$$

In this and in the following expressions, we write for the magnetic dipole operator $\mathbf{m} = i\mathbf{m}'$, where $\mathbf{m}'$ is real. The product $\langle a|\boldsymbol{\mu}|b\rangle \cdot \langle b|\mathbf{m}'|a\rangle = \mathrm{Im}(\langle a|\boldsymbol{\mu}|b\rangle \cdot \langle b|\mathbf{m}|a\rangle)$ is known as the *rotatory strength* of the transition [20] [see also Eq. (1.1) in Section 1.1.3].

On the basis of Eqs. (1.13a)–(1.14b), we write the following for *left circularly polarized* (L c.p.) radiation:

$$\mathbf{E}_- = (e_0/2)(+\mathbf{i} + i\mathbf{j}), \qquad \mathbf{E}_+ = (e_0/2)(+\mathbf{i} - i\mathbf{j}); \tag{1.54a}$$

$$\mathbf{B}_- = (b_0/2)(-i\mathbf{i} + \mathbf{j}), \qquad \mathbf{B}_+ = (b_0/2)(+i\mathbf{i} + \mathbf{j}). \tag{1.54b}$$

And for *right circularly polarized* (R c.p.) radiation we write

$$\mathbf{E}_- = (e_0/2)(+\mathbf{i} - i\mathbf{j}), \qquad \mathbf{E}_+ = (e_0/2)(+\mathbf{i} + i\mathbf{j}); \tag{1.55a}$$

$$\mathbf{B}_- = (b_0/2)(+i\mathbf{i} + \mathbf{j}), \qquad \mathbf{B}_+ = (b_0/2)(-i\mathbf{i} + \mathbf{j}). \tag{1.55b}$$

Introducing these expressions into Eq. (1.53), we find the following for the difference of the transition probability under L and R c.p. light:

$$\begin{aligned} \Delta w(a \to b) &= w(a \to b)_\mathrm{L} - w(a \to b)_\mathrm{R} \\ &= (4\pi/3\hbar^2)\langle a|\boldsymbol{\mu}|b\rangle \cdot \langle b|\mathbf{m}'|a\rangle e_0 b_0 \ \delta(\omega_{ba} - \omega) \\ &= (2/3\hbar^2)\langle a|\boldsymbol{\mu}|b\rangle \cdot \langle b|\mathbf{m}'|a\rangle e_0 b_0 \ \delta(\nu_{ba} - \nu). \end{aligned} \tag{1.56}$$

In CGS–Gauss units in vacuum, we note

$$e_0 = b_0; \qquad \rho(\nu) = (1/2\pi)\mathbf{E}_-(\nu) \cdot \mathbf{E}_+(\nu) = (1/4\pi)e_0^2;$$

Thus:

$$e_0 b_0 = {e_0}^2 = 4\pi\rho(\nu), \tag{1.57}$$

$\rho(\nu)$ being the radiation field energy density per unit frequency, at frequency ν. Consequently,

$$w(a \to b)_\mathrm{L} - w(a \to b)_\mathrm{R} = (8\pi/3\hbar^2)\langle a|\boldsymbol{\mu}|b\rangle \cdot \langle b|\mathbf{m}'|a\rangle \rho(\nu)\delta(\nu_{ba} - \nu). \tag{1.58a}$$

The relation to the experimental quantity, namely the difference of the absorption coefficient (Section 1.1.3) for left and right c.p. light, $\Delta\varepsilon$ (CD), is given by the proportionality:

$$\Delta\varepsilon(\mathrm{CD}) = \varepsilon_\mathrm{L} - \varepsilon_\mathrm{R} \sim w(a \to b)_\mathrm{L} - w(a \to b)_\mathrm{R}. \tag{1.58b}$$

The point of departure for our consideration of ORD is given by Eq. (1.40) in Section 1.2.4. In this expression we replace the electric dipole interaction with the radiation field by the magnetic dipole interaction, indicated by $-\omega(\mathrm{M})$, to get

$$\mathbf{p}^{(1)}(+\omega; -\omega(\mathrm{M})) = \sum_k \left\{ \frac{\langle a|\boldsymbol{\mu}|k\rangle(\langle k|m\boldsymbol{\mu}|a\rangle \cdot \mathbf{B}_-)}{\hbar(\omega_{ka} - \omega)} + \frac{(\langle a|\mathbf{m}|k\rangle \cdot \mathbf{B}_-)\langle k|\boldsymbol{\mu}|a\rangle}{\hbar(\omega_{ka} + \omega)} \right\}. \tag{1.59}$$

After *isotropic averaging*, we may write

$$\mathbf{p}^{(1)}(+\omega; -\omega(\mathrm{M})) = \chi^{(1)}(+\omega; -\omega(\mathrm{M}))\mathbf{B}_-, \tag{1.60a}$$

where $\chi^{(1)}(+\omega; -\omega(\mathrm{M}))$ is a pseudoscalar. From now on, we omit for convenience the pointed brackets $\langle \mathbf{p}^{(1)} \rangle$ used in Section 1.2.5 to indicate isotropic spatial averaging. In addition to (1.59) and (1.60a), we of course also obtain an analogous complex conjugate term:

$$\mathbf{p}^{(1)}(-\omega; +\omega(\mathrm{M})) = \chi^{(1)}(-\omega; +\omega(\mathrm{M}))\mathbf{B}_+. \tag{1.60b}$$

The susceptibility in Eq. (1.60a) is now found to be

$$\chi^{(1)}(+\omega; -\omega(\mathrm{M})) = \frac{1}{3}\sum_k \left\{ \frac{\langle a|\boldsymbol{\mu}|k\rangle \cdot \langle k|\mathbf{m}|a\rangle}{\hbar(\omega_{ka} - \omega)} + \frac{\langle a|\mathbf{m}|k\rangle \cdot \langle k|\boldsymbol{\mu}|a\rangle}{\hbar(\omega_{ka} + \omega)} \right\}. \tag{1.61a}$$

Assuming all wavefunctions $|k\rangle$ real, this is equal to

$$\chi^{(1)}(+\omega; -\omega(\mathrm{M})) = i\frac{2\omega}{3\hbar}\sum_k \frac{\langle a|\boldsymbol{\mu}|k\rangle \cdot \langle k|\mathbf{m}'|a\rangle}{(\omega_{ka}^2 - \omega^2)}. \tag{1.61b}$$

The numerators in the summation evidently contain the rotatory strengths of the transitions $a \to k$. We finally establish the connection to Eq. (1.15a) in Section 1.2.1. From our definition, $\mathbf{P}_- = \alpha\mathbf{E}_- + \beta i\mathbf{B}_-$ follows, N being the concentration of molecules:

$$\beta = -iN\chi^{(1)}(+\omega; -\omega(\mathrm{M})) = N\,\mathrm{Im}\{\chi^{(1)}(+\omega; -\omega(\mathrm{M}))\},$$

and thus

$$n_\mathrm{L} - n_\mathrm{R} = -8\pi iN\chi^{(1)}(+\omega; -\omega(\mathrm{M})) = 8\pi\beta. \tag{1.62}$$

The circular differential character of ORD may also be visualized in the following simple and straightforward way. As above, we of course assume *isotropic averaging*. Ordinary refraction is due to (see (1.43b)):

$$\mathbf{p}^{(1)}(\omega; -\omega) = \chi^{(1)}(\omega; -\omega)\mathbf{E}_-,$$

and optical activity [see (1.60a)]:

$$\mathbf{p}^{(1)}(+\omega; -\omega(\mathrm{M})) = \chi^{(1)}(+\omega; -\omega(\mathrm{M}))\mathbf{B}_- = \mathrm{Im}\{\chi^{(1)}(+\omega; -\omega(\mathrm{M}))\}i\mathbf{B}_-. \tag{1.63}$$

Introducing the field vectors $\mathbf{E}_-$ and $\mathbf{B}_-$ for left and right c.p. light, as given in Eqs. (1.54a)–(1.55b), we find that in the *left* c.p. case the vector $i\mathbf{B}_-$ *adds* to $\mathbf{E}_-$ whereas in the *right* c.p. case it *subtracts*. The absolute sign of the circular differential effect in a particular case evidently depends on the absolute sign of the pseudoscalar susceptibility $\mathrm{Im}\{\chi^{(1)}(-\omega; +\omega(\mathrm{M}))\}$, which of course is opposite for enantiomers, but which characteristically reflects the chiroptical properties of the molecule considered.

1.3.2. Optical Activity of Higher Order: Sum and Difference Frequency Generation

After having discussed the chiroptical effects of first order in the molecule–electromagnetic field interaction, we now briefly consider the influence of chirality on three- and four-wave mixing [61–63]. We begin here with sum and difference frequency generation [61]. For this purpose we return to Section 1.2.5, where for sum frequency generation we had found, after *isotropic averaging* [see Eq. (1.44b)], the following:

$$\mathbf{p}^{(2)}(\omega_1 + \omega_2; -\omega_1, -\omega_2) = \chi^{(2)}(\omega_1 + \omega_2; -\omega_1, -\omega_2)({}^2\mathbf{E}_- \times {}^1\mathbf{E}_-).$$

The detailed expression for $\chi^{(2)}(\omega_1 + \omega_2; -\omega_1, -\omega_2)$ may be deduced from Eqs. (1.41) and (1.44a). What we notice is that this molecular quantity is odd with respect to parity and therefore is a pseudoscalar. However, although sum frequency generation (as well as difference frequency generation) in liquids requires the presence of chiral molecules, the effect induced by pure electric dipole interactions in itself is *not* circular differential. A difference arises only if one adds contributions to $\mathbf{p}^{(2)}(\omega_1 + \omega_2; -\omega_1, -\omega_2)$ in which one interaction is of *magnetic dipole* (M) or *electric quadrupole* (Q) type. In the first case we have

$$\mathbf{p}^{(2)}(\omega_1 + \omega_2; -\omega_1(\mathrm{M}), -\omega_2) = \chi^{(2)}(\omega_1 + \omega_2; -\omega_1(\mathrm{M}), -\omega_2)({}^2\mathbf{E}_- \times i\,{}^1\mathbf{B}_-). \quad (1.64)$$

Here the susceptibility is defined to be real, and the factor i in the field part comes from the magnetic dipole operator, as in Eqs. (1.53) and (1.63). Of course, there is an additional contribution, arising from $\mathbf{p}^{(2)}(\omega_1 + \omega_2; -\omega_1 - \omega_2(\mathrm{M}))$, corresponding to the alternative replacement of the electric dipole operator by the magnetic dipole operator $\mathbf{m} = i\mathbf{m}'$ for the interaction with the field of frequency ω_2.

We now focus our attention on the field part of expressions (1.44b) and (1.64) in order to deduce the dependence of $\mathbf{p}^{(2)}$ on the state of polarization of the incident radiation. For sum frequency generation, parallel incidence and circular polarization, (ω_1) left–(ω_2) left (L–L), and, respectively, (ω_1) right–(ω_2) right (R–R), we obtain

$$\text{L–L}: \quad {}^2\mathbf{E}_- \times {}^1\mathbf{E}_- = 0; \qquad \text{R–R}: \quad {}^2\mathbf{E}_- \times {}^1\mathbf{E}_- = 0. \quad (1.65)$$

Here there cannot possibly be any circular differential effect. However, for sum frequency generation at parallel incidence and circular polarizations left–right (L–R) vs. right–left (R–L), one finds [see Eqs. (1.54a)–(1.55b)]

$$\text{L–R}: \quad {}^2\mathbf{E}_- \times {}^1\mathbf{E}_- = +(i/2)\,{}^2e_0\,{}^1e_0\mathbf{k}; \qquad {}^2\mathbf{E}_- \times i\,{}^1\mathbf{B}_- = +(i/2)\,{}^2e_0\,{}^1b_0\mathbf{k}. \quad (1.66a)$$

$$\text{R–L}: \quad {}^2\mathbf{E}_- \times {}^1\mathbf{E}_- = -(i/2)\,{}^2e_0\,{}^1e_0\mathbf{k}; \qquad {}^2\mathbf{E}_- \times i\,{}^1\mathbf{B}_- = +(i/2)\,{}^2e_0\,{}^1b_0\mathbf{k}. \quad (1.66b)$$

We notice that for L–R the contributions have the *same* sign, whereas for R–L they show an *opposite* sign. **k** is a unit vector in propagation direction. The added contributions lead to the inequality

$$| \mathbf{p}^{(2)}(\omega_1 + \omega_2)_{\mathrm{L-R}} | \neq | \mathbf{p}^{(2)}(\omega_1 + \omega_2)_{\mathrm{R-L}} | . \tag{1.67}$$

The procedure for *difference frequency generation* is similar, but there we find a characteristic difference in the selection rules; in particular,

$$\mathrm{L–R}: \quad {}^2\mathbf{E}_+ \times {}^1\mathbf{E}_- = 0; \qquad \mathrm{R–L}: \quad {}^2\mathbf{E}_+ \times {}^1\mathbf{E}_- = 0. \tag{1.68}$$

On the other hand:

$$\mathrm{L–L}: \quad {}^2\mathbf{E}_+ \times {}^1\mathbf{E}_- = +(i/2)\,{}^2e_0\,{}^1e_0\mathbf{k}; \qquad {}^2\mathbf{E}_+ \times i\,{}^1\mathbf{B}_- = +(i/2)\,{}^2e_0\,{}^1b_0\mathbf{k}. \tag{1.69a}$$

$$\mathrm{R–R}: \quad {}^2\mathbf{E}_+ \times {}^1\mathbf{E}_- = -(i/2)\,{}^2e_0\,{}^1e_0\mathbf{k}; \qquad {}^2\mathbf{E}_+ \times i\,{}^1\mathbf{B}_- = +(i/2)\,{}^2e_0\,{}^1b_0\mathbf{k}. \tag{1.69b}$$

For L–L the contributions add, while for R–R they subtract. We consequently find

$$| \mathbf{p}^{(2)}(\omega_1 - \omega_2)_{\mathrm{L-L}} | \neq | \mathbf{p}^{(2)}(\omega_1 - \omega_2)_{\mathrm{R-R}} | . \tag{1.70}$$

The reader will realize that one may also examine perpendicular incidence of the two radiation beams and other possible combinations of polarizations. Furthermore, one notices that the electric quadrupole–electric field gradient term does not average to zero, but must also be taken into consideration [61].

1.3.3. Optical Activity of Higher Order: Four-Wave Mixing

In Section 1.2.4, Eq. (1.42), we considered Raman-type four-wave mixing in the pure electric dipole approximation: $\mathbf{p}^{(3)}(\omega_1 - \omega_2 + \omega_3; -\omega_1, +\omega_2, -\omega_3)$. The numerators in the quantum mechanical terms describing this quantity lead, after isotropic averaging, to expressions of the form shown in Eq. (1.45). There we focused our attention on the vectorial field factors which read

$${}^3\mathbf{E}_-({}^2\mathbf{E}_+ \cdot {}^1\mathbf{E}_-), \qquad {}^2\mathbf{E}_+({}^3\mathbf{E}_- \cdot {}^1\mathbf{E}_-), \qquad {}^1\mathbf{E}_-({}^3\mathbf{E}_- \cdot {}^2\mathbf{E}_+).$$

If we now consider $\mathbf{p}^{(3)}(\omega_1 - \omega_2 + \omega_3; -\omega_1(\mathrm{M}), +\omega_2, -\omega_3)$, assuming that for the frequency ω_1 we have a magnetic dipole interaction (M), then in the molecular factors of Eq. (1.45) we must replace $\boldsymbol{\mu}_{ka}$ by $\mathbf{m}'_{ka}$, and the field factors correspondingly become

$$i\,{}^3\mathbf{E}_-({}^2\mathbf{E}_+ \cdot {}^1\mathbf{B}_-), \qquad i\,{}^2\mathbf{E}_+({}^3\mathbf{E}_- \cdot {}^1\mathbf{B}_-), \qquad i\,{}^1\mathbf{B}_-({}^3\mathbf{E}_- \cdot {}^2\mathbf{E}_+). \tag{1.71}$$

Proceeding here as in the previous section, we may ascertain that the added contributions of

$$\mathbf{p}^{(3)}(\omega_1 - \omega_2 + \omega_3; -\omega_1, +\omega_2, -\omega_3) \quad \text{and} \quad \mathbf{p}^{(3)}(\omega_1 - \omega_2 + \omega_3; -\omega_1(\mathrm{M}), +\omega_2, -\omega_3)$$

indeed are circular differential [61–63].

By successively also considering ω_2(M) and ω_3(M), as well as different combinations of the polarizations of the incident radiation beams, such as L–L–L versus R–R–R; L–L–R versus R–R–L, a large variety of possible nonlinear chiroptical effects may be conceived. The incidence of the beams may be parallel or perpendicular to each other. In addition, a comparable variety of electric dipole–electric quadrupole (Q) effects is possible, corresponding to [61–63] $\mathbf{p}^{(3)}(\omega_1 - \omega_2 + \omega_3; -\omega_1(Q), +\omega_2, -\omega_3)$, and so on.

1.3.4. Two-Photon CD and Raman Optical Activity

We now return to Section 1.2.6 and consider the matrix element of the transition operator for two-photon absorption $\langle b|R^{(2)}(-\omega_1,-\omega_2)|a\rangle$. As we know, the two-photon transition probability per unit time is proportional to

$$w^{(2)}(a\rightarrow b;\omega_1,\omega_2)\sim\langle b|R^{(2)}(-\omega_1,-\omega_2)|a\rangle\langle b|R^{(2)}(-\omega_1,-\omega_2)|a\rangle^*$$
$$=\langle a|R^{(2)}(-\omega_1,-\omega_2)^*|b\rangle\langle b|R^{(2)}(-\omega_1,-\omega_2)|a\rangle. \tag{1.72}$$

Introducing into (1.72) the right-hand side of Eq. (1.48) leads to a somewhat cumbersome formula that we shall not write out. However, after isotropically averaging the fourth rank tensor expressions that occur, the field factors may be recognized to be of the form

$$({}^1\mathbf{E}_+\cdot{}^2\mathbf{E}_+)({}^1\mathbf{E}_-\cdot{}^2\mathbf{E}_-),\qquad({}^1\mathbf{E}_+\cdot{}^1\mathbf{E}_-)({}^2\mathbf{E}_+\cdot{}^2\mathbf{E}_-),\qquad({}^1\mathbf{E}_+\cdot{}^2\mathbf{E}_-)({}^2\mathbf{E}_+\cdot{}^1\mathbf{E}_-). \tag{1.73}$$

We now assume a magnetic dipole interaction with the radiation field to occur for ω_1:$\langle b|R^{(2)}(-\omega_1(\mathrm{M}),-\omega_2)|a\rangle$. Following (1.72), but considering only *one* magnetic dipole interaction in all, this expression has to be multiplied by $\langle b|R^{(2)}(-\omega_1,-\omega_2)|a\rangle^*$, where the asterisk, as above, denotes complex conjugation. The field factors correspondingly now read

$$i({}^1\mathbf{E}_+\cdot{}^2\mathbf{E}_+)({}^1\mathbf{B}_-\cdot{}^2\mathbf{E}_-),\qquad i({}^1\mathbf{E}_+\cdot{}^1\mathbf{B}_-)({}^2\mathbf{E}_+\cdot{}^2\mathbf{E}_-),\qquad i({}^1\mathbf{E}_+\cdot{}^2\mathbf{E}_-)({}^2\mathbf{E}_+\cdot{}^1\mathbf{B}_-). \tag{1.74}$$

Making use of Eqs. (1.54a)–(1.55b), the reader may ascertain that these expressions have opposite signs for L and R c.p. light. A variety of additional circular differential terms is conceivable. A detailed theoretical treatment of two-photon CD is to be found in reference 64 describing different conditions for the incident radiation. A similar treatment of Raman optical activity may be developed by replacing $-\omega_2$ with $+\omega_2$ in expression (1.72). This entails a corresponding modification of the selection rules. For a general theoretical exposition of Raman optical activity, consult reference 65. The stimulated Raman effect is described in references 53 and 66. Concerning stimulated Raman optical activity, see references 62 and 63.

1.3.5. Magnetic Circular Dichroism: MCD

The Faraday effect, manifesting itself as magnetic circular birefringence, magnetic rotatory dispersion (MORD), and magnetic circular dichroism (MCD), is *circular differential* but *achiral*. It occurs in matter of any symmetry. Because we are mainly interested in general symmetry and selection rules, we shall limit ourselves to an elementary treatment of MCD. We consider, as in previous sections, a fluid in which the molecules are randomly oriented, and to which we now apply a *static magnetic* field $\mathbf{B}_0$. For simplicity, and possibly eschewing mathematical rigor, we treat the influence of the static field on the molecules in the frame of time-independent perturbation theory:

$$|a'\rangle=|a\rangle-\sum_{n\neq a}|n\rangle\frac{\langle n|\mathbf{m}|a\rangle\cdot\mathbf{B}_0}{\hbar\omega_{an}}, \tag{1.75a}$$

$$\langle b'| = \langle b| - \sum_{n\neq b} \frac{\langle b|\mathbf{m}|n\rangle \cdot \mathbf{B}_0}{\hbar\omega_{bn}} \langle n|. \tag{1.75b}$$

Introducing these relations into the expression for the transition probability per unit time,

$$w(a' \to b') = (1/\hbar^2)\langle b'|\boldsymbol{\mu} \cdot \mathbf{E}_-|a'\rangle\langle a'|\boldsymbol{\mu} \cdot \mathbf{E}_+|b'\rangle f(\nu),$$

we obtain the following after having, for practical reasons, shifted from the variable ω to the variable ν and after having replaced the delta function in Eq. (1.51) by a general and more realistic lineshape function $f(\nu)$:

$$w(a' \to b'; B_0) = \frac{4\pi^2}{3h^3} \left\{ \sum_{n\neq a} \frac{1}{\nu_{na}} \mathrm{Im}(\mathbf{m}_{na} \cdot \boldsymbol{\mu}_{ab} \times \boldsymbol{\mu}_{bn}) + \sum_{n\neq b} \frac{1}{\nu_{nb}} \mathrm{Im}(\mathbf{m}_{bn} \cdot \boldsymbol{\mu}_{ab} \times \boldsymbol{\mu}_{na}) \right\} \cdot (-i\mathbf{B}_0 \cdot \mathbf{E}_- \times \mathbf{E}_+) f(\nu). \tag{1.76}$$

We notice that the molecular part of this expression and also the field part are even with respect to the parity operation. The response to enantiomers must thus be the same. Writing $\mathbf{B}_0 = B_0\mathbf{k}$ and using expressions (1.54a) and (1.55a), we find

$$\text{For L c.p. light :} \qquad (-i\mathbf{B}_0 \cdot \mathbf{E}_- \times \mathbf{E}_+) = -B_0 \mathrm{e}_0{}^2/2, \tag{1.77a}$$

$$\text{For R c.p. light :} \qquad (-i\mathbf{B}_0 \cdot \mathbf{E}_- \times \mathbf{E}_+) = +B_0 \mathrm{e}_0{}^2/2. \tag{1.77b}$$

Thus,

$$w(a' \to b'; B_0)_\mathrm{L} - w(a' \to b'; B_0)_\mathrm{R} \sim -B_0 e_0{}^2. \tag{1.77c}$$

What we have derived here is the so-called *B-term* of MCD. We have assumed all zeroth-order wavefunctions, $|a\rangle, |n\rangle, |b\rangle$, to be nondegenerate. If, due to symmetry and/or spin properties, we encounter degeneracies, we also obtain *A terms*. If, in addition, the ground state is magnetically degenerate, there appears a *C term* [67–69]. However, the treatment of these aspects will be left to the specialized chapters.

1.3.6. Magnetochiral dichroism: MChD

MORD and MCD are induced in the presence of a static magnetic field by a pure electric dipole interaction with the radiation field. The only magnetic dipole interaction that occurs is with the static magnetic field. In magnetochiral dichroism (MChD) and birefringence, however, there occurs both a magnetic dipole interaction with the static field and a magnetic dipole interaction, as well as an electric quadrupole interaction, with the light field [70–73]. From that point of view, MChD may be considered as a combination of *natural* CD (hereafter denoted as NCD) and of MCD (see Figure 1.3). As we now shall see, MChD occurs only in chiral media, but, in contrast to MCD, it is *not circular differential*. For MChD we again combine in a formal sense Eq. (1.51) in

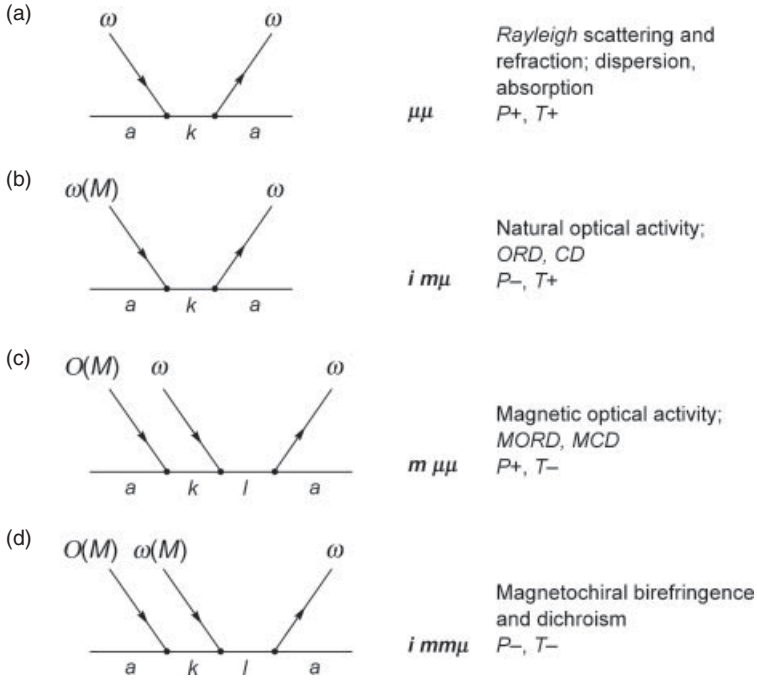

Figure 1.3. Graphs for the radiation-induced molecular polarization in the optical dispersion/absorption effects named at right. The general form of the tensor products of the corresponding molecular susceptibility are given: $\boldsymbol{\mu}$ stands for a parity-odd electric dipole interaction, and $\mathbf{m}$ stands for a parity-even magnetic dipole interaction. *i* represents the imaginary unit. The overall symmetry with respect to parity *P* and time reversal *T* is also noted for each case. (Reproduced with permission, from G. Wagnière, *On Chirality and the Universal Asymmetry*, VHCA-Wiley-VCH, Zurich, 2007.)

Section 1.3.1 with Eqs. (1.75a,b) in Section 1.3.5. The electric dipole–magnetic dipole contribution to the transition probability per unit time then reads [70]

$$w(a' \to b'; B_0; \text{el-mag}) = \frac{4\pi^2}{3h^3} \left\{ \begin{array}{l} \displaystyle\sum_{n\neq a} \frac{1}{\nu_{na}} (\boldsymbol{\mu}_{bn} \cdot \mathbf{m}_{ab} \times \mathbf{m}_{na} + \boldsymbol{\mu}_{ba} \cdot \mathbf{m}_{nb} \times \mathbf{m}_{an}) + \\ \displaystyle\sum_{n\neq b} \frac{1}{\nu_{nb}} (\boldsymbol{\mu}_{na} \cdot \mathbf{m}_{ab} \times \mathbf{m}_{bn} + \boldsymbol{\mu}_{ba} \cdot \mathbf{m}_{an} \times \mathbf{m}_{nb}) \end{array} \right\} \cdot (\mathbf{B}_0 \cdot \mathbf{E}_- \times \mathbf{B}_+) f(\nu). \tag{1.78}$$

We notice that the molecular part of this expression (inside the curly brackets) is odd with respect to the parity operation, and so is the field part. On the basis of Eqs. (1.54a)–(1.55b), we analyze the field part in the same way as in the previous section. We then find:

$$\text{For L c.p. light :} \qquad (\mathbf{B}_0 \cdot \mathbf{E}_- \times \mathbf{B}_+) = B_0 e_0 b_0/2, \tag{1.79a}$$

$$\text{For R c.p. light :} \qquad (\mathbf{B}_0 \cdot \mathbf{E}_- \times \mathbf{B}_+) = B_0 e_0 b_0/2. \tag{1.79b}$$

This confirms that the magnetochiral effect is *not* circular differential. MChD has the *same sign for left and right circularly polarized light*. It is consequently *independent of the polarization of the incident radiation* [70–73]. On the other hand, the effect changes its sign if the *direction of the static field* with respect to the *direction of propagation of the incident light beam is reversed:*

$$w(a' \to b'; B_0)_{\uparrow\uparrow} - w(a' \to b'; B_0)_{\downarrow\uparrow} \sim B_0 e_0 b_0. \tag{1.80}$$

We notice that the vector $\mathbf{E}_- \times \mathbf{B}_+$ is parallel and proportional to the Poynting vector, which is parallel to the wavevector $\boldsymbol{k}$ of the incident radiation. The electric dipole–electric quadupole contributions to MChD display similar symmetry properties.

In analogy to Eq. (1.76), we may consider Eq. (1.78) as a contribution to the *magnetochiral B term*. Where magnetic degeneracies occur, we will find *magnetochiral A terms* and possibly *C terms*. Magnetochiral dichroism and birefringence are Kronig–Kramers related, as are also all absorption/dispersion effects mentioned in previous sections.

Under ordinary laboratory conditions, the magnetochiral effect is small, because it requires for its detection a strong magnetic field. Considering that in Eq. (1.76) we replace termwise an electric dipole transition moment by a magnetic transition moment to obtain (1.78) (see also Figure 1.3), we conclude that the intensity I of MChD relates to that of MCD as that of natural CD relates to that of ordinary absorption. This ratio may be set approximately equal to the ratio of the energy of an elementary atomic (molecular) magnetic dipole and of an elementary atomic (molecular) electric dipole in the radiation field. It corresponds to the order of magnitude of the Bohr magneton, divided by the Bohr radius times the unit charge:

$$|I\,(\mathrm{MChD}|/|I\,(\mathrm{MCD})| \approx (e\hbar/2m_e c)/(a_0 e) = (1/2)(1/137) = 3.65 \times 10^{-3}. \qquad (1.81)$$

The first measurement of the magnetochiral effect was performed in emission [74], followed by an interferometric detection of magnetochiral birefringence [75], confirming the estimated order of magnitude.

As indicated above, the sign of the magnetochiral effect depends on the pseudoscalar product of the external magnetic field with the wavevector of light, $\mathbf{B}_0 \cdot \boldsymbol{k}$. The vector $\mathbf{B}_0$ is parity-even, time-odd; the vector $\boldsymbol{k}$ is parity-odd, time-odd. The product is parity-odd, time-even, which characterizes a chiral interaction [76]. These symmetry considerations allow us to understand that there must also exist a magnetochiral effect in *electric conduction*, depending for its relative sign on $\mathbf{B}_0 \cdot \mathbf{I}$ [77]. Indeed, the electric current vector $\mathbf{I}$ transforms with respect to both parity and time reversal like $\boldsymbol{k}$.

1.3.7. On Chirality and Magnetism: A Simple Model as Example

It was recently observed that magnetochiral dichroism may be significantly enhanced in chiral media that are *ferromagnetic* [78, 79]. Although ferromagnetism is usually due to the parallel alignment of electron spins, it is also of interest to study the interplay of chirality and *strong orbital paramagnetism*. A model which suggests itself in this context is that of a free electron on a quasi-infinite helix [80].

The model of a free electron on a helix has served to interpret fundamental aspects of *natural* circular dichroism (here denoted as NCD) [81, 82]. If one assumes periodic boundary conditions, then such a free electron (for simplicity here considered as spinless) displays not only *chirality*, but also *orbital angular momentum* pointed parallel or antiparallel to the helix axis. If we parametrically describe the helix as $(a\cos\varphi, a\sin\varphi, b\varphi)$, where a denotes the *radius* and $2\pi b$ represents the *pitch* of the helix, then the eigenfunctions will be of the form

$$|m\rangle = L^{-1/2}\exp(im\varphi/N), \qquad m = 0, \pm 1, \pm 2, \ldots, \qquad (1.82)$$

where N is the quasi-infinite number of turns and $L = 2\pi N(a^2 + b^2)^{1/2}$ is the curve length of the helix. We assume the degeneracies of the states $|m\rangle$ (for $m \neq 0$) to be

lifted by an external static magnetic field. The interaction of the free electron with an electromagnetic field incident along the helix axis is now considered and is described as indicated in Section 1.2.3, Eq. (1.26):

$$\mathcal{H}_{\text{int}} = (-e/m_e c)\mathbf{A}\cdot\mathbf{p} \equiv \mathcal{H}' \exp(-i\omega t) + \text{c.c.} \tag{1.83}$$

We calculate the *transition intensity* from a definite state n to a definite state m:

$$I(n \to m) \sim w(n \to m) \sim (2\pi/\hbar) \mid \langle m|\mathcal{H}'|n\rangle \mid^2 . \tag{1.84}$$

In contrast to Section 1.2.3, we do not multipole-expand the interaction Hamiltonian, but keep it in the exponential form (1.27a,b). Thanks to the simple exponential expressions, both of the wavefunctions (1.82) and of the interaction Hamiltonian (1.83), the calculation of (1.84) in closed form is relatively straightforward. Setting for simplicity $n = 0$, implying that the transition starts from the angular momentum-free ground state, we deduce the *anisotropy factors* for the transitions $|0\rangle \to |m\rangle$ in two basic situations: We begin by considering the *intensity difference between L and R c.p. incident light* for a *given direction of propagation*, denoted by (+) for *forward* and (−) for *backward* propagation, respectively. One finds [80]

$$g_{LR}(++) \equiv \frac{I_L(+) - I_R(+)}{I_L(+) + I_R(+)} = \frac{-2N^2kb + 2Nm}{m^2 - 2mNkb + N^2 + N^2k^2b^2}, \tag{1.85a}$$

$$g_{LR}(--) \equiv \frac{I_L(-) - I_R(-)}{I_L(-) + I_R(-)} = \frac{-2N^2kb - 2Nm}{m^2 + 2mNkb + N^2 + N^2k^2b^2}. \tag{1.85b}$$

The first term in the numerators of the right-hand side of Eqs. (1.85a,b) corresponds to NCD, and the second term corresponds to MCD. The NCD should exhibit the same sign, irrespective of the direction of incidence of the light, forward or backward. For a given direction of the angular momentum, however, the MCD must change its sign upon reversal of the direction of the light incidence. To fulfill these basic selection rules, the denominators should have the same (positive) sign and absolute value. This is conditionally fulfilled in the limit $kb = 2\pi b/\lambda \ll 1$. It implies that the wavelength of the light must be significantly larger than the pitch of the helix, and it corresponds to the *long-wavelength approximation*. If the pitch of the helix b is zero, evidently the natural optical activity vanishes, but not the MCD.

Next we examine the *difference between forward and backward propagation* for a *given chirality* of the light wave [80]:

$$g_{LL}(+-) \equiv \frac{I_L(+) - I_L(-)}{I_L(+) + I_L(-)} = \frac{2mNkb + 2mN}{m^2 + N^2 + 2N^2kb + N^2k^2b^2}, \tag{1.86a}$$

$$g_{RR}(+-) \equiv \frac{I_R(+) - I_R(-)}{I_R(+) + I_R(-)} = \frac{2mNkb - 2mN}{m^2 + N^2 - 2N^2kb + N^2k^2b^2}. \tag{1.86b}$$

The first term in the numerators of the right-hand side of Eqs. (1.86a,b) represents the MChD, the sign of which is *noncircular differential* and consequently is independent of the state of polarization of the incident radiation. The second term corresponds to MCD, which changes its sign on going from left to right circularly polarized light. We notice, however, that the obtention of these clear-cut selection rules again depends on the long-wavelength approximation and on N being large.

Both NCD and MChD are proportional to kb, the relation of the pitch of the helix to the wavelength of the light. In the limit where the magnetic quantum number m approaches N, we see from (1.85a,b) and (1.86a,b) that the absolute value of the MChD approaches that of the NCD. This suggests that the magnitude of the NCD signal may represent an upper limit to that of the MChD signal. In conclusion, this example illustrates the different selection rules for NCD, MCD, and MChD, as well as their dependence on the long-wavelength approximation.

1.4. CONCLUDING REMARKS

This introductory chapter aims at giving a brief overview of chiroptical effects in the frame of the semiclassical theory. It is hoped that it may serve as a point of departure for the study of the more detailed and topical expositions that follow, as well as an orientation for those readers who wish to enter the field of chirality and to get acquainted with its elements. However, the literature cited here is limited, and the choice of it subjective.

The phenomenon of optical activity was discovered two centuries ago. A hundred years later, in the first quarter of the twentieth century, it was recognized that the study of optical activity contributed very fundamentally and in a general way to the understanding of the spatial structure of molecules. Thus it became one of the cornerstones of modern stereochemistry.

The development of quantum mechanics opened the door to a physical understanding of optical activity. If one can calculate the wavefunctions of a chiral molecule, its optical activity may in principle be quantitatively derived. However, the task of obtaining good wavefunctions was, and still is, a major challenge. In spite of recent and spectacular advances in quantum chemical computation, this problem is not yet generally solved.

The development of lasers in the course of the five last decades has offered new possibilities in the experimental study of chiroptical phenomena. In particular, it has also made precise measurements of vibrational optical activity possible. It has opened the door to the study of many-photon, nonlinear optical and dynamical chiral effects.

The chemist is primarily interested in chiroptical phenomena as an analytical tool, in order to better understand the structure of, and reactions between, molecules. However, there is another aspect to chirality, namely the use of chosen chiral molecules to study, steer, and guide light. It seems to me that here the potential of chiroptical methods has not yet been systematically exploited. A combination of chiroptical and magneto-optical effects in chiral optical waveguides and fibers offers a variety of possibilities to independently control light polarization and phase, possibly leading to novel applications in optical transmission and switching [79, 83]. Finally, there is the fascinating field of optical teleportation [84] in which undoubtedly also significant discoveries related to chirality remain to be made.

REFERENCES

1. M. Born, E. Wolf, *Principles of Optics*, 6th ed., Cambridge University Press, Cambridge, **1997**.
2. J. D. Jackson, *Classical Electrodynamics*, John Wiley & Sons, New York, **1962**.
3. P. A. M. Dirac, *The Principles of Quantum Mechanics*, Oxford University Press, 4th ed., Oxford, **1958**.

4. J. J. Sakurai, *Advanced Quantum Mechanics*, Addison-Wesley, Reading, **1978**.
5. R. Loudon, *The Quantum Theory of Light*, Clarendon Press, Oxford, **1978**.
6. D. P. Craig, T. Thirunamachandran, *Molecular Quantum Electrodynamics*, Dover Publications, Mineola, NY, **1984**.
7. W. Heitler, F. London, *Z. Phys*. **1927**, *44*, 455–472.
8. M. Born, R. Oppenheimer, *Ann. Phys*. **1927**, *84*, 457–484.
9. L. Pauling, *J. Am. Chem. Soc*. **1931**, *53*, 1367–1400.
10. E. Hückel, *Z. Phys*. **1931**, *70*, 204–286; E. Hückel, *Z. Elektrochem*. **1937**, *43*, 752–788.
11. R. Hoffmann, *J. Chem. Phys*. **1963**, *39*, 1397–1412.
12. R. B. Woodward, R. Hoffmann, *J. Am. Chem. Soc*. **1965**, *87*, 395–397.
13. R. Hoffmann, R. B. Woodward, *J. Am. Chem. Soc*. **1965**, *87*, 2046–2048.
14. D. R. Hartree, *Proc. Cambridge Philos. Soc*. **1928**, *24*, 89,111.
15. V. Fock, *Z. Phys*. **1930**, *61*, 126–148.
16. C. C. J. Roothaan, *Rev. Mod. Phys*. **1951**, *23*, 69–89; C. C. J. Roothaan, *Rev. Mod. Phys*. **1960**, *32*, 179–185.
17. R. Pariser, R. G. Parr, *J. Chem. Phys*. **1953**, *21*, 466–471, 767–776.
18. J. A. Pople, D. P. Santry, G. A. Segal, *J. Chem. Phys*. **1965**, *43*, S129–S135.
19. J. P. Mathieu, *Activité Optique Naturelle, Handbuch der Physik*, Vol. 28, *Spektroskopie II*, Springer-Verlag, Berlin, **1957**, pp. 333–432.
20. L. Rosenfeld, *Z. Physik* **1928**, *52*, 161–174.
21. J. G. Kirkwood, *J. Chem. Phys*. **1937**, *5*, 479–491.
22. E. U. Condon, W. Altar, H. Eyring, *J. Chem. Phys*. **1937**, *5*, 753–775.
23. D. J. Caldwell, H. Eyring, *The Theory of Optical Activity*, Wiley-Interscience, New York, **1971**.
24. W. Moffitt, *J. Chem. Phys*. **1956**, *25*, 467–478.
25. I. Tinoco, Jr., *Theoretical Aspects of Optical Activity, Part Two: Polymers, Advances in Chemical Physics*, Vol. IV, Interscience Publishers, John Wiley & Sons, New York, **1962**, pp. 113–160.
26. S. F. Mason, B. J. Norman, *Chem. Phys. Lett*. **1968**, *2*, 22–24.
27. J. A. Schellman, *Accts. Chem. Res*. **1968**, *1*, 144–151.
28. S. F. Mason, *Molecular Optical Activity and the Chiral Discriminations*, Cambridge University Press, Cambridge, **1982**.
29. N. Harada, K. Nakanishi, *Circular Dichroic Spectroscopy—Exciton Coupling in Organic Stereochemistry*, University Science Books, Mill Valley, CA, **1983**.
30. R. W. Woody, *Monatshefte Chem*. **2005**, *136*, 347–366.
31. W. Moffitt, R. B. Woodward, A. Moscowitz, W. Klyne, C. Djerassi, *J. Am. Chem. Soc*. **1961**, *83*, 4013–4018.
32. A. Moscowitz, *Theoretical Aspects of Optical Activity, Part One: Small Molecules, Advances in Chemical Physics*, Vol. IV, Interscience Publishers, John Wiley & Sons, New York, **1962**, pp. 67–112.
33. J. A. Schellman, *J. Chem. Phys*. **1966**, *44*, 55–63.
34. W. Hug, G. Wagnière, *Tetrahedron* **1972**, *28*, 1241–1248; and references cited therein.
35. G. Wagnière, M. Iseli, R. Geiger, W. Gans, *Helv.Chim. Acta* **1977**, *60*, 1831–1844; M. Iseli, G. Wagnière, J. G. Brahms, S. Brahms, *Helv. Chim. Acta* **1979**, *62*, 921–931.
36. G. Snatzke, *Angew. Chem. Int. Ed*. **1979**, *18*, 363–377.
37. J. R. Escribano, L. D. Barron, *Mol. Phys*. **1988**, *65*, 327–344.
38. L. A. Nafie, *Annu. Rev. Phys. Chem*. **1997**, *48*, 357–386.

39. L. D. Barron, *Molecular Light Scattering and Optical Activity*, 2nd ed., Cambridge University Press, Cambridge, **2004**.
40. J. Costante, L. Hecht, P. L. Polavarapu, A. Collet, L. D. Barron, *Angew. Chem. Int. Ed*. **1997**, *36*, 885–887.
41. K. Ruud, T. Helgaker, P. Bouř, *J. Phys. Chem. A* **2002**, *106*, 7448–7455.
42. G. Zuber, W. Hug, *J. Phys. Chem. A* **2004**, *108*, 2108–2118.
43. F. Hund, *Z. Phys*. **1927**, *43*, 805–826.
44. R. A. Hegstrom, D. W. Rein, P. G. H. Sandars, *J. Chem. Phys*. **1980**, *73*, 2329–2341.
45. S. F. Mason, G. E. Tranter, *Chem. Phys. Lett*. **1983**, *94*, 34–37.
46. D. N. Stacey, *Physica Scripta* **1992**, *T40*, 15–22.
47. M. Quack, *Angew. Chem. Int. Ed*. **1989**, *28*, 571–586.
48. E. U. Condon, *Rev. Mod. Phys*. **1937**, *9*, 432–457.
49. H. Eyring, J. Walter, G. E. Kimball, *Quantum Chemistry*, John Wiley & Sons, New York, **1954**, Chapter 17.
50. M. Karplus, H. J. Kolker, *J. Chem. Phys*. **1963**, *39*, 1493–1506.
51. P. W. Langhoff, S. T. Epstein, M. Karplus, *Rev. Mod. Phys*. **1972**, *44*, 602–644.
52. N. Bloembergen, *Nonlinear Optics*, W. A. Benjamin, New York, **1965**.
53. Y. R. Shen, *The Principles of Nonlinear Optics*, John Wiley & Sons, New York, **1984**.
54. M. Sargent III, M. O. Scully, W. E. Lamb, Jr., *Laser Physics*, Addison-Wesley, Reading, MA, **1977**, Chapter II.
55. J. Fiutak, *Canad. J. Phys*. **1963**, *41*, 12–20.
56. A. D. Buckingham, *Advan. Chem. Phys*. **1967**, *12*, 107–142.
57. G. Wagnière, *Linear and Nonlinear Properties of Molecules*, VHCA/VCH, Weinheim, **1993**.
58. D. L. Andrews, T. Thirunamachandran, *J. Chem. Phys*. **1977**, *67*, 5026–5033; and references cited therein.
59. G. Wagnière, *J. Chem. Phys*. **1982**, *76*, 473–480; and references cited therein.
60. J. A. Giordmaine, *Phys. Rev*. **1965**, *138*, A1599–A1606.
61. G. Wagnière, *J. Chem. Phys*. **1982**, *77*, 2786–2792.
62. G. Wagnière, *Chem. Phys*. **1981**, *54*, 411–417.
63. J.-L. Oudar, C. Minot, B. A. Garetz, *J. Chem Phys*. **1982**, *76*, 2227–2237.
64. I. Tinoco, Jr., *J. Chem. Phys*. **1975**, *62*, 1006–1009.
65. L. D. Barron, A. D. Buckingham, *Annu. Rev. Phys. Chem*. **1975**, *26*, 381–396.
66. M. D. Levenson, *Introduction to Nonlinear Laser Spectroscopy*, Academic Press, New York, **1982**.
67. A. D. Buckingham, P. J. Stephens, *Annu. Rev. Phys. Chem*. **1966**, *17*, 399–432.
68. P. J. Stephens, W. Suëtaka, P. N. Schatz, *J. Chem. Phys*. **1966**, *44*, 4592–4602.
69. P. N. Schatz, A. J. McCaffery, *Q. Rev*. **1969**, *23*, 552–584.
70. G. Wagnière, A. Meier, *Chem. Phys. Lett*. **1982**, *93*, 78–81.
71. S. Woźniak, R. Zawodny, *Acta Phys. Pol*. **1982**, *A*61, 175–191.
72. L. D. Barron, J. Vrbancich, *Mol. Phys*. **1984**, *51*, 715–730.
73. G. Wagnière, *Chem Phys. Lett*. **1984**, *110*, 546–551.
74. G. L. J. A. Rikken, E. Raupach, *Nature* **1997**, *390*, 493–494.
75. P. Kleindienst, G. Wagnière, *Chem. Phys. Lett*. **1998**, *288*, 89–97.
76. L. D. Barron, *Chem. Soc. Rev*. **1986**, *15*, 189–223.
77. G. L. J. A. Rikken, J. Fölling, P. Wyder, *Phys. Rev. Lett*. **2001**, *87*, 236602,1–4.
78. C. Train, R. Gheorghe, V. Krstić, L.-M. Chamoreau, N. S. Ovanesyan, G. L. J. A. Rikken, M. Gruselle, M. Verdaguer, *Nat. Mat*. **2008**, *7*, 729–734.

79. L. D. Barron, *Nat. Mat*. **2008**, *7*, 691–692.
80. G. Wagnière, G. L. J. A. Rikken, *Chem. Phys. Lett*. **2009**, *481*, 166–168.
81. I. Tinoco, Jr., R. W. Woody, *J. Chem. Phys*. **1964**, *40*, 160–165.
82. D. Moore, I. Tinoco, Jr., *J. Chem. Phys*. **1980**, *72*, 3396–3400.
83. J. Zhou, J. Dong, B. Wang, T. Koschny, M. Kafesaki, C. M. Soukoulis, *Phys. Rev. B* **2009**, *79*, 121104(R),1–4.
84. C. S. Maierle, D. A. Lidar, R. A. Harris, *Phys. Rev. Lett*. **1998**, *81*, 5928–5931.

PART II

EXPERIMENTAL METHODS AND INSTRUMENTATION

2

MEASUREMENT OF THE CIRCULAR DICHROISM OF ELECTRONIC TRANSITIONS

John C. Sutherland

2.1. INTRODUCTION

2.1.1. Scope

This chapter describes the measurement of circular dichroism (CD) for absorption due to transitions between two distinct electronic states. This is distinguished from absorption of lower-energy photons, which are associated with changes of only the vibrational modes of the absorber and from the absorption of higher energy photons, which may result in ionizations. From the instrumental viewpoint, the chapter describes the measurement of CD that can be recorded using (a) a photomultiplier or avalanche photodiode to quantify the intensity of a light beam, (b) a photoelastic modulator to periodically alter the beam's polarization, and (c) a monochromator located between the light source and the modulator. Using either criterion, the focus is on the spectral domain spanning about a decade in wavelength (photon energy) from roughly 1.2 μm (1 eV ≈ 160 zJ) in the near infrared to 120 nm (10 eV ≈ 1.6 aJ) in the vacuum ultraviolet (VUV). In the near infrared, there is overlap between the domain of electronic and purely vibrational transitions, the use of photomultipliers or avalanche photodiodes versus other solid-state detectors, and the use of dispersive versus Fourier-transform spectrometers. There is also some overlap in the VUV with synchrotron beamlines that use arrays of magnets called "insertion devices" to cause the emitted synchrotron radiation to be elliptically polarized. To my knowledge, no single spectrometer spans the entire spectral domain discussed here, and the vast majority of laboratory instruments come nowhere close to either the upper or

Comprehensive Chiroptical Spectroscopy, Volume 1: Instrumentation, Methodologies, and Theoretical Simulations, First Edition. Edited by N. Berova, P. L. Polavarapu, K. Nakanishi, and R. W. Woody.
© 2012 John Wiley & Sons, Inc. Published 2012 by John Wiley & Sons, Inc.

lower limit. However, similar analytical approaches and types of instrumentation are employed throughout this spectral domain and thus are logically treated together.

The focus in this chapter is on the measurement of CD resulting from the inherent chirality of the absorbing system. There are several spectroscopic methods that are closely related in terms of science or instrumentation; some are treated in other chapters. These include magnetic circular dichroism (MCD), linear dichroism (LD) (Chapter 18), optical rotatory dispersion (ORD) (Chapter 11), fluorescence-detected circular dichroism (FDCD) (Chapter 3), circularly polarized luminescence (CPL) (Chapter 3) and fluorescence polarization anisotropy. A basic CD instrument of the type described here can be configured by temporary alterations of the sample compartment, an additional or repositioned detector, and modified electronics to perform many of the important experiments in the visible and UV regions [1]. These include unpolarized absorption and total fluorescence in addition to most of the experiments mentioned above. Except for absorption, such extensions of the basic technology will not be discussed. Other reviews of instrumentation related to CD have appeared, some containing information complementary to that included here [2–7].

2.1.2. Notation

In addition to standard mathematical notation, square brackets are used, when necessary, to indicate explicitly the argument of a function; braces are reserved for indicating lists, sets, and other collections; and parentheses are used exclusively to group terms. Vectors are denoted by an arrow above the symbol and average values by a bar in the same location. To avoid using more than one equals sign in a single mathematical expression, a right arrow ($\rightarrow$), indicates that the expression on the right is derived from the expression on the left. The same symbol connects a collection of equations on the left to one or more equations on the right. When more than one arrow is used, they are numbered and can be read "which becomes n."

2.2. THEORY

CD is a form of absorption spectroscopy, with the CD at a particular wavelength being defined as the difference in the absorbance of left- and right-circularly polarized light. Thus a brief review of absorbance is appropriate. CD is discussed first as an observable experimental parameter, which by convention can be expressed in several systems of units. Then, both CD and absorption are factored into extrinsic and intrinsic components.

2.2.1. Absorbance: Decadic and Eulerian

There is an inherent exponential relationship between the ratio of the intensity of a monochromatic light beam incident on a sample, I_0, and the transmitted intensity, I, as shown in the center panel of Figure 2.1. Optical intensity is the power per unit area (W/m^2) of the beam passing through an imaginary surface perpendicular to the propagation direction and the total power (W) in the beam must be determined by integration. For simplicity, a uniform beam of unit area will be assumed, so the intensity is effectively interchangeable with the total power of the beam. Because light, or more generally electromagnetic radiation, is a quantum phenomenon, the beam can also be characterized

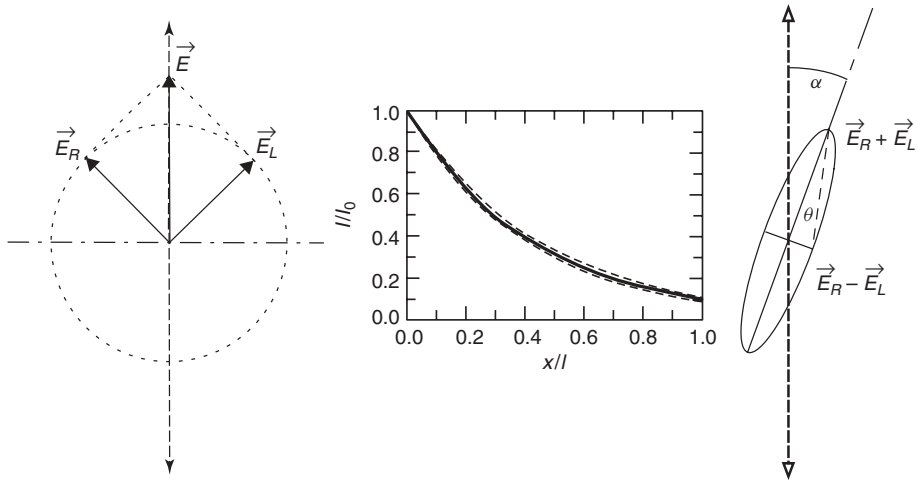

Figure 2.1. The center panel shows transmission as a function of position within a sample of thickness l. The average decadic absorbance for the sample is 1.0 and is indicated by the solid curve. The dashed curves are for the two circularly polarized components for which $\Delta A_{CD} = 0.1$, a value orders of magnitude larger than observed for most real samples. The left panel shows the decomposition of the electric vector of a vertically polarized beam into two circularly polarized components of equal magnitude and opposite directions of rotation. The right panel shows the effect of passing through the chiral absorbing sample on the components of the electric vector. Magnitudes are decreased due to absorption and the two circular components have different magnitudes due to CD, resulting in an elliptical trajectory for the electric vector. The major axis of the ellipse is twice the sum of the magnitudes of the left- and right-circularly polarized components, and the minor axis is twice their difference. The ellipticity, θ, is the angle whose tangent is the ratio of the semi-minor to the semi-major axes. The difference in refractive indices for the two circularly polarized components results in rotation of the major axis of the ellipse through an angle α with respect to the polarization of the incident beam. This is the parameter measured in ORD. The vector difference and angles shown are much greater than observed for real samples.

in terms of photons per unit time whenever convenient. The use of exponentials to relate intensities and absorption arises naturally from consideration of the interaction of the photons with the absorbing entities in a sample, as will be discussed further in Section 2.2.4. For now, the relationships between absorbance and incident and transmitted intensities at a particular wavelength are presented as definitions. In principal, any base could be used to express the exponential relationship, but only two (10 and e, also known as Euler's number) are of interest; they give rise to the decadic absorbance, A, and the Eulerian absorbance, a. They are related to the incident and transmitted monochromatic intensities as shown in (2.1), which also indicates the conventions used to express common and natural logarithms. Decadic absorbance is in widespread use in chemistry and biophysics and is more convenient for many purposes. However, Eulerian absorbance is more convenient for mathematical derivations. The simple relationship between the two absorbances, shown on the far right side of (2.1), also holds between the decadic and Eulerian forms of differential absorbances, such as CD. Thus, the measurement of CD will be analyzed using Eulerian absorbances and then translated to decadic absorbances in the final result. Absorbances are always defined for a particular wavelength, λ, but

the wavelength will be referenced explicitly only to indicate an extended spectrum, that is, $A[\lambda]$, or to indicate a particular wavelength of interest. Eulerian absorbance is also referred to as the Napierian absorbance in honor of John Napier (1550–1617), whose Naperian logarithms preceded the development of both common and natural logarithms.

$$\{I = I_0 10^{-A}, I = I_0 e^{-a}\} \rightarrow \left\{A = \log \frac{I_0}{I}, a = \ln \frac{I_0}{I}, a = A \ln 10\right\}. \tag{2.1}$$

2.2.2. Measurement of Circular Dichroism

In principal, we could measure the transmission of a sample at some defined wavelength using just right- or left-circularly polarized light, thereby obtaining the information required to compute the absorbance for each polarization component, and compute the CD by taking the difference. Indeed, some of the first measurements of the CD of electronic transitions of the heme ring in metalloproteins in the near infrared were recorded using a double-beam spectrophotometer with additional optical components that caused the sample and reference beams to be left- and right-circularly polarized, respectively [8]. In most cases, the differences in absorption are too small to be measured in such a direct fashion, but the concept provides a basis for showing how tiny differences in absorption can be measured using modulation techniques. Assume that the incident intensities of the right- and left-circularly polarized beams are identical and denoted by I_0 and that the transmitted components are denoted by I_R and I_L, respectively. The Eulerian absorbances for right- and left-circularly polarized light are related to I_R and I_L, as shown in the left set in (2.2). The ratio of the transmitted to incident intensity are shown as a function of relative position in the sample of thickness l within the center panel of Figure 2.1. The mean intensity and intensity difference due to CD are defined on the right of (2.2).

$$\{I_L = I_0 e^{-a_L}, I_R = I_0 e^{-a_R}\}, \qquad \left\{\overline{I} \equiv \frac{I_L + I_R}{2}, \Delta I_{CD} \equiv I_L - I_R\right\}. \tag{2.2}$$

The Eulerian CD, Δa_{CD}, and average absorbance are defined on the left side of (2.3) and rearranged on the right to give expressions for each polarized absorbance in terms of the mean absorbance and the CD.

$$\left\{\Delta a_{CD} \equiv a_L - a_R, \overline{a} \equiv \frac{a_L + a_R}{2}\right\} \rightarrow \left\{a_L = \overline{a} + \frac{\Delta a_{CD}}{2}, a_R = \overline{a} - \frac{\Delta a_{CD}}{2}\right\}. \tag{2.3}$$

In (2.4) the ratio of the differential and mean intensities is expressed using the definitions from the right side of (2.2). In step 1, this ratio is expanded in terms of the expressions given in the left side of (2.2) and the incident intensity, which is common to all of the terms of the ratio, is removed. In step 2, the absorbances for the left- and right-circularly polarized absorbances are replaced by the mean and differential values from the right side of (2.3) and the exponentials are factored, resulting in removal of the terms involving the mean absorbance. Rearranging slightly results in a ratio of exponentials recognized as a hyperbolic tangent, which is written as such in step 3 and then approximated by its argument. This is a good approximation for arguments less than about 0.1 and is

an excellent approximation as used here because the values of Δa_{CD} are rarely greater than 0.01.

$$\frac{\Delta I_{CD}}{\bar{I}} = 2\frac{I_L - I_R}{I_L + I_R} \underset{1}{\rightarrow} 2\frac{e^{-a_L} - e^{-a_R}}{e^{-a_L} + e^{-a_R}} \underset{2}{\rightarrow} -2\frac{e^{\frac{\Delta a_{CD}}{2}} - e^{-\frac{\Delta a_{CD}}{2}}}{e^{\frac{\Delta a_{CD}}{2}} + e^{-\frac{\Delta a_{CD}}{2}}} \underset{3}{\rightarrow}$$
$$-2\tanh\left[\frac{\Delta a_{CD}}{2}\right] \approx -\Delta a_{CD} \tag{2.4}$$

Equating the intensity ratio (far left) in (2.4) with the Eulerian CD (far right), converting to the decadic CD, and rearranging gives the simple expression for CD shown in (2.5). The negative sign results because an increase in absorbance yields a decrease in transmission.

$$\Delta A_{CD} = \frac{-1}{\ln 10}\frac{\Delta I_{CD}}{\bar{I}} \tag{2.5}$$

CD is thus obtained from the ratio of measured light intensities, as is absorption. However, in the case of CD, both intensities involve the beam transmitted through the same sample. Because absorption and CD are both obtained from the ratios of light intensities, it does not matter whether we measure these intensities in terms of photon flux or energy flux (power). It also follows that all absorption values are unitless, although they can be expressed on different scales—for example, decadic and Eulerian. There are other approaches that arrive at the same result [5]. As in absorption spectroscopy, a CD spectrum usually is reported as the difference between the CD of a sample containing the material or materials of interest and an otherwise identical "blank" sample without them.

2.2.3. Ellipticity

In the chemical and biochemical literature, CD is often expressed in ellipticity, θ, rather than absorbance, but there is a simple, linear relationship between these parameters. In the preceding discussion, light beams were characterized by their intensity. However, intensities are scalar quantities. The definition of ellipticity requires an analysis based on the behavior of the electric vector of a light beam, which is represented by $\vec{E}$. The intensity of a light beam is proportional to the square of the amplitude of the corresponding electric vector, that is, $I \propto |\vec{E}|^2$. The effect of a chiral absorbing medium on a beam of linearly polarized light is illustrated in the left and right panels of Figure 2.1, which shows the loci of the tip of the electric vector of a linearly polarized beam before and after passing through a chiral sample. According to the superposition principle [9], a linearly polarized light beam can be described as the sum of two circularly polarized beams with equal amplitudes and opposite directions of rotation. An absorbing chiral sample can attenuate one circular polarization more than the other and also shift their relative phases. The absorption differences cause the light emerging from the sample to be elliptically polarized, while the phase shift causes the major axis to be rotated through an angle α compared to the incident beam. This angle is the parameter measured in optical rotatory dispersion (ORD), the Kramers–Kronig transform of CD. The ellipticity, θ, in radians, is defined as the angle whose tangent is given by the ratio of the semi-minor to the semi-major axis of the ellipse. The semi-minor axis is the magnitude of the electric vector of the right-circularly polarized component minus that of the left circularly polarized component, while the semi-major axis is their sum. For typical applications, these

angles are much smaller that those shown, so θ can be approximated by its tangent. The tangent is computed using the square roots of the corresponding intensities, as shown in (2.6). The derivation proceeds much as described in (2.4). Note that the definition of ellipticity used here is right-minus-left, which effectively inserts a minus sign. Converting from radians to degrees and to decadic CD results in the expression shown in (2.7). Like all angles, ellipticity is inherently unitless, but, like absorbance, can be expressed using different scales—for example, radians and degrees.

$$\theta_{rad} \approx \tan\theta_{rad} = \frac{\sqrt{I_R}-\sqrt{I_L}}{\sqrt{I_R}+\sqrt{I_L}} \underset{1}{\rightarrow} \frac{e^{-\frac{a_R}{2}}-e^{-\frac{a_L}{2}}}{e^{-\frac{a_R}{2}}+e^{-\frac{a_L}{2}}} \underset{2}{\rightarrow} \frac{e^{\frac{\Delta a_{CD}}{4}}-e^{-\frac{\Delta a_{CD}}{4}}}{e^{\frac{\Delta a_{CD}}{4}}+e^{-\frac{\Delta a_{CD}}{4}}}$$
$$\underset{3}{\rightarrow} \tanh\left[\frac{\Delta a_{CD}}{4}\right] \approx \frac{\Delta a_{CD}}{4} \tag{2.6}$$

$$\theta_{deg} = \frac{360}{2\pi}\theta_{rad} \longrightarrow \frac{360}{2\pi}\ln 10\frac{\Delta A_{CD}}{4} \approx 32.98\Delta A_{CD} \tag{2.7}$$

2.2.4. Intrinsic Absorption and CD

Absorbance and CD are influenced both by the intrinsic properties of the material being studied and extrinsic properties such as the concentration of the absorbing entities and the distance the light beam travels through the sample. A major reason for recording the absorbance of a sample, as opposed to the fraction of the light transmitted or absorbed, is that absorbance facilitates separation of the contributions of the intrinsic and extrinsic properties. The same applies to circular dichroism. Consider a sample containing N identical absorbing entities per unit volume that are randomly located and oriented. For a sample consisting of small molecules, the absorbers are just the individual molecules. For macromolecules, however, the absorbers can be subunits, such as the peptide bonds of proteins or the bases of nucleic acids. Let σ represent the effective absorption cross section of each absorber. The adjective "effective" has two implications. The absorption is averaged over all equally probable orientations, so the effective absorption cross section is circular. Second, any photon intersecting this cross-sectional area will be absorbed, while photons not intersecting any such area will be transmitted. Consider a sample volume $\mathcal{A}l$, where $\mathcal{A}$ is a planar area perpendicular to a collimated photon beam moving along the positive x axis and l is the distance the beam travels through the sample. The intensity of the beam crossing the front face of the sample is I_0, the intensity exiting the rear surface is I_l, and the intensity at some intermediate position is $I[x]$. A thin slab of area $\mathcal{A}$ and depth Δx located a distance x from the front surface of the sample volume will contain $N\mathcal{A}\Delta x$ absorbers. As Δx approaches zero, it becomes impossible for any absorber to be behind any other. Thus the fraction of the incident beam absorbed in this incremental volume is equal to the fraction of the surface area occluded by the effective cross-sectional areas of the absorbers, leading to the difference equation on the left of (2.8). Integrating and taking antilogarithms results in the expression on the right of (2.8). Comparing this result with (2.1) results in the expression for the Eulerian absorption on the left in (2.9), which is a statement of the Beer–Lambert law and provides a tidy separation of the intrinsic properties of the absorber, which reside in σ, from the extrinsic properties of concentration and path length. An important intrinsic property is the dependence of the absorbance on wavelength/photon energy.

$$\Delta I = -\frac{\sigma N\mathcal{A}\Delta x}{\mathcal{A}} I \underset{1}{\rightarrow} \int_{I_0}^{I_l}\frac{dI}{I} = -\sigma N\int_0^l dx \underset{2}{\rightarrow} \ln\left[\frac{I_l}{I_0}\right] = -\sigma Nl \underset{3}{\rightarrow} I_l = I_0 e^{-\sigma Nl} \tag{2.8}$$

$$\{a = \sigma Nl,\ A = \varepsilon Cl\} \rightarrow \{\Delta a_{CD} = \Delta\sigma_{CD} Nl,\ \Delta A_{CD} = \Delta\varepsilon_{CD} Cl\} \tag{2.9}$$

Absorbance is unitless. Therefore, the units in which the cross section is expressed are determined by the units chosen for the concentration of absorbers and the pathlength. Using straightforward SI units, l would be in meters and N in absorbers per m^3, so the units of σ are m^2 per absorber. To avoid large numbers of zeros, cross sections are typically reported in nm^2. By (a decidedly non-SI) convention, the units used in the Beer–Lambert law for decadic absorption are cm for pathlength and moles/liter (M) for concentration. Thus, the units of the molar absorbance coefficient, ε, are M^{-1} cm^{-1} (or cm^2/m-mol). Defining analogous quantities for the left- and right-circularly polarized components and taking differences results in the expressions on the right-hand side of (2.9). The intrinsic counterpart of ellipticity is called molar ellipticity, denoted by $[\theta]$. By convention, the concentration of absorbers is defined as cm^2/d-mol, which has the effect of multiplying the numerical value by 100. Thus $[\theta]$ equals 3298 $\Delta\varepsilon_{CD}$. In addition to depending on wavelength, ε, $\Delta\varepsilon_{CD}$, and $[\theta]$ may be influenced by a variety of other factors such as temperature and pH. Converting from ΔA_{CD} to $\Delta\varepsilon_{CD}$ or $[\theta]$ requires knowledge of the product of the pathlength and the concentration of absorbers. They can be determined separately, but it is sometimes advantageous to obtain only their product—for example, when working with films. In such situations, the Cl product can be obtained from absorption measurements and then used to scale the CD spectrum. This is one of many situations in which simultaneous measurement of CD and absorption is desirable, because exactly the same beam size and position on the sample are assured.

2.2.4.1. CD–Absorbance Anisotropy Ratio and Multicomponent Spectra.

For a sample containing a single chiral species, the ratio of CD to absorbance is an intrinsic parameter that can be obtained without knowledge of optical pathlength, absorber concentration, or their product because $\Delta A_{CD}/A = \Delta\varepsilon_{CD}/\varepsilon = \Delta a_{CD}/a = \Delta\sigma_{CD}/\sigma$. This ratio, which is sometimes denoted by g, is the intrinsic chiral anisotropy at a particularly wavelength. Of course, such ratio spectra cannot be extended outside of the spectral region where the sample absorbs.

A major advantage of absorbance compared to transmission, is that at any wavelength, the observed absorbance is the sum of the absorbances of all of the individual components that may be present in a mixture, assuming they do not interact. The same is true for CD, except that some of the components can contribute negative values of the CD, that is, $\Delta A_{CD} = \sum_i \Delta A_{CD,i}$. The appearance of an isosbestic point in absorption spectra recorded during a titration of a sample suggests that the reaction is between just two states, initial and final. The observation of isodichroic points in the corresponding CD spectra support the same conclusion, and the observation of both is strong evidence that only two spectroscopically distinct species are present. In the case of multiple chiral species, the CD–absorbance anisotropy becomes characteristic of the mixture and independent of both optical path length and absolute concentrations of the components, as demonstrated in (2.10), where f_i is the fraction of the mixture associated with species i. For example, if the index i spans the various structural components of a protein (alpha helix, beta sheet, ...) and the decadic extinction and CD spectra of each structural are known, then the CD-absorption anisotropy spectrum provides enough data to determine the fractional component of each structural type [10–12]. This is attractive in studies of thin films of insoluble proteins but the sample may be partially oriented.

$$\frac{\Delta A_{CD}}{A} = \frac{\sum_i \Delta\varepsilon_{CD,i} C_i\ l}{\sum_i \varepsilon_i C_i\ l} \rightarrow \frac{\sum_i f_i \Delta\varepsilon_{CD,i}}{\sum_i f_i \varepsilon_i} \tag{2.10}$$

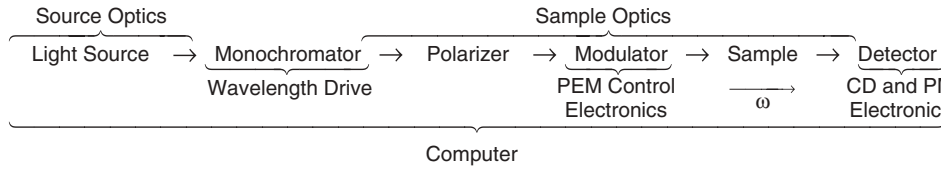

Figure 2.2. Schematic diagram showing the conceptual relationships of the typical subsystems found in dichrometers operating in the UV, visible, and near infrared. The arrows indicate the path of travel of the light beam and the electronic signals. Configurations of optical components typical of three classes of dichrometers are shown in Figures 2.4, 2.5, and 2.7. The electronic subsystems are shown in greater detail in Figure 2.9. Auxiliary subsystems (e.g., sample temperature controllers) are not shown, although frequently present in modern instruments. In some laboratory instruments, the function of the polarizer is incorporated with the internal components of the monochromator. In some synchrotron radiation CD (SRCD) instruments, the source optics and monochromator are tightly integrated with the synchrotron storage ring.

2.2.5. Components of a Conceptual CD Spectrometer

CD spectrometers operating in the spectral range characteristic of electronic transitions can be considered as composed of a dozen subsystems, as shown schematically in Figure 2.2. With the exceptions of the polarization modulator and electronics, the required components are found in a wide variety of instruments. Thus, the operation of these two subsystems will be discussed in detail, while criteria for the selection of the others will be presented in connection with the description of specific classes of dichrometers. For now, it suffices to say that the light source produces a broad spectrum, typically spanning the IR, visible, and UV. The source optics direct as much of the emitted light as possible into the monochromator, which transmits only a narrow spectral band. The sample optics ensure that the light beam from the monochromator passes through the linear polarizer (if present), polarization modulator, and sample before impinging on the light detector. However, the various components must be chosen to be compatible with one another, particularly in regard to the cone of radiation they can accept and the spectral range over which the instrument must perform.

2.2.5.1. Three Classes of Practical CD Spectrometers Based on Photoelastic Modulators. In current dispersive CD spectrometers, a beam of monochromatic, linearly polarized light is incident on a photoelastic modulator (PEM). The PEM must be oriented with its stress axis making an angle of 45° with respect to the polarization of the incident optical beam, as shown in the elevation view of Figure 2.3. This orientation of the PEM is compatible with incident light that is either vertically or horizontally polarized. The plan view of the PEM, shown in this figure, also appears in each subsequent instrument diagram. The operation of the PEM is discussed in Section 2.2.5.2.

Schematic diagrams of three classes of CD spectrometers are shown in the Figures 2.4, 2.5, and 2.7. Figure 2.4 is typical of instruments using a xenon arc light source and single-grating monochromator. Such instruments are best suited for studies in the near UV, visible, and near IR and can easily be adapted to function as a fluorometer, hence providing multifunctional capabilities for a modest investment. For operation in the visible and near infrared, tungsten–halogen light sources can also be considered. Restricting the spectral range to wavelengths greater than about 240 nm makes possible the use of calcite polarizers and thus monochromators with lower focal ratios, which

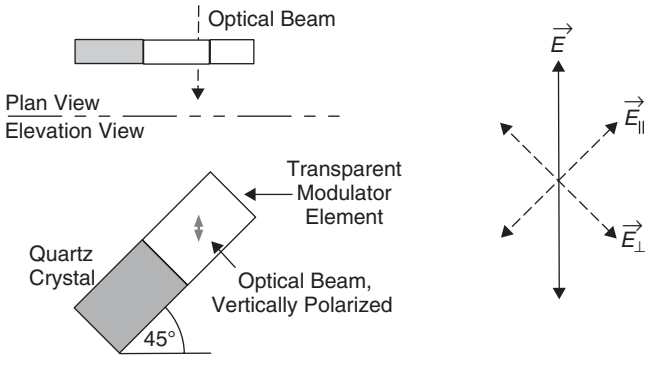

Figure 2.3. A beam of linearly polarized light passes through the optical element of a PEM, the principal axes of which are oriented at 45° with respect to the plane of polarization of the light beam. The orientation of the PEM shown is appropriate for either a vertically or a horizontally polarized incident beam. The electric vector for a vertically polarized incident beam is shown along with its decomposition into in-phase orthogonal components that are parallel and perpendicular to the stress axis of the PEM.

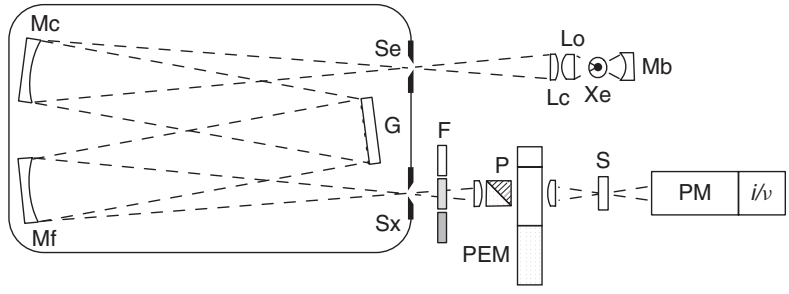

Figure 2.4. Schematic plan view of a simple CD spectrometer based on a high-pressure xenon arc, Xe; a single grating, G, Czerny–Turner monochromator; interchangeable order-sorting filters, F; crystal polarizer, P; photoelastic modulator, PEM; sample, S; and photomultiplier detector, PM, with integrated current-to-voltage converter, i/v. The source optics consist of an objective lens, Lo, that collects a large solid angle; a condensing lens, Lc, that focuses an image of the source onto the plane of the entrance slit, Se, of the monochromator; and a spherical mirror, Mb, behind the source, that increases the intensity of light reaching the monochromator by a factor of typically 1.2 to 1.5. The lamp housing and sample compartment enclosures are not shown.

deliver more light to the sample. Gratings are usually interchangeable, so it is easy to optimize performance of the monochromator for different spectral ranges. Most of the commercially built CD instruments currently in use employ a xenon arc light source combined with a double-prism monochromator, as shown in Figure 2.5. They permit operation into the far UV and are responsible for most published studies of protein secondary structure. Some use external polarizers. Others use a crystalline quartz prism or prisms to integrate the function of the polarizer with the monochromator.

That xenon arcs are the overwhelming choice for the light source for laboratory-based instruments reflects their superior radiance across much of the spectrum. There are, however, two negative features that are demonstrated by the spectrum shown in Figure 2.6. The precipitous drop in intensity for wavelengths less than 300 nm, which continues down to zero at about 160 nm, limits CD studies of protein secondary structure. In addition, the sharp spectral lines between 450 and 500 nm and also above 600 nm causes noise in CD instruments that acquire data while scanning the monochromator. The figure also shows that the output degrades slowly with time of operation, so xenon arcs must be replaced periodically.

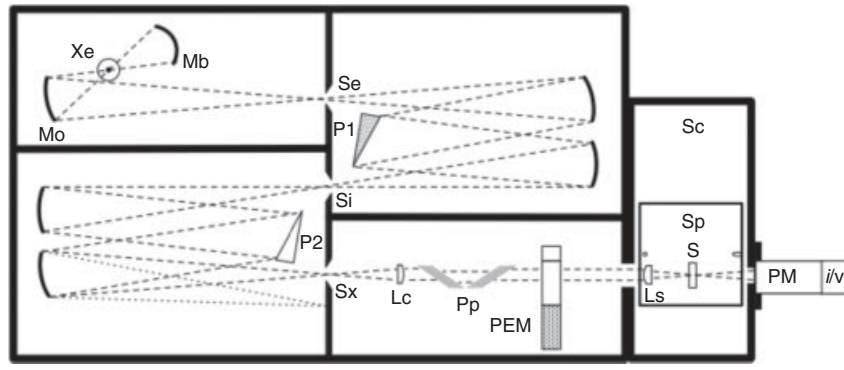

Figure 2.5. Schematic plan view of a laboratory dichrometer with double Czerny–Turner prism monochromators. Light from a high-pressure xenon arc, Xe, is focused on the entrance slit of the first monochromator, Se, by an off-axis ellipsoidal objective mirror, Mo. A spherical mirror, Mb, reflects light back through the xenon arc, increasing the light entering the monochromator by roughly 50%. In a Czerny–Turner monochromator, a spherical collimating mirror directs the incident beam onto the prism, P1, and a second spherical mirror focuses the dispersed spectrum onto the exit plane. The prism is rotated about a vertical axis, thus determining which wavelength of the dispersed spectrum is centered on the intermediate slit, Si. In this design, P1 is made of crystalline quartz, indicated by the stippling, so that two wavelengths of the dispersed spectrum enter the second monochromator; one is horizontally and the other vertically polarized. The second prism, P2, is of amorphous quartz and the orientation of the prism is chosen such that the horizontally polarized component (— — —) is focused on the exit slit, Sx, while the vertically polarized component (- - -) is blocked. A lens, Lc, approximately collimates the beam, which passes through a pile-of-plates polarizer, Pp; photoelastic modulator, PEM; and sample, S, before reaching the photomultiplier detector, PM. Pp is also referred to as a filter because the unwanted polarization that it removes is also predominately the unwanted second wavelength that enters the second-stage monochromator. A current-to-voltage converter, *i/v*, can be located within the PM housing. The sample is mounted on a platform, Sp, that is kinematically located in the sample compartment, Sc, which is bolted to the body of the dichrometer. Kinematically positioned sample platforms permit facile interchange of sample holders and can be used to enable a number of different experiments in addition to CD, including MCD, LD, ORD, FDCD, and fluorescence polarization anisotropy [1]. A lens, Ls, can be added to focus the beam to reduce the quantity of sample required or in LD, MCD, and fluorescence experiments [13, 14].

The third class of CD spectrometers, based on synchrotron radiation sources, first appeared in 1980 [15]. The spectrum generated by a synchrotron source increases with decreasing wavelength, as indicated in Figure 2.6. While heterogeneous in design, SRCD beamlines typically employ an ultra-high vacuum (UHV) single monochromator with a toroidal, ellipsoidal or parabolic holographic diffraction grating and a UHV window between the monochromator and the sample chamber, as shown in Figure 2.7. Windows and the PEM optical element are made of CaF_2 or LiF, while a polarizer, if required, is made of MgF_2. Exploitation of this extended range for studies of proteins has been limited by the high absorbance of water below 170 nm, but development of methods for studying hydrated films offers hope of progress in this area. CD measurements of a myoglobin film shown in Figure 2.8 demonstrate spectral features extending to the limits of the measurement. At present there are fewer than a dozen SRCD instruments

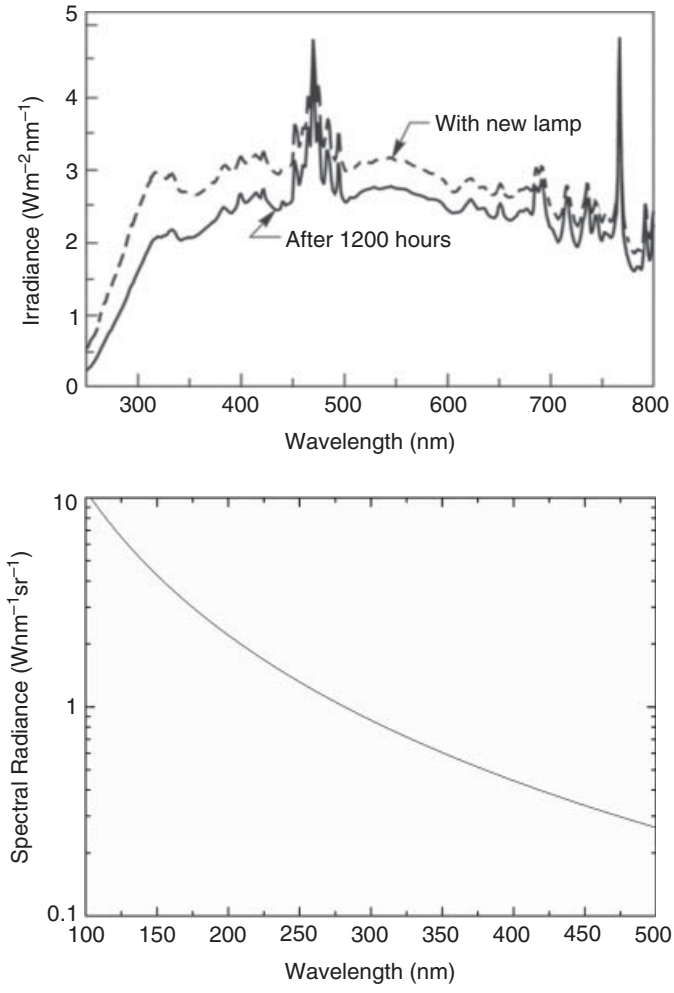

Figure 2.6. Upper: Spectral irradiance from a 300-W high-pressure xenon arcs on a surface located 500 mm from the source. An irradiance of 1 W m^{-2} nm^{-1} at this distance corresponds to a spectral radiance of 2.5 W nm^{-1} sr^{-1}, where it is assumed that the arc is a point source. Figure courtesy of the Newport Corporation's Oriel Instruments Group. Lower: Spectral radiance from port U11 of the National Synchrotron Light Source, also taken as a point source. Data computed for horizontal and vertical acceptances of 55 and 10 mrad, 1-nm band pass, and a stored electron beam of 500 mA, one-half of the maximum injection current. Data in the two figures cannot be compared directly because radiation from a larger solid angle can be collected from the xenon source, while for the synchrotron radiation, the solid angle is fixed by the design of the beamline. On the other hand, it is usually not possible to get all of the collected light from the xenon arc through the entrance slit of a monochromator. For the synchrotron instrument, in contrast, the entire photon beam is generated inside the monochromator, because the electron beam defines the entrance slit. The critical difference between the two sources is that in the far and vacuum UV, output from the xenon arc is decreasing rapidly, while the beam intensity from the synchrotron is increasing faster than exponentially.

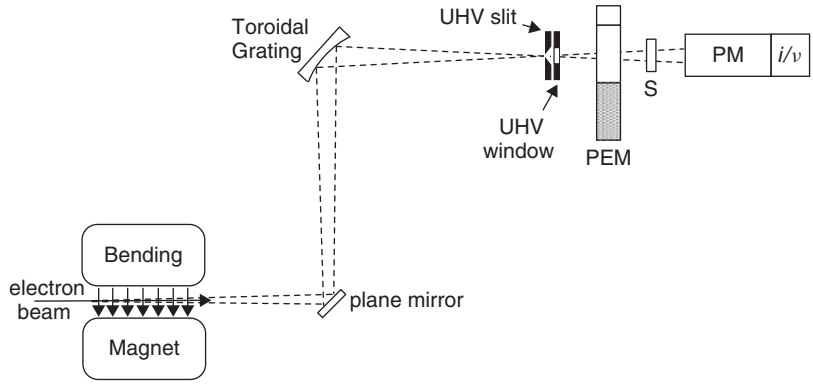

Figure 2.7. Schematic elevation view of a synchrotron-source CD spectrometer or ''beamline.'' A beam of photons generated by relativistic electrons passing through the field of a bending magnet is reflected by a plane mirror inclined as an angle of 45° to deflect the beam vertically onto an off-axis ellipsoidal or toroidal diffraction grating. The mirror may have to be water-cooled. The electron beam is deflected out of the plane of the figure by the magnetic field. In this design, the electron beam serves as the entrance aperture of the monochromator. A series of bending magnets cause the electrons to travel in a closed horizontal loop around the synchrotron storage ring. The electron beam and all of the components of the optical system up to a window are within a UHV vacuum system, which is not shown. The grating disperses the ''white'' synchrotron spectrum in a vertical plane, and a horizontal slit transmits the selected wave band, which then passes through a PEM and sample before impinging on the cathode window of a photomultiplier. The UHV window is made of CaF_2 or LiF, as is the optical element of the PEM. A MgF_2 polarizer may be placed before the PEM to ensure complete polarization of the beam. The components downstream of the window are contained in a housing which may be evacuable, permitting operation to below 130 nm. In some installations, a nonvacuum housing is used, but it must be purged with dry N_2, which permits CD measurements to below 150 nm.

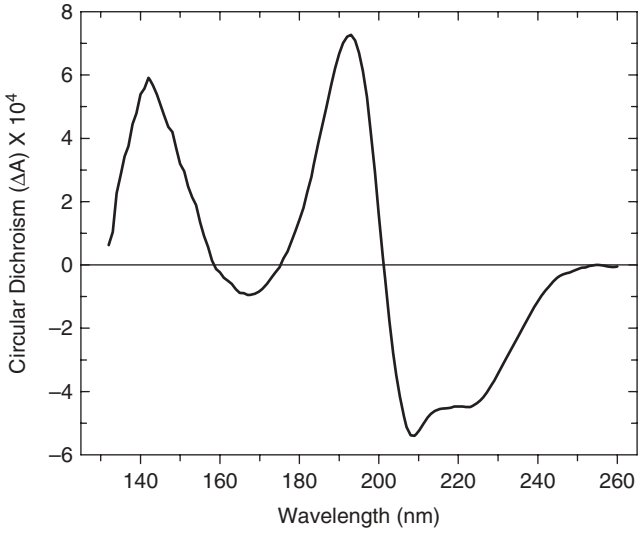

Figure 2.8. CD as a function of wavelength from 132 to 260 nm for a film of myoglobin on a CaF_2 substrate. A similar CaF_2 plate was used for the blank spectrum, which was subtracted before the data were plotted. Data were recorded on beamline U11 at the National Synchrotron Light Source at Brookhaven National Laboratory with a lock-in amplifier analog time constant of 1 s, digital integration period of 4 s, and spectral separation of one reading per nanometer. This spectrum is extended by almost 40 nm compared to what can be achieved using SRCD and aqueous samples, and 50 nm compared to conventional-source instruments.

in the world, but most are operated as user facilities and are thus available to many scientists. A recent review focused on (a) the methods required to exploit SRCD in protein characterization and (b) results obtained to date [16].

2.2.5.2. Photoelastic Modulator Operation. The analysis leading to (2.5) assumed that the absorbance of left- and right-circularly polarized light could be measured separately. To achieve the sensitivity required in practice, all modern CD spectrometers employ a polarization modulator, which makes the analysis slightly more complicated. The first generation of dichrometers employed Pockels cells to modulate the polarization of a linearly polarized photon beam [17–19]. These modulators have the advantage of being able to generate arbitrary sequences of polarization states, but suffered from severe limitations including: poor transmission in the VUV, high driving voltages that could damage the modulator at long wavelengths, and the need for near laser-like collimation to avoid the generation of multiple polarization states. The invention of the photoelastic modulator (PEM) [20–22] extended the spectral range of dichrometers into both the VUV and infrared while greatly increasing the angular acceptance of the modulator and thus the optical power reaching the sample. PEMs quickly became the device of choice for all dichrometers. However, they are resonant devices and thus operate at a fixed frequency. In addition, the degree of polarization produced and the driving voltage required to produce a given result at a particular wavelength are more involved than the corresponding situation for Pockels cells and can impact the operation of dichrometers and the interpretation of recorded spectra. Thus, consideration of the operation of PEMs is necessary for understanding the operation of all current CD instruments.

For PEMs operating in the spectral range addressed in this chapter, the device usually consists of a rectangular slab of some transparent, isotropic material bonded to a quartz crystal that acts as the frequency-determining element in an electronic oscillator circuit. Amorphous silica (synthetic quartz) is the material of choice for all instruments that do not need to operate at wavelengths less than about 165 nm; penetration further into the VUV requires either CaF_2 or LiF optical elements. The quartz crystal and the optical element bonded to it are cut to resonate at an ultrasonic frequency, typically near 50 kHz. A beam of linearly polarized light passes through the optical element of the PEM, the principal axes of which are oriented at 45° with respect to the plane of polarization of the incident light beam, as shown in Figure 2.3.

The quartz crystal transducer functions as the frequency-determining element of an electronic oscillator circuit, which is not shown in the figure. The alternating current flowing in this circuit causes the crystal to mechanically vibrate at the frequency of the oscillator due to the piezoelectric effect, inducing similar vibrations in the transparent optical element. As the optical element vibrates, the refractive index for the direction parallel to the long axis of the optical elements changes with respect to the refractive index for the orthogonal direction, thereby shifting the phase of the two components with respect to each other sinusoidally in time.

Suppose that for a particular wavelength of light, λ, the maximum difference in the refractive index for the parallel and perpendicular components is $\Delta n = n_{\parallel} - n_{\perp}$ and the thickness of the optical element is d. The instantaneous phase shift, $\delta[t]$, between the two orthogonal beams that emerge from the PEM is given by $\delta[t] = \frac{2\pi d\,\Delta n[t]}{\lambda} \underset{1}{\longrightarrow} \frac{2\pi dCS_0}{\lambda} \sin\omega t \underset{2}{\longrightarrow} \delta_0 \sin\omega t$, where C is the stress optical constant of the optical element, S_0 is the amplitude of the stress applied to the optical element by the quartz transducer, and ω is the angular frequency of the oscillations of the transducer, that is $\omega = 2\pi f$, where f is

the frequency of the PEM. When the instantaneous phase shift is zero, the light emerging from the modulator will have the came polarization as the incident beam. However, when the phase shift is $\pi/4$, the exiting beam will be circularly polarized. The instantaneous intensities of the exiting beam can therefore be represented as the sum of right- and left-circularly polarized beams, as shown in (2.11). The sine-of-a-sine term is expanded in terms of Bessel functions of the first kind as shown in (2.12). In subsequent discussions, all of the higher-order odd harmonics (3ω, 5ω, ...) are ignored, not because they are necessarily small but because measurement of their amplitudes is not required.

$$I_0[t] = I_{0,L}[t] + I_{0,R}[t], \quad \text{where } I_{0,L/R}[t] = \frac{I_0}{2}(1 \pm \sin\delta) \rightarrow \frac{I_0}{2}(1 \pm \sin[\delta_0 \sin\omega t]), \tag{2.11}$$

$$I_{0,L/R} = \frac{I_0}{2}(1 \pm 2J_1[\delta_0]\sin\omega t \pm 2J_3[\delta_0]\sin 3\omega t + \ldots). \tag{2.12}$$

Passage of the light beam through the sample attenuates both polarizations according to the expressions shown in (2.13). Applying the relevant expressions to the incident intensities shown in (2.12) results in the expression for the total time-dependent intensity shown in (2.13). In practical instruments, these intensities are converted to voltages, as described in Section 2.2.6.1.

$$\begin{aligned} I[t] = I_{0,L}e^{-a_L} + I_{0,R}e^{-a_R} \rightarrow \frac{I_0 e^{-\overline{a}}}{2}\Big(e^{\frac{\Delta a_{CD}}{2}} + e^{-\frac{\Delta a_{CD}}{2}} \\ -2J_1[\delta_0]\left(e^{\frac{\Delta a_{CD}}{2}} - e^{-\frac{\Delta a_{CD}}{2}}\right)\sin\omega t + \ldots\Big). \end{aligned} \tag{2.13}$$

2.2.6. Electronics and Computer Systems

2.2.6.1. Conversion of the Optical Beam Power to a Voltage. Some descriptions of the measurement of absorption and CD use the same symbols to describe the optical beam and the subsequent processing of the signals after detection. However, understanding the operation of a spectrometer and the source of potential artifacts is facilitated by distinguishing between the optical signals that exist before the detector, assumed to be a photomultiplier integrated with a current-to-voltage converter, and the electrical signals (voltages) that are processed downstream of the detector. This analysis is also necessary to understand the simultaneous measurement of CD and absorption spectra. Suppose that $v[t]$ represents the instantaneous voltage appearing at the output of the detector when the photocathode is illuminated with monochromatic light of wavelength λ and intensity $I[t,\lambda]$, which corresponds to the parameter on the left in (2.13), although the wavelength was not indicated explicitly there. Technically, this is the power in the optical beam, and not intensity, so the units are watts (W). Alternatively, the beam can be characterized in terms of light quanta, in which case the units are photons/s. The instantaneous signal current produced by the photomultiplier can be described as the product of the incident beam power, the sensitivity of the device at the particular wavelength, $\phi[\lambda]$ (amps/watt or amps/photon), and the internal gain of the photomultiplier, $G_{PM}[V]$ (dimensionless), which is controlled by the high voltage (or high tension), V, applied between the photocathode and anode. The value of $\phi[\lambda]$ includes both the sensitivity of the photocathode and the transmission of the window through which the photon beam must pass to reach the photocathode.

Various techniques are used to ensure that the signal generated by a modern photomultiplier are directly proportional to the power of the incident optical beam [23]. The current from the photomultiplier is converted to a voltage by the current-to-voltage converter, frequently integrated within the housing containing the photomultiplier and characterized by a gain, $G_{i/v}$ (volts/amp). Thus, the instantaneous signal voltage from the detector assembly is related to the instantaneous power in the photon beam incident on the photomultiplier as indicated in (2.14). The gain of a photomultiplier is an approximately exponential function of the applied high voltage. Increasing V by a few hundred volts can increase the gain by several orders of magnitude, a property critical to the operation of most CD spectrometers. The gain of the current-to-voltage converter can be adjusted in some instruments.

$$v[t] = G_{i/v} G_{PM}[V]\phi[\lambda] I[t, \lambda]. \tag{2.14}$$

2.2.6.2. Measurement of Circular Dichroism. The output of the detector assembly can also be viewed as the sum of a time-average signal, $\overline{v}$, plus very small sinusoidal signals at the frequency of the PEM, ω, and its harmonics ($2\omega, 3\omega, \ldots$). Measurement of CD requires determination of the amplitude of the fundamental, while experiments involving linear polarizations require determination of the amplitude of the first harmonic term. The amplitude of the signal at angular frequency ω is obtained with a phase-sensitive detector (PSD), also referred to as a lock-in amplifier. The output of the PSD is a steady or "dc" voltage, Δv_ω, equal to the amplitude of the sinusoidal signal at frequency ω times the gain of the PSD, G_{PSD}, as shown schematically in Figure 2.9. The other critical feature of the electronics shown in Figure 2.9 is a comparator circuit that controls the high voltage applied to the PM, so that the time-average output voltage is always equal to a reference value, $\overline{v}_C$, which can be adjusted so that the output of the lock-in is easily translated into absorbance or ellipticity. One way of setting the calibration of the CD scale of the dichrometer is by adjusting the value of $\overline{v}_C$. Combining the definitions of Δv_ω and $\overline{v}_C$ with the expressions in (2.13) and (2.14), rearranging, and simplifying will result in the expression for the decadic CD in terms of these instrumental parameters as shown in (2.15). In arriving at this result, the equality of the hyperbolic tangent and its argument was invoked, as was the assumption that the gain of the photomultiplier is independent of frequency, that is, G_{PM} is the same for both the static signals and those modulated at frequency ω, but the gain of the current-to-voltage converter may not be. The expressions in (2.15) demonstrate that a simple relationship can be established between CD and voltages that fall in some conveniently measured range such as ± 10 V. Implications of these results as regards the calibration of CD spectrometers are discussed in Section 2.3.1.

$$\Delta A_{CD} = \frac{-\Delta v_{CD}}{G_{PSD} \ln 10 J_1[\delta_0]\overline{v}} \frac{G_{i/v}[\omega]}{G_{i/v}[0]}. \tag{2.15}$$

Contrary to popular belief and ubiquitous product literature, in a CD experiment the phase amplitude of the PEM need not be set for exactly quarter-wave retardation, that is, $\delta_0 = \pi/4$ (90°). Indeed, the maximum value of J_1, and hence the largest CD signal, ΔI_{CD}, occurs for $\delta_0 \approx 0.587\pi$ (106°) [20]; but a wide range of values are acceptable, provided that the same value is maintained at all wavelengths. This is in contrast to linear dichroism, where δ_0 must be maintained at the "magic phase" of 0.765π (138°) to avoid an artifact that distorts large LD signals [1].

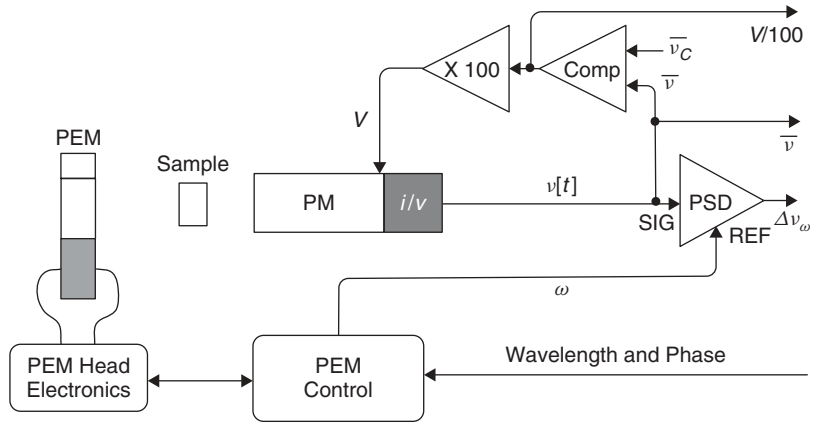

Figure 2.9. Electronic components used to extract the CD and absorption signals from the voltages produced by a photomultiplier, PM, detector and the circuit that controls the voltage, V, applied to it. The instantaneous voltage, $v[t]$, from the current-to-voltage converter, i/v, is connected to the signal input of a phase-sensitive detector, PSD, and to the input of a comparator circuit, Comp, and also read by the control computer. The two latter connections respond only to the time-average value of the signal voltage, $\overline{v}$. The PEM controller supplies a reference signal to the PSD, the output of which is a dc voltage, Δv_ω, proportional to the amplitude of the $\sin \omega t$ term in $v[t]$. The function of the comparator is to generate a signal that programs the voltage applied to the PM to maintain the time-average output signal at a preset calibration value, $\overline{v}_C$. This programming signal, or some other parameter that reflects the value of V, should also be recorded as part of a CD measurement.

2.2.6.3. An Alternate Approach to Extracting the CD Signal. In 1994, Richard DeSa introduced an alternate method of extracting CD signals from the instantaneous voltage signal that does not depend on a normal lock-in amplifier. Instead, both the instantaneous voltage signal, $v[t]$, from the detector and the reference signal from the PEM controller are digitized directly by a fast, high-resolution analog-to-digital converter located in the backplane of a control computer. The digital data stream is analyzed in real time to extract the time-average signal and the amplitude of the signal at the frequency of the PEM. CD instruments using this approach are marketed by OLIS, Inc., Bogart, Georgia, USA. While this system has not been described in the refereed literature, it has been discussed briefly in review articles [1, 5]. Product literature indicates that the design eliminates the need for external calibrations of the CD scale. Another unusual feature of DeSa's design is an operating mode in which both the ordinary and extraordinary beams from a Rochon polarizer pass through a single PEM and then through two sample cells before impinging on two photomultipliers. The CD from each beam is then analyzed as described above. The result is that two CD measurements can be performed independently and simultaneously. However, this capability should not be used to record the CD of a sample and its corresponding blank at the same time, because this would be comparable to measuring the two spectra in separate instruments with separate instrumental baselines.

2.2.6.4. Spectrometer Computer Systems. All modern dichrometers are controlled by and transfer data to a dedicated computer, and they can be classified based on the relationship between the optical and electronic components and the computer system.

Weakly coupled systems have most of the functionality of the instrument, including all of the analog electronics, integrated with the optical components. This integrated optical-electronics package is connected to a computer by a standard interface such as RS-232 or USB. Such instruments are often the descendants of stand-alone dichrometers, where the user interface was a collection of switches, knobs, and dials on the instrument and spectra were recorded on chart paper. The negative aspects of this arrangement are higher costs of construction because many components are specific for the particular brand of instrument, thus forfeiting the benefits of economies of scale. At the other end of the spectrum are instruments in which most of the electronics are integrated into the computer. This became a popular approach in the 1990s because standard input/output boards can be adapted to a specific purpose through software, thus making use of hardware components that are produced in higher volume. While software is expensive to develop, it is essentially free to "manufacture." The negative aspect of this approach is that the service life of the dichrometer tends to be determined by that of the computer system, which is usually much shorter than that of dedicated hardware. The use of proprietary software also makes it difficult to have an instrument serviced by the end user or a third party. Finally, laboratory-built instruments, including most synchrotron-source dichrometers, use a component model in which the optical and electronic components are purchased separately and integrated with a computer system. Initial costs are high, particularly if the costs of the personnel involved in construction are included. However, component instruments are essentially immortal, especially if control software is designed around a virtual instrument, rather than the particular components used in construction. Thus the electronic components and computer, which have a finite service life, can be replaced with improved models, while the optical components can be maintained indefinitely. The cost of the SRCD end station tends to be a small fraction of the cost of the complete beamline, particularly when the prorated cost of the entire facility is included.

Some instrument control computers are connected to a local area network (LAN), which may be connected to the internet, thus creating the possibility of additional layers of computing involved in the acquisition, storage, and analysis of CD and related data [24]. Such arrangements facilitate archival storage and analysis of experimental data while keeping the spectrometer control computer free to acquire new data. Recent additions to the computerized processing of CD data of proteins include the analysis of secondary structure over the internet using a suite of programs [25] and the Protein Circular Dichroism Data Base (PCDDB) [26], where analyzed spectra and their accompanying metadata can be deposited and made available to the broader community.

2.2.7. Simultaneous Measurement of Absorption

The operation of the high-voltage servo system makes it possible to record the information needed to obtain the (unpolarized) absorption spectrum of a sample at the same time the CD is recorded [27]. Two scans are required and they are the same sample and blank required for CD. The function of the comparator circuit is to adjust the voltage supplied to the PM such that the time-average current from the detector remains constant. Suppose we let A_S and A_B represent the time-average absorptions of the sample and blank solutions, respectively. Both, of course, are functions of wavelength. Suppose that, for each wavelength in the scans of the sample and the blank, the voltages applied to the PM are recorded (i.e., V_S and V_B), along with the intensities of the incident beam, $I_{0,S}$ and $I_{0,B}$, at the time the CD of both sample and blank are recorded. The servo loop ensures that the time-average signal currents are the same for both, so we can equate

them, as shown in (2.16). After rearrangement, the decadic absorption of the sample above background is found to be the difference in the corresponding pseudo absorptions, which are defined as the sum of the log of the PM gain plus the log of the intensity of the incident intensity recorded at each wavelength at the time of the measurement. Because these expressions involve the differences in logarithms, only relative values of the gains and incident intensities are required. If the light source is known to be stable in time, the intensity terms can be ignored. However, they cannot be ignored in current synchrotron spectrometers, because the intensity of the incident light at each wavelength decreases slowly as the circulating beam of electrons in the storage ring is depleted. The log of the gain of most photomultipliers is not quite a linear function of the applied high voltage, but can be represented by a second-order polynomial, that is, $\log[G_{PM}[V]] = c_1V + c_2V^2$. Performing this calibration requires the ability to control the high-voltage circuit independent of the servo circuit [6, 27]. There may be small differences between individual PM of the same type, so a calibration should be performed for each tube. The analysis requires that nothing other than the sample and the recorded intensities should change between the recording of the two pseudo-absorbances. This analysis was developed for and tested on CD spectrometers with fixed slits and may not be applicable to CD instruments in which the width of monochromator slits are changed during a spectral scan.

$$G_{PM}[V_S]I_{0,S}10^{-A_S} = G_{PM}[V_B]I_{0,B}10^{-A_B}$$
$$\underset{1}{\rightarrow} A_S - A_B = \log[G_{PM}[V_S]] + \log[I_{0,S}] - (\log[G_{PM}[V_B]] + \log[I_{0,B}]) \underset{2}{\rightarrow} pA_S - pA_B. \tag{2.16}$$

2.2.8. Selection of Optical Components

The selection of compatible optical components for a dichrometer is strongly influenced by the conservation of a parameter called étendue, which for a small light source or image is the product of the area of the source/image times the solid angle subtended by the conjugate aperture [28]. As light passes through a perfect optical system, étendue remains constant. It can never decrease, but can increase in a system containing imperfect optical components—for example, a lens that produces a poor image of its source. One complication in analyzing an optical system is that it can be difficult to determine solid angles. However, for an optical system involving circular apertures, such as lenses and mirrors, there is a simple relationship between the solid angle, Ω, subtended by the aperture and the corresponding and easily measured $f\#$, the ratio of the distance of the plane of the aperture from the source divided by the radius of the aperture [1], as shown in (2.17). For roughly square apertures, an approximate solid angle can be obtained by using the radius of the circle with the same area as the aperture, while for the very small solid angles characteristic of synchrotron radiation beamlines, the product of the divergence of the optical beam in the horizontal and vertical planes gives an excellent approximation of the solid angle.

$$\Omega = 2\pi\left(1 - \frac{1}{\sqrt{1 - (2f\#)^{-2}}}\right). \tag{2.17}$$

The design considerations inherent in the selection of optical components are illustrated by considering those shown in Figure 2.4. The radiation pattern for a xenon arc is approximately omnidirectional. Thus increasing the solid angle subtended by

the objective lens, Lo, increases the number of photons entering the optical train proportionately. However, the number of photons entering the monochromator peaks when the diameter of the circular image of the source equals the height of the entrance slit. Moving Lo closer to the source increases the number of photons collected, but they do not enter the monochromator. Even in the optimum configuration, most of the photons collected from the source do not enter the monochromator. Using a more powerful condenser lens, Lc, reduces the size of the image of the source on the entrance slit so more photons enter the monochromator, but if the $f\#$ of Lc with respect to the slit Se is less than that of the collimating mirror, Mc, with respect to Se, the additional photons will not reach the grating and thus are of no value. Actually, the excess photons are detrimental in that they can contribute to the level of stray light reaching the detector and are thus to be avoided. One of the excellent features of photoelastic modulators is that they have a large acceptance angle and thus, unlike Pockels cells, rarely are the limiting component in the optical train. The other component that is of concern is the polarizer. Crystal polarizers made of calcite have significantly larger acceptance angles than those made of quartz or MgF_2. Unfortunately, calcite becomes opaque between 200 and 250 nm, so conventional source VUV dichrometers must operate at a higher $f\#$, thus reducing throughput. In contrast to conventional-source systems, the solid angle of a synchrotron beam is tiny, so the image can be demagnified while maintaining comfortable solid angles that are compatible with downstream components.

2.3. OPERATIONS

2.3.1. Spectrometer Calibrations

In contrast to ORD, the need to use a transfer standard such as camphorsulfonic acid to calibrate the CD scale of a dichrometers is generally recognized. But why? According to (2.5), the measurement of CD requires only the measurement of two light intensities. Even the more detailed expression for CD in (2.15) indicates that measuring the output of the PSD is all that is required, provided that the servo-reference voltage, $\overline{v}_C$, PEM maximum phase shift, δ_0, and PSD and i/v gains are known. A plausible explanation is that in earlier generations of dichrometers, and even some current instruments, the PSD uses analog band-pass amplifiers. While sensitive and selective, the gain of such circuits may be difficult to determine *ab initio*. Velluz et al. [17] discussed the difficulties associated with predictable quantification of the CD signal in the first generation of commercial dichrometers, and Schippers and Dekkers [29] described a single-photon-counting detector that attempted to provide an empirical calibration for a dichrometer using a PEM, but the solution to the problem remains elusive. Uncertainties regarding PSDs should be less problematic for modern lock-ins that employ digital signal processing to extract the desired information. Another possible source of error is the assumption that the gain of the current-to-voltage converter, $G_{i/v}$, is independent of frequency. Such circuits are usually configured as low-pass amplifiers, which means that their response is constant below some frequency but declines exponentially for higher frequencies. It is tempting to set the circuits "roll-off" frequency too close to the 50-kHz modulator frequency because higher-frequency noise is suppressed. However, this invalidates the presumption of equal gain for the 50 kHz and "dc" signals. This possibility is considered explicitly in (2.15). As noted above, the dichrometers designed by Richard DeSa do not use separate analog circuits to process the 50-kHz and dc signals and are said not to require external calibration. An alternate approach to CD calibration would be a physical

device that is placed in the dichrometer. While standard in the infrared [30], they are not used in the ultraviolet.

Even if not formally required, frequent checks of instrument calibration represent good practice. The classic calibration for CD is the "two-point" method using (+)-10-camphorsulfonic acid (CSA) [31]. The strength of the CD band at 290.5 nm is $+2.36\ M^{-1}\ cm^{-1}$, while that of the band at 192.5 nm is −5 [5], which gives a ratio of 2.1. A simple way of obtaining the concentration of the CSA sample, while avoiding artifacts resulting from the fact that it is hygroscopic, is from its absorption spectrum. The molar extinction coefficient is $34.5\ M^{-1}\ cm^{-1}$ at 285 nm. Besides checking the calibration, the same $CD_{290.5}/CD_{192.5}$ ratio spectrum provides an indication that the PEM is being programmed correctly to maintain constant phase retardation as a function of wavelength. The CD spectrum also provides a low-resolution check on the wavelength calibration. More accurate procedures for checking monochromator wavelength calibration have been reviewed recently [1]. They use known wavelength standards identical to those used to calibrate spectrophotometers. In a dichrometer, peak absorbance can be determined by following the high voltage applied to the PM, or pseudo-absorbance, if available. The same review describes a rigorous procedure for checking PEM programming, although it is not practical for most end users [32]. The calibration of a PEM is influenced by environmental factors, including temperature and atmospheric pressure, and thus should be calibrated under the same conditions used to record experimental spectra. For this reason, some manufactures maintain the PEM at a constant temperature. The amplitude of modulation for a given driving voltage increases significantly when a PEM is in vacuum, so the same calibration program cannot be used when a VUV spectrometer is purged with N_2 as when it is evacuated. Other CD calibration issues and compounds that are believed to be more stable than CSA and which have more CD bands spanning a broader range of wavelengths have recently been described [33, 34] and may be offered commercially.

2.3.1.1. Cell Pathlength Calibration. A critical item of equipment for many studies and in particular studies of protein secondary structure, is the sample cell. For work in the far UV, synthetic quartz has long been the window material of choice. But to exploit the extended spectral range opened by synchrotron radiation, the focus has shifted to CaF_2 [35]. In either case, optical pathlengths must be kept very short, 5 to 50 μm being typical. Such dimensions pose a challenge to manufactures. An error of a few microns is insignificant for cells with a 1 cm, or even a 1 mm optical path, but is unacceptable for the shorter path cells that are required for the VUV. The solution is to calibrate each cell, which is a straightforward procedure that makes use of interference fringes generated between internal reflections from the front and back windows of the cell. Typical data are shown in Figure 2.10. To achieve the required level of reflectivity the cell must be empty, so there is the implicit assumption that the dimensions are unchanged by loading the sample. The pathlength, l, is given by the expression in (2.18), where n_{12} is the number of extrema (either minima or maxima) between two selected wavelengths. For the data shown in Figure 2.10, the pathlength was found to be 24 μm, 20% larger than the nominal 20-μm dimension of the cuvette [1]. The interference pattern also provides evidence that the front and rear windows of the cuvette are parallel. If the spectral resolution of a CD instrument is inadequate to record an interference pattern, the cell can be calibrated using a high-quality spectrophotometer.

$$l = \frac{n_{12}\lambda_1\lambda_2}{2(\lambda_2 - \lambda_1)} \tag{2.18}$$

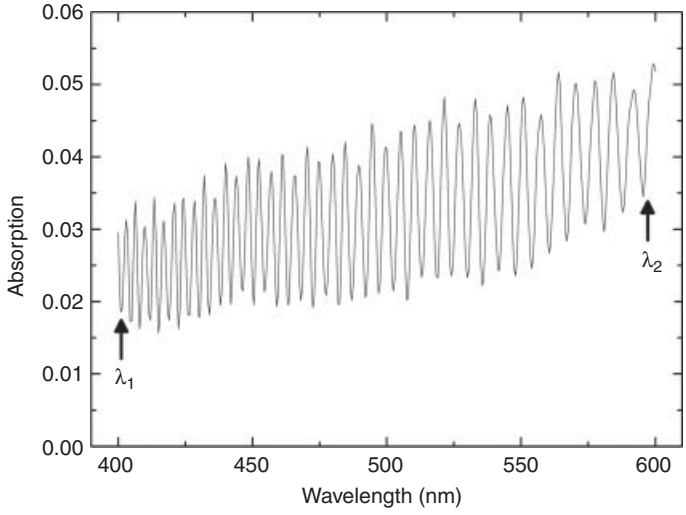

Figure 2.10. Interference pattern recorded from the pseudo-absorption of an empty nominal 20-μm path quartz cuvette. Data were recorded on beamline U9B at the National Synchrotron Light Source, Brookhaven National Laboratory.

2.3.2. Performance and Potential Artifacts

2.3.2.1. Signal-to-Noise Ratio and Optimum Absorbance. The critical signal measured in a CD experiment is ΔI_{CD}, which, according to (2.5), can be replaced by $-\Delta a_{CD} I$. The noise in a photomultiplier signal is statistical and thus proportional to $\sqrt{I}$. In (2.5) there is the implicit assumption that the only significant absorption is due to the chiral molecule being studied, but in considering factors that affect the signal-to-noise ratio (S/N), it is necessary to express the total absorption at a particular wavelength, a_T, as the sum of the absorption due to the chiral absorber(s) being studied, a_s, plus the absorption due to the buffer or other absorbers, including water, which may be present, a_B. The buffer is presumed to be nonchiral and hence does not contribute to the CD signal, but influences S/N by attenuating the photon beam. Therefore, the signal-to-noise ratio can be written as shown in (2.19), where the expression for Δa_{CD} is replaced using the chiral anisotropy relationship. The expression on the right in (2.19) indicates that four factors play a role in determining the signal-to-noise ratio of the CD measured at a particular wavelength. S/N is directly proportional to the intrinsic chiral anisotropy of the sample, to the absorption, and hence concentration, of the chiral components, to the square root of the intensity of the incident beam, and to the square root of the transmission of the sample, including absorption by both chiral and nonchiral components. The objective in preparing a sample is thus to achieve the highest practical ratio of chiral absorbers to nonchiral absorbers. Once that ratio is fixed, the absorbance of the chiral components is proportional to the total absorption of the sample at each wavelength. The optimum total absorption for a particular wavelength is found by replacing a_S by a constant times a_T in expression 2 in (2.19) and setting the derivative of this expression with respect to a_T equal to zero. Thus, the optimum value for the total Eulerian absorbance is 2 and the optimum decadic absorbance is $2/\ln 10 \approx 0.87$, as shown in Figure 2.11. However, the profile is asymmetric, with values greater than 80% of the maximum extending from about 0.4 to 1.6. In the absence of other considerations, it would thus be appropriate to have the maximum absorption of the chiral components encountered in a spectrum greater than 1.0. However, it is also important to avoid total absorbances that are too high because of artifacts that result from stray light and detector dark current, as discussed in Section 2.3.2.2. This is particularly true for VUV CD spectra of proteins recorded with

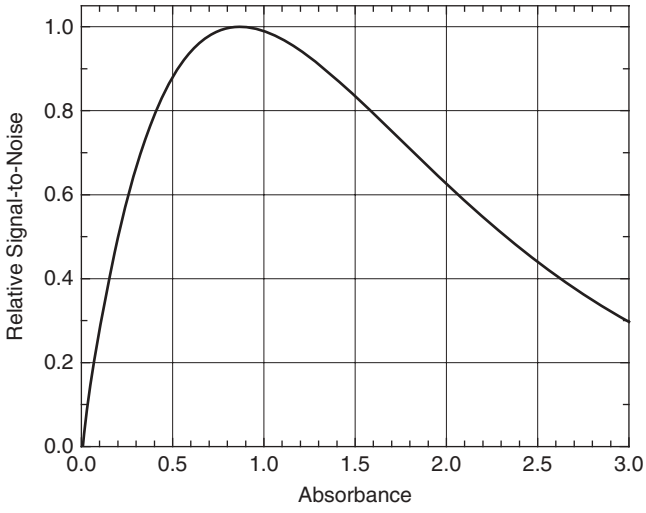

Figure 2.11. Relative-signal to-noise ratio as a function of decadic absorption from (2.19). The peak sensitivity is for $A = 2/\ln 10 \approx 0.87$ and the signal-to-noise is greater than eight-tenths of the maximum value for absorbances between 0.4 and 1.6.

a xenon-arc instrument because I_0 decreases and A_B increases near the short wavelength limit.

$$\frac{S}{N} = \frac{|\Delta I_{CD}|}{\sqrt{I}} \underset{1}{\rightarrow} |\Delta a_{CD}|\sqrt{I} \underset{2}{\rightarrow} \frac{|\Delta \varepsilon_{CD}|}{\varepsilon_S} a_S \sqrt{I_0 e^{-a_T}} \underset{3}{\rightarrow} \frac{|\Delta \varepsilon_{CD}|}{\varepsilon_S} \ln 10 A_S \sqrt{I_0 10^{-A_T}}. \quad (2.19)$$

2.3.2.2. Stray Light and Detector Dark Current. Any light reaching the detector that either has not passed through the sample or is outside the narrow range of wavelengths in the primary "monochromatic" beam emerging from the monochromator will result in an erroneous CD signal. In most cases, stray light will result in the apparent value of $\overline{I}$ in (2.5) being higher than the value produced by the primary wavelength, giving a low value for the CD. The trivial form of stray light is due to leaks in the sample compartment or the connections between it and the monochromator or detector. Such problems are easily detected by an increase in the PM voltage resulting when a black cloth is placed around the dichrometer or when the room lights are extinguished. Out-of-band light emerging from the monochromator and non-light-dependent signals (dark current) arising in the photomultiplier are more serious issues. They occur frequently in CD measurements in the far and vacuum UV at the short-wavelength limit of a scan where the absorption of the sample, and hence the high voltage applied to the photomultiplier, rises rapidly. These problems can be analyzed using a model that also suggests procedures to detect their existence and minimize their effects. The approach is to modify (2.14) to include the contribution to the observed time-average output voltage from the detector due to photomultiplier dark current and stray light, as shown in (2.20). The current from the photocathode is thus the sum of three terms, which are enclosed in parenthesis. The first term is the photocurrent generated by the primary light beam of intensity I_0 and wavelength λ_0, i.e., the true signal. The second term represents the contribution of out-of-band (stray) light reaching the photocathode. In this expression, $I_S[\lambda]$ represents the spectral density of the incident beam on the entrance slit of the monochromator that results in intensity I_0 at the primary wavelength and $R[\lambda, \lambda_0]$ is the ratio of the throughput of the monochromator for wavelength λ relative to the throughput for λ_0. For high-quality holographic grating and prism monochromators, R is typically less than 10^{-5} for wavelengths well separated from the primary wavelength [36, 37]. The third term is the Richardson–Dushman expression for the current from the photocathode

due to thermionic emission, where $\mathcal{A}$ is the area of the photocathode, C_R is Richardson's constant, T is the absolute temperature, W is the work function of the cathode surface, and k is the Boltzmann constant. This current is amplified along the dynode chain with the same gain as photon-induced cathode current [38], and thus the dark current at the anode increases exponentially as the applied high voltage increases. Other mechanisms that generate dark current are usually less important in CD experiments.

The sum of these three quantities are multiplied by the gain of the photomultiplier along the dynode string and the gain of the current to voltage converter to give the time-average signal voltage. CD is measured accurately only if the sum of the contributions of dark current and scattered light are insignificant compared to the signal from the primary wavelength.

$$\overline{v} = G_{i/v} G_{PM}[V] \left(\phi[\lambda_0] I_0[\lambda_0] e^{-a[\lambda_0]} + \int_{\lambda \neq \lambda_0} R[\lambda, \lambda_0] \phi[\lambda] e^{-a[\lambda]} d\lambda + \mathcal{A} C_R T^2 e^{\frac{-W}{kT}} \right). \tag{2.20}$$

Problems arise when the absorption of the sample plus background becomes large or the incident intensity at the primary wavelength decreases. Both conditions tend to occur near the short-wavelength limit of the spectrum of an aqueous sample. As the magnitude of the signal due to the light intensity at the primary wavelength decreases, the servo circuit increases the voltage applied to the photomultiplier and thus the internal gain to maintain $\overline{v} = \overline{v}_C$, but the contributions of the dark current and stray light may no longer be insignificant compared to the signal generated by the primary wavelength, and thus the output of the phase-sensitive detector will no longer be a valid measure of the CD of the sample.

There are three distinct failure modes in the limit of high sample absorption and/or low primary intensity, although the behavior of a particular instrument may reflect a combination of more than one of these limiting cases. Differential diagnosis of the failure modes is based on observation of the behavior of the high voltage applied to the photomultiplier and the effect of blocking the light beam with an opaque object or inserting a nonfluorescent short-wavelength cutoff filter. Because all photomultipliers are characterized by specified upper limit of the voltage difference that can be applied between the photocathode and the anode without damage, servo circuits are designed so that some maximum value, V_{MAX} cannot be exceeded. For an ideal dichrometer, there would be no dark current or stray light and when the beam reaching the detector is blocked by an opaque object, V goes to V_{MAX} and $\overline{v}$ drops to zero. For a practical instrument, $\overline{v}$ usually drops to a finite value that depends on the magnitude of the dark current. Insertion of a cutoff filter chosen to block the primary beam will have only a minor impact on the stray light term. Thus, this test indicates the sum of dark current plus stray light.

Analysis of the terms in (2.20) suggests various strategies for avoiding erroneous CD results due to detector dark current and stray light. They can be discussed both in terms of the technology used to improve performance and with respect to the regions of the spectrum for which they are applicable. Not surprisingly, the regions of concern are toward the limits of the spectral domain covered by this article: the far and vacuum UV and the red and infrared. Starting with the terms representing light intensity that appear in the first and second terms, it is obviously an advantage to have a source with high intensity where needed and lower intensity elsewhere. Synchrotron radiation sources are far superior to xenon arcs for CD studies in the far and vacuum UV because their radiance increases with decreasing wavelength, just the opposite of the xenon arc (Figure 2.6). The

same terms in (2.20) indicates the importance of having a detector with a high quantum yield and transparent window at the primary wavelength. Window transparency is an issue in the vacuum UV, as the best synthetic quartz becomes opaque at about 160 nm. Fortunately, photomultipliers are available with LiF, MgF_2, and CaF_2 windows. Low photocathode sensitivity is more of an issue for studies in the red and near infrared.

The expression for dark current due to thermionic emission in (2.20) provides rationales for three methods that are used to suppress dark current in photomultipliers: reducing the effective area, decreasing the temperature, and increasing the work function of the photocathode. Choosing a photomultiplier with a small photocathode is one means of achieving the first goal. Photomultipliers optimized for wavelengths less than 160 nm tend to have a small photocathode because of difficulties inherent in fabricating larger LiF and MgF_2 windows. Applying a magnetic field that permits electrons generated only from that area of the photocathode irradiated by the photon beam to reach the first dynode is another approach [39], but determining when this condition is fulfilled is problematic. In addition, limiting photocathode area can be counterproductive. For example, one approach to reducing anomalous CD signals due to scattered light is to position a photomultiplier with a large photocathode immediately behind the sample.

Another approach to reducing dark current is to cool the photocathode. Reducing photocathode temperature is effective until the dark current produced by thermionic emission drops below dark current due to dynode leakage, which is not included in (2.20). This transition temperature depends on the work function of the photocathode, with temperatures as low as $-60^{\circ}C$ being required for red- and infrared-sensitive detectors. While effective throughout the spectrum, cooling is particularly useful at longer wavelengths where the necessity of working with photocathodes with lower work functions results in higher thermionic emission and thus higher dark currents. Finally, choosing a photocathode with a higher work function is an effective way of reducing dark currents, but only relevant for UV studies, because such detectors do not respond to visible and near-UV radiation. The use of such a detector has an additional benefit because the response to stray light is also suppressed.

An effective, but expensive, strategy in the red and near infrared is to combine a cooled photomultiplier with a spectrometer in which the optical beam is periodically interrupted (chopped) at a frequency typically between 100 and 1000 Hz, as first described by Breeze and Ke [40]. A more sophisticated, and even more expensive, approach detects the time-average intensity with a lock-in amplifier tuned to the frequency of the chopper, while the CD is extracted from two sequential lock-ins: The first one is tuned to the PEM frequency and operated with a time constant set between the periods of the chopper and the PEM, and the second one is tuned to the frequency of the chopper [41].

Stray light is usually a problem only for studies in the ultraviolet, because short-wavelength blocking filters can remove potentially contaminating wavelengths for CD experiments in the red and infrared. As noted above, choosing a photomultiplier with a high work function, and hence little or no sensitivity to wavelengths outside the UV, reduces the response to stray light when the primary wavelength is in the UV. Another approach is to use a double monochromator, hence effectively squaring the value of W. This is typical for bench-top instruments with xenon arc sources operating in the UV because the source generates much higher intensities in the visible and near infrared than in the ultraviolet. The disadvantage is that the throughput of the primary wavelength is also reduced by the double monochromator. Chopping the optical beam with an opaque object, as described above, does not discriminate against stray light. However,

chopping the beam with a short wavelength cutoff filter would discriminate against both wavelengths transmitted by the filter and dark current.

2.3.2.3. Inhomogeneous and Anisotropic Samples and Photodegradation.

The theory describing measurement of absorption and CD presumes that the absorbing entities are randomly distributed and oriented throughout the sample. Sample inhomogeneity results in measurement errors that become progressively larger as the absorbance of the sample material increases. The simplest situation to understand is when a fraction of the incident beam never passes through the sample. No matter how opaque the sample, the transmission can never drop below this fraction, with corresponding effects on the measured absorbance and CD, thus "flattening" peak signals, and in the case of CD, possibly distorting spectral shapes. While the "incompletely filled cuvette syndrome" is classified as gross operator error, the formation of bubbles spanning the entire sample depth in cuvettes with very short pathlengths is far more insidious. Special precautions should be taken when working with submillimeter pathlengths, particularly if the sample temperature may increase after it is loaded into the cuvette. Degassing or saturating the sample with helium can be effective. Unlike most gases, the solubility of helium increases at higher temperatures. One of the several advantages of the simultaneous measurement of CD and absorption is that the optical beam samples exactly the same region of the sample. Even subtler is the situation in which absorbing moieties are clustered together as supramolecular structures with dimensions comparable with the wavelength of the radiation (i.e., 100 nm). Membrane fragments are particularly susceptible [42]. Castiglioni and co-workers have presented empirical approaches to correcting absorption flattening in such situations [43–45]. Samples involving materials such as compacted membrane fragments or insoluble proteins may not follow the Beer–Lambert law and may exhibit linear dichroism, which can result in spurious apparent CD signals [1]. Intense VUV radiation in some SRCD instruments can result in photodegradation of unbuffered protein samples [46].

ACKNOWLEDGMENTS

I thank Ettore Castiglioni, University of Brescia, Robert Woody, Colorado State University, and Alison Rodger, Warwick University, for helpful discussions and comments; Steven Hulbert, Brookhaven National Laboratory for the calculated radiance spectra from synchrotron beamline U11; John Trunk, also BNL, for recording the data in Figure 2.8 and Figure 2.10; and Lana Pryde, Newport Corporation, for permission to reproduce the xenon arc spectrum in Figure 2.6. Preparation of this chapter was supported by East Carolina University and by Brookhaven National Laboratory under contract with the U.S. Department of Energy.

REFERENCES

1. J. C. Sutherland, Measurement of circular dichroism and related spectroscopies with conventional and synchrotron light sources: Theory and instrumentation, in *Modern Techniques for Circular Dichroism and Synchrotron Radiation Circular Dichroism Spectroscopy*, B. A. Wallace and R. W. Janes, eds., IOS Press, Amsterdam, **2009**, pp. 19–72.
2. A. F. Drake, *J. App. Phys. E* **1986**, *19*, 170–181.
3. W. C. Johnson, Jr., *Proteins: Struct. Funct. Genet*. **1990**, *7*, 205–214.

4. D. R. Bobbitt, Instrumentation for the measurement of circular dichroism: Past, present and future developments, in *Analytical Applications of Circular Dichroism*, N. Purdie and D. R. Bobbitt, eds. Elsevier, Amsterdam, **1994**, pp. 15–52.
5. W. C. Johnson, Jr., Circular dichroism instrumentation, in *Circular Dichroism and the Conformational Analysis of Biomolecules*, G. D. Fasman, ed., Plenum Press, New York, **1996**, pp. 635–652.
6. J. C. Sutherland, Circular dichroism using synchrotron radiation: From ultraviolet to x-rays, in *Circular Dichroism and the Conformational Analysis of Biomolecules*, G. D. Fasman, ed., Plenum Press, New York, **1996**, pp. 599–633.
7. A. Rodger, B. Nordén, *Circular Dichroism and Linear Dichroism*, Oxford University Press, Oxford, **1997**.
8. W. A. Eaton, E. Charney, *J. Chem. Phys*. **1969**, *51*, 4502–4505.
9. J. D. Jackson, *Classical Electrodynamics*, John Wiley & Sons, New York, **1962**.
10. P. McPhie, *Anal. Biochem*. **2001**, *293*, 109–119.
11. P. McPhie, *Biopolymers* **2004**, *75*, 140–147.
12. B. R. Baker, R. L. Garrell, *Faraday Discuss*. **2004**, *126*, 209–222; Discussion, 245–254.
13. R. Marrington, T. R. Dafforn, D. J. Halsall, A. Rodger, *Biophys. J*. **2004**, *87*, 2002–2012.
14. D. E. Waldron, R. Marrington, M. C. Grant, M. R. Hicks, A. Rodger, *Chirality* **2010**, *22*, E136–E141.
15. J. C. Sutherland, E. J. Desmond, P. Z. Takacs, *Nuc.–Instr. Meth*. **1980**, *172*, 195–199.
16. B. A. Wallace, *Q. Rev. Biophys*. **2009**, *42*, 317–370.
17. L. Velluz, M. Legrand, M. Grosjean, *Optical Circular Dichroism*, Verlag Chemie, Academic Press, Weinheim, **1965**.
18. M. Billardon, J. Badoz, *Compt. Rend. Acad. Sci. Paris* **1966**, *262*, 1672–1675.
19. M. Billardon, J. Badoz, *Compt. Rend. Acad. Sci. Paris* **1966**, *263*, 139–142.
20. J. C. Kemp, *J. Opt. Soc. Am*. **1969**, *59*, 950–954.
21. S. N. Jasperson, S. E. Schnatterly, *Rev. Sci. Instrum*. **1969**, *40*, 761–767.
22. L. F. Mollenauer, D. Downie, H. Engstrom, W. B. Grant, *App–Opt*. **1969**, *8*, 661–665.
23. A. J. Diefenderfer, *Principles of Electronic Instrumentation*, W. B. Saunders, Philadelphia, **1979**.
24. J. C. Sutherland, D. C. Monteleone, B. M. Sutherland, *J. Photochem. Photobiol. B* **1997**, *40*, 14–22.
25. L. Whitmore, B. A. Wallace, *Nucleic Acids Rese*. **2004**, *32*, W668–W673.
26. B. A. Wallace, L. Whitmore, R. W. Janes, *Proteins* **2006**, *62*, 1–3.
27. J. C. Sutherland, P. C. Keck, K. P. Griffin, P. Z. Takacs, *Nuc–Instr. Meth*. **1982**, *195*, 375–379.
28. J. F. James, R. S. Sternberg, *The Design of Optical Spectrometers*, Chapman and Hall, London, **1969**.
29. P. H. Schippers, H. P. M. Dekkers, *Anal. Chem*. **1981**, *53*, 778–882.
30. G. A. Osborne, J. C. Cheng, P. J. Stephens, *Rev. Sci. Instrum*. **1973**, *44*, 10–15.
31. G. C. Chen, J. T. Yang, *Anal. Lett*. **1977**, *10*, 1195–1207.
32. T. C. Oakberg, J. Trunk, J. C. Sutherland, *Proc. SPIE* **2000**, *4133*, 101–111.
33. A. J. Miles, F. Wien, B. A. Wallace, *Anal. Biochem*. **2004**, *335*, 338–339.
34. A. J. Miles, F. Wien, J. G. Lees, A. Rodger, R. W. Janes, B. A. Wallace, *Spectroscopy* **2003**, *17*, 653–661.
35. F. Wien, B. A. Wallace, *Appl. Spectrosc*. **2005**, *59*, 1109–1113.
36. R. Donaldson, *J. Sci. Instrum*. **1952**, *29*, 151–153.
37. M. R. Sharp, D. Irish, *J. Mod. Optics* **1978**, *25*, 861–893.

38. Hamamatsu Photonics K. K. Editorial Committee, *Photomultiplier Tubes Basics and Applications*, Hamamatsu Photonics K.K. Electron Tube Division, Hamamatsy City, Japan, **2006**.
39. L. Frommhold, W. A. Feibelman, *J. Sci. Instrum*. **1967**, *44*, 182–183.
40. R. H. Breeze, B. Ke, *Anal. Biochem*. **1972**, *50*, 281–303.
41. W. A. Eaton, L. K. Hanson, P. J. Stephens, J. C. Sutherland, J. B. R. Dunn, *J. Am. Chem. Soc*. **1978**, *100*, 4991–5003.
42. B. A. Wallace, C. L. Teeters, *Biochemistry* **1987**, *26*, 65–70.
43. E. Castiglioni, S. Abbate, G. Longhi, R. Gangemi, R. Lauceri, R. Purrello, *Chirality* **2007**, *19*, 642–646.
44. E. Castiglioni, S. Abbate, G. Longhi, R. Gangemi, *Chirality* **2007**, *19*, 491–496.
45. E. Castiglioni, F. Lebon, G. Longhi, R. Gangemi, S. Abbate, *Chirality* **2008**, *20*, 1047–1052.
46. A. J. Miles, R. W. Janes, A. Brown, D. T. Clarke, J. C. Sutherland, Y. Tao, B. A. Wallace, S. V. Hoffmann, *J. Synchrotron Rad*. **2008**, *15*, 420–422.

3

CIRCULARLY POLARIZED LUMINESCENCE SPECTROSCOPY AND EMISSION-DETECTED CIRCULAR DICHROISM

James P. Riehl and Gilles Muller

3.1. INTRODUCTION

Since the very first observation of circular polarization in the luminescence from a chiral crystal of sodium uranyl acetate, $Na[UO_2(CH_3COO)_3]$, by Samoilov in 1948 [1], the measurement of the usually small net circular polarization from chiral molecular systems has become a useful probe of chiral molecular structure. This species crystallizes in the $P2_13$ space group, allowing for two enantiomeric forms, and the circular polarization is so large that it was easily detected with simple static optics. The much more difficult measurement of the usually small net circular polarization in the luminescence from chiral molecules in solution began with the pioneering studies of the research group of Professor Oosterhof at the University of Leiden in the late 1960s on chiral organic molecules [2, 3] and in the early 1970s by Professor Steinberg and coworkers at the Weizmann Institute on biomolecular systems [4, 5]. In recent years, this technique has developed into a reliable and useful spectroscopic tool for the study of a wide variety of chemical systems, but recent applications have overwhelmingly been concerned with CPL from chiral luminescent lanthanide (III) complexes since the first report of Luk and Richardson in 1974 [6] for reasons outlined later in this chapter. This phenomenon has been referred to as circularly polarized luminescence (CPL), circularly polarized emission (CPE), and other names. Here we will use the most common acronym CPL to describe this experimental technique. In this chapter we also discuss the measurement of the differential emission intensity due to differences in the absorption of left versus right circularly polarized light. This has been commonly referred to as fluorescence-detected

Comprehensive Chiroptical Spectroscopy, Volume 1: Instrumentation, Methodologies, and Theoretical Simulations, First Edition. Edited by N. Berova, P. L. Polavarapu, K. Nakanishi, and R. W. Woody.
© 2012 John Wiley & Sons, Inc. Published 2012 by John Wiley & Sons, Inc.

circular dichroism (FDCD), since almost all previous work and many new applications of this technique are based on the observation of organic fluorescence. In this chapter we will use the more general name of emission-detected circular dichroism (EDCD) for this measurement due to the recent application of this technique to luminescent lanthanide (III) ions with long emission lifetimes. There is no doubt that in the future that the interested reader will find both of these terms used in the literature. CPL spectroscopy has been the subject of numerous reviews [4, 7–12], whereas reviews or general discussions of EDCD (FDCD) results or techniques have been quite limited [10, 11, 13].

It should be noted that whereas EDCD spectroscopy (like conventional CD) probes the chiral structure of the ground state, CPL is a probe of the chirality of the excited state. These types of experiments are not redundant, since geometry changes may occur on electronic excitation. Furthermore, both of these experimental techniques have the potential of providing information concerning molecular dynamics and energetics that occur between the time of excitation and emission.

3.2. THEORETICAL PRINCIPLES

3.2.1. CPL Spectroscopy

In CPL spectroscopy, one is interested in measuring the difference in the luminescence intensity (ΔI) of left-circularly polarized light (I_L) versus right-circularly polarized light (I_R). By convention, this difference is defined as follows:

$$\Delta I \equiv I_L - I_R. \tag{3.1}$$

Just as in ordinary luminescence measurements, the determination of absolute emission intensities is quite difficult, so it is customary to report CPL measurements in terms of the ratio of the difference in intensity, divided by the average total luminescence intensity.

$$g_{lum} = \frac{\Delta I}{\frac{1}{2}I} = \frac{I_L - I_R}{\frac{1}{2}(I_L + I_R)}, \tag{3.2}$$

where g_{lum} is referred to as the luminescence dissymmetry ratio (or factor). The extra factor of 1/2 in Eq. (3.2) is included to make the definition of g_{lum} consistent with the definition of the related quantity in circular dichroism, CD, namely, g_{abs}:

$$g_{abs} = \frac{\Delta\varepsilon}{\varepsilon} = \frac{\varepsilon_L - \varepsilon_R}{\frac{1}{2}(\varepsilon_L + \varepsilon_R)}, \tag{3.3}$$

where in this equation ε_L and ε_R denote, respectively, the molar absorption coefficients for left- and right-circularly polarized light, and ε has always been explicitly defined as an average quantity.

The relationship of I and ΔI to molecular properties is through the transition probability (Fermi Golden Rule). In general, one must describe the probability of emitting a left- or right-circularly polarized photon at a time t following the excitation of the luminescing species to the excited or emitting state [7]. For organic fluorescence chromophores the excited-state lifetime is so short that one can normally consider the system as unchanged between excitation and emission, whereas for organic phosphorescence or other long-lived excited states such as lanthanide (III) emission, one can often consider

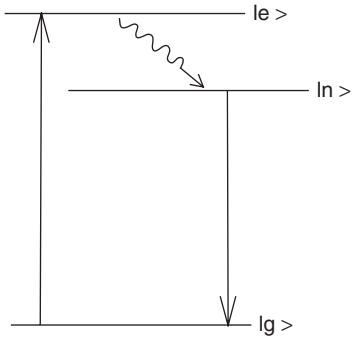

Figure 3.1. Schematic energy level diagram for absorption and emission transitions.

any photoinduced internal molecular structural changes as complete and the orientational distribution as completely isotropic by the time of emission.

Referring to the schematic energy level diagram presented in Figure 3.1, the steady-state differential intensity of left (L)- minus right (R)-circularly polarized light for a transition from an initial emitting state n to a final state g may be expressed as follows:

$$\Delta I(\lambda) = (\hbar c/\lambda) N_n \Delta W_{gn} f_\sigma(\lambda), \tag{3.4}$$

where we have introduced the differential transition probability ΔW_{gn},

$$\Delta W_{gn} \equiv W_{gn}^L - W_{gn}^R \tag{3.5}$$

a lineshape function, $f_\sigma(\lambda)$, and the population of the emitting state, N_n. In Eq. (3.4) we have ignored, for the reasons given above and simplicity, the time and orientation dependence of N_n and ΔW_{gn}. The probability of emitting a right- or left-circularly polarized photon may be related in the usual way to molecular transition matrix elements through Fermi's Golden Rule. Under the assumption that the emitted light is being detected in the laboratory 3 direction (see Figure 3.2), and allowing for only electric dipoles and magnetic dipoles in the expansion of the molecule–radiation interaction Hamiltonian, we

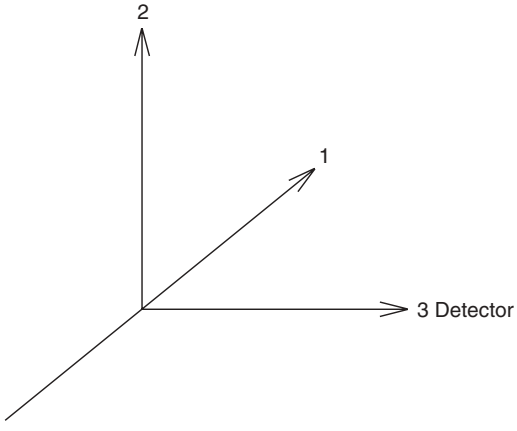

Figure 3.2. Laboratory coordinate system.

obtain the following expressions:

$$W_{gn}^{L} = K(\lambda^3)[|\mu_1^{gn}|^2 + |\mu_2^{gn}|^2 + |m_1^{gn}|^2 + |m_2^{gn}|^2 - 2i(\mu_1^{gn} m_1^{gn} + \mu_2^{gn} m_2^{gn})], \tag{3.6}$$

$$W_{gn}^{R} = K(\lambda^3)[|\mu_1^{gn}|^2 + |\mu_2^{gn}|^2 + |m_1^{gn}|^2 + |m_2^{gn}|^2 + 2i(\mu_1^{gn} m_1^{gn} + \mu_2^{gn} m_2^{gn})], \tag{3.7}$$

where **1** and **2** refer to laboratory axes and the electric dipole transition moment, μ^{gn}, and the imaginary magnetic dipole transition moment m^{gn} are defined as follows:

$$\begin{aligned} \mu_1^{gn} &\equiv < g|\mu_1|n >, \\ m_1^{gn} &\equiv < g|m_1|n > . \end{aligned} \tag{3.8}$$

The differential transition rate is, therefore,

$$\Delta W_{gn} = -K(\lambda^3)[4i(\mu_1^{gn} m_1^{gn} + \mu_2^{gn} m_2^{gn})]. \tag{3.9}$$

Note that the i in Eq. (3.9) results in the differential transition probability being a real number. The condition for this quantity to be nonzero is that the chromophore of interest must have a nonzero magnetic and electric transition dipole moment along the same molecular direction. In the absence of perturbing external fields, this is only true for molecules that are chiral.

The final connection between molecular properties and experimental observables requires knowledge of the orientational distribution of the emitting molecules with respect to the direction and polarization of the excitation light and the direction of detection. We consider here only the limiting cases in which the sample is "frozen," so the orientational distribution of emitting molecules is determined by (a) the distribution created by the excitation beam and (b) the *isotropic* or random distribution appropriate for a sample that has had sufficient time between absorption and emission to completely scramble any orientational distribution created by the excitation beam. The "frozen" limit is clearly appropriate when considering chiral crystals.

In order to measure CPL from crystals, the crystal system must be at least uniaxial with the optic axis oriented along the direction of emission detection, so circularly polarized luminescence may be propagated through the crystal without scattering which leads to depolarization. The implication is that the index of refraction of the crystal is uniform in directions perpendicular to the direction of emission detection. Of course, the other requirement is that the emitting species must be chiral. This situation is also true for randomly oriented "frozen" solutions of chiral molecules. In this case, of course, the orientational distribution of molecules is isotropic, and independent of the direction of emission detection.

Expressed in the laboratory (**1 2 3**) coordinate system, the total luminescence transition rate may be obtained by adding equations (3.6) and (3.7):

$$W_{gn} = 2K(\lambda^3)[|\mu_1^{gn}|^2 + |\mu_2^{gn}|^2 + |m_1^{gn}|^2 + |m_2^{gn}|^2]. \tag{3.10}$$

The luminescence dissymmetry ratio can then be related to the molecular transition matrix elements as follows:

$$g_{lum} = \frac{\Delta I}{\frac{1}{2}I} = \frac{I_L - I_R}{\frac{1}{2}(I_L + I_R)} = -4i\frac{\mu_1^{gn} m_1^{gn} + \mu_2^{gn} m_2^{gn}}{|\mu_1^{gn}|^2 + |\mu_2^{gn}|^2 + |m_1^{gn}|^2 + |m_2^{gn}|^2}, \tag{3.11}$$

where we have made the simplifying assumptions that the lineshapes for CPL and total luminescence are identical and that the number of molecules in the emitting state is independent of their orientation. The direct connection to molecular structure relies on relating the transition matrix elements from laboratory to molecular coordinate systems. For the case of a randomly oriented emitting distribution, the orientational averaging yields the following general result:

$$g_{lum}(\lambda) = 4\mathrm{Re}\left[\frac{\vec{\mu}^{gn} \cdot \vec{m}^{gn}}{|\vec{\mu}^{gn}|^2 + |\vec{m}^{gn}|^2}\right]. \tag{3.12}$$

A severe complication arises, however, with the fact that the orientational distribution of emitting molecules is determined by the orientation of the absorption dipole moment with respect to the polarization and direction of the incident beam. This is commonly referred to as photoselection. The problem here is not due to any inherent depolarization due to sample configuration, but rather the issue is that it is experimentally very difficult to measure circular polarization in the presence of linear polarization. The reasons for this will be discussed in some detail in Section 3.5.1. To our knowledge, there have been no reliable reports of CPL measurements in which linear polarization in the luminescence has been present. Although, in principle, there are experimental geometries that can be used to ensure no linear polarization in the luminescence, these rely on very precise control of incident excitation polarization and direction. This has limited the application of CPL to solutions composed of either (a) molecular systems in which the luminescent species is essentially a spherical emitter (such as lanthanides) or (b) small molecules that have a sufficient time between excitation and emission to completely scramble any photoselected orientational distribution.

The form of Eq. (3.12) illustrates an important characteristic of chiroptical spectroscopy. Larger dissymmetry values are seen when the transition involved is inherently weak. For electric-dipole-allowed transitions, the denominator in Eq. (3.12) will be dominated by the first term, $|\mu|^2$. An advantageous situation occurs when the transition is electric dipole forbidden and magnetic dipole allowed. The magnetic dipole transition moment is typically a thousand times smaller than the electric dipole term. These same arguments apply to CD spectroscopy where it is much easier, for example, to study the $n \rightarrow \pi^*$ transitions of chiral ketones than to study $\pi \rightarrow \pi^*$ transitions. As a result, it may be very difficult to apply CPL studies to chiral molecules that are strongly luminescent, such as organic dyes, due to the presence of allowed transition.

3.2.2. EDCD Spectroscopy

In EDCD we relate the extent of absorption of circularly polarized light to the intensity of emission observed following the excitation. This is expressed as follows:

$$g_{EDCD} = \frac{E_L - E_R}{\frac{1}{2}(E_L + E_R)} \tag{3.13}$$

where the emission intensity observed following left- or right-circularly polarized light is denoted E_L and E_R, respectively. In order to relate this measured quantity to the CD measured in the usual manner, one needs to take into account the fact that the relative intensity of the polarized excitations seen by an emitting species is going to depend on the how much differential absorption takes place between the sample cell wall and the location of the molecule in question. This is illustrated in Figure 3.3. Molecules close to

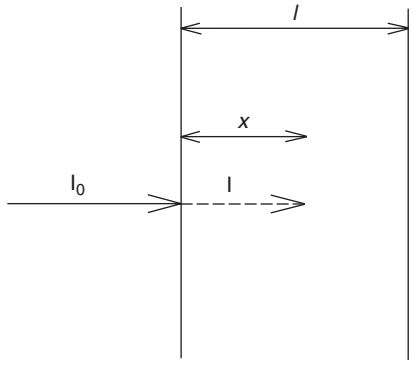

Figure 3.3. Absorption of the incident beam as it passes through the sample cell.

the cell wall in the direction of the excitation source will presumably see equal intensity of left- and right-circularly polarized light, whereas other molecules will see unequal amounts of circularly polarized light due to differential absorption. The issue of having to deal with a photoselected orientational distribution of emitting molecules also has severe consequences in EDCD spectroscopy, as will be described in Section 3.5.2.

The issues of absorption and photoselection have limited the application of EDCD. However, general expressions have been developed for situations in which the sample of interest contains absorbers other than the fluorescent species, as well as in cases where the fluorescent species have been excited through energy transfer from nonfluorescent absorbers [14–17]. Interpretation of the measurement of EDCD is much simpler if one is able to study a system in which the only chiral molecules in the sample are the same ones for which we are analyzing the luminescence, if we can assume an isotropic orientational distribution, and if we are able to ignore the presence of any other absorbing species. Under these conditions we can derive the following expression for the differential intensity of left- or right-polarized light, dE_L or dE_R, as a function of distance x:

$$dE_L = \alpha_L C \phi I_L(x)\, dx, \tag{3.14}$$

$$dE_R = \alpha_R C \phi I_R(x)\, dx, \tag{3.15}$$

where C denotes the concentration in moles per liter, the absorption coefficient, α, is related to the molar decadic extinction coefficient ($\alpha = 2.303\varepsilon$), and it is assumed that the fluorescence quantum yield, ϕ, is independent of incident polarization. The intensities of polarized excitation decrease exponentially as a function of distance into the cell:

$$I_L(x) = I_0 \exp(-\alpha_L C x), \tag{3.16}$$

$$I_R(x) = I_0 \exp(-\alpha_R C x) \tag{3.17}$$

Integrating equations (3.14) and (3.15) over the length of the cell, l, we obtain the following:

$$E_L = I_0 \phi (1 - e^{-\alpha_L C l}), \tag{3.18}$$

$$E_R = I_0 \phi (1 - e^{-\alpha_R C l}). \tag{3.19}$$

Substituting into Eq. (3.13), we obtain the following expression:

$$g_{EDCD} = \frac{2(e^{-\alpha_R Cl} - e^{-\alpha_L Cl})}{2 - e^{-\alpha_R Cl} - e^{-\alpha_L Cl}}. \tag{3.20}$$

At the usual low concentrations and low absorption coefficients seen in these types of measurements, the exponentials exp(-αCl) in Eq. (3.2) may be expanded as $(1 - \alpha Cl)$, and the equation is rewritten as

$$g_{EDCD} = \frac{2(\alpha_L Cl - \alpha_R Cl)}{\alpha_L Cl + \alpha_R Cl} = \frac{A_L - A_R}{\frac{1}{2}(A_L + A_R)}, \tag{3.21}$$

where the absorbance, A, has the customary Beer–Lambert definition

$$A = \varepsilon lC = \alpha Cl/2.303 \tag{3.22}$$

Thus under these somewhat limiting conditions and assumptions the EDCD and CD should yield identical information.

3.3. MEASUREMENT TECHNIQUES

3.3.1. The Measurement of Circularly Polarized Luminescence

Unlike circular dichroism where a number of commercial instruments have been available for more than 40 years, the measurement of circularly polarized luminescence has almost exclusively been performed on custom-built instruments that were designed, developed, and improved by a limited number of research groups over the last three decades [5, 8, 9, 18]. The basic design of a CPL instrument involves the use of a quarter-wave modulating circular polarization analyzer that converts alternately left then right circular polarization in a luminescence beam into linear polarization. Differences in the measured intensity of this linear polarization in phase with the modulation are directly proportional to the extent of circular polarization in the luminescence. The first CPL instruments used a lock-in amplifier referenced to the driving frequency of the modulator to measure the circular polarization. The more modern instruments have utilized photon-counting detection with various techniques of gated-photon counting. These have been shown to be more reliable, easier to calibrate, and less influenced by the electronic problems (i.e., ground loops) associated with the use of lock-in detection of usually weak CPL signals [7, 9, 19].

Another advantage of photon-counting methods versus the analog methods employed in the earlier equipment for the detection and analysis of CPL is that the standard deviation, σ_d, in the measurement of the luminescence dissymmetry factor follows a Poisson distribution [18, 20] and may be calculated directly from the total number of photon counts, N, that is, $\sigma_d = \sqrt{2/N}$. One can see that the determination of accurate g_{lum} values can be done in a short time for transitions associated with large g_{lum} values of highly luminescent compounds, whereas a longer time of collection is required for transitions associated with small g_{lum} values of weakly luminescent systems for achieving the same percent error. In general, one is not interested in having the same absolute error at each wavelength point, but rather, as is the case for analog instrumentation, one generally records spectra with the same relative error (or signal to noise ratio) at each wavelength.

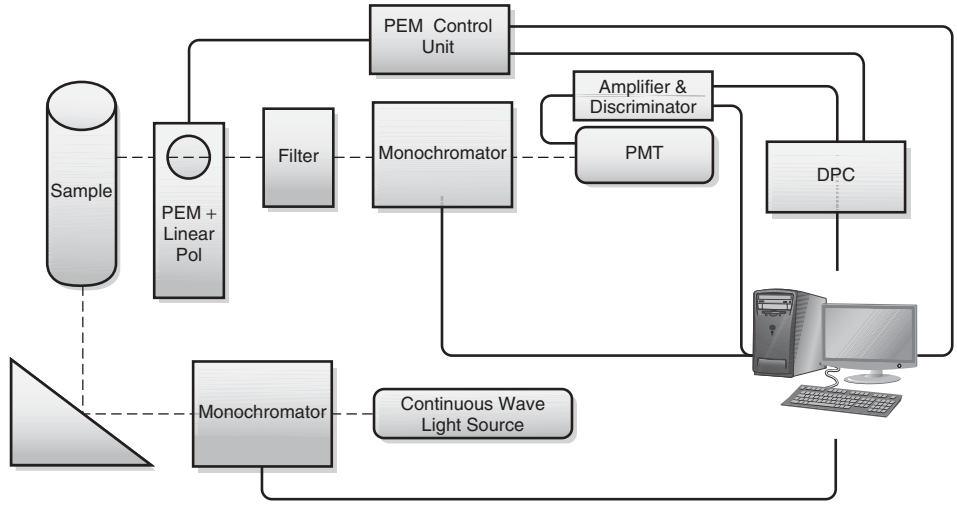

Figure 3.4. Schematic diagram for the instrumentation used for the measurement of CPL.

In order to do this, one simply counts photon pulses for a fixed amount of time at each wavelength.

All of the custom-made instruments use the same basic optical design. As a representative example, we present here a brief description of the CPL instrument used in the laboratory at San José State University. This CPL instrumentation follows the design shown in Figure 3.4. This instrument, as illustrated, is currently designed to measure "steady-state" CPL. A continuous wave excitation light source is provided by a tunable dye laser (Coherent-599) pumped by an argon-ion laser, an argon-ion laser without the dye laser (Coherent Sabre TSM 15 or Coherent Innova-70), or a 450-W xenon arc lamp. The choice of excitation light source (laser or xenon arc lamp) depends on the nature of the specific chiral system under study. A number of different types of applications of CPL spectroscopy are described in Section 3.6.1. In general, laser excitation is used when one desires either high-intensity wavelength, or polarization selectivity. In practice, laser excitation is used primarily for selective direct excitation of lanthanide (III) ions, whereas the arc lamp is used for excitation of the broad absorptions commonly seen in organic/polymeric systems or organic-based ligands.

With the exception of the excitation monochromator, the experimental setup for laser and xenon arc-lamp configurations are identical. In the laser configuration, the excitation wavelength is, of course, a property of the specific laser. For tunable laser sources, the specific excitation wavelength is set via a computer-controlled stepping motor. The emission wavelength is selected via a double monochromator (SPEX 1680), which is also controlled by the computer. In the xenon arc-lamp configuration, both excitation and emission wavelengths are selected via single-grating monochromators (SPEX 1681) and are controlled by the computer. It should be mentioned that in this experimental setup the laser beam is situated below the sample and emission light path and is reflected through the sample quartz fluorescence cuvette with a polished bottom surface. In addition, the polarization of the laser beam is aligned along the direction of emission (laboratory **3** direction) in order to minimize any polarization in the **12** plane for the reasons discussed in Section 3.5.1.

Situated between the sample and emission monochromator is the circular analyzer which is composed of a photoelastic (or elasto-optic) modulator (PEM) followed by a high-quality linear polarizer. The PEM is constructed from an isotropic clear optical material that becomes anisotropic on application of a periodic stress. For CPL measurements the PEM is set to act as a dynamic quarter-wave device, alternately converting the right- and then left-circularly polarized light emitted from the sample to linearly polarized light. The light is then directed toward the emission monochromator and ultimately to a cooled photomultiplier operating in photon-counting mode.

A plot of the modulation phase versus time is given in Figure 3.5. The time dependence of the phase shift, φ, is related to the sinusoidal periodic stress frequency, ω_{PEM}, (usually 50 kHz), as follows:

$$\varphi = A_m(\lambda_{EM}) \sin[\sin(\omega_{PEM} t)] \tag{3.23}$$

where we have explicitly noted that the amplitude, A_m, of the periodic stress is dependent on the wavelength of the emission. The maxima and minima of this function correspond to plus quarter-wave (+1/4) and minus quarter-wave (−1/4) retardation. Since a fixed oriented linear polarizer is placed after the PEM, the monochromator sees light of only one polarization throughout the modulation cycle. This is very important due to the polarization sensitivity of monochromators. The amplitude of the stress applied to the PEM for so-called wavelength tracking is controlled by the dedicated computer through application of an appropriate voltage to the optical head unit of the PEM. Since in such polarization-sensitive detection experiments it is obviously necessary to minimize sources of depolarization, one must avoid placing optical elements between the sample compartment and the PEM. This requirement is even more important for CPL-type measurements because the difference in intensities between the left- and right-circularly polarized emitted light are 10–100 times less than that normally observed in linearly polarized luminescence measurements. However, once the emitted light has passed through the PEM and the linear polarizer, it is strongly recommended that the emitted light travels through an appropriate filter to eliminate scattered excitation and other stray light. The emitted light, which is passing through the emission monochromator, is detected by the thermoelectrically cooled photomultiplier tube (PMT), operating in photon-counting mode, and converted to TTL-level pulses by the amplifier-discriminator for counting by the differential photon counter (DPC).

In our experimental setup the PEM control unit provides a 50-kHz reference signal to the DPC that is used to define a fixed time window for gated counting. This is

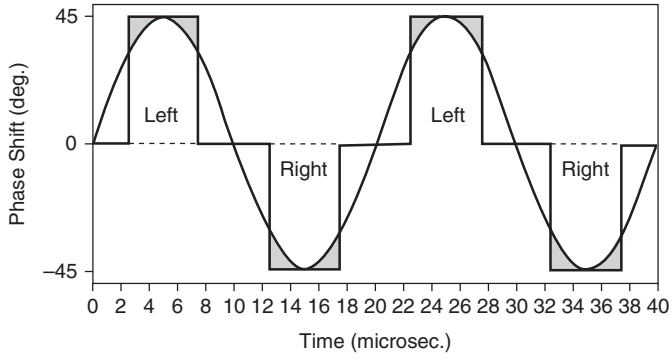

Figure 3.5. Plot of the phase modulation versus time for a 50-kHz PEM.

also illustrated in Figure 3.5. The beginning and ending of the two counting windows corresponding to left- and right-circularly polarized photons are determined by monitoring the reference signal as it crosses through 0 and then waiting a fixed number of clock cycles (10 GHz) before starting and stopping the counting of photon pulses. In our experimental setup the DPC is a stand-alone device that is set up and monitored by the computer. It is periodically probed to determine the number of counts corresponding to I_L and I_R detected in the two half-cycles of the polarization modulation. We usually set the time window to 50% of the modulation cycle as illustrated in Figure 3.5 and count all photons detected in this time window as either left- or right-circularly polarized. There is a slight error with this assumption associated with the phase shift being not exactly quarter-wave. The shaded area in this figure corresponds to the error in this approximation. Obviously, the shorter the time window, the less the error will be in g_{lum}. One can easily calculate the error by calculating the area of the shaded region and comparing it to the rectangular time windows. For a 50% window we calculate a theoretical error of less than 5%; and although a correction factor could be applied to the measurement, since there are numerous sources of other errors in optics, and statistical errors associated with the photon counting, we have decided to simply report the experimental results as measured. It should be emphasized that one of the most important aspect of this gated-counter technique is the requirement that the time windows for left- and right-circular polarization detections must be positioned properly, have a high temporal resolution, and be exactly equal in width.

In our laboratory, we use two custom-built DPCs. The older of the two DPCs was built at the University of Leiden, The Netherlands, under the supervision of H. P. J. M. Dekkers, and is a fixed-function design built from application-specific integrated circuits (ASICs). The DPC supports a variable sample size of 2×10^N photons, where $N = 4$, 5, 6, 7, or 8. This parameter is set via a physical setting on the device. Control of the device is performed using start, stop, and reset commands that are sent from a computer through a Keithley KPCI-3102 digital I/O board. When a start command is sent to the DPC, the DPC counts for the specified sample size and returns a final g_{lum} value. This value is also read through the digital I/O board. More recently, our research group at San José State University has developed a new DPC based on a Field Programmable Gate Array (FPGA) design. The immediate benefit of an FPGA is that it is a software design, one that is easily modified and replicated. Building a DPC is as easy as purchasing a commercially available Spartan 3AN FPGA board, loading the code implementing the design, and housing it in an enclosure. In our laboratory we currently have two such implementations, one intended for use with our laser instrumentation and another intended for use with instrumentation for near-infrared studies. The new DPC takes advantage of the serial port available on the Spartan 3AN board. All input and output functions are performed through this interface. This means that any computer with a serial port—as most PCs do—is able to use the new DPC without an expensive I/O board. Development and testing of DPC features are also greatly simplified, because serial port programming interfaces and terminal applications are readily available. Current commands supported by the new DPC include Count, Reset, and Toggle Mode. The mode Toggle is meant to enable switching between the standard photon counting mode and a pulse mode. This new DPC, in its current form, supports the counting of total photon pulses from any value from 1 to 2×10^9. This sample size is fixed in the sense that it is a constant value that is set in the FPGA code. It is flexible, however, in that this value can be changed and can be implemented simply by reloading the FPGA board with the new code. Also, given the expandable and easy-to-modify nature of FPGA designs, it would be possible

to implement a new feature in the future that would support the specification of a sample size via computer input.

One feature of the new DPC is that it does not return results in the form of a final g_{lum} value. Instead, the current FPGA design returns the individual left and right photon counters, leaving the calculation of the g_{lum} value to the computer [see Eq. (3.2)]. The advantage to this approach is that it provides more information, including total luminescence intensity, and allows for calculation of g_{lum} values across increments of the sample size (i.e., for a fixed sample size of a thousand, it would be easy to make counts for any positive, integer multiple of a thousand). As previously mentioned, the new DPC also includes a pulse mode. In our current experimental setups, all light sources are continuous wave. For laser setups, it is possible to break the continuous wave into pulses with the use of a chopper. Taking a reference signal from the chopper's controller, it is possible to perform photon counts based on the duration of the pulse, rather than for a fixed quantity of photons.

Advances in computer technology, and especially the commercial availability of very-high-speed counting/timing boards that may be easily programmed, will certainly lead to the development of new instrumentation for CPL in which the gated detection, calibration, and control will all be performed within a high-speed computer. Such an improvement in measurement technology is underway in our laboratory.

The overall principle and the optical components of CPL instruments capable of measuring the time-dependence of g_{lum} are similar to the ones described above, with the main difference being the excitation source. Unlike the use of a continuous excitation light source for the steady-state CPL instrumentation, a pulsed excitation light source is used in the time-resolved CPL equipment. This measurement involves determining g_{lum} at a series of times after the excitation pulse. The time measurement window needs to be some multiple of the phase modulation. In order to ensure equal sampling of the two half-cycles of modulation, corresponding to emission of left- and right-circular polarization, the excitation pulses must be coupled to the polarization modulation cycle [21] or be set to occur randomly throughout the modulation cycle [22].

Until very recently, all CPL measurements published in the literature were performed with custom-made instruments. The technique has developed to a point where the detection of CPL for moderately luminescent chiral systems can now be performed with a high degree of sensitivity ($\sim$1 part in 10^4–10^5) and reliability. There is some emerging interest in the development of chiral optical probes that take advantage of the inherent sensitivity of luminescence, especially involving lanthanide (III) ions, and this has led to the advertising and some availability of commercial instrumentation. The first commercial CPL spectrometer for which published data has appeared [23] is manufactured by JASCO Inc., one of the leading suppliers of commercial CD instruments. The JASCO CPL-200 instrument essentially consists of two CD spectrometers, with the second one used as the emission spectrometer. More recently, OLIS Inc. developed its *Polarization Toolbox* to support fluorescence, polarization of fluorescence, anisotropy, CPL, CD, and FDCD measurements for its CD instrumentation. As of August 2010, no CPL-based studies using the OLIS instrument has appeared in the literature, although several instruments have been sold.

3.3.2. The Measurement of Emission-Detected Circular Dichroism

In some aspects, an instrument capable of measuring EDCD (or FDCD) is the exact reverse of a CPL instrument. In this case, the excitation is modulated between left- and

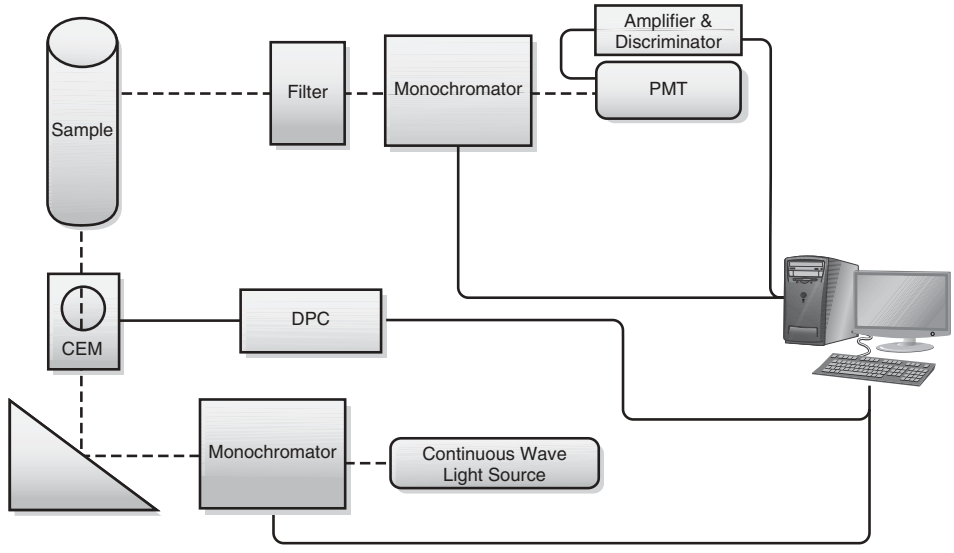

Figure 3.6. Schematic diagram showing instrumentation used for the measurement of EDCD.

right-circular polarization, and the total luminescence is detected in phase with the modulation and used to determine any difference in absorption. A schematic diagram of an EDCD instrument is given in Figure 3.6. As described earlier, there are some complications with the measurement of EDCD if one is interested in using this technique to report on the CD of a sample. The intrinsic problem of self-absorption has no consequence in terms of experimental design; one simply needs to take this into account during data analysis [17]. However, the problems associated with the presence of linear polarization in the luminescence do require the use of special experimental geometries or techniques to minimize or eliminate the unwanted effects. This phenomenon will be discussed in more detail in Section 3.5. In this section we will simply describe ways to eliminate the linear polarization in the direction of emission detection.

As can be seen in Figure 3.6, the incident excitation beam is passed through a polarization modulator before entering the sample compartment. Circularly polarized light is generated by first converting an excitation source to linear polarization before passing through the polarization modulator. It is obviously important that the modulation cycle time be much longer than the emission lifetime of the species under study if one is interested in associating the emission measured in phase with the circularly polarized excitation with the absorption event. For ordinary organic fluorescence with emission lifetimes on the order of nanoseconds, the PEM device described previously is the modulator of choice, since the cycle time is typically 20 μs. Earlier instruments employed Pockels cells for the generation of circularly polarized excitation. However, for organic phosphorescence, or for the usually long-lived lifetimes of luminescent lanthanide ions with lifetimes on the order of msec, we have employed a liquid crystal polarizer (LCP) operating as a quarter-wave device which can be programmed to modulate with a cycle time as slow as 1 s or longer [24]. It is important that the orientation of the linear polarizer be at 45° relative to the crystal axis of the PEM or vertical (or horizontal) axis of the LCP. As in CPL instrumentation, the computer controls the amplitude of the PEM or the alignment of the LCP to track with the wavelength of excitation. The LCP is switched between circular polarizations by the computer; and unlike the PEM, it is nearly exact

square-wave modulation. All the photons collected in phase with this square-wave modulation are counted, except for a small time period around the switching points that are excluded.

The luminescence is typically collected at 90° with respect to the excitation direction, and therefore, for nonisotropic emitters that do not have sufficient time between absorption and emission to randomize their orientational distribution, there will be linear polarization in the luminescence. There have been a number of suggestions to eliminate linear polarization. In principle, one can employ "magic angle" orientations for a linear polarizer/detector system [25], or orient two linear polarizer/detectors at specific angles [26, 27]. Applications of these techniques may be problematic due to the precise alignments that are necessary. More recently, the use of a carefully constructed ellipsoidal mirror has been employed to essentially collect all of the luminescence from a sample [28]. This has the result of eliminating any effects due to linear polarization.

3.4. STANDARDS FOR CPL

In the analog detection of CPL, the differential emission intensity, ΔI, is assumed to be proportional to the output of the lock-in amplifier, and the total emission intensity, I, is proportional to a DC output voltage. These are generally independent measurements, so that a determination of g_{lum} requires the use of a calibration standard. One of the main advantages of the photon counting method is that g_{lum} is determined directly, so that, in principal, no independent calibration is necessary.

It is obviously important that one be sure that the magnitude and sign of the CPL signal are being measured accurately. Although there have been efforts at standardization and calibration using variable quarter-wave plates [5], or passing unpolarized light through solutions of known CD [29], the most common approach is to use a solution containing a chiral species of known CPL. Brittain was the first to suggest the use of the commercially available NMR chiral shift reagent tris(3-trifluoroacetyl-*d*-camphorato)europium (III), Eu(facam)$_3$, as a CPL standard [30]. This complex is available in high purity, is readily soluble in DMSO, and may be excited either by a UV source at around 350 nm or by an Ar-ion laser excitation at 345 nm. This complex has also been used by Schippers [18]; three different Eu(III) transitions are observed with variable signs and magnitudes. It should be noted that Maupin has noted that the chirality of lanthanide facam complexes in DMSO are quite sensitive to the presence of water, so that care should be taken to ensure dry complex and dry solvent when using this species as a CPL standard [31]. In addition to the water sensitivity, the high cost of Eu((−)-facam)$_3$ with the other enantiomeric form of facam limits its use as an effective and reliable CPL standard for routine tests. Indeed, any CPL instrument needs to be regularly tested and calibrated for the accurate detection of small degrees of circular polarization in the total emitted light intensity.

Working along these lines, Bonsall et al. [32] reported on the use of an alternative CPL calibrating agent based on optical isomers of *N*,*N*′-bis(1-phenylethyl)-2,6-pyridinedicarboxamide (**1**) coordinated to Eu(III) ions in a Eu:**1** ratio of 1:3 (Figure 3.7). In particular, the advantages of these systems are (i) the ease of the ligand synthesis, (ii) their complex solution stability (i.e., several months), and (iii) the lack of a noticeable photochemical degradation under continuous UV excitation (i.e. 70 h, $\lambda_{exc} = 308$ nm). A g_{lum} (595.3 nm) value amounted to −0.18 for a $[\mathrm{Eu}((R,R)\text{-}\mathbf{1})_3]^{3+}$ complex solution in MeCN left on the shelf and measured seven months apart.

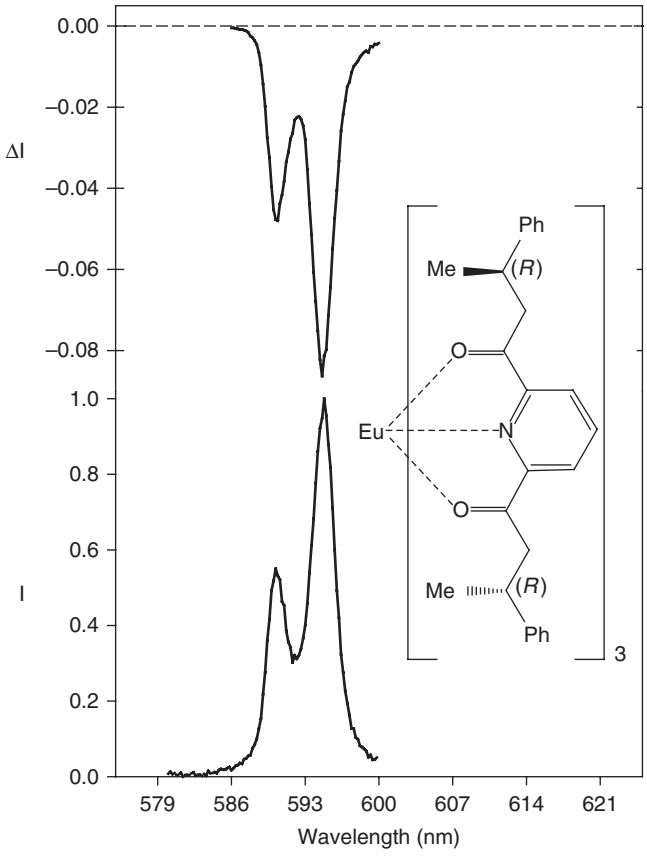

Figure 3.7. CPL (upper curves) and total luminescence (lower curves) spectra for the $^5D_0 \rightarrow {}^7F_1$ transition of $[Eu((R,R)\text{-}\mathbf{1})_3]^{3+}$ in 6.67×10^{-3} M MeCN at 295 K, following excitation at 308 nm. [See reference 32.]

It is important that standard samples be used in an appropriate manner. Due to the nature of the custom-built instruments that are used for this technique, some routine testing should be performed on a regular basis. If the values obtained for the particular standard are not obtained, then the source of the error needs to be identified and necessary modifications made to the instrument to get the accepted values. In general, it is not proper to compensate for any experimental and/or instrumental uncertainties that are evident by comparison with an accepted standard by applying a simple additive or multiplicative correction factor without some justification. Two recent reports of CPL measurements need to be examined in the light of the discussion in the previous paragraph. Coughlin et al. assumed that any instrumental and experimental errors could be corrected by adjusting the experimental values of ΔI and I for their CPL measurements with an additive factor determined from the measurement of the g_{lum} value of a racemic mixture of a luminescent bipyridyl hemicage complex [33]. The idea was that one would expect that a compound existing as a racemic mixture of both of its isomers in solution would result in no emitted circular polarization (a g_{lum} value of 0 should be obtained) assuming perfect operating conditions for the instrumentation. Since the authors recorded a g_{lum} value of -7.9×10^{-5}, they concluded that all of their CPL measurements should be corrected by this amount. This might be a valid approach, for example, if there was a slight phase offset from the modulation phase and the gated counter time windows. However, the accuracy and precision of CPL measurements are sample-specific and wavelength-dependent, since each compound may respond differently to the various

sources of error in polarization measurements that one may encounter. Note also the discussion in the next section concerning the presence of linear polarization. A similar concern is appropriate for experimental determination of g_{lum} values in the CPL study by Matsumoto et al. [34]. The experimental g_{lum} values of their Eu(III)-containing systems were corrected with a multiplication factor that was determined using the known g_{lum} value of the $Eu(facam)_3$ standard.

3.5. ARTIFACTS

3.5.1. Artifacts in CPL measurements

The principal source of artifacts in CPL spectroscopy is linear polarization in the luminescence beam. These effects should not be confused with the presence of a nonisotropic orientational distribution of luminescing species. In this latter case, one might be measuring the CPL of an oriented system that will most probably give different results than one would get from an isotropic system [35]; however, as long as the sample is isotropic in the plane perpendicular to the direction of emission detection, there will be no linear polarization in the **12** plane, and one would see no associated artifact signal. This, for example, is the situation encountered in the measurement of the CPL from chiral triarylamine helicenes by Field et al. [36] in which the authors used an excitation beam that was linearly polarized along the laboratory **3** axis to ensure no linear polarization in the **12** plane. Another approach was taken by Tsumatori et al., who excited their samples of chiral derivatized perylene aggregates at 0° in an epiluminescence measurement [37]. These authors depolarized the Ar-ion laser beam used for excitation to ensure no linear polarization in the luminescence.

It has long been recognized that the main source of artifacts in CPL measurements is the passing of linearly polarized light through the very slightly birefringent PEM [7, 38]. Even though this birefringence is usually small ($<5\%$), it may lead to a signal of comparable magnitude to many true CPL signals, since the extent of linear polarization is usually very much larger. Some success has been obtained in eliminating linear polarization effects by rotating the PEM and linear polarizer such that the birefringent axis of the PEM is parallel to the plane of polarization of the emitted light, or by using specific combinations of excitation/emission geometries and linear polarizers, for example, situated at so-called "magic angles" [25]. However, it is our experience that one can only be confident of the accuracy of a CPL measurement by verifying by experiment that the emitted light contains no linearly polarized component in the plane perpendicular to the emission direction. It is unfortunate that some of the earliest reports of CPL are the consequences of this artifact, and not due to molecular chirality.

The experimental consequences of the presence of linear polarization has limited the usefulness of CPL spectroscopy in studies involving fluorescence from chiral organic luminophores. Our attempts to overcome some of these problems through preparation of isotropic samples have had limited success. We have been able to measure CPL from lanthanide complexes dissolved in sol–gels [39], but all attempts to work with chiral molecules in KBr matrices have been unsuccessful. There have, in fact, been two recent reports of CPL from chiral organic molecules prepared in KBr, but these results have not been confirmed with racemic mixtures or by comparison with known solution samples [40, 41].

It is the case, however, that to date, no one has observed linear polarization in the luminescence from lanthanide (III) ions in ordinary solutions. This is due to the nature

of the electronic transitions involved and the fact that the lifetimes of the luminescent lanthanide (III) ions are long, allowing for any initial photoselected orientational distribution to randomize in the time between excitation and emission. It should be noted that Meskers et al. did report linear polarization in the individual crystal field components of an Eu(III) complex that had been prepared in a very viscous solution [42].

3.5.2. Artifacts in EDCD measurements

As mentioned earlier in this chapter, one of the difficulties that has impeded the use of EDCD spectroscopy is the artifacts caused by linear polarization. Again, here we should distinguish the normal effect of photoselection from the consequences of imperfect optical devices. Luminescence collected at right angles to the direction (**1**) of circularly polarized excitation by a single detector will lead to intensities that reflect differences in the distribution of emitting molecules that are oriented parallel versus perpendicular to the plane (**23**) of excitation. In the case of perfect alignment and optics, there should be no modulation of the total luminescence caused by this orientational distribution, but one would need to interpret the results as being from a nonisotropic sample. Comparison to CD results from isotropic solution would be somewhat problematic.

The polarization-induced artifact in EDCD measurements is caused by imperfections in the incident circular polarization modulation leading to some residual linear polarization [26, 43]. In principle, this artifact can be eliminated with the use of the two-detector scheme of Hug [26] that was effectively utilized by Lobenstein and Turner [43], or with the use of the ellipsoidal mirror configuration employed in the JASCO instrument [28].

3.6. EXAMPLE APPLICATIONS

The example applications presented in this section have been chosen to highlight the utility of CPL and EDCD to provide unique information concerning the chiral structure or structural changes to a range of molecular and biomolecular systems. For a more thorough treatment of the variety of applications of this chiroptical measurement, the reader is referred to the several reviews of CPL spectroscopy that have been published in recent years [7, 9, 12].

3.6.1. CPL

Although CPL spectroscopy has been a useful probe of some luminescent chiral organic molecules, liquid crystals, and polymers, the literature in the last 20 years is dominated by applications involving luminescent lanthanide (III) ions, particularly Eu(III) and Tb(III). These species are especially suited for CPL because of their long excited-state lifetimes, extremely narrow emission and absorption bands that are easily recognizable and well separated from the broad fluorescence bands of any organic fluorophores that may be present in the solution, the usually large Stokes shift, and, probably most importantly, the presence of formally forbidden intraconfigurational $f-f$ transitions that often show large circular polarization.

Many of the most recent applications of CPL from chiral lanthanide (III) containing systems have been driven by efforts to develop selective and sensitive probes of biomolecular structure [9, 12, 44]. Some of this work has involved the characterization of the structure, spectroscopic properties, and excited-state energetics of new chiral lanthanide (III) complexes, and other work has focused on the use of these chiral sensors as probes of specific biomolecular structure and dynamics.

3.6.1.1. CPL and Luminescence Selectivity. Unlike CD spectroscopy where all the absorbing chromophores contribute to the observed differential absorption measurement, CPL spectroscopy is limited to luminescent species. For example, in proteins the CD must be interpreted in terms of an average structure over the entire macromolecule reflecting a large number of chromophores in a multitude of different chiral environments. On the other hand, CPL measurements involving intrinsic fluorescence reflect the chiral environment surrounding the very few aromatic residues that emit [4]. In a similar way, the CPL from lanthanide (III) ions used as substitutional replacements for Ca(II) reflect the chiral structure surrounding the metal-ion binding sites [45, 46]. This selectivity has also been observed in small-molecule studies. For instance, Lunkley et al. recently showed the importance of using CPL for studying only luminescent chromophores present in solutions containing cesium and sodium tetrakis(3-heptafluoro-butylryl-(+)-camphorato = (+)-hfbc) Eu(III) complex solutions, $M^I[Eu \cdot (+)\text{-hfbc}_4]$ (M^I = Na or Cs), in EtOH. These authors showed a concentration-dependent exciton CD due to the dissociation of the tetrakis (+)-hfbc Eu(III) compound into the tris (+)-hfbc Eu(III) complex. The former species exhibited a strong CPL activity in solution, whereas the CPL activity of the latter compound was negligible [47].

It is obviously important to interpret CPL results in light of the selectivity of this technique and the manner of detection. Hilmes and Riehl have shown, for example, that the total luminescence intensity and CPL from a so-called "mixed" solution of Tb(III) with dipicolinic acid (DPA) and L-malic acid come from different species [48]. The total luminescence comes almost exclusively from tris $Tb(DPA)_3{}^{3-}$ and the CPL comes from some unknown mixture of Tb(III), L-malic acid, DPA and water. One must not simply divide ΔI by I in this system and interpret the result in terms of a single solution species.

3.6.1.2. CPL as a Chiral Structural Probe. Although the development of useful correlation between the CPL spectrum and chiral structure is still limited, there has been some useful information obtained. Bruce et al., for example, have studied well-defined DOTA-based macrocyclic Eu(III) complexes and showed that the sign and magnitude of CPL are affected by the degree of helical twist of the complex, the nature of the ligand field, and the axial donor group solvation [49]. These authors showed that the local helicity at the Ln(III) center is related to the angle, ϕ^{gn}, between the electric-dipole ($|P_{gn}|$) and magnetic-dipole ($|M_{ng}|$) transition moment vectors and, therefore, the rotatory strength, R_{gn}, associated with a given transition between two states g and n as described below.

$$R^{gn} = |P^{gn}||M^{ng}| \cos \phi^{gn}. \tag{3.24}$$

The rotatory strength can be shown to have a $\sin 2\theta \cos 2\theta$ (or $\sin 4\theta$) dependence, where θ is the twist angle between the N_4 and O_4 planes of the DOTA ring. It is, therefore, predicted to vanish at 0°, 45°, or 90° and to be a maximum at ±22.5° for square-antiprismatic complexes (SAPR) (see Figure 3.8). This latter value is closer to twist angles determined by crystallographic analysis for twisted square antiprismatic isomers (∼28°) than those associated with regular square antiprismatic species (∼40°).

Working along these lines, Lunkley et al., who reported the largest g_{lum} value (g_{lum}(595 nm) of +1.38) ever observed for any CPL studies of Ln(III)-containing compound solutions described in the literature, explained that the constant CPL activity of the tetrakis (+)-hfbc Eu(III) complex was due to the helical Δ-SAPR(C4) arrangement of the four (+)-hfbc ligands in the compound of interest [47]. This result is shown in

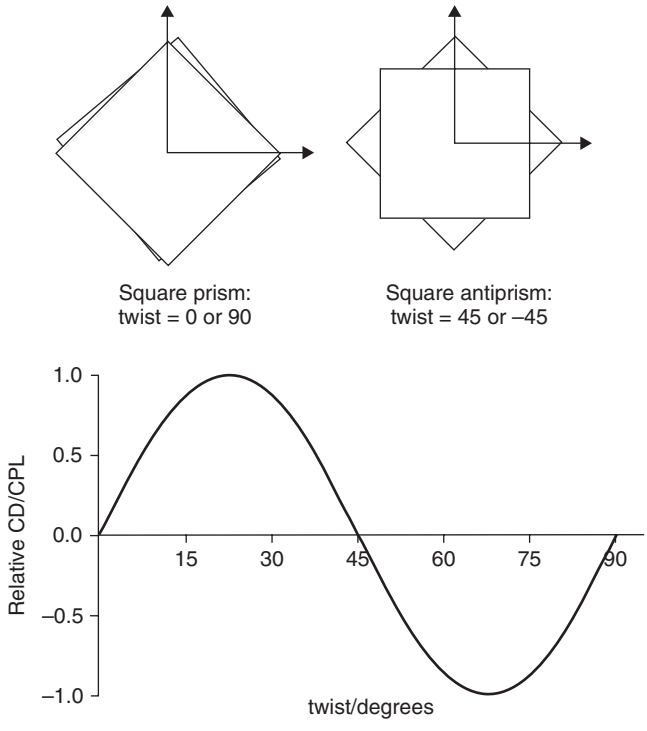

Figure 3.8. Correlation of the effect of twist angle in axially symmetric eight- and nine-coordinate antiprismatic lanthanide (III) complexes on their CPL or CD intensity. [See reference 49.]

Figure 3.9. In addition, they also showed that the solvent and alkali metal ion effects were due to the difference in susceptibility to solvation toward the alkali metal ion, but not toward the Eu(III) ion, unlike the case of axially symmetric DOTA-type complexes described by Bruce et al [49]. This conclusion was corroborated by the observation that the helical Δ-SAPR(C_4) arrangement of the four (+)-hfbc ligands in CH_3Cl and EtOH accounted for the CPL pattern of the M^I-Ln complexes, which in turn was controlled by the alkali metal ion sizes. The ninefold decrease in the magnitude of the CPL signal of the Na–Eu compound resulted from a less chiral environment for the Eu(III) ion in the Na–Eu compared to Cs–Eu. In addition, the authors indicated that the constant and large CPL activity substantiated the stereospecific formation of chiral Δ-SAPR-(C_4) configurations with the aid of $M^I \cdots FC$ (fluorocarbon) interactions as revealed by the X-ray analysis more clearly than the exciton CD spectra.

CPL has also been proven useful to monitor the formation of luminescent chiral aggregates from chiral monomers. A considerable amount of this work is aimed at developing a controllable molecular source for circularly polarized light. Tsumatori et al. have shown aggregation of chiral perylene derivatives as a function of concentration by observing increasing g_{lum} values as large as +0.006 for the excimer transition of these coupled aromatic systems [37]. Kawagoe et al. have employed CPL and CD to monitor the formation of chiral polymer structures by the addition of (*R*)- and (*S*)-limonene to achiral polymers [50]. In another interesting application, Goto and Akagi used CPL to monitor the formation of optically active conjugated polymers containing thiophene subunits prepared from achiral starting material in a chiral nematic solvent [51]. Especially for weakly luminescent organic systems, care must be taken to avoid photodegradation and photoracemization due to extended excitation exposure. This was seen, for example, by Solntsev et al. in a study involving chiral BINOLs [52]. In a more indirect approach,

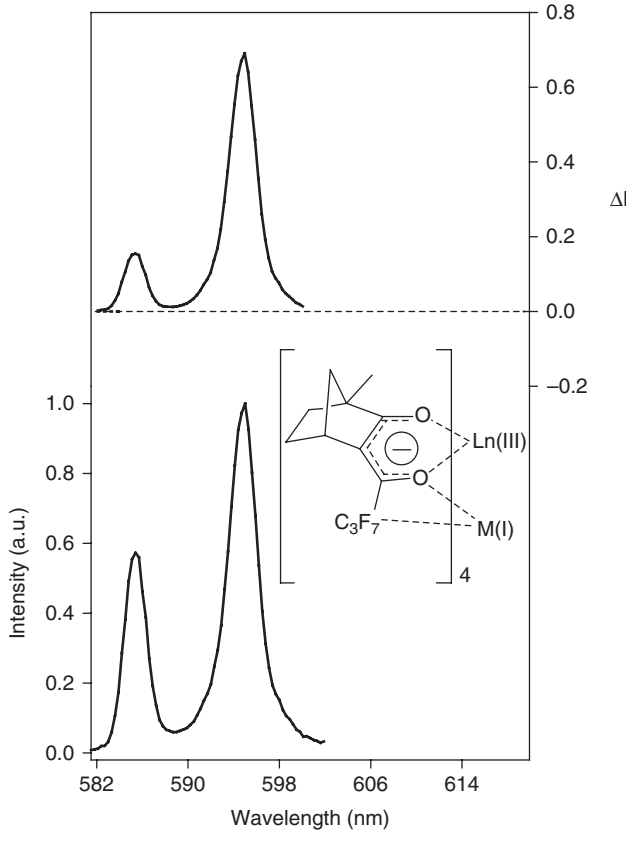

Figure 3.9. Chemical structure of M^I[Eu(III)-(+)-hfbc$_4$] (M^I = Cs); CPL (upper curves) and total luminescence (lower curves) spectra for the $^5D_0 \rightarrow {}^7F_1$ transition of the 2 mM Cs[Eu((+)-hfbc)$_4$] solution in $CHCl_3$ at 295 K, upon excitation at 352 nm. [See reference 47.]

Montgomery et al. used CPL from lanthanide complexes to probe certain aspects of protein structure; this work resulted in the discovery of a very unique chiroptical probe for serum albumin binding [53]. They showed that the Δ-conformer of the Ln(III) complexes with the enantiopure ligand (*SSS*)-**1** (Figure 3.10) bound selectively to "drug site II" in serum albumin. The novelty was that this binding process resulted in an inversion of the complex helicity (Δ to Λ), as signaled by a sign change in the CPL spectra, and was only observed for the Eu(III) and Tb(III) compounds with (*SSS*)-**1** and its analogues. No dynamic helicity inversion was observed for the related complexes with (*RRR*)-**1**, nor in the presence of excess of various substrates such as *B*- or *Z*-DNA, chiral anions (i.e., tartrate, lactate), (*S*)- or (*R*)-α-phenylsuccinate, or cyclodextrins. These findings were corroborated by the lack of changes in the sign and form of the measured CPL signals.

3.6.1.3. CPL from Racemic Mixtures. One of the unique aspects of CPL spectroscopy is the ability to study racemic mixtures. In this application, a circularly polarized excitation source is used to generate a nonracemic excited (emitting) state from a racemic ground sate by polarization-selective excitation. These experiments are successful only if the nonracemic excited state is shorter than the time required for racemization. Hilmes and Riehl [54] have shown that the measured g_{lum} value for the racemate is related to the CD and CPL of the individual enantiomer as follows:

$$g^L_{lum}(\lambda) = -\frac{1}{2} g^R_{abs}(\lambda') g^R_{lum}(\lambda) \tag{3.25}$$

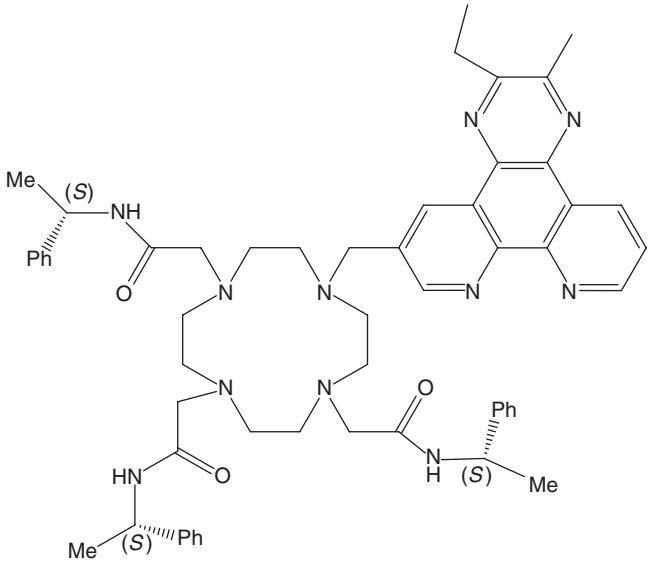

Figure 3.10. Chemical structure of ligand (*SSS*)-**1**. [From reference 53.]

where we have designated the excitation wavelength as λ'. Because this measurement depends on the product $g_{abs}g_{lum}$, and the detection limits of CPL are usually $>10^{-4}$, the experiment is limited to transitions with large dissymmetry values. Perhaps, the best example of this kind of experimental study are the numerous reports involving the 9-coordinate tris-terdentate complex of Ln(III) ions with 2,6-pyridine-dicarboxylate (DPA) derivatives. For example, CPL following circularly polarized excitation confirmed that the $[Eu(DPA)_3]^{3-}$ complex species exists as a racemic mixture of structural enantiomers, Λ and Δ, in basic aqueous solution that do not racemize significantly during the excited state lifetime at room temperature, but have been observed to racemize at higher temperatures from steady-state [55] and time-resolved [56] CPL measurements.

3.6.1.4. CPL as a Probe of Specific Molecular Chirality. Perturbation of the well-studied racemic equilibrium between the Δ and Λ enantiomers of the tris-terdentate complexes of lanthanides with DPA and related ligands through the addition of chiral "environment" compounds (the so-called Pfeiffer effect) has been exploited as a means of probing specific chiral structural aspects of the chiral additive. This work has involved a variety of optically active organic molecules such as tartrate substrates, amino acid, or sugar derivatives that are presumed to be involved in outer-sphere coordination [9, 44, 54, 57–69]. In these studies it is assumed here that the effect of adding chiral species (C^*) results in the preferential formation of diastereomeric outer-sphere association complexes [66]. The three relevant equilibrium expressions are defined as follows:

$$\Delta\text{-Ln(DPA)}_3{}^{3-} \leftrightarrows \Lambda\text{-Ln(DPA)}_3{}^{3-} \qquad (K_{rac} = 1) \tag{3.26}$$

$$\Delta\text{-Ln(DPA)}_3{}^{3-} + C^* \leftrightarrows \Delta\text{-Ln(DPA)}_3{}^{3-} : C^* \qquad (K_1) \tag{3.27}$$

$$\Lambda\text{-Ln(DPA)}_3{}^{3-} + C^* \leftrightarrows \Lambda\text{-Ln(DPA)}_3{}^{3-} : C^* \qquad (K_2) \tag{3.28}$$

where the outersphere association complex is denoted by a colon (:). Any success in using the direction of perturbation to determine chiral structure hinges on the ability

to understand the complex interactions between the chiral adduct and the enantiomeric metal complexes.

A significant amount of work has been focused on using this technique to probe chiral aspects of amino acid structure. For example, Muller et al. showed that the CPL sign and magnitude of specific Ln(III) transitions are dependent upon several factors and not simply the chiral identity of the enantiomerically pure amino acid [59]. They observed that (i) some simple modifications in the chiral adducts did not change the sign of the CPL signal (the same enantiomeric form was favored) and (ii) the magnitude of the CPL signal was influenced by the presence of additional aromatic groups in the perturbing molecule. It is clearly important in these systems to understand the effect of the various noncovalent chiral discriminatory interactions such as hydrogen bonding, coulombic forces, π-stacking, hydrophobic effects, experimental conditions (i.e., pH, temperature, ratio of system of interest to amino acid), and steric effects on the CPL sign and magnitude.

Working along these lines, Moussa et al. recently demonstrated that the chiral recognition of L-amino acids can be modulated by the nature of the ligand interface of the racemic 9-coordinate terbium(III) complexes and, in particular, by varying the substituent in the *para*-position of the pyridine ring of DPA [70]. For instance, the hydrogen-bond character of the negatively charged hydroxyl group in chelidamic acid, the *para*-hydroxylated derivative of DPA, led to a larger "Pfeiffer effect" with L-amino acids (i.e., L-proline or L-arginine) susceptible to form hydrogen bonds with negatively charged groups, while these hydrogen-bonding effects were less important with DPA. In another recent study, Kosareff et al. examined the chiral recognition of solutions containing various equivalents of L- and D-serine. Although their qualitative results are of a preliminary nature, they confirmed that CPL spectroscopy has potential for the chiral recognition of optical isomers of a given amino acid [12, 71].

3.6.1.5. CPL from Ln(III) Complexes with Chiral Ligands. One common use of CPL spectroscopy is to investigate solutions containing luminescent complexes to determine whether or not the source of the luminescence is one particular complex or a mixture of species. If only one emitting species contributes to the luminescence observed in the sample, then the CPL results should be independent of excitation polarization (i.e., left-, right-, or plane-polarized light). On the other hand, had the complex solution contained a mixture of species, the CPL signal would be dependent on the polarization of the excitation beam and, also, whether direct or indirect excitation would have be used. The usefulness of such experiments has recently being proven. Samuel et al. confirmed the diastereopurity of Tb(III)-containing compounds with chiral tetrapodal octadentate ligands containing 2-hydroxyisophtalamide (IAM) antenna chromophores and utilizing diaminocyclohexane (cYLI) and diphenylethylenediamine (dpenLI) backbones [72]. The CPL measurements confirmed the presence of a single and multiple emissive species in solution for the 2:1 cyLI-Tb and dpenLI-Tb compounds, respectively. The CPL signal of the former complex solution was similar whether direct or indirect excitation was used (consistent with one single emitting species in solution), whereas the g_{lum} values of the dpenLI-Tb solution were dependent on the polarization of the excitation beam and on whether direct or indirect excitation was used. These findings were confirmed by the lifetime data, which indicated the presence of two emitting species for dpenLI-Tb that differed in their hydration number, and, consequently, in their coordination environment. It should be noted that NMR is often used for assessing the diastereopurity of chiral systems. In addition to the sample requirement for NMR measurements, it is often the

case that Ln(III) complexes, namely Eu(III) and Tb(III), cannot be investigated in this way due to their strong paramagnetic nature. This is the reason why the CPL technique is suitable for a detailed examination of the diastereopurity of chiral Ln(III) systems, as demonstrated in this study.

3.6.2. EDCD

The measurement of the CD through the measurement of differential luminescence intensity is most suited for situations in which one is interested in exploiting the enhanced sensitivity and selectivity of luminescence methods. In the best cases, specific local chiral information may be obtained concerning the structure and environment of a luminescent chromophore without the presence of overlapping absorption CD bands that in large systems need to be interpreted in terms of an average structure. In other situations, EDCD (or FDCD) gives one the ability to probe chirality of substances only available in minute quantities.

Early applications of this technique focused on the selectivity. For example, Lobenstine et al. reported on the chirality of single fluorescent tryptophans in a series of proteins [27]. Although exploitation of EDCD has been limited due to data analysis and linear polarization caused artifacts, there has been some recent success in studying luminescent chiral systems composed of interacting transition dipoles [73, 74]. Applications of this type, in which so-called exciton coupling theory may be applied, have been shown to provide accurate chiral structures with a large increase in sensitivity than conventional electronic CD when using the ellipsoidal mirror attachment available from JASCO [75].

Until recently, all of the measurements of this type could properly be classified as based on fluorescence detection. The transitions involved all had very short lifetimes (fluorescence), and as a result the modulation frequency for the exciting beam (typically 50 kHz) for a photoelastic modulator was slow enough compared to the excited-state lifetime that the emission detected within the polarization time window could be associated with the excitation event in the identical window. Transitions with long-lived emitting states, such as those observed with many luminescent lanthanide (III) species, present a challenge because of the fact that widely used PEM devices are changing incident modulation every 10 μs whereas the lifetime of many complexes are on the order of milliseconds. Muller et al. have recently showed how a liquid crystal polarization modulator with a cycle time of seconds could be used to measure the EDCD of an aqueous solution of $Eu(DPA)_3^{3-}$ in which a chiral excess had been generated through the addition of a large excess of the noncoordinating chiral environment compound (+)-dimethyltartrate. These authors compared their results to the CD and CPL of the same transition as is illustrated in Figure 3.11 [24, 76]. The CD and EDCD spectra correspond to the intraconfigurational f $\leftrightarrow$ f transition from the thermally excited $^7F_1$ state to the nondegenerate $^5D_0$ excited state, and the CPL spectrum is for the reverse transition. The differences in relative height between absorption and emission of the two crystal field components, corresponding to the splitting of the $^7F_1$ state, reflect the fact that in absorption the two states (in D_3 symmetry) have a Boltzmann distribution.

Very recently there have been several reports on the ultimate sensitivity of measuring the EDCD from a single chiral helicenes molecule [77–79]. The authors report a distribution of dissymmetry ratios, along with an average dissymmetry that was significantly different from that determined from a bulk solution. They have interpreted this result as reflecting the CD of an oriented single luminescent chiral molecule [78]. This is obviously a difficult measurement, especially considering the artifacts associated with the presence

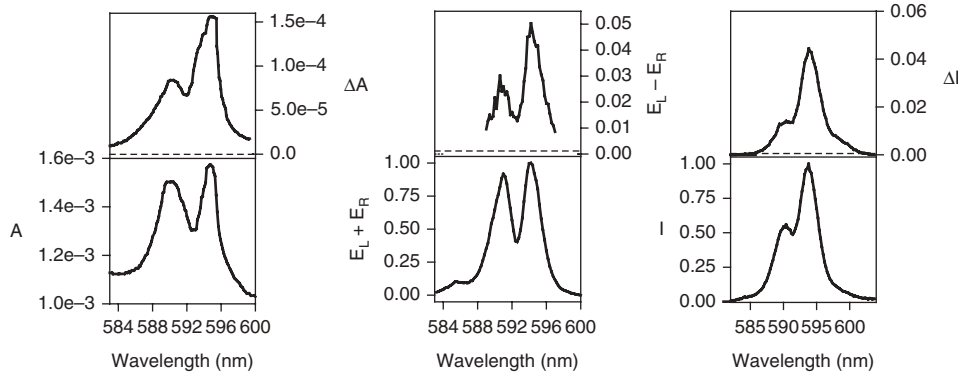

Figure 3.11. (Left) CD (upper curve) and absorption (lower curve) spectra for the $^5D_0 \leftarrow ^7F_1$ transition of an aqueous solution of 275:1 (+)-DMT:Eu(DPA)$_3^{3-}$. (Middle) EDCD (upper curve) and excitation (lower curve) spectra for the $^5D_0 \leftarrow ^7F_1$ transition monitored at 615 nm. (Right) CPL (upper curve) and total luminescence (lower curve) spectra for the $^5D_0 \rightarrow ^7F_1$ transition. [See reference 76]

of linear polarization that have plagued the measurement of EDCD in normal solutions. Tang et al. have commented that they were unable to reproduce theses single molecule chiroptical results, and concluded that Hassey et al. had not properly accounted for the effects of linear polarization [80]. This is currently an area of some dispute [81, 82].

3.7. SUMMARY

The measurement of the circularly polarized component in the luminescence from chiral molecules, along with the use of luminescence to monitor the differences in absorption of circularly polarized light, may provide unique information concerning chiral structure in certain applications. Advances in EDCD instrumentation, especially the commercial availability of the ellipsoidal mirror to both eliminate polarization artifacts and collect more of the luminescence, should lead to more applications of this technique especially for chiral samples only available in small quantities that can be chemically derivatized with luminescent chromophores that lend themselves to exciton coupling analysis. The continued development of EDCD involving long-lived lanthanide (III) species also shows promise to be an important chiral structural probe due to the large dissymmetry ratios that can be observed from these ions.

CPL applications in recent years have been dominated by applications involving luminescent lanthanide (III) ions, and there is no indication that this will change in the near future. Instrumentation for this measurement is becoming more available or easier to construct in one's own laboratory. What is most needed is the development of reliable correlations between CPL spectra and absolute chiral structure. The nature of the f electronic state makes this effort quite difficult, although some progress has been made in relatively high-symmetry species [66]. The lanthanide complexes that are being used as chiral structural probes tend to be very labile, so the experimental determination of the absolute structure from the sign of the CPL measurement is often not possible. There has been one recent example, however, in which this correlation has been made [83]. Applications of CPL involving carefully constructed racemic or chiral luminescent

complexes designed to probe specific aspects of biomolecular structure appears to be a potentially fruitful area of research. Continued development of time-resolved CPL instrumentation involving lanthanide (III) ions should also lead to interesting studies of biomolecules on a time scale (0.1–10 ms) reflecting structural changes associated with important biological processes.

ACKNOWLEDGMENTS

G.M. thanks the National Institute of Health, Minority Biomedical Research Support (1 SC3 GM089589-01 and 3 S06 GM008192-27S1) and the Henry Dreyfus Teacher–Scholar Award for financial support.

REFERENCES

1. B. N. Samoilov, *J. Exp. Theor. Phys*. **1948**, *18*, 1030–1040.
2. C. A. Emeis, L. J. Oosterhof, *Chem. Phys. Lett*. **1967**, *1*, 129–132.
3. C. A. Emeis, L. J. Oosterhof, *J. Chem. Phys*. **1971**, *54*, 4809–4819.
4. I. Z. Steinberg, in *Biochemical Fluorescence: Concepts*, I. R. F. Chen and H. Edelhoch, eds., Marcel Dekker, New York, **1975**.
5. I. Z. Steinberg, A. Gafni, *Rev. Sci. Instrum*. **1972**, *43*, 409–413.
6. C. K. Luk, F. S. Richardson, *J. Am. Chem. Soc*. **1974**, *96*, 2006–2009.
7. J. P. Riehl, F. S. Richardson, *Chem. Rev*. **1986**, *86*, 1–16.
8. F. S. Richardson, J. P. Riehl, *Chem. Rev*. **1977**, *77*, 773–792.
9. J. P. Riehl, G. Muller, in *Handbook on the Physics and Chemistry of Rare Earths*, K. A. Gschneidner and J.-C. G. Bünzli, eds., North-Holland Publishing Company, Amsterdam, **2005**, pp. 289–357.
10. J. P. Riehl, in *Analytical Applications of Circular Dichroism*, N. Purdie and H. G. Brittain, eds., Elsevier, Amsterdam, **1993**, pp. 539–553.
11. C. L. Maupin, J. P. Riehl, in *Encyclopedia of Spectroscopy and Spectrometry*, J. C. Lindon, G. E. Trantner, and J. L. Holmes, eds., Academic Press, New York, **2000**, pp. 319–326.
12. G. Muller, *Dalton Trans*. **2009**, 9692–9707.
13. B. Ehrenberg, I. Z. Steinberg, *J. Am. Chem. Soc*. **1976**, *98*, 1293–1295.
14. D. H. Turner, *Methods in Enzymology* **1978**, *49*, 199–214.
15. D. H. Turner, I. Tinoco Jr., M. Maestre, *J. Am. Chem. Soc*. **1974**, *96*, 4340–4342.
16. I. Tinoco Jr., D. H. Turner, *J. Am. Chem. Soc*. **1976**, *98*, 6453–6456.
17. T. G. White, Y.-H. Pao, M. M. Tang, *J. Am. Chem. Soc*. **1975**, *97*, 4751–4753.
18. P. H. Schippers, in *PhD. Dissertation*, University of Leiden, The Netherlands, **1982**, Chapter 1, pp. 12–25.
19. J. P. Riehl, F. S. Richardson, *Methods in Enzymology*, **1993**, *226*, 539–553.
20. P. H. Schippers, P. H. W. van der Ploeg, H. P. J. M. Dekkers, *J. Phys. E*, **1982**, *15*, 945.
21. D. H. Metcalf, S. W. Snyder, S. Wu, G. L. Hilmes, J. P. Riehl, J. N. Demas, F. S. Richardson, *J. Am. Chem. Soc*. **1989**, *111*, 3082–3083.
22. R. B. Rexwinkel, P. Schakel, S. C. J. Meskers, H. P. J. M. Dekkers, *Appl. Spectrosc*. **1993**, *47*, 731–740.
23. H. Goto, K. Akagi, *Angew. Chem.* **2005**, *117*, 4396–4402.
24. F. C. Muller, G. Muller, J. P. Riehl, *Chirality* **2007**, *19*, 826–832.

25. I. Tinoco Jr., B. Ehrenberg, I. Z. Steinberg, *J. Chem. Phys*. **1977**, *66*, 916–920.
26. W. Hug, *Appl. Spectrosc*. **1981**, *35*, 115–124.
27. E. W. Lobenstine, W. C. Schaefer, D. H. Turner, *J. Am. Chem. Soc*. **1981**, *103*, 4936–4940.
28. T. Nehira, K. Tanaka, T. Takakuwa, C. Ohshima, H. Masago, G. Pescitelli, A. Wada, N. Berova, *Applied Spectroscopy* **2005**, *59*, 121–125.
29. C. J. Barnett, A. F. Drake, S. F. Mason, *Bull. Soc. Chim. Belg*. **1979**, *88*, 853–862.
30. H. G. Brittain, *J. Am. Chem. Soc*. **1980**, *102*, 3693–3698.
31. C. L. Maupin, Ph.D. dissertation, Michigan Technological University, Houghton, **1999**.
32. S. D. Bonsall, M. Houcheime, D. A. Straus, G. Muller, *Chem. Commun*. **2007**, 3676–3678.
33. F. J. Coughlin, M. S. Westrol, K. D. Oyler, N. Byrne, C. Krami, E. Zysman-Colman, M. S. Lowry, S. Bernhard, *Inorg, Chem*. **2008**, *47*, 2039–2048.
34. K. Matsumoto, K. Suzuki, T. Tsukuda, T. Tsubomura, *Inorg, Chem*. **2010**, *49*, 4717–4719.
35. J. P. Riehl, F. S. Richardson, *J. Chem. Phys*. **1976**, *65*, 1011–1021.
36. J. E. Field, G. Muller, J. P. Riehl, D. Venkataraman, *J. Am. Chem. Soc*. **2003**, *125*, 11808–11809.
37. H. Tsumatori, T. Nakashima, T. Kawai, *Organic Lett*. **2010**, *12*, 2362–2365.
38. H. P. J. M. Dekkers, P. F. Moraal, J. M. Timper, J. P. Riehl, *Appl. Spectrosc*. **1985**, *39*, 818–821.
39. J. Sokolnicki, J. Legendziewicz, J. P. Riehl, *J. Phys. Chem. B* **2002**, *106*, 1508–1514.
40. Y. Imai, N. Shiota, T. Kinuta, T. Okuno, Y. Nakano, T. Harada, T. Sato, M. Fujiki, R. Kuroda, Y. Matsubara, *Eur. J. Org. Chem*. **2010**, 1353–1357.
41. T. Kinuta, K. Kamon, T. Harada, Y. Nakano, N. Tajima, T. Sato, M. Fujiki, R. Kuroda, Y. Matsubara, Y. Imai, *Eur. J. Org. Chem*. **2009**, 5760–5764.
42. S. C. J. Meskers, J. P. Riehl, H. P. J. M. Dekkers, *Chem. Phys. Lett*. **1993**, *216*, 241–246.
43. E. W. Lobenstine, D. H. Turner, *J. Am. Chem. Soc*. **1979**, *101*, 2205–2207.
44. D. Parker, R. S. Dickins, H. Puschmann, C. Crossland, J. A. K. Howard, *Chem. Rev*. **2002**, *102*, 1977–2010.
45. N. Çoruh, G. L. Hilmes, J. P. Riehl, *J. Luminesc*. **1988**, *40–41*, 227–228.
46. N. Çoruh, J. P. Riehl, *Collect. Czech. Chem. Commun*. **1991**, *56*, 3028–3031.
47. J. L. Lunkley, D. Shirotani, K. Yamanari, S. Kaizaki, G. Muller, *J. Am. Chem. Soc*. **2008**, *130*, 13814–13815.
48. G. L. Hilmes, J. P. Riehl, *Inorg. Chim. Acta* **1987**, *129*, 123–125.
49. J. I. Bruce, D. Parker, S. Lopinski, R. D. Peacock, *Chirality* **2002**, *14*, 562–567.
50. Y. Kawagoe, M. Fujiki, Y. Nakano, *New J. Chem*. **2010**, *34*, 637–647.
51. G. Goto, K. Akagi, *Angew. Chem.* **2005**, *117*, 4396–4402.
52. K. M. Solntsev, E.-A. Bartolo, G. Pan, G. Muller, S. Bommireddy, D. Huppert, L. M. Tolbert, *Isr. J. Chem*. **2009**, *49*, 227–233.
53. C. P. Montgomery, B. S. Murray, E. J. New, R. Pal, D. Parker, *Acc. Chem. Res*. **2009**, *42*, 925–937.
54. G. L. Hilmes, J. P. Riehl, *J. Phys. Chem*. **1983**, *87*, 3300–3304.
55. S. D. Belair, C. L. Maupin, M. W. Logue, J. P. Riehl, *J. Luminesc*., **2000**, *86*, 61–66.
56. D. H. Metcalf, S. W. Snyder, J. N. Demas, F. S. Richardson, *J. Phys. Chem*. **1990**, *94*, 7143–7153.
57. G. L. Hilmes, N. Çoruh, J. P. Riehl, *Inorg. Chem*. **1988**, *27*, 1136–1139.
58. F. Yan, R. A. Copeland, H. G. Brittain, *Inorg. Chem*. **1982**, *21*, 1180–1185.
59. G. Muller, J. P. Riehl, *J. Fluorescence* **2005**, *15*, 553–558.
60. H. G. Brittain, *J. Coord. Chem*. **1989**, *20*, 331–347.

61. H. G. Brittain, *J. Chem. Soc., Dalton Trans*. **1984**, 1367–1370.
62. H. G. Brittain, *Inorg. Chem*. **1981**, *20*, 3007–3013.
63. H. G. Brittain, *Pract. Spectrosc*. **1991**, *12*, 179–200.
64. S. Wu, G. L. Hilmes, J. P. Riehl, *J. Phys. Chem*. **1989**, *93*, 2307–2310.
65. E. Huskowska, J. P. Riehl, *Inorg. Chem*. **1995**, *34*, 5615–5621.
66. N. Çoruh, G. L. Hilmes, J. P. Riehl, *Inorg. Chem*. **1988**, *27*, 3647–3651.
67. J. S. Maradas, H. G. Brittain, *Inorg. Chem*., **1980**, *19*, 3841–3842.
68. H. Tsukube, S. Shinoda, *Chem. Rev*. **2002**, *102*, 2389–2403.
69. F. Yan, H. G. Brittain, *Polyhedron* **1982**, *1*, 195–199.
70. A. Moussa, C. Pham, S. Bommireddy, G. Muller, *Chirality*, **2009**, *21*, 497–506.
71. M. N. Kosareff, J. L. Lunkley, N. G. Nguyen, G. Muller (in preparation).
72. A. P. S. Samuel, J. L. Lunkley, G. Muller, K. N. Raymond, *Eur. J. Inorg. Chem*. **2010**, 3343–3347.
73. K. Tanaka, G. Pescitelli, K. Nakanishi, N. Berova, *Monatsh.Chem*. **2005**, *136*, 367–395.
74. T. Nehira, S. E. Boiadjiev, D. A. Lightner, *Monats. Chem*. **2008**, *139*, 591–595.
75. T. Nehira, K. Tanaka, T. Takakuwa, C. Ohshima, H. Masago, G. Pescitelli, A. Wada, N. Berova, *Appl. Spectrosc*. **2005**, *59*, 121.
76. G. Muller, F. C. Muller, C. L. Maupin, J. P. Riehl, *Chem. Commun*. **2005**, 3615–3617.
77. R. Hassey, E. J. Swain, N. I. Hammer, D. Venkataraman, M. D. Barnes, *Science* **2006**, *314*, 1437–1439.
78. R. Hassey, K. D. McCarthy, E. Swain, D. Basak, D. Venkataraman, M. D. Barnes, *Chirality* **2008**, *20*, 1039–1046.
79. R. Hassey-Paradise, A. Cyphersmith, A. M. Tilley, T. Mortsolf, D. Basak, D. Venkataraman, M. D. Barnes, *Chirality* **2009**, *21*, S265–S276.
80. Y. Tang, T. A. Cook, A. E. Cohen, *J. Phys. Chem. A* **2009**, *113*, 6213–6216.
81. M. D. Barnes, R. Hassey Paradise, E. Swain, D. Venkataraman, N. I. Hammer, *J. Phys. Chem. A* **2009**, *113*, 9757–9758.
82. A. Cohen, Y. Tang, *J. Phys. Chem. A* **2009**, *113*, 9759.
83. M. Cantuel, G. Bernardinelli, G. Muller, J. P. Riehl, C. Piguet, *Inorg. Chem*. **2004**, *43*, 1840–1849.

4

SOLID-STATE CHIROPTICAL SPECTROSCOPY: PRINCIPLES AND APPLICATIONS

Reiko Kuroda and Takunori Harada

4.1. INTRODUCTION

Chirality is generally measured in solution state, and the chiroptical spectra provide useful information on the conformation and handedness of the constituent molecules as well as their interactions with solvent. Historically, however, the phenomenon of optical activity was first discovered in quarts crystals. As early as in 1811, Arago inserted a quartz plate, which was cut perpendicular to the optic axis, between a polarizer and an analyzer. When he rotated the polarizer or analyzer, he observed a spectrum of colored image [1]. His colleague Biot showed [2] that this effect arises from the rotation of the plane of polarization by the quartz crystal and that there are two forms of quarts, one dextrorotatory and the other levorotatory, which induces the right-handed and left-handed rotation of the plane, respectively. Quartz crystals are made up of Si and O atoms and contain no chiral molecules. The helical arrangement of the Si and O atoms in the crystal generates chirality.

Chiroptical spectroscopy, thus started in the solid state, has soon extended to the liquid phase, first to chiral natural organic compounds such as turpentine oil and sucrose solution. Chirality as a molecular characteristic was first revealed by Pasteur [3]. Now the technique is extensively used in the field of organic chemistry, inorganic chemistry, and biochemistry, but the measurements are carried out almost all in solution.

Recently, solid-state chemistry is flourishing as one of the frontier areas in chemistry and bringing new aspects. For example, solid-state crystallization often produces crystals that are different from those obtained by solution crystallization [4–12]. We

Comprehensive Chiroptical Spectroscopy, Volume 1: Instrumentation, Methodologies, and Theoretical Simulations, First Edition. Edited by N. Berova, P. L. Polavarapu, K. Nakanishi, and R. W. Woody.
© 2012 John Wiley & Sons, Inc. Published 2012 by John Wiley & Sons, Inc.

have observed that co-grinding of crystals of benzoquinone (BQ) and *rac*-1,1′-bis-β-naphthol (*rac*-BN) in the total absence of liquid produces a novel crystal adduct through crystal sheering and molecular diffusion processes in the solid state [11a]. The crystal thus obtained is structurally distinct from adducts obtained from solution, particularly in terms of chiral discrimination. In both crystals, the triplet structure is found, where BQ is sandwiched by the naphthol rings of the two BN molecules in a near-parallel manner; however, in the crystals obtained in the solid phase, a racemic pair of BN forms the triplet, whereas, in the crystals produced in solution, a chiral pair of BN does. The hydrogen bonds which are present between the neighboring homochiral BN molecules within a helix in the *rac*-BN crystals are severed and new hydrogen bonds are formed among two BN of neighboring opposite-handed helices and an incoming BQ molecule. We have found many more examples of phase-dependent crystal formation in the series of charge transfer complexes [11b–f]. We envisage that the different behavior arises from the memory of the partial structure of the original crystal, and hence the phenomenon is conceptually very interesting [11f].

Photoreaction in the solid state sometimes achieves what solution chemistry cannot afford in terms of stereoselectivity and reaction yield [13–15]. Recently, we have found that molecules under the strong influence of neighboring molecules in a fixed orientation can adopt different reaction pathways and hence produce different reaction product from those of solution reactions [16]. Enantioselective reactions can be achieved sometimes only in chiral crystals. Furthermore, biomolecules *in vivo* may adopt structures that are different from those observed in aqueous buffered solutions *in vitro*. Particularly, for proteins/peptides such as β-amyloids whose aggregation is relevant to neurodegenerative diseases [17], the difference is expected to be big, and hence structural information in condensed phase is of necessity.

Thus, solid-state spectroscopy provides indispensable information on solid-state structures, supramolecular properties, and dynamics which is not obtainable from the conventional solution spectroscopy. However, very few solid-state chirality measurements have been reported to date [18–26]. This is because measurement of chiroptical properties in the solid state using commercially available circular dichroism (CD) and circular birefringence (CB = optical rotatory dispersion (ORD)) spectrophotometers is extremely difficult [27–29]. Chiroptical spectra are necessarily accompanied by artifacts that originate from the interaction between the macroscopic anisotropies of a sample such as linear birefringence (LB) and linear dichroism (LD) which are unique to the solid state, and the non-ideal characteristics of polarization–modulation instruments [28–30]. One exception is the measurement of a crystal along its unique optic axis, wherein the chiroptical signals are free from anisotropic effects [18, 19, 24, 25, 29, 30]. Taking the advantage of the fact, Mason [24], Judkins [26], and Kuroda [18, 19] studied transition metal complexes of D_3 symmetry which often crystallize in trigonal space groups with their molecular C3 axis parallel to the crystal optic axis. By combining single-crystal CD and microcrystalline CD in a KBr matrix, Kuroda assigned the two components of the first d–d transition band of Co(III) and evaluated the rotatory strengths, which cannot be achieved with solution spectra because the two components are opposite in sign and overlap substantially resulting in severe cancellation of the peaks [18, 19, 29].

These uniaxial crystals are an exception where optic and crystal axes are common. In the case of biaxial crystals in which most compounds are crystallized, there is no simple relationship between the two axes, and thus it is almost impossible to find optic axis and polish crystals perpendicular to the axes. Thus, to obtain true CD and CB spectra of solid

samples in general, we must either take away the parasitic artifacts from the observed spectra or devise a very special technique to detect artifact-free signals. Currently we are challenging the latter approach, developing a MC (multichannel) CD spectrophotomer [31] as well, which we shall discuss only briefly in Section 4.5. In this review, we shall mainly focus on the former technique we have been working on for a long time. By using the Stokes–Mueller matrix method that is particularly effective in understanding the physical meaning of signals observed in polarization–modulation spectroscopy, and in evaluating an instrument's performance, we have succeeded in designing and constructing a solid-state applicable chiroptical spectrophotometer (UCS-1:J-800KCM) [32]. Although it is based on the electrical and optical systems of a commercially available CD spectrophotometer (JASCO: J-820), the instrument is unique with two lock-in amplifiers (50 and 100 kHz) and an analyzer and is capable of measuring all polarization phenomena (i.e., LB, LD, CB, and CD) simultaneously.

UCS-1 is highly useful for measuring true CD and CB spectra of single crystals; however, we cannot always obtain single crystals big enough for the UCS-1 measurement. Furthermore, as described above, co-grinding of two kinds of crystals may produce microcrystallines of a new phase, which is different from crystals obtained from solution crystallization [4–12]. In these cases, chiroptical measurements must be carried out on the microcrystallines using either the KBr disk or the nujol-mull method. However, the methods sometimes suffer from reactions with the matrix material as reported by Braga [33] or dissolution of samples in nujol. We ourselves have noticed the collapse of crystal lattices by simple grinding of microcrystallines [34]. Thus, it is ideal to measure CD spectra of microcrystallines *in situ*. For this purpose, diffuse reflectance (DR) spectroscopy is the most suited. It is applicable to all crystallines irrespective of the size as well as to noncrystalline materials. The DRCD spectrophotometer was first developed by Biscarini and Kuroda et al. in 2002 [35]. However, due to the arrangement of the optical trains in the instrument and the low grade of the optical elements used, the CD measurement was limited to the visible wavelength range and the sensitivity was low.

To achieve high-quality *in situ* chirality measurements over a wide wavelength range with a higher sensitivity, we have designed and built UCS-2 (J-800KCMF) [36]. In fact, UCS-2 is designed as a dual-purpose spectrophotometer to measure not only DRCD but transmittance CD as well. It has a right-angle prism that makes it possible to set a sample on a horizontal stage, ideal to carry out measurement of loose powders and soft materials that suffer from gravity, or time-dependent measurements of liquid, mesophase, and condensed phases. Like UCS-1, UCS-2 is also equipped with two lock-in amplifiers (50 and 100 kHz) and an analyzer to measure LB, LD, CB, and CD simultaneously in the transmittance mode.

Although UCS-2 spectrophotometer is versatile and powerful for the measurement of DRCD spectra of powdered materials *in situ*, it has a limited spectral region of 250–800 nm, as the light intensity decreases sharply below 250 nm. To expand DRCD measurements down to 190 nm with high efficiency, we have improved UCS-2 and constructed UCS-3 (J-800KCMFII) [37].

In this chapter, theoretical background and instrumentation of UCS-1, -2, and -3, and their applications to organic, inorganic, and bio-related materials will be described.

4.2. THEORETICAL BACKGROUND [32]

For designing spectrophotometers and analyzing signals observed, we employed the Stokes–Mueller matrix method [38] and the Storks vector, $S = [S_0, S_1, S_2, S_3]$, which

expresses the polarized light. S_0, S_1, S_2, and S_3 indicate the total intensity, plus 45° preference, right-circular preference, and horizontal preference, respectively. By investigating the changes of the Storks vector after passing through the optical elements and a sample, we can easily find a polarization state of the coming out light. The Mueller matrix is the 4×4 matrices that was devised to express the optical characteristics of optical elements and a sample. Using the matrix calculation of $\hat{D} \cdot \hat{S}_{(\theta)} \cdot \hat{M} \cdot \hat{P} \cdot \hat{I}_0$, ($D$, photomultiplier; S, sample; M, photoelastic modulator; P, polarizer; and I_0, incident light), the signals observed of a sample having CD, CB, LD, and LB can be expressed as

$$\begin{aligned} I_d &= \hat{D} \cdot \hat{S}_{(\theta)} \cdot \hat{M} \cdot \hat{P} \cdot \hat{I}_0 \\ &= \frac{1}{2} e^{-\mathrm{Ae}} I_0 (P_x^2 + P_y{}^2)\{1 + \frac{1}{2}(\mathrm{LD}'^2 + \mathrm{LD}^2) + [\mathrm{CD} + \frac{1}{2}(\mathrm{LD}'\mathrm{LB} - \mathrm{LB}'\mathrm{LD})] \sin(\delta + \alpha) \\ &\quad + (\mathrm{LD}' \sin 2\theta + \mathrm{LD}\cos 2\theta) \cos(\delta + \alpha)\} + \frac{1}{2} I_0 (P_x{}^2 - P_y{}^2) \sin 2a\{-\mathrm{LD}' \cos 2\theta \\ &\quad + \mathrm{LD}\sin 2\theta + (\mathrm{LB}' \sin 2\theta - \mathrm{LB}\cos 2\theta) \sin(\delta + \alpha) + [-\mathrm{CB} \\ &\quad + \frac{1}{4}(\mathrm{LD}^2 + \mathrm{LB}^2 - \mathrm{LD}'^2 - \mathrm{LB}'^2) \sin 4\theta + (\mathrm{LD}'\mathrm{LD} + \mathrm{LB}'\mathrm{LB}) \cos 4\theta] \cos(\delta + \alpha)\} \\ &\quad + \frac{1}{2} I_0 (P_x{}^2 - P_y{}^2) \cos 2\mathrm{a}\{(-\mathrm{LD}' \sin 2\theta - \mathrm{LD}\cos 2\theta) \\ &\quad + (\mathrm{LB}' \cos 2\theta - \mathrm{LB}\sin 2\theta) \sin(\delta + \alpha) - [1 + \frac{1}{4}(\mathrm{LD}^2 - \mathrm{LB}'^2 - \mathrm{LD}'^2 + \mathrm{LB}^2) \cos 4\theta \\ &\quad + \frac{1}{2}(\mathrm{LD}'\mathrm{LD} + \mathrm{LB}'\mathrm{LB}) \sin 4\theta] \cos(\delta + \alpha)\}. \end{aligned} \tag{4.1}$$

Here, CB, LD, LD′, LB, and LB′ are circular birefringence, $(x-y)$ linear dichroism, 45° linear dichroism, $(x-y)$ linear birefringence, and 45° linear birefringence, respectively. $P_x{}^2$ and $P_y{}^2$ are the transmittance of the photomultiplier along the x and y directions, and "a" is the azimuth angle of its optical axis with respect to the x axis. θ is the rotation angle of the sample, and α is the residual static birefringence of the photoelastic modulator (PEM). δ is the periodic phase difference between the x and y axes of the PEM operating frequency $\omega/2\pi$ and is adjusted so as to act as a quarter-wave plate,

$$\delta = \delta_m{}^0 \sin \omega_m t, \tag{4.2}$$

where $\delta_m{}^0$ is the peak modulator retardation and in ordinal cases, $\omega/2\pi$ is 50 kHz. We can expand $\cos\delta$ and $\sin\delta$ in a Fourier series,

$$\sin(\delta_m{}^0 \sin \omega_m t) = 2J_1(\delta_m{}^0) \sin \omega_m t + 2J_3(\delta_m{}^0) \sin 3\omega_m t + \ldots, \tag{4.3}$$

$$\cos(\delta_m{}^0 \sin \omega_m t) = J_0(\delta_m{}^0) + 2J_2(\delta_m{}^0) \cos 2\omega_m t + \ldots, \tag{4.4}$$

where

$$\cos(\delta + \alpha) = 2J_2(\delta_m{}^0) \cos 2\omega_m t \cdot \cos \alpha - 2J_1(\delta_m{}^0) \sin \omega_m t \cdot \sin \alpha + J_0(\delta_m{}^0) \cos \alpha \ldots, \tag{4.5}$$

$$\sin(\delta + \alpha) = 2J_1(\delta_m{}^0) \sin \omega_m t \cdot \cos \alpha + 2J_2(\delta_m{}^0) \cos 2\omega_m t \cdot \sin \alpha + J_0(\delta_m{}^0) \sin \alpha \ldots. \tag{4.6}$$

$J_n(\delta_m{}^0)$ are Bessel functions of nth order. Hence, the 50-kHz signal detected at the photocurrent detected by the lock-in amplifier can be expressed as

$$\begin{aligned}\text{Signal}_{50\ \text{kHz}} = {} & \text{G}_1(P_x{}^2 + P_y{}^2)[\text{CD} + 1/2(\text{LD}'\text{LB} - \text{LB}'\text{LD}) \\ & + (\text{LD}' \sin 2\theta - \text{LDcos}\, 2\theta) \sin \alpha] \\ & + G_1(P_x{}^2 - P_y{}^2) \sin 2a\{\text{LB}' \sin 2\theta - \text{LBcos}2\theta \\ & + [-\text{CB} + \frac{1}{2}(\text{LD}^2 + \text{LB}^2 - \text{LD}'^2 - \text{LB}'^2) \sin 4\theta \\ & + (\text{LD}'\text{LD} + \text{LB}'\text{LB}) \cos 4\theta] \sin \alpha\} \\ & + G_1(P_x{}^2 - P_y{}^2) \cos 2\text{a}\{\text{LB}' \cos 2\theta - \text{LBsin}\, 2\theta \\ & - [1 + \frac{1}{4}(\text{LD}^2 - \text{LB}'^2 - \text{LD}'^2 + \text{LB}^2) \cos 4\theta \\ & + 1/2(\text{LD}'\text{LD} + \text{LB}'\text{LB}) \sin 4\theta] \sin \alpha\}, \end{aligned} \tag{4.7}$$

where G_1 is the apparatus constant related to the sensitivity of the spectrometer. Terms multiplied by $\sin\alpha$ are negligibly small because a PEM having a smaller residual static birefringence ($\alpha = 0.2$) was used in our CD spectrophotometer. We can also neglect the contribution of the term containing cos $2a$, because the photomultiplier (PM)'s azimuth angle was set so as to make cos $2a \approx 0$ in the baseline calibration. Thus, a 50-kHz signal is written as

$$\begin{aligned}\text{Signal}_{50\ \text{kHz}} = {} & G_1(P_x{}^2 + P_y{}^2)[\text{CD} + \frac{1}{2}(\text{LD}'\text{LB} - \text{LB}'\text{LD})] \\ & + G_1(P_x{}^2 - P_y{}^2) \sin 2a(\text{LB}' \sin 2\theta - \text{LBcos}2\theta). \end{aligned} \tag{4.8}$$

Similarly, the 100-kHz component of the photocurrent detected by the lock-in amplifier is given as

$$\begin{aligned}\text{Signal}_{100\ \text{kHz}} = {} & G_2(P_x{}^2 + P_y{}^2)\{\text{LD}' \sin 2\theta - \text{LDcos}\, 2\theta \\ & + [\text{CD} + \frac{1}{2}(\text{LD}'\text{LB} - \text{LB}'\text{LD})] \sin \alpha\} \\ & + G_2(P_x{}^2 - P_y{}^2) \sin 2a\{-\text{CB} + 1/4(\text{LD}^2 + \text{LB}^2 - \text{LD}'^2 - \text{LB}'^2) \sin 4\theta \\ & + (\text{LD}'\text{LD} + \text{LB}'\text{LB}) \cos 4\theta + (\text{LB}' \sin 2\theta - \text{LBcos}2\theta) \sin \alpha\} \\ & + G_2(P_x{}^2 - P_y{}^2) \cos 2a\{1 + \frac{1}{4}(\text{LD}^2 - \text{LB}'^2 - \text{LD}'^2 + \text{LB}^2) \cos 4\theta \\ & + \frac{1}{2}(\text{LD}'\text{LD} + \text{LB}'\text{LB}) \sin 4\theta + (\text{LB}' \cos 2\theta - \text{LBsin}\, 2\theta) \sin \alpha\}. \end{aligned} \tag{4.9}$$

In the same way as the 50-kHz signal, the above equation can be expressed as

$$\begin{aligned}\text{Signal}_{100\ \text{kHz}} = {} & G_2(P_x{}^2 + P_y{}^2)(\text{LD}' \sin 2\theta - \text{LDcos}\, 2\theta) \\ & + G_2(P_x{}^2 - P_y{}^2) \sin 2a\{-\text{CB} + \frac{1}{4}(\text{LD}^2 + \text{LB}^2 - \text{LD}'^2 - \text{LB}'^2) \sin 4\theta \\ & + (\text{LD}'\text{LD} + \text{LB}'\text{LB}) \cos 4\theta\}. \end{aligned} \tag{4.10}$$

Here G_2 is the apparatus constant related to the sensitivity of the spectrometer at 100 kHz.

When an analyzer with 45-degree optical axis was inserted into optical path, from a matrix calculation of $\hat{D} \cdot \hat{A} \cdot \hat{S}_{(\theta)} \cdot \hat{M} \cdot \hat{P} \cdot \hat{I}_0$, the light intensity, I_d, detected by photomultiplier can be expressed as

$$\begin{aligned} I_{\mathrm{d}} &= \hat{D} \cdot \hat{A} \cdot \hat{S}_{(\theta)} \cdot \hat{M} \cdot \hat{P} \cdot \hat{I}_0 \\ &= \frac{1}{4} e^{-\mathrm{Ae}} I_0 \{(P_x{}^2 + P_y{}^2) + (P_x{}^2 - P_y{}^2) \sin 2a\} \{1 + \frac{1}{2}(\mathrm{LD}^2 + \mathrm{LD}'^2) \\ &\quad - (\mathrm{LD}' \cos 2\theta + \mathrm{LDsin}2\theta) + [\mathrm{CD} + \frac{1}{2}(\mathrm{LD}'\mathrm{LB} - \mathrm{LDLB}') \\ &\quad - (\mathrm{LBcos}2\theta + \mathrm{LB}' \sin 2\theta)] \sin(\delta + \alpha) - [(\mathrm{LD}' \sin 2\theta + \mathrm{LDcos}\, 2\theta) - \mathrm{CB} \\ &\quad + \frac{1}{2}(\mathrm{LD}^2 + \mathrm{LB}^2 - \mathrm{LD}'^2 - \mathrm{LB}'^2) \sin 4\theta \\ &\quad + (\mathrm{LDLD}' + \mathrm{LBLB}') \cos 4\theta] \cos(\delta + \alpha)\}. \end{aligned} \tag{4.11}$$

In the same way as without an analyzer, the 50-kHz signal detected at the photocurrent detected by the lock-in amplifier can be expressed as

$$\mathrm{Signal}_{50\ \mathrm{kHz}} = G_3\{\mathrm{CD} + \frac{1}{2}(\mathrm{LD}'\mathrm{LB} - \mathrm{LDLB}') - \mathrm{LBcos}2\theta + \mathrm{LB}' \sin 2\theta\}. \tag{4.12}$$

where G_3 is the apparatus constant related to the sensitivity of the spectrometer with the analyzer inserted at 50 kHz. Similarly, the 100-kHz signal also can be expressed as

$$\begin{aligned} \mathrm{Signal}_{100\ \mathrm{kHz}} &= G_4\{-\mathrm{LD}' \sin 2\theta + \mathrm{LDcos}\, 2\theta + \mathrm{CB} \\ &\quad - 1/2(\mathrm{LD}^2 + \mathrm{LB}^2 - \mathrm{LD}'^2 - \mathrm{LB}'^2) \sin 4\theta \\ &\quad - (\mathrm{LDLD}' + \mathrm{LBLB}') \cos 4\theta\} \\ &= G_4\{\mathrm{CB} + (\mathrm{LD}^2 + \mathrm{LD}'^2)^{1/2} \cos(2\theta + \eta) \\ &\quad - 1/2[(\mathrm{LB}^2 + \mathrm{LB}'^2) \sin(4\theta + \gamma) \\ &\quad + (\mathrm{LD}^2 + \mathrm{LD}'^2) \sin(4\theta + \zeta)]\}. \end{aligned} \tag{4.13}$$

where $\eta = \tan^{-1}[\mathrm{LD}/\mathrm{LD}']$, $\gamma = \tan^{-1}[\mathrm{LBLB}'/\frac{1}{2}(\mathrm{LB}^2 + \mathrm{LB}'^2)]$, and $\zeta = \tan^{-1}[\mathrm{LDLD}'/1/2(\mathrm{LD}^2 - \mathrm{LD}'^2)]$. Here G_4 is the apparatus constant related to the sensitivity of the spectrometer with the analyzer inserted at 100 kHz. The 100-kHz signal contains not only CB but also LD and LB terms and changes with θ during the sample rotation at an arbitrary wavelength. If the contribution of LD is much larger than LB, the signal changes with $\cos 2\theta$ periodicity, whereas if the contribution of LB is much larger than LD, the change follows $\sin 4\theta$ periodicity [Eq. (4.13)]. Generally, LD is 10 times smaller than LB, and thus Eq. (4.13) can be approximated as

$$\mathrm{Signal}_{100\ \mathrm{kHz}} = G_4\{\mathrm{CB} - \frac{1}{2}(\mathrm{LB}^2 + \mathrm{LB}'^2) \sin(4\theta + \gamma)\}. \tag{4.14}$$

If there is no macroscopic anisotropy, Eqs. (4.8) and (4.14) give CD and CB, respectively, and this is the case of solution experiments. In other cases, polarization phenomena, LB, LD, CB, and CD, are intermingled with each other in several detecting modes. Based on these analyses, apparatuses UCS-1, −2, and −3 have been developed.

4.3. DEVELOPMENT OF NEW APPARATUSES

4.3.1. Universal Chiroptical Spectrophotometer UCS-1

To obtain true chiroptical signals by removing the parasitic artifacts from the observed spectra, we have designed and constructed a solid-state applicable universal chiroptical spectrophotometer (UCS-1: J-800KCM) based on the Stokes–Mueller matrix analyses as described in Section 4.2.

Figure 4.1 shows the block diagram of the optical system of J-800KCM together with the axis orientations of the optical and electric components. UCS-1 has the following components: 450-W xenon lamp, pile of plate and PEM of JASCO J-820 CD spectrometer, sample stage, sample holder, Halle Glan-Taylor polarizing prism (ZETA International Corporation, TY-LS-10), Hamamatsu R-376 head-on type photomultiplier, lamp and photomultiplier power supply of JASCO, two lock-in amplifiers (SRS SR830 and JASCO), two-pen recorder SS 250F (SECONIC), and phase-locked-loop (PLL) circuit.

Light emitted from a 450-W xenon lamp is monochromatized by a double-prism monochrometor. The monochromatic light is converted to plane-polarized radiation having an electric vector parallel to the Y axis by the polarizer. The linearly polarized light passes through a PEM whose optic axis is at 45 degrees with respect to X and Y axis. The PEM is modulated by the ac voltage $V_0 \sin \omega_m t$ with the frequency $\omega_m = 50$ kHz so as to act as a quarter-wave plate at arbitrary wavelength. Here, note that the linearly polarized light modulated at 50 kHz and 100 kHz is converted into various unmodulated and modulated polarized light [27]. After passing through a sample, the light emitted from the sample passes through the analyzer and then falls on the photomultiplier. The output from the photomultiplier is a dc signal superimposed by ac components modulated. The dc level is kept at a constant value $V_{\mathrm{dc}} = 500$ mV, independent of the total amount of the light, by a servo control of a photomultiplier power supply through the feedback of the dc component. The ac components are processed by using two lock-in

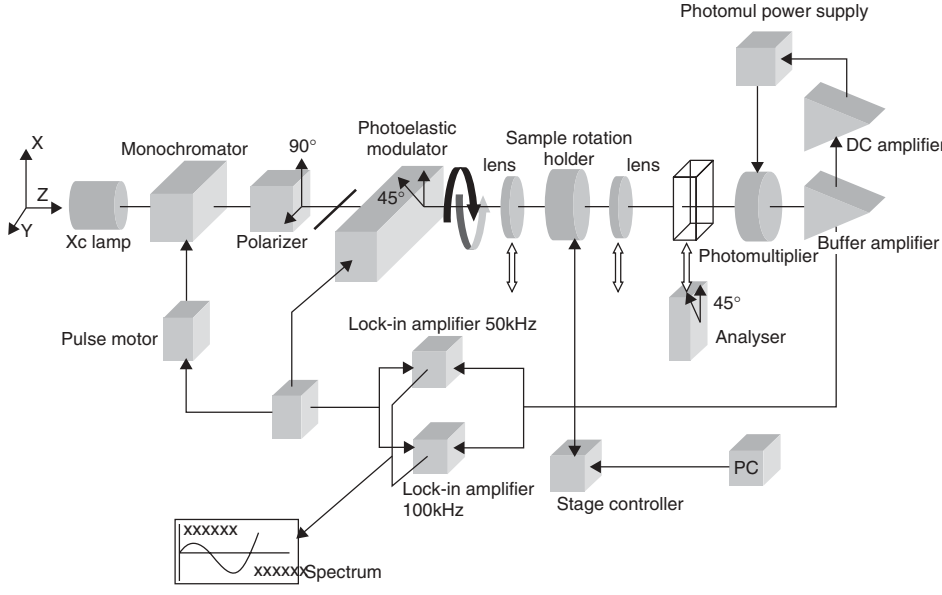

Figure 4.1. Block diagram of the universal chiroptical spectrophotometer (UCS-1).

amplifiers of JASCO and Stanford Research Systems. The signal processing is set up to take the ratio of the ac to the dc signals. Electric signals processing by lock-in amplifiers are transmitted into a two-pen recorder and a personal computer.

Using this instrument, we have measured several solid samples such as single crystals of α-Ni$(H_2O)_6 \cdot SO_4$ [32, 39, 40], $NaClO_3$ [40], and CaF_2 [40], films of a polymer (polyvinyl alcohol [39, 42]) and biopolymers (bovine serum albumin [43] and β-amyloid peptides [44]), microcrystallines of porphyrin derivatives [45], chiral supramolecular fluorophores [46], and metal complexes [47], and obtained physicochemical information that was not obtainable on commercially available CD spectrophotometers.

4.3.2. Dual-Purpose transmittance CD and Diffuse Reflectance CD Spectrophotometers (UCS-2 and -3)

UCS-2 (J-800KCMF) [36] and UCS-3 (J-800KCMFII) [37] are designed as dual-purpose spectrophotometers to measure DRCD as well as transmittance CD to achieve high-quality *in situ* chirality measurements with high sensitivity over a wide wavelength range. Because of this purpose, they have a unique design distinct from that of commercially available CD instruments. A block diagram of UCS-2 is shown in Figure 4.2. UCS-2/3 have the following characteristics: (1) They can measure both DRCD and transmittance CD, and for that purpose they house two photomultipliers; (2) they equip with two lock-in amplifiers (50 and 100 kHz) and an analyzer so that it is capable of measuring all polarization phenomena (i.e., LB, LD, CB, and CD) simultaneously in the transmittance mode; and (3) they equip with an integrating sphere for the measurement of DRCD.

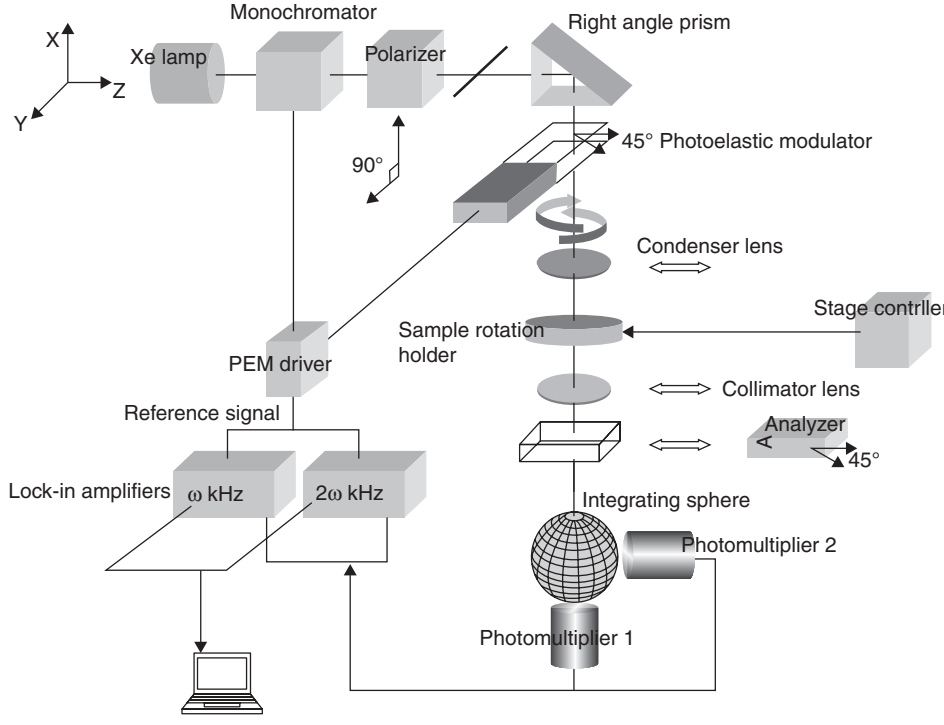

Figure 4.2. Block diagram of a dual-purpose universal chiroptical spectrophotometer (UCS-2).

The integrating sphere is a highly reflective enclosure that is placed in close proximity to the sample, so that the incident light enters the sphere, bounces around the highly reflective diffuse surface of the sphere wall, is reemitted after incident on samples, and finally impinges upon the detector part of the integrating sphere assembly. (4) *In situ* chirality measurement without any pretreatment can be carried out as a right-angle prism is installed in the instrument, which makes it possible to set a sample on a horizontal plane. This is ideal to carry out not only *in situ* measurements of solid samples including loose powders without any pretreatment, but also time-dependent measurements of liquid, mesophase, and fluid-type condensed phases.

By investigating the PEM position and selecting high-quality optical elements, we could overcome the defect of the prototype DRCD spectrophotometer [35] and succeed in developing a UCS-2 that can measure signals over the UV–Vis regions, 250–800 nm. However, the spectral region is not satisfactory. The limit is mainly due to the large decrease in the intensity of the light below 250 nm because of the size of the integrating sphere (ϕ 120 mm in diameter) and the inappropriate material used for coating the inner side of the sphere. $BaSO_4$ used in UCS-2 shows a relatively high diffuse reflectance only above 250 nm.

Thus, we have constructed UCS-3 [37], the substantially upgraded version of UCS-2 in the DR mode, which enables the DRCD measurements down to 190 nm with high reflectivity and sensitivity. Optical components newly used in UCS-3 are the integrating sphere of optimum size and material to achieve high performance, particularly in the shorter-wavelength region. An integrating sphere (Labsphere Co. Ltd. Sutton, NH; IS-020-SL; ϕ 2 inches ($\approx$51 mm) in diameter) was adopted which is made of thermoplastic resin spectralon, a material with reflectance higher than 95% for UV–vis wavelength region. A baffle made of spectralon was installed to reduce the first specular reflection signals, and a condenser lens was used to increase light intensity per area for small samples. As a result, UCS-3 has become a very powerful instrument to measure DRCD spectra of powdered samples *in situ*, with $\approx$20 times sensitivity of UCS-2. We could show that to achieve similar-quality DRCD spectra, only 50 μg of (*S*)-(+)-1,1′-binaphthyl-2,2′-diyl hydrogen phosphate is required on UCS-3, as compared with 1.12 mg for UCS-2 [37].

DRCD measurement mode can remove artifact signals arising from an LD that is not coupled with LB. LB contribution cannot be measured on UCS-2/3 at the moment. Using UCS-2/3, we have measured artifact-signal-free CD and DRCD spectra of several solid samples such as microcrystallines and a co-grinding complex that exhibit supramolecular chirality, [48] as well as β-amyloid peptides related to the neurodegenerative Alzheimer's disease, [44] to understand the molecular events underlying the protein aggregation.

4.4. APPLICATION TO SOLID SAMPLES

4.4.1. Method for True CD Measurement

As seen in Eq. (4.8), the apparent CD component of 1/2(LD′LB − LDLB′) is independent of the rotation of the sample, whereas terms including the coupling of LB with the polarization characteristic of the photomultiplier change with rotation of the sample. Taking into consideration this fact, we have developed a set of procedures for the measurement of true CD, as follows: (1) With an analyzer, LB measurement was carried out by rotating the sample 360° in the ($X-Y$) plane at the wavelength of an absorption maximum. Then, the LB spectrum was obtained by the wavelength scanning at the LB_{max} position. (2) Without an analyzer, LD was measured by rotating the sample at the absorption

maximum. Then, LD spectrum was obtained by the wavelength scanning at the LD_{max} position. (3) Similarly, CD measurement was carried out by rotating the sample at the absorption maximum. If the CD value changes on rotating the sample 360° around the z axis, it is clear that the macroscopic anisotropies contribute to the CD spectrum. From the measurements, we can tell the extent of contribution of LD and LB signals to the observed CD signals. As is obvious from Eq. (4.8), if LB and LD signals are negligibly small compared with CD, or if there are no macroscopic anisotropies like solution samples, the signal observed is a true CD. If the two 50-kHz spectra obtained with and without the analyzer are different, the 50-kHz signal detected without the analyzer contains an apparent CD signal, and the signal detected with the analyzer is an LB signal. (4) From the data obtained in step 1, we can locate the LB_{max} and LB_{min} positions. The sample was rotated 45° from the LB_{max} position, wherein the LB value becomes 0 and the LB′ value maximum. The wavelength scan was then carried out without an analyzer. From Eq. (4.8), the apparent CD signal of the face side is given as

$$[\text{appCD}]_{\text{face}} = G_1\{(P_x{}^2 + P_y{}^2)(\text{CD} - \frac{1}{2}\text{LB}'\text{LD}) + (P_x{}^2 - P_y{}^2)\sin 2a(\text{LB}')\}. \quad (4.15)$$

(5) The sample was then rotated by 180° about the Y axis, and the wavelength scan was carried out. This corresponds to the back-side measurement. By this rotation, the CD and LD do not change their signs, but LB′ becomes −LB′. Hence, the apparent CD signal of the back side becomes

$$[\text{appCD}]_{\text{back}} = G_1\{(P_x{}^2 + P_y{}^2)(\text{CD} + \frac{1}{2}\text{LB}'\text{LD}) - (P_x{}^2 - P_y{}^2)\sin 2a(\text{LB}')\}. \quad (4.16)$$

It is obvious that the addition of Eqs. (4.15) and (4.16) gives Eq. (4.17):

$$2G_1(P_x{}^2 + P_y{}^2)\text{CD}. \quad (4.17)$$

Thus, measurement of $[\text{appCD}]_{\text{face}}$ and $[\text{appCD}]_{\text{back}}$ spectra using our special sample holder, the addition of the two spectra and division by a factor of 2 should give the true CD spectrum. The method is best applied when the LB value is not too large, that is, less than ∼30°.

4.4.2. Method for True CB measurement [41]

Because the CB signal is usually 10^2 to 10^3 times smaller compared with LB and LB′ signals and thus is buried under large macroscopic anisotropy signals, it is difficult to detect. However, we have found that the following set of measurements makes this possible. At (+) maximum position during sample rotation, a signal 2ω becomes

$$(+)\text{max}[\text{Signal } 2\omega] = G_4\{\text{CB} + \frac{1}{2}(\text{LB}^2 + \text{LB}'^2)\}. \quad (4.18)$$

At the negative maximum position, or at the position rotated 45° from the positive maximum position if the signal changes with sin 4θ periodicity, the signal detected is given as

$$(-)\text{max}[\text{Signal } 2\omega] = G_4\{\text{CB} - \frac{1}{2}(\text{LB}^2 + \text{LB}'^2)\}. \quad (4.19)$$

Thus, if we average the (+)max[Signal 2ω] and (−)max[Signal 2ω] spectra, we can obtain CB. The method is best applied when the LB value is less than ∼30°.

4.4.3. Kramers–Kronig (K–K) Relationship

Correctness of the solid-state CD and CB spectra obtained by the set of procedures described in Sections 4.4.1 and 4.4.2, respectively, were checked by the Kramers–Kronig (K–K) relationship for a cast film having macroscopic anisotropies, LB and LD. The numerical evaluation of K–K relationship was thoroughly studied for isotropic medium previously [49]. It is well known that CD and CB are related by the K–K relationship, which always holds between true CD and CB. However, if the solid-state CD and CB spectra contain artifact signals of LB and LD, it cannot hold. Figure 4.3 shows that K–K relationships holds well in the case of a cast film for β-amyloid(1–42) peptide related to Alzheimer's disease; that is, CB spectrum calculated from the observed true CD spectrum based on the K–K relationship agrees well with the observed true CB spectrum [44]. These prove the integrity of our instrumentation and procedures for the study of solid-state chiroptical properties.

4.4.4. True CD Spectra of Achiral Films [32]

PVA (polyvinyl alcohol) film dyed with Congo red was used as an achiral sample. Thus, the rather strong CD spectra observed must be due to artifact resulting from the coupling of LB with the nonideal characteristics of the instrument. The LB value of a highly stretched PVA film employed in this study was 1.9λ at 546 nm. We assumed that the PVA film is optically homogeneous, and there is no face-side and back-side difference. In the homogeneous case, the Mueller matrix of the sample can be expressed as

$$\hat{S} = \mathrm{e}^{-\mathrm{Ae}} \begin{pmatrix} 1 & -\mathrm{LD}' & 0 & -\mathrm{LD} \\ -\mathrm{LD}' & 1 & -\mathrm{LB} & 0 \\ 0 & \mathrm{LB} & 1 & -\mathrm{LB}' \\ -\mathrm{LD} & 0 & \mathrm{LB}' & 1 \end{pmatrix} \times \begin{pmatrix} 1 & -\mathrm{LD}' & 0 & -\mathrm{LD} \\ -\mathrm{LD}' & 1 & -\mathrm{LB} & 0 \\ 0 & \mathrm{LB} & 1 & -\mathrm{LB}' \\ -\mathrm{LD} & 0 & \mathrm{LB}' & 1 \end{pmatrix} \tag{4.20}$$

Thus, from the simple Mueller matrix computation of $\hat{D} \cdot \hat{S} \cdot \hat{M} \cdot \hat{P} \cdot \hat{I}_0$, we can obtain the light intensity at the detector I_d as

$$\begin{aligned} I_d = {} & \frac{1}{2} e^{-\mathrm{Ae}} I_0 ({P_x}^2 + {P_y}^2)[1 + \mathrm{LD}'^2 + \mathrm{LD}^2 + (\mathrm{LD}'\mathrm{LB} - \mathrm{LB}'\mathrm{LD}) \sin(\delta + \alpha) \\ & + 2\mathrm{LD}\cos(\delta + \alpha)] + 1/2 I_0 ({P_x}^2 - {P_y}^2) \sin 2a[-\mathrm{LD}' - (\mathrm{LD}'\mathrm{LD} \\ & + \mathrm{LB}'\mathrm{LB}) \cos(\delta + \alpha) - 2\mathrm{LB}\cos 2\theta) \sin(\delta + \alpha)] \end{aligned}$$

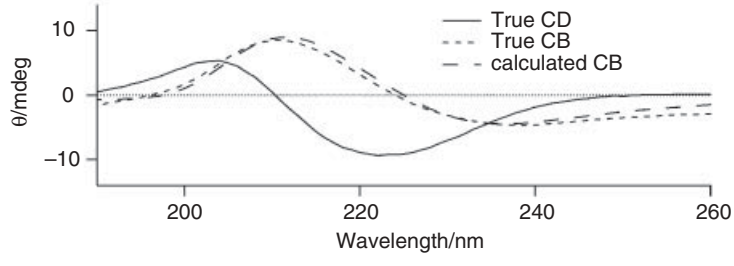

Figure 4.3. True CD (solid line), true CB (short dashes), and CB (long dashes) calculated from the CD assuming the Kramers–Kronig relation spectra of β-amyloid (1–42) cast film.

$$+ 1/2\mathrm{I}_0(P_x{}^2 - P_y{}^2)\cos 2a[-2\mathrm{LD} - (\mathrm{LD}^2 - \mathrm{LB}'^2 + 1)\cos(\delta + \alpha) + 2\mathrm{LB}'\sin(\delta + \alpha)]. \quad (4.21)$$

For simplicity and as we selected the best detector for UCS-1, we assumed that the detector is ideal, and hence the 50-kHz signal detected by the photomultiplier is expressed as

$$\mathrm{signal}^{\mathrm{face}}_{50\ \mathrm{kHz}} = G_1[\mathrm{LD}'\mathrm{LB} - \mathrm{LB}'\mathrm{LD}]. \quad (4.22)$$

When we rotate the sample 180° with respect to the vertical (y) axis, LD and LB do not change their signs, but LD′ and LB′ become −LD′ and −LB′, respectively. Therefore, the 50-kHz signal of the back side detected by the photomultiplier is expressed as

$$\mathrm{signal}^{\mathrm{back}}_{50\ \mathrm{kHz}} = G_1[-\mathrm{LD}'\mathrm{LB} + \mathrm{LB}'\mathrm{LD}]. \quad (4.23)$$

If we add up Eqs. (4.22) and (4.23), the sum becomes 0. Thus, the apparent CD spectra due to macroscopic anisotropies should cancel out by this procedure.

This expectation is what we have actually observed. As shown in Figure 4.4, the substantially strong CD spectra observed for the face and back of the film are almost mirror images to each other, and they cancel out when added. This proves that the observed CD for the PVA film is not a true CD but simply an artifact.

4.4.5. Assessing the Contribution of Macroscopic Anisotropies to CD Spectra: Single Crystal of α-Ni$(H_2O)_6 \cdot SO_4$ [32]

α-Ni$(H_2O)_6 \cdot SO_4$ exhibits a chiral nature only in the crystalline state. Its single crystal belongs to a uniaxial system with the enantiomorphic tetragonal space group of $P4_12_12$ or $P4_32_12$ [50–52]. Solid-phase circular birefringence CB and CD spectra of α-Ni$(H_2O)_6 \cdot SO_4$ were studied in the 250- to 600-nm region to investigate how macroscopic anisotropies affect CD spectra. Because the crystal belongs to a uniaxial crystal system, there is no macroscopic anisotropies along the optic axis. By tilting the crystal from the position, we introduced some macroscopic anisotropies on purpose. Following the set of procedure we have developed, CD of two α-Ni$(H_2O)_6 \cdot SO_4$ single crystals, one with large and the other with very small LB, were measured. In the case of a large LB sample, by comparing LB, LD, and CD spectra (Figure 4.5a), we could recognize that the LB signal was larger than the CD signal, and the second and third terms in Eq. (4.12) contributed to the CD spectrum. By adopting the procedure described in Section

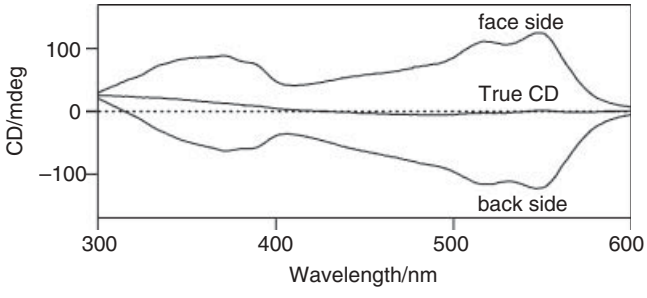

Figure 4.4. CD spectra of a stretched PVA film dyed with Congo Red. The top and bottom spectra are the apparent CD of face side and back side, respectively. The middle trace is the true CD spectrum.

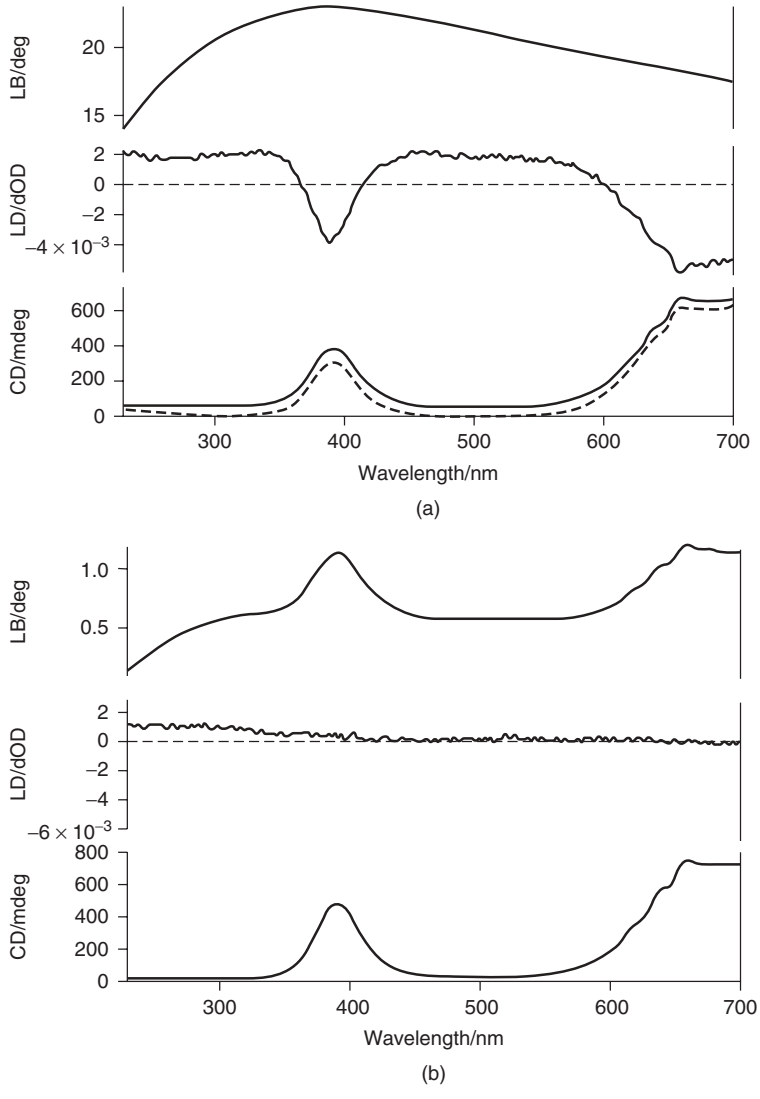

Figure 4.5. Single crystal of α-$Ni(H_2O)_6 \cdot SO_4$ exhibiting a large LB (a) and a small LB (b): LB spectra at LB_{max} positions, LD spectra at LD_{max} positions, and an apparent CD spectra at arbitrary angles (dotted line) and true CD spectra (solid line).

4.4.1, we successfully eliminated these terms and obtained a true CD spectrum. The true CD and an apparent CD spectra are compared in Figure 4.5a.

In the case of slight tilting from the unique orientation, both LD and LB signals are negligibly small compared with the CD signal (Figure 4.5b). The figure shows that the apparent and true CD spectra are virtually the same, and the LB spectrum is also almost identical to the CD. Thus, we can regard the measured CD of a single crystal of α-$Ni(H_2O)_6 \cdot SO_4$ as the true CD, when the LB value is less than 1° at 390 nm.

4.4.6. Cubic Crystal Is Not Optically Homogeneous: Presence of LB Signal [41]

In almost all textbooks, cubic crystals are described to be optically isotropic from whichever direction light travels. The crystal of $NaClO_3$ belongs to the chiral cubic

tetrahedral class (T-23) with the space group $P2_13$ [53]. Cubic shape crystals of $NaClO_3$ having [1 0 0] facets were usually obtained from the solution, whereas tetrahedral shape crystals with [1 1 1] facets were grown by adding sodium thiosulfate into the solution [54]. The polished single crystals having faces parallel to either the (1 0 0) or (1 1 1) were mounted with the plane perpendicular to the light, and their chiroptical spectra were measured for both (d)- and (l)-crystals of $NaClO_3$. Figure 4.6a shows rotational measurements of 50-kHz (LB) and 100-kHz (CB) signals at 250 nm on rotating a single crystal of (l)-$NaClO_3$ placed with the (1 1 1) face perpendicular to the incident light. As expected, when light beam was incident to the crystal almost exactly normal to the (1 1 1) face, hardly any LB signal appeared (Figure 4.6a, solid line). In contrast, when the crystal was mounted slightly tilted from the perpendicular orientation, a weak LB and CB signals both with $\sin 2\theta$ periodicity were detected in the rotational measurements (Fig. 4.6a, dotted line). From Eq. (4.13), it is found that the contribution of LD is much bigger than LB, because the CB signal changes with $\cos 2\theta$ periodicity.

Figure 4.6b shows a typical LB rotational measurement at 250 nm of a (l)-$NaClO_3$ crystal that was mounted with the (1 0 0) plane perpendicular to the light beam (polished with 1.85-mm thickness). The signals are much stronger than in the slightly tilted (1 1 1) cases (Figure 4.6a dotted line), and LB and CB changed with $\sin 2\theta$ and $\sin 4\theta$ periodicity on rotating the sample, respectively (Figure 4.6b). In this case, the contribution of LB is much bigger than LD. Contrary to the common belief that cubic crystal is homogeneous in all directions, we could prove experimentally that chiral cubic crystal of $NaClO_3$ has intrinsic LB in any direction except for the along the [1 1 1] axes [41].

Based on the set of procedures described in Section 4.4.2. Artifact-free CB spectra of $NaClO_3$ crystals were measured with the (1 0 0) plane perpendicular to the light beam for both of the enantiomers and with various thicknesses. Figure 4.6c plots absolute values of artifact-free CB signals at 250 nm against the sample thickness. Calculation of a least-squared linear line shows that the linear relationship holds well, including the CB value previously reported by Chandrasekhar [55]. This indicates that even in the cases where LB is substantial, the true CB spectra can be obtained on UCS-1 by our set of procedures.

4.4.7. Cast Film CD of Bovine Serum Albumin (BSA) [43]

Solid-state spectroscopy provides valuable information on solid-state structure and supramolecular properties. This applies not only to organic or inorganic compounds but also to biological substances. CD spectroscopy of proteins in dry thin films may provide useful information on their unique conformation in an aggregate or in the condensed phase. The information may be particularly relevant to some neurodegenerative disorders, such as Alzheimer's and prion diseases, in which the production of abnormal aggregates of α-amyloid peptide or prion protein seems to constitute an important step [56, 57]. Relating to this, CD spectra of nine proteins/peptides in both solution and in dry films were published [23]. For one class of proteins (e.g., BSA and α-synuclein), their CD spectra in the solid and solution states were different, whereas for the other class of proteins (e.g., insulin, lysozyme, and luciferase), the two CD spectra were similar. Based on these findings, it was claimed [23] that first-class proteins undergo structural transformation from native structures in solution into β-sheet predominant structures in the solid state. In their work, no macroscopic anisotropies of solid samples were considered. Thus, we have independently studied CD of BSA on UCS-1.

We made a BSA cast film by slow evaporation (24 h) to obtain a relatively strain-free film of even thickness. The LB and the LD signals were small, and photomultiplier

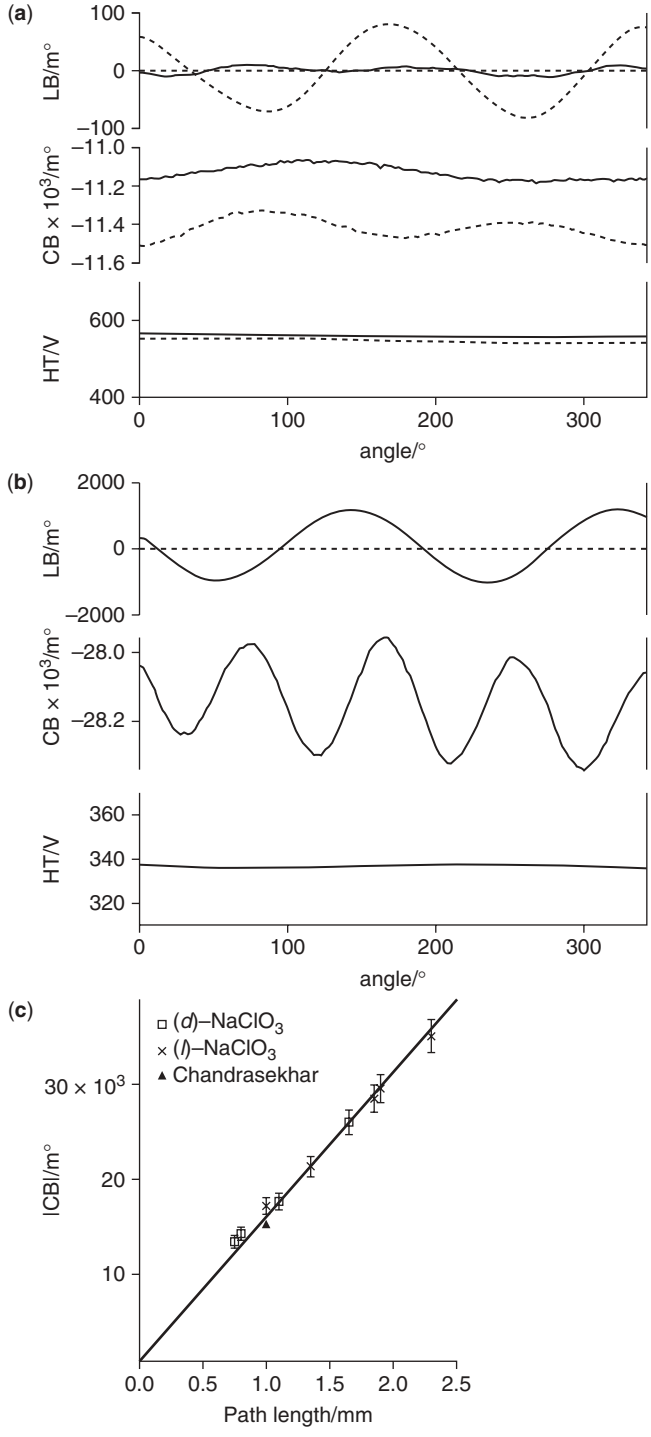

Figure 4.6. LB and CB rotation measurements (at 250 nm) of an (*l*)-$NaClO_3$ single crystal (0.6-mm thickness). In the case when the light beam is exactly normal to the (a) (1 1 1) or (b) (1 0 0) face (solid line), or slightly tilted from it (dotted line). (c) Absolute values of CB signals [(□) for the (*d*)- and (×) for the (*l*)-isomers], at 250 nm, against the pathlength of the crystals polished parallel to the (1 0 0) face. Linear relationship holds only with the true LB or CB. The CB value at 253 nm reported by Chandrasekhar is indicated by a filled triangle.

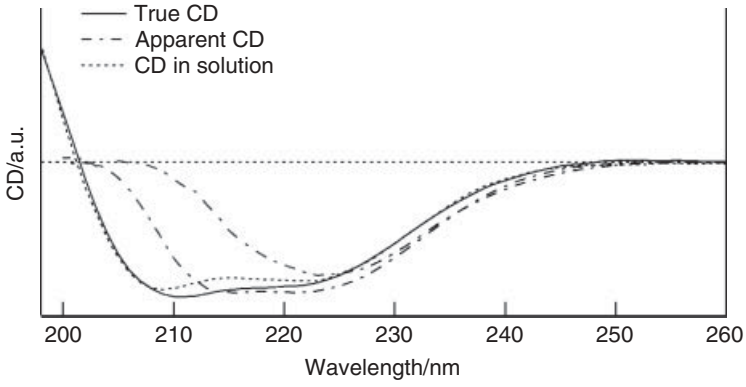

Figure 4.7. CD spectra of the bovine serum albumin (BSA) cast films having large and small anisotropies: film with large anisotropies at the CD_{max} and CD_{min} positions and film small anisotropy. The solution CD spectrum (red) is shown for comparison.

voltage was almost constant throughout the rotation of the sample 360° in the plane perpendicular to the light beam at 210 nm, to ensure the even thickness and strain-free nature of the sample. We could obtain true CD spectrum of the film by using the procedures of removing artifact signals as described in Section 4.4.1. The solid-state spectrum is similar to the solution CD spectrum, which presents a double-negative broad spectrum with a peak at 209 nm and a shoulder at 222 nm (Figure 4.7), typical of proteins with a high α-helical content.

Experiments were also carried out by making BSA cast film very fast (10 min) on purpose. From the CD rotation measurement, we can locate the $\mathbf{CD_{max}}$ and $\mathbf{CD_{min}}$ positions where the CD signal becomes the maximum and minimum values, respectively. The wavelength scans carried out at these positions are quite different from each other: CD_{max} spectrum exhibits a negative peak at 223 nm, while CD_{min} spectrum shows a broader negative band (Figure 4.7). Thus, the CD spectra differed substantially, depending on the sample rotational positioning, θ. The solid-state CD at the CD_{max} position is incidentally similar to what was reported in the literature [23]. The CD was interpreted as the structure containing β-sheets, and it was claimed that BSA transforms to a β-sheet aggregate in the condensed phase as it exhibited different CD from that in the solution. Our results unambiguously deny their statement. We can conclude that the structural change of BSA does not occur in the process of film formation. The spectral difference is simply due to the artifacts arising from the substantial macroscopic anisotropies, mainly LB and its coupling with LD.

If LB and LD signals are mixed into the CD signals, different CD spectra are obtained for films made with different evaporation speed, although they are made from the same stock solution, or for films at different rotation positions even for the same film. If samples are homogeneous, the procedures for obtaining true CD can be applied; however, inhomogeneous cases (e.g., uneven thickness) cannot be dealt with. For the CD measurement of samples with possible macroscopic anisotropies such as films, gels, micells, and liquid crystals, it is necessary to measure the anisotropies using specially designed spectrophotometer such as our UCS's. Only with this consideration, important information on protein and peptide characteristics in the condensed phase will be elucidated.

In the case of β-amyloid (1–40) and (1–42) peptides, we could show a clear structure transition from α-helix dominant structure in solution to β-sheet dominant one in cast films [44]. Figure 4.3 shows a representative true CD of β-amyloid (1–42) peptide in a cast film.

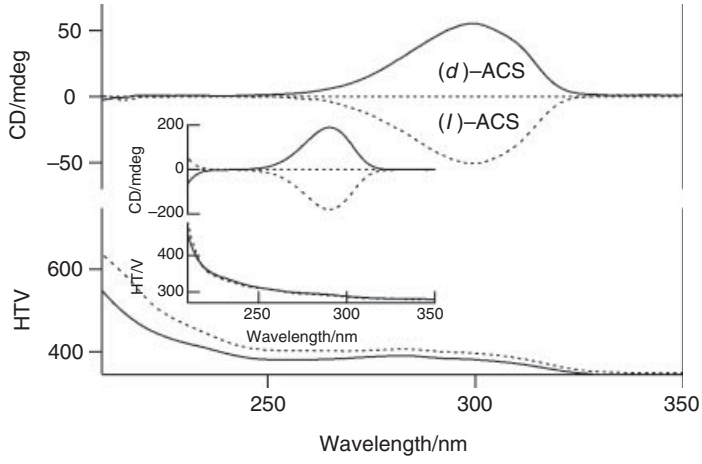

Figure 4.8. DRCD spectra of (*d*)-(solid line) and (*l*)-ACS (dotted line) microcrystallines pulverized to small particles. (Inset) Their transmittance CD spectra in the solution state.

4.4.8. Diffuse Reflectance CD (DRCD): Specular Component

In order to evaluate the performance of DRCD mode of dual-purpose UCS-2 or UCS-3, we measured powdered ammonium-10-camphorsulfonate (ACS), which is usually used as a standard sample for CD spectrophotometer calibration in UV wavelength region [58, 59]. As shown in Figure 4.8, DRCD spectra of the microcrystalline ACS enantiomers are mirror images of each other, indicating that all the equipments, both optical and electric, work well. The spectra are compared with the solution spectra (Figure 4.8 inset). The agreement in general is quite good, but slight red shifts of the peak maximum, 9 and 6 nm, were observed compared to the transmission CD in solution and in the solid state (KBr matrix method, data not shown), respectively. The observed slight red shift (~3 nm) in transmission CD of the KBr disk as compared with the solution CD may be due to the effect originated from the densely packed neighboring molecules in crystals, although dispersion effect cannot be ignored completely. The depolarization at grain boundaries of a sample may cause serious experimental problems. We have noticed that even with an apparently translucent KBr disk there may be a large depolarization of the light beam due to reflection and refraction at the grain boundaries which influence transmittance CD as well [18, 19, 60]. The dispersion effect on the transmittance CD was first studied by Kuroda when she calculated the rotatory strengths of $d-d$ transition by using the microcrystalline CD as a KBr disk quantitatively [18, 19]. In the case of nujol mull method, generally the particle size cannot be made smaller than the KBr matrix and hence cause bigger red shift of the CD peak maxima [18, 60].

The red shifts in the DRCD measuremnts is due to the intrinsic nature of solid samples. It has been reported that the red shifts in DR spectra depend on specular reflectance [61–66], which is defined as the reflected radiation that reaches the detector but never penetrates the sample particles. In contrast, DR is defined as the reflected radiation that is transmitted and/or refracted through one or more sample particles and finally reflected onto the detector. Thus, it might be suggested that the observed DRCD signal contains both specular and DR lights. It is exremely difficult to segregate specular and diffuse reflectance components and to remove the specular component from the obtained spectra completely. In UCS-3, a baffle made of spectralon was installed to reduce the first specular reflection signals.

The effect of specular reflections on the DRCD spectra was experimentally studied by comparing DRCD of neat microcrystallines with various grinding time, that of samples diluted with KBr, and nujol mull methods [36, 48]. These results indicate that the effect of specular reflections in the detected signal can be reduced by using small-particle-size microcrystallines and diluting the light-absorbing sample with an inert low-absorbing matrix such as KCl, KBr, and MgO microcrystalline [35, 48].

4.4.9. DRCD: First CD Measurement of 1:1 BQ–PYR Complex [48]

The 1:1 complex (**1**) of BQ and PYR(pyrene) exhibits optical activity only in the crystalline state due to the chiral supramolecular arrangement of the nonchiral components. But, its chirality has never been studied. It crystallizes in a chiral uniaxial crystal system with the space group of either $P4_1$ or $P4_3$. The CD measurement method for uniaxial crystals with the light propagated along the unique axis to avoid the effect of macroscopic anisotropies is, however, hampered by the strong absorption ($\varepsilon = 10^4 - 10^5$) in the UV–vis wavelength range. It is difficult to prepare extremely thin-plate-like specimens appropriate for the direct transmittance CD measurement. Alternative matrix methods [18, 19, 26], that are now widely used in the solid-state chirality measurements cannot be applied to this complex, because BQ sublimes easily from the complex crystals, especially during the KBr disk formation processes (due to increased surface areas and under vacuum condition). The nujol mull method is also not applicable to **1** because it dissolves in nujol.

DRCD measurement [35] is most suitable for this type of samples. A single crystal of **1** was co-ground with KBr (or separately ground) to microcrystalline powders (grain size: 20–53 μm, dilution: 10–20 wt%) in order to decrease the specular reflection [63–66] and the parasitic signals originating from the intrinsic macroscopic anisotropies (LB and LD) as well as to reduce the large absorption coefficient. X-ray powder diffraction (XRPD) analysis showed that the grinding process does not alter the crystal lattice. To avoid the sublimation of BQ, the sample holder was covered with a quartz plate. Figure 4.9a shows DRCD spectra of **1** measured on UCS-3 for both of the enantiomeric crystals. They are almost mirror images of each other. Because the absorption coefficient of a charge transfer (CT) band at around 450 nm is very small ($\varepsilon_{453} = 323$) [67], spectra in the 400- to 250-nm wavelength region are shown. Absolute configuration of crystal **1** cannot be determined by X-ray anomalous dispersion method as it contains no heavy atom. Thus, we made a 1:1 complex crystal, **2**, with 2-chloro-1,4-benzoquinone (2-ClQ) and PYR, and determined the absolute crystal configuration. Crystal **2** is isomorphous to **1** and exhibits similar DRCD to **1**. Thus, we could correlate the sign of DRCD spectra of **1** and **2** with the absolute configuration of the crystals: $P4_1$ crystals exhibit negative peaks at the 350-325 nm wavelength range, whereas $P4_3$ crystals positive peaks.

The DRCD spectra were checked for the effect of artifact signals which arise from the interaction between the macroscopic anisotropies of the sample and the non-ideal characteristics of the polarization-modulation instruments [32]. UCS-2/3 cannot record signals with analyzer inserted in the DRCD mode, thus only the aritifact signals arising from LD which does not couple with LB can be taken care of. Thus, we have estimated the contribution of LB as follows. The artifact signals have terms dependent as well as independent on the sample rotation in the plane perpendicular to the light beam [32]. DRCD signals of **1** hardly changed with sample rotation, and hence the angular-dependent terms multiplied by the polarization characteristics of the detector, P, are negligible. Here the polarization characteristics, P, of the detector is expressed as $(P_x{}^2 - P_y{}^2) \sin 2a$,

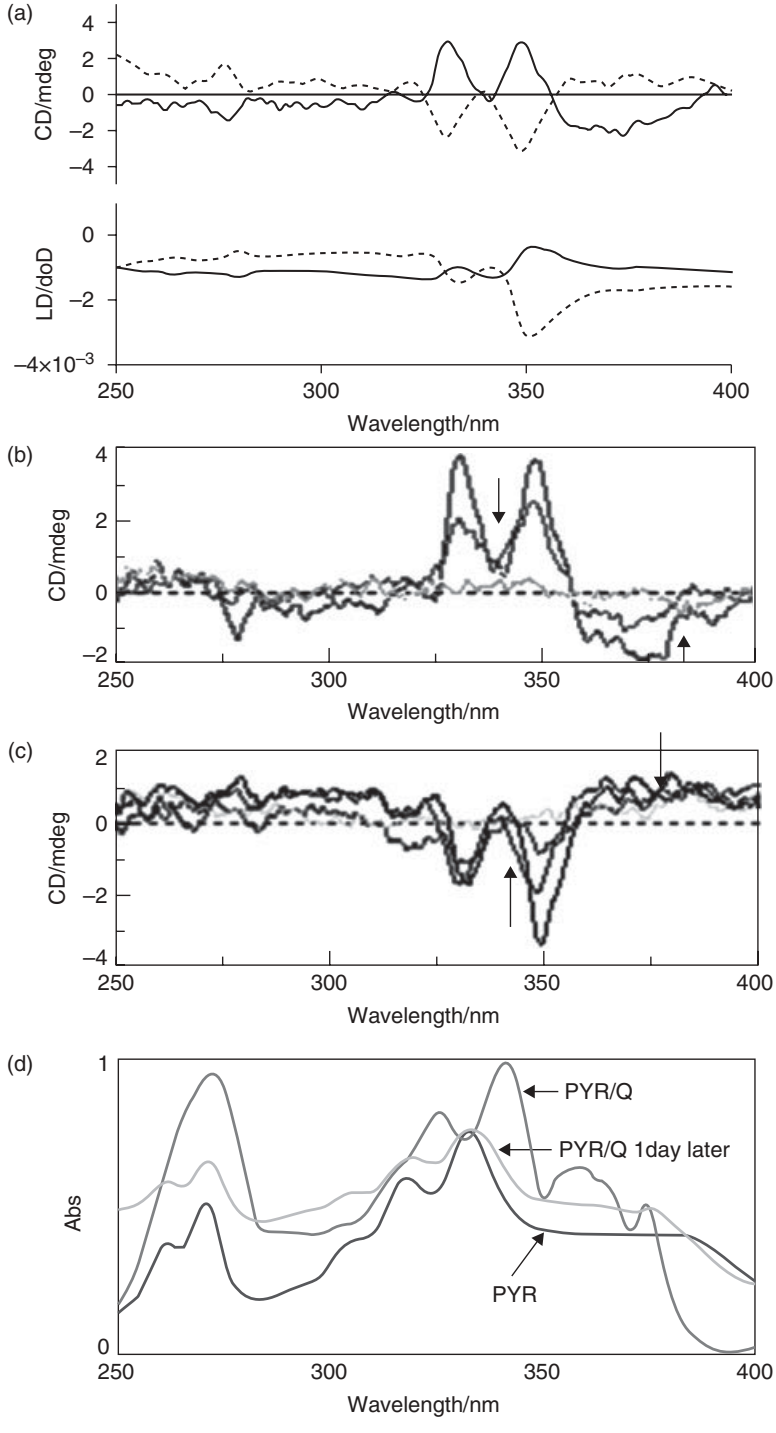

Figure 4.9. (a) DRCD and (b) LD spectra of **1** measured on UCS-3 for the enantiomeric crystals (diluted with KBr matrix: 17 wt% (solid line) and 10 wt% (broken line)). (c) Time-dependent change of the DRCD spectra over 24 h due to sublimation of Q: red, green, and blue spectra correspond to after 0, 3 and 24 h of exposure, respectively. (d) Corresponding electronic absorption spectra at the initial state and after 24 h. PYR spectrum is shown for comparison.

where P_x^2 and P_y^2 are the transmittance of the detector along the x and y directions and a is the azimuth angle of its optical axis with respect to the x axis. LB values of the sample were expected to be less than 10^{-3} OD because the value of P of UCS-3 was estimated to be on the order of 10^{-3} at 350 nm [68]. LD signals of current samples were measured to be on the order of 10^{-3}–10^{-4} OD (Figure 4.9b), and hence the angular-independent terms are 10–100 times smaller than the true DRCD signal. Thus, we can conclude that the DRCD spectra of **1** recorded on UCS-3 are free from LD and LB effects.

We observed time-dependent change of the DRCD spectra over 24 h (Figure 4.9c) when the sample was left without a cover. The DRCD spectra for both of the enantiomeric crystals decreased the absolute intensities, and after 24 h all the CD peaks disappeared completely (Figure 4.9c). The absorption spectra after 24-h exposure coincided with that of PYR crystal (Figure 4.9d). Thus, the absorption and the DRCD spectra observed at the initial state originate from the supramolecular structure of **1**.

This is the first measurement of CD spectra of crystals **1** and **2**, which exhibit optical activity only in the crystalline state due to chiral supramolecular arrangement of nonchiral components. DRCD is the only available method for measuring CD of sublimable samples, samples that react with KBr during the disk formation or that dissolve in nujol.

4.5. MULTICHANNEL (MC) CD METHOD: A NOVEL METHOD FOR DIRECT TRUE CD MEASUREMENT

So far we have succeeded in obtaining true CD and CB spectra of solid samples, by developing a series of UCSs and devising a set of measuring/analyzing procedures for UCSs. Many interesting results have been obtained on UCSs by investigating the structures of organic, inorganic, and bio samples in the condensed phase and the dynamics of relatively slow structural change of peptides from solution to solid-phase transition. UCSs adopt the method of taking away the parasitic artifacts signals from the observed spectra, and hence cumbersome procedures as described in Sections 4.4.1 and 4.4.2 are necessary.

Alternative method adopts entirely novel concept/technique for measuring CD spectra—that is, to detect only artifact-free signals. This is a MC (multichannel) CD spectrophotometer we are currently developing in our laboratory [31]. The new spectrophotometer is designed to subtract the absorption for the left-circularly polarized light form that for the right-circularly polarized light directly, thus the spectra will not be affected by the macroscopic anisotropies which are intrinsic to solid samples. It also employs nonmonochromated white light and measures spectra like a snapshot with a multichannel detector to provide simultaneous detection of whole wavelength ranges. Because wavelength scan is unnecessary, high-speed data acquisition is possible. This is ideal for studying dynamics of moderately fast structural changes if the molecules are chiral, like proteins. We hope to improve in the near future the prototype we are currently developing. Accuracy and S/N ratio of UCSs are expected to surpass those of the MC CD spectrophotometer, and thus we believe that both techniques are complementary to each other.

4.6. CONCLUDING REMARKS

This chapter discussed the principles and applications of chiroptical spectroscopy in the solid state. As biological world is homochiral consisting of proteins made up of only

L-amino acids and nucleic acids of only D-(deoxy)ribose, the effect of medicinal and agricultural chemicals are quite different, depending on the handedness of the compounds. For the development of new therapeutic drugs, agricultural chemicals, food etc, which are related to many biological processes, the chiral recognition and resolution must be considered. Also, because the biological world is homochiral, physical chemistry and biochemistry underlying many biological phenomena such as gene expression, recombination, metabolism, disease development, organismal development, etc, may be elucidated through chirality measurement. Thus, chirality is important in both basic and applied sciences.

The solid-state chemistry is one of the most advancing frontiers because strong intermolecular interactions and fixed molecular conformations can open up unique areas of research. Because solid-state reactions do not require environmentally damaging organic solvents, it is regarded as green chemistry. Limiting to chirality, solid-state chiral chemistry offers unique chemistry, since chirality generation, transfer, and amplification occur most strongly in the solid state. As we have seen in this chapter, the solid-state chiroptical spectroscopy provides indispensable information on many molecular events underlying many interesting phenomena. The most powerful chiroptical technique for the chirality measurements is the circular dichroism spectroscopy, and it is necessary to use spectrophotometers that can handle solid-state measurements. We have designed and constructed solid-state applicable CD spectrophotometers (UCS-1, UCS-2, and UCS-3) and devised analytical procedures based on the Stokes–Mueller matrix. They can measure true CD and CB spectra of samples having macroscopic anisotropies such as gels, films, and crystals. It can also carry out *in situ* measurement of solid samples without any pretreatment, as well as dynamics of relatively slow structural changes. A new concept of measuring only pure chiroptical signals rather than removing artifact from observed signals is on its way. It is hoped that the versatile chiroptical spectroscopy becomes a basic tool in the world to advance the frontier of science even further.

REFERENCES

1. F. Arago, *Mem. CI. Sci. Math. Phys. Inst*. **1811**, *12*, 93–110.
2. J. B. Biot, *Me. Inst France* **1812**, *1*, 1–32.
3. L. Pasteur, *Ann. Chim. Phys*. **1848**, *24*, 442–459.
4. D. Braga, S. L. Giaffreda, F. Grepioni, A. Pettersen, L. Maini, M. Curzi, M. Polito, *Dalton Trans*. **2006**, 1249–1263 and references in the review articles.
5. T. Friscic, A. V. Trask, W. Jones, W. S. S. Motherwell, *Angew. Chem. Int. Ed*. **2006**, *45*, 7708–7712.
6. F. Toda, K. Tanaka, H. Miyamoto, H. Koshima, I. Miyahata, K. Hirotsu, *J. Chem. Soc. Perkin Trans*. **1997**, *9*, 1877–1885.
7. (a) V. R. Pedireddi, W. Jones, A. P. Chorlton, R. Docherty, *Chem. Commun*. **1996**, 987–988; (b) A. V. Trask, W. D. S. Motherwell, W. Jones, *Chem. Commun*. **2004**, *7*, 890–891.
8. P. J. Nichols, C. L. Raston, J. W. Steed, *Chem. Commun*. **2001**, 1062–1063.
9. (a) D. Braga, L. Maini, M. Polito, L. Mirolo, F. Grepioni, *Chem. Commun*. **2002**, *24*, 2960–2961; (b) D. Braga, *Chem. Commun*. **2003**, 2751–2754; (c) D. Braga, L. Maini, M. Polito, L. Mirolo, F. Grepioni, *Chem. Eur. J*. **2003**, *9*, 4362–4370; (d) D. Braga, L. Maini, G. de Sanctis, K. Rubini, F. Grepioni, M. R. Chierotti, R. Gobetto, *Chem. Eur. J*. **2003**, *9*, 5538–5548; (e) D. Braga, S. L. Giaffreda, F. Grepioni, M. Polito, *CrystEngComm*. **2004**, *6*, 458–462; (f) D. Braga, M. Curzi, F. Grepioni, M. Polito, *Chem. Commun*. **2005**, 2915–2917.

10. K. Chadwick, R. Davey, W. Cross, *CrystEngComm*. **2007**, *9*, 732–734.
11. (a) R. Kuroda, Y. Imai, N. Tajima, *Chem. Commun*. **2002**, 2848–2849; (b) R. Kuroda, Y. Imai, T. Sato, *Chirality*. **2001**, *13*, 588–594; (c) Y. Imai, N. Tajima, T. Sato, R. Kuroda, *Chirality*. **2002**, *14*, 604–609; (d) R. Kuroda, K. Higashiguchi, S. Hasebe, Y. Imai, *CrystEngComm*. **2004**, *6*, 463–468; (e) Y. Imai, N. Tajima, T. Sato, R. Kuroda, *Organic Lett*. **2006**, *8*, 2941–2944; (f) E. Y. Cheung, S. J. Kitchin, K. D. M. Harris, Y. Imai, N. Tajima, R. Kuroda, *J. Am. Chem. Soc*. **2003**, *125*, 14658–14659; (g) R. Kuroda, T. Sato, Y. Imai. *CrystEngComm*. **2008**, *10*, 1881–1890.
12. A. Nakamura, T. Sato, R. Kuroda, *Chem. Commun*. **2004**, 2858–2859.
13. (a) G. M. J. Schmidt, *J. Chem. Soc*. **1964**, 2014–2021; (b) G. M. J. Schmidt, *Pure Appl. Chem*. **1987**, *87*, 433–481.
14. (a) L. R. MacGillivray, J. L. Reid, J. A. Ripmeester, *J. Am. Chem. Soc*. **2000**, *122*, 7817–7818, (b) X. Gao, T. Caronna, T. Friscic, L. R. MacGillivray, *Angew. Chem. Int. Ed*. **2004**, *43*, 232–236.
15. K. Tanaka, F. Toda, *Chem. Rev*. **2000**, *100*, 1025–1074.
16. (a) R. Kuroda, ACS fall meeting, Washington DC, **2009**; (b) R. Sekiya, R. Kuroda, *Chem. Commun*. **2011**, *47*, 10097–10099.
17. M. Stefani, C. M. Dobson, *J. Mol. Med*. **2003**, *81*, 678–699, and references therein.
18. R. Kuroda, Ph.D Thesis, The University of Tokyo, **1975**.
19. R. Kuroda, Y. Saito, *Bull. Chem. Soc. Japan* **1976**, *49*, 433–434.
20. F. Livolant, W. Mickols, M. F. Maestre, *Biopolymers* **1988**, *27*, 1761–1769.
21. J. Safar, P. P. Roller, G. C. Ruben, D. Carleton Gajdusek, C. J. Gibbs, Jr., *Biopolymers* **1993**, *33*, 1461–1476.
22. J. Lang, M. Liu, *J. Phys. Chem. B*. **1999**, *103*, 11393–11397.
23. H.-Y. Hu, Q. Li, H.-C. Cheng, H.-N. Du, *Biopolymers* **2001**, *62*, 15–21.
24. A. J. McCaffery, S. F. Mason, *Trans Faraday Soc*. **1963**, *59*, 1–11.
25. B. Norden, I. Grenthe, *Acta Chem. Scand*. **1972**, *26*, 407–409.
26. R. R. Judkins, D. J. Royer, *Inorg. Chem*. **1974**, *13*, 945–950.
27. Y. Shindo, M. Nishio, S. Maeda, *Biopolymers* **1990**, *30*, 405–413.
28. Y. Shindo, *Opt. Eng*. **1995**, *34*, 3369–3384.
29. R. Kuroda, *Circular Dichroism: Principles and Applications*, 2nd edition, N. Berova, K. Nakanishi, and R. W. Woody, eds., John Willey & Sons, Hoboken, NJ, **2000**, pp. 159–184.
30. R. Kuroda, *Chiral Photochemistry*, Y. Inoue and V. Ramamurthy, eds., Marcel Dekker, New York, **2004**, pp. 385–414.
31. R. Kuroda, CD2011, Oxford, U.K., **2011**, p24; T. Harada, H. Takahashi, R. Kuroda, to be submitted.
32. R. Kuroda, T. Harada, Y. Shindo, *Rev. Sci. Instrum*. **2001**, *72*, 3802–3810; Japanese Patent No. 3,942,800, April 28, **2000**; and Japanese Patent No. 4,010,760, October 13, **2000**.
33. D. Braga, L. Maini, M. Polito, F. Grepioni, *Chem. Commun*. **2002**, 2302–2303.
34. T. Harada, R. Kuroda, to be submitted.
35. I. Bilotti, P. Biscarini, F. Ferranti, E. Castiglioni, R. Kuroda, *Chirality*, **2002**, *14*, 750–756.
36. T. Harada, H. Hayakawa, R. Kuroda, *Rev. Sci. Instrum*. **2008**, *79*, 373103.
37. T. Harada, Y. Miyoshi, R. Kuroda, *Rev. Sci. Instrum*. **2009**, *80*, 046101.
38. J. A. Schellman, *Polarized Spectroscopy of Ordered Systems*, B. Samori and E. W. Thulstrup, eds., Kluwer Academic, Dordrecht, **1988**, pp. 231–274; H. P. Jensen, J. A. Schellman, T. Troxell, *Appl. Spectrosc*. **1978**, *32*, 192–200; J. Schellman, H. P. Jensen, *Chem. Rev*. **1987**, *87*, 1359–1399; Y. Shindo, M. Nakagawa, Y. Ohmi, *Appl. Spectosc*. **1985**, *39*, 860–868; Y. Shindo, Y. Ohmi, *Rev. Sci. Instrum*. **1985**, *56*, 2237–2242.
39. T. Harada, Y. Shindo, R. Kuroda, *Chem. Phys. Lett*. **2002**, *360*, 217–222.

40. T. Harada, T. Sato, R. Kuroda, *Chem. Phys. Lett*. **2008**, *456*, 268–271.
41. T. Harada, T. Sato, R. Kuroda, *Chem. Phys. Lett*. **2005** *413*, 445–449.
42. Y. Shindo, K. Kani, J. Horinaka, R. Kuroda, T. Harada, *J. Plast. Film. Sheeting* **2001**, *17*, 164–183.
43. T. Harada, R. Kuroda, *Chem. Lett*. **2002**, *31*, 326–327.
44. T. Harada, R. Kuroda, *Biopolymers* **2011**, *95*, 127–134.
45. V. V. Borovkov, T. Harada, G. A. Hembury, Y. Inoue, R. Kuroda, *Angew. Chem*. **2003**, *42*, 1746–1749; V. V. Borovkov, Y. Inoue, T. Harada, R. Kuroda, *Angew. Chem*. **2002**, *41*, 1378–1381.
46. Y. Imai, K. Kawaguchi, T. Harada, T. Sato, M. Ishikawa, M. Fujiki, R. Kuroda, Y. Matsubara, *Tetrahedron Lett*. **2007**, *48*, 2927–2930.
47. S. G. Telfer, T. Sato, T. Harada, R. Kuroda, J. Lefebvre, D. B. Leznoff, *Inorg. Chem*. **2004**, *43*, 6168–6176; S. G. Telfer, N. D. Parker, R. Kuroda, T. Harada, J. Lefebvre, D. B. Leznoff, *Inorg. Chem*. **2008**, *47*, 209–218; S. Khatua, H. Stoeckli-Evans, T. Harada, R. Kuroda, M. Bhattacharjee, *Inorg. Chem*. **2006** *45*, 9619–9621; S. Khatua, T. Harada, R. Kuroda, M. Bhattacharjee, *Chem. Commun*. **2007**, 3927–3929.
48. N. Asano, T. Harada, T. Sato, N. Tajima, R. Kuroda, *Chem. Commun*. **2009**, 899–901.
49. C. A. Emeis, L. J. Oosterhoff, G. De Vries, *Proc. R. Soc. London Ser. A* **1967**, *297*, 54–65.
50. C. A. Beevers, H. Z. Lipson, *Krist*. **1932**, *83*, 123–135.
51. B. H. O'Connor, D. H. Dale, *Acta Cryst*. **1966**, *21*, 705–709.
52. K. Stadnica, A. M. Glazer, M. Koralewski, *Acta Cryst. B* **1987**, *43*, 319–325.
53. G. N. Ramachandran, K. S. Chandrasekaran, *Acta Cryst*. **1957**, *10*, 671–675; D. Xue, S. Zhang, *Chem. Phys. Lett*. **1998**, *287*, 503–508.
54. H. E. Buckley, *Z. Krist*. **1930**, *73*, 15–29.
55. S. Chandrasekhar, *Proc. R. Soc. A* **1961**, *259*, 531–553.
56. E. H. Koo, P. T. Lansbury, J. W. Kelly, *Proc. Natl.Acad. Sci. USA* **1999**, *96*, 9989–9990.
57. P. B. Tran, R. J. Miller, *Trends Neurosci*. **1999**, *22*, 194–197.
58. T. Takakuwa, T. Konno, H. Meguro, *Anal. Sci*. **1985**, *1*, 215–218.
59. D. F. DeTar, *Anal. Chem*. **1969**, *41*, 1406–1408.
60. R. Kuroda, T. Honma, *Chirality* **2000**, *12*, 269–277.
61. R. K. Vincent, G. R. Hunt, *Appl. Opt*. **1968**, *7*, 53–59.
62. M. Mamiya, *J. Spectrosc. Soc. Jpn*. **1976**, *25*, 99–117.
63. G. Kortüm, W. Braun and G. Herzog, *Angew. Chem. Int. Ed*. **1963**, *2*, 333–341.
64. J. W. Childers, R. Röhl, R. A. Palmer, *Anal. Chem*. **1986**, *58*, 2629–2636.
65. E. Castiglioni, P. Albertini, *Chirality*. **2000**, *12*, 291–294.
66. M. G. Lagorio, *J. Chem. Educ*. **2004**, *81*, 1607–1611.
67. R. E. Merrifield, W. D. Phillips, *J. Am. Chem. Soc*. **1958**, *80*, 2778–2782; R. K. Gupta, R. A. Singh, *J. Crystal Growth*. **2004**, *267*, 340–347.
68. Y. Shindo, M. Nakagawa, *Rev. Sci. Instrum*. **1985**, *56*, 32–39.

5

INFRARED VIBRATIONAL OPTICAL ACTIVITY: MEASUREMENT AND INSTRUMENTATION

Laurence A. Nafie

5.1. INTRODUCTION

This chapter is devoted to the measurement and instrumentation associated with the rapidly growing field of infrared vibrational optical activity (VOA) [1–8]. Preceding chapters have focused on optical activity and linear dichroism associated with *electronic* transitions, and this is the first of two chapters devoted to optical activity in *vibrational* transitions, the second being the chapter on vibrational Raman optical activity (ROA) instrumentation and measurement by Werner Hug. As a result, our primary focus will be on vibrational circular dichroism (VCD), which is the central topic of infrared vibrational optical activity. Nevertheless, a number of aspects of VCD will not be covered in this chapter since they will be described elsewhere. The first is VCD measured with picosecond or femtosecond time resolution, which will be covered in the chapter by Minhaeng Cho, and in yet another chapter, Sergio Abbate will describe VCD in the near-infrared spectral region where vibrational overtone and combination band transitions occur.

While it is beneficial to consider various forms of optical activity from different perspectives, nature does not restrict herself to sharp divisions of topics. For example, in both infrared VCD and visible-laser-excited ROA, spectra have been observed involving *electronic* transitions, namely infrared electronic circular dichroism (IR-ECD) and electronic, as opposed to vibrational, Raman optical activity (EROA). In addition, the effects of overtone and combination bands, normally observed in the near-IR region, can also occur in the region of fundamental vibrational transitions arising from multiple mode transitions of low-frequency vibrations. As a result of these overlaps and the growth in

Comprehensive Chiroptical Spectroscopy, Volume 1: Instrumentation, Methodologies, and Theoretical Simulations, First Edition. Edited by N. Berova, P. L. Polavarapu, K. Nakanishi, and R. W. Woody.
© 2012 John Wiley & Sons, Inc. Published 2012 by John Wiley & Sons, Inc.

the forms and spectral regions covered by optical activity, it is becoming increasingly important to distinguish the electronic and vibrational forms of optical activity as EOA and VOA. If follows that the term CD should only be used when it can be applied to both ECD and VCD. Furthermore, with the growth of research and application of VCD in recent years, it is important to distinguish ECD and VCD explicitly as separate phenomena. This will become even more important in future years when vibronically resolved ECD can be measured and explicitly calculated. Such spectra are simultaneous ECD and VCD spectra, perhaps to be called EVCD spectra.

In view of these overlaps, as well as the growing diversity of the field of optical activity, there is value in considering the broader view of these various fields of optical activity. Thus we begin with a short comprehensive description of the field of VOA so that it is clear where the material of this chapter fits into the grander scheme of VOA, in particular, and natural optical activity, in general.

5.1.1. Definition of Vibrational Optical Activity

Natural vibrational optical activity can be defined as the differential interaction of a chiral molecule, or chiral assembly of molecules, with left- versus right-circularly polarized radiation for a vibrational transition. It should be mentioned, but only once briefly here, that there is the phenomenon of magnetic optical activity, including magnetic ECD (MECD), magnetic VCD (MVCD), and magnetic Raman optical activity (MROA), that follows a similar definition except that all molecules and assemblies, not just chiral molecules and assemblies, can exhibit magnetic optical activity spectra where a magnetic field must be applied either parallel or antiparallel to the beam propagation direction of the circularly polarized radiation interacting with the sample. The definition of natural VOA can be applied to *any* vibrational transition, fundamental, overtone or combination tone, within *any* electronic state of a molecule. The foundations of VOA rest upon two fundamental phenomena, namely (a) VCD associated with first-order one-photon absorption processes and (b) vibrational ROA associated with a second-order two-photon scattering processes. Besides these main phenomena, the circular polarization (CP) forms of VOA, there are also linear polarization forms of VOA, namely vibrational optical rotatory dispersion (VORD), also named vibrational circular birefringence (VCB), and corresponding forms of linear polarization ROA. These involve the rotation of linearly polarized radiation from its initial orientation before the sample to its final orientation after the sample interaction. Linear polarization VOA also is contained within the general definition of VOA since linear polarized radiation is the simultaneous in-phase occurrence of left- and right-circular polarization (LCP and RCP) radiation. For example, for VCB, differences in the speed of light for RCP and LCP radiation, even in the absence of significant absorption, give rise to the rotation of plane polarized light as it passes through the sample.

5.1.2. Forms of Infrared VOA

There are two forms of infrared vibrational optical activity, namely, vibrational circular dichroism (VCD) and, most recently, as mentioned above, vibrational circular birefringence (VCB). These two forms of infrared VOA are related by Kramers–Kronig transformation as described formally below and share a common spectroscopic invariant, namely the rotational strength. We begin by considering first the definition of VCD, ΔA, as the difference in the absorbance of a molecule for LCP (L) versus RCP (R) radiation

for a vibrational transition in electronic state e between vibrational sublevels υ and υ' of normal mode a:

$$(\Delta A)^a_{e\upsilon',e\upsilon} = (A_L)^a_{e\upsilon',e\upsilon} - (A_R)^a_{e\upsilon',e\upsilon}, \tag{5.1}$$

where the convention for the sign of the VCD intensity is left minus right. The corresponding average of the LCP and RCP intensities is the ordinary vibrational absorbance (VA) intensity, A, defined as

$$(A)^a_{e\upsilon',e\upsilon} = \frac{1}{2}[(A_L)^a_{e\upsilon',e\upsilon} + (A_R)^a_{e\upsilon',e\upsilon}]. \tag{5.2}$$

These definitions apply only to a *single* transition that can be computed theoretically or measured experimentally if one isolates the peak or band in the measured spectrum corresponding to the particular vibrational mode of interest. The entire VCD or VA spectrum can be described as a linear sum of intensities, $(\Delta A)^a_{e\upsilon',e\upsilon}$ or $(A)^a_{e\upsilon',e\upsilon}$, times a lineshape function $f'_a(\nu)$ which describes the frequency-dependent shape of the vibrational band as well as the location of the vibrational peak frequency in the spectrum as

$$\Delta A(\nu) = \sum_a (\Delta A)^a_{e\upsilon',e\upsilon} f'_a(\nu), \tag{5.3}$$

$$A(\nu) = \sum_a (A)^a_{e\upsilon',e\upsilon} f'_a(\nu). \tag{5.4}$$

The most common bandshape function for individual vibrational transitions is the Lorentzian lineshape given by the expression

$$f'_a(\nu) = \frac{1}{\pi}\left[\frac{\gamma_a}{(\nu_a - \nu)^2 + \gamma_a^2}\right]. \tag{5.5}$$

This is a symmetric function centered with a maximum value $1/\pi\gamma_a$ at $\nu = \nu_a$, where γ_a is the half-width of the Lorentzian band at its half-maximum value. This can be seen by setting $\nu = \nu_a \pm \gamma_a$ in Eq. (5.5) and seeing that the band intensity there is $1/2\pi\gamma_a$, half the peak value. The factor of $1/\pi$ in Eq. (5.5) provides a normalization property to the Lorentzian lineshape such that the area under band is equal to unity, namely

$$\int_{-\infty}^{\infty} f'_a(\nu)\, d\nu = 1. \tag{5.6}$$

The VCD and VA spectra, $\Delta A(\nu)$ and $A(\nu)$, defined in Eqs. (5.3) and (5.4), are instrument-independent quantities as we will explain in more detail later in this chapter; however, they do depend on the choice of sampling, namely the pathlength, l, and molar concentration, C, of the sample. This dependence on sampling conditions can be removed by dividing $\Delta A(\nu)$ and $A(\nu)$ by pathlength and concentration that yields definitions of VCD and VA in terms of molar absorptivities, $\Delta\varepsilon(\nu)$ and $\varepsilon(\nu)$:

$$\Delta\varepsilon(\nu) = \Delta A(\nu)/(ee)bC, \tag{5.7}$$

$$\varepsilon(\nu) = A(\nu)/bC. \tag{5.8}$$

Here (ee) is the enantiomeric excess of the sample that is required to correct for the possible deviation of the chiral sample from 100% pure chirality of the major enantiomer of the molecule being measured. The (ee) can be defined as the concentration of the major enantiomer, C_M, minus that of the minor enantiomer, C_m, divided by their sum, the total concentration C.

$$(ee) = \frac{C_M - C_m}{C_M + C_m} = \frac{C_M - C_m}{C}. \tag{5.9}$$

The value of (ee) can vary from 1 for a sample of only a single enantiomer to zero for a racemic mixture of both enantiomers such that neither enantiomer is in excess. Equations (5.7) and (5.8) assume Beer–Lambert's law. This law breaks down if there are significant levels of intermolecular interactions between solute molecules which usually can be avoided at sufficiently low levels of concentration. These definitions of $\Delta\varepsilon(\nu)$ and $\varepsilon(\nu)$ are pure molecular properties and can be compared directly to the results of theoretical calculations.

The theoretical expressions for VCD and VA intensities defined in Eqs. (5.1) and (5.2) are given by the rotational strength, $R^a_{g\upsilon',g\upsilon}$, for VCD and the dipole strength, $D^a_{g\upsilon',g\upsilon}$, for VA as

$$R^a_{e\upsilon',e\upsilon} = \mathrm{Im}[\langle\psi^a_{e\upsilon}|\boldsymbol{\mu}|\psi^a_{e\upsilon'}\rangle \cdot \langle\psi^a_{e\upsilon'}|\boldsymbol{m}|\psi^a_{e\upsilon}\rangle], \tag{5.10}$$

$$D^a_{e\upsilon',e\upsilon} = |\langle\psi^a_{e\upsilon}|\boldsymbol{\mu}|\psi^a_{e\upsilon'}\rangle|^2. \tag{5.11}$$

Here $\boldsymbol{\mu}$ is the electric dipole moment operator, and $\boldsymbol{m}$ is the magnetic dipole moment operator given by

$$\boldsymbol{\mu} = \sum_j e_j \boldsymbol{r}_j, \qquad \boldsymbol{m} = \sum_j \frac{e_j}{2m_j c} \boldsymbol{r}_j \times \boldsymbol{p}_j, \tag{5.12}$$

where the summation index j is over all electrons and nuclei in the molecule, and e_j is the charge, $\boldsymbol{r}_j$ is the position, $\boldsymbol{p}_j$ is the momentum, m_j is the mass, and c is the speed of light. From these definitions we can see that the dipole strength is always a positive quantity, namely the absolute square of the electric dipole transition moment. On the other hand, VCD is the scalar product of two vectors, the electric dipole and the magnetic dipole transition moments. This product can be either positive or negative, depending on whether the angle between the two vectors is less than 90° or between 90° and 180°. Given these theoretical definitions for the rotational and dipole strengths, we now can write the expressions for $\Delta\varepsilon(\nu)$ and $\varepsilon(\nu)$ in terms rotational and dipole strengths, respectively, in units is esu^2-cm^2 as

$$\Delta\varepsilon(\overline{\nu}) = \frac{32\pi^3 N\overline{\nu}}{3000hc\ln(10)} \sum_a R_a f'_a(\overline{\nu}) = \frac{\overline{\nu}}{2.236\times10^{-39}} \sum_a R_a f'_a(\overline{\nu}), \tag{5.13}$$

$$\varepsilon(\overline{\nu}) = \frac{8\pi^3 N\overline{\nu}}{3000hc\ln(10)} \sum_a D_a f'_a(\overline{\nu}) = \frac{\overline{\nu}}{9.184\times10^{-39}} \sum_a D_a f'_a(\overline{\nu}). \tag{5.14}$$

Using Eqs. (5.7) and (5.13), one can compare measured and calculated VCD, and similarly for comparing measured and calculated VA intensities using Eqs. (5.8) and (5.14). Of particular interest in these comparisons is the dimensionless ratio of $\Delta\varepsilon_a(\overline{\nu})$ to $\varepsilon_a(\overline{\nu})$

for a given transition called the anisotropy ratio, $g_a = \Delta\varepsilon_a(\overline{\nu})/\varepsilon_a(\overline{\nu})$. This ratio is a measure of VCD intensity relative to its parent VA intensity for a given transition. If the definition of g_a is applied to Eqs. (5.13) and (5.14), one obtains four times the rotational strength divided by the dipole strength since all other factors cancel, including the individual line shapes, which are equal for VCD and VA to a very good approximation.

$$g_a = \frac{\Delta\varepsilon_a(\overline{\nu})}{\varepsilon_a(\overline{\nu})} = \frac{4R_a}{D_a} \tag{5.15}$$

The anisotropy ratio is a measure of the expected signal noise ratio of a VCD measurement.

We next consider the other form of infrared VOA, vibrational circular birefringence (VCB), which can also be called vibrational optical rotatory dispersion (VORD). It is well known that CD and ORD are related mathematically by a transform pair called the Kramers–Kronig transform. This transform states that any point in an ORD spectrum can be specified by the entire CD spectrum over all frequencies and *vice versa*. This means that if one has, for example, the complete CD spectrum of a molecule, there is no new information in the corresponding ORD spectrum.

These ideas can be expressed in a simple way by considering the normalized complex Lorentzian lineshape function:

$$\tilde{f}_a(\nu) = \frac{1}{\pi}\left[\frac{1}{(\nu_a - \nu) - i\gamma_a}\right] = f_a(\nu) + if'_a(\nu). \tag{5.16}$$

Here, the tilde signifies a complex quantity, and the real and imaginary parts are given by Eqs. (5.17) and (5.5), respectively.

$$f_a(\nu) = \frac{1}{\pi}\left[\frac{\nu_a - \nu}{(\nu_a - \nu)^2 + \gamma_a^2}\right]. \tag{5.17}$$

The imaginary part of the complex lineshape $\tilde{f}_a(\nu)$ is designated by a prime $f'_a(\nu)$ whereas the real part is unprimed, $f_a(\nu)$. The function $f_a(\nu)$ is sometimes called a dispersion lineshape function compared to the absorption lineshape, $f'_a(\nu)$. These two normalized lineshape functions are displayed in Figure 5.1. The dispersion lineshape has a value of zero at the band center frequency, ν_a, and is negative on the high-frequency side and positive on the low-frequency side. Far from the center frequency the intensity for the dispersion lineshape diminishes toward zero as $1/(\nu_a - \nu)$ whereas the absorption lineshape approaches zero much faster as $1/(\nu_a - \nu)^2$. For the complex Lorentzian lineshape, the real and imaginary parts are Kramer–Kronig transforms of one another. A result, VCD and VCB can be interconverted just by changing only the lineshape function. To compare corresponding expressions for VCD and VCB we make a minor change in notation involving primes and write the complex molar absorptivity as

$$\Delta\tilde{\varepsilon}(\nu) = \Delta\varepsilon(\nu) + i\,\Delta\varepsilon'(\nu), \tag{5.18}$$

$$\Delta\varepsilon(\nu) = \frac{32\pi^3 N\nu}{3000hc\ln(10)}\sum_a R_a f_a(\nu) = \frac{\nu}{2.236\times10^{-39}}\sum_a R_a f_a(\nu), \tag{5.19}$$

$$\Delta\varepsilon'(\nu) = \frac{32\pi^3 N\nu}{3000hc\ln(10)}\sum_a R_a f'_a(\nu) = \frac{\nu}{2.236\times10^{-39}}\sum_a R_a f'_a(\nu), \tag{5.20}$$

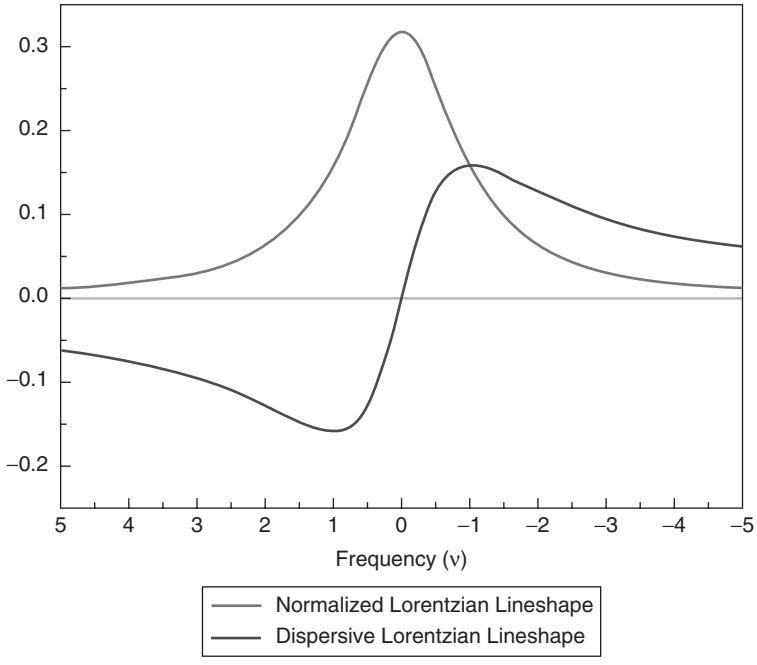

Figure 5.1. The real and imaginary parts, Eqs. (5.17) and (5.5) respectively, of the complex normalized Lorentzian lineshape, Eq. (5.16), are plotted in frequency units of half-width at half-maximum of the absorption lineshape where the real and imaginary parts cross each other. The band center frequency is chosen to be zero. (From reference 9, reproduced with permission.)

where $\Delta\varepsilon(\overline{\nu})$ is the VCB spectrum and $\Delta\varepsilon'(\overline{\nu})$ is the VCD spectrum. From these expressions it is clear how to calculate VCB given the means to calculate a VCD spectrum. Later in this chapter we will provide a description of how to convert a VCD spectrometer to one that can measure VCB spectra.

We conclude this section with an example of both the measured and calculated VA and VCD spectra described theoretically with the preceding equations. In Figure 5.2 we present a comparison published recently of the measurement and calculations of the two forms of infrared VOA as well as the parent VA for the molecule (−)-*S*-α-pinene [9]. The experimental and theoretical expressions given in this section were used for presenting these spectra on the same intensity scale without any adjustable parameters except for the choice of lineshape for the individual vibrational bands including the choice of bandwidth set at half-width at half-maximum to be 6 cm^{-1}. The measured and calculated spectra are offset from each other for clarity. The close agreement between measured and calculated spectra attests to the overall accuracy of density functional theory (DFT) to describe quantum mechanically the equilibrium geometry, vibrational force field, nuclear displacements, vibrational frequencies, and response of electron density in the molecule to changes in the nuclear positions and velocities. The triple zeta basis sets (cc-pVTZ and TZVP) are very similar to one another, and both of these agree noticeably better with the measured spectra than the double zeta basis set 6-31G(d). It was found that TZVP required significantly less computational time than the cc-pVTZ basis set and is recommended if improvement over the 6-31G(d) basis set is desired.

5.1.3. Overview of Infrared VOA

The scope of this chapter covers both the original dispersive VCD instrumentation and the now established Fourier transform infrared (FT-IR) VCD instrumentation. The fundamental optical equations governing the measurement of VCD using a photoelastic modulator

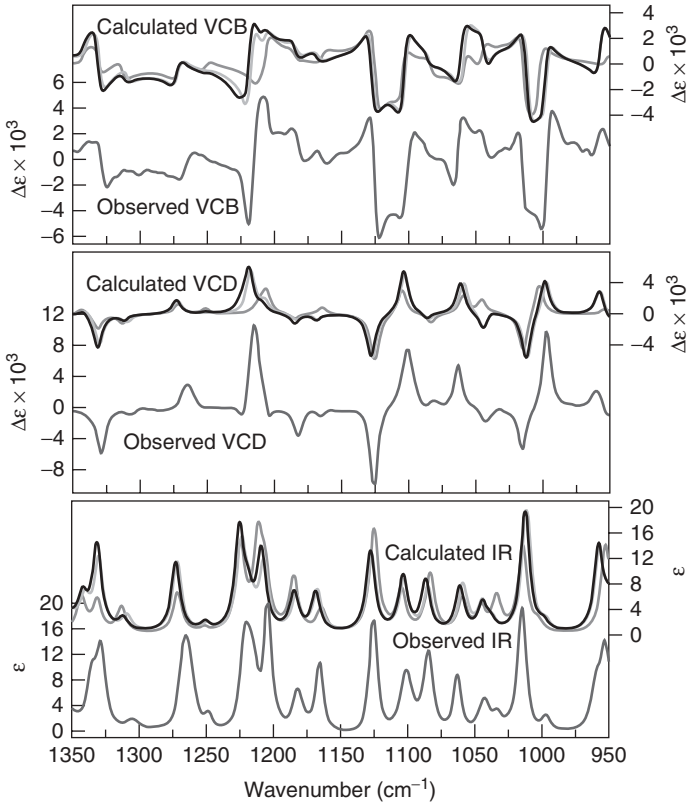

Figure 5.2. Comparison of observed neat liquid (dark grey) and calculated VCB (upper), VCD (middle), and VA (IR, lower) of $(-)-S-\alpha$-pinene. The three sets of calculated spectra are DFT 6-31G(d)/B3LYP (grey), cc-pVTZ/B3PW91 (black), and TZVP/B3PW91 (light grey). (From reference 9, reproduced with permission.)

(PEM) oscillating with a sine wave modulation cycle is unchanged from the first papers that reported the experimental discovery [10] and confirmation of the discovery [11] of VCD. The first detailed description of a VCD spectrometer, including intensity calibration and polarization scrambling using a second PEM [12], was described in the first full paper devoted to the measurement of VCD [13]. Subsequent advances in dispersive VCD instrumentation included extension of the long-wavelength range into the mid-IR region, first to the carbonyl stretching region [14] and then deeper into the mid-IR to near 1250 cm^{-1} or 8 μm [15].

About this same time a new approach was being explored for the measurement of VCD, a method that combined the band of Fourier frequency modulations of FT-IR spectroscopy with the higher-frequency polarization modulation of the PEM needed for VCD measurement. This approach is called double-modulation FT-IR spectroscopy and was first described theoretically [16] with application to circular and linear dichroism measurement. This was followed by the first report of FT-VCD in the hydrogen-stretching region [17–19] and subsequently in the mid-IR for a wide variety of molecules [20]. FT-VCD using the double-modulation approach provided a striking advance in the methodology of VCD measurement for two reasons. First, FT-VCD spectra realized all of the advantages of FT-IR spectroscopy relative to dispersive IR technology for which today there is no longer a standard, commercially available IR spectrometer. The result was a breakthrough in spectral acquisition giving an unsurpassed combination of spectral resolution, signal-to-noise ratio, and breadth of spectral coverage down to 14 μm or approximately 800 cm^{-1}. The second reason is that a VCD instrument could be

constructed from a modification of an existing, computer-controlled FT-IR spectrometer that facilitates the construction of a VCD spectrometer and brings VCD technology closer to commercial availability. The first detailed review of FT-VCD methodology in the mid-IR region was published in 1988 and continues to be a good fundamental source of knowledge about theory and practice of VCD measurement [21].

The next major development of FT-VCD instrumentation was the exploration by two research groups of the polarization division interferometer. The group at Syracuse University used a modification of a Bomem FT-IR spectrometer equipped with plane mirrors [22], while the group at Vanderbilt University used the original Martin–Pupplet design with rooftop mirrors [23]. Both groups reported circular dichroism results at around the same time: The Syracuse group reported VCD measurement in the mid-IR region [24], while the Vanderbilt group achieved CD measurements in the far-IR region [23, 25]. The motivation for the development of the polarization division approach to VCD is to bypass the need for a PEM that has optical limitation to lower vibrational frequencies. The basic idea with polarization division FT-VCD measurement is to replace the usual FT-IR beamsplitter with a wire grid polarizer at 45° to the incident linear polarization state. The two arms of the interferometer carry IR beams with orthogonal linear polarization. When the beams combine, they do not interfere in intensity but they do recombine coherently to produce Fourier modulation cycles in relative polarization phase starting from vertical polarization at 0 degrees, RCP at 90 degrees, horizontal at 180 degrees, and LCP at 270 (or equivalently −90) degrees. The modulation cycle with reference points at 0 and 180 degrees probes linear dichroism in the sample with dichroic axes oriented vertical and horizontal as a cosine transform, whereas the cycle with reference points at 90 and 270 degrees probes the circular dichroism of the sample. After performing a phase correction on the measured interferogram, the real part of the interferogram yields the linear dichroism spectrum and the imaginary part yields the circular dichroism spectrum. The ordinary FT-IR interferogram can be measured by inserting a vertical or horizontal polarizer into the polarization modulated beam, thereby converting polarization modulation to the usual intensity modulation at the usual Fourier frequencies of the instrument. Polarization division interferometry continued to be explored by the Vanderbilt group [26–30], including a report of VCD observed below 600 cm^{-1} [30], but the technique has yet to be adopted for widespread use which would require a commercially available instrument.

In the past decade, several reports of advances in FT-VCD instrumentation have been reported aimed at increasing the signal-to-noise ratio and reducing spectral artifacts that interfere with the measurement of the true VCD spectrum and reduce the stability and reproducibility of VCD measurements. The first of these is the dual polarization modulation (dual-PEM) methodology [31]. Here, a second PEM is placed after the sample in an FT-VCD spectrometer, and by dynamically subtracting the output signal of the second PEM, properly adjusted, from that of the first PEM, the bulk of the artifact signal is eliminated, thus greatly enhancing the stability and reproducibility of VCD measurements. A second improvement is the simultaneous use of two sources for VCD measurements [32]. The two source beams enter the interferometer from orthogonal directions, and the resulting IR beam is partially canceled by their opposite Fourier phases. If in addition the two sources are equipped with linear polarizers of orthogonal orientation, the two beams generate VCD intensities of opposite sign. But instead of canceling the VCD intensities of the two beams, add because they also have opposite Fourier phases. This lead to a near doubling of the signal-to-noise ratio for each scan of

the interferometer, equivalent to several VCD spectrometers operating in parallel with combined detector signals.

Parallel to these advances, the potential advantage of using digital signal processing for interferogram digitization and demodulation were explored [33]. Also explored have been a variety of methods for reducing artifacts including a rotating quarter-wave plate [34], a rotating half-wave plate [35], and more recently a rotating sample cell [36]. The potential benefits of the use of step-scan FT-IR instrumentation for VCD measurements have been explored [37–40], but no significant benefits relative the more recent rapid-scan instrumentation and detection were found, and hence the use of step-scan methods for VCD measurement have not been pursued further. Another advance of FT-VCD instrumentation in recent years has been extension of the spectral region into the near-IR as far as $10,000\ \mathrm{cm}^{-1}$ through the second overtone region [41]. More recently, Keiderling and co-workers have described in detail and compared dispersive and Fourier transform VCD as background for a review of applications of VCD to biological molecules [42]. Finally we note that the newest commercial VCD instrumentation from BioTools, Inc. uses a new high-speed digital processing software that permits three interferograms to be simultaneously measured, digitized, and processed without the use of any external lock-in amplifiers or filters, thereby significantly reducing digitization noise associated the many analog-to-digital and digital-to-analog steps that are required when using external digital lock-in amplifiers and filters.

In this review, we will focus on the principles of VCD instrumentation and measurement that lead directly instrumentation that is available today from commercial sources. Dispersive instrumentation, although not widely used, will be covered for its pedagogical value in seeing the process of VCD measurement in its simplest and purest form. The review will be structured around the optical analysis tools of Stokes vectors and Mueller matrices. Once familiar with these methods, the reader can easily check the various intensity expressions presented in this chapter and, if desired, extend these optical analyses to explore new approaches to VCD instrumentation and measurement.

5.2. STOKES–MUELLER REPRESENTATIONS OF INTENSITIES

5.2.1. Stokes Vectors and Mueller Matrices

A Stokes vector, $\boldsymbol{S}$, is four-element column vector that empirically describes the polarization state of any beam of electromagnetic radiation as follows:

$$\boldsymbol{S} = \begin{pmatrix} S_0 \\ S_1 \\ S_2 \\ S_3 \end{pmatrix} = \begin{pmatrix} I_{Total} \\ I_0 - I_{90} \\ I_{45} - I_{135} \\ I_R - I_L \end{pmatrix}. \tag{5.21}$$

The uppermost element of the Stokes vector, S_0, represents the total intensity of the radiation beam. This intensity is the combination of both the polarized and unpolarized intensities. The next three elements describe the intensity balance of the beam between two independent pairs of orthogonal linear polarization states, vertical (0°) minus horizontal (90°) intensities and ($+45^\circ$) and (-45°), and one pair of circular polarization intensties, right and left. These three Stokes elements represent pure polarization states. The following relation holds for the values of first element versus the other three elements.

$$S_0^2 \geq S_1^2 + S_2^2 + S_3^2. \tag{5.22}$$

The equality holds if there is no unpolarized intensity present in the beam, and the inequality holds if some or all of the light is unpolarized. We assume here that no unpolarized radiation is present, a condition that is easily met by initiating the optical path with a linear polarizer. A few simple examples of Stokes vectors are

$$\boldsymbol{S}_0 = \begin{pmatrix} 1 \\ 1 \\ 0 \\ 0 \end{pmatrix}, \quad \boldsymbol{S}_{90} = \begin{pmatrix} 1 \\ -1 \\ 0 \\ 0 \end{pmatrix}, \quad \boldsymbol{S}_{45} = \begin{pmatrix} 1 \\ 0 \\ 1 \\ 0 \end{pmatrix},$$

$$\boldsymbol{S}_{135} = \begin{pmatrix} 1 \\ 0 \\ -1 \\ 0 \end{pmatrix}, \quad \boldsymbol{S}_R = \begin{pmatrix} 1 \\ 0 \\ 0 \\ 1 \end{pmatrix}, \quad \boldsymbol{S}_L = \begin{pmatrix} 1 \\ 0 \\ 0 \\ -1 \end{pmatrix}. \tag{5.23}$$

A Mueller matrix, $\boldsymbol{M}$, is a 4×4 matrix that operates on a the ith Stokes vector, $\boldsymbol{S}_i$, to transform it to the jth Stokes vector, $\boldsymbol{S}_j$. The action of $\boldsymbol{M}$ operating on $\boldsymbol{S}_i$ represents the effect of an optical element on the beam which changes the Stokes vector before entering the optical element to the Stokes vector after passing through the optical element. This optical process is represented by $\boldsymbol{S}_j = \boldsymbol{M} \cdot \boldsymbol{S}_i$ and is given in explicit expanded form by

$$\begin{pmatrix} S_{j,0} \\ S_{j,1} \\ S_{j,2} \\ S_{j,3} \end{pmatrix} = \begin{pmatrix} M_{00} & M_{10} & M_{20} & M_{30} \\ M_{01} & M_{11} & M_{21} & M_{31} \\ M_{02} & M_{12} & M_{22} & M_{32} \\ M_{03} & M_{13} & M_{23} & M_{33} \end{pmatrix} \begin{pmatrix} S_{i,0} \\ S_{i,1} \\ S_{i,2} \\ S_{i,3} \end{pmatrix} \tag{5.24}$$

Four basic Mueller matrices are needed for the optical analyses to be presented in this chapter. The first is the Mueller matrix of a linear polarizer $\boldsymbol{M}_P(\theta)$ orientated at an angle of θ relative to the vertical direction.

$$\boldsymbol{M}_P(\theta) = \frac{1}{2} \begin{pmatrix} 1 & \cos 2\theta & \sin 2\theta & 0 \\ \cos 2\theta & \cos^2 2\theta & \sin 2\theta \cos 2\theta & 0 \\ \sin 2\theta & \sin 2\theta \cos 2\theta & \sin^2 2\theta & 0 \\ 0 & 0 & 0 & 0 \end{pmatrix} \tag{5.25}$$

Here it is clear that all entries along the bottom row and fourth column, the ones involved with states of circular polarization, are zero as is expected of a device that produces only linearly polarized light. The second fundamental Mueller matrix that we need is the linear birefringence (LB) retardation plate, $\boldsymbol{M}_{LB}(\theta, \delta)$, such as a quarter-waveplate, a half-waveplate, or even a PEM.

$$\boldsymbol{M}_{LB}(\theta, \delta) = \begin{pmatrix} 1 & 0 & 0 & 0 \\ 0 & \cos^2(\delta/2) + \cos 4\theta \sin^2(\delta/2) & \sin 4\theta \sin^2(\delta/2) & -\sin 2\theta \sin \delta \\ 0 & \sin 4\theta \sin^2(\delta/2) & \cos^2(\delta/2) - \cos 4\theta \sin^2(\delta/2) & \cos 2\theta \sin \delta \\ 0 & \sin 2\theta \sin \delta & -\cos 2\theta \sin \delta & \cos \delta \end{pmatrix}. \tag{5.26}$$

Here the angle δ represents the retardation angle of the plate—for example, $\delta = \pi$ for a half-wave plate—and θ represents the angle of the slow axis of the plate from vertical. We assume a right-handed coordinate system in which the beam propagates along the Z direction, vertical is the Y direction, and a positive angle of rotation of an optical element is from the positive Y direction to the positive X direction. A simple but important example of an LB plate is a retardation plate with a slow axis at $+45^\circ$ from the vertical direction:

$$\boldsymbol{M}_{LB}(45^\circ, \delta) = \begin{pmatrix} 1 & 0 & 0 & 0 \\ 0 & \cos\delta & 0 & -\sin\delta \\ 0 & 0 & 1 & 0 \\ 0 & \sin\delta & 0 & \cos\delta \end{pmatrix}. \tag{5.27}$$

Another important limiting case of Eq. (5.26) is a quarter-wave plate (QWP) obtained by setting $\delta = \pi/2$ and applying the half-angle trigonometric identities $(1 + \cos 4\theta)/2 = \cos^2 2\theta$, $(1 - \cos 4\theta)/2 = \sin^2 2\theta$, and $\sin 4\theta = 2 \sin 2\theta \cos 2\theta$, which yields

$$\boldsymbol{M}_{LB}(\theta, \pi/2) = \begin{pmatrix} 1 & 0 & 0 & 0 \\ 0 & \cos^2 2\theta & \sin 2\theta \cos 2\theta & -\sin 2\theta \\ 0 & \sin 2\theta \cos 2\theta & \sin^2 2\theta & \cos 2\theta \\ 0 & \sin 2\theta & -\cos 2\theta & 0 \end{pmatrix}. \tag{5.28}$$

This matrix would be useful for describing the effects of a rotating QWP in an optical train. It can be seen from the nonzero elements that such a QWP interconverts linear and circular polarization states. A similar result is obtained for a half-waveplate (HWP) oriented at an arbitrary angle about the beam propagation direction, obtained by setting $\delta = \pi$:

$$\boldsymbol{M}_{LB}(\theta, \pi) = \begin{pmatrix} 1 & 0 & 0 & 0 \\ 0 & \cos 4\theta & \sin 4\theta & 0 \\ 0 & \sin 4\theta & -\cos 4\theta & 0 \\ 0 & 0 & 0 & -1 \end{pmatrix}. \tag{5.29}$$

Here, no interconversion between linear and circular polarization states takes place. Linear polarization states are interconverted between the two orthogonal linear polarization reference frames, $\pm 45^\circ$ and VH, and all circular polarization components are reversed from RCP to LCP and vice versa as designated by the lower right element, -1.

Yet another important limit of the general linear birefringence plate in Eq. (5.26) can be obtained by assuming small values of linear birefringence. For small values of δ we can expand the trigonometric functions of δ as $\sin\delta = \delta - \delta^3/3! \ldots$ and $\cos\delta = 1 - \delta^2/2 + \ldots$. We need only keep terms through first order in δ since higher-order terms would be negligibly small. This yields the matrix

$$\boldsymbol{M}_{LB}(\theta, \delta) = \begin{pmatrix} 1 & 0 & 0 & 0 \\ 0 & 1 & 0 & -\delta \sin 2\theta \\ 0 & 0 & 1 & \delta \cos 2\theta \\ 0 & \delta \sin 2\theta & -\delta \cos 2\theta & 1 \end{pmatrix}. \tag{5.30}$$

The $\delta \sin 2\theta$ terms correspond to birefringence with slow and fast axes at $+45^\circ$ and -45°, respectively, while the $\delta \cos 2\theta$ terms correspond to LB with slow and fast axes at 0° and $+90^\circ$, respectively. This matrix can be further simplified by writing $\delta = \delta \sin 2\theta$

and $\delta' = \delta \cos 2\theta$ where δ and δ' that correspond to the two kinds of LB ($\pm 45^\circ$ and VH) that might occur at different locations with different intensities and orientations across an optical element. This simple but important Mueller matrix is given by

$$\boldsymbol{M}_{LB}(\delta, \delta') = \begin{pmatrix} 1 & 0 & 0 & 0 \\ 0 & 1 & 0 & -\delta \\ 0 & 0 & 1 & \delta' \\ 0 & \delta & -\delta' & 1 \end{pmatrix}. \tag{5.31}$$

The third general Mueller matrix needed is that for an arbitrary sample that can possess, including the sample-cell windows, linear and circular dichroism (LD and CD) and linear and circular birefringence (LB and CB). Through first order this matrix can be represented by

$$\boldsymbol{M}_S = 10^{-A} \begin{pmatrix} 1 & -\mathrm{LD} & -\mathrm{LD}' & \mathrm{CD} \\ -\mathrm{LD} & 1 & \mathrm{CB} & -\mathrm{LB} \\ -\mathrm{LD}' & -\mathrm{CB} & 1 & \mathrm{LB}' \\ \mathrm{CD} & \mathrm{LB} & -\mathrm{LB}' & 1 \end{pmatrix}. \tag{5.32}$$

The LB and LD entries have unprimed and primed forms corresponding to the two orthogonal reference frames described above. Here A is the decadic absorbance of the sample, LD is the vertical–horizontal linear dichroism, $(\ln 10/2)(A_0 - A_{90})$, LD′ is linear dichroism at 45° from vertical–horizontal, $(\ln 10/2)(A_{45} - A_{135})$, CD is the circular dichroism, $(\ln 10/2)(A_L - A_R)$, and $(\ln 10/2) = 1.1513$. The linear birefringence entries, LB and LB′, and the circular birefringence, CB, are the corresponding birefringence differences, $n_0 - n_{90}$, $n_{45} - n_{135}$, and $n_L - n_R$, respectively, where n in the real part of the complex index of refraction of the sample.

Finally, we present the Mueller matrix of a detector that has a different response, p_X and p_Y, to radiation polarized along its X and Y axes, respectively, and where the optical axis of this response is at an angle of α with respect to the laboratory X axis. We also assume that the detector is not chiral and cannot respond differently to RCP and LCP radiation.

$$\boldsymbol{D}(\alpha) = [1 \quad (p_X^2 - p_Y^2)\cos 2\alpha \quad (p_X^2 - p_Y^2)\sin 2\alpha \quad 0]. \tag{5.33}$$

In general, the Mueller matrix is a 4×4 matrix; but in the case of the detector, only the total intensity of the final Stokes vector is measured, and thus only the top row of the detector Mueller matrix is needed or is nonzero. Another way to think about this is that there is no longer any polarization information associated with the beam of radiation once photons strike the detector. The first entry is 1, but equally it could be represented by $(p_X^2 + p_Y^2)$ if one prefers not to assume a detector response normalized to unity. Typically the quantity $(p_X^2 - p_Y^2)$ is approximately two orders of magnitude smaller than unity, indicating that the linear polarization sensitivity of the detector is relatively small compared to its overall response. In the case of the detector, the result of the detector Mueller matrix operating on the Stokes vector of the incoming beam is simply a scalar quantity representing the total intensity of the beam at the detector. In particular, we

can write

$$I_D = \boldsymbol{D}(\alpha)\cdot\boldsymbol{S}_f = \begin{pmatrix}1 & (p_X^2 - p_Y^2)\cos 2\alpha & (p_X^2 - p_Y^2)\sin 2\alpha & 0\end{pmatrix}\begin{pmatrix}S_{f0}\\ S_{f1}\\ S_{f2}\\ S_{f3}\end{pmatrix}$$

$$= S_{f0} + S_{f1}(p_X^2 - p_Y^2)\cos 2\alpha + S_{f2}(p_X^2 - p_Y^2)\sin 2\alpha. \qquad (5.34)$$

The Stokes vectors and Mueller matrices presented in this section provide the means to describe quantitatively the polarization states along a complete optical pathway between a source and a detector. We now use this methodology to describe VCD and VCB instrumental intensities for any such instrumentation using a PEM to effect the required polarization modulation of the beam.

5.2.2. Measurement of Circular Dichroism

In this section, we provide a step-by-step application of the Stokes–Mueller formalism to illustrate in detail how it is used to obtain the detector signal for a CD spectrometer. As mentioned above, we will assume a dispersive spectrograph to avoid the unnecessary complications at this stage due to Fourier transformation instrumentation. The optical path needed to describe the measurement of either ECD or VCD can be represented by the following expression:

$$\text{Source} \rightarrow \text{Polarizer}(0^\circ) \rightarrow \text{PEM}(45^\circ) \rightarrow \text{Sample} \rightarrow \text{Detector}$$

The intensity at the detector for this optical path using the Stokes–Mueller formalism is given by

$$I_D(\overline{\nu}) = \boldsymbol{D}(\alpha)\cdot\boldsymbol{M}_S(\overline{\nu})\cdot\boldsymbol{M}_{PEM}(\overline{\nu})\cdot\boldsymbol{M}_P(0^\circ\cdot\boldsymbol{S}_0(\overline{\nu}). \qquad (5.35)$$

Notice that the optical train is described right to left, opposite that of the diagram above, since by convention Mueller matrices operate to the right on Stokes vectors. The IR beam from the source is assumed to be unpolarized with a spectral distribution $I_0(\overline{\nu})$ which then passes through a polarizer at an angle of 0°. This results in vertically polarized light with half the original unpolarized intensity.

$$\boldsymbol{S}_1(\overline{\nu}) = \boldsymbol{M}_P(0^\circ)\cdot\boldsymbol{S}_0(\overline{\nu}) = \frac{1}{2}\begin{pmatrix}1 & 1 & 0 & 0\\ 1 & 1 & 0 & 0\\ 0 & 0 & 0 & 0\\ 0 & 0 & 0 & 0\end{pmatrix} I_0(\overline{\nu})\begin{pmatrix}1\\0\\0\\0\end{pmatrix} = \frac{I_0(\overline{\nu})}{2}\begin{pmatrix}1\\1\\0\\0\end{pmatrix}. \qquad (5.36)$$

This beam then passes through the PEM with retardation angle $\alpha_M(\overline{\nu})$ and stress axes at 45°. Using the Mueller matrix in Eq. (5.27) gives rise to the Stokes vector, $\boldsymbol{S}_2(\overline{\nu})$, after the PEM:

$$\boldsymbol{S}_2(\overline{\nu}) = \boldsymbol{M}_{PEM}[45^\circ, \alpha_M(\overline{\nu})]\cdot\boldsymbol{S}_1(\overline{\nu})$$

$$= \begin{pmatrix}1 & 0 & 0 & 0\\ 0 & \cos\alpha_M(\overline{\nu}) & 0 & -\sin\alpha_M(\overline{\nu})\\ 0 & 0 & 1 & 0\\ 0 & \sin\alpha_M(\overline{\nu}) & 0 & \cos\alpha_M(\overline{\nu})\end{pmatrix}\frac{I_0(\overline{\nu})}{2}\begin{pmatrix}1\\1\\0\\0\end{pmatrix} = \frac{I_0(\overline{\nu})}{2}\begin{pmatrix}1\\ \cos\alpha_M(\overline{\nu})\\ 0\\ \sin\alpha_M(\overline{\nu})\end{pmatrix}. \qquad (5.37)$$

The beam next passes through the sample with reference to Eq. (5.32). This gives rise to the last Stoke vector before the detector

$$\begin{aligned}\boldsymbol{S}_3(\overline{\nu}) &= \boldsymbol{M}_S(\overline{\nu}) \cdot \boldsymbol{S}_2(\overline{\nu}) \\ &= \frac{I_0(\overline{\nu})}{2} 10^{-A(\overline{\nu})} \begin{pmatrix} 1 & 0 & 0 & \mathrm{CD}(\overline{\nu}) \\ 0 & 1 & \mathrm{CB}(\overline{\nu}) & -\mathrm{LB}(\overline{\nu}) \\ 0 & -\mathrm{CB}(\overline{\nu}) & 1 & \mathrm{LB}'(\overline{\nu}) \\ \mathrm{CD}(\overline{\nu}) & \mathrm{LB}(\overline{\nu}) & -\mathrm{LB}'(\overline{\nu}) & 1 \end{pmatrix} \begin{pmatrix} 1 \\ \cos\alpha_M(\overline{\nu}) \\ 0 \\ \sin\alpha_M(\overline{\nu}) \end{pmatrix} \\ &= \frac{I_{DC}(\overline{\nu})}{2} \begin{pmatrix} 1 + \mathrm{CD}(\overline{\nu}) \sin\alpha_M(\overline{\nu}) \\ \cos\alpha_M(\overline{\nu}) - \mathrm{LB}(\overline{\nu}) \sin\alpha_M(\overline{\nu}) \\ -\mathrm{CB}(\overline{\nu}) \cos\alpha_M(\overline{\nu}) + \mathrm{LB}'(\overline{\nu}) \sin\alpha_M(\overline{\nu}) \\ \mathrm{CD}(\overline{\nu}) + \mathrm{LB}(\overline{\nu}) \cos\alpha_M(\overline{\nu}) + \sin\alpha_M(\overline{\nu}) \end{pmatrix}. \end{aligned} \tag{5.38}$$

Here we have assumed a nonoriented sample, such as a solution or disordered solid, so that all four linear dichroism (LD) elements from Eq. (5.32) are set equal to zero. The LB terms have been retained to represent linear birefringence due to optical imperfections or strain in the transparent sample-cell windows. This last Stokes vector is converted to a scalar intensity by the detector Mueller matrix as discussed above.

$$\begin{aligned} I_D(\overline{\nu}) = \boldsymbol{D}(\alpha) \cdot \boldsymbol{S}_3(\overline{\nu}) = \frac{I_{DC}(\overline{\nu})}{2} \{ &[1 + \mathrm{CD}(\overline{\nu}) \sin\alpha_M(\overline{\nu})] \\ &+ (p_X^2 - p_Y^2) \cos 2\alpha [\cos\alpha_M(\overline{\nu}) - \mathrm{LB}(\overline{\nu}) \sin\alpha_M(\overline{\nu})] \\ &+ (p_X^2 - p_Y^2) \sin 2\alpha [-\mathrm{CB}(\overline{\nu}) \cos\alpha_M(\overline{\nu}) + \mathrm{LB}'(\overline{\nu}) \sin\alpha_M(\overline{\nu})] \}. \end{aligned} \tag{5.39}$$

If for simplicity we assume that the detector has no polarization sensitivity, only the first of the three detector terms is nonzero, and we can write

$$I_D(\overline{\nu}) + I_{DC}(\overline{\nu}) + I_{AC}(\overline{\nu}) = \frac{I_{DC}(\overline{\nu})}{2} [1 + \mathrm{CD}(\overline{\nu}) \sin\alpha_M(\overline{\nu})]. \tag{5.40}$$

The angle of retardation of the PEM, $\alpha_M(\overline{\nu})$, oscillates in a sine wave pattern that can be expressed to lowest order in the PEM frequency as

$$\sin[\alpha_M(\overline{\nu}, t)] = 2J_1[\alpha_M^{\circ}(\overline{\nu})] \sin\omega_M t, \tag{5.41}$$

where $\alpha_M^{\circ}(\overline{\nu})$ is the maximum retardation value in the PEM oscillation cycle and $J_1[\alpha_M^{\circ}(\overline{\nu})]$ is the first-order Bessel function. Using the definition of the CD given above equal to $(1/2)\ln 10[A_L(\overline{\nu}) - A_R(\overline{\nu})] = 1.1513\Delta A(\overline{\nu})$, the expressions for $I_{AC}(\overline{\nu})$ and $I_{DC}(\overline{\nu})$ are given by

$$I_D(\overline{\nu}) = I_{DC}(\overline{\nu}) + I_{AC}(\overline{\nu}) = \frac{I_{DC}(\overline{\nu})}{2} [1 + 2J_1[\alpha_M^{\circ}(\overline{\nu})][1.1513\Delta A(\overline{\nu})]]. \tag{5.42}$$

The intensities $I_{AC}(\overline{\nu})$ and $I_{DC}(\overline{\nu})$ can be measured separately by virtue of their different time modulation frequencies, distinguished for the measurement of $I_{AC}(\overline{\nu})$ by a lock-in amplifier synchronized to the PEM reference signal. Once separated and measured, the

ratio of $I_{AC}(\overline{\nu})$ by $I_{DC}(\overline{\nu})$ removes characteristic features of the VCD instrument and yields an expression proportional the CD spectrum $\Delta A(\overline{\nu})$ as

$$\frac{I_{AC}(\overline{\nu})}{I_{DC}(\overline{\nu})} = 2J_1[\alpha_M^{\circ}(\overline{\nu})][1.1513\Delta A(\overline{\nu})]. \tag{5.43}$$

As described previously [13], it is possible to calibrate this ratio using a multiple-waveplate and a polarizer in place of the sample. The calibration spectrum is essentially a measure of CD intensity equal to unity. The result of the VCD calibration measurement is

$$\left[\frac{I_{AC}(\overline{\nu})}{I_{DC}(\overline{\nu})}\right]_{cal,\omega_M} = 2J_1[\alpha_M^{\circ}(\overline{\nu})]. \tag{5.44}$$

Calibrated VCD spectra can then be obtained from the expression

$$\Delta A(\overline{\nu}) = \frac{1}{1,1513}\left[\frac{I_{AC}(\overline{\nu})}{I_{DC}(\overline{\nu})}\right] \Big/ \left[\frac{I_{AC}(\overline{\nu})}{I_{DC}(\overline{\nu})}\right]_{cal,\omega_M}. \tag{5.45}$$

The corresponding VA spectrum can be obtained from the ratio of $I_{DC}(\overline{\nu})$ with the sample in place to $I_{DC}^0(\overline{\nu})$ without the sample or with some suitable reference in place of the sample as

$$A(\overline{\nu}) = -\log_{10}\frac{I_{DC}(\overline{\nu})}{I_{DC}^0(\overline{\nu})}. \tag{5.46}$$

These instrumental expressions for the measurement of VCD and VA spectra can be connected to the general and theoretical definitions of these same quantities given in Section 5.1.

5.2.3. Measurement of Vibrational Circular Birefringence

A VCD spectrometer can be converted to a VCB spectrometer by two simple changes, one optical and other electronic. A detailed description of this change including comparison of the measured VCB spectra to quantum chemistry density function theory calculations has recently been published [9]. The optical change involves placing a linear polarizer at 45° from vertical after the sample in the VCD optical train. The electronic change to be explained below is referencing the PEM lock-in amplifier to twice the PEM frequency rather than the fundamental of the PEM frequency as in VCD measurement. The Stokes–Mueller intensity expression is given by

$$\begin{aligned} I_D(\overline{\nu}) &= \boldsymbol{D}(\alpha)\cdot\boldsymbol{M}_A(45^{\circ})\boldsymbol{M}_S(\overline{\nu})\cdot\boldsymbol{M}_{PEM}(\overline{\nu})\cdot\boldsymbol{M}_P(0^{\circ})\cdot\boldsymbol{S}_0(\overline{\nu}) = \boldsymbol{D}(\alpha)\cdot\boldsymbol{M}_A(45^{\circ})\boldsymbol{S}_3(\overline{\nu}) \\ &= \boldsymbol{D}(\alpha)\cdot\frac{1}{2}\begin{pmatrix}1&0&1&0\\0&0&0&0\\1&0&1&0\\0&0&0&0\end{pmatrix}\frac{I_{DC}(\overline{\nu})}{2}\begin{pmatrix}1+\mathrm{CD}(\overline{\nu})\sin\alpha_M(\overline{\nu})\\ \cos\alpha_M(\overline{\nu})-\mathrm{LB}(\overline{\nu})\sin\alpha_M(\overline{\nu})\\ -\mathrm{CB}(\overline{\nu})\cos\alpha_M(\overline{\nu})+\mathrm{LB}'(\overline{\nu})\sin\alpha_M(\overline{\nu})\\ \mathrm{CD}(\overline{\nu})+\mathrm{LB}(\overline{\nu})\cos\alpha_M(\overline{\nu})+\sin\alpha_M(\overline{\nu})\end{pmatrix}. \end{aligned} \tag{5.47}$$

Here we have taken advantage of the fact the VCD and VCB optical paths are identical through the position of the sample and hence we can start the analysis with the Stokes vector $\boldsymbol{S}_3(\overline{\nu})$ from the VCD set up in Eq. (5.38). Evaluating this expressions yields

$$I_D(\overline{\nu}) = \frac{I_{\mathrm{DC}}(\overline{\nu})}{4}[1 + CD(\overline{\nu})\sin\alpha_M(\overline{\nu}) - CB(\overline{\nu})\cos\alpha_M(\overline{\nu}) + LB'(\overline{\nu})\sin\alpha_M(\overline{\nu})]. \quad (5.48)$$

The term $\cos\alpha_M(\overline{\nu}, t)$ including its time dependence as in Eq. (5.41) can be expressed as

$$\cos\alpha_M(\overline{\nu}, t) = J_0[\alpha_M^{\mathrm{o}}(\overline{\nu})] + 2J_2[\alpha_M^{\mathrm{o}}(\overline{\nu})]\sin 2\omega_M t. \quad (5.49)$$

If the AC part of this signal is detected with a lock-in amplifier synchronized at the twice the PEM frequency, $2\omega_M$, the AC and DC detector intensities are

$$\mathrm{I}_D(\overline{\nu}) = I_{DC}(\overline{\nu}) + I_{AC}(\overline{\nu}) = \frac{I_{DC}(\overline{\nu})}{4}[1 - CB(\overline{\nu})2J_2[\alpha_M^{\mathrm{o}}(\overline{\nu})]\cos 2\omega_M t]. \quad (5.50)$$

The CB spectrum, $\Delta n_{LR}(\overline{\nu})$, can be obtained from the ratio

$$\frac{I_{AC}(\overline{\nu})}{I_{DC}(\overline{\nu})} = -2J_2[\alpha_M^{\mathrm{o}}(\overline{\nu})][\Delta n_{\mathrm{LR}}(\overline{\nu})]. \quad (5.51)$$

The VCB intensity expression can be calibrated by using a vertical or horizontal polarizer in the place of the sample which, with an appropriate average of $I_{DC}(\overline{\nu})$ for the two orientations of the polarizer gives the calibrated intensity

$$\left[\frac{I_{AC}(\overline{\nu})}{I_{DC}(\overline{\nu})}\right]_{cal,2\omega_M} = 2J_2[\alpha_M^{\mathrm{o}}(\overline{\nu})]. \quad (5.52)$$

This is precisely the intensity need to calibrate the measurement of CB given in Eq. (5.51). As a result, we can write the following expression for the calibration CB spectrum:

$$\Delta n_{LR}(\overline{\nu}) = -\left[\frac{I_{AC}(\overline{\nu})}{I_{DC}(\overline{\nu})}\right] / \left[\frac{I_{AC}(\overline{\nu})}{I_{DC}(\overline{\nu})}\right]_{cal,2\omega_M}. \quad (5.53)$$

5.3. FOURIER TRANSFORM INSTRUMENTATION

5.3.1. General Principles

The expressions for VA, VCD, and VCB measurement developed in the previous section are quite general and can applied to measurements in any spectral region where the circular polarization modulation was generated using a PEM. In this section we turn to the combination of CD measurement with Fourier transform (FT) spectroscopy. Virtually all infrared (IR) or near-IR (NIR) measurements are carried out using FT spectroscopy. As mentioned above, there are several ways in which one can consider combining CD measurements with FT-IR (or FT-NIR) spectroscopy. By far the most successful of these is the one in which a PEM is placed before the sample in the FT instrument that generates two interferograms at the same time at the detector. One interferogram is the normal transmission IR interferogram, and the other is the transmission VCD interferogram that is also modulated at the PEM frequency, ω_M.

There is a convenient analogy between the measurement of VCD spectra using dispersive versus FT instrumentation. For dispersive instrumentation, a light chopper is needed for the measurement of the ordinary transmission spectrum because the detector has a nonzero signal if the IR source is blocked. The IR detector sees the constant IR background from its room temperature environment, and this background is the overwhelming source of noise for IR measurements. In addition, for the measurement of dispersive VCD spectra a lock-in amplifier (LIA) tuned to the chopper frequency is placed after the PEM LIA to discriminate the background radio-frequency radiation generated by the PEM. The chopper frequency is the same for all wavelengths that are selected one resolution element at a time by a grating monochromator. In FT-VCD measurements the chopper is replaced by the FT interferometer that "chops" each wavelength at its own Fourier frequency. The wavelengths can be measured at the same time, each with its own chopper (Fourier) frequency, by taking the Fourier transform of the interferogram signal that emerges from the PEM LIA.

5.3.2. Measurement of FT-VCD and FT-VCB

As a point of reference for considering not only the optical path but also the electronic pathway in a CD measurement we can consider Figure 5.3. This simplified figure applies equally well to dispersive and FT CD measurements. When applied to FT-VCD measurements, the signals coming from the LIA for $I_{AC}(\delta)$ and directly from the detector D for $I_{DC}(\delta)$ are given by

$$I_{DC}(\delta) = \int_0^\infty I_{DC}(\overline{\nu}) \cos[2\pi\delta\overline{\nu} + \theta_{DC}(\overline{\nu})]\, d\overline{\nu}, \tag{5.54}$$

$$I_{AC}(\delta) = \int_0^\infty I_{AC}(\overline{\nu}) \cos[2\pi\delta\overline{\nu} + \theta_{AC}(\overline{\nu})]\, d\overline{\nu}. \tag{5.55}$$

These electronic signals $I_{DC}(\delta)$ and $I_{AC}(\delta)$ are interferograms expressed as integral superpositions of the transmission intensities of all the spectral frequencies in the spectrum multiplied by a cosine function that depends on the wavenumber frequency, $\overline{\nu}$, and the retardation, δ, the path difference of the interferometer from the central equal-mirror position. The units of length of the retardation parameter δ are usually centimeters.

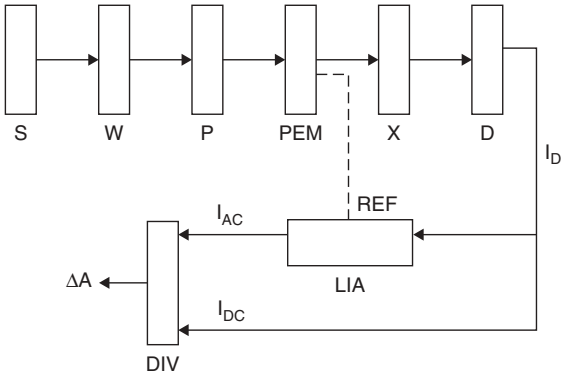

Figure 5.3. Optical electronic diagram illustrating the measurement of CD, where S is the source, W the wavelength selection device (a monochromator or Fourier transform interferometer), P a linear polarizer, PEM a photoelastic modulator, X the sample, D the detector, I_D the detector signal, LIA the lock-in amplifier referenced to the PEM, and DIV a software division step to divide I_{DC} into I_{AC} to produce the VCD spectrum ΔA. (From reference 31, reproduced with permission.)

A rapid-scan interferometer operating with constant mirror velocity V_m in centimeters/second has a retardation length that is related to the time-base Fourier frequency $f_{F,\overline{\nu}} = \omega_F/2\pi$ in cycles per second, or hertz (Hz), for each wavenumber, $\overline{\nu}$, by the relations

$$2\pi\delta\overline{\nu} = 2\pi(2V_M t)\overline{\nu} = 2\pi(2V_M\overline{\nu})t = 2\pi f_{F,\overline{\nu}}t = \omega_F t. \tag{5.56}$$

A common time-based Fourier frequency is 16 kHz (16,000 Hz) for the HeNe reference laser frequency. From Eq. (5.56) this Fourier frequency corresponds to a retardation velocity $2V_M$ of approximately 1 cm/s since the wavenumber frequency $\overline{\nu}$ of an HeNe laser at 623.8 nm is nearly 16,000 cm^{-1}. This is a convenient mirror velocity since the Fourier frequency corresponding to any wavenumber frequency is just the numerical value of that frequency. Thus the Fourier frequencies associated with the mid-IR region from 1000 to 2000 cm^{-1} have values between 1 and 2 kHz.

In order to obtain the transmission spectra, $I_{DC}(\overline{\nu})$ and $I_{AC}(\overline{\nu})$, in the integrals of Eqs. (5.54) and (5.55), the interferogram must be Fourier transformed. This is represented by the following expressions:

$$I_{DC}(\overline{\nu}) = \text{FT}[I_{DC}(\delta)] = \frac{1}{2\pi}\int_0^\infty I_{DC}(\delta)\cos(2\pi\delta\overline{\nu})\ d\delta, \tag{5.57}$$

$$I_{AC}(\overline{\nu}) = \text{FT}[I_{AC}(\delta)] = \frac{1}{2\pi}\int_0^\infty I_{AC}(\delta)\cos(2\pi\delta\overline{\nu})\ d\delta. \tag{5.58}$$

Before the Fourier transform can be performed mathematically, the phase correction spectra, $\theta_{DC}(\overline{\nu})$ and $\theta_{AC}(\overline{\nu})$, must be determined and removed from the expression for $I_{DC}(\delta)$ and $I_{AC}(\delta)$ in Eqs. (5.54) and (5.55). This is an operation that is automatically performed for $\theta_{DC}(\overline{\nu})$ by software that controls the operation of the FT-IR spectrometer, and several kinds of phase-correction algorithms are available for this purpose. The phase function $\theta_{AC}(\overline{\nu})$ is not the same as the phase function $\theta_{DC}(\overline{\nu})$. The reason is that these two interferograms pass through different electronic pathways with different phase shifts for the same Fourier frequencies. The algorithm that determines this phase correction function automatically assumes that all detector intensities are positive. This is true for $I_{DC}(\overline{\nu})$, but the intensities $I_{AC}(\overline{\nu})$ can be either positive or negative across the spectrum depending on whether the VCD intensity is negative or positive. As a result, a method for measuring $I_{AC}(\overline{\nu})$ when only positive CD intensities are present is needed, after which that phase correction function can be transferred to the measurement of $I_{AC}(\overline{\nu})$ when both positive and negative intensities are present. Such a single-signed CD spectrum can be obtained from stressed optical plate, usually made of ZeSe, followed by a polarizer located at the sample position.

Once the interferograms $I_{AC}(\delta)$ and $I_{DC}(\delta)$ are Fourier transformed to the transmission spectra $I_{AC}(\overline{\nu})$ and $I_{DC}(\overline{\nu})$, the determination of the VCD and VA spectra, $\Delta A(\overline{\nu})$ and $A(\overline{\nu})$, proceeds according to Eqs. (5.45) and (5.46) presented in the previous section. Similarly, for the measurement of VCB, an AC phase function must be measured using the same electronic pathway as used for VCB measurement before Fourier transformation. Here the corresponding AC and DC interferograms yield the VCB and VA spectra, $\Delta n_{RL}(\overline{\nu})$ and $A(\overline{\nu})$, as presented above in Eqs. (5.53) and (5.46).

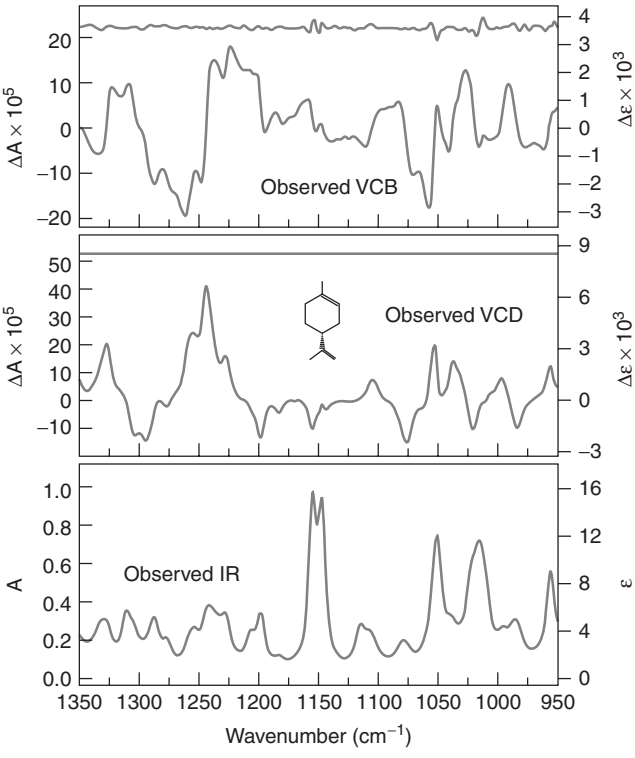

Figure 5.4. VCB (upper), VCD (middle), and VA (lower) spectra of (+)-*R*-limonene as a neat liquid are shown measured with a pathlength of 50 μm. Also displayed above the VCB and VCD spectra are the corresponding VCB and VCD noise spectra. (From reference 9, reproduced with permission.)

5.3.3. Infrared VOA and VA Spectra of Alpha Pinene

In this section we present, as a standard example, the VCD, VCB, and VA spectra of limonene [9]. In Figure 5.4, the VCB upper, VCD middle, and VA lower spectra of (+)-*R*-limonene as a neat liquid is presented for the spectral region from 1350 to 950 cm^{-1}. The convention in VOA spectroscopy is to plot the parent VA spectrum beneath the VOA spectrum so that features in the VA spectrum can be correlated to features in the VOA spectrum. This is important since peak values in the VOA spectra can be shifted from the resonance band center by overlaps of oppositely signed spectral features. Also provided in the figure are the VCB and VCD noise spectra plotted just above their corresponding VCB and VCD spectra. The VOA spectra were collected in two blocks. The blocks were added and divided by 2 to produce the displayed VCB and VCD spectra and were subtracted and divided by 2 to produce the corresponding noise spectra. The noise spectra provide a measure of confidence in the authenticity of small features in the VOA spectra. Finally, the ordinate axis units are unitless absorbance, ΔA or A, on the left and molar absorptivity in units of mol^{-1} cm^2, $\Delta\varepsilon$ or ε, on the right. The molar absorptivity scale was obtained from the absorbance scale by dividing the latter by the pathlength in cm and by the molar concentration in moles/cm^3. Absorbance units are useful judging the signal-to-noise conditions of the measurement since the signal-to-noise ratio is maximized for ΔA or A at a value of approximately 0.4. Absorbance levels should never exceed approximately 1.0 due to significant loss of IR throughput and attendant much higher noise levels. The molar absorptivity units are useful for comparing intensities to the results of quantum mechanical calculations or to other molecules of similar structure and size.

5.3.4. Comparison of Dispersive and Fourier Transform VCD

Although FT-VCD instrumentation has many significant advantages over the older dispersive VCD instrumentation, there still remains an area of application where dispersive VCD instrumentation is at least comparable in performance and reliability, if not superior. This area of application involves optimization of instrumentation for a relatively narrow spectral region of 100–200 cm^{-1} in width. Under these circumstances, it is possible to increase substantially the intensity of the IR source without saturating the detector, an ever-present danger in FT-VCD measurements, and to optimize all other components such as spectrograph, grating, and filters that would not be appropriate for measurements covering a wider spectral frequency range. With such optimized dispersive instrumentation signal-to-noise ratios comparable to those of wide-spectral-coverage FT-VCD over the same region, can be obtained. Recently, two papers have appeared that featured comparisons of dispersive VCD and FT-VCD spectra. The first one is a review by Keiderling [43] at the University of Illinois, Chicago, that contains many such comparisons, and the second one is a more recent paper carried out at Syracuse that focuses on comparisons of the FT-IR and FT-NIR VCD of proteins and also includes a single comparison between FT and dispersive VCD in the amide I region for the protein α-chymotripsin [44].

Comparisons of dispersive and FT VCD are difficult due to differing natures of the sources of noise in the VCD spectra. FT-VCD spectra have noise that is distributed smoothly over the entire spectrum and is the result of the aggregate noise of the spectral measurement over all frequencies measured simultaneously. The noise does vary with absorbance level in the usual way, but the noise itself comes from a broadband average. The difficulty in seeing this smooth kind of noise is one reason why it is important to show a separate noise curve for VCD spectra as is in Figure 5.4. Noise in dispersive VCD spectra is much more local in a spectroscopic sense and somewhat easier to see. The noise is manifested as sharper features that vary while the VCD spectrum is being measured one resolution element at a time. There seems to be advantages to both types of VCD measurement, and it may well be that there will always be a place for specially designed dispersive VCD instrument for a particular spectral region such as the amide I region of protein IR and VCD spectra.

A final point of comparison concerns kinetic measurements of VCD spectra as a function of time. Here, there is an intrinsic advantage of FT-VCD instrumentation since all frequencies in the spectrum are measured simultaneously. The time resolution can be determined by the length of time for each unit of co-added VCD scans that could vary from a few tens of seconds to as long as an hour. Dispersive VCD spectra will always contain a time bias associated with the time it takes to make a single scan over the frequency range measured. For slow kinetics, on the order of hours, there is no significant level of time bias since in effect for say a 5-minute single scan there may be essentially no detectable change in the kinetic state of the sample. Nevertheless, FT-VCD with simultaneous collection of AC and DC interferograms enjoys a significant advantage in principle for kinetic measurements.

5.4. ADVANCED METHODS FOR FT-VCD MEASUREMENT

In this section we describe advances in FT-VCD instrumentation and measurement that involve the introduction of new optical elements or changes in the optical beam path that have demonstrated a significant improvement in the measurement of VCD spectra.

5.4.1. Dual Polarization Modulation FT-VCD

The advance of dual polarization modulation for FT-VCD measurement was described for the first time approximately 10 years ago [31]. The method is related to the earlier technique called polarization scrambling [12], but differs in several significant ways. In both polarization scrambling and dual polarization modulation, a second PEM with slow and fast axes aligned parallel to the first PEM is placed in the optical train after the sample. For polarization scrambling, the control voltage of the second PEM is continuously changed as the dispersive monochromator scans the spectrum in order to keep this PEM at retardation value of optimum scrambling that reduces the magnitude and severity of the VCD background baseline offset. Polarization scrambling cannot be carried out with the same level of efficiency for FT-VCD measurement since all frequencies are measured simultaneously and only for one narrow region of the spectrum can the PEM setting correspond to optimum polarization scrambling.

For dual polarization modulation, the control voltages of the first and second PEMs are adjusted to have the same retardation setting, and the FT-VCD spectrum of each of the two PEMs is measured using its own lock-in. The first PEM records the FT-VCD of the sample plus the VCD baseline offset spectrum, while the second PEM, placed after the sample, records only the VCD baseline offset spectrum. Subtraction of the two AC interferograms in real time during each interferogram scan dynamically cancels the baseline offset spectrum and yields the VCD spectrum of the sample free of the interfering baseline distortions and other kinds of spectral artifacts.

The optical-electronic block diagram for the dual PEM setup is provided in Figure 5.5.

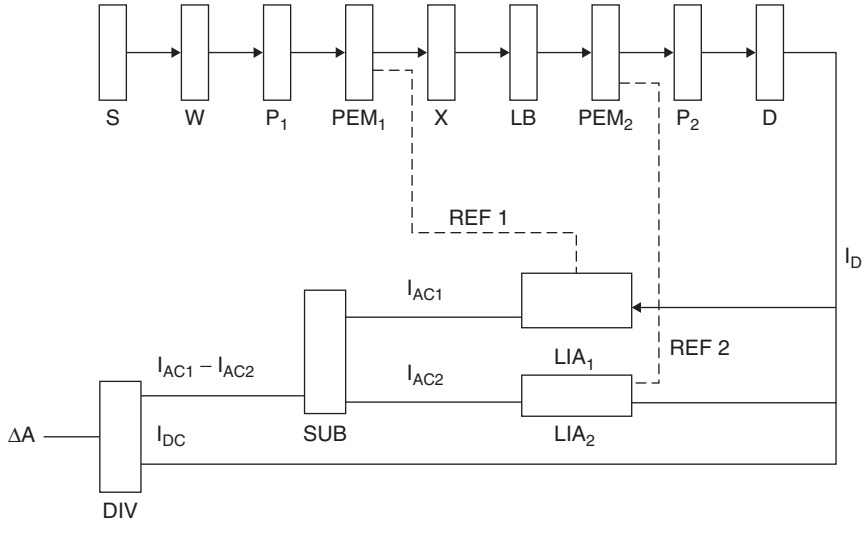

Figure 5.5. Optical-electronic block diagram illustrates the dual polarization modulation setup. The optical and electronic labels are the same, except for additional numbering, as those used in Figure 5.3 except for the addition of a real-time electronic subtraction stage (SUB) that filters and subtracts the outputs of PEM_1 and PEM_2 before their difference AC interferogram is Fourier-transformed and ratioed to the Fourier transform of the DC interferogram to produce the measured VCD spectrum. (From reference 31, reproduced with permission.)

The optical path between the source and detector is described as

$$\text{Source} \rightarrow \text{Pol.}(0^\circ) \rightarrow \text{PEM}_1(45^\circ) \rightarrow \text{Sample} \rightarrow \text{PEM}_2(45^\circ) \rightarrow \text{Pol.}(0^\circ) \rightarrow \text{Detector}$$

and the Stokes–Mueller formalism for the intensity at the detector is given by

$$I_D(\overline{\nu}) = \boldsymbol{D}(\alpha) \cdot \boldsymbol{M}_{P2}(0^\circ) \cdot \boldsymbol{M}_{PEM2}(\overline{\nu}) \cdot \boldsymbol{M}_S(\overline{\nu}) \cdot M_{PEM1}(\overline{\nu}) \cdot \boldsymbol{M}_{P1}(0^\circ) \cdot \boldsymbol{S}_0(\overline{\nu}). \quad (5.59)$$

This expression is the same as that of the single PEM theory through the Mueller matrix of the sample which produces $\boldsymbol{S}_3(\overline{\nu})$ given above in Eq. (5.38). If the Mueller matrix of the second PEM operates on $\boldsymbol{S}_3(\overline{\nu})$, the new Stokes vectors $\boldsymbol{S}_4(\overline{\nu})$ is obtained by the following expressions:

$$\begin{aligned}
\boldsymbol{S}_4(\overline{\nu}) &= \boldsymbol{M}_{PEM2}[45^\circ, \alpha_{M2}(\overline{\nu})] \cdot \boldsymbol{S}_3(\overline{\nu}) \\
&= \begin{pmatrix} 1 & 0 & 0 & 0 \\ 0 & \cos\alpha_{M2}(\overline{\nu}) & 0 & -\sin\alpha_{M2}(\overline{\nu}) \\ 0 & 0 & 1 & 0 \\ 0 & \sin\alpha_{M2}(\overline{\nu}) & 0 & \cos\alpha_{M2}(\overline{\nu}) \end{pmatrix} \frac{I_{DC}(\overline{\nu})}{2} \\
&\quad \begin{pmatrix} 1 + CD(\overline{\nu})\sin\alpha_{M1}(\overline{\nu}) \\ \cos\alpha_{M1}(\overline{\nu}) - LB(\overline{\nu})\sin\alpha_{M1}(\overline{\nu}) \\ -\text{CB}(\overline{\nu})\cos\alpha_{M1}(\overline{\nu}) + \text{LB}'(\overline{\nu})\sin\alpha_{M1}(\overline{\nu}) \\ \text{CD}(\overline{\nu}) + LB(\overline{\nu})\cos\alpha_{M1}(\overline{\nu}) + \sin\alpha_{M1}(\overline{\nu}) \end{pmatrix} \\
&= \frac{I_{DC}}{2} \begin{pmatrix} 1 + \text{CD}\sin\alpha_{M1} \\ \cos\alpha_{M1}\cos\alpha_{M2} - \text{LB}\sin\alpha_{M1}\cos\alpha_{M2} - \text{CD}\sin\alpha_{M2} \\ -\text{LB}\cos\alpha_{M1}\sin\alpha_{M2} - \sin\alpha_{M1}\sin\alpha_{M2} \\ -\text{CB}\cos\alpha_{M1} + \text{LB}'(\overline{\nu})\sin\alpha_{M1} \\ \cos\alpha_{M1}\sin\alpha_{M2} - \text{LB}\sin\alpha_{M1}\sin\alpha_{M2} + \text{CD}\cos\alpha_{M2} \\ +LB\cos\alpha_{M1}\cos\alpha_{M2} + \sin\alpha_{M1}\cos\alpha_{M2} \end{pmatrix}.
\end{aligned} \quad (5.60)$$

Here, to save space, the wavenumber frequency dependence has been dropped in the last expression. We now introduce the Bessel functions $J_0(\alpha_M)$ and $J_1(\alpha_M)$ from Eqs. (5.41) and (5.49) through first order in the modulation frequency, and we eliminate terms that depend on the product $\sin\alpha_{M1}\sin\alpha_{M2}$ since the PEMs are not synchronized and the product of sine waves averages to zero. Also eliminated are the terms $\cos\alpha_{M1}\cos\alpha_{M2}$ and $\text{CD}\cos\alpha_{M2}$ since they are small relative to unity, the main DC term. This gives

$$\boldsymbol{S}_4(\overline{\nu}) = \frac{I_{DC}}{2} \begin{pmatrix} 1 + 2J_1(\alpha_{M1})\text{CD} \\ -2J_1(\alpha_{M1})J_0(\alpha_{M2})\text{LB} - 2J_1(\alpha_{M2})\text{CD} - 2J_0(\alpha_{M1})J_1(\alpha_{M2})\text{LB} \\ -J_0(\alpha_{M1})\text{CB} + 2J_1(\alpha_{M1})\text{LB}' \\ 2J_0(\alpha_{M1})2J_1(\alpha_{M2}) + 2_1(\alpha_{M1})J_0(\alpha_{M2}) \end{pmatrix}. \quad (5.61)$$

If we complete the last two Mueller matrix operations for the second polarizer and the detector in Eq. (5.59), the final scalar intensity is given by

$$\begin{aligned}
I_D = \frac{I_{DC}}{4}[1 + (p_X^2 - p_Y^2)\cos 2\alpha][1 + 2J_1(\alpha_{M1})\text{CD} - 2J_1(\alpha_{M1})J_0(\alpha_{M2})\text{LB} \\
-2J_1(\alpha_{M2})\text{CD} - 2J_0(\alpha_{M1})J_1(\alpha_{M2})\text{LB}].
\end{aligned} \quad (5.62)$$

Here the first two terms in square brackets are close to unity with a small term depending on the magnitude and angle of the polarization sensitivity of the detector. The second set of terms in square brackets has a DC term (1) and four AC terms comprised of two equivalent terms associated with each PEM, one carrying the VCD signal and the other carrying an LB artifact term. These two terms associated with each PEM are measured separately by the two lock-in amplifiers in Figure 5.5. It is possible to exactly separate the VCD intensity from the LB intensity by reversing the sign of one of the lock-ins by changing the lock-in phase by 180°. If, in addition, the two PEMs are set to the same retardation value such that $J_0(\alpha_{M2})J_1(\alpha_{M1}) = J_0(\alpha_{M1})J_1(\alpha_{M2})$, the LB terms cancel while the CD terms add, giving

$$I_D = \frac{I_{DC}}{4}[1 + (p_X^2 - p_Y^2)\cos 2\alpha][1 + 2J_1(\alpha_{M1})\mathrm{CD} + 2J_1(\alpha_{M2})\mathrm{CD}]. \tag{5.63}$$

The two VCD terms compensate for the loss of light that occurs when the second polarizer is placed in the beam. Although this is optically and electronically a perfect solution to the VCD artifact problem, it suffers from a major drawback that has so far prevented its use in everyday applications. This drawback is the fact that placing a polarizer in the beam after the second PEM magnifies the size of the LB by a factor of approximately 100, which places too large a demand on the accuracy of the cancellation of the LB terms relative to the size of the VCD intensity.

An alternative solution is to not place a polarizer after the sample. Applying the Mueller matrix of the detector to $\boldsymbol{S}_4(\overline{\nu})$ in Eq. (5.61) yields

$$\begin{aligned} I_D = \frac{I_{DC}}{2}\{&1 + 2J_1(\alpha_{M1})\mathrm{CD} \\ &+ (p_X^2 - p_Y^2)\cos 2\alpha[-2J_1(\alpha_{M1})J_0(\alpha_{M2})\mathrm{LB}] \\ &-2J_1(\alpha_{M2})\mathrm{CD} - 2J_0(\alpha_{M1})J_1(\alpha_{M2})\mathrm{LB}] \\ &+(p_X^2 - p_Y^2)\sin 2\alpha[2J_1(\alpha_{M1})\mathrm{LB}']\}. \end{aligned} \tag{5.64}$$

Here, we have again ignored terms that are small or average to zero. Now there is twice as much light reaching the detector, but only a very small CD term coming from the second PEM. All AC terms beyond the CD term of PEM1 are reduced to the level of the polarization sensitivity of the detector, and again changing the sign of the LIA of the second PEM cancels the two LB terms when the PEMs are set to the same retardation value. Carrying out this operation, we obtain

$$\begin{aligned} I_D = \frac{I_{DC}}{2}\{&1 + 2J_1(\alpha_{M1})\mathrm{CD} + (p_X^2 - p_Y^2)\cos 2\alpha[2J_1(\alpha_{M2})\mathrm{CD}] \\ &+ (p_X^2 - p_Y^2)\sin 2\alpha[2J_1(\alpha_{M1})\mathrm{LB}']\}. \end{aligned} \tag{5.65}$$

Because there was no polarizer in place at the vertical or horizontal orientation, a single LB′ term remains in this expression that is not present in Eq. (5.63). Later in this section we demonstrate two practical ways to eliminate this remaining source of linear birefringence. Further analysis reveals (not shown here but easily verified if desired) that the dual PEM method without a second polarizer eliminates all sources of LB and LB′ artifacts before and after the two PEMs as well as all LB terms between the two PEMs. Only the LB′ terms between the two PEM are not eliminated unless a polarizer is placed in the beam after the second PEM as demonstrated above.

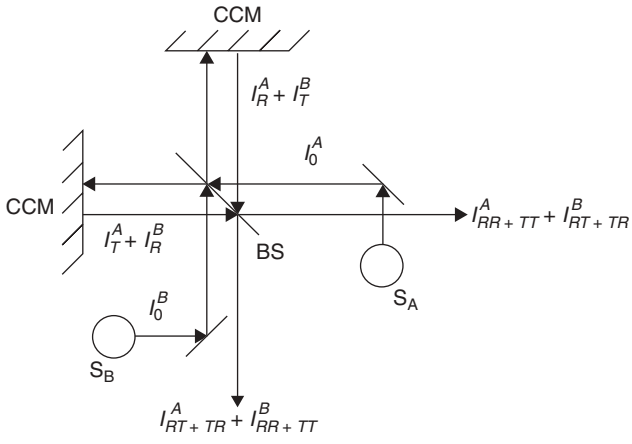

Figure 5.6. Diagram illustrating the optical layout of a dual-source FT-IR spectrometer. The beam from the two sources, S_A and S_B, are each divided into two beams at the beamsplitter, BS. These four beams reflect at cube-corner mirrors (CCM) and recombine at the beamsplitter. The subscripts *R* and *T* refer to reflection and transmission, respectively, as described in the text. (From reference 32, reproduced with permission.)

5.4.2. Dual Source FT-VCD

A relatively recent advance in VCD instrumentation is the use of two sources in an FT-IR spectrometer [32]. The basic optical layout is illustrated in Figure 5.6. The source S_A is located in the usual position, whereas source S_B is located in a nonstandard position. The interferometer used for the dual source measurement employs cube-corner mirrors instead of flat plane mirrors. Using such mirrors, it is possible for the light beam incident on the beamsplitter to be in the lower portion of the beamsplitter and it is possible for the recombined beams after mirror reflection to be in the upper part of the beamsplitter. In this way, there are four available in-out ports for the interferometer. In Figure 5.6, the beam exiting the interferometer toward the sample is comprised of a beam from S_A, $I_{RT+TR}^{A,DC}(\delta)$, where the two split beams each experiences one reflection and one transmission at the beamsplitter as indicated by the subscripts $RT + TR$. For this same beam in intensity originating from S_B, $I_{RR+TT}^{B,DC}(\delta)$, one of the split beams experiences two reflections and the other two transmissions, labeled $RR + TT$. These two beams have opposite Fourier phases and hence contribute with opposite signs at the detector as indicated here:

$$I_{DC}^{AB}(\delta) = I_{RT+TR}^{A,DC}(\delta) + I_{RR+TT}^{B,DC}(\delta) = \int_0^\infty (I_{DC}^A(\overline{\nu}) - I_{DC}^B(\overline{\nu})) \cos[2\pi\delta\overline{\nu} + \theta_{DC}(\overline{\nu})]\, d\overline{\nu}. \tag{5.66}$$

For the dual-source AC interferogram, one first replaces the single polarizer in front of the PEM with two polarizers oriented orthogonally, one in front of each source. Thus, although beams from S_A and S_B are nearly the same, their different polarization states with respect to reflection and transmission at the beamsplitter lead to different intensities for $I_{DC}^A(\overline{\nu})$ and $I_{DC}^B(\overline{\nu})$, for the outgoing beams. As a result, even though the beams $I_{RT+TR}^A(\delta)$ and $I_{RR+TT}^A(\delta)$ have opposite Fourier phase, their Fourier modulations do not cancel but rather add as shown in the following equation:

$$I_{AC}^{AB}(\delta) = I_{RT+TR}^{A,AC}(\delta) + I_{RR+TT}^{B,AC}(\delta) = \int_0^\infty (I_{AC}^A(\overline{\nu}) + I_{AC}^B(\overline{\nu})) \cos[2\pi\delta\overline{\nu} + \theta_{AC}(\overline{\nu})]\, d\overline{\nu} \tag{5.67}$$

Experimentally, it is found that for such an arrangement with two sources the ratio $I^A_{DC}(\overline{\nu})/I^B_{DC}(\overline{\nu})$ is approximately 1.6 times the ratio with a single source. This increase in signal against a fixed detector noise background makes the dual-source setup equivalent to nearly three otherwise identical single source FT-VCD spectrometers operating in parallel. Alternatively, collection time is reduced by a factor of three with dual source operation compared to single source operation.

An additional advantage of dual source operation, beyond the increased intensity of the AC signal, is the reduction in saturation sensitivity of the DC part of the signal. Because in the DC mode, the two interferograms combine with opposite signs, one or both beams can be above the saturation limit of the detector, but their difference as measured can still be below the saturation limit.

For dual-source operation, the VCD intensity is proportional to the ratio of the combined AC and DC interferograms. This ratio, relative to single-source operation, is found experimentally to be approximately

$$\left|\frac{I^A_{AC}(\overline{\nu})+I^B_{AC}(\overline{\nu})}{I^A_{DC}(\overline{\nu})-I^B_{DC}(\overline{\nu})}\right| = \left|\frac{1+1.6}{1-1.6}\right| \approx 4.3. \tag{5.68}$$

This represents the increase in the uncalibrated dual-source VCD intensity relative to the corresponding uncalibrated single-source VCD intensity. This factor represents the gain in AC transmission intensity relative to the reduction in DC transmission intensity, and it is compensated when the final calibrated dual-source VCD spectrum is determined.

5.4.3. Rotating Achromatic Half-Wave plate

It has been demonstrated recently that placing a rotating achromatic half-waveplate (HWP) after the second PEM in a dual-PEM FT-VCD instrument eliminates all sources of artifacts throughout the optical train [35]. The plate rotates slowly on the order of 10 revolutions per minute asynchronously with respect to all other modulation frequencies in the instrument. We also add an additional source of linear birefringence (LB_2) after the rotating HWP, to demonstrate how the effects of this plate are eliminated, followed by the detector. The optical setup for the dual-PEM rotating HWP is

$$\begin{aligned}\text{Source} \rightarrow \text{Pol.} \rightarrow \text{PEM}_1(45^\circ) \rightarrow \text{Sample} \rightarrow \text{PEM}_2(45^\circ)\\ \rightarrow \text{RHWP} \rightarrow \text{LB2} \rightarrow \text{Detector}\end{aligned}$$

The Mueller matrix for a HWP as a function of its orientation angle was provided above in Eq. (5.29). For a rotating plate, the effect of the HWP can be averaged over all angles by integration between the 0 and 2π, as

$$\boldsymbol{M}_{RHWP} = \frac{1}{2\pi}\int_0^{2\pi}\begin{pmatrix}1 & 0 & 0 & 0\\ 0 & \cos 4\theta & \sin 4\theta & 0\\ 0 & \sin 4\theta & -\cos 4\theta & 0\\ 0 & 0 & 0 & -1\end{pmatrix} d\theta = \begin{pmatrix}1 & 0 & 0 & 0\\ 0 & 0 & 0 & 0\\ 0 & 0 & 0 & 0\\ 0 & 0 & 0 & -1\end{pmatrix}. \tag{5.69}$$

This Mueller matrix averages to zero all LP states and converts any component of circular polarization from right to left or vice versa. If a rotating HWP is placed after the second

PEM in a dual PEM optical train, the resulting Stokes vector $\boldsymbol{S}_5(\overline{\nu})$ can be obtained starting from the Stokes vector after PEM_2, $\boldsymbol{S}_4(\overline{\nu})$, given in Eq. (5.61), by

$$\boldsymbol{S}_5(\overline{\nu}) = \boldsymbol{M}_{RHWP} \cdot \boldsymbol{S}_4(\overline{\nu}) = \frac{I_{DC}}{2} \begin{pmatrix} 1 + 2J_1(\alpha_{M1})\mathrm{CD} \\ 0 \\ 0 \\ -2J_0(\alpha_{M1})2J_1(\alpha_{M2}) - 2J_1(\alpha_{M1})J_0(\alpha_{M2}) \end{pmatrix}. \quad (5.70)$$

If a second source of small linear birefringence LB_2 is included after the rotating HWP, it can be described by the Mueller matrix from Eqs. (5.31) and (5.32):

$$\boldsymbol{M}_{\mathrm{LB2}} = \begin{pmatrix} 1 & 0 & 0 & 0 \\ 0 & 1 & 0 & -\mathrm{LB2} \\ 0 & 0 & 1 & \mathrm{LB2}' \\ 0 & \mathrm{LB2} & -\mathrm{LB2}' & 1 \end{pmatrix}. \quad (5.71)$$

This source of this birefringence can be due to the detector focusing lens or the detector window. The Stokes vector after this additional source of LB is given by

$$\begin{aligned} \boldsymbol{S}_6(\overline{\nu}) &= \boldsymbol{M}_{LB2} \cdot \boldsymbol{S}_5(\overline{\nu}) \\ &= \frac{I_{DC}}{2} \begin{pmatrix} 1 + 2J_1(\alpha_{M1})\mathrm{CD} \\ \mathrm{LB2}[2J_0(\alpha_{M1})2J_1(\alpha_{M2}) + 2J_1(\alpha_{M1})J_0(\alpha_{M2})] \\ -\mathrm{LB2}'[2J_0(\alpha_{M1})2J_1(\alpha_{M2}) + 2J_1(\alpha_{M1})J_0(\alpha_{M2})] \\ -(1 + \mathrm{LB2} - \mathrm{LB2}')[2J_0(\alpha_{M1})2J_1(\alpha_{M2}) + 2J_1(\alpha_{M1})J_0(\alpha_{M2})] \end{pmatrix}. \end{aligned} \quad (5.72)$$

The terms in square brackets which are due simply to the circular polarization term of the Stokes vector after the rotating HWP in Eq. (5.61) become zero if the two PEMs are set to be equal retardation strength and the LIA1 and LIA2 signals are subtracted electronically as describe above. If this is done, the last entry in Eq. (5.70) or all the square bracket terms expressions in Eq. (5.72) are zero and then all LB and LB′ terms cancel and the final Stokes vector before the detector is given by

$$\boldsymbol{S}_6(\overline{\nu}) = \frac{I_{DC}}{2} \begin{pmatrix} 1 + 2J_1(\alpha_{M1})\mathrm{CD} \\ 0 \\ 0 \\ 0 \end{pmatrix}. \quad (5.73)$$

The signal at the detector, with or without polarization sensitivity at the detector, is given by

$$\begin{aligned} I_D(\overline{\nu}) &= \boldsymbol{D}(\alpha) \cdot \boldsymbol{M}_{LB2}(\overline{\nu}) \cdot \boldsymbol{M}_{RHWP} \cdot \boldsymbol{M}_{PEM2}(\overline{\nu}) \cdot \boldsymbol{M}_S(\overline{\nu}) \cdot \boldsymbol{M}_{PEM1}(\overline{\nu}) \cdot \boldsymbol{M}_P(0^\circ) \cdot \boldsymbol{S}_0(\overline{\nu}) \\ &= \boldsymbol{D}(\alpha) \cdot \boldsymbol{S}_6(\overline{\nu}) = \frac{I_{DC}}{2}[1 + 2J_1(\alpha_{M1})\mathrm{CD}(\overline{\nu})]. \end{aligned} \quad (5.74)$$

This is birefringent artifact-free VCD spectrum. The dual-PEM setup eliminates all sources of birefringence except for the LB′ contributions located between the two PEMs, primarily due to the sample cell windows in the case of a liquid or solution sample and orientational effects in a solid-phase sample. By contrast, the rotating HWP eliminates all sources of birefringence before it in the optical train but has no effect on birefringence

that occurs after it, such as in the detector focusing lens or detector windows. Together, and only together, they eliminate all birefringent artifact signals.

The principal drawback of the rotating HWP is acquisition of an achromatic HWP in the IR region. The fabrication is fairly straightforward. For the NIR region with a lower limit of 2000 cm^{-1} the cost of acquisition in 2004 of a super achromatic plate (B. Halle Nachfolger in Berlin, Germany) was approximately the same cost as a PEM [35]. Extension beyond this limit into the mid-IR is still untested optical technology for VCD measurements.

5.4.4. Rotating Sample Cell

A simpler solution to the LB artifact problem that remains after incorporation of the dual-PEM setup is rotation of the sample about the optic axis of the IR beam. Here, both sources of linear birefringence, $\mathrm{LB}(\overline{\nu})$ and $\mathrm{LB}'(\overline{\nu})$, associated the sample cell, and included in the Mueller matrix of the sample in Eq. (5.32), are averaged to zero over the course of the measurement. This yields a VCD baseline that is the same as the baseline of the spectrometer with the same optical aperture but no optical elements between the two PEMs. The optical arrangement to be described by Mueller analysis is given below:

$$\text{Source} \rightarrow \text{Pol.} \rightarrow \text{PEM}_1(45^\circ) \rightarrow \text{RSC} \rightarrow \text{PEM}_2(45^\circ) \rightarrow \text{LB}_2 \rightarrow \text{Detector}$$

Here the sample cell is replaced by a rotating sample cell (RSC), and we again include an additional source of birefringence by LB_2 to account for the optical strain effects of the detector focusing lens and detector window.

We first generalize the Mueller matrix of the sample used in Eq. (5.38) to be valid for any angle of orientation of the sample cell.

$$\boldsymbol{M}_S(\theta) = 10^{-A}\begin{pmatrix} 1 & 0 & 0 & \mathrm{CD} \\ 0 & 1 & \mathrm{CB} & -\mathrm{LB}\cos 2\theta - \mathrm{LB}'\sin 2\theta \\ 0 & -\mathrm{CB} & 1 & \mathrm{LB}'\cos 2\theta - \mathrm{LB}\sin 2\theta \\ \mathrm{CD} & \mathrm{LB}\cos 2\theta + \mathrm{LB}'\sin 2\theta & -\mathrm{LB}'\cos 2\theta + \mathrm{LB}\sin 2\theta & 1 \end{pmatrix} \tag{5.75}$$

Averaging over all orientation angles as was done for the rotation HWP in Eq. (5.69), one obtains

$$\boldsymbol{M}_{RS} = \int_0^{2\pi} \boldsymbol{M}_S(\theta)\, d\theta = 10^{-A}\begin{pmatrix} 1 & 0 & 0 & \mathrm{CD} \\ 0 & 1 & \mathrm{CB} & 0 \\ 0 & -\mathrm{CB} & 1 & 0 \\ \mathrm{CD} & 0 & 0 & 1 \end{pmatrix}. \tag{5.76}$$

Integration over all angles eliminates through first order all sources of LB arising from the sample. The action of PEM_2 eliminates all remaining LB terms. The detector signal has only pure VCD intensity at the fundamental PEM frequency with no artifact terms.

$$\begin{aligned} I_D(\overline{\nu}) &= \boldsymbol{D}(\alpha)\cdot\boldsymbol{M}_{LB2}(\overline{\nu})\cdot\boldsymbol{M}_{PEM2}(\overline{\nu})\cdot\boldsymbol{M}_{RSC}(\overline{\nu})\cdot\boldsymbol{M}_{PEM1}(\overline{\nu})\cdot\boldsymbol{M}_P(0^\circ)\cdot\boldsymbol{S}_0(\overline{\nu}) \\ &= \boldsymbol{D}(\alpha)\cdot\boldsymbol{S}_6(\overline{\nu}) = \frac{I_{DC}(\overline{\nu})}{2}\{1 + 2J_1[\alpha^0_{M1}(\overline{\nu})]\mathrm{CD}(\overline{\nu}) - 2J_2[\alpha^0_{M2}(\overline{\nu})]\mathrm{CB}(\overline{\nu})\}. \end{aligned} \tag{5.77}$$

For completeness we retain the VCB intensity that can be measured at twice the PEM frequency and is proportion to $2J_2(\alpha_{M1})$ as described above. VCB cannot be measured with the achromatic RHWP since the linear polarization states used in VCB measured are averaged to zero by the RHWP.

5.5. MEASUREMENT OF DISPERSED SOLIDS AND FILMS

Most measurements of VCD spectra have been carried for neat liquids or solutions. As seen from considerations above, all such measurements have been carried out in a sample cell with windows. While the windows, such as BaF_2, are transparent in the regions measured, they nevertheless can display varying degrees of strain birefringence that can distort the circular polarization balance of the IR beam between RCP and LCP states leading to artifacts. The method of dual polarization modulation with two PEMS, combined with sample cell rotation, eliminates all sources of the LB in the optical train. In this section we discuss the issues associated with measuring the VCD in solid-phase samples, primarily dispersed solids and films.

5.5.1. Sampling Methods for Dispersed Solids

The most significant difference between a solid sample for VCD measurement and the cell windows using for a solution-state VCD measurement is that the solid sample has a significant level of absorption. The absorption bands cause sharp changes in the index of refraction of the sample as a function of wavenumber frequency. In a solid the index of refraction can be different for different directions in the solid, and as a result there can be both linear dichroism from the absorption bands and linear birefringence from the index of refraction differences in different direction.

One approach to reducing these effects is to grind the solid to small particle sizes and disperse the solid to reduce the effects of LD or LB on the VCD spectrum. A complicating factor is the particle size. If particles are not smaller than the wavelength of the light, scattering from the so-called Christiansen effect will occur that affects both the IR absorption spectrum and the VCD spectrum. If the particle size is sufficiently small, the VCD of dispersed solids, such as mulls or KBr pellets, can be obtained without concern about LB artifacts, provided that two PEMs are used together with the rotating sample cell.

As has been shown in detail using second-order Stoke–Mueller analysis, one remaining source of CD artifacts for solid samples can arise for samples with both LB and LD with axes oriented 45° from one another—that is, independent of the angle of sample orientation [45]. The final expression, even after integrating uniformly over all possible angles of orientation, is

$$I_D = \frac{I_{DC}}{2}\left[1 + J_1(\alpha_{M_1})\left[\mathrm{CD} + \frac{1}{2}(\mathrm{LBLD} - \mathrm{LB'LD'})\right]\right]. \tag{5.78}$$

This is the same as Eq. (5.74) or Eq. (5.77) except for the addition of a term that depends on the product of LD and LB for the two reference systems. The way these quantities were defined, the term LBLD represents the second-order Mueller matrix effect of LB with axes at 45° from vertical, that converts CP light to LP light in the vertical horizontal orientation, with LD orientated in the vertical versus horizontal direction. The term LB′LD′ is analogous except all angles are changed by 45°. A signature of this artifact is its reversal if the solid sample is rotated 180° about any axis perpendicular to the propagation axis such that the front and back faces of the sample are interchanged. If this is done, the sign of this artifact is reversed and this artifact cancels for sum of the VCD measurements with the sample facing front and back. While in principle, this artifact could arise from the individual crystals for a dispersed solid, no such artifact has

yet been reported. Most likely, this artifact is important only for oriented solid-phase samples displaying a significant level of both LD and LB spectra.

An example of a solid-phase VCD spectrum for *S*-propanolol is presented in Figure 5.7. This example illustrates one advantage of measuring the VCD of solid-phase samples, in this case a drug substance, where slight modifications of the composition, free base versus hydrochloride salt, can lead to distinct differences in the VCD related to its detailed stereochemical structure in the solid. For these samples, the solid was ground to small particle size to avoid particle scattering. The absence of observable levels of particle scattering can be ascertained from the bandshapes of the IR spectra since particle scattering, which depends on the index of refraction of the solid particles relative to the hydrocarbon oil used to make the mull, leads to distortion of the symmetry of the lineshapes. Symmetric lineshapes can be interpreted as the absence of particle scattering effects.

5.5.2. Sampling Methods for Films

Another solid-phase sampling method used in VCD is the measurement of films. If films are prepared without care, spurious orientation effects due to strain birefringence can lead to artifacts that prevent reproducibility of the VCD of film samples. As noted from the Stokes–Mueller analysis of samples with LB and LD effects, two sets of orientation effects can be present that differ by 45° from one another, LB and LD as well as LB′ and LD′, and hence checking a film sample for the differences in VCD at positions that differ only by 90° is insufficient to check for the absence of orientation artifact. In addition, as noted above, it is important to check for front and back face orientations of a film sample to ensure the absence of second-order LBLD artifacts described for Eq. (5.78). We cite here a number of examples of methods of measuring VCD of films that do not suffer

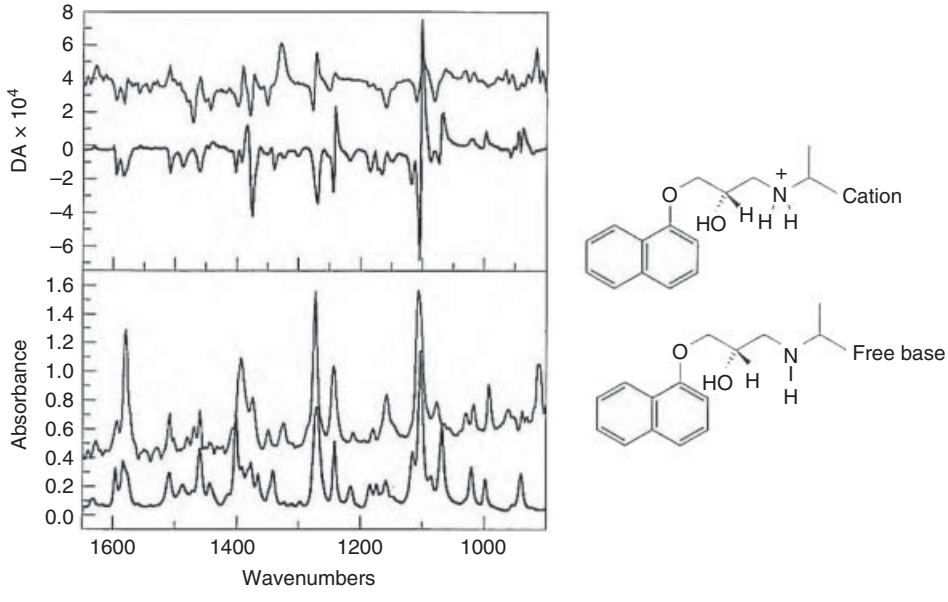

Figure 5.7. VA and VCD spectra of *S*-propranolol in the solid phase for two different forms, the hydrochloride salt (cation) and free base. (From reference 5, reproduced with permission.)

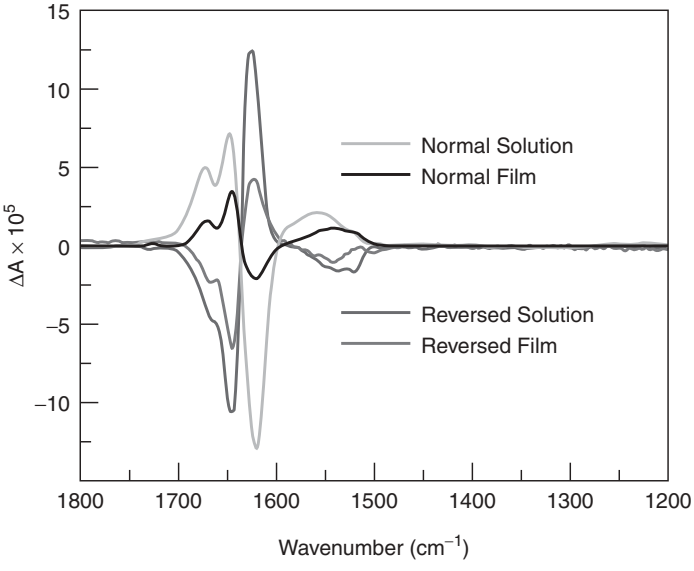

Figure 5.8. Enhanced VCD of insulin fibrils in the solution and film states prepared by heating at 65°C for 2 h at pH ~2 for two samples showing opposite supramolecular chirality. (From reference 48, reproduced with permission.)

from measurable orientation artifacts. The first is a spin-coated film of a conducting polymer that showed no effects of orientation about the beam propagation direction [46]. A second example is spray-dried films, which are fast-drying films formed by two-dimensional layering from a solution sprayed onto an IR transparent window that has been heated to promote rapid evaporation of the solvent to form the crystalline film [36]. A third example is films of amino acids prepared from a solution containing cyclodextrin that, as a supporting matrix for the film, promotes a uniform film without orientation effects in the VCD spectra that are seen in the absence of cyclodextrin [47]. In this case, cyclodextrin acts to replace hydrogen bonding interactions present in the aqueous solutions of the amino acids, and thus VCD spectra can be obtained with a minimum level of interference of solvent as films with aqueous-like molecular properties. Finally, we note that recently, as shown in Figure 5.8, VCD spectra of solutions and films were presented for samples of insulin amyloid fibrils that show a reversal of enhanced VCD and of supramolecular chirality as a function of the pH [48]. The film and solution VCD spectra were approximately the same size when normalized to the same IR absorbance intensity, and no orientation effects including front to back sampling, was observed.

5.6. CONCLUSIONS

Instrumentation for the measurement of infrared vibrational optical activity has advanced in many ways from the discovery of vibrational circular dichroism in the 1970s. In this chapter, we have presented many of these advances using the Stoke–Mueller formalism of optical analysis. Since a number of these advances have taken place relatively recently, it is likely that the process of instrumentation development and improvement for VCD measurement is still ongoing and that the future will see further improvements as methods are sought to routinely measure VCD as rapidly as possible without interferences from effects of the optical elements required for its measurement.

REFERENCES

1. L. A. Nafie, *Annu. Rev. Phys. Chem*. **1997**, *48*, 357–386.
2. P. L. Polavarapu, *Vibrational Spectra*: *Principles and Applications with Emphasis on Optical Activity*, Elsevier, Amsterdam **1998**.
3. R. K. Dukor, L. A. Nafie, Vibrational optical activity of pharmaceuticals and biomolecules, in *Encylopedia of Analytical Chemistry: Instrumentation and Applications*, R. A. Meyers, ed., John Wiley & Sons, Chichester, **2000**, pp. 662–676.
4. L. A. Nafie, T. B. Freedman, Vibrational optical activity theory, in *Circular Dichroism*, 2nd ed., N. Berova, K. Nakanishi, and R. W. Woody, eds., John Wiley & Sons, New York, **2000**, pp. 97–131.
5. L. A. Nafie, R. K. Dukor, Applications of vibrational optical activity in the pharamaceutical industry, in *Applications of Vibrational Spectroscopy in Pharmaceutical Research and Development*, D. Pivonka, J. M. Chalmers, and P. R. Griffiths, eds., John Wiley & Sons, Chichester, **2007**, pp. 129–154.
6. L. A. Nafie, R. K. Dukor, Vibrational optical activity in chiral analysis, in *Chiral Analysis*, K. W. Busch, and M. A. Busch, eds., Elsevier, Amsterdam, **2006**, pp. 505–544.
7. L. D. Barron, A. D. Buckingham, *Chem. Phys. Lett*. **2010**, *492*, 199–213.
8. L. A. Nafie, Vibrational optical activity: Principles and applications, John Wiley & Sons, Chichester, **2011**.
9. R. A. Lombardi, L. A. Nafie, *Chirality* **2009**, *21*, E277–E286.
10. G. Holzwarth, E. C. Hsu, H. S. Mosher, T. R. Faulkner, A. Moscowitz, *J. Am. Chem. Soc*. **1974**, *251*, 251–252.
11. L. A. Nafie, J. C. Cheng, P. J. Stephens, *J. Am. Chem. Soc*. **1975**, *97*, 3842.
12. J. C. Cheng, L. A. Nafie, P. J. Stephens, *J. Opt. Soc. Am*. **1975**, *65*, 1031–1035.
13. L. A. Nafie, T. A. Keiderling, P. J. Stephens, *J. Am. Chem. Soc*. **1976**, *98*, 2715–2723.
14. P. J. Stephens, R. Clark, *NATO Adv. Study Inst. Ser., Ser. C: Math. Physi. Sci*. **1979**, *48*, 263–287.
15. C. N. Su, V. J. Heintz, T. A. Keiderling, *Chem. Phys. Lett*. **1980**, *73*, 157–159.
16. L. A. Nafie, M. Diem, *Appl. Spectrosc*. **1979**, *33*, 130–135.
17. L. A. Nafie, M. Diem, D. W. Vidrine, *J. Am. Chem. Soc*. **1979**, *101*, 496–498.
18. L. A. Nafie, D. W. Vidrine, *Fourier Transform Infrared Spectrosc*. **1982**, *3*, 83–123.
19. L. A. Nafie, E. D. Lipp, C. G. Zimba. Fourier transform infrared circular dichroism: a double modulation approach, in *Proceedings of SPIE–The International Society for Optical Engineering*, **1981**.
20. E. D. Lipp, L. A. Nafie, *Appl. Spectrosc*. **1984**, *38*, 20–26.
21. L. A. Nafie, *Polarization Modulation FTIR Spectroscopy in Advances in Applied FTIR Spectroscopy*, M. W. Mackenzie, ed., John Wiley & Sons, New York, **1988**, pp. 67–104.
22. L. A. Nafie, N. S. Lee, G. Paterlini, T. B. Freedman, *Microchim. Acta* **1988**, *1987*(III), 93–104.
23. P. L. Polavarapu, *Infrared Phys*. **1988**, *28*, 109.
24. N. Ragunathan, N.-S. Lee, T. B. Freedman, L. A. Nafie, C. Tripp, H. Buijs, *Appl. Spectrosc*. **1990**, *44*, 5–7.
25. P. L. Polavarapu, P. G. Quincey, J. R. Birch, *Infrared Phys*. **1990**, *30*, 175.
26. P. L. Polavarapu, G.-C. Chen, *Appl. Spectrosc*. **1994**, *48*, 1410–1418.
27. P. L. Polavarapu, Z. Deng, G.-C. Chen, *Appl. Spectrosc*. **1995**, *49*, 229–236.
28. P. L. Polavarapu, Z. Deng, S. Weibel, *Appl. Spectrosc*. **1996**, *50*, 98–101.
29. P. L. Polavarapu, ed., *Principles and Applications of Polarization—Division Interferometry*, John Wiley & Sons, Ltd., Chichester, **1998**.

30. P. L. Polavarapu, Z. Y. Deng, *Appl. Spectrosc*. **1996**, *50*, 686–692.
31. L. A. Nafie, *Appl. Spectrosc*. **2000**, *54*, 1634–1645.
32. L. A. Nafie, H. Buijs, A. Rilling, X. Cao, R. K. Dukor, *Appl. Spectrosc*. **2004**, *58*, 647–654.
33. J. Hilario, D. Drapcho, R. Curbelo, T. A. Keiderling, *Appl. Spectrosc*. **2001**, *55*, 1435–1448.
34. P. Malon, T. A. Keiderling, *Appl. Spectrosc*. **1996**, *50*, 669–674.
35. X. Cao, R. K. Dukor, L. A. Nafie, *Theor. Chem. Accts*. **2008**, *119*, 69–79.
36. L. A. Nafie, R. L. Lombardi, **2010**, Unpublished results.
37. B. Wang, T. A. Keiderling, *Appl. Spectrosc*. **1995**, *49*, 1347–1355.
38. M. Niemeyer, G. G. Hoffmann, B. Schrader, *J. Mol. Struct*. **1995**, *349*, 451–454.
39. F. Long, T. B. Freedman, T. J. Tague, L. A. Nafie, *Appl. Spectrosc*. **1997**, *51*, 508–511.
40. F. Long, T. B. Freedman, R. Hapanowicz, L. A. Nafie, *Appl. Spectrosc*. **1997**, *51*, 504–507.
41. C. Guo, R. D. Shah, R. K. Dukor, T. B. Freedman, X. Cao, L. A. Nafie, *Vibr. Spectrosc*. **2006**, *42*, 254–272.
42. T. A. Keiderling, J. Kubelka, J. Hilario, Vibrational circular dichroism of biopolymers: Summary of methods and applications, in *Vibrational Spectroscopy of Biological and Polymeric Materials*, V. G. Gregariou, and M. B. Braiman, eds., CRC Press, Boca Raton, FL, **2005**, pp. 253–323.
43. T. A. Keiderling, *Curr. Opin. Chem. Biol*. **2002**, *6*, 682–688.
44. S. Ma, T. B. Freedman, R. K. Dukor, L. A. Nafie, *Appl. Spectrosc*. **2010**, *64*, 615–626.
45. R. Kuroda, T. Harada, Y. Shindo, *Rev. Sci. Instr*. **2001**, 3802–3810.
46. D. M. Tigelaar, W. Lee, K. A. Bates, A. Sapringin, V. N. Prigodin, X. Cao, L. A. Nafie, M. S. Platz, A. J. Epstein, *Chem. Mater*. **2002**, *14*, 1430–1438.
47. P. Zhang, P. L. Polavarapu, *Appl. Spectrosc*. **2006**, *60*, 378–385.
48. D. Kurouski, R. A. Lombardi, R. K. Dukor, I. Lednev, K., L. A. Nafie, *Chem. Comm*. **2010**, *46*, 7154–7156.

6

MEASUREMENT OF RAMAN OPTICAL ACTIVITY

Werner Hug

6.1. INTRODUCTION

The theoretical understanding of optically active Rayleigh scattering was reached at the beginning of the 1970s. Decisive insight came through the identification, by Barron and Buckingham [1], of the interference terms of the electric dipole–electric dipole polarizability tensor with the optical activity tensors, namely the electric dipole–magnetic dipole tensor and the appropriately contracted electric dipole–electric quadrupole tensor. Moreover, it appeared plausible that the Placzek polarizability treatment of Raman scattering could be extended to Raman optical activity. This theoretical insights, which suggested that Raman optical activity (ROA) should be measurable, led to a number of early reports on its presumed observation. The early data were spurious, however, with published spectra of an unreasonable size and apparance, and it was only by the measurement of individual ROA bands of the enantiomers of α-phenylethanol, α-phenylethylamin, and α-phenylethylisocyanate by Barron et al. in 1973 [2, 3] that the existence of ROA was experimentally established. The subsequent measurement of the ROA spectra of (+)-α-phenyletylamine and (−)-α-pinene by Hug et al. [4] confirmed these first data and expanded measurements to whole ROA spectra. It is noteworthy to point out that the ROA data reported by Barron et al. actually represent the first observation of vibrational optical activity of molecular origin. VCD of molecular origin was observed in the following year by Holzwarth et al. [5] and was subsequently confirmed by Nafie et al. [6] with higher-quality spectra.

With electronic optical activity, at first ORD and later also CD, routinely measurable for decades, one might ask what the experimental obstacles were which delayed the

Comprehensive Chiroptical Spectroscopy, Volume 1: Instrumentation, Methodologies, and Theoretical Simulations, First Edition. Edited by N. Berova, P. L. Polavarapu, K. Nakanishi, and R. W. Woody.
© 2012 John Wiley & Sons, Inc. Published 2012 by John Wiley & Sons, Inc.

observation of vibrational optical activity until the 1970s. In the case of Raman optical activity, there is a simple answer: the lack of the availability of a sufficiently powerful laser with an appropriate wavelength. It is no exaggeration to state that it was the invention of the argon ion laser which made the experimental demonstration of ROA possible and relatively straightforward. Other helpful technologies that had become available in the 1970s were single-photon counting and KD*P electro-optic polarization modulators developed for the purpose of laser Q-switching.

Early ROA measurements were tedious and prone to offset. The advances that have happened over the past three decades can roughly be divided into three cathegories. The first reflects the general progress in Raman instrumentation, such as optical multichannel detection originally with intensified linear self-scanned diode arrays [7] and more recently with backthinned charge-coupled devices (CCDs) combined with (a) high-luminosity spectrographs with holographic gratings and (b) solid-state lasers that replace gas lasers. The second is the solution of the offset problem ubiquitous in optical activity, in early right-angle scattering by a dual-lens light collection system [8], and more recently in a general way by the creation of a virtual enantiomer [9]. The third are improvements in light collection, sample cells, and sample handling techniques that have allowed a reduction in the amount of substance required down to less than 50 μg in the case of aqueous solutions. Right-angle scattering was supplanted with back- and forward scattering [10–12]. The exclusive modulation of the circular polarization of the incident light, which dominated the first decade of ROA measurements, was complemented by the circular polarization analysis of the scattered light [13–17].

The discussion of these experimental advances will occupy most of the remainder of this chapter. One should not overlook, however, that the theoretical foundations of ROA have also been revised to include novel polarization schemes and the general resonance case [18], with an explicit formulation of the singly excited state limit [19, 20]. There have been various formulations of nonlinear ROA [21–23] which so far have not found practical applications.

6.2. OPTICAL ACTIVITY MEASURED BY LIGHT SCATTERING

Spontaneous light scattering is a two-photon process. In contrast to luminescence, Raman scattering cannot be separated into two consecutive one-photon processes, and the design of an optically active light scattering experiment thus needs to take the properties of the scattering tensor into account. A ROA instrument can be used to conduct an optically active luminescence experiment, but the opposite is not neccessarily true.

The light scattering nature of ROA opens up the possibility of different scattering geometries and polarization schemes for measuring it. This permits the collection of far more information on the structure of a molecule, on the molecule's electronic properties, and on the nature of its vibrations than is possible with a transmission or luminescence experiment. It also complicates the discussion of the measurement of ROA.

We describe in the following the main scattering arrangements and how they relate to the properties of the scattering tensor. The information they provide, and aspects related to offset control, will be addressed in later sections.

6.2.1. Scattering Geometries and Polarization Schemes

The relevant physical quantity in a scattering experiment is the scattering cross section σ. In a light-scattering experiment, it measures the rate at which energy is removed

by scattering from the incident beam of exciting light, relative to the rate at which energy crosses a unit area perpendicular to the direction of propagation of the incident beam. In ROA, where the diastereomeric interaction between left- and right-circularly polarized light with a chiral molecule is measured, the difference scattering cross section $\Delta\sigma = \sigma(\text{left}) - \sigma(\text{right})$ takes this place.

The direct measurement of light scattered into a solid angle $\Omega = 4\pi$ is not feasible in Raman and ROA spectroscopy. In ordinary Raman spectroscopy, $d\sigma(\theta)/d\Omega$ is measured, the differential scattering cross section per unit of solid angle for scattering under an angle θ into an infinitesimally small element $d\Omega$. In ROA, $\Delta d\sigma(\theta)/d\Omega$, the difference differential scattering cross section per unit of solid angle, is used accordingly. In practice, in view of the need to collect a finite amount of light, the use of a substantial solid light collection angle is unavoidable. Experimental data described as, for example, "ROA measured in foreward scattering" thus do not correspond precisely to the theoretical expression pertaining to $\Delta d\sigma(0)/d\Omega$.

The three distinguished scattering geometries are right-angle scattering ($\theta = \pi/2$), backward scattering ($\theta = \pi$), and forward scattering ($\theta = 0$). For each of these scattering geometries there are three basic circular polarization schemes depending on whether the circular polarization of the incident light (ICP, incident circular polarization), of the scattered light (SCP, scattered circular polarization), or of both (DCP, dual circular polarization) is modulated or analyzed. In addition, for ICP the scattered light can or cannot be analyzed with respect to its content polarized perpendicular ($\perp$) or parallel ($\parallel$) to the scattering plane. Likewise, in SCP the incident light can be naturally (n) polarized or linearly polarized perpendicularly or parallel to the scattering plane. In DCP, the left- (right-) circularly polarized component of the scattered light can be detected when the exciting light is left- (right-) circularly polarized (DCP_I), or the circular polarization of the incident and detected light can be opposite (DCP_II) [15, 16]. Outside resonance, DCP_II vanishes, and the information obtained with ICP and SCP is identical.

The indication of the polarization arrangement is part of the notation of scattering cross sections. It is best illustrated by an example. For a SCP experiment with a scattering angle θ undertaken with naturally (n) polarized exciting light, one has

$$^{n}d\sigma_p(\theta)_{\text{SCP}} = \frac{1}{2}(^{n}d\sigma_{p,R}(\theta) + ^{n}d\sigma_{p,L}(\theta)), \tag{6.1}$$

$$-\Delta^{n}d\sigma_p(\theta)_{\text{SCP}} = -(^{n}d\sigma_{p,L}(\theta) - ^{n}d\sigma_{p,R}(\theta)). \tag{6.2}$$

where p indicates the molecular vibration underlying the Raman band one observes. This index is often omitted because the vibrational assignement may not be known in an experiment. The notation is then identical to that for Rayleigh scattering, but the symbols in formulae stand for different molecular quantities.

L and R obviously refer to the left- and right-circularly polarized component of the scattered light. The minus sign in front of $\Delta d\sigma$ has been introduced because molecular properties in optical activity are defined as the quantity measured for left-circularly polarized light minus that for right-circularly polarized light, while in ROA the opposite sign convention was adopted for measured scattering intensities [7, 24, 25]. Outside resonance with electronic transitions, and except for the infrequent cases where the comparison of the sign of a ROA and a VCD band may be of interest (the mechanisms that generate ROA and VCD are not identical), the sign convention adopted for representing ROA data causes few problems. It is a source of confusion, on the other hand, in resonance ROA [19].

Absolute values for differential scattering cross sections [26] are rarely measured in Raman scattering and have not so far been determined in ROA. In most cases, scattered intensities are indicated in what amounts to arbitrary units, such as ADC (analog-to-digital converter) counts or electrons detected by a CCD (charge coupled device) detector. The indication of the exciting power and recording time—which is not neccessarily the actual illumination time of the sample during which the scattered light was collected—is useful for judging the experimental conditions but gives an approximate idea only of the ROA scattering power of a compound. Specifying detected electrons per joule of exciting power for a spectrum recorded with a particular instrument and sample cell does, in principle at least, allow the computation of scattering cross sections, provided that a comparative measurement can be made for Raman bands for which absolute scattering cross sections are known. Optical corrections will have to be made for the index of refraction of the sample, the finite size of the light collection angle, instrumental resolution, and the variation of the detectivity of the instrument with wavelength. Moreover, absolute scattering cross sections are available for molecules in the gas phase while ROA is measured for liquids. Passing from a gas to a liquid profoundly modifies the intensity of Raman scattering [26].

6.2.2. Scattering Cross Sections and Invariants of the ROA Scattering Tensor

In a ROA experiment, the polarization properties of either the exciting light, the scattered light, or both need to be conserved. This requires samples to be optically isotropic on a scale of less than a quarter of the wavelength of the light. The samples measured in ROA therefore are in general liquids, and the scattering cross sections that one measures correspond to molecules for which the spatial orientation has been averaged. They can therefore be expressed through rotational invariants of the ROA scattering tensor. The understanding of the properties of the ROA scattering tensor was crucial for the success of the first observations of ROA [2, 4]. This has remained so for the design of modern ROA spectrometers.

The currently most often used ROA scattering arrangement is SCP collinear scattering. For forward scattering, which depends on all five Raman and ROA invariants and which is thus chosen as example, the theory yields the expressions

$$^{n}d\sigma_p(0)_{\mathrm{SCP}} = K_p(90a_p^2 + 14\beta_p^2)\,d\Omega, \tag{6.3}$$

$$-\Delta^{n}d\sigma_p(0)_{\mathrm{SCP}} = \frac{4K_p}{c}(90aG_p' + 2\beta_{Gp}^2 - 2\beta_{Ap}^2)\,d\Omega, \tag{6.4}$$

where

$$K_p = \frac{1}{90}\left(\frac{\mu_0}{4\pi}\right)^2 \omega_0\omega_p^3 = \frac{10^7}{9}\pi^2\mu_0^2c^4\tilde{\nu}_p^3\tilde{\nu}_0, \tag{6.5}$$

$$\tilde{\nu}_p = \frac{\omega_p}{200\pi c} = \frac{\omega_0}{200\pi c} \pm \Delta\tilde{\nu}_p, \tag{6.6}$$

where $\omega_0 = 2\pi\nu_0$ and $\omega_p = 2\pi\nu_p$ are the pulsations of the exciting and the scattered light, respectively, $\Delta\tilde{\nu}_p$ is the frequency of vibration p and $\pm\Delta\tilde{\nu}_p$ is thus the Raman wavenumber shift (in cm^{-1}), c is the speed of light (in ms^{-1}), and μ_0 is the permeabilty of the vacuum. The notation implies that a single vibrational mode undergoes a transition. The formulae are valid for 0 K. For other temperatures, they have to be modified to include appropriate Boltzmann factors [27].

a_p^2 is the isotropic and β_p^2 the anisotropic invariant of the molecular electric dipole–electric dipole transition tensor $\alpha_{\mu\nu,p}$. aG'_p and β_{Gp}^2 are the isotropic and anisotropic invariants due to the interference terms of this tensor with the electric dipole–magnetic dipole transition tensor $G'_{\mu\nu,p}$, and β_{Ap}^2 is the anisotropic invariant due to the interference term with the tensor $A_{\mu\nu,p} = \varepsilon_{\mu\rho\sigma} A_{\rho,\sigma\nu,p}$, where $A_{\rho,\sigma\nu,p}$ is the electric dipole–electric quadrupole transition tensor and $\varepsilon_{\mu\rho\sigma}$ is the antisymmetric unit tensor of Levi-Civita.

In the Placzek polarizability theory approach, in the far from resonance limit, the transition tensor is written as a molecular electronic tensor $T_{\mu\nu}^e$ effecting a transition between an initial molecular vibrational state $|i\rangle$ and a final state $\langle f|$:

$$T_{\mu\nu,p} \approx \left(\frac{\partial T_{\mu\nu}^e}{\partial Q_p}\right) \langle f|Q_p|i\rangle \approx \left(\frac{\partial T_{\mu\nu}^e}{\partial Q_p}\right)_0 \sqrt{\frac{\hbar}{400\pi c \Delta\tilde{\nu}_p}}, \tag{6.7}$$

where we have additionally assumed that the vibration is described by normal mode Q_p and thus harmonic, that the electrical harmonic approximation holds, and that $f \leftarrow i$ is a fundamental transition. The electronic property tensors have the form

$$\alpha_{\mu\nu}^e = \frac{2}{\hbar} \sum_{j \neq n} \frac{\omega_{jn}}{\omega_{jn}^2 - \omega_0^2} \mathrm{Re}(\langle n|\hat{\mu}_\mu|j\rangle\langle j|\hat{\mu}_\nu|n\rangle), \tag{6.8}$$

$$G'^e_{\mu\nu} = -\frac{2}{\hbar} \sum_{j \neq n} \frac{\omega_0}{\omega_{jn}^2 - \omega_0^2} \mathrm{Im}(\langle n|\hat{\mu}_\mu|j\rangle\langle j|\hat{m}_\nu|n\rangle), \tag{6.9}$$

$$A_{\rho,\sigma\nu}^e = \frac{2}{\hbar} \sum_{j \neq n} \frac{\omega_{jn}}{\omega_{jn}^2 - \omega_0^2} \mathrm{Re}(\langle n|\hat{\mu}_\rho|j\rangle \left\langle j|\hat{\Theta}_{\sigma\nu}|n\right\rangle), \tag{6.10}$$

with $\hat{\mu}_\mu$ and $\hat{m}_\nu$ representing the electric and magnetic dipole operator, respectively, and $\hat{\Theta}_{\sigma\nu}$ the electric quadrupole operator.

Formulae for scattering cross sections for practically important SCP and DCP arrangements are collected in Table 6.1. In the far from resonance case, ICP cross sections are obtained from the SCP ones by multiplying them by a factor of two [28, 29]. The reason for this factor is that in a SCP experiment, scattering into the

TABLE 6.1. Comparison of SCP and $\mathrm{DCP_I}$ Scattering Cross Sections

Scattering Angle	Cross Section	Difference $\frac{}{4(K/c)}$	Sum $\frac{}{K}$
0	SCP, unpolarized	$90aG' + 2\beta_G^2 - 2\beta_A^2$	$90a^2 + 14\beta^2$
	$\mathrm{DCP_I}$	$180aG' + 4\beta_G^2 - 4\beta_A^2$	$180a^2 + 4\beta^2$
π	SCP, unpolarized	$12\beta_G^2 + 4\beta_A^2$	$90a^2 + 14\beta^2$
	$\mathrm{DCP_I}$	$24\beta_G^2 + 8\beta_A^2$	$24\beta^2$
$\pi/2$	SCP, polarized	$45aG' + 7\beta_G^2 + \beta_A^2$	$90a^2 + 14\beta^2$
	SCP, depolarized	$6\beta_G^2 - 2\beta_A^2$	$12\beta^2$
	SCP, unpolarized	$\frac{45}{2}aG' + \frac{13}{2}\beta_G^2 - \frac{1}{2}\beta_A^2$	$45a^2 + 13\beta^2$
	$\mathrm{DCP_I}$	$45aG' + 13\beta_G^2 - \beta_A^2$	$45a^2 + 13\beta^2$
Integral	SCP	$\frac{2\pi}{3}(180aG' + 40\beta_G^2)$	$\frac{4\pi}{3}(180a^2 + 40\beta^2)$

left- and right-circular polarization channel of an instrument is recorded simultaneously, while in an ICP measurement the scattering cross sections for left- and right-circularly polarized exciting light are separately determined and then subtracted. The actual equivalent measurement times for SCP and ICP are, of course, the same. Three measurements with different scattering geometries and polarization schemes are required for determining the three ROA invariants [30].

The persistence of quadrupole contributions in the theoretical expressions for ROA scattering of rotational averages of molecules was originally not well understood because such contributions are absent in the optical activity expressions for transmission. Integral scattering cross sections [28, 29] are included in Table 6.1 because they show that in a scattering experiment, quadrupole interaction likewise does not contribute to the energy difference taken out of the transmitted light by circular intensity differential scattering. While integral ROA scattering cross sections cannot be measured directly, their invariant combination can be obtained as the linear combination $\frac{2}{3}\Delta^{\perp}d\sigma_p(\pi/2) + \frac{1}{3}\Delta^{||}d\sigma_p(\pi/2)$ of a polarized and a depolarized right-angle SCP scattering measurement. Initial interest in this linear combination was the elimination of quadrupole contributions considered computationally demanding [31].

6.2.3. Building Blocks of a ROA Scattering Instrument

ROA instruments share a laser, a spectrograph, and a data acquisition system with ordinary Raman instrumentation. They similarly contain optics for focusing the laser beam into the sample and for collecting Raman scattered light. Such optics has to be carefully optimized in a ROA instrument for not perturbing the polarization properties. Polarization optics is required for creating circularly polarized light (ICP), for analyzing the circularly polarized content of light (SCP), or for both (DCP). Additional polarization conditioning optics for scrambling undesirable polarization components is also needed in order to reduce offsets.

Figure 6.1 gives an overview of a modern SCP backscattering instrument permitting the simultaneous detection of the intensity of the right- and the left-circularly polarized component in the scattered light. Circular components other than those due to the ROA of the sample, as well as components of linear polarization, are undesirable in such an instrument, and the polarization conditioning optics is designed to eliminate them. In a DCP modification of the SCP instrument, the incident light would be modulated between right and left circular. The two arms of the dual arm system in Figure 6.1 will then detect DCP_I and DCP_{II}.

6.3. SCATTERING ZONE, LIGHT COLLECTION, AND SPECTRAL ANALYSIS

Arguably two of the most important aspects of a light-scattering experiment are (a) the formation of the light collection zone and (b) the collection of light from it. The considerations for optimizing both of them are different for right-angle scattering and for collinear scattering. In right-angle scattering, the waist of the focused beam of the laser used to excite scattering is imaged onto the entrance slit of the spectrograph used for analyzing its spectral content, while in collinear scattering it is the light collected from circular cross sections of the beam that has to be passed through a spectrograph's rectangular entrance slit. Different considerations from those discussed in the following would apply if the spectral analyzis would be performed by Fourier transform spectroscopy.

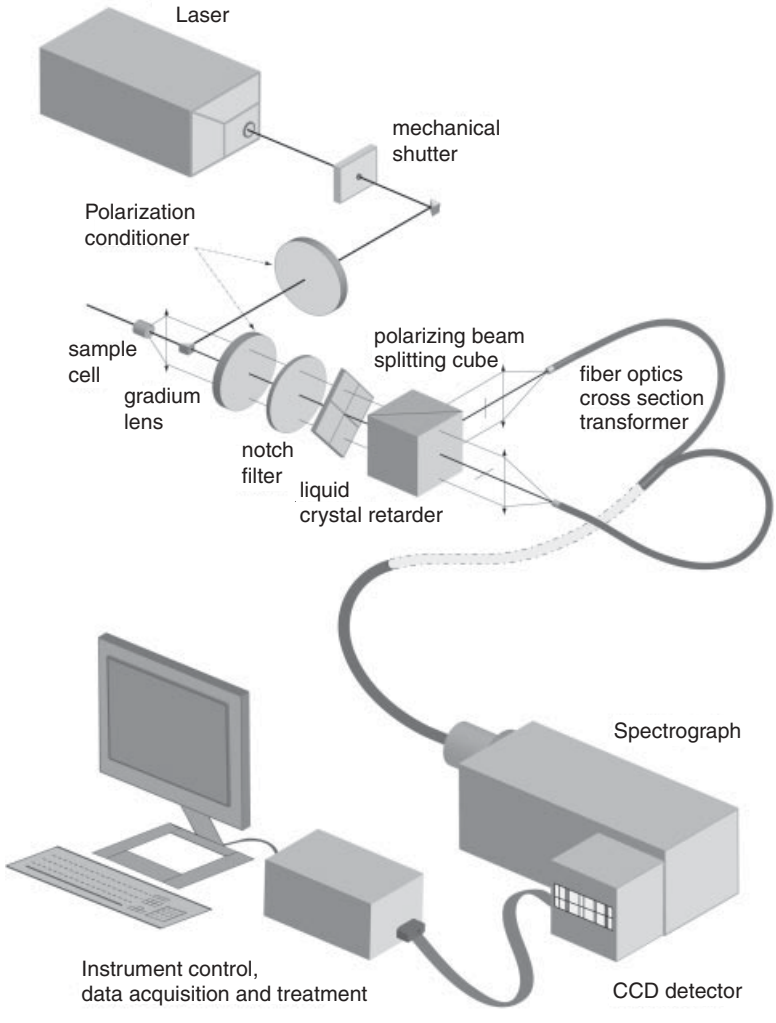

Figure 6.1. Building blocks of an SCP ROA spectrometer.

6.3.1. A Spectrograph Optimized for ROA Scattering

Etendue. As one of the main considerations in ROA is detecting as many scattered photons as possible, a high-throughput dispersive system is required. The luminosity of a spectrograph can be quantified by its étendue, or geometric extent G, which is a measure for the product of the area S of the field stop, in general the entrance slit, and the solid angle subtended at the entrance aperture by the collimator or the dispersing element (whichever is smaller) [32]:

$$G = \pi S \sin^2 \alpha \approx \frac{\pi S}{(2 \times \text{focal ratio})^2}, \tag{6.11}$$

where α is the half-angle of the light acceptance cone with $\text{NA} = \sin\alpha$ the numerical aperture. In the second half of the equation, the usual approximation $2\text{NA} \approx \frac{1}{(\text{focal ratio})}$ is used.

Before the advent of concave holographic reflective and planar holographic transmission gratings, and of steep notch and edge filters obviating the need for dispersive pre-monochromators, it was generally the étendue of the dispersive system which limited the throughput of a Raman instrument. In contrast, the étendue of modern holographic transmission grating spectrographs is so large that the shape of the scattering zone, along with the light collection optics, tends to limit the amount of light which reaches the detector. For calcultating the étendue of the standard Kaiser Holospec which we assume as the base design, the detector width (which determines the slit length) must be known. If we assume a CCD detector with 256 × 1024 square pixels of 26-μm edge length, then the 0.1-mm × 6.656-mm slit (9.5-cm^{-1} resolution with a 2400-lines/mm holographic VPT grating HSG-532-LF, Kaiser Optical) leads to an étendue of 0.16 mm sr ($f = 85$ mm, $f/1.8$ entrance lens, $f = 85$ mm, $f/1.4$ output lens). Hadamard or Fourier transform spectroscopy would thus provide no Jacquinot throughput advantage.

Entrance Speed Optimized for Interfacing. A high output speed is a desirable spectrograph characteristic because it keeps the detector size small. The benefit of high input speed is a reduction of the diameter of the input optics and thus the size and cost of the spectrograph.

A decisive consideration in optimizing the spectrograph design [33] was to facilitate interfacing with the remainder of the optics of the ROA instrument. To this end, the focal length of the entrance optics was increased from 85 mm to 200 mm by the use of a 76-mm-diameter achromatic doublet. The large diameter of the entrance optics renders (if the size of the grating is not taken into account) the $f = 85$ mm, $f/1.4$ output optics the element which determines a $f/3.3$ input focal ratio. The grating size of 53mm × 64mm reduces étendue by cutting off marginal rays, and the actual average focal ratio is slightly better than 4. Because resolution requirements in ROA are modest, the use of a single achromatic doublet does not lead to a noticable degradation.

At 7-cm^{-1} resolution, the entrance slit width amounts to 0.175 mm with the modified optics. With the same 6.656-mm-wide detector as above, the slit length amounts to 15.6 mm and the étendue reaches the same value as for the unmodified spectrograph, albeit at better resolution. An appropriate notch or edge filter has to be used in the external optics because the modified spectrograph lacks such a prefilter.

The reduced entrance speed allows the direct coupling with low focal-ratio degradation fiber optics needed in collinear scattering, and it does not impose the requirement of a high numerical aperture onto the transfer optics of the dual lens light collection optics we describe for right-angle scattering.

Image Distortion. A major disadvantage of a spectrograph with the simple optical layout shown in Figure 6.2, as compared to the concave holographic grating spectrograph [34] used in the first high-throughput ROA instrument [7], is the curved image it creates from a straight entrance slit [32].

For the angles θ and ϕ in Figure 6.2, for rays passing a straight vertical entrance slit at the height of the optical axis (field angle $\alpha = 0$), the dispersion equation holds:

$$\sin\theta + \sin\phi = \frac{m\lambda}{d}, \tag{6.12}$$

where m is the grating order, λ the wavelength, d the spacing between lines on the grating, and ϕ and θ the angles that the wavefront normals of the incoming wave and the dispersed ray, respectively, make with the grating normal. ϕ is fixed and θ

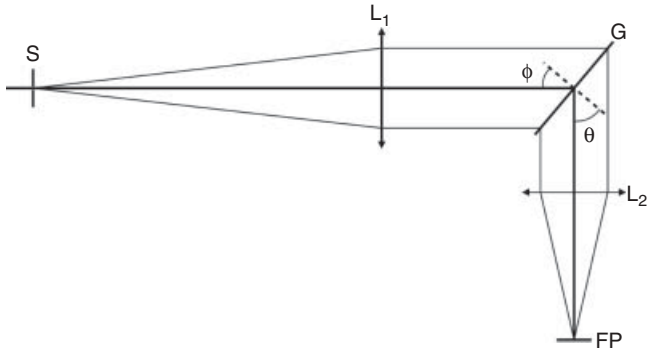

Figure 6.2. Optical layout of the modified holographic transmission grating spectrograph. S, entrance slit; L_1, $f = 200$-mm entrance lens; G, grating; L_2, $f = 85$ mm, $f/1.4$ photographic lens; FP, output focal plane with CCD detector.

varies with λ, with both angles measured in a horizontal plane. Let θ_0 be the the value for a particular λ_0. A ray passing the entrance slit at a different height will have a field angle α. This will cause a deviation $\Delta\theta = \theta - \theta_0$ with respect to the value θ_0 [32]:

$$\Delta\theta = \frac{1}{2}\frac{\sin\theta_0 + \sin\phi}{\cos\theta_0}\alpha^2. \tag{6.13}$$

The equation describes a parabola. It is valid, provided that the slit is short compared to the focal length of the instrument, as the approximation $\frac{1}{\cos\alpha} \approx 1 + (\frac{\alpha^2}{2})$ is used in its derivation, with angles understood to be introduced in radians. The deviation of the slit image from a straight line, and hence its curvature as a function of the field angle α, can be calculated as $\tan\theta$ times the focal length of the output lens, which is 85 mm in our case.

With a 6.656-mm-wide detector, the field angle reaches $\pm 2.25^\circ$. For the standard plane, holographic gratings used with green exciting wavelengths $\phi = 40^\circ$ and $\theta_0 = 50^\circ$ hold at the center of the spectral range projected onto the detector. This leads to a displacement of 0.143 mm at the lower and upper edges of the detector, which must be compared to the 0.075 mm (7-cm^{-1} spectral width) image of the slit on the detector. One notices that $\Delta\theta$ varies with θ_0 and therefore depends on the spectral position.

In ordinary Raman spectroscopy, the curvature of the slit image can be corrected by software, provided that the CDD detector is read pixelwise. In a ROA experiment, where the detector is read hundreds of times in order to attain a sufficient signal-to-noise ratio, the overhead incurred by a pixelwise reading of the detector would inordinately increase data acquisitions times.

There are two practical approaches for solving this problem. The optical one is to use a curved entrance slit that produces a straight-line image on the detector at the center of the observed spectral range [33]. In order to calculate its curvature, the angles ϕ and θ are interchanged. For convenience of manufacturing, the parabola can be approximated by a circular arc with a radius of 108.5 mm. There will remain some curvature at positions off-center; but even at the extreme ends of a typical CCD detector with 26.6-mm length, the degradation of resolution remains acceptable. The software solution is to read the detector in binned slices of different width chosen to combine a sufficient read-out speed with an acceptable loss of resolution. An estimate for loss of resolution with the size of the slices can be found in reference [33].

From Eq. (6.13) it is seen that the slit curvature does not depend on the wavelength at which one is working. This is fortunate as the Raman wavenumber range of about 4000 cm^{-1} is in general covered by two different gratings, with the HSG-532-LF grating cited earlier typically covering a -85- to $+2400$-cm^{-1} range. Provided that the same values of ϕ and θ apply to both, the same compensating curvature of the entrance slit can be used.

6.3.2. Right-Angle Scattering

In order to maximize light throughput, the brightness of the scattering zone and the solid light collection angle must be maximized subject to the following conditions:

- The image of the scattering zone projected onto the entrance slit must fill the slit's length.
- It must not overfill its width.
- The numerical aperture of the spectrograph must be matched.

We assume the same light collection optics as will subsequently be discussed for collinear scattering, namely a $f = 30$ mm Gradium lens with a fast $f/1.1$ speed for collimating the scattered light, followed by a $f = 100$ mm achromatic lens for focusing it onto the entrance slit of the spectrograph. Thin-lens formulae yield a combined focal length of the two lenses of $f = 23$ mm and thus a speed of $f/0.85$. This is about as fast as practical light collection optics can get. The image magnification amounts to 3.3, and the $f/3.6$ cone of collected light projected onto the the spectrograph's entrance slit fills its numerical aperture.

Beam Waist Considerations. For a length of a straight entrance slit of 15.6 mm and a width of 0.175 mm (7-cm^{-1} resolution), the zone in the sample from which light can be collected has a length of 4.73 mm and a width of 0.053 mm. The confocal parameter b_f of the waist of the laser beam focused into the sample should correspond to the length, and the beam's diameter at the ends of the confocal zone, amounting to $\sqrt{2}$ of the value at the center, should not substantially exceed the width. b_f is equal to twice the Rayleigh length and is given by

$$b_f = \frac{2\pi w_f^2}{\lambda}, \tag{6.14}$$

where w_f is the radius of the waist of the focused beam which is close to the ideal value of $0.053/(2 \times \sqrt{2}) = 0.0187$ mm, and λ is the wavelength of the laser light, which we assume to be 532 nm. The radius of a beam with a Gaussian profile (TM00 mode) is generally considered to be equal to the distance from the center to where the intensity has dropped to $1/e^2$ of the center value, with the cross section it describes comprising 86.5% of the beam's power.

The beam waist in the sample is the transform of the waist of the beam exiting the laser, often located at the output mirror. The considerations for generating it by beam transfer and focusing optics can be simplified by making the assumptions that the waist of the beam entering the focusing lens has a Rayleigh length substantially larger than the waist's distance from the lens' entrance focal point and that this Rayleigh length is far larger than the lens' focal length. Conversely, for the beam leaving the lens, one assumes the Rayleigh length of the waist to be small compared to the focal length of the lens.

The focus region is then treated as a point source when looking backward to the lens. One finds that the new beam waist created by the lens is located at its image-side focal point, and the confocal parameter b_f and the radius w_f of the waist are related by

$$d = 4f\frac{w_f}{b_f}, \tag{6.15}$$

where f is the focal length of the lens and d is the diameter of the beam when entering the lens. Results from Eq. (6.15) are approximate for finite values of b_f. Small deviations in the waist's position can easily be corrected by slightly displacing the lens. With $w_f = 0.020$ mm, $b_f = 4.73$ mm, and an $f = 50$ mm focusing lens, a value of 0.79 mm follows for d.

Practical working distances between the output mirror of the laser and the sample cell are of the order of 1 m or more in a ROA instrument. The change of the beam's radius $w(z)$ as a function of distance z from the waist w_0, assumed to be located at the output mirror, is given by

$$w(z) = w_0\sqrt{1 + \left(\frac{\lambda z}{\pi w_0^2}\right)^2}. \tag{6.16}$$

One readily finds that there is no value for w_0 which for $z = 1000$ mm yields $d = 2w(z) = 0.79$ mm. Thus, either beam transfer optics must be employed or the requirements for the confocal length in the sample must be reduced.

Dual Lens Light Collection and Sample Considerations. Figure 6.3 shows a dual lens light collection system that allows filling the spectrograph's étendue with a beam waist of half the length discussed above. This yields a value of $d = 1.58$ mm and requires a diameter of the beam leaving the laser of about 1.5 mm, with the possibility of adjusting this value by varying the focal length f of the focusing lens.

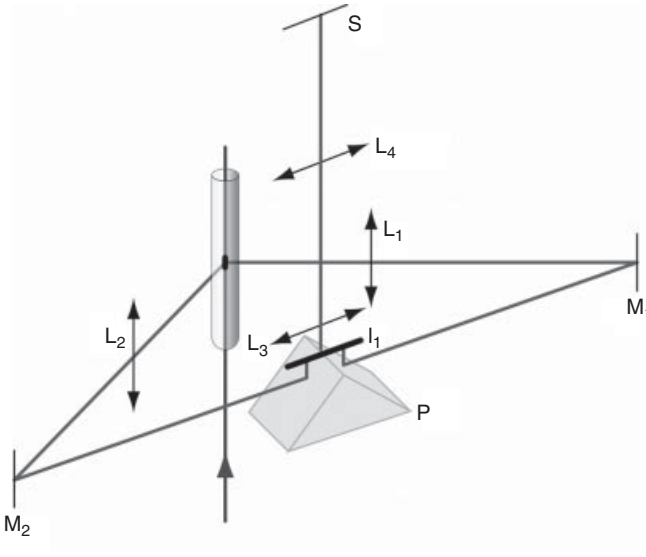

Figure 6.3. Dual lens light collection system for right-angle scattering. L_1 and L_2, light collection lenses composed of an $f = 30$-mm Gradium lens and an $f = 100$-mm achromatic doublet; I_1, intermediate image; P, mirrored prism; L_3, field lens; L_4, lens for focusing I_1 onto the entrance slit S of the spectrograph.

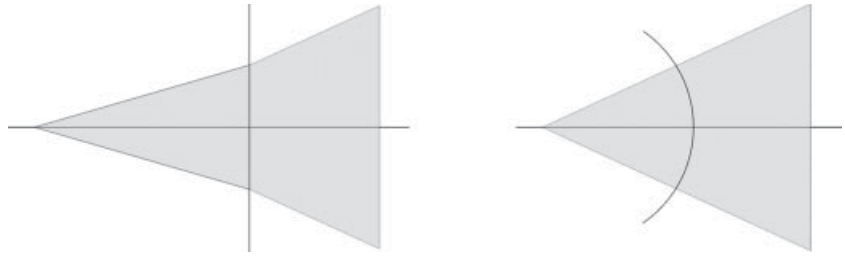

Figure 6.4. Light collection cone inside a flat-window sample cell and a capillary, in the plane perpendicular to the capillary's axis.

A further advantage of a smaller collimated segment needed in the sample is a reduced sensibility to thermal lensing, which is a problem for samples that show a tiny amount of absorption. In the case of a planar grating spectrograph suffering from image distortion, a dual lens light collection system can be adapted so that the directions of the line images formed by the two lenses are not collinear but parallel to the tangents of two halfs of a curved entrance slit.

The measurement of ROA in right-angle scattering has some definite advantages over collinear scattering. For one, it requires a smaller sample volume if a capillary is used as the sample cell: Its diameter does not need to be much larger than the waist of the laser beam from which light is collected [4], with a length of barely 2.5 mm, and the capillaries' cylindrical surface increases the brightness of the image, as compared to a flat surface cell (see Figure 6.4). For another, the danger of collecting Raman light and light due to fluorescence of the windows of the sample cell is negligible compared to collinear scattering. And last but not least, the lack of the need of a fiber-optics cross-section transformer eliminates an important source of loss of light, so that light throughput is higher with a dual-lens system than can be achieved in collinear scattering. The main drawback, which matters for the measurement of solutions, is the smaller ratio of ROA to Raman scattering for depolarized Raman bands, as compared to backward scattering (see Table 6.1).

Except for size, sample considerations are similar in right-angle and collinear ROA scattering. The samples need to be nonfluorescing transparent isotropic liquids. Solutions have to be reasonably concentrated due to Raman spectroscopy's limited dynamic range, which translates to a few percent for aqeuous solutions and 10% or more for a solvent such as acetonitrile. The measurement of suspensions of particles smaller than a quarter of the wavelength of the exciting light might be possible but has not yet been demonstrated.

6.3.3. Collinear Scattering

The backscattering geometry yields the highest ratio of ROA to Raman scattering. For depolarized Raman bands, this ratio is similar for SCP, ICP, and DCP_I. The suppression of isotropic Raman contributions in DCP_I can sizably enhance the ratio for strongly polarized bands (Table 6.1), though such bands also tend to carry little ROA information. In forward scattering, on the other hand, the ratio favors DCP_I for depolarized bands for which a^2 and aG'_p vanish. The throughput that can be achieved with the same spectrograph and detector in collinear and right-angle scattering is compared in Table 6.2.

As compared to right-angle scattering, the demands for the quality of the waist of the beam focused into the sample are lesser, and TM00 operation of the exciting laser is

TABLE 6.2. Comparison of Collinear Dual Arm and Right-Angle Dual Lens Light Collection

	Polarization Scheme	Throughput Gain	$1/f$ Noise Gain
Dual arm, collinear	SCP	—	√
	DCP_I static	—	—
	DCP_I switched[a]	—	√
Dual lens, right angle	SCP	—	√
	ICP static	√	—
	ICP switched[a]	—	√
	DCP_I static	√	—
	DCP_I switched[a]	—	√

[a] "Switched" means switching of scattered light between CCD halves for incident polarization states, see Section 6.5.

not required. Multimode beams are less prone to trapping particles in their center by the optical tweezer effect than are TM00 beams.

The Role of Fiber Optics. The first backscattering ROA instrument used the ICP scheme and fiber optics optimized for matching the large étendue of a concave holographic grating spectrograph [10]. If matching is not carefully done, focal-ratio degradation will lead to a loss of light, and a number of later instruments used direct coupling [11, 12]. Because far higher throughput can be achieved in collinear scattering with well-designed optics, the instrument depicted in Figure 6.1 is based on fiber optics. In the case of SCP, fiber optics also permits an elegant simultaneous detection of left- and right-circularly polarized scattered light. It is unlikely that other cross-section transforming optics, such as holographic optical elements, might accomplish this dual function.

The fibers form the curved entrance slit of the spectrograph. Two groups of 31 low numerical aperture (NA = 0.22) fibers with a diameter, including buffer, of 0.245 mm are separated by a 0.3-mm spacer, yielding a slit of 15.5-mm length. The active surface due to the core of 0.215-mm diameter of the fibers amounts to 2.25 mm^2, which is 69% of the surface. Without cladding, if the fibers would be joined core by core, an object of 13.33-mm length would result. The average width of the active surface therefore amounts to 0.169 mm and yields the desired resolution of about 7 cm^{-1}. Bends in the fibers below a 200-mm radius are to be avoided in order to avoid focal ratio degradation. Shallow right-angle bends in orthogonal planes are used to achieve a substantial depolarization of the transmitted light. A discussion on how best to arrange the fibers from the slit-like end on the circular entrance ends can be found in reference [33].

Scattering Zone and Light Collection. Figure 6.5 shows a combined back- and forward-scattering arrangement. The waist of the laser beam is createt by an $f = 100$-mm achromat at the common focus of two fast $f = 30$-mm, $f/1.1$ Gradium lenses. The beam passes through a hole in the lens which collects the backscattered light. This permits different focal lenths for focusing and collecting light and allows a better adjustment of the beam waist of the transverse multimode disk laser used in the instrument. It also avoids undesirable Raman scattering in the light collection lens, which can be a problem when very weakly scattering samples, such as gases, are measured.

Light collected from the center of the focused beam is collimated by the Gradium lenses. After passing an edge filter and the circular polarization analyzer, it is focused

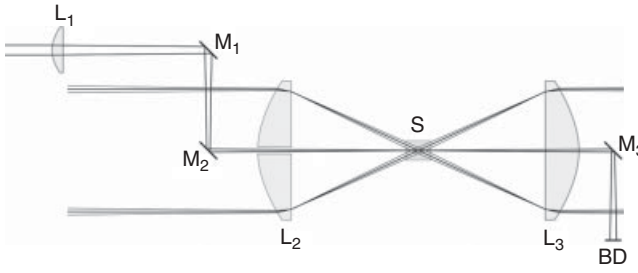

Figure 6.5. Combined forward and backward scattering arrangement. L_1, lens focusing the laser beam into the the sample S; L_2 and L_3, $f = 30$-mm Gradium light collection lenses; M_1 and M_2, turning mirrors for deviating the exciting laser beam in two orthogonal planes; M_3, mirror deviating the beam into the beam dump BD.

for each scattering direction by two $f = 100$-mm achromats onto the approximately circular ends of the two tails of a fiber-optics cross-section transformer. As discussed for right-angle scattering, the ratio of the focal lengths of the Gradium lenses to that of the achromats yields an $f/3.6$ cone to fill the numerical aperture of the spectrograph.

Either the exciting light or the scattered light needs to be deviated in a backscattering instrument. In an ICP experiment it is preferable to deviate the scattered light, while in an SCP experiment it is the deviation of the incident light which is less critical with respect to polarization conservation. Polarization changes can further be minimzed by combining two right-angle deviations of the laser beam in orthogonal planes, and the two deviations schematically indicated in Figure 6.5 are chosen this way.

The light collection optics is nonimaging. Light is collected, for either backward or foreward scattering, from a volume of two cones intersecting at the center of the the light collection zone. Figure 6.6 depicts a cut through it for a cell with flat windows and assuming the index of refraction of the sample to be that of fused quartz ($n = 1.47$). One cone extends to the light collection lens, whereas the other extends, in principle, to infinity. It is for this reason that forward and backward ROA scattering cannot be simultaneously measured. Light collection for one of the two lenses in Figure 6.5 has to be blocked because otherwise light reflected back from one of the collection channels tends to causes offsets in the other.

The radius at the locus where the cones of light collection intersect corresponds to the image of the round-fiber optics ends formed backwards by the light collection optics. In a diamond-shaped central zone, light with a solid angle filling the 27.3-mm diameter of the $f/1.1$ Gradium lens is collected. Outside this boundary, collection efficiency falls off. On-axis collection is blocked by the small mirrors used to deviate the exciting laser beam.

Figure 6.7 shows the measured dependence of the light collection efficiency on the longitudinal position of the sample [35]. The "sample" used for this test was a 0.17-mm-thick microscope cover glass. Its thickness is not neglegible and its index of refraction slightly modifies optical paths, but the qualitative agreement with theoretical expectations is satisfactory.

Sample Cells and Sample Size. In collinear scattering, the shape of the light collection zone leads to the collection of light due to Raman scattering and fluorescence from the windows of the scattering cell. The shorter the cell and the thicker its windows, the more pronounced this problem becomes. Relatively large amounts of substance are further required for low offset as the cone of scattered light has to be able to leave the sample without polarization degradation, and the required sample volume therefore tends to increase with the third power of the length of the cell.

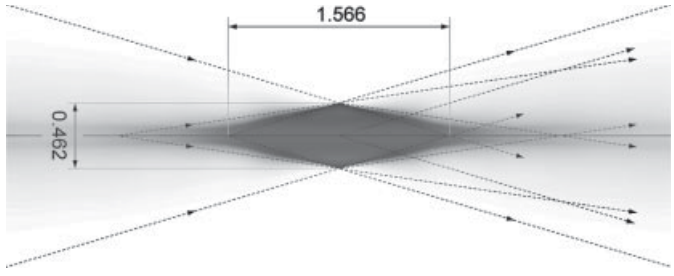

Figure 6.6. Light collection from the scattering zone in a collinear experiment. Light is collimated by an $f = 30$-mm Gradium lens as in Figure 6.5 and is then focused onto the circular entrance ends of the fiber-optics cross-section transformer by an $f = 100$-mm achromatic doublet. The index of refraction of the sample is assumed to correspond to that of quartz.

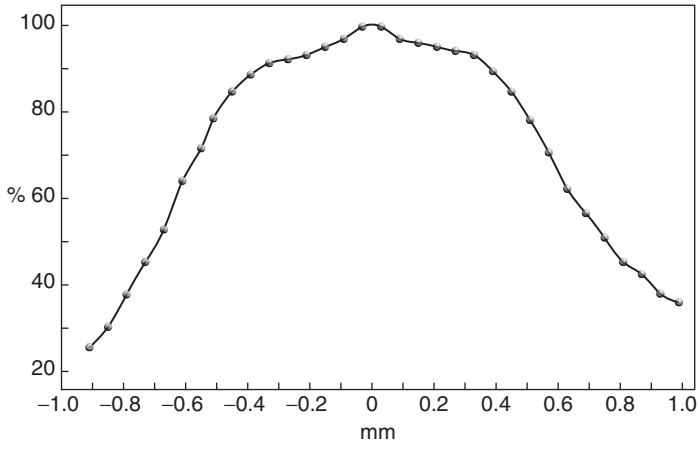

Figure 6.7. Measured longitudinal dependence of collection of Raman light from the 920-cm^{-1} band of a 0.17-mm thick microscope cover glass slide. The spectrum corresponds to that of the Teflon cell in Figure 6.8.

Figure 6.8 shows Raman and fluorescence spectra from empty cells with the light collection zone placed at their center. The fused quartz cell (Hellma) of 5-mm pathlength depicted in Figure 6.9 produces the smallest background signal, despite its 1-mm-thick windows. Its volume of 35 μL is also the largest one, and its diameter-to-length ratio of only 0.6 can lead to small offsets due to the collection of Raman-light-reflected multiple times from the boundaries of the sample volume. Placing the focus of the light collection optics deeper than halfway into the cell avoids this but increases light collection from the back window. The cell made from black Teflon, also shown in Figure 6.8, has a volume of only 21 μL. Its pathlength of 3 mm, its black side walls, and its diameter-to-length ratio of 1 reduce the collection of light-reflected multiple times. Its more closely spaced glass windows, though only 0.17 mm thick, produce a larger signal than the windows of the quartz cell.

The spectra of two empty glass capillaries of 1.46- and 1.21-mm inner diameter shown in Figure 6.8 demonstrate the influence of glass on parasitic light. The thinner-walled melting point capillary produces a higher background signal than does the disposable precision capillary pipette tip ("minicaps," Hirschmann). The 20% smaller diameter of the melting point capillary is partly responsible for this, but it cannot explain either the extent of the increase or the change in shape of the parasitic signal.

Of practical importance is the ratio of the parasitic signal of the cell to the Raman signal of the sample. Compared to the Raman intensities of the chiral compounds of interest in ROA, the intensities of the spectra in Figure 6.8 are weak. In Figure 6.10 the spectra of a 5% solution of ascorbic acid in water, measured in the quartz cell and in the precision capillary of Figure 6.8, are compared. For the capillary, the contribution of the glass envelope can be identified below 500 cm^{-1} in the Raman spectrum but does not lead to

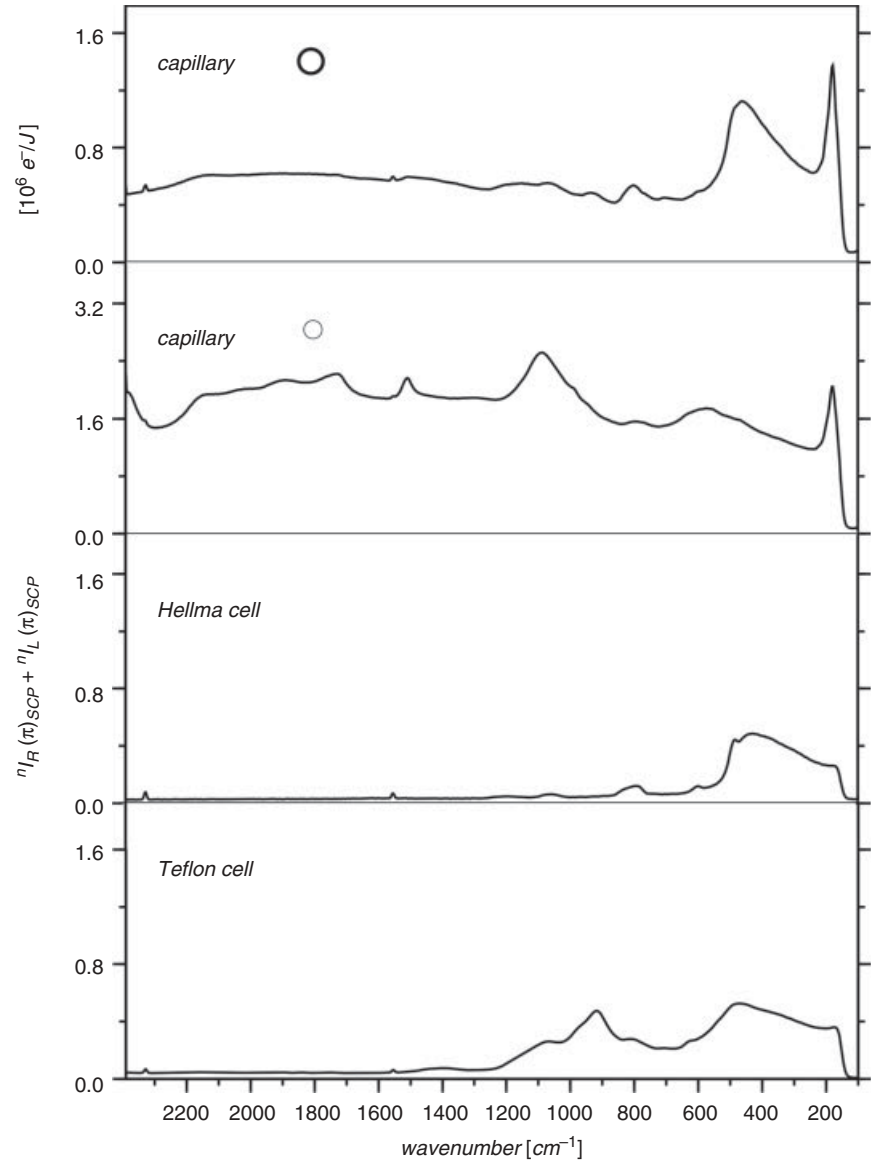

Figure 6.8. Spectra of different sample cells. From top to bottom: Precision capillary ID = 1.46 mm, OD = 1.85 mm. Melting point capillary, ID = 1.214 mm, OD = 1.250 mm. Precision quartz cell with 5-mm pathlength and 1-mm-thick windows. Black Teflon cell with 3-mm pathlength and 0.17-mm-thick windows.

an offset in the ROA spectrum. For the fused quartz cell, a parasitic signal cannot be identified. In addition to the expected smaller size of the parasitic signal, the Raman and ROA signals of the sample are larger than those measured in the capillary. The reduction in scattering intensity of about 50% is typical for water solutions measured in capillaries of the kind shown in Figure 6.8. The decrease in signal strength is less pronounced for

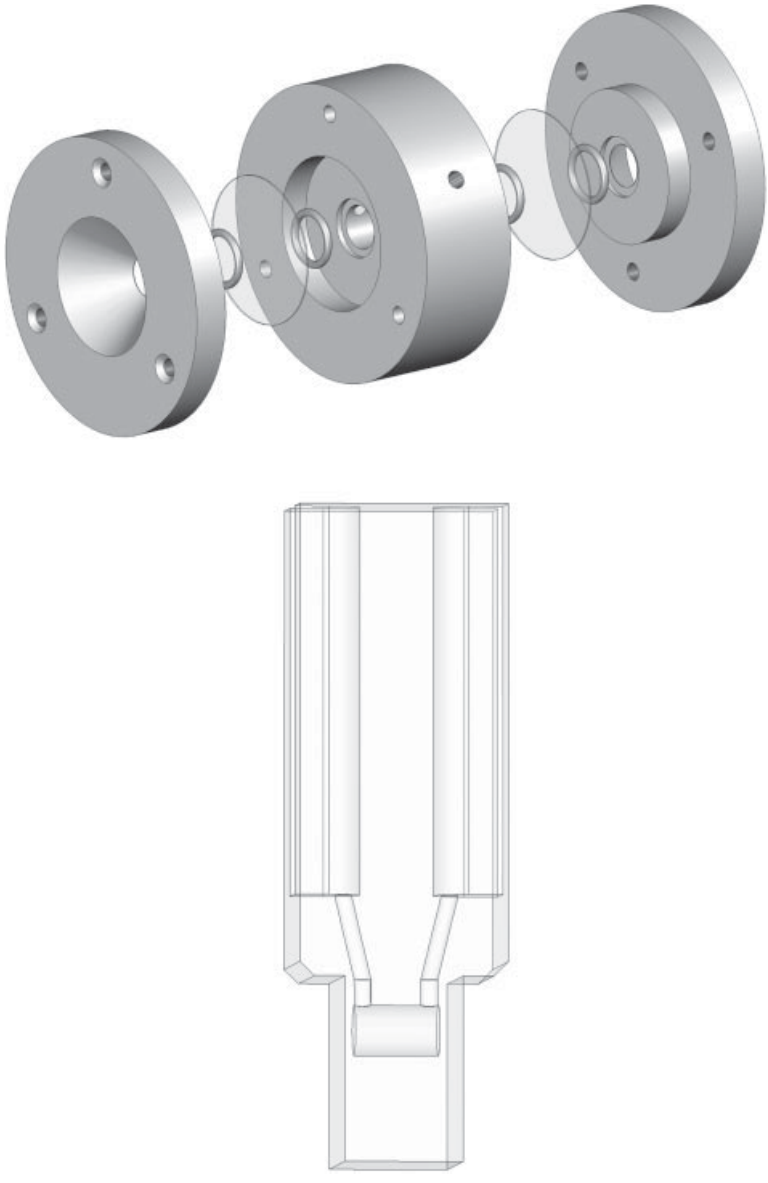

Figure 6.9. 35-μL precision quartz cell (bottom) and exploded view of black Teflon cell (top) with microscope cover glass windows. Joints are black Kalrez.

compounds with higher indices of refraction because the cylindrical surface of the capillary then provides more of an advantage over flat windows (see Figure 6.4).

Offset free collinear measurements in capillaries require a length of the column of the liquid about twice the capillaries' inner diameter [35]. This translates into about 100 μg of substance if a 5% solution is used in a 1.46-mm-diameter capillary. If small offsets are not a concern, a situation that is often encountered in the determination of absolute configurations, smaller-diameter capillaries and liquid volumes of 1 μL or less [36] are possible in backscattering.

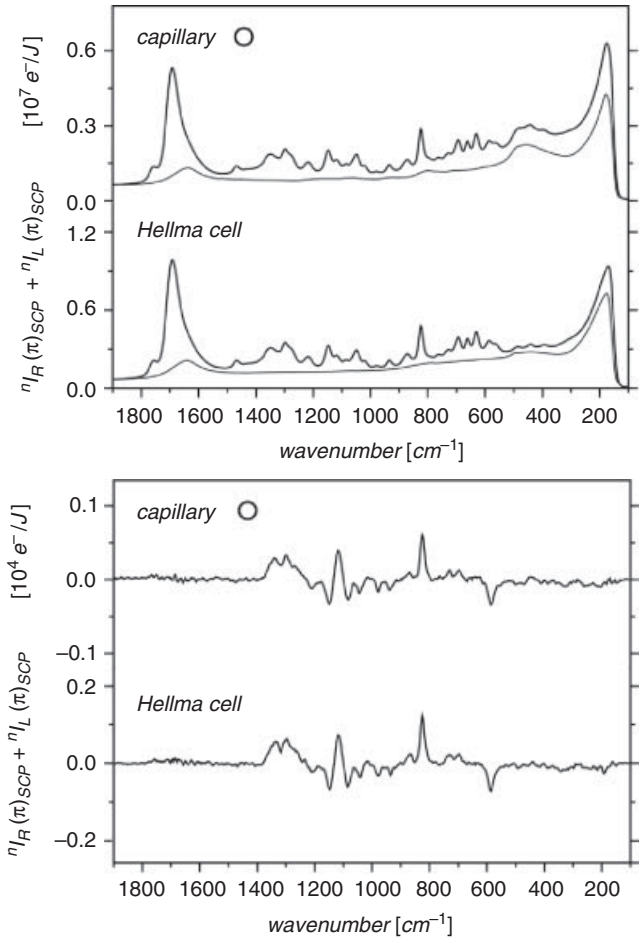

Figure 6.10. Backscattering spectra of a 5% by weight solutions in water of ascorbic acid (vitamin C) measured in the precision capillary and quartz cell. Top: Raman spectra with indication of background by cell material and solvent. Bottom: SCP ROA spectra. Illumination time for both cases: 60 min with 500 mW of laser power. The curves were smoothed with a third-order seven-point Savitzky–Golay procedure.

6.4. SIGNAL DETECTION AND NOISE

Signal-to-noise problems have been a companion to ROA since its inception. The first recording of an entire spectrum and not just individual bands with an optical single-channel instrument typically took several weeks [4], with beam walk-off of the exciting laser, stability of the polarization modulation, and stability of the sample posing major problems for such extended measurement times. While shot noise is the reason for the long recording times, two distinct additional noise sources matter in a ROA experiment, namely flicker noise and deterministic offset. Deterministic offset will be discussed in the section on polarization control because it is related to the polarization properties of the light.

6.4.1. Noise

Shot Noise. The two root causes for the shot noise problem of ROA are the weakness of the Raman effect and the fact that optical activity represents the difference of two much larger quantities. The ratio of ROA to Raman scattering is generally less than 1 part in 1000. A typical value of the number of detected Raman photons, per joule

of exciting energy passed through the sample, is 2.6×10^7 for the medium to strong band due to the carbonyl stretch vibration of 3-methylcyclohexanone. This value refers to a 2.4-cm^{-1}-wide window representing one column on the CCD detector at the peak of the band. The geometry is backscattering with the instrument shown in Figure 6.1 equipped with the spectrograph of Figure 6.2, and with an exciting wavelength of 532 nm. Measured at a resolution of 7 cm^{-1}, the band has a full width at half-maximum height of 25 cm^{-1} or about 10 columns on the detector.

The Raman signal corresponds to $N_R + N_L$, where N_R and N_L are the number of detected photons for right- and left-circularly polarized scattered light, respectively. The root mean square shot noise for their sum and difference is $\sqrt{N_R + N_L}$. In order to detect the ROA signal of the band, which has a ratio $\Delta = \frac{N_R - N_L}{N_R + N_L} \approx 10^{-5}$, at least 10^{10} photons per column of the CCD must be detected. If the laser power passing through the sample amounts to 250 mW, this means a measurement time of 26 minutes, not counting read-out time of the detector.

It is illustrative to consider the laser power that one would need at other exciting wavelengths. We disregard differences in the quantum efficiency of the detector and in the throughput of the spectral analyzing system and solely consider the wavelength dependence of the Raman and ROA scattering cross sections. For Raman, if we neglect the difference between the frequency of the exciting and scattered light, then cross sections vary like the fourth inverse power of the wavelength of the light. For a detector yielding a signal proportional to the number of detected photons, the exciting laser energy required for a constant signal therefore varies as the third power of the wavelength. Thus, we will need an exciting laser power of approximately 2 W at 1064 nm and 32 mW at 266 nm. In ROA we have to take the variation of the Δ-ratio with the wavelength into account. For a band with $\Delta = 10^{-5}$ at 532 nm, one will have $\Delta = 5 \times 10^{-6}$ at 1064 nm and $\Delta = 2 \times 10^{-5}$ at 266 nm, which translates into 8 W and 8 mW, respectively.

Required laser power is just one criterion of many for the measurability of ROA. Sample decomposition by photochemistry or heating, fluorescence, and offset problems are others. Ample power is easily available, for example, at 1064 nm from undoubled YAG lasers but appropriate detectors for optical multichannel spectroscopy are not. Fourier transform spectroscopy can provide the Fellgett (multiplex) advantage of dispersive optical multichannel systems. However, it cannot alleviate the sample heating problem due to the absorption of overtones of stretching vibrations involving hydrogen atoms.

Flicker Noise. In contrast to shot noise, which has a white power spectrum and increases like the square root of measurement time, flicker noise, often also called $1/f$ noise, increases with decreasing frequency f. In clock works, after the elimination of all deterministic drifts, there remains an error due to flicker noise that is known to increase at least linearly with time [37]. This makes flicker noise one of the most vexing problems in ROA measurement as it tends to lead to slow, drifting offset in ROA spectra.

Though flicker noise is a generally observed penomenon in nature, its origin is not well understood. In ROA, there are many potential sources of flicker noise. Obvious ones are instabilities of the laser source, density fluctuations in the sample due to local heating by the laser beam, and oscillating dust particles trapped in the beam by the optical tweezer effect.

There are two ways to combat the effect of flicker noise. Either one can use a frequency above the onset of $1/f$ noise for switching between right- and left-circular polarization of the exciting light in ICP and DCP, or one can simultaneously measure the intensity of both in SCP. In view of the read-out time of the detector, either approach

requires the subdivision of its surface into two halves, sacrificing half of the etendue of the spectrograph. Table 6.2 compares the different options for right-angle and collinear scattering.

6.4.2. Detectors

Early optical multichannel systems relied on image-intensified low-light-level television tubes. Image distortion, low geometric stability, low stability of the sensitivity, a small dynamic range, blooming, and read-out lag rendered them unsuitable for providing Fellgett multiplexing gain to ROA spectroscopy. The use of linear self-scanned diode arrays rectified many of these deficiencies. They made the multichannel recording of good-quality ROA spectra [38] possible with image intensification, while the recording of ordinary Raman spectra was made possible without intensification [34, 39]. Limitations were the relatively high read-out noise and the small width of self-scanned diode arrays.

Modern back-thinned charge coupled device (CCD) detectors combine the high sensitivity and stability of self-scanned diode arrays with a lower read-out noise and a larger light-sensitive area. The CCD 30-11-0-232 (EEV) detector used in reference 33 has 256 × 1024 pixels with a 26-μm square shape providing a 6.656-mm × 26.624-mm light-sensitive area. Quantum efficiency can exceed 70% in the yellow spectral range, and deep depletion can extend good quantum efficiency into the red and near infrared. Because the goal in ROA is to register as many photons as possible rather than to detect individual photons, the low read-out noise of CCDs obsoletes image intensification. Exposure times are of the order of a few 100 ms to a few seconds. Thermoelectric cooling therefore suffices for reducing charge loss by dark current.

Illumination of the CCD creates a charge pattern that is treated as 256 lines of 1024 pixels each. The charge of a pixel is read by shifting the whole pattern over the width of the CCD, line by line, into a read-out register of 1024 cells. For a shifted line, the charges of the 1024 cells of the register are clocked out, converted into a voltage, and then analog-to-digital (A/D) converted. Because this is a relatively slow process, on-chip binning is used to move the charge of several lines, combined into a single slice, into the read-out register, before reading and A/D converting it. Charge removal by reading the CCD only once is far from complete, and additional charge clearing cycles, without A/D conversion, are required.

Typical parameters for A/D conversion are a 16-bit resolution with one bit set to the charge of 10 electrons. The full-scale charge of 655,360 e^- matches the capacity of the read-out register, and the 16-bit resolution avoids aliasing and thus potential spurious ROA signals for low-intensity Raman bands.

The saturation charge of individual pixels is a few hundred thousand electrons. The value depends on the design of the CCD and strongly on its mode of operation. The cells of the read-out register can hold a somewhat larger charge, which remains for the quoted CDD below the A/D converters maximum capacity. For the instrument described in reference [33], rms read-out noise amounts to a mere 15 electrons for each address of a slice, even if the slice is read in as little as 5 ms. In comparison, read-out noise (including charge resetting and fixed pattern subtraction) is about 1000 electrons per address for reading the whole of a CMOS linear self-scanned diode array used in earlier instrumentation in a mere 20 ms [7]. Such a diode array has about one-third of the surface of the CCD, and each address can hold about two-thirds of the saturation charge of an entire column of 256 pixels of the CCD.

Saturation charge of individual pixels and of the read-out register are limiting parameters in a ROA instrument: Overloading either of them leads to offset through nonlinearity

and blooming, with charge flowing uncontrollably into adjacent cells. The presence of a strong Raman band requires reducing exposure in order not to saturate individual pixels. Reduced binning to protect the read-out register makes reading of the CCD even slower. Blocking light from known strong solvent bands from reaching the detector, by optical filters or mechanical stops, is possible but cumbersome. Modern backthinned CMOS diode arrays with less sensitivity to overload might make an eventual comeback as a solution to CCDs' unsatisfactory dynamic range. An added advantage would be their higher quantum efficiency in the red, making the deep depletion required for CCDs, with its increased sensitivity toward cosmic particles, unneccessary.

In the SCP instrument of Figure 6.1, the surface of the CCD is treated as two halfs of 128 lines each for registering the intensity of left- and right-circularly polarized light. The charge of the two halves must be shifted over a different number of addresses into the read-out register. Interchanging the function of the two branches of the instrument, as described in the section on polarization modulation, eliminates this source of offset.

6.5. POLARIZATION CONTROL AND DETECTION

Precise polarization control is one of the most important aspects of the measurement of ROA as the determination of scattering differences for left- and right-circularly polarized light down to the 10^{-5} level of their sum is required. At first sight, this appears to be best achievable by determining the ellipticity of the scattered light. In practice, the determination of the scattering difference via an intensity measurement has proved more efficient because nulling for establishing a baseline is not needed.

6.5.1. Circular Polarization Modulation and Analysis

The circular polarization analyzer in a SCP instrument consists of a polarizing beam-splitting cube preceded by a quarter-wave plate with its axes oriented at $+45^\circ$ and -45° to either the *s* or *p* polarization direction of the cube. Circular polarization is generated in ICP and DCP instruments by the inverted arrangement—that is, a linear polarizer preceding a quarter-waveplate or a Fresnel rhomb. Modulation is required between right and left circular in ICP and DCP, so either (a) the axes of the quarter-waveplate have to be interchanged or (b) the linear polarization incident on it needs to be rotated by 90°.

In current instruments, switching of circular polarization states is synchronized to the CCD read-out cycle, which requires modulation periods of 100 m or more. This precludes the use of photoelastic modulators otherwise common in optical activity measurements.

Exciting Light. KD*P (potassium dideuteriumphosphate) modulators representing quarter-wave plates with electrically interchangable fast and slow optical axes have been the modulators of choice in ICP instruments [2, 4]. One of their disadvantages is the high modulation voltage they require, of the order of 1.5 kV for light in the green wavelength region; another disadvantage is the temperature dependence of their retardation. Temperature dependence is likewise pronounced for switchable liquid crystal retarders (LCR). They exhibit, moreover, a transmission change of about 2 parts in 10^3 for the two switching states [33] which has to be compensated. Switching of LCRs is slow and needs to be done during the read-out time of the CCD detector. Optomechanical approaches for the circular polarization modulation of the exciting light in ICP and DCP are rotating a quarter-waveplate in linearly polarized light, or moving a half-waveplate into and out of circularly polarized light.

Scattered Light. The transmission difference of the two switching states of LCRs is of little consequence in the SCP instrument shown in Figure 6.1 because switching here merely serves the purpose of interchanging the functions of the two arms of the instrument, with one carrying the information of the intensity of the left- and the other that of the right-circular component of the scattered light. The limited precision of LCRs—the retardation can vary over their aperture, and the induced optical axes are not precisely aligned for the two switching states—would, however, make them unsuitable as parts of the circular polarization analyzer if it were not for the additional polarization conditioning optics of the instrument.

The large acceptance angle of LCRs is a potential advantage over other switchable retarders for analyzing scattered light. It is not actually required in the SCP instrument of Figure 6.1, because deviations of the collimated light from the direction of the optical axis are kept below 1° by design, in order to match the small acceptance angle of the polarizing beamsplitting cube of the circular polarization analyzer. Large-aperture KD*P retarders, which can be manufactured to closer tolerances, and which have smaller retardance oscillations [9] and higher switching speeds than LCRs, might increase measurement precision. They were avoided because of their large size and their high voltage requirements.

6.5.2. Polarization as a Source of Deterministic Offset

One can distinguish offset caused by the electronics and the optics. Placing a signal amplifier or A/D converter into close proximinity to a voltage synchronized with the acquisition cycle is bound to lead to electronic offset. The origin of optical offsets ranges from an intensity modulation of the exciting light through backreflection of light into the laser cavity, synchronized to the data acquisition cycle, to polarization interconversion by optical elements yielding an excess of right- or left-circular light unrelated to the ROA of the sample.

We limit the discussion here to polarization related deterministic offset. On the one hand, it has in the past been the most awkward one to deal with; and on the other hand, it has found a conceptual solution by scrambling linear and circular polarization components.

Linear Polarization Scrambling. Linear polarization of the exciting or of the scattered light is prone to create offsets in a SCP instrument. Stray bifrefringences in optical elements, as well as reflections under oblique angles from mirrors, the surfaces of lenses, and the walls of the sample cell, tend to convert linearly into elliptically polarized light. The circular polarization analyzer itself is likely to exhibit linear polarization dependence that likewise results in a spurious ROA signal.

Linear components can similarly lead to offset in an ICP experiment. Imperfections of the circular polarization modulator entail elliptically instead of precisely circularly polarized exciting light, and circularly polarized light can become elliptical through birefringences and reflections in the optical train. The axes of the ellipses will not, in general, have the same size and orientation for the left and right modulation period. This can lead to offset through the polarization sensitivity of the spectrograph and, in a polarized right-angle scattering experiment, the properties of the Raman scattering tensor.

Dual Lens Light Collection. Described earlier in the context of optimizing light collection in right-angle scattering, dual lens light collection (Figure 6.3) can also eliminate

the influence that linearly polarized components in the incident light have on scattered intensities in an ICP experiment [8]. With respect to polarization, dual lens light collection is equivalent to collecting light in a circle around the sample. This amounts to an effective scrambling of the linear polarization information of the exciting light.

Lyot Depolarizer. Lyot depolarizers are not ordinarily usable for narrow bandwith light such as that of an individual Raman band. By placing them into the divergent light ahead of the light collection lens [10], an effective scrambling can be achieved of linear as well as circular polarization components. Such an arrangement was successfully used in the recording of collinear ICP scattering [11, 12].

Linear Rotators. A half-waveplate rotates the plane of polarization of linearly polarized light by twice the angle it makes with the plate's fast axis. If the plate is rotated, the plane of polarization rotates with twice its speed. Formally, the time-averaged result of the action of a regularly rotating half-waveplate on light described by the Stokes vector $\boldsymbol{S} = (I, P_1, P_2, P_3)$ can be expressed as the product

$$\langle \boldsymbol{S} \rangle = \langle \boldsymbol{L} \rangle \boldsymbol{S}, \tag{6.17}$$

where $\langle \boldsymbol{L} \rangle$ is the time-averaged Mueller matrix [9] of the rotating half-waveplate given by

$$\langle \boldsymbol{L} \rangle = \left\langle \begin{pmatrix} 1 & 0 & 0 & 0 \\ 0 & \cos 4\phi & \sin 4\phi & 0 \\ 0 & \sin 4\phi & -\cos 4\phi & 0 \\ 0 & 0 & 0 & -1 \end{pmatrix} \right\rangle = \begin{pmatrix} 1 & 0 & 0 & 0 \\ 0 & 0 & 0 & 0 \\ 0 & 0 & 0 & 0 \\ 0 & 0 & 0 & -1 \end{pmatrix}, \tag{6.18}$$

with ϕ being a momentary angle between the plates fast axis and the horizontal plane.

The resulting time-averaged Stokes vector is $\langle \boldsymbol{S} \rangle = (I, 0, 0, -P_3)$. The intensity I remains unchanged, P_1 and P_2, which describe the preponderance of horizontal over vertical and of $+45^\circ$ over -45° oriented linear polarization, respectively, are rendered 0, and the right- and left-circular polarization states specified by P_3 are interconverted. Time-averaged scrambling of linear polarization can therefore be achieved by a rotating half-waveplate. In view of its effect, one might call such a device a linear rotator. As rotation has to be accomplished by mechanical means, the method lacks the elegance of the previous approaches, but it has the advantage of being more generally applicable, including to collimated monochromatic light.

The precision of the retardation of half-wave plates, along with the fact that their transmission depends slightly on the orientation of their axes with respect to the plane of polarization of the light incident on them, limits the degree of depolarization that can be achieved with a single plate. A higher precision is possible by using two counter-rotating plates. This provides, moreover, the benefit of doubling the rotation speed of the plane of polarization, and it reduces the influence an even tiny wobble of the laser beam, synchronized with the orientation of the plane of polarization, can have. A combination of two low-order quartz half-wave plates is suitable for depolarizing the quasi-monochromatic exciting laser beam, and a zero-order one is used for the limited range of wavelengths encountered in the Raman scattered light.

Figure 6.11 shows an arrangement of two motors with hollow axles, specifically developed for scrambling linear polarization components, equipped with half-wave plates

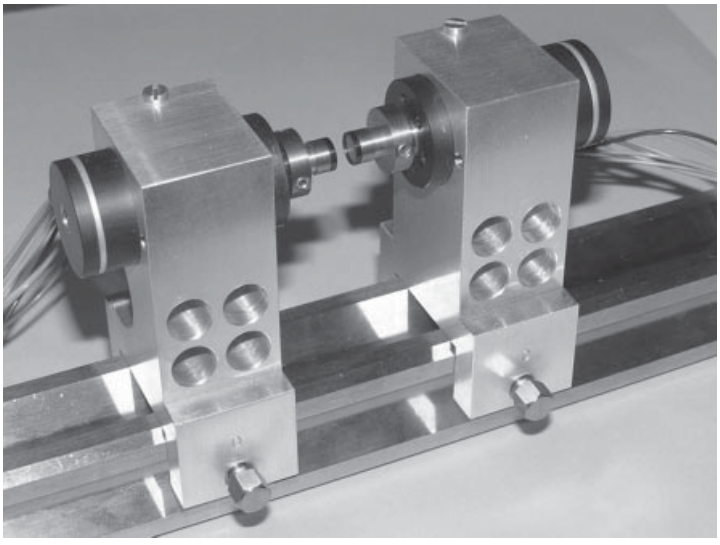

Figure 6.11. Dual high-speed hollow axle motor arrangement equipped with low-order quartz half-wave retardation plates. The counter-rotating motors are synchronized to the data-acquisition cycle.

through which the laser beam passes. Their precisely synchronized rotation speeds of 13,488.75 and 11,853.75 rpm are chosen so that their fast optical axes cross at 180° /31 intervalls, with the speed of rotation of the plane of polarization reaching 50,685 rpm. The rotation speeds yield completed rotations for acquisition and read-out times that are multiples of 4/109 s. The base interval of 1/109 is chosen to avoid interference by accidental synchronization of acquisition cycles with either the European 50-Hz or the US 60-Hz line frequency.

Scrambling Circular Polarization: The Virtual Enantiomer. Because it is circular polarization which carries the ROA information, scrambling it must be done compatible with recovering this information. The strategy is to carry out the measurement in a way that makes the elements of the optical train, including the circular polarization modulator in an ICP and the circular polarization analyzer in a SCP experiment, time-averaged agnostic of the circular polarization state used for probing the handedness of the sample. This is equivalent to alternatingly measuring the chiral molecule that one is interested in, along with its enantiomer. While using the actual enantiomer is not a generally useful approach, it is possible to create the chiroptical properties of a molecule's optical antipode by purely optical means. We will call this a virtual enantiomer.

The property of half-waveplates to interconvert left- and right-circularly polarized light is the key for achieving this. It can be shown in a general way [9] that placing a chiral molecule between half-waveplates makes it look, if observed from the outside, as if it were its enantiomer. This is true for all its chiroptical properties. If, moreover, the axes of the half-waveplates are aligned so that together they form a full-wave retardation plate, then their presence becomes transparent to an observer probing the molecule from the outside. Practical half-waveplates entail an optical pathlength change, and in an actual experiment they therefore have to be placed into sections of the optical train with parallel light paths, in order to minimize optical disturbances they cause.

The scrambling of linear components, as described in the previous section, simplifies the description of the action that half-waveplates have in creating a virtual enantiomer. Their only effect then becomes that of interconverting left- and right-circularly polarized

light, and one might therefore call them circularity converters. This is seen from their action on the Stokes vector of time-average linearly depolarized light obtained by a linear rotator:

$$\begin{pmatrix} 1 & 0 & 0 & 0 \\ 0 & \cos 4\phi & \sin 4\phi & 0 \\ 0 & \sin 4\phi & -\cos 4\phi & 0 \\ 0 & 0 & 0 & -1 \end{pmatrix} \begin{pmatrix} I \\ 0 \\ 0 \\ P_3 \end{pmatrix} = \begin{pmatrix} I \\ 0 \\ 0 \\ -P_3 \end{pmatrix}. \tag{6.19}$$

If circularity converters are preceded by linear rotators, then their angular orientation ϕ becomes unimportant.

Combination of Linear and Circular Polarization Scrambling. Linear polarization scrambling by rotating half-waveplates and the creation of a virtual enantiomer can be applied to the ICP, SCP, and DCP polarization scheme. Scrambling is applicable to chiroptical measurements other than ROA, with the limitation being the availability of appropriate retarders.

Figure 6.12 shows schematically a practical implementation in a SCP instrument. The counter-rotating linear rotators LR_1 and LR_2 eliminate linear polarization from the exciting laser beam. Ideally they should, as is also the case for the circularity converter CC_1, be placed directly in front of the sample cell, but this is not possible in a backscattering experiment. The light path between them and the sample is therefore kept as polarization neutral as possible by the use of two 90° deviations in orthogoal planes instead of a single one. The influence of small residual linear components produced by optical imperfections is reduced by the linear rotator LR_3 in the scattered light. The slightly different transmission of the low-order retarder CC_1 for light-polarized parallel and perpendicular to its fast axis is an example of such an imperfection.

We will analyze the effectiveness of the arrangement for the case of arbitrarily polarized exciting light $\boldsymbol{S} = (I, P_1, P_2, P_3)$ of the laser. We will see that the influence of P_3, which would normally lead to huge offsets in a SCP measurement, is suppressed, and that a linear component described by P_1 and P_2 is prevented from reaching the circular polarization analyzer. Offset mechanisms other than due to the exciting light are amenable to a similar analysis.

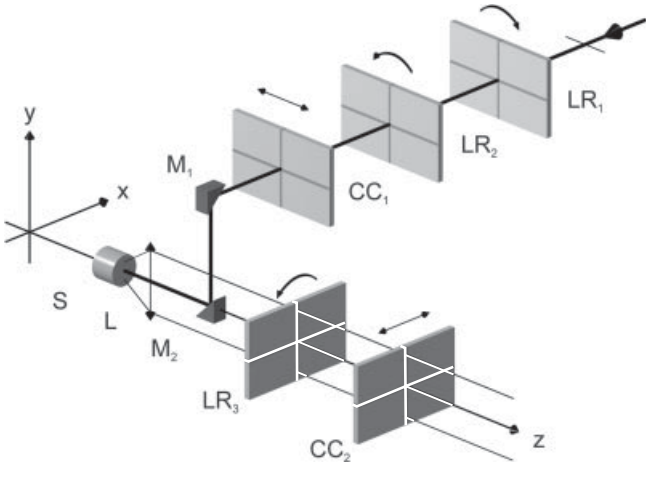

Figure 6.12. Combination of linear and circular polarization scrambling in an SCP backscattering instrument. LR_1 and LR_2, high-speed counter-rotating linear rotators in the exciting light; CC_1 and CC_2, circularity converters in the exciting and scattered light, respectively; LR_3, slow-rotation linear rotator in the scattered light. Other optical elements are as in Figure 6.5.

For the situation where the actual molecule is measured, the time-averaged Stokes vector on the entrance of the circular polarization analyzer is given by

$$\langle \boldsymbol{S}'(00)\rangle = \langle \boldsymbol{L}_3\rangle \boldsymbol{X} \langle \boldsymbol{L}_2\rangle \langle \boldsymbol{L}_1\rangle \boldsymbol{S}\,. \tag{6.20}$$

where $\langle \boldsymbol{L}_1\rangle$, $\langle \boldsymbol{L}_2\rangle$, and $\langle \boldsymbol{L}_3\rangle$ are the Mueller matrices of the linear rotators $\mathrm{LR}_1, \mathrm{LR}_2$, and LR_3, and $\boldsymbol{X}$ stands for the scattering matrix of the sample, which we assume to include the influence of the optics between the polarization correcting elements. The notation (00) indicates that the circularity converters are removed from the optical path, and a prime distinguishes the scattered from the exciting light.

For the measurement of the virtual enantiomer, where both circularity converters are moved into the optical train, one likewise has

$$\langle \boldsymbol{S}'(11)\rangle = \boldsymbol{C}_2 \langle \boldsymbol{L}_3\rangle \boldsymbol{X} \boldsymbol{C}_1 \langle \boldsymbol{L}_2\rangle \langle \boldsymbol{L}_1\rangle \boldsymbol{S}\,, \tag{6.21}$$

with $\boldsymbol{C}_1$ and $\boldsymbol{C}_2$ representing the matrices of the circularity convertes CC_1 and CC_2. The products of the various Mueller matrices can be separately evaluated, and one has

$$\langle \boldsymbol{L}_2\rangle \langle \boldsymbol{L}_1\rangle = \begin{pmatrix} 1 & 0 & 0 & 0 \\ 0 & 0 & 0 & 0 \\ 0 & 0 & 0 & 0 \\ 0 & 0 & 0 & 1 \end{pmatrix}, \tag{6.22}$$

$$\boldsymbol{C}_1 \langle \boldsymbol{L}_2\rangle \langle \boldsymbol{L}_1\rangle = \begin{pmatrix} 1 & 0 & 0 & 0 \\ 0 & 0 & 0 & 0 \\ 0 & 0 & 0 & 0 \\ 0 & 0 & 0 & -1 \end{pmatrix}, \tag{6.23}$$

$$\boldsymbol{C}_2 \langle \boldsymbol{L}_3\rangle = \begin{pmatrix} 1 & 0 & 0 & 0 \\ 0 & 0 & 0 & 0 \\ 0 & 0 & 0 & 0 \\ 0 & 0 & 0 & 1 \end{pmatrix}. \tag{6.24}$$

For $\boldsymbol{X}$ we assume the general form

$$\boldsymbol{X} = \frac{I'}{I} \begin{pmatrix} X_{00} & X_{01} & X_{02} & X_{03} \\ X_{10} & X_{11} & X_{12} & X_{13} \\ X_{20} & X_{21} & X_{22} & X_{23} \\ X_{30} & X_{31} & X_{32} & X_{33} \end{pmatrix}, \tag{6.25}$$

where I'/I is the ratio of the intensity of the scattered to that of the exciting light.

The Stokes vectors for the scattered light are obtained as $\langle \boldsymbol{S}'(00)\rangle = I'/I \times (X_{00}I + X_{03}P_3, 0, 0, -X_{30}I - X_{33}P_3)$ and $\langle \boldsymbol{S}'(11)\rangle = I'/I \times (X_{00}I - X_{03}P_3, 0, 0, X_{30}I - X_{33}P_3)$. For an achiral sample, X_{03} and X_{30} of the scattering matrix vanish [40] and X_{33} represents the reversal ratio. Subtraction of the Stokes vectors then yields

$$\langle \Delta \boldsymbol{S}'\rangle = \langle \boldsymbol{S}'(00)\rangle - \langle \boldsymbol{S}'(11)\rangle = I'/I \times (0, 0, 0, 0). \tag{6.26}$$

This means that time-average scrambling of circular and linear components effectively eliminates any influence that such components of the exciting light have on the scattered light. The term surviving for a chiral sample, for exciting light devoid of a circular

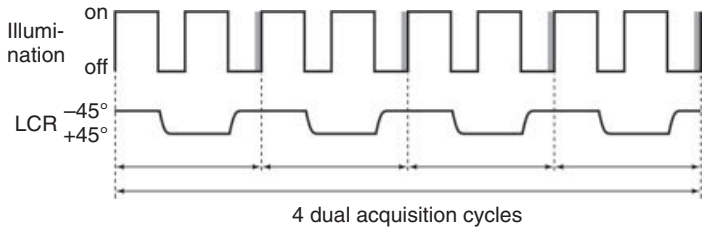

Figure 6.13. Timing diagram of an SCP acquisition cycle for a single fixed position of the circularity converters. The liquid crystal retarder is switched while the exciting light is switched off and the CCD is read (dark interval). The circularity converters are moved to the next one of four relative positions during the last (8th) dark interval. Every second dark interval is increased by one basic timing unit of 1/109 s (see text) to eliminate the influence of systematic deviations of the shutter opening and closing speeds.

component, is $-2I'X_{30}$; that is, subtraction of a measurement with CC_1 and CC_2 moved into the optical train from one where they have been removed leads to addition of the terms responsable for chiral scattering.

Perfect half-wave plates do not exist. In practice it is therefore best to limit the size of net circular components of the exciting light in an SCP instrument, either by a high-quality linear polarizer or by a rotating quarter-wave plate.

6.5.3. Acquisition Cycle

A basic acquisition cycle of a circular intensity difference measurement consists of separately measuring and subtracting the Raman signal for right-and left-circular polarization. In the SCP instrument of Figure 6.1 the two intensities are determined simultaneously by the two arms, and a basic acquisition cycle therefore comprises illuminating the sample and reading the CCD detector. Switching the state of the liquid crystal retarder in the circular polarization analyzer interchanges the function of the two arms. The sum for two switching states, a dual acquisition cycle, has a vastly increased precision because differences in the arms' transmission are eliminated.

The linear rotators LR_1 and LR_2 are synchronized so that an integral number of turns of the plane of polarization of the exciting light results for each illumination period. The mechanical shutter used to cut off the laser beam tends to lead to a systematic deviation of the period's length. The deviation's influence can be eliminated by combining four dual acquisition cycles into a block and by starting consecutive dual cycles with the plane of polarization rotated by 45°. To this end, every second dark period is extended by one basic timing unit of 1/109 s (see section on linear polarization scrambling). Figure 6.13 shows a timing diagram for a block of four dual cycles.

Synchronization of the polarization scrambler LR_3 in the scattered light is not required for long acquisition times. It is important for short acquisitions as demonstrated in the recording of ROA spectra of the anomers of glucose [41].

The circularity converters are moved into and out of the optical path after each block of four dual acquisition cycles. The required optical precision is generally more demanding for CC_1 than for CC_2. It can be shown [9] that a vastly increased offset suppression is achieved for half-wave plates of limited precision by not moving the converters together but in a pattern (00), (01), (10), (11), with the circularity converter CC_1 in the incident light moving like the lower and the converter in the scattered light

like the higher bit. For the optical arrangement in Figure 6.12 the ROA and Raman information is then obtained from the average Stokes vector components $\overline{P_3'}$ and $\overline{I'}$, respectively, of the scattered light, given by

$$\overline{P_3'} = -\frac{1}{4}\{P_3'(00) + P_3'(01) - P_3'(10) - P_3'(11)\}, \tag{6.27}$$

$$\overline{I'} = \frac{1}{4}\{I'(00) + I'(01) + I'(10) + I'(11)\}. \tag{6.28}$$

The modification of the acquisition cycle for a slow modulation DCP_I experiment is straightforward. The exciting light is modulated between right and left circular, and a basic acquisition cycle now consists of reading the CCD detector twice, with the desired signal once on its upper and once on its lower half. A fast modulation DCP_I instrument can be obtained with a shutter provided by a synchronized rotating wheel at the entrance of the spectrograph [33].

6.6. FINAL REMARKS

Stereochemical information and the determination of absolute configurations have been the main areas of practical interest of ROA so far. In the context of the present chapter, we have stressed the measurement of ROA with different scattering geometries and polarization schemes. Such measurements render differing information, which reflects ROA's dependence on the various invariants of the scattering tensor and, thus, on a molecule's electronic structure and the nature of its vibrational modes.

The potential value of such information for sterochemistry can be illustrated by the example of the depolarization ratio in ordinary Raman spectroscopy. A glance at it in the Raman spectrum of a polyatomic molecule can allow the identification of, for example, a ring breathing mode, due to the polarized nature of the band it produces, without any calculation. In a similar way, the comparison of the forward and backward scattering ROA spectra of a molecule might permit, with more experience at hand than presently available, a judgment on the role that interaction between fragments plays in generating a particular ROA band's sign and size.

Figure 6.14 compares the forward and backward scattering SCP ROA spectra of (R)-(+)-propylene oxide. The Raman spectra are identical for the two scattering geometries except for differencies in the detectivity of the two scattering channels, and the ROA spectra are normalized to the Raman intensity measured in backward scattering. The two ROA spectra are, except for band positions, starkly different, as one might expect from the formulae in Table 6.1. A closer analysis reveals that forward scattering spectra are exclusively determined by intrinsic terms, with no dependence on the distance between molecular fragments. Backward scattering spectra, on the other hand, depend on intrinsic terms as well as on terms proportional to the distance.

Apart of the expected wider future use of ROA data obtained with different scattering geometries and polarization schemes, a move of exciting laser wavelengths from the presently preferred green toward the red or near infrared appears inevitable. Δ values will suffer, but longer exciting wavelengths solve much of Raman spectroscopy's ubiquitous fluorescence problem. Spectrographs and optics present no obstacle to such a move. Power levels of semiconductor lasers have been insufficient so far in the red, but appropriate Raman fiber lasers hold promise. The overload problem of CCD detectors is a temporary technological limit and is bound to find a solution in the form of low-noise

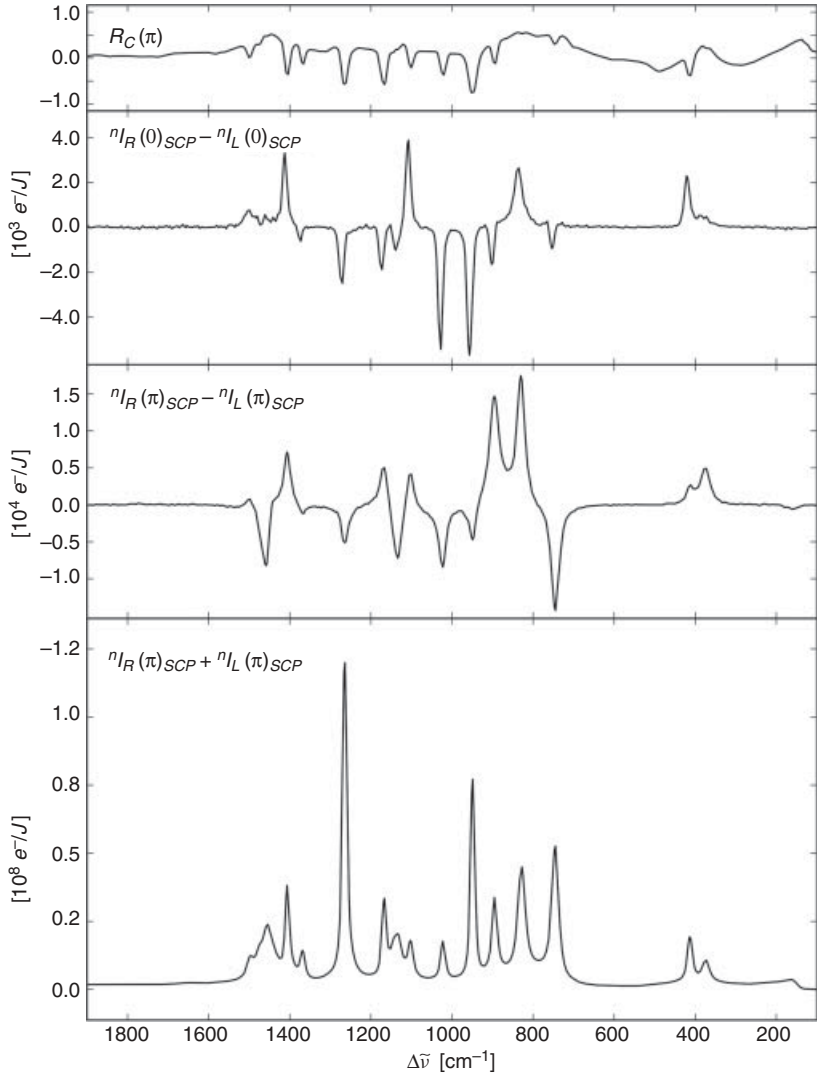

Figure 6.14. Comparison of forward and backward scattering ROA spectra of (R)-(+)-propylene oxide (methyloxirane). Top curve: degree of circularity ${}^RC(\pi)$ indicating the degree of polarization of bands; −1 represents a fully polarized band and +5/7 denotes a fully depolarized band. Middle curves: ROA spectra. Bottom curve: Raman measured in backscattering. Measurement parameters: 150 (270)-mW laser power and 120 (36.6)-min illumination time for forward (backward) scattering, respectively. The curves are slightly smoothed by a third-order five-point Savitzky–Golay procedure.

CMOS line scanners or similar devices. Raman spectroscopy's low dynamic range, which makes ROA measurements in most solvents except water difficult, might be alleviated by the use of fine grained mulls with a particle size similar to what is being used to render lenses made from organic materials scratch resistant. Technological advances made the first ROA measurements possible in the seventies of the last century, and they will render them a standard tool of chiral chemistry in the future.

REFERENCES

1. L. D. Barron, A. D. Buckingham, *Mol. Phys*. **1971**, *20*, 1111.
2. L. D. Barron, M. P. Bogaard, A. D. Buckingham, *J. Am. Chem. Soc*. **1973**, *95*, 603.
3. L. Barron, M. Bogaard, A. D. Buckingham, *Nature* **1973**, *241*, 113.
4. W. Hug, S. Kint, G. F. Bailey, J. R. Scherer, *J. Am. Chem. Soc*. **1975**, *97*, 5589.
5. G. Holzwarth, E. C. Hsu, H. S. Mosher, T. R. Faulkaner, A. Moscowitz, *J. Am. Chem. Soc*. **1974**, *96*, 251.
6. L. A. Nafie, J. C. Cheng, P. J. Stephens, *J. Am. Chem. Soc*. **1975**, *97*, 3842.
7. W. Hug, H. Surbeck, *Chem. Phys. Lett*. **1979**, *60*, 186.
8. W. Hug, *Appl. Spectrosc*. **1981**, *35*, 115.
9. W. Hug, *Appl. Spectrosc*. **2003**, *57*, 1.
10. W. Hug, in *Raman Spectroscopy, Linear and Non-linear*, J. Lascomb and P. Huong, eds., Wiley-Heyden, Chichester, **1982**, p. 3.
11. L. Hecht, L. D. Barron, A. R. Gargaro, Z. Q. Wen, W. Hug, *J. Raman Spectrosc*. **1992**, *23*, 401.
12. L. D. Barron, L. Hecht, A. R. Gargaro, W. Hug, *J. Raman Spectrosc*. **1990**, *21*, 375.
13. K. M. Spencer, T. B. Freedman, L. A. Nafie, *Chem. Phys. Lett*. **1988**, *149*, 367.
14. L. Hecht, D. Che, L. A. Nafie, *Appl. Spectrosc*. **1991**, *45*, 18.
15. L. A. Nafie, T. B. Freedman, *Chem. Phys. Lett*. **1989**, *154*, 260.
16. D. Che, L. Hecht, L. A. Nafie, *Chem. Phys. Lett*. **1991**, *180*, 182.
17. M. Vargek, T. B. Freedman, L. A. Nafie, *J. Raman Spectrosc*. **1997**, *28*, 627.
18. L. Hecht, L. A. Nafie, *Mol. Phys*. **1991**, *72*, 441.
19. L. A. Nafie, *Chem. Phys. Lett*. **1996**, *205*, 309.
20. M. Vargek, T. B. Freedman, E. Lee, L. A. Nafie, *Chem. Phys. Lett*. **1998**, *287*, 359.
21. J. O. Bjarnason, H. C. Anderson, B. S. Hudson, *J. Chem. Phys*. **1980**, *72*, 4132.
22. G. Wagniére, *Chem. Phys*. **1981**, *54*, 411.
23. J.-L. Oudar, C. Minot, B. A. Garetz, *J. Chem. Phys*. **1982**, *76*, 2227.
24. L. D. Barron, J. F. Torrance, *Chem. Phys. Lett*. **1983**, *102*, 285.
25. L. A. Nafie, *Chem. Phys. Lett*. **1983**, *102*, 287.
26. H. W. Schrötter, H. W. Klöckner, in *Raman Spectroscopy of Gases and Liquids, Topics Currents in Physics*, Vol. *11*, A. Weber, ed., Springer, Berlin, **1979**, p. 123.
27. D. A. Long, *The Raman Effect*, John Wiley & Sons, Hoboken, NJ, **2002**.
28. W. Hug, *Chem. Phys*. **2001**, *264*, 53.
29. W. Hug, in *Handbook of Vibrational Spectroscopy*, Vol. 1, J. M. Chalmers and P. R. Griffiths, eds., John Wiley & Sons, Chichester, **2002**, p. 745.
30. D. Che, L. A. Nafie, *Chem. Phys. Lett*. **1992**, *189*, 35.
31. L. Hecht, L. D. Barron, *Spectrochim. Acta, Part A* **1989**, *45*, 671.
32. J. F. James, R. S. Sternberg, *The Design of Optical Spectrometers*, Chapman and Hall, London, **1969**.
33. W. Hug, G. Hangartner, *J. Raman Spectrosc*. **1999**, *30*, 841.
34. H. Surbeck, W. Hug, M. Gremaud, M. Bridoux, A. Deffontaine, and E. DaSilva, *Optics Commun*. **1981**, *38*, 57.
35. E. Hasanova, W. Hug, unpublished results.
36. M. A. Lovchik, G. Frater, A. Goeke, W. Hug, *Chem. Biodiversity* **2008**, *5*, 126.
37. D. W. Allan, M. A. Weiss, T. K. Peppler, *IEEE Trans. Instrum. Meas*. **1989**, *38*, 624.

38. W. Hug, A. Kamatari, K. Srinivasan, H.-J. Hansen, H.-R. Sliwka, *Chem. Phys. Lett*. **1980**, *76*, 469.
39. W. Hug, H. Surbeck, *J. Raman Spectrosc*. **1982**, *13*, 38.
40. Y. Shi, W. M. McClain, R. A. Harris, *Chem. Phys. Lett*. **1993**, *205*, 91.
41. W. Hug, in *Encyclopedia of Spectroscopy and Spectrometry*, 2nd edition, Vol. 3, J. Lindon, G. Tranter, D. Koppenaal, ed., Elsevier, Oxford, **2010**, p. 2387.

7

NANOSECOND TIME-RESOLVED NATURAL AND MAGNETIC CHIROPTICAL SPECTROSCOPIES

David S. Kliger, Eefei Chen, and Robert A. Goldbeck

7.1. INTRODUCTION

Kinetic studies have long been recognized as critical to understanding the mechanisms of chemical reactions. As with other mechanistic studies, understanding how biomolecular reactions work, such as in the functional and folding reactions of proteins, requires an understanding of their kinetics. Early studies of proteins focused on understanding their reaction products and their structures. From these, the mechanisms by which proteins produced those products could often be deduced. More recently, however, it has become clear that natively folded proteins are dynamic entities and that protein structures can change as they carry out their functions. Studies of the kinetics of protein reactions have thus become increasingly important. It has also become clear in recent years that the mechanistic steps in the folding and function of proteins can occur on very rapid timescales.

Studies of rapid kinetics have generally involved the use of time-resolved optical spectroscopies because these are most amenable to measurements on short time scales. Rapid time-resolved absorption studies have been feasible since the middle of the past century, with the advent of millisecond flash lamps for initiating photochemical reactions [1, 2]. Flash lamps were later created with microsecond pulse durations, followed by the advent of pulsed lasers with pulse durations of nanoseconds, soon shortened to picoseconds and then femtoseconds [3]. Today, lasers are even available with attosecond pulse durations [4]. The development of such pulsed light sources, together with the development of light detection systems with both high time resolution and multiwavelength capabilities, has made optical studies of reaction kinetics on very rapid time scales possible.

Comprehensive Chiroptical Spectroscopy, Volume 1: Instrumentation, Methodologies, and Theoretical Simulations, First Edition. Edited by N. Berova, P. L. Polavarapu, K. Nakanishi, and R. W. Woody.
© 2012 John Wiley & Sons, Inc. Published 2012 by John Wiley & Sons, Inc.

While rapid measurements of absorption spectra have added tremendously to our understanding of fast reactions in proteins, such spectra are not particularly sensitive to protein structural changes. Thus a number of more structure-sensitive time-resolved spectral techniques have been developed over the years that have been important tools for protein mechanistic studies [5]. These include time-resolved fluorescence, IR, resonance Raman, and even time-resolved X-ray techniques. Over the years we have also developed a number of chiroptical spectroscopic techniques to monitor the time evolution of protein structures [6]. This development began with techniques to measure time-resolved circular dichroism (TRCD) with nanosecond [7] and later picosecond [8, 9] resolution. This approach was later extended to techniques for the time-resolved measurement of magnetic circular dichroism (TRMCD), optical rotatory dispersion (TRORD), and magnetic optical rotatory dispersion (TRMORD), as well as very sensitive time-resolved measurements of linear dichroism (TRLD) [10–14]. These techniques, as well as more recent related developments and a number of applications, will be described in the rest of this chapter.

7.2. NEAR-NULL ELLIPSOMETRIC CD MEASUREMENTS

Realizing the potential importance of structure-sensitive spectral measurements with high time resolution to studies of protein function and protein folding, our group worked to develop a capability for measuring CD spectra with high time resolution as far back as the 1980s. At that time, the standard method for making CD measurements was to use photoelastic modulators (PEM) with frequencies on the order of 100 kHz to create light that rapidly alternated between right- and left-circular polarizations. Phase-sensitive detection was then used to sensitively measure the difference in absorption between light of these two polarizations. This sensitivity is important because the difference between absorption of left- and right-circularly polarized light is typically on the order of 10^{-2} to 10^{-5} times the magnitude of the absorption itself. However, given the frequency of the modulators, it would not be possible to measure CD kinetics with this approach with time resolution better than milliseconds. Furthermore, to get modulators that would be significantly faster than this would require much smaller modulators, and this would result in optical throughputs that would be too small for measurements with reasonable signal to noise. We thus sought a different approach to CD measurements which could be capable of high time resolution.

The approach we used took advantage of the vectorial properties of the electric field component of light. As shown in Figure 7.1, these properties make it possible to convert one form of light to another with relative ease. Thus linearly polarized light with any orientation can be created by adding linear light components of vertical and horizontal polarized light with different amplitudes. Circularly polarized light can be created by the addition of vertically and horizontally polarized electric field vectors of identical amplitudes that are 90° out of phase. Elliptically polarized light can be created by the addition of 90° out-of-phase vertical and horizontal electric field vectors of different amplitudes or by the addition of left and right circular components with different amplitudes. In other words, one can easily convert light between different polarization types through controlling the amplitudes and/or phases of the light components.

Because elliptically polarized light can be thought of as comprising left- and right-circularly polarized components of different amplitude and the eccentricity of the elliptical polarization changes when the relative amplitudes of the left and right components change, ellipticity provides a different and, it turns out, sensitive way to measure circular

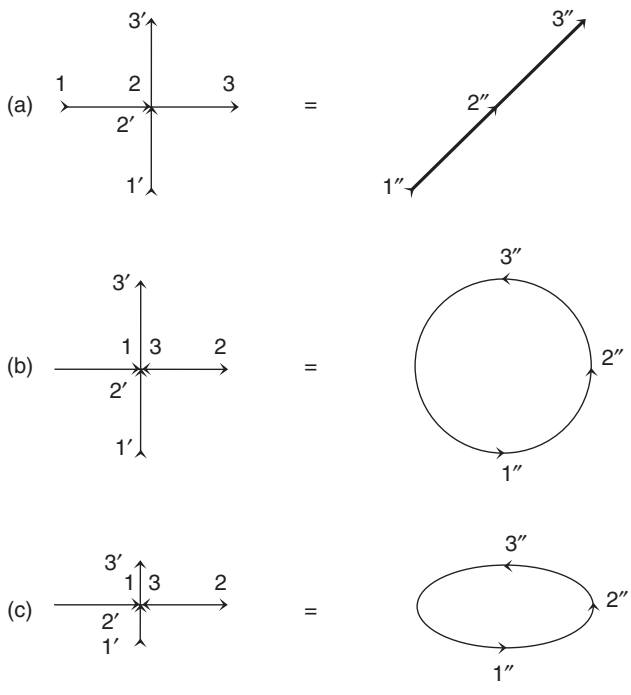

Figure 7.1. The manipulations of light polarization used in CD measurements can be visualized with the aid of electric field polarization vectors. Viewing the light facing toward its source, the tip of its electric field vector traces out over time a pattern that depends on its polarization as it oscillates with a frequency ν. Linearly polarized light traces out a straight line, with its phase of oscillation at a given instant being indicated in the figure by an arrowhead. (a) Two linearly polarized light vectors with the same phase add together in simple vector addition to give a sum field that is also linearly polarized (the numbered arrowheads indicate times that are 90° apart in phase). (b) A more interesting case is when the two linear polarization vectors have different phases. When perpendicular vectors of equal magnitude but 90° phase difference are added together, the result is circularly polarized light. (c) Finally, if the out-of-phase vectors have different magnitudes, then elliptical polarization results.

dichroism. Thus, if one passes an elliptically polarized light beam (with highly eccentric ellipticity) through a circularly dichroic sample, the relative amplitudes of the circular components will change, thus changing the eccentricity of the elliptically polarized light. Measuring the change in eccentricity thus provides a way to measure a sample's circular dichroism.

In practice this can be accomplished with an apparatus like that shown in Figure 7.2. One starts by using a high-intensity flashlamp to produce light with sufficiently high peak intensity that measurements with good signal-to-noise ratios can be made without exposing the sample to the damagingly high levels of light energy absorption over time that might be caused by a continuous light source. This light is then passed through a high-quality linear polarizer (i.e., one with high extinction so the light emerging from the polarizer has linear polarization to a very high degree) followed by a birefringent element that converts the linearly polarized light into highly eccentric elliptically polarized light. To accomplish this, one can simply take a strain-free quartz plate and apply a mechanical strain along a well-defined axis. This produces elliptically polarized light with eccentricity determined by the amount of strain applied to the plate. By orienting the strain axis along a $\pm 45^\circ$ axis relative to the axis of linear polarization, one produces left or right elliptically polarized light oriented along the original axis of the linearly polarized light. After passing this light through the sample, the change in ellipticity can be monitored by passing the light through a second linear polarizer with polarization axis perpendicular to that of the first polarizer. Monitoring the intensity of the resulting light for both left and right elliptically polarized beams then yields the sample circular dichroism according to the following formula:

$$\text{Signal} = (I_{\text{REP}} - I_{\text{LEP}})/(I_{\text{REP}} + I_{\text{LEP}}) = 2.3\Delta\varepsilon c\ell/\delta, \tag{7.1}$$

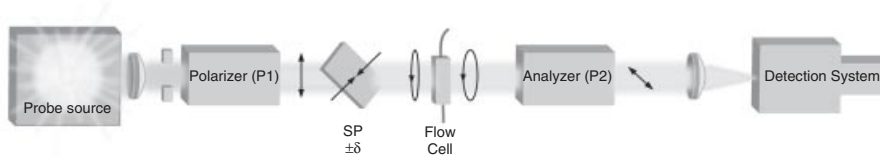

Figure 7.2. Apparatus used for near-null ellipsometric measurements of time-resolved circular dichroism. A circularly dichroic sample will change the eccentricity of elliptically polarized light because this light comprises components of LCP and RCP light with different amplitudes. Highly eccentric elliptically polarized light is generated by passing linearly polarized light, which is unpolarized before meeting the first linear polarizer, through a strain plate (SP) that introduces a small phase retardance (δ). When the compression (fast) strain axis of this birefringent element is oriented at 45° from the linear polarization axis, the major axis of the elliptically polarized light that is produced is parallel to the original linear polarization axis. REP and LEP light ($+45°$ and $-45°$) are obtained by rotating SP around its vertical axis by 180°. CD in a sample will change the polarization ellipticity of the REP and LEP probe beams, with the minor axis (horizontally polarized light) of each being monitored after the probe beam passes through the second analyzing polarizer and detected by either an intensified photodiode array or intensified charge coupled device.

where I_{REP} and I_{LEP} are the intensities of right elliptically and left elliptically polarized light, respectively, $\Delta\varepsilon$ is the circular dichroism, c is the concentration of a sample of pathlength ℓ, and δ is the retardation in radians of the birefringent element used to produce elliptically polarized light from the linearly polarized light. It is clear from this formula that the more eccentric the elliptically polarized light (i.e., the smaller the δ), the larger the signal produced from a sample of given circular dichroism.

Initial implementation of this approach to CD measurements involved making time-resolved measurements at single wavelengths. Expansion of this implementation soon followed by extending measurements into the far-UV region and making multi-wavelength measurements by replacing a monochromator/photomultiplier detection system with a spectrograph/multichannel analyzer [initially using gated diode array detectors and more recently using gated charge-coupled device (CCD) detectors] [15]. Given the sensitivity of this CD measurement approach to a number of artifacts (discussed below), the ability to measure multi-wavelength spectra is very useful to ensure that the measured signals truly reflect CD spectra of interest rather than optical artifacts.

7.3. NEAR-NULL ELLIPSOMETRIC MCD MEASUREMENTS

While natural CD results only from molecules with chiral structures, CD can be induced in either chiral or achiral molecules placed in a magnetic field. Magnetic circular dichroism (MCD) is closely related to the Zeeman effect, which causes splitting of degenerate energy levels in molecules placed in a magnetic field. The electric dipole transitions between Zeeman levels are circularly polarized, so splitting of these levels results in a CD signal when light propagating parallel to the magnetic field direction passes through the sample. The size of the MCD signal is proportional to the strength of the magnetic field as well as the magnetic moments of the molecule's electronic energy levels. Since MCD is produced from the splitting of degeneracies, it is a sensitive measure of molecular

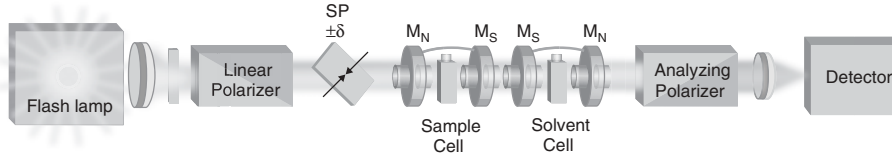

Figure 7.3. Apparatus for time-resolved magnetic circular dichroism measurements. The TRMCD measurement is an extension of that for TRCD, with addition of a magnet (M_N, M_S) surrounding the sample and a compensator to counteract the Faraday rotation of the probe beam polarization as it travels though the sample cell windows and the solvent in a magnetic field. The compensator, comprising a solvent blank in a cell matched with the sample cell and a magnetic field matched in magnitude but opposite in direction to that for the sample, rotates the beam polarization back to its original orientation.

structures and environments that perturb the electronic states. The sensitivity of natural CD to asymmetries in molecules makes it particularly useful in studying proteins, which naturally exhibit asymmetric structural motifs. Because of the sensitivity of MCD to the splitting of degenerate electronic states, it produces large signals in aromatic molecules and thus is particularly useful in studying heme proteins and proteins that contain aromatic residues. In heme proteins, MCD is particularly sensitive to the axial ligation, spin, and oxidation states of the heme iron. MCD measurements are thus a very useful complement to natural CD measurements in such proteins.

The approach to measuring MCD spectra with high time resolution is basically the same as the TRCD approach, but with a couple of changes. First, and most obvious, one must add a magnet around the sample with the magnetic field oriented along the axis of light propagation. This requires the use of magnets surrounding the sample with holes in the pole pieces through which the light passes. The second change involves the use of a compensator to correct for Faraday rotation of light passing through the sample cell windows and solvent. Although the windows and solvent will be transparent at the probe wavelength, they will produce an optical rotation (Faraday effect) in the beam because of the MCD associated with their far-UV absorption bands, since absorption and refraction are fundamentally linked by the Kramers–Kronig integral transform. Thus, the polarization ellipse of elliptically polarized light passing through such a sample in a magnetic field will rotate. However, the TRCD technique relies on a measurement of the change in minor axis intensity of the elliptically polarized light; therefore, if the ellipse is rotated, the intensity of the minor axis would appear to increase due to the rotation rather than to a dichroism. This Faraday rotation effect can be quite large compared with the dichroism of the sample since the concentrations of molecules under study are generally very small relative to solvent concentrations and window densities. Thus a Faraday compensator is used to rotate the elliptical polarization axis back to its original orientation before the light passes through the polarization analyzer and on to the detector. The apparatus for TRMCD measurements is shown in Figure 7.3.

Two approaches have been used to compensate for the Faraday rotation in MCD measurements. The first approach to Faraday compensation involves use of an optically

active material, such as a sugar solution, placed between the sample cell and the analyzing polarizer. If measurements are made far from an absorption band, the Faraday effect varies with wavelength as $1/\lambda^2$. When the magnet is oriented in a configuration parallel to the light propagation, the rotation of the sample will be levorotatory, so use of a dextrorotatory sugar such as sucrose will rotate the plane of elliptically polarized light to the original orientation if the sucrose concentration is adjusted properly. Similarly, when the magnet is oriented in an antiparallel configuration, the rotation will be dextrorotatory and a levorotatory sugar, such as fructose, can be used.

The approach of using sugars in a Faraday compensator works well in spectral regions far from the sugar or solvent UV absorption bands, but it does not work well for measurements in the UV region. In the latter case, a more accurate approach is to add a compensator comprising a second cell that is matched to the sample cell and placed in a magnetic field matched in magnitude but opposite in orientation to the sample magnetic field. This approach provides an accurate cancellation of Faraday rotation at all wavelengths.

The dependence of the MCD effect on the magnetic field makes it possible to separate CD signals from MCD signals in samples exhibiting both effects. Circular dichroism measurements on a sample that exhibits both natural CD and MCD will detect the sum of the two effects, CD + MCD, in an applied magnetic field that is parallel (north to south) with the light propagation vector. Since the MCD signal depends on the magnitude and orientation (parallel or antiparallel) of the magnetic field, the signal produced by the same sample when the orientation of the magnetic field is reversed will be CD − MCD. Thus, taking measurements at both orientations of the magnetic field and adding the two signals will give two times the CD, whereas subtracting the two signals will give two times the MCD.

7.4. NEAR-NULL POLARIMETRIC ORD AND MORD MEASUREMENTS

We discussed above the methods for measuring TRCD and TRMCD using an ellipsometric approach. We will discuss below artifacts of which one must be careful in applying these methods. Some of these artifacts arise from the fact, as discussed in reference to TRMCD measurements, that absorption changes are always accompanied by refractive changes. The latter can cause birefringence artifacts when making dichroism measurements. In making TRCD and TRMCD measurements, therefore, one must take care to minimize the effects of birefringence. However, there are closely related polarimetric techniques that can provide similar molecular information with less sensitivity to linear birefringence (LB) artifacts and with the higher signal-to-noise ratios that are possible away from absorption bands. Just as CD and MCD spectra are useful in providing information about molecular structures, the wavelength dependence of circular birefringence [i.e., optical rotatory dispersion (ORD) and magnetic optical rotatory dispersion (MORD)] also contains valuable molecular structural information. This is an obvious result of the fact that CD and ORD, as well as MCD and MORD, are directly related to each other through the Kramers–Kronig relationships [16].

It is more common these days for researchers to measure CD spectra than ORD spectra because CD is more easily interpreted in terms of molecular structures than ORD. This is because CD transitions report on the dichroic properties of individual electronic (or vibrational in the case of VCD measurements) transitions, whereas ORD reflects more widely dispersed refractive index changes and thus typically reports on

the combined contributions of multiple electronic transitions. However, there are applications, particularly for fast time-resolved measurements, wherein signal-to-noise ratios are limited by the amount of light collected, when the ability to measure an ORD signal outside of an absorption band of a molecule can be an advantage that outweighs any inconvenience in interpretation. A good example is the study of protein folding (as discussed below in Section 7.7.2), in which monitoring ORD changes near 230 nm was found to give a similar picture of the kinetics of secondary structure change as that observed in TRCD monitored at 222 nm, despite the presence of overlapping contributions from other CD bands in the ORD. An even more straightforward biomolecular example is provided by the MORD of heme proteins. In this case, the Soret and visible heme bands are typically well separated in wavelength from each other and the electronic transitions of other protein chromophores, permitting their MCD spectra to be obtained conveniently by Kramers–Kronig transform of their MORD [12].

TRORD measurements can be made using an approach that is similar to, yet simpler than, the ellipsometric TRCD approach. The approach is shown in Figure 7.4. The basic idea of this measurement is that circular birefringence rotates the polarization axis of linearly or elliptically polarized light. Thus, if the polarization axis of a probe beam is rotated in either a clockwise or counterclockwise direction by a small fixed angle, the optical rotation of the sample will add to or subtract from that rotation, allowing a determination of the sample-induced rotation by taking the difference of the magnitudes of the total rotations. This is accomplished by placing the sample between two crossed polarizers in the probe beam path, as with the TRCD approach, but eliminating the birefringent element (strain plate) used in the latter apparatus. Instead, the first polarizer is rotated off the crossed position by a small angle, β, and the intensity of light passing through the sample and analyzing polarizer is measured. The measurement is repeated with the first polarizer rotated off by an angle $-\beta$. The result of these measurements depends on the orientation of the crossed polarizers relative to the polarization axis of the excitation laser. In one limiting case, orientation 1, the laser excitation polarization axis is taken to be vertical and the polarizer axes are horizontal and vertical. In another limiting case, orientation 2, the laser axis is vertical and the polarization axes are at $+45^\circ$ and -45°. The signal, defined as the difference of these two intensities divided by their

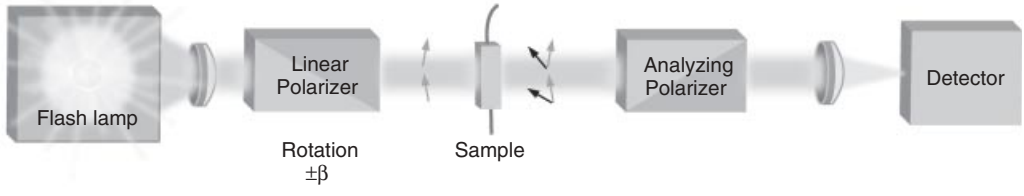

Figure 7.4. Schematic diagram of a time-resolved optical rotatory dispersion apparatus. ORD data are collected by measuring the intensities of the probe beam that pass through the sample and the fixed, analyzing polarizer to the detector when the first linear polarizer is rotated (off the crossed position of the two polarizers) first by a small angle, β, and then by $-\beta$. The underlying concept of this measurement is that the optical rotation of the sample will either add to or subtract from the reference rotation, $\pm\beta$, because CB rotates the polarization axis of linearly or elliptically polarized light. By orienting the axes of the linear polarizers at $+45^\circ$ and -45° relative to the vertical (0°) axis of the pump laser polarization axis, the signal yields LD of the sample and when the polarizer axes are at 0° and 90° the signal yields the sample ORD.

sum, can be shown by using Mueller calculus to be

$$S_1 \equiv [I(\beta) - I(-\beta)]/[I(\beta) + I(-\beta)] \approx -[\mathrm{LD}' + \mathrm{CB}]/\beta \tag{7.2}$$

and

$$S_2 \equiv [I(\beta) - I(-\beta)]/[I(\beta) + I(-\beta)] \approx [\mathrm{LD} - \mathrm{CB}]/\beta, \tag{7.3}$$

where S_1 and S_2 are the signals for orientations 1 and 2, respectively, $I(\beta)$ and $I(-\beta)$ are the probe intensities reaching the detector after rotation of the polarizer by angles of $+\beta$ and $-\beta$, respectively, LD′ is the linear dichroism in orientation 1, LD is the linear dichroism in orientation 2, and CB is the circular birefringence [11].

As can be seen in these formulae, signals produced with this approach have contributions from both linear dichroism and circular birefringence (or ORD in multi-wavelength measurements, Figure 7.5). However, separating these two effects is generally straightforward. If the chromophores in the sample are randomly oriented, then there would be no linear dichroism and each measurement would yield only CB (ORD). If the sample is anisotropic or is made to be transiently anisotropic through laser excitation from the photoselection effect [17], then a linear dichroism can result. For measurements made at times significantly longer than the rotational diffusion time of the chromophore, the sample will again be isotropic and will yield no LD signal. For faster measurements, the photoselection axis will be that of the excitation laser polarization axis. Therefore, for measurements using orientation 1, LD′ will be zero and the signal will be due only to CB (ORD). In orientation 2, the LD signal will generally be much larger than the ORD signal so the signal is essentially due only to LD. In both cases, β is generally small (typically about 0.01 radians) so the signal amplifies the effects of CB or LD, making this approach a very sensitive way of measuring LD or ORD. In general, CB or LD $\ll \beta \ll 1$ radian.

This same approach can be used to measure TRMORD by compensating for the Faraday rotation of the sample cell and solvent as in TRMCD measurements. Polarization orientation 2 is used, with probe beam polarizers oriented in the vertical and horizontal

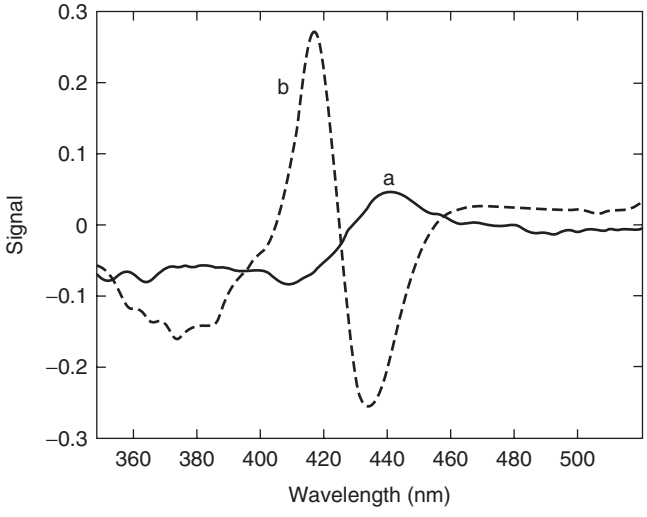

Figure 7.5. Discrimination between time-resolved optical rotatory dispersion and linear dichroism measurements using different polarization orientations. These intermediate spectra were obtained 100 ns after photolysis of HbCO, with the linear and the analyzing polarizers initially oriented in (a) the crossed position (horizontal and vertical directions) for ORD (solid line) measurements and in (b) the diagonal direction (or 45°) to obtain LD (dotted line) spectra. The ORD signal shown was magnified 5 times for comparison with the LD spectrum. On this scale an ORD signal of 0.1 corresponds to a 0.006° rotation and an LD signal of 0.3 corresponds to a difference in absorption of 0.009.

directions. However, the excitation beam, which propagates along an axis perpendicular to the probe beam propagation direction, is polarized along an axis parallel to the probe beam propagation axis to minimize artifacts due to coupling of photoselection-induced LD with the solvent and cell window Faraday rotation [13].

7.5. LIMITATIONS OF NEAR-NULL TECHNIQUES

The methods described above provide measurements of CD and ORD, along with their magnetic counterpart measurements, with high sensitivity because they use near-null approaches. That is, rather than measuring small changes in large signals, such as the small difference in extinction coefficient between left- and right-circularly polarized light relative to the extinction coefficient itself, the measurements involve determining the relatively large difference in the intensity of the minor axis elliptical polarization intensity. While this approach yields measurements with high sensitivity, it also is prone to the introduction of artifacts which must be controlled or accounted for. Figure 7.6 shows how elliptically polarized light can be affected by linear and circular dichroism, as well as linear and circular birefringence. One must account for the coupling of these effects to avoid artifacts in measurements of interest.

As discussed above and shown in Figure 7.1, REP or LEP light can be described in terms of the vector addition of unequal amplitude left- and right-circular components or by the vector addition of out-of-phase linear components. Figure 7.6 shows how CD, CB, LD, or LB would affect these vector components and thus alter REP or LEP light. For a measurement of CD, consider what artifacts might be caused by the CB, LD, or LB of a sample. To first order, CB and LD each change REP and LEP in the same way. Therefore, taking the difference over the sum of the REP and LEP intensities will yield no CD signal. On the other hand, LB effects will be very different for REP and LEP light and can thus produce a signal large enough to completely mask CD effects. Recalling that the elliptically polarized light is produced by a linearly birefringent element, it should not be surprising that a sample exhibiting LB would strongly affect a measurement that depends on careful control and measurement of changes in polarization ellipticity. For CD measurements, it is thus important to understand LB contributions and how to minimize them.

A potentially significant source of linear birefringence besides the strain plate is inadvertent strain in optical elements along the optical path of the CD instrument. It is thus important to use high-quality optics that exhibit retardations of less than 10^{-4} radians. In addition to artifacts due to static linear birefringence of optical elements, time-resolved measurements are susceptible to artifacts from transient linear birefringence caused by photoselection-induced anisotropy in an excited sample or even from cell window birefringence due to thermally induced window strain [a particular problem when using laser temperature jumps (T-jump) coupled to ellipsometric measurements]. In the case of photoselection-induced birefringence, the effects will disappear as the excited molecules rotate to become randomly oriented, but this could take picoseconds for small molecules or hundreds of nanoseconds for typical proteins, or even milliseconds for proteins embedded in membrane patches.

Fortunately, while photoselection-induced LB effects can be large, they can also be eliminated, or at least greatly minimized, by proper orientation of the polarization axis of the excitation laser. Precise alignment of this axis along the vertical or horizontal axes minimizes induced birefringence for perpendicular pump-probe geometries. In practice, horizontal polarization alignment (excitation polarization parallel to the probe beam propagation axis) is generally more effective because misalignments produce smaller signals.

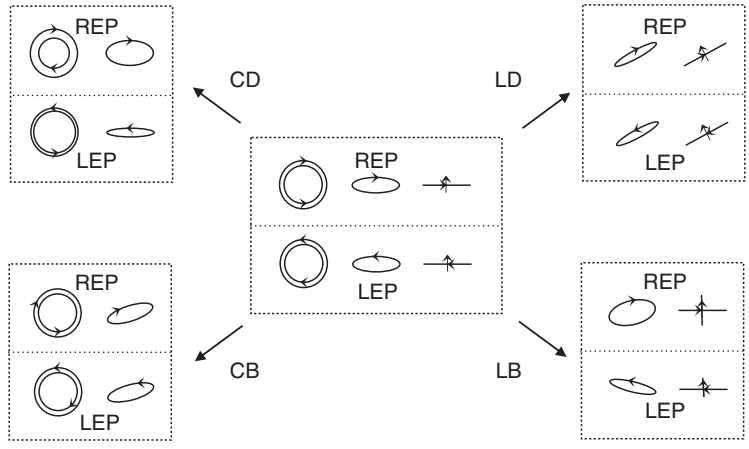

Figure 7.6. A schematic diagram of how the optical properties of a sample can change the polarization of light [73]. The center box shows the decomposition of right elliptically polarized (REP) and left elliptically polarized (LEP) light into two orthogonal polarization bases: circular and linear. In the circular basis, elliptical light results from the addition of unequal amounts of right-circularly polarized (RCP) and left-circularly polarized (LCP) light. The relative phases of RCP and LCP (indicated by the arrowheads) determine the orientation of the ellipse (see Figure 7.1). Diagrams at each of the four corners show the effect of optical properties—circular dichroism (CD), linear dichroism (LD), circular birefringence (CB), and linear birefringence (LB)—on initially elliptically polarized light. The effects of LD and LB are most easily visualized in terms of the changes in the linear components, whereas CD and CB are most easily visualized in terms of the circular components. The box in the upper left shows the effect of a positive CD on REP and LEP. More LCP than RCP is absorbed, fattening the REP ellipse (which becomes more RCP-like) and thinning the LEP ellipse (which becomes closer to linearly polarized). A positive CB, shown in the lower left, retards RCP relative to LCP and thus rotates REP and LEP in the same direction by an angle equal to half of the retardance angle. Shown in the lower right is the effect of a small LB for the most general case, the birefringence axes askew from the elliptical axes by a nonintegral multiple of 45° (15° retarder with fast axis rotated 30° counterclockwise from horizontal in the example shown). When LB is small, its effect on the orientation and ellipticity are opposite for REP and LEP. (The more complicated effect of large LB is best visualized with the aid of the Poincaré sphere [19].) The rotation results from the relative phase difference induced in the linear basis states so that they are no longer 90° out of phase. This rotation vanishes when the fast LB axis is at a 45° angle from the elliptical axes. The change in eccentricity is caused by the skew between the LB and initial ellipse axes and is at a maximum at 45°. The effect of a skewed LB acting separately on each of the linear basis vectors is to produce polarization ellipses of opposite handedness. The handedness associated with the major axis, REP in this case, determines whether the net eccentricity of the total polarization ellipse is increased or decreased. The effect of LD (shown in the upper right) is to both rotate and change the eccentricity of the polarization ellipse identically for REP and LEP light. As the magnitude of LD increases and approaches the limit of a perfect linear polarizer, the major axis of the ellipse rotates toward the axis of highest transmission and the eccentricity approaches unity. (Adapted from reference 73 with permission of the American Chemical Society.)

For those applications where it is not possible to eliminate birefringence artifacts in TRCD measurements, TRORD measurements can be a useful alternative because birefringence affects ORD signals to second order rather than to first order, as is the case for TRCD measurements. One recent development where this was shown to be important is in T-jump experiments, as discussed above. A temperature jump on the order of 10–20°C produces a shock wave in the sample and significant strain in cell windows. This makes T-jump TRCD measurements more difficult, but T-jump ORD measurements have been produced successfully [18].

Linear birefringence artifacts can actually be less problematic for TRMCD measurements than for TRCD measurements because the "raw" MCD signals for chiral molecules like proteins typically comprise MCD plus natural CD, so that pure MCD is determined by taking the difference between the signals measured with parallel and antiparallel orientations of the magnetic field. The birefringence effects are the same for both field orientations, so they tend to cancel from the difference in such MCD measurements. While this reduces the susceptibility of MCD measurements to LB effects, other artifacts are of concern. For one, the laser polarization axis must be controlled with respect to the magnetic field direction, as well as the probe beam polarization axis. Another factor for MCD measurements that is not present for CD measurements is the homogeneity of the magnetic fields of both the magnet surrounding the sample and the magnet surrounding the compensator because inhomogeneities result in different optical rotations in different parts of the probe beam.

7.6. CD AND MCD IN SAMPLES ORIENTED BY LASER PHOTOSELECTION

Besides potentially affecting near-null TRCD/ORD and TRMCD/MORD measurements in an indirect manner, by inducing the linear dichroism and birefringence artifacts discussed above, laser excitation-induced anisotropy may also directly alter the CD/ORD and MCD/MORD properties of a sample. When laser excitation partially orients a molecular sample through the process of photoselection, the extent of orientation depends on the symmetry properties of the chromophoric transition, the intensity, polarization, and propagation properties of the light, and the orientation and excitation relaxation properties of the sample [17]. In fluid samples, both the direct and indirect effects of photoselection decay with the rotational diffusion lifetime, so that (in the absence of population decay back to the prephotolysis state) the return to the isotropic TRCD or TRMCD signal, $\Delta\alpha_{t=\infty}$ (and similarly for TRORD or TRMORD), is given by

$$\Delta\alpha(t) - \Delta\alpha_{t=\infty} = (\Delta\alpha_{t=0+} - \Delta\alpha_{t=\infty}) \exp[-6D_R t], \tag{7.4}$$

where $\Delta\alpha = \alpha_L - \alpha_R$ is the apparent difference in absorption coefficients for left- and right-circularly polarized probe light, respectively, $\Delta\alpha_{t=0+}$ is the rotationally unrelaxed TRCD/MCD immediately after photolysis, and D_R is the rotational diffusion constant. The diffusion constant for isotropic molecules is given by $D_R = k_B T/(6\eta V)$, where η is the viscosity, k_B is the Boltzmann constant, T is absolute temperature, and V is the hydrodynamic volume of the solute.

Expressions for the natural CD and MCD of photoselection-oriented molecules, $\Delta\alpha_{PS}$, are given in the following subsections. (Note that they were derived using the assumption that depletion of the isotropic sample existing before photo-excitation can be ignored.) Those results are connected to the time dependence contained in Eq. (7.4) through the expression $\Delta\alpha_{t=0+} - \Delta\alpha_{t=\infty} = \Delta\alpha_{PS} - \Delta\alpha_{-ISO}$, where $\Delta\alpha_{-ISO}$ is the pre-photoconversion dichroism of that subset of isotropic molecules that will undergo photoconversion. (Note that $\Delta\alpha_{-ISO}$ will reflect the same photoselection orientation factors as $\Delta\alpha_{PS}$.) If no pre-conversion transitions overlap the probe frequency ν, then $\Delta\alpha_{-ISO}(\nu) = 0$. If pre-conversion transitions do overlap with ν, then $\Delta\alpha_{-ISO}$ can be calculated from the expressions below for $\Delta\alpha_{PS}$ by replacing all quantities referenced to the probe beam (e.g., bandshape functions, matrix elements) with their pre-photoconversion equivalents.

Expressions for oriented ORD and MORD (not shown) can be calculated by Kramers–Kronig transformations of the corresponding CD and MCD expressions. More general discussions of the spectroscopy of photoselection-oriented samples can be found in [19] and [20].

7.6.1. CD of Samples Oriented by Photoselection

The orientation-averaged CD of a photoselected sample with nondegenerate transitions [bandshape function $= g(\nu)$] at the probe frequency ν and the pump frequency ν' is given for a collinear excitation geometry by

$$\Delta\alpha_{PS} = \alpha_L - \alpha_R = \frac{2}{15} kk' N\phi I \, g(\nu) g(\nu') \{3|\boldsymbol{\mu}'|^2 \mathrm{Im}(\boldsymbol{\mu} \cdot \mathbf{m}) + (\boldsymbol{\mu} \cdot \boldsymbol{\mu}')\mathrm{Im}(\boldsymbol{\mu}' \cdot \mathbf{m}) + (\pi\nu/c)(\boldsymbol{\mu}' \times \boldsymbol{\mu})\mathbf{Q}\boldsymbol{\mu}'\}, \tag{7.5}$$

where ϕ is quantum efficiency of photoconversion, I is laser light fluence (photons/cm^2), N is solute concentration (molecules/cm^3), $k = 8\pi^3\nu/hc, h$ is Planck's constant, c is speed of light, $\boldsymbol{\mu}$, $\mathbf{m}$, and $\mathbf{Q}$ are the electric dipole, magnetic dipole, and electric quadrupole moments for the probe transition, respectively, and primes indicate the corresponding pump transition parameters [21]. The quadrupole term in Eq. (7.5) does not appear in the CD of isotropic samples and also vanishes from the analogous expression for the degenerate transition case. More general expressions for the CD of photoselected samples (that are initially isotropic) and their applications to special symmetry cases can be found in reference 21.

7.6.2. MCD of Samples Oriented by Photoselection

The orientation averaged MCD of a photoselected sample excited by a linearly polarized pump beam propagating perpendicularly to the probe beam (crossed beam geometry, X-beam) is given by

$$\Delta\alpha_{PS} = \Delta\alpha^{X-beam} = \frac{-2Hkk' NI\phi}{15} g'(\nu) \left[\frac{a}{h} \frac{\partial g(\nu)}{\partial \nu} + \left(b + \frac{c}{k_B T} \right) g(\nu) \right], \tag{7.6}$$

where

$$a = \overline{A}_1 + \overline{A}_2 \sin^2\theta + \overline{A}_3 \cos^2\theta,$$

$$b = -\mathrm{Im}\{\overline{B}_1 + \overline{B}_2 \sin^2\theta + \overline{B}_3 \cos^2\theta\},$$
$$c = \overline{C}_1 + \overline{C}_2 \sin^2\theta + \overline{C}_3 \cos^2\theta, \tag{7.7}$$

θ is the azimuthal angle of the pump polarization relative to the pump-probe propagation plane, and H is the applied longitudinal field strength [22]. The subscripted *A, B*, and *C* MCD terms, generalized for photoselection, are given by

$$\overline{A}_1 = \overline{D'}\,\overline{A},$$

$$\overline{A}_2 = \frac{i}{dd'} \sum_{\substack{aa'a'' \\ bb'b''}} \tilde{\boldsymbol{\mu}}^*(i_{a''}f_{b''}) \cdot \tilde{\boldsymbol{\mu}}^*(i'_{a'}f'_{b'})\, \tilde{\boldsymbol{\mu}}(i_a f_b) \times \tilde{\boldsymbol{\mu}}(i'_{a'}f'_{b'}) \cdot [\tilde{\mathbf{m}}(f_b f_{b''})\delta_{aa''} - \tilde{\mathbf{m}}(i_{a''}i_a)\delta_{bb''}],$$

$$\overline{A}_3 = \frac{i}{dd'} \sum_{\substack{aa'a'' \\ bb'b''}} \tilde{\boldsymbol{\mu}}(i_a f_b) \times \tilde{\boldsymbol{\mu}}^*(i_{a''}f_{b''}) \cdot \tilde{\boldsymbol{\mu}}(i'_{a'}f'_{b'})\, \tilde{\boldsymbol{\mu}}^*(i'_{a'}f'_{b'}) \cdot [\tilde{\mathbf{m}}(f_b f_{b''})\delta_{aa''} - \tilde{\mathbf{m}}(i_{a''}i_a)\delta_{bb''}],$$

$$\overline{B}_1 = \frac{\overline{D'}}{d} \sum_{ab} \tilde{\boldsymbol{\mu}}(i_a f_b) \cdot \left[\sum_{j\neq f} \frac{\tilde{\boldsymbol{\mu}}^*(i_a j) \times \tilde{\mathbf{m}}^*(j f_b)}{E_j - E_f} + \sum_{j\neq i} \frac{\tilde{\boldsymbol{\mu}}^*(j f_b) \times \tilde{\mathbf{m}}^*(i_a j)}{E_j - E_i} \right],$$

$$\overline{B}_2 = \frac{1}{dd'} \left\{ \sum_{\substack{aa' \\ bb'}} \tilde{\boldsymbol{\mu}}^*(i'_{a'}f'_{b'}) \cdot \left[\sum_{j\neq f} \frac{\tilde{\boldsymbol{\mu}}^*(i_a j)\tilde{\mathbf{m}}^*(j f_b)}{E_j - E_f} + \sum_{j\neq i} \frac{\tilde{\boldsymbol{\mu}}^*(j f_b)\tilde{\mathbf{m}}^*(i_a j)}{E_j - E_i} \right] \cdot \tilde{\boldsymbol{\mu}}(i_a f_b) \times \tilde{\boldsymbol{\mu}}(i'_{a'}f'_{b'}) \right.$$
$$\left. - \sum_{\substack{aa' \\ bb'}} \tilde{\boldsymbol{\mu}}(i'_{a'}f'_{b'}) \cdot \left[\sum_{j\neq f} \frac{\tilde{\boldsymbol{\mu}}(i_a j) \times \tilde{\mathbf{m}}(j f_b)}{E_j - E_f} + \sum_{j\neq i} \frac{\tilde{\boldsymbol{\mu}}(j f_b) \times \tilde{\mathbf{m}}(i_a j)}{E_j - E_i} \right] \tilde{\boldsymbol{\mu}}^*(i_a f_b) \cdot \tilde{\boldsymbol{\mu}}^*(i'_{a'}f'_{b'}) \right\},$$

$$\overline{B}_3 = \frac{2}{dd'} \sum_{\substack{aa' \\ bb'}} \tilde{\boldsymbol{\mu}}(i'_{a'}f'_{b'}) \times \tilde{\boldsymbol{\mu}}(i_a f_b) \cdot \left[\sum_{j\neq f} \frac{\tilde{\boldsymbol{\mu}}^*(i_a j)\tilde{\mathbf{m}}^*(j f_b)}{E_j - E_f} + \sum_{j\neq i} \frac{\tilde{\boldsymbol{\mu}}^*(j f_b)\tilde{\mathbf{m}}^*(i_a j)}{E_j - E_i} \right] \cdot \tilde{\boldsymbol{\mu}}^*(i'_{a'}f'_{b'}),$$

$$\overline{C}_1 = \overline{D'}\,\overline{C},$$

$$\overline{C}_2 = \frac{i}{dd'} \sum_{\substack{aa'a'' \\ bb'}} \tilde{\boldsymbol{\mu}}^*(i_{a''}f_b) \cdot \tilde{\boldsymbol{\mu}}^*(i'_{a'}f'_{b'})\, \tilde{\boldsymbol{\mu}}(i_a f_b) \times \tilde{\boldsymbol{\mu}}(i'_{a'}f'_{b'}) \cdot \tilde{\mathbf{m}}(i_{a''}i_a),$$

$$\overline{C}_3 = \frac{i}{dd'} \sum_{\substack{aa'a'' \\ bb'}} \tilde{\boldsymbol{\mu}}(i_a f_b) \times \tilde{\boldsymbol{\mu}}^*(i_{a''}f_b) \cdot \tilde{\boldsymbol{\mu}}(i'_{a'}f'_{b'})\, \tilde{\boldsymbol{\mu}}^*(i'_{a'}f'_{b'}) \cdot \tilde{\mathbf{m}}(i_{a''}i_a), \tag{7.8}$$

where E_i, E_f, and E_j denote the energies of initial (i), final (f), and intermediate (j) states, d and d' indicate the (ground state) degeneracies of probe and pump transitions, respectively, and the subscripts a and b label degenerate levels within initial and final states. The *A, B, C*, and *D* (dipole strength) terms for the isotropic case appearing in the

equations above are given by

$$\overline{A} = \frac{i}{2d} \sum_{\substack{aa' \\ bb'}} \tilde{\boldsymbol{\mu}}(i_a f_b) \times \tilde{\boldsymbol{\mu}}^*(i_{a'} f_{b'}) \cdot [\tilde{\mathbf{m}}(f_b f_{b'}) \delta_{aa'} - \tilde{\mathbf{m}}(i_{a'} i_a) \delta_{bb'}],$$

$$\overline{B} = \frac{1}{d} \sum_{ab} \mathrm{Im} \left\{ \tilde{\boldsymbol{\mu}}(i_a f_b) \times \left[\sum_{j \neq f} \frac{\tilde{\mathbf{m}}^*(j f_b) \cdot \tilde{\boldsymbol{\mu}}^*(i_a j)}{E_j - E_f} + \sum_{j \neq i} \frac{\tilde{\mathbf{m}}^*(i_a j) \cdot \tilde{\boldsymbol{\mu}}^*(j f_b)}{E_j - E_i} \right] \right\},$$

$$\overline{C} = \frac{i}{2d} \sum_{aa'b} \tilde{\boldsymbol{\mu}}(i_a f_b) \times \tilde{\boldsymbol{\mu}}^*(i_{a'} f_b) \cdot \tilde{\mathbf{m}}(i_{a'} i_a),$$

$$\overline{D} = \frac{1}{d} \sum_{ab} |\tilde{\boldsymbol{\mu}}(i_a f_b)|^2. \tag{7.9}$$

More general expressions for the oriented MCD as a function of excitation geometry and polarization are given in reference 22 for samples that are initially isotropic. The orientation factor approach described in reference 20 can be used to derive the natural or magnetic circular dichroism of photoselected samples that are not initially isotropic—for example, crystals, membranes, and stretched films.

7.7. APPLICATIONS OF NANOSECOND CHIROPTICAL SPECTROSCOPIES

The million-fold improvement in time resolution presented by near-null ellipsometric (TRCD and TRMCD) and polarimetric (TRORD and TRMORD) techniques, compared with conventional instrumentation, has opened up a range of rapid physicochemical and biophysical processes for study [5–7, 10, 23, 24]. Fast TRCD/ORD methods have been applied to the electronic excited states of inorganic complexes [25–29], RNA photochemistry [30], protein conformational changes in hemoglobin [7, 11, 31] and myoglobin [32, 33], folding reactions in cytochrome *c*, RNase A, and polypeptides [18, 34–41], and the photocycles of phytochrome [42, 43], photoactive yellow protein [44], Phot1 LOV2 protein [45], and the visual pigment rhodopsin [46]. Applications of TRMCD/MORD methods have included functional studies of mammalian cytochrome *c* oxidase [47, 48], the bacterial oxidase cytochrome ba_3 [49], cytochrome c_3 [50], myoglobin [12, 51], and hemoglobin [52, 53], as well as folding studies of cytochrome *c* [34, 54–56]. Data from a selection of these studies are shown in Figure 7.7, and we discuss several of these applications in more detail in the following subsections.

7.7.1. Inorganic Complexes

Nanosecond TRCD spectroscopy can be used to assign the electronic states of metal complexes and examine their ligand–ligand electronic interactions, as has been demonstrated in TRCD spectral studies of the excited states of ruthenium [27, 28], chromium [25], and iron complexes [26]. Chiroptical information can be obtained for short-lived states, as demonstrated in the latter study of iron(II) trisbipyridyl, which measured the CD spectrum of an electronic excited state having an 800-ps lifetime.

7.7.2. Protein Folding

Stopped-flow and rapid mixing far-UV CD studies of protein folding typically have been unable to resolve the most rapid secondary structure formation processes in proteins, as the so-called burst phase may proceed to completion within the ~1 ms or longer dead times characteristic of conventional approaches to time-resolved CD measurements [57, 58]. The first CD study to resolve the submillisecond formation of helical structure in a protein, cytochrome *c*, was reported by Chen et al. in 1998 [34]. That study, which used near-null ellipsometric far-UV TRCD techniques and CO photolysis as a folding trigger, was soon followed by a TRCD study that used photoreduction to trigger folding in this protein [37]. The advantage of the latter method for initiating folding was that it permitted the kinetics of α-helical structure formation to be followed over a much longer time range (from microseconds to several hundred milliseconds) than was practicable with the ligand photolysis method. The signal-to-noise ratio advantage of far-UV TRORD for the detection of ultra-fast secondary structure processes has also been combined with photoreduction triggering to explore the dependence of the submicrosecond to microsecond "burst phase" dynamics on denaturant concentration (Figure 7.8) and the mutation of key protein residues (Figures 7.7e and 7.7f) [35, 36, 39]. The results of these cytochrome *c* TRCD/ORD folding studies, which exploited the redox and photochemical properties of the heme moiety to achieve fast triggering, have been useful in addressing such questions as the simultaneity and cooperativity of ultrafast secondary structure formation (time constant of $\sim 10^{-5}$ s to submicrosecond) with the early collapse phase of unfolded chains observed in Trp fluorescence studies of small globular proteins like cytochrome *c* [59].

What about far-UV TRCD/ORD studies of more general protein sequences that lack a cofactor, such as the heme found in cytochrome *c*, that can provide the chemical reactivity suitable for rapidly initiating secondary structural changes with light? The synthetic addition of photoactive groups, such as azobenzenes, is one way to introduce such a photochemical folding trigger that has been realized in nanosecond TRORD studies of polypeptides [40, 41]. An even more general approach is to use the photophysics of solvent heating by laser pulses. The absorption of brief IR laser pulses by the solvent water can be used to generate temperature jumps of ~10°C that rapidly perturb the folded/unfolded protein conformational equilibrium. However, as mentioned above, because of the stray linear birefringence issues associated with the shock wave produced by rapid solvent heating, this trigger method has been more conveniently coupled with nanosecond near-null TRORD methods than with TRCD [18]. Folding of RNase A and cytochrome *c* has been triggered by rapid heating and probed with TRORD using an apparatus diagrammed in Figure 7.9. This work demonstrated the applicability of the T-jump TRORD method to protein studies [18]. Currently, the kinetics of the α-helix to β-sheet transition (which plays a key role in the folding of many functional proteins and in the formation of the deadly β-sheet structure in many diseases) in poly-L-lysine is being studied with this method. Preliminary data for this study are shown in Figure 7.7d.

The intrachain conformational diffusion rate of unfolded proteins is a fundamental parameter in the dynamics of folding that appears explicitly in energy landscape models and is implicit in the barrier crossing frequency of transition state theory descriptions of folding rates. Despite its theoretical importance, it has been difficult to measure experimentally, particularly for folding-competent protein sequences. However, one route to measuring this parameter has been through near-null polarimetric TRMORD spectroscopy of heme-residue recombination reactions in unfolded cytochrome *c* and Kramers–Kronig transformation of the rotation data to TRMCD spectra [54, 55]. Being more sensitive to

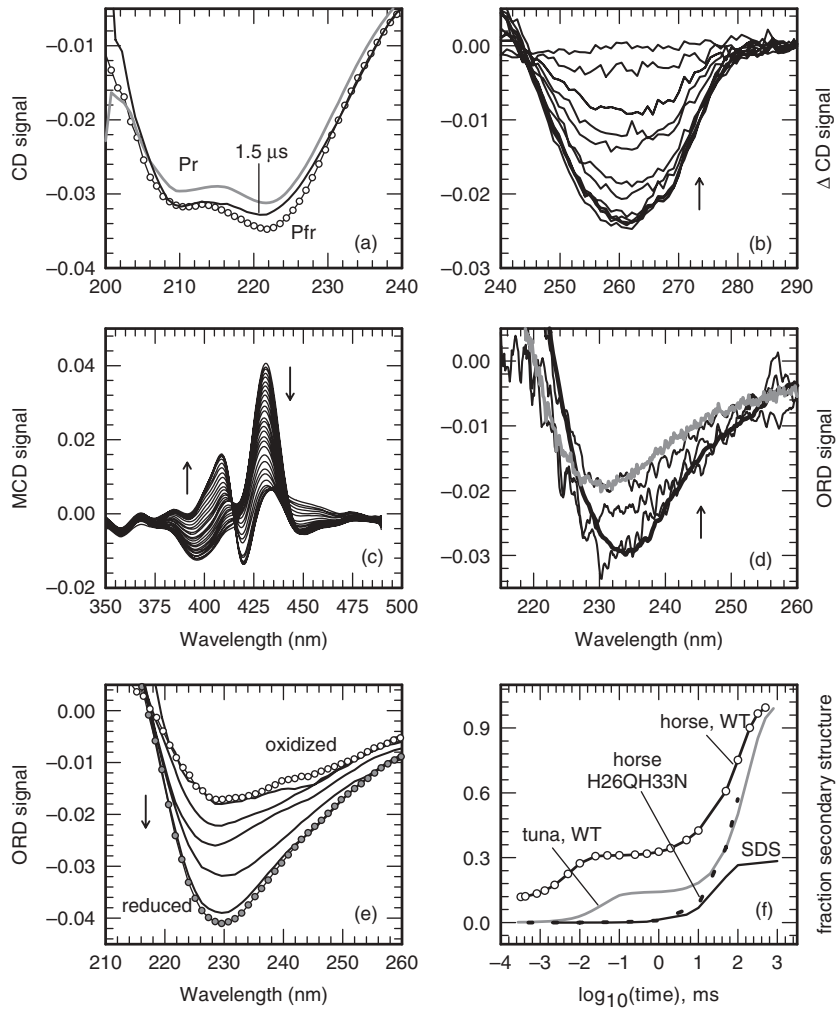

Figure 7.7. Results of protein folding and function studies using time-resolved polarization spectroscopy. (a) Far-UV TRCD data of the phytochrome A photoactivation (not shown) and photoreversion reactions [42, 43]. The spectra of the switch-off (Pr, gray line) and switch-on (Pfr, white circles) forms of phytochrome are shown with the spectrum measured 1.5 μs after photoinitiation of the reversion (Pfr → Pr) reaction. N-terminal α-helical unfolding during photoreversion was assigned to a single exponential process with a time constant of 310 μs, whereas folding of the N-terminal α-helix during photoactivation was slower ($\tau \sim 113$ ms). (b) Near-UV TRCD spectra of MbCO following CO photolysis [33]. The data are shown as the difference between the photoproduct CD spectra measured at 18 time delays from 220 ns to 10 ms after photolysis and the ground-state MbCO CD spectrum. The temporal behavior of the CD data was fit to two exponential processes with lifetimes of 110 μs and 1.5 ms. Together with near-UV TROD results, the 110-μs near-UV TRCD component was proposed to reflect early motions of tyrosines and/or nearby aromatic groups in response to an event that triggers ligand rebinding. (c) Heme ligand dynamics during reduced cytochrome *c* folding (4.6 M guanidine hydrochloride (GuHCl)) probed with TRMORD/MCD spectroscopy in the Soret region [54]. These 32 TRMCD spectra were calculated from TRMORD signals that were measured from 330 ns to 25 ms after CO-photodissociation-initiated folding of reduced cytochrome *c*. The time-dependent changes of the MCD data were best described by four exponential processes ($\tau = 3$, 50, 300, and 700 μs) and suggested that the heme ligand kinetics during folding are better interpreted by a heterogeneous

the nature of the heme ligand than ordinary absorption, MCD of the heme Soret bands is better able to detect the influence of finite intrachain diffusion on the microsecond-timescale kinetic competition between methionine and histidine residues for binding to the heme site vacated by CO photolysis.

7.7.3. Protein Function

The photocycle of rhodopsin, which activates the firing of visual neurons, appears to comprise a large number of distinct intermediates. However, the absorption spectra of many of the intermediates are similar, which tends to obscure the structural basis of the activation process. Turning to a more structure-sensitive chiroptical approach, an initial (near-null ellipsometric) TRCD study of rhodopsin in the UV–vis spectral bands of its *N*-retinylidene Schiff base prosthetic chromophore revealed a ∼10–100-μs timescale spectral evolution that was not seen in ordinary absorption, a finding that could point to a chromophore conformational change that is the earliest direct trigger for activation [46].

Early evidence from time-resolved absorption studies suggested that hemoglobin's R → T quaternary structural change happened about 20 μs after removal of the heme ligands from the R state (typically accomplished by photolyzing the CO complex) [60]. However, near-UV TRCD spectroscopy of the aromatic residue bands revealed a much faster spectral evolution with a spectral signature characteristic of quaternary structural changes [31]. This finding suggested the existence of an early kinetic step along a compound R → T pathway. The compound nature of the allosteric transition was then confirmed by near-UV TRMCD spectroscopy. TRMCD showed that a Trp–Asp hydrogen

←

Figure 7.7. (*Continued*) versus homogeneous folding model. (d) T-jump TRORD studies of the α-helix to β-sheet transition in poly-L-lysine (PLL). TRORD signals (thin black lines) measured at 500 ns, 4 μs, and 25 μs after a 7 K T-jump are compared to the equilibrium signal for α-helix PLL (pH 12, thick black line) at 314 K. The equilibrium ORD signal for PLL measured at 321 K (gray line) is about 67% of that for α-helix PLL. ORD data measured at 500 ns, 4 μs, and 25 μs show a corresponding 0%, 20%, and 33% decrease in signal intensity. (e and f) TRORD studies of reduced wild-type tuna heart cytochrome *c* folding (3.3 M GuHCl) in the far-UV region [35]. Rapid laser-induced reduction of the initially unfolded oxidized species (white circles) forms an immediate photoproduct characterized by a reduced heme iron and unfolded protein. Because the reduced state of cytochrome *c* favors the folded protein, folding is triggered, as observed in the ORD signals measured at 200 ns, 25 μs, 10 ms, 100 ms, and 500 ms after photoreduction (e). These signals represent only a few time points measured in this experiment and are shown relative to the final folded reduced state of the protein (gray circles). Global kinetic analysis of all the data (27 time delays) yields two exponential processes with time constants of 40 μs and 185 ms. A comparison of the time-dependent formation of secondary structure in 3.3 M GuHCl for wild-type tuna heart (gray line) and wild-type horse heart (black line, white circles) [36] cytochromes *c* shows the absence of the fast folding phase [observed for the latter (see Figure 7.8)] in the tuna protein (f). That there is a sequence dependence of the ultrafast helix formation and that this fast-folding phase may be attributed to the formation of a molten globule intermediate is supported by the kinetic traces measured for folding of the horse heart variant H26QH33N (dotted line) [39] and of horse heart cytochrome *c* in the presence of sodium dodecyl sulfate (SDS) (black line) [38], where folding is initiated from the molten globule state of reduced cytochrome *c*.

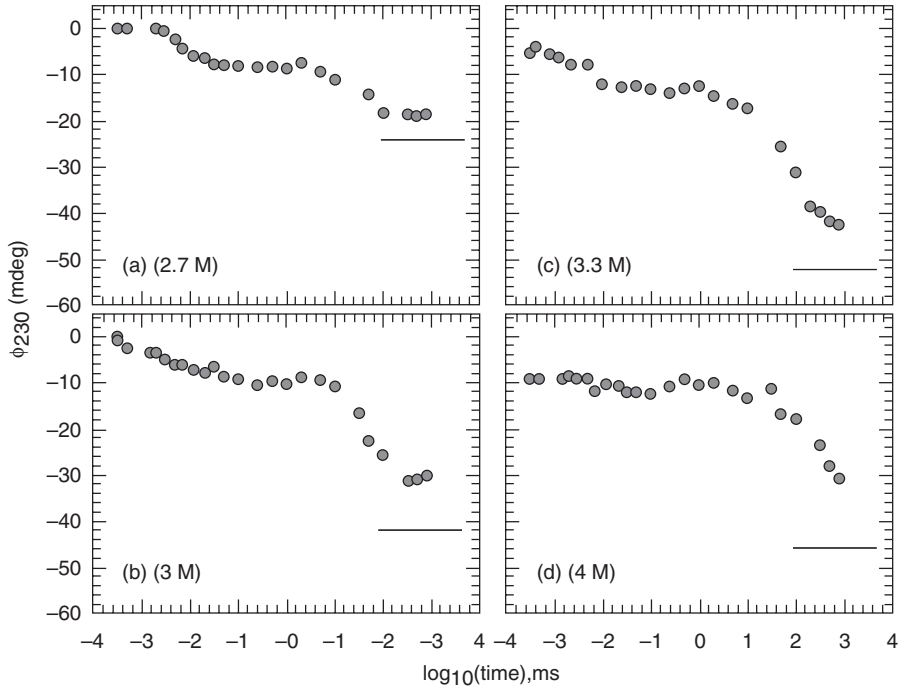

Figure 7.8. Far-UV TRORD studies of the submillisecond (fast phase) kinetics of wild-type horse heart cytochrome *c* secondary structure folding in (a) 2.7 M, (b) 3 M, (c) 3.3 M, and (d) 4 M guanidine hydrochloride (GuHCl) [36]. These studies, which coupled the rapid photoreduction trigger method with time-resolved CD and ORD measurements, report noncanonical behavior of the kinetics of reduced cytochrome *c* folding as a function of GuHCl. On increasing the concentration of denaturant, the behavior of the ORD signal shows formation of secondary structure only after about 5 μs in 2.7 M GuHCl versus formation of 20% secondary structure within the instrument time resolution ($\tau < 400$ ns) in 4 M GuHCl. The solid lines in (a)–(d) indicate the signal intensity for the natively folded reduced cytochrome *c*. The results of these studies suggested the formation of a submillisecond molten-globule-like intermediate during folding of reduced cytochrome *c*.

bond, extending across the dimer–dimer interface and known to be a component of the R → T structural shift that is crucial to allostery and cooperativity in hemoglobin, was formed with a 2-μs time constant, much faster than the canonical R → T step observed in absorption (Figure 7.10) [52].

7.8. OTHER APPROACHES TO FAST AND ULTRAFAST TRCD MEASUREMENTS

In this section we briefly consider other approaches to fast time-resolved chiral spectroscopy. Those alternative approaches that use PEM methods tend to bracket in time the nanosecond to microsecond time regime that is the focus of the near-null ellipsometric and polarimetric methods primarily discussed in this chapter. This is largely because of the kilohertz resonant frequencies characteristic of photoelastic modulators. At timescales much faster than nanoseconds, PEM frequencies are so relatively slow that

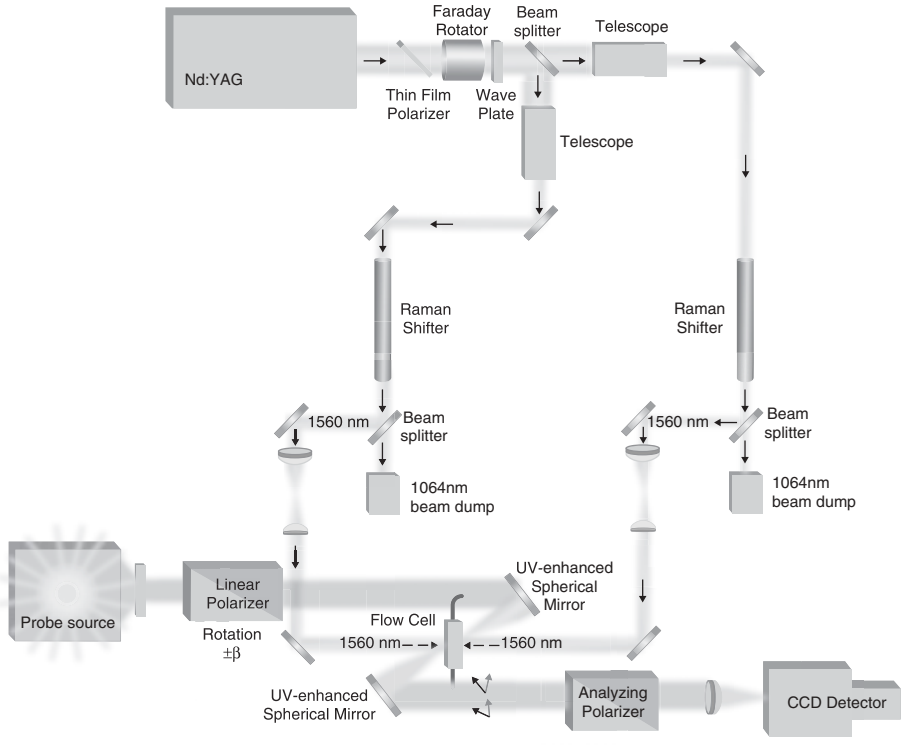

Figure 7.9. A temperature-jump time-resolved optical rotatory dispersion apparatus. This T-jump TRORD system uses a rapid-heater folding trigger that is generated using a stimulated Raman scattering approach coupled to a small-volume TRORD detection method. The output of a Nd:YAG laser, which is protected from potentially deleterious back-reflections with an optical isolater (thin-film polarizer, Faraday rotator, and wave plate), passes through a 50:50 beam splitter to produce two 9-mm 1064-nm beams that are subsequently compressed in diameter to about 4 mm with two separate 2:1 telescopes. After traveling through two D_2-filled Raman shifters, the 1560-nm wavelengths are selected and directed with 1560-nm high reflector mirrors to the sample along counterpropagating paths. The diameters of the 1560-nm beams are controlled with a second set of telescopes for optimal overlap with the probe beam. The ~300-μm probe beam in this small-volume TRORD system is a modification of the TRORD system that is described in Figure 7.4, wherein two UV-enhanced spherical mirrors are used to focus the probe beam into the sample.

they do not interfere with time-resolved measurements. High repetition-rate picosecond and femtosecond lasers can then be synchronized to the PEM frequency to produce circularly polarized probe pulses whose differential absorption by a dichroic sample can be extensively signal averaged in a manner that is broadly similar to that used in conventional PEM-based CD spectroscopy. On the other hand, at timescales much slower than tens of microseconds, PEM frequencies can be fast enough that PEM-based detection methods are again applicable and are typically implemented by using a conventional CD instrument and rapid microfluidic mixing of reactants.

Finally, we will end this chapter by mentioning recent variations of CD ellipsometry that have been applied to ultrashort timescales.

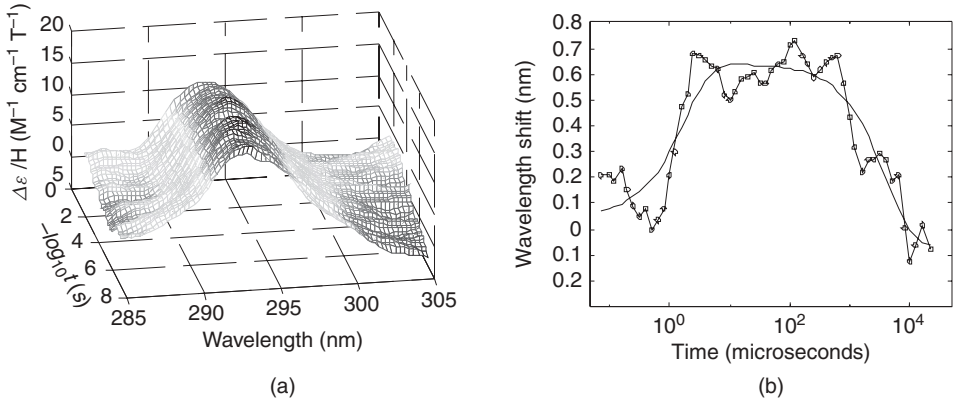

Figure 7.10. An early step in the R → T quaternary transition of hemoglobin detected by TRMCD spectroscopy of the tryptophan bands after photolysis of the CO complex. (a) Near-UV TRMCD spectra collected at delay times ranging from 63 ns to 25 ms after photolysis. (b) A plot of the near-UV Trp band position versus time shows a red shift at 2 μs that corresponds to formation of a Trp–Asp hydrogen bond between the two dimers of the Hb tetramer. (Adapted from reference 52 with permission from the American Chemical Society.) (*See insert for color representation of the figure.*)

7.8.1. PEM-Based Picosecond CD and MCD

Simon and co-workers first implemented picosecond CD detection by using a 1-kHz PEM synchronized to two pulsed dye lasers tunable from 560 to 950 nm [8, 9, 23, 61]. One of the laser beams was passed through a polarizer and the PEM to produce alternating left- and right-circularly polarized probe light, while the second beam was passed though a variable delay line before exciting the sample. Output from the photomultiplier tube (PMT) monitoring the probe beam was fed into a lock-in amplifier referenced to the PEM frequency. Additionally, passing the pump beam though a depolarizer and spinning half-waveplate was found to be necessary to eliminate photoselection-induced linear dichroism artifacts in the CD signal measured by the lock-in amplifier. Also, a servo-controlled neutral density filter placed in the probe beam was used to maintain a constant time-averaged output voltage from the PMT, minimizing distortion of the CD signal that might be caused by nonlinearity of the PMT response when large changes in optical density occur in the sample. This approach has been applied to ultrafast processes in myoglobin and in photosynthetic reaction centers [8, 62] and has been extended to picosecond MCD measurements [63].

7.8.2. Rapid Mixing

The mixing dead-time characteristic of conventional stopped-flow instruments (several milliseconds) can be reduced by an order of magnitude using microfluidic mixing techniques. For instance, an ultrafast solution mixer (for denaturant dilution) was coupled with a commercial CD dichrograph to obtain time-resolved measurements of cytochrome *c* folding with ~400-μs dead time [58]. One caveat to this approach is that strain birefringence caused by high flow pressures may distort the CD signal, as reported in reference 58.

7.8.3. Ultrafast Ellipsometric CD

The near-null polarimetric and ellipsometric techniques for nanosecond TRORD and TRCD spectroscopy presented above can in principle be extended to ultrafast measurements by replacing the microsecond flashlamp as a probe source with an ultrafast white light continuum pulse. Indeed, both single- and multi-wavelength approaches to ultrafast chiroptical spectroscopy using variations of these near-null techniques have been developed.

Hache has described an implementation of ultrafast near-null ellipsometric TRCD that uses 150-femtosecond laser pulses for the pump and probe beams, the former being mechanically chopped and the latter being tunable for single-wavelength CD measurements over the wavelength ranges 230–350 and 400–500 nm [64–66]. This approach uses a Babinet–Soleil compensator as a variable source of reference birefringence (in place of a strain plate). The light intensity transmitted between crossed polarizers is analyzed to second order as a function of the reference birefringence in order to determine the sample CD (as opposed to the first-order analysis described above for ns TRCD). This approach relies on detecting a small shift between two intensity versus retardation parabolas, the first measured by time averaging the transmitted light intensity over the pump chopping frequency and the second measured by a lock-in amplifier referenced to the pump chopping frequency, in order to determine the pump-induced change in sample CD. This parabolic analysis approach is most useful when the pump-induced absorption changes in the sample are not too large. It has been applied to the excited states of ruthenium tris(bipyridyl) and tris(phenanthroline), and the dynamics of conformational change in photoexcited binaphthol, photolyzed carboxymyoglobin, and a photoreceptor protein thought to be involved in light avoidance behavior in the protozoan *Blepharisma japonicum* [67–71].

In a recent multi-wavelength implementation of ultrafast near-null TRORD and TRCD spectroscopy, Mangot et al. focused 150-femtosecond pulses from a 5-kHz Ti:sapphire laser into a CaF_2 crystal to obtain a supercontinuum probe source extending from 350 to 800 nm [72]. Using near-null measurements of the light intensity transmitted by a sample placed between crossed polarizers, the TRORD of the sample after excitation by a femtosecond laser pump pulse was obtained by analyzing the polarizer–analyzer off-rotation angle dependence of the transmitted intensities to second order (similar to the parabolic CD analysis approach of Hache), rather than to first order as described above for nanosecond near-null polarimetric measurements. This apparatus can be modified for multi-wavelength TRCD measurements by placing a broadband quarter-wave plate before the analyzing polarizer.

REFERENCES

1. R. G. W. Norrish, G. Porter, *Nature* **1949**, 164, 658–658.
2. G. Porter, *Proc. R. Soc. London Ser. A* **1950**, 200, 284–300.
3. N. Bloembergen, *Prog. Optics* **2007**, 50, 1–12.
4. P. Agostini, L. F. DiMauro, *Rep. Prog. Phys*. **2004**, 67, 813–855.
5. E. F. Chen, R. A. Goldbeck, D. S. Kliger, *Annu. Rev. Biophys. Biomol. Struct*. **1997**, 26, 327–355.
6. R. A. Goldbeck, D. B. Kim-Shapiro, D. S. Kliger, *Annu. Rev. Phys. Chem*. **1997**, 48, 453–479.

7. J. W. Lewis, R. F. Tilton, C. M. Einterz, S. J. Milder, I. D. Kuntz, D. S. Kliger, *J. Phys. Chem*. **1985**, 89, 289–294.
8. X. L. Xie, J. D. Simon, *J. Am. Chem. Soc*. **1990**, 112, 7802–7803.
9. X. L. Xie, J. D. Simon, *J. Opt. Soc. Am. B* **1990**, 7, 1673–1684.
10. R. A. Goldbeck, T. D. Dawes, S. J. Milder, J. W. Lewis, D. S. Kliger, *Chem. Phys. Lett*. **1989**, 156, 545–549.
11. D. B. Shapiro, R. A. Goldbeck, D. P. Che, R. M. Esquerra, S. J. Paquette, D. S. Kliger, *Biophys. J*. **1995**, 68, 326–334.
12. R. M. Esquerra, R. A. Goldbeck, D. B. Kim-Shapiro, D. S. Kliger, *J. Phys. Chem. A* **1998**, 102, 8749–8758.
13. R. M. Esquerra, R. A. Goldbeck, D. B. Kim-Shapiro, D. S. Kliger, *J. Phys. Chem. A* **1998**, 102, 8740–8748.
14. D. P. Che, D. B. Shapiro, R. M. Esquerra, D. S. Kliger, *Chem. Phys. Lett*. **1994**, 224, 145–154.
15. C. F. Zhang, J. W. Lewis, R. Cerpa, I. D. Kuntz, D. S. Kliger, *J. Phys. Chem*. **1993**, 97, 5499–5505.
16. A. Moscowitz, *Adv. Chem. Phys*. **1962**, 4, 67–112.
17. A. C. Albrecht, *J. Mol. Spectrosc*. **1961**, 6, 84–108.
18. E. F. Chen, Y. X. Wen, J. W. Lewis, R. A. Goldbeck, D. S. Kliger, C. E. M. Strauss, *Rev. Sci. Instrum*. **2005**, 76, 083120.
19. D. S. Kliger, J. W. Lewis, C. E. Randall, *Polarized Light in Optics and Spectroscopy*, Academic Press, Boston, **1990**.
20. J. Michl, E. W. Thulstrup, *Spectroscopy with Polarized Light: Solute Alignment by Photoselection, in Liquid Crystals, Polymers, and Membranes*, VCH, Deerfield Beach, FL, **1986**.
21. D. P. Che, R. A. Goldbeck, D. S. Kliger, *J. Chem. Phys*. **1994**, 100, 8602–8613.
22. R. A. Goldbeck, D. P. Che, D. S. Kliger, *J. Chem. Phys*. **1996**, 104, 6930–6937.
23. J. W. Lewis, R. A. Goldbeck, D. S. Kliger, X. L. Xie, R. C. Dunn, J. D. Simon, *J. Phys. Chem*. **1992**, 96, 5243–5254.
24. E. Chen, R. A. Goldbeck, D. S. Kliger, *Curr. Protein Pept. Sci*. **2009**, 10, 464–475.
25. S. J. Milder, J. S. Gold, D. S. Kliger, *Inorg. Chem*. **1990**, 29, 2506–2511.
26. S. J. Milder, J. S. Gold, D. S. Kliger, *J. Am. Chem. Soc*. **1986**, 108, 8295–8296.
27. S. J. Milder, J. S. Gold, D. S. Kliger, *Chem. Phys. Lett*. **1988**, 144, 269–272.
28. J. S. Gold, S. J. Milder, J. W. Lewis, D. S. Kliger, *J. Am. Chem. Soc*. **1985**, 107, 8285–8286.
29. Y. X. Wen, E. F. Chen, J. W. Lewis, D. S. Kliger, *Rev. Sci. Instrum*. **1996**, 67, 3010–3016.
30. S. J. Milder, P. S. Weiss, D. S. Kliger, *Biochemistry* **1989**, 28, 2258–2264.
31. S. C. Bjorling, R. A. Goldbeck, S. J. Paquette, S. J. Milder, D. S. Kliger, *Biochemistry* **1996**, 35, 8619–8627.
32. S. J. Milder, S. C. Bjorling, I. D. Kuntz, D. S. Kliger, *Biophys. J*. **1988**, 53, 659–664.
33. E. F. Chen, D. S. Kliger, *Inorg. Chim. Acta* **1996**, 242, 149–158.
34. E. Chen, M. J. Wood, A. L. Fink, D. S. Kliger, *Biochemistry* **1998**, 37, 5589–5598.
35. E. F. Chen, R. A. Goldbeck, D. S. Kliger, *J. Am. Chem. Soc*. **2004**, 126, 11175–11181.
36. E. F. Chen, R. A. Goldbeck, D. S. Kliger, *J. Phys. Chem. A* **2003**, 107, 8149–8155.
37. E. F. Chen, P. Wittung-Stafshede, D. S. Kliger, *J. Am. Chem. Soc*. **1999**, 121, 3811–3817.
38. E. Chen, V. Van Vranken, D. S. Kliger, *Biochemistry* **2008**, 47, 5450–5459.
39. E. Chen, C. J. Abel, R. A. Goldbeck, D. S. Kliger, *Biochemistry* **2007**, 46, 12463–12472.
40. E. Chen, G. A. Woolley, D. S. Kliger, Time-resolved optical rotatory dispersion studies of azobenzene cross-linked peptides, in *Methods in Protein Structure and Stability Analysis: NMR and EPR Spectroscopies, Mass-Spectrometry, and Protein Imaging*, V. N. Uversky and E. A. Permyakov, eds., Nova Science, Hauppauge, **2008**, pp. 235–255.

41. E. F. Chen, J. R. Kumita, G. A. Woolley, D. S. Kliger, *J. Am. Chem. Soc*. **2003**, 125, 12443–12449.
42. E. F. Chen, W. Parker, J. W. Lewis, P. S. Song, D. S. Kliger, *J. Am. Chem. Soc*. **1993**, 115, 9854–9855.
43. E. F. Chen, V. N. Lapko, P. S. Song, D. S. Kliger, *Biochemistry* **1997**, 36, 4903–4908.
44. E. Chen, T. Gensch, A. B. Gross, J. Hendriks, K. J. Hellingwerf, D. S. Kliger, *Biochemistry* **2003**, 42, 2062–2071.
45. E. F. Chen, T. E. Swartz, R. A. Bogomolni, D. S. Kliger, *Biochemistry* **2007**, 46, 4619–4624.
46. Y. G. Thomas, I. Szundi, J. W. Lewis, D. S. Kliger, *Biochemistry* **2009**, 48, 12283–12289.
47. R. A. Goldbeck, T. D. Dawes, O. Einarsdottir, W. H. Woodruff, D. S. Kliger, *Biophys. J*. **1991**, 60, 125–134.
48. W. H. Woodruff, O. Einarsdottir, R. B. Dyer, K. A. Bagley, G. Palmer, S. J. Atherton, R. A. Goldbeck, T. D. Dawes, D. S. Kliger, *Proc. Natl. Acad. Sci. USA* **1991**, 88, 2588–2592.
49. R. A. Goldbeck, O. Einarsdottir, T. D. Dawes, D. B. O'Connor, K. K. Surerus, J. A. Fee, D. S. Kliger, *Biochemistry* **1992**, 31, 9376–9387.
50. D. B. O'Connor, R. A. Goldbeck, J. H. Hazzard, D. S. Kliger, M. A. Cusanovich, *Biophys. J*. **1993**, 65, 1718–1726.
51. R. M. Esquerra, R. A. Goldbeck, D. B. Kim-Shapiro, D. S. Kliger, *Biochemistry* **1998**, 37, 17527–17536.
52. R. A. Goldbeck, R. M. Esquerra, D. S. Kliger, *J. Am. Chem. Soc*. **2002**, 124, 7646–7647.
53. D. J. Vitale, R. A. Goldbeck, D. B. Kim-Shapiro, R. M. Esquerra, L. J. Parkhurst, D. S. Kliger, *Biochemistry* **2000**, 39, 7145–7152.
54. R. A. Goldbeck, Y. G. Thomas, E. F. Chen, R. M. Esquerra, D. S. Kliger, *Proc. Natl. Acad. Sci. USA* **1999**, 96, 2782–2787.
55. C. J. Abel, R. A. Goldbeck, R. F. Latypov, H. Roder, D. S. Kliger, *Biochemistry* **2007**, 46, 4090–4099.
56. Y. G. Thomas, R. A. Goldbeck, D. S. Kliger, *Biopolymers* **2000**, 57, 29–36.
57. G. A. Elove, A. F. Chaffotte, H. Roder, M. E. Goldberg, *Biochemistry* **1992**, 31, 6876–6883.
58. S. Akiyama, S. Takahashi, K. Ishimori, I. Morishima, *Nat. Struct. Biol*. **2000**, 7, 514–520.
59. R. A. Goldbeck, E. Chen, D. S. Kliger, *Int. J. Mol. Sci*. **2009**, 10, 1476–1499.
60. J. Hofrichter, J. H. Sommer, E. R. Henry, W. A. Eaton, *Proc. Natl. Acad. Sci. USA* **1983**, 80, 2235–2239.
61. X. L. Xie, J. D. Simon, *Rev. Sci. Instrum*. **1989**, 60, 2614–2627.
62. X. L. Xie, J. D. Simon, *Biochim. Biophys. Acta* **1991**, 1057, 131–139.
63. X. L. Xie, J. D. Simon, *J. Phys. Chem*. **1990**, 94, 8014–8016.
64. F. Hache, *J. Photochem. Photobiol. A: Chem*. **2009**, 204, 137–143.
65. C. Niezborala, F. Hache, *J. Opt. Soc. Am. B* **2006**, 23, 2418–2424.
66. C. Niezborala, F. Hache, *J. Opt. Soc. Am. B* **2007**, 24, 1012–1012.
67. T. Dartigalongue, F. Hache, *Chem. Phys. Lett*. **2005**, 415, 313–316.
68. T. Dartigalongue, F. Hache, *Chirality* **2006**, 18, 273–278.
69. T. Dartigalongue, C. Niezborala, F. Hache, *Phys. Chem. Chem. Phys*. **2007**, 9, 1611–1615.
70. C. Niezborala, F. Hache, *J. Am. Chem. Soc*. **2008**, 130, 12783–12786.
71. F. Hache, M. T. Khuc, J. Brazard, P. Plaza, M. M. Martin, G. Checcucci, F. Lenci, *Chem. Phys. Lett*. **2009**, 483, 133–137.
72. L. Mangot, G. Taupier, M. Romeo, A. Boeglin, O. Cregut, K. D. Dorkenoo, *Opt. Lett*. **2010**, 35, 381–383.
73. S. C. Bjorling, R. A. Goldbeck, S. J. Milder, C. E. Randall, J. W. Lewis, D. S. Kliger, *J. Phys. Chem*. **1991**, 95, 4685–4694.

8

FEMTOSECOND INFRARED CIRCULAR DICHROISM AND OPTICAL ROTATORY DISPERSION

Hanju Rhee and Minhaeng Cho

8.1. INTRODUCTION

The property of light propagating through a medium differs from that through a vacuum, because its velocity and intensity are modulated due to the frequency-dependent refractive index $n(\omega)$ and absorption coefficient $\kappa(\omega)$ of the medium, respectively, which reflect the intrinsic optical properties of the medium. Consequently, frequency-dependent phase retardation and attenuation processes occur simultaneously [1]. In the case that the optical medium is spatially isotropic and contains no chiral molecules, these quantities at a given frequency remain the same irrespective of radiation polarization state, meaning that the transmitted light polarization state does not change by the medium. However, for a solution including chiral molecules, this is not the case for circular polarization (left, LCP; right, RCP) because the parameters, $n(\omega)$ and $\kappa(\omega)$, leading the dispersion and absorption processes vary with its handedness; that is, we have $n_L(\omega) \neq n_R(\omega)$ and $\kappa_L(\omega) \neq \kappa_R(\omega)$ [2]. The circular dichroism (CD) and circular birefringence (CB), referred to as the *optical activity*, are directly related to the frequency-dependent differential absorption coefficient, $\Delta\kappa(\omega) = \kappa_L(\omega) - \kappa_R(\omega)$, and the differential refractive index, $\Delta n(\omega) = n_L(\omega) - n_R(\omega)$, respectively. Throughout this chapter, we will use the terms *optical rotatory dispersion* (ORD) and *circular birefringence* (CB) together when denoting Δn because the optical rotation of linearly polarized light is the actual observable, which is solely related to the CB.

These chiroptical properties are manifested by almost all natural products and drugs, and they are highly sensitive to their conformations and absolute configurations. The

Comprehensive Chiroptical Spectroscopy, Volume 1: Instrumentation, Methodologies, and Theoretical Simulations, First Edition. Edited by N. Berova, P. L. Polavarapu, K. Nakanishi, and R. W. Woody.
© 2012 John Wiley & Sons, Inc. Published 2012 by John Wiley & Sons, Inc.

CD or ORD spectroscopy has therefore been extensively used to elucidate secondary structures of biomolecules such as polypeptides and proteins and to determine absolute configurations of chiral drugs dissolved in condensed phases or bound to target proteins [2]. In principle, $\kappa(\omega)$ and $n(\omega)$ are related to each other via the *Kramers–Kronig* relations [3–5], but in practice, the two observables, CD and ORD spectra, should be measured independently due to the limitation in the experimentally achievable frequency range. Before the 1990s, the CD spectroscopy was more widely used than the ORD measurement in studying structural details of chiral molecules, which was not only because the measurement is comparatively easy but also because direct comparisons between experimental and quantum mechanically calculated results were possible. In particular, the electronic CD spectrum was interpreted using sector rules and exciton coupling models. The conventional CD spectroscopy relies on a differential intensity measurement technique, where the absorbance difference of LCP and RCP lights by the chiral sample is selectively measured. In the case of the vibrational CD (VCD) [6, 7], which is the vibrational analog of electronic CD, the chiral susceptibilities for nuclear vibrations are far much smaller than the corresponding signals in the UV–vis range, which originate from the angular motions of electronic degrees of freedom. Consequently, it is by no means an easy measurement because one has to differentiate such a weak effect by using the differential measurement scheme with relatively largely fluctuating incident IR beams. This is why it still takes a long time (typically a few hours) to acquire a statistically meaningful VCD spectrum with commercially available VCD spectrometers.

Despite the successes of the conventional VCD measurement methods, they still pose certain limitations that prevented further methodological advancements for a wide range of applications including time-resolved VCD studies of biomolecules. Understanding this difficulty starts from realizing that the vibrational response of chiral molecule is related to helical oscillations of charged particles that are associated with nuclear motions in a given chiral molecule. Such helical oscillations can be decomposed into angular and linear components representing chiral and achiral effects, respectively. A major difficulty of the conventional differential absorbance (ΔA) measurement technique is associated with the fact that such angular components (magnetic dipole responses) of the nuclear motions are extremely small in comparison to the linear components (electric dipole responses). Consequently, the VCD (measuring ΔA) signal is masked by the strong achiral IR absorption signal ($\Delta A/A = 10^{-4}–10^{-6}$), which is in this case a huge fluctuating achiral background noise. Recently, it has been shown that the electric field measurement [8–11] and calculation [12, 13] methods based on a time-domain characterization of infrared optical activity (IOA) are alternative and promising approaches overcoming some of the problems hampering the differential intensity measurement and gas-phase *ab initio* calculation methods, respectively.

To provide an explanation on the underlying principles of the electric field approaches, we find it useful to consider the fundamental difference between quantum mechanical and classical mechanical descriptions of particle dynamics, which is essentially the phase factor of quantum mechanical wavefunction [14]. Phase information is lost when the absolute square of the wavefunction is experimentally measured. Similarly, a free-induction-decay (FID) field $\mathbf{E}$ generated by the linear polarization of a given material interacting with an incident radiation is a complex function containing an additional time- and space-dependent phase factor, $\exp(i\phi)$, compared to the incident electric field [2]. Conventional circular dichroism is usually based on an intensity measurement technique so that the intensities $|\mathbf{E}|^2$ of the transmitted fields when a chiral solution sample interacts with LCP and RCP radiations are separately measured. Note

that the imaginary part of the phase factor is responsible for the differential absorbance of chiral molecules for LCP and RCP radiations, whereas its real part is associated with the optical rotation of an incident linearly polarized radiation. Direct characterization of such a complex phase factor thus requires special measurement methods. Recently, it was shown that a combination of cross-polarization analyzer and heterodyned interferometric detection method is capable of measuring both the phase and the amplitude of the IOA FID field $\mathbf{E}$ instead of $|\mathbf{E}|^2$ with respect to the incident radiation [8–11]. We shall refer these measurement and calculation methods to as electric field approaches. In this chapter, we will provide discussions on both theoretical and experimental aspects of the time-domain IOA of chiral molecules in condensed phases.

8.2. TIME CORRELATION FUNCTION THEORY

The radiation–matter interaction Hamiltonian in the minimal coupling scheme is given by the inner product of the vector potential of the electromagnetic field and the momentum operator of charged particles [15]. Then, the multipolar expansion form of the interaction Hamiltonian, which is valid up to the first order in the wavevector $\mathbf{k}$, is given as [8, 12, 13, 16, 17]

$$H_I = -\boldsymbol{\mu} \cdot \mathbf{E}(\mathbf{r},t) - \mathbf{M} \cdot \mathbf{B}(\mathbf{r},t) - (1/2)\mathbf{Q} : \nabla \mathbf{E}(\mathbf{r},t). \tag{8.1}$$

Here, $\mathbf{E}$ and $\mathbf{B}$ are the electric and magnetic fields, respectively. $\boldsymbol{\mu}$, $\mathbf{M}$, and $\mathbf{Q}$ are the electric dipole, magnetic dipole, and electric quadrupole operators, respectively. Using the linear response theory, one can find that the linear polarization is given as [8]

$$\mathbf{P}^{(1)}(\mathbf{r},t) = < \boldsymbol{\mu}\rho^{(1)}(\mathbf{r},t) > + < (\mathbf{M} \times \hat{\mathbf{k}})\rho^{(1)}(\mathbf{r},t) > -(i/2) < (\mathbf{k} \cdot \mathbf{Q})\rho^{(1)}(\mathbf{r},t) >, \tag{8.2}$$

where $\hat{\mathbf{k}} \equiv \mathbf{k}/|\mathbf{k}|$ and $\rho^{(1)}(\mathbf{r},t)$ is the first-order perturbation-expanded density operator with respect to the above radiation–matter interaction Hamiltonian H_I in Eq. (8.1). Then, the linear polarization in Eq. (8.2) can be rewritten in terms of the corresponding linear response functions [16]:

$$\begin{aligned}\mathbf{P}^{(1)}(\mathbf{r},t) = \rho_0 \int_0^\infty d\tau \{&\phi_{\mu\mu}(\tau) + \phi_{\mu M}(\tau) + (i/2)\phi_{\mu Q}(\tau) + \phi_{M\mu}(\tau) \\ &- (i/2)\phi_{Q\mu}(\tau)\} \cdot \mathbf{e}E(\mathbf{r}, t-\tau),\end{aligned} \tag{8.3}$$

where $\mathbf{e}$ is the unit vector in the polarization direction of the external electric field and ρ_0 is the number density N/V. The linear response functions in Eq. (8.3) are defined as [16]

$$\begin{aligned}
\phi_{\mu\mu}(\tau) &\equiv \frac{i}{\hbar}\theta(\tau) < [\boldsymbol{\mu}(\tau), \boldsymbol{\mu}(0)]\rho_{eq} >, \\
\phi_{\mu M}(\tau) &\equiv \frac{i}{\hbar}\theta(\tau) < [\boldsymbol{\mu}(\tau), \mathbf{M}(0) \times \hat{\mathbf{k}}]\rho_{eq} >, \\
\phi_{\mu Q}(\tau) &\equiv \frac{i}{\hbar}\theta(\tau) < [\boldsymbol{\mu}(\tau), \mathbf{k} \cdot \mathbf{Q}(0)]\rho_{eq} >, \\
\phi_{M\mu}(\tau) &\equiv \frac{i}{\hbar}\theta(\tau) < [\mathbf{M}(\tau) \times \hat{\mathbf{k}}, \boldsymbol{\mu}(0)]\rho_{eq} >, \\
\phi_{Q\mu}(\tau) &\equiv \frac{i}{\hbar}\theta(\tau) < [\mathbf{k} \cdot \mathbf{Q}(\tau), \boldsymbol{\mu}(0)]\rho_{eq} > .
\end{aligned} \tag{8.4}$$

Here, $< \ldots >$ denotes the trace over the bath states and ρ_{eq} is the thermal equilibrium density operator. The first term on the right-hand side of Eq. (8.3), which represents the electric dipole response against the external electric field, is typically two to three orders of magnitude larger than the other terms for *electronic* transition or four to six orders for *vibrational* transition.

Without loss of generality, it is assumed that the incident field propagates along the z axis in a space-fixed frame,—that is, $\mathbf{k} = (\omega_0/c)\hat{\mathbf{z}}$, where ω_0 is the center frequency of the electric field—and that $\mathbf{e} = \hat{\mathbf{y}}$. The rotationally averaged y component of $\mathbf{P}^{(1)}(t)$, which is the temporal amplitude of $\mathbf{P}^{(1)}(\mathbf{r}, t)$, is then found to be

$$P_y^{(1)}(t) = \int_0^\infty d\tau \chi_{\mu\mu}(\tau) E(t-\tau), \tag{8.5}$$

where

$$\chi_{\mu\mu}(t) \equiv \rho_0 \left(\frac{i}{\hbar}\right) \langle [\mu_y(t), \mu_y(0)] \rho_{eq} \rangle. \tag{8.6}$$

In this case that the y component of $\mathbf{P}^{(1)}(t)$, which is parallel to the polarization direction of the incident beam, is measured, the magnetic dipole and electric quadrupole contributions to the linear polarization in Eq. (8.3) vanish. From the electric dipole–electric dipole response function given in Eq. (8.6), the linear susceptibility in frequency domain is defined as

$$\chi(\omega) = \int_0^\infty dt \chi_{\mu\mu}(t) e^{i\omega t} = \chi'(\omega) + i\chi''(\omega). \tag{8.7}$$

The imaginary part of $\chi(\omega)$, denoted as $\chi''(\omega)$, can be rewritten as

$$\begin{aligned} \chi''(\omega) &= \frac{\pi\rho_0}{\hbar} \sum_{a,b} P(a) |\mu_{ab}|^2 [\delta(\omega - \omega_{ba}) - \delta(\omega + \omega_{ba})] \\ &= \frac{\pi\rho_0}{\hbar} (1 - e^{-\beta\hbar\omega}) \sum_{a,b} P(a) |\mu_{ab}|^2 \delta(\omega - \omega_{ba}), \end{aligned} \tag{8.8}$$

where $P(a)$ is the population of the initial state $|a\rangle$ and μ_{ab} is the transition dipole moment defined as $\mu_{ab} = \langle a|\mu_y(0)|b\rangle$. $\beta = 1/k_B T$ where k_B is the Boltzmann constant. The absorption lineshape function $g(\omega)$ in an isotropic medium is then given as

$$g(\omega) = \frac{3\hbar\varepsilon''(\omega)}{4\pi^2(1 - e^{-\beta\hbar\omega})} = \frac{\rho_0}{2\pi} \int_{-\infty}^{\infty} dt e^{i\omega t} \langle \boldsymbol{\mu}(t) \cdot \boldsymbol{\mu}(0) \rangle, \tag{8.9}$$

where the imaginary part of the dielectric constant is related to the imaginary part of the susceptibility as $\varepsilon''(\omega) = 4\pi\chi''(\omega)$.

We next consider the linear optical activity such as circular dichroism and circular birefringence. When the incident radiation is circularly polarized, the unit vector $\mathbf{e}$ is given as $\mathbf{e}_L = (\hat{x} + i\hat{y})/\sqrt{2}$ and $\mathbf{e}_R = (\hat{x} - i\hat{y})/\sqrt{2}$ for the left- and right-circularly polarized lights, respectively. The difference polarization, which is related to the linear optical activity, is defined as $\Delta\mathbf{P}(\mathbf{r}, t) = \mathbf{P}^L(\mathbf{r}, t) - \mathbf{P}^R(\mathbf{r}, t)$, where $\mathbf{P}^{L,R}(\mathbf{r}, t)$ is the linear

polarization induced by the left- or right-circularly polarized light. Instead of considering the y component of these linear polarizations, we now consider the rotationally averaged x components of the linear polarizations $\mathbf{P}^L(\mathbf{r},t)$ and $\mathbf{P}^R(\mathbf{r},t)$ that are found to be

$$P_x^L(\mathbf{r},t) = \frac{1}{\sqrt{2}}\int_0^\infty d\tau\{\chi_{\mu\mu}(\tau) + \chi_{\mu M}(\tau) + \chi_{M\mu}(\tau)\}E(\mathbf{r},t-\tau), \tag{8.10}$$

$$P_x^R(\mathbf{r},t) = \frac{1}{\sqrt{2}}\int_0^\infty d\tau\{\chi_{\mu\mu}(\tau) - \chi_{\mu M}(\tau) - \chi_{M\mu}(\tau)\}E(\mathbf{r},t-\tau), \tag{8.11}$$

where

$$\chi_{\mu M}(t) \equiv \rho_0\left(\frac{i}{\hbar}\right)\langle[\mu_x(t), -iM_x(0)]\rho_{eq}\rangle, \tag{8.12}$$

$$\chi_{M\mu}(t) \equiv \rho_0\left(\frac{i}{\hbar}\right)\langle[M_x(t), i\mu_x(0)]\rho_{eq}\rangle. \tag{8.13}$$

Note that the y components of $\mathbf{P}^L(\mathbf{r},t)$ and $\mathbf{P}^R(\mathbf{r},t)$ are the same, so that the y component of the difference polarization $\Delta\mathbf{P}(\mathbf{r},t)$ is zero. From Eqs. (8.10) and (8.11), we find that the rotationally averaged x component of the difference polarization is

$$\Delta P_x(t) = \frac{1}{\sqrt{2}}\int_0^\infty d\tau\,\Delta\chi(t-\tau)E(\tau), \tag{8.14}$$

where the linear optical activity susceptibility, $\Delta\chi(t)[\equiv \chi_L(t) - \chi_R(t)]$, is related to the electric dipole–magnetic dipole response functions in Eqs. (8.12) and (8.13) as

$$\Delta\chi(t) \equiv 2\{\chi_{\mu M}(t) + \chi_{M\mu}(t)\}, \tag{8.15}$$

Note that the electric dipole–electric dipole and the electric dipole–electric quadrupole responses do not contribute to $\Delta P_x(t)$ because they all vanish after rotational averaging of the corresponding second- and third-rank tensorial response functions over randomly oriented chiral molecules in solutions. From Eq. (8.15), one can obtain the linear optical activity susceptibility in frequency domain,

$$\begin{aligned}\Delta\chi(\omega) &= \frac{\rho_0}{\hbar}\int_0^\infty dt\ e^{i\omega t}\{\langle[\mu_x(t), M_x(0)]\rho_{eq}\rangle - \langle[M_x(t),\mu_x(0)]\rho_{eq}\rangle\} \\ &= \frac{\rho_0}{\hbar}(1-e^{-\beta\hbar\omega})\sum_{a,b}P(a)(\mu_{ab}M_{ba} - M_{ab}\mu_{ba})\int_0^\infty dt\ e^{i(\omega-\omega_{ba})t},\end{aligned} \tag{8.16}$$

where $\mu_{ab} = \langle a|\mu_x(0)|b\rangle$ and $M_{ab} = \langle a|M_x(0)|b\rangle$. Using the relationship $\int_{-\infty}^\infty dt\ e^{i\omega t}\langle A(t)B(0)\rangle = \left(\int_{-\infty}^\infty dt\ e^{i\omega t}\langle B(t)A(0)\rangle\right)^*$, the lineshape function of the circular dichroism $\Delta g(\omega)$ in an isotropic medium is then given as

$$\Delta g(\omega) = \frac{3\hbar\Delta\varepsilon''(\omega)}{4\pi^2(1-e^{-\beta\hbar\omega})} = \frac{\rho_0}{\pi}\mathrm{Im}\int_{-\infty}^\infty dt\ e^{i\omega t}\langle\boldsymbol{\mu}(t)\cdot\mathbf{M}(0)\rangle. \tag{8.17}$$

This result shows that the cross-correlation function of electric dipole and magnetic dipole is directly related to the CD spectrum via Fourier transformation. Consequently, a direct calculation of the cross-correlation function in time is enough to obtain the CD spectrum.

8.3. DIFFERENTIAL INTENSITY MEASUREMENT METHOD

In this section, we present a brief discussion on the conventional differential intensity measurement of VCD with LCP and RCP radiations, for the sake of comparison. Figure 8.1 depicts the differential intensity measurement scheme. An equal amount of LCP or RCP beam (I_0) is alternately created by a phase-retarder (PR) and injected into the chiral sample (CS). Then, each intensity ($I_{L,R}$) attenuated by the optical sample is separately recorded at spectrometer. By taking the difference of their logarithmic scales, the CD spectrum (ΔA) is finally obtained as

$$\Delta A = A_L - A_R = -\log\left(\frac{I_L}{I_0}\right) + \log\left(\frac{I_R}{I_0}\right) = \log\left(\frac{I_R}{I_L}\right). \tag{8.18}$$

The sign and intensity of ΔA are determined by the relative magnitudes of I_L and I_R at a given frequency. With $\Delta I = I_L - I_R$ and $I = (I_L + I_R)/2$, ΔA is approximately given by $-\Delta I/(2.303 \times I)$. When the absorption intensity of LCP or RCP beam is measured, most of absorbed photons correspond to the achiral noise originating from the electric dipole free-induction-decay field. These extra photons act as a largely fluctuating noise along the light source fluctuation, which in turn increase shot noise and deteriorate the signal-to-noise ratio significantly. In the case of the VCD, where ΔA value is typically about 10^{-4}–10^{-5} at absorbance $A \sim 1$, even if the incident light is fairly stable and its fluctuation amplitude level is just about 0.1% of its average intensity, it is still very difficult to discriminate such a weak chiral signal (ΔI) from the large fluctuating background noise (I). This is a fundamental problem of the differential measurement method. In the following section, we will show an alternative time-domain approach based on a spectral interferometry that is capable of overcoming some of these difficulties.

8.4. PHASE-AND-AMPLITUDE MEASUREMENT OF IR OPTICAL ACTIVITY

The governing principles of the electric field measurement method can be understood from an explanation of the nondifferential amplitude-level detection scheme, where the

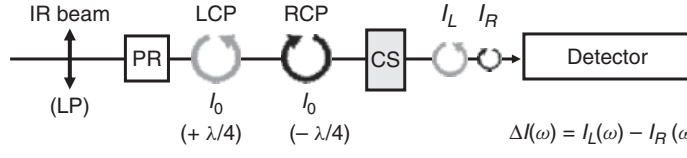

Figure 8.1. Conventional differential VCD intensity measurement scheme. PR, phase-retarder; CS, chiral sample. The PR converts an incident IR LP beam into LCP and RCP ones by alternately controlling the phase retardation ($\pm\lambda/4$). Their attenuated intensity spectra ($I_{L,R}(\omega)$) by the CS are separately measured, and their difference ($\Delta I(\omega)$) corresponds to the VCD spectrum.

IOA field is isolated from the achiral background field and its handedness (phase) and magnitude are subsequently characterized. The transmitted electric field through the cross-polarization analyzer accounts for the chirospecific IR response of chiral solution sample and forms a wave packet of IOA FID field carrying complete IOA (VCD and VORD) information over the whole frequency range of the incident IR pulse spectrum. Secondly, direct phase-and-amplitude measurement of the IOA FID field can be achieved by employing a Fourier-transform spectral interferometry (FTSI) [18–25], which is a useful method for characterizing an unknown weak electric field in terms of its spectral phase and amplitude with respect to a reference field called local oscillator and has been widely used in heterodyne-detected two-dimensional (2D) optical spectroscopy [21–24]. Such a heterodyne detection of the IOA FID using a modified Mach–Zehnder interferometer, where a time delay between the signal and a local oscillator is experimentally controlled, simultaneously provides both VCD and VORD spectra.

8.4.1. Cross-Polarization Detection (CPD) Technique: Enhancement of Chiral Selectivity

The main problems of the conventional intensity measurement method are, as briefly mentioned, that (1) the huge achiral background noise is unnecessarily detected and (2) the differential intensity measurement scheme thus needed to remove such achiral noise is very vulnerable to the light intensity fluctuation. The electric field measurement approach based on a cross-polarization detection (CPD) technique enables us to overcome those problems and to significantly enhance the chiral selectivity. Let us first consider chiral aspects of molecules and radiations. When equal amounts of left- and right-handed enantiomers of a chiral molecule are mixed in solution, such solutions are called *racemate* that is macroscopically nonchiral due to a homogeneous mixing of the two forms and therefore optically inactive. Similarly, two LCP and RCP fields with opposite handedness properties can be combined with equal amount to form a linearly polarized (LP) light field that is nonchiral much like a racemate. If the LP beam transmits through a chiral medium with excess of one enantiomer, its polarization state becomes elliptically polarized by the differential interactions between the two opposite field components, LCP and RCP, with the chiral molecules. Such field chiralization is observed through the VCD and VORD effects.

Figure 8.2a describes the basic concept of the CPD technique and provides a simplified sketch of detailed chiroptical polarization changes involved. A linear polarizer (P1) ensures that an incident IR field becomes a vertical LP beam (= 50% LCP + 50% RCP). While traveling through the chiral sample, each opposite-handed field component experiences different chiroptical responses so that one of the two components is more attenuated and delayed with respect to the other, depending on the molecular chirality. As a result, the incident LP beam is transformed into an elliptically polarized (EP) one whose major axis is a little bit rotated left or right from the vertical axis. With a close inspection of the transmitted EP beam, it becomes possible to decompose it into three different polarization components: vertical LP(V), horizontal LP(H), and circular polarization (CP). The LP(V), which accounts for the achiral electric dipole response signal, is completely removed by another linear polarizer (P2) placed after the sample cell in an ideal case, where its optic axis is perpendicular to that of P1. In contrast, the LP(H) and CP components that are created by the chiral responses, Δn (VORD) and $\Delta\kappa$ (VCD), respectively, are allowed to transmit through the P2.

The phase relationship between the polarization components will be characterized in a subsequent measurement procedure. The LP(H) component (VORD) has 0° or 180°

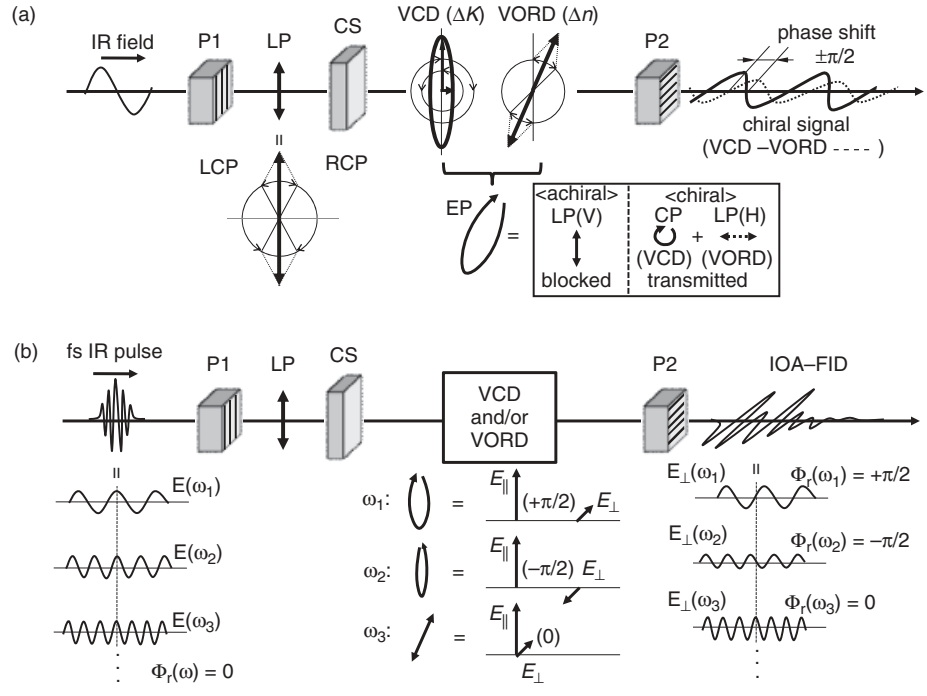

Figure 8.2. Cross-polarization detection (CPD) scheme. P1 and P2, linear polarizers; CS, chiral sample. (a) Monochromatic chiroptical response. The LP beam by the P1 (vertical) is a linear combination of an equal amount of LCP and RCP beams. After passing through the CS, unequal absorption ($\Delta\kappa$, VCD) and phase shift (Δn, VORD) of the two oppositely handed field components lead to a linear-to-elliptical polarization change and at the same time its optical rotation, respectively. The P2 (horizontal) is used to eliminate the vertical LP (achiral) component and allows only the CP (VCD) and the horizontal LP (VORD) components to be transmitted through it. It should be noted that a phase relationship between the VCD and VORD signal fields is in-quadrature ($\pm\pi/2$). (b) Impulsive chiroptical response. A femtosecond IR pulse can be viewed as a collection of multiple longitudinal modes of the laser. The individual frequency components ($\omega_1, \omega_2, \omega_3, \ldots$) experience different chiroptical responses (VCD/VORD). As a result, each horizontally emitted electric field ($E_\perp$) has different amplitude and relative phase (Φ_r). All the phase-and-amplitude modulated field components are superimposed to form a chiral wave packet called IOA FID.

phase shift with respect to the all electric dipole polarization, depending on whether the optical rotation of EP is actually left or right. On the other hand, the horizontal component of LCP or RCP (VCD) is phase-shifted by either $+90^\circ$ or -90°. Therefore, the VCD and VORD components in the transmitted field also have a well-defined in-quadrature phase relationship between the two, since the optical rotation is negligibly small in general. If a proper IR electric field measurement technique that is phase-sensitive is developed, the handedness and intensity of VCD and VORD signals can be simultaneously obtained by directly measuring the phase (handedness) and amplitude (intensity) of the chiral IR electric field without relying on a differential intensity measurement method. This is essentially the basis of the enhanced chiral selectivity achievable in the present electric field approach.

8.4.2. Time-Domain IR Optical Activity Free Induction Decay

For one's better understanding, we have so far simply focused on the monochromatic chiroptical response regarding just a single frequency field component. We shall now consider its impulsive characteristics induced by a femtosecond IR pulse that in fact has a broad range of frequency components (FWHM $\sim$200 cm^{-1}). The mode-locked femtosecond IR pulse can be regarded as a superposition state of longitudinal modes (sine waves) from the laser cavity, whose amplitude distribution is determined by Fourier transformed function of the pulse shape and whose relative phases are all zero. While the incident femtosecond LP pulse transmits through the chiral medium, the individual field components experience frequency-dependent IR responses, which can be divided into the achiral $[n(\omega), \kappa(\omega)]$ and chiral $[\Delta n(\omega), \Delta\kappa(\omega)]$ ones. Then, its phase (dispersion) and amplitude (absorption) are also frequency-dependently modulated and their polarization states are correspondingly altered, depending on a specific chiral property of a target chiral molecule. Figure 8.2b depicts a specific case where three IR frequency components $(\omega_1, \omega_2, \omega_3)$ chosen in the IR pulse spectrum have different polarization states. These differently modulated waves are superimposed to form an IR wave packet in time domain. We have referred to it as *IR optical activity free induction decay* (*IOA FID*) because it contains the whole linear chiral responses.

To establish the relationship between the generated electric field (experimental observables) and the underlying chiroptical response ($\Delta\chi$), let us consider the CPD configuration and the theory described in Section 8.2. With the CPD scheme, the unit vector of the incident beam is given as $\mathbf{e} = \hat{\mathbf{y}}$ in Eq. (8.3) and the rotationally averaged x component of the linear polarization $P_x^{CPD}(t)$ over the ensemble of randomly oriented chiral molecules in solution is then given as

$$\begin{aligned} P_x^{CPD}(t) &= -i \int_0^\infty d\tau \{\chi_{\mu M}(\tau) + \chi_{M\mu}(\tau)\} E(t-\tau) \\ &= -\frac{i}{2} \int_0^\infty d\tau \Delta\chi(\tau) E(t-\tau). \end{aligned} \tag{8.19}$$

From this, we find that $P_x^{CPD}(t)$ is essentially the same as the difference polarization, $\Delta P_x(t)$, in Eq. (8.14) except for the constant factor and that the CPD geometry enables direct measurement of the chiral response without relying on the conventional differential measurement scheme.

In practice, however, the experimentally measured quantity is not the polarization itself but the electric field $\mathbf{E}(t)$. For the x and y components of the emitted signal electric field at position z inside the sample, $E_x(z,t)$ and $E_y(z,t)$, we found that the Maxwell equation is given as [8]

$$\nabla^2 E_x(z,t) - \frac{1}{c^2}\frac{\partial^2}{\partial t^2} E_x(z,t) = \frac{4\pi}{c^2}\frac{\partial^2}{\partial t^2} P_x^{CPD}(z,t), \tag{8.20}$$

where

$$P_x^{CPD}(z,t) = -\frac{i}{2} \int_0^\infty d\tau \Delta\chi(\tau) E_y(z, t-\tau) + \int_0^\infty d\tau \chi_{\mu\mu}(\tau) E_x(z, t-\tau). \tag{8.21}$$

Note that $P_x^{CPD}(z,t)$, determined by both $E_x(z,t)$ and $E_y(z,t)$, acts as the source generating $E_x(z,t)$. By solving this equation in the frequency domain, it was found that the

x component of the emitted electric field (i.e., IOA FID) after the sample length L is given as

$$E_{\perp}(\omega) = \left(\frac{\pi\omega L}{cn(\omega)}\right)\Delta\chi(\omega)E_{||}(\omega), \tag{8.22}$$

where $n(\omega)$ and c is the refractive index and speed of light, respectively. We will hereafter denote $E_x(\omega)$ and $E_y(\omega)$ as $E_{\perp}(\omega)$ and $E_{||}(\omega)$, respectively, because $E_x(\omega)$ and $E_y(\omega)$ are the perpendicular and parallel components, respectively, with respect to the incident electric field polarization direction (y axis). The complex function $\Delta\chi(\omega)$ corresponds to the linear chiral susceptibility in frequency domain. This clearly shows that once the phases and amplitudes of both $E_{\perp}(\omega)$ and $E_{||}(\omega)$ are measured in the frequency domain, the linear optical activity susceptibility $\Delta\chi(\omega)$ whose imaginary and real parts correspond to the VCD and VORD spectra, respectively, can be fully characterized.

8.4.3. Fourier-Transform Spectral Interferometry of IOA FID

A simple way to characterize the spectral phase-and-amplitude information would be to record the FID signal in the time domain and then to Fourier-transform it into a complex spectrum. In pulsed NMR spectroscopy, a RF-pulse-induced FID signal is relatively slowly varying because its frequency is in the range of a few hundred megahertz. Therefore, its time-domain signal variation can be directly measured with high-speed detector and electronics currently available. However, this is not the case for much faster optical signal fields such as the present IOA FID. Therefore, to measure the highly oscillating IOA FID field, we need to use an interferometric detection technique.

Fourier-transform spectral interferometry (FTSI) has proven to be of exceptional use to precisely determine both the phase and amplitude of an unknown optical field and has been widely used in linear and nonlinear spectroscopy [18–25]. The prominent features of the FTSI method are that the heterodyned interferometric detection is achieved in the frequency domain and that the resultant spectral interferogram is analyzed using a well-established inverse-FT-and-FT procedure [18]. To obtain phase information, the former is necessary; note that such information is lost in the conventional FT-IR spectroscopy that is based on the homodyned interferometric detection. Figure 8.3 depicts the spectral interferometric heterodyned detection scheme. A reference field called *local oscillator* whose phase and amplitude are well-defined is combined with the signal field, and the interference spectrum called the spectral interferogram is recorded. In contrast to the time-domain interferometry requiring a large number of data points with high time accuracy, a spectral interferogram between the pulsed signal (E_s) and local oscillator (E_{LO}) fields is measured in the frequency domain at a fixed time delay (τ_d) without any time scanning as

$$S^{het}(\omega) = 2\mathrm{Re}\left[E_s(\omega)E_{LO}^{*}(\omega)\exp(i\omega\tau_d)\right]. \tag{8.23}$$

Since the measured spectral interferogram $S^{het}(\omega)$ itself is a real function, it does not directly provide spectral phase information of $E_s(\omega)$. The standard inverse-FT (F^{-1}) and FT (F) transformation enables one to convert such real function into its complex form, and its stepwise procedure follows as (1) inverse FT of $S^{het}(\omega) \rightarrow F^{-1}\{S^{het}(\omega)\}$, (2) multiplying the time-domain signal $F^{-1}\{S^{het}(\omega)\}$ by a Heavyside step function $\theta(t) \rightarrow \theta(t)F^{-1}\{S^{het}(\omega)\}$, and (3) FT of the positive time-domain

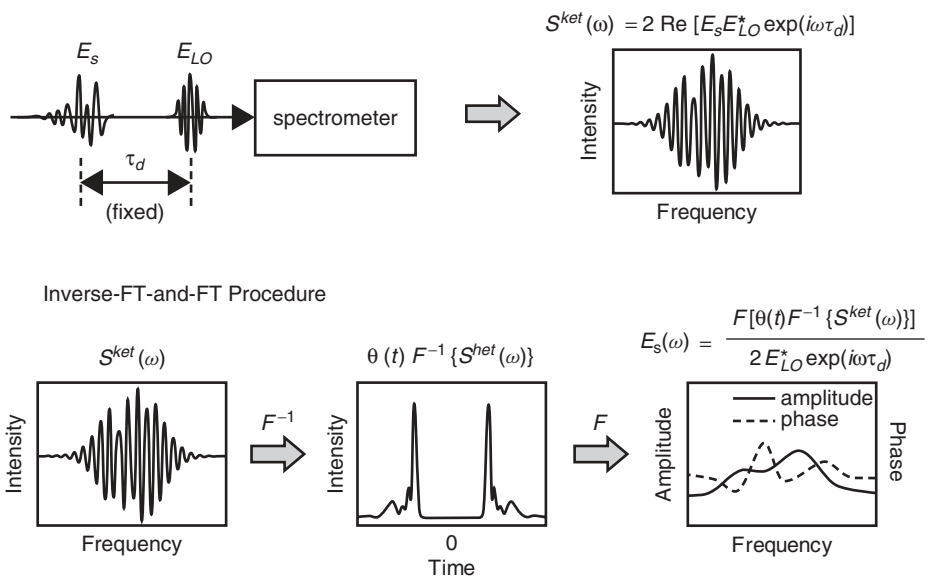

Figure 8.3. Standard FTSI procedure for phase-and-amplitude measurement of an unknown signal electric field (E_s). (a) Frequency-domain heterodyned interferometric detection. (b) Stepwise inverse-FT-and-FT transformation procedure.

signal $\rightarrow F[\theta(t)F^{-1}\{S^{het}(\omega)\}]$. Therefore, the complex electric field $E_s(\omega)$ can be retrieved as

$$E_s(\omega) = \frac{F\left[\theta(t)F^{-1}\{S^{het}(\omega)\}\right]}{2E_{LO}^{*}(\omega)\exp(i\omega\tau_d)}. \tag{8.24}$$

Here, $E_{LO}(\omega)$ and τ_d should be predetermined to obtain the phase and amplitude of $E_s(\omega)$ with Eq. (8.24).

In principle, a complete characterization of the local oscillator field $E_{LO}(\omega)$ is possible by using well-known nonlinear techniques such as FROG [26], SPIDER [27], and so on. However, such field characterization unfortunately requires an additional complicated measurement equipment, which is by no means an easy task. Furthermore, a precise determination of τ_d within an optical period (less than a few femtoseconds) is still quite a challenging problem. We found that such difficulties can be overcome using the linear relationship between the complex chiral susceptibility $\Delta\chi(\omega)$ and the ratio of the chiral field ($E_\perp(\omega)$) to the achiral field ($E_{||}(\omega)$), that is, $\Delta\chi(\omega) \propto E_\perp(\omega)/E_{||}(\omega)$. This requires measurements of both $E_\perp(\omega)$ and $E_{||}(\omega)$ by controlling the second linear polarizer P2 in Figure 8.2. From Eq.(8.24), they can be, in practice, obtained by using the following equation,

$$E_{\perp,||}(\omega) = \frac{F[\theta(t)F^{-1}\{S_{\perp,||}^{het}(\omega)\}]}{2E_{LO}^{*}(\omega)\exp(i\omega\tau_d)}, \tag{8.25}$$

where $S_{\perp}^{het}(\omega)$ and $S_{||}^{het}(\omega)$ are the perpendicular- and parallel-detected spectral interferograms. Here, for example, the perpendicular detection means that the direction of the

heterodyne-detected signal field is perpendicular to that of the incident beam. Since both electric fields $E_{\perp,||}(\omega)$ have common factor in the denominator of Eq. (8.25), the ratio $E_{\perp}(\omega)/E_{||}(\omega)$ does not depend on the details of $E_{LO}(\omega)$ and τ_d. However, still sufficiently good phase stability of the entire setup during the measurements of $S_{\perp}^{het}(\omega)$ and $S_{||}^{het}(\omega)$ is required. Finally, combining these results, we find that the chiral susceptibility is experimentally measured as

$$\Delta\chi(\omega) \propto \frac{F[\theta(t)F^{-1}\{S_{\perp}^{het}(\omega)\}]}{F[\theta(t)F^{-1}\{S_{||}^{het}(\omega)\}]}. \tag{8.26}$$

This clearly demonstrates that the present method is capable of characterizing the complex $\Delta\chi(\omega)$ without precise characterizations of $E_{LO}(\omega)$ and τ_d.

8.5. ACTIVE- AND SELF-HETERODYNE DETECTIONS OF IR OPTICAL ACTIVITY

The electric field approach discussed here can be viewed as an active heterodyne-detection technique because the signal field itself is deliberately allowed to interfere with an additional reference field. Here, the cross-polarization geometry for selective elimination of the achiral background field was one of the important elements for the success of this measurement method. In this regard, it should be mentioned that the so-called ellipsometric technique using a quasi-null geometry with two linear polarizers [2, 28, 29], which was pioneered by Kliger and co-workers, shares a very similar optical setup (Figure 8.4). Much like the cross-polarization scheme, two crossed linear polarizers were used. However, instead of a linearly polarized radiation, an elliptically polarized beam with vertical major axis (y axis), which is produced by a phase-retarder, was used to generate an electronic OA FID field in visible frequency domain. It is then detected by allowing its interference with the residual horizontal (parallel to the x axis) component of the incident elliptically polarized beam; note that an elliptically polarized radiation can be described as a linear combination of linearly polarized (along the y axis) and circularly polarized beams. Even though this technique is still an intensity (not phase-and-amplitude) measurement method, it can be considered to be a self-heterodyne-detection scheme because the in-quadrature phase-different horizontal beam component essentially acts like a local oscillator interfering with the generated chiral signal field whose polarization direction is parallel to the x axis. Recently, Helbing and co-workers experimentally demonstrated that such an ellipsometric technique can be extended to the IR region to measure the VCD and VORD spectra with a significantly enhanced detection sensitivity [30].

A major difference between this and ours is how to control the relative phase between signal and reference fields during the heterodyning process. In the ellipsometric detection geometry, the chiral signal field interferes with the incident horizontal electric field itself, which acts as a local oscillator (for self-heterodyning) as well as an excitation field. Thus, the phase delay between the chiral signal and intrinsic local oscillator fields is not experimentally controllable. As a result, the imaginary (VCD) and real (VORD) parts of the IOA response should be measured separately. On the other hand, the present cross-polarization interferometric technique utilizing a Mach–Zehnder interferometer shown in Figure 8.4 (upper left) uses an external local oscillator (for active-heterodyning) so that both the imaginary and real parts of $\Delta\chi(\omega)$ can be simultaneously obtained via the FTSI procedure discussed above.

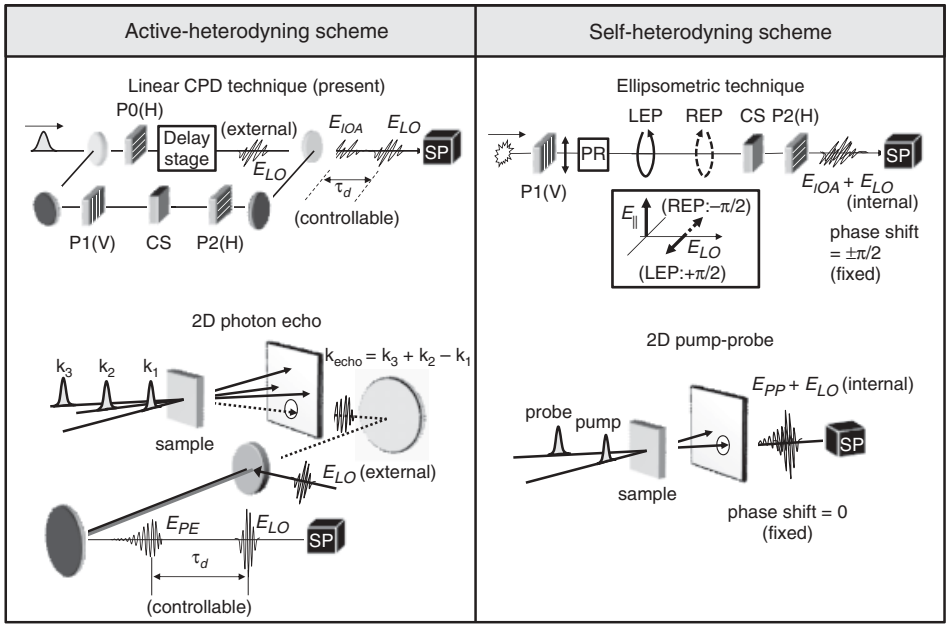

Figure 8.4. Comparison between active- and self-heterodyning schemes for optical activity (upper) and 2D signal (lower) measurements. P0–P2; linear polarizers; (V), vertical; (H), horizontal; PR, phase-retarder; SP, spectrometer; CS, chiral sample. In the active-heterodyning scheme, the local oscillator (E_{LO}) is externally controlled so that the time delay between E_{LO} and the signal (E_{IOA}/E_{PE}) is controllable. In contrast, the phase shift between them is fixed in the self-heterodyning scheme because the incident excitation field itself acts as the local oscillator.

Interestingly, the relationship between these two methods is quite similar to that between self-heterodyne-detected pump probe with two pulses and active-heterodyne-detected stimulated photon echo with four pulses (lower panel of Figure 8.4). These measurement methods have been widely used to obtain the 2D optical spectra of biomolecules [31–33], light-harvesting systems [23, 34], semiconductors [24, 35, 36], chemical exchange systems [37, 38], and so on. In the case of the self-heterodyned pump-probe spectroscopy, essentially only two pulses are enough to carry out such a measurement. The first two field-matter interactions occur with the pump pulse, and the third field-matter interaction with a time-delayed (T) probe pulse creates a third-order polarization $\mathbf{P}^{(3)}_{PP}(t,T)$, which is linearly proportional to the generated signal electric field, i.e., $\mathbf{E}^{(3)}_{PP}(t,T) \propto i\omega\mathbf{P}^{(3)}_{PP}(t,T)$. If a homodyne detection of the signal field is performed, the measured quantity is the intensity $|\mathbf{E}^{(3)}_{PP}(t,T)|^2$ of the pump-probe signal not its amplitude. Consequently, the homodyne-detected pump-probe signal does not carry information on the phase of the signal field. On the other hand, one can use the probe pulse itself as a local oscillator so that the measured transient dichroism signal in this case is given as

$$S_{PP}(T) \propto \mathrm{Re}\left[\int_{-\infty}^{\infty} dt\ \mathbf{E}^{*}_{probe}(t) \cdot \mathbf{E}^{(3)}_{PP}(t,T)\right]. \tag{8.27}$$

As can be seen in Eq. (8.27), the measured pump-probe signal is linearly proportional to the third-order polarization (or signal field).

In contrast, the heterodyne-detected photon echo uses the same type of Mach–Zehnder interferometer to record the spectral interferogram,

$$S_{PE}^{het}(\omega) = 2\mathrm{Re}[E_{PE}(\omega)E_{LO}^{*}(\omega)\exp(i\omega\tau_d)], \tag{8.28}$$

where the spectrum of the photon echo signal field generated by the third-order polarization is denoted as $E_{PE}(\omega)$. Then, the measured spectral interferogram can be converted into the photon echo spectrum by using the same inverse-FT-and-FT procedure. A notable difference between the present interferometric detection technique for the IOA measurement and the 2D photon echo measurement is that the latter requires accurate characterization of $E_{LO}(\omega)$ and τ_d. In fact, this phasing problem was indirectly resolved by comparing the projected 2D spectrum with the dispersed pump-probe spectrum; note that the two spectra should be the same so that an arbitrary phase correction factor is multiplied to the measured 2D spectrum to make the two spectra identical. Overall, despite the fact that the frequency-resolved pump-probe experiment is comparatively easy to perform, information on the absorptive part of the 2D response spectrum can only be extracted from the measured pump-probe signal. In contrast, the heterodyned photon echo techniques can be of use to measure both the absorptive and dispersive parts of the complex 2D response spectrum.

8.6. EXPERIMENTAL DEMONSTRATION: VCD AND VORD SPECTRA OF (1S)-β-PINENE

To demonstrate the experimental feasibility of the present IOA FID measurement method, we considered (1S)-β-pinene dissolved in CCl_4, which is a standard chiral organic molecule studied before. By tuning the center frequency of the femtosecond IR pulse whose spectral width is $\sim$200 cm^{-1}, we examined four distinctively different groups of vibrational modes: C–C stretch modes (1000–1350 cm^{-1}), C–H bending modes (1400–1500 cm^{-1}), a C=C stretch mode (1600–1700 cm^{-1}) and C–H stretch modes (2850–3000 cm^{-1}). One of the crucial optical elements is a pair of crossed linear polarizers (P1 and P2 in Figure 8.2) having extremely small extinction ratio to effectively remove huge vertically polarized achiral background noise. For typical chiral molecules with $\Delta A(\mathrm{VCD}) = 10^{-4}$–$10^{-5}$, the ratio of the chiral signal to the achiral noise (horizontal-to-vertical signal ratio) is about 10^{-9} so that extremely high-quality polarizers are required to suppress such noise. Brewster's angle germanium polarizers having extinction ratio of about 10^{-9} over the broad IR frequency range from 20 to 10,000 cm^{-1} [11, 39] have been used for this purpose.

Figure 8.5 depicts the step-by-step FTSI procedure for retrieving the frequency-(VCD and VORD spectra) and time-domain chiral susceptibilities from the measured spectral interferograms $S_{\perp,||}^{het}(\omega)$. The dispersed heterodyned spectral interferograms $S_{\perp}^{het}(\omega)$ (solid) and $S_{||}^{het}(\omega)$ (dashed) measured in each target vibrational mode region are plotted in Figure 8.5a, and they exhibit distinct spectral shapes (phases and amplitudes). In particular, a highly oscillating feature of $S_{\perp}^{het}(\omega)$ in comparison to that of $S_{||}^{het}(\omega)$ immediately shows that the $S_{\perp}^{het}(\omega)$ contains more complicated positive/negative sign information on the optical activity. As a first step of the retrieval procedure, an inverse FT (iFT) is performed to convert the frequency-domain interferograms $S_{\perp,||}^{het}(\omega)$ into time-domain signals $F^{-1}\{S_{\perp}^{het}(\omega)\}$ (black) and $F^{-1}\{S_{||}^{het}(\omega)\}$ (gray) that are displayed in Figure 8.5b. Then, these are multiplied by a Heavyside step function $\theta(t)$ to obtain

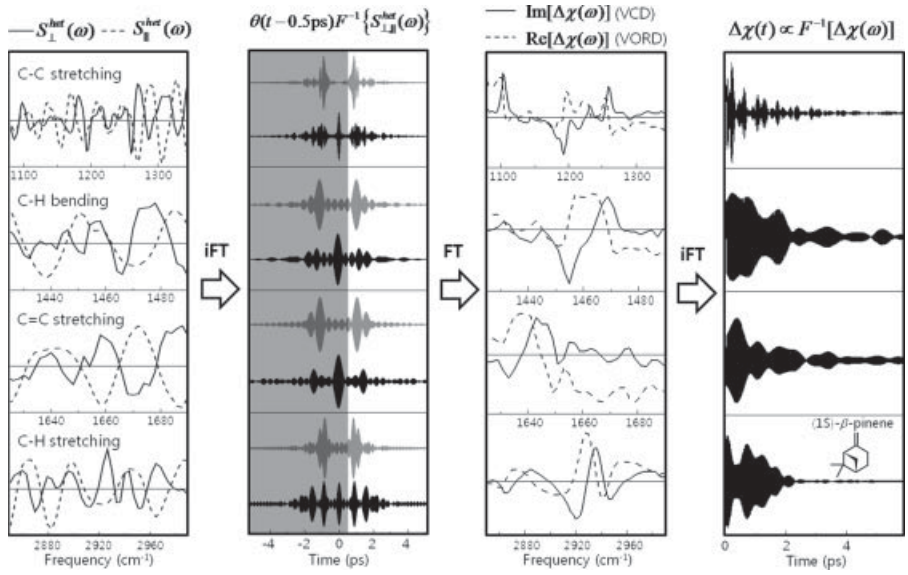

Figure 8.5. Stepwise procedure for retrieving the IR chiral susceptibilities of four different vibrational modes of (1S)-β-pinene. (a) Perpendicular- and parallel-detected spectral interferograms $S_{\perp}^{het}(\omega)$ (solid) and $S_{||}^{het}(\omega)$ (dashed). (b) Inverse-Fourier-transformed (iFT) time-domain signals $F^{-1}\{S_{\perp}^{het}(\omega)\}$ (lower black) and $F^{-1}\{S_{||}^{het}(\omega)\}$ (upper gray). For the sake of comparison, $F^{-1}\{S_{||}^{het}(\omega)\}$ is offset from $F^{-1}\{S_{\perp}^{het}(\omega)\}$. To take the positive time-domain part of $F^{-1}\{S_{\perp,||}^{het}(\omega)\}$ as well as to remove residual DC noise near time zero, $\theta(t - 0.5$ ps) is multiplied to the time-domain functions $F^{-1}\{S_{\perp,||}^{het}(\omega)\}$. (c) Imaginary (VCD, solid) and real (VORD, dashed) part spectra of chiral susceptibility $\Delta\chi(\omega)$ obtained from Eq. (8.26). (d) Time-domain chiral response function $\Delta\chi(t)$ obtained by carrying out an inverse-Fourier-transformation of the $\Delta\chi(\omega)$.

a complex form of $\Delta\chi(\omega)$. In practice, $\theta(t - 0.5$ ps) instead of $\theta(t)$ was used to take the signal in the positive time domain and to remove any residual DC noise of $S_{\perp,||}^{het}(\omega)$ that appears near time zero. The time-domain function $\theta(t)F^{-1}\{S_{||}^{het}(\omega)\}$ is essentially the convolution product of $E_{LO}(t)$ and $E_{||}(t)$, which is the interference term between the input field and the achiral FID. On the other hand, $\theta(t)F^{-1}\{S_{\perp}^{het}(\omega)\}$ corresponds to that of $E_{LO}(t)$ and $E_{\perp}(t)$, which is in turn given by the convolution between $\Delta\chi(t)$ and $E_{||}(t)$. It is noted that such transformed signals $\theta(t)F^{-1}\{S_{\perp,||}^{het}(\omega)\}$ can be obtained in a different way—that is, time-domain interferometry, which measures the convolution product of $E_{LO}(t)$ and $E_{\perp,||}(t)$ directly in the time domain.

Next, an FT conversion of the $\theta(t)F^{-1}\{S_{\perp,||}^{het}(\omega)\}$ yields the complex spectra $F[\theta(t)F^{-1}\{S_{\perp,||}^{het}(\omega)\}]$. The complex chiral susceptibility $\Delta\chi(\omega)$ is then simply obtained by taking their ratio [see Eq. (8.26)]. The imaginary (solid) and real (dashed) part spectra of the $\Delta\chi(\omega)$ associated with the VCD and VORD, respectively, are plotted in Figure 8.5c. Characteristic VCD features of (1S)-β-pinene are observed and found to be fully consistent with the results obtained by using a FT-IR VCD spectrometer [40]. The VCD spectrum of the C=C stretch mode (1600–1700 cm^{-1}) appears to be comparatively noisy, however. This is likely to be due to IR absorption by water vapor.

The perpendicular-detected time-domain signal $\theta(t)F^{-1}\{S_{\perp}^{het}(\omega)\}$ shown in Figure 8.5b is not identical to the chiroptical response function $\Delta\chi(t)$ itself, but it is

given by a complicated convolution product of $\Delta\chi(t), E_{||}(t)$, and $E_{LO}(t)$ as mentioned above. Although it is not an easy task to deconvolute such signal in the time domain, by performing the inverse FT of the $\Delta\chi(\omega)$, the time-domain chiral susceptibility $\Delta\chi(t)$ can be obtained. Figure 8.5d depicts the $\Delta\chi(t)$ of the four different vibrational modes probed here, and each of them is closely related to the electric dipole–magnetic dipole correlation function $\langle\boldsymbol{\mu}(t)\cdot\mathbf{M}(0)\rangle$ of the corresponding vibrational mode.

8.7. SUMMARY AND A FEW CONCLUDING REMARKS

In this chapter, we presented a detailed discussion on the time-domain measurement method for vibrational CD and ORD spectra of chiral molecules in condensed phases, where a femtosecond IR pulse is used to create IOA FID field and to detect it in a phase-and-amplitude-sensitive manner. We first discussed the time-correlation function theory for the optical activity, where the chiral signal field was expressed in terms of the electric dipole–magnetic dipole cross-correlation function. It was shown that a combination of cross-polarization detection and spectral interferometry with a properly designed Mach–Zehnder interferomer is useful to selectively eliminate the achiral background signal and to characterize the relative phase of the chiral field with respect to the local oscillator. The present electric field measurement method using an active heterodyne-detection scheme was compared with the self-heterodyned ellipsometric electronic and vibrational CD spectroscopy. The relationship between the two is analogous to that between the heterodyne-detected photon echo and the self-heterodyned pump-probe measurement methods. To illustrate the underlying principles and experimental procedures, we specifically considered (1S)-β-pinene solution and presented measured spectral interferograms and VCD and VORD spectra. The present phase-and-amplitude-sensitive VCD and VORD measurement technique utilizing a femtosecond IR pulse has a superior time-resolution in comparison to the VCD spectroscopy based on the differential absorption measurement with a continuous-wave radiation source. Consequently, one can directly extend this method to study ultrafast dynamics of chiral molecules in solutions with unprecedented time-resolution achievable, which is what we are currently investigating in our laboratory.

ACKNOWLEDGMENTS

This work was supported by KBSI grant T30401.

REFERENCES

1. M. Born, E. Wolf, *Principles of Optics*, Cambridge University Press, Cambridge, **1999**.
2. N. Berova, K. Nakanishi, R. W. Woody, *Circular Dichroism: Principles and Applications*, Wiley-VCH, New York, **2000**.
3. R. de L. Kronig, *J. Opt. Soc. Am*. **1926**, *12*, 547–557.
4. H. A. Kramers, *Atti Congr. Intern. Fisici, Como* **1927**, *2*, 545–557.
5. H. M. Nusenzveig, *Causality and Dispersion Relations*, Academic Press, New York, **1972**.
6. G. Holzwarth, E. C. Hsu, H. S. Mosher, T. R. Faulkner, A. Moscowitz, *J. Am. Chem. Soc*. **1974**, *96*, 251–252.

7. N. A. Nafie, T. A. Keiderling, P. J. Stephens, *J. Am. Chem. Soc*. **1976**, *98*, 2715–2723.
8. H. Rhee, J.-H. Ha, S.-J. Jeon, M. Cho, *J. Chem. Phys*. **2008**, *129*, 094507.
9. H. Rhee, Y.-G. June, J.-S. Lee, K.-K. Lee, J.-H. Ha, Z. H. Kim, S.-J. Jeon, M. Cho, *Nature* **2009**, *458*, 310–313.
10. H. Rhee, Y.-G. June, Z. H. Kim, S.-J. Jeon, M. Cho, *J. Opt. Soc. Am. B* **2009**, *26*, 1008–1017.
11. H. Rhee, S.-S. Kim, S.-J. Jeon, M. Cho, *ChemPhysChem* **2009**, *10*, 2209–2211.
12. J. Jeon, S. Yang, J.-H. Choi, M. Cho, *Acc. Chem. Res*. **2009**, *42*, 1280–1289.
13. S. Yang, M. Cho, *J. Chem. Phys*. **2009**, *131*, 135102.
14. P. A. M. Dirac, *The Principles of Quantum Mechanics*, Oxford University Press, New York, **1958**.
15. R. Loudon, *The Quantum Theory of Light*, Oxford University Press, New York, **1983**.
16. M. Cho, *Two-Dimensional Optical Spectroscopy*, CRC Press, Boca Raton, FL, **2009**.
17. C. Cohen-Tannoudji, I. DuPont-Roc, G. Grynberg, *Photons and Atoms: Introduction to Quantum Electrodynamics*, John Wiley & Sons, New York, **1989**.
18. L. Lepetit, G. Cheriaux, M. Joffre, *J. Opt. Soc. Am. B* **1995**, *12*, 2467–2474.
19. D. N. Fittinghoff, J. L. Bowie, J. N. Sweetser, R. T. Jennings, M. A. Krumbugel, K. W. DeLong, R. Trebino, I. A. Walmsley, *Opt. Lett*. **1996**, *21*, 884–886.
20. W. J. Walecki, D. N. Fittinghoff, A. L. Smirl, R. Trebino, *Opt. Lett*. **1997**, *22*, 81–83.
21. M. T. Zanni, N.-H. Ge, Y. S. Kim, R. M. Hochstrasser, *Proc. Natl. Acad. Sci. USA* **2001**, *98*, 11265–11270.
22. M. Khalil, N. Demirdoven, A. Tokmakoff, *J. Phys. Chem. A* **2003**, *107*, 5258–5279.
23. T. Brixner, J. Stenger, H. M. Vaswani, M. Cho, R. E. Blankenship, G. R. Fleming, *Nature* **2005**, *434*, 625–628.
24. T. H. Zhang, C. N. Borca, X. Li, S. T. Cundiff, *Opt. Express* **2005**, *13*, 7432–7441.
25. S.-H. Lim, A. G. Caster, S. R. Leone, *Opt. Lett*. **2007**, *32*, 1332–1334.
26. D. J. Kane, R. Trebino, *IEEE J. Quantum Electron*. **1993**, *29*, 571–579.
27. C. Iaconis, I. A. Walmsley, *Opt. Lett*. **1998**, *23*, 792–794.
28. J. W. Lewis, R. F. Tilton, C. M. Einterz, S. J. Milder, I. D. Kuntz, D. S. Kliger, *J. Phys. Chem*. **1985**, *89*, 289–294.
29. R. A. Goldbeck, D. B. Kim-Shapiro, D. S. Kliger, *Annu. Rev. Phys. Chem*. **1997**, *48*, 453–479.
30. J. Helbing, M. Bonmarin, *J. Chem. Phys*. **2009**, *131*, 174507.
31. C. Kolano, J. Helbing, M. Kozinski, W. Sander, P. Hamm, *Nature* **2006**, *444*, 469–472.
32. S.-H. Shim, R. Gupta, Y. L. Ling, D. B. Strasfeld, D. P. Raleigh, M. T. Zanni, *Proc. Natl. Acad. Sci. USA* **2009**, *106*, 6614–6619.
33. N. Demirdoven, C. M. Cheatum, H. S. Chung, M. Khalil, J. Knoester, A. Tokmakoff, *J. Am. Chem. Soc*. **2004**, *126*, 7981–7990.
34. N. S. Ginsberg, Y.-C. Cheng, G. R. Fleming, *Acc. Chem. Res*. **2009**, *42*, 1352–1363.
35. K. W. Stone, K. Gundogdu, D. B. Turner, X. Li, S. T. Cundiff, K. A. Nelson, *Science* **2009**, *324*, 1169–1173.
36. X. Li, T. Zhang, C. N. Borca, S. T. Cundiff, *Phys. Rev. Lett*. **2006**, *96*, 057406.
37. Y. S. Kim, R. M. Hochstrasser, *Proc. Natl. Acad. Sci. USA* **2005**, *102*, 11185–11190.
38. J. Zheng, K. Kwak, J. Asbury, X. Chen, I. R. Piletic, M. D. Fayer, *Science* **2005**, *309*, 1338–1343.
39. D. J. Dummer, S. G. Kaplan, L. M. Hanssen, A. S. Pine, Y. Zong, *Appl. Opt*. **1998**, *37*, 1194–1204.
40. C. Guo, R. D. Shah, R. K. Dukor, T. B. Freedman, X. Cao, L. A. Nafie, *Vib. Spectrosc*. **2006**, *42*, 254–272.

9

CHIROPTICAL PROPERTIES OF LANTHANIDE COMPOUNDS IN AN EXTENDED WAVELENGTH RANGE

Lorenzo Di Bari and Piero Salvadori

9.1. INTRODUCTION

Lanthanides constitute a fascinating family of elements, endowed with some unusual chemical and photophysical properties, which make them useful in the most diverse fields of chemistry, material science, and biomedicine. At the same time, they constitute powerful and widely used probes for studying structure and dynamics of molecules. It is most common that in an Ln^{3+} coordination sphere a high degree of stereodiscrimination takes place, which justifies their use as enantioselective catalysts or as chiral auxiliaries and reagents, for example. The correct understanding of these processes calls for appropriate investigation techniques; to this end, chiroptical methods play a major role.

9.2. THE *F* SHELL

Lanthanides are also called f elements, because they are characterized by the progressive filling of the $4f$ shell: The (III) ions go from the f^0 configuration of La^{3+} to the completely filled f^{14} of Lu^{3+} through, for example, the semifilled Gd^{3+} (f^7). These orbitals are inner with respect to those with 5- and 6-principal quantum number, which constitute the outer shell of Ln^{3+} and display weak hybridization with them. This is the main origin of their peculiar properties. In the first place, they're characterized by similar chemical behavior, since they interact with the environment practically with the same frontier. Moreover, it

Comprehensive Chiroptical Spectroscopy, Volume 1: Instrumentation, Methodologies, and Theoretical Simulations, First Edition. Edited by N. Berova, P. L. Polavarapu, K. Nakanishi, and R. W. Woody.
© 2012 John Wiley & Sons, Inc. Published 2012 by John Wiley & Sons, Inc.

also justifies that they have very weak tendency to forming covalent bonds, but rather give rise to electrostatic interactions, similarly to alkali or alkali earth ions. The result is a very poor directionality of the bonds, variable coordination numbers, and marked Lewis acidity of their salts, which must be classified as *hard* and oxophilic, small crystal field interactions with the ligands [1].

To a first order, one may neglect the existence of the ligands environment and obtain a series of electronic states (terms) whose relative energies are determined primarily by angular momentum (spin orbit and *jj* couplings) interactions and not by the influence of crystal field. The first very simple example is provided by Ce^{3+}, which has only one unpaired electron in the f orbitals. It is endowed with spin quantum number $S = \frac{1}{2}$ and orbital quantum number $L = 3$, which combine to a total value of $J = L \pm S = 7/2, 5/2$ and are represented through the symbols $^2F_{5/2}$ (fundamental) and $^2F_{7/2}$ (excited). The energy splitting between these two terms is about 2250 cm^{-1} in all Ce^{3+} compounds. The situation is closely similar for Yb^{3+}, having f^{13} configuration (i.e., with just one hole): The two terms describing this ion are again $^2F_{7/2}$ and $^2F_{5/2}$, but this time with this inverted order and a splitting of 10,200 cm^{-1}. The other paramagnetic elements have more unpaired electrons and give rise to richer manifolds of terms, as found e.g. in refs. 1 and 3 and depicted in Figure 9.1.

In a completely symmetrical environment, all the projections of J (M_J) are degenerate, which means that, for example, $^2F_{7/2}$ contains four degenerate Kramers doublets with $M_J = \pm 7/2, \pm 5/2, \pm 3/2, \pm 1/2$. Crystal field splitting (CFS) may lift this degeneracy, conducting to up to four nondegenerate states for this level: In the absence of a magnetic field acting on the electron spins, Kramers doublets degeneracy persists. The number of nondegenerate states after introducing CFS depends upon its symmetry and upon J. Since we shall not enter into any further detail about this, we refer the reader to more specific literature [1–3].

The extinction coefficients of lanthanides are very small, because the purely intraconfigurational f–f transitions are Laporte forbidden (can't interact with electric field radiation); thus most Ln^{3+} salts and compounds are colorless or display pale hues.

On the contrary, almost all Ln^{3+} compounds are luminescent: Ce^{3+}, Pr^{3+}, Sm^{3+}, Eu^{3+}, Tb^{3+}, Dy^{3+}, and Ho^{3+} emit in the visible, Gd^{3+} emits in the UV, and Pr^{3+}, Nd^{3+}, Ho^{3+}, Er^{3+}, and Yb^{3+} are near-infrared (NIR) emitters [4]. Consequently, they find wide applications in light-emitting devices. We shall not enter the complex field of how sensitization of a Ln^{3+} is achieved and the general principles of lanthanide isotropic luminescence, but only consider its chiroptical counterpart: circular polarization of luminescence (CPL) [4, 5].

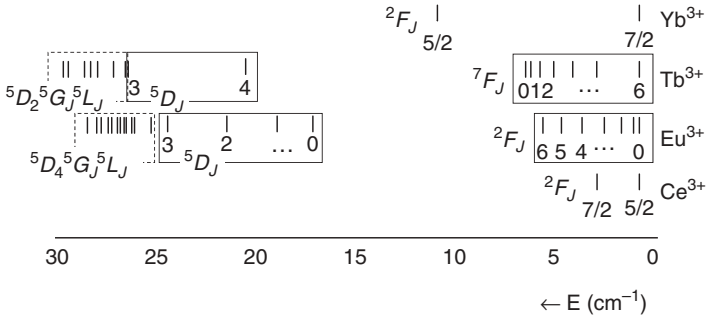

Figure 9.1. Partial diagram of the electronic states of some Ln^{3+} aquo ions. The relevant electronic terms are indicated and the *J*-components are specified below the states. From reference 3.

Both absorption and emission spectra of Ln^{3+} have narrow lines, typical of atomic spectroscopy, which is once more due to the weak coupling of f orbitals with the environment. Thus, they result in multiplets, which are often well-resolved. We can divide the structure of these spectra into two levels: A coarse spacing is provided by spin–orbit coupling—that is, by the individual terms, shown in Figure 9.1; to make things clearer, for example the absorption spectrum of Tb^{3+} has the $^7F_6 \rightarrow {}^7F_5$ at 2115 cm^{-1}, the $^7F_6 \rightarrow {}^7F_4$ at 3270 cm^{-1}, and so on. A finer structure arises because the crystal field splits each electronic state (like $^7F_6$ in the above example) into sublevels. Owing to the weak interaction between f electrons and ligands, this latter fine structure is usually of the order of 10–1000 cm^{-1} [6].

9.3. ELECTRONIC CIRCULAR DICHROISM AND CIRCULARLY POLARIZED LUMINESCENCE

Electronic optical activity may take place in absorption (electronic circular dichroism, ECD) and in emission (circularly polarized luminescence, CPL), the former associated with the difference in absorbance (A) toward left- and right-circularly polarized radiation ($\Delta A = A^{left} - A^{right}$), the latter with differential intensity of left- and right-polarized luminescence ($\Delta I = I^{left} - I^{right}$). In both cases, a relevant derived quantity is the so-called anisotropy g factor, which we can define as

$$g_{Abs} = \frac{\Delta A}{A} = \frac{A^{left} - A^{right}}{A} \tag{9.1}$$

for ECD (in absorption), and

$$g_{lum} = \frac{\Delta I}{I} = \frac{I^{left} - I^{right}}{I} = 2\frac{I^{left} - I^{right}}{I^{left} + I^{right}} \tag{9.2}$$

for CPL (in emission).

We may recall that optical activity (ECD or CPL) of an electronic transition $a \rightarrow b$ is gauged by the rotational strength

$$R_{ab} = \mathrm{Im}\{\boldsymbol{\mu}_{ab} \cdot \mathbf{m}_{ab}\}, \tag{9.3}$$

where $\boldsymbol{\mu}_{ab}$ and $\mathbf{m}_{ab}$ are the electric and magnetic dipole transition moments (EDTM and MDTM) vectors relative to the transition $a \rightarrow b$, respectively. If the energy of the initial state a is less than that of b, then during the transition a photon is absorbed and R_{ab} refers to ECD; if a is above b, we deal with an emission process and R_{ab} is allied to CPL.

The rotational strength can be rewritten with explicit reference to the scalar product between $\boldsymbol{\mu}_{ab}$ and $\mathbf{m}_{ab}$ expressed in Eq. (9.3) as

$$R_{ab} = |\boldsymbol{\mu}_{ab}||\mathbf{m}_{ab}| \cos \tau_{ab}, \tag{9.4}$$

where τ_{ab} is the angle between the EDTM and MDTM vectors.

The fundamental rule for magnetic dipole transitions is $\Delta J = 0, \pm 1$ (excluding $J = J' = 0$). On the contrary, for electric dipole we should expect vanishing moment, because

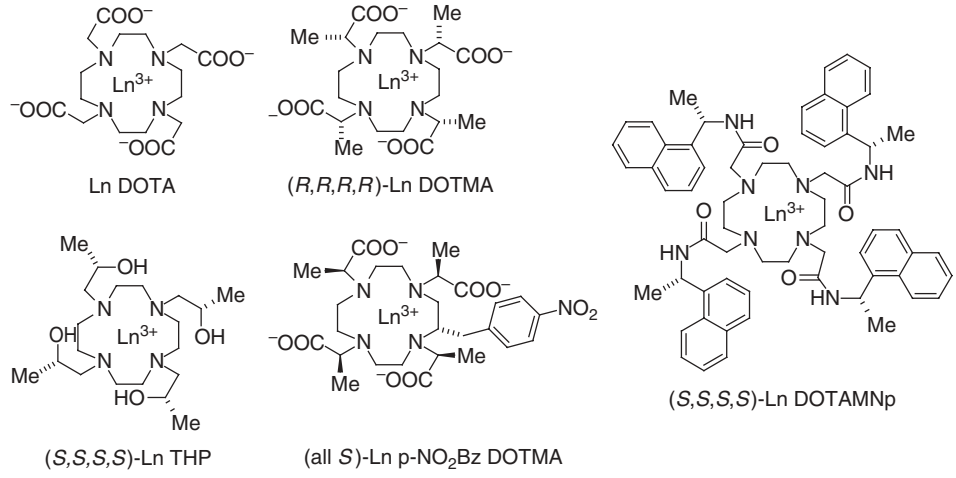

Scheme 9.1. Molecular structures of DOTA derivatives.

f–f transitions are intraconfigurational and consequently parity-forbidden, hence the very small extinction coefficients mentioned above [2].

We shall see now the two fundamental mechanisms through which the chiral environment brings about the necessary EDTM to give rise to optical activity. We shall represent static and dynamic couplings as separate and alternative, although in the general case they must be regarded as two facets contributing simultaneously to the observed ECD or CPL spectra [2].

9.3.1. Static Coupling

For a purely Ln^{3+}-centered transition, in order to have $\boldsymbol{\mu}_{ab} \neq 0$, some degree of hybridization must be invoked, which means that the $4f$ orbitals mix (for example) with the $5d$, gaining the necessary odd-parity interconfigurational character. This can be actuated by a dissymmetric ligand field in the so-called "static coupling" mechanism. To make an analogy with what is customary in the description of ECD of organic molecules, we can consider this case as an intrinsically chiral chromophore [7], because we must identify the whole coordination sphere as the locus where radiation absorption or emission takes place.

An example may be provided by Ln DOTMA (Scheme 9.1; see also Section 9.5.4). The stereochemistry of this molecule has been extensively studied [8–10], because it is closely analogue to one of the most successful contrast agents for magnetic resonance imaging (MRI), namely Gd DOTA (Scheme 9.1) [10–12], the difference between DOTMA and DOTA consisting in the fact that the latter lacks the four methyl groups in the side arms and is therefore achiral.

The coordination polyhedron of Ln DOTMA is defined by the four nitrogen and the four carboxylate oxygen atoms and is a twisted square antiprism, shown in Figure 9.2, which is obviously chiral. It is worth noting that the ligand is essentially devoid of significant chromophores, the strongest one being the carboxylate with only a weak absorption at about 200 nm. Thus, we may consider Ln DOTMA as an intrinsically chiral lanthanide chromophore, essentially not perturbed from polarizable groups.

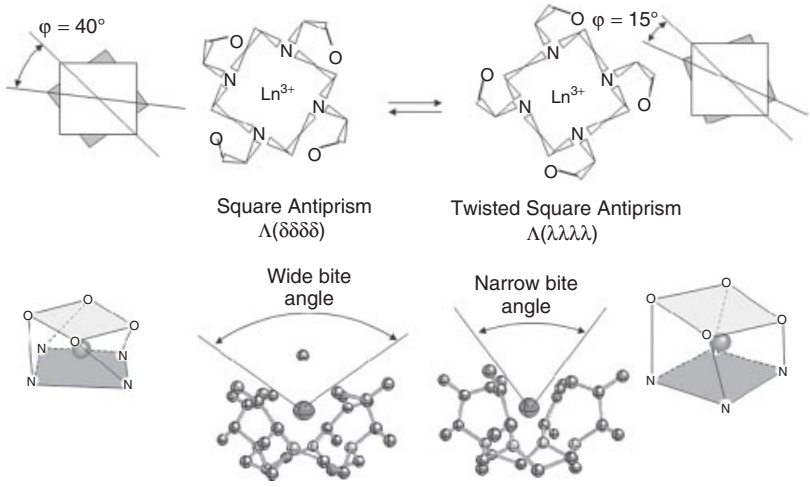

Figure 9.2. The coordination cage of Ln DOTMA in its two main diastereomeric conformations.

Accordingly, metal-centered transitions can be considered as solely responsible for the observed ECD. Because of the lack of significant couplings, the f shell must be considered as practically isolated and the sum rule must apply to it. This means that the integral of the CD spectrum over all the f transitions must be vanishing. In some cases this may be hard to check or to be useful, because a very wide spectral range should be covered, often extending from the IR (possibly NIR) to UV. For the simplest systems having one electron or one hole, instead, it has an immediate consequence. The two ions where this applies are Ce^{3+} and Yb^{3+}, respectively, with f^1 and f^{13} configuration. They have only one term, $^2F_{5/2} \rightarrow {}^2F_{7/2}$ for Ce^{3+} in IR and the $^2F_{7/2} \rightarrow {}^2F_{5/2}$ for Yb^{3+}, which is in the NIR, rather close to the edge of visible light and reached by some commercial ECD instruments working in the UV–vis. The ECD of Ce^{3+} may be coupled to vibrational transitions (see Section 9.4) and will not be considered here. On the contrary, there are many reports about Yb^{3+} chiroptical spectroscopy [13]. The first ECD spectrum of a structurally well-defined Yb^{3+} compound is the one of Yb DOTMA and is reproduced in Figure 9.3 [8].

It is evident that it is composed of a manifold of lines allied to positive and negative Cotton effects. One can appreciate that the integral over the whole ECD multiplet is close to zero, because positive and negative rotational strengths largely compensate. The same feature can be found in the spectra of similar species. One immediate consequence is that, within the limit of perfect static coupling, we are able to see an ECD or a CPL spectrum only if the crystal field components of the multiplet are sufficiently splitted, because otherwise they would sum up to zero. "Sufficient" in this context means that the lines must be separated more than their apparent widths, which in turn is a combination of a natural linewidth, plus a broadening term depending on the instrument and on its settings. The most relevant aspects to take into account are the passing band, which is regulated by the slit opening and the combination scan speed/time constant (this latter is an interval over which the instrument averages the signal). A rule of the thumb states that

$$\frac{\text{time constant(s)} \cdot \text{scan speed(nm} \cdot \text{s}^{-1})}{\text{passing band(nm)}} \leq \frac{1}{2} \tag{9.5}$$

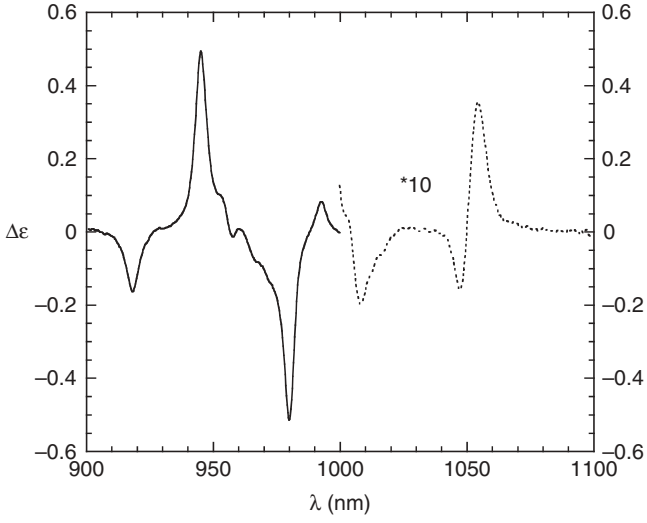

Figure 9.3. Absorption and NIR-ECD spectrum of Yb DOTMA in water ($c = 14.5$ mM, pathlength 1 cm).

Of course one has to make sure that the passing band is not wider than the natural linewidths (remember that lanthanides spectra have very narrow lines!). The entity of the ligand field splitting is very sensitive to the geometry and although there are no general rules, we shall discuss some aspects in Section 9.3.4.

9.3.2. Dynamic Coupling

A completely different situation is shown by compounds where the coordination polyhedron is symmetrical with reference to rotoreflection operations; that is, it is achiral. This is well represented by the family of complexes Ln Na_3 $BINOLate_3$, also known as heterobimetallic Shibasaki's catalysts (Scheme 9.2; see also Section 9.5.5).

Here the six oxygen atoms (anionic) define an almost perfect trigonal antiprism (Figure 9.4) and the lanthanide chromophore must be considered intrinsically achiral, notwithstanding the stereodefined axes of the BINOLate units. This can't break the parity of the f orbitals and should result in vanishing metal-centered ECD. A different type

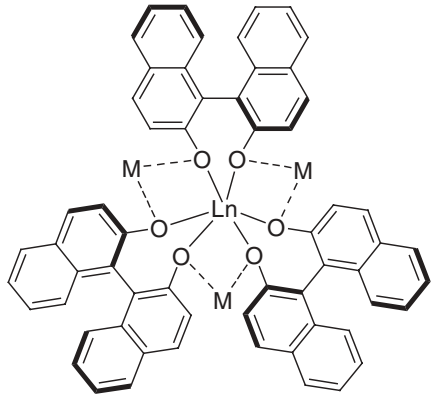

M = Li, Na, K

Scheme 9.2. Chemical structure of Shibasaki's heterobimetallic catalysts.

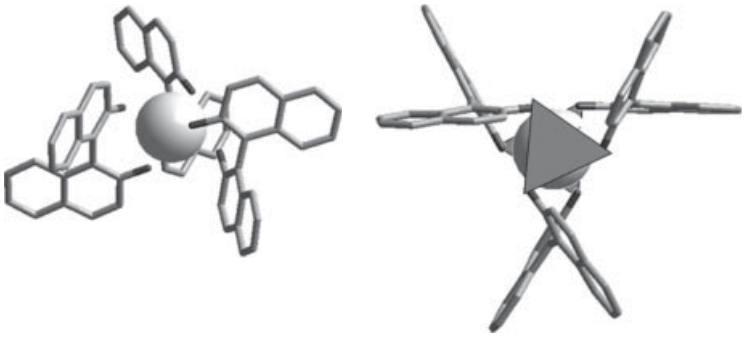

Figure 9.4. Solution structure and coordination polyhedron of of Yb Na_3 $BINOLate_3$ Left: View from the side. Right: View along the C_3 symmetry axis, the two dark gray triangles enhance the top and bottom faces of the trigonal antiprism defined by the oxygen atoms.

of interaction can be invoked in this case, referred to as "dynamic coupling" or ligand polarization, whereby the spectroscopic basis set is expanded to include ligand-localized excitations. Indeed the ligands bring about six naphthoate groups, disposed as the blades of a pinwheel around Ln^{3+} and endowed with a manifold of electronic transitions with EDTM character.

The result of this expansion is a coupling where the f–f transition borrows electric dipole character from the ligand-centered ones. Symmetrically, this also brings about some magnetic dipole onto the naphthoate transitions [14].

The NIR-ECD spectrum of Ln Na_3 $BINOLate_3$ is depicted in Figure 9.5 and we can see that, although bands of different sign alternate in this case as well, the integral over the whole multiplet is grossly negative. The sum rule implies that positive rotational strength compensating for this unbalance must be found elsewhere in the ECD spectrum of this molecule. This very likely occurs in connection with the naphthoate transitions in the UV. Unfortunately, this spectral region is dominated by very intense ECD bands, largely determined by degenerate and nondegenerate exciton coupling (described, for example, in Chapter 3 of Volume 2), which makes it unviable to recognize the relatively small missing rotational strength.

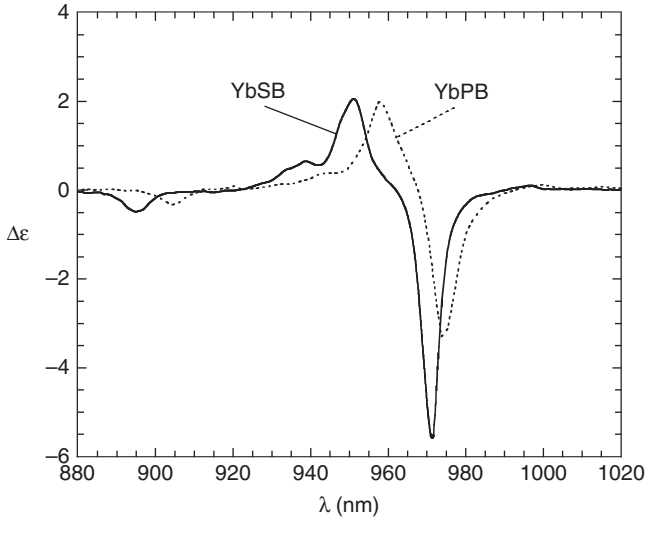

Figure 9.5. NIR-ECD spectrum of Yb Na_3 $BINOLate_3$ (YbSB, continuous line) and Yb K_3 $BINOLate_3$ (YbPB, dashed line) in acetonitrile ($c = 5$ mM, pathlength 1 cm).

Significantly here one can observe ECD or CPL also in cases when the ligand field splitting is very small or when the spectral resolution is poorer. Notably, this may be the case when one is forced to open the slit in order to harvest more light. We may quote at least two such situations, from our personal experience. In the first place, when one has background absorbance, which reduces the light reaching the detector. Lanthanide transitions often fall in uncommon spectral regions, where there are hardly contributions from other sources, but it may nonetheless be that there are tails from, for example, the solvent or other chromophores. This is true in particular for Yb^{3+} in water, because around 1000 nm there is a relevant contribution from H_2O (but not from D_2O) due to an O–H stretching overtone which makes it difficult to use optical paths above 2 cm, unless opening the slit. Secondly, this may be the case with CPL with poorly emissive samples; here one may try to collect as many photons as possible. A third situation we encountered sometimes is the presence of turbid samples, which scatter light and sizably reduce transmittance, which should be anyway avoided because it may be a source of artifacts.

9.3.3. Total and Relative Intensity of Chiroptical Properties

Lanthanides offer practically isostructural complexes throughout the transition with most ligands. The main differences between one versus the other Ln^{3+}, from the point of view of chemical behavior, must be found: (1) in the more or less accessible reduced or oxidized states (e.g. Ce^{4+} or Sm^{2+}); (2) in the variable coordination number, as a consequence of lanthanide contraction. The latter primarily affects one labile coordination site (often identified as *axial*), which can be more or less occupied by water or by another ligand [15–17]. In this family of very similar members, how does one choose between one or another? While structure and chemistry can be considered homogeneous, the spectroscopic properties of the various Ln^{3+} are very diverse. We shall naturally concentrate on chiroptical properties and make reference to the electronic terms depicted in Figure 9.1. It is evident that for most elements there is a manifold of transitions, spanning a wide spectral range. As mentioned, to a first approximation, all of them are electric dipole forbidden and must borrow intensity from the surroundings via static coupling, dynamic coupling, or both.

In the following we shall make reference to the absorption part, ECD, although the same arguments may be used for CPL, as well. We can elaborate Eqs. (9.1) and (9.2) by recalling that for a given transition $a \rightarrow b$, $\Delta A \propto R_{ab}$ and A is proportional to the dipolar strength D_{ab}, primarily determined by $|\boldsymbol{\mu}_{ab}|^2$. Taking advantage of (9.4) and assuming the same lineshape in absorption and in ECD, we may write

$$g_{Abs} = \frac{4R_{ab}}{D_{ab}} = \frac{4|\boldsymbol{\mu}_{ab}||\mathbf{m}_{ab}|\cos\tau_{ab}}{|\boldsymbol{\mu}_{ab}|^2} = \frac{4|\mathbf{m}_{ab}|}{|\boldsymbol{\mu}_{ab}|}\cos\tau_{ab}. \tag{9.6}$$

The angle τ_{ab} depends on the specific geometry of the system and does not lend itself to general considerations, but the two electric and magnetic dipole do provide some indications. In order to have strong ECD, both $\mathbf{m}_{ab}$ and $\boldsymbol{\mu}_{ab}$ must be nonvanishing, but to have large dissymmetry, the best situation is when $\boldsymbol{\mu}_{ab} \approx 0$. This means that good transitions to observe chiroptical spectra are all those with $\Delta J = 0, \pm 1$, which ensures $\mathbf{m}_{ab} \neq 0$ (ΔM_J also plays a role, which we'll neglect for simplicity here), while those with largest dissymmetry factors are those where J or $J' = 0$. We notice immediately that among a multitude, a few transitions stand out in Figure 9.1 and they are indicated in Table 9.1. Table 9.1 helps choosing the lanthanide to use, according to the following guidelines: (a) if one wants to focus of ECD or CPL; (b) the type of interferences one

TABLE 9.1. List of Ln^{3+} Transitions with Strong Rotational Strength [2]

Ion	Transition	$\tilde{\nu}$ (cm^{-1})
Ce^{3+}	$^2F_{5/2} \rightarrow {}^2F_{7/2}$	2100
Pr^{3+}	$^3H_4 \rightarrow {}^3H_5$	2150
Nd^{3+}	$^4I_{9/2} \rightarrow {}^4I_{11/2}$	2000
Sm^{3+}	$^5I_4 \rightarrow {}^5I_5$	1600
Eu^{3+}	$^7F_1 \rightarrow {}^7F_2$	1400
Tb^{3+}	$^7F_6 \rightarrow {}^7F_5$	1100
Dy^{3+}	$^6H_{15/2} \rightarrow {}^6H_{13/2}$	2100
Ho^{3+}	$^5I_8 \rightarrow {}^5I_7$	3500
Er^{3+}	$^4I_{15/2} \rightarrow {}^4I_{13/2}$	5000
Tm^{3+}	$^3H_6 \rightarrow {}^3H_5$	5800
Yb^{3+}	$^2F_{7/2} \rightarrow {}^2F_{5/2}$	10000

likes to avoid (e.g., blank absorbance); (c) which wavelength range one's instrumentation can cover.

In our own experience about Ln^{3+} ECD, working with Yb^{3+} in the NIR offers several advantages: The manifold $^2F_{7/2} \rightarrow {}^2F_{5/2}$ is among the intense ECD. Its transitions are often associated to very high g_{Abs} factors, often above 10%. Moreover, they is hardly ever perturbed by other absorptions apart from the OH stretching overtone, mentioned above, which may be a problem only when working with long paths (and may be reduced by using deuterated solvents).

For CPL, in the visible range, the most popular ones are $Eu^{3+} {}^5D_0 \rightarrow {}^7F_1$ around 17,000 cm^{-1} and $Tb^{3+} {}^5D_4 \rightarrow {}^7F_5$ at 18,000 cm^{-1} and $^5D_0 \rightarrow {}^7F_3$ at 16,000 cm^{-1} while in the Near infrared Yb^{3+} and Nd^{3+} were reported. In emission, however, there is one more aspect that needs to be taken into account: a suitable condition to excite luminescence. This is a very important issue in emission spectroscopy, which has been recently and very clearly reviewed by Bünzli and Piguet and will not be treated here [4].

In our opinion, the good understanding of the nature and the geometry of the complex under investigation is a necessary requisite for a rational approach. We shall see in Section 9.3.4 how chiroptical spectroscopy can contribute to this knowledge, but in general most of the information must come from other techniques, and very notably from paramagnetic NMR. The degree of structural detail that one can obtain from the analysis of lanthanide-induced pseudocontact shifts and relaxation rates—that is, from the analysis of NMR spectra (^1H, ^{13}C as well as of other nuclei)—is often impressive and can be compared to *X* rays. In contrast to diffractometric methods, NMR measurements are run in solution—that is, exactly on the same species that one often wants to observe by means of chiroptical methods. From this point of view, ytterbium is again the ideal choice, because it provides the highest accuracy of the ligand geomtetry in a sphere of about 7-nm radius [13].

9.3.4. Multiplet Structures in Yb^{3+} Complexes

The Yb^{3+} NIR-ECD multiplet is rich in information concerning the structure, nature, and charge distribution of the donor atoms participating in the coordination polyhedron. Some aspects relative to structure and nature will be discussed in Section 9.4.1 below, while here we wish to briefly treat charge distribution.

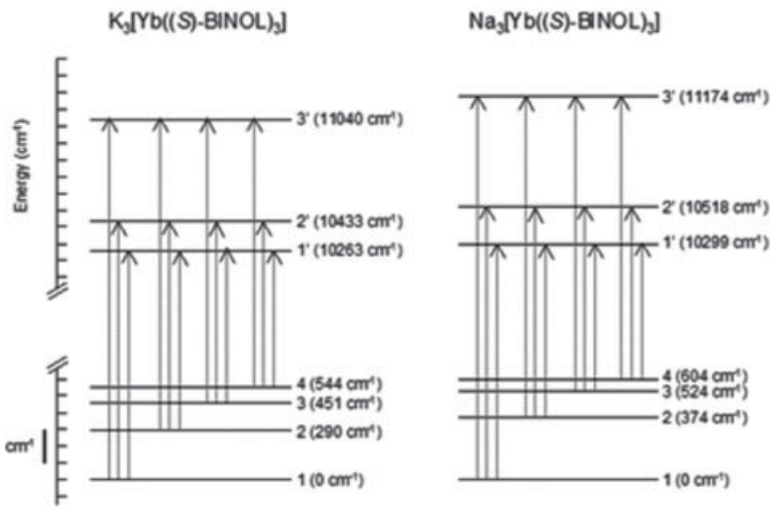

Figure 9.6. Energy level diagrams for the *f* states of Yb^{3+} in the complexes K_3 Yb(BINOLate)$_3$ (left) and Na_3 Yb(BINOLate)$_3$ (left) (right) [19].

Shibasaki's heterobimetallic complexes of formula M_3 Ln (BINOLate)$_3$ introduced in Section 9.3.2 change significantly their chemical behavior according to the alkali ion $M^+ = Li^+, Na^+, K^+$, which bridge to adjacent oxygen atoms on different BINOLate units [18]. This is very clearly reflected in the NIR-ECD spectrum of the Yb compounds, shown in Figure 9.5. Paramagnetic NMR data clearly demonstrated that the structure of the complexes in solution are independent of the nature of M [14], which proves that any difference in NIR-ECD must arise from crystal field parameters. Indeed even if static coupling can't be a source of ECD, because the coordination polyhedron is achiral (Section 9.3.2), the coordination polyhedron nonetheless modulates the splitting of the ground and excited electronic states of Yb^{3+}. Because this is only a small perturbation, the barycenter of the multiplet is preserved at 10,200 cm^{-1} (980 nm), while the individual wavenumbers of the bands become closer to or farther from this value like an accordion, depending on crystal field parameters. The complete analysis of the transition, by means of low temperature measurements, as described below, provides the energy levels shown in Figure 9.6. A nice feature of this finding is that it correlates very well with NMR parameters, specifically with the paramagnetic anisotropy constant [13].

Similarly, in Yb THP (Scheme 9.1), a complex based on tetraazacyclododecane, by changing the solution pH one can modulate the state of protonation of the hydroxyls and the charge borne on the oxygen atoms, which again is reflected in a similar accordion movement of the Cotton effects [20].

We should observe that the intensity of the CD bands is also modulated by the CFS, although to a rather modes extent.

9.3.5. Low-Temperature Measurements

Variable temperature (VT) is a well-known practice especially in conformational analysis through ECD. The idea is simply to change the distribution of conformers according to Boltzmann's law in order to disentangle the contributions arising from each single form and to provide temperature-dependent mole fraction for each component, which are related to the relative formation enthalpies. Such an approach has been applied in many cases and is thoroughly discussed in Lightner and Gurst's book [21].

In the context of Ln^{3+}, VT-ECD measurements may play a different and really major role, because they provide insight not only into conformational manifolds but also on the true structure of transitions manifolds. Consequently, within the literature on Ln^{3+}, they have been used relatively more often than for the rest of chiroptical studies.

The ligand field splitting is usually small compared to kT at room temperature (about 0.6 kcal $\cdot$ mol^{-1} or 2.4 kJ $\cdot$ mol^{-1}), which gives rise to so called "hot bands." These are transitions originating not from the state of lowest energy, but rather from the fact that the first excited one(s) may be (partially) populated according to Boltzmann distribution.

Consequently, the ECD spectrum contains a manifold of bands, which are necessarily at lower frequency to the those starting from the fundamental state. In itself this is a nice feature, because a highly structured ECD spectrum can be regarded as a fingerprint of the complex and of its structure. On the contrary, for its quantitative interpretation this feature needs to be simplified, which can be achieved by means of low-temperature ECD data.

Suitable solvents for low temperatures (down to -80°C or even lower) provide several advantages: a conformationally homogeneous system and significant population of only the fundamental electronic state. This should be regarded as the most correct way to obtain crystal field parameters through ECD.

ECD and CPL of a single term-to-term transition normally consist (or at least should consist) of a series of lines arising from CFS sublevels of the initial and final states. Let us take, for example, once more Yb DOTMA (Scheme 9.1), introduced in Section 9.3.1. The C_4 coordination polyhedron splits the fundamental $^2F_{7/2}$ into four and the excited state $^2F_{7/2}$ into three sublevels. Since the splitting is small, not only the lowest energy, but all the sublevels, may be populated at a given temperature, to an extent determined by Boltzmann distribution, as shown in Table 9.2. The observed absorption or ECD spectrum will consist of up to 12 components, whose position (wavenumber or wavelength) is solely determined by the CFS, but whose intensities depend on (a) the intrinsic dipolar or rotational strength of the transition and (b) the temperature-dependent Bolzmann population of the initial sublevel [8].

At 0 K, only the lowest energy state would be populated, and only three transitions should survive, which justifies the fact that the other ones are called "hot bands."

The multiplet structure may be analyzed in terms of energy levels of the fundamental and excited states by exploiting such temperature dependence—that is, by recording a spectrum at high and low temperature (provided that the sample does not undergo phase transitions or any other modification). One fundamental advantage of using ECD compared to total absorption consists of the fact that chiroptical spectra may contain bands of alternate sign, which enhances the resolution when two lines are nearer than their linewidth: If they have the same sign, they will simply merge into one (broader) peak, but if one is positive and the other is negative, there is a cancellation effect,

TABLE 9.2. Energy Sublevels and Relative Boltzmann Populations B(T) at Room (298 K) and Low (193 K) Temperature of the Fundamental State ($^2F_{7/2}$) of Yb DOTMA in Water

Energy (cm^{-1})	Sublevel	B(298 K)	B(193 K)
0	1	0.616	0.718
124	2	0.338	0.283
652	3	0.029	0.005
715	4	0.015	0.003

which anyway leaves two components, which may be recognized. This fact is of utmost importance in degenerate exciton coupling in ECD of organic chromophores (ECCD): In most cases the exciton couplet, consisting of a sigmoidal feature (bisignated doublet of bands) in ECD, corresponds to one absorption band where there is hardly any trace of the interaction between the chromophores.

Another, more elegant and possibly reliable way of achieving the assignment of the CFS sublevels would consist of combining ECD and CPL data.

Our long experience on Yb^{3+} complexes allows us to generalize what follows: Usually C_4 symmetry is allied to larger CFS compared to threefold, although other parameters such as the degree of twist or axial coordination may also play a role [15–17, 22]. This has an immediate consequence on the appearance and ultimately on the possibility of detection of ECD spectra. In the case of static coupling, where one can expect that the rotational strength integrated over the whole multiplet vanishes, only fourfold symmetry guarantees sufficient separation of the components to see a strong ECD spectrum. On the contrary, for threefold symmetry, the static coupling contribution may often get lost and only one line survives, thanks to dynamic coupling. From this point of view, it is indeed remarkable that most (pseudo)-C_4 complexes that have been studied, such as those depicted in Scheme 9.1, lack strongly polarizable groups in the first coordination sphere of Ln^{3+}; that is, they are likely under a strong influence from static coupling. On the contrary, (pseudo)-C_3 systems are practically dominated by conjugated ligands like diketonates or binaphthoates, endowed with strong electric-dipole-allowed transitions, responsible for relevant dynamic coupling.

9.4. COUPLING OF ELECTRONIC AND VIBRATIONAL STATES AND VCD ENHANCEMENT

This is a new field that will require further investigation, but may be expected to provide new pieces of information.

In the stem paper on VCD, Nafie, Keiderling, and Stephens reported the spectra of a wide range of compounds, fully demonstrating the power of this technique [23], which has become since a reference method for stereochemical assignments (see Chapters 4 and 24 of this volume). Among the others, they took into account two lanthanide complexes Pr $(tfc)_3$ and Eu $(tfc)_3$ (tfc stands for trifluoromethyl hydroxymethylene-*d*-camphorate; at the time of that paper the complexes were abbreviated as Pra-Opt and Eu-Opt), in the C–H stretching region. The two spectra, reproduced in Figure 9.7, are remarkably similar in position, sign, and relative amplitudes of the bands, although the Eu derivative has much stronger Cotton effects that the Pr. This fact was interpreted as a possible contribution from the *electronic* CD of Eu^{3+}, which has several states in the IR region. Against this explanation is the fact that the electronic transition nearest to 3000 cm^{-1} is $^7F_0 \rightarrow {}^7F_4$, at about 2870 cm^{-1}, which is magnetic dipole forbidden because $\Delta J = 4$ and, consequently, should also have very weak ECD (note that the rules for optical activity of Ln^{3+} compounds were reported by Richardson in 1980 [2] while Stephens' paper was published in 1976).

A few years later, Mason et al. described an interesting effect, assigned to the coupling of C–H stretching with a broad underlying d–d transition in Co^{2+} and Ni^{2+}-spartein complexes [7, 24]. There are two main aspects that characterize this phenomenon: (1) the fact that the metal-centered transition has nonvanishing strength at the stretching energy and (2) the VCD lineshape is dispersive, changing sign within the width of the

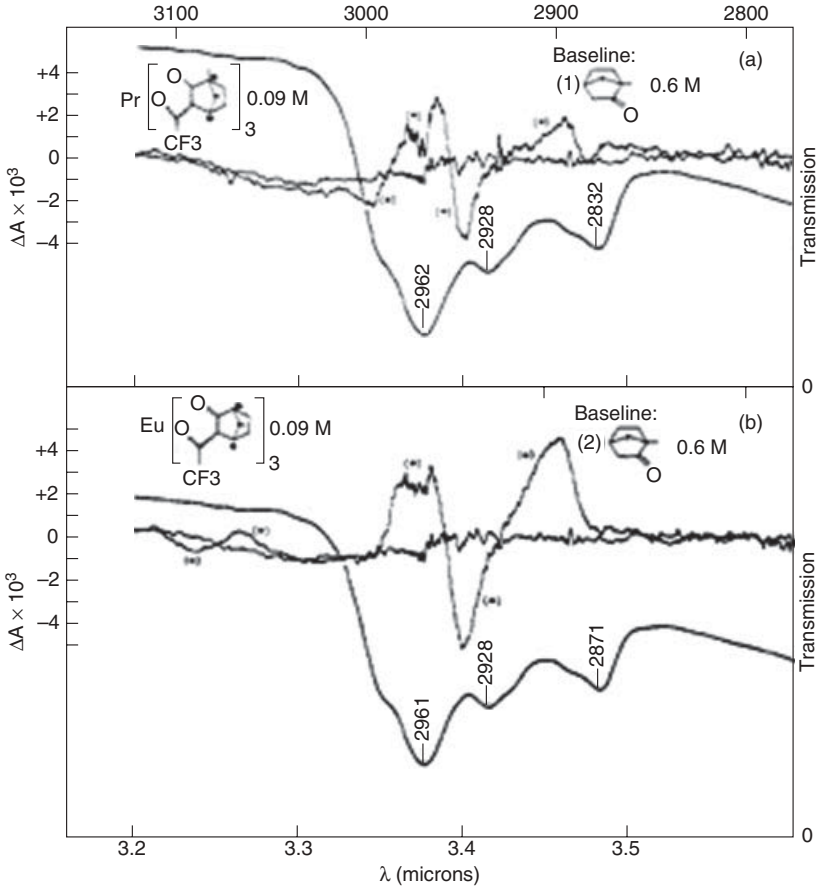

Figure 9.7. Total absorption, VCD, and baseline of Pr (tfc)$_3$ (top) and Pr (tfc)$_3$ (bottom) [23].

corresponding absorption [24]. This is strongly at variance with what had been observed by Stephens et al. for lanthanides: The spectra of Eu (tfc)$_3$ and Pr (tfc)$_3$ are very similar in shape and definitely share the same sign sequence [23].

In 2001 Nafie et al. reported that for Co^{2+} and Ni^{2+}-spartein complexes not only the C–H stretching region but also the mid-IR is strongly affected by the presence of an open-shell metal center, although the oscillator strength of the d–d electronic transitions of the metal cations in this spectral region can be considered negligible [25]. A few more recent articles related to d-metal complexes can be found in the literature [26, 27], and very recently some degree of VCD variation depending on the specific nucleus (Ln = La, Eu, Yb) in camphorate derivatives has been observed [26].

A complete theory accounting for the interaction of low-lying electronic states (LLES), as often found in metal complexes, was provided by Nafie [28]; but although it is meant for d metals as well as for f metals, the question for lanthanides seems to have been completely overlooked in the literature.

What we have seen in the previous sections demonstrates that Ln^{3+} are indeed peculiar and may not always be looked at with the same eye as d metals. As we repeatedly said, the degree of orbital mixing between metal and ligand is very modest, which means

that the electronic properties of the ligand are perturbed to some extent by the interaction, but not completely mixed up, which is at odds with transition metal complexes. Essentially, the ligand oscillators, responsible for vibrational spectra, are independent of the coupling with a Ln^{3+} and are responsible for a good deal of EDTM. Once more, we deal with ligand-centered electric dipole transitions, which couple with the magnetic dipole brought about from f–f terms—that is, with a dynamic coupling, which this time involves *vibrational* states of the ligand and is observed on these latter ones.

The effect of this coupling is to increase the rotational strength of intrinsically weak VCD bands, but what makes it particularly interesting and appealing is the fact that the overall appearance of the VCD spectrum is not really altered; that is, position and signs of the bands remain the same, while the amplitudes of the Cotton effects are larger. An example is provided in Figure 9.8, where the VCD spectra in the mid-IR of Yb, Gd, and La DOTMA are compared. This figure demonstrates that some of the low-energy Cotton effects are strongly enhanced in Yb DOTMA, compared to the other two compounds. This may be ascribed to the fact that La^{3+} is diamagnetic, while Gd^{3+} has f^7 configuration, two situations preventing the existence of LLES. On the contrary, Yb^{3+} features a fundamental state $^2F_{7/2}$, which generates four CFS sublevels, as discussed above. This indeed provides electronic states that are splitted by up to about 1000 cm^{-1} and which may provide an MDTM, useful to generate rotational strength.

9.5. APPLICATIONS

9.5.1. Lanthanides as Spectroscopic Probes for Ca^{2+} Binding Biomolecules

There are many reports on some similarities between lanthanide and alkali earth ions, notably Ca^{2+} and Mg^{2+}, two very relevant cations in biological chemistry, which are unfortunately spectroscopically silent. There have been many reports where alkali earth

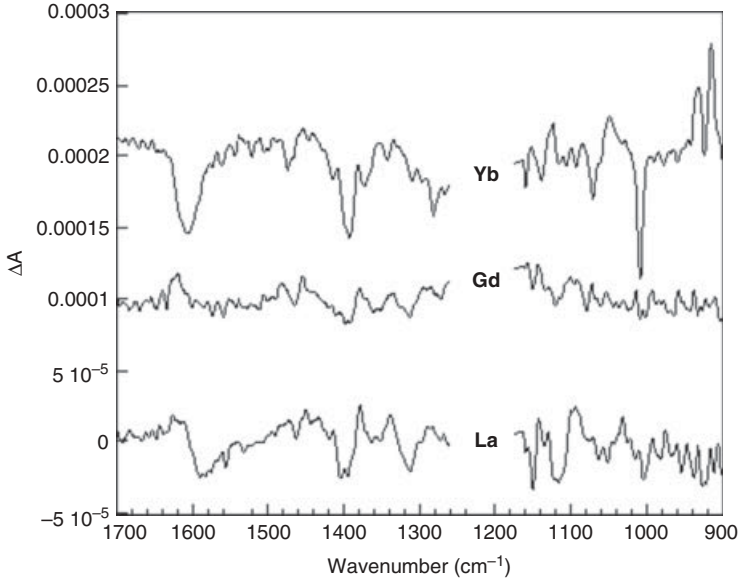

Figure 9.8. VCD spectra of La, Gd, and Yb DOTMA in water solution. The spectra have been vertically offset for clarity. A region between 1175 and 1260 cm^{-1} has been obscured because it is dominated by a solvent absorption.

metals have been substituted isostructurally with Ln^{3+}, with the benefit that, one can take advantage of the rich variety of spectral data made available by *f* elements. The two techniques that by and large have dominated this field of applications are emission spectroscopy and NMR [29].

Chiroptical methods may be a formidable tool for investigating biomolecule Ln^{3+} binding events, because the ions by themselves are achiral and all observed ECD or CPL must arise from adducts involving the biomolecule. The small extinction coefficients and the possibly large anisotropy factors are very suitable for ECD applications, especially considering the transitions listed in Table 9.1. Indeed, the first ECD of Yb^{3+} around 980 nm was measured for its complex with calcium-binding antibiotic rifampicin and is depicted in Figure 9.9 [30].

Unfortunately, the small absorption of Ln^{3+} means also that dichroism is weak and requires the use of rather concentrated solutions. Typically, 1–10 mM in a 1-cm cuvette must be used even for most sensitive cases, like Yb^{3+}. Of course, one may use longer pathlengths, which may have two consequences. First, solvent or blank absorbance may be no longer negligible, which is the case for the 980-nm band of Yb^{3+}, where a vibrational overtone of OH around 1000 nm may disturb the measurement. Second, by increasing the pathlength, one increases the volume, which ultimately means that the quantity of sample required may be a limiting factor, when dealing with costly or difficult to isolate biomolecules. It may be interesting to observe, however, that the type of sample suited for ECD measurements may match (quantity, concentration and solvent) those required for NMR, and in our experience exactly the same solution may be used for both (at least when using a 1-cm semi-micro cuvette). Thus, one may take advantage of the structural detail made available by paramagnetic NMR and of the chiral response

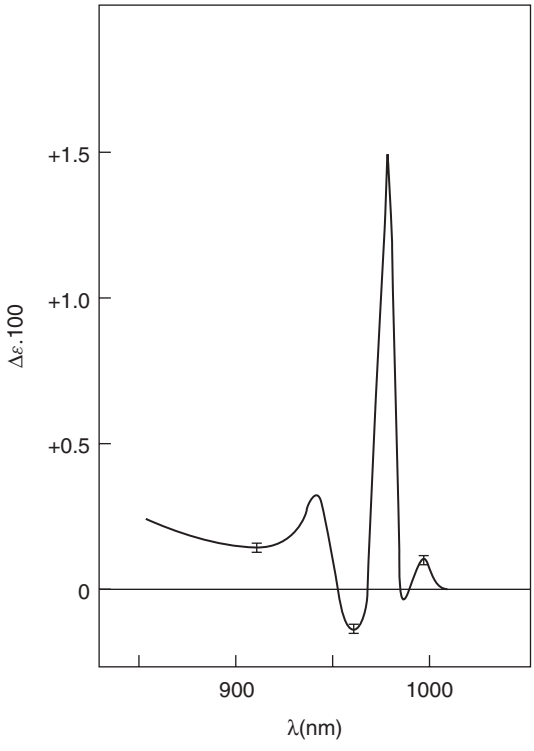

Figure 9.9. NIR-ECD spectrum of the complex Yb-rifampicin in MeOH/water [30].

at once. This kind of approach has been used successfully in at least two cases: the anthracycline family of anticancer drugs [31] and the widely used veterinary antibiotic lasalocid A [32].

NMR allows one to identify which parts of the ligand molecule are close to the paramagnetic center, and it can also provide conformational restraints about the way the ligand folds around Ln^{3+}. In the last few years, we have developed the program PERSEUS, which takes as input: (a) experimental data readily accessible from NMR experiments and (b) a tentative structure for the complex. The NMR data are used as constraints to build an optimized ("ultimate") solution structure, which best fits the paramagnetic shifts and nuclear relaxation information [13]. Of course, chirality is completely out of reach for NMR, which at best may provide insight into relative configuration but is insensitive to mirror-image structures and here is where chiroptical methods come into play.

The three cases cited so far (rifampicin, anthracycline, lasalocid A) and shown in Figures 9.9 and 9.10 fall largely in the category of dynamic coupling. Indeed, all of them feature one line dominating the NIR-ECD spectrum (which reveals also that at least for rifampicin and anthacycline the ligand field splitting is small). This is not surprising, considering the presence of UV–vis chromophoric groups in the ligands.

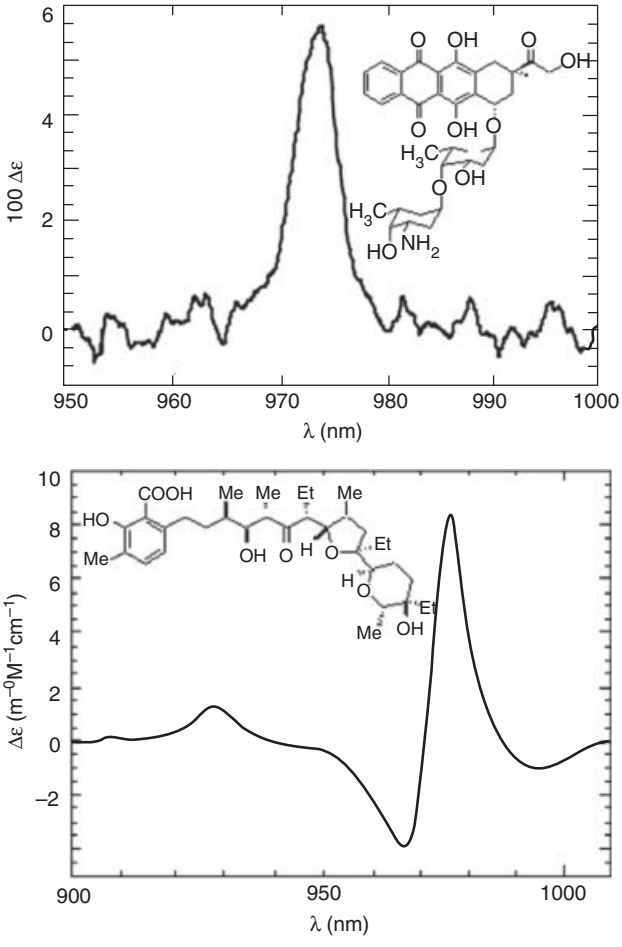

Figure 9.10. NIR-ECD spectra of Yb bound to drug molecules. Left: An anthracyclin (MEN 10755) [31]. Right: Lasalocid A [32].

It should be noted that these results are especially interesting because ytterbium (or any other lanthanide) may play the same structural role of biologically relevant ions, notably Ca^{2+}. This assumption may be proved *inter alia* by using *ligand*-centered ECD: One should measure the ECD spectrum of the drug molecule alone, in the presence of the spectroscopically silent cation (Ca^{2+}, Mg^{2+}) and in the presence of the Ln^{3+} probe. Identity of the latter two cases (and possibly difference from the free form) are a positive indication of isostructurality. Of course this is possible only for chromophoric ligands.

Emission spectroscopy is one of the spectroscopic tools able to reveal the interaction between Ln^{3+} and biomolecules. Thus, Eu^{3+} and Tb^{3+}, which have red and green fluorescence, have been largely used to this end. Ln^{3+} emission is efficiently quenched by O–H oscillators [4]. Upon binding to inner pockets e.g. of proteins, where water is excluded, they may yield a bright state, leading to a rather optimal situation of a probe that is *off*, when it is not ligated, or *on*, when it is ligated to a hydrophobic pocket of the biomolecules and thus sheltered from water. In principle, one should be able to observe CPL, as well, because biomolecules are usually chiral nonracemic, which would lead to an independent demonstration of binding. For example, interaction between Tb^{3+} and sugars has been demonstrated through CPL, as shown in Figure 9.11 [33].

Here we may notice at least one relevant feature: The integral over the multiplet is close to 0, which agrees well with the fact that ribose has no chromophores and that static coupling should largely dominate in determining the spectrum. Note also that for an ion with a rich manifold of f–f transitions like Tb^{3+}, it is the integral over the whole set which should vanish, not for one individual term-to-term component.

Spectra like those shown in Figure 9.11 demonstrate the interaction between lanthanide and sugars. They also encode relevant information on the organic moiety chirality and on the complex structure, aspects that will require further studies in the future.

9.5.2. Studies in the Solid State and Ln $(ODA)_3$

For many years the literature on chiroptical properties of lanthanide compounds has been dominated by the work of Richardson group on single crystals of Ln^{3+} $(ODA)_3$ (ODA

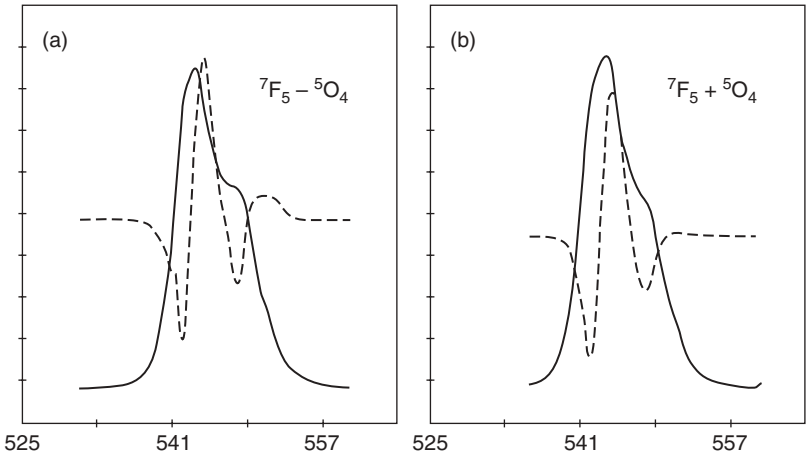

Figure 9.11. Total luminescence (continuous line) and CPL (dashed) spectra for (a) 1:3 Tb^{3+}/D-arabinose and (b) Tb^{3+}/D-fructose in DMF. $[Tb^{3+}] = 10$ mM and $\lambda_{exc} = 488$ nm. Adapted from reference 33.

stands for 1,3-oxydiacetate). The ligand is achiral and the complex in solution consists of the rapidly exchanging enantiomers due to Λ and Δ pseudooctaedric coordination. It crystallizes from water as a conglomerate and gives rise to a spontaneous resolution, whereby each crystal is of homogeneous chirality. ECD and CPL measurements on single crystals for a variety of Ln^{3+} ions provided extremely high resolution spectra, covering the whole UV–*vis* range. These data were used in connection with a comprehensive theoretical treatment of static and dynamic couplings. Covering this subject goes far beyond our scope, and we shall refer the reader to the literature [34–38].

9.5.3. Ln^{3+} in the Determination of Absolute Configurations with No Interferences

Determination of absolute configuration of chiral molecules is still a very urgent question, which has not yet found a general solution, as largely demonstrated in this book. One specific issue that raised a special interest is the 1,2-diol moiety, a common feature in natural as well as in synthetic products and intermediates. A wide set of methods for assigning the configuration of this moiety have been proposed, each one with merits and limitations; among them, at least two make use of lanthanide ECD and, more specifically, of Yb^{3+} NIR ECD.

At the time when spectral resolution was a major problem in NMR, one would often use lanthanide shift reagents; among them, Ln $(fod)_3$ (Figure 9.12) was a popular choice, because it can bind to mono- and bifunctional groups such as 1,2-diols. The fact is that Ln $(fod)_3$ is only formally achiral, because it is indeed the racemate of Λ and Δ pseudooctaedric coordination, which rapidly (typically in the s^{-1} range) exchange. When these bind to a chiral 1,2-diol, an asymmetric transformation of the first kind takes place; that is, the Λ/Δ mixture deracemizes on account of the diastereomeric interactions with the chiral species. As a consequence, there is an ECD signature both in the UV, allied to the exciton coupling of the diketonates chromophores, and in the vis-NIR, allied to the metal-centered f–f transitions. These two chiroptical signatures are both very important and useful. The former gives rise to an intense couplet, about 300 nm, which is strong and falls in a spectral region covered by every ECD instrument; although it occurs at relatively low energies, it may suffer from some interferences, when the analyte is endowed with red-shifted transitions or possibly due to other absorbing entities in solution. As for the latter, one can choose the Ln^{3+} that best suits one's needs and the available experimental setup, as described above; once more, we can take advantage of Yb^{3+} at the very start of NIR [39]. As one can appreciate from Figure 9.12, the NIR-ECD consists of essentially one band, which should be mostly due to the dynamic coupling between metal-centered magnetic dipole transitions and the diketonates EDTM.

The induction of stereoselection operated by the chiral diol upon Yb $(fod)_3$ can hardly be predicted *a priori*; but by observing coherence over a wide range of products, one can put forward an empirical rule, by which if the diol is of (*R*)- or of (*R,R*)-configuration (provided that the sequence rule reflects the size and bulk of the substituents), the observed NIR-ECD band is negative. The only weakness point in this correlation is provided by the simplest structure, namely 2,3-butandiol, which apparently leads to a complex of different structure. Interestingly, its NIR-ECD signature is completely different from the others, because it contains a large band at high energy, which renders clear that one deals with a unique species that can't be considered analogous to the other ones [39].

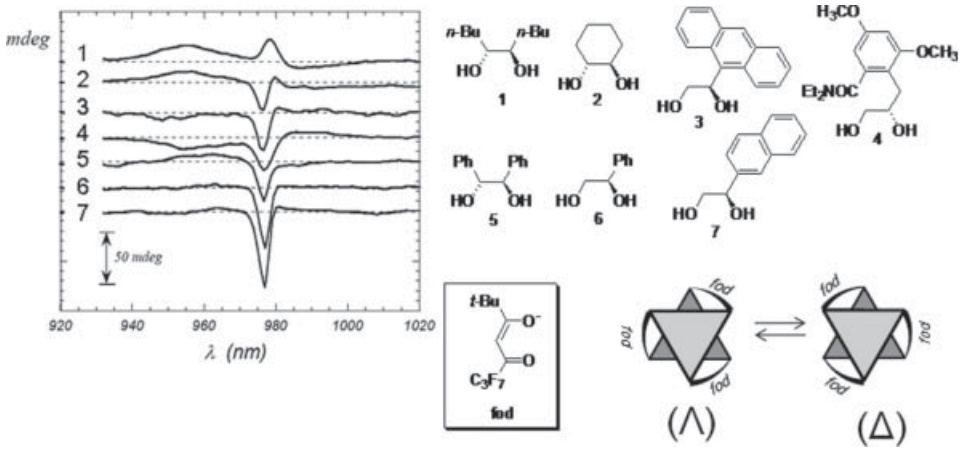

Figure 9.12. NIR ECD spectra of Yb $(fod)_3$ bound to the diols depicted on the right.

Taking inspiration from this correlation and also from the experience of the mixtures of sugars (which contain several 1,2-diol moieties) with Tb^{3+} salts (see Figure 9.11), it becomes easily rationalized that one can obtain relevant NIR-ECD spectra by simply mixing chiral nonracemic diols with Yb salts like chloride or triflate. [40]. Here, the only element of chirality is the diol itself, and the only spectroscopically active part is Yb^{3+}. The fact that a non-vanishing NIR-ECD spectrum is observed reveals the intimate interaction between cation and chiral ligand. Moreover, since the diol lacks relevant electronic transitions, dynamic coupling can't be the source of metal-centered ECD, but rather a static coupling mechanism. Luckily, the CFS induced by the diol is strong enough to split the electronic sublevels of the excited state ($^2F_{5/2}$) of Yb^{3+}, as a necessary requisite to observe a nonvanishing CD spectrum (see Section 9.3.2). Figure 9.13 represents the spectrum obtained by mixing Yb $(TfO)_3$ with (*R,R*)-2,3-butanediol in different solvents. One can immediately note that (1) the spectra are complex and consist in a series of bands within at least 60 nm (about 650 cm^{-1}), (2) the integral over the whole multiplet is close to 0, and (3) the overall multiplet shape is very similar in different solvents. On analyzing different diols, one can find again a regularity in the sequence of bands, which can once more be used as an empirical tool for assigning the absolute configuration of diols. For both correlations outlined above, namely Yb $(fod)_3$ and Yb X_3 (X = Cl or TfO), not only diols with one but also with two chiral centers (of like chirality) were employed and provided coherent results [39].

In principle, not only ECD but also CPL can be used to monitor the formation of chiral nonracemic Ln^{3+} chelates with 1,2-diols [41].

9.5.4. MRI: Conformation SAP/TSAP

One of the fields where lanthanide compounds have found the most applications is MRI (magnetic resonance imaging) contrast agents, where Gd DOTA constitutes a successful example in clinical practice and a benchmark for the evaluation of alternative products. A wide number of structural variations of this motif have been prepared; and all of them, to a larger or a smaller extent, feature a common stereochemical problem. When the four nitrogen atoms are engaged in Ln^{3+} coordination, tetraazacyclododecane (cyclen) can exist in one conformationm represented by the symbol [3333]. This indicates that the

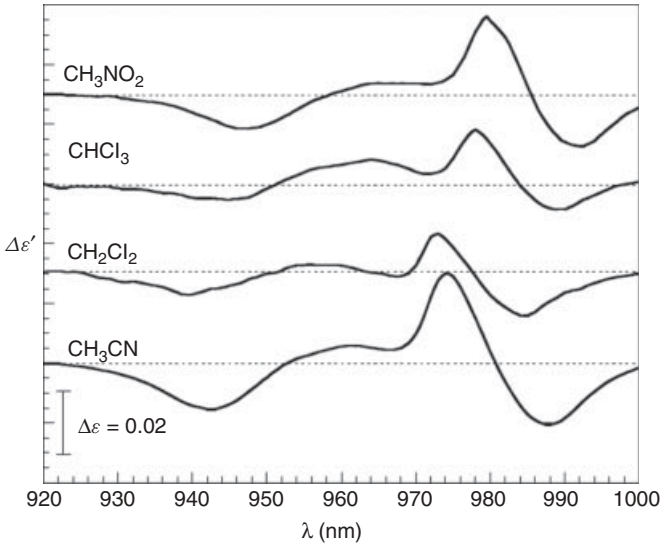

Figure 9.13. NIR-ECD spectra of a 1:4 mixture of Yb X_3 and (*R,R*)-2,3-butanediol NIR CD in different solvents. In CH_3CN and in CH_3NO_2, X = OTf; in $CHCl_3$ and CH_2Cl_2, X = Cl.

macrocycle consists of four "straight" segments of *three* bonds each (hence four times "3"), as depicted in Figure 9.14 (see also paragraph 11-5.d, pp. 762–769 in reference 42).

The [3333] form is chiral, because it consists of the repetition of *gauche* conformations of the same sign for all the four ethylene groups. Two enantiomers are possible: They are named (λλλλ) and (δδδδ) according to the g^-/g^+ geometry of the four NCCN moieties, as shown in Figure 9.14 [5, 43]. The pendant acetate arms bearing further donor groups must all lean from the same side (Figure 9.14). The concerted arrangement of these pendant groups leads to a type of chirality similar to the Λ and Δ metal coordination of octahedric complexes with bidentate ligands. These two conformational chirality elements, namely the macrocycle arrangement described through (λλλλ)/(δδδδ) and the side-arm orientation, leading to Λ/Δ metal coordination combine to provide four stereoisomers, which are two pairs of enantiomers and otherwise diastereomers. In all Ln DOTA complexes the rate of interconversion at room temperature is around 1 s^{-1}, and consequently the four species must be considered labile and cannot be isolated.

This stereochemical issue is particularly relevant in the context of MRI contrast agents, because the two diastereomeric forms as Λ (λλλλ) and Λ (δδδδ) have a different bite angles (O–Ln–O) and consequently different access to a nineth-coordination site along the C_4 axis, where water binds. The fact is that the exchange rate between bulk and ligated water is one of the primary parameters determining the contrast agent properties of a compound, which makes a correct knowledge of the bite angle of paramount importance.

Paramagnetic NMR has provided a rich harvest of structural and dynamic detail on these compounds but, very surprisingly, it may fail to distinguish between the two diastereomers.[9, 11–13, 44, 45] NIR-ECD applied on Yb DOTA derivatives containing chiral centers on the side arm [8, 16, 20] or on the macrocycle [22] have demonstrated that they have completely different chiroptical signatures and that they can immediately be recognized by a simple spectrum, as demonstrated in Figure 9.15, where one takes advantage of conformationally locked derivatives, obtained by introducing a bulky *p*-nitrobenzyl group onto the macrocyclic ring of DOTMA (see Scheme 9.1 for the structures). Moreover, the fine structure of the NIR-ECD spectrum is a faithful reporter of the state of axial binding [17].

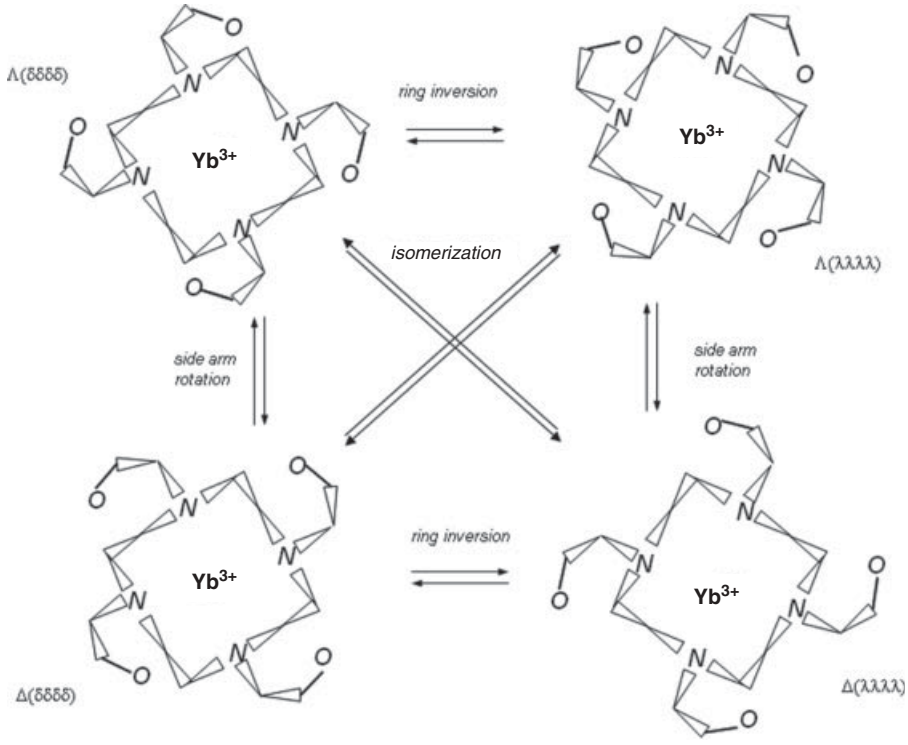

Figure 9.14. Stereochemistry of Yb-DOTA. The species across the diagonals are enantiomers, while between top and bottom lines and between left and right columns, there is a conformational diastereomer relation.

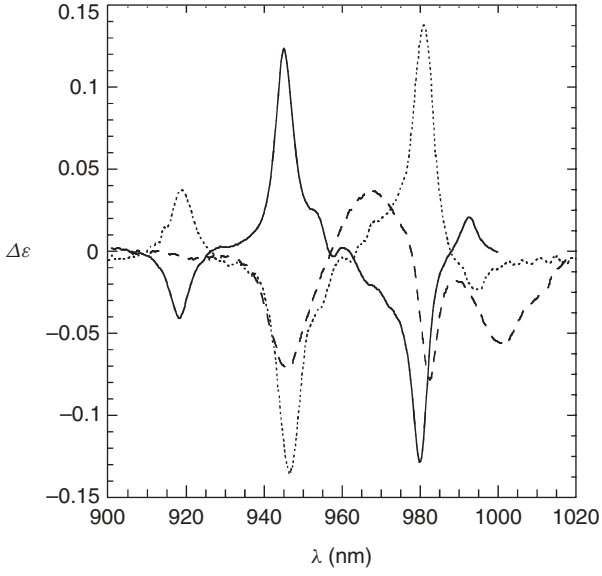

Figure 9.15. NIR CD spectra of (*RRRR*) Yb DOTMA (continous line), *S*(*SSSS*) Yb *p*-NO_2Bz DOTMA (dotted line), and *S*(*RRRR*) Yb *p*-NO_2Bz DOTMA (dashed line). For the structures, see Scheme 9.1.

In the literature, one can find several other cases where NIR-CD was used to monitor extent and type of ligation at a labile axial positions at least for Yb^{3+}, a fact that can be possibly extrapolated to the other Ln^{3+} [15, 16].

The spectral signature of the two diastereomers is so characteristic that it could be used for studying the inclusion process of Ln DOTA into γ-cyclodextrin [46]. It is known that the lanthanide complex can be hosted in the large macrocyclic cavity of the sugar, but while paramagnetic NMR provided insight into the thermodynamics of the process, it could not access safely which of the four stereoisomers of Ln DOTA, namely Λ ($\lambda\lambda\lambda\lambda$), Δ ($\delta\delta\delta\delta$), Δ ($\lambda\lambda\lambda\lambda$), Λ ($\delta\delta\delta\delta$), would bind to γ-cyclodextrin. This problem was easily solved by means of NIR-ECD of Yb-DOTA, which revealed that there is total stereoselection and that only Λ ($\delta\delta\delta\delta$) binds [47].

Parker and Dickins used achiral analogues of Ln DOTA to report the chirality of anions, which would bind to the lanthanide cation and by so doing would enforce a definite configuration of the macrocycle, which is profitably observed by metal-centered ECD or CPL [48–50].

9.5.5. Catalysts: Structure and Dynamics

The field where stereodefined lanthanide compounds have met the largest interest at the moment appears to be enantioselective catalysis [51, 52]. In several cases, metal-centered ECD has greatly helped understanding structural details of the catalytic precursors and about the reaction pathways. The most successful family in this context has been the so-called heterobimetallic Shibasaki catalysts, of general formula M_3 Ln $BINOLate_3$, introduced above in Sections 9.3.2 and 9.3.4.

There is at least one more interesting feature that one can observe, and measure *only* by means of metal-centered ECD: it is the ligand-exchange process, through the following experiment.

One can start with a homochiral complex prepared with enantiopure (*R*)-BINOLate, which we shall briefly call *RRR*. This has well-defined UV-ECD as well as NIR-ECD spectra. The former is allied to (*R*)-BINOLate and is largely dominated by the negative couplet due to the exciton coupling between the ^1B_b transitions of directly connected naphthoates. *Inter*-binaphthoate coupling—that is, between transitions located on different ligands—also plays a role, because they are kept closed in space by participating in the coordination of the same Yb^{3+}. The metal-centered NIR-ECD only senses the chirality of the coordination polyhedron of Yb^{3+}. If we now add to the solution a 20% molar excess of the ligand of opposite configuration (*S*)-BINOL, we may have a certain degree of ligand exchange, while keeping in mind that NMR demonstrates that the amount of heterochiral diastereomers of the complex, (i.e., species like *RRS*) is in any case small (below 10%). The UV-ECD of such a mixture is difficult to interpret and disentangle, because the contributions arising from free and bound ligand are superimposed and can hardly be separated. On the contrary, the NIR-ECD shown in Figure 9.16 is very neat and informative, revealing that complete reversal of chirality can be attained by the dynamic ligand shuffling. It is noteworthy that this process is very rapid and it is completed within a few seconds.

More recently, an apparently very similar system based on a modification of BINOL was proposed for enantioselective aldol reaction [53–55]. In this case the formation of diastereomers occurs to a much lesser extent and indeed it cannot be revealed by NMR. Nevertheless, the very same exchange experiment briefly described above could be followed by NIR-ECD, demonstrating that the same chirality inversion takes place in

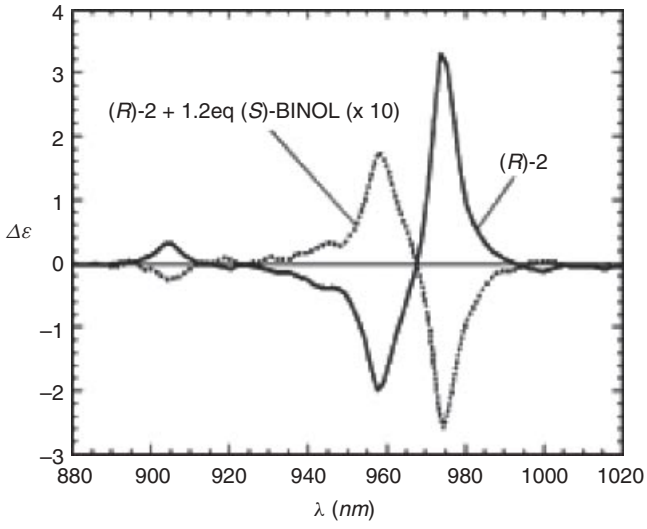

Figure 9.16. NIR-ECD spectrum of the complex (*R*)-Na_3 Yb (BINOLate)$_3$ before (continuous line) and after (dotted) the addition of 1.2 equivalents of (*S*)-BINOL.

this case as well, although on a much slower pace (it takes several hours and its kinetics can be easily followed) [56].

9.5.6. Frontier Applications of Ln^{3+} CPL

We wish to conclude this overview by mentioning a field that we believe may be relevant in the future: namely, applications of CPL in new and potentially "responsive" materials. As we've discussed at length, lanthanides nicely join several very useful features: (1) They can be strongly emissive, with high g_{lum} anisotropy factors; (2) the experience of MRI contrast agents provides a solid knowledge of stable chelates that are globally achiral but can sense the chirality of ancillary ligands; (3) mostly from the field of enantioselective catalysis one can derive concepts and inspiration for preparing stable nonracemic chelates of known or predictable structures; and (4) paramagnetic NMR provides the necessary structural detail for understanding what goes on in solution (or even in the solid state). There are at least two fields where all of this may find applications: luminescent devices such as LEDs and stains for fluorescence microscopy. Recently, Kaizaki et al. proposed a stable chiral Eu^{3+} diketonate, Cs[Eu((+)-hfbc)$_4$], with the exceptional $g_{lum} = 1.38$, which means that there is an enantiomeric excess of the emerging photons at 595 nm close to 70% (Figure 9.17a, 9.17b) [57].

It is interesting to observe that in our own finding this high degree of CPL is maintained also after dispersing this product in a polyvinyl carbazole (PVK) polymeric film—that is, i.e. in the solid state, as shown in Figure 9.17c.

9.6. CONCLUSIONS

At the end of this discussion, we may conclude that not only chiral lanthanide compounds are interesting per se, but rather they can be used as powerful spectroscopic and chiroptical probes to address a large number of very different questions and to solve structural problems in a manifold of situation. Their almost homogeneous chemical behavior together with their widely different spectroscopic signatures lends itself to a fine tuning

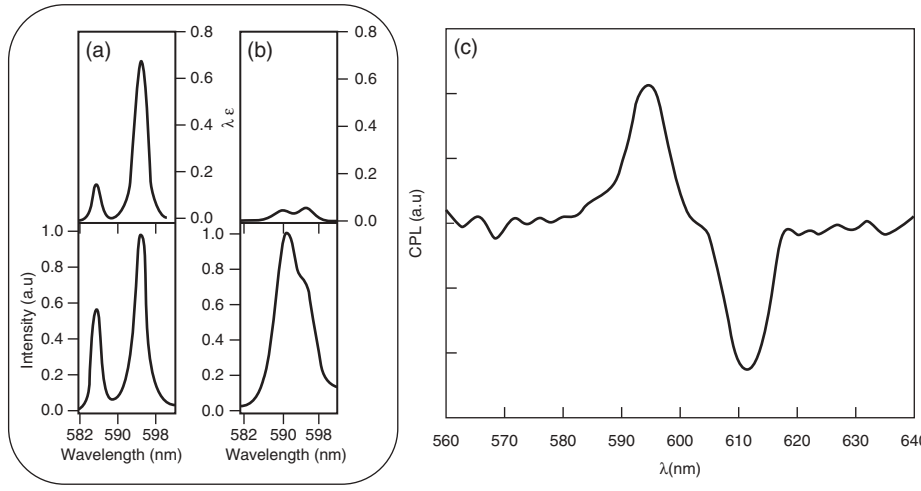

Figure 9.17. (a, b) CPL (upper curves) and total luminescence (lower curves) spectra for the $^5D_0 \rightarrow {}^5F_1$ transition of the complex Cs[Eu((+)-hfbc)$_4$] (a) and Na[Eu((+)-hfbc)$_4$] (b) solutions in $CHCl_3$ ([Eu] = 2 mM, λ_{exc} = 352 and 335 nm, respectively) [57]. (c) CPL spectrum of Cs[Eu((+)-hfbc)$_4$] dispersed in a PVK film. Notice that only the low-energy band (590 nm) should be compared with those depicted in (a) or (b), because the one at 610 nm belongs to $^5D_1 \rightarrow {}^7F_0$ transition.

of the choice of the specific lanthanide to be used as a probe according to the specific problem under investigation. We are aware that in this limited space we could give just the taste of it, but we hope this will stimulate the readers.

ACKNOWLEDGMENT

Financial support from the program FIRB RBPR05NWWC is gratefully acknowledged.

LIST OF ABBREVIATIONS

CFS	Crystal field splitting
CPL	Circular polarization of luminescence
ECD	Electronic circular dichroism
EDTM	Electric dipole transition moment
LLES	Low-lying electronic states
MDTM	Magnetic dipole transition moment
MRI	Magnetic resonance imaging
NIR	Near infrared
PCS	Pseudocontact shift
PVK	Polyvinyl carbazole
UV	Ultraviolet
VCD	Vibrational circular dichroism
vis	Visible
VT	Variable temperature

REFERENCES

1. S. Cotton, *Lanthanide and Actinide Chemistry*, John Wiley & Sons, Chichester, **2006**.
2. F. S. Richardson, *Inorg. Chem*. **1980**, *19*, 2806–2812.
3. S. Hüfner, Optical spectroscopy of the lanthanides in crystalline matrix, in *Systematics and the Properties of the Lanthanides*, Vol. 109, S. P. Sinha, ed., NATO-ASI, **1983**, pp. 313–388.
4. J.-C. G. Bünzli, C. Piguet, *Chem. Soc. Rev*. **2005**, *34*, 1048–1077.
5. D. Parker, R. S. Dickins, H. Puschmann, C. Crossland, J. A. K. Howard, *Chem. Rev*. **2002**, *102*, 1977–2010.
6. L. Smentek, B. G. Wybourne, *Optical Spectroscopy of the Lanthanides*, CRC Press, Taylor and Frances, Boca Raton, FL, **2007**.
7. S. Mason, F., *Molecular Optical Activity and the Chiral Discriminations*, Cambridge University Press, Cambridge, **1982**.
8. L. Di Bari, G. Pintacuda, P. Salvadori, *J. Am. Chem. Soc*. **2000**, *122*, 5557–5562.
9. L. Di Bari, G. Pintacuda, P. Salvadori, *Eur. J. Inorg. Chem*. **2000**, 75–82.
10. H. G. Brittain, J. F. Desreux, *Inorg. Chem*. **1984**, *23*, 4459–4466.
11. S. Aime, M. Botta, G. Ermondi, *Inorg. Chem*. **1992**, *31*, 4291–4299.
12. S. Aime, M. Botta, M. Fasano, M. P. M. Marques, C. F. G. C. Geraldes, D. Pubanz, A. E. Merbach, *Inorg. Chem*. **1997**, *36*, 2059–2068.
13. L. Di Bari, P. Salvadori, *Coord. Chem. Rev*. **2005**, *249*, 2854–2879.
14. L. Di Bari, M. Lelli, G. Pintacuda, G. Pescitelli, F. Marchetti, P. Salvadori, *J. Am. Chem. Soc*. **2003**, *125*, 5549–5558.
15. J. Lisowski, S. Ripoli, L. Di Bari, *Inorg. Chem*. **2004**, *43*, 1388–1394.
16. L. Di Bari, G. Pintacuda, P. Salvadori, R. S. Dickins, D. Parker, *J. Am. Chem. Soc*. **2000**, *122*, 9257–9264.
17. R. S. Dickins, D. Parker, J. I. Bruce, D. J. Tozer, *Dalton Trans*. **2003**, 1264–1271.
18. A. J. Wooten, P. J. Carroll, P. J. Walsh, *J. Am. Chem. Soc*. **2008**, *130*, 7407–7419.
19. M. Lelli, *Solution Structure and Solution Dynamics in Chiral Ytterbium(III) Complexes*, Edizioni della Normale, Pisa, **2009**.
20. M. Lelli, G. Pintacuda, A. Cuzzola, L. Di Bari, *Chirality* **2005**, *17*, 201–211.
21. D. A. Lightner, J. E. Gurst, *Organic Conformational Analysis and Stereochemistry from Circular Dichroism Spectroscopy* Wiley-VCH, New York, **2000**.
22. L. Di Bari, G. Pescitelli, A. D. Sherry, M. Woods, *Inorg. Chem*. **2005**, *44*, 8391–8398.
23. L. A. Nafie, T. A. Keiderling, P. J. Stephens, *J. Am. Chem. Soc*. **1976**, *98*, 2715–2723.
24. C. J. Barnett, A. F. Drake, R. Kuroda, S. F. Mason, S. Savage, *Chem. Phys. Lett*. **1980**, *70*, 8–10.
25. Y. N. He, X. L. Cao, L. A. Nafie, T. B. Freedman, *J. Am. Chem. Soc*. **2001**, *123*, 11320–11321.
26. H. Sato, T. Taniguchi, A. Nakahashi, K. Monde, A. Yamagishi, *Inorg. Chem*. **2007**, *46*, 6755–6766.
27. C. Johannessen, P. W. Thulstrup, *Dalton Trans*. **2007**, 1028–1033.
28. L. A. Nafie, *J. Phys. Chem. A* **2004**, *108*, 7222–7231.
29. C. H. Evans, *Biochemistry of the lanthanides* Plenum Press, New York, **1990**.
30. P. Salvadori, C. Rosini, C. Bertucci, *J. Am. Chem. Soc*. **1984**, *106*, 2439–2440.
31. L. Di Bari, G. Pintacuda, S. Ripoli, P. Salvadori, *Magn. Reson. Chem*. **2002**, *40*, 396–405.
32. S. Ripoli, S. Scarano, L. Di Bari, P. Salvadori, *Bioorg. Med. Chem*. **2005**, *13*, 5181–5188.
33. J. P. Riehl, F. S. Richardson, *Chem. Rev*. **1986**, *86*, 1–16.
34. P. S. May, C. K. Jayasankar, F. S. Richardson, *Chem. Phys*. **1989**, *138*, 139–156.

35. F. S. Richardson, *J. Less Common Metals* **1989**, *149*, 161–177.
36. M. T. Berry, C. Schwieters, F. S. Richardson, *Chem. Phys*. **1988**, *122*, 125–139.
37. M. T. Berry, C. Schwieters, F. S. Richardson, *Chem. Phys*. **1988**, *122*, 105–124.
38. P. S. May, M. F. Reid, F. S. Richardson, *Mol. Phys*. **1987**, *62*, 341–364.
39. L. Di Bari, M. Lelli, G. Pintacuda, P. Salvadori, *Chirality* **2002**, *14*, 265–273.
40. M. Lelli, L. Di Bari, P. Salvadori, *Tetrahedron-Asymm*. **2007**, *18*, 2876–2855.
41. T. A. Hopkins, D. H. Metcalf, F. S. Richardson, *Chirality* **2008**, *20*, 511–523.
42. E. L. Eliel, S. H. Wilen, L. N. Mander, *Sterechemistry of Organic Compounds*, John Wiley & Sons, New York, **1994**.
43. L. Di Bari, P. Salvadori, Stereochemistry of macrocyclic lanthanide chelates: Structure and dynamics in Ln DOTA analogues, in *Organometallic Chirality*, G. Pàlyi, L. Caglioti, C. Zucchi, eds., Mucchi Editore, Modena, **2008**, pp. 227–246.
44. F. Benetollo, G. Bombieri, L. Calabi, S. Aime, M. Botta, *Inorg. Chem*. **2003**, *42*, 148–157.
45. R. S. Ranganathan, R. K. Pillai, N. Raju, H. Fan, H. Nguyen, M. F. Tweedle, J. F. Desreux, V. Jacques, *Inorg. Chem*. **2002**, *41*, 6846–6855.
46. E. Zitha-Bovens, H. van Bekkum, J. A. Peters, C. Geraldes, *Eur. J. Inorg. Chem*. **1999**, 287–293.
47. L. Di Bari, G. Pintacuda, P. Salvadori, *Chirality* **2010**, *22*, E11–E16.
48. R. S. Dickins, A. S. Batsanov, J. A. K. Howard, D. Parker, H. Puschmann, S. Salamano, *Dalton Trans*. **2004**, 70–80.
49. R. S. Dickins, A. Badari, *Dalton Trans*. **2006**, 3088–3096.
50. R. S. Dickins, S. Aime, A. S. Batsanov, A. Beeby, M. Botta, J. Bruce, J. A. K. Howard, C. S. Love, D. Parker, R. D. Peacock, H. Puschmann, *J. Am. Chem. Soc*. **2002**, *124*, 12697–12705.
51. H. C. Aspinall, *Chem. Rev*. **2002**, *102*, 1807–1850.
52. M. Shibasaki, N. Yoshikawa, *Chem. Rev*. **2002**, *102*, 2187–2209.
53. F. Tur, S. J. M., *Org. Lett*. **2007**, *9*, 5079–5082.
54. J. M. Saá, F. Tur, J. Gonzalez, M. Vega, *Tetrahedron-Asymm*. **2006**, *17*, 99–106.
55. J. M. Saá, F. Tur, J. González, *Chirality* **2009**, *21*, 836–842.
56. L. Di Bari, S. Di Pietro, G. Pescitelli, F. Tur, J. Mansilla, J. M. Saá, *Chemistry—A European Journal* **2010**, *16*, 14190–14201.
57. J. L. Lunkley, D. Shirotani, K. Yamanari, S. Kaizaki, G. Muller, *J. Am. Chem. Soc*. **2008**, *130*, 13814–13815.

10

NEAR-INFRARED VIBRATIONAL CIRCULAR DICHROISM: NIR-VCD

Sergio Abbate, Giovanna Longhi, and Ettore Castiglioni

10.1. INTRODUCTION

In a general way, near-infrared (NIR) spectroscopy may be defined as the spectroscopy in the ~4000 to 15,000 cm^{-1} (or equivalently, from ~2500 to 700 nm) region; the latter figures bring us to the edge of the visible region. In 1976 Keiderling and Stephens, in their effort toward measuring circular dichroism (CD) spectra in the infrared region (a technique named, a few years later, vibrational circular dichroism or VCD), reported [1] the first examples of NIR-VCD spectra. They did not make any attempt to interpret their nice data, and VCD in this region remained unattended for years. Even now, after considerable progress has been made in instrumentation, measurements, theory, and calculations of NIR-VCD spectra [2], the usefulness of this form of chiroptical spectroscopy is not yet fully recognized. The low-lying electronic transitions, namely either atomic $f-f$ or $d-d$ transitions, as in inorganic complexes, or transitions associated with largerly delocalized π states, as in organic solids, can appear in the NIR region, and CD spectra associated with such transitions [3] are discussed in another chapter of this book. Our concern here is just vibrational spectroscopy. The fact that the sea is blue is due to NIR absorption by the higher OH-stretching overtones of water molecules [4], which allow only lower-wavelength light to emerge after passing through meter- to kilometer-long layers of seawater. NIR absorption spectroscopy has been used extensively in the food industry to determine and quantify the parameters for highly absorbing materials, tied to smell, taste, and other organolectic characteristics; in the pharma industry, NIR absorption data [5] have been employed for quality controls. Are there similar reasons

Comprehensive Chiroptical Spectroscopy, Volume 1: Instrumentation, Methodologies, and Theoretical Simulations, First Edition. Edited by N. Berova, P. L. Polavarapu, K. Nakanishi, and R. W. Woody.
© 2012 John Wiley & Sons, Inc. Published 2012 by John Wiley & Sons, Inc.

that may support the use of NIR-VCD? The answer is still difficult, but some significant steps forward have been made recently such as to justify moderate optimism, both in the direction of fundamental knowledge and in that of applied research.

Before entering this discussion, however, let us identify the vibrational transitions that appear in the NIR-VCD spectra. They are from the ground state toward two sets of vibrational states: The first set is the succession of the overtones of XH-stretching vibrations (X = C, O, N, etc.), together with their own proper combinations, and the second one is the succession of the combination bands of v quanta XH stretching excitations with one quantum HXH bending excitation or with one quantum C=O stretching excitation [6, 7]. These last ones will be ignored here because their detection is increasingly difficult with increasing vibrational energy level due to intrinsically weaker signals. Furthermore, the interpretation of the first set of transitions appears simpler or at least is more studied in the literature for NIR absorption spectroscopy [8, 9], as discussed later in Section 10.2.2. As an example of the first set of transitions, we report in Figure 10.1, the absorption and VCD spectra of (+)-(*R*)-limonene, for transitions from the ground vibrational state ($v = 0$) to excited vibrational states, $v = 1$, 2, 3, 4, and 5 of CH stretchings. These transition regions are, respectively, called the fundamental transition ($\Delta v = 1$) region, the first overtone ($\Delta v = 2$) transition region, the second overtone ($\Delta v = 3$) transition region, and so on. All these spectra were taken in our lab, with different instruments and cells. For $\Delta v = 1$, we employed a Jasco-FVS 4000 FTIR spectrometer with a InSb detector measuring a 0.33 M CCl_4 solution in a 0.1 mm BaF_2 cell; for $\Delta v = 2$, 3, and 4 we employed a home-made instrument, described in reference 2, with the neat sample in a 0.1-cm, 0.5-cm, and 10-cm quartz cell, respectively. For $\Delta v = 2$ an extended InGaAs Peltier-cooled detector was employed, whereas for $\Delta v = 3$ and 4 a narrow-band InGaAs Peltier-cooled detector was used. Finally the spectrum for $\Delta v = 5$ was obtained by using a Jasco 815 SE spectrometer with its standard multiakali photomultiplier tube, but with a large enough sample compartment to fit a specially manufactured 19-cm quartz cell, which was a generous gift from Professor Dave Lightner of the University of Nevada, Reno. The acquisition times for the spectra were ~1 h for $\Delta v = 1$ and 2, 20 min for $\Delta v = 3$ and 4, and several hours for $\Delta v = 5$: the required times correspond to measuring different numbers of spectra and adding them up, for need of signal averaging. The data for $\Delta v = 5$ are in accordance with earlier measurements on a Jasco J600 instrument [10]. The fact that our instrumentation is optimized for $\Delta v = 3$ and 4 is proven by the signal-to-noise ratio of the spectra. The $\Delta v = 1$, 2, and 3 data are in good agreement with the data reported independently by Nafie and co-workers [11]. We have chosen limonene, since it was the first compound, together with a related group of molecules, on which systematic studies were conducted [12]. An important feature of Figure 10.1 is that the ratio of the VCD $\Delta\varepsilon$ values to the absorbance ε values, called g ratio, as defined for example in reference 13, is in the 10^{-4} range for all Δv. This interesting feature was predicted first by Faulkner et al. for $\Delta v = 2$ [14]. In a context more appropriate to the present chapter and for a generic Δv, Polavarapu [15] and Abbate et al. [16] showed that the same magnitude of g is expected for all Δv, on the basis of a simplified local Morse oscillator model and of an anharmonically perturbed normal mode model, respectively. Noticeably, reference 14 predicts also a decrease of two orders of magnitude in $\Delta\varepsilon$ and ε values, individually, while going from the fundamental to the first overtone transitions, as indeed observed. The $\Delta v = 3$, 4, and 5 NIR-VCD spectra of Figure 10.1 look very similar, with a negative feature corresponding to the absorption maximum and a positive feature of slightly higher intensity at higher wavelengths. The same bisignate feature can be recognized also in the $\Delta v = 1$ and $\Delta v = 2$ NIR-VCD

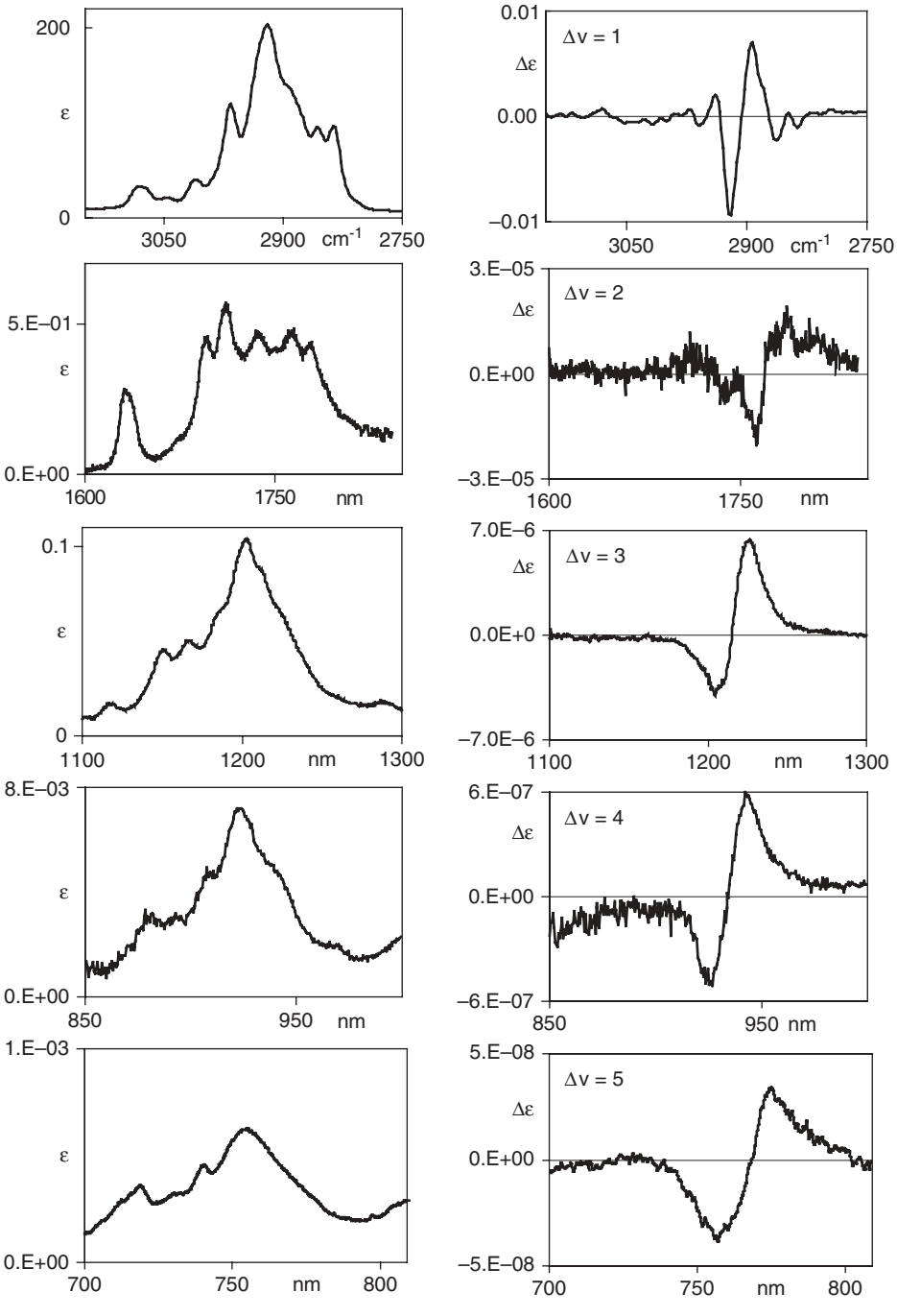

Figure 10.1. (*R*)-limonene absorption (left) and VCD (right) spectra in the fundamental ($\Delta v = 1$, topmost panels) and overtone regions ($\Delta v = 2$–5). For details on how the spectra were run, see text. Spectra for fundamentals plotted in wavenumbers (cm^{-1}), all other spectra in wavelength (nm).

spectra; however, the latter spectra and the corresponding absorption spectra look more structured and more complicated. Do these simple observations bear simple explanations based on *ab initio*-type calculations, without resorting to modeling arguments, as, for example, done in references 15 and 16? As will be shown later in Sections 10.2 and 10.3, we can now conduct *ab initio* analyses with just very few simplifying hypotheses on a number of cases obtaining quite good results.

10.2. ACQUIRING AND INTERPRETING NIR-VCD SPECTRA

The NIR region is special for several reasons. It requires dedicated or, at least, extended instrumentation from the one that had been originally designed for other spectroscopic regions. At the same time it requires adequate theoretical modeling, which, in large part, may be viewed (probably incorrectly) as an extension of the approach employed in the mid-IR region (4000–900 cm^{-1}), but with some complications that are not encountered in the mid-IR region. In this section we will consider the basic features of these two aspects, starting with instrumentation. Before this discussion, we wish to remind the reader that the cells that need to be employed for NIR are also different from those employed for the mid-IR region, and the needed sample concentrations are different as well. One should remember that the signals, both in absorbance and in CD, are progressively less intense with the overtone order. This point may be appreciated by going back to Figure 10.1, where one may notice that the ε and $\Delta\varepsilon$ decrease approximately by two orders of magnitude in going from $\Delta v = 1$ to $\Delta v = 2$ and then by one order of magnitude for each next higher Δv. This means that one has to employ progressively longer pathlength cells or more concentrated samples. In reality, the OH stretching overtone region is more difficult to investigate than the CH stretching overtone region, and beyond $\Delta v = 2$ not as many experiments have been reported for the OH stretching overtones due, among other reasons, to a different decrease behavior in absorption from fundamental to overtones and also due to complications related to hydrogen bonding. On the other hand, the cells that one uses for the NIR region are made of quartz and thus are easier to handle, to fill, and to clean than those used for the mid-IR region, which are porous, sometimes hygroscopic, and prone to breaking.

10.2.1. Instrumentation

As stated above, one may use standard mid-IR instrumentation modified for the NIR region. However, we should state that the data of Nafie and co-workers [11] were obtained with FTIR instrumentation, while those from our lab at Brescia [2, 17], were obtained on specially designed dispersive instruments. Indeed the data for $\Delta v = 2$, 3, and 4 of Figure 10.1 and most of the VCD data of the NIR region published by us [2, 17] were obtained with a noncommercial instrument, the picture of which is presented in Figure 10.2. A brief description of this instrument is given here: On the left-hand side is the source, a 20-W halogen lamp, followed by an Optometrics *f* 3/9 74-mm focal length Ebert single grating monochromator equipped with an 830-grooves/mm ruled grating blazed at 1.2 μm. Next to the monochromator is a big compartment divided in two halves: In the first half, just after the monochromator exit slit, there is a collimating lens to create a nearly parallel beam and a Glan Taylor linear polarizer to generate linearly polarized (LP) light in the vertical plane which passes through the sample and a PEM crystal. Note that this instrument is designed with two sample compartments (*vide infra*).

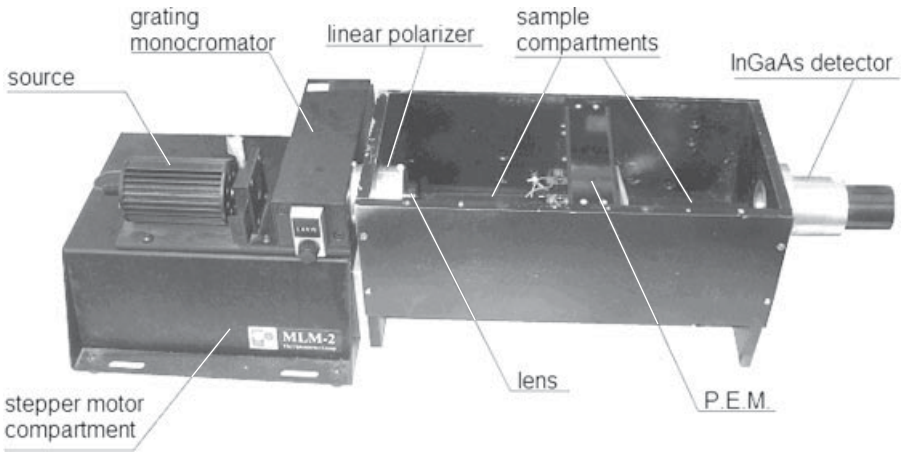

Figure 10.2. Picture of the instrument used for NIR-VCD spectroscopy ($\Delta v = 2$–4), located in Brescia.

The PEM, mounted with the principal optical axis at 45° to the axis of LP, introduces a phase difference (maximum $\pm\lambda/4$) between the two orthogonal components of LP light. The PEM is driven by a sinusoidal signal (~50 kHz) with circularly polarized (CP) light of two sorts generated at the extrema of the sinusoidal wave. Following the PEM, there is another sample holder. Finally, at the extreme right, one has an additional quartz lens focusing the beam on to the sensitive surface of a InGaAs detector. For $\Delta v = 2$ we use another detector (1 mm ϕ active area), which, at −20°C, has a useable sensitivity range from 1.3 μm to 2.5 μm. For $\Delta v = 3$ and 4 we use the standard InGaAs detector (2 mm ϕ active area), with useable sensitivity range from 0.9 μm to 1.7 μm (at −20°C). The low temperature of the detector is ensured by Peltier cooling working in the interval from −50°C to RT. The PEM is kept at 40°C all the time. The AC signal at the detector is synchronously amplified and demodulated by a lock-in amplifier (both lock-in and PEM were taken from a JASCO polarimeter).

An important feature of our instrument is the double sample compartment: For the CD measurements we place the sample on the right of the PEM. After collecting CD data in the right compartment, we take another spectrum by placing the sample in the left half, in a position that is normally called the absorption baseline (ABL) position. The CD spectrum that we provide, as done for example in Figure 10.1 for $\Delta v = 2$–4, is the difference of the CD and ABL spectra divided by the DC signal (which is related to the transmittance spectrum) and is taken simultaneously with the modulated data. This procedure, which we first adopted in reference 18, after making the first measurements in just the CD mode [17] is quite efficacious and was first suggested in the context of VCD by Holzwarth and Chabay [19, 20]; they stressed that most CD artifacts are due to "leaks" of the absorption DC features into the AC demodulated signals as well as from residual linear anisotropies of the optical components. The simple approach illustrated here is very effective in this regard, since the ABL spectrum is collected using the chiral sample itself and not its solvent (if any) or its racemic form, whose CD, ABL, and DC signals may be recorded independently. The scanning system is controlled directly from the old Jasco electronics (J-500A) and we output simultaneously the AC demodulated and the DC signals into a recently assembled microprocessor-controlled data logger interfaced to a PC, from which we can fully control scan parameters, spectra

acquisition/real time visualization, and, when necessary, spectra accumulation for signal-to-noise (s/n) improvements.

10.2.2. Theory

The interpretation of NIR-VCD experimental spectra is associated with calculating NIR-VCD spectra on the basis of the following quantities to be computed for each vibrational transition: (**a**) frequency ω; (**b**) rotational strength, defined as [21]

$$R = \mathrm{Im} \sum_{i=1}^{3} \langle 0|\mu_i|\mathbf{v}\rangle\langle \mathbf{v}|m_i|0\rangle \tag{10.1}$$

where μ_i and m_i are the Cartesian components ($i = 1, 2, 3$ or x, y, z) of the electric and magnetic dipole moment operators, respectively; $|0>$ represents the ground state and $|\mathbf{v}>$ the vibrational excited state defined by a set of quantum numbers, which we collectively denote by the boldface symbol **v; (c)** bandwidths associated with the transitions under study. Together with the NIR-VCD spectra, it is useful or even necessary to study the NIR absorption spectra, which implies the calculation of the quantities recalled in parts **a** and **c**, plus the step **(d)** for calculating dipole strengths:

$$D = \sum_{i=1}^{3} |\langle 0|\mu_i|\mathbf{v}\rangle|^2. \tag{10.2}$$

The above quantities are the same as those for the mid-IR region, where they can all, except for bandwidth, be obtained nowadays using *ab initio* programs such as those of reference 22; the method for conducting these calculations was set up more than 25 years ago [23]. In the NIR, there are, however, fundamental differences that prevent one from making full *ab initio* calculations unlike in the mid-IR case: Indeed there is a much larger number of states to deal with (*dimensionality*), and vibrational motions imply large displacements (*anharmonicity*, *i.e*. *nonlinearity*). Regarding the first type of difficulty, one should remember that in the mid-IR range one has to deal, in principle, with $(3N - 6)$ vibrational excited states, when N is the number of atoms in the molecule, each state depending on just one coordinate, called the *normal mode* coordinate. The states are described by special wavefunctions, built from Hermite's polynomials [6, 7]; vibrational transitions in the IR imply going from the ground state $|0> = |0, 0, \ldots>$ to a fundamental state $|\mathbf{v}> = |0, \ldots, 1, \ldots, 0>$, with excitation of just one quantum number of the $(3N - 6)$ possible. On the contrary, the transitions giving rise to NIR absorption or VCD imply more than one quantum number being excited and/or one quantum number being excited more than once—in the first case originating *combination* bands, in the second case *overtone* bands [6, 7]. This makes the dimensionality of the problem in the NIR too large, if no approximations are made. Indeed in Eqs. (10.1) and (10.2), **v** is meant to be a collection of integer quantum numbers $(v_1, v_2, \ldots, v_{3N-6})$ for all stretching and bending modes. The earliest interpretations of NIR absorption spectra, however, were prompted by the observation that signals are intense only for vibrations involving XH stretchings, and, despite the increasing number of states, spectra get simpler with increasing quantum number [24]. This observation provided a basis for simplified models, enough to describe the so-called "bright modes" (see, e.g., reference 25); the latter do not include the contributions of XY-bond stretching modes (X and Y both different from H), of XYZ bending modes, and of XYZW deformation modes (torsions,

out-of-plane modes, puckering modes, etc.). This approximation is useful to interpret the spectral regions of the sort presented in Figure 10.1. This is justified by the fact that larger v_i quantum numbers are needed for the bending and for the XY stretching modes than for the XH stretching modes to participate in the NIR region, and it is known that transition probabilities decrease with increasing powers of v_i [6, 7]. We may call the latter modes "dark modes," borrowing the name from the literature of IVR (internal vibrational redistribution) phenomena [25]: Only through resonance the latter modes may contribute to the spectra of Figure 10.1. It should be reminded that some of the NIR spectra that were recorded in references 1, 11, and 18 contain combination bands of $\Delta v \geq 1$ XH stretching modes with specific deformation modes, namely the $\Delta v = 1$ bending modes or the $\Delta v = 1$ C=O stretching modes, but we will not consider them here.

Due to all these considerations, one can assume a model of just XH stretching modes (X = C, O, N, etc.) that we may call "bright modes." The problem starts to show a tractable dimensionality, since one has, for each overtone order Δv, transitions from the ground state to manifolds of vibrational states $|\mathbf{v}> = |v_1, v_2, \ldots>$ in a limited energy range ("almost degenerate") and thus possibly influencing each other, depending on v and m, the latter integer number being the number of interacting XH stretching modes. v is given by

$$v = \|\mathbf{v}\| = \sum_{i=1}^{\mathrm{m}} v_i \tag{10.3}$$

where $v_i (= 0, 1, 2, 3, \ldots)$ is the vibrational quantum number for the ith XH stretching in the homogeneous group of m XH bonds (let us say aromatic or aliphatic CHs or something else). The number $v = \|\mathbf{v}\|$, which we have defined through Eq. (10.3), is kind of the norm of vector with integer components $\mathbf{v}$ and is the number that we refer to in defining the overtone order in, for example, Figure 10.1. The dimensionality $N(v, m)$ of the problem is, by standard combination analysis, $\frac{(m+v-1)!}{v!(m-1)!}$. $N(v, m)$ increases with v approximately as the vth power of m (for limonene at $v = 5$, one has a figure of the order of 13^5 for aliphatic CHs). For small v and small m, $N(v, m)$ is a small enough number. The dimensionality of the problem can be still high, if one wants to calculate all anharmonic corrections, and this initially discouraged setting up *ab initio* methods. A fruitful hypothesis has then been put forward on an empirical basis, which was justified first with classical mechanics arguments, namely the "*local mode*" hypothesis [8, 9]. In 1983 Lehman [26] was able to demonstrate that for $m = 2$ vibrational modes are completely equivalently described assuming as zero-order modes either normal modes, which are mixed at high v by Darling–Dennison anharmonicities, or strongly anharmonic local modes, having the form of Morse oscillators [7], mixed by harmonic couplings. The implication of this—discussed thereafter for $m \geq 3$ by Mills and Robiette [27], Sibert [28], Halonen [29], and many others—is that a system of m equivalent or almost equivalent XH stretchings is well represented by normal modes when $v = 1$, while the local mode scheme is more appropriate at high v. For this reason, when considering the NIR spectroscopy of m XH stretching systems, one can examine electrical and magnetic properties referring to local modes, and one may assume pure overtones [29] as the principal bright states.

This hypothesis allowed F. Gangemi et al. [2, 30, 31] to arrive at an interpretation of NIR-VCD spectra on a quantitative basis, adopting *ab initio*/DFT procedures previously devised by Bak et al. [32], who used the classic APT/AAT approach (*vide infra*) developed by Stephens [23, 33]. Let us briefly review their approach by reporting the

fundamental equations to calculate frequencies, dipole strengths, and rotational strengths, which will be used in the next paragraph to calculate the NIR-VCD spectra of (*S*)- and (*R*)-epichlorohydrin. This approach is based on the use of vibrational Morse eigenfunctions and eigenvalues [9, 34] that allow one to derive the vibrational frequencies and dipole and rotational strengths, comprised in the steps **a**, **b**, and **d** outlined above, as follows.

(a) Calculations of Frequencies. ω_{nv} for the nth local mode excited v times. One has

$$\omega_{n\mathrm{v}} = \omega_{0n}\left(v+\frac{1}{2}\right) - \chi_n\left(v+\frac{1}{2}\right)^2, \tag{10.4}$$

where ω_{0n} is the harmonic frequency and χ_n is the anharmonicity of the nth XH local mode under the action of a Morse potential function of the form [9, 34]

$$U_n(z) = D_n(1-e^{a_n(z-z_e)})^2, \tag{10.5}$$

$$a_n = \sqrt{\frac{8\pi^2 m_R c\,\chi_n}{h}}, \tag{10.5'}$$

$$D_n = \frac{\omega_{0n}^2}{4\chi_n}, \tag{10.5''}$$

where $\omega_{0\mathrm{n}}$ and χ_{n} are calculated in our approach as follows. One first calculates *ab initio* (at the Hartree–Fock or DFT level) the molecular energies at equilibrium and by displacing the nth XH bond under investigation (backward and forward) in several steps. The plots of energy values as function of the $(z-z_e)$ XH stretching coordinate are fit with a polynomial interpolation. The second, third, and fourth derivative of the potential energy are K_{nn}, K_{nnn}, and K_{nnnn}, which represent harmonic and anharmonic force constants. Therefrom, according to a suggestion of Kjaergaard et al. [35], one derives ω_{0n} from K_{nn}, and χ_n from the relation

$$\chi_n = \frac{h}{64\pi^2 mc}\left(\frac{5}{3}\frac{K_{nnn}^2}{K_{nn}^2} - \frac{K_{nnnn}}{K_{nn}}\right). \tag{10.6}$$

A fourth-order anharmonic local oscillator Hamiltonian treated by perturbation theory, up to second order for the cubic term and at first order for the quartic, gives the energy levels of Eq. (10.4) if χ satisfies Eq. (10.6) [27].

(b and d) Calculations of Dipole and Rotational Strengths. Looking at Eqs. (10.1) and (10.2) of Section 10.2.2, one understands that it is necessary to derive an expression for the transition probabilities for the electric dipole moment and magnetic dipole moment operators. An *ab initio* program, like Gaussian03 or Gaussian09 [22] or other similar packages (like ADF, GAMESS, TURBOMOLE, or DALTON [36–39]), provides such information (completely or in part) generally only for one-quantum number transitions (we have used the Gaussian package so far and throughout this work). The following procedure deals also with higher quantum numbers taking into account electric and magnetic anharmonic terms as well as mechanical ones (Morse eigenfunctions) and treats just local mode coordinates with no cross terms. One calculates the first and higher

derivatives with respect to the XH stretching coordinates $(z - z_e)$ of the electric dipole moment (called APT, which stands for atomic polar tensor) and of the magnetic dipole moment (called AAT, which stands for atomic axial tensor) as explained later and inserts them in Eqs. (10.7) and (10.8) [30–32].

$$\langle 0|\mu_i|v\rangle = \sum_{\alpha=H,X} \Pi^0_{\alpha i3} L^n_{\alpha 3} \sqrt{\frac{m_R}{m_G}} \langle 0|z - z_e|v\rangle + \frac{1}{2} \sum_{\alpha=H,X} \left(\frac{\partial \Pi_{\alpha i3}}{\partial z}\right)_0 L^n_{\alpha 3} \sqrt{\frac{m_R}{m_G}} \langle 0|(z-z_e)^2|v\rangle + \frac{1}{6} \sum_{\alpha=H,X} \left(\frac{\partial^2 \Pi_{\alpha i3}}{\partial z^2}\right)_0 L^n_{\alpha 3} \sqrt{\frac{m_R}{m_G}} \langle 0|(z - z_e)^3|v\rangle + \cdots, \tag{10.7}$$

$$\langle v|m_i|0\rangle = 2\hbar \sum_{\alpha=H,X} A^0_{\alpha i3} \frac{L^n_{\alpha 3}}{\sqrt{m_R m_G}} \langle v|p|0\rangle + 2\hbar \sum_{\alpha=H,X} \left(\frac{\partial A_{\alpha i3}}{\partial z}\right)_0 \frac{L^n_{\alpha 3}}{\sqrt{m_R m_G}} \langle v|(z-z_e)p|0\rangle + \frac{1}{2}\hbar \sum_{\alpha=H,X} \left(\frac{\partial^2 A_{\alpha i3}}{\partial z^2}\right)_0 \frac{L^n_{\alpha 3}}{\sqrt{m_R m_G}} (\langle v|(z - z_e)^2 p|0\rangle - \langle 0|(z - z_e)^2 p|v\rangle) + \cdots. \tag{10.8}$$

In Eqs. (10.7) and (10.8), $m_R = M_H M_X/(M_X + M_H)$ and $m_G = [\sum_{\alpha j} (S^n_{\alpha j})^2]^{-1}$ are mass coefficients; the first one is the reduced mass of the XH bond, and the second one is the normalization constant of the vibrational eigenvectors, $L^n_{\alpha j} = \sqrt{m_G} S^n_{\alpha j} \cdot S^n_{\alpha j}$ relates the nth normal mode (here the local XH oscillator: $z - z_e = Q_n/\sqrt{m_R}$) to the Cartesian jth coordinate of the αth atom, namely, $r_{\alpha j} = \sum_n S^n_{\alpha j} Q_n$.

In Eqs. (10.7) and (10.8) the coordinate number 3 is coincident with the z coordinate and thus

$$L^n_{H3} = \frac{M_X}{\sqrt{M_H^2 + M_X^2}}, \qquad L^n_{X3} = -\frac{M_H}{\sqrt{M_H^2 + M_X^2}}$$

(as a consequence, $m_G = m_R \frac{M_{XH}^2}{M_H^2 + M_X^2}$). The integrals $< 0|z - z_e|v) >, \ldots, < v|(z - z_e)^2 p|0 >$ are known if one assumes the wavefunctions $|v >$ to be eigenfunctions of the vibrational one-dimensional problem with the Morse potential. These eigenfunctions are constructed from Laguerre's polynomial and are known [9, 34]. The integrals are tabulated in many papers and books. For convenience we refer to reference 30.

Last but most important, let us discuss the APTs, $\Pi_{\alpha i3}$, and their derivatives and AATs, $A_{\alpha i3}$, and their derivatives. We point out first that in Eqs. (10.7) and (10.8) we need to take into account only the APTs and AATs of the X and H atoms of the XH stretching local mode we are interested in, and that each local oscillator is treated in its own reference system, with the z axis directed from X to H. Then we consider the plots of the *x, y, z* components of the H and X APTs and AATs versus $(z - z_e)$; as done for the calculations of ω_{0n} and χ_n in point **a** above, we perform polynomial interpolations of the derived plots. The zeroth-order term gives the first coefficient in Eqs. (10.7) and (10.8), namely $\Pi^0_{\alpha i3}$ and $A^0_{\alpha i3}$; the first-order terms yield coefficients $\left(\frac{\partial \Pi_{\alpha i3}}{\partial z}\right)_0$ and $\left(\frac{\partial A_{\alpha i3}}{\partial z}\right)_0$, and so on.

After calculating **a, b**, and **d**, the program would be considered complete, if one were content with a bar representation of the calculated spectra. In other words, one could place a bar whose height is proportional to R_{nv} (with the calculated + or − sign)

or D_{nv} at frequencies ω_{nv} for each local mode. However, a more direct representation of the NIR and NIR-VCD spectra is obtained by applying a bandshape that accounts for the heterogeneous phenomena undergone by the molecule in the solvent or in the neat liquid. As a matter of fact, not much work has been done in this sense; only a general discussion has been provided for VCD at reference 40. So, as done in mid-IR VCD, one attributes Lorentzian bandshapes to all transitions; the half-width at half-height is decided on an empirical basis, and it increases with overtone order as indicated by Reddy et al. [41] for transitions up to $\Delta v = 10$, in a study of NIR–vis absorption spectra. We may say that this is the only empirical part of the calculation scheme presented here, if one abstracts from the local mode hypothesis made above. We wish to conclude this section by stating that the local mode hypothesis and the approach just presented has allowed us to go from a mere generic discussion of NIR-VCD spectra to a quantitative interpretation thereof, with the consequent possibility of gaining physical insight into phenomena such as conformations, hydrogen bonding, differences in the electrical behavior of XH bonds, solvent effects, and so on.

10.3. A WORKED-OUT EXAMPLE: EPICHLOROHYDRIN

Epichlorohydrin is a small molecule, used for the synthesis of chiral compounds of pharmaceutical interest. Both enantiomers have been obtained from Sigma-Aldrich, and measurements have been done without further purification on neat liquids and, in the case of the fundamental stretching region, for 2.5 M CCl_4 solutions. For this spectroscopic region, absorption and VCD measuraments have been made with a JASCO 4000-FVS instrument equipped with an InSb detector, using a BaF_2 0.1-mm pathlength cell. The spectra are presented in Figure 10.3 (left) after solvent subtraction. In the NIR spectroscopic regions, 1800–1600 nm for $\Delta v = 2$ and 1250–1050 nm for $\Delta v = 3$, spectra have been measured with the instrument and the procedure described in a previous section. The absorption spectra for $\Delta v = 4$ and $\Delta v = 5$ transitions have been recorded with a commercial Jasco V-670 instrument. The absorption spectrum is intrinsically weak for $\Delta v = 1$, as may be realized by comparing the data of Figure 10.3 with the data of Figure 10.1; on the other hand, overtone absorption data exhibit comparable intensities to the data of Figure 10.1. VCD is quite weak for epichlorohydrin, and in the following we will provide the reasons why this happens.

Assuming that the observed wavenumber at the absorption maximum corresponds to the average transition frequency of the m oscillators $\omega_v - \omega_{v=0}$, the Birge–Sponer plot, $(\omega_v - \omega_{v=0})/v$ versus v, is obtained (see Figure 10.4a). If Eq. (10.4) holds, one obtains that $(\omega_v - \omega_{v=0})/v$ is proportional to v, namely, $(\omega_v - \omega_{v=0})/v = (\omega_0 - \chi) - \chi v$. Figure 10.4a indicates that this is indeed valid for epichlorohydrin: the slope of the straight line is a direct measure of χ (58.2 cm^{-1} from Figure 10.4a) and intercept yields the harmonic frequency ω_0 (3114 cm^{-1}); these are the "experimental" ω_0 and χ values.

In the following we calculate the observed NIR absorption and VCD spectra without introducing ad hoc parameters except for bandwidths, using the approximate methods based on the local mode scheme previously discussed. Before doing this, we recall what already is known in the literature, and we present a "standard" calculation for fundamentals.

Epichlorohydrin has already been studied by VCD spectroscopy in the mid-IR region [42]. A thorough discussion of its conformational properties as determined by various spectroscopic techniques is given in the same paper, where different population ratios for

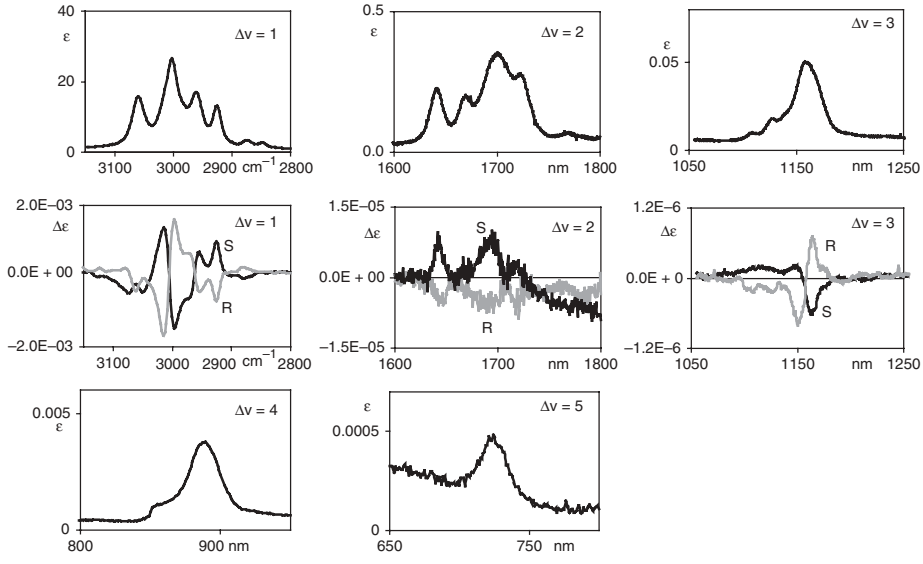

Figure 10.3. Epichlorohydrin: absorption and VCD spectra for fundamental and successive overtone regions. Absorption spectra for $\Delta v = 1$–5 (top and bottom panels) and VCD spectra for $\Delta v = 1$–3 (middle panels): black traces (*S*)-(+)-epichlorohydrin, gray traces (*R*)-(−)-epichlorohydrin. See text for experimental conditions.

the three conformers are proposed for different solvents, as deduced by mid-IR absorption spectra (thereafter confirmed by VCD data). Figure 10.5 displays the three conformers of (*S*)-epychlorohydrin, along with the adopted atom numbering: As done in reference 42, we keep the nomenclature of *cis*, *gauche* I and *gauche* II with reference to the dihedral angle formed by the C–Cl bond and the bisector of the ring. Based on the study in reference 42, we assume as population ratios *gauche* II:*gauche* I:*cis* the values 35.7%:54.6%:9.7% in the case of neat liquid, and 58.6%:34.0%:7.4% in the case of CCl_4 solution. Since a good interpretation of the recorded mid-IR spectra was obtained with B3LYP functional and 6-311G(2d,2p) basis sets, we have adopted the same DFT method also in our case to interpret the VCD of fundamental and overtone CH stretchings.

When considering the data relating to $\Delta v = 1$, we calculate transition frequencies, dipole strength, and rotational strength within the harmonic approximation; however, a frequency scaling factor (in this case we have preferred to apply a shift related to anharmonicity) is necessary. We present in Figure 10.6 the spectra calculated for the three conformers and their weighted average, assuming the population factors proposed for CCl_4 solutions. First of all, it should be noted that the calculations also predict intrinsically low intensities, both for absorption and for VCD spectra. Furthermore, we observe that the two most populated conformers *gauche* I and *gauche* II show VCD spectra that are nearly mirror images. The matching between calculated and experimental spectra is less satisfactory than that obtained for the mid-IR [42]; it is good enough, though, for a configurational assignment since the plus and minus sign pattern is reproduced. It is clear, however, that something important has not been taken into account: In particular, there can be Fermi resonances between bending overtones or combinations and CH stretching fundamentals affecting the region between 2800 and 2900 cm^{-1}. The treatment of these anharmonic interactions between bending and stretching modes and their signature in a VCD spectrum is beyond the scope of this work.

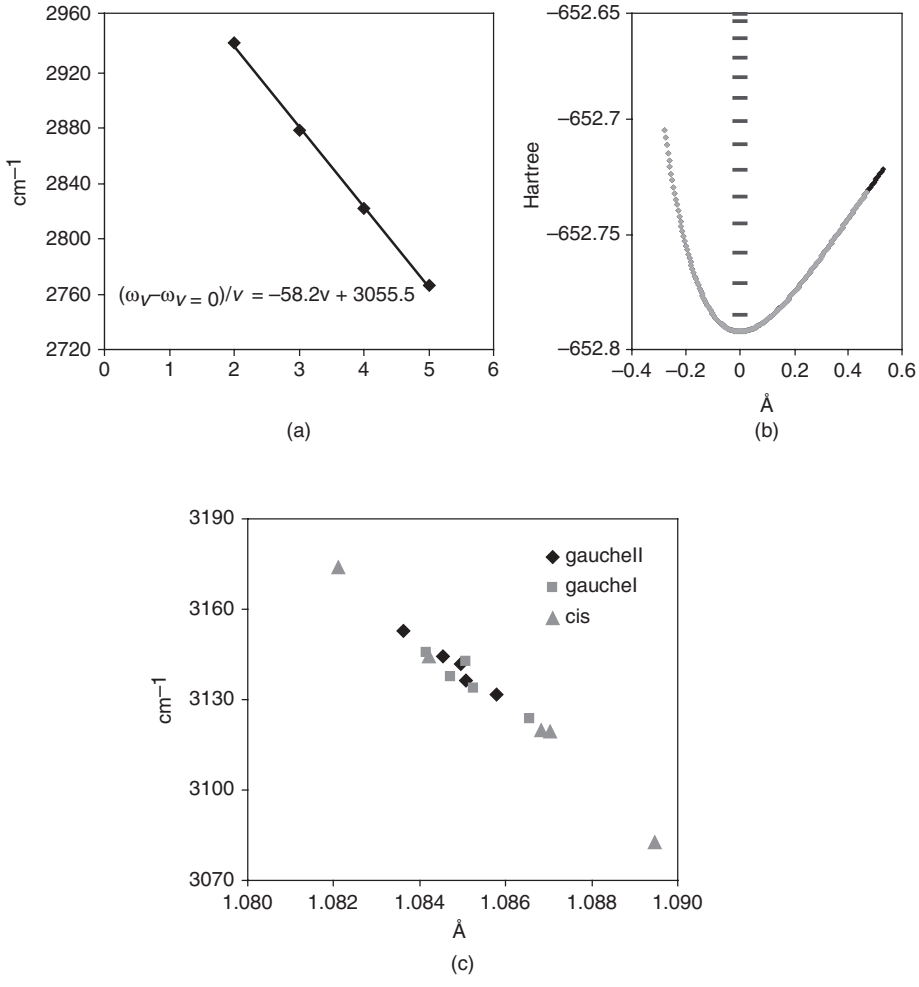

Figure 10.4. Characterization of harmonic and anharmonic mechanical parameters for epichlorohydrin CH bonds. (a) Birge–Sponer plot as deduced from the observed absorption bands in overtone spectra. (b) Example of numerically obtained energy curve for one CH stretching coordinate, with superimposed energy levels. (c) Correlation diagram between DFT calculated harmonic frequencies ω_0 and equilibrium bond lengths for all epiclorohydrin CH bonds for all conformers.

To calculate overtone spectra, we consider the molecule as a set of five CH oscillators generating five local modes: As explained in the previous section, for the case of CH stretchings, $\Delta v > 2$, this local mode scheme accounts well for the pattern observed for the absorption spectra; a higher-order approximation introducing couplings is necessary to account for possible combination bands and to gain the normal mode pattern, which on the contrary is based on coupled purely harmonic oscillators. For the set of local oscillators we have first calculated the mechanical parameters as explained in point **a**. Single-point energy calculations have been carried out to obtain the potential energy as function of each internal stretching coordinate; the harmonic frequency and the anarmonicity can be obtained from the lower derivatives [second, third, and fourth from Eq. (10.6)] of the

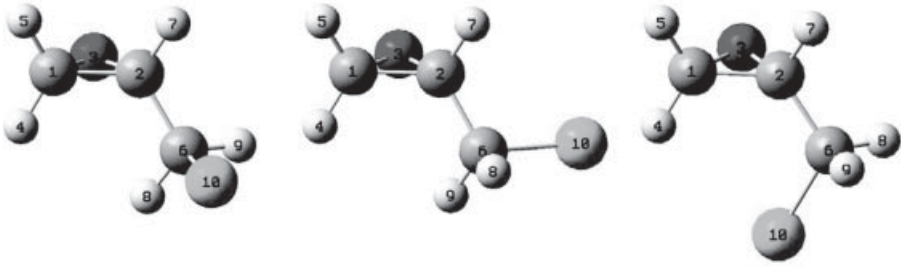

Figure 10.5. Optimized structures of the three conformers of (*S*)-(+)-epichlorohydrin with atom numbering.

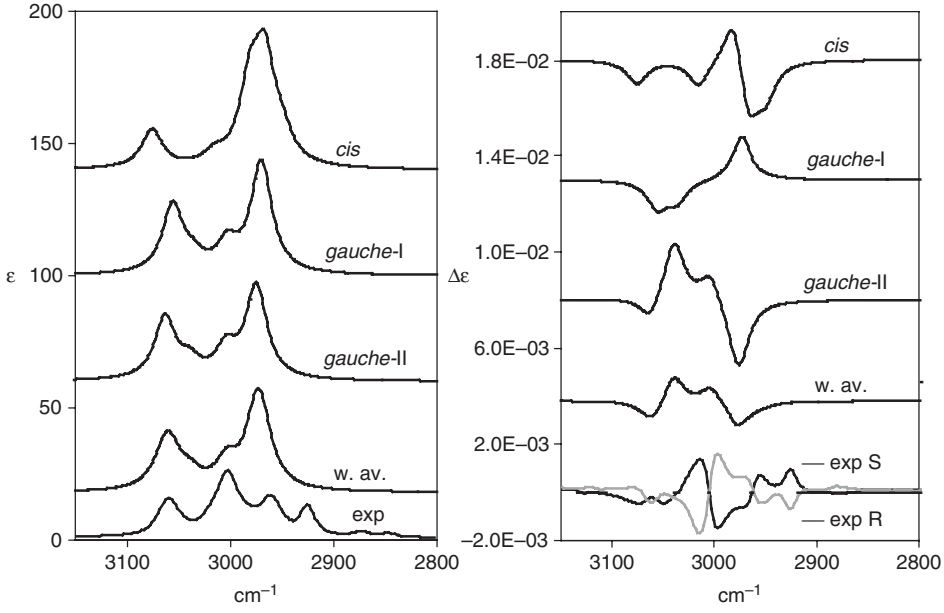

Figure 10.6. $\Delta v = 1$ experimental and calculated absorption (left) and VCD spectra (right) for epichlorohydrin. Calculations performed for (*S*)-epichlorohydrin at B3LYP/6-311G(2d,2p) level; experimental spectra for both enantiomers. Calculated frequencies in the harmonic approximation have been shifted downward by 122 cm^{-1}, consistently with the calculated average anharmonicity, full bandwidth 24 cm^{-1}; weighted average (trace labeled ''w.av.'') has been obtained as discussed in the text.

polynomial curve that best fits the calculated energy values. The χ value is quite sensitive to the uncertainties in the numerical calculations: We find that, in the fitting procedure, one needs, at least, sixth-order polynomial. The lower derivatives needed in Eq. (10.6) are stable for polynomial fittings of degrees 6–12. In our case we have considered quite a small step of 0.01 Å and an interval of about (−0.27 Å, +0.52 Å) around the equilibrium geometry since vibrations are asymmetric due to anharmonicity. An example of calculated energy curve for one of the considered CH bonds is shown in Figure 10.4B. Also, steps of 0.025 Å give comparable results. With the mechanical parameters ω_0 and χ derived from

TABLE 10.1. Calculated Mechanical and Electrical Parameters for CH Bonds of (*S*)-Epichlorohydrin in Its Three Conformers[a]

Configuration	$\mathbf{r}_0$	χ	ω_0	Π^0_{H33}	$\left(\frac{\partial \Pi_{H33}}{\partial z}\right)_0$	$\left(\frac{\partial^2 \Pi_{H33}}{\partial z^2}\right)_0$	$\sqrt{{A^0_{H13}}^2 + {A^0_{H23}}^2}$
gauche II							
4	1.0845	61.4	3144	−0.11	−0.51	−0.19	0.17
5	1.0836	61.6	3153	−0.12	−0.61	−0.21	0.11
7	1.0851	61.9	3136	−0.10	−0.57	−0.34	0.04
8	1.0850	60.7	3142	−0.05	−0.44	−0.36	0.11
9	1.0858	61.6	3132	−0.07	−0.54	−0.49	0.10
gauche I							
4	1.0847	62.1	3138	−0.12	−0.55	−0.21	0.20
5	1.0841	61.7	3145	−0.13	−0.65	−0.21	0.14
7	1.0853	61.9	3134	−0.10	−0.55	−0.33	0.06
8	1.0866	62.1	3123	−0.07	−0.52	−0.50	0.09
9	1.0851	60.8	3143	−0.05	−0.42	−0.36	0.09
cis							
4	1.0821	60.1	3174	−0.06	−0.42	−0.13	0.13
5	1.0842	62.0	3144	−0.15	−0.66	−0.20	0.09
7	1.0895	63.6	3083	−0.15	−0.68	−0.33	0.05
8	1.0868	61.7	3120	−0.07	−0.53	−0.51	0.11
9	1.0870	61.9	3119	−0.07	−0.53	−0.46	0.12

[a]Equilibrium bond length r_0 (Å), anharmonicity $\chi(\mathrm{cm}^{-1})$, mechanical Frequency $\omega_0(\mathrm{cm}^{-1})$, $\Pi^0_{\alpha 33}$ (e: electron charge), first and second derivatives (e/Å and e/Å^2), and modulus of AAT transverse component ($(ea_0)/(\hbar c)$, where a_0 is the Bohr radius, h is the reduced Planck's constant, and c is the velocity of light) (see Figure 10.5 and text).

such curves and reported in Table 10.1, we can easily calculate all transition frequencies using Eq. (10.4). We observe that all CH bonds are quite similar in all conformations, the only relevant differences being observed in the *cis* conformer for the H7 atom trans to the chlorine atom (low frequency and high anarmonicity) and for H4. It is well known [43] that the harmonic frequencies correlate nicely with the equilibrium bond lengths. NIR absorption spectroscopy has been used in cases more favorable than here (larger differences among CH bonds and higher resolution), but, just on the basis of calculations we still may appreciate from Figure 10.4C that this correlation holds.

After characterizing mechanical coefficients, we next need to calculate the electric and magnetic parameters of Eqs. (10.7) and (10.8): $\Pi^0_{\alpha i3}$ and $A^0_{\alpha i3}$ and their derivatives with respect to the internal coordinate z. Tensors of both atoms C and H for each bond need to be considered and, due to the local mode scheme, just the variation along the local coordinate z (index 3) is needed. Each atomic tensor APT and AAT is referred to the local Cartesian system assuming the z axis along the CH bond; the two perpendicular axes x and y are consequently chosen. Similar to what was previously done for evaluating anharmonicity χ, tensors are calculated for 25 steps of +0.08 Å and −0.08 Å. We present plots of the results for $\alpha = H$ in Figures 10.7A and 10.7B. All components $\Pi^0_{\alpha i3}$ and $A^0_{\alpha i3}$ are interpolated by an eighth-order polynomial. The zeroth-order term and the first and second derivatives thus obtained are used in Eqs. (10.7) and (10.8). This calculation is less problematic than that for the mechanical anharmonicity; that is, it does not show a strong dependence on the polynomial degree and on the chosen step. As expected, $\Pi^0_{\alpha 33}$ and its derivatives assume values higher than the other components,

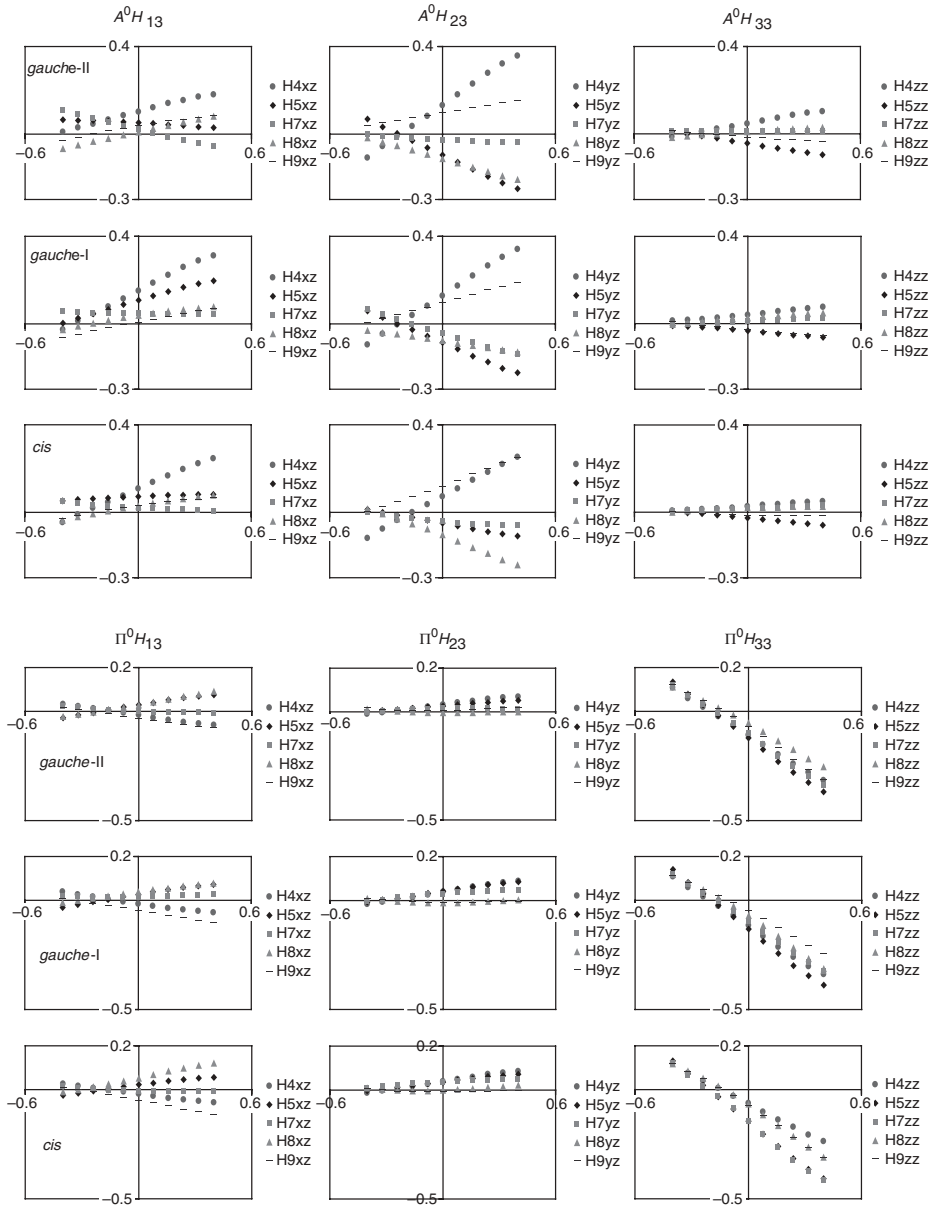

Figure 10.7. (*S*)-(+)-epichlorohydrin: Dependences of the components Π^0_{Hi3} (A) and A^0_{Hi3} (B) ($i = 1, 2, 3$) on corresponding CH bond length displacements in Å (z directions). APTs are in units of e (electron charge), and AATs are in units of $(ea_0)/(\hbar c)$, where a_0 is the Bohr radius, $\hbar$ is the reduced Planck's constant, and c is the velocity of light. Local Cartesian reference system: z axis ($i = 3$) directed from C to H along the CH bond under study; y axis ($i = 2$) in the plane HCO, pointing toward O for atoms 4, 5, and 7; in the plane HCC, pointing toward C for atoms 8 and 9.

which, however, must be taken into account to calculate rotational strenghts. Π^0_{H33} are negative for all H atoms, as it is well known in the overtone intensity literature [44]; the opposite holds for OH stretchings [31]. Since the latter values are related to the electro-optical parameters, we report in Table 10.1 just these components: all hydrogen atoms exhibit a quite similar behavior, even though a clear effect of chlorine in lowering these parameters for the nearby hydrogens is observed. Opposite to the case of APT, the most important contributions of AAT are the components xz and yz, transverse to the CH z axis. In any case, the electric dipole term is not exactly parallel to the CH bond, and the magnetic contribution is not perpendicular to the bond direction, a condition that would generate vanishing rotational strengths.

Using the calculated $\Pi^0_{\alpha i3}$ and $A^0_{\alpha i3}$ and their derivatives, and after evaluating the transition elements of Eqs. (10.7) and (10.8) on the basis of Morse oscillator eigenfunctions, we have computed dipole and rotational strength for each transition, which we report in Table 10.2. Through introduction of a Lorentzian bandshape for the transitions, with an *ad hoc* bandwith value (the same for all transitions in each overtone region), we have obtained the calculated spectra. For each conformer we show them in Figures 10.8 and 10.9 for $\Delta v = 2$ and $\Delta v = 3$, respectively; we show there the different contributions of the successive "electric" anharmonic corrections. We use the following notation: ABS0 and CD0 for the use of only the first term of Eqs. (10.7) and (10.8), that is, no tensor derivative; ABS1 and CD1 for the use of also the second term of Eqs. (10.7) and (10.8) with the first tensor derivatives; ABS2 and CD2 for the use of also the third term of the two equations, with second tensor derivatives. As expected from the trends observed for absorbtion intensities [44] and VCD signals [12] and from perturbative theory [45, 46] the successive correction terms increase in importance with quantum number v: the first corrections ABS1 and CD1 are sufficient for the first overtone region, the second order corrections have some influence for the second overtones. These facts may be appreciated also from Table 10.2. We notice that, while for absorption the perturbative terms count only for increasing intensity, for VCD the different expansion terms can generate also a change in sign of some rotational strengths. One could easily get average

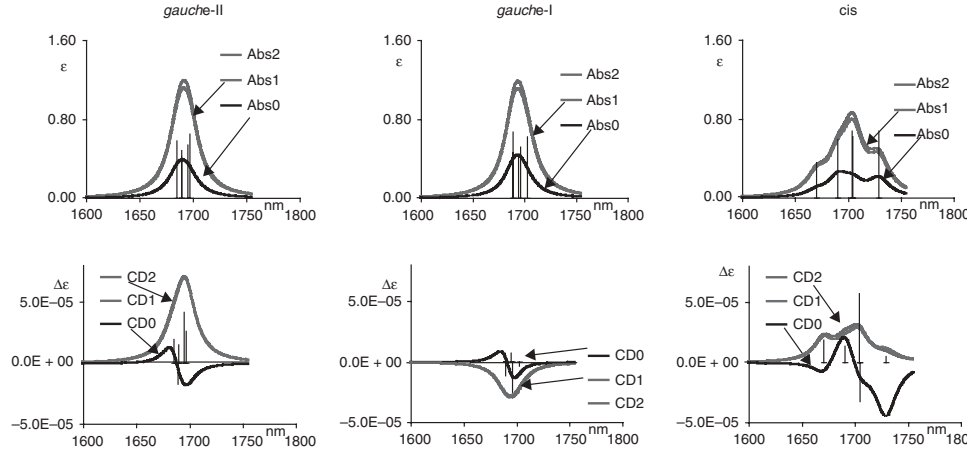

Figure 10.8. (*S*)-(+)-epichlorohydrin: $\Delta v = 2$ calculated absorption (top) and VCD spectra (bottom) for the three conformers. Contributions of the different approximations are evidenced as explained in the text. A 10-nm bandwidth was adopted.

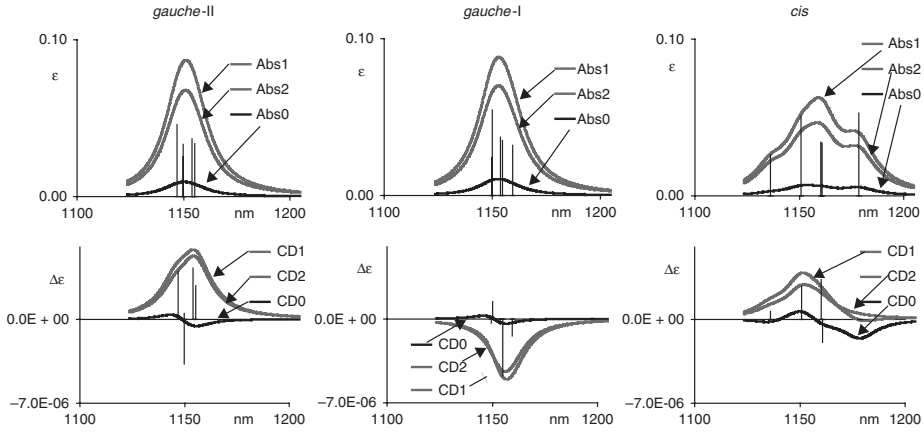

Figure 10.9. (*S*)-(+)-epichlorohydrin: $\Delta v = 3$ calculated absorption (top) and VCD spectra (bottom) for the three conformers. Contributions of the different approximations are evidenced as explained in the text. A 10-nm bandwidth was adopted.

rules for the relative signs of the successive corrections involving the z component of μ, since they depend on the sign of $< 0|(z - z_e)^n|v >$ and of $\Pi^0_{\alpha 33}$ and its derivatives, which have usually the same sign for all CHs. In fact the opposite sign of $< 0|z - z_e|v >$ and $< 0|(z - z_e)^2|v >$ [30], in conjunction with the fact that $\Pi^0_{\alpha 33}$ and $(\partial \Pi^0_{\alpha 33}/\partial z)_0$ are calculated with the same sign (Table 10.1), explains the larger decrease in intensity from the fundamental to the first overtone as compared to the decrease observed for successive overtones. On the contrary, the correct sign of the rotational strengths requires detailed calculations of all components of APT and AAT. From Figures 10.8 and 10.9 it is clear that zero-order results are not acceptable for overtones so that in general the electric anharmonic terms are crucial.

Given these calculations, we present in Figure 10.10 the comparison of experimental and calculated spectra, after due average over contribution from the three conformers, assuming the population factors proposed in reference 42. The comparison appears quite good, considering that we obtain the correct sign for $\Delta v = 2$: Due to our approximation we cannot obtain bands on the high-energy side of the spectroscopic region (1640 nm) which are most probably due to combinations, $|0, 0> \rightarrow |1, 1>$ transitions. In the case treated here, the interpretation is facilitated by the fact that the two principal conformers generate practically monosignate spectra of opposite sign: Thus combination of local modes, due to possible couplings, neglected here, would in any case conserve the sign. Also at $\Delta v = 3$, where the local mode hypothesis is more appropriate, we obtain good results. The two features of opposite sign are generated by the two principal conformers: the positive band at higher energy is due to *gauche* II, oscillator 5 (see Figure 10.5 for numbering); at lower energy, oscillator 4 brings in negative rotational strength followed by positive contributions of oscillators 7 and 9. The latter are balanced by the negative band of the conformer *gauche* I which is largely due to oscillator 7: The specific rotational strength of *gauche* I is smaller than that due to *gauche* II at the same wavelength (higher than 1150 nm), but *gauche* I has a larger population factor.

The case presented here is just an illustrative example, which we have used to analyze the role of the terms that enter in the calculations; in fact we have assumed population values derived by studies of other spectroscopic regions: However, this study provides an independent support for the existence of two main conformers in neat liquid

TABLE 10.2. Calculated Wavelengths (nm) and Dipole and Rotational Strengths (three levels of approximation) for $\Delta v = 2$ and $\Delta v = 3$ CH bond stretching transitions for (*S*)-epichlorohydrin in its Three Conformers[a]

$\Delta v = 2$ local mode #	nm	D0	D1	D2	R0	R1	R2
gauche II							
4	1689	2.2E-01	4.0E-01	4.1E-01	−1.9E-01	−7.0E-02	−7.7E-02
5	1685	2.7E-01	5.6E-01	5.8E-01	2.1E-01	7.6E-02	8.9E-02
7	1695	1.9E-01	5.0E-01	5.4E-01	−5.6E-02	2.0E-01	1.9E-01
8	1689	7.4E-02	4.5E-01	4.9E-01	5.0E-02	5.7E-02	6.9E-02
9	1697	1.1E-01	6.0E-01	6.5E-01	−3.9E-02	1.2E-01	1.2E-01
gauche I							
4	1694	2.7E-01	4.3E-01	4.5E-01	−1.4E-01	4.3E-02	3.4E-02
5	1689	3.0E-01	6.5E-01	6.7E-01	1.6E-01	−2.6E-02	−1.4E-02
7	1696	1.9E-01	4.8E-01	5.2E-01	−7.9E-02	−1.1E-01	−1.1E-01
8	1702	1.2E-01	5.7E-01	6.2E-01	2.8E-02	−1.5E-02	−1.6E-02
9	1689	8.4E-02	4.3E-01	4.6E-01	1.8E-02	−4.9E-02	−5.2E-02
cis							
4	1670	1.0E-01	3.5E-01	3.6E-01	−5.6E-02	8.3E-02	8.6E-02
5	1690	3.7E-01	5.7E-01	6.0E-01	1.6E-01	4.7E-02	6.2E-02
7	1729	3.6E-01	6.3E-01	6.8E-01	−2.2E-01	3.5E-02	2.2E-02
8	1704	1.2E-01	6.1E-01	6.8E-01	1.5E-02	2.4E-01	2.6E-01
9	1704	1.4E-01	5.7E-01	6.2E-01	−9.3E-02	−1.3E-01	−1.5E-01
$\Delta v = 3$							
gauche II							
4	1150	6.1E-03	3.9E-02	3.3E-02	−7.6E-03	−2.1E-02	−1.7E-02
5	1147	7.5E-03	5.4E-02	4.6E-02	8.5E-03	2.4E-02	1.8E-02
7	1154	5.4E-03	4.8E-02	3.7E-02	−2.3E-03	1.7E-02	1.9E-02
8	1150	2.0E-03	3.5E-02	2.6E-02	2.0E-03	3.7E-03	2.1E-03
9	1155	3.2E-03	4.9E-02	3.4E-02	−1.6E-03	1.7E-02	1.3E-02
gauche I							
4	1154	7.6E-03	4.4E-02	3.7E-02	−5.6E-03	−4.8E-03	−2.3E-03
5	1150	8.4E-03	6.2E-02	5.4E-02	6.5E-03	1.0E-02	6.5E-03
7	1155	5.3E-03	4.6E-02	3.5E-02	−3.2E-03	−2.3E-02	−2.2E-02
8	1159	3.4E-03	4.7E-02	3.2E-02	1.1E-03	−1.1E-02	−6.6E-03
9	1150	2.3E-03	3.3E-02	2.4E-02	7.1E-04	6.9E-05	−1.8E-03
cis							
4	1136	2.7E-03	3.0E-02	2.6E-02	−2.2E-03	4.5E-03	3.0E-03
5	1151	1.0E-02	5.9E-02	5.1E-02	6.7E-03	1.8E-02	1.2E-02
7	1178	1.0E-02	6.6E-02	5.3E-02	−9.4E-03	−4.0E-03	−1.3E-05
8	1160	3.4E-03	5.0E-02	3.4E-02	6.1E-04	1.7E-02	1.5E-02
9	1161	3.8E-03	4.8E-02	3.4E-02	−3.8E-03	−1.0E-02	−8.8E-03

[a] D0 and R0 were obtained with only the first term of Eqs. (10.7) and (10.8), D1 and R1 were obtained using also the second term of Eqs. (10.7) and (10.8), and D2 and R2 were obtained using the complete expressions of the two equations. Units for dipole strengths are 10^{-40} esu^{2}cm^2, and units for rotational strengths are 10^{-44} esu^{2}cm^2.

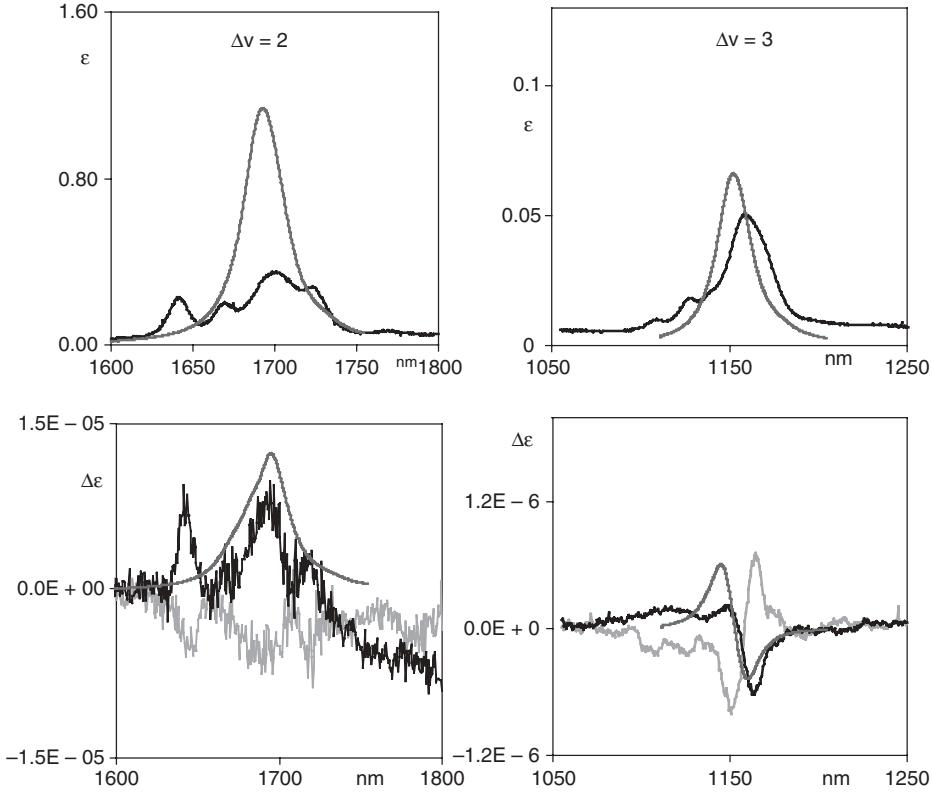

Figure 10.10. Comparison of $\Delta v = 2$ (left) and $\Delta v = 3$ (right) experimental absorption and VCD spectra of (*S*)- and (*R*)-epichlorohydrin (black and gray respectively) with the calculated spectra for (*S*)-epichlorohydrin. Population factors are used from reference 42.

epichlorohydrin, as was evaluated earlier by Wang and Polavarapu [42]. Next we will describe other situations in which NIR-VCD provides precious physical insight in other molecular systems.

10.4. PERSPECTIVES AND CONCLUSIONS

In this conclusive paragraph we examine first what is possible to investigate by NIR-VCD and what kind of information one may get from NIR-VCD spectra, and we then indicate what is needed in order to make NIR-VCD to advance. In thinking of possible applications of NIR-VCD, one should remember that nonlinear phenomena enter into several aspects of NIR-VCD spectra. Not all anharmonic phenomena are fully under control, as we shall see later. However, two types of problems can be considered at a satisfactory point on both theory and experimentation with respect to what has been expounded above, and we start this conclusive chapter just from them.

(a) Exploiting the* Δν = 2 *OH-Stretching Region, for Truly Local Mode Problems. As presented in reference 31, recording the $\Delta v = 2$ NIR-VCD and NIR absorption spectra of dilute 0.1 M solutions of (1*R*)- and (1*S*)-borneol and applying the

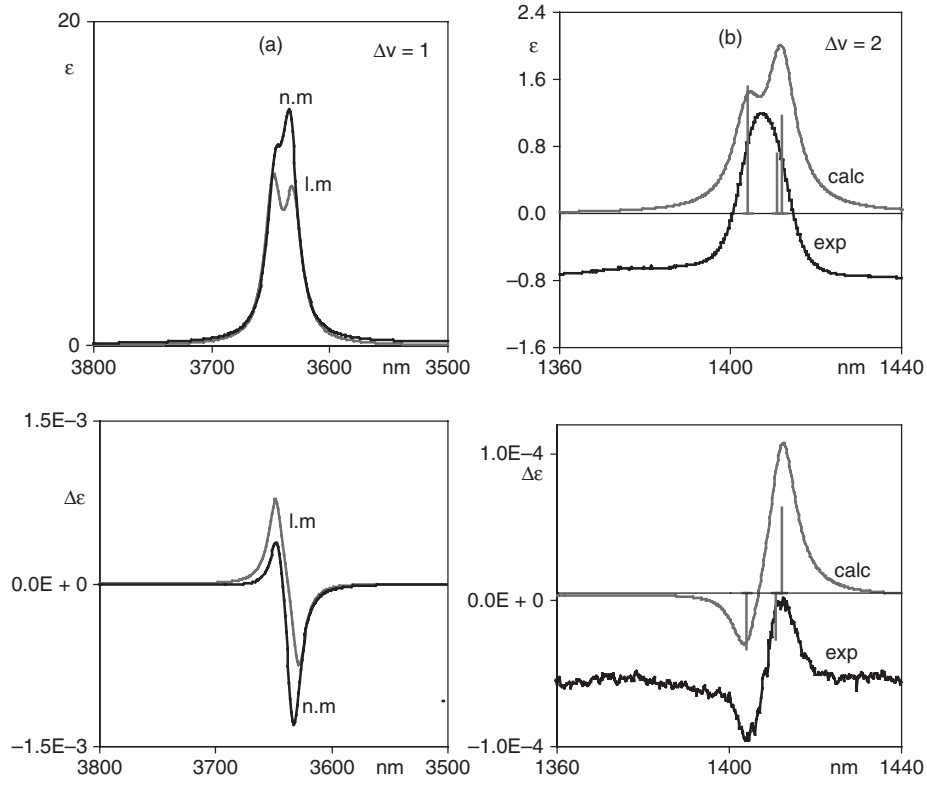

Figure 10.11. (a) Calculated spectra for (1*S*)-(+)-*endo*-borneol in the fundamental OH stretching region: full normal modes calculation as obtained by Gaussian03 (n.m), with a frequency shift of 176 cm^{-1} accounting for anharmonicity (black); isolated local OH stretching characterized as explained in Section 10.2 (l.m). (b) Comparison of experimental (black) and calculated (gray) spectra of (1*S*)-(+)-*endo*-borneol at the $\Delta v = 2$ OH stretching region. Bars indicating dipole or rotational strengths at calculated frequencies are reported in arbitrary units. Experiments conducted on 0.06 M/CCl_4 solution in a 5-cm pathlength cell. In both cases, calculated spectra are obtained from averages with statistical weights based on ΔG. B3LYP functional and 6-31G** basis set were used.

theory of Section 10.2.2 allowed us to "detect" and characterize with good confidence the conformational states of the single and isolated OH bond. This is similar to what was reported for epichlorohydryn in Section 10.3, where different conformers have been associated to bands of opposite sign. We reproduce from reference 31 the comparison of calculations and experiments in Figure 10.11b. The theoretical approach of Section 10.2.2, adopted in reference 31, is quite appropriate in this case, since the main assumption of the theory, namely the uncoupled local mode hypothesis, is intrinsic to the system. Indeed borneol has just one OH oscillator, with ω_0 and χ values quite different from those of the CH bonds in the same molecule [30, 31]; this prevents interaction among the CH and OH oscillators. Besides, for $\Delta v = 2$ the difference in frequency between local modes is larger than that for $\Delta v = 1$ [see Eq. (10.4) of Section 10.2.2)], and this increases the resolution of the signals associated with different conformational states of the OH bond in the overtone with respect to the fundamental region. Moreover, we notice that the predicted VCD spectrum of the fundamental $\Delta v = 1$ OH-stretching exhibits a

couplet of low intensity and in reverse order with respect to the first overtone (see Figure 10.11a).

Considering intermolecular hydrogen bonding phenomena, we may expect that the $\Delta v = 2$ OH stretching signals be spread out on a twice wider spectroscopic region than that for $\Delta v = 1$; this has the consequence that intramolecular hydrogen bonding phenomena be easier to study by NIR-VCD $\Delta v = 2$ spectroscopy. We think that this kind of expectation motivated the very early studies by Sugeta and co-workers [47] on $\Delta v = 2$ NIR VCD spectra of alcohols, esters, and amines. On the basis of what we have just reported, we may expect some indication on internal hydrogen bonds from the $\Delta v = 2$ NIR-VCD spectra. An example is provided in Figure 10.12 with the NIR-VCD spectra of 2,2,2-trifluorophenylethanol, where we tentatively assign the intense negative band for the (*R*)-species to the OH stretching in the conformational state where the OH is pointing toward the CF_3 group. All of this is quite important, since the OH or NH/CF_3 interaction is under investigation nowadays [48]. Calculations are underway to support our assignment.

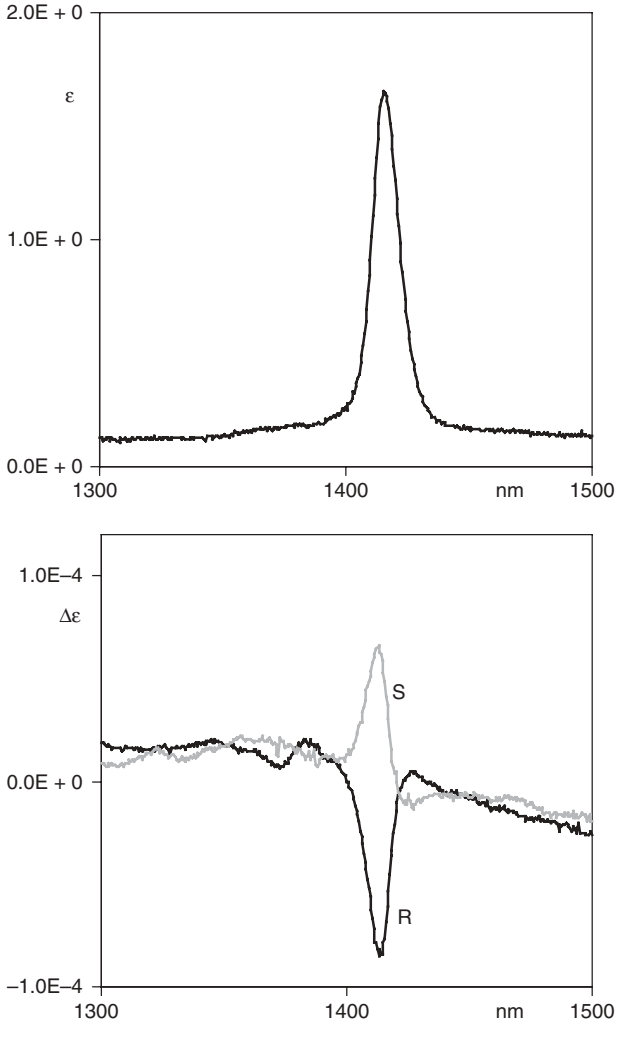

Figure 10.12. Experimental absorption and VCD spectra of both enantiomers of 2,2,2-trifluorophenylethanol in the $\Delta v = 2$ OH stretching region; 0.13 M/CCl_4 solution, 2-cm pathlength.

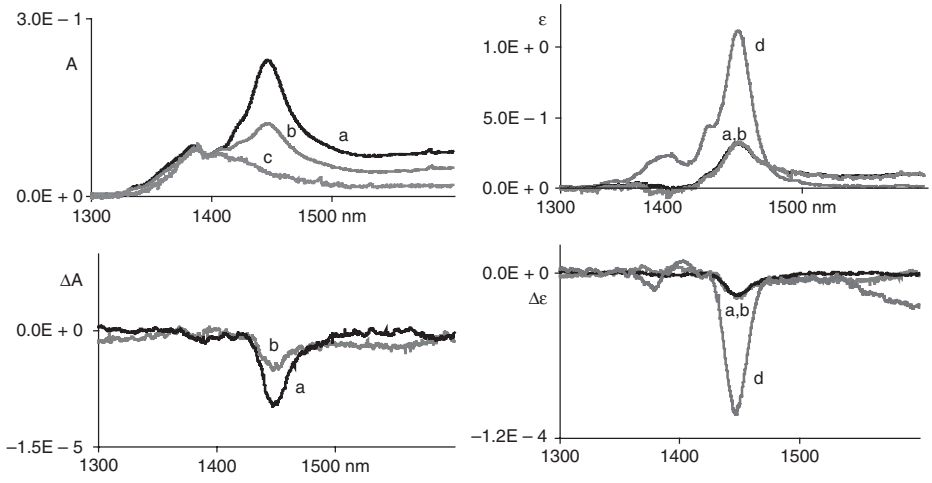

Figure 10.13. Experimental absorption (top) and VCD spectra (bottom) of D-dimethyltartrate (DDT) in CCl_4 in the presence of AOT, for the first overtone OH stretching region. Left panels: (a) DDT/AOT/CCl_4 ([AOT] = 0.158 M; $R = 2$), (b) DDT/AOT/CCl_4 ([AOT] = 0.158 M; $R = 0.7$), (c) AOT/CCl_4 ([AOT] = 0.158 M); 2-cm pathlength. Right panels: (a, b) DDT/AOT/CCl_4: superimposed spectra at two different concentrations, AOT absorption subtracted; (d) DDT/CCl_4 0.04M solution absorption and VCD spectra.

Another, similar example of the use of the OH overtone NIR-VCD spectroscopy is provided in Figure 10.13, where we present on the left the superposition of the NIR and NIR-VCD spectra of D-dimethyltartrate (DDT) in the presence of AOT (sodium-ethyl-bis-octyl-succinate) surfactant molecule in CCl_4 in two different ratios $R = [DDT]/[AOT]$. AOT is known to aggregate in the form of reverse micelles in the presence of apolar solvents and provides a means to solubilize larger tartrate quantities [49]. In this spectroscopic region we observe also absorption due to AOT (combination bands corresponding to one quantum CH stretching and one bending) which does not, however, interfere with the DDT NIR-VCD signals. On the right, after subtraction of AOT absorption, we observe how for the two R ratios one has superimposable ε and $\Delta\varepsilon$ spectra; we compare them to the corresponding spectra for a 0.04 M solution of DDT in CCl_4. We may assume the 0.04 M solution to be representative or close to what happens for the isolated molecule. On the contrary, in the presence of AOT, DDT molecules form intermolecular hydrogen bonds with themselves and with AOT; we surmise that in the latter case the DDT molecules are not associated to the surfactant molecules. From the literature it is known that association through intermolecular H bonds increases OH stretching fundamental absorption intensity, while it decreases intensity at the first overtone [50, 51].

(b) Exploiting the CH Stretching Regions for $\Delta v \geq 3$ for Qualitative Characterization of Different Types of CH Bonds. It is well known that aromatic CH bonds and aliphatic CH bonds have quite distinct IR fundamental frequencies and intensities [44]: The aromatic ω_0 is higher than the aliphatic ω_0, and the aromatic intensities are much weaker than the aliphatic ones. The NIR absorption spectra provide a different perspective, since the NIR aromatic intensities are comparable to the NIR

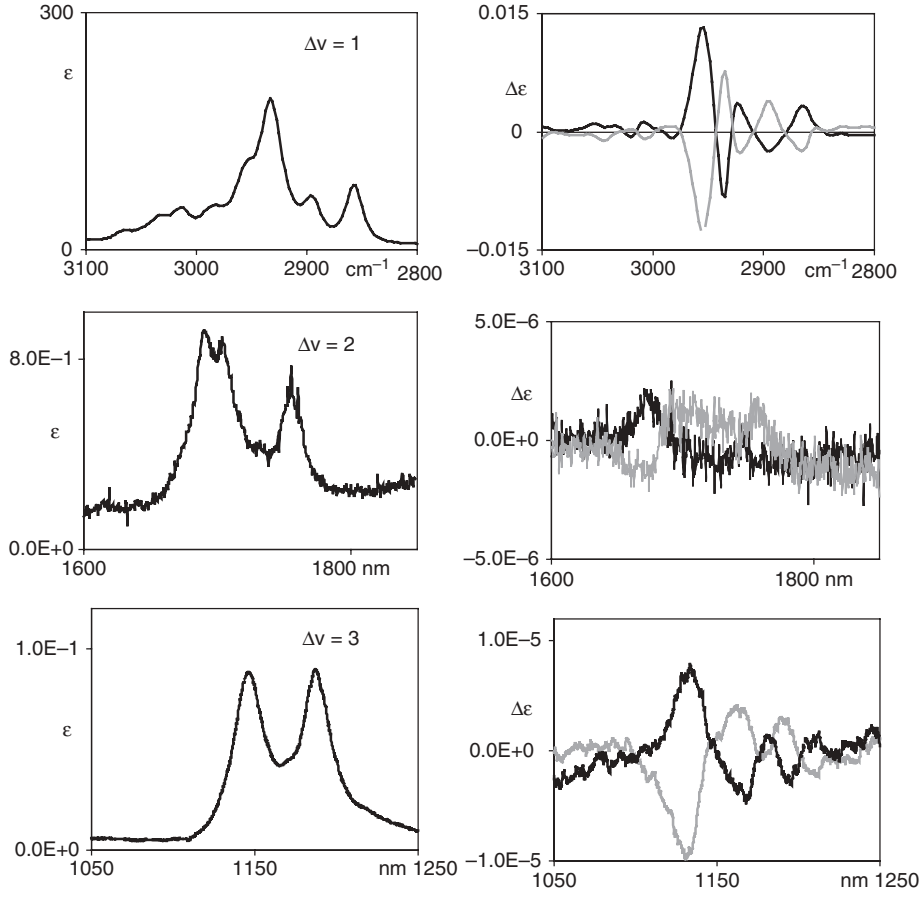

Figure 10.14. Experimental absorption and VCD spectra in the fundamental and overtone CH stretching regions $\Delta v = 2$, 3 for 4-methoxy-d_3-carbonyl[2.2] paracyclophane (0.5 M/$CDCl_3$ solutions; 100 μm, 0.5 cm, and 2 cm cells, respectively). Black trace (*R*)- and gray trace (*S*)-4-methoxy-d_3-carbonyl[2.2]paracyclophane.

aliphatic intensities [44]. This is dramatically seen when the two types of oscillators, aromatic and aliphatic, are co-present as in the 4-$COOCD_3$-[2.2]-paracyclophane case [52]. We provide in Figure 10.14 the succession of $\Delta v = 1$ to $\Delta v = 3$ spectra of 4-$COOCD_3$-[2.2]-paracyclophane in CCl_4 and the succession of $\Delta v = 1, \Delta v = 2$, and $\Delta v = 3$ NIR VCD spectra of (*R*)-and (*S*)-4-$COOCD_3$-[2.2]-paracyclophane. Not only do the aromatic overtones have comparable NIR absorption spectra as the aliphatic ones, but they have even larger NIR-VCD spectra at $\Delta v = 3$ (and possibly at $\Delta v = 2$, where the signal is quite noisy since in that region the detector is less efficient). In reference 52 a semiquantitative explanation was provided in terms of the $\left(\frac{\partial \Pi_{H33}}{\partial z}\right)_0 = \left(\frac{\partial^2 \mu}{\partial z^2}\right)_0$ parameter, on the basis of the local mode hypothesis for the CH stretching vibrations (see Figure 10.15). In that paper it was also noticed that the correct sign of the NIR-VCD spectrum could be obtained only by introducing electrical anharmonicity. The calculated rotational strengths, compared to experimental values, are weak due to the approximations adopted: (1) Just two different values for $(\partial \mu / \partial z)_0$ and two for $(\partial^2 \mu / \partial z^2)_0$ were proposed to represent on the average aromatic and aliphatic CHs, and (2) no magnetic anharmonicity correction

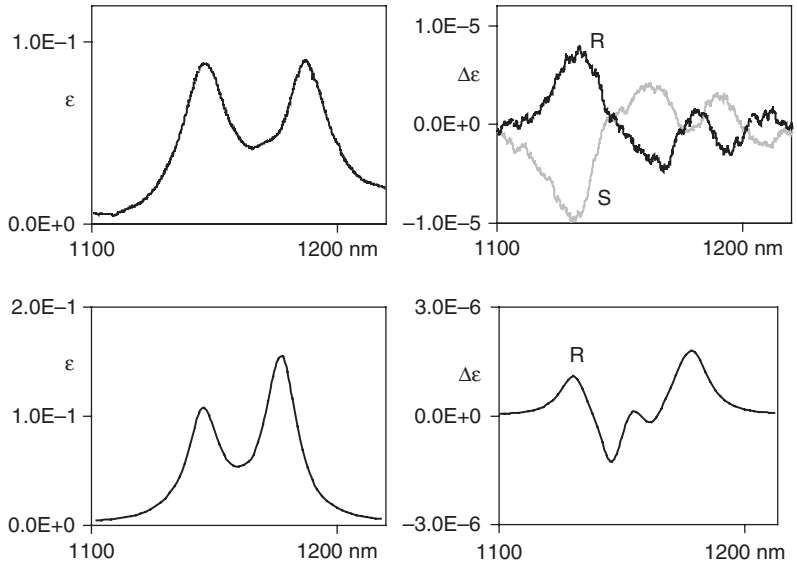

Figure 10.15. Comparison of calculated NIR-VCD spectra for $\Delta v = 3$ of (*R*)-4-methoxy-d_3-carbonyl[2.2]paracyclophane with the corresponding experimental data for both enantiomers. Absorption and rotational strengths have been evaluated as explained in the text (see also reference 52).

was taken into account as the magnetic contribution was obtained just from calculations of the fundamental region, with due correction factor deduced from the dependence of transition moments $\langle 0|z - z_e|v\rangle$ and $\langle v|p|0\rangle$ on quantum number v.

In the same line of reasoning, following the theory of Section 10.2.2 with both electric and magnetic anharmonic corrections of Eqs. (10.7) and (10.8), it was shown for camphorquinone in reference 30 that the CH bond in position 4, close to the C=O bond in position 3, has a special nonlinear electrical and mechanical behavior, giving rise to an intense and isolated NIR-VCD band.

(c) Future Directions in Instrumentation and Measurements. The instrument used in our laboratory (Figure 10.2) is somewhat limited because the light source has very low power (20 W); the monochromator has a low reciprocal linear dispersion (∼15 nm/mm) and uses only fixed (even if interchangeable) 300-μm slits, and the working wavelength range of the quartz PEM itself is limited to 2.0 μm. Progress in these aspects is easily possible and will be pursued. We also point out that FTIR-based NIR-VCD measurements are pursued by Nafie and co-workers [53], especially in the region 4000–6000 cm^{-1}. Quite recently they have been able to characterize the NH overtone stretchings bands and the NH stretching C=O stretching combination bands for peptides and proteins. This is an exciting success that opens the door to important applications.

(d) Future Directions in Calculations/Theory. The derivation of the anharmonicity constant χ illustrated in Sections 10.2 and 10.3, while giving pretty accurate predictions of the NIR absorption and NIR VCD bands, is time-consuming. It involves studying molecular properties for large numbers of geometries, corresponding to stretching XH bonds off-equilibrium for at least 10 positions. We are currently exploring

alternative methods [54], possibly less accurate but more efficient, especially in view of the fact that it will be necessary to consider stretching simultaneously more than one XH bond, when relaxing the pure local mode hypothesis. This last remark takes us to the direction that we wish to explore, which, as a matter of fact, constitutes the very early motivation of our research in this area [12]: the normal mode/local mode transition. The two vibrational regimes are simultaneously accounted for with coupled anharmonic oscillator models as illustrated in the literature as well as with anharmonically perturbed harmonic normal modes [29, 46, 55, 56]. After defining multidimensional mechanical and electrical anharmonic constants—that is, after calculating cross anharmonic force constants and after calculating the APT and AAT dependence on more than one $(z - z_e)$ XH stretching coordinate—a perturbative treatment needs to be conducted. One can follow a second-order perturbative treatment taking into account effective intramanifold couplings [29, 55, 56] or a Van Vleck perturbation treatment based on S matrices [14, 15, 32, 57]. We applied the latter method in references 16 and 45 for model systems, without the *ab initio* determination of electrical and mechanical quantities. We expect to gain much insight from this approach, especially for understanding the $\Delta v = 2$ region. The latter region is transitional from normal to local modes and does not require, on the experimental side, the large amounts of samples needed at higher Δv. Also, for this reason we think that progress in this area could attract more people to explore NIR VCD.

Of course the above steps are not at all exhaustive to make the experiments and theory better. Other studies are also necessary, but we defer them to a more distant future: On theoretical grounds, calculating higher-order terms in the electrical anharmonicity constants [see Eqs. (10.7) and (10.8)] to study the $\Delta v \geq 4$ NIR-VCD spectra and, related to this, worrying about the influence of non-Born–Oppenheimer effects, as expounded in reference 2, are needed; relaxing the separation of bending/deformation and XH stretching modes could enlighten the role of large-amplitude motions in highly excited states. In the experimental direction, the use of alternate sources, like lasers, could allow one to study less abundant samples or in vapor phase. Finally, measurements should also regard the NH stretching overtone regions, which are important for proteins and peptides, as done for example in reference 53 and the CH stretching overtone regions of heterocyclic molecules as model systems for the nucleic acid bases.

REFERENCES

1. T. A. Keiderling, P. J. Stephens, *Chem. Phys. Lett*. **1976**, *41*, 46–48.
2. S. Abbate, E. Castiglioni, F. Gangemi, R. Gangemi, G. Longhi, *Chirality* **2009**, *21*, S242–S252.
3. (a) P. Salvadori, C. Rosini, C. Bertucci, *J. Am. Chem. Soc*. **1984**, *106*, 2439–2440. (b) X. Peng, N. Komatzu, S. Battacharya, T. Shinawaki, S. Aonouma, T. Kimura, A. Osuka, *Nature Nanotechnol*. **2002**, *2*, 361–365.
4. L. J. F. Hermans, "Blue Skies, blue seas", *Eur. Phys. J*. **2006**, *37*, 16–16.
5. H. W. Siesler, Y. Ozaki, S. Kawata, Editors *Near Infrared Spectroscopy. Principles, Instruments, Applications*, Wiley-VCH, Weinheim, **2002**.
6. E. B. Wilson, Jr., J. C. Decius, P. C. Cross, *Molecular Vibrations*, McGraw-Hill, New York, **1955**.
7. G. Herzberg, *Molecular Spectra and Molecular Structure, I. Spectra of Diatomic Molecules*, 2nd ed., Van Nostrand Reinhold, New York, **1950**.
8. M. S. Child, L. Halonen, *Adv. Chem. Phys*. **1985**, *57*, 1–58.

9. B. R. Henry, *Acc. Chem. Rev*. **1987**, *20*, 429–435.
10. S. Abbate, G. Longhi, J. W. Givens, S. Boiadjiev, D. A. Lightner, A. Moscowitz, *Appl. Spectrosc*. **1996**, *50*, 642–643.
11. C. Guo, R. D. Shah, R. K. Dukor, T. B. Freedman, X. Cao, L. A. Nafie,. *Vibr. Spectrosc*. **2006**, *42*, 254–272.
12. S. Abbate, G. Longhi, L. Ricard, C. Bertucci, C. Rosini, P. Salvadori, A. Moscowitz, *J. Am. Chem. Soc*. **1989**, *111*, 836–840.
13. J. A. Schellman, *Chem. Rev*. **1975**, *75*, 323–331.
14. T. R. Faulkner, C. Marcott, A. Moscowitz, J. Overend, *J. Am. Chem. Soc*. **1977**, *99*, 8160–8168.
15. P. L. Polavarapu, *Mol. Phys.* **1996**, *89*, 1503–1510.
16. S. Abbate, G. Longhi, C. Santina, *Chirality* **2000**, *12*, 180–190.
17. E. Castiglioni, F. Lebon, G. Longhi, S. Abbate, *Enantiomer* **2002**, *7*, 161–173.
18. G. Longhi R. Gangemi, F. Lebon, E. Castiglioni, S. Abbate, V. M. Pultz, D. A. Lightner, *J. Phys. Chem. A* **2004**, *108*, 5338–5352.
19. I. Chabay, E. C. Hsu, G. Holzwarth, *Chem. Phys. Lett*. **1972**, *15*, 211–214.
20. I. Chabay, Infrared Circular Dichroism Measurements, Ph.D. thesis, University of Chicago, **1972**.
21. L. Rosenfeld, *ZS Phys*. **1928–29**, *52*, 161–174.
22. GAUSSIAN 09, M. J. Frisch, G. W. Trucks, H. B. Schlegel, G. E. Scuseria, M. A. Robb, J. R. Cheeseman, J. A. Montgomery, Jr., T. Vreven, K. N. Kudin, J. C. Burant, J. M. Millam, S. S. Iyengar, J. Tomasi, V. Barone, B. Mennucci, M. Cossi, G. Scalmani, N. Rega, G. A. Petersson, H. Nakatsuji, M. Hada, M. Ehara, K. Toyota, R. Fukuda, J. Hasegawa, M. Ishida, T. Nakajima, Y. Honda, O. Kitao, H. Nakai, M. Klene, X. Li, J. E. Knox, H. P. Hratchian, J. B. Cross, V. Bakken, C. Adamo, J. Jaramillo, R. Gomperts, R. E. Stratmann, O. Yazyev, A. J. Austin, R. Cammi, C. Pomelli, J. W. Ochterski, P. Y. Ayala, K. Morokuma, G. A. Voth, P. Salvador, J. J. Dannenberg, V. G. Zakrzewski, S. Dapprich, A. D. Daniels, M. C. Strain, O. Farkas, D. K. Malick, A. D. Rabuck, K. Raghavachari, J. B. Foresman, J. V. Ortiz, Q. Cui, A. G. Baboul, S. Clifford, J. Cioslowski, B. B. Stefanov, G. Liu, A. Liashenko, P. Piskorz, I. Komaromi, R. L. Martin, D. J. Fox, T. Keith, M. A. Al-Laham, C. Y. Peng, A. Nanayakkara, M. Challacombe, P. M. W. Gill, B. Johnson, W. Chen, M. W. Wong, C. Gonzalez, J. A. Pople, Gaussian Inc., Pittsburgh, **2009**.
23. P. J. Stephens, *J. Phys. Chem*. **1985**, *89*, 748–750.
24. (a) R. L. Swofford, M. S. Burberry, J. A. Morrell, A. C. Albrecht, *J. Chem. Phys*. **1977**, *66*, 5245–5246. (b) M. S. Burberry, A. C. Albrecht, *J. Chem. Phys*. **1979**, *71*, 4631–4640. (c) M. S. Burberry, A. C. Albrecht, *J. Chem. Phys*. **1979**, *70*, 147–152.
25. (a) G. A. Bethardy, X. Wang, D. S. Perry, *Can. J. Chem*. **1994**, *92*, 652–659. (b) E. L. Sibert III, W. P. Reinhardt, J. T. Hynes, *J. Chem. Phys*. **1984**, *81*, 1115–1134.
26. K. K. Lehman, *J. Chem. Phys*. **1983**, *79*, 1098–1099.
27. I. M. Mills, A. G. Robiette, *Mol. Phys*. **1985**, *56*, 743–765.
28. E. L. Sibert III, *J. Chem. Phys*. **1988**, *88*, 4378–4390.
29. L. Halonen, *Adv. Chem. Phys*. **1998**, *104*, 41–179.
30. F. Gangemi, R. Gangemi, G. Longhi, S. Abbate, *Vibr. Spectrosc*. **2009**, *50*, 257–267.
31. F. Gangemi, R. Gangemi, G. Longhi, S. Abbate, *Phys. Chem. Chem. Phys*. **2009**, *11*, 2683–2689.
32. K. L. Bak, O. Bludskỳ, P. Jørgensen, *J. Chem. Phys*. **1995**, *103*, 10548–10555.
33. P. J. Stephens, F. J. Devlin, J. J. Pan, *Chirality* **2008**, *20*, 643–663.
34. (a) P. M. Morse, *Phys. Rev*. **1929**, *34*, 57–64; (b) D. Ter Haar, *Phys. Rev*. **1946**, *70*, 222–223.
35. D. A. Howard, P. Jørgensen, H. G. Kjaergaard, *J. Am. Chem. Soc*. **2005**. *127*, 17096–17103.

36. ADF: Amsterdam Density Functional program. Theoretical Chemistry, Vrjie Universiteit, Amsterdam. URL: http://www.scm.com V. P. Nicu, J. Neugebauer, S. K. Wolf, E. J. Baerends, *Theor. Chem. Acc*. **2008**, *119*, 245–263.
37. GAMESS: General Atomic and Molecular Electronic Structure System, M. Dupuis, D. Spangler, J. J. Wendoloski, NRCC, Software Catalog, University of California, Berkeley, **1980**.
38. TURBOMOLE: V6.3 2011, A development of University of Karlsruhe and Forschungszentrum Karlsruhe GmbH, 1989–2007, TURBOMOLE GmbH, since 2007; available from http://www.turbomole.com.
39. DALTON: A molecular electronic structure program, Hans Ågren et al. Release Dalton, **2011**, see http://daltonprogram.org/
40. S. Abbate, G. Longhi, K. Kwon, A. Moscowitz, *J. Chem. Phys*. **1998**, *108*, 50–62.
41. K. V. Reddy, D. F. Heller, M. J. Berry, *J. Chem. Phys*. **1982**, *76*, 2814–2837.
42. F. Wang, P. L. Polavarapu, *J. Chem.Phys. A* **2000**, *104*, 6189–6196.
43. K. M. Gough, B. R. Henry, *J. Phys. Chem*. **1984**, *88*, 1298–1302.
44. G. Longhi, L. Ricard, S. Abbate, G. Zerbi, *J. Chem. Phys*. **1988**, *88*, 6733–6742.
45. (a) S. Abbate, R. Gangemi, G. Longhi, *J. Chem. Phys*. **2002**, *117*, 7575–7586. (b) R. Gangemi, G. Longhi, S. Abbate, *Chirality* **2005**, *17*, 530–539.
46. (a) I. Scheck, J. Jortner, M. L. Sage, *Chem. Phys. Lett*. **1979**, *64*, 209. (b) M. L. Sage, J. Jortner, *Adv. Chem. Phys*. **1981**, part I, 293–322.
47. Y. Nakao, H. Sugeta, Y. Kyogoku, *Chem. Lett*. **1984**, 623–626.
48. F. Hof, D. M. Scofield, W. B. Schweizer, F. Diederich, *Angew. Chem. Intl. Ed*., **2004**, *43*, 5056–5059.
49. S. Abbate, G. Longhi, A. Ruggirello, V. Turco Liveri, *Coll. Surf. A Physicochem. Eng. Aspects* **2008**, *327*, 44–54.
50. C. Sandorfy, *J. Mol. Struct*. **2002**, *614*, 365–366.
51. Z. Rong, H. G. Kjaergaard, *J. Phys. Chem. A* **2002**, *106*, 6242–6253.
52. S. Abbate, E. Castiglioni, F. Gangemi, R. Gangemi, G. Longhi, R. Ruzziconi, S. Spizzichino, *J. Phys. Chem. A* **2007**, *111*, 7031–7040.
53. S. Ma, T. B. Freedman, R. K. Dukor, L. A. Nafie, *Appl. Spectrosc*. **2010**, *64*, 615–626.
54. C. Y. Lim, A. T. Gilbert, P. M. W. Gill, *Theor. Chem. Acc*. **2008**, *120*, 23–35.
55. H. G. Kjaergaard, B. R. Henry, *J. Chem. Phys*. **1991**, *96*, 4841–4851.
56. E. L. Sibert III, *J. Chem. Phys*. **1988**, *88*, 4378–4390.
57. G. Amat, H. H. Nielsen, G. Tarrago, *Rotation-Vibration of Polyatomic Molecules*, Marcel Dekker, NY, **1971**.

11

OPTICAL ROTATION AND INTRINSIC OPTICAL ACTIVITY

Patrick H. Vaccaro

11.1. INTRODUCTION

In the transparent region of the spectrum, natural optical activity commonly manifests itself as a rotation in the plane of polarization for electromagnetic radiation passing through an isotropic ensemble of enantiomerically enriched chiral molecules [1, 2]. The resulting "optical rotation" represents the progenitor of all chiroptical phenomena, having first been discovered by Arago [3] in 1811 during investigations of crystalline quartz and subsequently elaborated by Biot [4, 5] in seminal studies performed on solids, liquids, and gases. Reduced to most basic terms, this effect arises from the action of an intrinsic (optical) anisotropy known as circular birefringence, whereby the index of refraction in a chiral medium differs slightly for the two helical "directions" of light polarization. The characteristic dependence of optical rotation on incident wavelength, sample concentration, and other experimental variables was recognized from the onset and exploited extensively as an analytical tool [6]; however, the precise relationship of such physical measurements to underlying molecular structure took a substantially longer time to mature. Indeed, as highlighted by recent reviews [7–13], much of the current interest in chiroptical spectroscopy stems from the emergence of reliable computational paradigms for correlating the unique signatures of these processes to the absolute stereochemistry of targeted substrates.

Electromagnetic radiation propagating through an isotropic chiral medium experiences a complex index of refraction that differs in both the real (in-phase) and imaginary (in-quadrature) parts for the right-circular and left-circular polarization states that together

Comprehensive Chiroptical Spectroscopy, Volume 1: Instrumentation, Methodologies, and Theoretical Simulations, First Edition. Edited by N. Berova, P. L. Polavarapu, K. Nakanishi, and R. W. Woody.
© 2012 John Wiley & Sons, Inc. Published 2012 by John Wiley & Sons, Inc.

define the helicity basis [1, 2]. The resulting phenomena of circular birefringence (CB) and circular dichroism (CD) lead to observable effects in the form of dispersive rotation and absorptive elliptization for an impinging beam of plane-polarized light, which commonly are measured under conditions of nonresonant and resonant excitation, respectively. The molecules of opposite handedness that compose an enantiomeric pair long have been known to display wavelength-resolved optical activities (CB and CD) of equal magnitude yet inverse sign, thereby affording a viable means for their relative discrimination [14]. Unfortunately, the *a priori* correlation of a specific chiroptical response with an individual enantiomer still presents formidable challenges, usually requiring supplementary physical and/or chemical information to reach a definitive assignment [15, 16]. Historically, this crucial task has relied on empirical rules (e.g., chromophore-based octant/sector correlations [14] and the conformational dissymmetry relationships of Brewster [17]) or quasi-classical models (e.g., the induced polarization-anisotropy schemes proposed by Kirkwood [18] and Applequist [19]); however, recent years have witnessed the rapid development of quantum-chemical techniques designed to compute such properties from first principles [7–13]. The advent of robust *ab initio* methods for reliably predicting the frequency-dependent response evoked from a chiral molecule has led to a veritable renaissance in the applications of chiroptical spectroscopy [7, 20], with numerous experimental and theoretical endeavors highlighting the ability to determine absolute stereochemical configurations, as well as secondary structural and conformational parameters, for diverse species.

This chapter focuses on the dispersive phenomena of natural optical rotation or circular birefringence (CB) exhibited by isotropic ensembles of chiral molecules maintained under thermally equilibrated liquid-phase and vapor-phase conditions. Particular emphasis will be directed towards elucidation of the intrinsic behavior obtained in the absence of environmental perturbations, the quantitative measurement of which has been made possible by recent advances in polarimetric instrumentation. Ancillary discussion of the absorptive events arising from resonant circular dichroism (CD) will be presented, thereby affording a means for relating the provenance and manifestation of these complementary linear processes (viz., observed signals scale in direct proportion to the intensity of incident electromagnetic radiation) [21–23]. While electronic variants of chiroptical spectroscopy, as revealed by wavelength-resolved optical rotatory dispersion (ORD) and electronic circular dichroism (ECD) profiles, will be of primary concern, the need to consider nuclear motion (e.g., vibrational displacements and conformational flexibility) will be made apparent by the consequences arising from nonrigidity of the molecular framework. Indeed, the recommended protocol and *de facto* standard for stereochemical studies based upon such probes advocates the simultaneous use of multiple techniques [24], including the vibration-mediated schemes [13] of vibrational circular dichroism [10, 25] (VCD) and Raman optical activity [26] (ROA) that explicitly rely on nuclear degrees of freedom for their spectral signatures. The International System of Units [27] (*SI*) will be employed throughout the ensuing discussion; however, measurable chiroptical parameters often will be converted to their commonly accepted (albeit nonstandard) metrics.

11.2. THEORETICAL BACKGROUND

11.2.1. Notation and Conventions

The semiclassical treatment of matter–field interactions, whereby quantized molecules are acted upon by classical electromagnetic radiation, affords a convenient framework

for describing chiroptical phenomena [1, 2]. From this viewpoint, light can be decomposed into coherently oscillating electric-field, $\mathbf{E}(\mathbf{r},t)$ (in V/m), and magnetic-field, $\mathbf{B}(\mathbf{r},t)$ (in tesla or Vs/m^2), vectors that propagate through free space at a characteristic speed related to the electric permittivity (ε_0) and magnetic permeability (μ_0) of a vacuum, $c = (\varepsilon_0\mu_0)^{-1/2}$. For a monochromatic plane wave having angular frequency ω (rad/s) and angular wavevector $\mathbf{k}$ (rad/m), the spatial and temporal dependencies of these quantities can be specified by [21, 28]:

$$\mathbf{E}(\mathbf{r},t) = \mathbf{E}_\omega e^{i(\mathbf{k}\cdot\mathbf{r}-\omega t)} \Rightarrow \frac{1}{2}[\mathbf{E}_\omega e^{i(\mathbf{k}\cdot\mathbf{r}-\omega t)} + \mathbf{E}_\omega^* e^{-i(\mathbf{k}\cdot\mathbf{r}-\omega t)}], \tag{11.1}$$

$$\mathbf{B}(\mathbf{r},t) = \mathbf{B}_\omega e^{i(\mathbf{k}\cdot\mathbf{r}-\omega t)} \Rightarrow \frac{1}{2}[\mathbf{B}_\omega e^{i(\mathbf{k}\cdot\mathbf{r}-\omega t)} + \mathbf{B}_\omega^* e^{-i(\mathbf{k}\cdot\mathbf{r}-\omega t)}], \tag{11.2}$$

where the exponential representation provides a compact means for simultaneously encoding amplitude and phase information. As highlighted by the final equalities in these expressions, the transcription of complex fields into their physically meaningful counterparts implicitly assumes that only the real part is of significance. The angular wavevector points in the direction of wave propagation, with the angular wavenumber derived from its magnitude, $k = |\mathbf{k}|$ (rad/m), being related to the corresponding linear wavenumber $\tilde{\nu}$ (osc/m) and wavelength λ (m/osc) by $k = 2\pi\tilde{\nu} = 2\pi/\lambda$. Similarly, the angular frequency can be recast in terms of the linear frequency ν (osc/s) and period of oscillation T (s/osc) such that $\omega = 2\pi\nu = 2\pi/\mathrm{T}$. The spatial ($k$) and temporal ($\omega$) properties for any viable wave phenomenon must be connected through a specific dispersion relationship [29], which can be formulated as $\omega = ck$ (or $\nu = c/\lambda$) for electromagnetic radiation traversing a vacuum. In the case of a transparent (nonabsorbing) dielectric medium characterized by (pure-real) index of refraction $n(\omega)$ [30], this expression must be modified by introducing the frequency-dependent speed of light, $\upsilon = c/n(\omega)$ [where $n(\omega) = 1$ *in vacuo*].

The vector amplitude of the electric field in Eq. (11.1) can be partitioned as the product of a complex scalar amplitude (E_ω) and a vector of unit magnitude ($\vec{\boldsymbol{\varepsilon}}$) such that $\mathbf{E}_\omega = E_\omega\vec{\boldsymbol{\varepsilon}}$ [28]. In particular, $\vec{\boldsymbol{\varepsilon}}$ specifies the direction of optical polarization [31], with the arrow symbol affixed to this quantity (and others below) reinforcing its status as a unit vector. The vector amplitude for the magnetic (induction) field in Eq. (11.2) can be decomposed in a similar fashion, $\mathbf{B}_\omega = B_\omega\vec{\mathbf{b}}$, where $\vec{\mathbf{b}}$ and $\vec{\boldsymbol{\varepsilon}}$ are orthogonal to $\mathbf{k}$. Since Maxwell's Equations demand that electromagnetic radiation propagating through a transparent dielectric satisfy $\mathbf{k}\times\mathbf{E}_\omega = \omega\mathbf{B}_\omega$ where $|\mathbf{k}| = k = \omega/\upsilon$, it also follows that $\vec{\mathbf{b}}\perp\vec{\boldsymbol{\varepsilon}}$ and $B_\omega = E_\omega/\upsilon$ [29]. While the monochromatic plane wave defined by Eqs. (11.1) and (11.2) affords a convenient framework for discussing matter–field interactions, this ansatz can be extended to encompass the more realistic situation of quasi-monochromatic excitation by incorporating temporal envelope functions, $E_\omega(t)$ and $B_\omega(t)$, that vary slowly on the timescale of ω^{-1} (where ω now represents the central or carrier frequency) [21, 28].

For a monochromatic plane wave propagating along the z axis such that $\mathbf{k} = k\vec{\mathbf{e}}_z$ (where $\vec{\mathbf{e}}_z$ denotes the pertinent Cartesian unit vector), the optical polarization vector must reside in the transverse x–y plane and have the general form [28, 31]

$$\vec{\boldsymbol{\varepsilon}} = \varepsilon_x\vec{\mathbf{e}}_x + \varepsilon_y\vec{\mathbf{e}}_y, \tag{11.3}$$

with proper normalization demanding that the complex scalar quantities ε_x and ε_y satisfy $|\varepsilon_x|^2 + |\varepsilon_y|^2 = 1$. Of special importance for analyses of optical activity are the definitions

of right-circular (R) and left-circular (L) polarization [1, 31]:

$$\vec{\boldsymbol{\varepsilon}}_{R/L} = \frac{1}{\sqrt{2}}(\vec{\mathbf{e}}_x + e^{\mp\pi/2}\vec{\mathbf{e}}_y) = \frac{1}{\sqrt{2}}(\vec{\mathbf{e}}_x \mp i\vec{\mathbf{e}}_y), \tag{11.4}$$

which (following the convention used in optics as opposed to that of physics) [30, 31] represent clockwise (for R) and anticlockwise (for L) rotation of the electric field vector as viewed by an observer towards whom the wave is propagating. The two vectors of Eq. (11.4) define a helicity basis for describing all situations of pure polarization (i.e., *sans* depolarization effects [31]), with the orthogonal states of linear (or plane) polarization along the x and y axes being readily decomposed as linear combinations of their right-circular and left-circular counterparts [1, 31]:

$$\vec{\boldsymbol{\varepsilon}}_x = \frac{\sqrt{2}}{2}(\vec{\boldsymbol{\varepsilon}}_R + \vec{\boldsymbol{\varepsilon}}_L) = \vec{\mathbf{e}}_x, \qquad \vec{\boldsymbol{\varepsilon}}_y = i\frac{\sqrt{2}}{2}(\vec{\boldsymbol{\varepsilon}}_R - \vec{\boldsymbol{\varepsilon}}_L) = \vec{\mathbf{e}}_y. \tag{11.5}$$

The exponential notation introduced by Eqs. (11.1) and (11.2) proves especially useful when dealing with states of complex polarization. For example, the time derivative of the magnetic vector for a right-/left-circularly polarized monochromatic plane wave, $\dot{\mathbf{B}}^{R/L}(\mathbf{r},t) \equiv \partial\mathbf{B}^{R/L}(\mathbf{r},t)/\partial t$, readily can be shown to be proportional to the corresponding electric field vector, $\mathbf{E}^{R/L}(\mathbf{r},t)$:

$$\dot{\mathbf{B}}^{R/L}(\mathbf{r},t) = -i\omega\mathbf{B}^{R/L}(\mathbf{r},t) = -i\mathbf{k}\times\mathbf{E}^{R/L}(\mathbf{r},t) = \pm\frac{\omega}{c}\mathbf{E}^{R/L}(\mathbf{r},t). \tag{11.6}$$

Other quantities of interest for spectroscopy can be evaluated with similar ease, including the intensity of light, I (W/m^2), passing through a transparent dielectric medium [29, 30]:

$$I = \frac{1}{\mu_0}\langle\langle|\mathbf{E}(\mathbf{r},t)\times\mathbf{B}(\mathbf{r},t)|\rangle\rangle_{\mathrm{T}} = \frac{1}{2\mu_0}\mathrm{Re}[E^*(\mathbf{r},t)B(\mathbf{r},t)] = \frac{1}{2}\varepsilon_0 cn(\omega)|E_\omega|^2, \tag{11.7}$$

where $\langle\langle\cdots\rangle\rangle_{\mathrm{T}}$ denotes the temporal (or cycle) average taken over one oscillation period [28].

11.2.2. Phenomenological Description of Optical Activity

As first elaborated by Fresnel after advancing his hypothesis that light is a transverse wave phenomenon [32, 33], natural optical activity can be ascribed to the circular differential properties of matter. From this perspective, dispersive (ORD) and absorptive (ECD) chiroptical effects can be rationalized uniformly by postulating a complex, frequency-dependent index of refraction, $\tilde{n}(\omega)$, that differs slightly for left-circular and right-circular polarizations [1, 2]:

$$\tilde{n}_{R/L}(\omega) = n_{R/L}(\omega) + i\,n'_{R/L}(\omega), \tag{11.8}$$

where the real and imaginary parts (distinguished by affixing a prime to the latter) respectively govern the velocity and the amplitude of a propagating electromagnetic wave [29, 30]. Circularly polarized light passing along the z axis through a homogeneous (spatially isotropic) and steady (temporally invariant) medium characterized by

$\tilde{n}_R(\omega) \neq \tilde{n}_L(\omega)$ will display an electric field vector that depends explicitly on the initial state of helicity (R or L):

$$\mathbf{E}^{R/L}(z,t) = \mathbf{E}_{\omega}^{R/L} e^{i\left(\frac{\omega \tilde{n}_{R/L}(\omega)}{c} z - \omega t\right)} = E_{\omega} \vec{\boldsymbol{\varepsilon}}_{R/L}\, e^{-\frac{\omega n'_{R/L}(\omega)}{c} z} e^{i\left(\frac{\omega n_{R/L}(\omega)}{c} z - \omega t\right)}, \tag{11.9}$$

where the angular wavenumber has been recast as $k_{R/L} = \omega \tilde{n}_{R/L}(\omega)/c$. The chiral nature of the medium thus has been transcribed onto the properties of the traversing light, with the real part of the refractive index, $n_{R/L}(\omega)$, imparting a circular-differential phase shift (or CB) while its imaginary counterpart, $n'_{R/L}(\omega)$, introduces a circular-differential attenuation (or CD) [1, 2].

Owing to the small disparity that exists between $\tilde{n}_L(\omega)$ and $\tilde{n}_R(\omega)$, it proves convenient to introduce average [$\overline{n}(\omega)$ and $\overline{n}'(\omega)$] and differential [$\Delta n(\omega)$ and $\Delta n'(\omega)$] quantities for describing their real and imaginary parts:

$$n_{R/L}(\omega) = \overline{n}(\omega) \mp \frac{\Delta n(\omega)}{2}, \tag{11.10}$$

$$n'_{R/L}(\omega) = \overline{n}'(\omega) \mp \frac{\Delta n'(\omega)}{2}, \tag{11.11}$$

with summation and subtraction of the two helicity components yielding:

$$\overline{n}(\omega) = \frac{1}{2}[n_L(\omega) + n_R(\omega)], \qquad \overline{n}'(\omega) = \frac{1}{2}[n'_L(\omega) + n'_R(\omega)], \tag{11.12}$$

$$\Delta n(\omega) = n_L(\omega) - n_R(\omega), \qquad \Delta n'(\omega) = n'_L(\omega) - n'_R(\omega). \tag{11.13}$$

For the transparent region of the spectrum, where the frequency of impinging electromagnetic radiation is far removed from resonant transitions [i.e., $\overline{n}'(\omega) \approx 0$ and $\Delta n'(\omega) \approx 0$], the dispersive phenomena of circular birefringence typically dominate [1, 2]. Assuming the light incident on a sample of length ℓ to be plane-polarized along the x axis, $\vec{\boldsymbol{\varepsilon}}_{in} = \sqrt{2}[\vec{\boldsymbol{\varepsilon}}_R + \vec{\boldsymbol{\varepsilon}}_L]/2$, the transmitted wave will exhibit a normalized polarization vector of the form

$$\begin{aligned} \vec{\boldsymbol{\varepsilon}} &= \frac{\sqrt{2}}{2}[\vec{\boldsymbol{\varepsilon}}_R e^{-i\omega\Delta n(\omega)\ell/2c} + \vec{\boldsymbol{\varepsilon}}_L e^{+i\omega\Delta n(\omega)\ell/2c}] \\ &= \cos\left[\frac{\omega\Delta n(\omega)}{2c}\ell\right]\vec{\mathbf{e}}_x - \sin\left[\frac{\omega\Delta n(\omega)}{2c}\ell\right]\vec{\mathbf{e}}_y, \end{aligned} \tag{11.14}$$

with the emerging electric-field vector specified by $\mathbf{E}(\ell,t) = E_{\omega}\vec{\boldsymbol{\varepsilon}} e^{i(\omega\overline{n}(\omega)\ell/c - \omega t)}$. These expressions describe a linearly polarized beam of light that has its plane of polarization reoriented from the (initial) x axis by a frequency-dependent angle, $\phi(\omega)$ (rad) [1, 31]:

$$\phi(\omega) = \frac{\omega\ell}{2c}\Delta n(\omega), \tag{11.15}$$

which defines the direction and magnitude of optical rotation in terms of the associated circular birefringence, $\Delta n(\omega) = n_L(\omega) - n_R(\omega)$. In particular, a positive (negative) value of $\phi(\omega)$ implies that the incident plane of polarization has been rotated clockwise (counterclockwise) as viewed by an observer looking towards the light source, thereby leading to the designation dextrorotatory (levorotatory) for the traversed medium.

Measurements of circular birefringence typically are expressed in terms of the specific optical rotatory power (or specific optical rotation), $[\alpha]_{\lambda}^{T}$, which describes the angle of linear polarization rotation (deg) observed at a specified temperature T (°C) and wavelength λ (nm) per pathlength (dm) and per concentration (g/mL) [1, 34]. This pivotal quantity follows directly from Eq. (11.15) by taking into account the requisite conversion between angular units:

$$[\alpha]_{\lambda}^{T} = \frac{180}{\pi}\frac{\phi(\omega = 2\pi c/\lambda)}{C\ell}, \tag{11.16}$$

where, by convention, the sample pathlength (ℓ) and species concentration (C) are expressed in dm and g/mL, respectively, with the latter reflecting either the density (ρ) for a pure liquid or the mass concentration (γ) for a solution. A less common metric for circular birefringence is the molar optical rotatory power, α_m, which requires C in Eq. (11.16) to be replaced by the molarity $[C]$ (mol/L) of the target medium [34].

The absorptive phenomena of CD usually dominate the chiroptical response when the incident frequency of electromagnetic radiation is proximate to a molecular resonance [1, 2]. By neglecting circular-differential dispersion effects [$\Delta n(\omega) \approx 0$] and assuming the light incident on a chiral medium of length ℓ to be plane-polarized along the x axis, the normalized polarization vector for the emerging wave now will have the form:

$$\begin{aligned}\vec{\boldsymbol{\varepsilon}} &= \frac{\sqrt{2}}{2}\frac{\vec{\boldsymbol{\varepsilon}}_R e^{+\omega\Delta n'(\omega)\ell/2c} + \vec{\boldsymbol{\varepsilon}}_L e^{-\omega\Delta n'(\omega)\ell/2c}}{[e^{+\omega\Delta n'(\omega)\ell/c} + e^{-\omega\Delta n'(\omega)\ell/c}]^{1/2}} \\ &= \mathcal{N}\left\{\cosh\left[\frac{\omega\Delta n'(\omega)\ell}{2c}\right]\vec{\mathbf{e}}_x - i\sinh\left[\frac{\omega\Delta n'(\omega)\ell}{2c}\right]\vec{\mathbf{e}}_y\right\},\end{aligned} \tag{11.17}$$

with the electric-field vector specified by $\mathbf{E}(\ell,t) = E_{\omega}\vec{\boldsymbol{\varepsilon}}e^{-\omega\overline{n}'(\omega)\ell/c}e^{i(\omega\overline{n}(\omega)\ell/c-\omega t)}/\mathcal{N}$ where $\mathcal{N}^2 = \mathrm{sech}[\omega\Delta n'(\omega)\ell/c]$. These expressions describe an elliptically polarized electromagnetic wave that has major and minor semi-axes of lengths $a = \mathcal{N}\cosh[\omega\Delta n'(\omega)\ell/2c]$ and $b = \mathcal{N}\sinh[\omega\Delta n'(\omega)\ell/2c]$ oriented along $\vec{\mathbf{e}}_x$ and $\vec{\mathbf{e}}_y$, respectively [1, 31]. The frequency-dependent ellipticity of this polarization state, $\eta(\omega)$, is defined by [1, 35]:

$$\tan[\eta(\omega)] = \frac{b}{a} = \frac{|\mathbf{E}^R(\ell,t)| - |\mathbf{E}^L(\ell,t)|}{|\mathbf{E}^R(\ell,t)| + |\mathbf{E}^L(\ell,t)|} = \tanh\left[\frac{\omega\Delta n'(\omega)\ell}{2c}\right], \tag{11.18}$$

where $|\mathbf{E}^R(\ell,t)|$ and $|\mathbf{E}^L(\ell,t)|$ denote the distinct transmitted field amplitudes of the helicity components. For typically small values of $\eta(\omega)$ and $\Delta n'(\omega)$, truncated power-series expansions of the trigonometric and hyperbolic functions in Eq. (11.18) lead to

$$\eta(\omega) \approx \frac{\omega\ell}{2c}\Delta n'(\omega), \tag{11.19}$$

which defines the direction and magnitude of optical ellipticity in terms of the associated circular dichroism, $\Delta n'(\omega) = n'_L(\omega) - n'_R(\omega)$. In particular, a positive (negative) value of $\eta(\omega)$ implies a net clockwise (counterclockwise) sense of circulation for the emerging polarization vector when viewed by an observer looking towards the light source, as demanded by preferential absorption of the left-handed (right-handed) circular polarization component.

Measurements of circular dichroism can be expressed in terms of the specific ellipticity, $[\theta]_\lambda^T$ [deg $dm^{-1}(g/mL)^{-1}$], as defined by analogy to Eq. (11.16) [1, 31]:

$$[\theta]_\lambda^T = \frac{180}{\pi}\frac{\eta(\omega = 2\pi c/\lambda)}{C\ell}, \tag{11.20}$$

or the related molar ellipticity, θ_m, obtained upon replacing concentration C by molarity $[C]$; however, the intimate relationship that exists between the imaginary part of the refractive index and the process of absorption affords other metrics for characterizing such phenomena. The dimensionless transmittance $\mathcal{T}$ for light passing through a medium that spans the $0 \le z \le \ell$ region is defined by the ratio of transmitted (I_ℓ) and incident (I_0) intensities:

$$\mathcal{T} = \frac{I_\ell}{I_0} = e^{-\overline{\kappa}(\omega)\ell} = 10^{-\overline{\varepsilon}(\omega)[C]\ell}, \tag{11.21}$$

where $\overline{\kappa}(\omega) = \frac{1}{2}[\kappa_L(\omega) + \kappa_R(\omega)]$ and $\overline{\varepsilon}(\omega) = \frac{1}{2}[\varepsilon_L(\omega) + \varepsilon_R(\omega)]$ denote the linear-napierian and molar-decadic absorption coefficients [27], with $\overline{\kappa}(\omega) = \overline{\varepsilon}(\omega)[C]\ln 10 = 2\omega\overline{n}'(\omega)/c$ [the factor of two in the final equality follows from $I(z) \propto |E(z,t)|^2 \propto \left|E_\omega e^{-\omega\overline{n}'(\omega)z/c}\right|^2$]. The circular-differential variants of these quantities similarly are related by:

$$\Delta n'(\omega) = \frac{c}{2\omega}\Delta\kappa(\omega) = \frac{c}{2\omega}\Delta\varepsilon(\omega)[C]\ln 10, \tag{11.22}$$

thus allowing the circular dichroism to be recast as absorption-related metrics: [1, 2, 35]

$$\Delta\kappa(\omega) = \frac{4}{\ell}\eta(\omega) = \frac{2\omega}{c}\Delta n'(\omega), \tag{11.23}$$

$$\Delta\varepsilon(\omega) = \frac{4}{\ell[C]\ln 10}\eta(\omega) = \frac{2\omega}{c[C]\ln 10}\Delta n'(\omega), \tag{11.24}$$

where $\Delta\kappa(\omega) = \kappa_L(\omega) - \kappa_R(\omega)$ and $\Delta\varepsilon(\omega) = \varepsilon_L(\omega) - \varepsilon_R(\omega)$ commonly are expressed in units of dm^{-1} and L dm^{-1} mol^{-1}, respectively.

While the phenomenological description of natural optical activity presented above has separated the dispersive [$\Delta n(\omega) \neq 0$] and absorptive [$\Delta n'(\omega) \neq 0$] aspects of linear chiroptical response, actual chiral species will manifest both effects simultaneously, thereby leading to concurrent reorientation and elliptization of impinging plane-polarized light [1, 2, 31]. The distinct frequency dependencies of CB and CD will govern the behavior observed during a given laboratory measurement, with the polarization rotation arising from the former usually found to dominate in transparent spectral regions far removed from molecular resonances.

11.2.3. Microscopic Origins of Optical Activity

Theoretical treatments of frequency-dependent dispersion and absorption in achiral media typically invoke the electric-dipole ($E1$) approximation [36], where the assumption that molecular dimensions (d) are much smaller than the wavelength of incident light ($\lambda \gg d$) leads to strong matter–field interactions induced by a spatially uniform (albeit time-varying) electric field. Quantitative analyses of chiroptical phenomena necessitate moving

beyond this $E1$ premise [1, 2, 37], so as to incorporate higher-order magnetic-dipole ($M1$) and electric-quadrupole ($E2$) processes mediated, respectively, by the magnetic field and the electric-field gradient of an impinging electromagnetic wave. The $M1$ and $E2$ interactions are substantially weaker than their $E1$ counterparts (i.e., by a factor of $d/\lambda \approx 10^{-4}$) [38]; however, enantiomer-specific interferences among these processes (viz., $E1$–$M1$ and $E1$–$E2$) are responsible for the linear manifestation of natural optical activity. While the $M1$ and $E2$ terms stem from the same order of the multipole expansion used to classify the hierarchy of matter–field couplings [38], the averaging over all spatial orientations required to model an isotropic ensemble of target molecules causes the inherently anisotropic electric-quadrupole contributions to vanish [1, 2]. In the case of oriented samples (e.g., crystals [39] or single molecules [40]), $E1$–$E2$ chiroptical effects have been shown to be important, often surpassing in magnitude those arising from analogous $E1$–$M1$ mechanisms.

The first quantitative attempts to rationalize the microscopic origins of chiroptical phenomena can be traced back to before the dawn of modern quantum theory. Following initial proposals for matter–field couplings that could lead to the appearance of circular birefringence when incorporated into Maxwell's Equations [41], Born [42], Oseen [43], and Gray [44] independently formulated rigorous classical explanations for the optical activity of chiral ("dissymmetric") species. This ansatz was extended to the semiclassical framework of quantum mechanics by Rosenfeld [45] in 1928, with subsequent refinements being introduced by Condon [46], Eyring [47], and others. Such treatments build upon the oscillating electric and magnetic multipoles created in a target medium by an impinging electromagnetic wave of angular frequency ω. In the absence of static external fields, time-dependent perturbation theory predicts a chiral molecule to exhibit an electric dipole moment vector, $\boldsymbol{\mu}(t)$, that embodies two distinct optically induced contributions [1]:

$$\boldsymbol{\mu}(t) \equiv \langle \Psi(t)|\hat{\boldsymbol{\mu}}|\Psi(t)\rangle = \boldsymbol{\mu}(0) + \boldsymbol{\alpha}(\omega)\cdot\mathbf{E}(t) + \frac{1}{\omega}\mathbf{G}'(\omega)\cdot\frac{\partial\mathbf{B}(t)}{\partial t} + \cdots, \tag{11.25}$$

where $\hat{\boldsymbol{\mu}}$ denotes the electric dipole moment operator. The absence of spatial arguments in electromagnetic field vectors implies that these quantities are being evaluated at the origin of the coordinate system (i.e., the location of the molecule), while the time derivative of $\mathbf{B}(t)$ reflects the quadrature phase of its contribution relative to that of $\mathbf{E}(t), \dot{\mathbf{B}}(t) = -i\omega\mathbf{B}(t)$ [cf. Eq. (11.6)]. Analogous expressions can be derived for the induced magnetic-dipole and electric-quadrupole vectors [1], $\mathbf{m}(t) \equiv \langle \Psi(t)|\hat{\mathbf{m}}|\Psi(t)\rangle$ and $\boldsymbol{\Theta}(t) \equiv \langle \Psi(t)|\hat{\boldsymbol{\Theta}}|\Psi(t)\rangle$, where $\hat{\mathbf{m}}$ and $\hat{\boldsymbol{\Theta}}$ represent the magnetic-dipole and electric-quadrupole operators, respectively.

The induced electric-dipole moment of Eq. (11.25) contains two dynamic molecular property tensors of the second rank that quantify the frequency-dependent response of the system to impinging electromagnetic radiation [1]: (*i*) the electric dipole ($E1$) polarizability tensor, $\boldsymbol{\alpha}(\omega)$, which governs achiral dispersion/absorption and (*ii*) the mixed electric dipole–magnetic dipole ($E1$–$M1$) polarizability tensor, $\mathbf{G}'(\omega)$, which is responsible for the manifestation of optical activity. The Cartesian components of $\boldsymbol{\mu}(t)$ follow from expansion of the tensor contractions:

$$\mu_\alpha(t) = \mu_\alpha(0) + \sum_\beta \alpha_{\alpha\beta}(\omega)E_\beta(t) + \frac{1}{\omega}\sum_\beta G'_{\alpha\beta}(\omega)\dot{B}_\beta(t) + \cdots, \tag{11.26}$$

where subscripts α and β independently can assume indices x, y, or z. The putative role of $\mathbf{G}'(\omega)$ as a mediator of chiroptical response readily can be appreciated by considering the case of incident light having either right-circular (R) or left-circular (L) polarization [48]:

$$\begin{aligned}\mu_\alpha^{R/L}(t) &= \mu_\alpha(0) + \sum_\beta \alpha_{\alpha\beta}(\omega) E_\beta^{R/L}(t) + \frac{1}{\omega}\sum_\beta G'_{\alpha\beta}(\omega)\dot{B}_\beta^{R/L}(t) + \cdots \\ &= \mu_\alpha(0) + \sum_\beta \left[\alpha_{\alpha\beta}(\omega) \pm \frac{1}{c} G'_{\alpha\beta}(\omega)\right] E_\beta^{R/L}(t) + \cdots,\end{aligned} \tag{11.27}$$

where the second equality follows from Eq. (11.6). Taking into account that the induced electric dipole moment $\boldsymbol{\mu}^{R/L}(t)$ (when scaled by the target number density) serves as the source term for radiating a new electromagnetic wave, the circular-differential response of the system clearly resides in the components of the mixed $E1$–$M1$ polarizability tensor, $G'_{\alpha\beta}(\omega)$, which exhibit opposing signs for the two species constituting an enantiomeric pair. For an isotropic and homogeneous ensemble of chiral molecules having pathlength ℓ (m) and number density N (m^{-3}), detailed calculations predict the optical rotation $\phi(\omega)$ (rad) sustained by linearly polarized light of angular frequency ω (rad/s) to be [1]

$$\phi(\omega) = -\mu_0 \ell N \omega G'(\omega), \tag{11.28}$$

where μ_0 ($4\pi \times 10^{-7}\mathrm{Hm}^{-1}$) denotes the permeability of free space. The chiroptical coupling constant that appears in this expression, $G'(\omega)$ ($\mathrm{C}^2\mathrm{m}^3\mathrm{J}^{-1}\mathrm{s}^{-1}$), stems from averaging of the $\mathbf{G}'(\omega)$ tensor over all spatial orientations [1, 2], a quantity that can be defined in terms of the corresponding trace over Cartesian components:

$$G'(\omega) = \frac{1}{3}\mathrm{Tr}[\mathbf{G}'(\omega)] = \frac{1}{3}\sum_\alpha G'_{\alpha\alpha}(\omega). \tag{11.29}$$

Since the three elements of the mixed $E1$–$M1$ polarizability tensor added in Eq. (11.29) often are found to partially cancel one another [e.g., $G'_{xx}(\omega) \approx -G'_{yy}(\omega)$ with $|G'_{yy}(\omega)| \gg |G'_{zz}(\omega)|$], theoretical calculations of optical rotation in isotropic media must be capable of predicting these quantities reliably with high levels of intrinsic accuracy.

Explicit expressions for $\alpha_{\alpha\beta}(\omega)$ and $G'_{\alpha\beta}(\omega)$ follow from time-dependent perturbation theory [1, 2], where eigenstates of the unperturbed (field-free) molecular Hamiltonian, $\hat{\mathrm{H}}^{(0)}$, afford a basis for expanding properties of interest [38]. In particular, the (lower-lying) ground and (higher-lying) excited electronic states of the field-free system are denoted by $|g\rangle$ and $|e\rangle$, respectively, with the attendant energy eigenvalues of E_g and E_e allowing the angular frequency for the $|e\rangle \leftrightarrow |g\rangle$ resonance to be specified as $\omega_{eg} = (E_e - E_g)/\hbar$. By focusing on wavelengths that reside in the transparent region of the spectrum (*sans* resonant absorption) and assuming that only the ground state is populated prior to the onset of matter–field interactions, the tensor elements for $\boldsymbol{\alpha}(\omega)$ are found to be given by [1, 2]

$$\alpha_{\alpha\beta}(\omega) = \frac{2}{\hbar}\sum_{e\neq g} \frac{\omega_{eg}\mathrm{Re}[\langle g|\hat{\mu}_\alpha|e\rangle\langle e|\hat{\mu}_\beta|g\rangle]}{\omega_{eg}^2 - \omega^2} = \frac{2}{\hbar}\sum_{e\neq g} \frac{\omega_{eg}}{\omega_{eg}^2 - \omega^2}\, {}^{eg}S_{\alpha\beta}, \tag{11.30}$$

where ω denotes the incident optical frequency and the summation is taken over all (excited) states excluding the initial (ground) state. The product of electric dipole moment matrix elements in this expression can be recast as the elements (${}^{eg}S_{\alpha\beta}$) of a second-rank tensor specifying spatial properties of the $E1$ transition moment for the $|e\rangle \leftrightarrow |g\rangle$ resonance, ${}^{eg}\mathbf{S}$. The associated transition strength, ${}^{eg}S$, which quantifies achiral dispersion and absorption effects in an isotropic medium, follows from the trace of this quantity over Cartesian components:

$$ {}^{eg}S = \mathrm{Tr}[{}^{eg}S] = \sum_{\alpha} {}^{eg}S_{\alpha\alpha} = \mathrm{Re}[\langle g|\hat{\boldsymbol{\mu}}|e\rangle \cdot \langle e|\hat{\boldsymbol{\mu}}|g\rangle] = |\langle g|\hat{\boldsymbol{\mu}}|e\rangle|^2, \tag{11.31} $$

where the final equality reflects the Hermitian nature of the electric dipole moment operator [38]. The canonical spectroscopic oscillator strength for the $|e\rangle \leftrightarrow |g\rangle$ transition, ${}^{eg}f$, is linearly related to ${}^{eg}S$ by a proportionality constant that depends on the mass (m_e) and charge ($-e$) of the electron [49], ${}^{eg}f = (2\omega_{eg}m_e/3\hbar e^2){}^{eg}S$.

For the transparent region of the spectrum, time-dependent perturbation theory predicts the components of the mixed $E1$–$M1$ polarizability tensor to have the form [1, 2]

$$ G'_{\alpha\beta}(\omega) = -\frac{2\,\omega}{\hbar} \sum_{e\neq g} \frac{\mathrm{Im}[\langle g|\hat{\mu}_\alpha|e\rangle\langle e|\hat{m}_\beta|g\rangle]}{\omega_{eg}^2 - \omega^2} = -\frac{2}{\hbar} \sum_{e\neq g} \frac{\omega}{\omega_{eg}^2 - \omega^2}\, {}^{eg}R_{\alpha\beta}, \tag{11.32} $$

where the pure-imaginary product of electric-dipole and magnetic-dipole matrix elements (*vide infra*) defines the elements (${}^{eg}R_{\alpha\beta}$) of the second-rank rotatory tensor for the $|e\rangle \leftrightarrow |g\rangle$ transition, ${}^{eg}\mathbf{R}$. The corresponding rotatory strength, ${}^{eg}R$, as required for the description of chiroptical phenomena in isotropic media, follows from the trace of this quantity:

$$ {}^{eg}R = \mathrm{Tr}[{}^{eg}\mathbf{R}] = \sum_{\alpha} {}^{eg}R_{\alpha\alpha} = \mathrm{Im}[\langle g|\hat{\boldsymbol{\mu}}|e\rangle \cdot \langle e|\hat{\mathbf{m}}|g\rangle]. \tag{11.33} $$

The operators governing electric-dipole ($\hat{\boldsymbol{\mu}}$) and magnetic-dipole ($\hat{\mathbf{m}}$) transitions are proportional to those for linear momentum ($\hat{\mathbf{P}}$) and angular momentum ($\hat{\mathbf{J}}$) [38], respectively, which, in turn, represent the generators for infinitesimal translation (along the direction of $\mathbf{P}$) and infinitesimal rotation (about the direction of $\mathbf{J}$) [50]. Consequently, the juxtaposition of matrix elements for these quantities in the definition of ${}^{eg}R$ suggests that both a displacement and a (nonorthogonal) reorientation of electron charge density must transpire for a contributing $|e\rangle \leftrightarrow |g\rangle$ resonance, thereby imbuing an effective helical motion to the attendant chiroptical process (the handedness of which depends on the relative phases of $\langle g|\hat{\boldsymbol{\mu}}|e\rangle$ and $\langle e|\hat{\mathbf{m}}|g\rangle$).

Since Eq. (11.32) shows that $G'_{\alpha\beta}(\omega)$ is proportional to the frequency of incident electromagnetic radiation, the mixed $E1$–$M1$ polarizability tensor will vanish in the static ($\omega \to 0$) limit, as will the manifestation of corresponding chiroptical effects. Such behavior is subsumed by definition of the related Rosenfeld tensor, $\boldsymbol{\beta}(\omega)$ [9]:

$$ \beta_{\alpha\beta}(\omega) = -\frac{1}{\omega} G'_{\alpha\beta}(\omega). \tag{11.34} $$

For isotropic media, averaging of $\boldsymbol{\beta}(\omega)$ over all spatial orientations yields the scalar Rosenfeld optical-activity parameter $\beta(\omega)$:

$$\beta(\omega) = \frac{1}{3}\mathrm{Tr}[\boldsymbol{\beta}(\omega)] = \frac{1}{3}\sum_{\alpha}\beta_{\alpha\alpha}(\omega) = -\frac{1}{\omega}G'(\omega), \tag{11.35}$$

with the predicted polarization rotation of Eq. (11.28) now being reformulated as:

$$\phi(\omega) = \mu_0 \ell N \omega^2 \beta(\omega). \tag{11.36}$$

11.2.4. Resonant Chiroptical Behavior

While the expressions presented above for $\boldsymbol{\alpha}(\omega)$ and $\mathbf{G'}(\omega)$ suffice for analyses of optical phenomena taking place in the transparent region of the spectrum, they are not appropriate for the description of resonant matter–field interactions (e.g., absorption) [1, 2]. This assertion can be seen readily from the form of $G'_{\alpha\beta}(\omega)$ in Eq. (11.32), where the simple poles that exist at $\omega = \omega_{eg}$ lead to unphysical divergence of the mixed $E1$–$M1$ susceptibility whenever the incident frequency of electromagnetic radiation (ω) approaches the resonance frequency of a specific $|e\rangle \leftrightarrow |g\rangle$ transition (ω_{eg}). Such aberrant behavior can be attributed to the implicit neglect of relaxation processes, which effectively assumes molecular states to be infinitely long-lived. Nevertheless, since the frequency-integrated intensity for an isolated ECD feature scales in proportion to the rotatory strength, ${}^{e'g}R$, for the pertinent $|e'\rangle \leftrightarrow |g\rangle$ excitation [1, 2], requisite spectroscopic information still can be deduced from the corresponding residue of $G'(\omega)$:

$${}^{e'g}R = \hbar \lim_{\omega \to \omega_{e'g}} [(\omega - \omega_{e'g})G'(\omega)]. \tag{11.37}$$

As shown below, proper introduction of depopulation and dephasing rates will lead to complex frequency-dependent property tensors [akin to $\tilde{n}(\omega) = n(\omega) + i\,n'(\omega)$], the real and imaginary parts of which respectively serve to describe the dispersive and absorptive aspects of the system.

A comprehensive scheme for elaborating molecular response properties can be found in the density operator formalism [51], where temporal evolution of the system under the simultaneous influence of electromagnetic fields and relaxation processes is described through perturbative solution of the quantum-mechanical Liouville equation. This approach has become the standard for frequency-domain analyses of nonlinear optical spectroscopy [21, 22], with diagrammatic techniques serving to organize and interpret successively higher orders of matter–field coupling. Application to linear chiroptical phenomena yields a complex variant of the mixed $E1$–$M1$ polarizability tensor, $\boldsymbol{\chi}(\omega)$, the components of which can be specified by:

$$\chi_{\alpha\beta}(\omega) = -\frac{i}{\hbar}\sum_{e \neq g}\left[\frac{\langle g|\hat{\mu}_\alpha|e\rangle\langle e|\hat{m}_\beta|g\rangle}{\omega_{eg} - \omega - i\Gamma_{eg}} + \frac{\langle g|\hat{m}_\beta|e\rangle\langle e|\hat{\mu}_\alpha|g\rangle}{\omega_{eg} + \omega + i\Gamma_{eg}}\right], \tag{11.38}$$

where the two terms stem from complementary events taking place in the dual ket (absorption) and bra (emission) spaces [22, 28]. The set of Γ_{eg} rate parameters appearing in this expression reflect the temporal dissipation of optical coherences induced between the excited (e) and ground (g) states [51], where only the latter is populated initially.

As such, these quantities embody the effects of intrinsic relaxation processes (e.g., radiative/nonradiative decay) and extrinsic environmental perturbations (e.g., collisions and other intermolecular interactions). Under quite general circumstances [22], they can be related to the rates of population removal (Γ_{nn}) or, equivalently, to the effective lifetimes ($\tau_n = 1/\Gamma_{nn}$) for the optically coupled states:

$$\Gamma_{eg} = \frac{1}{2}(\Gamma_{ee} + \Gamma_{gg}) + \Gamma'_{eg} \xrightarrow{\Gamma_{gg}\approx 0 \;\&\; \Gamma'_{eg}\approx 0} \frac{1}{2}\Gamma_{ee} = \frac{1}{2\tau_e}, \tag{11.39}$$

where Γ'_{eg} denotes the rate of pure-dephasing processes (e.g., elastic collisions) that destroy molecular coherence without disrupting corresponding populations. The final equality in Eq. (11.39) follows from the common assumption of an infinite ground-state lifetime ($\Gamma_{gg} \approx 0$) combined with pure-dephasing mechanisms of negligible consequence ($\Gamma'_{eg} \approx 0$).

By assuming unperturbed wavefunctions for the ground (g) and excited (e) states of the system to be nondegenerate (i.e., pure real), the matrix elements describing electric-dipole ($E1$) and magnetic-dipole ($M1$) interactions will be pure real and pure imaginary, respectively [1, 2]:

$$\langle g|\hat{\mu}_\alpha|e\rangle^* = \langle e|\hat{\mu}_\alpha|g\rangle = \langle g|\hat{\mu}_\alpha|e\rangle, \tag{11.40}$$

$$\langle g|\hat{m}_\beta|e\rangle^* = \langle e|\hat{m}_\beta|g\rangle = -\langle g|\hat{m}_\beta|e\rangle. \tag{11.41}$$

As such, the products of these quantities present in Eq. (11.38) must be pure imaginary:

$$\langle g|\hat{\mu}_\alpha|e\rangle\langle e|\hat{m}_\beta|g\rangle = i\,\mathrm{Im}[\langle g|\hat{\mu}_\alpha|e\rangle\langle e|\hat{m}_\beta|g\rangle], \tag{11.42}$$

$$\langle g|\hat{m}_\beta|e\rangle\langle e|\hat{\mu}_\alpha|g\rangle = i\,\mathrm{Im}[\langle g|\hat{m}_\beta|e\rangle\langle e|\hat{\mu}_\alpha|g\rangle], \tag{11.43}$$

and are related by:

$${}^{eg}R_{\alpha\beta} = \mathrm{Im}[\langle g|\hat{\mu}_\alpha|e\rangle\langle e|\hat{m}_\beta|g\rangle] = -\mathrm{Im}[\langle g|\hat{m}_\beta|e\rangle\langle e|\hat{\mu}_\alpha|g\rangle], \tag{11.44}$$

where the leftmost equality restates the definition of rotatory tensor elements, ${}^{eg}R_{\alpha\beta}$, in Eq. (11.33). The complex $E1$–$M1$ polarizability tensor now can be separated into real and imaginary parts, $\chi_{\alpha\beta}(\omega) = \mathrm{Re}[\chi_{\alpha\beta}(\omega)] + i\,\mathrm{Im}[\chi_{\alpha\beta}(\omega)]$, which have the following forms:

$$\begin{aligned}\mathrm{Re}[\chi_{\alpha\beta}(\omega)] &= \frac{1}{\hbar}\sum_{e\neq g}\left[\frac{\omega_{eg}-\omega}{(\omega_{eg}-\omega)^2+\Gamma_{eg}^2} - \frac{\omega_{eg}+\omega}{(\omega_{eg}+\omega)^2+\Gamma_{eg}^2}\right]{}^{eg}R_{\alpha\beta} \\ &= \frac{1}{\hbar}\sum_{e\neq g}\frac{2\,\omega(\omega_{eg}^2-\omega^2-\Gamma_{eg}^2)\;{}^{eg}R_{\alpha\beta}}{[(\omega_{eg}-\omega)^2+\Gamma_{eg}^2][(\omega_{eg}+\omega)^2+\Gamma_{eg}^2]},\end{aligned} \tag{11.45}$$

$$\begin{aligned}\mathrm{Im}[\chi_{\alpha\beta}(\omega)] &= \frac{1}{\hbar}\sum_{e\neq g}\left[\frac{\Gamma_{eg}}{(\omega_{eg}-\omega)^2+\Gamma_{eg}^2} + \frac{\Gamma_{eg}}{(\omega_{eg}+\omega)^2+\Gamma_{eg}^2}\right]{}^{eg}R_{\alpha\beta} \\ &= \frac{1}{\hbar}\sum_{e\neq g}\frac{2\Gamma_{eg}(\omega_{eg}^2+\omega^2+\Gamma_{eg}^2)\;{}^{eg}R_{\alpha\beta}}{[(\omega_{eg}-\omega)^2+\Gamma_{eg}^2][(\omega_{eg}+\omega)^2+\Gamma_{eg}^2]}.\end{aligned} \tag{11.46}$$

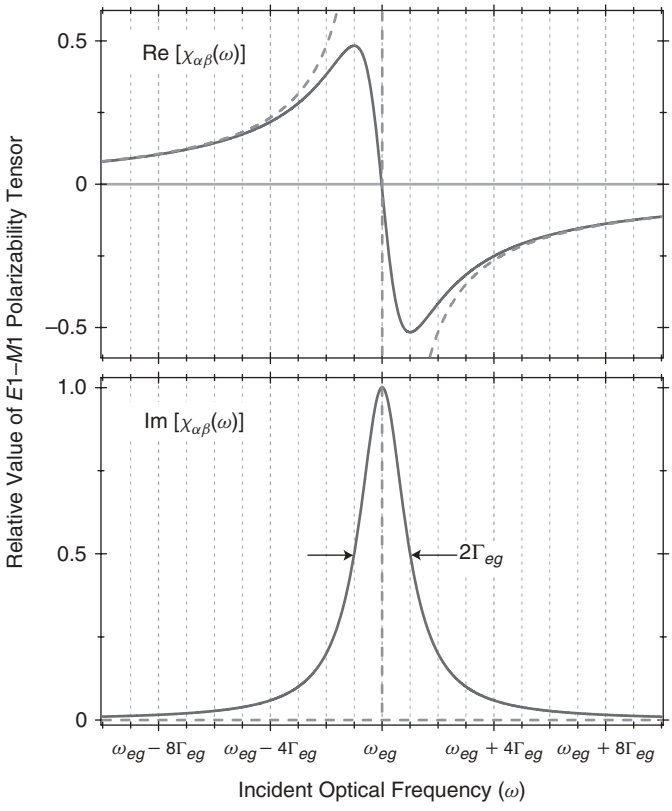

Figure 11.1. Resonant chiroptical response. The real (dispersive) and imaginary (absorptive) parts of the complex $E1$–$M1$ polarizability tensor, $\chi_{\alpha\beta}(\omega)$, are plotted as functions of the incident frequency ω in the vicinity of an isolated electronic resonance ω_{eg} ($\omega_{eg} \gg 0$). Solid curves denote the forms obtained in the presence of dephasing and/or depopulation processes characterized by rate Γ_{eg}, while dashed lines illustrate the behavior expected in the limit of infinite lifetimes ($\Gamma_{eg} \to 0$). For each graph, the ordinate scale is defined in units of ${}^{eg}R_{\alpha\beta}/\hbar\Gamma_{eg}$, where ${}^{eg}R_{\alpha\beta}$ denotes the corresponding element of the rotatory tensor for the $|e\rangle \leftrightarrow |g\rangle$ transition.

Figure 11.1 depicts the characteristic shapes of these quantities for an isolated $|e\rangle \leftrightarrow |g\rangle$ resonance ($\omega_{eg} \gg 0$), highlighting the dispersive nature of $\mathrm{Re}[\chi_{\alpha\beta}(\omega)]$ (which passes through zero at $\omega = \omega_{eg}$) and the absorptive nature of $\mathrm{Im}[\chi_{\alpha\beta}(\omega)]$ (which attains a maximum value at $\omega = \omega_{eg}$). The homogeneous linewidth of the Lorentzian absorption profile (full-width at half-maximum height) is specified by $2\Gamma_{eg}$, with the same quantity also defining the separation between the positive and negative extrema of the dispersion curve.

To make a formal connection with the previous expression for $\mathbf{G}'(\omega)$, it proves useful to consider the limit of $\chi_{\alpha\beta}(\omega)$ when the dephasing parameters Γ_{eg} uniformly approach zero, which is tantamount to assuming that all excited states display infinite lifetimes. Under such conditions, the real portion of the complex $E1$–$M1$ susceptibility tensor collapses to yield

$$\begin{aligned}\lim_{\Gamma_{eg}\to 0}\{\mathrm{Re}[\chi_{\alpha\beta}(\omega)]\} &= \frac{1}{\hbar}\sum_{e\neq g}\left[\frac{1}{\omega_{eg}-\omega}-\frac{1}{\omega_{eg}+\omega}\right]{}^{eg}R_{\alpha\beta} \\ &= \frac{2}{\hbar}\sum_{e\neq g}\frac{\omega}{\omega_{eg}^2-\omega^2}\,{}^{eg}R_{\alpha\beta}, \end{aligned} \tag{11.47}$$

which equals the negative of $G'_{\alpha\beta}(\omega)$ as defined in Eq. (11.32). As such, the frequency-dependent optical rotation predicted for an isotropic ensemble of chiral molecules can

be reformulated as

$$\phi(\omega) = \mu_0 \ell N \omega \mathrm{Re}[\chi(\omega)], \tag{11.48}$$

where $\chi(\omega)$ follows from averaging of the complex $E1$–$M1$ polarizability tensor over all spatial orientations [1, 2]:

$$\chi(\omega) = \frac{1}{3}\mathrm{Tr}[\boldsymbol{\chi}(\omega)] = \frac{1}{3}\sum_{\alpha}\chi_{\alpha\alpha}(\omega). \tag{11.49}$$

Equation (11.48) affords a consistent description of ORD that spans the nonresonant and resonant portions of the spectrum, with the top panel of Figure 11.1 highlighting the disparity that exists between $\mathrm{Re}[\chi_{\alpha\beta}(\omega)]$ and $-G'_{\alpha\beta}(\omega)$ when $\omega \approx \omega_{eg}$.

Evaluation of $\mathrm{Im}[\chi_{\alpha\beta}(\omega)]$ in the limit of negligible dephasing requires use of the Dirac delta function, $\delta(b)$, as defined by [50]:

$$\lim_{\Gamma\to 0^+}\frac{a\Gamma}{b^2+\Gamma^2} = a\pi\delta(b). \tag{11.50}$$

Application of this identity to Eq. (11.46) yields:

$$\begin{aligned}\lim_{\Gamma_{eg}\to 0}\{\mathrm{Im}[\chi_{\alpha\beta}(\omega)]\} &= \frac{\pi}{\hbar}\sum_{e\neq g}[\delta(\omega_{eg}-\omega)+\delta(\omega_{eg}+\omega)]\ {}^{eg}R_{\alpha\beta} \\ &\xrightarrow[\omega_{e'g}>0]{\omega\approx\omega_{e'g}} \frac{\pi}{\hbar}\delta(\omega_{e'g}-\omega)\ {}^{e'g}R_{\alpha\beta},\end{aligned} \tag{11.51}$$

where the final equality assumes that the excitation source has been tuned to coincide with an isolated $|e'\rangle \leftrightarrow |g\rangle$ transition having $\hbar\omega_{e'g} = E'_e - E_g > 0$. The bottom panel of Figure 11.1 contrasts the infinitely sharp frequency dependence of this expression with the gradual (finite-bandwidth) behavior suggested by Eq. (11.46); however, in both cases the absorptive nature of the response is manifest. The imaginary part of the complex $E1$–$M1$ susceptibility tensor thus provides a uniform description of ECD that encompasses both the resonant and nonresonant regions of the spectrum. For an isotropic ensemble of chiral molecules characterized by number density N and pathlength ℓ, detailed analyses predict that the ellipticity, $\eta(\omega)$, acquired by an impinging beam of plane-polarized light, will be [1, 2]:

$$\eta(\omega) = -\mu_0 \ell N \omega \mathrm{Im}[\chi(\omega)], \tag{11.52}$$

where the complex (orientation-averaged) quantity $\chi(\omega)$ has been defined by Eq. (11.49). Owing to the superposition of contributions from neighboring electronic manifolds and the presence of fine structure from nuclear degrees of freedom (viz., vibrations), ECD spectral profiles often appear congested, displaying effective (inhomogeneously broadened [36]) linewidths far in excess of those expected for an isolated (homogeneously broadened [36]) transition.

The $E1$–$M1$ polarizability in Eq. (11.38) represents the Fourier transform of an analogous time-domain response tensor, $\boldsymbol{\chi}(t)$, which is subject to the principle of temporal causality (i.e., the "cause" must precede the "effect"). Aside from requiring the poles of $\boldsymbol{\chi}(\omega)$ to reside in the lower half of the complex frequency plane [22, 52], this causes

the real and imaginary parts of $\chi_{\alpha\beta}(\omega)$ to be linked by extensions of the canonical Kramers–Kronig (KK) relationships [1]:

$$\mathrm{Re}[\chi_{\alpha\beta}(\omega)] = \frac{1}{\pi}\wp\int_{-\infty}^{+\infty}\frac{\mathrm{Im}[\chi_{\alpha\beta}(\omega')]}{\omega'-\omega}d\omega' \xrightarrow{\chi^*(\omega)=\chi(-\omega)} \frac{2}{\pi}\wp\int_{0}^{+\infty}\frac{\omega'\mathrm{Im}[\chi_{\alpha\beta}(\omega')]}{\omega'^2-\omega^2}d\omega', \tag{11.53}$$

$$\mathrm{Im}[\chi_{\alpha\beta}(\omega)] = -\frac{1}{\pi}\wp\int_{-\infty}^{+\infty}\frac{\mathrm{Re}[\chi_{\alpha\beta}(\omega')]}{\omega'-\omega}d\omega' \xrightarrow{\chi^*(\omega)=\chi(-\omega)} -\frac{2}{\pi}\wp\int_{0}^{+\infty}\frac{\omega\mathrm{Re}[\chi_{\alpha\beta}(\omega')]}{\omega'^2-\omega^2}d\omega', \tag{11.54}$$

where the symbol $\wp$ signifies the Cauchy principal value of an integral. The caveat that real electromagnetic fields must induce real molecular moments also demands $\boldsymbol{\chi}^*(\omega) = \boldsymbol{\chi}(-\omega)$, [1, 22], thereby constraining $\mathrm{Re}[\chi_{\alpha\beta}(\omega)]$ and $\mathrm{Im}[\chi_{\alpha\beta}(\omega)]$ to be even and odd functions of ω, respectively. As shown by the final equalities in Eqs. (11.53) and (11.54), the KK relationships thus can be manipulated such that their limits of integration span only positive values of frequency.

While the Kramers–Kronig relationships afford a mathematically rigorous approach for interconverting the dispersive (ORD) and absorptive (ECD) components of a complex molecular property tensor, their practical application often has been limited by the need to have high-quality information spanning a wide range of frequencies (literally $0 \leq \omega \leq \infty$). Such procedures historically have been employed to compensate for inadequacies and/or restrictions of instrumentation that either encumbered or prohibited one type of experimental measurement relative to another (i.e., dispersive ORD versus absorptive ECD) [53, 54]. Modern developments in analytical spectroscopy have eliminated most of these issues; however, the advent of reliable quantum-chemical methods for predicting chiroptical response has brought renewed interest to this topic, with disparities between recorded ORD profiles and their KK-transformed ECD counterparts proposed as a means to enumerate and characterize higher-lying (experimentally inaccessible) electronic manifolds that contribute to the observed frequency dependence of CB. Systematic analyses of these capabilities have been reported by Polavarapu and coworkers [55], while Autschbach et al. [56] have demonstrated the utility of exploiting multiply subtractive KK algorithms that incorporate fixed "anchor points" of known value.

The sum-over-states expressions given above for the elements of $\boldsymbol{\alpha}(\omega), \mathbf{G}'(\omega)$, and $\boldsymbol{\chi}(\omega)$ suffer from slow convergence and seldom are used in conjunction with modern quantum-chemical methods since an unphysically large number of electronic manifolds would need to be considered before asymptotically stable results are obtained [57]. Instead, most calculations make use of linear response theory [58, 59], which affords a comprehensive framework for computing chiroptical properties that requires neither knowledge of nor summation over eigenstates of the unperturbed molecular Hamiltonian. This approach enables elements of the dynamic molecular property tensors in Eqs.

(11.25) and (11.26) to be reformulated as [8, 9]:

$$\alpha_{\alpha\beta}(\omega) = -\langle\langle \hat{\mu}_\alpha; \hat{\mu}_\beta \rangle\rangle_\omega, \qquad G'_{\alpha\beta}(\omega) = -\mathrm{Im}[\langle\langle \hat{\mu}_\alpha; \hat{m}_\beta \rangle\rangle_\omega], \tag{11.55}$$

where $\langle\langle \hat{A}; \hat{V}_\omega \rangle\rangle_\omega$ denotes a linear response function for operator $\hat{A}$ defined in terms of specific Fourier components for the time-dependent perturbation (i.e., $\hat{V}^{E1}_\omega = -\hat{\boldsymbol{\mu}} \cdot \mathbf{E}_\omega$ or $\hat{V}^{M1}_\omega = -\hat{\mathbf{m}} \cdot \mathbf{B}_\omega$). General strategies for computing these quantities efficiently are based upon economical parameterization of the electronic wavefunction, with the first-order perturbative response to external electric and magnetic fields usually being obtained from the relatively straightforward solution to a coupled system of algebraic equations [59]. Most quantum-chemical implementations of the linear-response formalism have assumed molecular states to be infinitely long-lived, thus making them ill-suited for predictions of the frequency dependence displayed by near-resonant chiroptical properties. Several extensions to incorporate dephasing and/or depopulation effects have been reported [60, 61]; however, such efforts typically rely on a single phenomenological decay rate (Γ_{eg}) that uniformly describes all electronic manifolds and, therefore, excludes pertinent differences among their relaxation processes.

11.3. EXPERIMENTAL METHODS

Instruments designed to probe the dispersive components of natural optical activity (CB) commonly are referred to as polarimeters or spectropolarimeters, with the distinction between the two nominally depending on whether fixed-frequency or continuously tunable electromagnetic radiation is utilized. While the diversity of such devices reflects their long history of development and broad range of applications [6, 53, 62], they all usually can be reduced to three basic ingredients that must appear in succession: (i) a wavelength-resolved (or near-monochromatic) source of incident plane-polarized light; (ii) a chiral sample of interest; and (iii) an analyzer capable of discriminating changes in the polarization state for transmitted light. The accuracy of CB studies performed under isotropic liquid-phase or vapor-phase conditions typically scales in direct proportion to the pathlength (ℓ), concentration (C), and enantiomeric purity (*%ee*) of the targeted molecules [cf. Eq. (11.16)]; however, a myriad of other factors will contribute to the sensitivity and resolution attained by a particular apparatus, including the quality of polarization optics (used to create and analyze optical polarization) and the precision with which they can be adjusted (so as to gauge the rotation of optical polarization). For modern quantitative work, the venerable manual polarimeter, where the ability to discern chiroptical effects is subject to the limitations of human perception and judgment, has been supplanted by fully automatic instruments based upon sophisticated digital signal-processing algorithms.

Commercial liquid-phase polarimeters usually employ filtered light from atomic resonance lamps (e.g., Na I and Hg I) as the excitation source, thereby permitting CB measurements to be performed at discrete wavelengths spanning the visible and ultraviolet regions, the most common of which (for historical reasons) corresponds to the 589.3 nm *D*-line emission of neutral sodium [6]. Based upon a nominal pathlength of $\ell = 1$ dm, such instruments typically have specified angular resolutions and accuracies of $\leq$1 mdeg and $\leq\pm$3 mdeg, respectively, with at least one manufacturer claiming an accuracy of $\pm$0.3 mdeg for samples of low rotation ($|\phi(\omega)| < 1$ deg) [63]. Standalone spectropolarimeters, as required for the acquisition of continuous ORD profiles, were once commonplace [53], but now have been relegated to an accessory on modern ECD

spectrometers, where grating monochromators often are used to disperse and isolate frequency components from a broadband light source.

The unique properties of laser radiation [64] have been exploited to develop a variety of specialized polarimetric instruments, with the enhancement of chiroptical sensitivity and concomitant reduction of requisite sample volumes making such devices particularly well suited for integration into modern analytical separation technologies (e.g., liquid chromatography) [65]. At least one commercial laser polarimeter presently is available [66], where use of 670 nm diode-laser excitation in a unique flow-cell geometry leads to a specified angular resolution of 25 μdeg and a linear dynamic range that approaches 10^6. Based upon a scheme first introduced by Yeung et al. [67] with subsequent refinements following from the work of Bobbitt [68] and others [69], this apparatus relies on a magnetic Faraday rotator to modulate the incident direction of linear polarization at a high frequency. Phase-sensitive detection of optical rotation induced by the chiral sample thus serves to alleviate the deleterious effects arising from amplitude fluctuations inherent to the laser source.

The intrinsic spatial/temporal coherence of laser radiation affords unique opportunities for implementing interferometric probes of dispersive chiroptical properties. Such efforts have culminated in the recent work of Chou et al. [70], where a stabilized Zeeman helium–neon laser operating at 638.3 nm was used to generate correlated pairs of orthogonally plane-polarized P and S ($\vec{\boldsymbol{\varepsilon}}_x$ and $\vec{\boldsymbol{\varepsilon}}_y$) photons that had slightly different frequencies ($\Delta\nu = \nu_P - \nu_S = 2.6$ MHz). Common-path propagation of this unique light source though a chiral medium introduced equal optical rotations into the coupled P–/S–states, which subsequently were separated and detected in a balanced configuration designed to mitigate intensity fluctuations and background noise. The desired angle of polarization rotation [$\phi(\omega)$] was encoded in the differential amplitude of the emerging antisymmetric heterodyne waveforms and could be extracted at shot-noise-limited levels by means of conventional demodulation techniques. The resulting scheme of polarized photon-pair heterodyne interferometry was shown to have an angular sensitivity of better than 55 μdeg/cm for aqueous solutions of glucose [70], representing perhaps the best detection limit demonstrated to date for a single-pass static geometry. Chou and co-workers have documented a variety of applications for this powerful methodology, including investigations of CB phenomena associated with crystalline quartz [71] and the Faraday effect [72].

The circular birefringence that gives rise to most nonresonant manifestations of natural optical activity, $\Delta n(\omega) = n_L(\omega) - n_R(\omega)$, is extremely small, amounting to no more than a few parts per million of $\overline{n}(\omega)$ even for a pure chiral liquid. This situation is exacerbated further in the case of dilute solutions or vapors, where $\Delta n(\omega)$ can be expected to scale in proportion to the concentration or pressure of the dominant enantiomer. The demands placed on the angular resolution and sensitivity of optical-rotation measurements performed under such rarefied conditions can be daunting; however, as shown by Eq. (11.15), the magnitude of $\phi(\omega)$ observed at a given excitation frequency and for a specified target number density can be enhanced readily by expanding the length of sample, ℓ, traversed by electromagnetic radiation. Building upon this basic premise, historical efforts to probe dispersive chiroptical phenomena in the vapor phase have relied on single-pass instruments that required substantial pressure–pathlength products to achieve meaningful results [5, 73–75]. Obviously, it is desirable to increase the effective value of ℓ without simultaneously augmenting the size or volume of the chiral medium, a capability made possible by recent advances in cavity-/resonator-based polarimetric techniques.

The basic scheme for implementing ultrasensitive vapor-phase polarimetry in a tabletop instrument relies upon a high-finesse optical cavity constructed from mirrors of superior quality ($R \approx 1$, where $0 \leq R \leq 1$ is the intensity reflection coefficient), thereby enabling electromagnetic radiation to traverse an entrained chiral sample repeatedly. While the traveling-wave geometry of a ring resonator offers the potential benefit of unidirectional operation [64], this advantage will be tempered by the intrinsic anisotropies incurred from oblique mirror reflections [31]. Consequently, ongoing efforts to develop cavity-enhanced polarimeters have focused primarily on variants of the Malus Fabry–Perot interferometer [76], where polarized light is introduced into one end of a linear resonator formed from two mirrors and the polarization state of light emerging from the opposing end subsequently is analyzed. The normal-incidence reflections (or retroreflections) inherent to this simple experimental configuration greatly facilitate the ability to discern and extract minute birefringence/dichroism signals; however, fruitful application in the realm of chiroptical spectroscopy demands careful consideration of fundamental symmetry principles. In particular, the physical observables associated with ORD and ECD measurements in isotropic media, $\phi(\omega)$ and $\eta(\omega)$ [cf. Eqs. (11.48) and (11.52)], are time-even pseudoscalars [1], implying that they change sign under action of the parity (space-inversion) operator, $\hat{\Pi}$, yet remain unaffected when subjected to transformation by the time-reversal operator, $\hat{\mathrm{T}}$. These properties lead to the precise cancellation of any polarization effects accrued during each *round-trip* pass of electromagnetic radiation through a linear cavity that only contains a substance having natural (field-free) optical activity. Such reciprocal behavior can be attributed to the characteristic inversion of polarization helicity caused by the retroreflection of light from a mirror surface [31].

For natural optical activity to accrue in a linear-resonator configuration, the sign of the chiroptical response experienced by electromagnetic radiation propagating in one direction effectively must be reversed for the (retroreflected) beam that travels in the opposite direction. This can be accomplished by preceding each mirror with an intracavity quarter-wave ($\lambda/4$) retardation plate aligned to compensate for the polarization effects that accompany normal-incidence reflection. Frequency-domain implementations of this scheme have been reported for both liquid-phase [77] and vapor-phase [78] media, with the chirospecific phase/frequency shifts imposed on the helicoidal eigenmodes of a passive interferometer, which had been servo-locked to a stabilized 633 nm (helium–neon) laser source, affording a robust means for detecting chiroptical signatures. When compared to a single-pass instrument of comparable dimensions, the polarimeter developed by Poirson et al. [78] was found to give a signal enhancement factor of $4KF^2/\pi^2 \approx 1700$, where K and F respectively denote the transmission coefficient ($\sim$0.3) and the finesse ($\sim$120) of the Fabry–Perot cavity, the latter being related, in part, to mirror reflectivity through $F = \pi\sqrt{R}/(1-R)$. Although quantitative measurements of $[\alpha]_\lambda^T$ were not attempted, the estimated angular sensitivity of 1 μdeg attained over a pathlength of $\ell = 30$ cm readily enabled the optical rotation of enantiomerically enriched limonene vapor to be observed under ambient conditions. An intriguing variant of this approach has been suggested by Vollmer and Fischer [79], where free-space coupling of a chiral liquid ($\ell = 10$ cm) into a fiber-loop (ring) resonator ($\lambda \approx 763$ nm) allowed attendant CB phenomena to be encoded as differential frequency shifts appearing on the circularly polarized cavity modes.

Figure 11.2 schematically illustrates the experimental configuration for cavity ring-down polarimetry (CRDP) [80–82], which extends the basic concepts of Malus Fabry–Perot interferometry into the time domain. The depicted polarimetric scheme builds upon the exquisite trace-species sensitivity afforded by long-pathlength cavity

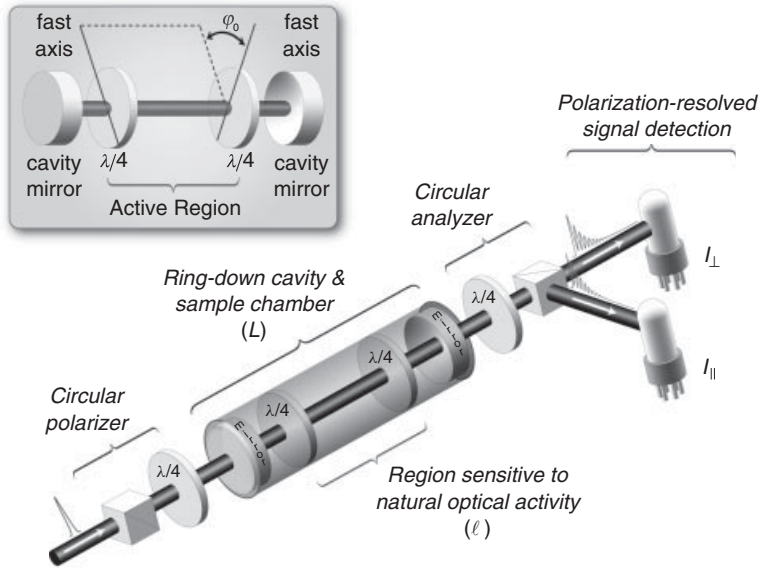

Figure 11.2. Schematic diagram of CRDP apparatus. Pulsed laser radiation traverses a circular polarizer consisting of a tandem calcite prism and quarter-wave plate ($\lambda/4$) before being coupled into a high-finesse linear cavity of length L. Matched intracavity $\lambda/4$ retardation plates are aligned to produce a stable linearly polarized field over the intervening region of length ℓ, thereby making this portion of the apparatus sensitive to the accruing effects of natural optical activity. Emerging light is imaged onto two identical detectors that separately monitor temporal profiles for the two linear components (parallel and perpendicular) generated by a circular polarization analyzer. The inset depicts the arrangement of cavity optics, highlighting the relative offset, φ_0, purposely introduced between the fast axes of intracavity waveplates so as to resolve the sign of measured specific rotation. (*See insert for color representation of the figure.*)

ring-down spectroscopy (CRDS), [83] as augmented by inserting polarization-specific components into the light-injection stage, stable linear-resonator assembly, and signal-detection train of a conventional (pulsed) CRDS instrument. Variants of this approach designed to probe dispersive and absorptive chiroptical phenomena have been elaborated [81], with studies of vapor-phase circular birefringence achieving an angular resolution of $<2\,\mu$deg/cm for (single-pass) sample lengths of $\ell \leq 1$m [80, 84, 85]. The related technique of polarization-dependent CRDS has enabled Engeln et al. [86] to measure the Faraday effect in achiral gases with an estimated noise floor of $\sim 0.6\,\mu$deg/cm. In part, this detection limit reflects the time-odd/parity-even nature of the underlying (magnetically induced) matter-field interaction [1], which dispenses with the need to introduce lossy retardation plates into a high-finesse optical cavity.

The CRDP scheme benefits from two features inherent to all ring-down techniques [83]: (i) long effective sample pathlengths arising from numerous passes of light through the apparatus and (ii) relative immunity to fluctuations of the excitation source owing to the measurement of signal accumulation *rates* rather than cumulative signal *amplitudes*. For a stable cavity of length L constructed from identical mirrors of reflectivity R, the active fraction of the resonator that will respond to the effects of natural optical activity, $f_{act} = \ell/L$, is governed by the separation between intracavity waveplates, ℓ.

Initial alignment of these retardation elements in an evacuated polarimeter establishes a recurrent state of plane polarization over the intervening region, the characteristics of which are analyzed by projecting the light that emerges from the cavity onto orthogonal linear-polarization detection channels (designated as "$\parallel$" and "$\perp$"). The resulting signal intensities can be expressed in terms of the number of round trips, N_{rt}, undergone by a laser pulse injected into the apparatus at reference time $t = 0$ [81, 84]:

$$I_{\parallel}(N_{rt}) = \frac{1}{2}R^{2N_{rt}}e^{-2(N_{rt}+\frac{1}{2})\overline{\kappa}(\omega)L} \left\{\cosh[(N_{rt}+\tfrac{1}{2})\Delta\kappa(\omega)\ell] + \cos[4(N_{rt}+\tfrac{1}{2})(\varphi_0+\varphi(\omega)\ell)]\right\}, \tag{11.56}$$

$$I_{\perp}(N_{rt}) = \frac{1}{2}R^{2N_{rt}}e^{-2(N_{rt}+\frac{1}{2})\overline{\kappa}(\omega)L} \left\{\cosh[(N_{rt}+\tfrac{1}{2})\Delta\kappa(\omega)\ell] - \cos[4(N_{rt}+\tfrac{1}{2})(\varphi_0+\varphi(\omega)\ell)]\right\}, \tag{11.57}$$

where $\overline{\kappa}(\omega)$ and $\Delta\kappa(\omega)$ denote the average and circular-differential linear-napierian absorption coefficients for an entrained chiral vapor [cf. Eqs. (11.21) and (11.23)] with the associated polarization rotation per unit length being specified by $\varphi(\omega) = \phi(\omega)/\ell$ [cf. Eq. (11.15)]. The quantity φ_0, which represents a fixed angular offset mechanically imposed between retardation axes of the intracavity waveplates (cf. inset of Figure 11.2), leads to a progressive (pass-by-pass) rotation of linear polarization in the active region of the evacuated polarimeter. The quadrature modulation of $I_{\parallel}(N_{rt})$ and $I_{\perp}(N_{rt})$ waveforms produced by nonzero φ_0 allows for the phase-sensitive (signed) detection of $\phi(\omega)$ and simultaneously ameliorates the effects of instrumental imperfections [81]. The CRDP signal expressions can be recast as functions of time, $t = N_{rt}t_{rt}$, by taking into consideration the round-trip period for an optical pulse propagating through the resonator, $t_{rt} = 2L/c$. Consequently, the factors of $R^{2N_{rt}}$ lead to exponentially decaying temporal profiles for the empty apparatus, e^{-t/τ_0}, where the characteristic lifetime of the cavity (*sans* chiral sample) is defined by $\tau_0 = L/(c|\ln R|)$. In practice, the effective value of R employed in these expressions embodies the intrinsic reflectivity of each mirror substrate as well as the inevitable losses incurred from the adjacent intracavity waveplate.

The CRDP configuration of Figure 11.2 has been optimized for dispersive chiroptical (CB) analyses [81, 84], with subtraction of Eqs. (11.56) and (11.57) leading to:

$$I_{-}(t) = I_{\parallel}(t) - I_{\perp}(t) = Ae^{-t/\tau}\cos[\Omega t + \Phi], \tag{11.58}$$

where $A = e^{-\overline{\kappa}(\omega)L}$, $1/\tau = 1/\tau_0 + c\overline{\kappa}(\omega)$, $\Omega = 2c(\varphi_0+\varphi(\omega)\ell)/L$, and $\Phi = 2(\varphi_0+\varphi(\omega)\ell)$. This expression has the form of an idealized free-induction decay, as often encountered in studies of Fourier-transform magnetic resonance spectroscopy [87]. In particular, the extracted frequency of oscillation, Ω, encodes both the sign and the magnitude of vapor-phase circular birefringence:

$$\Omega = \Omega_0 + \Omega_N N = \frac{2c}{L}\varphi_0 + 2c\left(\frac{\ell}{L}\right)\varphi(\omega), \tag{11.59}$$

where the subscript on Ω_N emphasizes the fact that this quantity scales in direct proportion to the number density (N) or pressure ($p = Nk_BT$) of the chiral medium, as shown explicitly by the definition of $\phi(\omega) = \varphi(\omega)\ell$ [cf. Eqs. (11.28) and (11.48)]. For

the modulated mode of CRDP operation obtained by having $\varphi_0 \neq 0$ [81], the action of natural optical activity will either increase or decrease Ω relative to that of the empty polarimeter ($\Omega_0 \equiv 2c\varphi_0/L$), with the phase of the observed frequency shift, $\Delta\Omega = \Omega - \Omega_0 = \Omega_N N = 2c f_{act}\varphi(\omega)$, reflecting the enantiomeric form of the targeted species. Consequently, the coveted vapor-phase specific optical rotation, $[\alpha]_\lambda^T$, can be extracted readily from the (signed) slope of the linear curve that results from plotting $\Delta\Omega$ as a function of p. This procedure has been applied successfully to a wide variety of volatile organic compounds [84, 85, 88, 89] where effective sample pathlengths in excess of 1 km (i.e., for an apparatus of $L \approx 1.2$-m physical length) have permitted the first quantitative measurements of dispersive chiroptical phenomena to be performed on ambient gases.

All of the aforementioned polarimetric instruments rely on the pathlength-dependent phase shifts that a chiral medium introduces between left-circular and right-circular polarization components, ultimately leading to a discernable optical rotation for transmitted light. Such behavior stems from the difference in refractive index (or CB) that exists for the helicity basis, $\Delta n(\omega) = n_L(\omega) - n_R(\omega) \neq 0$ [cf. Section 11.2.2]; however, as first noted by Fresnel [33, 90], the ensuing chiroptical properties also should be manifest in refraction and reflection (which implicitly depend on $\Delta n(\omega)$ through Snell's Law [30]). Ghosh and Fischer [91] have exploited this concept to implement new variants of liquid-phase polarimetry whereby the double refraction or reflection of plane-polarized light at a chiral–achiral interface causes a characteristic bifurcation of the emerging beam. The angular deviation between the resulting pairs of refracted/reflected waves was shown to be in quantitative agreement with canonical ORD profiles acquired simultaneously for pure chiral liquids and enantiomerically enriched solutions. Analogous circular-differential techniques have been demonstrated by these authors for diffractive scattering [92] and the magnetically induced Faraday effect [93]. Since the underlying interfacial phenomena take place over distances amounting to only a few wavelengths of light, the apparatus can be miniaturized readily without suffering an appreciable loss in sensitivity. Consequently, the double refraction/reflection methodology promises to open new vistas in the realm of chiroptical spectroscopy, potentially enabling optical activity to be studied in novel substrates (e.g., thin films) and otherwise inaccessible environments (e.g., microfluidic devices).

11.4. INTRINSIC OPTICAL ACTIVITY

11.4.1. The Optical Rotation of Isolated Molecules

The investigation of electronic optical activity (ORD and ECD) in condensed media has enjoyed a long and fruitful history [14, 53], serving to elucidate many of the key features that distinguish chiral molecules and their interactions. Through careful consideration of pertinent experimental parameters, such efforts, in principle, can reveal *intrinsic* chiroptical properties, which can be defined broadly as the response evoked from a nominally isolated species that is perturbed negligibly by its surroundings. For polarimetric studies of circular birefringence in the solution phase, this demands selection of innocuous or non-interacting solvents (e.g., cyclohexane), with concentrations being kept sufficiently low so as to minimize any solute–solute coupling that might lead to the formation of aggregates and/or complexes (processes of interest in their own right) [94–97]. Even for the most auspicious of circumstances, Polavarapu et al. [98] have emphasized the importance of extrapolating optical-rotation measurements and resulting specific rotatory powers to the hypothetical limit of infinite dilution.

The top panel of Figure 11.3 presents ORD data acquired for (*S*)-methyloxirane under both solvated and isolated (vapor-phase) conditions. Owing to its conformational rigidity and computational tractability, this small epoxide has emerged as a model system for *ab initio* predictions of optical activity. The dotted curves follow from interpolation of canonical solution-phase polarimetric measurements performed at discrete excitation frequencies (ω) denoted by the individual symbols, with concentrations being

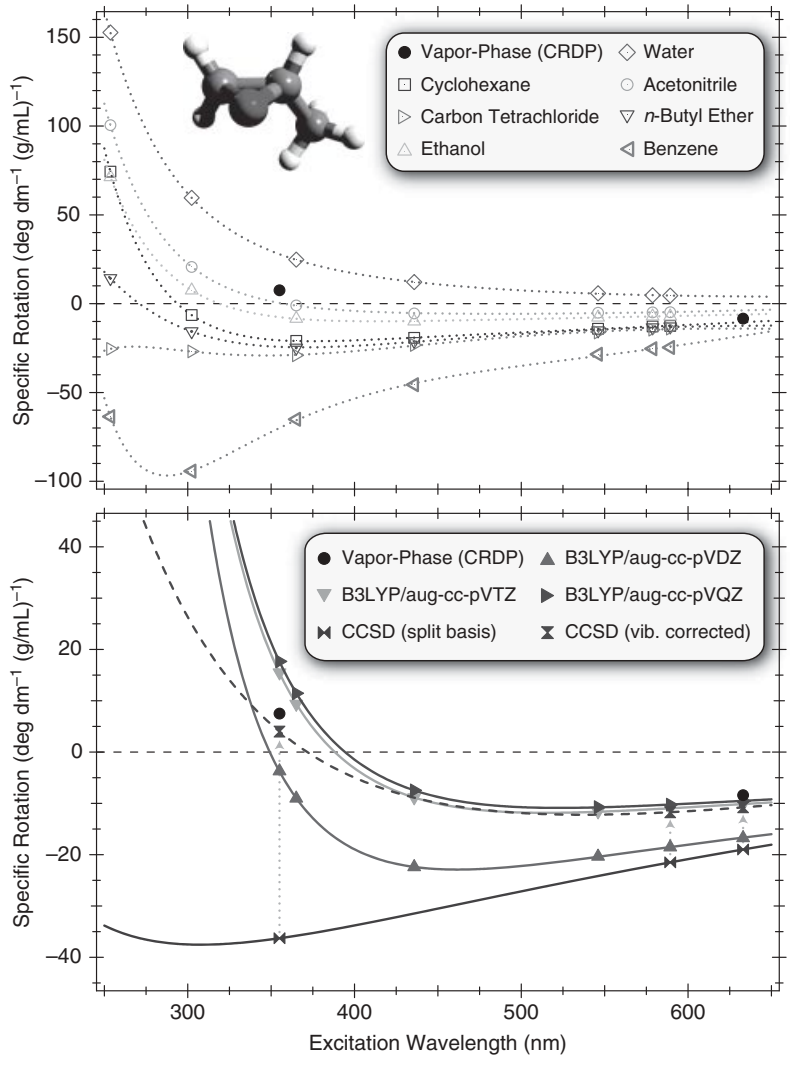

Figure 11.3. Optical Rotation of (*S*)-Methyloxirane. The top panel contrasts optical rotatory dispersion profiles acquired for (*S*)-methyloxirane under complementary solution-phase (opened symbols and dotted curves) and vapor-phase (closed circular symbols) conditions, where the latter isolated-molecule results stem from CRDP measurements. The bottom panel compares the intrinsic chiroptical response to predictions obtained at density-functional (triangular symbols) and coupled-cluster (hourglass symbols) levels of theory, with the dashed curve and associated arrows depicting the correction of CCSD linear-response calculations for vibrational motion of the nuclear framework [110, 111] (cf. Table 11.1).

kept low enough to minimize solute–solute interactions. The selected solvents (cf. legend) possess a broad spectrum of chemical and physical attributes, including distinct permanent electric-dipole moments μ, static dielectric constants $\varepsilon = \varepsilon(0)$, and refractive indices $n(\omega) \approx \sqrt{\varepsilon(\omega)}$. Even a cursory inspection of this figure reveals marked differences among the solution-phase results, thereby demonstrating conclusively that the observed behavior does not reflect an intrinsic property of the solute molecule entrained in an otherwise passive medium. While the CB of methyloxirane appears to be especially susceptible to environmental perturbations [99], numerous studies performed on species having diverse structural motifs and functional moieties have documented the pronounced influence that solvation can exert on dispersive/absorptive chiroptical phenomena [14].

The application of cavity-enhanced techniques to gas-phase polarimetry has provided a new means for extracting intrinsic properties from rarefied environments [80, 84]. The isolated-molecule results in Figure 11.3 stem from CRDP analyses performed independently at $\lambda = 355$ nm and $\lambda = 633$ nm, where CB signals could be resolved readily for ambient (25°C) samples of (*S*)-methyloxirane having pressures of $p \ll 1$ Torr. The unparalleled sensitivity of this polarimetric scheme comes at the expense of limited spectral versatility, because the underlying long-pathlength advantage depends critically on the quality of narrow-band dielectric coatings applied to mirror substrates (for reflectivity) and intracavity waveplates (for antireflectivity). Since the requisite high finesse of the resonator assembly only can be maintained over a limited range of incident wavelengths, all optical components must be replaced whenever a substantive change in excitation frequency is desired. Four historical attempts to explore circular birefringence in gaseous media have been reported prior to modern cavity-based measurements [5, 73–75], including the seminal 1817 study of Biot that first demonstrated the existence of such phenomena in an $\ell = 30$ m column of vapor from boiling turpentine, but failed to obtain quantitative information prior to conflagration of the apparatus [5]. Efforts to probe gas-phase ORD in single-pass instruments appear to have culminated in the 1931 work of Lowry and Gore [75], which examined camphor and camphorquinone at elevated temperatures (180–200°C) in the near-ultraviolet region proximate to their ketonic and quinonoid absorption bands.

Direct comparison of the complementary solution-phase and vapor-phase results depicted in Figure 11.3 highlights the pronounced and, oftentimes, counterintuitive effects incurred by complex solvation phenomena. This assertion is demonstrated most succinctly by the values of specific optical rotation deduced for (*S*)-methyloxirane at 355 nm excitation, where removal of the surrounding solvent (except water) leads to a reversal of sign for $[\alpha]^{25^\circ\mathrm{C}}_{355\ \mathrm{nm}}$. Indeed, analogous polarimetric studies performed on a wide variety of conformationally rigid chiral species have shown that solvents possessing high dielectric constants (e.g., acetonitrile) consistently provide better mimics for intrinsic (vapor-phase) chiroptical response than their less-polar counterparts (e.g., cyclohexane) [84, 88, 89], a finding that would appear to contradict conventional wisdom regarding the nature of solute-solvent interactions.

The dispersive aspects of chiroptical behavior (CB or ORD) impose unique challenges for quantitative theoretical calculations, even if the complications arising from environmental perturbations (e.g., solvation) are ignored. Rather than depending on the characteristics of a localized chromophore as is the case for absorptive CD phenomena [14], CB is a composite molecular property that reflects the dynamical response of the entire electronic distribution to oscillating electromagnetic fields, an assertion reinforced by the explicit summation over all excited states appearing in definitions of the mixed

$E1-M1$ polarizability tensor [cf. Eqs. (11.32) and (11.38)]. Consequently, the reliability of computational predictions for optical activity should scale directly with the ability of the underlying *ab initio* method to successfully reproduce the excitation energies ($\hbar\omega_{eg}$) and transition moments (^{eg}R) of the targeted chiral species. Aside from incorporating extensive sets of diffuse basis functions designed to describe the periphery of the electronic wavefunction accurately [100, 101], such analyses must be capable of treating pervasive electron-correlation effects at high levels of theory.

The vast majority of optical activity calculations reported to date have exploited density functional theory (DFT) [102], specifically the time-dependent variant of TDDFT [103], which offers an effective balance between computational cost and accuracy. Despite use of correlation-exchange models that typically have been optimized for the elucidation of thermochemical (rather than linear-response) characteristics [104], numerous studies have documented the ability of DFT to predict ORD and ECD profiles quantitatively. In particular, Stephens and coworkers have performed extensive TDDFT analyses of CB [105, 106], with targeted sets of conformationally rigid chiral species found to exhibit root-mean-square deviations of $\sigma \approx 29\,\mathrm{deg\,dm^{-1}\,(g/mL)^{-1}}$ between their computed (solvent-free) and measured (solvated) specific rotatory powers at sodium D-line excitation (589.3 nm). Such results have prompted these authors to propose a "zone of indeterminacy" amounting to $\pm 2\sigma$ within which DFT-calculated values of $[\alpha]^{T}_{589.3\ \mathrm{nm}}$ cannot be used to determine absolute stereochemical configuration reliably (i.e., with $> 95\%$ confidence) [106]. The shortcomings inherent to DFT have prompted several research groups to pursue alternative treatments of chiroptical response built upon the potent coupled-cluster (CC) paradigm [107], a wavefunction-based approach capable of incorporating dynamic electron-correlation effects rigorously in a convergent framework that systematically can be improved to reach the exact (Born–Oppenheimer) electronic wavefunction. Although demanding substantially more computational resources than their DFT counterparts, CC methods have been shown to provide exceptionally accurate predictions for diverse molecular properties [108, 109].

Since gas-phase polarimetry dispenses with the need to model complex solvation processes, information gleaned from such studies can be used to critically assess burgeoning *ab initio* predictions of chiroptical behavior. The bottom panel of Figure 11.3 contrasts CRDP measurements of intrinsic optical rotation for (S)-methyloxirane with ORD profiles computed by applying density-functional (hybrid B3LYP correlation-exchange functional) and coupled-cluster (CCSD with a polarization-augmented basis of split double-ζ and triple-ζ character) [110, 111] techniques to equilibrium geometries optimized, respectively, at the MP2/aug-cc-pVQZ and B3LYP/aug-cc-pVTZ levels of theory. A subset of these linear-response calculations has been compiled in Table 11.1, where tabulated DFT parameters demonstrate the effect of successively improving basis quality. While the B3LYP/aug-cc-pVDZ scheme has been suggested to provide a reasonable compromise between computational costs and predictive accuracy for dispersive chiroptical phenomena [100, 105, 106], the resulting $[\alpha]^{T}_{\lambda}$ values for methyloxirane differ markedly from those obtained by analogous B3LYP/aug-cc-pVTZ and B3LYP/aug-cc-pVQZ treatments, which are presumed to more closely approximate the complete basis-set limit [112].

All of the quantum-chemical results depicted in Figure 11.3 concur in predicting a negative specific rotatory power for (S)-methyloxirane vapor at 633 nm, thereby corroborating the absolute stereochemical configuration of the chiral species targeted by CRDP experiments. While B3LYP/aug-cc-pVTZ and B3LYP/aug-cc-pVQZ linear-response calculations reproduce the positive value of $[\alpha]^{25^{\circ}\mathrm{C}}_{\lambda}$ measured at $\lambda = 355$ nm, their double-ζ counterparts, as well as CCSD analyses for the rigid equilibrium structure, suggest the

TABLE 11.1. Intrinsic Optical Rotation of (*S*)-Methyloxirane[a]

Quantity	Specific Optical Rotation ($\deg\,dm^{-1}(g/mL)^{-1}$)		
	633.0 nm	589.3 nm	355.0 nm
Experimental (CRDP)	−8.39 ± 0.20	−7.27 ± 0.38	7.49 ± 0.30
DFT(B3LYP)			
aug-cc-pVDZ	−16.74	−18.53	−3.71
aug-cc-pVTZ	−10.19	−10.98	15.47
aug-cc-pVQZ	−9.56	−10.25	17.69
CCSD(*split basis*)			
Equilibrium contribution: $[\alpha]_\lambda^{eq}$	−18.99	−21.50	−36.29
Anharmonic contribution: $[\alpha]_\lambda^{anh}$	+3.02	+3.56	+12.84
Harmonic contribution: $[\alpha]_\lambda^{har}$	+5.19	+6.22	+27.46
Corrected response: $[\alpha]_\lambda^{25^\circ C}$	−10.78	−11.72	4.01

[a] The specific optical rotation for isolated (*S*)-methyloxirane is compared with predictions obtained from density-functional theory and coupled-cluster calculations. The experimental value at 589.3 nm is interpolated from vapor-phase CRDP measurements performed at 633 nm and 355 nm by applying a quadratic Drude-like model of the form $[\alpha]_\lambda^T = a_0 + a_2/\lambda^2$, where $a_0 = -15.68 \pm 0.32\,\deg\,dm^{-1}(g/mL)^{-1}$ and $a_2 = (2.920 \pm 0.066) \times 10^6\,\deg\,dm^{-1}(g/mL)^{-1}\,nm^2$. DFT results are presented for various basis sets used in conjunction with the hybrid B3LYP correlation-exchange functional (geometry optimized at MP2/aug-cc-pVQZ), while the CCSD treatment reported by Kongsted et al. [110, 111] utilized a split basis consisting of aug-cc-pVDZ on carbon, aug-cc-pVTZ on oxygen, and daug-cc-pVDZ on hydrogen (geometry optimized at B3LYP/aug-cc-pVTZ). In the latter case, the vibrationally corrected chiroptical response, $[\alpha]_\lambda^T$, has been partitioned into equilibrium (electronic), anharmonic, and harmonic (thermally averaged at $T = 298.15$ K) contributions, denoted by $[\alpha]_\lambda^{eq}$, $[\alpha]_\lambda^{anh}$, and $[\alpha]_\lambda^{har}$, respectively.

opposite sign. At first glance, the ORD profiles computed by DFT techniques seem to be in much better agreement with vapor-phase data than those emerging from analogous CC treatments, a finding that would appear to contradict the superior accuracy expected for coupled-cluster schemes [108]. However, as demonstrated by the detailed investigations of Tam et al. [113], this behavior stems from a fortuitous cancellation of errors inherent to the density-functional approach, which can be related directly to the incorrect prediction of excited-state transition energies. In particular, underestimation of $\hbar\omega_{eg}$ for the lowest-lying (Rydberg) electronic manifold shifts the corresponding first-order pole in the mixed $E1$–$M1$ polarizability, $G'(\omega)$, to longer wavelengths and leads to a concomitant displacement of the computed ORD curve towards more positive values. Since the CCSD paradigm correctly predicts the location of absorptive resonances in isolated methyloxirane molecules, the glaring discrepancies that exist between observed and calculated chiroptical properties must reflect the action of ancillary effects, such as those arising from vibrational motion of the nuclear framework.

11.4.2. Vibrational Effects

While the fundamental underpinnings of chiroptical spectroscopy performed in the visible and ultraviolet regions of the spectrum usually attribute such phenomena to electronic origins (cf. Section 11.2) [1, 2], the contributing roles of nuclear motion should not be discounted. Even in the absence of conformational flexibility (*vide infra*) or other large-amplitude degrees of freedom, localized vibrational displacement of the molecular

framework can exert a pronounced influence on both dispersive (CB) and absorptive (CD) processes. This assertion is demonstrated succinctly by the family of ostensibly achiral compounds that become optically active upon isotopic substitution [16] (e.g., (*S,S*)-[2,3-$^2H_2$] oxirane [114]), where the underlying isotopically engendered chirality (IEC) must reflect vibrational perturbations acting on the otherwise achiral electronic wavefunction (the latter being implied by strict application of the adiabatic Born–Oppenheimer approximation). The precise mechanism for IEC has been a subject of considerable speculation [115], leading to suggestions of vibrationally averaged structures that are made chiral by the effects of mechanical anharmonicity (e.g., imbuing minute differences between the lengths of C–H and C–D bonds) and of reoriented electric/magnetic transition moments induced by vibronic coupling among electronic manifolds.

The putative influence of nuclear motion upon electronic optical activity (CB) is illustrated graphically in Figure 11.4 for the case of (*S*)-methyloxirane. The top panel depicts the threefold-symmetric potential energy curve computed at the B3LYP/aug-cc-pVTZ level of theory by performing restricted geometry optimizations as a function of methyl-group torsional displacement, the latter being quantified by the dihedral angle, τ_{HCCO}, that describes the orientation of a selected hydrogen atom in the $-CH_3$ moiety. Three equivalent minima (maxima) are evident over this cyclic coordinate, being located at τ_{HCCO} values of 44.1° (−15.9° or 344.1°), 164.1° (104.1°), and 284.1° (224.1°). The quantized energy levels (E_v) and associated probability densities ($|\psi_v(\tau_{HCCO})|^2$) superimposed on this figure follow from an approximate treatment of the internal rotor Hamiltonian [116], with different colors being used to distinguish alternating eigenstates of *A* (nondegenerate) and *E* (doubly degenerate) character under the C_3 rotational subgroup.

The bottom panel of Figure 11.4 depicts the specific rotatory power of (*S*)-methyloxirane calculated as a function of $-CH_3$ torsion by applying the B3LYP/aug-cc-pVTZ linear-response formalism at three excitation wavelengths: 633 nm, 589.3 nm, and 355 nm. Surprisingly large changes in the magnitude of $[\alpha]_\lambda^T$ are predicted to occur as the orientation of the methyl group is varied, with the sign of this quantity also found to switch in a periodic fashion. While higher-lying (torsional) eigenstates show unmistakable evidence for tunneling among the potential minima, their less-energetic counterparts remain fairly well localized, in keeping with the rigid structural assumption often invoked under ambient (thermal) conditions. Nevertheless, even the zero-point level exhibits significant probability density over wide swaths of the accessible τ_{HCCO} parameter space, thereby suggesting that the computed optical activity must be averaged over the corresponding range of nuclear coordinates. Torsional motion has been found to be an especially potent mediator of ORD profiles in methyloxirane and related rigid species [110, 117–119]; however, other vibrational degrees of freedom certainly contribute to the observed chiroptical response, as well as to its dependence on temperature and other environmental variables.

The influence of nuclear motion on molecular properties long has been a subject of experimental and theoretical interest [120]. Recent advances in this area (including those directed towards the elucidation of chiroptical behavior) have been motivated by the development of evermore accurate and reliable electronic-structure calculations, with quantitative comparison of such *ab initio* predictions to laboratory measurements often demanding the explicit consideration of zero-point (vibrational) effects [117, 119, 121–123] and of temperature-dependent contributions arising from the population of excited (vibrational/rotational) manifolds [124, 125]. In the canonical treatment, the property under investigation, $P \equiv P(\mathbf{Q})$, is expanded as a multidimensional Taylor series of nuclear coordinates, $\mathbf{Q} \equiv \{Q_1, Q_2, \ldots, Q_{N_{vib}}\}$, the latter often being described by the N_{vib} normal modes of vibration [126]. The resulting expression formally contains

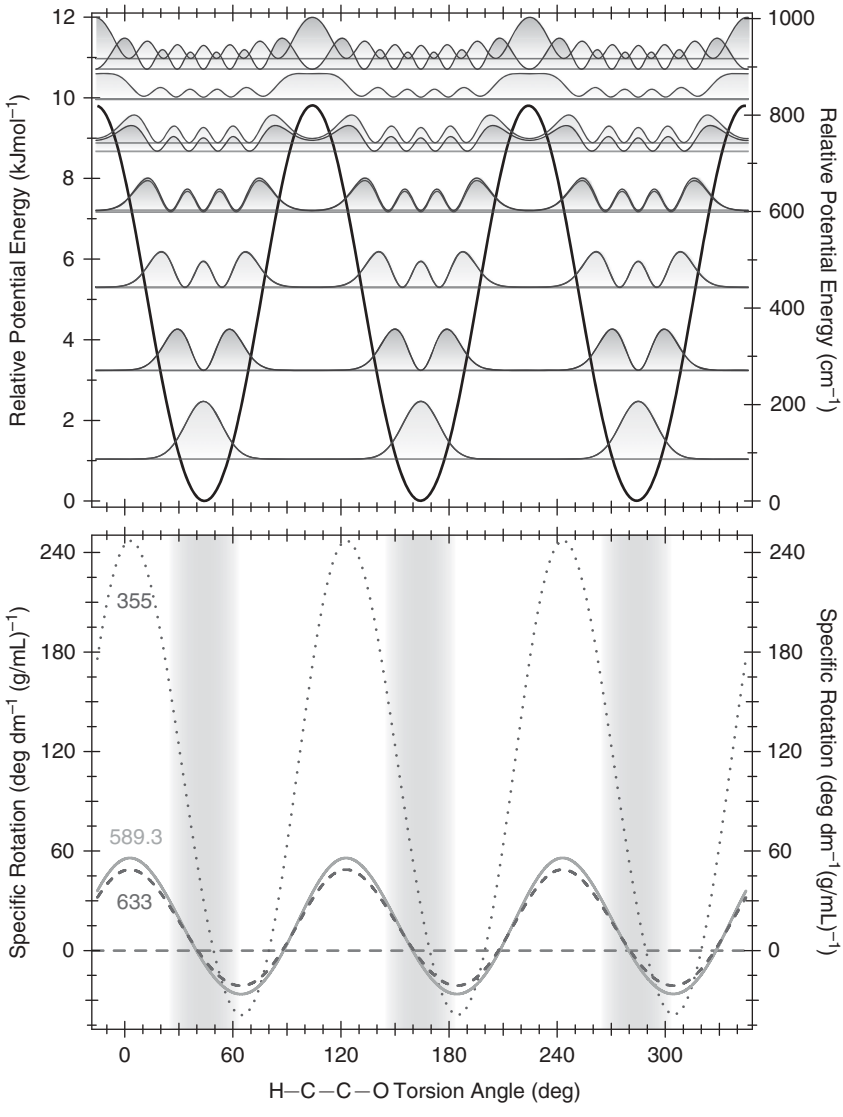

Figure 11.4. Torsional displacements in (*S*)-methyloxirane. The top panel presents the threefold symmetric torsional potential for (*S*)-methyloxirane computed at the B3LYP/aug-cc-pVTZ level of theory. Probability densities for the lowest-lying eigenstates are superimposed, with different colors being used to distinguish alternating levels of *A* and *E* character under the C_3 rotational subgroup (note that near degeneracy of first few *A* and *E* levels leads to a merged green coloration). The bottom panel depicts the torsional dependence of specific optical rotation predicted by B3LYP/aug-cc-pVTZ linear-response calculations performed at 633 nm (dashed curve), 589.3 nm (solid curve), and 355 nm (dotted curve).

an infinite number of terms that entail successively higher-order derivatives of P with respect to the Q_i:

$$P = \sum_{n=0}^{\infty} P_n = P_0 + \sum_{i=1}^{N_{\text{vib}}} \left(\frac{\partial P}{\partial Q_i} \right)_0 Q_i + \frac{1}{2} \sum_{i=1}^{N_{\text{vib}}} \sum_{j=1}^{N_{\text{vib}}} \left(\frac{\partial^2 P}{\partial Q_i \partial Q_j} \right)_0 Q_i Q_j + \cdots, \tag{11.60}$$

where the point about which the expansion is taken (designated by subscript "0") usually coincides with the equilibrium (minimum-energy) configuration of the nuclear framework (*vide infra*). For a given vibrational eigenstate $|\psi_{\mathbf{v}}\rangle \equiv \psi_{\mathbf{v}}(\mathbf{Q})$, as specified by the collective set of quantum numbers $\mathbf{v} \equiv \{\mathrm{v}_1, \mathrm{v}_2, \ldots, \mathrm{v}_{N_{\text{vib}}}\}$, the expectation (or average) value of P follows from

$$\langle P \rangle_{\mathbf{v}} = \sum_{n=0}^{\infty} \langle P_n \rangle_{\mathbf{v}} = P_0 + \sum_{i=1}^{N_{\text{vib}}} \left(\frac{\partial P}{\partial Q_i} \right)_0 \langle Q_i \rangle_{\mathbf{v}} + \frac{1}{2} \sum_{i=1}^{N_{\text{vib}}} \sum_{j=1}^{N_{\text{vib}}} \left(\frac{\partial^2 P}{\partial Q_i \partial Q_j} \right)_0 \langle Q_i Q_j \rangle_{\mathbf{v}} + \cdots, \tag{11.61}$$

where $\langle A \rangle_{\mathbf{v}} \equiv \langle \psi_{\mathbf{v}} | A | \psi_{\mathbf{v}} \rangle$ and $\langle \psi_{\mathbf{v}'} | \psi_{\mathbf{v}} \rangle = \delta_{\mathbf{v}',\mathbf{v}} \equiv \prod_{i=1}^{N_{\text{vib}}} \delta_{\mathrm{v}_i',\mathrm{v}_i}$.

Quantitative descriptions of multidimensional nuclear dynamics in polyatomic species often require explicit consideration of effects arising from intrinsic anharmonicity of the potential energy surface, $V(\mathbf{Q})$. Although potent variational methods exist for predicting the rotation–vibration structure of small molecules with near-spectroscopic accuracy [127], analyses performed on larger systems commonly rely on the techniques of time-independent perturbation theory [122, 123, 128], which afford a reasonable compromise between computational cost and reliability. For vibrational degrees of freedom, this approach usually exploits the separable harmonic-oscillator eigenbasis, $|\psi_{\mathbf{v}}^{(0)}\rangle \equiv \psi_{\mathbf{v}}^{(0)}(\mathbf{Q}) = \prod_{i=1}^{N_{\text{vib}}} \psi_{\mathrm{v}_i}^{(0)}(Q_i)$, with the unperturbed (zero-order) eigenvalues being specified by $E_{\mathbf{v}}^{(0)} = \sum_{i=1}^{N_{\text{vib}}} \hbar\omega_i(\mathrm{v}_i + 1/2)$, where the angular (linear) frequency, $\omega_i(\nu_i)$, for each eigenmode can be related to the attendant wavenumber, $\tilde{\nu}_i$, through $\omega_i = 2\pi\nu_i = 2\pi c\tilde{\nu}_i$. Second-order perturbative expansions generally are preferred so as to generate closed-form expressions for energy-related parameters [122, 123, 128]; however, for the present discussion of vibrational averaging, it proves convenient to consider only first-order wavefunction corrections:

$$|\psi_{\mathbf{v}}\rangle \approx |\psi_{\mathbf{v}}^{(0)}\rangle + |\psi_{\mathbf{v}}^{(1)}\rangle = |\psi_{\mathbf{v}}^{(0)}\rangle + \sum_{\mathbf{v}'} a_{\mathbf{v}',\mathbf{v}}^{(1)} |\psi_{\mathbf{v}'}^{(0)}\rangle. \tag{11.62}$$

The coefficients $a_{\mathbf{v}',\mathbf{v}}^{(1)}$ are defined formally by matrix elements of the perturbation Hamiltonian, $\hat{\mathrm{H}}_{\text{vib}}^{(1)}$, that describes the effects of vibrational anharmonicity:

$$a_{\mathbf{v}',\mathbf{v}}^{(1)} = \langle \psi_{\mathbf{v}'}^{(0)} | \psi_{\mathbf{v}}^{(1)} \rangle = \frac{\langle \psi_{\mathbf{v}'}^{(0)} | \hat{\mathrm{H}}_{\text{vib}}^{(1)} | \psi_{\mathbf{v}}^{(0)} \rangle}{E_{\mathbf{v}}^{(0)} - E_{\mathbf{v}'}^{(0)}} \qquad (\mathbf{v}' \neq \mathbf{v}), \tag{11.63}$$

where proper normalization of $|\psi_{\mathbf{v}}\rangle$ demands that $\langle \psi_{\mathbf{v}}^{(0)} | \psi_{\mathbf{v}}^{(1)} \rangle + \langle \psi_{\mathbf{v}}^{(1)} | \psi_{\mathbf{v}}^{(0)} \rangle = 0$ [50]. The molecular potential energy surface commonly is expanded as a multidimensional Taylor series about the equilibrium nuclear configuration, with truncation at quadratic

terms leading to the canonical normal modes of vibration. Consequently, $\hat{\mathrm{H}}^{(1)}_{\mathrm{vib}}$ reflects the lowest-order (cubic) contributions neglected by this harmonic approximation:

$$\hat{\mathrm{H}}^{(1)} = \frac{1}{6}\sum_{j=1}^{N_{\mathrm{vib}}}\sum_{k=1}^{N_{\mathrm{vib}}}\sum_{l=1}^{N_{\mathrm{vib}}}\left(\frac{\partial^3 V(\mathbf{Q})}{\partial Q_j \partial Q_k \partial Q_l}\right)_0 Q_i Q_j Q_l = \frac{1}{6}\sum_{j,k,l=1}^{N_{\mathrm{vib}}} \Phi_{jkl} Q_j Q_k Q_l, \tag{11.64}$$

where Φ_{ijl} denotes the cubic force constant. Building upon this perturbative framework, the coordinate expectation values in Eq. (11.61) can be evaluated readily to find [129]:

$$\begin{aligned}\langle Q_i\rangle_{\mathbf{v}} &= \langle\psi_{\mathbf{v}}|Q_i|\psi_{\mathbf{v}}\rangle \approx \langle\psi^{(1)}_{\mathbf{v}}|Q_i|\psi^{(0)}_{\mathbf{v}}\rangle + \langle\psi^{(0)}_{\mathbf{v}}|Q_i|\psi^{(1)}_{\mathbf{v}}\rangle \\ &= -\frac{\hbar}{2\omega_i^2}\sum_{j=1}^{N_{\mathrm{vib}}}\frac{\Phi_{ijj}}{\omega_j}\left(\mathrm{v}_j+\frac{1}{2}\right),\end{aligned} \tag{11.65}$$

$$\begin{aligned}\langle Q_i Q_j\rangle_{\mathbf{v}} &\equiv \langle\psi_{\mathbf{v}}|Q_i Q_j|\psi_{\mathbf{v}}\rangle \approx \langle\psi^{(0)}_{\mathbf{v}}|Q_i Q_j|\psi^{(0)}_{\mathbf{v}}\rangle \\ &= \delta_{ij}\langle\psi^{(0)}_{\mathbf{v}}|Q_i^2|\psi^{(0)}_{\mathbf{v}}\rangle = \delta_{ij}\frac{\hbar}{\omega_i}\left(\mathrm{v}_i+\frac{1}{2}\right),\end{aligned} \tag{11.66}$$

with $\langle Q_i\rangle_{\mathbf{v}}$ vanishing in the strictly harmonic limit (i.e., where $\Phi_{ijj}\to 0$). The vibrational average of property P in eigenstate $|\psi_{\mathbf{v}}\rangle$ now can be expressed as:

$$\begin{aligned}\langle P\rangle_{\mathbf{v}} &= P_0 \;+\left[-\frac{\hbar}{2}\sum_{i=1}^{N_{\mathrm{vib}}}\frac{1}{\omega_i^2}\left(\frac{\partial P}{\partial Q_i}\right)_0\sum_{j=1}^{N_{\mathrm{vib}}}\frac{\Phi_{ijj}}{\omega_j}\left(\mathrm{v}_j+\frac{1}{2}\right)\right]+\frac{\hbar}{2}\sum_{i=1}^{N_{\mathrm{vib}}}\frac{1}{\omega_i}\left(\frac{\partial^2 P}{\partial Q_i^2}\right)_0\left(\mathrm{v}_i+\frac{1}{2}\right) \\ &= P^{eq} + \qquad P^{anh} \qquad + \qquad P^{har},\end{aligned} \tag{11.67}$$

where the second equality highlights the partitioning of $\langle P\rangle_{\mathbf{v}}$ into equilibrium (P^{eq}), anharmonic (P^{anh}) , and harmonic (P^{har}) contributions, the latter two depending, respectively, on the slope and the curvature of the property function, $P(\mathbf{Q})$, proximate to the reference nuclear configuration.[1] The effects of zero-point displacement follow from this expression by setting all vibrational quantum numbers to zero (viz., $\mathbf{v}\to\mathbf{0}$) to obtain $\langle P\rangle_{\mathbf{0}}$. Likewise, contributions arising from the manifold of vibrational states occupied in a thermally equilibrated ensemble of molecules can be described by averaging $\langle P\rangle_{\mathbf{v}}$ over the corresponding Boltzmann distribution:

$$P_T \equiv \sum_{\mathbf{v}}\langle P\rangle_{\mathbf{v}} f_{\mathbf{v}}(T) = \sum_{\mathbf{v}}\langle P\rangle_{\mathbf{v}}\;\frac{e^{-E_{\mathbf{v}}/k_B T}}{q_{\mathrm{vib}}}, \tag{11.68}$$

[1] In keeping with the terminology used to describe vibrational transitions, the P^{anh} terms in Eq. (11.67) embody the effects of "mechanical" anharmonicity (arising from derivatives of the electronic potential energy surface beyond second order) while their P^{har} counterparts reflect the action of "property" anharmonicity (arising from derivatives of the molecular property surface beyond first order). The latter quantities often are equated with "electrical" anharmonicity, since the molecular property surface of interest in vibrational spectroscopy is typically the electric dipole moment.

where $f_{\mathbf{v}}(T) = e^{-E_{\mathrm{v}}/k_B T}/q_{\mathrm{vib}}$ represents the normalized population of quantum state $|\psi_{\mathbf{v}}\rangle$ at absolute temperature T and $q_{\mathrm{vib}} = \sum_{\mathbf{v}} e^{-E_{\mathrm{v}}/k_B T}$ denotes the vibrational partition function. The components of P^{har} and P^{anh} entering into this thermal average can be evaluated as follows:

$$\sum_{\mathbf{v}} \left(\mathrm{v}_i + \frac{1}{2}\right) f_{\mathbf{v}}(T) = \sum_{\mathbf{v}} \left(\mathrm{v}_i + \frac{1}{2}\right) \frac{e^{-E_{\mathrm{v}}/k_B T}}{q_{\mathrm{vib}}} \approx \frac{1}{2}\coth\left[\frac{\hbar\omega_i}{2k_B T}\right], \tag{11.69}$$

where the final equality stems from the harmonic approximation of $E_{\mathbf{v}} \approx E_{\mathbf{v}}^{(0)}$.

The analyses outlined above are based upon expansion of the potential-energy and property-function surfaces about the equilibrium configuration; however, other choices for this reference point have been proposed. In particular, Ruud et al. [117, 121] have advocated use of an effective geometry defined formally by minimizing the sum of electronic and vibrational zero-point energies. This variational approach closely approximates the vibrationally averaged structure of the molecule, with the leading (anharmonic) terms in the perturbative development of the vibrational wavefunction found to vanish such that $|\psi_{\mathbf{v}}\rangle \approx |\psi_{\mathbf{v}}^{(0)}\rangle$. Consequently, the expectation value for a property now can be decomposed into two quantities, $\langle P\rangle_{\mathbf{v}} = P^{eff} + P'^{har}$, where P'^{har} embodies property-curvature values (evaluated at the effective geometry) and the contributions of anharmonicity are incorporated implicitly by the shift between the effective and equilibrium nuclear frameworks, $P^{anh} \approx P^{eff} - P^{eq}$.

The computational scheme embodied in Eqs. (11.67) and (11.68) has been applied fruitfully to interpret diverse molecular phenomena, including dispersive chiroptical effects where $P(\mathbf{Q})$ becomes $[\alpha]_\lambda(\mathbf{Q})$. Wiberg and coworkers [130] have reported detailed measurements for the temperature dependence (0–100°C) of the specific rotatory power displayed by a series of conformationally rigid bicyclic compounds entrained in dilute ethylcyclohexane solutions. The resulting plots of $[\alpha]_\lambda^T$ versus T were essentially linear in form; however, the attendant slopes varied greatly (in both magnitude and sign) from one targeted species to the next. By combining the TDDFT linear-response framework with property-averaging procedures that accounted for the thermal population of excited (vibrational) states, Mort and Autschbach [124] have shown that many of the trends noted in this polarimetric study can be attributed to intrinsic vibrational displacements. These authors found that corrections arising from property-curvature terms $[\propto (\partial^2[\alpha]_\lambda/\partial Q_i^2)_0]$ usually dominated over those attributed to anharmonicity of the potential energy surface $[\propto (\partial[\alpha]_\lambda/\partial Q_i)_0]$, with the proper treatment of low-frequency modes (*e.g.*, the torsional motion of methyl rotors) requiring special consideration [125]. While experimental complications (*e.g.*, solvation) and theoretical deficiencies (e.g., for treating Rydberg states) [131] limited the extent of agreement achieved between observed and predicted behavior, this work clearly demonstrates the latent roles played by nuclear degrees of freedom.

One might expect the effects of nuclear motion to represent only a minor constituent of measured ORD profiles; however, the magnitudes of such effects can be comparable to or even larger than those of their purely electronic counterparts, especially for species possessing small rotatory powers [132]. This statement is bolstered by the (*S*)-methyloxirane results compiled in Table 11.1, which follow from the CC linear-response calculations of Kongsted et al. [110, 111]. Aside from specific rotations computed for the rigid minimum-energy (equilibrium) structure at three excitation wavelengths, $[\alpha]_\lambda^{eq}$, the corresponding anharmonic, $[\alpha]_\lambda^{anh}$, and harmonic, $[\alpha]_\lambda^{har}$, vibrational corrections are tabulated, where the latter property-curvature quantity has been averaged over a

$T = 298.15$ K thermal ensemble [cf. Eqs. (11.68) and (11.69)]. While $[\alpha]_\lambda^{eq}$ is predicted to be uniformly negative at the CCSD level of theory (cf. Figure 11.3), the $[\alpha]_\lambda^{anh}$ and $[\alpha]_\lambda^{har}$ parameters are positive with $[\alpha]_\lambda^{har} > [\alpha]_\lambda^{anh}$. Consequently, vibrational correction of the specific rotation, $[\alpha]_\lambda^{T} = [\alpha]_\lambda^{eq} + [\alpha]_\lambda^{anh} + [\alpha]_\lambda^{har}$, shifts the innate ORD curve (as described by $[\alpha]_\lambda^{eq}$ alone) toward positive values and produces near-quantitative agreement with gas-phase polarimetric measurements performed on isolated (*S*)-methyloxirane molecules (cf. dashed line in Figure 11.3). In contrast, analogous considerations applied to DFT analyses exacerbate the discrepancies between theory and experiment [110, 118], overestimating the rotatory power at 355 nm by nearly an order of magnitude and giving the incorrect sign of optical rotation at 589.3 nm and 633 nm.

While CC methods generally are considered to be more accurate and reliable than their DFT counterparts, the latter are considerably less demanding from a computational perspective. Such considerations are of prime importance for treatments of vibrational phenomena, where the enumerated degrees of freedom escalate rapidly as molecular size increases. Even given the simplifications obtained by a strictly harmonic description of normal modes (e.g., $\langle Q_i \rangle_{\mathbf{v}} = 0$), the sheer number of property-curvature calculations needed to account for the effects of nuclear motion in a moderately large chiral species can prove to be prohibitive for arduous CC schemes. To remedy this situation, recent efforts have explored the possibility of cobbling efficient density-functional analyses of vibrational properties with dependable coupled-cluster estimates of electronic chiroptical response [133]. This hybrid approach has been shown to provide a reasonable compromise between accuracy and cost, with B3LYP zero-point corrections of CCSD specific-rotation values usually found to better approximate the intrinsic (isolated-molecule) behavior revealed by gas-phase polarimetric measurements.

11.4.3. Conformational Flexibility

Conformational flexibility, whereby internal motion of functional/structural moieties gives rise to distinct minima within an encompassing electronic potential energy hypersurface, can impact both the dispersive (CB) and absorptive (CD) components of natural optical activity. Interconversion of the resulting stereoisomers through large-amplitude vibrational displacements commonly is hindered by the presence of substantial potential barriers, thereby leading to essentially independent entities that often exhibit opposing chiroptical properties. The separate "species" obtained under such circumstances can produce contrasting sets of vibronic features in ECD spectra [14], with the unique signature of each conformer reflecting the different local environment of its absorbing chromophore. Similar considerations apply for ORD profiles, where even a rudimentary description of observed behavior demands knowledge of population distributions for the contributing structural isomers. Consequently, any attempt to quantitatively model or interpret the response evoked from a nonrigid chiral species must be preceded by a comprehensive hunt for all accessible configurations of the nuclear framework. This formidable task can be guided by chemical intuition; however, semiautomated procedures, based upon low-level search algorithms followed by optimization of identified geometries at higher levels of theory, have been implemented to explore the potential-energy landscape of larger systems. Detailed analyses of specific rotation have been reported for a variety of flexible substrates probed, primarily, under solvated conditions, including prototypical organic compounds [85, 89, 134–147], molecular aggregates [95, 96, 148], and complex natural products [149, 150].

The putative roles that molecular conformations can play in dispersive chiroptical phenomena are illustrated graphically by Figure 11.5 for the case of (*S*)-epichlorohydrin,

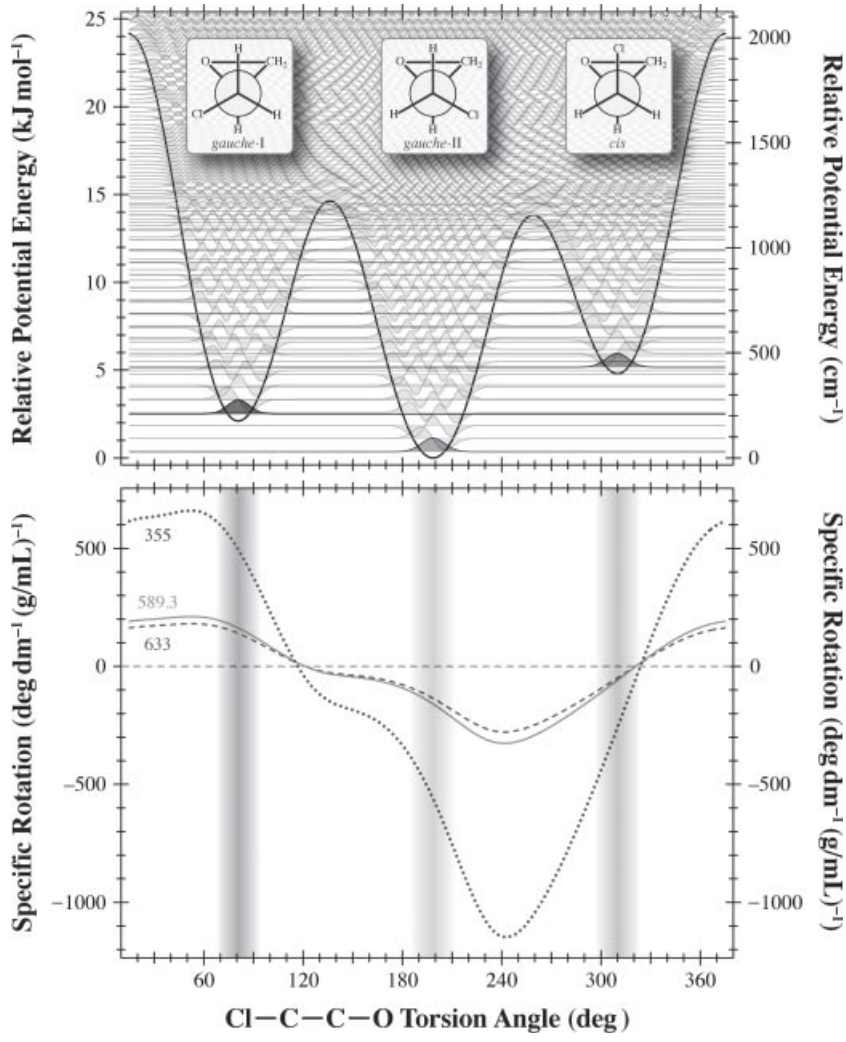

Figure 11.5. Conformational flexibility in (*S*)-epichlorohydrin. The top panel presents the torsional potential for (*S*)-epichlorohydrin computed at the MP2/aug-cc-pVTZ level of theory. The insets depict idealized Newman projections for the three stable conformers of the nuclear framework, which are designated as *gauche* I, *gauche* II, and *cis*. Approximate wavefunctions obtained for the lowest-lying torsional eigenstates are superimposed, with the effective ''zero-point level'' for each potential minimum highlighted. The bottom panel shows the conformational dependence of specific optical rotation as predicted by B3LYP/aug-cc-pVTZ linear-response calculations performed at 633 nm (dashed curve), 589.3 nm (solid curve), and 355 nm (dotted curve).

a flexible chiral species that has been the subject of several investigations [85, 134, 139]. The top panel presents a relaxed potential-energy scan obtained at the MP2/aug-cc-pVTZ level of theory by performing partial geometry optimizations as a function of the Cl–C–C–O dihedral angle, τ_{ClCCO}, which describes relative orientation of the chloromethyl group with respect to the epoxide ring. As shown by the idealized Newman projections in the insets, the ground electronic surface is predicted to support

three stable low-lying conformers designated as *gauche* I ($\tau_{\mathrm{ClCCO}} = 80.8^{\circ}$), *gauche* II ($\tau_{\mathrm{ClCCO}} = 198.5^{\circ}$), and *cis* ($\tau_{\mathrm{ClCCO}} = 310.0^{\circ}$). While the *gauche*-II form represents the global minimum-energy configuration of the isolated nuclear framework, the *gauche*-I and *cis* structures reside only 2.11 kJ/mol (176.0 cm^{-1}) and 4.80 kJ/mol (400.9 cm^{-1}) higher in energy, implying that all three will exist in an ambient ensemble of equilibrated (*S*)-epichlorohydrin molecules.

The bottom panel of Figure 11.5 depicts the circular birefringence of (*S*)-epichlorohydrin predicted as a function of the τ_{ClCCO} coordinate for three excitation wavelengths: 633 nm, 589.3 nm, and 355 nm. These results follow from B3LYP/aug-cc-pVTZ linear-response calculations performed on partially optimized geometries emerging from the aforementioned potential-energy scan. The orientation of the chloromethyl group, which mediates interchange among the stable ground-state minima, clearly exerts a pronounced influence upon dispersive chiroptical response, promoting marked shifts in both magnitude and sign of the computed specific rotation, $[\alpha]_{\lambda}$. In particular, the localized segments of the abscissa nominally attributed to each conformer display contrasting behaviors, with the *gauche*-I and *gauche*-II forms respectively having positive and negative $[\alpha]_{\lambda}$ values of comparable size while the *cis* species displays roughly half the rotatory power of its *gauche*-II counterpart. Experimental measurements of optical activity in (*S*)-epichlorohydrin should reflect such antagonistic properties by depending strongly on temperature and other environmental variables that affect the distribution of population among the potential wells.

Since the stable conformations of (*S*)-epichlorohydrin constitute distinct minima within a *single* electronic manifold, their properties can be described uniformly by solving the associated nuclear Schrödinger equation to obtain multidimensional vibrational eigenfunctions, $\psi_{\mathbf{v}}(\mathbf{Q})$, and eigenvalues, $E_{\mathbf{v}}$. In particular, for sufficiently low barriers to interconversion, the resulting $\psi_{\mathbf{v}}(\mathbf{Q})$ will display delocalized probability amplitudes that span all three of the potential wells. Such information, in conjunction with knowledge of the coordinate-dependence for wavelength-resolved specific rotation, $[\alpha]_{\lambda}(\mathbf{Q})$, should enable the observed optical activity, $[\alpha]_{\lambda}^{T}$, to be predicted from Eq. (11.68). Even if the complications incurred from environmental perturbations (e.g., solvation) are neglected, this represents a computationally formidable task that proves to be prohibitively expensive for all but the simplest of species. Consequently, most theoretical treatments of chiroptical behavior in conformationally flexible molecules have relied on a simple Boltzmann-weighted average, in which each thermally accessible conformer is regarded as an independent entity with its rotatory power often approximated by that of the corresponding equilibrium configuration, $[\alpha]_{\lambda}^{eq}$. By using the index η to enumerate structural isomers, this approach predicts the specific rotation at temperature T to have the form:

$$[\alpha]_{\lambda}^{T} = \sum_{\eta} [\alpha]_{\lambda,\eta}^{eq} \, f_{\eta}(T) = \sum_{\eta} [\alpha]_{\lambda,\eta}^{eq} \, \frac{e^{-\Delta E_{\eta}/k_B T}}{q}, \tag{11.70}$$

where ΔE_{η} denotes the relative energy for species η and $q = \sum_{\eta} e^{-\Delta E_{\eta}/k_B T}$ ensures overall normalization of the fractional populations defined by $f_{\eta}(T)$. Since laboratory studies of conformer-mediated properties typically are conducted under conditions of thermal equilibrium that reflect both enthalpic and entropic constraints, relative values of the Gibbs free energy, ΔG_{η}, often supersede their ΔE_{η} counterparts [85]. Crawford and Allen [140] have performed detailed analyses of the successive approximations required to transform the theoretically rigorous vibrational-averaging procedure of Eq. (11.68) into

the computationally expedient approach of Eq. (11.70). By focusing on the pragmatic case of (*R*)-3-chloro-1-butene [137] and exploiting model potentials of adjustable barrier height, these authors documented the robust nature of the simplistic Boltzmann-weighted ansatz, proposing that its overall success stems from a favorable cancellation of otherwise sizable errors.

As suggested by the form of the potential energy curve in Figure 11.5 and reinforced by the shapes of the superimposed vibrational wavefunctions, the conformers of (*S*)-epichlorohydrin are predicted to be essentially independent entities at ambient temperatures, with delocalized behavior only being obtained once the substantial barriers to interconversion have been surmounted. Consequently, the Boltzmann-weighted average of Eq. (11.70) should afford a reasonable description for the attendant optical activity. Figure 11.6 contrasts ORD profiles computed at the B3LYP/aug-cc-pVDZ level of linear-response theory with analogous vapor-phase and solution-phase measurements of specific rotation, where the latter will be discussed in the ensuing section. These results follow from the polarimetric analyses of Wilson and coworkers [85] which exploited composite Gaussian-3 (G3) [151] calculations to determine requisite ΔG_η parameters for the

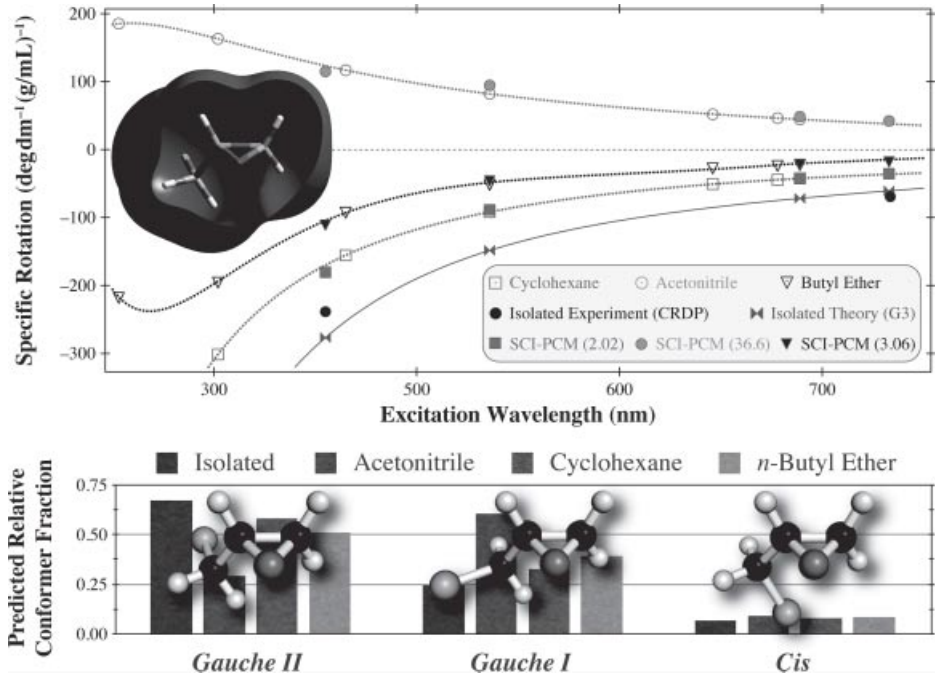

Figure 11.6. Solvation and optical activity of conformationally flexible molecules. Measured and computed ORD curves are shown for (*S*)-epichlorohydrin, a nonrigid chiral molecule where the antagonistic properties of three lowing-lying conformers mediate overall chiroptical response. Optical activity predictions are based on B3LYP/aug-cc-pVDZ linear-response calculations that were thermally averaged by using Gaussian-3 (G3) and self-consistent isodensity polarizable continuum model (SCI-PCM) estimates for the relative Gibbs free energies (i.e., Boltzmann-weighted populations) of the isolated and solvated stereoisomers, respectively. Aside from vapor-phase polarimetric measurements, solution-phase results are shown for acetonitrile (36.6), di-*n*-butylether (3.06), and cyclohexane (2.02) media, where parentheses denote static dielectric constants.

solvent-free species. The accompanying bar graph depicts the relative population for each conformer, as dictated by the ordering of their energies, with dominance of the *gauche*-II form under isolated-molecule conditions (where $\Delta G_{gauche-\mathrm{II}} < \Delta G_{gauche-\mathrm{I}} \ll \Delta G_{cis}$) leading to the overall negative sign for $[\alpha]_{\lambda}^{T}$ (as expected from the bottom panel of Figure 11.5). Reasonable accord is found between experiment and theory in the case of (*S*)-epichlorohydrin; however, Wilson et al. [85] have reported less satisfactory agreement for (*S*)-epifluorohydrin and (*S*)-1,2-epoxybutane, which respectively exhibit comparable and more extensive degrees of conformational flexibility. These authors also examined sources of error contributing to Boltzmann-weighted predictions, asserting that ΔG_{η} must be computed with <10% accuracy for emerging $[\alpha]_{\lambda}^{T}$ values to display a propagated uncertainty (*sans* that attributed to $[\alpha]_{\lambda}^{eq}$) on the order of $\pm 1\,\mathrm{deg\,dm^{-1}\,(g/mL)^{-1}}$.

11.4.4. Solvation Dynamics

The presence of a solvent long has been known to markedly influence chiroptical response [14], potentially changing both the magnitude and the sign of measured spectral signatures. In the case of flexible solutes like epichlorohydrin (cf. Figures 11.5 and 11.6), these observations commonly have been attributed to geometrical relaxation of the nuclear framework that leads to the differential stabilization of conformers, each of which possesses unique and, oftentimes, antagonistic properties. Nevertheless, as demonstrated by the methyloxirane data in Figure 11.3, even nominally rigid species can exhibit pronounced solvation phenomena that ultimately must be ascribed to static/dynamic adaptations taking place in attendant distributions of electron density. Building upon the theoretical description for natural optical activity given in Section 11.2, nonspecific solute–solvent interactions can be expected to alter excitation energies ($\hbar\omega_{eg}$), transition moments (^{eg}R), and dephasing rates (Γ_{eg}) for excited states in a distinct manner that reflects their underlying provenance. Aside from shifting the locations, linewidths, and (signed) intensities of resonant ECD features, such effects will modify the role that a given electronic manifold plays in constituting the composite property of ORD, which is exquisitely sensitive to "molecular shape" and strongly affected by perturbations at the periphery of the electronic wavefunction [101]. Cooperative solvation mechanisms, including the formation of asymmetric (chiral) solvent shells [152] and the action of solvent-mediated vibronic coupling [153], also have been invoked to interpret the complex behavior encountered in condensed media.

While the coupling between solute and solvent degrees of freedom clearly exerts a profound influence on measured chiroptical response, analyses of such phenomena historically have been relegated to the venerable (albeit now largely discredited) [105, 106, 154] Lorentz local-field correction [18, 46, 47]. Modern theoretical approaches for solvation can be classified broadly as being either explicit or implicit in nature, depending on whether they approximate the solvent as distinct entities (e.g., molecular frameworks with appended point charges) that give rise to a cooperative supramolecular "complex" or as an infinite and structureless "fluid" characterized by a set of macroscopic parameters (e.g., density and dielectric constant). Explicit models are capable of faithfully portraying specific interactions mediated by the innermost solvent shell; however, they generally afford less satisfactory descriptions of properties attributed to long-range (bulk) forces and polarization of the medium. Monte Carlo and molecular dynamics simulations commonly are integrated into these schemes, with extraction of desired information predicated upon delicate statistical averages deduced from ensembles of uncorrelated solute–solvent "snapshots." In the case of optical activity, the inherent difficulty of this

task is compounded by the need to perform arduous quantum-mechanical calculations of chiroptical behavior for each identified arrangement of solute and solvent. Implicit solvation methods, as exemplified by variants of the Polarizable Continuum Model (PCM) [155], alleviate this computational burden by implicitly incorporating configurational averaging into definition of the solvent. Most implementations of this scheme embed the solute in a cavity of predetermined size/shape (i.e., selected either for mathematical convenience or to mimic molecular features) and encode solute–solvent coupling in the form of an apparent charge distribution spread over the surface of the cavity. Although first solvation-shell effects that distinguish the cybotactic region typically are neglected [155], the continuum formalism does provide an accurate description of bulk electrostatic and polarization properties.

Mennucci and coworkers [154] have combined DFT linear-response calculations of dispersive optical activity with a continuum-dielectric (PCM) model of solvation designed primarily to account for electrostatic interactions. While specific rotatory powers evaluated at the sodium D-line (589.3 nm) for a series of rigid compounds were in reasonable accord with polarimetric measurements performed in dilute cyclohexane, acetone, methanol, and acetonitrile, serious discrepancies were noted for other solvent systems ($CCl_4, C_6H_6, CHCl_3$) and were attributed to the action of strong nonelectrostatic effects (e.g., dispersion/repulsion forces). This study and implicit treatments of related electronic phenomena [142, 156] have documented the need to incorporate dynamical aspects of solvent response through inertial polarization components that are not equilibrated with instantaneous changes in the solute charge distribution. Analogous DFT-PCM analyses of absorptive chiroptical properties by Pecul et al. [157] also emphasized the nonequilibrium nature of solvation accompanying resonant (electronic) excitation and highlighted the important roles played by deformations of electron distribution in dielectric environments. The quality of resulting ECD predictions was found to depend markedly on the provenance of each feature, with the relatively poor description of transitions terminating on diffuse Rydberg manifolds reflecting possible tunneling of electron density into the surrounding medium and inherent inadequacies of correlation-exchange functionals [131].

The influence of solvation upon the optical activity of conformationally flexible solutes is demonstrated vividly by Figure 11.6, which presents ORD profiles recorded for (*S*)-epichlorohydrin in dilute acetonitrile (36.6), di-*n*-butylether (3.06), and cyclohexane (2.02) media [85], where numbers in parentheses denote the corresponding static ($\omega \rightarrow 0$) dielectric constants, $\varepsilon \equiv \varepsilon(0)$. Studies performed on rigid chiral species consistently have found solvents of high polarity such as acetonitrile to best mimic isolated-molecule behavior (cf. Figure 11.3) [84, 88, 89]; however, the epichlorohydrin results seem to show diametrically opposite trends, with acetonitrile producing specific rotation values of inverted sign relative to those measured in the vapor phase while solvation by cyclohexane appears to most closely reproduce the intrinsic chiroptical response. Although in keeping with the expectations of chemical intuition, such observations reflect a much more complex scenario that involves the combined effects of differential stabilization and antagonistic properties for individual conformers [85].

The analyses of solution-phase chiroptical behavior in Figure 11.6 have exploited a B3LYP/6-311+G* implementation of the polarizable continuum model that constructs the solute cavity self-consistently on the basis of its electron isodensity surface (SCI-PCM). Since this implicit treatment of solvation emphasizes electrostatic interactions, pronounced effects are anticipated whenever changes in molecular structure lead to substantial modifications of charge distribution. In particular, owing to inherent polarity of the C–Cl bond, the optimized (solvent-free) *gauche*-I, *gauche*-II, and *cis* forms of

ground-state (*S*)-epichlorohydrin are predicted to have permanent electric dipole moment magnitudes, μ, of 3.66 D, 0.61D, and 3.02 D, respectively, at the MP2/aug-cc-pVTZ level of theory. As illustrated by the accompanying bar graphs, the Gibbs free energies, ΔG_η, and fractional populations, $f_\eta(T) = e^{-\Delta G_\eta / k_B T}/q$, emerging from SCI-PCM calculations reflect the repercussions of these first-order multipoles. While solvents of low dielectric constant (e.g., cyclohexane) yield results comparable to those of the vapor phase, strongly polar media (e.g., acetonitrile) are found to markedly lower the energies of stereoisomers that possess larger values of μ. Such differential stabilization is sufficient to alter the relative energy ordering from $\Delta G_{gauche-\mathrm{II}} < \Delta G_{gauche-\mathrm{I}} \ll \Delta G_{cis}$ for the isolated molecule to $\Delta G_{gauche-\mathrm{I}} < \Delta G_{gauche-\mathrm{II}} < \Delta G_{cis}$ in the case of an acetonitrile environment, with commensurate changes taking place in conformer populations.

Given the distinct CB expected for each of the stable conformations in ground-state (*S*)-epichlorohydrin (cf. Figure 11.5), the solvent-dependent $f_\eta(T)$ parameters emerging from SCI-PCM analyses should produce dramatic changes in the composite optical activity. As highlighted by Figure 11.6, ORD profiles computed from Eq. (11.70) for acetonitrile, di-*n*-butylether, and cyclohexane media show near-quantitative accord with measured values of specific rotation. In particular, the change in sign of $[\alpha]_\lambda^{25^\circ\mathrm{C}}$ observed upon dissolution in acetonitrile is reproduced by this treatment, reflecting preferential stabilization of the *gauche*-I form that makes $[\alpha]_{\lambda,\eta}^{eq}$ contributions of opposite polarity to those of its *gauche*-II and *cis* counterparts. The quality of agreement between experiment (opened symbols) and theory (closed symbols) is perhaps fortuitous in view of the approximations inherent to the present model, which has cobbled together estimates of solvent-mediated energies/populations for localized stereoisomers with vapor-phase predictions for chiroptical response. Analogous efforts to interpret epichlorohydrin behavior in CH_2Cl_2, $CHCl_3$, and CCl_4 environments have not proven to be as successful [139], owing, in part, to known deficiencies of PCM descriptions for such chlorinated solvents [154].

Solvation phenomena for nominally rigid chiral species can be especially challenging to interpret, as illustrated by the (*S*)-methyloxirane data in Figure 11.3 where the sign of specific rotation measured over the 250–650 nm range flips from being all negative in a benzene environment to being completely positive in an aqueous medium. Kongsted et al. [111] have reported extensive coupled-cluster analyses of circular birefringence for this deceptively simple epoxide under both isolated and solvated conditions, the latter being modeled implicitly by forming a spherical cavity in a continuum dielectric fluid and considering successive orders of truncation for the multipole expansion of the embedded solute molecule. Despite affording an accurate description for important electron-correlation effects, this treatment failed to reproduce the trends exhibited by experimental ORD profiles. At the CCSD level of theory, solvents of high (low) polarity were found to slightly decrease (increase) the magnitudes of negative $[\alpha]_\lambda^{eq}$ values predicted for (*S*)-methyloxirane in the vapor phase, thereby suggesting (in contrast to observations) that optical activity should be dominated by the intrinsic solute response.

To probe the possible roles of specific solute-solvent coupling in (*S*)-methyloxirane, Mukhopadhyay and coworkers [158, 159] have combined an explicit (atomistic) treatment of innermost solvation shells with an implicit (continuum) model designed to mimic bulk behavior. Classical molecular dynamics simulations were exploited to obtain feasible structures for the solvent-decorated solute, with the optical activity calculated by DFT linear-response techniques (in the presence of a continuum dielectric) being averaged over an ensemble of such instantaneous "snapshots." For aqueous media [158], this hybrid approach found contributions arising from interactions between water and methyloxirane to overwhelm the intrinsic (solvent-free) chiroptical response, causing predicted

ORD profiles to shift towards positive values in accord with the results of polarimetric measurements. Subsequent inspection of $[\alpha]^{25^{\circ}C}_{589.3nm}$ parameters as a function of the angular position for water molecules in the first hydration shell revealed a clear bias for *anti* configurations (water and methyl group on opposite faces of the epoxide ring) over their *syn* counterparts (water and methyl group on the same face of the epoxide ring). Fourier-transform microwave spectroscopy performed on binary methyloxirane–water complexes synthesized in a rovibrationally cold molecular beam have suggested the opposite preference (viz., *syn* being more prevalent than *anti*); [160] however, this diastereofacial discrimination switches upon introduction of a second water ligand to create the tertiary methyloxirane–$(water)_2$ species [161]. Losada et al. [162] have reported extensive computational and experimental investigations of aqueous methyloxirane, confirming that the *anti* conformer of the binary adduct dominates under ambient conditions. These authors also documented a pronounced nonmonotonic dependence of specific rotatory power on solute concentration, which was interpreted as being indicative of attendant changes in the cooperative hydrogen-bonding network formed by surrounding water molecules (*vide infra*).

In contrast to the negligible contributions made by the independent solute and solvent in aqueous (*S*)-methyloxirane, the analogous ORD profile recorded in benzene is believed to arise mostly from the environment. Building upon their hybrid treatment of explicit/implicit solvation, Mukhopadhyay et al. [159] showed that dissymmetric imprinting of the chiral epoxide substrate on the surrounding configuration of achiral benzene molecules dominates the predicted chiroptical response. Precedence for this behavior can be found in suggestions that an appreciable fraction of the total ECD signal evoked from an optically active chromophore stems from chiral ordering of the adjacent solvent [152]. Losada and coworkers [162] have reported experimental evidence for related chirality-transfer phenomena in aqueous methyloxirane, where reorganization of the solvent network proximate to the entrained solute imparts optical activity to features residing in the water bending-mode region of the vibrational absorption spectrum. Similar solute-mediated VCD signatures have been demonstrated in a variety of systems capable of cooperatively accepting and/or donating hydrogen bonds [96, 97, 163], thereby affording a new tool for characterizing subtle solute–solvent interactions and elucidating their potential roles in chirospecific discrimination/recognition events.

While computational investigations of chiral solvation processes can provide invaluable information regarding the microscopic origins of environmental perturbations, considerable insight also can be gleaned from the more qualitative aspects of such phenomena. For example, Fischer et al. [164] have reported the specific rotation for (*S*)-α-methylbenzylamine dissolved in 39 different solvents, with measurements performed at various concentrations being extrapolated to the limit of infinite dilution [98]. Since this amphoteric species has the ability to both donate and accept hydrogen bonds, a comprehensive description of experimental results only could be achieved by invoking models based upon the threefold Kamlet–Taft parameterization of solvent acidity, basicity, and polarity/polarizability [165]. Figure 11.7 presents another attempt to correlate solvent-mediated chiroptical response with physical properties of the surrounding medium. The depicted analyses build upon the progenitor of implicit solvation methods, Onsager reaction field theory [166], where the multipole moments of a potentially polarizable solute molecule, imbedded in an isotropic and homogeneous continuum-dielectric fluid (characterized by static dielectric constant ε), induce reflection moments (in the surrounding medium) that, in turn, act to electrostatically stabilize the solute. In simplest form, this

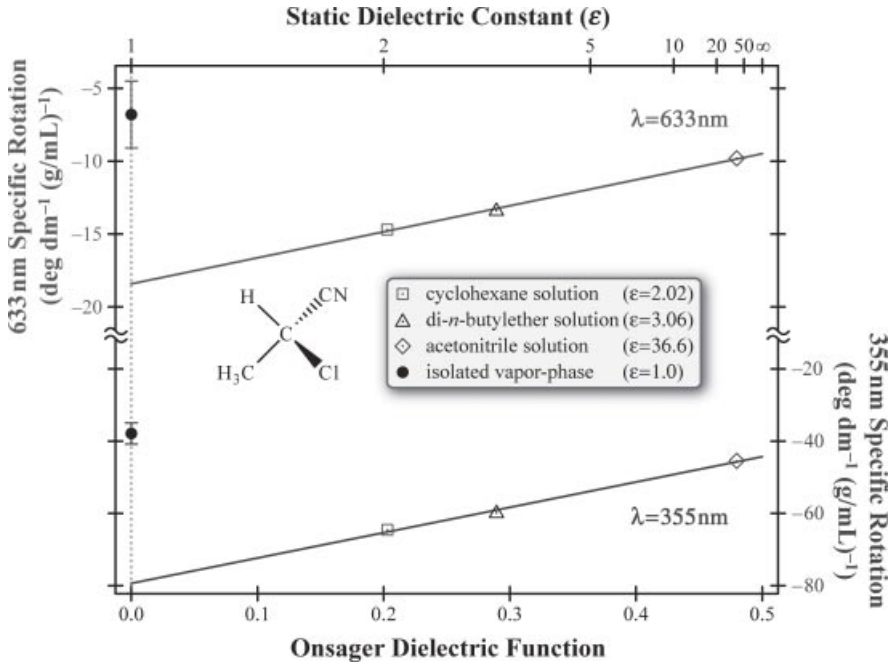

Figure 11.7. Dielectric Scaling of Circular Birefringence. The specific rotatory power of (*S*)-2-chloropropionitrile, $[\alpha]_{\lambda}^{25^{\circ}C}$, is plotted against the Onsager dielectric function, $f(\varepsilon)$. Solid symbols reflect vapor-phase CRDP measurements performed at 633 nm (top) and 355 nm (bottom), while opened symbols distinguish results interpolated from dilute solution-phase polarimetric studies conducted in acetonitrile (36.6), di-*n*-butylether (3.06), and cyclohexane (2.02) media (parentheses denote respective values of the static dielectric constant). Superimposed lines illustrated the predicted extrapolation of solvated response ($\varepsilon > 1$) to the isolated-molecule limit ($\varepsilon = 1$).

venerable approach encloses the solute in a spherical cavity of radius a and only considers its permanent electric dipole moment $\boldsymbol{\mu}$, thereby giving rise to an analytically calculable reaction electric field (as generated by the polarized continuum solvent) of the form [167]:

$$\mathbf{E} = \frac{2f(\varepsilon)}{a^3}\boldsymbol{\mu}, \tag{11.71}$$

where the Onsager dielectric function, $f(\varepsilon) = (\varepsilon - 1)/(2\varepsilon + 1)$, spans the range $0 \leq f(\varepsilon) \leq 0.5$ as the medium changes from completely nonpolar ($\varepsilon = 1$) to infinite polarity ($\varepsilon \gg 1$). The corresponding solute–solvent interaction energy is given by $E_{\text{solv}} = -\boldsymbol{\mu} \cdot \mathbf{E} = -(2f(\varepsilon)/a^3)\mu^2$, thus affording a tractable means for exploring nonspecific solvation phenomena dominated by dipolar electrostatic coupling.

Figure 11.7 highlights the specific rotatory power deduced for (*S*)-2-chloropropionitrile at 633 nm (top trace) and 355 nm (bottom trace) as a function of $f(\varepsilon)$, contrasting the response measured under isolated (gas-phase) conditions with that obtained in solvents selected to span an appreciable fraction of the accessible ordinate scale [88]. The chiral species targeted by this study is nominally rigid and possesses a substantial permanent electric dipole moment ($\mu = 3.7$ D), thereby satisfying criteria imposed for fruitful application of the dipolar reaction-field model. Similar analyses have been used

to examine equilibrium solvation effects for diverse chemical processes (e.g., conformational shifts [168], internal-rotation barriers [169], and activation energies [170]), with analogous plots allowing for the linear extrapolation of solution-phase ($\varepsilon > 1$) results to their vapor-phase ($\varepsilon = 1$) counterparts. Obviously such expectations are not realized in the case of dispersive chiroptical properties since measurements of $[\alpha]^{25^{\circ}\mathrm{C}}_{633\mathrm{nm}}$ and $[\alpha]^{25^{\circ}\mathrm{C}}_{355\mathrm{nm}}$ for isolated (*S*)-2-chloropropionitrile molecules are found to be two to three times smaller in magnitude than the values predicted from ordinate intercepts.

While the static value of ε employed by the dipolar reaction-field model affords a first-order approximation for nonspecific equilibrium solvation processes, straightforward extensions of this approach to describe nonequilibrium phenomena have been reported [171, 172]. Nevertheless, the behavior exhibited by (*S*)-2-chloropropionitrile in Figure 11.7 is representative of that found for a wide variety of rigid chiral species, reinforcing previous assertions (cf. Figure 11.3) that solvents of high dielectric constant (e.g., acetonitrile) consistently provide better mimics for the dispersive optical activity of isolated molecules than their less polar counterparts (e.g., cyclohexane). Such anomalous dielectric scaling suggests that a serious incongruity exists between specific rotation parameters acquired under solvated and isolated conditions, thereby casting doubts on the relevance and validity of comparisons often made between canonical (solution-phase) polarimetric measurements and *ab initio* predictions of intrinsic (vapor-phase) chiroptical properties. The origins of this discrepancy are an active subject of research; however, it would appear that the differential effects of solvation on individual excited state, perhaps reflecting the Rydberg or valence nature of their electronic parentage, might ultimately be responsible.

11.5. SUMMARY AND OUTLOOK

This chapter has outlined the conceptual foundations and practical considerations associated with quantitative measurements of the dispersive electronic components in natural optical activity, where the innate circular birefringence of an isotropic chiral medium manifests itself through nonresonant optical (polarization) rotation. Particular emphasis was placed on recent developments in polarimetric instrumentation (e.g., cavity-enhanced schemes) that have enabled these phenomena to be interrogated under isolated (rarefied vapor-phase) conditions, thereby revealing the intrinsic chiroptical response of targeted species. Nuclear degrees of freedom (i.e., vibrational displacements and/or conformational flexibility) were shown to influence such properties markedly, with the surrounding environment (e.g., solvation) also found to be capable of affecting both the magnitude and the sign of the observed rotatory power.

As the tools exploited for investigations of molecular properties have continued to evolve, the need for complementary theoretical advancements designed to understand and interpret their findings has become an evermore pressing concern. This especially is evident in the realm of electronic chiroptical spectroscopy, where the current resurgence of interest in these venerable techniques largely stems from the development of dependable quantum-chemical paradigms for predicting enantiomer-specific ORD and ECD profiles. The emerging synergism between laboratory measurements and computational analyses of natural optical activity has been demonstrated by numerous endeavors, which also have served to highlight the enormous potential of transforming relatively facile polarimetric methods into quantitative instruments for assigning the absolute stereochemical configuration of a targeted species. In the case of optical rotation, several issues need

to be addressed before these burgeoning capabilities can be realized fully, including the inevitable complications incurred by extrinsic environmental perturbations and intrinsic nuclear couplings. Nevertheless, as documented by the diverse contributions found in the present monograph, the future application of such chiroptical probes to problems of molecular structure and dynamics seems very promising indeed!

ACKNOWLEDGMENTS

The author wishes to sincerely thank his Yale colleague and collaborator Professor Kenneth B. Wiberg, as well as the graduate/undergraduate students, postdoctoral fellows, and research scientists who have participated in our joint investigations of chiroptical phenomena, including Ms. Priyanka Lahiri, Mr. John E. Wolff, Dr. Shaun M. Wilson, Mr. Michael J. Murphy, Dr. Thomas Müller, Dr. Yi-gui Wang, and Dr. James R. Cheeseman (Gaussian, Inc.). This chapter was prepared under the auspices of grants provided by the Chemistry Division of the United States National Science Foundation, the continuing support of which is gratefully acknowledged.

REFERENCES

1. L. D. Barron, *Molecular Light Scattering and Optical Activity*, 2nd ed., Cambridge University Press, Cambridge, **2004**.
2. G. H. Wagnière, *Linear and Nonlinear Optical Properties of Molecules*, VCH Publishers, New York, **1993**.
3. F. J. D. Arago, Mémoire sur une Modification Remarquable Qu'Éprouvent les Rayons Lumineux dans Leur Passage a Travers Certains Corps Diaphanes, et Sur Quelques Autres Nouveaux Phénomènes d'Optique, in *Mémoires de la Classe des Sciences Mathématiques et Physiques de l'Institut Impérial de France: Part I (Paris)*, **1811**, pp. 93–134.
4. J. B. Biot, Mémoire sur un Nouveau Genre d'Oscillation que les Molécules de la Lumière Éprouvent en Tranversant Certains Cristaux, in *Mémoires de la Classe des Sciences Mathématiques et Physiques de l'Institut Impérial de France: Part I (Paris)*, **1812**, pp. 1–372.
5. J.-B. Biot, Mémoire sur les Rotations que Certains Substances Impriment aux Axes de Polarisation des Rayons Lumineux, in *Mémoires de l'Académie Royale des Sciences de l'Institut de France*, **1817**, pp. 41–136.
6. T. M. Lowry, *Optical Rotatory Power*, Longmans, Green, and Co., London, **1935**.
7. P. L. Polavarapu, *Chirality* **2002**, *14*, 768–781; P. L. Polavarapu, *Chirality* **2002**, *15*, 284–285.
8. T. D. Crawford, *Theor. Chem. Acc*. **2006**, *115*, 227–245; T. D. Crawford, M. C. Tam, M. L. Abrams, *J. Phys. Chem. A* **2007**, *111*, 12057–12068.
9. M. Pecul, K. Ruud, *Adv. Quantum Chem*. **2005**, *50*, 185–212.
10. P. J. Stephens, F. J. Devlin, J.-J. Pan, *Chirality* **2008**, *20*, 643–663.
11. J. Autschbach, *Chirality* **2009**, *21*, E116–E152.
12. P. Mukhopadhyay, P. Wipf, D. N. Beratan, *Accounts Chem. Res*. **2009**, *42*, 808–819.
13. L. D. Barron, A. D. Buckingham, *Chem. Phys. Lett*. **2010**, *492*, 199–213.
14. N. Berova, K. Nakanishi, R. W. Woody, eds., *Circular Dichroism: Principles and Applications*, John Wiley & Sons, New York, **2000**; E. L. Eliel, S. H. Wilen, M. P. Doyle, Chiroptical properties, in *Basic Organic Stereochemistry*, John Wiley & Sons, New York, **2001**, Chapter 12, pp. 534–609.

15. J. H. Brewster, Assignment of stereochemical configuration by chemical means, in *Techniques of Chemistry*, Vol. IV: *Elucidation of Organic Structure by Physical and Chemical Methods*, Part III, 2nd ed., K. W. Bentley and G. W. Kirby, eds., Wiley-Interscience, New York, **1972**, Chapter I, pp. 1–249.
16. E. L. Eliel, S. H. Wilen, M. P. Doyle, *Basic Organic Stereochemistry*, John Wiley & Sons, New York, **2001**.
17. J. H. Brewster, *J. Am. Chem. Soc*. **1959**, *81*, 5475–5483; J. H. Brewster, *J. Am. Chem. Soc*. **1959**, *81*, 5483–5493; J. H. Brewster, *J. Am. Chem. Soc*. **1959**, *81*, 5493–5500; J. H. Brewster, *Tetrahedron Lett*. **1959**, *1*, 23–28; J. H. Brewster, *Tetrahedron* **1961**, *13*, 106–122.
18. J. G. Kirkwood, *J. Chem. Phys*. **1937**, *5*, 479–491; J. G. Kirkwood, *J. Chem. Phys*. **1939**, *7*, 139.
19. J. Applequist, J. R. Carl, K.-K. Fung, *J. Am. Chem. Soc*. **1972**, *94*, 2952–2960; J. Applequist, *J. Chem. Phys*. **1973**, *58*, 4251–4259; J. Applequist, *J. Am. Chem. Soc*. **1973**, *95*, 8258–8262; J. Applequist, *J. Am. Chem. Soc*. **1973**, *95*, 8255–8258; J. Applequist, *Accounts Chem. Res*. **1977**, *10*, 79–85.
20. P. L. Polavarapu, *Chem. Rec*. **2007**, *7*, 125–136.
21. P. N. Butcher, D. Cotter, *The Elements of Nonlinear Optics*, Cambridge University Press, Cambridge, **1990**.
22. S. Mukamel, *Principles of Nonlinear Optical Spectroscopy*, Oxford University Press, New York, **1995**.
23. P. Fischer, F. Hache, *Chirality* **2005**, *17*, 421–437.
24. P. L. Polavarapu, *Chirality* **2008**, *20*, 664–672.
25. L. A. Nafie, T. B. Freedman, Vibrational optical activity theory, in *Circular Dichroism*, N. Berova, K. Nakanishi, R. W. Woody, eds., John Wiley & Sons, New York, **2000**, Chapter 4, pp. 97–132; P. J. Stephens, F. J. Devlin, A. Aamouche, Determination of the structures of chiral molecules using vibrational circular dichroism spectroscopy, in *Chirality: Physical Chemistry*, J. M. Hicks, ed., American Chemical Society, Washington, D.C., **2002**, Chapter 2, pp. 18–33; T. B. Freedman, X. Cao, R. A. Dukor, L. A. Nafie, *Chirality* **2003**, *15*, 743–758.
26. L. D. Barron, L. Hecht, Vibrational Raman optical activity: From fundamentals to biochemical applications, in *Circular Dichroism*, N. Berova, K. Nakanishi, R. W. Woody, eds., John Wiley & Sons, New York, **2000**, Chapter 23, pp. 667–702; L. D. Barron, E. W. Blanch, A. F. Bell, C. D. Syme, L. Hecht, L. A. Day, New insights into solution structure and dynamics of proteins, nucleic acids, and viruses from Raman optical activity, in *Chirality: Physical Chemistry*, J. M. Hicks, ed., American Chemical Society, Washington, D.C., **2002**, Chapter 3, pp. 34–49; L. D. Barron, F. Zhu, L. Hecht, *Vib. Spectrosc*. **2006**, *42*, 15–24; L. D. Barron, F. Zhu, L. Hecht, G. E. Tranter, N. W. Isaacs, *J. Mol. Struct*. **2007**, 834–836, 7–16.
27. E. R. Cohen, T. Cvitaš, J. G. Frey, B. Homström, K. Kuchitsu, R. Marquardt, I. Mills, F. Pavese, M. Quack, J. Stohner, H. L. Strauss, M. Takami, A. J. Thor, eds., *Quantities, Units and Symbols in Physical Chemistry*, 3rd ed., Royal Society of Chemistry Publishing, Cambridge, **2007**.
28. T. A. W. Wasserman, P. H. Vaccaro, B. R. Johnson, *J. Chem. Phys*. **2002**, *116*, 10099–10121.
29. J. D. Jackson, *Classical Electrodynamics*, 2nd ed., John Wiley & Sons, New York, **1975**; J. R. Reitz, F. J. Milford, R. W. Christy, *Foundations of Electromagnetic Theory*, 3rd ed., Addison-Wesley, Reading, MA, **1979**.
30. E. Hecht, *Optics*, 4th ed., Addison-Wesley, Reading, MA, **2002**.
31. D. S. Kliger, J. W. Lewis, C. E. Randall, *Polarized Light in Optics and Spectroscopy*, Academic Press, Boston, **1990**.
32. A. J. Fresnel, *Bull. Soc. Philomat*. **1824**, 147–158.

33. A. J. Fresnel, Mémoire sur la double réfraction, in *Œuvres Complètes d'Augustin Fresnel*, Vol. 2, H. de Sénarmont, E. Verdet, L. Fresnel, eds., Imprimerie Impériale, Paris, **1866**, pp. 479–596.
34. P. Crabbé, *Optical Rotatory Dispersion and Circular Dichroism in Organic Chemistry*, Holden-Day, San Francisco, **1965**; P. Crabbé and A. C. Parker, Optical rotatory dispersion and circular dichroism, in *Techniques of Chemistry*, Vol. I: *Physical Methods of Chemistry*, Part III(C): *Optical, Spectroscopic, and Radioactive Methods (Polarimetry)*, A. Weissberger B. W. Rossiter, eds., Wiley-Interscience, New York, **1972**, Chapter III, pp. 183–270.
35. L. Velluz, M. Legrand, M. Grosjean, *Optical Circular Dichroism: Principles, Measurements, and Applications*, Verlag Chemie, GMBH, Weinheim, **1965**.
36. W. Demtröder, *Laser Spectroscopy: Basic Concepts and Instrumentation*, 2nd ed., Springer-Verlag, Berlin, **1996**.
37. J. Michl, E. W. Thulstrup, *Spectroscopy with Polarized Light: Solute Alignment by Photoselection, in Liquid Crystals, Polymers, and Membranes*, VCH Publishers, New York, **1986**.
38. M. Weissbluth, *Atoms and Molecules*, Academic Press, San Diego, **1978**; B. H. Bransden, C. J. Joachain, *Physics of Atoms and Molecules*, 2nd ed., Pearson Education Ltd., Harlow, England, **2003**.
39. K. Claborn, J. H. Cedres, C. Isborn, A. Zozulya, E. Weckert, W. Kaminsky, B. Kahr, *J. Am. Chem. Soc*. **2006**, *128*, 14746–14747; C. Isborn, K. Claborn, B. Kahr, *J. Phys. Chem. A* **2007**, *111*, 7800–7804; K. Claborn, C. Isborn, W. Kaminsky, B. Kahr, *Angew. Chem. Int. Ed*. **2008**, *47*, 5706–5717.
40. R. Hassey, E. J. Swain, N. I. Hammer, D. Venkataraman, M. D. Barnes, *Science* **2006**, *314*, 1437–1439; R. Hassey, K. D. McCarthy, E. Swain, D. Basak, D. Venkataraman, M. D. Barnes, *Chirality* **2008**, *20*, 1039–1046.
41. P. Drude, *Lehrbuch der Optik*, S. Hirzel, Leipzig, **1900**.
42. M. Born, *Z. Phys*. **1915**, *16*, 251–258; M. Born, *Proc. R. Soc. A* **1935**, *150*, 84–105.
43. C. W. Oseen, *Ann. Phys*. **1915**, *48*, 1–56.
44. F. Gray, *Phys. Rev*. **1916**, *7*, 472–488.
45. L. Z. Rosenfeld, *Physik* **1928**, *52*, 161–174.
46. E. U. Condon, *Rev. Mod. Phys*. **1937**, *9*, 432–457; E. U. Condon, W. Altar, H. Eyring, *J. Chem. Phys*. **1937**, *5*, 753–775.
47. W. Kauzmann, J. Walter, H. Eyring, *Chem Rev* **1940**, *26*, 339–407; H. Eyring, H. C. Liu, D. Caldwell, *Chem. Rev*. **1968**, *68*, 525–540; D. J. Caldwell, H. Eyring, *The Theory of Optical Activity*, Wiley-Interscience, New York, **1971**; D. J. Caldwell, H. Eyring, Theory of optical rotation, in *Techniques of Chemistry*, Vol. I: *Physical Methods of Chemistry*, Part III(C): *Optical, Spectroscopic, and Radioactive Methods (Polarimetry)*, A. Weissberger, B. W. Rossiter, eds., Wiley-Interscience, New York, **1972**, Chapter I, pp. 1–50.
48. P. L. Polavarapu, *Vibrational Spectra: Principles and Applications with Emphasis on Optical Activity*, Elsevier, Amsterdam, **1998**.
49. R. C. Hilborn, *Am. J. Phys*. **1982**, *50*, 982–986.
50. B. H. Bransden, C. J. Joachain, *Introduction to Quantum Mechanics*, Longman Scientific and Technical, Harlow, England, **1989**; J. J. Sakurai, *Modern Quantum Mechanics*, Addison-Wesley, Redwood City, CA, **1985**.
51. K. Blum, *Density Matrix Theory and Applications*, 2nd ed., Plenum Press, New York, **1996**.
52. A. D. Buckingham, P. Fischer, *Phys. Rev. A* **2000**, *61*, 035801/1–4.
53. C. Djerassi, *Optical Rotatory Dispersion: Applications to Organic Chemistry*, McGraw-Hill Book Company, New York, **1960**.
54. A. Moscowitz, *Rev. Mod. Phys*. **1960**, *32*, 440–443; A. Moscowitz, *Tetrahedron* **1961**, *13*, 48–56.

55. P. L. Polavarapu, *J. Phys. Chem. A* **2005**, *109*, 7013–7023; P. L. Polavarapu, A. G. Petrovic, P. Zhang, *Chirality* **2006**, *18*, 723–732.
56. M. Krykunov, M. D. Kundrat, J. Autschbach, *J. Chem. Phys*. **2006**, *125*, 194110/1–13; M. Rudolph, J. Autschbach, *Chirality* **2008**, *20*, 995–1008.
57. K. B. Wiberg, Y. Wang, S. M. Wilson, P. H. Vaccaro, J. R. Cheeseman, *J. Phys. Chem. A* **2006**, *110*, 13995–14002.
58. P. Jørgensen, J. Simons, *Second Quantization Based Methods in Quantum Chemistry*, Academic Press, New York, **1981**; J. Oddershede, P. Jørgensen, D. L. Yeager, *Comput. Phys. Rep* **1984**, *2*, 33–92; J. Linderberg, Y. Öhrn, *Propagators in Quantum Chemistry*, John Wiley & Sons, Hoboken, NJ, **2004**.
59. J. Olsen, P. Jørgensen, *J. Chem. Phys*. **1985**, *82*, 3235–3264; P. Jørgensen, H. J. A. Jensen, J. Olsen, *J. Chem. Phys*. **1988**, *89*, 3654–3661.
60. P. Norman, D. M. Bishop, H. J. A. Jensen, J. Oddershede, *J. Chem. Phys*. **2001**, *115*, 10323–10334; P. Norman, K. Ruud, T. Helgaker, *J. Chem. Phys*. **2004**, *120*, 5027–5035; A. Jiemchooroj, P. Norman, *J. Chem. Phys*. **2007**, *126*, 134102/1–7; H. Solheim, K. Ruud, S. Coriani, P. Norman, *J. Chem. Phys*. **2008**, *128*, 094103/1–7.
61. L. Jensen, J. Autschbach, G. C. Schatz, *J. Chem. Phys*. **2005**, *122*, 224115/1–11; J. Autschbach, L. Jensen, G. C. Schatz, Y. C. Electra Tse, M. Krykunov, *J. Phys. Chem. A* **2006**, *110*, 2461–2473.
62. R. Descamps, *Trans. Farad. Soc*. **1930**, *26*, 357–370; M. K. Hargreaves, *J. Chem. Soc*. **1953**, 2953–2954; E. Brand, E. Washburn, B. F. Erlanger, E. Ellenbogen, J. Daniel, F. Lippmann, M. Scheu, *J. Am. Chem. Soc*. **1954**, *76*, 5037–5040; H. Rudolph, *J. Opt. Soc. Am*. **1955**, *45*, 50–59; W. Heller, H. G. Curmè, Optical rotation—Experimental techniques and physical optics, in *Techniques of Chemistry*, Vol. I: *Physical Methods of Chemistry*, Part III(C): *Optical, Spectroscopic, and Radioactive Methods (Polarimetry)*, A. Weissberger, B. W. Rossiter, eds., Wiley-Interscience, New York, **1972**, Chapter II, pp. 51–181.
63. Specifications for AUTOPOL VI Polarimeter (Rudolf Research Analytical, 2010), retrieved July 5, **2010**, `http://www.rudolphresearch.com/polarimeters/autopol vi.php`.
64. P. W. Milonni, J. H. Eberly, *Lasers*, John Wiley & Sons, New York, **1988**.
65. D. J. Bornhop, S. Dotson, Micro-Scale Polarimetry, in *Chiral Analysis*, K. W. Busch, M. A. Busch, eds., Elsevier, Amsterdam, **2006**.
66. Technical Specifications for Advanced Laser Polarimeter (ALP) (PDR-Chiral, Inc., 2006), retrieved July 6, **2010**, `http://www.pdf-chiral.com/pdr documents/p&s/alpmar06.pdf`.
67. E. S. Yeung, L. E. Steenhoek, S. D. Woodrugg, J. C. Kuo, *Anal. Chem*. **1980**, *52*, 1399–1402; D. R. Bobbitt, E. S. Yeung, *Anal. Chem*. **1984**, *56*, 1577–1581; D. R. Bobbitt, E. S. Yeung, *Anal. Chem*. **1985**, *57*, 271–274; D. R. Bobbitt, E. S. Yeung, *Appl. Spectrosc*. **1986**, *40*, 407–410; X. Xi, E. S. Yeung, *Appl. Spectrosc*. **1989**, *43*, 1337–1341; P. D. Rice, D. R. Bobbitt, *Anal. Chem*. **1990**, *62*, 1661–1665.
68. P. D. Rice, Y. Y. Shao, D. R. Bobbitt, *Talanta* **1989**, *36*, 985–988; K. Ng, T. J. Edkins, D. R. Bobbitt, *Chirality* **1999**, *11*, 187–194; D. R. Bobbitt and S. W. Linder, *Trac-Trend Anal. Chem*. **2001**, *20*, 111–123; S. W. Linder, G. W. Yanik, D. R. Bobbitt, *Microchem. J*. **2004**, *76*, 105–112.
69. D. K. Lloyd, D. M. Goodall, H. Scrivener, *Anal. Chem*. **1989**, *61*, 1238–1243; D. K. Lloyd, D. M. Goodall, *Chirality* **1989**, *1*, 251–264; D. M. Goodall, *Trac-Trend Anal. Chem*. **1993**, *12*, 177–184.
70. C. Chou, K.-H. Chiang, K.-Y. Liao, Y.-F. Chang, C.-E. Lin, *J. Phys. Chem. B* **2007**, *111*, 9919–9922; C.-E. Lin, C.-J. Yu, C.-L. Chen, L.-D. Chou, C. Chou, *J. Phys. Chem. A* **2010**, *114*, 1665–1669.
71. C. Chou, W.-C. Kuo, C.-Y. Han, *Appl. Opt*. **2003**, *42*, 5096–5100; C. Chou, H.-M. Tsai, K.-Y. Liao, L.-D. Chou, P.-H. Huang, *Appl. Opt*. **2006**, *45*, 3733–3739.

72. C.-E. Lin, C.-J. Yu, Y.-C. Li, C.-C. Tsai, C. Chou, *J. Appl. Phys*. **2008**, *104*, 033101/1–4.
73. D. Gernez, *D. Ann. Sci. Ec. Norm. Sup*. **1864**, *1*, 1–38.
74. P.-A. Guye, A.-P. do Amaral, *Arch. Sci. Phys. Nat*. **1895**, *33*, 513–529.
75. T. M. Lowry, H. K. Gore, *Proc. R. Soc. London, Ser. A* **1931**, *A*135, 13–22.
76. M. Vallet, F. Bretenaker, A. Le Floch, R. Le Naour, M. Oger, *Opt. Comm*. **1999**, *168*, 423–443.
77. Y. Le Grand, A. Le Floch, *Opt. Lett*. **1992**, *17*, 360–362.
78. J. Poirson, M. Vallet, F. Bretenaker, A. Le Floch, J.-Y. Thépot, *Anal. Chem*. **1998**, *70*, 4636–4639.
79. F. Vollmer, P. Fischer, *Opt. Lett*. **2006**, *31*, 453–455.
80. T. Muller, K. B. Wiberg, P. H. Vaccaro, *J. Phys. Chem. A* **2000**, *104*, 5959–5968.
81. T. Muller, K. B. Wiberg, P. H. Vaccaro, J. R. Cheeseman, M. J. Frisch, *J. Opt. Soc. Am. B* **2002**, *19*, 125–141.
82. T. Muller, K. B. Wiberg, P. H. Vaccaro, *Rev. Sci. Instrum*. **2002**, *73*, 1340–1342.
83. J. J. Scherer, J. B. Paul, A. O'Keefe, R. J. Saykally, *Chem. Rev*. **1997**, *97*, 25–51; G. Berden, R. Peeters, G. Meijer, *Int. Rev. Phys. Chem*. **2000**, *19*, 565–607; M. D. Wheeler, S. M. Newman, A. J. Orr-Ewing, M. N. R. Ashfold, *J. Chem. Soc. Faraday Trans*. **1998**, *94*, 337–351; C. Vallance, *New J. Chem*. **2005**, *29*, 867–874.
84. S. M. Wilson, K. B. Wiberg, J. R. Cheeseman, M. J. Frisch, P. H. Vaccaro, *J. Phys. Chem. A* **2005**, *109*, 11752–11764.
85. S. M. Wilson, K. B. Wiberg, M. J. Murphy, P. H. Vaccaro, *Chirality* **2008**, *20*, 357–369.
86. R. Engeln, G. Berden, E. van den Berg, G. Meijer, *J. Chem. Phys*. **1997**, *107*, 4458–4467.
87. C. P. Slichter, *Principles of Magnetic Resonance*, 3rd ed., Springer-Verlag, Berlin, **1990**.
88. K. B. Wiberg, Y.-G. Wang, S. M. Wilson, P. H. Vaccaro, J. R. Cheeseman, *J. Phys. Chem. A* **2005**, *109*, 3448–3453.
89. K. B. Wiberg, Y.-G. Wang, S. M. Wilson, P. H. Vaccaro, W. L. Jorgensen, T. D. Crawford, M. L. Abrams, J. R. Cheeseman, M. Luderer, *J. Phys. Chem. A* **2008**, *112*, 2415–2422.
90. A. J. Fresnel, *Ann. Chim. Phys*. **1825**, *28*, 147–161.
91. A. Ghosh, P. Fischer, *Phys. Rev. Lett*. **2006**, *97*, 173002/1–4.
92. A. Ghosh, F. M. Fazal, P. Fischer, *Opt. Lett*. **2007**, *32*, 1836–1838.
93. A. Ghosh, W. Hill, P. Fischer, *Phys. Rev. A* **2007**, *76*, 055402/1–4.
94. H. DeVoe, *J. Chem. Phys*. **1965**, *43*, 3199–3208; B. R. Jennings, G. Spach, T. M. Schuster, *Biopolymers* **1968**, *6*, 635–652.
95. M.-R. Goldsmith, N. Jayasuriya, D. N. Beratan, P. Wipf, *J. Am. Chem. Soc*. **2003**, *125*, 15696–15697.
96. G. Yang, Y. Xu, *Phys. Chem. Chem. Phys*. **2008**, *10*, 6787–6795.
97. M. Losada, H. Tran, Y. Xu, *J. Chem. Phys*. **2008**, *128*, 014508/1–11.
98. P. L. Polavarapu, A. Petrovic, F. Wang, *Chirality* **2003**, *15*, S143–S149.
99. Y. Kumata, J. Furukawa, T. Fueno, *Bull. Chem. Soc. Jpn*. **1970**, *43*, 3920–3921.
100. J. R. Cheeseman, M. J. Frisch, F. J. Devlin, P. J. Stephens, *J. Phys. Chem. A* **2000**, *104*, 1039–1046.
101. K. B. Wiberg, Y.-G. Wang, P. H. Vaccaro, J. R. Cheeseman, G. Trucks, M. J. Frisch, *J. Phys. Chem. A* **2004**, *108*, 32–38.
102. R. G. Parr, W. Yang, *Density-Functional Theory of Atoms and Molecules*, Oxford University Press, New York, **1989**.
103. R. Bauernschmitt, R. Ahlrichs, *Chem. Phys. Lett*. **1996**, *256*, 454–464; M. E. Casida, Time-dependent density-functional response theory for molecules, in *Recent Advances in Density*

Functional Methods, Part I, D. P. Chong, ed., World Scientific Publishing Co., Singapore, **1995**, pp. 155–192.

104. A. D. Becke, *J. Chem. Phys*. **1993**, *98*, 5648–5652; C. Lee, W. Yang, R. G. Parr, *Phys. Rev. B* **1988**, *37*, 785–789.
105. P. J. Stephens, F. J. Devlin, J. R. Cheeseman, M. J. Frisch, *J. Phys. Chem. A* **2001**, *105*, 5356–5371.
106. P. J. Stephens, D. M. McCann, J. R. Cheeseman, M. J. Frisch, *Chirality* **2005**, *17*, S52–S64; D. M. McCann, P. J. Stephens, *J. Org. Chem*. **2006**, *71*, 6074–6098.
107. R. J. Bartlett, Coupled-cluster theory: An overview of recent developments, in *Modern Electronic Structure Theory*, D. R. Yarkony, ed., World Scientific, Singapore, **1995**, Chapter 16, pp. 1047–1131; T. D. Crawford, H. F. Schaefer, An introduction to coupled cluster theory for computational chemists, in *Reviews in Computational Chemistry*, K. B. Lipkowitz and D. B. Boyd, eds., VCH Publishers, New York, **2000**, Chapter 2, pp. 33–136.
108. T. J. Lee, G. E. Scuseria, Achieving chemical accuracy with coupled-cluster theory, in *Quantum Mechanical Electronic Structure Calculations with Chemical Accuracy*, S. R. Langhoff, ed., Kluwer Academic Publishers, Dordrecht, **1995**, pp. 47–108; T. Helgaker, P. Jørgensen, J. Olsen, *Molecular Electronic Structure Theory*, John Wiley & Sons, New York, **2000**; T. Helgaker, T. A. Ruden, P. Jørgensen, J. Olsen, W. Klopper, *J. Phys. Org. Chem*. **2004**, *17*, 913–933.
109. T. Helgaker, W. Klopper, D. P. Tew, *Mol. Phys*. **2008**, *106*, 2107–2143.
110. J. Kongsted, T. B. Pedersen, L. Jensen, A. E. Hansen, K. V. Mikkelsen, *J. Am. Chem. Soc*. **2006**, *128*, 976–982.
111. J. Kongsted, T. B. Pedersen, M. Strange, A. Osted, A. E. Hansen, K. V. Mikkelsen, F. Pawlowski, P. Jørgensen, C. Hättig, *Chem. Phys. Lett*. **2005**, *401*, 385–392.
112. C. T. Campos, F. E. Jorge, T. P. Silva, M. R. Coppo, *Chem. Phys. Lett*. **2010**, *494*, 170–173.
113. M. C. Tam, N. J. Russ, T. D. Crawford, *J. Chem. Phys*. **2004**, *121*, 3550–3557.
114. T. B. Freedman, M. G. Paterlini, N.-S. Lee, L. A. Nafie, J. M. Schwab, T. Ray, *J. Am. Chem. Soc*. **1987**, *109*, 4727–4728; T. B. Freedman, K. M. Spencer, C. McKarthy, S. J. Cianciosi, J. E. Baldwin, L. A. Nafie, J. A. Moore, J. M. Schwab, *Proc. SPIE Int. Soc. Opt. Eng*. **1989**, *1145*, 273–274; T. B. Freedman, K. M. Spencer, N. Ragunathan, L. A. Nafie, J. A. Moore, J. M. Schwab, *Can. J. Chem*. **1991**, *69*, 1619–1629.
115. M. Dierksen, S. Grimme, *J. Chem. Phys*. **2006**, *124*, 174301/1–12.
116. W. Gordy, R. L. Cook, *Microwave Molecular Spectra*, John Wiley & Sons, New York, **1984**.
117. K. Ruud, P. R. Taylor, P.-O. Åstrand, *Chem. Phys. Lett*. **2001**, *337*, 217–223.
118. K. Ruud, R. Zanasi, *Angew. Chem. Int. Ed*. **2005**, *44*, 3594–3596.
119. B. C. Mort, J. Autschbach, *J. Phys. Chem. A* **2005**, *109*, 8617–8623.
120. C. W. Kern, R. L. Matcha, *J. Chem. Phys*. **1968**, *49*, 2081–2091; W. C. Ermler, C. W. Kern, *J. Chem. Phys*. **1971**, *33*, 4851–4860; A. D. Buckingham, W. Urland, *Chem. Rev*. **1975**, *75*, 113–117; G. Riley, W. T. Raynes, P. W. Fowler, *Mol. Phys*. **1979**, *38*, 877–892; D. M. Bishop, *Rev. Mod. Phys*. **1990**, *62*, 343–374; A. J. Russell, M. A. Spackman, *Mol. Phys*. **1995**, *84*, 1239–1255; D. M. Bishop, *Adv. Chem. Phys*. **1998**, *104*, 1–40.
121. K. Ruud, P.-O. Åstrand, P. R. Taylor, *J. Chem. Phys*. **2000**, *112*, 2668–2683; P.-O. Åstrand, K. Ruud, D. Sundholm, *Theor. Chem. Acc*. **2000**, *103*, 365–373; P.-O. Åstrand, K. Ruud, P. R. Taylor, *J. Chem. Phys*. **2000**, *112*, 2655–2667.
122. D. A. Clabo, Jr., W. D. Allen, R. B. Remington, Y. Yamaguchi, H. F. Schaefer III, *Chem. Phys*. **1988**, *123*, 187–239.
123. V. Barone, *J. Chem. Phys*. **2004**, *120*, 3059–3065; V. Barone, *J. Chem. Phys*. **2005**, *122*, 014108/1–10.
124. B. C. Mort, J. Autschbach, *J. Phys. Chem. A* **2006**, *110*, 11381–11383; B. C. Mort, J. Autschbach, *Chem. Phys. Chem*. **2007**, *8*, 605–616.

125. B. C. Mort, J. Autschbach, *Chem. Phys. Chem*. **2008**, *9*, 159–170.

126. E. B. Wilson, Jr., J. C. Decius, P. C. Cross, *Molecular Vibrations: The Theory of Infrared and Raman Vibrational Spectroscopy*, 1980 corrected edition, Dover Publications, New York, **1955**.

127. J. M. Bowman, *Acc. Chem. Res*. **1986**, *19*, 202–208; J. Tennyson, Variational calculations of rotation–vibration spectra, in *Computational Molecular Spectroscopy*, P. Jensen, P. R. Bunker, eds. John Wiley and Sons, Chichester, **2000**, Chapter 9, pp. 305–323; J. M. Bowman, S. Carter, N. C. Handy, *Progress in the Quantum Description of Vibrational Motion in Polyatomic Molecules*, Elsevier B.V., Amsterdam, **2005**.

128. H. H. Nielsen, *Rev. Mod. Phys*. **1951**, *23*, 90–136; I. M. Mills, Vibrational-Rotation Structure in Asymmetric- and Symmetric-Top Molecules, in *Molecular Spectroscopy: Modern Research*, K. N. Rao, ed., Academic Press, New York, **1972**, pp. 115–140.

129. M. Toyama, T. Oka, Y. Morino, *J. Mol. Spectrosc*. **1964**, *13*, 193–213; S. P. A. Sauer, M. J. Packer, The *ab initio* calculation of molecular properties other than the potential energy surface, in *Computational Molecular Spectroscopy*, P. Jensen, P. R. Bunker, eds., John Wiley & Sons, Chichester, **2000**, Chapter 7, pp. 221–252.

130. K. B. Wiberg, Y.-G. Wang, M. J. Murphy, P. H. Vaccaro, *J. Phys. Chem. A* **2004**, *108*, 5559–5563.

131. D. J. Tozer, R. D. Amos, N. C. Handy, B. O. Roos, L. Serrano-Andrés, *Mol. Phys*. **1999**, *97*, 859–868; D. J. Tozer, N. C. Handy, *Phys. Chem. Chem. Phys*. **2000**, *2*, 2117–2121; R. Burcl, R. D. Amos, N. C. Handy, *Chem. Phys. Lett*. **2002**, *355*, 8–18; A. Dreuw, J. L. Weisman, M. Head-Gordon, *J. Chem. Phys*. **2003**, *119*, 2943–2946.

132. T. B. Pedersen, J. Kongsted, T. D. Crawford, K. Ruud, *J. Chem. Phys*. **2009**, *130*, 034310/1–7.

133. T. B. Pedersen, J. Kongsted, T. D. Crawford, *Chirality* **2009**, *21*, E68–E75.

134. F. Wang, P. L. Polavarapu, *J. Phys. Chem. A* **2000**, *104*, 6189–6196.

135. J. He, A. Petrovic, P. L. Polavarapu, *J. Phys. Chem. A* **2004**, *108*, 1671–1680; J. He, A. G. Petrovic, P. L. Polavarapu, *J. Phys. Chem. A* **2004**, *108*, 20451–20457; A. G. Petrovic, P. L. Polavarapu, J. Drabowicz, P. Łyżwa, M. Mikołajczyk, W. Wieczorek, A. Balińska, *J. Org. Chem*. **2008**, *73*, 3120–3129; P. L. Polavarapu, N. Jeirath, S. Walia, *J. Phys. Chem. A* **2009**, *113*, 5423–5431.

136. P. J. Stephens, F. J. Devlin, J. R. Cheeseman, M. J. Frisch, C. Rosini, *Org. Lett*. **2002**, *4*, 4595–4598; P. J. Stephens, F. J. Devlin, J. R. Cheeseman, M. J. Frisch, *Chirality* **2002**, *14*, 288–296; P. J. Stephens, F. J. Devlin, J. R. Cheeseman, M. J. Frisch, O. Bortolini, P. Besse, *Chirality* **2003**, *15*, S57–S64.

137. K. B. Wiberg, P. H. Vaccaro, J. R. Cheeseman, *J. Am. Chem. Soc*. **2003**, *125*, 1888–1896.

138. K. B. Wiberg, Y.-G. Wang, P. H. Vaccaro, J. R. Cheeseman, M. R. Luderer, *J. Phys. Chem. A* **2005**, *109*, 3405–3410; K. B. Wiberg, S. M. Wilson, Y.-G. Wang, P. H. Vaccaro, J. R. Cheeseman, M. R. Luderer, *J. Org. Chem*. **2007**, *72*, 6206–6214.

139. M. C. Tam, T. D. Crawford, *J. Phys. Chem. A* **2006**, *110*, 2290–2298.

140. T. D. Crawford, W. D. Allen, *Mol. Phys*. **2009**, *107*, 1041–1057.

141. M. Pecul, K. Ruud, A. Rizzo, T. Helgaker, *J. Phys. Chem. A* **2004**, *108*, 4269–4276; D. Marchesan, S. Coriani, C. Forzato, P. Nitti, G. Pitacco, K. Ruud, *J. Phys. Chem. A* **2005**, *109*, 1449–1453.

142. S. Coriani, A. Baranowska, L. Ferrighi, C. Forzato, D. Marchesan, P. Nitti, G. Pitacco, A. Rizzo, K. Ruud, *Chirality* **2006**, *18*, 357–369.

143. M. D. Kundrat, J. Autschbach, *J. Phys. Chem. A* **2006**, *110*, 4115–4123; M. D. Kundrat, J. Autschbach, *J. Phys. Chem. A* **2006**, *110*, 12908–12917; M. D. Kundrat, J. Autschbach, *J. Chem. Theory Comput*. **2008**, *4*, 1902–1914; M. D. Kundrat, J. Autschbach, *J. Am. Chem. Soc*. **2008**, *130*, 4404–4414; M. D. Kundrat, J. Autschbach, *J. Chem. Theory Comput*. **2009**, *5*, 1051–1060.

144. S. Grimme, A. Bahlmann, G. Haufe, *Chirality* **2002**, *14*, 793–797.

145. W. Al-Basheer, R. M. Pagni, R. N. Compton, *J. Phys. Chem. A* **2007**, *111*, 2293–2298.

146. R. K. Kondru, P. Wipf, D. N. Beratan, *J. Phys. Chem. A* **1999**, *103*, 6603–6611.

147. J. Kaminsky, I. Raich, K. Tomcakova, P. Bour, *J. Comput. Chem*. **2010**, *31*, 2213–2224.

148. T. Mori, Y. Inoue, S. Grimme, *J. Org. Chem*. **2006**, *71*, 9797–9806; T. Mori, Y. Inoue, S. Grimme, *J. Phys. Chem. A* **2007**, *111*, 7995–8006.

149. R. K. Kondru, P. Wipf, D. N. Beratan, *J. Am. Chem. Soc*. **1998**, *120*, 2204–2205; S. Ribe, R. K. Kondru, D. N. Beratan, P. Wipf, *J. Am. Chem. Soc*. **2000**, *122*, 4608–4617; R. K. Kondru, D. N. Beratan, G. K. Friestad, A. B. Smith, III, P. Wipf, *Org. Lett*. **2000**, *2*, 1509–1512; K. M. Specht, J. Nam, D. M. Ho, N. Berova, R. K. Kondru, D. N. Beratan, P. Wipf, R. A. Pascal, Jr., D. Kahne, *J. Am. Chem. Soc*. **2001**, *123*, 8961–8966; G. Zuber, M.-R. Goldsmith, T. D. Hopkins, D. N. Beratan, P. Wipf, *Org. Lett*. **2005**, *7*, 5269–5272.

150. E. Giorgio, R. G. Viglione, C. Rosini, *Tetrahedron: Asymmetry* **2004**, *15*, 1979–1986; E. Giorgio, M. Roje, K. Tanaka, Z. Hamersak, V. Sunjic, K. Nakanishi, C. Rosini, N. Berova, *J. Org. Chem*. **2005**, *70*, 6557–6563; E. Giorgio, K. Tanaka, L. Verotta, K. Nakanishi, N. Berova, C. Rosini, *Chirality* **2007**, *19*, 434–445.

151. L. A. Curtiss, K. Raghavachari, P. C. Redfern, V. Rassolov, J. A. Pople, *J. Chem. Phys*. **1998**, *109*, 7764–7776.

152. J. Fidler, P. M. Rodger, A. Rodger, *J. Chem. Soc. Perkin Trans. 2* **1993**, *1993*, 235–241; J. Fidler, P. M. Rodger, A. Rodger, *J. Am. Chem. Soc*. **1994**, *116*, 7266–7273.

153. G. Fischer, *Vibronic Coupling: The Interaction Between the Electronic and Nuclear Motions*, Academic Press, London, **1984**; M. F. Ruiz-Lopez, D. Rinaldi, J. L. Rivail, *Chem. Phys*. **1986**, *110*, 401–414.

154. B. Mennucci, J. Tomasi, R. Cammi, J. R. Cheeseman, M. J. Frisch, F. J. Devlin, S. Gabriel, P. J. Stephens, *J. Phys. Chem. A* **2002**, *106*, 6102–6113.

155. J. Tomasi, M. Persico, *Chem. Rev*. **1994**, *94*, 2027–2094; C. J. Cramer, D. G. Truhlar, *Chem. Rev*. **1999**, *99*, 2161–2200; J. Tomasi, R. Cammi, B. Mennucci, C. Cappelli, S. Corni, *Phys. Chem. Chem. Phys*. **2002**, *4*, 5607–5712; J. Tomasi, *Theor. Chem. Acc*. **2004**, *112*, 184–203; J. Tomasi, B. Mennucci, R. Cammi, *Chem. Rev*. **2005**, *105*, 2999–3093; B. Mennucci, *J. Phys. Chem. Lett*. **2010**, *1*, 1666–1674.

156. M. A. Aguilar, F. J. Olivares del Valle, J. Tomasi, *J. Chem. Phys*. **1993**, *98*, 7375–7384; B. Mennucci, *Theor. Chem. Acc*. **2006**, *116*, 31–42; B. Mennucci, C. Cappelli, C. Achille Guido, R. Cammi, J. Tomasi, *J. Phys. Chem. A* **2009**, *113*, 3009–3020.

157. M. Pecul, D. Marchesan, K. Ruud, S. Coriani, *J. Chem. Phys*. **2005**, *122*, 024106/1–9.

158. P. Mukhopadhyay, G. Zuber, M.-R. Goldsmith, P. Wipf, D. N. Beratan, *Chem. Phys. Chem*. **2006**, *7*, 2483–2486.

159. P. Mukhopadhyay, G. Zuber, P. Wipf, D. N. Beratan, *Angew. Chem. Int. Ed*. **2007**, *46*, 6450–6452.

160. Z. Su, Q. Wen, Y. Xu, *J. Am. Chem. Soc*. **2006**, *128*, 6755–6760.

161. Z. Su, Y. Xu, *Angew. Chem. Int. Ed*. **2007**, *46*, 6163–6166.

162. M. Losada, P. Nguyen, Y. Xu, *J. Phys. Chem. A* **2008**, *112*, 5621–5627.

163. M. Losada, Y. Xu, *Phys. Chem. Chem. Phys*. **2007**, *9*, 3127–3135; E. Debie, L. Jaspers, P. Bultinck, W. Herrebout, B. Van Der Veken, *Chem. Phys. Lett*. **2008**, *250*, 426–430; E. Debie, P. Bultinck, W. Herrebout, B. van der Veken, *Phys. Chem. Chem. Phys*. **2008**, *10*, 3498–3508.

164. A. T. Fischer, R. N. Compton, R. M. Pagni, *J. Phys. Chem. A* **2006**, *110*, 7067–7071.

165. M. J. Kamlet, J. L. Abboud, R. W. Taft, *J. Am. Chem. Soc*. **1977**, *99*, 6027–6038; M. J. Kamlet, J. L. Abboud, M. H. Abraham, R. W. Taft, *J. Org. Chem*. **1983**, *48*, 2877–2887.

166. L. Onsager, *J. Am. Chem. Soc*. **1936**, *58*, 1486–1493.

167. J. B. Foresmann, T. A. Keith, K. B. Wiberg, J. Snoonian, M. J. Frisch, *J. Phys. Chem*. **1996**, *100*, 16098–16104; M. W. Wong, M. J. Frisch, K. B. Wiberg, *J. Am. Chem. Soc*. **1991**, *113*, 4776–4782.

168. K. B. Wiberg, T. A. Keith, M. J. Frisch, M. Murko, *J. Phys. Chem*. **1995**, *99*, 9072–9079; O. W. Kolling, *Trans. Kansas Acad. Sci*. **1998**, *101*, 89–94.

169. K. B. Wiberg, P. R. Rablen, D. J. Rush, T. A. Keith, *J. Am. Chem. Soc*. **1995**, *117*, 4261–4270; K. B. Wiberg, D. J. Rush, *J. Am. Chem. Soc*. **2001**, *123*, 2038–2046.

170. H. Castejon, K. B. Wiberg, *J. Am. Chem. Soc*. **1999**, *121*, 2139–2146.

171. C. N. R. Rao, S. Singh, V. P. Senthilnathan, *Chem. Soc. Rev*. **1976**, *5*, 297–316; M. G. Giorgini, G. Fini, P. Mirone, *J. Chem. Phys*. **1983**, *79*, 639–643; P. Suppan, *J. Photochem. Photobiol*. **1990**, *50*, 293–330; B. Linder, *J. Phys. Chem*. **1992**, *96*, 10708–10712.

172. O. W. Kolling, *J. Phys. Chem*. **1992**, *96*, 6217–6220; O. W. Kolling, *J. Phys. Chem*. **1996**, *100*, 16087–16091; O. W. Kolling, *Appl. Spectrosc*. **1999**, *53*, 29–32; O. W. Kolling, *Appl. Spectrosc*. **2000**, *54*, 890–893.

12

CHIROPTICAL IMAGING OF CRYSTALS

John Freudenthal, Werner Kaminsky, and Bart Kahr

12.1. INTRODUCTION

Chiroptical imaging, in the main, is the use of circular birefringence (CB, optical rotation) or circular dichroism (CD) as contrast mechanisms for substances that are inhomogeneous in the object plane [1]. The term is a misnomer because nonenantiomorphous systems can surely give rise to CB and CD [2]. Nevertheless, we yield to common usage. Chiroptical imaging may also refer to less common effects such as circular intensity differential scattering (CIDS), observed when the size of scatterers such as biopolymers approach the wavelength of light [3]. This discussion emphasizes the real and imaginary parts of the linear susceptibility [nonlinear chiroptics is considered elsewhere in this volume (Chapters 13 and 14)] of circularly polarized light most commonly investigated (CB and CD). Other chiroptical effects are also considered such as Faraday rotation, a magneto-optical phenomenon, because of its close phenomenological relationship to CB. On the other hand, we will not cover magnetic circular dichroism imaging in the X-ray region of the electromagnetic spectrum [4–6]. X-rays skirt the troublesome linear anisotropies in crystalline media that make chiroptical imaging in less energetic parts of the spectrum so vexing and interesting.

Chiroptical images are trivial to make in some special cases. Three examples follow. For instance, in basal {0001} sections of quartz, the left- and right-handed so-called Brazil twins are differentiated by rotating an analyzer by a small amount (3° in the case shown in Figure 12.1) [7]. The optical rotation of only one enantiomorph is nulled. This experiment is easy to execute for visible light passed along the optic axis of quartz because there

Comprehensive Chiroptical Spectroscopy, Volume 1: Instrumentation, Methodologies, and Theoretical Simulations, First Edition. Edited by N. Berova, P. L. Polavarapu, K. Nakanishi, and R. W. Woody.
© 2012 John Wiley & Sons, Inc. Published 2012 by John Wiley & Sons, Inc.

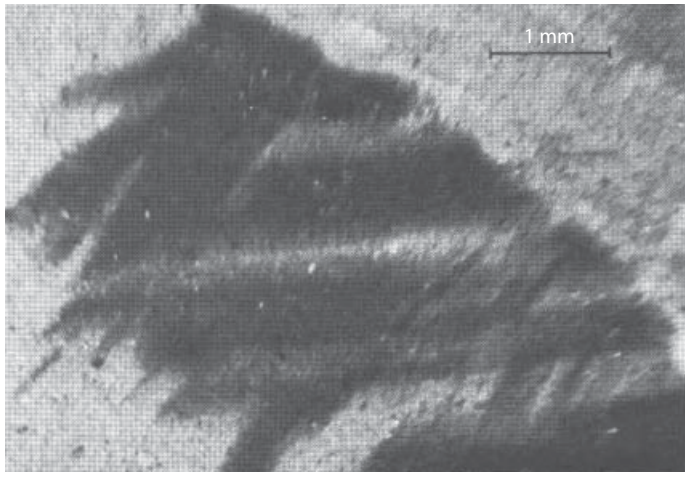

Figure 12.1. Enantiomorphous Brazil twinning in (0001) quartz plate. Analyzer rotated by 3°. Scale bar = 0.2 mm. (Reproduced from reference 7 with permission of the American Mineralogical Society.)

is no absorption and CB is the only mechanism allowed by symmetry for shifting the phase of the light passing through the medium. The perturbation of the light polarization can be described by a simple rotation matrix.

In isotropic media, chiroptical contrast is likewise trivial. Enantiomorphous domains of helical filamentous liquid crystals with large optical rotations have been photographed [8], as was quartz in Figure 12.1. CD images of disordered *d*-camphorsulfonic acid films with a spatial resolution of <1 μm were obtained by Yamada et al. [9] by applying a polarizing undulator to near-UV synchrotron radiation, although this experiment can hardly be described as trivial. A film of cubic yttrium iron garnet appears optically active, however, in this case, the spontaneous magnetization causes Faraday rotation of linearly polarized light (Figure 12.2).

What makes chiroptical imaging a fitting subject for a chapter in *Comprehensive Chiroptical Spectroscopy* are the challenges that are introduced when CB or CD is the desired contrast mechanism for a system that also exhibits much larger linear anisotropies, namely LB and LD, well known to be 10^3–10^4 times larger than their

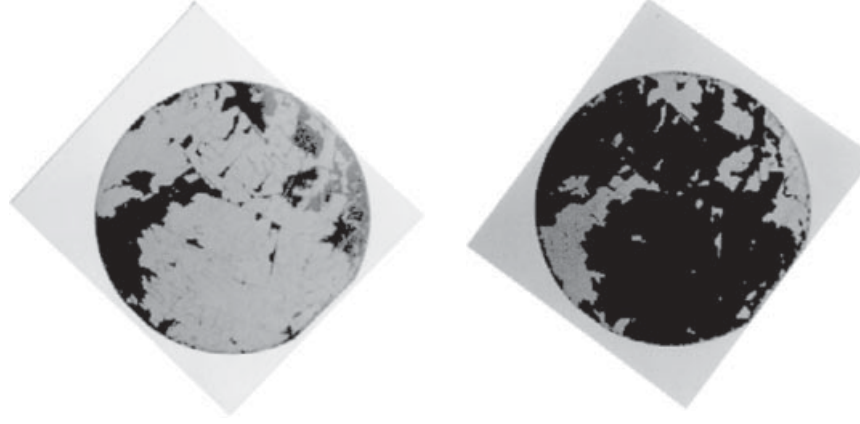

Figure 12.2. Film of yttrium iron garnet (8-cm diameter) between slightly uncrossed polarizers. (Reproduced from reference 10 with permission of IOP Publishing.)

circular counterparts [10]. Measuring CB and CD in crystals of arbitrary symmetry has for two centuries been likened to the search for a needle in a haystack. For this reason, we know virtually nothing from experiment about the orientational dependence of chiroptics of molecules, an enormous hole in the science of molecular chirality [2, 10].

12.2. DIFFERENTIAL POLARIZATION IMAGING

Often additional information about complex samples can be extracted from a comparison of images made with different incident polarization states, or different analyzing states. This general strategy is called differential polarization imaging (DPI). A simple, albeit alarming, example of DPI was given by researchers of the US Army Research Laboratories [11]. A lyrical field with some trees was captured in an ordinary aerial photograph, but when the same scene was displayed as the difference of intensity captured with orthogonal analyzers, two trucks in shadow that polarize radiation by reflection were exposed.

In the 1980s, Tinoco, Maestre, and Bustamante, working together in Berkeley, California, developed DPI to a high art for application to problems in biophysics [12]. Much of their work was motivated by the desire for a chiroptical microscope for complex, organized structures. Maestre et al. first adapted a Carey spectropolarimeter to a microscope [13–16] for single-point measurements of the CD spectra of chromatin. In this early work, they faced instrumental artifacts [17, 18] arising from imperfect polarization states [19]. Residual ellipticities, when coupled with LB and LD of ordered media, generate artifactual CD signals, a recurrent theme in the study of the chiroptical properties of organized systems [20–23].

In 1985, the Berkeley group introduced an imaging device [24]. The transmission through a microscope was analyzed by a linear 256-diode array detector that was translated to produce an image. The difference between the left- and right-circular polarization states could then be plotted, in principle, as CD. Alternatively, a sample micro-positioning stage was used to make images in conjunction with a photomultiplier tube detector for the analysis of spermatocyte nuclei [25]. The DPI microscope was fitted with a pinhole for confocal measurements [26] for CD microscopy of heterochiral domains of associated chromophores in spinach chloroplasts [27].

The propagation of light through complex samples interposed between trains of optical elements can be treated by the Jones calculus or the Stokes–Mueller calculus. The Berkeley group relied mainly on the Stokes–Mueller formalism because it is most suited to depolarizing effects introduced by biological samples. In what follows, we adhere to the Stokes–Mueller formalism for coherence, even though many of the original papers cited, especially those dealing with slightly depolarizing single crystals, employed the Jones calculus. Moreover, no sample is wholly free of depolarization.

12.3. COMPLETE VERSUS INCOMPLETE POLARIMETERS

The Stokes–Mueller calculus is based upon the description of partially polarized light by a so-called Stokes vector (S), a 4×1 matrix, and the transformation of the Stokes vector by an operator, the 4×4 Mueller matrix, embodying the behavior of an optical

system [28]. $S_{\text{out}} = MS_{\text{in}}$ where

$$S = \begin{bmatrix} I \\ Q \\ U \\ V \end{bmatrix} = \begin{bmatrix} |E_x|^2 + |E_y|^2 \\ |E_x|^2 - |E_y|^2 \\ 2E_xE_y\cos\varphi \\ 2E_xE_y\sin\varphi \end{bmatrix} = \begin{bmatrix} I_o = I_x + I_y \\ I_x - I_y \\ I_{45^\circ} - I_{-45^\circ} \\ I_R - I_L \end{bmatrix},$$

$$M = \begin{bmatrix} M_{00} & M_{01} & M_{02} & M_{03} \\ M_{10} & M_{11} & M_{12} & M_{13} \\ M_{20} & M_{21} & M_{22} & M_{23} \\ M_{30} & M_{31} & M_{32} & M_{33} \end{bmatrix}. \tag{12.1}$$

E_x and E_y in Eq. (12.1) are the electric field amplitudes for light propagating in the z direction, and φ is the phase shift that the medium introduces between these modes. S is defined by the following four parameters: I for the total intensity, Q for the difference in intensities of linear polarized light at 0° and 90°, U for the difference in intensities of linearly polarized light at $\pm 45^\circ$, and V for the difference between left- and right-circularly polarized light (CPL) intensities. The broad applicability of the Stokes–Mueller formalism provides a framework for presenting a variety of polarimeters. The elements of the sample's Mueller matrix that can be extracted depend on the nature of the optical elements before and after the sample.

An imaging polarimeter that functions by analogy with a CD spectropolarimeter is shown in Figure 12.3a. We call it a circular extinction (CE) microscope since extinction is a more general term than dichroism, because it embodies mechanisms of differential circular transmission other than absorption (A). The CE microscope outlined below measures the M_{03} Mueller matrix element. A linear polarizer produces E_x polarized light characterized by the Stokes vector $S_{in} = [1, 1, 0, 0]$. A polarizer oriented at $\pm 45^\circ$ with Mueller matrix $M_{pol}(\pm\pi/4)$, transmits its output through a variable

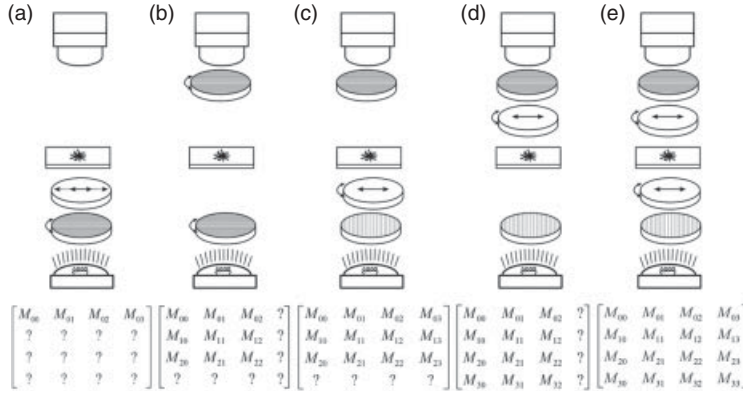

Figure 12.3. (a) CE microscope. (b) High-accuracy universal polarimeter (HAUP) instrument. (c, d) Standard ellipsometer configurations. (e) Mueller matrix microscope. All instruments are bounded by a camera on top and by a light source on the bottom, and they have samples on slides in the middle. Ruled disks are linear polarizers. Disks with double-headed arrows or variable double-headed arrows (as in *a*) are waveplates and compensators, respectively. Curved arrows indicate rotating components. Microscope objectives or other kind of lenses (not pictured) are likely to be present in the instruments.

Babinet–Soleil compensator with a retardance of a quarter wave, $M_{ret}(\pi/2)$. Each optical element is characterized by its own Mueller matrix. The Mueller matrices for a linear polarizer $M_{pol}(\theta)$ and waveplate $M_{ret}(\delta,\theta)$ with a variable retardance δ are shown in Eqs. (12.2).

$$M_{pol}(\theta) = \frac{1}{2}\begin{bmatrix} 1 & \cos 2\theta & \sin 2\theta & 0 \\ \cos 2\theta & \cos^2 2\theta & \sin 2\theta \cos 2\theta & 0 \\ \sin 2\theta & \sin 2\theta \cos 2\theta & \sin^2 2\theta & 0 \\ 0 & 0 & 0 & 0 \end{bmatrix},$$

$$M_{ret}(\delta,\theta) = \begin{bmatrix} 1 & 0 & 0 & 0 \\ 0 & \cos^2 2\theta + \cos\delta \sin^2 2\theta & (1-\cos\delta)\sin 2\theta \cos 2\theta & -\sin\delta \sin 2\theta \\ 0 & (1-\cos\delta)\sin 2\theta \cos 2\theta & \sin^2 2\theta + \cos\delta \cos^2 2\theta & \sin\delta \cos 2\theta \\ 0 & \sin\delta \sin 2\theta & -\sin\delta \cos 2\theta & \cos\delta \end{bmatrix}. \tag{12.2}$$

The combination $M_{ret}(\frac{\pi}{2})M_{pol}(\pm\frac{\pi}{4})S_{in}$ produces right and left CPL: $S_R = [1,0,0,1]$ and $S_L = [1,0,0,-1]$. The relationship $S_{out} = M_{sample}S_{R/L}$ yields $M_{03} = (I_R - I_L)/I_o$.

A polarimeter with a rotating linear polarizer and a rotating linear analyzer (Figure 12.3b) is capable of measuring 9 of the 16 Mueller matrix elements. By adding a rotating birefringent element before or after the sample (Figure 12.3c,d), 12 of the 16 Mueller matrix elements can be measured. Two rotating waveplates affect the measurement of all 16 Mueller matrix elements (Figure 12.3e). An expression for such a device is shown in Eq. (12.3):

$$S_{out} = M_{pol}(\theta_{pol})M_{ret}(\delta_A,\theta_{An})M_{sample}M_{ret}(\delta_G,\theta_{Gn})M_{pol}(0)S_{in}. \tag{12.3}$$

S_{in} is the Stokes vector of the monochromatic source illumination, θ_{Gn} is the alignment of the retarder in the polarization state generator (PSG) for measurement n, δ_G is the PSG's retardance, θ_{An} is the alignment of the retarder in the polarization state analyzer (PSA) for measurement n, δ_A is the PSA's retardance, θ_{pol} is the angle of the PSA's polarizer, and S_{out} is the output Stokes vector.

The greater the number of polarization states generated, and the greater the number of analyzed states, the greater the information content in the Mueller matrix. However, a crystal containing all manner of optical phenomena scatters the effects of fundamental phenomena of interest (*LD, LB, CD, CB*) among Mueller matrix elements [29].

To separate linear and circular anisotropies, one can implement the lamellar approximation for light propagating through a homogeneous medium first pioneered by Jones [30] and later developed for Mueller matrices by Azzam [31]. We express the infinitesimal change in the Stokes vector's input by the differential equation in Eq. (12.4):

$$dS/dz = mS, \qquad \text{where } m = \lim_{\Delta z \to 0} \frac{M_{z,\Delta z} - I}{\Delta z} = \begin{bmatrix} A & -LD & -LD' & CD \\ -LD & A & CB & LB' \\ -LD' & -CB & A & -LB \\ CD & -LB' & LB & A \end{bmatrix}. \tag{12.4}$$

Matrix m is a Mueller matrix that describes the passage through a complex medium through which light travels an infinitessimal distance Δz with the following parameters, Eqs. (12.5):

$$A = \ln 10\frac{A_x + A_y}{2}, \qquad LD = \ln 10\frac{A_x - A_y}{2}, \qquad LB = \frac{2\pi(n_x - n_y)L}{\lambda},$$
$$LD' = \ln 10\frac{A_{45} - A_{135}}{2}, \qquad LB' = \frac{2\pi(n_{45} - n_{135})L}{\lambda}, \qquad CD = \ln 10\frac{A_L - A_R}{2},$$
$$CB = \frac{2\pi(n_L - n_R)L}{\lambda}. \tag{12.5}$$

A is absorbance, and n is refractive index, and L is the sample thickness. *LB'* and *LD'* refer the linear birefringence and linear dichroism along a secondary set of axes bisecting the primary set. These latter parameters permit the measurement of arbitrarily aligned samples.

Analytical methods for the extraction of the relevant optical parameters from an experimental Mueller matrix have been deduced only recently [32–34]. According to the rather compact method of Arteaga and Canillas [34], a Jones matrix is expressed in polar coordinates whose amplitudes (r_{ij}) and phase factors (q_i) are in turn expressed in terms of the elements of a nondepolarizing Mueller matrix [Eqs. (12.6)]:

$$r_{00} = \sqrt{\frac{M_{00} + M_{01} + M_{10} + M_{11}}{2}}, \qquad r_{01} = \sqrt{\frac{M_{00} - M_{01} + M_{10} - M_{11}}{2}},$$
$$r_{10} = \sqrt{\frac{M_{00} + M_{01} - M_{10} - M_{11}}{2}}, \qquad r_{11} = \sqrt{\frac{M_{00} - M_{01} - M_{10} + M_{11}}{2}},$$
$$q_1 = e^{i\tan^{-1}\left(\frac{-M_{03} - M_{13}}{M_{02} + M_{12}}\right)}, \qquad q_2 = e^{i\tan^{-1}\left(\frac{M_{30} + M_{31}}{M_{20} + M_{21}}\right)},$$
$$q_3 = e^{i\tan^{-1}\left(\frac{M_{32} - M_{23}}{M_{22} + M_{33}}\right)}. \tag{12.6}$$

These parameters are then combined as K, to yield T, from which Ω is computed [see Eqs. (12.7)]:

$$K = (r_{00}r_{11}q_3 - r_{01}r_{10}q_1q_2)^{-1/2}, \quad T = \cos^{-1}\left(\frac{K(r_{00} + r_{11}q_3)}{2}\right), \quad \Omega = \frac{TK}{\sin(T)}. \tag{12.7}$$

Finally, we solve for the fundamental optical quantities as components of generalized retardances [29] L, L', and C, defined in Eqs. (12.8):

$$L = i\Omega(r_{00} - r_{11}q_3) = LB - iLD,$$
$$L' = i\Omega(r_{01}q_1 + r_{10}q_2) = LB' - iLD', \tag{12.8}$$
$$C = \Omega(r_{01}q_1 - r_{10}q_2) = CB - iCD.$$

12.4. OPTICAL ROTATION

To measure CB along a general direction of a transparent crystal, the influence of LB must be deconvolved from the CB. Although the intensity of light passing through a polarizer, a chiral anisotropic sample, and an analyzer contains the necessary information for extracting CB, implementation of this idea prior to the invention of electrophotometry and stable, high-intensity light sources was impossible. For generations, most researchers conceded that measuring CB in the presence of large LB was not a realistic goal. In 1983, Uesu and Kobayashi pushed through this perceived impasse by using lasers, photon counting, and computerized modulation of polarizer and analyzer orientations to determine CB in crystals for directions off the optic axes [35]. This experiment was named HAUP (high-accuracy universal polarimetry) whose basic geometry is given in Figure 12.3b.

To apply the HAUP technique to heterogeneous crystals, the polarimeter was fitted with a translation stage in order to produce topographs of the optical parameters. In this way, maps were made comprising 100 × 100 pixels at a resolution of about 30 μm per pixel. This experiment, S-HAUP for scanning high accuracy universal polarimetry, provided the first image of CB measured along a birefringent direction in a crystal, in this case the ferroelastic mineral langbeinite, $K_2Cd_2(SO_4)_3$ [36]. This measurement also involved LB variation by tilting [37] the crystal about an axis perpendicular to the wavevector. Tilting introduces an analytical modulation to the measured intensities that can be fit with CB as a variable parameter. In this way, ferroelastic domains in langbeinite with optical activity were revealed. However, given the time-consuming measurement process requiring successive scanning and tilting, the resolution of the image was low.

Domains in triglycine sulfate, a model ferroelectric, cannot be detected by ordinary polarization microscopy because the optical plane has the same orientation no matter the direction of the polar axis. But, when the paraelectric phase (C_{2h}) becomes ferroelectric (C_2), the material becomes chiral. Enantiomorphs were then revealed by the S-HAUP method [38].

Topographs (Figure 12.4) of the spontaneous Faraday effect in $FeBO_3$ were recorded below the Curie temperature [39]. Unlike the yttrium iron garnet (Figure 12.2) discussed in the introduction, identifying these domains required careful polarimetry by the S-HAUP method because of the large LB.

These early examples of chiroptical imaging were of admittedly complex, ferroic materials: ferroelastic, ferroelectric, and ferromagnetic, respectively. In the case of triglycine sulfate, the optical rotation is most likely a convolution of natural optical activity and electrogyration [9] in the ferroelectric phase.

The quintessential, *simple* chiral crystals are $NaClO_3$ and $NaBrO_3$. These substances have long puzzled crystallographers ever since Marbach observed that levorotatory crystals of $NaClO_3$ nucleated dextrorotatory crystals of its isomorph $NaBrO_3$ and vice versa [40, 41]. Bijvoet [42] ultimately established, on the basis of the anomalous dispersion of X-rays, that homochiral crystals of $NaClO_3$ and $NaBrO_3$ do indeed have opposite signs of optical rotation. Why? An experiment that might lend some insight into this problem would exploit the miscibility of the two halates to determine whether the contributions from the components to the rotatory power were independent of one another. This question has not been addressed because the mixed crystals display anomalous LB [43–45] that preclude measurements of CB. The as-grown crystal S-HAUP topographs showed a chaotic ensemble of dextro- and levorotatory domains (Figure 12.5d) indicating the segregation of BrO_3^- and ClO_3^- on the microscale, a judgment supported by

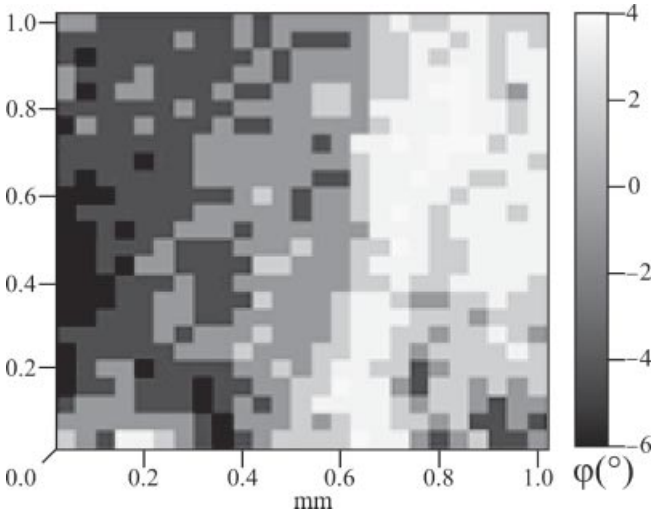

(a)

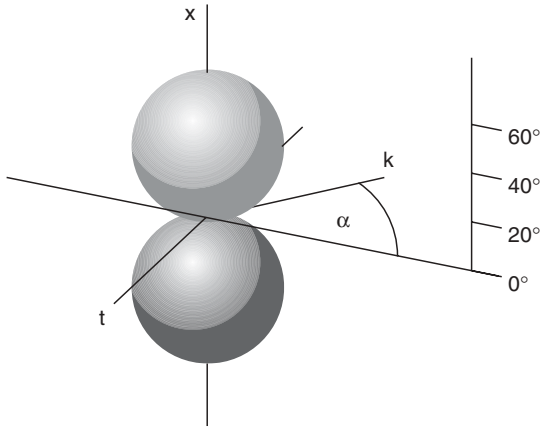

(b)

Figure 12.4. $FeBO_3$. (a) Topography of spontanous Faraday rotation. Grayscale in degrees/mm. (b) Representation surface of spontaneous Faraday effect in degrees/mm. The distance from the origin represent the size of the effect. Black is positive rotation, white is negative. The experimental tilt axis is **t, n** is the crystal plate normal, and **k** is the wavevector.

independent researchers [46]. Annealing near the melting temperature can remove the anomalous birefringence and restore $P2_13$ symmetry. While annealing, these domains merged into homogeneous regions as the anions diffused at higher temperatures [47]. S-HAUP topographs in Figures 12.5e–h display the separation of the transmission, LB, extinction, and CB of a mixed halate crystal grown after partial annealing at 200°C.

Quantitative imaging of chiral crystals can be achieved using the configuration in Figure 12.3d (albeit the waveplate is fixed), coupled with additional components for conoscopic illumination including a microscope substage condenser and a lens to carry the back focal plane of the objective to the eyepiece or camera. In this way, the so-called Airy's spiral, a twisting of the isogyres in the conoscope, becomes vivid. Geday and Glazer used this technique to determine the sign and rotation of quartz crystals as shown in Figure 12.6 [48]. Airy's spirals associated with cholesteric liquid crystals were likewise measured [49].

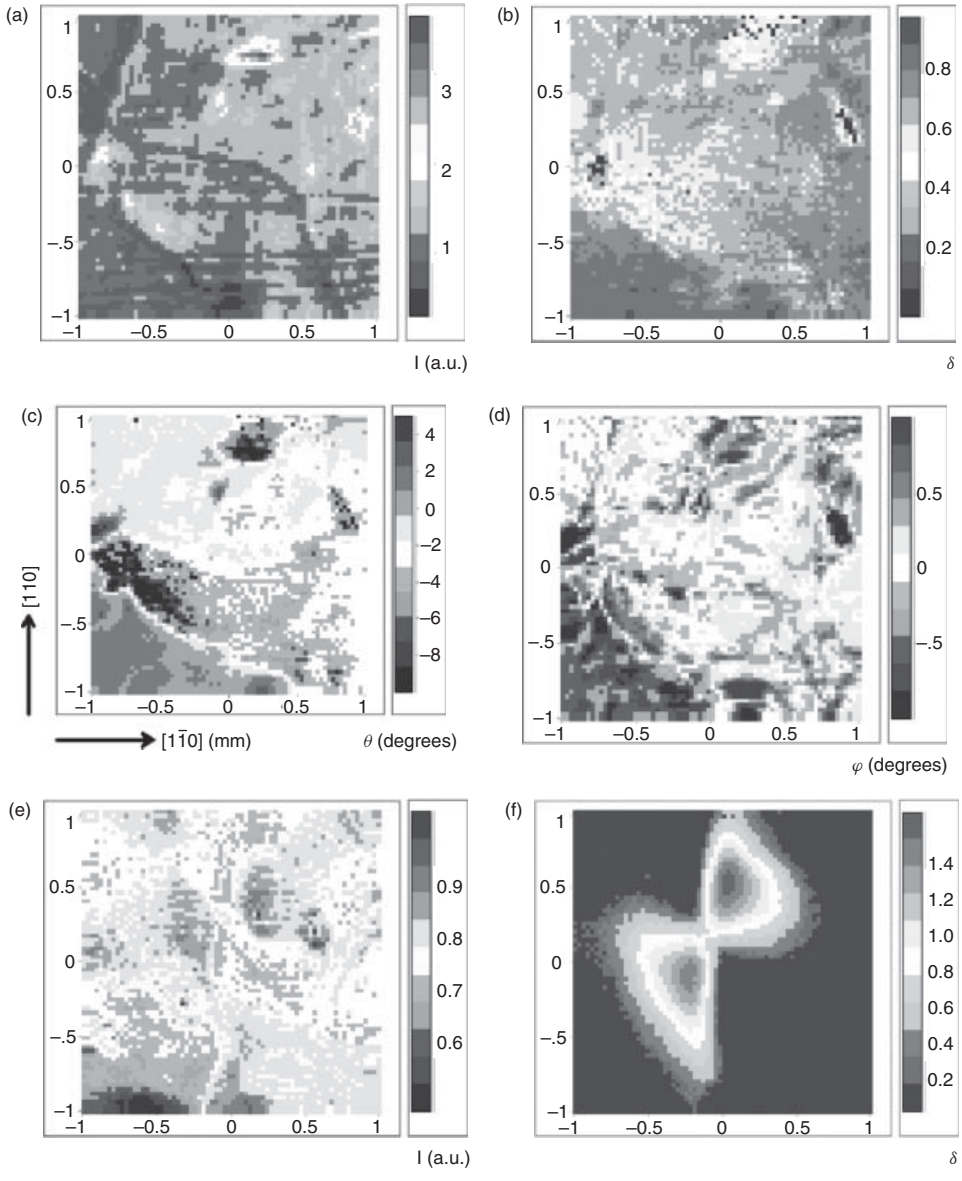

Figure 12.5. S-HAUP generated topographs of optical properties of a mixed halate ($NaCl_{0.5}Br_{0.5}O_3$, 0.435-mm-thick) crystal. Scan direction **x** is along [110]. Crystals grown at room temperature: (a) transmission (arbitrary units, a.u.), (b) phase difference δ, (c) extinction θ (deg); (d) optical rotation φ(deg) $= \frac{1}{2}$(CB). After annealing at 200°C: (e) transmission (arbitrary units, a.u.), (f) phase difference δ, (g) extinction θ(deg); (h) optical rotation φ (deg). (Parts a–d reproduced from reference 47 with permission of the Royal Society of Chemistry.)

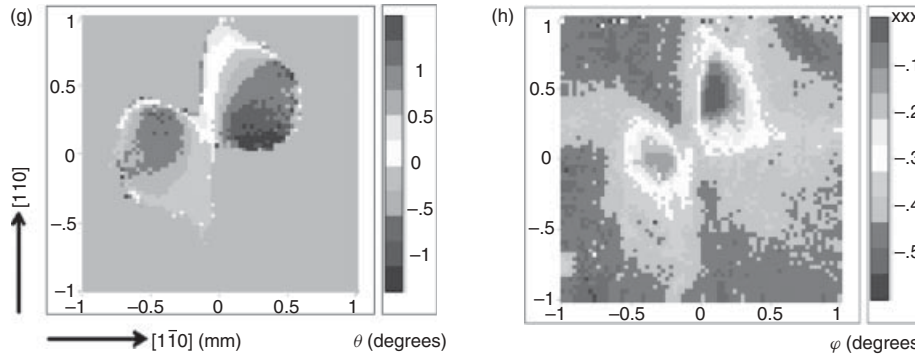

Figure 12.5. (*Continued*)

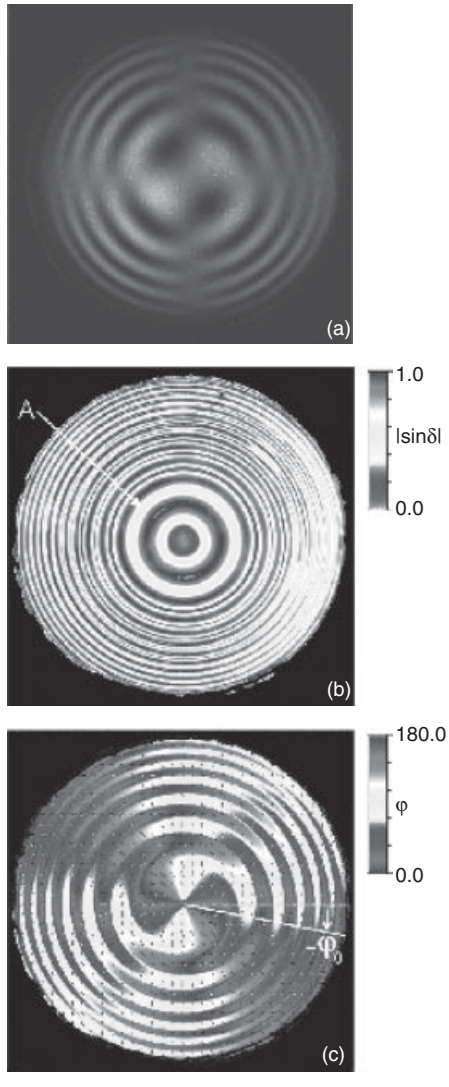

Figure 12.6. Conoscopic images of a 1-mm-thick (0001) quartz slice. (a) Live camera image in polarized light, (b) Resolved $|\sin\delta|$ image, (c) Resolved orientation φ (deg) image. Angle indicates direction of the slow axis plotted counterclockwise from the horizontal. (Reproduced from reference 48 with permission of Blackwell.)

12.5. CIRCULAR DICHROISM/EXTINCTION

Tetragonal crystals of 1,8-dihydroxyanthraquinone (DHA) were examined by the S-HAUP method. They appeared to have both dextro- and levorotatory domains. However, the images were of poor quality because of the nonuniform extinction across the crystal plate. The HAUP technique uses linearly polarized input requiring samples of uniform extinction. In other words, the optical indicatrices should have a common orientation in each part of the sample. Clearly, another tool would be required to further explore this contrast.

CE imaging is well suited for studying the crystals of DHA [47]. CE is equivalent to CD in the absence of artifacts. Indeed, CE micrographs of CD in Figure 12.7, recorded at 515 nm, show mirror image domains that can be attributed to CD-positive and CD-negative heterochiral pinwheels. These images are independent of the orientation of the microscope stage, which is the surest way to rule out linear biases in the optical train. At first blush, it appears that DHA is like Brazil quartz showing enantimorphous twinning along the optic axis. However, the DHA crystals are challenging because they display anomalous LB along the ostensible fourfold axis [50, 51].

There is a dearth of measurements of CD along low symmetry crystal directions. Exceptions are the work of Kuroda and co-workers [52, 53] on the tetragonal crystals of nickel sulfate hexahydrate and also Moxon and Renshaw [54, 55] on nickel sulfate hexahydrate and benzil.

CD can be imparted to transparent crystals through dyeing during growth from solution. $NaClO_3$ crystals stained with a textile dye, a propeller-shaped triarylmethane cation, possessed a confluence of properties—CD as well as anomalous CE (ACE). ACE was previously framed in terms of Jones matrices. However, we can see that this effect is akin to the mixing of linear and circular anisotropies incompletely separated by an incomplete Mueller matrix measurement. Schellman and Jensen explained that the following combinations gives rise to artifacts: $L' + C = L$ artifact, $C + L = L'$ artifact, $L + L' = C$ artifact.

These relationships arise because of formal similarities to the Pauli spin matrices [29].

The relative magnitudes of CD and ACE depended upon the direction from which the oriented dyes in the crystal were analyzed [56, 57]. The CD response was bisignate with respect to energy (Figure 12.8) by virtue of two nearly equienergetic transitions with opposite signed Cotton effects and bisignate with respect to wave vector (Figure 12.9). To

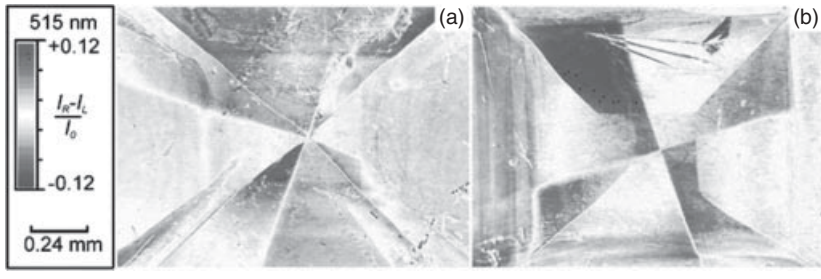

Figure 12.7. CD micrographs of the tetragonal form of 1,8-dihydroxyanthraquinone. Parts (a) and (b) show different crystals. Images made with device represented in Figure 12.3a. (Reproduced from reference 47 with permission of the American Chemical Society.)

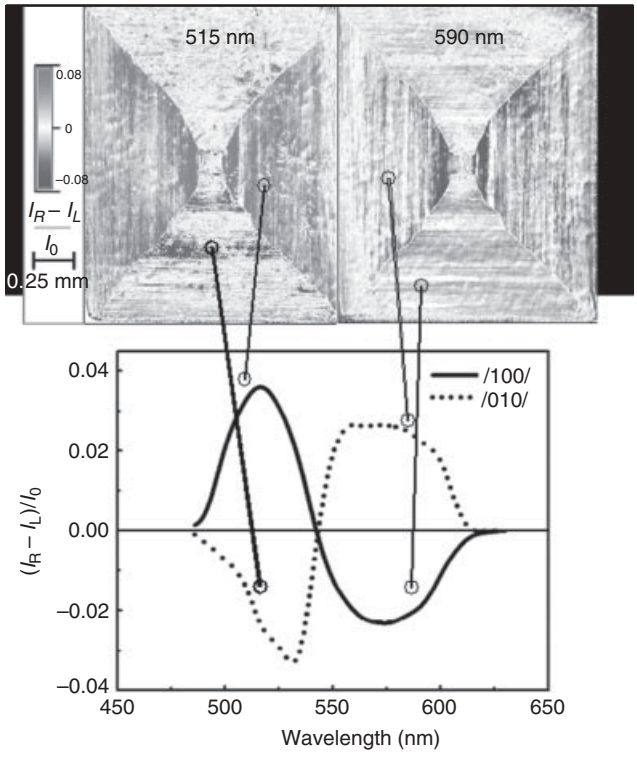

Figure 12.8. The wavelength dependence of circular dichroism (CD) in crystals of $NaClO_3$ dyed with a triarylmethane dye. The different sectors of the crystal show opposite signs of CD due to the varying CD tensor rotation of the dye in each sector. (Reproduced from reference 57 with permission of the American Chemical Society.)

read this figure, imagine that you are looking from the top at a crystal slice represented in gray. The sign of the response is given by the intersection of the section by the tensor representation surfaces associated with three growth sectors related by the threefold axis of the cube body diagonal.

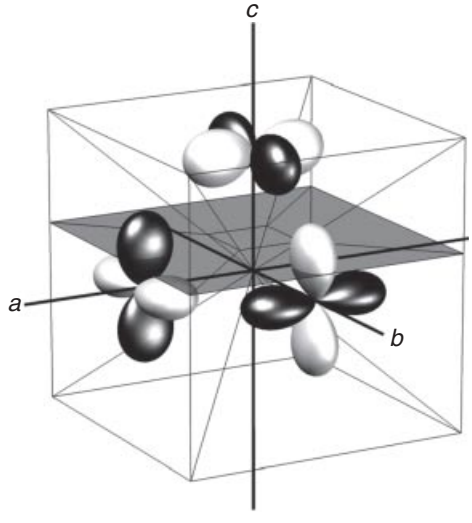

Figure 12.9. The orientation of the circular dichroism (CD) tensor of a triarylmethane dye grown into a host crystal of $NaClO_3$. (Reproduced from reference 56 with permission of the American Chemical Society.)

12.6. NANOSCALE

Recently, chiroptical imaging has found applications at the nanoscale, and a brief discussion of this emerging enterprise is warranted. While this is not an application specific to crystals, single-molecule spectroscopy was born in crystals [58, 59], and transparent single crystals are excellent hosts for single molecules [60–64]. Moreover, fascinating chiroptical images have been obtained from *J*-aggregates of dyes in solution, the beginnings of crystals so to speak [65].

Single-molecule microscopy is now routine. Consequently, chiroptical measurement of a single molecules was a natural step. Hassey et al. reported the first such claim and stimulated a field inquiry in so doing [66–68]. They showed that helicenes luminescence unequally when excited with left and right CPL. These results were bolstered by control experiments with highly anisotropic dyes to ensure that their input polarization states were pure. Nevertheless, the dissymmetry factors $(I_R - I_L)/I_o$ reported were larger than those anticipated from *ab initio* calculations. Tang et al. reexamined the same helicenes, but chose to compensate for ellipticities introduced by optical components in polarized light input. In this way, they obtained smaller dissymmetry factors [69]. A consensus has not yet been established, but most likely this will be an active area of research in the future. This debate has directed researchers to consider not only single-molecule chiroptics, but also chiroptics at the nanoscale (generally speaking). Savoini et al. showed that CPL can be delivered to a sample in the near field through the tip of an optical probe. They offered submicron maps of the dissymmetry factors of luminescent polymers [70]. Researchers have further considered CPL sources narrower than the diffraction limit for applications in magneto-optical recording [71]. Reflected CPL was collected by Mastai and co-workers through a near-field scanning optical microprobe [72]. Line profiles were reported for D- and L-histidine crystallites even though differential circularly polarized reflection is a tiny effect. The line profiles could easily be converted to images.

Chiroptical images have also been derived from insects that produce nanostructures that control the propagation of light. Goldstein showed Stokes vector images of Scarabaeidae beetles [73]. Confocal micrographs of the circularly polarized luminescence of *Chrysina gloriosa* was studied by Srinivasarao and co-workers [74]. Chiroptical effects among all scarab beetles were surveyed by Pye [75].

12.7. MUELLER MATRIX MICROSCOPY

In order to measure a complete Mueller matrix, a PSG and a PSA must be placed before and after the sample. There are many ways to construct a PSG or PSA [76]. If the modulation is mechanical, a fixed linear polarizer and rotating retarder is a common configuration. Alternatively, the concomitant sensitivity that accompanies fast polarization switching may be achieved with photoelastic modulators [77].

The PSG must be capable of generating a broad range of Stokes vectors. This can be evaluated by plotting the range of Stokes vectors generated on the Poincaré sphere (Figure 12.10). Calibrating a Mueller matrix microscope requires fitting intensities for different settings of the PSG and PSA [78].

The equations for a complete Mueller matrix polarimeter were given in Eq. (12.3). The alignment of the two retarders is changed 16 times to solve for the 16 elements of the Mueller matrix. The algorithm is given in Chipman's classic chapter on polarimetry

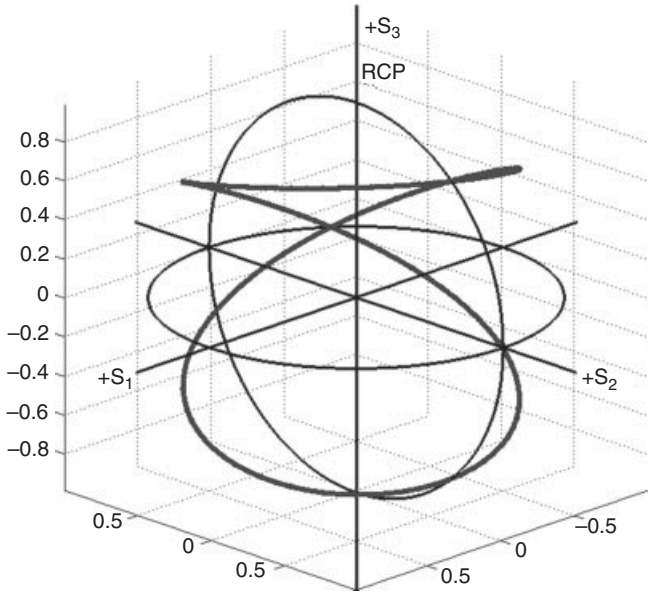

Figure 12.10. The heavy black line represents the attainable Stokes vectors projected onto the Poincaré sphere for a PSG composed of a polarizer and two quarter wave plates offset by 26°.

[76]. First the Mueller matrix is flattened to a Mueller vector, Eq. (12.9).

$$\vec{M}_{sample} = [M_{00} \quad M_{01} \quad M_{02} \quad M_{03} \quad M_{10} \quad M_{11} \quad \cdots \quad M_{33}]. \tag{12.9}$$

A polarimetric measurement vector, W_n for the nth setting of the polarimeter is given as a product of the first column of the PSG Mueller matrix (G_{ni}) and the first row of the analyzer Mueller matrix (A_{ni}), Eq. (12.10).

$$W_n = [A_{n0}G_{n0} \quad A_{n0}G_{n1} \quad A_{n0}G_{n2} \quad A_{n0}G_{n3} \quad A_{n1}G_{n0} \quad A_{n1}G_{n1} \quad \cdots \quad A_{n3}G_{n3}]. \tag{12.10}$$

Then, the measured intensities can be expressed as follows, Eq. (12.11):

$$I = \begin{bmatrix} I_1 \\ I_2 \\ I_3 \\ \vdots \\ I_N \end{bmatrix} = W\vec{M}_{sample} = \begin{bmatrix} W_1 \\ W_2 \\ W_3 \\ \vdots \\ W_N \end{bmatrix} \vec{M}_{sample}. \tag{12.11}$$

Inversion of $W, \vec{M}_{sample} = W^{-1}I$, yields the sample Mueller matrix elements.

Generally, more than 16 measurements are taken in order to reduce noise. In addition, the W defined as the N x 16 matrix where the n^{th} row is W_n, matrix must be well-conditioned for inversion and multiplication [79]. This is possible only if the Poincaré space is well-covered. Naturally, the PSG and PSA must be well-calibrated.

The choice of modulation determines the manner in which images are made. We have used slow mechanical light modulation with a CCD camera as a detector. Greater sensitivity in chiroptical measurements may be achieved by rapid sampling concomitant with photoelastic modulation at rates of ~50 kHz. However, photoelastic modulators

(PEMs) are too fast for CCD cameras, and photomultiplier tubes are typically used as detectors. To yield images, they must be operated with sample scanning.

Arteaga and Canillas built an instrument based on two PEMs pioneered by Jellison and Modine [80, 81], to which they added quartz rotators that obviate the need for reorienting the modulators [82]. With this polarimeter, they analyzed recrystallized melts of benzil [83], a well-studied chiral crystal in the enantiomorphous space groups $P3_121$ and $P3_221$. Thin polycrystalline films can be grown from the melt that arguably contains both enantiomorphs. Figures 12.11a, 12.11b, and 12.11c show CD, CB, and the fraction of polarized light [β, Eq. (12.12)], respectively, associated with an absorption band

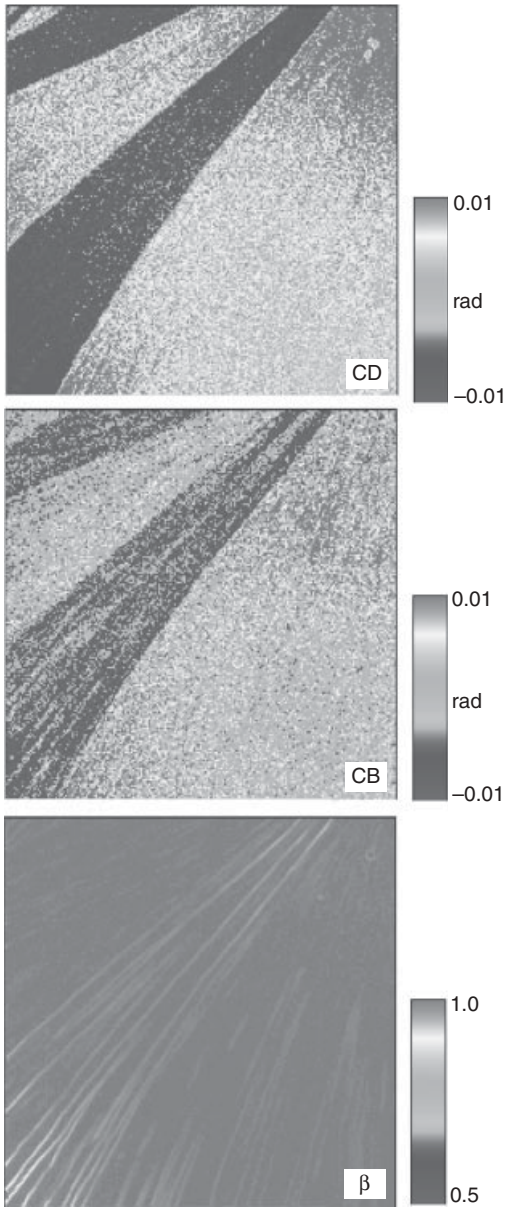

Figure 12.11. Circular dichroism (CD), circular birefringence (CB), and depolarization (β) images of polycrystalline benzil films. The distinct regions are enantiomorphous ($P3_121$ and $P3_221$) crystals of benzil grown from the same melt. Images made with dual PEM Stokes–Mueller imaging polarimeter. (Image courtesy of O. Arteaga.)

at 400 nm. The oppositely signed regions, viewed along low-symmetry directions, are self-evident.

$$\beta = \frac{\sqrt{(\sum_{ij} m_{ij}^2) - m_{00}^2}}{\sqrt{3} m_{00}}. \tag{12.12}$$

Arteaga et al. have further used the generalized two-photoelastic-modulator transmission ellipsometer, with scanning of the sample, to produce topographs of the CB remnant in sections of meteorites [84]. Their detection of CB, while preliminary, supports the notion that optically active material, produced extraterrestrially, was brought to earth.

12.8. ARTIFACTS

Transparent polycrystalline ensembles of achiral crystals have made striking patterns of CE in some instances. For instance, Figure 12.12 shows rhythmic precipitates of phthalic acid in the form radial aggregates [85]. Each such spherulite is bisected along one diameter. One half gives a positive CE signal and the other half gives a negative signal. These effects are not chiroptical effects *per se*. Even though they are made with CPL, their origin does not involve magnetic dipoles or electric quadrupoles. When orthogonal circular polarization states enter an anisotropic medium, the exiting light is in orthogonal elliptical states. If the exiting surface is not normal to the wavevector, Fresnel reflection at the interface may discriminate between orthogonal elliptical states. This differential scattering was shown to be a consequence of mesoscale chiral texture wholly consistent with the C_{2h} symmetry of the initial phthalic acid nucleus [86].

As previously stated, CD measurements of anisotropic media may contain artifacts that result from mixed linear anisotropies. Such artifacts are generally considered a nuisance. However, artifacts, carefully measured, may contain valuable information. Pairs of intergrown, dyed polycrystalline sorbitol spherulites [87] developed strong apparent CB and CD signals at their boundaries. The signs and magnitudes of these signals were sensitive to the angle of overlapping sorbitol fibrils (Figure 12.13) and their relative heights

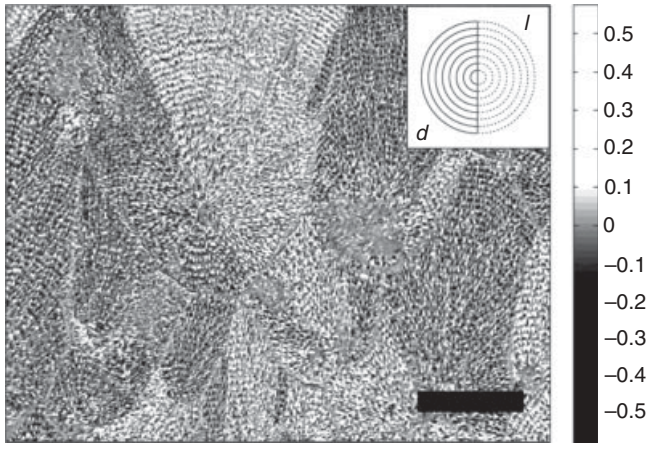

Figure 12.12. Phthalic acid spherulites grown from ethanol. Micrograph made with a Stokes–Mueller imaging polarimeter as in Figure 12.3e. Scale at right is $(I_R - I_L)/I_o$. Scale bar is 0.3 mm. Inset shows schematically the ''right-handed'' and ''left-handed'' halves of the spherulites. (Reproduced from reference 84 with permission of Wiley.)

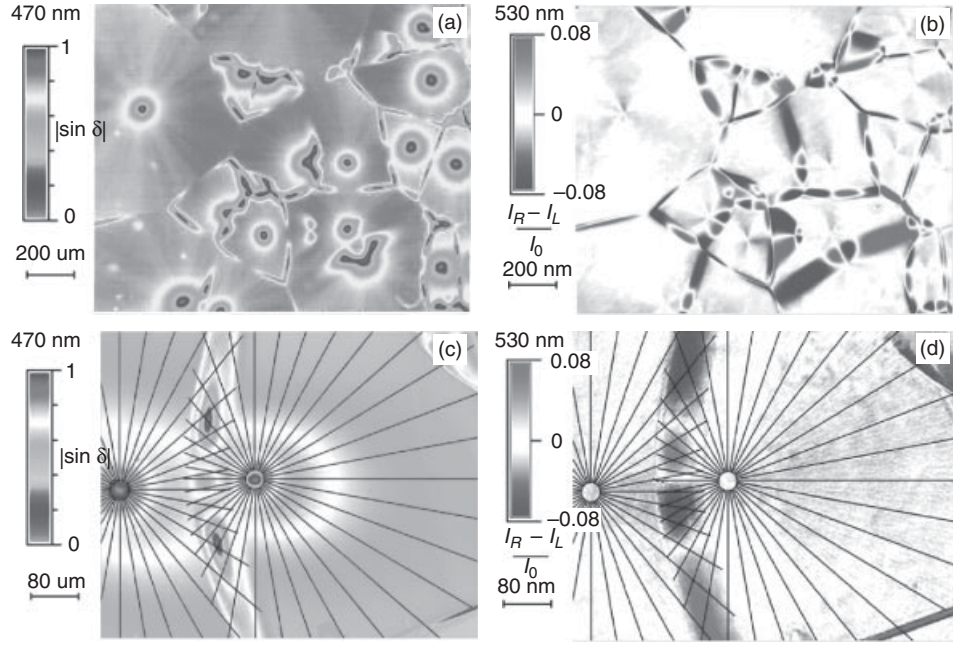

Figure 12.13. (a, b) Images of $|\sin\delta|$ for 1 wt% amaranth doped D-sorbitol spherulites made with LB imaging system. (c, d) Corresponding images of circular extinction. Nuclei in (c) and (d) are overlaid with radial grids that indicate directions of fibril growth. The signals are null where grid lines are parallel or perpendicular. In other words, where the eigenmodes are aligned, the medium behaves as if it were homogeneous. (Reproduced from reference 85 with permission of Wiley.)

along the optical path [88]. Systematic chiroptical artifacts should not be dismissed reflexively; they are comprehensible effects that serve to define mesoscale structure.

The S-HAUP technique can be expanded for imaging CB in simple centrosymmetric crystals that had adsorbed, oriented, and overgrown chiral dye molecules. Chiroptical effects such as CB and CD were expected when equilibrium racemic mixtures of dyes selectively recognized chiral facets of achiral crystalline hosts. Crystals of K_2SO_4 grown in the presence of trypan blue, a linear azo dye, were colored in the {110} and {111} growth sectors. The {111} faces are unusual in the D_{2h}-symmetric crystals because they are chiral. As such, the biaryl dye must be adsorbed enantioselectively to these faces [89]. S-HAUP topographs of a K_2SO_4/trypan (010) section are shown in Figure 12.14, where the dyed regions exhibit opposite signals consistent with crystal mirror symmetry. The first row in Figure 12.14 represents the phase δ, which changes sign when the fast and slow axes are exchanged. In the second row, contrary to expectation, the sign of the apparent CB changes with sample reorientation, that is, the sign of the effect changes whenever the sample is turned by 90° about the wave vector ("rotation") or rotated 180° around the vertical or horizontal axes perpendicular to the wave vector ("flip"). Intrinsic CB (and CD) would be invariant to these transformations. This is a consequence of the fact that $L+L'$ gives rise to a C artifact [29]. We called the effect anomalous azimuthal rotation (AAR) [90].

The ACE effect is analogous to AAR. $LiKSO_4$ forms hexagonal crystals ($P6_3$) that have oriented and overgrown the dye Chicago sky blue [91]. Because the crystals are

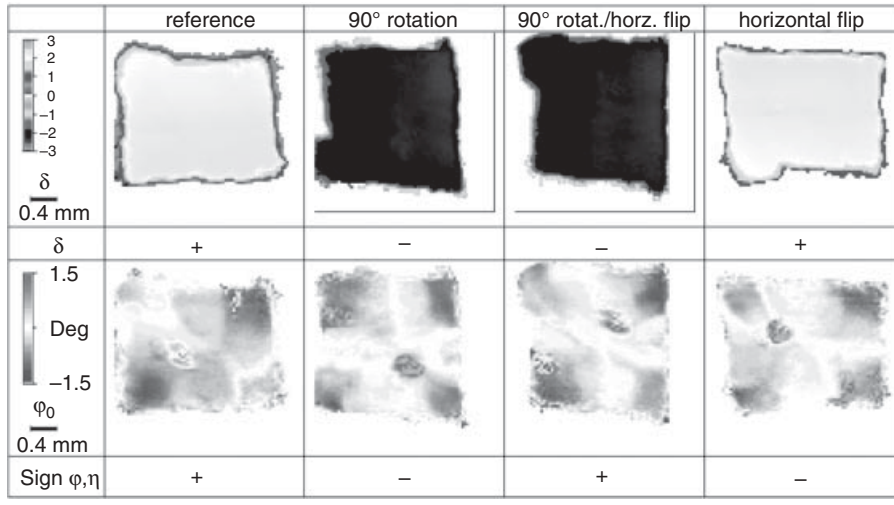

Figure 12.14. Optical topographs of K_2SO_4/trypan blue (010) plate (~90 μm) using the S-HAUP technique. First row: Phase difference $\delta, \lambda = 670$ nm, for various crystal orientations. The shape of the sample seen in the images in this row guide for the eye as the sample is reoriented in the columns of this table. Second row: Apparent optical rotation φ. The signs of the quantities refer to the top-left quadrant in the first image. ''Rotation'' = 90° rotation about wavevector. ''Flip'' = 180° rotation about horizontal or vertical axes of the crystal plate. (Reproduced from reference 88 with permission of the American Chemical Society.)

enantiomorphously twinned [92], mirror-image-related faces that potentially incorporate conformationally chiral guest molecules selectively during growth. An instrument sensitive enough and sufficiently free of artifacts could be used with such crystals, and those of K_2SO_4 above could be used to measure anisotropies of a dye's induced chiroptical properties. Although mirror-image-related domains in the twinned $LiKSO_4$ crystals displayed marked CE, the signal changed sign with inversion of the sample with respect to the light path, a transformation inconsistent with natural CD. The anisotropy of the host generates elliptical states that will differentially interact with the absorbing sublattice of rod like dipoles so long as the electric dipole transition moments are twisted in the same sense from the eigenmodes of the crystal [93]. A bias therefore becomes manifest in the interaction of dyes and the two elliptical light forms.

Unlike intrinsic CB or CD, AAR and ACE do not convey absolute configuration but may be used instead to determine the *absolute orientation* of adsorbed dye molecules and thereby resolve an ambiguity present in polarized absorption measurements.

12.9. OUTLOOK

Chiroptical imaging is still in its infancy, but adolescence is not far off. Here, the credit is due largely to the manufacturers of increasing stable PEMs, CCD with increasing resolution, and, it goes without saying, faster computers. The greatest challenges to chiroptical imaging are sensitivity and speed of acquisition. Opportunities abound in combining the inherent accuracy of rapid photoelastic modulation and the imaging capacity of CCD cameras. Research groups are actively trying to force PEMs and CCD to work in concert

with clever schemes that overcome their incompatible timescales of operation [94–96]. Continual improvements in liquid crystal modulators will also allow for higher-speed Mueller matrix imaging without the complications of microsecond pixel timing [97].

REFERENCES

1. I. Tinoco, W. Mickols, M. F. Maestre, C. Bustamante, *Annu. Rev. Biophys. Biophys. Chem*. **1987**, *16*, 319–349.
2. K. Claborn, C. Isborn, W. Kaminsky, B. Kahr, *Angew. Chem. Int. Ed. Engl*. **2008**, *47*, 5706–5717.
3. C. Bustamante, M. F. Maestre, I. Tinoco Jr. *J. Chem. Phys*. **1982**, *76*, 3440–3446.
4. B. P. Tonner, D. Dunham, T. Droubay, J. Kikuma, J. Dellinger, *J. Electr. Spectr. Rel. Phenom*. **1996**, *78*, 13–18.
5. K. Sato, Y. Ueji, K. Okitsu, T. Matsushida, Y. Amemiya, *J. Synchrotron. Rad*. **2001**, *8*, 1021–1026.
6. A Locatelli, S. Cherifi, S. Heun, M. Marsi, K. Ono, A. Pavlovska, E. Bauer, *J. Surf. Rev. Lett*. **2002**, *9*, 171–176.
7. A. Spry, R. Turner, R. Tobin, *Am. Mineral*. **1969**, *54*, 117–133.
8. L. E. Hough, H. T. Jung, D. Kruerke, M. S. Heberling, M. Nakata, C. D. Jones, D. Chen, D. R. Link, J. Zasadzinski, G. Heppke, et al., *Science* **2009**, *325*, 456–460.
9. T. Yamada, H. Onuki, M. Yuri, S. Ishizaka, *Jpn. J. Appl. Phys*. **2000**, *39*, 310–315.
10. W. Kaminsky, *Rep. Prog. Phys*. **2000**, *63*, 1575–1640.
11. J. S. Tyo, D. L. Goldstein, D. B. Chenault, J. A. Shaw, *Appl. Opt*. **2006**, *45*, 5453–5469.
12. C. Bustamante, I. Tinoco, M. F. Maestre, *Proc. National Acad. Sci. USA*, **1983**, *80*, 3568–3572.
13. M. F. Maestre, J. E. Katz, *Biopolymers* **1982**, *21*, 1899–1908.
14. M. Maestre, G. Salzman, R. Tobey, C. Bustamante, *Biochem*. **1985**, *24*, 5152–5157.
15. F. Livolant, M. F. Maestre, *Biochem*. **1988**, *27*, 3056–3068.
16. F. Livolant, W. Mickols, M. F. Maestre, *Biopolymers* **1988**, *27*, 1761–1769.
17. Y. Shindo, M. Nakagawa, *Appl. Spectrosc*. **1985**, *39*, 32–38.
18. Y. Shindo, M. Nakagawa, T. Ohmi, *Appl. Spectrosc*. **1985**, *39*, 860–868.
19. K. W. Hipps, G. A. Crosby, *J. Phys. Chem*. **1979**, *83*, 555–562.
20. R. L. Disch, D. I. Sverdlik, *Anal. Chem*. **1969**, *41*, 82–86.
21. B. Nordén, H. J. Jakobsen, H. J. Jakobsen, H. A. Øye, S. Svensson, *Acta Chem. Scand*. **1972**, *26*, 1763–1776.
22. AA. Davidsson, B. Norden, *Spectrochim. Acta Part A: Molec. Spectr*. **1976**, *32*, 717–722.
23. AA. Davidsson, B. Nordén, S. Seth, *Chem. Phys. Lett*. **1980**, *70*, 313–316.
24. W. Mickols, I. Tinoco, J. E. Katz, M. F. Maestre, C. Bustamante, *Rev. Sci. Instrum*. **1985**, *56*, 2228–2236.
25. W. Mickols, M. F. Maestre, I. Tinoco, *Nature* **1987**, *328*, 452–454.
26. C. Juang, L. Finzi, C. J. Bustamante, *Rev. Sci. Instrum*. **1988**, *59*, 2399–2408.
27. L. Finzi, C. Bustamante, G. Garab, C. B. Juang, *Proc. Natl. Acad. Sci. USA*, **1989**, *86*, 8748–8752.
28. D. H. Goldstein, *Polarized Light*, Marcel Drekker, New York, **2003**.
29. J. Schellman, H. P. Jensen, *Chem. Rev*. **1987**, *87*, 1359–1399.
30. C. R. Jones, *J. Opt. Soc. Am*. **1948**, *38*, 671–685.

31. R. M. A. Azzam, *J. Opt. Soc. Am*. **1978**, *68*, 1756–1767.
32. I. Abdulhalim, *J. Opt. A: Pure Appl. Opt*. **1999**, *1*, 646–653.
33. J. Mosiño, A. Starodumov, O. Barbosa-García, V. N. Filippov, *J. Opt. B: Quantum Semiclass. Opt*. **2001**, *3*, S159–S165.
34. O. Arteaga, A. Canillas, *Opt. Lett*. **2010**, *35*, 559–561.
35. J. Kobayashi, Y. Uesu, H. Takehara, *J. Appl. Crystallogr*. **1983**, *16*, 212–219.
36. W. Kaminsky, *Phase Transitions*, **1996**, *59*, 121–133.
37. W. Kaminsky, A. M. Glazer, *Ferroelectrics* **1996**, *183*, 133–141.
38. W. Kaminsky, A. M. Glazer, *Phase Trans*. **1998**, *66*, 1–21.
39. W. Kaminsky, *Ferroelectric* **1997**, *204*, 233–246.
40. H. Marbach, *Ann. Phys. Chem*. **1856**, *9*, 459.
41. H. Marbach, *Ann Phys. Chem*, **1858**, *99*, 451.
42. J. M. Bijvoet, *Acta Crystallogr*. **1960**, *13*, 1100–1101.
43. G. Crundwell, P. Gopalan, A. Bakulin, M. L. Peterson, B. Kahr, *Acta Crystallogr. B Struct. Sci*. **1997**, *53*, 189–202.
44. P. Gopalan, M. L. Peterson, G. Crundwell, B. Kahr, *J. Am. Chem. Soc*. **1993**, *115*, 3366–3367.
45. A. G. Shtukenberg, I. V. Rozhdestvenskaya, D. Y. Popov, Y. O. Punin, *J. Solid St. Chem*. **2004**, *177*, 4732–4742.
46. S. N. Bocharov, P. Gille, A. E. Glikin, *Cryst. Res. Technol*. **2009**, *44*, 13–18.
47. W. Kaminsky, K. Claborn, B. Kahr, *Chem. Soc. Rev*. **2004**, *33*, 514–525.
48. M. A. Geday, A. M. Glazer, *J. Appl Crystallogr*. **2002**, *35*, 185–190.
49. K. Bjorknas, M. A. Geday, E. P. Raynes, *Liquid Crystals* **2003**, *30*, 889–897.
50. B. Kahr, J. M. McBride, *Angew. Chem. Int. Ed. Engl*. **1992**, *31*, 1–26.
51. A. Shtukenberg, I. I. Punin, *Optically Anomalous Crystals*, B. Kahr, ed., Springer, Dordtrecht, **2007**.
52. H. Takunori, Y. Shindo, R. Kuroda, *Chem. Phys. Lett*. **2002**, *360*, 217–222.
53. H. Takunori, T. Sato, R. Kuroda, *Chem. Phys. Lett*. **2008**, *456*, 268–271.
54. J. L. M. Moxon, A. R. Renshaw, *J. Phys.: Condens. Matter*, **1990**, *2*, 6807–6836.
55. J. L. M. Moxon, A. R. Renshaw, *J. Phys. D, Appl. Phys*. **1991**, *24*, 1187–1192.
56. B. Kahr, Y. Bing, W. Kaminsky, D. Viterbo, *Angew. Chem. Int. Ed*. **2009**, *48*, 3744–3748.
57. Y. Bing, D. Selassie, R. H. Paradise, C. Isborn, N. Kramer, M. Sadilek, W. Kaminsky, B. Kahr, *J. Am. Chem. Soc*. **2010**, *132*, 7454–7465.
58. W. E. Moerner, L. Kador, *Phys. Rev. Lett*. **1989**, *62*, 2535–2538.
59. M. Orrit, J. Bernard, *Phys. Rev. Lett*. **1990**, *65*, 2716–2719.
60. K. L. Wustholz, B. Kahr, P. J. Reid, *J. Phys. Chem. B* **2005**, *109*, 16357–16362.
61. K. L. Wustholz, E. Bott, C. Isborn, X. Li, B. Kahr, P. Reid, *J. Phys. Chem. C* **2007**, *111*, 9146–9156.
62. K. L. Wustholz, E. D. Bott, B. Kahr, P. J. Reid, *J. Phys. Chem. C* **2008**, *112*, 7877–7885.
63. E. D. Bott, E. A. Riley, B. Kahr, P. J. Reid, *ACS Nano*, **2009**, *3*, 2403–2411.
64. E. D. Bott, E. A. Riley, B. Kahr, P. J. Reid, *J. Phys. Chem. A* **2010**, *114*, 7331–7337.
65. Z. El-Hachemi, O. Arteaga, A. Canillas, J. Crusats, C. Escudero, R. Kuroda, T. Harada, M. Rosa, J. Ribó, *Chem. Eur. J*. **2008**, *14*, 6438–6443.
66. R. Hassey, E. J. Swain, N. I. Hammer, D. Venkataraman, M. D. Barnes, *Science* **2006**, *314*, 1437–1439.
67. R. Hassey, K. D. McCarthy, E. Swain, D. Basak, D. Venkataraman, M. D. Barnes, *Chirality* **2008**, *20*, 1039–1046.

68. R. Hassey-Paradise, A. Cyphersmith, A. M. Tilley, T. Mortsolf, D. Basak, D. Venkataraman, M. D. Barnes, *Chirality* **2009**, *21*, E265–E276.
69. Y. Tang, T. A. Cook, A. E. Cohen, *J. Phys. Chem. A* **2009**, *113*, 6213–6216.
70. M. Savoini, P. Biagioni, G. Lakhwani, S. C. J. Meskers, L. Duò, M. Finazzi, *Opt. Lett*. **2009**, *34*, 3571–3573.
71. E. Öğüt, G. Kızıltas, K. Sendur, *Appl. Phys. B* **2009**, *99*, 67–74.
72. D. H. Dressler, A. Landau, A. Zaban, Y. Mastai, *Chem. Commun*. **2008**, 945–947.
73. D. H. Goldstein, *Appl. Opt*. **2006**, *45*, 7944–7950.
74. V. Sharma, M. Crne, J. O. Park, M. Srinivasarao, *Science*, **2009**, *325*, 449–451.
75. J. D. Pye, *Biol. J. Linnean Soc*. **2010**, *100*, 585–596.
76. R. A. Chipman, in *Handbook of Optics*, Vol. II, M. Bass, ed., McGraw-Hill, New York, **1995**, Chapter 22.
77. S. N. Jasperson, S. E. Schnatterly, *Rev. Sci. Instr*. **1969**, *40*, 761–767.
78. De Martino, A. *Thin Solid Films* **2004**, *455–456*, 112–119.
79. M. H. Smith, *Appl. Opt*. **2002**, *41*, 2488–2493.
80. G. E. Jellison, F. A. Modine, *Appl. Opt*. **1997**, *36*, 8184–8189.
81. G. E. Jellison, F. A. Modine, *Appl. Opt*. **1997**, *36*, 8190–8198.
82. O. Arteaga, *Mueller matrix polarimetry of anisotropic chiral media*, Ph.D. dissertation, University of Barcelona, **2010**.
83. O. Arteaga, Z. El-Hachemi, A. Canillas, J. M. Ribó, *Thin Solid Films,* **2011**, *519*, 2617–2623.
84. O. Arteaga, A. Canillas, J. Crusats, Z. El-Hachemi, G. E. Jellison, J. Llorca, J. M. Ribó, *Orig. Life Evol. Biosph*. **2009**, *40*, 27–40.
85. B. Kahr, J. H. Freudenthal, *Chirality* **2008**, *20*, 973–977.
86. E. Gunn, R. Sours, J. B. Benedict, W. Kaminsky, B. Kahr, *J. Am. Chem. Soc*. **2006**, *128*, 14234–14235.
87. J. B. Benedict, J. H. Freudenthal, E. Hollis, B. Kahr, *J. Am. Chem. Soc*. **2008**, *130*, 10714–10719.
88. J. H. Freudenthal, E. Hollis, B. Kahr, *Chirality*, **2009**, *21*, E20–E27.
89. W. Kaminsky, M. A. Geday, J. Herreros-Cedrés, B. Kahr, *J. Phys. Chem. A*, **2003**, *107*, 2800–2807.
90. W. Kaminsky, J. Herreros-Cedrés, M. A. Geday, B. Kahr, *Chirality*, **2004**, *16*, S55–S61.
91. K. Claborn, A.-S. Chu, S.-H. Jang, F. Y. Su, W. Kaminsky, B. Kahr, *Cryst. Growth Des*. **2005**, *5*, 2117–2123.
92. H. Klapper, Th. Hahn, S. Chung, *Acta Cryst. Struct. Sci*. **1987**, *B43*, 147–159.
93. W. Kaminsky, J. Herreros Cedres, M. Geday, B. Kahr, *Chirality*, **2004**, *16*, S55–S61.
94. D. J. Diner, A. Davis, B. Hancock, S. Geier, B. Rheingans, V. Jovanovic, M. Bull, D. M. Rider, R. A. Chipman, A. Mahler, et al., *Appl. Opt*. **2010**, *49*, 2929–2946.
95. P. Gleyzes, A. C. Boccara, H. Saint-James, *Opt. Lett*. **1997**, *22*, 1529–1531.
96. C. Y. Han, Y.-F. Chao, *Rev. Sci. Instr*. **2006**, *77*, 023107.
97. R. L. Heredero, N. Uribe-Patarroyo, T. Belenguer, G. Ramos, A. Sánchez, M. Reina, V. M. Pillet, A. Álvarez-Herrero, *Appl. Opt*. **2007**, *46*, 689–698.

13

NONLINEAR OPTICAL SPECTROSCOPY OF CHIRAL MOLECULES

Peer Fischer

13.1. INTRODUCTION

The enantiomers of a chiral molecule are exactly alike in all chemical and physical properties except those that involve a left–right difference. This makes the observation and detection of chirality challenging. Only under a chiral influence, such as circularly polarized light, can interactions distinguish between the mirror-image forms of a chiral molecule. Optical methods are often the only practical physical means to probe molecular chirality, and a liquid's ability to rotate the plane of polarization of a linearly polarized light beam traversing it (in the absence of a static magnetic field) is the classical distinguishing characteristic of a chiral liquid—that is, one that is "optically active." Conventional optical activity phenomena, such as optical rotation and circular dichroism, are based on the interference of induced oscillating electric and magnetic moments, and they arise from a differential response to left- and right-circularly polarized light. In these linear chiroptical phenomena, neither the angle of rotation of a polarized light beam nor its ellipticity (circular dichroism) is expected to change with the intensity of the light. However, at typical peak powers of pulsed lasers the optical field strength can become comparable to the field that binds the valence electrons to the nucleus of an atom or a molecule, and under these conditions the optical properties will have contributions that depend nonlinearly on the applied electromagnetic fields. This is the realm of nonlinear optics [1–3]. The usual linear refractive indices observed at low light intensities are then augmented by additional contributions that depend on the intensity of the light. Hence, nonlinear (intensity-dependent) contributions to optical activity (optical rotation and circular dichroism) may be observed in chiral media under appropriate experimental conditions.

Comprehensive Chiroptical Spectroscopy, Volume 1: Instrumentation, Methodologies, and Theoretical Simulations, First Edition. Edited by N. Berova, P. L. Polavarapu, K. Nakanishi, and R. W. Woody.
© 2012 John Wiley & Sons, Inc. Published 2012 by John Wiley & Sons, Inc.

Nonlinear optical phenomena can also be used to generate light at new frequencies. For instance, nonlinear second-harmonic generation in an appropriate crystal allows an infrared laser beam to be converted (frequency doubled) into green radiation, a process that is used in green laser pointers. If two different frequencies "mix" in a suitable nonlinear medium, then colors corresponding to the sum and difference frequencies can be generated. Surprisingly, such a frequency-mixing process can also be a probe of chirality in solution. In contrast to conventional linear optical activity, the nonlinear chiral mixing process can arise entirely in the electric dipole approximation (i.e., without magnetic or quadrupolar transitions) and is not circular differential. Hence, no polarization modulation is needed and the generated photons themselves are a measure of the solution's chirality. Since an achiral solvent does not contribute to the signal, the technique is a sensitive, background-free probe of molecular chirality.

Nonlinear optical phenomena are generally discussed in terms of an induced polarization $\vec{P}(t)$, written here in the electric dipole approximation as a power series in the applied electric field $\vec{E}$ [2]:

$$\vec{P}(t) = \varepsilon_0(\overleftrightarrow{\chi}^{(1)}\vec{E} + \overleftrightarrow{\chi}^{(2)}\vec{E}\vec{E} + \overleftrightarrow{\chi}^{(3)}\vec{E}\vec{E}\vec{E} + \overleftrightarrow{\chi}^{(4)}\vec{E}\vec{E}\vec{E}\vec{E} + \cdots). \tag{13.1}$$

Most linear optical phenomena such as refraction, absorption, and Rayleigh scattering are described by the first term in Eq. (13.1), where $\overleftrightarrow{\chi}^{(1)}$ is the linear susceptibility tensor. The higher-order terms and susceptibilities are responsible for nonlinear optical effects. The second-order susceptibility tensor $\overleftrightarrow{\chi}^{(2)}$ depends quadratically on the incident electric field and can give rise to sum-frequency generation (SFG) in solution. It may also give rise to second-harmonic generation (SHG) and be used to observe chiral molecules at a surface or an interface. Linearly polarized as well as circularly polarized light can probe the nonlinear optical response from a chiral molecular monolayer. Remarkably, the nonlinear intensity differentials in SHG can be much larger than for linear optical activity.

The third-order term, $\overleftrightarrow{\chi}^{(3)}$, underlies many nonlinear optical effects, including the intensity-dependent refractive index, the optical Kerr effect, pump-probe spectroscopy, and coherent Raman processes. To describe nonlinear optical activity phenomena at this order of nonlinearity, it becomes necessary to consider susceptibilities other than the electric dipole susceptibilities in Eq. (13.1). Similar to linear chiroptical phenomena, higher-order multipolar contributions to the susceptibility must be considered in order to understand nonlinear optical activity; that is, the dependence on the magnetic field components of the electromagnetic wave is required to describe these processes. Chiral processes at third order include nonlinear circular dichroism and nonlinear optical rotation, as well as pump-probe and two-photon absorption spectroscopy. These effects depend on the combined interaction of several light fields and therefore allow for time-resolved experiments.

The fourth-order $\overleftrightarrow{\chi}^{(4)}$ susceptibility is in the electric dipole approximation intrinsically chirally sensitive and has been predicted to give rise to a new form of Raman spectroscopy (BioCARS) that is coherent unlike conventional Raman optical activity (ROA).

Under which conditions nonlinear susceptibilities permit the observation of chiral molecules either in solution or at a surface is the topic of this chapter, which is in part based on two recent reviews [4, 5] and is organized as follows:

In Section 13.3 we discuss the nonlinear optical properties of isotropic liquids and solutions composed of chiral molecules. We consider nonlinear optical activity phenomena as well as nonlinear chiroptical effects that have no counterpart in linear optics, such

as sum-frequency generation and BioCARS. Nonlinear chiroptics at surfaces is discussed in Section 13.4. We briefly introduce some computational approaches that can be used to estimate the nonlinear chiral response tensors and susceptibilities (Section 13.5). Conclusions are drawn in Section 13.6, and in the Appendix (Section 13.7) we collect some useful formulae and derivations.

In order to properly introduce the nomenclature and in order to discuss nonlinear optical activity, we first briefly review the theoretical basis of linear chiroptics (Section 13.2). The reader who is primarily interested in nonlinear chiral processes that have no counterpart in linear optics (e.g., SHG, SFG, BioCARS) may begin with Section 13.3.

13.2. LINEAR CHIROPTICS IN LIQUIDS: $\chi^{(1)}$

Optical fields that are incident upon a molecule induce time-varying molecular moments which themselves radiate. Most linear optical phenomena such as refraction (and absorption) of light, and hence the refractive index (and the absorptivity), as well as Rayleigh scattering can be interpreted through a molecule's oscillating electric dipole moment $\vec{\mu}_{\text{ind}}$ linear in the electric field, $\vec{E}$,[1]

$$\vec{\mu}_{\text{ind}} = \overleftrightarrow{\alpha}\vec{E} + \cdots, \tag{13.2}$$

where $\overleftrightarrow{\alpha}$ is the polarizability of the molecule. In general, $\overleftrightarrow{\alpha}$ relates the three components of the electric field vector to those of the dipole moment and is therefore a tensor with nine components. Molecular symmetry may reduce the number of independent components. The induced dipole moments in an ensemble of molecules give rise to an average macroscopic polarization $\vec{P}$ in the medium:

$$\vec{P} = N\langle\vec{\mu}_{\text{ind}}\rangle, \tag{13.3}$$

where the angular brackets denote an orientational average over a region of space containing N molecules per unit volume. This leads to the first term in Eq. (13.1):

$$\vec{P} = \varepsilon_0 \overleftrightarrow{\chi}^{(1)}\vec{E}, \tag{13.4}$$

where ε_0 is the permittivity of the vacuum. The linear susceptibility $\overleftrightarrow{\chi}^{(1)}$ is the macroscopic analog of the molecular polarizability. It relates the electric field vector to the macroscopic polarization vector. In a liquid the linear susceptibility is a scalar (see Section 13.7.1) and is related to the molecular polarizability via

$$\chi^{(1)} = \frac{N}{\varepsilon_0}\frac{1}{3}(\alpha_{xx} + \alpha_{yy} + \alpha_{zz}) \equiv \frac{N}{\varepsilon_0}\overline{\alpha}. \tag{13.5}$$

The linear refractive index n_0 of an isotropic medium is a function of the susceptibility:

$$n_0 = (1 + \chi^{(1)})^{1/2} \equiv \sqrt{\varepsilon}. \tag{13.6}$$

[1] In condensed media, such as liquids, the field at the molecule will be different from the externally applied electric field, $\vec{E}$. To account for the effect of dipole–dipole interactions of the surrounding molecules, the electric field $\vec{E}$ in macroscopic expressions, such as Eq. (13.4), should be replaced with a "local field," which is in the Lorentz model approximately given by $\vec{E}(\varepsilon + 2)/3$.

To describe the refractive index of an optically active liquid, it becomes necessary to go beyond the electric dipole approximation in Eq. (13.2) and to include the induced magnetic dipole moment $\vec{m}_{\text{ind}}$ (and for oriented samples also the induced electric quadrupole moment $\overleftrightarrow{\Theta}_{\text{ind}}$) [6]. The macroscopic magnetization, and the macroscopic quadrupole density are respectively $\vec{M} = N\langle\vec{m}_{\text{ind}}\rangle$ and $\overleftrightarrow{Q} = N\langle\overleftrightarrow{\Theta}_{\text{ind}}\rangle$. For an optically active liquid we need to consider [7–9]

$$\begin{aligned}\vec{\mu}_{\text{ind}} &= \overleftrightarrow{\alpha}\vec{E} + \omega^{-1}\overleftrightarrow{G}'\dot{\vec{B}} + \cdots,\\ \vec{m}_{\text{ind}} &= -\omega^{-1}\overleftrightarrow{G}'\dot{\vec{E}} + \cdots,\end{aligned} \tag{13.7}$$

where the dot denotes a derivative with respect to time and where $\overleftrightarrow{G}'$ is the optical rotation tensor, which is a function of the rotational strength. The inclusion of the higher-order multipolar moments leads to an effective susceptibility (for a derivation see Section 7.2)

$$\vec{P}_{\text{eff}} = \varepsilon_0\chi_{\text{eff}}\vec{E} \tag{13.8}$$

and results in a contribution to the refractive index that depends on the circularity of the light:

$$n^{(\pm)} \approx n_0 \pm g_0, \qquad \text{where } g_0 = \frac{N\overline{G}'}{\varepsilon_0 c}, \tag{13.9}$$

where $\overline{G}'$ is the isotropic part of the optical rotation tensor and $\overline{G}' \equiv (G'_{xx} + G'_{yy} + G'_{zz})/3$. Time-dependent perturbation theory may be used to obtain a sum-over-states expression for $\overline{G}'$ away from resonance [8, 9]:

$$\overline{G}' = -\frac{2}{3\hbar}\sum_{j\neq g}\frac{\omega}{\omega_{jg}^2 - \omega^2}\text{Im}[\langle g|\vec{\mu}|j\rangle \bullet \langle j|\vec{m}|g\rangle], \tag{13.10}$$

where ω_{jg} is the Bohr angular frequency in the basis set for which g is the ground state, and all the other symbols have their usual meaning. The optical rotation θ in radians developed over a pathlength l is a function of the wavelength λ and the circular birefringence and is given by [9]

$$\theta = \frac{\pi l}{\lambda}(n^{(-)} - n^{(+)}) \approx -\frac{2\pi l}{\lambda}\frac{N}{\varepsilon_0 c}\overline{G}'. \tag{13.11}$$

$\overline{G}'$ is a scalar that changes sign under mirror-image symmetry and hence is opposite for the two enantiomeric forms of a chiral solution. $\overline{G}'$ underlies linear chiroptics (see Chapter 11).

We now consider the symmetry of optical response tensors and in particular discuss nonlinear chirality-specific *pseudoscalars* that, similar to $\overline{G}'$, permit the observation of chiral effects in nonlinear optics.

13.3. NONLINEAR CHIROPTICS IN LIQUIDS

An optical effect in a liquid, an isotropic medium, cannot depend on direction. A light ray "sees" the same liquid irrespective of whether it traverses the solution from left to right or

vice versa. Consequently, observables in liquids, such as the refractive index, are scalars. However, in the case of chiral liquids there is an additional symmetry requirement. Under mirror symmetry, or more generally under parity or space inversion, a chiral solution changes its handedness and it follows that those properties that are chirality-specific must also change sign. Under space inversion all coordinates (x, y, z) are replaced everywhere by $(-x, -y, -z)$. A chirality-specific response in a liquid thus requires that the isotropic component of the corresponding response tensor or susceptibility changes sign (is odd) under space inversion [10]. A scalar that changes sign under mirror-image symmetry (space-inversion) is called a *pseudoscalar*. Pseudoscalars—independent of the choice of coordinate axes and of opposite sign for enantiomers—underlie chiral observables in liquids. For nonlinear chiroptics in liquids we therefore seek nonlinear pseudoscalars. Generally, we also require that the pseudoscalars are even with respect to time-reversal symmetry for a true chiral observable [9, 10], but it may be shown that this requirement can be satisfied for all the optical processes that are of interest in this review, and henceforth we will assume that the optical response also obeys the correct time-reversal symmetry. Susceptibilities at all orders can satisfy these requirements, but only those at even-order ($\overleftrightarrow{\chi}^{(2)}, \overleftrightarrow{\chi}^{(4)} \ldots$) can do so within the electric dipole approximation. The appropriate scalars (isotropic components) are obtained from an orientational average, and these are listed in Section 13.7.1. In order to examine which scalars are parity-odd, we consider the symmetry of the fields and molecular properties.

13.3.1. Symmetry

Parity inverts all coordinates and hence the electric field and the electric dipole are odd under parity, whereas the magnetic field is even. Time reversal inverts the direction of momenta and spins but leaves charges invariant. It follows that an electric field and an electric dipole moment is symmetric under time reversal, whereas a magnetic field and a magnetic dipole are time-antisymmetric. Table 13.1 shows the effect of $\hat{P}$ and $\hat{T}$ on the electromagnetic field and dipole operators.

We now discuss the pseudoscalars at the different orders.

13.3.2. Pseudoscalars

The isotropic components of the hyperpolarizability and susceptibility tensors are required to describe the optical response—linear and nonlinear—in a solution. The spatial symmetry of a response tensor may be deduced by considering the symmetry of the fields it connects. For example, the optical rotation tensor $\overleftrightarrow{G}'$ in Eq. (13.7) connects a (time derivative of a) magnetic field with an electric moment and must therefore be parity-odd

TABLE 13.1. Symmetry of Fields and Electric and Magnetic Dipole Operators Under Parity $\hat{P}$ and Time Reversal $\hat{T}$

Field or Property	(Vectors)	$\hat{P}$	$\hat{T}$
$\boldsymbol{E}$	Electric field	−	+
$\boldsymbol{\mu}$	Electric dipole moment	−	+
$\boldsymbol{P}$	Electric polarization	−	+
$\boldsymbol{B}$	Magnetic field	+	−
$\boldsymbol{m}$	Magnetic dipole moment	+	−

for the equality to hold. Alternately, one may deduce the spatial symmetry by considering the operators that enter the response tensor's quantum mechanical expression. For the optical rotation tensor, it is seen that the product of one electric dipole and one magnetic dipole transition moment operator in Eq. (13.10) renders the optical rotation tensor parity-odd.

It will be shown that at second-order no magnetic dipole contributions are required to obtain a chirality-specific response, because a product of three electric dipole transition moment vectors is already parity-odd. However, a third-order process requires magnetic dipole contributions in order to be parity-odd. Some pseudoscalars that arise at order n are tabulated in Table 13.2.

The pseudoscalar $\hat{m}\hat{m}\hat{\mu}$ underlies the magnetochiral effect in linear optics (see Chapter 16, this volume).

13.3.3. Sum-Frequency Generation: $\chi^{(2)}$

In sum-frequency generation (SFG) spectroscopy, pulses with distinct frequencies are overlapped in a medium and the light generated at the sum of the two incident frequencies is detected, which is a coherent and highly directional beam. Its molecular basis is an induced dipole quadratic in the electric field:

$$\vec{\mu}_{\text{ind}} = \overleftrightarrow{\beta}\vec{E}\vec{E}. \tag{13.12}$$

With $\vec{E} \propto \vec{E}_0 \cos(\omega t)$, the induced moment has a static term and a term that oscillates at twice the applied frequency, since $\cos^2(\omega t) \propto 1 + \cos(2\omega t)$. The induced dipole oscillating at 2ω radiates and is the source of second-harmonic generation. In the case of an optical field with two distinct frequencies ω_1 and ω_2, radiation at the sum frequency $(\omega_1 + \omega_2)$ and the difference frequency $(\omega_1 - \omega_2)$ may be generated. Sum (and difference) frequencies can only be generated in a liquid if the liquid is chiral.

TABLE 13.2. Some Chirality-Specific Susceptibilities in Liquids and the Operators that Enter the Numerator of the Corresponding Quantum Mechanical Expressions

$\chi^{(n)}$	Operators	Pseudoscalar	Associated Optical Phenomena
$n = 1$	$\mathrm{i}\,\hat{m}\hat{\mu}$	$g_0, \overline{G'}$	Optical activity (optical rotation, circular dichroism)
$n = 2$	$\hat{\mu}\hat{\mu}\hat{\mu}$ $\hat{m}\hat{m}\hat{\mu}$	$\chi^{(2)}, \overline{\beta}$	Three-wave mixing: Sum and difference frequency generation
	$\mathrm{i}\hat{\Theta}\hat{m}\hat{\mu}$		magnetochiral effect, inverse magnetochiral birefringence, etc.
$n = 3$	$\mathrm{i}\hat{m}\hat{\mu}\hat{\mu}\hat{\mu}$ $\hat{\Theta}\hat{\mu}\hat{\mu}\hat{\mu}$	g_2	Four-wave mixing: Nonlinear optical activity (nonlinear optical rotation, nonlinear circular dichroism), coherent Raman optical activity, two-photon absorption CD
$n = 4$	$\hat{\mu}\hat{\mu}\hat{\mu}\hat{\mu}\hat{\mu}$	$\chi^{(4)}$	Five-wave mixing (e.g., BioCARS)

The corresponding macroscopic polarization for a sum-frequency generation process is described by[2]

$$\vec{P}(\omega_1+\omega_2)=\varepsilon_0\overleftrightarrow{\chi}^{(2)}(\omega_1+\omega_2)\vec{E}(\omega_1)\vec{E}(\omega_2), \tag{13.13}$$

where the second-order susceptibility tensor $\overleftrightarrow{\chi}^{(2)}$ is here written with its frequency argument. The intensity of the sum frequency is proportional to $|\vec{P}(\omega_1+\omega_2)|^2$. In a liquid, one needs to consider an isotropic average (see Section 13.7.1) in Eq. (13.13), with the result that the polarization is given by the vector cross product of the incident fields

$$\vec{P}(\omega_1+\omega_2)=\varepsilon_0\chi^{(2)}(\omega_1+\omega_2)(\vec{E}(\omega_1)\times\vec{E}(\omega_2)), \tag{13.14}$$

and the susceptibility is a scalar of the form

$$\chi^{(2)}=\frac{N}{\varepsilon_0}\frac{1}{6}(\beta_{xyz}-\beta_{xzy}+\beta_{yzx}-\beta_{yxz}+\beta_{zxy}-\beta_{zyx})\equiv\frac{N}{\varepsilon_0}\overline{\beta}. \tag{13.15}$$

The term in parentheses vanishes for any molecule that possesses reflection planes, a center of inversion, or rotation-reflection axes, and $\overline{\beta}$ is thus only nonzero for a chiral molecule. It is of opposite sign for the enantiomers of a chiral molecule, and is therefore a pseudoscalar and a chiral observable.

In Rayleigh–Schrödinger perturbation theory the isotropic component of the first electric dipolar hyperpolarizability at $\omega_3=\omega_1+\omega_2$ may be written as

$$\begin{aligned}\overline{\beta}=&\frac{(\omega_2-\omega_1)}{6\hbar^2}\sum_{j,k}\vec{\mu}_{gk}\bullet(\vec{\mu}_{kj}\times\vec{\mu}_{jg})\\&\left\{\frac{1}{(\tilde{\omega}_{jk}-\omega_3)(\tilde{\omega}_{jg}-\omega_2)(\tilde{\omega}_{jg}-\omega_1)}+\frac{1}{(\tilde{\omega}^*_{kj}+\omega_3)(\tilde{\omega}^*_{kg}+\omega_2)(\tilde{\omega}^*_{kg}+\omega_1)}\right.\\&\left.+\frac{1}{(\tilde{\omega}_{kg}-\omega_3)(\tilde{\omega}_{jg}-\omega_2)(\tilde{\omega}_{jg}-\omega_1)}+\frac{1}{(\tilde{\omega}^*_{jg}+\omega_3)(\tilde{\omega}^*_{kg}+\omega_2)(\tilde{\omega}^*_{kg}+\omega_1)}\right\},\end{aligned} \tag{13.16}$$

where the summation is over all excited states j,k. By allowing the transition frequency to be the complex quantity defined by $\tilde{\omega}_{jk}=\omega_{jk}-(\mathrm{i}/2)\Gamma_k$, where ω_{jk} is the real transition frequency and Γ_k is the population decay rate of the upper level k, the theory is appropriate for near-resonant frequencies. The asterisk denotes complex conjugation. The electric dipole transition moments are defined as $\vec{\mu}_{gj}=\langle g|\vec{\mu}|j\rangle$. It is seen in Eq. (13.16) that all diagonal contributions ($j=k$) to $\overline{\beta}$ vanish. Furthermore, $\overline{\beta}$ has no static limit and its dispersion is consequently much more dramatic than that of a regular nonzero tensor component of the first hyperpolarizability. In practice, the pseudoscalar $\overline{\beta}$ needs to be near resonance for there to be an appreciable sum-frequency response. The wave-mixing energy level diagram describing the nonlinear SFG process is depicted in Figure 13.1.

[2] The polarization oscillating at the sum frequency is the source of a new wave, so one has to consider the interaction of several (incident and generated) coupled waves in the medium. Efficient frequency conversion occurs when the vector sum of the incoming photon momenta matches the momentum of the generated wave (phase-matching).

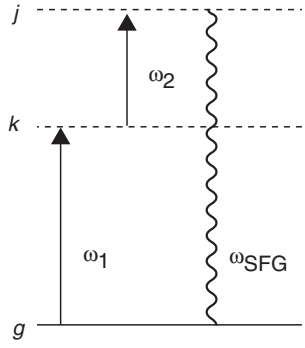

Figure 13.1. Wave-mixing energy level diagram [92] that illustrates the SFG process, which is characterized by three transition matrix elements formed between the ground state *g* and the intermediate virtual states *k,j* (dashed lines). The incident fields at ω_1 and ω_2, as well as the generated field at the sum-frequency, interact with the molecule via electric dipole transition matrix elements. The diagram represents one of a total of six that describe the quantum mechanical expression [cf. Eq. (13.16)]. In the density matrix description of SFG, there are a total of eight diagrams.

13.3.3.1. SFG Experiments. The intrinsic symmetry-breaking in chiral molecules causes a nonracemic liquid to be noncentrosymmetric and, as predicted by Giordmaine, allows for electric dipolar SFG [11]. Sum-frequency generation from chiral liquids has been reexamined [12] and has been observed experimentally [13–18]. We now discuss some of its salient features.

It follows from the vector cross product in Eq. (13.14) that the electric fields at ω_1, ω_2, and $(\omega_1 + \omega_2)$ need to span the *X, Y*, and *Z* directions of a Cartesian frame. Hence, a noncollinear beam geometry is required where two beams are polarized parallel, and one beam is polarized perpendicular to the plane defined by the input beams. This would suggest that the two incident beams make a right angle, where all three beams lie in the same plane. However, momentum conservation favors collinear beams. The optimum angle to observe SFG in an optically active solution is thus a balance of these two requirements. Figure 13.2 shows a schematic of the experimental arrangement. Whereas linear optical activity probes chirality with left- and right-circularly polarized light, the chiral probe in SFG corresponds to the three linearly polarized field directions that form either a left-handed or a right-handed coordinate frame. Chiral SFG spectroscopy therefore needs no circularly polarized light and no polarization modulation. Rather, it is the detection of photons at the sum frequency which constitutes the chiral measurement.

One can immediately see that there can be no chiral probe if two of the three waves have the same frequency, as is the case for SHG. The electric field vectors of the frequency-degenerate fields add and the three waves no longer make a coordinate frame.

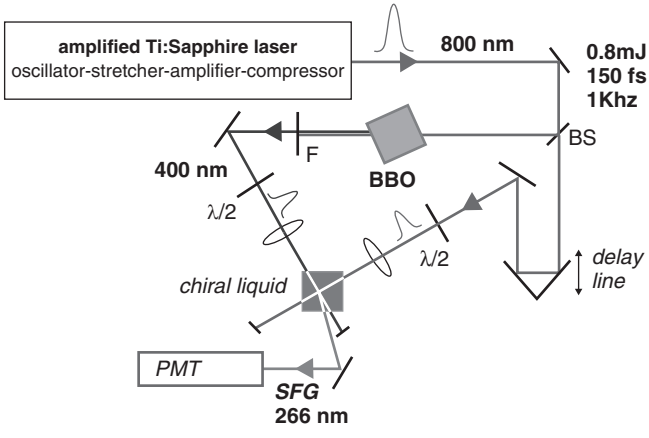

Figure 13.2. Experimental arrangement for the observation of SFG from a chiral liquid. The optical elements shown include a beam splitter (BS), a filter (F), a photomultiplier tube (PMT), and a nonlinear crystal (BBO) [5].

This is also borne out by the quantum mechanical expression for $\overline{\beta}$ [Eq. (13.16)], which is proportional to $\omega_1 - \omega_2$ and therefore goes to zero for SHG, where $\omega_1 = \omega_2$ [19].

For a liquid that contains only two optically active molecular species, namely the *R* and *S* enantiomers of a chiral molecule, we can write the isotropic part of the electric dipolar second-order susceptibility as

$$\chi^{(2)} = \frac{1000 N_A}{\varepsilon_0}([R] - [S])\overline{\beta}_R, \tag{13.17}$$

where the square brackets denote a concentration in mol/L, and where N_A is Avogadro's number. $\overline{\beta}_R$ is the $\overline{\beta}$ of the *R* enantiomer and is given by

$$\overline{\beta}_R = \frac{1}{6}(\beta_{R,xyz} - \beta_{R,xzy} + \beta_{R,yzx} - \beta_{R,yxz} + \beta_{R,zxy} - \beta_{R,zyx}), \tag{13.18}$$

as is required for a pseudoscalar: $\overline{\beta}_R = -\overline{\beta}_S$, so that $\chi^{(2)}$ is zero for a racemic solution (where $[R] = [S]$). The intensity at the sum frequency is proportional to $|\chi^{(2)}|^2$ and the sum-frequency signal thus depends quadratically on the difference in concentration of the two enantiomers. A sum-frequency experiment therefore measures the chirality of a solution and not its handedness, and SFG does not distinguish between optical isomers [20]. This is shown in Figure 13.3 where a quadratic dependence of a SFG signal on the (fractional) concentration difference of the *R*-(+) and *S*-(−) enantiomers of 1,1′-bi-2-naphthol (BN) is observed [15]. Within the noise of the experiment, no signal is recorded for the racemic mixture. SFG is thus effectively background free. As seen in Table 13.3, this is in contrast to linear optical activity phenomena which always contain an achiral and a chiral response. Several other differences between optical activity and chiral SFG are also listed in Table 13.3. For instance, linear optical activity phenomena require both

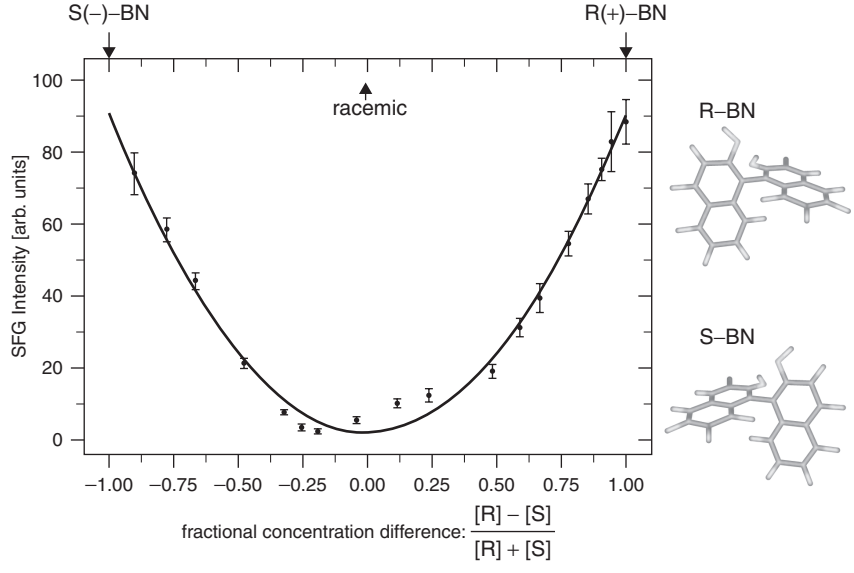

Figure 13.3. Structures of 1,1′-bi-2-naphthol (BN) and continuous titration of two 0.5 M solutions of R-(+)-BN and S-(−)-BN in tetrahydrofuran [4]. The sum-frequency intensity is observed at 266 nm with the incident beams at 800 nm and 400 nm.

TABLE 13.3. Comparison Between Linear Optical Activity and Nonlinear Optical Sum-Frequency Generation from a Chiral Liquid

	Optical Activity	Sum-Frequency Generation
Pseudoscalar	$\overline{G}' \propto \omega\ \mathrm{Im}[\vec{\mu}_{gj} \cdot \vec{m}_{jg}]$ electric and magnetic dipolar	$\overline{\beta} \propto (\omega_1 - \omega_2)\vec{\mu}_{gk} \cdot [\vec{\mu}_{kj} \times \vec{\mu}_{jg}]$ electric dipolar
Signal	$\sim \overline{G}'$ Circular differential	$\sim \lvert\overline{\beta}\rvert^2$ Intensity at sum frequency
Chiral probe	Circularly polarized light	x,y,z components of linearly polarized light beams
Signal contains	Chiral and achiral response	Only chiral response, no background

electric dipolar and magnetic dipolar transitions, whereas SFG from an optically active liquid is entirely electric dipolar. This is significant, as magnetic dipole (and electric quadrupole) transitions are typically much (~1000 times) weaker than electric dipole transitions. This is used to great effect in the study of chiral molecules at surfaces (see Section 13.4). Even though the absolute strength of the nonlinear SFG (and SHG) signals is low, the nonlinear signals can be detected effectively as the there is little or no background. However, in practice at least one of the three frequencies needs to be near or on (electronic or vibrational) resonance for there to be a measurable SFG signal. The conversion efficiency is low because the SFG process cannot be phase-matched in liquids.

Sum-frequency generation can also be used to probe vibrational transitions. If one of the lasers is tunable in the infrared, SFG may be used to record the vibrational spectrum of a chiral molecule. SFG vibrational spectra from neat limonene in the region of the CH stretch have been reported [13, 21]. The strength of the chiral CH stretch in the limonene solutions $|\chi^{(2)}|$ was reported to be about three orders of magnitude smaller than a typical achiral stretch [13]. The liquids from the two enantiomers can be distinguished if beam polarizations are used that permit the observation of mixed chiral/achiral SFG [13].

Time-resolved vibrational SFG optical activity measurements with circularly polarized infrared light have been proposed [22].

13.3.3.2. Electric-Field-Induced Sum-Frequency Generation. Because the sum-frequency signal is proportional to the square of the enantiomeric concentration difference, SFG can in general not distinguish between the enantiomers of a chiral solute. However, it has been shown that the application of a static electric field to SFG makes it possible to determine the sign of the pseudoscalar $\chi^{(2)}$ and thus the absolute configuration of the chiral solute [23]. The static field does not change the phase matching conditions of the sum-frequency process, but it gives rise to an electric-field-induced contribution to the signal. The combined sum-frequency polarization along x is given by

$$P_x(\omega_3) = \varepsilon_0 \left[\underbrace{\chi^{(2)} E_y(\omega_1) E_z(\omega_2)}_{\text{chiral}} + \underbrace{\chi^{(3)} E_y(\omega_1) E_y(\omega_2) E_x(0)}_{\text{achiral}} \right], \tag{13.19}$$

where we assume that the ω_1 beam travels along the z direction and has its electric field vector oscillating along y, and we also assume the ω_2 beam to be plane-polarized

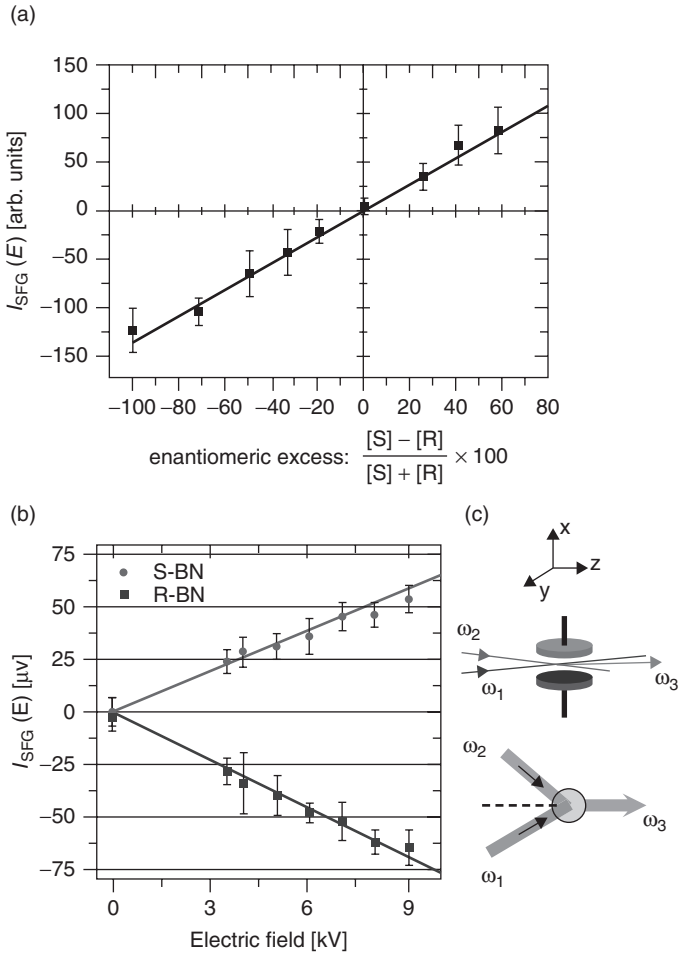

Figure 13.4. (a) Intensity of SFG linear in the static field measured as a function of the fractional concentration difference in S(−)-BN and R-(+)-BN. (b) SFG intensity as a function of the applied electric field for the two enantiomers S-BN and R-BN. (c) Beam geometry for SFG(E) [18].

in the yz plane (see Figure 13.4). The beat between chirality-sensitive SFG (a parity-odd second-order process) and achiral electric-field-induced sum-frequency generation (a parity-even third-order process) yields a contribution to the intensity ($I_{SFG} \propto |\vec{P}(\omega_3)|^2$) that changes sign with the enantiomer. The cross-term linear in the static electric field is [18]

$$I_{SFG}(E) \propto \mathrm{Re}[\chi^{(2)}(\chi^{(3)})^*]E(0)I(\omega_1)I(\omega_2). \tag{13.20}$$

The effect can therefore be used to determine the absolute sign of the isotropic part of the sum-frequency hyperpolarizability. The effect has been observed in solutions of 1,1′-bi-2-naphthol [18]. Figure 13.4 shows that the $I_{SFG}(E)$ signals depend linearly on the strength of the static electric field, and linearly on the enantiomeric excess, and that the $I_{SFG}(E)$ signals changes sign with the enantiomer. *Ab initio* computations can be used to relate the sign of the pseudoscalar to the absolute configuration of the enantiomers [18].

13.3.4. Third-Order Nonlinear Chiroptics: $\chi^{(3)}$

Thus far we have discussed nonlinear optical effects which are quadratic in the optical fields and which give rise to the generation of light at a new frequency—different from that of the incident laser. We now turn to those nonlinear optical effects that modify the optical properties of an optically active liquid at the frequency of (one of) the incident fields.

In two-beam coupling, one laser beam changes the optical properties of the medium for the second laser beam. Interaction of the two different frequency components in a medium via a third-order susceptibility of the form $\overleftrightarrow{\chi}(\omega_1 - \omega_2 + \omega_2)$, for instance, causes a change of the refractive index at ω_1 due to the presence of ω_2. The same nonlinearity also describes pump-probe experiments where the fields at ω_1 and ω_2 are short pulses that are incident with variable time delays in order to observe dynamical effects resulting from the induced polarization as a function of the time between the pulses [24–28].

It is also possible for a single laser beam at third-order to change the optical properties of a medium. The optical response then depends on the cube of the incident optical field and has a component that oscillates at the frequency of the laser. The so-called "degenerate four-wave mixing" process or "optical Kerr effect" occurs in any medium and gives rise to a nonlinear contribution to the refractive index. We can write the corresponding macroscopic polarization as

$$\vec{P}(\omega) = \varepsilon_0 \overleftrightarrow{\chi}(\omega - \omega + \omega)|\vec{E}(\omega)|^2 \vec{E}(\omega), \tag{13.21}$$

where the third-order susceptibility is electric dipolar with a frequency argument of $\omega - \omega + \omega$ (which is $= \omega$). Apart from the intensity-dependent refractive index (see Section 13.3.4.1), many important nonlinear optical phenomena, including self-focusing, self-phase modulation, and two-photon absorption, are directly related to the susceptibility in Eq. (13.21) [2].

We now discuss how frequency-degenerate third-order processes may become specific to chiral molecules. These lead to nonlinear extensions of well-known linear chiroptical effects.

13.3.4.1. Nonlinear Optical Activity. In order to describe nonlinear optical activity, we need to consider the induced moments expanded in powers of the electromagnetic field. The induced electric dipole moment of Eq. (13.2) oscillating at ω becomes

$$\vec{\mu}_{\text{ind}} = \overleftrightarrow{\alpha}\vec{E} + \overleftrightarrow{\gamma}\vec{E}\vec{E}\vec{E} + \cdots. \tag{13.22}$$

For an electric field $\vec{E} \propto \vec{E}_0 \cos(\omega t)$ the term cubic in the electric field has a time dependence $\cos^3(\omega t)$, and since $\cos^3(\omega t) \propto 3\cos(\omega t) + \cos(3\omega t)$ there is a term that oscillates as $\cos(\omega t)$ and therefore contributes to the refractive index at ω. The term quadratic in the electric field $\overleftrightarrow{\beta}\vec{E}\vec{E}$ has been omitted from Eq. (13.22) because it has no term that oscillates at the input angular frequency ω. $\overleftrightarrow{\gamma}$ is known as the second hyperpolarizability.

The refractive index that includes the nonlinear (intensity-dependent) electric dipolar contribution follows from Eqs. (13.8) and (13.22). We define $\chi^{(3)} \equiv N\overline{\gamma}/\varepsilon_0$ and write

$$\vec{P} = \varepsilon_0(\chi^{(1)} + \chi^{(3)}|\vec{E}_0|^2)\vec{E}, \tag{13.23}$$

such that $n \approx n_0 + \chi^{(3)}|\vec{E}_0|^2/(2n_0)$.[3] We can write the refractive index in terms of the intensity, $I \propto |\vec{E}_0|^2$, and use a more compact notation by introducing the nonlinear index of refraction, n_2 [3]:

$$n \approx n_0 + n_2 I. \tag{13.24}$$

By considering cubic field terms in Eq. (13.7), the intensity-dependent refractive index of an optically active liquid can be derived, and inspection of Eqs. (13.9) and (13.24) suggests its general form:

$$n^{(\pm)} \approx (n_0 + n_2 I) \pm (g_0 + g_2 I), \tag{13.25}$$

where we have introduced a "nonlinear optical activity index," g_2. Hence, the circular birefringence of an optically active liquid is modified in the presence of intense light. In analogy to the Rosenfeld equation, we can write a generalized equation that describes linear and nonlinear optical rotation:

$$\theta \approx -\frac{2\pi l}{\lambda}(g_0 + g_2 I). \tag{13.26}$$

The corresponding absorptivities describe linear and nonlinear circular dichroism.

Nonlinear optical rotation has been observed experimentally in a gas [29] and in solutions [30], and has been computed *ab initio* [31]. Nonlinear circular dichroism has been observed in solutions of the ruthenium(II) tris(bipyridyl) salt [28, 32, 33]. One particular form of nonlinear chiral absorption is two-photon circular dichroism, which has recently been measured in binapthol solutions [34].

13.3.4.2. Coherent Raman Optical Activity. Nonlinear extensions of natural optical activity phenomena are not restricted to optical rotation and circular dichroism. Nonlinear optical analogues of Raman optical activity (ROA) have also been considered and their theory has been discussed [35, 36]. ROA measures a small difference in the vibrational Raman spectrum for left- and right-circularly polarized incident light [37, 38]. Although Raman optical activity is now routinely used to study chiral (bio)molecules in aqueous solutions (see Chapter 23 of Volume 2), it is an incoherent spectroscopy and the signals are thus weak. Spontaneous Raman scattering can easily be masked by light emitted from competing processes such as fluorescence. Nonlinear Raman spectroscopies could be of value in the study of vibrational optical activity, because they make it possible to probe Raman resonances through coherent rather than incoherent scattering [36]. The signal strength in nonlinear Raman spectroscopies, such as coherent anti-Stokes Raman scattering (CARS) and stimulated raman scattering (SRS), is therefore several orders of magnitude larger than in spontaneous Raman scattering [39]. Nonlinear Raman spectroscopy would make it possible to eliminate interference from fluorescence and would allow previously unavailable temporal information about a molecule's vibrations to be obtained. Nonlinear Raman optical activity is described by a nonlocal third-order susceptibility of the form $\chi^{\mu\mu\mu m}(\omega_1 - \omega_2 + \omega_1)$ with three electric dipole and one magnetic

[3] Other definitions of the fields and polarizations can be found in the nonlinear optics literature. The numerical factors that enter the expression for the refractive index and that accompany the susceptibilities (here and elsewhere in this volume) may therefore differ from those used in other conventions.

dipole transition in its numerator ($\hat{\mu}\hat{\mu}\hat{\mu}\hat{m}$) [35, 36]. In CARS the laser at ω_2 is tuned and whenever the difference in angular frequencies $\omega_1 - \omega_2$ is proportional to a vibrational energy $\hbar\omega_{\text{vib}}$, then a resonantly enhanced Raman signal is observed at $\omega_1 + \omega_{\text{vib}}$. To our knowledge, there is only one preliminary report of a nonlinear Raman optical activity measurement from a chiral liquid to date [40]. Nonlinear ROA effects are larger near electronic resonance. The wave-mixing energy level diagrams of CARS and SRS are depicted in Figure 13.5.

13.3.5. BioCARS: $\chi^{(4)}$

The nonlinear polarization in a liquid is at fourth order given by a vector cross product [41, 42]:

$$\vec{P}(3\,\omega_1 - \omega_2) = \varepsilon_0 \chi^{(4)}(3\,\omega_1 - \omega_2)(\vec{E}(\omega_1) \times \vec{E}(\omega_2))(\vec{E}(\omega_1) \cdot \vec{E}(\omega_1)), \tag{13.27}$$

here illustrated for a mixing process of the form $3\omega_1 - \omega_2$. Such a fourth-order process in an optically active liquid has been predicted to exist on theoretical grounds [41]. It would allow for the observation of a background-free, electric dipolar chiral signal. Although $\chi^{(4)}$ is, in general, much weaker than $\chi^{(2)}$, a fourth-order process has the distinct advantage that it can be realized in a phase-matched geometry.

A new coherent chiral Raman spectroscopy, which arises when $3\omega_1 - \omega_2$ in Eq. (13.27) is equal to the angular frequency of a vibration, has been proposed and dubbed "BioCARS" to indicate that this spectroscopy would constitute an extension of CARS to chirality and hence biology [43]. BioCARS would exclusively probe chiral Raman vibrations that are simultaneously Raman and hyper-Raman active [43, 44] (see Figure 13.6). The spectroscopy does not require the use of circularly polarized light to detect chirality and would allow for a complete rejection of fluorescence, but it could not distinguish between optical isomers. Apart from the inherent weakness of a nonlinear optical susceptibility responsible for BioCARS, fourth-order processes are weak because they require a noncollinear beam geometry—due to the vector cross product in Eq. (13.27)—which

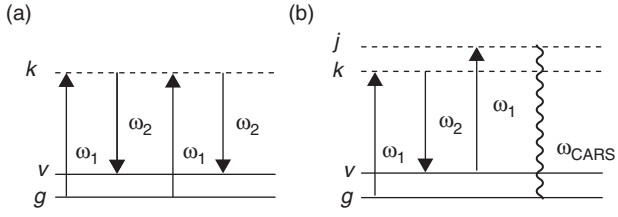

Figure 13.5. Wave-mixing energy diagram of two four-wave mixing ([92]) processes: (a) Spontaneous or stimulated Raman. (b) Coherent anti-Stokes Raman (CARS).

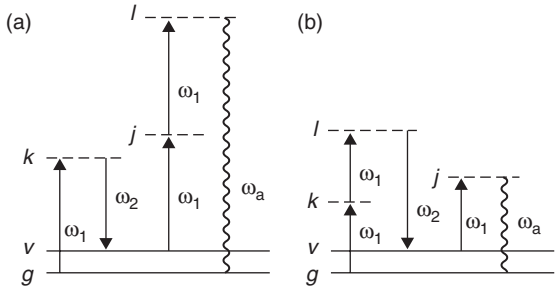

Figure 13.6. Five-wave mixing BioCARS: (a) The difference between the two incident frequencies drives a Raman transition at $v \leftarrow g$ which is then up-converted by two field actions. (b) Hyper-Raman resonance with $2\omega_1 - \omega_2$ matching a vibrational frequency [43].

further reduces the interaction length. The use of a waveguide may constitute a promising alternative because it would allow for a collinear beam geometry and therefore a more efficient implementation of this five-wave mixing process [45].

BioCARS has not yet been observed, but a number of five-wave mixing processes have been discussed [42, 46], including some recent experiments of five-wave mixing at surfaces and interfaces [47, 48].

13.3.6. Incoherent Processes and SHG from Chiral Crystals

The strength of nonlinear spectroscopy is often its coherence—for example, coherent Raman spectroscopy. Nevertheless, incoherent nonlinear processes do occur and they can be useful molecular probes when the corresponding coherent wave-mixing effect is symmetry-forbidden, as is for instance the case with second-harmonic generation in liquids. Similar to incoherent linear Rayleigh and Raman scattering, nonlinear, or hyper-Rayleigh scattering arises from (density) fluctuations in the liquid. The frequency-doubled light is not phase-matched and is emitted in all spatial directions. Its molecular description arises from an orientational average of the product of two first hyperpolarizabilities (a scalar of rank 6), and it may also contain chirally sensitive hyperpolarizability elements [49, 50].

An interesting development in analytical science is the detection of protein crystals in crystallizing solutions via SHG microscopy [51]. SHG can be generated in noncentrosymmetric (i.e., chiral) crystals, including suspensions that contain protein crystals. Unlike ordinary light microscopy, SHG has the advantage that it does not "see" agglomerated or precipitated proteins.

13.4. NONLINEAR CHIROPTICS AT SURFACES

Surface-specific spectroscopies probe molecular order at surfaces and interfaces—for example, the liquid–air interface [52, 53]. In second-harmonic generation (SHG) a light wave from a laser is incident on a surface or an interface at a fixed angle with respect to the surface normal (Figure 13.7). The incident field at the frequency ω induces dipole moments that oscillate at 2ω. Coherent addition of these moments from the surface leads to a macroscopic polarization

$$\vec{P}(2\omega) = \varepsilon_0 \overleftrightarrow{\chi}^{(2)}(\omega + \omega)\vec{E}(\omega)\vec{E}(\omega), \tag{13.28}$$

which radiates a lightwave at the second harmonic (2ω) in the specular direction. The intrinsic surface specificity of SHG originates from the symmetry-breaking that occurs at an interface. Whereas $\overleftrightarrow{\chi}^{(2)}(\omega + \omega)$ vanishes in the bulk of isotropic media, it is nonzero at surfaces and interfaces where the molecules may adopt a preferred orientation. Compared to linear optical spectroscopies, SHG can probe a single layer of molecules on a surface with little background from the bulk. Furthermore, because SHG is a nonlinear optical process, it relies on several parameters, such as the directions or the polarizations of the incoming light beams, and is therefore experimentally more versatile than a linear optical technique.

In 1993 Hicks and co-workers discovered that circular intensity differences in SHG are a probe of surface chirality [54]. Since the first applications of SHG to the study of chiral molecules at interfaces [54–56], including imaging applications of SHG [57],

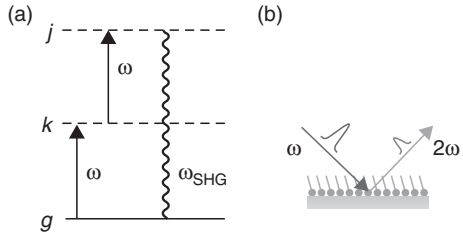

Figure 13.7. Second-harmonic generation (SHG): (a) Wave-mixing energy diagram of nonresonant SHG. (b) Schematic of an SHG process at a surface containing a layer of molecules that are characterized by a molecular axis of symmetry and a tilt angle with respect to the surface normal.

numerous studies on chiral surface SHG have appeared and we refer the interested reader to Chapter 14 in this volume for further details.

In the case of SHG from a surface layer of chiral molecules, symmetry breaking is twofold: First, the interface breaks centrosymmetry such that surface SHG may occur; and second, the symmetry breaking in chiral molecules gives rise to additional contributions to the SHG signal. Both contribute to surface SHG from chiral molecules. It is important to note that SHG can be observed from an achiral surface as well as from a chiral surface. Even for a chiral surface the dominant signals can be electric dipolar (or "local"). In this case, surface SHG probes chirality, similar to sum-frequency generation from the bulk of a liquid, via susceptibility tensor elements that depend on the three orthogonal spatial directions "*XYZ*."

Second-harmonic generation is symmetry-forbidden in a liquid, even if the solution is optically active. In SHG, $\omega_1 = \omega_2$ and the hyperpolarizability components in Eq. (13.16) become symmetric in the corresponding indices (e.g. $\beta_{xyz} = \beta_{xzy}$ etc.) such that their antisymmetric sum vanishes. However, both sum-frequency generation (SFG) and second-harmonic generation (SHG) are allowed at a surface, provided that the molecules at the interface adopt a preferred orientation. This is, for instance, the case for a thin layer of dipolar molecules that lie between two isotropic media with different properties, such as the liquid–air interface.

Generally, one assumes that such a surface is symmetric about its normal, giving C_∞ symmetry for chiral molecules and $C_{\infty v}$ for achiral molecules. The interface is then characterized by one axis, the surface normal, around which it is rotationally invariant and which is parallel to the direction of the average dipole moment. In addition, the arrangement of the molecules at the interface can often be characterized by an average tilt angle θ of the molecular axis (below taken to be along "z") with respect to the surface normal (along "Z"). The nonvanishing components of the second-order surface susceptibility tensor, evaluated in the frame of the laboratory which contains the optical fields, are then related to the first hyperpolarizability tensor, which is expressed in molecular coordinates, by the following matrix equations [58].

$$\begin{pmatrix} \chi^{(2)}_{ZZZ} \\ \chi^{(2)}_{ZXX} \\ \chi^{(2)}_{XZX} \\ \chi^{(2)}_{XXZ} \end{pmatrix} = \frac{N_\sigma}{\varepsilon_0} \begin{bmatrix} a & 2b & 2b & 2b \\ 2b & c & -b & -b \\ 2b & -b & c & -b \\ 2b & -b & -b & c \end{bmatrix} \begin{pmatrix} \beta_{zzz} \\ \beta_{zxx} + \beta_{zyy} \\ \beta_{xzx} + \beta_{yzy} \\ \beta_{xxz} + \beta_{yyz} \end{pmatrix}, \tag{13.29}$$

where N_σ is the number of molecules per unit area and where $a = \cos^3\theta, b = \frac{1}{4}(\cos\theta - \cos^3\theta), c = \frac{1}{4}(\cos\theta + \cos^3\theta)$. In addition, the following identities hold:

$$\chi^{(2)}_{ZXX} = \chi^{(2)}_{ZYY}, \chi^{(2)}_{XZX} = \chi^{(2)}_{YZY}, \chi^{(2)}_{XXZ} = \chi^{(2)}_{YYZ}.$$

For chiral molecules there are additional components

$$\begin{pmatrix} \chi^{(2)}_{XYZ} \\ \chi^{(2)}_{YZX} \\ \chi^{(2)}_{ZXY} \end{pmatrix} = \frac{N_\sigma}{\varepsilon_0} \begin{bmatrix} d & e & e \\ e & d & e \\ e & e & d \end{bmatrix} \begin{pmatrix} \beta_{xyz} - \beta_{yxz} \\ \beta_{yzx} - \beta_{xzy} \\ \beta_{zxy} - \beta_{zyx} \end{pmatrix}, \tag{13.30}$$

where $d = \frac{1}{2}\cos^2\theta, e = \frac{1}{4}(1 - \cos^2\theta)$ and where

$$\chi^{(2)}_{XYZ} = -\chi^{(2)}_{YXZ}, \chi^{(2)}_{YZX} = -\chi^{(2)}_{XZY}, \chi^{(2)}_{ZXY} = -\chi^{(2)}_{ZYX}.$$

The above matrix equations hold for SFG and SHG. In addition, the following identities apply in the case of SHG:

$$\chi^{(2)}_{XZX} = \chi^{(2)}_{XXZ} = \chi^{(2)}_{YZY} = \chi^{(2)}_{YYZ}, \chi^{(2)}_{XYZ} = -\chi^{(2)}_{YXZ} = -\chi^{(2)}_{YZX} = \chi^{(2)}_{XZY}. \tag{13.31}$$

Only chiral molecules—that is, molecules with the point group symmetry C_n, D_n, O, T, or I—can give rise to the surface susceptibility elements in Eq. (13.30). Hence an experimental geometry that probes one of the "*XYZ*" surface susceptibility elements is a probe of molecular chirality. For example, *Y*-polarized SHG that is observed in reflection from a C_∞ surface, when the input beam is polarized parallel to the plane of incidence (*ZX*), requires the surface to be chiral. The components of the polarization from the surface are in this case given by

$$P_Y(2\omega) = 2\varepsilon_0 \chi^{(2)}_{YXZ} \cos\varphi \sin\varphi |\vec{E}_0(\omega)|^2, \tag{13.32}$$

where φ is the angle of incidence. In addition there will be achiral contributions

$$\begin{aligned} P_Z(2\omega) &= \varepsilon_0(\chi^{(2)}_{ZZZ} \sin^2\varphi + \chi^{(2)}_{ZXX} \cos^2\varphi)|\vec{E}_0(\omega)|^2, \\ P_X(2\omega) &= 2\varepsilon_0 \chi^{(2)}_{XZX} \cos\varphi \sin\varphi |\vec{E}_0(\omega)|^2, \end{aligned} \tag{13.33}$$

where we have used the identities in Eq. (13.31). The second-harmonic's plane of polarization is thus seen to "rotate" as a function of $\chi^{(2)}_{YXZ}$ and as a function of the enantiomeric excess at the interface. This effect has been termed "SHG-ORD" [59]. Similarly, the circular SHG intensity differential has been termed "SHG-CD," and "SHG-LD" describes linear SHG intensity differentials [54]. These descriptions are widely used, however, we would like to stress that these SHG processes do not arise from differences in the refractive and absorption indices that respectively underlie optical rotatory dispersion and circular dichroism in linear optical activity. Further details regarding the use of polarization in surface nonlinear spectroscopy may be found in references 56, 60–62.

Surface second-order optical measurements are not restricted to SHG. Sum-frequency generation (SFG) is equally versatile [63, 64]. SFG has the advantage that the incident frequencies can be tuned independently and that vibrational resonances can be probed [17]; and promising applications of SFG to the study of biomolecules, especially proteins at interfaces, have been reported [65–67].

13.5. COMPUTATION

Apart from analytical calculations based on phenomenological models [12, 68–71], the (chiral) nonlinear optical susceptibilities and hyperpolarizabilities may also be calculated quantum chemically. Quantum chemical calculations can be based on a perturbation approach that directly evaluates sum-over-states (SOS) expressions as in Eq. (13.16), or on differentiation of the energy or induced moments for which (electric field) perturbed wavefunctions and/or electron densities are explicitly calculated. These techniques may be implemented at different levels of approximation ranging from semiempirical to density functional methods that account for electron correlation through approximations to the exact exchange-correlation functionals to high-level *ab initio* calculations that systematically include electron correlation effects.

Additional approximations are typically made. The application of external electric fields not only perturbs the electron densities, but also can modify the nuclear configuration. However, a global calculation that evaluates hyperpolarizabilities with a sum over rovibronic states [72] is often computationally too demanding for polyatomic molecules. Instead, one can use a two-step procedure that sequentially, rather than simultaneously, treats the effects of the applied electric fields upon the motion of the electrons and nuclei. Often the clamped-nucleus approximation [73] is applied to determine the effects of the electric field on the electron distribution. Computation of the vibrational contribution to the susceptibilities and hyperpolarizabilities is computationally more demanding. Nevertheless, these corrections have been considered for compounds of practical interest to nonlinear optics [74, 75].

13.5.1. Configuration Interaction Singles Sum-Over-States (CIS-SOS)

Working within the clamped-nucleus approximation, one approach is to directly implement the sum-over-states (SOS) expression for the molecular response tensors obtained from the perturbation expression. The transition moments and frequencies that are required for the SOS can be directly related to spectroscopic quantities. The use of phenomenological damping terms ensures that the SOS expressions can also be used near resonance. Accurate SOS calculations of the first hyperpolarizabilities, in turn, require accurate ground and excited state wavefunctions and derived properties, including excitation energies, dipole transition moments, and dipole moments. The excited-state wavefunctions and energies are typically calculated at the configuration interaction singles (CIS) level of approximation, and a large number of such studies on conjugated compounds employing semiempirical Hamiltonians have been published [76]. *Ab initio* SOS/CIS studies are less frequent [77]. They can be applied to any kind of system, but suffer from two drawbacks: the truncation of the sum (also present in semiempirical calculations) and an overestimation of the excitation energies. Limited computational resources often make it necessary that the SOS is truncated after inclusion of only a few excited states. In order to reduce the overestimation of the excitation energies, it is customary to reduce the excited-state energies such that the calculation agrees with the experimental absorption spectrum. The correction is particularly important for calculations that concern the SFG hyperpolarizability/pseudoscalar near resonance [16]. Extensions of this scheme have been proposed and are based on the second-order perturbative correction of the excitation energies in the CIS(D) method [78]. The limitations of the SOS approach—due to both the approximate nature of the wavefunctions and energies and the truncation of the sum-over-states—can be assessed

by comparing the traditional Orr–Ward–Bishop expression [79, 80] with dipole-free SOS expressions [81].

13.5.2. Time-Dependent Hartree–Fock (TDHF)

Apart from SOS approaches, hyperpolarizabilities can be evaluated by differentiating the energy or the dipole moment with respect to the applied electric field(s):

$$\beta = \left(\frac{\partial^2 \mu(\mathrm{E})}{\partial \mathrm{E}^2}\right)_{\mathrm{E}=0} = -\left(\frac{\partial^3 \mathrm{W}(\mathrm{E})}{\partial \mathrm{E}^3}\right)_{\mathrm{E}=0}. \tag{13.34}$$

In principle, the differentiation is done either numerically (finite-field method) or in an analytical scheme, or a combination of both. Numerical finite-field calculations are limited to derivatives with respect to static fields. Since SFG is an optical process that involves dynamic oscillating fields, it becomes necessary to use an analytical approach, such as the time-dependent Hartree–Fock (TDHF) method.

TDHF [82, 83] is one of the most widely employed *ab initio* techniques to evaluate nonlinear-optical response tensors. The TDHF approach is size consistent but cannot account for the finite lifetime of the excited states. The matrices of the TDHF equation are expanded in a Taylor series of the perturbation due to the static and/or dynamic electric fields and are solved for each order [82, 83]. The so-obtained successive field derivatives of the density matrix are then inserted into the expressions for the hyperpolarizability.

Apart from calculations at the *ab initio* level, the TDHF scheme has also been used with semiempirical Hamiltonians. This makes it possible to calculate larger molecules while partially accounting for electron correlation effects. Indeed, when estimating the dynamic first hyperpolarizability of reference push–pull-conjugated compounds, the semiempirical TDHF scheme performs generally better than the *ab initio* TDHF approach in comparison with high-level *ab initio* methods [84].

TDHF schemes that account explicitly for electron correlation effects have been proposed, in particular within the frame work of propagators or response function approaches [85–87]. These have been employed at the multiconfigurational self-consistent-field (MCSCF) or coupled cluster (CC) level, not only for systems with few atoms and large electron correlation effects, but also for model push–pull π-conjugated molecules like *p*-nitroaniline [88].

13.5.3. Density Functional Theory (DFT)

In addition to the traditional wavefunction CIS-SOS and TDHF methods, density functional theory (DFT) can be used to calculate frequency-dependent hyperpolarizabilities. For small to medium-sized molecules, DFT methods calculate hyperpolarizabilities that are in good agreement with *post*-Hartree–Fock methods. However, the conventional exchange-correlation functionals are local functions of the density (and its derivatives) and cannot properly describe the nonlocal effects associated with the hyperpolarizabilities of large (conjugated) molecules [89].

13.6. CONCLUSIONS

The principles of nonlinear optical probes of chiral molecules in solution and on surfaces have been reviewed and several selected applications of the various spectroscopies have

been presented. Nonlinear spectroscopies require pulsed lasers and often some form of resonance enhancement and thereby can reveal aspects of molecular chirality not accessible to linear optics. Surprisingly, nonlinear chiroptics can sometimes give correspondingly larger signals or be more sensitive than conventional optical activity probes. For instance, a monolayer of chiral molecules may be studied by second-harmonic and sum-frequency generation at surfaces with little contribution from the bulk of the liquid, whereas such a monolayer cannot be detected in linear optical ORD or CD experiments.

Interestingly, nonlinear spectroscopies based on pseudoscalars at even order ($\chi^{(2)}, \chi^{(4)}$) arise within the electric dipole approximation and have no analog in linear optics. They give rise to frequency conversion processes only if the liquid is optically active. Examples are $\chi^{(2)}$ sum- and difference-frequency generation in solutions and processes that involve five field actions (four incident, one generated), as in $\chi^{(4)}$ BioCARS. Care has to be taken that the expression is not frequency-degenerate (far from resonance) in those indices that require antisymmetry. The latter follows from the nature of the isotropic components that involve the Levi-Civita operator that vanishes if repeated indices are symmetric. It is the generation of a photon itself which becomes the measure of a liquid's chirality.

The largest number of nonlinear optical effects arises at third order via $\chi^{(3)}$. This susceptibility couples three incident field actions with a generated (induced) polarization. It is in itself not chiral. In order for the product of four transition moments in the numerator of the corresponding quantum mechanical expression for $\chi^{(3)}$ to be parity-odd (and hence chiral), one of operators has to be magnetic-dipolar. If the applied field is frequency degenerate, then intensity-dependent contributions to optical rotation and circular dichroism may be observed in nonlinear optical activity. Processes involving distinct frequencies in the incident radiation such as coherent Raman and certain pump-probe spectroscopies may similarly become chirality-specific if magnetic-dipolar susceptibilities with transitions of the form $\hat{\mu}\hat{\mu}\hat{\mu}\hat{m}$ are considered. In contrast to linear chiroptics, nonlinear $\chi^{(3)}$ effects make it possible to study the conformation of molecules at ultrafast timescales.

Much remains to be discovered in nonlinear chiroptics. We expect that nonlinear optical spectroscopies will become important tools in the investigation of molecular and biomolecular chirality.

13.7. APPENDIX

13.7.1. Isotropic Tensors

A Cartesian polarizability or susceptibility tensor $\overleftrightarrow{X}xy\ldots$ describing the optical response due to incident fields along the Cartesian directions $xy\ldots$ may in an isotropic medium be replaced by an appropriate scalar. The Greek subscripts indicate Cartesian components; that is, $\vec{u}_\alpha$ is the vector with components (u_x, u_y, u_z). Repeated subscripts denote summation (Einstein summation convention).

The isotropic components are obtained from an orientational average $\langle\ldots\rangle$ over all orientations and are given by [9]

$$\langle \overleftrightarrow{X}^{(1)}_{\alpha\beta} \rangle = X^{(1)}\delta_{\alpha\beta}, \tag{13.35}$$

$$\langle \overleftrightarrow{X}^{(2)}_{\alpha\beta\gamma} \rangle = X^{(2)}\epsilon_{\alpha\beta\gamma}, \tag{13.36}$$

$$\langle \overleftrightarrow{X}^{(3)}_{\alpha\beta\gamma\delta} \rangle = X^{(3)}_1\delta_{\alpha\beta}\delta_{\gamma\delta} + X^{(3)}_2\delta_{\alpha\gamma}\delta_{\beta\delta} + X^{(3)}_3\delta_{\alpha\delta}\delta_{\beta\gamma}, \tag{13.37}$$

where

$$X^{(1)} = \frac{1}{3}\overleftrightarrow{X}^{(1)}_{\alpha\beta}\delta_{\alpha\beta} = \frac{1}{3}\overleftrightarrow{X}^{(1)}_{\alpha\alpha} = \frac{1}{3}(\overleftrightarrow{X}^{(1)}_{xx} + \overleftrightarrow{X}^{(1)}_{yy} + \overleftrightarrow{X}^{(1)}_{zz}), \tag{13.38}$$

$$X^{(2)} = \frac{1}{6}\overleftrightarrow{X}^{(2)}_{\alpha\beta\gamma}\epsilon_{\alpha\beta\gamma} = \frac{1}{6}(\overleftrightarrow{X}^{(2)}_{xyz} - \overleftrightarrow{X}^{(2)}_{xzy} + \overleftrightarrow{X}^{(2)}_{yzx} - \overleftrightarrow{X}^{(2)}_{yxz} + \overleftrightarrow{X}^{(2)}_{zxy} - \overleftrightarrow{X}^{(2)}_{zyx}), \tag{13.39}$$

$$X^{(3)}_1 = \frac{1}{30}(4\overleftrightarrow{X}^{(3)}_{\alpha\alpha\beta\beta} - \overleftrightarrow{X}^{(3)}_{\alpha\beta\alpha\beta} - \overleftrightarrow{X}^{(3)}_{\alpha\beta\beta\alpha}),$$

$$X^{(3)}_2 = \frac{1}{30}(-\overleftrightarrow{X}^{(3)}_{\alpha\alpha\beta\beta} + 4\overleftrightarrow{X}^{(3)}_{\alpha\beta\alpha\beta} - \overleftrightarrow{X}^{(3)}_{\alpha\beta\beta\alpha}), \tag{13.40}$$

$$X^{(3)}_3 = \frac{1}{30}(-\overleftrightarrow{X}^{(3)}_{\alpha\alpha\beta\beta} - \overleftrightarrow{X}^{(3)}_{\alpha\beta\alpha\beta} + 4\overleftrightarrow{X}^{(3)}_{\alpha\beta\beta\alpha})$$

and $\delta_{\alpha\beta}$ is the Kronecker delta and $\epsilon_{\alpha\beta\gamma}$ is the antisymmetric Levi-Civita tensor.

13.7.2. Linear Optical Activity

We consider a monochromatic circularly polarized plane wave traveling along the z direction. In the optically active medium the electric field $\vec{E}^{\pm}$ with amplitude E_0, and the magnetic field $\vec{B}^{\pm}$ can (at a point $z = 0$) be written as

$$\vec{E}^{\pm} = E_0(\vec{x}\cos(\omega t) \mp \vec{y}\sin(\omega t)),$$
$$\vec{B}^{\pm} = E_0\frac{n_0}{c}(\pm\vec{x}\sin(\omega t) + \vec{y}\cos(\omega t)). \tag{13.41}$$

The upper sign corresponds to right-circularly polarized and the lower sign to left-circularly polarized light. $\vec{x}$ and $\vec{y}$ are unit vectors, and c is the speed of light in vacuum.

Substitution of the fields into $\vec{\mu}_{\text{ind}}$ in Eq. (13.7) and use of Eq. (13.4) yields

$$\overleftrightarrow{P}^{\pm} = \varepsilon_0\left(\frac{N\overline{\alpha}}{\varepsilon_0} \pm \frac{N\overline{G}'n_0}{\varepsilon_0 c}\right)\vec{E}^{\pm} \tag{13.42}$$

for a liquid, where the isotropic component $\overline{G}' \equiv (G'_{xx} + G'_{yy} + G'_{zz})/3$ (see Section 13.7.1). The induced magnetic dipole term is best included by considering an effective polarization that contains the contributions due to the magnetization and the quadrupole density [90, 91]

$$\vec{P}_{\text{eff}} = \vec{P} + \frac{\mathrm{i}}{\omega}\vec{\nabla}\times\vec{M} - \vec{\nabla}\cdot\overleftrightarrow{Q}, \tag{13.43}$$

such that

$$\overleftrightarrow{P}^{\pm}_{\text{eff}} = \varepsilon_0\left(\frac{N\overline{\alpha}}{\varepsilon_0} \pm \frac{2N\overline{G}'n_0}{\varepsilon_0 c}\right)\vec{E}^{\pm}. \tag{13.44}$$

The effective polarization is of the form

$$\vec{P}_{\text{eff}} = \varepsilon_0\chi_{\text{eff}}\vec{E}, \tag{13.45}$$

and since the refractive index of a dielectric is, in general, given by $n = (1 + \chi_{\text{eff}})^{1/2}$, we obtain the refractive index of an optically active liquid for right (+)- and left (−)-circularly polarized light:

$$n^{(\pm)} \approx n_0 \pm g_0, \qquad \text{where} \quad g_0 = \frac{N\overline{G}'}{\varepsilon_0 c}. \tag{13.46}$$

The optical rotation in radians developed over a pathlength l is a function of the wavelength λ and the circular birefringence and is given by [9]

$$\theta = \frac{\pi l}{\lambda}(n^{(-)} - n^{(+)}). \tag{13.47}$$

ACKNOWLEDGMENTS

The author is grateful to Professor B. Champagne for helpful comments regarding the section on computational methods.

REFERENCES

1. G. H. Wagnière, *Linear and Nonlinear Optical Properties of Molecules*, VCH, Basel, **1993**.
2. P. N. Butcher, D. Cotter, *The Elements of Nonlinear Optics*, Cambridge University Press, Cambridge, **1990**.
3. R. W. Boyd, *Nonlinear Optics*, Academic Press, London, **1992**.
4. P. Fischer, F. Hache, *Chirality* **2005**, *17*, 421–437.
5. P. Fischer, B. Champagne, Nonlinear optical properties of chiral liquids, in *Non-linear Optical Properties of Matter*, M. G. Papadopoulos, A. J. Sadlej, and J. Leszczynski, eds., Springer, Dordrecht, **2006**, pp. 359.
6. A. D. Buckingham, M. B. Dunn, *J. Chem. Soc. A Inorg. Phys. Theo*. **1971**, 1988–1991.
7. E. U. Condon, *Rev. Mod. Phys*., **1937**, *9*, 432–457.
8. A. D. Buckingham, in *Advances in Chemical Physics*, J. O. Hirschfelder, ed., Interscience, New York, **1967**, pp. 107–142.
9. L. D. Barron, *Molecular Light Scattering and Optical Activity*, Cambridge University Press, Cambridge, **2004**.
10. L. D. Barron, A. D. Buckingham, *Acc. Chem. Res*. **2001**, *34*, 781–789.
11. J. A. Giordmaine, *Phys. Rev*. **1965**, *138*, 1599–1606.
12. P. Fischer, D. S. Wiersma, R. Righini, B. Champagne, A. D. Buckingham, *Phys. Rev. Lett*. **2000**, *85*, 4253–4256.
13. M. A. Belkin, T. A. Kulakov, K. H. Ernst, L. Yan, Y. R. Shen, *Phys. Rev. Lett*. **2000**, *85*, 4474–4477.
14. M. A. Belkin, S. H. Han, X. Wei, Y. R. Shen, *Phys. Rev. Lett*. **2001**, *8711*, 113001.
15. P. Fischer, K. Beckwitt, F. W. Wise, A. C. Albrecht, *Chem. Phys. Lett*. **2002**, *352*, 463–468.
16. P. Fischer, F. W. Wise, A. C. Albrecht, *J. Phys. Chem. A* **2003**, *107*, 8232–8238.
17. M. A. Belkin, Y. R. Shen, *Phys. Rev. Lett*. **2003**, *91*, 213907.
18. P. Fischer, A. D. Buckingham, K. Beckwitt, D. S. Wiersma, F. W. Wise, *Phys. Rev. Lett*. **2003**, *91*, 173901.
19. P. Fischer, A. D. Buckingham, A. C. Albrecht, *Phys. Rev. A* **2001**, *64*, 053816, 1–7.

20. R. A. Harris, *J. Chem. Phys*. **2001**, *115*, 10577–10580.
21. M. A. Belkin, T. A. Kulakov, K. H. Ernst, S. H. Han, Y. R. Shen, *Opt. Mater*. **2003**, *21*, 1–5.
22. M. H. Cho, *J. Chem. Phys*. **2002**, *116*, 1562–1570.
23. P. Fischer, A. D. Buckingham, *J. Opt. Soc. Am. B* **1998**, *15*, 2951–2957.
24. M. H. Cho, *Chem. Rev*. **2008**, *108*, 1331–1418.
25. D. Abramavicius, S. Mukamel, *Chem. Phys*. **2005**, *318*, 50–70.
26. M. Cho, *Two-Dimensional Optical Spectroscopy*, CRC Press (Taylor and Francis), Boca Raton, FL, **2009**.
27. S. Mukamel, *Principles of Nonlinear Optical Spectroscopy*, Oxford University Press, Oxford, **1999**.
28. F. Hache, *J. Photochem. Photobio. A Chem*. **2009**, *204*, 137–143.
29. R. Cameron, G. C. Tabisz, *Mol. Phys*. **1996**, *90*, 159–164.
30. R. Cameron, G. C. Tabisz, *J. Chem. Phys*. **2007**, *126*, 224507.
31. W. Qu, G. C. Tabisz, *J. Chem. Phys*. **2006**, *124*, 184305.
32. H. Mesnil, F. Hache, *Phys. Rev. Lett*. **2000**, *85*, 4257–4260.
33. F. Hache, H. Mesnil, M.-C. Schanne-Klein, *Phys. Rev. B* **1999**, *60*, 6405–6411.
34. L. De Boni, C. Toro, F. E. Hernandez, *Opt. Lett*., **2008**, *33*, 2958–2960.
35. J. O. Bjarnason, H. C. Andersen, B. S. Hudson, *J. Chem. Phys*., **1980**, *72*, 4132–4140.
36. J. L. Oudar, C. Minot, B. A. Garetz, *J. Chem. Phys*., **1982**, *76*, 2227–2237.
37. L. D. Barron, L. Hecht, Vibrational Raman optical activity: From fundamentals to biochemical applications, in *Circular Dichroism*, N. Berova, K. Nakanishi, and R. W. Woody, eds., Wiley-VCH, New York, **2000**, p. 877.
38. L. A. Nafie, *Annu. Rev. Phys. Chem*. **1997**, *48*, 357–386.
39. M. D. Levenson, *Introduction to Nonlinear Laser Spectroscopy*, Academic Press, New York, **1982**.
40. H. Spiegel, F. W. Schneider, First measurement of Raman optical activity by CARS, in *Spectroscopy of Biological Molecules—State of the Art*, A. Bertoluzza, C. Fagnano, P. Monti, eds., John Wiley & Sons, New York, **1989**, pp. 317–322.
41. N. I. Koroteev, Novel nonlinear optical techniques for studying chiral molecules of biological importance, in *Frontiers in Nonlinear Optics. The Serguei Akhmanov Memorial Volume*, H. Walther, N. I. Koroteev, M. Scully, eds., Institute of Physics Publishing, Bristol, **1993**, pp. 228–239.
42. L. C. D. Romero, S. R. Meech, D. L. Andrews, *J. Phys. B Atom. Mol. Opt. Phys*. **1997**, *30*, 5609–5619.
43. N. I. Koroteev, *Biospectroscopy* **1995**, *1*, 341–350.
44. S. N. Volkov, N. I. Konovalov, N. I. Koroteev, V. A. Makarov, *Quantum Electron*. **1995**, *25*, 62–65.
45. A. M. Zheltikov, A. N. Naumov, *Quantum Electron*. **1999**, *29*, 607–612.
46. A. P. Shkurinov, A. V. Dubrovskii, N. I. Koroteev, *Phys. Rev. Lett*. **1993**, *70*, 1085–1088.
47. C. Voelkmann, M. Reichelt, T. Meier, S. W. Koch, U. Hofer, *Phys. Rev. Lett*. **2004**, *92*, 127405.
48. S. Yamaguchi, T. Tahara, *J. Phys. Chem. B* **2005** *109*, 24211–24214.
49. V. Ostroverkhov, R. G. Petschek, K. D. Singer, L. Sukhomlinova, R. J. Twieg, S. X. Wang, L. C. Chien, *J. Opt. Soc. Am. B* **2000**, *17*, 1531–1542.
50. P. Fischer, A. Salam, *Mol. Phys*. **2010**, *108*, 1857–1868.
51. R. D. Wampler, D. J. Kissick, C. J. Dehen, E. J. Gualtieri, J. L. Grey, H. F. Wang, D. H. Thompson, J. X. Cheng, G. J. Simpson, *J. Am. Chem. Soc*. **2008**, *130*, 14076–14078.

52. Y. R. Shen, *Surf. Sci*. **1994**, *299/300*, 551–562.
53. T. F. Heinz, Second-order nonlinear optical effects at surfaces and interfaces, in *Nonlinear Surface Electromagnetic Phenomena*, H. E. Ponath and G. I. Stegeman, eds., North Holland, Amsterdam, **1991**, pp. 353–416.
54. T. P. Petralli-Mallow, T. M. Wong, J. D. Byers, H. I. Yee, J. M. Hicks, *J. Phys. Chem*. **1993**, *97*, 1383–1388.
55. J. D. Byers, H. I. Yee, J. M. Hicks, *J. Chem. Phys*. **1994**, *101*, 6233–6241.
56. M. Kauranen, T. Verbiest, J. J. Maki, A. Persoons, *J. Chem. Phys*. **1994**, *101*, 8193–8199.
57. M. A. Kriech, J. C. Conboy, *J. Am. Chem. Soc*. **2005**, *125*, 2834–2835.
58. B. Dick, *Chem. Phys*. **1985**, *96*, 199–215.
59. J. D. Byers, H. I. Yee, T. Petralli-Mallow, J. M. Hicks, *Phys. Rev. B* **1994**, *49*, 14643–14647.
60. M. Kauranen, S. Cattaneo, Polarization techniques for surface nonlinear optics, in *Progress in Optics*, E. Wolf, ed., Elsevier, Amsterdam, **2008**, pp. 69–120.
61. M. Kauranen, S. Van Elshocht, T. Verbiest, A. Persoons, *J. Chem. Phys*. **2000**, *112*, 1497–1502.
62. S. Foerier, I. A. Kolmychek, O. A. Aktsipetrov, T. Verbiest, V. K. Valev, *ChemPhysChem* **2009**, *10*, 1431–1434.
63. P. Fischer, A. D. Buckingham, *J. Opt. Soc. Am. B* **1998**, *15*, 2951–2957.
64. S. H. Han, N. Ji, M. A. Belkin, Y. R. Shen, *Phys. Rev. B* **2002**, *66*, 165415/1–6.
65. J. Wang, X. Y. Chen, M. L. Clarke, Z. Chen, *Proc. Natl. Acad. Sci*. **2005**, *102*, 4978–4983.
66. K. T. Nguyen, J. T. King, Z. Chen, *J. Phys. Chem. B* **2010**, *114*, 8291–8300.
67. L. Fu, G. Ma, E. C. Y. Yan, *J. Am. Chem. Soc*. **2010**, *132*, 5405–5412.
68. G. J. Simpson, *ChemPhysChem* **2004**, *5*, 1301–1310.
69. M. A. Belkin, Y. R. Shen, C. Flytzanis, *Chem. Phys. Lett*. **2002**, *363*, 479–485.
70. F. Hache, *J. Phys. Chem. A* **2010**, *DOI: 10.1021/jp105123m*.
71. A. J. Moad, G. J. Simpson, *J. Phys. Chem. B* **2004**, *108*, 3548–3562.
72. D. M. Bishop, *Rev. Mod. Phys*. **1990**, *62*, 343–374.
73. D. M. Bishop, B. Kirtman, B. Champagne, *J. Chem. Phys*. **1997**, *107*, 5780–5787.
74. J. M. Luis, M. Duran, B. Champagne, B. Kirtman, *J. Chem. Phys*. **2000**, *113*, 5203–5213.
75. O. Loboda, R. Zalesny, A. Avramopoulos, J. M. Luis, B. Kirtman, N. Tagmatarchis, H. Reis, M. G. Papadopoulos, *J. Phys. Chem. A* **2009**, *113*, 1159–1170.
76. V. J. Docherty, D. Pugh, J. O. Morley, *J. Chem. Soc. Faraday Trans. II* **1985**, *81*, 11791192.
77. M. Spassova, V. Monev, I. Kanev, B. Champagne, D. H. Mosley, J. M. Andre, in *Quantum Systems in Chemistry and Physics*, A. Hernandez-Laguna, ed., Kluwer, Dordrecht, **2000**, p. 101.
78. B. Champagne, B. Kirtman, *J. Chem. Phys*. **2006**, *125*, 024101/1–7.
79. B. J. Orr, J. F. Ward, *Mol. Phys*. **1971**, *20*, 513–526.
80. D. M. Bishop, *J. Chem. Phys*. **1994**, *100*, 6535–6542.
81. M. G. Kuzyk, *Phys. Rev. A* **2005**, *72*, 053819.
82. H. Sekino, R. J. Bartlett, *J. Chem. Phys*. **1986**, *85*, 976–989.
83. S. P. Karna, M. Dupuis, *J. Comp. Chem*. **1991**, *12*, 487–504.
84. E. Botek, B. Champagne, *Appl. Phys. B* **2002**, *74*, 627–634.
85. F. Aiga, R. Itoh, *Chem. Phys. Lett*., **1996**, *251*, 372–380.
86. O. Christiansen, P. Jørgensen, C. Hättig, *Int. J. Quantum Chem*. **1998**, *68*, 1–52.
87. L. Ferrighi, L. Frediani, C. Capelli, P. Salek, H. Ågren, T. Helgaker, K. Ruud, *Chem. Phys. Lett*. **2006**, *425*, 267–272.
88. J. R. Hammond, K. Kowalski, *J. Chem. Phys*. **2009**, *130*, 194108.

89. B. Champagne, E. A. Perpete, D. Jacquemin, S. J. A. van Gisbergen, E. J. Baerends, C. Soubra-Ghaoui, K. A. Robins, B. Kirtman, *J. Phys. Chem. A* **2000**, *104*, 4755–4763.

90. L. Rosenfeld, *Theory of Electrons*, Dover, New York, **1965**.

91. P. S. Pershan, *Phys. Rev*. **1963**, *130*, 919–929.

92. D. Lee, A. C. Albrecht, in *Advances in Infrared and Raman Spectroscopy*, R. J. H. Clark and R. E. Hester, eds.,, John Wiley & Sons, New York, **1985**, p. 179.

14

IN SITU MEASUREMENT OF CHIRALITY OF MOLECULES AND MOLECULAR ASSEMBLIES WITH SURFACE NONLINEAR SPECTROSCOPY

Hong-fei Wang

The previous chapter (Chapter 13 by Peer Fischer) [1] covers the general principles on nonlinear optical spectroscopy of chiral molecules. This chapter shall discuss the developments in *in situ* measurement and quantitative analysis of chirality of molecules and molecular assemblies with the surface nonlinear spectroscopy. The message to take home is that surface second-order nonlinear spectroscopies are not only sensitive techniques to detect and characterize molecular chirality, but also unique techniques to detect and characterize structural chirality. These emerging chiroptical techniques shall potentially find broad applications in general chemistry of chiral molecules, material sciences, and biological sciences.

14.1. INTRODUCTION

By definition, a molecule or molecular structure is chiral when it lacks an internal plane of mirror and inversion symmetry—that is, when its mirror image is nonsuperimposable with itself. Because chiral amino acids, carbohydrate, lipids, and nucleic acids are the building blocks of life, and many of them form three-dimensional chiral structures or assemblies in the biological membranes, *in situ* measurement and analysis to identify their presence and to determine their structure, structural changes, and interactions at various interfaces and membranes are the keys to understand the mechanisms of life. It has been convincingly argued that it is important to simultaneously use more than one chiroptical spectroscopic method for determining the structure of chiral molecules and structures [2]. However, in the main stream discussions on chiroptical methods, the

Comprehensive Chiroptical Spectroscopy, Volume 1: Instrumentation, Methodologies, and Theoretical Simulations, First Edition. Edited by N. Berova, P. L. Polavarapu, K. Nakanishi, and R. W. Woody.
© 2012 John Wiley & Sons, Inc. Published 2012 by John Wiley & Sons, Inc.

nonlinear spectroscopy, especially surface nonlinear spectroscopy, is yet to be recognized as one of the newest additions in the arsenal of chiroptical spectroscopic techniques. It is safe to say that in terms of the molecular chirality studies, nonlinear spectroscopy is still in its infancy.

The second-order nonlinear chiroptical techniques are intrinsically surface-sensitive and chiral-selective spectroscopic probes that are ideal for fundamental understanding of surface chirality and for *in situ* measurement and detection of the surface chirality and interactions [3–9]. The second-order nonlinear optical process is the process when two incoming photons with certain frequencies interact simultaneously with the same set of atoms or molecules to generate a new emitting photon at the sum or the different frequency of the two incoming photons. When the frequencies of the two incoming photons are identical and the frequency of emitting photon is twice that of incident photons, the process is called second-harmonic generation (SHG), or called optical rectification when the resulted field is with zero frequency; when the frequencies of the two photons are different, the process is called sum-frequency generation (SFG) or difference-frequency generation (DFG) [10, 11]. Varying the frequencies and polarizations of the incoming photons can probe both the vibrational spectroscopy (VS) and electronic spectroscopy (ES) of the surface molecules. The spectral detail and the polarization dependence can provide structural and interaction details of all the surface molecular moieties [12–26]. Since the pioneering works using SHG to study chiral interfaces by the groups of Hicks and Persoons in the early 1990s [4, 27–32], there have been many developments on the understanding of the nonlinear chiroptical phenomenon [4–6, 33–47] and on the applications of the SHG and SFG techniques for characterization and imaging of the chiral surfaces [48–62].

The motivations behind the attempt to connect the second-order nonlinear chiroptical techniques to the molecular chirality studies were clearly summarized by Janice M. Hicks more than 15 years ago as follows [4]:

> *There are at least two motivations for accomplishing a connection between (surface) nonlinear processes and chiral optical responses. Even-order nonlinear optical processes are surface-sensitive; thus it is possible to develop a probe of chiral structures at interfaces at submonolayer densities* ($<10^{14}$ molecules cm^{-2}). *Secondly, because of the symmetry properties of higher-order optical tensors, more spectroscopic details about the chiral medium can be obtained.*

Currently, SHG and SFG-VS are capable of measuring good-quality spectra in the sample area of less than 100 μm in diameter at submonolayer density. This corresponds to less than 10^{10} molecules, or 1.6×10^{-14} mole. In contrast to SHG and SFG, the common linear optical techniques, such as the circular dichroism (CD) spectroscopy, optical rotatory dispersion (ORD), vibrational circular dichroism (VCD), and vibrational Raman optical activity (ROA), have neither the surface selectivity nor the monolayer sensitivity [63–69].

The surface selectivity of SHG and SFG comes from the inherent symmetry requirement of the second-order nonlinear optical process, which dictates that for centrosymmetric systems, such as bulk liquids and amorphous solids, the leading dipolar contribution term has to vanish [13, 14, 70]. While the SHG process is a completely dipole-forbidden process in the centrosymmetric liquid (chiral or achiral), SFG or DFG processes are only dipole-forbidden processes for the liquid of achiral molecules and are dipole-allowed processes for the chiral terms of the liquid of chiral molecules, even though the achiral terms are still dipole-forbidden [1, 3, 5, 7, 33]. Because the resulting SHG or SFG signal is at

a completely different frequency in comparison to the two incoming frequencies or other photoinduced emissions, they are basically background-free. The second-order SHG and SFG processes are very weak processes. Nevertheless, submonolayer sensitivity can be readily achieved with femtosecond or picosecond pulse lasers, which provides enough peak intensity. Very sensitive detectors, such as single-photon counting photomultiplier tubes (PMTs), in single-wavelength or scanning SHG/SFG [71, 72], and charge-coupled device (CCD), in broadband or so-called "multiplex" SHG and SFG [72–76], are needed for the measurements. Using heterodyne techniques, SHG or SFG from the interface can also be further amplified to improve the sensitivity by at least one or two orders of magnitude, in addition to the ability to measure the absolute phase of the SHG or SFG optical field [77–82].

The chiral selectivity of the surface SHG and SFG comes from the fact that the third-rank second-order nonlinear optical susceptibility tensors can uniquely describe the intrinsic chiroptical interactions between the chiral molecule and the optical fields [3, 7]. Because we know that in the linear absorption (infrared or UV–visible) spectroscopy and Raman spectroscopy, the molecular response to the optical field is described with transition moments (vector) or Raman polarizability (second rank tensor). Neither the vector nor the second-rank tensors can describe the chiroptical responses of the molecule, because any chiroptical response has to reflect the three-dimensional chiral structure that lacks the mirror and inversion symmetry. This is why in the absorption or Raman spectroscopy, the higher-order coupling tensors between the dipole and magnetic dipole terms need to be considered to describe the molecular chiroptical responses. In contrast, in SHG or SFG, the dipolar responses already included the chiroptical terms described by the third-rank second-order nonlinear susceptibility tensors. Therefore, no higher-order coupling, which generally involves much weaker effects, needs to be invoked [3, 7]. These facts not only enable explicit interpretation of the SHG and SFG experimental data, but also can be used to simplify the theoretical treatment and first principle computation of the molecular responses in the SHG and SFG processes.

The most important aspect of the chiral selectivity of the surface SHG and SFG processes is their ability to selectivity probe the "structural chirality," or "orientational chirality" as called by Simpson et al., of the molecular assembly or macromolecules over the "intrinsic chirality" of each chiral building block [6, 8, 83–85]. At the molecular level, the values of the chiral terms are in general two orders of magnitude smaller than the values of the achiral terms [5, 7, 9, 44, 86, 87]. Therefore, in any macroscopic SHG and SFG-VS measurements, the "structural chirality" that comes from the achiral molecular terms through the three-dimensional chiral arrangements of molecular units or segments dominates over the "intrinsic chirality," which is the result of the chiral molecular terms. [6, 8, 83–85]. Thus, surface SHG and SFG are uniquely sensitive probes of the 3-D structure of the protein and DNA molecules. In the linear VCD, ECD, and ROA spectroscopy of proteins, the spectrum is usually dominated by the "intrinsic chirality" of the chromophore or the amino acid units [88]. Still, the sensitivity of far-UV protein CD spectra to protein secondary structure is widely used to determine the secondary structure and composition of proteins [89–92]. Therefore, successful application of surface SHG and SFG electronic and vibrational spectroscopy in such studies is expected to have great impact.

There has been numerous reviews on the chiroptical nonlinear SHG and SFG techniques [4–9, 93]. There is also a chapter in this book to cover the general principles on nonlinear optical spectroscopy of chiral molecules [1]. Therefore, this chapter shall focus on the SHG and SFG linear dichroism (LD) methods, because they are the simplest

and more informative in terms of quantitative measurement and analysis of the surface chirality. A thorough understanding of the SHG-LD and SFG-LD can lead to important applications, and extension to the SHG/SFG circular dichroism (CD) or optical rotation dichroism (ORD) techniques can be carried out accordingly, whenever such additional measurements and analysis are desired.

14.2. THEORY AND FORMALISM OF SHG-LD AND SFG-LD

14.2.1. Some General Issues in Surface SHG and SFG

The principles and descriptions on the surface second-order nonlinear optics can be found in books and reviews [13–19, 22, 94–97] More detailed technical description and applications with quantitative analysis with SHG and SFG-VS can be found in the reviews and research papers [14–17, 22, 94, 96, 97]. Descriptions and examples on the SHG-CD and SHG-ORD for interface and SFG for bulk molecular chirality studies can be found in the literature [5–7, 28, 48, 93, 98, 99].

The key issue for the application of the SHG and SFG vibrational spectroscopy (SFG-VS) techniques for the achiral and chiral surface studies lies in how accurate and quantitative the experimental measurement and data analysis can be achieved. The past few years have witnessed the developments in quantitative measurement and analysis with SHG and SFG-VS studies of the achiral surfaces [15–17, 94, 100]. These developments were based on the careful studies using the polarization and experimental configuration control in designing SHG and SFG-VS experiments and in SHG and SFG-VS data analysis [100–112] and employing the unified treatment and analysis of the macroscopic susceptibility tensors in relationship to the microscopic molecular tensors, as well as the molecular optical theory on the microscopic local field factors [15–17, 94, 96]. Techniques on quantitative treatment in SHG and SFG-VS have been extensively reviewed [15–17, 22, 94, 113].

In SFG-VS, a set of polarization selection rules were established for assignment and detail analysis of the symmetry and interference of the vibrational spectra peaks and features [15, 102, 103, 114, 115]. Based on these polarization selection rules, it was then found that many of the spectral assignments in SFG-VS disagreed with the established IR and Raman assignments even for the C–H stretching vibrations of the commonly studied simple molecules, such as ethylene glycol, ethanol, and so on [102, 103, 117, 116]. Another successful application of this new practice with polarization and symmetry analysis was well demonstrated in the assignment and analysis of the O–H stretching vibrational spectra of the air–water interface [104]. In SHG and SFG-VS or SFG-ES, the chiral spectral features appear also in different polarization combinations from the achiral spectra features; the assignment of these various spectral features, especially when they are congested or overlapping with each other in the IR or Raman, is straightforward and relatively easy using the polarization selection rules. This shall help clarify many questions or confusions in the IR and Raman spectral assignment and analysis of the chiral molecules in the bulk samples. This also tells us that surface SHG and SFG should not be only considered as the surface spectroscopic tools.

14.2.2. SHG-LD, SFG-LD and the Degree of Chiral Excess (DCE)

The unique aspect of the simplicity and effectiveness of the surface nonlinear chiroptical techniques (i.e., SHG or SFG), is their linear dichroism (LD) [35, 118]. In linear

spectroscopy, such as IR and Raman, only circular dichroism (CD) and optical rotatory dispersion (ORD) were possible for randomly oriented liquid-phase samples. There is no analog of the linear dichroism in the linear optical activity of the bulk sample as in the surface nonlinear spectroscopy.

In general, there are three kinds of experiments to study chiral surfaces using the SHG and SFG techniques. Two of them use the linearly polarized light, including the SHG (SFG) linear dichroism (SHG-LD) and SHG (SFG) optical rotators dispersion (SHG-ORD), and the third uses the circularly polarized light, including the SHG (SFG) circular dichroism (SHG-CD) [5, 6, 35, 93, 118]. There is also an approach using the counterpropagating geometry for SHG to separately probe the chiral and achiral surface susceptibility elements [48, 57]. Comparison of the LD, CD, and ORD in SHG techniques were carefully reviewed in the literatures [5, 6, 35].

It has been understood that the SHG-LD is the simplest and direct measurement among these three experiments [5, 35, 58, 93]. In addition, it has been shown that the half-waveplate technique can be used to make more accurate determination of the interface second-order nonlinear susceptibility tensor elements than the quarter-waveplate technique used for SHG-CD experiments [16, 58, 119]. SFG-LD also follows the same arguments as above. In short, in the SHG-LD experiment one varies the linear polarization of the incident beam using a half-waveplate and detects SHG signal in certain linear polarizations, such as the s and the p polarization. The difference of the SHG intensity at the input linear polarizations of 45° and -45° (or 135°) measures the chirality of the monolayer or film. Thus, a quantitative description of the degree of chiral excess (DCE) can be defined [118]. Here the s polarization is defined when the vector of the optical field is perpendicular to the incident plane formed with the propagation direction of incident light and the surface normal; while the p-polarization is when the optical field vector is within the incident plane.

In the SHG-LD, as well as in the SFG-LD, the degree of chiral excess (DCE) of the interface or film is used to quantify the chirality of the interface. It is [118]

$$\Delta I/I = \frac{2(I_{-45^\circ} - I_{+45^\circ})}{(I_{-45^\circ} + I_{+45^\circ})}. \tag{14.1}$$

Here in SHG/SFG, the intensities are measured with either the s- or p-polarization detection, and I_{-45° denotes the SHG/SFG intensity when the incident laser polarization is -45°, and so on. The chiral and achiral Langmuir or Gibbs monolayer at the air–liquid or liquid–liquid interfaces are usually considered rotationally isotropic with respect to the interface normal. For the achiral Langmuir or Gibbs interface, $I_{-45^\circ} = I_{+45^\circ}$ and consequently $\Delta I/I = 0$; while for the chiral Langmuir or Gibbs interface, $I_{-45^\circ} \neq I_{+45^\circ}$ and consequently $\Delta I/I \neq 0$ [118]. It is clear that when $I_{-45^\circ} > I_{+45^\circ}$, $\Delta I/I > 0$; while when $I_{-45^\circ} < I_{+45^\circ}$, $\Delta I/I < 0$. Thus, the sign of the $\Delta I/I$ indicates whether the chiral interface is predominantly in one chiral enantiomer state or in the opposite chiral enantiomer state, even though the absolute chirality of the interface is not known from the SHG-LD measurement [118].

It was recently demonstrated that the accuracy of the DCE value of a chiral surface can be experimentally determined as accurate as $\sim$2% or better using the s-detection SHG-LD [101] or using the twin polarization angle (TWA) method in SFG-VS [120] measurements. With the DCE value accurately quantified, the s-detection SHG-LD was subsequently applied to systematically investigate, and clarify, the mechanism of chirality formation and changes in the Langmuir monolayer of achiral molecules [101, 121]. The examples will be presented in the section below.

14.2.3. Theory of SHG-LD

Details for quantitative experimental measurements on the achiral surface using SHG have been extensively discussed in recent reviews [16]. The basic theory of SHG as a general surface analytical probe has been well described in literature [14, 96, 100, 122, 123].

14.2.3.1. SHG-LD for Chiral Surface. SHG-LD was first demonstrated by Persoons and co-workers in the early 1990s. Its advantages over the SHG-CD or SHG-ORD were also demonstrated [35, 118]. However, SHG-LD so far has only found limited applications, partly due to its formulations in literature that are not targeted for chemists.

Generally, the SHG Intensity $I(2\omega)$ reflected from an interface is [96]

$$I(2\omega) = \frac{32\pi^3\omega^2 \sec^2\Omega}{c_0^3 n_1(\omega)n_1(\omega)n_1(2\omega)}|\chi_{eff}|^2 I^2(\omega), \tag{14.2}$$

$$\chi_{eff} = [\mathbf{L}(2\omega) : \hat{e}(2\omega)] \cdot \chi_{ijk} : [\mathbf{L}(\omega) : \hat{e}(\omega)] \cdot [\mathbf{L}(\omega) : \hat{e}(\omega)]. \tag{14.3}$$

In Eq. (14.2), $I(\omega)$ is the incoming laser intensity, c_0 is the speed of the light in the vacuum, and Ω is the incident angle from the surface normal. In Eq. (14.3), χ_{ijk} is the macroscopic second-order susceptibility tensor, which has $3 \times 3 \times 3 = 27$ elements; $\hat{e}(2\omega)$ and $\hat{e}(\omega)$ are the unit vectors of the electric field at 2ω and ω; $\mathbf{L}(2\omega)$ and $\mathbf{L}(\omega)$ are the tensorial Fresnel factors for 2ω and ω, respectively. Here in χ_{ijk}, the index i corresponds to the polarization vector direction of the second harmonic (2ω) field, and j and k correspond to the two polarization vector directions of the incoming fundamental (ω) field.

χ_{eff} itself contains all molecular information of SHG measurement. There are three independent achiral χ_{eff} terms, namely, s-in/p-out (χ_{sp}), 45°-in/s-out ($\chi_{45°s}$), and p-in/p-out (χ_{pp}), with one additional $\chi_{eff,chiral}$ chiral term for an rotationally isotropic chiral interface (C_∞). Here, in the experimental coordinate system (x,y,z), z is the interface normal, and we choose the xz plane as the incident plane. Subsequently, p polarization is defined as polarization within the xz plane, and s is perpendicular to the xz plane. These χ_{eff} terms are directly related to the interfacial macroscopic susceptibilities χ_{ijk} tensor elements as discussed below [96, 97].

The seven nonvanishing achiral χ_{ijk} tensors of the rotationally isotropic chiral interface (C_∞) are $\chi_{zyy} = \chi_{zxx}$, $\chi_{yzy} = \chi_{yyz} = \chi_{xzx} = \chi_{xxz}$, and χ_{zzz}, and the four nonvanishing chiral terms are $\chi_{xyz} = \chi_{xzy} = -\chi_{yzx} = -\chi_{yxz}$ [30]. Since any nonzero chiral susceptibility tensor has to have no mirror symmetry, the chiral susceptibility tensor cannot have exchangeable indexes; that is, all the three subscripts have to be different. Because of the rotational symmetry along the z axis (surface normal), the $\chi_{zxy} = \chi_{zyx} = 0$ terms have to vanish. Because the last two indexes correspond to the indistinguishable incoming fundamental photons, we have $\chi_{xyz} = \chi_{xzy}$ and $\chi_{yzx} = \chi_{yxz}$. Finally, since there is no mirror symmetry, we have $\chi_{xyz} = \chi_{xzy} = -\chi_{yzx} = -\chi_{yxz}$.

One has [16]

$$\begin{aligned}
\chi_{eff,sp} &= L_{zz}(2\omega)L_{yy}^2(\omega)\sin\Omega\chi_{zyy},\\
\chi_{eff,45°s} &= L_{yy}(2\omega)L_{zz}(\omega)L_{yy}(\omega)\sin\Omega\chi_{yzy},\\
\chi_{eff,pp} &= L_{zz}(2\omega)L_{xx}^2(\omega)\sin\Omega\cos^2\Omega\chi_{zxx}\\
&\quad - 2L_{xx}(2\omega)L_{zz}(\omega)L_{xx}(\omega)\sin\Omega\cos^2\Omega\chi_{xzx}\\
&\quad + L_{zz}(2\omega)L_{zz}^2(\omega)\sin^3\Omega\chi_{zzz}
\end{aligned} \tag{14.4}$$

with

$$\chi_{eff,chiral} = 2L_{xx}(2\omega)L_{yy}(\omega)L_{zz}(\omega)\sin\Omega_\omega\cos\Omega_\omega\chi_{xyz}. \tag{14.5}$$

The general expression for Eq. (14.4) is

$$\chi_{eff,\alpha_{in}-\gamma_{out}} = \left[\chi_{eff,45^\circ s}\sin 2\alpha + \chi_{eff,chiral}\cos^2\alpha\right]\sin\gamma + \left[\chi_{eff,sp}\sin^2\alpha + \chi_{eff,pp}\cos^2\alpha + \frac{1}{2}\chi_{eff,chiral}\sin 2\alpha\right]\cos\gamma. \tag{14.6}$$

Here the Fresnel factor $L_{ii}(\omega)$ terms were clearly defined by Zhuang and Wei et al. [96, 97], and α and γ are the polarization angles measured from the optical plane of the incident laser beam and the detection polarization angle in the outgoing signal beam, respectively. Equation (14.6) shows that χ_{eff} in any experimental configuration with linearly polarized light can be directly expressed as a linear combination of these four independently measurable χ_{eff} terms. It is clear that when $\chi_{eff,chiral} = 0$, the interface is achiral, Eq. (14.6) is reduced back to the expression for the achiral surface [16]. When the interface chirality is changed from one enantiomer to its mirror image, both χ_{xyz} and $\chi_{eff,chiral}$ change sign.

Since the values of the chiral terms are generlly two orders of magnitude smaller than the values of the achiral terms [5, 7, 9, 44, 86], the $\chi_{eff,chiral}$ term is much smaller than the $\chi_{eff,achiral}$ terms. Using Eq. (14.6), there are various ways to make the SHG-LD measurement on the chiral as well as achiral interface. The simplicity and accuracy of the SHG-LD technique for *in situ* quantitative measurement and analysis of the chiral interfaces is clear.

For the s-detection with the fixed $\gamma = 90^\circ$ and $\alpha = 0^\circ$, the $\chi_{eff,ps} = \chi_{eff,chiral}$ term is purely chiral. Because the pure chiral term is generally very small compared to the achiral terms, the pure chiral terms usually cannot be directly measured. However, fitting the $I^s_\alpha(2\omega)$ at $\gamma = 90^\circ$ [Eq. (14.7)] can quite accurately determine the relative sign and amplitude of the $\chi_{eff,sp}$ and the $\chi_{eff,chiral}$ terms. One has

$$I^s_\alpha(2\omega) \propto |\chi_{eff,45^\circ s}\sin 2\alpha + \chi_{eff,chiral}\cos^2\alpha|^2, \tag{14.7}$$

$$I^s_{45^\circ}(2\omega) \propto |\chi_{eff,45^\circ s} + \frac{1}{2}\chi_{eff,chiral}|^2,$$

$$I^s_{-45^\circ}(2\omega) \propto |-\chi_{eff,45^\circ s} + \frac{1}{2}\chi_{eff,chiral}|^2. \tag{14.8}$$

Whether $I^s_{45^\circ}(2\omega) > I^s_{-45^\circ}(2\omega)$ or $I^s_{45^\circ}(2\omega) < I^s_{-45^\circ}(2\omega)$ solely depends on the relative sign of the $\chi_{eff,45^\circ s}$ and the $\chi_{eff,chiral}$ terms. With the $I^s_{45^\circ}(2\omega)$ and $I^s_{-45^\circ}(2\omega)$ values, the degree of the chiral excess (DCE) can be readily calculated according to Eq. (14.1).

Even though Eq. (14.7) is simple and easy to use, it has not been explicitly written in the literature only until recently [17, 35, 58, 118], and there were recent cases where the s-detection SHG-LD data were observed but not properly interpreted [124], missing the opportunity for important applications.

Now let's look at the p-detection with the fixed $\gamma = 0^\circ$. One has

$$I^p_\alpha(2\omega) \propto \left|\chi_{eff,sp}\sin^2\alpha + \chi_{eff,pp}\cos^2\alpha + \frac{1}{2}\chi_{eff,chiral}\sin 2\alpha\right|^2, \tag{14.9}$$

$$I^{p}_{45^\circ}(2\omega) \propto \left|\frac{1}{2}[\chi_{eff,sp} + \chi_{eff,pp} + \chi_{eff,chiral}]\right|^2,$$
$$I^{p}_{-45^\circ}(2\omega) \propto \left|\frac{1}{2}[\chi_{eff,sp} + \chi_{eff,pp} - \chi_{eff,chiral}]\right|^2. \quad (14.10)$$

Here, it is difficult to fit the data with Eq. (14.9) to accurately determine the values of all three $\chi_{eff,sp}$, $\chi_{eff,pp}$, and the $\chi_{eff,chiral}$ terms, especially the much smaller $\chi_{eff,chiral}$ term [16]. This fact limits the accuracy and application of the SHG-LD p-detection in the chiral surface studies [16, 101].

14.2.3.2. Symmetry Relationships Between the χ_{ijk} and $\beta_{i'j'k'}$ Terms. Generally, χ_{ijk} is the ensemble orientational average of the second-order molecular polarizability tensor elements $\beta_{i'j'k'}$ in the molecular system [15, 95, 96].

$$\chi_{ijk} = N_s \sum_{i'j'k'=abc} \langle R_{ii'} R_{jj'} R_{kk'} \rangle \beta_{i'j'k'}, \quad (14.11)$$

where N_s is the molecule number density; the operator $\langle\rangle$ denotes the orientational ensemble average over the Euler rotation matrix transformation element $R_{\lambda\lambda'}$ from the molecular coordinate $\lambda'(a,b,c)$ to the laboratory coordinate $\lambda(x,y,z)$ [107], through the three Euler angles (θ,ψ,ϕ) [125]. The subscript (i,j,k) of the χ_{ijk} corresponds to the laboratory coordinate (x,y,z), and the subscript (i',j',k') of the $\beta_{i'j'k'}$ corresponds to the molecular coordinate (a,b,c). Here in Eq. (14.11), the convention to incorporate the local field factors into effective refractive indices, which are needed to calculate the $L_{zz}(\omega)$ or $L_{zz}(2\omega)$ in Eqs. (14.4) and (14.5), is followed [96].

For a rotationally isotropic chiral molecular interface or thin film, there are seven nonzero achiral χ_{ijk} tensor elements (i.e., $\chi_{zzz}, \chi_{zxx} = \chi_{zyy}, \chi_{yzy} = \chi_{yyz} = \chi_{xzx} = \chi_{xxz}$) and four chiral χ_{ijk} tensor elements (i.e., $\chi_{xyz} = \chi_{xzy} = -\chi_{yzx} = -\chi_{yxz}$) [16, 30, 126].

The connections between the macroscopic χ_{ijk} tensor elements and the microscopic $\beta_{i'j'k'}$ tensor elements as defined in Eq. (14.11) were derived in literature for both SHG [16, 36, 119] and SFG [15, 94, 127]. However, special attention needs to be paid to the correctness of the expressions [127] or the conventions of the Euler transformation used [36, 94]. As pointed out above, there are 12 different ways to perform the Euler angle transformation [125], and in each of them the definition of the Euler angles and the order of the rotational transformations are slightly different. These transformations are usually classified into the X convention [15, 16, 36], as adopted here, or the Y convention [94].

It is conceptually important to understand the simple symmetry-invariant relationships between the χ_{ijk} and $\beta_{i'j'k'}$ terms. The $\beta_{i'j'k'}$ tensor elements belonging to different molecular symmetry categories are listed and classified in Table 14.1. It should be noted that many of the $\beta_{i'j'k'}$ tensor elements with the similar symmetry properties are grouped together and are inseparable in the macroscopic tensor expressions. They are labeled as β_1, β_2, and β_3, as listed in Table 14.1. Using these classification, general expressions between χ_{ijk} and $\beta_{i'j'k'}$ can be reached for the achiral $C_{\infty v}$ and chiral C_∞ interfaces.

For a rotationally isotropic achiral or chiral molecular interface—that is, $C_{\infty v}$ or C_∞, respectively—the achiral terms generally satisfy

$$\frac{\chi_{zxx}}{\chi_{xzx}} = \frac{(\beta_1+\beta_2-2\beta_3)D - (\beta_1-\beta_2-2\beta_3)}{(\beta_1-\beta_2)D - (\beta_1-\beta_2-2\beta_3)},$$
$$\frac{\chi_{zzz}}{\chi_{xzx}} = \frac{2(\beta_2+2\beta_3)D + 2(\beta_1-\beta_2-2\beta_3)}{(\beta_1-\beta_2)D - (\beta_1-\beta_2-2\beta_3)}, \quad (14.12)$$

TABLE 14.1. Independent Nonvanishing elements of $\beta_{i'j'k'}$ for various molecular symmetries [16][a]

Symmetry Classes	Location of Mirror Plane	Nonvanishing Independent Tensor Elements	$\beta_1, \beta_2, \beta_3$ of $C_{\infty v}$ surface		
			β_1	β_2	β_3
C_1	No mirror	$(\beta_{ccc}, \beta_{caa}, \beta_{cbb})$ $\langle \beta_{aca} = \beta_{aac}, \beta_{bcb} = \beta_{bbc} \rangle$ $[\beta_{aaa}, \beta_{abb}, \beta_{bab} = \beta_{bba}]$ $[\beta_{bbb}, \beta_{baa}, \beta_{aba} = \beta_{aab}]$ $[\beta_{acc}, \beta_{cac} = \beta_{cca}]$ $[\beta_{bcc}, \beta_{cbc} = \beta_{ccb}]$ $\{\beta_{cab} = \beta_{cba}, \beta_{abc} = \beta_{acb}, \beta_{bac} = \beta_{bca}\}$	β_{ccc}	$\frac{\beta_{caa}+\beta_{cbb}}{2}$	$\frac{\beta_{aca}+\beta_{bcb}}{2}$
$C_{1v}(C_s)$	$\hat{x}\hat{z}$	$(\beta_{ccc}, \beta_{caa}, \beta_{cbb})$ $\langle \beta_{aca} = \beta_{aac}, \beta_{bcb} = \beta_{bbc} \rangle$ $[\beta_{aaa}, \beta_{abb}, \beta_{bab} = \beta_{bba}]$ $[\beta_{acc}, \beta_{cac} = \beta_{cca}]$	β_{ccc}	$\frac{\beta_{caa}+\beta_{cbb}}{2}$	$\frac{\beta_{aca}+\beta_{bcb}}{2}$
C_2	No mirror	$(\beta_{ccc}, \beta_{caa}, \beta_{cbb})$ $\langle \beta_{aca} = \beta_{aac}, \beta_{bcb} = \beta_{bbc} \rangle$ $\{\beta_{cab} = \beta_{cba}, \beta_{abc} = \beta_{acb}, \beta_{bac} = \beta_{bca}\}$	β_{ccc}	$\frac{\beta_{caa}+\beta_{cbb}}{2}$	$\frac{\beta_{aca}+\beta_{bcb}}{2}$
C_{2v}	$\hat{x}\hat{z}, \hat{y}\hat{z}$	$(\beta_{ccc}, \beta_{caa}, \beta_{cbb})$ $\langle \beta_{aca} = \beta_{aac}, \beta_{bcb} = \beta_{bbc} \rangle$	β_{ccc}	$\frac{\beta_{caa}+\beta_{cbb}}{2}$	$\frac{\beta_{aca}+\beta_{bcb}}{2}$
C_3	No mirror	$(\beta_{ccc}, \beta_{caa} = \beta_{cbb})$ $\langle \beta_{aca} = \beta_{aac} = \beta_{bcb} = \beta_{bbc} \rangle$ $[\beta_{abb} = \beta_{bab} = \beta_{bba} = -\beta_{aaa}]$ $[\beta_{aab} = \beta_{aba} = \beta_{baa} = -\beta_{bbb}]$ $\{\beta_{abc} = -\beta_{bac} = \beta_{acb} = -\beta_{bca}\}$	β_{ccc}	β_{caa}	β_{aca}
C_{3v}	$\hat{x}\hat{z}$	$(\beta_{ccc}, \beta_{caa} = \beta_{cbb})$ $\langle \beta_{aca} = \beta_{aac} = \beta_{bcb} = \beta_{bbc} \rangle$ $[\beta_{abb} = \beta_{bab} = \beta_{bba} = -\beta_{aaa}]$	β_{ccc}	β_{caa}	β_{aca}
C_4, C_6, C_∞	No mirror	$(\beta_{ccc}, \beta_{caa} = \beta_{cbb})$ $\langle \beta_{aca} = \beta_{aac} = \beta_{bcb} = \beta_{bbc} \rangle$ $\{\beta_{abc} = -\beta_{bac} = \beta_{acb} = -\beta_{bca}\}$	β_{ccc}	β_{caa}	β_{aca}
$C_{4v}, C_{6v}, C_{\infty v}$	$\hat{x}\hat{z}, \hat{y}\hat{z}$	$(\beta_{ccc}, \beta_{caa} = \beta_{cbb})$ $\langle \beta_{aca} = \beta_{aac} = \beta_{bcb} = \beta_{bbc} \rangle$	β_{ccc}	β_{caa}	β_{aca}

[a]Here the $\beta_{i'j'k'}$ tensors are classified according to their symmetry properties and whether they appear in the macroscopic χ_{ijk} terms when the interface is with $C_{\infty v}$ symmetry. The terms in ( ) are symmetric terms that appear in the nonvanishing macroscopic susceptibility tensor terms (χ_{ijk}), terms in $\langle\rangle$ are asymmetric terms that appear in χ_{ijk} terms, terms in [ ] are asymmetric terms that do not appear in the χ_{ijk} terms, and terms in {} are chiral terms only for chiral molecules.

Source: W. K. Zhang, H. F. Wang, D. S. Zheng, *Phys. Chem. Chem. Phys* **2006**, *8*, 4041–4052. Reproduced with permission of the PCCP Owner Societies [16].

For the four nonzero chiral elements [14, 126]—that is, $\chi_{xyz} = \chi_{xzy} = -\chi_{yxz} = -\chi_{yzx}$ of the surface of chiral liquids—the molecules need to be chiral (C_1, C_2, C_3, C_4, C_6, and C_∞ as in Table 14.1), which is the case of the so-called "intrinsic chirality" [8], one has [16]

$$\begin{aligned}\chi_{xyz} &= \chi_{xzy} = -\chi_{yxz} = -\chi_{yzx} \\ &= \frac{1}{2}N_s[\langle\cos^2\theta\rangle(\beta_{abc} - \beta_{bac}) \\ &\quad -\frac{1}{2}\langle\sin^2\theta\rangle(\beta_{bca} - \beta_{acb})].\end{aligned} \tag{14.13}$$

If the molecule is achiral, macroscopic chirality arises only when the molecule cannot rotate freely around its axis; that is, the Euler angle ψ (the twist angle) cannot be integrated or ensemble-averaged [94]. This is the case of the so-called "orientational chirality" or 'structural chirality' [8]. One has [16, 36, 94]

$$\begin{aligned}\chi_{xyz} &= \chi_{xzy} = -\chi_{yxz} = -\chi_{yzx} \\ &= \frac{1}{2}N_s[\langle \sin^2\theta \sin\psi \cos\psi\rangle(\beta_{aca} - \beta_{bcb} - \beta_{caa} + \beta_{cbb}) \\ &\quad + \langle \sin\theta \cos\theta \sin\psi\rangle(\beta_{abb} - \beta_{acc} - \beta_{bab} + \beta_{cac}) \\ &\quad + \langle \sin\theta \cos\theta \cos\psi\rangle(-\beta_{aba} + \beta_{baa} - \beta_{bcc} + \beta_{cbc})]. \end{aligned} \tag{14.14}$$

When both "intrinsic chirality" and "orientational chirality" exist, whether the observed surface chirality is from the "intrinsic chirality" or the "orientational chirality" is an issue that needs to be discussed [8]. In general, both the chiral and achiral tensors in the molecular microscopic polarizability $\beta_{i'j'k}$ are to be present in the macroscopic susceptibility tensors through Eq. (14.11) [8, 36, 94, 127]. However, at the molecular level, the values of the chiral $\beta_{i'j'k'}$ tensor elements are, in general, two orders of magnitude smaller than the values of the achiral terms [5, 7, 9, 44, 86]. Therefore, it is expected that in such cases, the "orientational chirality" contribution shall dominate over the "intrinsic chirality" contribution in the macroscopic chiral χ_{ijk} tensors, as going through the ensemble average as in Eq. (14.11). This fact shall make the SHG-LD measurement of the "intrinsic chirality" difficult. It also raises questions on the interpretations in the early SHG-CD studies on the mechanism of the significant chiral response [4, 93]. However, this suggests that in the SHG-LD or SHG-CD measurement of the protein or DNA helix or β-sheet 3-D structures, only the "orientational chirality" from the achiral molecular terms need to be considered, and the more complex "intrinsic chirality" contributions can be neglected because they are much smaller. Equation (14.14) is therefore also a valid approximation for the case when the molecule is chiral.

The discussion here on the χ_{ijk} and $\beta_{i'j'k'}$ tensor elements are equally valid for the SHG and SFG. The only difference is that in SFG, the three indices in the χ_{ijk} denote the polarization vector of optical electric field directions for the sum frequency, the visible, and the infrared, respectively.

14.2.4. Theory of SFG-LD

Chiral SFG-VS signal from monolayer or membrane interfaces was only obtained recently in specific polarization combinations from interface or membrane [59, 83, 87, 99, 128]. All these measurements used the chiral only polarization combinations. Since the values of the chiral terms are, in general, two orders of magnitude smaller than the values of the achiral terms [5, 7, 9, 44, 86, 87], the $\chi_{eff,chiral}$ term is generally much smaller than the $\chi_{eff,\ achiral}$ terms, and the chiral-term-only measurement is usually subject to large errors. Similar to the SHG-LD, SFG-LD measurement can also be carried out. Since the chiral SFG-VS is allowed and dominating in the chiral liquid, the first SFG-LD experiment for the bulk chiral liquid was carried out by Shen and co-workers for the (*S*)- and (*R*)-limonene bulk liquids in 2000 [33]. The first SFG-LD measurement of the chiral liquid surface, where the achiral signal is dominating, was reported in 2009 [120].

With SHG-LD formulation established, the case for the SFG-LD from the linearly polarized incident lights is straightforward. However, unlike SHG, where the frequencies

of two incoming optical fields are always identical, in SFG, each of the three optical fields are different and unexchangeable. The consequence is that in order to make the SFG-LD measurement as accurately as the *s*-detection SHG-LD for chiral surface measurement, the polarizations, of the sum frequency and the visible fields need to be fixed with a certain relationship, and this shall make the SFG-LD with similar accuracy as the *s*-detection SHG-LD. This technique is called the twin polarization angle (TPA) method.

14.2.4.1. SFG-LD for Chiral Surface. Sum frequency generation (SFG) is the second-order nonlinear process when two photons at the frequency ω_1 and ω_2 simultaneously interact with a molecule to generate a photon with the frequency at the sum of the two frequencies, that is, $\omega = \omega_1 + \omega_2$. In the SFG-VS, ω_1 is usually fixed at a visible light frequency, and the SFG signal at ω is recorded varying ω_2 in the infrared region. When ω_2 is in resonance with the vibrational frequency of the interfacial molecules, the SFG signal is enhanced to give the spectroscopic response of the interfacial molecular vibrations [15, 96]. When ω_1 or ω is also in resonance with or close to the electronic resonances, the SFG process is called double resonance SFG (DR-SFG), and the SFG signal can be greatly enhanced [87, 129]. However, because the DR-SFG involves processes in the electronically excited states, quantitative analysis and interpretation of the of the DR-SFG signal is more complicated [130]. The discussion in this chapter is therefore limited to the non-DR-SFG cases.

The schematics representations of the surface SFG is in Figure 14.1.

The intensity of the SFG signal ($I(\omega)$) from a surface is proportional to the intensities of the incident visible and infrared light beams ($I(\omega_1)$ and $I(\omega_2)$, respectively), as well as the square of the effective susceptibility χ_{eff} of the interface [15, 96].

$$I(\omega) = \frac{8\pi^3\omega^2 sec^2\beta}{c^3 n_1(\omega)n_1(\omega_1)n_1(\omega_2)}|\chi_{eff}|^2 I(\omega_1)I(\omega_2), \tag{14.15}$$

$$\chi_{eff} = [\hat{\mathbf{e}}(\omega)\cdot\mathbf{L}(\omega)]\cdot\chi_{ijk} : [\mathbf{L}(\omega_1)\cdot\hat{\mathbf{e}}(\omega_1)][\mathbf{L}(\omega_2)\cdot\hat{\mathbf{e}}(\omega_2)], \tag{14.16}$$

where c is the speed of light in the vacuum; ω, ω_1, and ω_2 are the frequencies of the SFG signal, visible, and IR laser beams, respectively; $n_j(\omega_i)$ is the refractive index of bulk medium j at frequency ω_i; β_i is the angle of incidence or reflection from interface normal of the ith laser beam; $I(\omega)$ and $I(\omega_i)$ are the intensities of the SFG signal and the incident laser beams, respectively; χ_{ijk} represents the macroscopic second-order nonlinear susceptibility tensor elements of the interface; and the $\hat{\mathbf{e}}(\omega_i)$ and the $\mathbf{L}(\omega_i)$ are the unit polarization vector and the Fresnel factor at frequency ω_i, respectively.

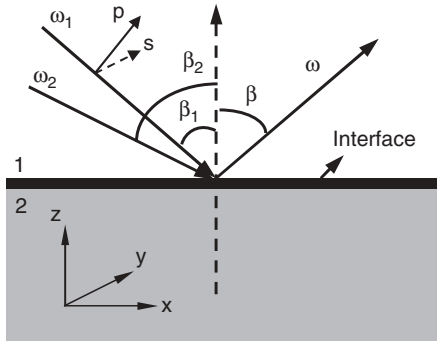

Figure 14.1. Schematic representation of reflection-geometry SFG measurement [105]. The laser light at frequency ω_i is incident on the interface at angle β_i. The input polarization angle α_i is clockwise from the *p*-polarization direction. The frequency and angles of the SFG signal beam is denoted with the subscript *s*. The dielectric constants of medium 1, medium 2, and interfacial film at frequency ω_i are $\epsilon_1(\omega_i)$, $\epsilon_2(\omega_i)$, and $\epsilon'(\omega_i)$, respectively.

For an azimuthally isotropic interface formed by the chiral molecules (symmetry C_∞), there are seven nonvanishing macroscopic susceptibility tensor elements χ_{ijk}, that is, $\chi_{xxz} = \chi_{yyz}, \chi_{xzx} = \chi_{yzy}, \chi_{zxx} = \chi_{zyy}$, and χ_{zzz}; and there are six nonvanishing chiral tensor elements, that is, $\chi_{xyz}, \chi_{yxz}, \chi_{zxy}, \chi_{zyx}, \chi_{xzy}$, and χ_{yzx} [5, 16, 94]. One has

$$\begin{aligned}\chi_{eff} &= [\sin\Omega\cos\Omega_1\chi_{sps} + \cos\Omega\sin\Omega_1\chi_{pss} \\ &\quad + \cos\Omega\cos\Omega_1\chi_{pps}]\sin\Omega_2 \\ &\quad + [\sin\Omega\sin\Omega_1\chi_{ssp} + \sin\Omega\cos\Omega_1\chi_{spp} \\ &\quad + \cos\Omega\sin\Omega_1\chi_{psp} + \cos\Omega\cos\Omega_1\chi_{ppp}]\cos\Omega_2 \end{aligned} \tag{14.17}$$

with the achiral responses in ssp, sps, pss, and ppp polarization combinations as

$$\begin{aligned}\chi_{ssp} &= L_{yy}(\omega)L_{yy}(\omega_1)L_{zz}(\omega_2)\sin\beta_2\chi_{yyz}, \\ \chi_{sps} &= L_{yy}(\omega)L_{zz}(\omega_1)L_{yy}(\omega_2)\sin\beta_1\chi_{yzy}, \\ \chi_{pss} &= L_{zz}(\omega)L_{yy}(\omega_1)L_{yy}(\omega_2)\sin\beta\chi_{zyy}, \\ \chi_{ppp} &= -L_{xx}(\omega)L_{xx}(\omega_1)L_{zz}(\omega_2)\cos\beta\cos\beta_1\sin\beta_2\chi_{xxz} \\ &\quad - L_{xx}(\omega)L_{zz}(\omega_1)L_{xx}(\omega_2)\cos\beta\sin\beta_1\cos\beta_2\chi_{xzx} \\ &\quad + L_{zz}(\omega)L_{xx}(\omega_1)L_{xx}(\omega_2)\sin\beta\cos\beta_1\cos\beta_2\chi_{zxx} \\ &\quad + L_{zz}(\omega)L_{zz}(\omega_1)L_{zz}(\omega_2)\sin\beta\sin\beta_1\sin\beta_2\chi_{zzz}, \end{aligned} \tag{14.18}$$

and the chiral SFG responses for polarization combinations of pps, spp, and psp as χ_{pps}, χ_{spp}, and χ_{psp}, respectively.

$$\begin{aligned}\chi_{spp} &= L_{yy}(\omega)L_{zz}(\omega_1)L_{xx}(\omega_2)\sin\beta_1\cos\beta_2\chi_{yzx} \\ &\quad + L_{yy}(\omega)L_{xx}(\omega_1)L_{zz}(\omega_2)\cos\beta_1\sin\beta_2\chi_{yxz}, \\ \chi_{pps} &= L_{zz}(\omega)L_{xx}(\omega_1)L_{yy}(\omega_2)\sin\beta\cos\beta_1\chi_{zxy} \\ &\quad - L_{xx}(\omega)L_{zz}(\omega_1)L_{yy}(\omega_2)\cos\beta\sin\beta_1\chi_{xzy}, \\ \chi_{psp} &= L_{zz}(\omega)L_{yy}(\omega_1)L_{xx}(\omega_2)\sin\beta\cos\beta_2\chi_{zyx} \\ &\quad - L_{xx}(\omega)L_{yy}(\omega_1)L_{zz}(\omega_2)\cos\beta\sin\beta_2\chi_{xyz}. \end{aligned} \tag{14.19}$$

With the laboratory coordinates defined such that z is along the surface normal, and the xy plane is the plane of interface, $L_{ii}(i = x, y, z)$ is the Fresnel coefficient determined by the refractive indices of the two bulk phases and the interface layer, as well as by the incident and reflected angles [15, 96, 97]. The p polarization is within the xz plane, and the s polarization is perpendicular to the xz plane. The polarization combination ssp indicates that the SF signal, the visible beam, and the IR beam are in s, s, and p polarization, respectively, and so on.

These terms are grouped with the polarization angle of the infrared optical field (Ω_2) because in the SFG experiment usually the detection is performed with the IR polarization fixed either at the $s(\Omega_2 = 90^\circ)$ or $p(\Omega_2 = 0^\circ)$ polarizations. Since the SFG-VS intensities can be normalized to those obtained for z-cut quartz crystals, the absolute values for the three chiral elements $\chi_{pps}, \chi_{spp}, \chi_{psp}$ and the four nonchiral elements $\chi_{sps}, \chi_{pss}, \chi_{ssp}, \chi_{ppp}$ can be obtained with these experimental measurements.

The connection between the macroscopic χ_{ijk} tensors and the microscopic molecular polarizability $\beta_{i'j'k'}$ tensors follows the same discussions in the Section 14.2.3.2. Detailed expressions can be found in the literature, and attention needs to be paid to the convention used for the Euler transformation [15, 36, 94, 96, 97, 127].

In the single vibrationally resonant SFG-VS, the IR frequency is near resonance to molecular vibrational transition, and the second-order molecular polarizability is

$$\beta = \beta_{NR} + \sum_q \frac{\beta^q}{\omega_{IR} - \omega_q + i\Gamma_q} \tag{14.20}$$

and the tensor elements of β^q is related to the IR and Raman properties of the vibrational mode [97],

$$\beta^q_{i'j'k'} = -\frac{1}{2\epsilon_0\omega_q}\frac{\partial\alpha_{i'j'}}{\partial Q_q}\frac{\partial\mu_{k'}}{\partial Q_q}. \tag{14.21}$$

These two equations define the vibrational spectral response as observed in the SFG-VS from the interfaces. In Eq. (14.20), the first term β_{NR} represents nonresonant contributions; β^q, ω_q, and Γ_q are the sum frequency strength factor tensor, resonant frequency, and damping constant of the qth molecular vibrational mode, respectively [131–134]. In Eq. (14.21), $\partial\alpha_{i'j'}/\partial Q_q = \alpha'_{i'j'}$ and $\partial\mu_{k'}/\partial Q_q = \mu'_{k'}$ are partial derivatives, respectively, of the electric dipole polarizability tensor and electric dipole moment with respect to the qth vibrational mode; and Q_q is the normal coordinate of the same mode [97]. Therefore, any nonzero sum frequency vibrational mode has to be both IR- and Raman-active. This is the transition selection rule for SFG-VS.

The experimentally measured SFG-VS intensity can be directly related to the microscopic molecular polarizability tensor $\beta^q_{i'j'k'}$ through orientational average. Detailed treatment and consideration of the issues in the quantitative measurement and analysis in the SFG-VS of the achiral molecular interfaces have been well established [15, 17, 94, 96, 97]. The key idea in the quantitative analysis is to systematically employ the polarization dependence and experimental configuration dependence in the coherent SFG-VS spectra to elucidate (a) the vibrational spectral details and (b) the orientation and conformation as well as their changes of the interfacial molecular groups. One important and very useful result from these analysis is the development of a set of polarization selection rules that can be used for vibrational and electronic spectral assignment [15, 102–104]. These analyses have led to advances of SFG-VS as spectroscopic tool for the interface studies.

14.2.4.2. Chiral SFG Selectively Probes Structural Chirality. Unlike SHG, one important fact for the chiral SFG is that its chiral terms are not surface-selective for surface of chiral liquids [3]. However, the achiral terms shall remain surface-selective. This makes the surface SFG a good probe for the chirality of the bulk chiral liquid.

Since the values of the chiral terms are, in general, two orders of magnitude smaller than the values of the achiral terms [5, 7, 9, 44, 86, 87], the $\chi_{eff,chiral}$ term is much smaller than the $\chi_{eff,achiral}$ terms. Therefore, it is known that measurement of the chiral SFG signal from a molecular monolayer is extremely difficult. Shen and co-workers used the double resonance enhancement effect to demonstrate the first observation of the chiral SFG signal from the molecular monolayer [87], and they also questioned the likeliness and validity of the observation of the chiral only SFG-VS spectra of a protein monolayer without such enhancement effect [9, 128]. However, recent works do show that such

chiral signal can arise from the 3-D protein structures, even though the signal is indeed small [83, 85].

The ability for SHG and SFG to separate the "orientational chirality" (or "structural chirality") and "intrinsic chirality" can have great implications in protein and DNA structure studies. In the linear VCD, ECD, and ROA spectroscopy of proteins, the spectrum is usually dominated by the "intrinsic chirality" of the chromophore or the amino acid units [88]. Still, the sensitivity of far-UV protein CD spectra to protein secondary structure is widely used to determine the secondary structure and composition of protein [89–92]. In comparison, surface SHG and SFG are not only submonolayer-sensitive, but also selective to the "structural chirality." With double resonance SHG and SFG, protein chromophores can also be selectively probed [87, 129]. In addition, all the polarization dependence and tensorial elements can provide much more information about the structural information of the proteins. A good example was recently published by Yan and co-workers using SFG to probe the misfolding of human islet amyloid polypeptide at the air–water interface [83].

14.2.4.3. Experimental Methods for SFG-LD Determination of the Chiral and Achiral Elements. It was shown recently [120] that (a) direct measurement of the pure chiral elements in SFG-LD is not only subject to significant experimental errors, but also incapable of obtaining the sign or phase information of the χ_{chiral} terms; (b) single polarization angle method in SFG-VS can obtain the sign or relative phase of the χ_{chiral} and $\chi_{achiral}$ terms, but it is subject to significant experimental errors in the determination of the smaller chiral terms; and (c) twin polarization angle (TPA) method in SFG-LD can obtain both the sign or relative phase and the most accurate values for the χ_{chiral} and $\chi_{achiral}$ terms.

Here the unique accuracy and sensitivity with the so-called twin polarization angle (TPA) is discussed [120]. Discussions on the pure chiral term and single polarization method can be found in the literature [120].

In the SHG-LD s-polarization detection, the unique accuracy comes from the $\cos^2\alpha$ and $\sin 2\alpha$ functions associated with the small chiral and much larger achiral terms, respectively, as shown in Eq. (14.7). Here α is the polarization angle of the input fundamental beam in the SHG measurement. Because the achiral term is much larger than the chiral term, the maximum intensity is going to be around $\alpha = \pm 45^\circ$, and the interference between the chiral and achiral terms is going to be maximized around $\alpha = \pm 45^\circ$. This not only allows direct recognition of the surface chirality by looking at the different SHG intensities at the $\alpha = 45^\circ$ and $\alpha = -45^\circ$, but also allows accurate determination of the DCE value.

Similarly, one simple way to make the SFG-VS-LD similar to the SHG-LD is to have $\Omega_2 = 90^\circ$ and let $\Omega_1 = \pm\Omega$ in Eq. (14.17). Thus, one has

$$I_{\pm}^{S}(\Omega) = |\chi_{eff}(\Omega)|^2 = |\chi_{pps}\cos^2\Omega + \frac{1}{2}(\chi_{sps} \pm \chi_{pss})\sin 2\Omega|^2. \tag{14.22}$$

Another option is to have $\Omega_2 = 0^\circ$ and let $\Omega_1 \pm \Omega = 90^\circ$. One has

$$I_{\pm}^{P}(\Omega) = |\chi_{eff}(\Omega)|^2 = |\chi_{psp}\cos^2\Omega \pm \chi_{spp}\sin^2\Omega + \frac{1}{2}(\chi_{ssp} \pm \chi_{ppp})\sin 2\Omega|^2. \tag{14.23}$$

The reason not to have the two cases of $\Omega_2 = 90^\circ$ with $\Omega_1 \pm \Omega = 90^\circ$ and $\Omega_2 = 0^\circ$ with $\Omega_1 = \pm\Omega$ is that in these two cases the $\cos^2\Omega$ and $\sin^2\Omega$ terms are associated

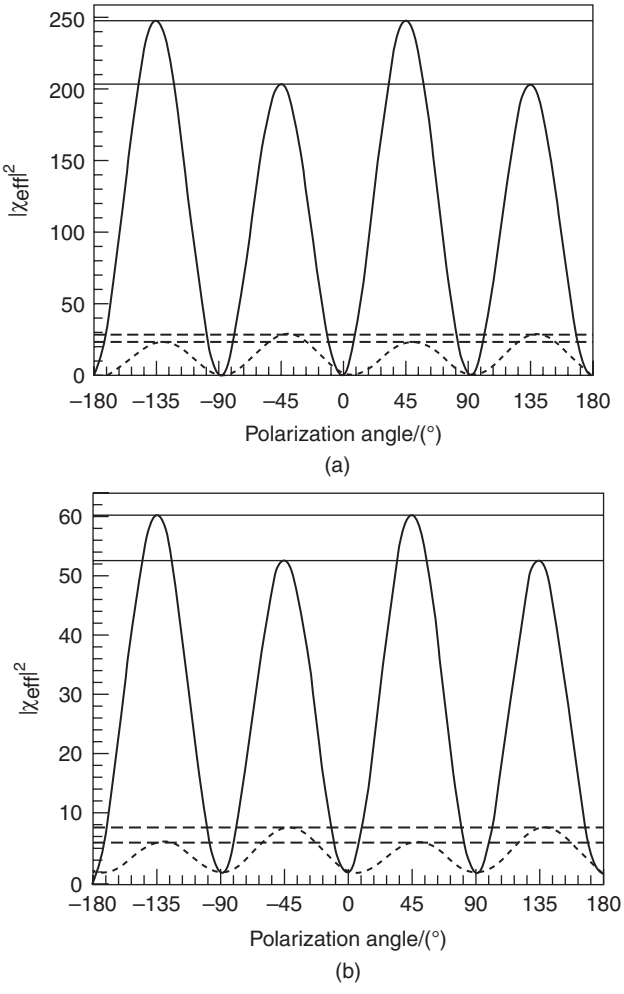

Figure 14.2. TPA simulation results with $\chi_{pps} = 0.5$, $\chi_{spp} = 1$, $\chi_{psp} = 0.5$, $\chi_{sps} = 5$, $\chi_{pss} = 10$, $\chi_{ssp} = 10$, $\chi_{ppp} = 20$. (a) Solid curve, $I_+ = I_{\Omega,90-\Omega,0^\circ}$; dashed curve, $I_- = I_{\Omega,90+\Omega,0^\circ}$. (b) Solid curve, $I_+ = I_{\Omega,\Omega,90^\circ}$; dashed curve, $I_- = I_{\Omega,-\Omega,90^\circ}$. The horizontal lines indicates the different intensities at the peaks—that is, when $\Omega = 45^\circ$ and $\Omega = -45^\circ$, and so on. These differences are the explicit indication of the chiral contribution. (From F. Wei, Y. Y. Xu, Y. Guo, S. L. Liu, H. F. Wang, *Chin. J. Chem. Phys.* **2009**, *22*, 592–600. Copyright 2009 Chinese Physical Society [120]. Reproduced with permission.)

with the larger achiral susceptibility terms, while the $\sin 2\Omega$ term is associated with the much smaller chiral susceptibility terms. In these two cases, the surface chirality is not going to be explicit in the measurement and the DCE values shall be subject to large experimental errors.

Figure 14.2 illustrates the simulation results for $I_{\pm}^{P}(\Omega)$ and $I_{\pm}^{P}(\Omega)$ with the following values for the chiral and achiral susceptibility tensors: $\chi_{pps} = 0.5$, $\chi_{spp} = 1$, $\chi_{psp} = 0.5$, $\chi_{sps} = 5$, $\chi_{pss} = 10$, $\chi_{ssp} = 10$, $\chi_{ppp} = 20$. The choosing of these values is rather arbitrary except that it is used to make the chiral susceptibility terms much smaller than the achiral susceptibility terms. Also, the choice of the values is also in general agreement with the fact that the ssp and ppp intensity in the SFG-VS measurement are usually larger than the sps and pss terms.

It is clear that the $I_{+}^{P}(\Omega)$ and $I_{+}^{S}(\Omega)$ curves have larger SFG intensity and also larger chiral modulations at the peaks around $\Omega = \pm 45^\circ$. Therefore, the relative magnitude of the SFG peak signal strengths for the $+$ and $-$ detection curves can directly tell whether the ssp/ppp pair or the sps/pss pair have the same or opposite signs.

It is to be noted that in the above discussion all the susceptibility tensors are treated as real numbers. This is generally valid when the frequency factor is the common denominator for the different χ_{eff} terms in Eq. (14.20).

14.3. APPLICATION OF SHG-LD AND SFG-LD

Here two examples are provided to illustrate the applications of quantitative measurement and analysis in SHG-LD and SFG-LD. In one example, SHG-LD is applied to measure the chirality and chiral formation mechanism of a chiral Langmuir monolayer formed by achiral molecules. In another example, SFG-LD is applied to measure the chiral vibrational spectra of the pure chiral liquid surfaces.

14.3.1. Chirality of Langmuir Molecular Assembly Measured with SHG-LD

Quantitative SHG-LD *in situ* measurement of the chiral Langmuir monolayer formed by the achiral long-chain molecule 5-octadecyloxy-2-(2-pyridylazo)phenol (PARC18, Figure 14.3) at the air–water interface not only quantitatively characterized its chirality, but also provided an answer for its chiral structure and mechanism [101].

Previously, no chirality has been observed for the PARC18 Langmuir–Blodgett (LB) multilayer film [135], even though the LB multilayer film of the achiral molecules with similar structures—that is, the 5-(octadecyloxy)-2-(2-(thiazolylazo)phenol (TARC18)—exhibits chirality, which was probed with UV–vis CD spectra of the LB multilayer [136, 137].

In recent years, various studies have revealed that several achiral molecules formed macroscopically chiral Langmuir–Blodgett (LB) or Langmuir–Schaefer (LS) films with the assemblies of achiral molecules [136–152]. It has been believed that in these cases each constituent molecule in the macroscopically chiral multilayer films remains achiral as a single entity, but spontaneous symmetry breaking in the close-packed monolayer and/or the assembly during the monolayer compression leads to the macroscopic surface chirality, in which two enantiomers coexist with only one of the enantiomers being predominant [136, 137, 142, 143, 153].

The importance of this subject is obvious [154–156]. However, the mechanism of this formation is not clear. Previous experiments with scanning microscopy or UV–visible CD spectra were all conducted *ex situ*—that is, on the transferred Langmuir–Blodgett (LB) multilayers [136, 137]—instead of *in situ* spectroscopic measurement of the Langmuir monolayer as it forms [157]. It was believed that the surface chirality was formed through the compression-induced mechanism. That is, when the monolayer is not fully packed, there should be no chiral structure; while when the monolayer is fully packed, the chirality should stay the same under further compression. Such mechanism was supported by flawed SHG-LD experimental results and interpretation [121, 160]. However, careful *in situ* SHG-LD measurement revealed that such surface chirality was not only

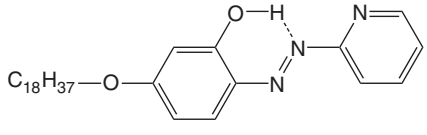

Figure 14.3. The stable configuration of the PARC18 molecule as optimized with the DFT calculation [101].

inhomogeneous in the fully packed monolayer, but also spontaneously formed when the monolayer is not fully packed [101, 121].

The SHG-LD experimental setup is standard [100, 119, 158]. A broadband tunable (700–1100 nm) mode-locked femtosecond Ti:sapphire laser is now widely available and its high-repetition rate (usually ~80 MHz) and short pulse width (<100 fs) make it suitable for detection of the weak second-harmonic signals. Typically with the laser power at about 200 mW, even the nonresonant SHG signal from the neat air–water interface, which usually generates the least SHG signal than any other interface, can reach >100 counts per second, with the typical dark noise level of less than 1 count per second. In comparison, the SHG signal from the PARC18 monolayer surface is typically a few thousand counts per second. Therefore, the SHG-LD experiment is simple and can be easily realized.

Comparison of the SHG-LD data (Figure 14.4) in both the *s* detection and *p* detection of the chiral PARC18 and the achiral 4′-*n*-octyl-4-cyanobiphenyl (8CB) Langmuir monolayer is revealing [101]. All data have excellent signal/noise ratio and can be described with Eqs. (14.7) and (14.9). In the *s*-detection curve of the achiral 8CB monolayer, the four peaks are with identical intensity; while in the *s*-detection curve of the chiral PARC18 monolayer, the four peaks are with two different intensities. According to Eq. (14.7), this is the result of the existence of the nonzero $\chi_{eff,chiral}$ term in the PARC18 monolayer. From the calculated DCE value of the PARC18 and 8CB data as in Figure 14.4, it is obvious that the *s* detection resulted in accurate DCE values for both monolayers, while the uncertainty of the DCE value from the *p* detection is much higher. One can easily conclude that the *s* detection is not only a straightforward way to visualize the existence of the surface chirality, but also an accurate way to measure the small changes in the surface chirality. Detailed analysis and simulation using Eqs. (14.7) and (14.9) well demonstrated the above conclusions [101].

The *s*-detection SHG-LD data in Figure 14.5 and calculated DCE values in Figure 14.6 of PARC18 Langmuir monolayer at different surface densities indicate that the chirality in the PARC18 Langmuir monolayer is not only inhomogeneous, but also spontaneously formed. In Figure 14.6, nonzero DCE values were obtained when the monolayer is still in the condensed-phase/gas-phase coexistence region. These clearly indicate that the PARC18 monolayer possesses chirality well before it became a compact monolayer. It is to be noted that only with the accuracy provided by the SHG-LD *s* detection, such phenomena were able to be nailed down.

The spatial chiral inhomogeneity of the PARC18 monolayer at different positions was further demonstrated with the SHG-LD data in Figure 14.7. Fitting the data with Eq. (14.7) resulted in the achiral $\chi_{45^\circ s}$ values and the chiral χ_{chiral}, as well as the DCE values as plotted in Figure 14.8. It clearly indicated that the chiral inhomogeneity is indeed from the chiral term, which is mainly determined by the twist angle, instead of the achiral term, which is mainly determined by the tilt angle. Quantitative analysis of these data also concluded that the chiral signal is not from the so-called "in-plane anisotropy" [159]. The statistical criterion for the "in-plane anisotropy" using SHG-LD *s* detection is [101],

$$\frac{\delta_{\chi_{45^\circ s}}}{\delta_{\chi_{chiral}}} = \left| \frac{1}{2\cos\beta} \right|. \tag{14.24}$$

Here $\delta_{\chi_{45^\circ s}}$ and $\delta_{\chi_{chiral}}$ are the statistical variation of the achiral and chiral terms in the random position in the monolayer. β is the incident angle of the fundamental beam from

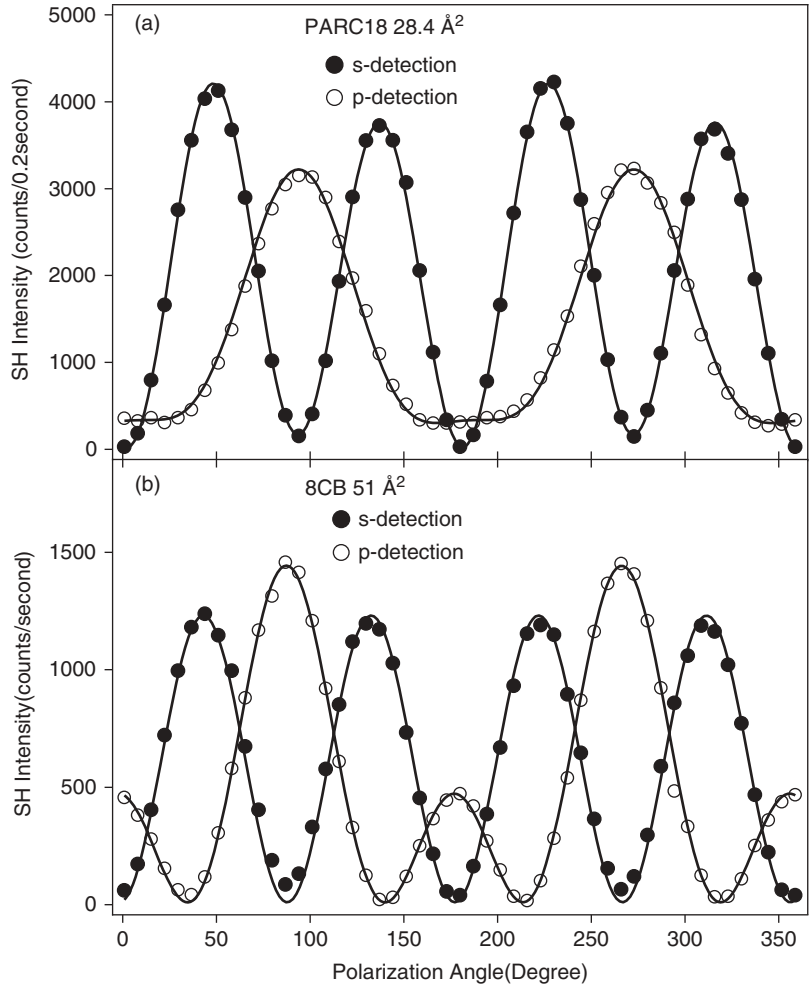

Figure 14.4. Comparison of the *s*- and *p*-polarization detection of the 400-nm SHG signal from the PARC18 Langmuir monolayer and the 8CB Langmuir monolayer at the air–water interface against the input linear polarization of the fundamental light at 800 nm. The laser power for the PARC18 experiment was 200 mW, and it was 600 mW for the 8CB. The solid lines are the fitting results using Eqs. (14.7) and (14.9), respectively. For the PARC18, $I_{+135^\circ} < I_{+45^\circ}$ in the *s*-detection curve and thus $\Delta I/I = 22.1\% \pm 1.8\%$, while for the 8CB, $I_{+135^\circ} \approx I_{+45^\circ}$ in the *s*-detection curve and $\Delta I/I = -1.8\% \pm 2.9\%$, indicating that the PARC18 monolayer is chiral and the 8CB Langmuir monolayer is achiral. The DCE values from the *p*-detection data are $\Delta I/I = -17.3\% \pm 7.5\%$ for PARC18 and $\Delta I/I = 3.2\% \pm 12.5\%$, respectively. The similar pattern for the two *p*-detection curves for the PARC18 and 8CB is owing to their similar molecular symmetry. It is clear that comparison of the SH intensities at the $+45^\circ$ ($+225^\circ$) and $+135^\circ$ ($+315^\circ$) in the *s* detection is a straightforward way to determine whether the surface is chiral or not. (From Y. Y. Xu, Y. Rao, D. S. Zheng, Y. Guo, M. H. Liu, H. F. Wang, *J. Phys. Chem. C* **2009**, *113*, 4088–4098. Copyright 2009 American Chemical Society [101]. Reproduced with permission.)

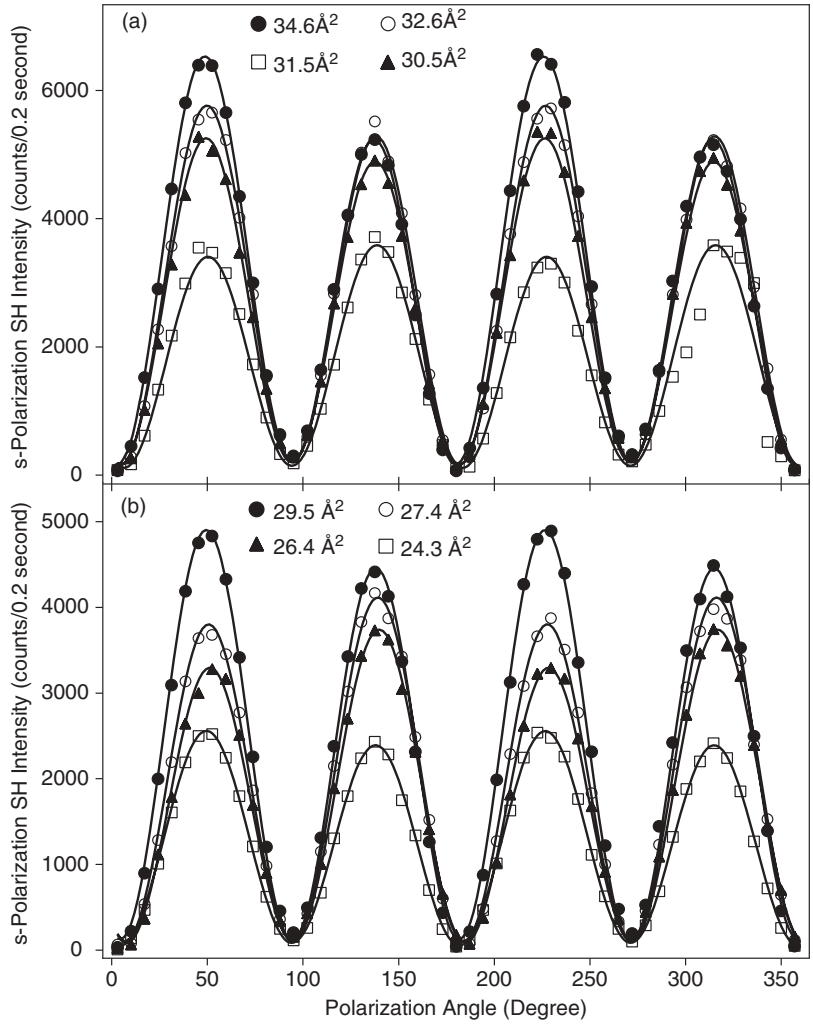

Figure 14.5. Results of the *s*-polarization SHG measurements at 380 nm of the PARC18 Langmuir monolayer at different surface densities at the air–water interface. All the curves were recorded during one consecutive film compression process. It is clear that the overall chirality of the monolayer changes not only with the amplitude, but also with the sign at different surface densities. (From Y. Y. Xu, Y. Rao, D. S. Zheng, Y. Guo, M. H. Liu, H. F. Wang, *J. Phys. Chem. C* **2009**, *113*, 4088–4098. Copyright 2009 American Chemical Society [101]. Reproduced with permission.)

the interface normal, which is usually 70°. Therefore, if the monolayer is with the so-called "in-plane anisotropy," instead of the true chiral structure, the ratio is 1.46. The measured ratio $\frac{\delta_{\chi_{45^\circ s}}}{\delta_{\chi_{chiral}}} = 0.2 - 0.5$. Further analysis of this ratio using the χ_{xyz} tensors in Eq. (14.14) can quantitatively determine the average chiral twist angle in the PARC18 molecular assembly.

The $\chi_{45^\circ s}$ value is only about 10 times of the χ_{chiral}, as shown in Figure 14.8. This is consistent with the analysis in Section 14.2.3.2 that the macroscopic surface chirality for the PARC18 monolayer is "orientational chirality" instead of the "intrinsic chirality."

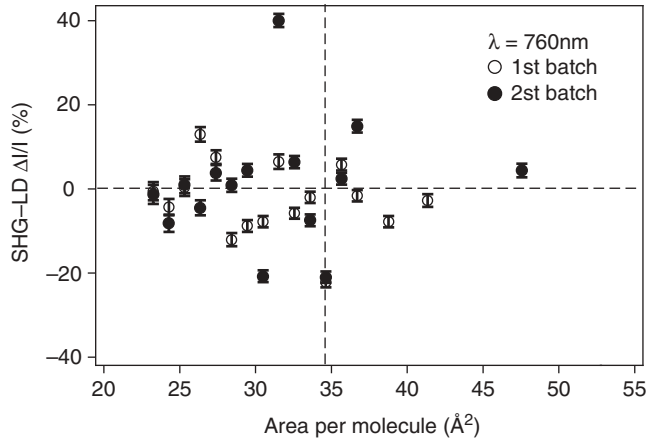

Figure 14.6. SHG-LD values measured at 380 nm of the PARC18 Langmuir monolayer at different surface densities in two batches of film upon compression. The dotted line is $\Delta I/I = 0$, indicating the achiral state. The overall chirality of the monolayer switches sign randomly at different surface density, and it is different from batch to batch. The vertical dashed line is drawn at 34.5-Å^2 surface density, indicating the separation of the liquid condensed phase and the gas–liquid condensed coexistence phase in the PARC18 surface phase diagram. The monolayer is clearly chiral even in the coexistence region before the whole monolayer entered the liquid condensed phase around the surface density of 34.5 Å^2, indicating that the monolayer chirality is not compression induced. (From Y. Y. Xu, Y. Rao, D. S. Zheng, Y. Guo, M. H. Liu, H. F. Wang, *J. Phys. Chem. C* **2009**, *113*, 4088–4098. Copyright 2009 American Chemical Society [101]. Reproduced with permission.)

In addition to the PARC18 Langmuir monolayer studies, SHG-LD measurement and quantitative analysis of the 4-(4-(dihexadecylamino)styryl)-*N*-methylpyridinium iodide (DiA) and 4-(4-(*N*-methyl,*N*-octadecyl-amino)styryl)-*N*-methylpyridinium iodide (HTC) chiral Langmuir monolayers also confirmed the inhomogeneous nature and the spontaneous formation mechanism of these chiral monolayers [121, 160]. Another conclusion from this study is that there is no evidence to support the claim that there is significant magnetic dipole contribution to the chirality of the DiA Langmuir monolayer, as well as other Langmuir films [121].

The issues on the origin of the surface SHG or SFG signal have been examined using quantitative measurement and analysis. Historically, the complexity of the tensorial analysis in SHG and SFG often resulted dubious and confusing attributions of signals appeared to have unknown origins in the SHG or SFG measurements to the bulk quadruple or molecular magnetic dipole terms [7, 10, 27, 160]. Recent detailed experimental and theoretical studies, including the results discussed here, have shown that there has been no substantial evidence to support the non-negligible quadrupole and magnetic dipole contributions to the SHG and SFG signals from molecular surface, as well as SFG from molecular chiral liquids [33, 34, 119, 121, 161, 162]. These developments have cleared the way for quantitative analysis and interpretation of the surface SHG and SFG data using only the tensorial dipolar terms [15–17, 94].

Of course, SHG-LD is not limited to be applied to the chiral molecular assemblies from the achiral molecules. SHG-LD as described in this chapter can readily be applied to study the chirality of the monolayer and membrane of the proteins, DNA, and other chiral molecules. The above SHG-LD experimental data and results demonstrated the

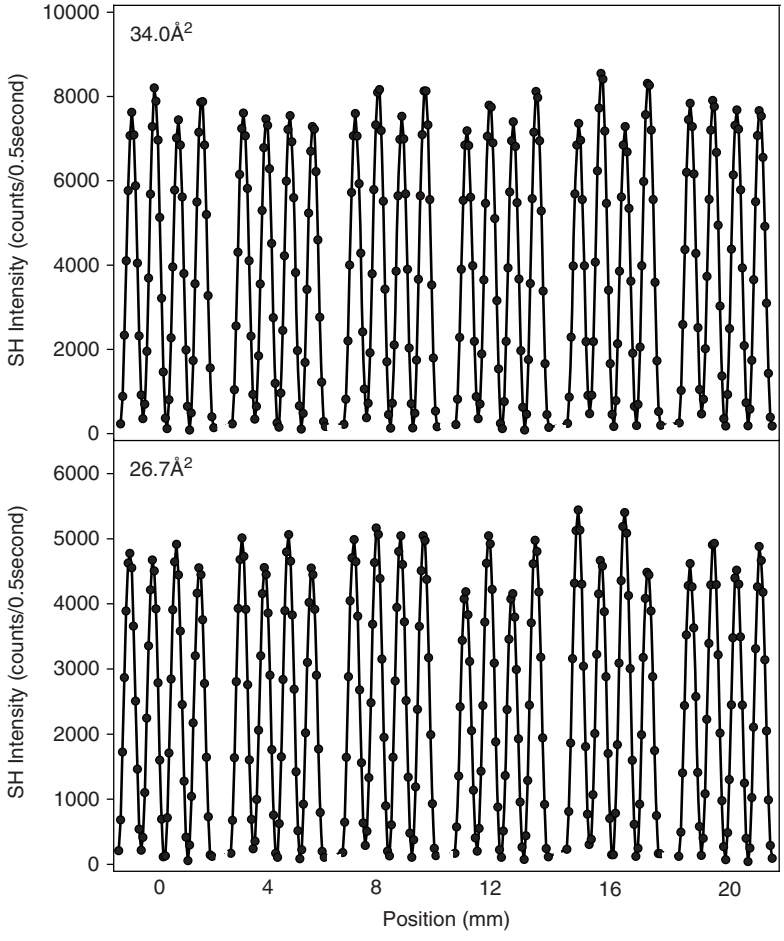

Figure 14.7. The 360° periodical *s*-detection curve of the SHG-LD data at six different positions (4 mm apart from each other) of monolayer with the surface densities at 34.0 Å^2 and 26.7 Å^2. These two surface densities are in the liquid condensed phase of the PARC18 phase diagram [101]. It is clear that both the degree and sign of the chirality change with the location in the PARC18 Langmuir monolayer. (From Y. Y. Xu, Y. Rao, D. S. Zheng, Y. Guo, M. H. Liu, H. F. Wang, *J. Phys. Chem. C* **2009**, *113*, 4088–4098. Copyright 2009 American Chemical Society [101]. Reproduced with permission.)

power of the SHG-LD in interface chirality studies. It showed that the *s*-polarization detection in the SHG-LD experiment can be used to accurately determine the degree of chiral excess (DCE) for the chiral surfaces. These results also indicated that the SHG-LD technique, as well as other nonlinear optical spectroscopic techniques, such as SFG-LD and SHG/SFG-CD, and so on, are not only effective and quantitative *in situ* probes of the interface chirality, but also effective tools to study the dynamic processes in the close-packed monolayer or in the self-assembled films at the microscopic scale using nonlinear optical microscopy. Using these techniques, future *in situ* experimental and theoretical investigations on the chirality and dynamics behaviors in the Langmuir monolayer, Langmuir–Blodgett films, and biological membranes can be established on a quantitative foundation.

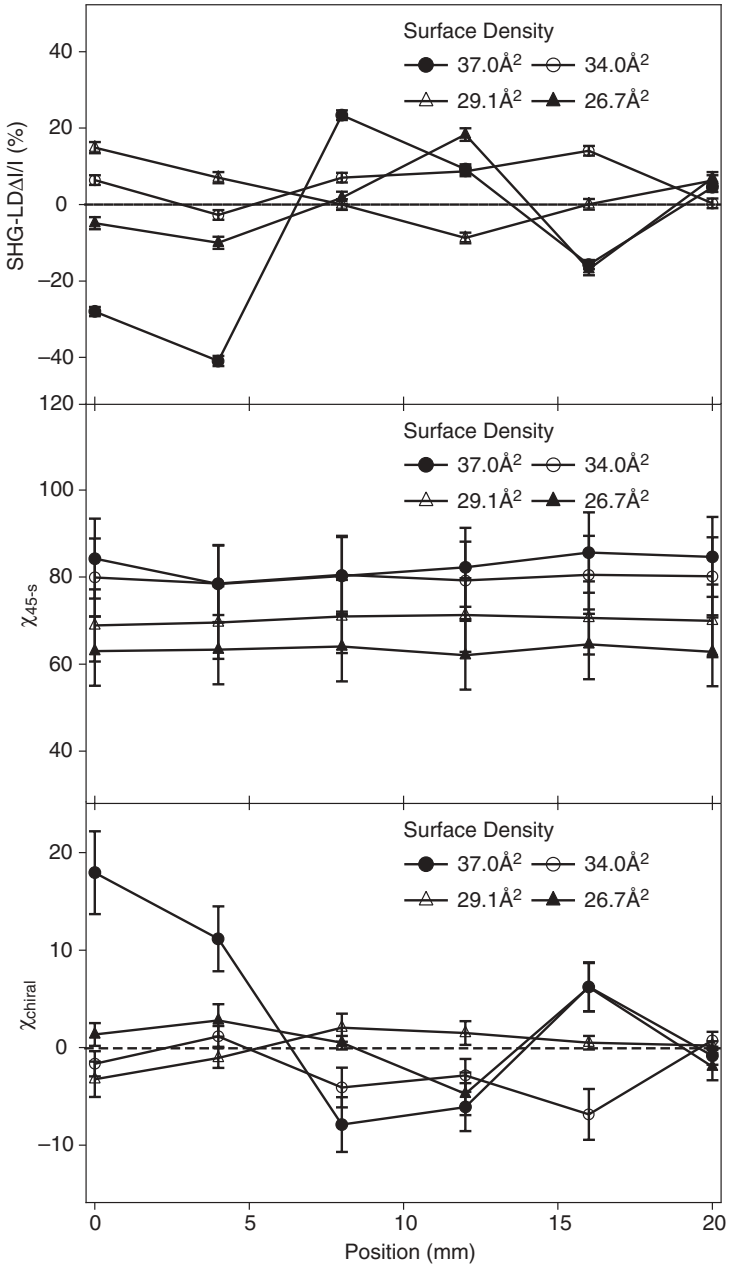

Figure 14.8. The SHG-LD DCE values, $\chi_{45°-s}$ and $\chi_{eff,chiral}$ values at different positions of the PARC18 Langmuir monolayer at the surface densities of 37.0 Å^2 and 34.0 Å^2, 29.1 Å^2 and 26.7 Å^2 from fitting the *s*-detection curve with the Eq. (14.7). Note that according to the definition of the SHG-LD DCE value and the relative signs between the χ_{chiral} and the $\chi_{45°-s}$ terms in the Eq. (14.7), the SHG-LD DCE values at each point are with opposite sign to the corresponding χ_{chiral} values. Furthermore, the inhomogeneity of the SHG-LD DCE values are the results of the inhomogeneity of the χ_{chiral} term, while the $\chi_{45°-s}$ term remains homogeneous in the PARC18 Langmuir monolayer. (From Y. Y. Xu, Y. Rao, D. S. Zheng, Y. Guo, M. H. Liu, H. F. Wang, *J. Phys. Chem. C* **2009**, *113*, 4088–4098. Copyright 2009 American Chemical Society [101]. Reproduced with permission.)

14.3.2. Chiral Spectra and Chirality of Chiral Liquid Surface with SFG-LD

Here the surface SFG-LD technique with both the single polarization angle (SPA) and twin polarization angle (TPA) methods is applied to obtain the chiral and achiral SFG-VS spectra of the (*S*)-limonene and (*R*)-limonene air–liquid interfaces. From the comparison of the achiral and chiral spectra, the vibrational spectral peaks of the limonene molecule can be assigned explicitly. Using the TPA measurement, the surface degree of chiral

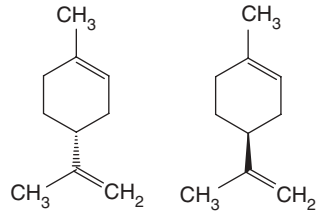

Figure 14.9. The chemical structure of the enantiomer pair (*S*)-limonene and (*R*)-limonene.

excess (DCE) and the absolute values for the chiral and achiral susceptibilities can be accurately measured.

Limonene is one of the benchmark molecules for VCD and ROA studies [163, 164] as well as chiral SFG-VS studies [33]. The structure of (*S*)- and (*R*)-limonene is shown in Figure 14.9.

The SFG-LD experiment was carried out with a 10-Hz 23-ps scanning SFG spectrometor [102, 165, 166], and the details can be found in the literature [120]. The incident angle of the visible beam is 63° (β_1) and it is 50° (β_2) for the IR beam, and the SFG signal was collected around 62° (β) at the reflection geometry. To perform the single polarization angle (SPA) detection, the visible wavelength was fixed at 532.1 nm and the IR beam was tuned from 2800 cm^{-1} to 3000 cm^{-1} with 2-cm^{-1} increment. To perform the twin polarization angle (TPA) experiment, the wavelength of the IR beam was set at a specific value and the SFG signal was recorded when the polarization angles of the visible beam and SFG signal were varied accordingly. The spectral intensity is normalized to the intensities of the corresponding visible and IR laser pulses, and then to the z-cut α-quartz surface signal to obtain the absolute value of the surface SFG response. The details of the normalization procedure were described previously [104].

Figure 14.10 shows the achiral ssp and ppp surface SFG-VS spectra of the air–liquid interfaces of the (*S*)-limonene, (*R*)-limonene, and their racemic mixture at room temperature [167]. Figure 14.11 shows the chiral $\Delta I = I_{p45^\circ p} - I_{p-45^\circ p}$ spectra for air–liquid interface of the (*S*)-limonene and (*R*)-limonene. In the achiral spectra, those for the (*S*)-limonene and (*R*)-limonene are slightly different from each other. The origin of these differences are yet to be determined. No doubt that the signal-to-noise ratios in these spectra still need to be improved. Nevertheless, the spectral peak positions for the (*S*)-limonene and (*R*)-limonene agree with each other very well. The ssp spectra have apparent spectral peaks at 2830 cm^{-1}, 2860 cm^{-1}, and 2915cm^{-1}, while the ppp spectra have apparent spectral peaks at 2835cm^{-1} (weak), 2880 cm^{-1}, 2925 cm^{-1}, and 2965 cm^{-1}, respectively. The spectral features in the ssp polarization combination are apparently different from those in the ppp polarization combinations. According to the well-established polarization selection rules in surface SFG-VS [15, 102, 103], the stronger ssp peaks belong to the symmetric C–H stretches; while the stronger ppp peaks belong to the asymmetric C–H stretches. It is interesting to note that the number of spectral features can be resolved from the polarization dependent SFG-VS is generally more than the number of peaks can be identified in the IR or Raman spectra in the liquid phase under the same condition [15, 102, 103]. Therefore, the polarization selection rules in SFG-VS help greatly on assigning these spectral features.

In Figure 14.11, the two $\Delta I = I_{s45^\circ p} - I_{s-45^\circ p}$ spectra for the (*S*)- and (*R*)-limonene are almost mirror image to each other. This indicates the chiral nature of the SFG-VS spectra thus obtained. In comparison, the chiral spectra features in Figure 14.11 are

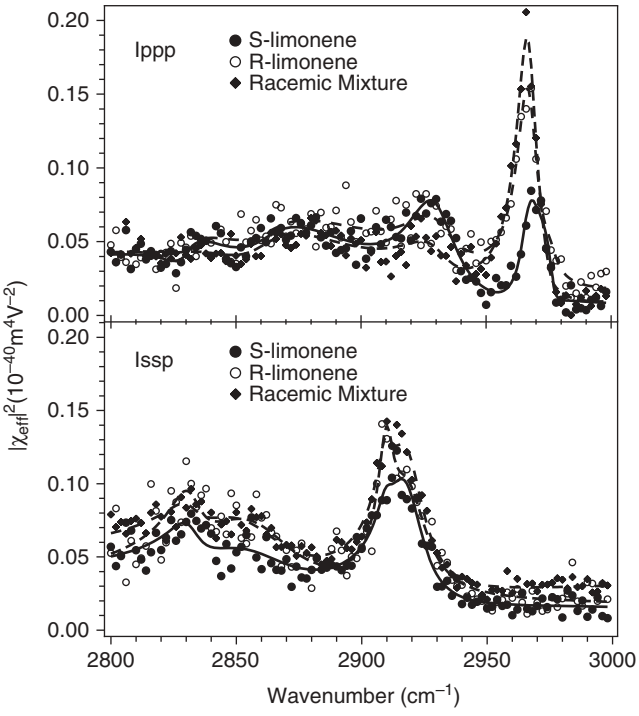

Figure 14.10. The achiral *ssp* and *ppp* SFG-VS spectra for (*S*)- and (*R*)-limonene, as well as the racemic mixture at $\beta_{Vis} = 63^\circ$ and $\beta_{IR} = 50^\circ$. The apparent peaks in the *ssp* spectra are 2830 cm^{-1}, 2860 cm^{-1}, and 2915 cm^{-1}; while the apparent peaks in the *ppp* spectra are 2835 cm^{-1} (weak), 2880 cm^{-1}, 2925 cm^{-1}, and 2965 cm^{-1}, respectively.

2835 cm^{-1}, 2880 cm^{-1} and possibly the 2920–2930 cm^{-1} (weak). These spectral peak positions are in agreement with the chiral SFG-VS spectral features of the (*S*)- and (*R*)-limonene bulk liquid, as reported by Belkin and co-workers previously [7, 33]. As discussed above, the surface chiral spectra as measured here should be dominated with the bulk chiral SFG contributions. Therefore, there is no surprise that the surface chiral SFG-VS spectral features are at the same positions as the SFG-VS spectra from the bulk liquid. However, the relative strengths of these peaks are different due to reasons unknown so far.

Moreover, these three chiral peaks are in agreement with the peak positions in the ppp spectra from the air–liquid interface except for the missing 2965 cm^{-1} in the chiral spectra. The absence of the 2965-cm^{-1} peak (attributed to the asymmetric C–H stretches of the $-CH_3$ groups in the limonene molecule) in the chiral spectra suggests that the $-CH_3$ groups are with insignificant chiral characteristics. Furthermore, all three chiral spectral positions are different from the positions of the peaks observed in the ssp spectra, as shown in Figure 14.10. These facts explicitly suggested that all the chiral spectral features have the character of the asymmetric C–H vibration. This is consistent with the fact that all the chiral susceptibilities have to have no mirror symmetry. Therefore, none of these chiral spectral features can be assigned to the symmetric C–H stretching modes as in the literature [33, 163, 164].

The above discussion indicates the importance to compare the achiral and chiral surface SFG-VS spectra in different polarization combinations for understanding both the chiral and achiral spectral features for (*S*)- and (*R*)-limonene. It also suggests that the surface SFG-VS is a very important addition to the VCD, ROA, and bulk chiral SFG-VS techniques.

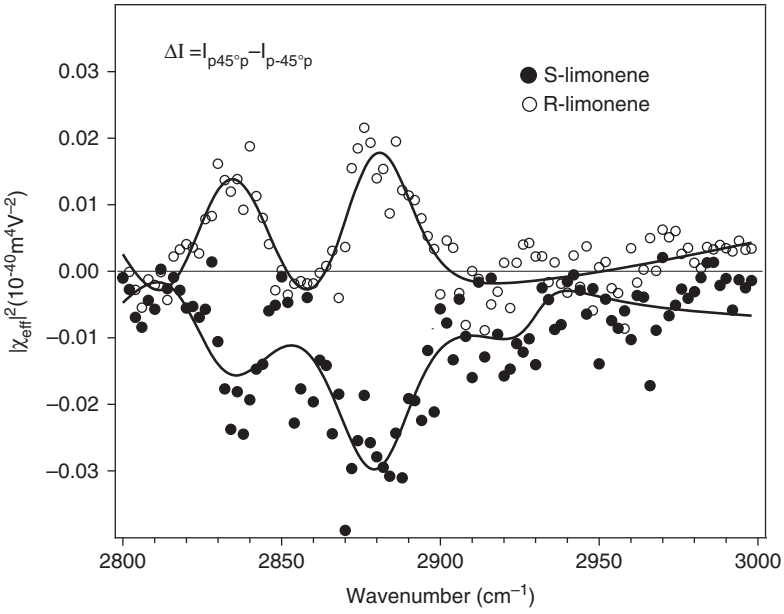

Figure 14.11. The chiral SFG-VS spectra for (*S*)- and (*R*)-limonene as obtained using the single polarization angle (SPA) measurement. The vertical axis is the normalized absolute value for the $\Delta I = I_{p45^\circ p} - I_{p-45^\circ p}$. The chiral spectra indicates that there are three chiral vibrational bands in the 2800- to 3000-cm^{-1} region, that is, the 2835-cm^{-1}, the 2880-cm^{-1}, and possibly the 2920- to 2930-cm^{-1} bands. It is clear that these peaks are the same as the peaks in the *ppp* spectra, but different from the peaks in the *ssp* spectra in the Figure 14.10. These facts are consistent with the fact that the chiral peaks have to have the asymmetric characters instead of the symmetric characters [120].

Now using the various TPA techniques discussed above, the DCE and absolute values of the macroscopic susceptibility tensors of the air–liquid interface of the (*S*)- and (*R*)-limonene can be accurately determined. TPA measurement was performed for the three chiral peaks at 2835 cm^{-1}, 2880 cm^{-1}, and 2920 cm^{-1} [120]. Here only the $I_{\pm}^{P}(\Omega)$ results for the 2880 cm^{-1} are presented in Figure 14.12. The different intensities at $\Omega = 45^\circ$ and $\Omega = -45^\circ$ explicitly indicate that the surface is chiral. The $I_{\pm}^{S}(\Omega)$ curves are with small SFG intensity and not presented. The reason is clear from Eqs. (14.22) and (14.23), because of the fact that the sps and pss terms are relatively small in comparison to the ssp and ppp terms.

The polarization-dependent $I_{\pm}^{P}(\Omega)$ TPA curves behaved just as predicted by the theoretical treatment and simulation in the Section 14.2.4.3. The fitting results of these TPA curves with Eq. (14.23) as well as the calculated DCE values using Eq. (14.1) are listed in Table 14.2.

According to these results, the following conclusions can be made.

1. The DCE values obtained from the $I_{+}^{P}(\Omega)$ curves are accurate. This is because the ssp and ppp terms are with the same sign, and thus the $I_{+}^{P}(\Omega)$ signals are much stronger. The error bar for DCE thus obtained is only ~1%. This indicates that the TPA method can be used to accurately measure the chirality of chiral surfaces. Considering the fact that the polarization angle was manually adjusted

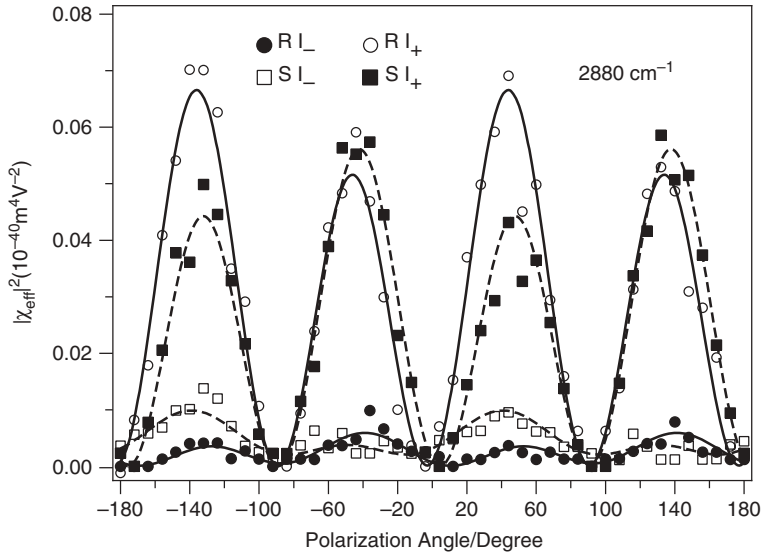

Figure 14.12. $I^P_{\pm}(\Omega)$ TPA results of (*S*)-limonene and (*R*)-limonene air–liquid interfaces at 2880 cm^{-1}. Solid circle, $IP_{-}(\Omega)$ for (*R*)-limonene; open circle; $I^P_{+}(\Omega)$ for (*R*)-limonene; Open square, $I^P_{-}(\Omega)$ for (*S*)-limonene; solid square, $I^P_{+}(\Omega)$ for (*S*)-limonene [120].

TABLE 14.2. Calculated DCE Values as Well as the Susceptibility Tensor Elements from the TPA Data as in Figure 14.2 for the 2835-cm^{-1}, 2880-cm^{-1}, and 2920-cm^{-1} Peaks[a]

Peak	Position	2835 cm^{-1}	2880 cm^{-1}	2920 cm^{-1}
R	DCE_{-}	−6.4±5.0%	−53.1±15.0%	−7.0±1.4%
	DCE_{+}	25.1±0.9%	25.4±1.3%	11.6±0.8%
S	DCE_{-}	−15.5±7.9%	84.8±55.0%	4.3±0.2%
	DCE_{+}	−25.9±2.3%	−23.7±0.4%	−9.1±0.8%
R	χ_{ppp}	0.26±0.06%	0.29±0.01%	0.25±0.05%
	χ_{ssp}	0.28±0.06%	0.20±0.01%	0.38±0.03%
	χ_{spp}	0.01±0.02%	0.004±0.01%	0.001±0.01%
	χ_{psp}	0.03±0.02%	0.03±0.01%	0.02±0.01%
S	χ_{ppp}	0.24±0.01%	0.30±0.02%	0.21±0.02%
	χ_{ssp}	0.30±0.01%	0.20±0.02%	0.40±0.01%
	χ_{spp}	0.01±0.02%	0.02±0.01%	0.02±0.01%
	χ_{psp}	−0.05±0.02%	−0.05±0.01%	−0.03±0.01%

[a]The TPA data for the 2835-cm^{-1} and 2920-cm^{-1} peaks are not shown. The unit of the susceptibilities is $10^{-20}m^2 \cdot V^{-1}$.

Source: F. Wei, Y. Y. Xu, Y. Guo, S. L. Liu, H. F. Wang, *Chin. J. Chem. Phys*. **2009**, *22*, 592–600. Copyright 2009 Chinese Physical Society [120]. Reproduced with permission.

in this experiment, much better data quality and less experimental error can be expected when automation and computer controls are introduced.

2. The DCE values for the (*S*)- and (*R*)-limonene are almost identical in magnitude but opposite in sign from the more accurate DCE_{+} values. This suggests that the surface structures of the (*S*)- and (*R*)-limonene are indeed similar.

3. The absolute values for the ssp, ppp, psp, and spp macroscopic susceptibility tensors for the (*S*)- and (*R*)-limonene air–liquid surfaces are obtained directly from the TPA measurement. The spp term value is small and below the noise level. This suggests that the TPA approach can be used as a standard technique for measurement of the nonlinear susceptibilities for the molecular surfaces. Quantitative calculation and comparison with the SFG measurement of the (*S*)- and (*R*)-limonene bulk liquid are yet to be done. It is expected to generate much more information on the chirality of the (*S*)- and (*R*)-limonene.

Here the difference between the chiral psp/spp and the achiral ssp/ppp susceptibilities is about 1 to 10. This is also consistent with the fact that the chiral psp/spp terms contain significant bulk contributions, while the ssp/ppp terms are dominated by the surface contribution. One would expect that the chiral terms of the (*S*)- or (*R*)-limonene monolayer is going to be at least one or two more orders of magnitude smaller. How to accurately measure the intrinsic monolayer chiral susceptibility is still an yet to be accomplished task, except for the case with double resonance SFG as demonstrated by Shen and co-workers [34].

Comparison of the surface chiral psp/spp values measured here with the bulk psp/spp values obtained in the literature gives the information on the depth of the bulk liquid to the measured surface SFG chiral signal. Here in Table 14.2 the surface psp $\chi_{eff,chiral}$ value at 2880 cm^{-1} is on the order of 0.05×10^{-20} $m^2 \cdot V^{-1}$, while the psp $|\chi_{chiral}|^2$ at 2880 cm^{-1} is about 1.75×10^{-28} $m^2 \cdot V^{-2}$, as measured by Shen and co-workers [33]. From the definition of the surface susceptibility, one knows that the surface $\chi_{eff,chiral}$ differs from the bulk χ_{chiral} by the factor of Fresnel factors and a length (depth) factor [17, 168]. It is known that for dielectric liquid surfaces the Fresnel factors are usually not all very different from unity [169]; the length (depth) factor is therefore about 4×10^{-8}m, that is, ~40 nm. Considering the fact that in the typical SFG measurement the spot size is usually about 0.5 mm, this gives a volume of 1×10^{-10} cm^{-3}. The molecular weight of limonene is about 136. Thus, this volume corresponds to 7×10^{-13} moles of the limonene molecules. In comparison to the large amount of sample required in the bulk or linear chiroptical spectroscopic measurement, the measurement with surface SFG is indeed very sensitive.

Even though the surface SFG-LD in chiral studies is still in its infancy, the data and discussion above demonstrated the power of the chiral and achiral surface SFG-LD techniques for studying both the surface and bulk chirality. Not only the chiral and achiral contribution to the vibrational spectra can be explicitly assigned and analyzed, but also the surface susceptibility of the chiral liquid or membrane can be quantitatively measured.

14.4. PERSPECTIVES AND FUTURE DIRECTIONS

In this chapter, the principles and detailed formulation of the surface SHG-LD and SFG-LD are presented with examples for their application to the *in situ* measurement of the surface chirality of molecules and molecular assemblies. In particular, the *s* detection in the surface SHG-LD and the twin polarization angle (TPA) in the SFG-LD can be used for accurate surface chirality measurement.

With the discussion on the connections between the macroscopic surface susceptibility tensors and the microscopic molecular polarizability tensors, the mechanisms for the

contribution to the surface chirality as observed in the SHG-LD and SFG-LD measurement are clarified. One important conclusion is that in the surface SHG-LD and SFG-LD measurement, the "intrinsic chirality" is significantly smaller than the "structural chirality." Therefore, surface SHG-LD and SFG-LD are sensitive to the 3-D structure of the protein, instead of the "intrinsic chirality" of its amino acid units. This simple fact makes SHG-LD and SFG-LD ideal techniques for elucidation and determination of the structure of the proteins, as well as other chiral structures in the biological system. Similar treatment can also be systematically developed for the SHG/SFG CD and SHG/SFG ORD techniques. In principle, they shall provide complementary or more detailed information to the SHG/SFG LD techniques.

The formulations presented in this chapter allows not only quantitative measurement using the surface SHG-LD and SFG-LD, but also quantitative analysis and interpretation of the data by directly connecting the observed macroscopic surface nonlinear optical properties to the microscopic molecular nonlinear optical properties, which can in principle be readily calculated or computed using *ab initio* or non-*ab initio* computational methods. All these are possible because the interface provides a simple and clear reference frame for such analysis. With the surface as the reference frame, the achiral and chiral (including intrinsic chirality and structural chirality) contributions can be well separated in the surface SHG and SFG measurement and analysis, allowing further explicit theoretical treatment of each. For example, the polarization dependence in the SHG-LD and SFG-LD allowed development of the polarization selection rules for explicit spectral assignment and allowed development of orientational/structural determination of the surface molecular moieties [15]. Future studies using these concepts and analysis shall provide unique information on the spectroscopy, structure, and interactions of the chiral and achiral molecules at the interface and in the membrane.

The surface SHG and SFG can directly benefit the study and understanding of the chirality of molecules and molecular assemblies in three directions.

Firstly, surface SHG and SFG are sensitive analytical tools for unambigeous chiral detection. It is very promising to develop them into routine laboratory analytical tools for sensitive chiral detection and structural determination. Because the relative signs between the chiral terms and the achiral terms depend on the chirality of the molecule or structure, this in principle can be used as the effective tool for absolute chirality determination.

Secondly, surface SHG and SFG have great potentials and promises in studying the protein and biological membrane structure. The ability for surface SHG and SFG to separate and quantitatively measure the achiral, structural chiral and intrinsic chiral contributions allows direct comparison with the theoretical modeling and computation. In comparison to the linear chiroptical spectroscopy, the tensorial nonlinear susceptibilities and their polarization dependence shall have great advantages for the purpose of 3-D structural determination.

Thirdly, the unique ability for sensitive detection and spectral analysis with the surface SHG and SFG vibrational and electronic spectroscopy can shed new lights on the understanding of the molecular spectra of both chiral and achiral molecules. Surface SHG and SFG can help solve a great deal of uncertainties, confusions, and puzzles in the linear spectroscopy. Understanding these issues can significantly enhance our ability to determine the absolute configuration of the simple chiral molecules with the synergetic efforts of different chiroptical spectroscopic techniques.

Applications of surface SHG and SFG spectroscopic techniques to chiral and achiral molecular studies require synergy of the experiment and theory. Because traditionally it was considered a very difficult task to obtain and interpret the SHG and SFG data

into properties that can be easily compared with theoretical predictions, relatively little has been explored to synergize the SHG and SFG experimental and theoretical efforts in more quantitative fashion. Recent developments in surface SHG and SFG measurement and quantitative analysis, as shown in the formulations and examples in this chapter, have removed most of such obstacles. With the development of the laser technology and detection techniques, not only SHG and SFG experiments can be much more easily designed and conducted, but also the accuracy in the SHG and SFG experiment can allow detailed comparison of the experimental data and the results of theoretical predictions. Calculation and computation of the tensorial second-order nonlinear optical and chiroptical properties is not trivial. However, the problem can be simplified since for most of the cases only the dipolar terms need to be considered, in comparison to the linear chiroptical spectroscopy where the coupling between the dipolar and the magnetic dipolar terms needs to be treated. Joined with the theory, surface nonlinear spectroscopy shall reveal great details in the spectra, structure, and interactions of chiral molecules and chiral structures.

In comparison to other chiroptical spectroscopic techniques, surface SHG and SFG are still in their infancy. Nevertheless, even with simple examples as presented in this chapter, as well as the previous Chapter 13, the tremendous potentials and promises of the surface nonlinear chiroptical methods can be noticed. It is up to the researchers in various fields with all sorts of scientific problems to grab the opportunities in this relatively open field.

REFERENCES

1. P. Fischer, Nonlinear optical spectroscopy of chiral molecules, in *Advances in Chiroptical Methods*, N. Berova, P. L. Polavarapu, K. Nakanishi, R. W. Woody, John Wiley & Sons, Hoboken, NJ, **2011**, Chapter 13, pp. 373–406.
2. P. L. Polavarapu, *Chirality* **2008**, *20*, 664–672.
3. J. A. Giordmaine, *Phys. Rev*. **1965**, *138*, A1599–A1606.
4. J. M. Hicks, T. Petralli-Mallow, J. D. Byers, *Faraday Discuss*. **1994**, *99*, 341–357.
5. P. Fischer, F. Hache, *Chirality* **2005**, *17*, 421–437.
6. G. J. Simpson, *ChemPhysChem* **2004**, *5*, 1301–1310.
7. M. A. Belkin, Y. R. Shen, *Int. Rev. Phys. Chem*. **2005**, *24*, 257–299.
8. L. M. Haupert, G. J. Simpson, *Annu. Rev. Phys. Chem*. **2009**, *60*, 345–365.
9. N. Ji, Y. R. Shen, *Chirality* **2006**, *18*, 146–158.
10. Y. R. Shen, *The Principles of Nonlinear Optics*, Wiley-Interscience, New York, **1984**.
11. R. W. Boyd, *Nonlinear Optics*, 3rd ed., Academic Press, New York, **2008**.
12. Y. R. Shen, in *Proceedings of the International School of Physics Enrico Fermi*, Course CXX, Frontiers in Laser Spectroscopy; T. W. Hansch, and M. Inguscio, eds., North Holland, Amsterdam, **1994**, p. 139.
13. Y. R. Shen, *Nature* **1989**, *337*, 519–525.
14. Y. R. Shen, *Annu. Rev. Phys. Chem*. **1989**, *40*, 327–350.
15. H. F. Wang, W. Gan, R. Lu, Y. Rao, B. H. Wu, *Int. Rev. Phys. Chem*. **2005**, *24*, 191–256.
16. W. K. Zhang, H. F. Wang, D. S. Zheng, *Phys. Chem. Chem. Phys*. **2006**, *8*, 4041–4052.
17. D. S. Zheng, Y. Wang, A. A. Liu, H. F. Wang, *Int. Rev. Phys. Chem*. **2008**, *27*, 629–664.
18. Y. R. Shen, *Annu. Rev. Mater. Sci*. **1986**, *16*, 69–86.
19. G. L. Richmond, J. M. Robinson, V. L. Shannon, *Prog. Surf. Sci*. **1988**, *28*, 1–70.

20. V. Vogel, Y. R. Shen, *Annu. Rev. Mater. Sci*. **1991**, *21*, 515–534.
21. K. B. Eisenthal, *Acc. Chem. Res*. **1993**, *26*, 636–643.
22. C. D. Bain, *J. Chem. Soc. Faraday Trans*. **1995**, *91*, 1281–1296.
23. K. B. Eisenthal, *Annu. Rev. Phys. Chem*. **1992**, *43*, 627–661.
24. R. M. Corn, D. A. Higgins, *Chem. Rev*. **1994**, *94*, 107–125.
25. K. B. Eisenthal, *Chem. Rev*. **1996**, *96*, 1343–1360.
26. M. Buck, M. Himmelhaus, *J. Vac. Sci. Technol. A* **2001**, *19*, 2717–2736.
27. M. Kauranen, T. Verbiest, J. J. Maki, A. Persoons, *J. Chem. Phys*. **1994**, *101*, 8193–8199.
28. J. D. Byers, H. I. Yee, T. Petralli-Mallow, J. M. Hicks, *Phys. Rev. B* **1994**, *49*, 14643–14647.
29. T. Petralli-Mallow, T. M. Wong, J. D. Byers, H. I. Yee, J. M. Hicks, *J. Phys. Chem*. **1993**, *97*, 1383–1388.
30. J. J. Maki, M. Kauranen, A. Persoons, *Phys. Rev. B* **1995**, *51*, 1425–1434.
31. J. D. Byers, J. M. Hicks, *Chem. Phys. Lett*. **1994**, *231*, 216–224.
32. T. Verbiest, M. Kauranen, A. Persoons, M. Ikonen, J. Kurkela, H. Lemmetyinen, *J. Am. Chem. Soc*. **1994**, *116*, 9203–9205.
33. M. A. Belkin, T. A. Kulakov, K. H. Ernst, L. Yan, Y. R. Shen, *Phys. Rev. Lett*. **2000**, *85*, 4474–4477.
34. M. A. Belkin, S. H. Han, X. Wei, Y. R. Shen, *Phys. Rev. Lett*. **2001**, *87*, 113001.
35. J. J. Maki, T. Verbiest, M. Kauranen, S. Van Elshocht, A. Persoons, *J. Chem. Phys*. **1996**, *105*, 767–772.
36. G. J. Simpson, *J. Chem. Phys*. **2002**, *117*, 3398–3410.
37. S. H. Han, N. Ji, M. A. Belkin, Y. R. Shen, *Phys. Rev. B* **2002**, *66*, 165415.
38. M. A. Belkin, Y. R. Shen, C. Flytzanis, *Chem. Phys. Lett*. **2002**, *363*, 479–485.
39. J. M. Hicks, T. Petralli-Mallow, *Appl. Phys. B* **1999**, *68*, 589–593.
40. T. Petralli-Mallow, A. L. Plant, M. L. Lewis, J. M. Hicks, *Langmuir* **2000**, *16*, 5960–5966.
41. T. Verbiest, M. Kauranen, A. Persoons, *J. Mater. Chem*. **1999**, *9*, 2005–2012.
42. V. L. Brudny, W. L. Mochán, *Phys. Stat. Sol. A* **1999**, *175*, 183–188.
43. M. J. Crawford, S. Haslam, J. M. Probert, Y. A. Gruzdkov, J. G. Frey, *Chem. Phys. Lett*. **1994**, *229*, 260–264.
44. P. Fischer, A. D. Buckingham, A. C. Albrecht, *Phys. Rev. A* **2001**, *64*, 053816.
45. L. Hecht, L. D. Barron, *Mol. Phys*. **1996**, *89*, 61–80.
46. P. K. Yang, J. Y. Huang, *J. Opt. Soc. Am. B* **1998**, *15*, 1698–1706.
47. D. L. Andrews, I. D. Hands, *J. Phys. B: Atom. Mol. Phys*. **1998**, *31*, 2809–2824.
48. M. A. Kriech, J. C. Conboy, *J. Opt. Soc. Am. B* **2004**, *21*, 1013–1022.
49. P. J. Campagnola, A. C. Millard, M. Terasaki, P. E. Hoppe, C. J. Malone, W. A. Mohler, *Biophys. J*. **2002**, *81*, 493–508.
50. P. J. Campagnola, M. D. Wei, A. Lewis, L. Loew, *Biophys. J*. **1999**, *77*, 3341–3349.
51. L. Moreaux, O. Sandre, M. Blanchard-Desce, J. Mertz, *Opt. Lett*. **2000**, *25*, 320–322.
52. E. Brown, T. McKee, E. Tomaso, A. Pluen, B. Seed, Y. Boucher, R. K. Jain, *Nature Med*. **2003**, *9*, 796–800.
53. A. Zoumi, A. Yeh, B. J. Tromberg, *Proc. Natl. Acad. Sci. USA* **2002**, *99*, 11014–11019.
54. W. R. Zipfel, R. M. Williams, R. Christie, A. Y. Nikitin, B. Hyman, W.W. Webb, *Proc. Natl. Acad. Sci. USA* **2003**, *100*, 7075–7080.
55. D. A. Dombeck, K. A. Kasischke, H. D. Vishwasrao, M. Ingelsson, B. Hyman, W.W. Webb, *Proc. Natl. Acad. Sci. USA* **2003**, *100*, 7081–7086.
56. V. Ostroverkhov, K. D. Singer, R. G. Petschek, *J. Opt. Soc. Am. B* **2001**, *18*, 1858–1865.
57. M. A. Kriech, J. C. Conboy, *J. Am. Chem. Soc*. **2005**, *127*, 2834–2835.

58. B. J. Burke, A. J. Moad, M. A. Polizzi, G. J. Simpson, *J. Am. Chem. Soc*. **2003**, *125*, 9111–9115.
59. S. R. Walter and F. M. Geiger, *J. Phys. Chem. Lett*. **2010**, *1*, 9–15.
60. V. K. Valev, A. V. Silhanek, N. Smisdom, B. De Clercq, W. Gillijns, O. A. Aktsipetrov, M. Ameloot, V. V. Moshchalkov, T. Verbiest, *Optics Express* **2010**, *18*, 8286–8293.
61. V. K. Valev, A. V. Silhanek, N. Verellen, W. Gillijns, G.A.E. Vandenbosch, O. A. Aktsipetrov, V. V. Moshchalkov, T. Verbiest, *Phys. Rev. Lett*. **2010**, *104*, 127401.
62. V. K. Valev, N. Smisdom, A. V. Silhanek, B. De Clercq, W. Gillijns, M. Ameloot, V. V. Moshchalkov, T. Verbiest, *Nano. Lett*. **2009**, *9*, 3945–3948.
63. L. D. Barron, A. D. Buckingham, *Mol. Phys*. **1971**, *20*, 1111–1119.
64. L. D. Barron, M. P. Bogaard, A. D. Buckingham, *J. Am. Chem. Soc*. **1973**, *95*, 603–605.
65. E. Charney, *The Molecular Basis of Optical Activity*, John Wiley & Sons, New York, **1979**.
66. N. Berova, K. Nakanishi, R. W. Woody, *Circular Dichroism: Principles and Applications*, John Wiley & Sons, New York, **2002**.
67. L. A. Nafie, *Ann. Rev. Phys. Chem*. **1997**, *48*, 357–386.
68. L. A. Nafie, T. B. Freedman, in *Circular Dichroism: Principles and Applications*, 2nd ed., K. Nakanishi, N. Berova, R. W. Woody, eds., John Wiley & Sons, New York, **2002**, p. 97.
69. L. D. Barron, *Molecular Light Scattering and Optical Activity*, 2nd ed., Cambridge University Press, Cambridge, **2004**.
70. T. F. Heinz, in *Nonlinear Surface Electromagnetic Phenomena*, H. E. Ponath and G. I. Stegeman, eds., North-Holland, Amsterdam, **1994**, Chapter 5.
71. Ekspla Co., Vilnius, Lithuania. `http://www.ekspla.com`.
72. J. P. Smith, V. Hinson-Smith, *Ana. Chem*. **2004**, *76*, 287A–290A.
73. L. J. Richter, T. P. Petralli-Mallow, and J. C. Stephenson, *Opt. Lett*. **1998**, *23*, 1594–1596.
74. E. L. Hommel, G. Ma, H. C. Allen, *Ana. Sci*. **2001**, *17*, 1–5.
75. T. Ishibashi, H. Onishi, *Appl. Phys. Lett*. **2002**, *81*, 1338–1340.
76. S. Yamaguchi, T. Tahara, *J. Phys. Chem. B*, **2004**, *108*, 19079–19082.
77. K. Kemnitz, K. Bhattacharyya, J. M. Hicks, G. R. Pinto, K.B. Eisenthal, T. F. Heinz, *Chem. Phys. Lett*. **1986**, *131*, 285–290.
78. R. Superfine, J. Y. Huang, Y. R. Shen, *Opt. Lett*. **1990**, *15*, 1276–1278, 1990.
79. R. Superfine, J. Y. Huang, Y. R. Shen, *Chem. Phys. Lett*. **1990**, *172*, 303–306.
80. R. Lu, Y. Rao, W. K. Zhang, H. F. Wang, *Proceedings of the SPIE Conference on Nonlinear Spectroscopy*, **2002**, No.4812–15, pp. 115–124.
81. I. V. Stiopkin, H. D. Jayathilake, A. N. Bordenyuk, A V. Benderskii, *J. Am. Chem. Soc*. **2008**, *130*, 2271–2275.
82. S. Nihonyanagi, S. Yamaguchi, T. Tahara, *J. Chem. Phys*. **2009**, *130*, 204704.
83. L. Fu, G. Ma, E. C. Y. Yan, *J. Am. Chem. Soc*. **2010**, *132*, 5405–5412.
84. G.J. Simpson, J. M. Perry, C. L. Ashmore-Good, *Phys. Rev. B* **2002**, *66*, 165437.
85. J. M. Perry, A. J. Moad, N. J. Begue, R. D. Wampler, G. J. Simpson, *J. Phys. Chem. B* **2005**, *109*, 20009–20026.
86. P. Fischer, D. S. Wiersma, R. Righini, B. Champagne, A. D. Buckingham, *Phys. Rev. Lett*. **2000**, *85*, 4253–4256.
87. M. A. Belkin, Y. R. Shen, *Phys. Rev. Lett*. **2003**, *91*, 213907.
88. G. Pescitelli, N. Sreerama, P. Salvadori, K. Nakanishi, N. Berova, R. W. Woody, *J. Am. Soc. Chem*. **2008**, *130*, 6170–6181.
89. J. T. Yang, C. -S. C. Wu, H. M. martinez, *Methods Enzymol*. **1986**, *130*, 208–269.
90. N. Sreerama, S. Y. Venyaminov, R. W. Woody, *Anal. Biochem*. **2000**, *287*, 243–251.
91. N. Sreerama, R. W. Woody, *Anal. Biochem*. **2000**, *287*, 252–260.

92. N. Sreerama, and R. W. Woody, *Protein Sci*. **2004**, *13*, 100–112.
93. S. Sioncke, T. Verbiest, A. Persoons, *Mat. Sci. Eng. R* **2003**, *42*, 115–155.
94. A. J. Moad, G. J. Simpson, *J. Phys. Chem. B* **2004**, *108*, 3548–3562.
95. P. F. Brevet, *Surface Second Harmonic Generation*, Press Polytechniques et Universitaires Romandes, Lausanne, **1997**.
96. X. Zhuang, P. B. Miranda, D. Kim, Y. R. Shen, *Phys. Rev. B*, **1999**, *59*, 12632–12640.
97. X. Wei, S. C. Hong, X. W. Zhuang, T. Goto, Y. R. Shen, *Phys. Rev. E* **2000**, *62*, 5160–5172.
98. M. Kauranen, T. Verbiest, E. W. Meijer, E. E. Havinga, M. N. Teerenstra, A. J. Schouten, R. J. M. Nolte, A. Persoons, *Adv. Mater*. **1995**, *7*, 641–644.
99. X. Chen, M. L. Clarke, J. Wang, Z. Chen, *Int. J. Mod. Phys. B* **2005**, *19*, 691–713.
100. Y. Rao, Y. S. Tao, H. F. Wang, *J. Chem. Phys*. **2003**, *119*, 5226–5236.
101. Y. Y. Xu, Y. Rao, D. S. Zheng, Y. Guo, M. H. Liu, H. F. Wang, *J. Phys. Chem. C* **2009**, *113*, 4088–4098.
102. R. Lu, W. Gan, B. H. Wu, H. Chen, H. F. Wang, *J. Phys. Chem. B* **2004**, *108*, 7297–7306.
103. R. Lu, W. Gan, B. H. Wu, Z. Zhang, Y. Guo, H. F. Wang, *J. Phys. Chem. B* **2005**, *109*, 14118–14129.
104. W. Gan, D. Wu, Z. Zhang, R. R. Feng, H. F. Wang, *J. Chem. Phys*. **2005**, *123*, 114705.
105. R. Lu, W. Gan, H. F. Wang, *Chin. Sci. Bull*. **2003**, *48*, 2183–2187.
106. R. Lu, W. Gan, H. F. Wang, *Chin. Sci. Bull*. **2004**, *49*, 899–899.
107. H. F. Wang, *Chin. J. Chem. Phys*. **2004**, *17*, 362–369.
108. M. A. Polizzi, R. M. Plocinik, G. J. Simpson, *J. Am. Chem. Soc*. **2004**, *126*, 5001–5007.
109. W. Gan, B. H. Wu, H. Chen, Y. Guo, H. F. Wang, *Chem. Phys. Lett*. **2005**, *406*, 467–473.
110. W. Gan, D. Wu, Z. Zhang, H. F. Wang, *Chin. J. Chem. Phys*. **2006**, *19*, 20–24.
111. N. J. Begue, A. J. Moad, G. J. Simpson, *J. Phys. Chem. C* **2009**, *113*, 10158–10165.
112. N. J. Begue, R. M. Everly, V. J. Hall, L. Haupert, G. J. Simpson, *J. Phys. Chem. C* **2009**, *113*, 10166–10175.
113. M. J. Shultz, in *Advances in Multi-photon Processes and Spectroscopy*, Vol. 18, S. H. Lin, A. A. Villaeys, and Y. Fujimura, eds., World Scientific, Singapore, **2008**, p. 133.
114. W. Gan, B. H. Wu, Z. Zhang, Y. Guo, H. F. Wang, *J. Phys. Chem. C* **2007**, *111*, 8716–8725.
115. W. Gan, Z. Zhang, R. R. Feng, H. F. Wang, *J. Phys. Chem. C* **2007**, *111*, 8726–8738.
116. Y. Q. Yu, K. Lin, X. G. Zhou, H. Wang, S. L. Liu, X. X. Ma, *J. Phys. Chem. C* **2007**, *111*, 8971–8978.
117. W. Gan, Z. Zhang, R. R. Feng, H. F. Wang, *Chem. Phys. Lett*. **2006**, *423*, 261–265.
118. T. Verbiest, M. Kauranen, J. J. Maki, M. N. Teerenstra, A. J. Schouten, R. J. M. Nolte, A. Persoons, *J. Chem. Phys*. **1995**, *103*, 8296–8298.
119. W. K. Zhang, D. S. Zheng, Y. Y. Xu, H. T. Bian, Y. Guo, H. F. Wang, *J. Chem. Phys*. **2005**, *123*, 224713.
120. F. Wei, Y. Y. Xu, Y. Guo, S. L. Liu, H. F. Wang, *Chin. J. Chem. Phys*. **2009**, *22*, 592–600.
121. Y. Y. Xu, F. Wei, H. F. Wang, *J. Phys. Chem. C* **2009**, *113*, 4222–4226.
122. T. G. Zhang, C. H. Zhang, G. K. Wong, *J. Opt. Soc. Am. B* **1990**, *7*, 902–907.
123. M. B. Feller, W. Chen, Y. R. Shen, *Phys. Rev. A* **1991**, *43*, 6778–6792.
124. J. S. Salafsky, *J. Chem. Phys*. **2006**, *125*, 074701.
125. H. Goldstein, *Classical Mechanics*, Addison-Wesley, Inc., New York, **1980**, p. 147.
126. P. Fischer, A. D. Buckingham, *J. Opt. Soc. Am. B* **1998**, *15*, 2951–2957.
127. C. Hirose, N. Akamatsu, K. Domen, *Appl. Spectro*. **1992**, *46*, 1051–1072.

128. J. Wang, X. Y. Chen, M. L. Clarke, Z. Chen, *Proc. Natl. Acad. Sci. USA* **2005**, *102*, 4978–4983.
129. M. B. Raschke, M. Hayashi, S. H. Lin, Y. R. Shen, *Chem. Phys. Lett*. **2002**, *359*, 367–372.
130. D. Wu, G. H. Deng, Y. Guo, H. F. Wang, *J. Phys. Chem. A* **2009**, *113*, 6058–6063.
131. C. D. Bain, P. B. Davies, T. H. Ong, R. N. Ward, M. A. Brown, *Langmuir* **1991**, *7*, 1563–1566.
132. T. H. Ong, P. B. Davies, C. D. Bain, *Langmuir* **1993**, *9*, 1836–1845.
133. G. R. Bell, Z. X. Li, C. D. Bain, P. Fischer, D. C. Duffy, *J. Phys. Chem. B* **1998**, *102*, 9461–9472.
134. M. G. Brown, E. A. Raymond, H. C. Allen, L. F. Scatena, G. L. Richmond, *J. Phys. Chem. A* **2000**, *104*, 10220–10226.
135. M. H. Liu, K. Ushida, A. Kira, H. Nakahara, *Thin Sol. Films* **1998**, *327–329*, 491–494.
136. P. Z. Guo, L. Zhang, M. H. Liu, *Adv. Mater*. **2006**, *18*, 177–180.
137. P. Z. Guo, M. H. Liu, *Langmuir* **2005**, 21, 3410–3412.
138. R. Viswanathan, J. A. Zasadzinski, D. K. Schwartz, *Nature* **1994**, *368*, 440–443.
139. X. Huang, S. G. Jiang, M. H. Liu, *J. Phys. Chem. B* **2005**, *109*, 114–119.
140. L. Zhang, Q. Lu, M. H. Liu, *J. Phys. Chem. B* **2003**, *107*, 2565–2569.
141. X. Huang, C. Li, S. G. Jiang, X. S. Wang, B. W. Zhang, M. H. Liu, *J. Coll. Inter. Sci*. **2005**, *285*, 680–685.
142. X. Huang, C. Li, S. G. Jiang, X. S. Wang, B. W. Zhang, M. H. Liu, *J. Am. Chem. Soc*. **2004**, *126*, 1322–1323.
143. J. Yuan, M. H. Liu, *J. Am. Chem. Soc*. **2003**, *125*, 5051–5056.
144. P. Z. Guo, R. P. Tang, C. X. Cheng, F. Xi, M. H. Liu, *Macromolecules* **2005**, *38*, 4874–4879.
145. S. G. Jiang, M. H. Liu, *J. Phys. Chem. B* **2004**, *108*, 2880–2884.
146. Y. Q. Zhang, P. L. Chen, M. H. Liu, *Langmuir* **2006**, *22*, 10246–10250.
147. P. L. Chen, X. G. Ma, M. H. Liu, ChemPhysChem **2006**, 7, 2419–2423.
148. P. Z. Guo, M. H. Liu, *Coll. Surf. A Physicochem. Eng. Aspects* **2006**, *284–285*, 70–73.
149. Z. X. Guo, T. F. Jiao, M. H. Liu, *Langmuir* **2007**, *23*, 1824–1829.
150. P. L. Chen, X. G. Ma, M. H. Liu, *Macromolecules* **2007**, *40*, 4780–4784.
151. L. Zhang, J. Yuan, M. H. Liu, *J. Phys. Chem. B* **2003**, *107*, 12768–12773.
152. X. Huang, M. H. Liu, *Chem. Comm*. **2003**, 66–67.
153. I. Weissbuch, L. Leiserowitz, M. Lahav, *Curr. Opin. Coll. Inter. Sci*. **2008**, *13*, 12–22.
154. K. H. Ernst, *Topics Curr. Chem*. **2006**, *265*, 209–252.
155. I. Kuzmenko, H. Rapaport, K. Kjaer, J. Als-Nielsen, I. Weissbuch, M. Lahav, L. Leiserowitz, *Chem. Rev*. **2001**, *101*, 1659–1696.
156. N. Nandy, D. Vollhardt, *Chem. Rev*. **2003**, *103*, 4033–4076.
157. P. Dynarowicz-Latka, A. Dhanabalanb, O. N. Oliveira, Jr. *Adv. Coll. Interface Sci*. **2001**, *91*, 221–293.
158. H. F. Wang, E. Borguet K. B. Eisenthal, *J. Phys. Chem. A* **1997**, *101*, 713–718.
159. T. Verbiest, M. Kauranen, A. Persoons, *J. Opt. Soc. Am. B* **1998**, *15*, 451–457.
160. G. Martin-Gassin, E. Benichou, G. Bachelier, I. Russier-Antoine, Ch. Jonin, P. F. Brevet, *J. Phys. Chem. C* **2008**, *112*, 12958–12965.
161. B. Champagne, P. Fischer, A. D. Buckingham, *Chem. Phys. Lett*. **2000**, *331*, 83–88.
162. P. Fischer, F. W. Wise, A. C. Albrecht, *J. Phys. Chem. A* **2003**, *107*, 8232–8238.
163. P. L. Polavarapu, M. Diem, L. A. Nafie, *J. Am. Chem. Soc*. **1980**, *102*, 5449–5453.

164. F. P. Ureña, J. R. A. Moreno, J. J. L. González, *Tetrahedron:Asymmetry* **2009**, *20*, 89–97.
165. J. Feng, D. Wu, J. Wen, S. L. Liu, H. F. Wang, *Chin. J. Chem. Phys*. **2008**, *21*, 314–323.
166. Z. Zhang, D. S. Zheng, Y. Guo, H. F. Wang, *Phys. Chem. Chem. Phys*. **2009**, *11*, 991–1002.
167. F. Wei, H. F. Wang, unpublished data of the author's group.
168. N. Bloembergen, P. S. Pershan, *Phys. Rev*. **1962**, *128*, 606–622.
169. X. Wei, Y. R. Shen, *Phys. Rev. Lett*. **2001**, *86*, 4799–4802.

15

PHOTOELECTRON CIRCULAR DICHROISM

Ivan Powis

15.1. INTRODUCTION

Chiral asymmetry in the angular distribution of photoelectrons that are emitted upon ionization with circularly polarized radiation is one of the more recent, and remarkable, chiroptical phenomena to be investigated. Perhaps the most immediately striking characteristic of this effect is the magnitude of the asymmetry factors that are encountered from a sample of randomly oriented, isolated (i.e. noninteracting) molecular enantiomers. Routinely, these are found to be in the range 0.01–0.4 and thus are many orders of magnitude greater than typical chiroptical asymmetries, such as seen for example in conventional absorption circular dichroism (CDA) spectroscopy.

A more extensive list—contrasting the features expected of photoelectron circular dichroism [1] (PECD), the technique developed to record chiral angular distribution parameters, with, for example, CDA—suggests some of the potential of this newer approach. First, the giant asymmetry factors indicate a sensitivity advantage that is sufficient to enable work with dilute, solvent-free samples. In fact, experimental constraints on the electron detection mandate working in a high-vacuum environment with low-density vapors, thereby focusing attention on the bare, isolated molecular system. But compatible molecular beam techniques may also be introduced, perhaps augmented by simultaneous detection of the accompanying parent ion in coincidence with the emitted photoelectrons. That permits selective examination by electron spectroscopy of well-characterized cluster species. PECD investigations can thus be readily extended to examine intermolecular interactions in molecular recognition phenomena, or to create controlled microsolvation to better understand the role of solvent effects on a chiral species.

Comprehensive Chiroptical Spectroscopy, Volume 1: Instrumentation, Methodologies, and Theoretical Simulations, First Edition. Edited by N. Berova, P. L. Polavarapu, K. Nakanishi, and R. W. Woody.
© 2012 John Wiley & Sons, Inc. Published 2012 by John Wiley & Sons, Inc.

Secondly, the spectral range available is not then restricted by any solvent cutoff and extends, effectively, from the molecular ionization threshold (typically around 155 nm, or 8 eV photon energy) through to core excitation regions in the soft X ray range (2 nm, 600 eV, and beyond). The PECD spectrum is dispersed not only by photon energy, $h\nu$, but also by electron energy, E_{kin}, which is recorded along with the photoelectron angular distribution. This provides for the creation of a feature-rich two-dimensional map ($h\nu$ *vs.* E_{kin}) of the chiral asymmetry parameters. As in conventional photoelectron spectroscopy (PES), the electron energy coordinate allows the differentiation of contributions made by the ionization of different molecular orbitals, and these prove to each have distinctive PECD signatures. In certain circumstances, especially core orbital photoionization, the molecular orbital will itself be highly localized, offering some capability for probing specific regions in the molecular structure. Even when individual orbital contributions are not resolvable due to spectral congestion, and so the conventional PES appears broad and relatively featureless, the PECD curves may still be strongly structured; and guided by realistic theoretical modeling of the PECD phenomenon, unambiguous assignments of absolute chiral configuration may still be achieved [2].

Of equal surprise to those already familiar with studies of molecular photoionization is the sensitivity of the PECD measurement to more subtle features of molecular structure, such as conformation and chemical substitution. The traditional form of the photoelectron angular distribution function, $I(\theta)$, is well known in this context:

$$I(\theta) = 1 + \beta P_2(\cos\theta), \tag{15.1}$$

with θ being the angle of electron emission measured from the electric vector of a linearly polarized light source and P_2 the second Legendre polynomial function. The so-called anisotropy parameter,[1] β, ranges $-1 \leq \beta \leq +2$ with $\beta = 0$ describing a fully isotropic distribution. Many molecular studies have established that β typically rises in a semiquantitatively predictable manner from approximately zero at threshold toward its positive limit with increasing electron kinetic energy. In the absence of resonances, the information content of β is then perhaps somewhat limited. In contrast, the additional chiral distribution parameter that will be introduced to describe ionization with circular polarizations varies dramatically with the above-mentioned factors in a manner that, although reliably predictable from quantum mechanical calculations of the photoionization dynamics, has detail that defies simple intuition.

The author's own interest in this topic was motivated by a challenge to propose instrumental ways to identify and distinguish the optical isomers of volatile odorant molecules in real-time breath analysis [3], since in many cases these are perceived to have very different smells/tastes. Thus motivation comes from a defined analytical need, although to date our own studies, and those by other groups, have been directed toward developing a sound theoretical and experimental base for the technique. Experimentally, PECD has been investigated for a range of molecules running from small chiral prototypes such as methyl-oxirane [4–6] and glycidol [7, 8] through to some terpene natural products such as carvone [9, 10], camphor [11–14], fenchone [15, 16], and endo-borneol [2]. The catalogue of studies also includes investigations on bromocamphor [11, 17], alaninol [18],

[1] Also known as the asymmetry parameter, although the distribution it describes has inversion symmetry and thus is not actually asymmetric. Here we will avoid this terminology to prevent confusion with the additional chiral distribution parameter that has been introduced to describe the true forward–backward asymmetry in the angular distribution probed by PECD.

and 3-hydroxytetrahydrofuran [19]. Recently the author and co-workers have started to examine the effects of clustering on PECD obtained from *n*-mers of camphor [20], epichlorohydrin, and glycidol [21] as anticipated above.

15.2. THE PHOTOELECTRON ANGULAR DISTRIBUTION AND CIRCULAR DICHROISM

A more complete, but much less widely recognized, form of the photoelectron angular distribution expression, Eq. (15.1), can be given:

$$I^{\{p\}}(\theta) = 1 + b_1^{\{p\}} P_1(\cos\theta) + b_2^{\{p\}} P_2(\cos\theta). \tag{15.2}$$

Both equations apply to the single-photon ionization of a randomly oriented molecular sample. Here the P_j are now first- and second-order Legendre polynomials, whose coefficients, $b_j^{\{p\}}$, have an explicit dependence on the light polarization state or helicity, p. For linearly polarized light the index p equals 0, while p is ± 1 for, respectively, left- and right-circular polarizations. It should also be noted that the angle θ is understood to be measured from the electric vector in the case of linear polarization, but is taken from the direction of light propagation for circularly polarized light (CPL).

A full derivation of Eq. (15.2) can be found elsewhere [1, 22, 23], but here we will summarize its key characteristics. The coefficients, $b_j^{\{p\}}$, are determined by the quantum mechanical photoionization dynamics and thus will depend on the identity of the ionized orbital and vary with ionization energy. Constraints implied by conservation of photon and electron angular momentum impart certain symmetry related properties to these coefficients. First,

$$b_1^{\{0\}} = 0 \tag{15.3}$$

so that the first Legendre polynomial term is always absent for linear polarizations. Hence, in this case Eq. (15.2) has just a single remaining anisotropic term given by the $P_2(\cos\theta)$ function and thus reduces to the more common form [Eq. (15.1)] with the identity $\beta \equiv b_2^{\{0\}}$.

For photoionization with CPL, one finds that the additional P_2 coefficients are symmetric,

$$b_2^{\{+1\}} = b_2^{\{-1\}} \left(= -\frac{1}{2} b_2^{\{0\}} \right), \tag{15.4}$$

but the P_1 coefficients are antisymmetric,

$$b_1^{\{+1\}} = -b_1^{\{-1\}}; \tag{15.5}$$

that is, the first anisotropic (P_1) term in Eq. (15.2) changes sign with switch of the light helicity. Similarly, the $b_1^{\{p\neq 0\}}$ coefficients will swap sign with an exchange of the molecular helicity (enantiomer):

$$b_1^{\{p\}}(R) = -b_1^{\{p\}}(S). \tag{15.6}$$

Conversely, however, for an *achiral* molecule $b_1^{\{p\}}$ is necessarily always zero. This is due to a complete internal cancellation of the dipole matrix elements contributing to this parameter in such cases. Consequently, it is only for the specific combination of photoionization of a chiral molecule by CPL that the first Legendre polynomial term in Eq. (15.2) may contribute to the observed angular distribution; otherwise the simplified form [Eq. (15.1)] is sufficient.

The expansion of the first Legendre polynomial term appearing in Eq. (15.2) in fact gives just $b_1^{\{\pm 1\}} \cos\theta$. The cosine is of course odd with respect to the inversion $\theta = 0^\circ \rightarrow \theta = 180^\circ$ so that some forward–backward asymmetry in the photoelectron angular distribution (PAD) can be anticipated for chiral molecule photoionization with CPL. One can thus define

$$G_{AD} = I^{\{p\}}(0^\circ) - I^{\{p\}}(180^\circ) = b_1^{\{p\}} \cos(0^\circ) - b_1^{\{p\}} \cos(180^\circ) = 2b_1^{\{p\}}, \tag{15.7}$$

where use has been made of the fully normalized distribution functions, Eq. (15.2), and the relation $P_2(\cos 0^\circ) = P_2(\cos 180^\circ)$.

Alternatively, the antisymmetry of the $b_1^{\{\pm 1\}}$ coefficients displayed in Eq. (15.5) suggests a dichroism associated with the angle-resolved electron yield. The asymmetry factor for this can be defined, again in terms of the fully normalized distributions functions of Eq. (15.2), for a given detection angle, θ, as the difference between the yield obtained with left and right CPL:

$$\gamma(\theta) = I^{\{+1\}}(\theta) - I^{\{-1\}}(\theta) = 2b_1^{\{+1\}} P_1(\cos\theta) = 2b_1^{\{+1\}} \cos\theta, \tag{15.8}$$

where it is noted that the invariance of $b_2^{\{\pm 1\}}$ with helicity switches expressed in Eq. (15.4) causes the P_2 terms to be eliminated.

The alternative asymmetry factors, Eqs. (15.7) and (15.8), are seen to provide essentially the same information content, namely the sign and magnitude of a specific choice of $b_1^{\{p\}}(R/S)$ parameter, which is then trivially related to the others via Eqs. (15.5) and (15.6). In principle, therefore, a single measurement that determined the angular distribution would be sufficient to extract information contained in the chiral $b_1^{\{\pm 1\}}$ parameters, although in practice, as will be seen, two or more measurements obtained with switched circular polarizations of the ionizing radiation to yield the dichroism from the difference signal are preferred.

The derivation of Eq. (15.2) [1, 23, 24], and thus also the dichroism it predicts in an angle-resolved photoelectron spectrum [Eq. (15.8)], proceeds in the pure electric dipole (E1) approximation for the light–matter interaction, and it requires no recourse to consideration of the typically much weaker magnetic dipole (M1), or electric quadrupole (E2) interaction terms. This contrasts with the situation in CDA, where the dichroism results from E1·M1 or E1·E2 interaction terms and is consequently weak compared to the overall electric dipole transition strength. Photoelectron circular dichroism can therefore be expected to be much the stronger effect. The first realistic numerical calculations [23, 25] predicted asymmetry factors ranging from a few percent up to ~40%, and subsequent experimental work has fully borne out these expectations.

That such strong anticipated dichroism is present already in the electric dipole approximation can be attributed to the *differential* nature of the PECD measurement; detection of an angle-resolved electron allows the final state in the photoabsorption process to be probed more completely. On the other hand, the electric dipole PECD disappears in a fully *integral* cross-section measurement (as in CDA), as can be seen

by considering the asymmetry expression [Eq. (15.8)] integrated over all θ. At the level of the pure electric dipole approximation, there is no dichroism associated with the *total* photoionization cross section. Extending the derivation of, for example, Eq. (15.2) to include higher order radiation–matter interaction terms [26] introduces additional dichroism associated with the isotropic term in the angular distribution (proportional to the total photoionization cross section) and with the anisotropic Legendre polynomial terms (including a further P_3 term for the case of E1·E2 interactions). However, these much weaker asymmetries are effectively swamped by the electric dipole contribution in an angle-resolved PECD measurement, and Eq. (15.2) has proven fully adequate to deal with experimental data to date.

While the present chapter stops short of repeating the full derivation for Eq. (15.2), it should be noted that the theoretical treatment underpinning this phenomenological description describes, essentially, a specific transfer of photon angular momentum to the outgoing electron, which is mediated via a scattering of the photoelectron off the chiral molecular ion, as it departs the molecular region. It will be seen from results to be discussed that this scattering by the chiral molecular potential plays a major role in many cases.

An analogy can be offered which, although inexact, can help an appreciation of why there should be a forward–backward scattering asymmetry of the photoelectrons. Imagine a length of threaded rod (molecular framework), carrying a nut (electron), held away from an observer. Spinning the nut (representing exciting the electron to be ejected) will cause it to travel toward one end or the other of the rod (molecule). Which direction it departs will depend on the thread (enantiomer) and the sense of the rotation imparted to the nut. For a normal right-hand screw thread, a right-handed rotation imparted by the observer will cause the nut to move away. Conversely, a left-handed spin of the nut will see it move toward the observer. Turning the rod/nut assembly through 180° and repeating will not change these (lab-frame) directions of travel relative to the observer. Hence the orientation of the rod/molecule is unimportant; instead, what causes a specific forward or backward motion is the handedness of the thread/enantiomer and of the angular momentum given the nut when its motion is excited. The rod's thread, like the chiral molecular potential, thus plays its role in the chirally specific model of photon–electron–molecule interaction and in creating the resulting strong forward–backward asymmetry in the nut/electron angular distribution.

This mechanical analogy cannot be developed further. In the real molecular case the interactions are quantum mechanical in nature, with many interference terms whose mutual cancellation and/or reinforcement varies rapidly with changing energy etc., such that the realistic outcome cannot be guessed by intuition, but instead requires a full numerical calculation of the photoionization matrix elements.

15.3. EXPERIMENTAL APPROACHES

Equation (15.2) was first derived by Ritchie [22] over three decades ago, but its specific significance for the photoionization of randomly oriented chiral molecules with circularly polarized light (CPL) was not exploited until a decade ago, when advances in the technology of so-called insertion devices for synchrotron radiation sources provided for the first time convenient and reproducible highly polarized radiation across the vacuum ultraviolet (VUV) and soft X-ray (SXR) regions that is required for valence and inner-shell ionization studies.

15.3.1. Light Sources

Synchrotron radiation itself is produced when electrons (or positrons) are accelerated around a storage ring, and it can be emitted in a very broad energy band extending from the infrared to the hard X ray [27]. Although naturally linearly polarized in the plane of the storage ring, light emitted in a direction slightly above and below this plane of circulation becomes elliptically polarized, and this was exploited in the first attempts to measure PECD [17]. However, this approach carries a number of practical difficulties for a dichroism measurement with two opposing polarizations; the light intensity falls on moving out of plane, and achieving two CPL beams with well-balanced intensities and known, matched degrees of polarization is very challenging. Even then, the different propagation directions of the alternately polarized beams introduces severe instrumental alignment difficulties, such that the implied measurement approach with alternating light helicity has to be effectively abandoned. These first studies were then made by switching not polarization, but the handedness of the molecular enantiomers in front of a fixed CPL beam [11, 17]. While fine for a demonstration experiment, this clearly has limitations when both enantiomers may not be readily available, or indeed one may have a sample of unknown configuration to investigate.

Insertion devices (undulators, wigglers) are magnetic arrays that are introduced into straight sections of the storage ring [28, 29]. Initially introduced to increase brilliance of the light source in a selected wavelength region, these devices also allow full polarization control by causing rapid oscillating deviations of the circulating electron packets as they pass through. Two such matched arrays, placed to produce fields in the horizontal and vertical planes, can introduce orthogonal excursions of the traversing electrons, resulting in components of horizontal and vertical polarization in the emitted light beam. If these oscillations are in phase, a linear light polarization results, which may be rotated as the amplitude of horizontal and vertical excursions is varied. Moreover, a relative displacement of the two magnetic arrays along the electron beam direction introduces a defined phase shift between the orthogonal oscillations, allowing controllable elliptically polarized light to be produced. A complete corkscrew path for the electron beam, created by such a two-axis device, will result in emission of fully circularly polarized light [30].

The undulator light output has to be transmitted along a beamline to the experimental end station via various optical elements, including a monochromator. In the wavelength regions considered, these are all reflection optics (gratings, mirrors) that can introduce polarization changes due to different reflectivities of s and p components. In a beamline designed for polarization studies, care will have been taken to compensate for depolarization at different elements and to have a predictive model for this where possible. Nevertheless, there can be long-term shifts in beamline depolarization effects due to, for example, pollution buildup on optical surfaces. Consequently, some form of *in situ* polarimetry to measure the degree of polarization actually achieved at the sample can be beneficial [31–33].

Various elliptically polarizing undulators have been introduced (e.g., references 34–40). More traditional designs utilize permanent magnets, and these have the disadvantage that changing the phase to switch between left and right CPL requires very precise mechanical movement of magnet assemblies of substantial mass; polarization switching can thus be slow (perhaps several minutes). One solution to this has been adopted at the BESSY II synchrotron [36, 37]. Here two undulators are placed in series, one behind the other, with a very small angular displacement between the output light beams. One may then be set for right CPL, the other for left CPL, and the two optical beams will pass almost in parallel through the beamline optical path to the final focusing

mirror before the experimental chamber, where they are refocused to a common spot. The spatial separation achieved in the central beamline is sufficient to allow insertion of an *in vacuo* mechanical chopper to alternately block the left and right beams, thereby providing a much more rapid polarization switch at the experiment. Alternatively, electromechanical designs [34, 38, 39] permit simpler switching of a single undulator by reversal of one set of coil currents.

Either of the above approaches allows polarization switching frequencies of the order of 0.1–0.001 Hz, which is probably about optimum for these measurements. This is clearly well below the 50 kHz familiar in CDA, but the strength of PECD means that there is no need for recourse to lock-in detection to extract very low level signals. Rather, the switches during the course of a measurement cycle are intended to minimize effects of medium-term drifts in light intensity, sample vapor pressures, and possibly alignment, which may occur on these timescales; short-term stability is typically not a problem.

Technical improvements in modern synchrotrons continue to provide better signal through increased brightness and focusing of optical beams, along with much improved beam stability. Additionally, the introduction of continuous "top-up" operating modes to maintain a constant stored beam current can now eliminate the long-term quasi-exponential ($\tau \approx$ *hours*) decay in light intensity that used to be typical at such light sources.

15.3.2. Fixed-Angle-Resolved Electron Detection

The simplest experimental arrangement consists of placing a single-electron analyzer system, with a defined angular acceptance (typically $\pm 3^{\circ}$) at some fixed angle, θ, with respect to the light-beam propagation direction (Figure 15.1), and then measuring the asymmetry or dichroism spectrum as the polarization is switched. The experimental asymmetry factor is then defined as the normalized difference between the background

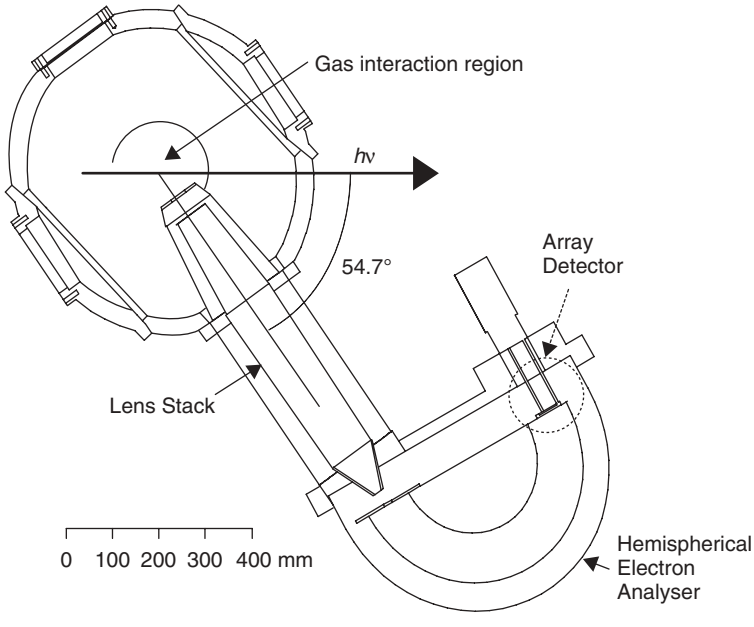

Figure 15.1. Schematic showing an angle-resolving hemispherical electron analyzer system used for PECD experiments at the BESSY synchrotron.

corrected spectra, $S^{\{\pm1\}}(\theta)$, recorded with left and right CPL, respectively:

$$\Gamma(\theta) = \frac{(S^{\{+1\}}(\theta) - S^{\{-1\}}(\theta))}{((S^{\{+1\}}(\theta) + S^{\{-1\}}(\theta))/2)}. \tag{15.9}$$

It is assumed that each angle-resolved spectrum can be expressed in terms of a total ionization rate, $N^{\{\pm1\}}$, and an angular distribution function; hence $S^{\{\pm1\}} = N^{\{\pm1\}}I^{\{\pm\}}(\theta)$. The experimental methodology developed for these measurements aims to ensure that the overall ionization rates are set, or otherwise compensated, so as to be equal for the two helicities [10]. This entails switching polarization rapidly enough to eliminate medium-term drifts, plus other steps necessary to minimize instrumental contributions to the asymmetry. If then it is assumed that $N^{\{+1\}} = N^{\{-1\}}$, Equation (15.9) can be written directly in terms of the angular distribution functions, $I^{\{\pm\}}(\theta)$, defined in Eq. (15.2). Thus,

$$\Gamma(\theta) = \frac{(I^{\{+1\}}(\theta) - I^{\{-1\}}(\theta))}{((I^{\{+1\}}(\theta) + I^{\{-1\}}(\theta))/2)} = \frac{2b_1^{\{+1\}}P_1(\cos\theta)}{1 + b_2^{\{\pm1\}}P_2(\cos\theta)}, \tag{15.10}$$

where the second step exploits the symmetries of the $b_j^{\{p\}}$ coefficients [Eqs. (15.4) and (15.5)]. This measure of the dichroism is seen to depend also on the $b_2^{\{\pm1\}}$ coefficient (equivalently the β anisotropy parameter), but it is common to choose $\theta = 54.7^\circ$, the so-called magic angle at which $P_2(\cos\theta) = 0$ so that by writing the remaining P_1 polynomial explicitly, one obtains

$$\Gamma(54.7^\circ) = 2b_1^{\{+1\}}\cos(54.7^\circ). \tag{15.11}$$

Consequently, at the magic angle the experimental dichroism asymmetry defined in Eq. (15.9) allows direct determination of the chiral b_1 coefficient, whereas at other observation angles some prior knowledge or associated determination of the b_2 parameter would also be necessary. The observed asymmetry is reduced from the maximum value of $2b_1^{\{+1\}}$ that might be obtained at 0° (or 180°) by the factor of $\cos(54.7^\circ)$. This is approximately a half, and the sensitivity disadvantage is easily outweighed by the convenient simplification seen in Eq. (15.11).

It ought to be noted that Eq. (15.2) applies to light polarization rates of 100% and has to be modified for elliptical polarization (i.e., when we have the Stokes parameter $0 < S_3 < 1$) [41]. This introduces an additional dependence on ϕ, the detector azimuthal angle from the principal axis of the polarization ellipse. In such cases, more care may need to be taken to either estimate, or eliminate, a potential "contamination" of the measured dichroism, Γ, by additional terms including the $b_2^{\{p\}}$ parameters [8, 18].

This arrangement, with a standard hemispherical electrostatic energy analyzer, has been used for various core-level PECD measurements at BESSY II [8, 10, 14, 16]. The spectrometer was, however, fitted with an array detector in the analyzer's image plane to allow multichannel detection of the dispersed electrons. The consequent energy multiplexing provides an obvious advantage in data acquisition rate but, equally important, allows parallel, simultaneous detection across an energy range sufficient to span one or more bands in the measured photoelectron spectrum. Eliminating a need to scan the analyzer during data acquisition means that any effects of pressure and intensity drifts are uniform across the studied band profile.

Other groups have used an arrangement with dual, opposing hemispherical analyzers set to observe directions θ and $\theta + 180^{\circ}$ [11, 18]. In principle, simultaneous observation of the electrons scattered in diametrically opposed directions should permit the forward–backward asymmetry in the angular distribution to be recorded with a single, fixed circular polarization, thus providing access to the chiral $b_1^{\{p\}}$ coefficient. However, in practice, there are considerable practical difficulties in ensuring that the two analyzer systems have equal transmission and detection efficiency and have the same field of view of the ionization volume. Consequently, these instruments still employ switching of the molecular handedness (enantiomer) or photon helicity. The second analyzer data channel then provides a check on reproducibility of the measured dichroism, or may be suitably combined in the data treatment to effectively merge both data streams when extracting the dichroism.

15.3.3. Photoelectron Imaging

An alternative method that has been developed for studying valence-shell PECD is based upon photofragment velocity map imaging (VMI), a technique that has been widely adopted for molecular photoionization and reaction dynamics studies [42]. The basic principle of this approach may be understood with reference to Figure 15.2.

An electron emitted from a molecule will, after some specified time, be found to lie on the surface of a sphere having a radius determined by the velocity (energy) of the electron. A large number of electrons of the same energy would be distributed over the surface of this sphere according to their angular distribution. If, as the electron shell expands, the electrons are being uniformly accelerated by an electrostatic field, away from the ionization region towards a position sensitive detector, then a two-dimensional projection of this three-dimensional shell can be recorded. The strength of the electric field can be varied to control the flight time and, thus, control the physical size of the expanded electron shell, allowing it to be made commensurate with the area of the detector.

Figure 15.2 also shows what happens if a second ionization channel were to yield electrons of an alternative, lower kinetic energy. In that case a second, smaller shell of electrons can be anticipated, appearing as a smaller diameter feature in the 2-D projection. Isotropic distributions for both channels have been assumed in the figure, but it should be obvious that any variations in electron angular distribution will appear as intensity variations in the detected 2-D image. The projection from 3-D electron distribution to 2-D image implies some loss of information; however, it is often the case that some cylindrical symmetry must exist in the experimental arrangement (for example, in the

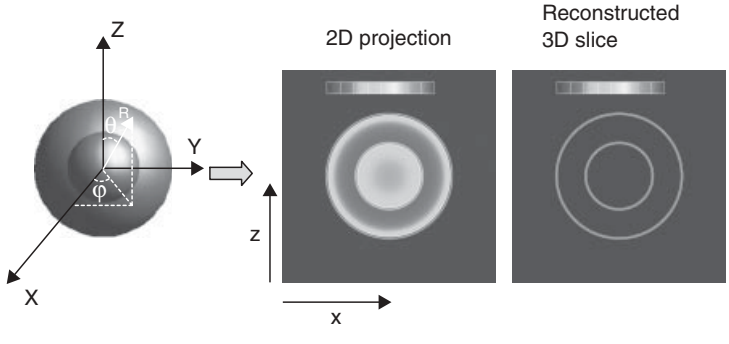

Figure 15.2. The photofragment imaging technique. A 3-D angular distribution of emitted electrons and their projection onto a 2-D imaging detector. Mathematical inversion of the projection recovers a slice through the 3-D distribution along with the energy and angular distribution functions. (*See insert for color representation of the figure*.)

PECD situation the propagation direction of a beam of CPL along the **Z** axis, parallel to the detector plane, creates such a symmetry axis). In such cases, mathematical inversion techniques can recreate the full 3-D distribution, displayed in Figure 15.2 as a slice through the expanded shells [42]. This provides a "cleaner" image, with electrons of different energy dispersed at different radius, and in the process it also allows the angular distribution around **Z** to be quantitatively extracted. Consequently, the radial distribution in the inverted 3-D image provides a spectrum of the electron energy, with angular distribution parameters available across this spectrum as a function of the energy/radius.

A limitation of this approach arises when, in a realistic situation, the ionization volume is of finite size. The consequent uncertainty in the starting position of any electron leads to a blurring of the detected image, with a corresponding smearing of the rings seen after inversion and hence a limitation on achievable resolution. Velocity map imaging [43] seeks to overcome this limitation by means of a simple electrostatic lens arrangement incorporated into the electron acceleration region. By analogy with optical lenses, the operation of such a lens can be described by a transfer matrix formulation, such that the position, r, and direction, $r' = dr/dY$, of each ray or electron trajectory at the image plane of the detector can be directly expressed in terms of the initial position and direction, R, R':

$$\begin{pmatrix} r \\ r' \end{pmatrix} = \begin{pmatrix} a_{11} & a_{12} \\ a_{21} & a_{22} \end{pmatrix} \begin{pmatrix} R \\ R' \end{pmatrix}. \tag{15.12}$$

Normal optical imaging, as in a camera, would prefer $a_{12} = 0$, such that each point R in the object uniquely maps to a point r in the image, independent of the ray's initial direction R' (i.e., there is no spherical aberration), with a linear magnification given by a_{11}. Velocity map imaging, in contrast, seeks to establish the converse lens condition that $a_{11} = 0$. Hence, for a given electron energy or speed one finds $r \approx a_{12}R'$, showing that all electron trajectories having the same speed and the same initial angle (i.e., having the same velocity vector) will be mapped, to a reasonable approximation, to a single point r in the 2-D image—independent of initial position, R, in the ionization source. Blurring and resolution loss due to finite interaction region dimensions can thus be minimized.

The electron imaging approach has both conceptual and practical appeal for PECD studies. The full 4π electron angular distribution may be collected, and the detection scheme offers both energy and angle multiplexing, with obvious advantages for data acquisition rates. For PECD measurements made with synchrotron radiation the VMI spectrometer design originally proposed by Eppink and Parker [43] has been modified with an additional lens structure to extend the useful kinetic energy range that can be recorded [44]. Recorded images can then immediately offer visual insight into the electron distribution. In principle, the chiral asymmetry in the electron angular distribution could be observed directly from a single image recorded with a fixed helicity light. For practical purposes, however, recording the dichroism by subtracting images recorded with interleaved left and right CPL is preferred. With carefully planned data-acquisition procedures, the subtraction can be used to eliminate apparent instrumental asymmetries (e.g., due to nonuniform sensitivity across the face of the imaging electron detector) and, because the full angular distribution is observed, detailed prior knowledge of β parameters is not required [12].

Example dichroism images obtained at two different photon energies in a study of *S*-methyl oxirane PECD [45] are displayed in Figure 15.3. In the left-hand column the raw 2-D projection images appear (with the photon beam propagating vertically up relative to the displayed images). The lower photon energy (10.8 eV) is a little above the first

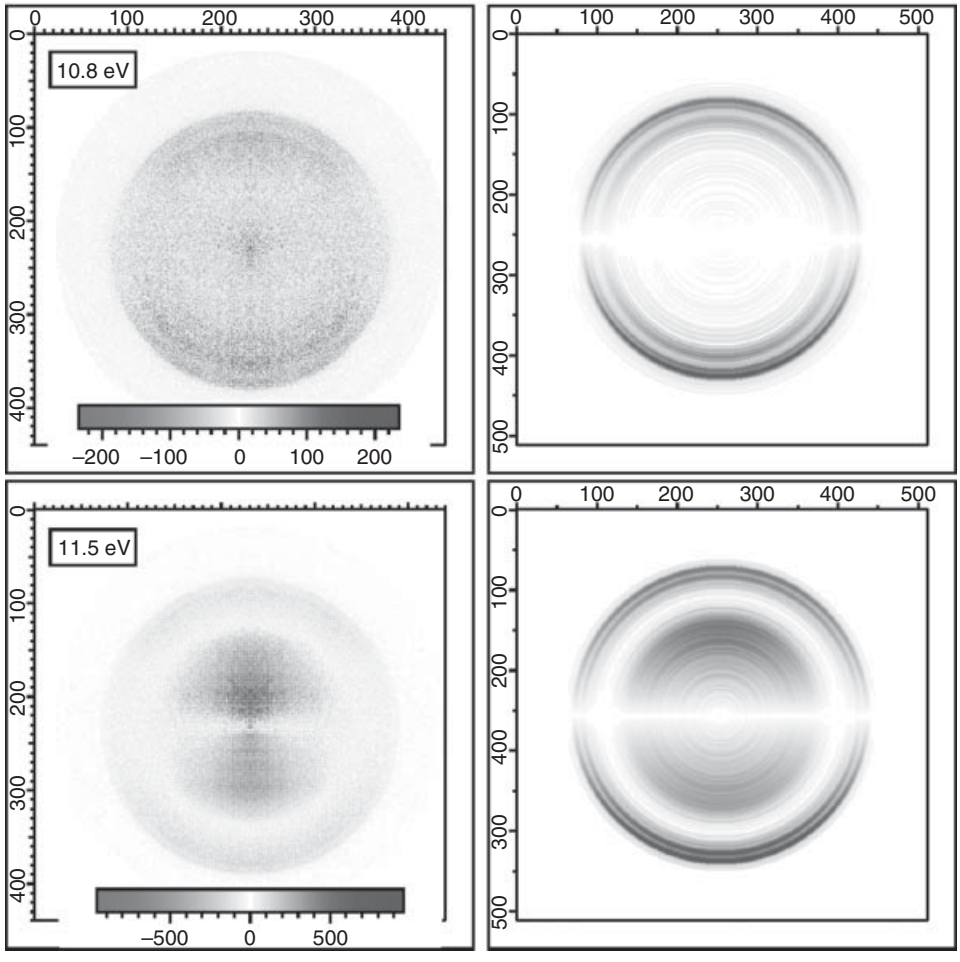

Figure 15.3. VMI images showing PECD in (*S*)-methyloxirane, with pseudo-color mapped intensities and **X, Y** axes that are marked in detector pixel units. The photon beam propagates vertically upwards, parallel to the image plane in these recordings. Left column: unprocessed 2-D photoelectron dichroism image (left CPL-right CPL). Right column: after treatment with pBaseX algorithm. (*See insert for color representation of the figure.*)

ionization potential. The electrons thus come from the HOMO orbital, and one readily sees the electron angular asymmetry with a negative difference (L-R) in the forward (up) direction and a counterbalancing positive difference in the backward (down) direction.

A variety of algorithms have been introduced for the mathematical inversion of 2-D projection images recovering the full 3-D distribution [42]. The pBaseX method developed by the author and colleagues [46] is particularly well-adapted for the present circumstances. In particular, it can handle both positive and negative pixel values encountered in these bipolar dichroism images and will yield directly the Legendre polynomial coefficients, $b_j^{\{p\}}$, as a function of electron energy (radius).

3-D slice images recovered using the pBaseX method are shown alongside the 2-D projection images in the right-hand column of Figure 15.3. The structure that can be discerned in the $h\nu = 10.8$ eV 2-D image is now much clearer in the processed 3-D

slice. The two prominent outer rings correspond to vibrational structure in the HOMO ionization as does other, less intense, inner structure seen on closer examination. All have a qualitatively similar forward-backward asymmetry which the full analysis shows to have a magnitude of 10–20%.

In the second example in Figure 15.3 a higher photon energy was used (11.5 eV) which is now sufficient to ionize both the HOMO and the next, HOMO-1, orbitals in methyl oxirane. Because the more tightly bound HOMO-1 orbital has a higher ionization energy, these electrons are emitted with a lower kinetic energy than the HOMO electrons, and so in these images the HOMO-1 electrons fall inside the rings just attributed to the HOMO band. Again, the detail is more apparent in the 3-D slice generated by mathematical inversion of the 2-D projection image, but in either case it is very clear that the forward–backward asymmetry along the photon beam direction is in the opposite sense for the HOMO-1 electrons.

15.4. EXPERIMENTAL RESULTS AND DISCUSSION

In this section some recent, representative results are presented with the intention that they introduce and highlight some of the capabilities of the PECD technique.

15.4.1. Carbon 1s core electron PECD

15.4.1.1. Fenchone. Fenchone, $C_{10}H_{16}O$, is a camphor-like molecule with a rigid bicyclic skeletal framework. The structure of the 1*R*, 4*S*-fenchone enantiomer and its C 1s X-ray photoelectron spectra (XPS) are shown in Figure 15.4. These particular data were recorded using a photon energy of 299.5 eV and a detection angle of 54.7° to the photon beam direction [16]. A moderately heated (50°C–80°C) sample inlet and gas cell were used to generate sufficient vapor pressure from the solid fenchone sample.

Two peaks are evident in the XPS, the less intense one being readily assigned to ionization of the carbonyl C 1*s* orbital as it experiences a shift in binding energy attributable to the attached O atom. The main, unshifted peak consists of superimposed contributions from all other C atom sites in the molecule. Included in the figure are

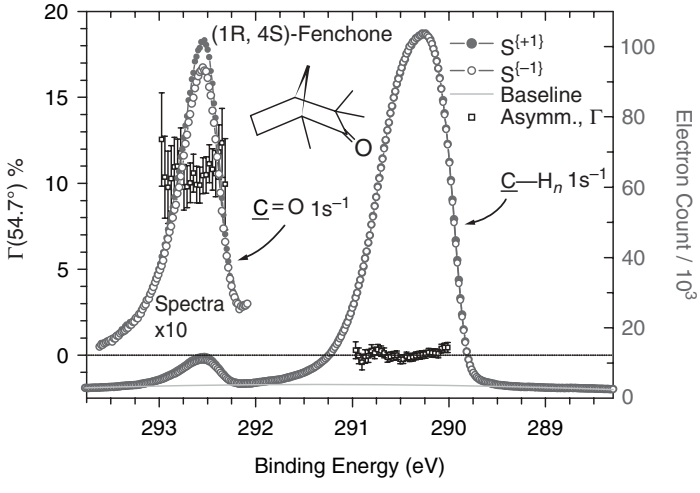

Figure 15.4. XPS of (1*R*, 4*S*)-fenchone recorded at a photon energy $h\nu = 299.5$ eV. The asymmetry, Γ, between peaks in the spectra $S^{\{+1\}}$ recorded with left-CPL and $S^{\{-1\}}$ recorded with right-CPL at 54.7° to the photon beam direction is also plotted (left-hand axis). (Redrawn from reference 16.)

individual spectra, $S^{\{\pm 1\}}$, that have been recorded with the two different helicities of the circularly polarized X-ray beam. While the main peak intensities appear to be identical, a difference arises for the carbonyl C atom peak, so that the dichroism for photoionization at this site is clearly visible in the expanded view (Figure 15.4). With due allowance in the data treatment to ensure that the observations made with either helicity are strictly comparable in terms of integrated photon flux etc. [16], and following removal of any achiral background signal, the asymmetry, $\Gamma(54.7^{\circ})$, defined in Eq. (15.9) is simply obtained from the normalized subtraction $S^{\{+1\}} - S^{\{-1\}}$. Values for this asymmetry are plotted point by point across the two XPS peaks in Figure 15.4. For the example given in this figure, it is seen that this asymmetry averages around 11% across the carbonyl peak. Then from Eq. (15.11), after factoring out the $\cos(54.7^{\circ})$ term, one estimates $2b_1^{\{+1\}}$ to be almost 0.2. This also, of course, indicates an expected magnitude approaching 20% for the forward–backward asymmetry factor, G_{AD} [Eq. 15.7], pertaining to the carbonyl C 1*s* electron angular distribution.

The conventional view of core XPS is that it provides essentially an elemental probe, the photoemission from each atomic site having a characteristic atomic binding energy that responds only weakly to the molecular environment via shifts induced by changes in the valence electron distribution of the molecule. In the present case, the carbonyl C 1*s* orbital can be considered to be spherical (thus achiral) and highly localized at a site which, although adjacent, is not itself one of the asymmetric carbons. From such a standpoint, the huge PECD displayed in the photoemission from the carbonyl site is all the more surprising, because the initial orbital would seem to be essentially unaware of the handedness of the molecular framework. In fact, this observation provides very clear evidence for the importance of final-state interactions—a scattering of the outgoing photoelectron off the chiral molecular framework—as the origin of the asymmetry in the asymptotic photoelectron angular distribution. This does not imply that the nature of the initial orbital is necessarily unimportant or makes no contribution (as will be clearly demonstrated in the valence region), but does indicate that PECD is likely to be sensitive to relatively long-range, delocalized interactions within the molecular system.

Therefore, successful theoretical modeling of PECD has to incorporate the final, continuum-state electron-scattering effects and thus go beyond nowadays routine bound-state electronic structure treatments. Although relevant computational approaches are not discussed further in this chapter, details may be found in, for example, references 5, 23, and 47.

Determinations of the PECD asymmetry, Γ, such as shown in Figure 15.4, were made for a range of photon energies just above the C K-edge and were repeated with the (1*S*, 4*R*)-fenchone enantiomer. The extracted values for the carbonyl C $1s^{-1}b_1^{\{+1\}}$ parameters are averaged over the relevant XPS band profile at each energy and then plotted in Figure 15.5. One sees a variation of the $b_1^{\{+1\}}$ parameter with photon energy (and correspondingly with electron kinetic energy) and also that the resulting PECD spectrum for the (1*R*)- enantiomer is reliably mirrored by that of the (1*S*)- enantiomer, as anticipated in the electric dipole treatment. This is in fact useful for corroborating the true *molecular* nature of the observed asymmetry, as any residual instrumental asymmetry or artefacts would not switch with sample exchange.

Qualitatively, one observes that from ~10 eV above the ionization threshold, the magnitude of the chiral asymmetry diminishes with further increase in the ejected electron's kinetic energy. Similar trends have been observed in a number of other studies. Such behavior can be roughly rationalized since it would be expected that slower emitted electrons will be more strongly scattered by the chiral molecular potential, whereas faster

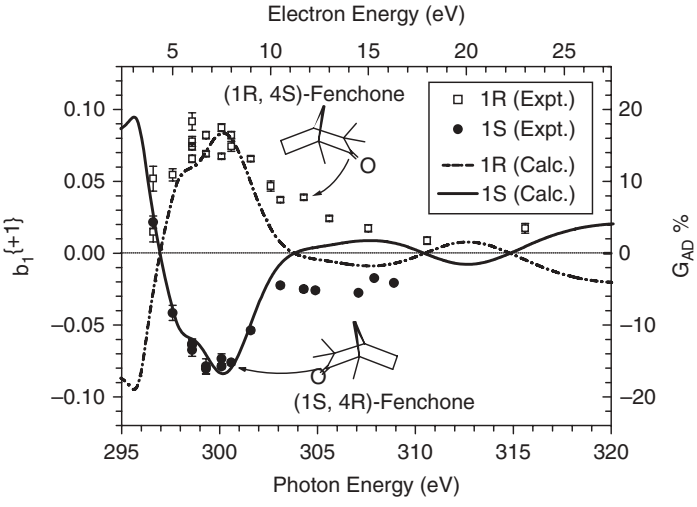

Figure 15.5. PECD for ionization of the carbonyl C = O C 1*s* electron of either enantiomer of fenchone. The experimental data points are presented as the chiral $b_1^{\{+1\}}$ parameters (left axis), although equivalent angular distribution asymmetry factors may be read off the right axis. The curves are theoretical predictions from a CMS-Xα calculation. (Redrawn from reference 16.)

electrons would be less strongly deviated as they pass out of the molecular vicinity. Nevertheless, some caution needs to be exercised in applying this as a statement of principle, because often the high-energy attenuation of the PECD is far from monotonic.

Figure 15.5 includes computed $b_1^{\{+1\}}$ parameter curves for either enantiomer, calculated using a continuum multiple-scattering (CMS-Xα) method [16]. Below 10 eV kinetic energy the theoretical treatment works well, with the calculations reproducing the sign, and indeed the magnitude, of the experimental data. This degree of theory–experiment concurrence would certainly be sufficient to allow a confident assignment of the absolute configuration of an unknown enantiomeric sample. The greater discrepancy that appears at higher energy, centered around 12.5 eV, can be tentatively ascribed to a continuum resonance state, by analogy with a similar feature observed in the closely related camphor molecule [47].

The above discussion has focused on the carbonyl C 1*s* ionization as the most favorable case. The strong core-electron binding energy shift at the carbonyl site means that it is fully separated from all other C $1s^{-1}$ features in the XPS and thus allows the PECD to be studied for a single, well-characterized, highly localized initial orbital. In contrast, only the net asymmetry of the other C $1s^{-1}$ ionizations can be recorded experimentally because all photoemission from these atomic sites is superimposed under the principal XPS peak. At the 299.5 eV photon energy shown in Figure 15.4 the composite $1s^{-1}$ asymmetry from the tetrahedral C atomic sites is essentially zero, although at other photon energies that were included in this study of fenchone [16] more varied behavior was observed. However, for now the large number of variables involved precludes fully quantitative modeling of this composite peak PECD.

15.4.1.2. Carvone. The enantiomers of the terpene molecule carvone provide a classic example of a pair of optical isomers having very different perceived odors. Carvone displays a simple carbon region XPS with a minor carbonyl C 1*s* photoemission peak shifted some 2 eV to higher binding energy from the principal photoemission line, which is again a superposition of the other saturated C atomic sites. Like the fenchone molecule considered above, this therefore provides an opportunity for the study of PECD from a single localized and well-characterized initial orbital. Unlike fenchone, carvone is a more flexible molecule that can adopt several distinct conformations.

It was already apparent in some of the earliest theoretical PECD calculations for the amino acid alanine that a very strong dependence on molecular conformation was predicted [25], a view reinforced by subsequent theoretical PECD calculations [19, 48, 49]. Indeed, the seemingly enhanced sensitivity to conformation of the PECD phenomenon has been a recurring feature of several more recent combined theoretical/experimental PECD investigations (e.g., references 2, 7, 8, 18, and 19). Carvone presents another opportunity to examine this facet.

A schematic for the (*S*)-carvone enantiomer and its conformer structures are shown in Figure 15.6. The six identified conformers are associated with positioning of the isopropenyl tail group, and they subdivide into those with either axial or equatorial structures. Within each subgroup, three rotational conformations of the tail group are possible. Generally the three equatorial conformers are expected to be the more stable due to the reduced steric hindrance between tail group and the ring. This expectation is confirmed by electronic structure calculations [9], the **Eq1** structure being found the most stable. Suggested thermal populations at the experimental temperature (~350 K) lie in the range 30% to 50% for **Eq1** and approximately 20% to 25% for **Eq2** or **Eq3**; the expected axial conformer populations total 5% to 25%. The uncertainty in these Boltzmann populations stems from the variations in results obtained with different computational methods, but in all cases it is clear that axial conformers are a minority population.

An experimental PECD spectrum of (*S*)-carvone was obtained following the same procedures as outlined for fenchone [9, 10]. Asymmetries were estimated from the difference spectra of the carbonyl C 1*s* XPS band recorded with alternating CPL over a range of photon energies in the 300 eV region. Values for the $b_1^{\{+1\}}$ parameters were then extracted as intensity-weighted averages formed over the band profile at each photon energy, and these are plotted as a function of energy in Figure 15.7.

Figure 15.8 shows individual carbonyl C $1s^{-1}$ PECD curves calculated using the CMS-Xα method for (*S*)-carvone conformers [9, 48]. There are, as anticipated, significant variations between the different conformers. A broad distinction can be drawn between the equatorial and axial conformer results; in the region centered around 10 eV electron

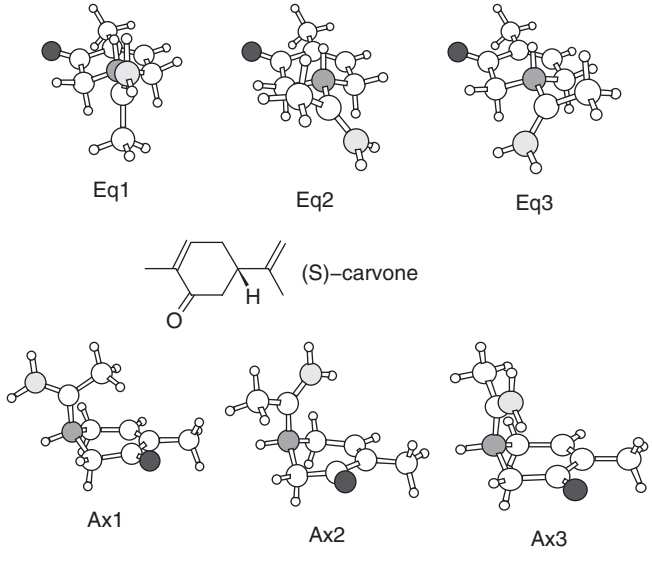

Figure 15.6. The conformers of (*S*)-carvone. The oxygen atom is shaded dark gray, the asymmetric carbon is shown in mid-gray, and the unsaturated carbon in the isopropenyl tail is reproduced in light gray for greater clarity. (Redrawn from reference 9.)

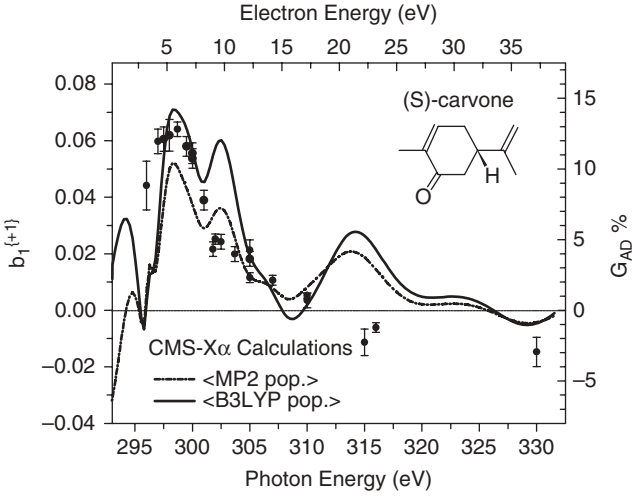

Figure 15.7. PECD for ionization of the carbonyl C = O C 1*s* electron from (*S*)-carvone. The data are presented as the chiral $b_1^{\{+1\}}$ parameters (left axis). Equivalent angular distribution asymmetry factors may be read off the right axis. The experimental data points are compared with theoretical CMS-Xα results in which the conformer averages follow thermal populations obtained from either MP2/6-31G* or B3LYP/6-31G* calculations. (Redrawn from reference 9.)

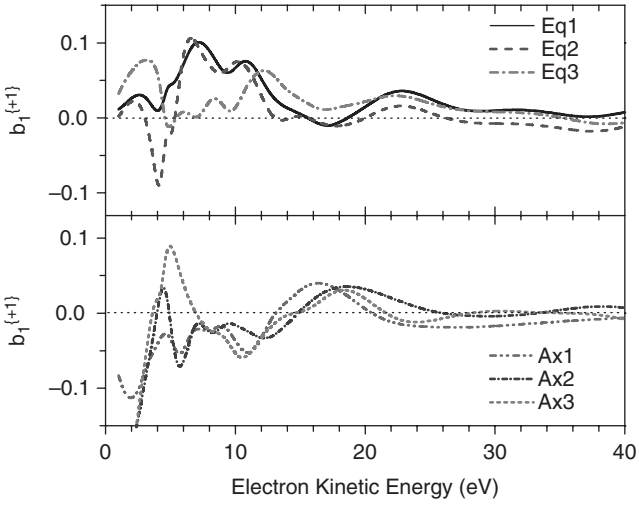

Figure 15.8. CMS-Xα calculations showing carbonyl C 1*s* PECD of individual conformers of (*S*)-carvone. (Redrawn from reference 9.)

kinetic energy the former are predicted to have positive $b_1^{\{+1\}}$ parameters, the latter negative. Even within the equatorial conformer subgroup (and also within the axial group) there are clear differences expected between conformers; in particular, around 10 eV the **Eq3** conformer curve is quite different from either the **Eq1** or **Eq2**. A simple visual comparison between the experimental PECD (Figure 15.7) and predicted conformer PECD (Figure 15.8) reveals the close similarity between experiment and **Eq1, Eq2** conformer calculations in the 10 eV region where the asymmetry peaks. These are, of course, the conformers expected to dominate a thermal sample. Conversely, the different sign of the experiment and the axial conformer predictions tend to rule out a dominant presence for these.

Somewhat more quantitatively, an appropriate 350 K thermal average of the different conformer curves can be formed using calculated energetics of the conformers to estimate thermal populations. Two such thermally averaged curves are included in Figure 15.7 for direct comparison with experiment, based upon alternative MP2/6-31G**

and B3LYP/6-31G** calculations for the relative stabilities [9]. Neither produces perfect agreement, but both corroborate the broad, semiquantitative conclusions of the previous paragraph.

Reflecting upon the differences seen, even amongst the equatorial conformers, it may seem remarkable that an initial electron, localized on the carbonyl group, should be so sensitive to rotational orientation of a substituent group on the opposite side of the molecular ring. Perhaps, however, the structural sensitivity of PECD is less surprising if, recalling above discussions of the importance of final state scattering in these localized carbonyl C $1s^1$ photoemissions, one considers that the processes studied are essentially akin to low-energy diffraction of electrons generated *in situ* from a point source. At another level, it has been argued that this enhanced structural sensitivity occurs because of the unique way that even very small shifts in the phase of the outgoing electron waves can make a significant contribution to the chiral term in the photoelectron angular distribution, Eq. (15.2) [1, 48]. Attenuation of scattering effects induced by small or remote structural changes is thus countered in the detailed photoionization dynamics, in a manner that is only seen for the chiral term.

15.4.2. Valence Shell PECD

15.4.2.1. Glycidol. The PECD of glycidol has been studied in both the core (O $1s^{-1}$, C $1s^{-1}$) [8] and valence [7] ionization regions; here we focus on the latter. Measurements were made using the velocity-map imaging method described above. Figure 15.9 shows the PECD of the *R*- and *S*-enantiomers, recorded at a photon energy of 21.2 eV. The equal magnitude, but opposite sign, of the two enantiomers' PECD is an obvious feature, and again it helps underscore the true molecular origin of the chiral asymmetry.

Also included in the figure, on the same energy scale but with arbitrary intensity scaling, are two corresponding photoelectron spectra. The first is the VMI spectrum, obtained from the radial intensity distribution of the same images from which the PECD was extracted. The normal VMI PES and PECD spectra are thus derived from the same data with, consequently, identical experimental conditions including energy resolution. The second PES is a He(I) spectrum (also $h\nu = 21.2$ eV), recorded in a separate instrument by scanning a dispersive electrostatic analyzer at a resolution estimated $\leq$50 meV [7]. This affords somewhat better energy resolution than VMI can achieve when, as here, it is asked to disperse a full $\sim$12 eV ($h\nu$−I.P.) energy range across the detector image.

The He(I) PES has several distinct bands, which have been assigned to the different valence orbital ionizations of glycidol [7]. In comparison, the more modest VMI resolution provides a spectrum that, though structured, lacks some of the distinctive peaks to be seen in the He(I) spectrum. It is then significant that the spectrum of the PECD displays more prominent structure than does the simultaneously recorded VMI PES. Using the He(I) spectrum as a guide to the expected positions of the individual orbital structure that must underlie the measured VMI curves, there is a clear correlation between some of the additional structure visible in the PECD and the expected orbital energies. The VMI PECD measurement yields, in effect, better resolution of the orbital structure than the accompanying VMI PES despite the identical energy dispersion.

A reason for this is found by considering the different characteristics of the data. While adjacent bands in the photoelectron spectra will typically have commensurate intensity, adjacent orbitals will have PECD that, at any given photon energy, may differ not only in absolute magnitude but also in sign. Moreover, away from any resonant

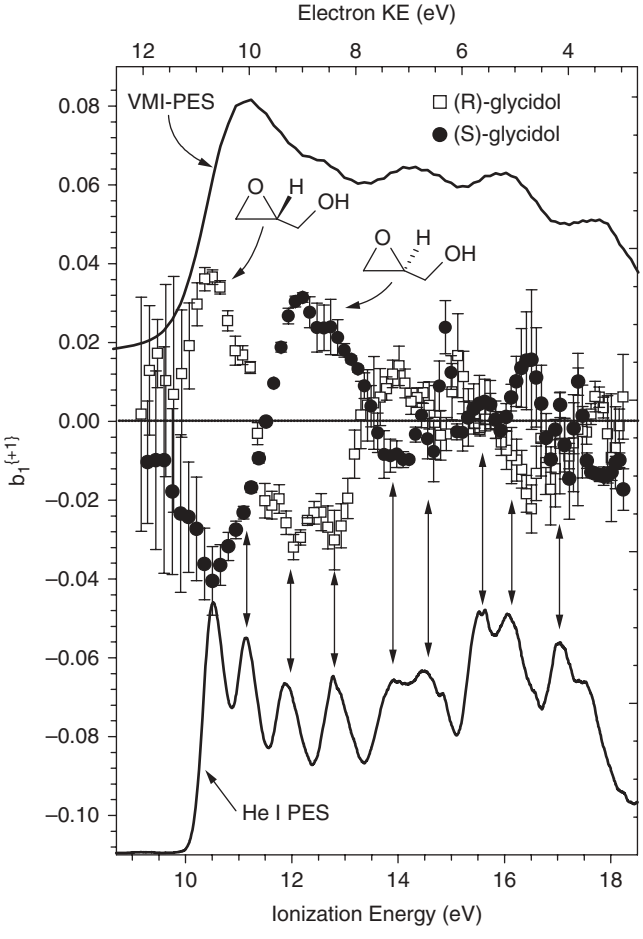

Figure 15.9. PECD for the (*R*-), (*S*-) enantiomers of glycidol, recorded at a photon energy of 21.2 eV. The PES derived from the same VMI images is plotted on the same energy scale above, and an He (I) PES is plotted below; both the latter have their intensity arbitrarily scaled. Arrows are used to guide the eye in tying together features in the PECD and He (I) spectra. (Redrawn from reference 7.)

behavior the photoelectron relative intensities will be only a very slowly varying function, of photon energy, while the PECD has regularly been found to vary much more rapidly.

Deconvolution of the PECD curves appearing in Figure 15.9 to extract the $b_1^{\{+1\}}$ parameter values associated with individual valence orbitals requires minimal effort. This can be repeated for VMI measurements made at different photon energies. An example of such $b_1^{\{+1\}}$ versus $h\nu$ data for the HOMO orbital is shown in Figure 15.10. The figure is drawn as for the *R*-enantiomer of glycidol. In fact, some of the data were obtained from measurements made with the *S*-enantiomer. These have been negated for plotting to eliminate the enantiomer mirroring as seen, for example, in Figure 15.9.

Equilibrium structures of gaseous glycidol have been investigated theoretically and experimentally [8, 50, 51]. Each of the two torsional angles, H-O_H-C-C and O_H-C-C-O_R (see Figure 15.11; here H and R subscripts are used to distinguish the hydroxyl and ring O atoms, respectively), can adopt gauche$^{\pm}$, or anti, positions, generating $3 \times 3 = 9$ possible conformers. The four lowest-energy conformers are drawn in Figure 15.11. Two of these, **C1**(g^+g^-) and **C2**(g^-g^+), are stabilized by intramolecular hydrogen bonding and are predicted to account for nearly all the population of a thermal sample of glycidol having an approximate 2:1 ratio of **C1** to **C2**. Experimental data are consistent with these predictions [50, 51].

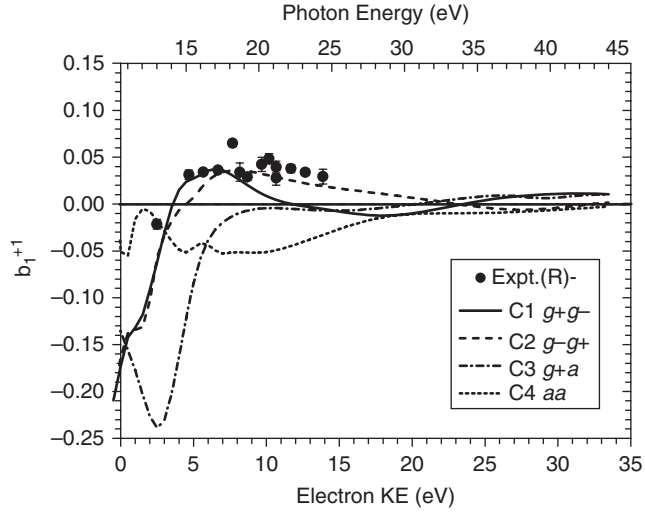

Figure 15.10. Glycidol HOMO orbital PECD as a function of energy. CMS-Xα calculations are shown for the four most stable conformers **C1**–**C4** (see Figure 15.11). (Redrawn from reference 7.)

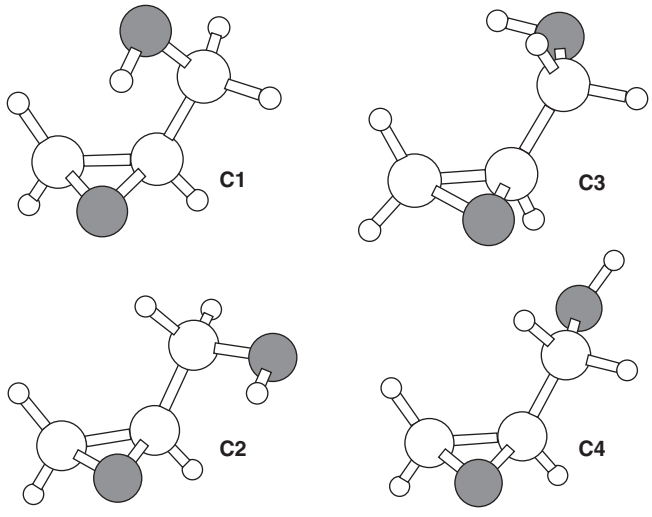

Figure 15.11. The four lowest-energy glycidol conformations, **C1**–**C4**. Note that the ground-state **C1** and next-lying **C2** structures are both stabilized by an intramolecular H-bonded ring structure formed from the hydroxyl group to the epoxy ring O atom. (Redrawn from reference [8].)

Figure 15.10 includes CMS-Xα calculations of the glycidol HOMO orbital PECD for each of these conformer structures **C1**–**C4**, which can thus be separately compared against experiment and one another. Again the differences predicted for the different conformers are quite striking. In particular, neither the **C3** nor **C4** PECD displays the same sign as the experimental observations in the key region around 10 eV electron kinetic energy. The comparison of the **C3** and **C4** calculated PECD with the experimental data thus appears to be sufficient to rule out a dominant contribution from either in the experimental sample; this, of course, is just as predicted from the calculated stabilities [7, 8] and by previous experimental observation [50, 51]. Extending such comparisons to the PECD observed for other orbitals with the relevant calculations for these, and other, conformer structures provides, in totality, convincing corroboration for the **C1**, and to a lesser extent **C2**, conformations as the dominant experimental structures [7, 8]. Further

refinements to the model, allowing for the intramolecular H bond in the ground-state conformation, lead to further improved agreement with experiment.

The differences seen between the predicted conformers' PECD merit further comment. Not only do the **C3**(g^+a) and **C4**(aa) display pronounced differences compared to experiment as seen in Figure 15.11, they also are quite distinct from one another. However, from Figure 15.11 it may be noticed that these structures differ, principally, in the positioning of the hydroxyl H atom. While the HOMO orbital of glycidol, which is the subject of the data in Figure 15.11, has some O *2p* character, it is relatively delocalized without any significant density at the hydroxyl H atom. Nevertheless, this H atom evidently exerts a profound influence on the chiral scattering dynamics of the emitted photoelectron. So while valence PECD data, such as that shown in Figure 15.9, clearly demonstrate an important effect stemming from *initial* state (orbital) influences, results here continue to show an important role for *final* state (scattering) in controlling the phenomenon.

15.4.2.2. endo-Borneol. Presentation of selected results obtained in a recent investigation [2] of the bicyclic terpene molecule endo-borneol allows further development of some of the themes introduced in preceding sections. Endo-borneol ($C_{10}H_{18}O$) is a camphor derivative, with the ketone, C═O, replaced by an alcohol, CH—OH. In consequence there are thus three low energy conformers of *endo*-borneol, corresponding to the minima expected in the C—OH torsional potential. One should by now expect that quite different PECD behavior would be predicted for the photoionization of these conformers and this indeed proves to be the case.

In consideration of the HOMO orbital PECD, recorded over a range from 10 eV to 24 eV, an equally weighted average of the three conformer predictions gave good agreement with the experimental data, significantly better than any one conformer PECD curve alone [2]. Electronic structure calculations that were performed at various levels of treatment indicated little effective difference in stability of the three *endo*-borneol conformers, such that an approximately 1:1:1 population ratio is a reasonable expectation for the vapor of this compound, supporting the deduction made from the experimental HOMO PECD data.

The full valence photoelectron spectrum of *endo*-borneol may be expected to be very heavily congested, due to the high density of electronic states. From calculations, one estimates that ~27 orbitals per conformer would have an ionization energy falling in the region below 22 eV. Allowing for shifts between the conformers' ionization energies, a high degree of intrinsically overlapping orbital band structure appears inevitable, such that experimental resolution of the majority of the individual orbital contributions is not feasible. Figure 15.12 shows the VMI results obtained for (*S*)-*endo*-borneol at a photon energy of 23.6 eV [2]. The VMI-PES has some structure, but it is clear that assignment to individual orbital bands cannot be contemplated.

Appearing on the same energy scale in Figure 15.12, are the PECD measurements. While the modulation of these across the energy range is a little greater than that of the PES, the individual data points must clearly still represent a superposition of contributions from several underlying orbitals. A full theoretical simulation has been attempted, based upon first simulating the PES of each conformer from calculated ionization potentials and photoionization cross sections and then folding the resulting stick spectrum with realistic instrumental and rovibrational width functions [2]. Calculated $b_1^{\{+1\}}$ parameters for each orbital are then blended with a relative weighting dictated by the intensity distribution of the simulated PES to generate an overall PECD curve from this purely theoretical model.

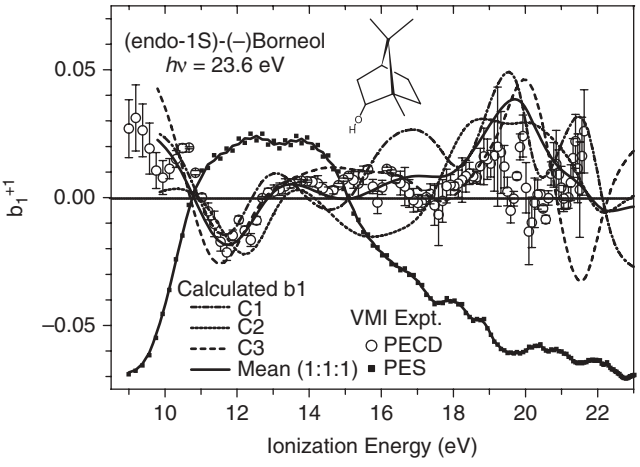

Figure 15.12. (*S*)-*endo*-borneol PECD and PES obtained from VMI images recorded at a fixed photon energy of 23.6 eV. The PES intensity has arbitrary scaling. Simulated PECD curves, considering contributions from all orbitals with predicted ionization thresholds below 23 eV, are shown for each individual conformer, along with their thermally averaged resultant. (Redrawn from reference 2.)

These conformer specific $b_1^{\{+1\}}$ curves are included in Figure 15.12, as is the 1:1:1 weighted average of these, as suggested by the probable conformer populations under the relevant experimental conditions. Considering the range of parameters required to produce the simulations, the agreement with experiment that these demonstrate, especially for the 1:1:1 conformer average, is very good. In particular, the latter accurately captures the absolute magnitude, and sign, of the experimental PECD over much of the electron energy range. These findings and conclusions were replicated in further individual simulations that spanned a range of different photon energies [2]. Photon-energy-dependent trends evident in the experiment appeared to be reliably reproduced in the theoretical model.

The overall quality of the theoretical model in reproducing the experimental PECD in a system of this complexity, without the introduction of empirical parameterization, is quite significant. The agreement in sign and magnitude, demonstrated over a range of electron and photon energies, provides a clear, unambiguous basis for assignment of absolute configuration from the calculation.

15.4.2.3. Camphor Dimers. Although inherently a gas-phase technique, the instrumentation developed for PECD measurements can readily be extended by use in conjunction with supersonic molecular beam sources. This greatly widens the opportunities for study—for example, by creating (a) partially solvated molecules and (b) van der Waals or hydrogen-bonded cluster species [52]. The last example selected for inclusion in this chapter highlights these capabilities and summarizes recent results obtained for homochiral dimers of camphor [20], which can ultimately be compared with benchmark results previously established for PECD in the monomer [11–13, 47].

In this context, a further capability of the technique can be introduced. Formation of the photoelectron is, of course, accompanied by creation of the corresponding residual ion (or possibly by fragmentation products thereof). In the VMI method, these photoions can be extracted by means of the same electrostatic source field applied to the electrons; the ions are accelerated in the opposite direction and pass through a time-of-flight mass analyzer before being detected [44, 53], so ion mass spectra and PES/PECD spectra of the sample can be recorded simultaneously. But the technique is more potent than just this. Using timing detectors, individual ion–electron pairs can be detected in delayed coincidence. The temporal correlation thus established, with allowance for a longer flight

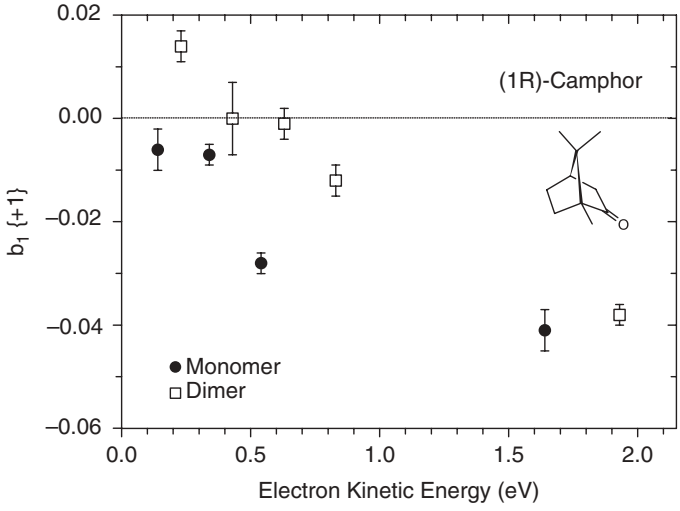

Figure 15.13. Mean PECD recorded for the HOMO band regions of the monomer and dimer of (*R*)-camphor, displayed as a function of increasing electron energy (i.e., the excess of photon energy over the respective adiabatic ionization potentials). (Redrawn from reference 20.)

time of the ion from the source to the ion detector, identifies an ion and electron originating from the same molecular photoionization event. Consequently it is possible, for example, to filter out (usually by post-processing software) all but those electrons formed in coincidence with a selected ion mass, thus recording the PES/PECD spectra from a selected molecular mass.

Coincidence detection schemes have an obvious advantage for the present context, in distinguishing the PECD signals from dimer and monomer camphor species. A general difficulty arises when fragmentation of the monomer and/or dimer ion occurs on a short timescale before mass analysis of the ion. If this cannot be positively ruled out, there is thus some ambiguity whether the recorded mass is that of the parent neutral species that was ionized, or merely a fragment thereof. The latter could potentially derive from either monomer or a larger n-mer species. In this camphor investigation, however, the cooling provided in the supersonic beam source additionally allowed vibrationally resolved photoionization spectra to be recorded [20], even for such a large system. This, together with careful analysis of the threshold yield behavior allowed clear, unambiguous selection of distinct monomer and dimer photoionization behavior over a range of 2 eV from threshold to be established.

The $b_1^{\{+1\}}$ parameters derived for low-energy HOMO band photoionization of the homochiral $R{-}R$ camphor dimer species are compared with those of the (*R*)-camphor monomer in Figure 15.13. Although the data are at present limited, there are clear differences in the PECD of the monomer and dimer. No such differences were observed in the more traditional angular distribution term, the β parameter, measured in the same experiments [20]. The chiral measurement does, therefore, provide the prospect for a greater sensitivity to clustering reactions in this and, by extension, other systems.

15.5. PROSPECTS

The requirement for a source of circularly polarized ionizing radiation has, to date, limited experimental investigations to a small number of groups with access to appropriate synchrotron radiation sources. The focus of investigations in such circumstances has been to establish the underlying quantum physics rather than development of applications,

although potential applications in breath odor analysis initially stimulated this author's interest in the topic. The principles and understanding of the phenomenon are now firmly established, allowing one to look to applications founded on a secure theoretical basis. The use of laboratory-based (laser), circularly polarized photoionization sources would be a major step in making the technique more widely available, and this can now be foreseen.

The principles of the phenomenon, and theoretical modeling built on these, are sufficiently well established to allow confident treatment of new systems, with the possibility to identify structural conformation and absolute configuration from a theory–experiment comparison. These comparisons are not clouded by any uncertainty in the induced chirality and response of a solvent shell. The range of photon energies that may be examined is enormous, and some elemental sensitivity can be achieved by measurement near an atomic edge. Alternatively, a 2D-mapping of PECD response versus photon energy versus electron energy (target orbital) is capable of providing a very richly detailed response map, which could prove to have some "finger print" capabilities even before quantitative modeling is performed.

Simultaneous recording of a sample's mass spectrum could well be convenient for proposed analytical applications, perhaps in conjunction with resonance-enhanced laser multiphoton ionization schemes that offer additional selectivity in the photoionization analysis of mixtures. More explicitly, electron–ion coincidence detection (or covariance mapping [54, 55]) could be adopted to allow PECD information to be associated to specific ion mass-selected channels.

A prospect that is already now being actively pursued is the use of molecular beam sources to generate and sample cluster and micro-solvated species. The unique capabilities of PECD suggest a role in probing chiral molecular recognition phenomena, a topic of significant current interest.

Finally, the extraordinary magnitude of the chiral asymmetry exhibited in the phenomenon suggests that it perhaps ought to be considered in astrophysical models speculating upon terrestrial homochirality [56].

ACKNOWLEDGMENTS

The author wishes to acknowledge the great role played by co-workers in pursuing this work. Most important is the ongoing collaboration with Laurent Nahon and with my former student and colleague Gustavo Garcia at the Synchrotron Soleil (and formerly LURE). Uwe Hergenhahn, and numerous former members of his group, especially Emma Rennie, were likewise central in establishing the core ionization experiments at BESSY. Mauro Stener has also been helpful in comparative benchmarking of our alternative computational methods. Finally, members of my own research group, past and present, have been deeply involved in these investigations, particularly Gustavo Garcia, Chris Harding, and Steven Daly.

REFERENCES

1. I. Powis, *Adv. Chem. Phys*. **2008**, *138*, 267–329.
2. G. A. Garcia, H. Soldi-Lose, L. Nahon, I. Powis, *J. Phys. Chem. A* **2010**, *114*, 847–853.
3. A. J. Taylor, *Crit. Rev. Food Sci. Nutr*. **1996**, *36*, 765–784.

4. S. Stranges, S. Turchini, M. Alagia, G. Alberti, G. Contini, P. Decleva, G. Fronzoni, M. Stener, N. Zema, T. Prosperi, *J. Chem. Phys*. **2005**, *122*, 244303.
5. M. Stener, G. Fronzoni, D. Di Tommaso, P. Decleva, *J. Chem. Phys*. **2004**, *120*, 3284–3296.
6. S. Turchini, N. Zema, G. Contini, G. Alberti, M. Alagia, S. Stranges, G. Fronzoni, M. Stener, P. Decleva, T. Prosperi, *Phys. Rev. A* **2004**, *70*, art. no.014502.
7. G. A. Garcia, L. Nahon, C. J. Harding, I. Powis, *Phys. Chem. Chem. Phys*. **2008**, *10*, 1628–1639.
8. I. Powis, C. J. Harding, S. Barth, S. Joshi, V. Ulrich, U. Hergenhahn, *Phys. Rev. A* **2008**, *78*.
9. I. Powis, *Chirality* **2008**, *20*, 961–968.
10. C. J. Harding, E. A. Mikajlo, I. Powis, S. Barth, S. Joshi, V. Ulrich, U. Hergenhahn, *J. Chem. Phys*. **2005**, *123*, 234310.
11. T. Lischke, N. Böwering, B. Schmidtke, N. Müller, T. Khalil, U. Heinzmann, *Phys. Rev. A* **2004**, *70*, art. no.022507.
12. L. Nahon, G. A. Garcia, C. J. Harding, E. A. Mikajlo, I. Powis, *J. Chem. Phys*. **2006**, *125*, 114309.
13. G. A. Garcia, L. Nahon, M. Lebech, J. C. Houver, D. Dowek, I. Powis, *J. Chem. Phys*. **2003**, *119*, 8781–8784.
14. U. Hergenhahn, E. E. Rennie, O. Kugeler, S. Marburger, T. Lischke, I. Powis, G. Garcia, *J. Chem. Phys*. **2004**, *120*, 4553–4556.
15. I. Powis, C. J. Harding, G. A. Garcia, L. Nahon, *ChemPhysChem* **2008**, *9*, 475–483.
16. V. Ulrich, S. Barth, S. Joshi, U. Hergenhahn, E. A. Mikajlo, C. J. Harding, I. Powis, *J. Phys. Chem. A* **2008**, *112*, 3544–3549.
17. N. Böwering, T. Lischke, B. Schmidtke, N. Müller, T. Khalil, U. Heinzmann, *Phys. Rev. Lett*. **2001**, *86*, 1187–1190.
18. S. Turchini, D. Catone, G. Contini, N. Zema, S. Irrera, M. Stener, D. D. Tommaso, P. Decleva, T. Prosperi, *ChemPhysChem* **2009**, *10*, 1839–1846.
19. A. Giardini, D. Catone, S. Stranges, et al., *ChemPhysChem* **2005**, *6*, 1164–1168.
20. L. Nahon, G. A. Garcia, H. Soldi-Lose, S. Daly, I. Powis, *Phys. Rev. A* **2010**, *82*, art. no. 032514.
21. Powis, I., Daly, S., Garcia, G. A., Nahon, L., in preparation.
22. B. Ritchie, *Phys. Rev. A* **1976**, *13*, 1411–1415.
23. I. Powis, *J. Chem. Phys*. **2000**, *112*, 301–310.
24. B. Ritchie, B. R. Tambe, *J. Chem. Phys*. **1978**, *68*, 755–761.
25. I. Powis, *J. Phys. Chem. A* **2000**, *104*, 878–882.
26. B. Ritchie, *Phys. Rev. A* **1976**, *14*, 359–362.
27. G. Margaritondo, *Elements of Synchrotron Light: For Biology, Chemistry, and Medical Research*, Oxford University Press, Oxford, **2002**.
28. J. A. Clarke, *The Science and Technology of Undulators and Wigglers*, Oxford University Press, Oxford, **2004**.
29. H. Onuki, P. Elleaume, *Undulators, Wigglers and Their Applications*, Taylor and Francis CRC Press, London, **2003**.
30. H. Onuki, N. Saito, T. Saito, *Appl. Phys. Lett*. **1988**, *52*, 173–175.
31. F. Schäfers, H. C. Mertins, A. Gaupp, et al., *Appl. Opt*. **1999**, *38*, 4074–4088.
32. L. Nahon, F. Polack, B. Lagarde, R. Thissen, C. Alcaraz, O. Dutuit, K. Ito, *Nucl. Instrum. Methods Phys. Res. Sect. A Accel. Spectrom. Dect. Assoc. Equip*. **2001**, *467*, 453–457.
33. C. Alcaraz, R. Thissen, M. Compin, A. Jolly, M. Drescher, L. Nahon, *SPIE* **1999**, *3773*, 250–261.
34. A. Derossi, F. Lama, M. Piacentini, T. Prosperi, N. Zema, *Rev. Sci. Inst*. **1995**, *66*, 1718–1720.

35. R. P. Walker, B. Diviacco, *Rev. Sci. Inst*. **1992**, *63*, 332–335.
36. M. R. Weiss, R. Follath, K. J. S. Sawhney, et al., *Nucl. Instrum. Methods Phys. Res. A* **2001**, *467*, 449–452.
37. J. Bahrdt, W. Frentrup, A. Gaupp, M. Scheer, W. Gudat, G. Ingold, S. Sasaki, *Nucl. Instrum. Methods Phys. Res. A* **2001**, *467*, 21–29.
38. L. Nahon, C. Alcaraz, *Applied Optics* **2004**, *43*, 1024–1037.
39. L. Nahon, R. Thissen, C. Alcaraz, M. Corlier, P. Peaupardin, F. Marteau, O. Marcouille, P. Brunelle, *Nucl. Instrum. Methods Phys. Res. A* **2000**, *447*, 569–586.
40. `http://www.synchrotron-soleil.fr/Recherche/LignesLumiere/DESIRS`.
41. K. N. Huang, *Phys. Rev. A* **1980**, *22*, 223–239.
42. B. J. Whitaker, *Imaging in Molecular Dynamics*, Cambridge University Press, Cambridge, **2003**.
43. A. T. J. B. Eppink, D. H. Parker, *Rev. Sci. Inst*. **1997**, *68*, 3477–3484.
44. G. A. Garcia, L. Nahon, C. J. Harding, E. A. Mikajlo, I. Powis, *Rev. Sci. Inst*. **2005**, *76*, 053302.
45. S. Daly, G. Garcia, L. Nahon and I. Powis, unpublished work.
46. G. A. Garcia, L. Nahon, I. Powis, *Rev. Sci. Inst*. **2004**, *75*, 4989–4996.
47. M. Stener, D. D. Tommaso, G. Fronzoni, P. Decleva, I. Powis, *J. Chem. Phys*. **2006**, *124*, 024326.
48. C. J. Harding, I. Powis, *J. Chem. Phys*. **2006**, *125*, 234306.
49. D. Di Tommaso, M. Stener, G. Fronzoni, P. Decleva, *ChemPhysChem* **2006**, *7*, 924–934.
50. N. Borho, M. A. Suhm, *Phys. Chem. Chem. Phys*. **2002**, *4*, 2721–2732.
51. K. M. Marstokk, H. Mollendal, Y. Stenstrom, *Acta Chem. Scand*. **1992**, *46*, 432–441.
52. M. Kappes, S. Leutwyler, in *Atomic and Molecular Beam Methods, Part 1*., G. Scoles, ed., Oxford University Press, Oxford, **1988**, pp. 380–415.
53. G. A. Garcia, H. Soldi-Lose, L. Nahon, *Rev. Sci. Inst*. **2009**, *80*, Art. no. 023102.
54. D. A. Card, E. S. Wisniewski, D. E. Folmer, A. W. Castleman, Jr., *Int. J. Mass. Spec*. **2003**, *223–224*, 355–363.
55. L. J. Frasinski, K. Codling, P. A. Hatherly, *Science* **1989**, *246*, 1029–1031.
56. L. Nahon, G. Garcia, I. Powis, U. Meierhenrich, A. Brack, *Proc. SPIE Int. Soc. Opt. Eng*. **2007**, *6694*, 669403.

16

MAGNETOCHIRAL DICHROISM AND BIREFRINGENCE

G. L. J. A. Rikken

16.1. INTRODUCTION

Natural circular birefringence (NCB) or natural optical activity, which occurs exclusively in chiral media, and magnetic circular birefringence (MCB), better known as the Faraday effect, which is induced by a longitudinal magnetic field, show a strong phenomenological resemblance. In both cases, the direction of polarization of linearly polarized light is rotated during propagation through the medium. Interpreting magnetic optical activity as a sign of magnetically induced chirality, Pasteur was the first to search—in vain—for an enantioselective effect of magnetic fields [1]. These searches were partly motivated by the hope of finding an explanation for the homochirality of life [2]. Although several positive results were reported, all were revoked or could not be confirmed [3, 4].

The symmetry requirements for any process to yield a chiral result were formulated by Barron, who pointed out that no enantioselectivity of magnetic fields *per se* is allowed [5, 6]. In 1962 the first implicit prediction appeared of a cross effect between natural and magnetic optical activity, which discriminates between the two enantiomers of chiral molecules [7], but the author apparently did not recognize the importance of his result. Later on, this was followed independently by a prediction of magnetospatial dispersion in noncentrosymmetric crystalline materials [8]. This cross effect has been called magnetochiral anisotropy and has since then been predicted independently several more times [9–12]. Its existence can be most easily appreciated by expanding the dielectric tensor of a chiral medium subject to a magnetic field to first order in the wavevector k and

Comprehensive Chiroptical Spectroscopy, Volume 1: Instrumentation, Methodologies, and Theoretical Simulations, First Edition. Edited by N. Berova, P. L. Polavarapu, K. Nakanishi, and R. W. Woody.
© 2012 John Wiley & Sons, Inc. Published 2012 by John Wiley & Sons, Inc.

magnetic field B, retaining all symmetry-allowed terms [8]:

$$\varepsilon_{ij}(\omega, k, B) = \varepsilon_{ij}(\omega) + \alpha_{ijl}(\omega)k_l + \beta_{ijl}(\omega)B_l + \gamma_{ijlm}(\omega)k_l B_m. \tag{16.1}$$

For high-symmetry media like gases, liquids, cubic crystals, or uniaxial crystals with their optical axis parallel to B, and the propagation direction of the light parallel to B, the optical eigenmodes are right- and left-handed circularly polarized waves, denoted by $+$ and $-$. For such media, Eq. (16.1) can be simplified to [8, 9]

$$\varepsilon_{\pm}(\omega, k, B) = \varepsilon(\omega) \pm \alpha^{D/L}(\omega)k \pm \beta(\omega)B + \gamma^{D/L}(\omega)k \cdot B, \tag{16.2}$$

where $x^D(\omega) = -x^L(\omega)$ refers to right (D)- and left (L)-handed media, α describes natural optical activity and β describes magnetic optical activity. The material parameters $\varepsilon, \alpha, \beta$, and γ are all generally complex-valued, and we will denote their real and imaginary parts by x' and x'', respectively. From the above equation, the essential features of MChA become immediately clear. They are (i) the dependence on the *relative orientation* of k and B, (ii) the dependence on the handedness of the chiral medium (i.e., *enantioselectivity*), and (iii) the *independence* of the polarization state of the light. A simple, intuitive physical picture behind MChA is that any spinning particle, which also moves parallel to its rotation axis, is a chiral object [5]. An electron in a magnetic field is spinning due to the induction of a net spin or orbital angular momentum by the field. When it moves parallel to the magnetic field—for example, because it has absorbed linear momentum from a photon or an external static electric field—it is chiral, and its interaction with the chiral geometry of the molecule depends on the relative handedness of the electronic motion and the molecular framework.

Baranova and co-workers were the first to present a simple microscopic model [10] that can give an order-of-magnitude estimate for MChA in optical absorption. It is an extension of the classical Becquerel model for NCB [13] and it interprets MChA as a result of the Larmor precession in NCB. Baranova and co-workers find (CGS units)

$$\gamma(\omega) = \frac{e}{2mc}\frac{\partial \alpha}{\partial \omega}, \tag{16.3}$$

where e and m are the electron charge and mass. When studying NCD or MCD, it is convenient to normalize the dichroism by the normal absorption in dimensionless dissymmetry factors $g \equiv 2(A_+ - A_-)/(A_+ + A_-)$, where $A_\pm$ is the optical extinction coefficient for right/left-circularly polarized light. If the absorption strength is not too large (i.e., $\varepsilon'_\pm \gg \varepsilon''_\pm$), the dissymmetry factors for NCD and MCD can be simply expressed in the imaginary parts of the terms of Eq. (16.2):

$$g_{NCD} = \frac{2\alpha'' k}{\varepsilon''}, \tag{16.4}$$

$$g_{MCD} = \frac{2\beta'' B}{\varepsilon''}. \tag{16.5}$$

Here we define the magnetochiral anisotropy factor similarly:

$$g_{MChA} \equiv 2\frac{A(B \uparrow\uparrow k) - A(B \uparrow\downarrow k)}{A(B \uparrow\uparrow k) + A(B \uparrow\downarrow k)} = \frac{2\gamma'' kB}{\varepsilon''}. \tag{16.6}$$

The g_{NCD} is usually quite constant across one given optical transition. Then we can write $\alpha''(\omega) \equiv C \cdot \varepsilon''(\omega)$, where C is a constant. Using the classical Becquerel result $\beta(\omega) = e/2mc \cdot \partial\varepsilon/\partial\omega$, our definition for g_{MChA} leads to

$$g_{MChA} = \frac{eCkB}{mc\varepsilon''} \frac{\partial\varepsilon''}{\partial\omega} = g_{NCD} g_{MCD}/2. \tag{16.7}$$

This simple model therefore gives as an estimate for the relative strength of MChA in absorption the product of the relative strengths of NCD and MCD, a result that seems in line with physical intuition for a cross effect. A more sophisticated model is given in Chapter 1 by G. H. Wagnière. A detailed molecular theory for MChA in molecular liquids and gases has been formulated for the first time by Barron and Vbrancich [14]. It requires complete knowledge of all molecular transition moments involved and therefore cannot be easily used to obtain quantitative predictions. More recently, the first *ab initio* calculations of MChA in simple molecules have appeared [15, 16].

Before continuing, it should be noted that the words "birefringence" and "dichroism" in the names of these effects is confusing, as these terms are usually reserved to differences for different optical polarizations in refractive index and absorption coefficient, respectively. More adequate names would be "magnetochiral nonreciprocal refraction" and "magnetochiral nonreciprocal absorption." However, in the following we will adopt the historically accepted terminology.

16.2. MChD IN LUMINESCENCE

Although there always seemed to be theoretical unanimity on the existence of magnetochiral anisotropy, it had not been observed experimentally until a few years ago. One of the reasons is certainly that MChA is always accompanied by MCD and NCD, which complicates its unequivocal experimental observation. It is therefore essential to try to devise experiments that are intrinsically insensitive to the presence of these two unwanted effects. We will see below that that is not always possible. For a claim of an observation of MChA to be credible, it is therefore crucial that all fundamental characteristics of the effect are experimentally confirmed. Furthermore, as the above arguments showed, MChA is a product of magnetic and chiral effects on the optical properties of the systems. As each of them individually is in general not very strong, it will be intuitively clear that the MChA effect will usually be very weak and thus difficult to observe. The best chances for its observation are therefore provided by systems in which both the magnetic field and the chirality have simultaneously a relatively large influence on the optical properties.

The most strongly chiral optical transitions reported in literature are the $^5D_0 \rightarrow {}^7F_{1,2}$ luminescent transitions in tris(3-trifluoroacetyl-(±)-camphorato) europium(III) complexes (Eu((±)tfc)$_3$). Although some discussion exists on the exact value of their anisotropy factor, it is close to unity. These transitions also have been shown to have a considerable MCD. According to the argument above, such complexes are therefore likely candidates to show a significant magnetochiral effect. These transitions are most conveniently studied in luminescence, because the $^7F_{1,2}$ level is hardly populated at room temperature, and the absorption transition $^7F_{1,2} \rightarrow {}^5D_0$ has therefore very low extinction, whereas its luminescence can be efficiently excited by exciting the ligands, which have a strong and broad UV absorption and can transfer this excitation to the Eu ion. An additional advantage of these transitions is that no self-absorption of the luminescence occurs for realistic

sample sizes. Such a self-absorption would have severely complicated the quantitative analysis because it would depend on handedness, polarization, and magnetic field.

The experiment performed by us to observe MChA measures the difference in the luminescence intensity of the $^5D_0 \rightarrow {}^7F_{1,2}$ transition in the directions parallel and antiparallel to B [17, 18] (Figure 16.1) of a solution of one handedness of the complex in deuterated dimethylsulfoxide, in which the largest NCD has been observed. The luminescence is captured by optical fibers and guided to monochromators, after which it is detected by photodiodes. Because such fibers have a finite numerical aperture (in our case 0.45), they also capture light that is not exactly parallel or antiparallel to the field. This will reduce somewhat the observed value of the MChA. In order to increase sensitivity, the magnetic field is alternated and the intensity difference $I_{\widehat{B}\uparrow\uparrow\widehat{k}} - I_{\widehat{B}\uparrow\downarrow\widehat{k}}$ as given by the difference between the two photodiode signals is phase-sensitively detected by a lock-in amplifier. Factors related to excitation intensity, complex concentration, and sample geometry are eliminated by dividing the lock-in output by the total, static luminescence signal, as given by the sum of the two photodiode signals. To avoid problems with MCD, the luminescence excitation was done along the direction perpendicular to the magnetic field, with unpolarized light from a UV lamp. The magnetochiral luminescence anisotropy factor g_{MChA} can then be expressed as

$$g_{MChA} = \frac{\frac{\partial}{\partial B}(I_{\widehat{B}\uparrow\uparrow\widehat{k}} - I_{\widehat{B}\uparrow\downarrow\widehat{k}})}{I_{\widehat{B}\uparrow\uparrow\widehat{k}} + I_{\widehat{B}\uparrow\downarrow\widehat{k}}} B. \tag{16.8}$$

Figure 16.2 shows the experimental results for g_{MChA} for the two enantiomers of the complex, showing significant MChA at the two transitions $^5D_0 \rightarrow {}^7F_1$ and $^5D_0 \rightarrow {}^7F_2$. An essential characteristic of MChA is that g_{MChA} should be of opposite sign for the two enantiomers, as observed. The results shown in the inset confirm the expected linear magnetic field dependence of g_{MChA}. Figure 16.2 therefore constitutes the complete proof for the existence of MChA in luminescence and all of its characteristics. The Baranova model Eq. (16.7), using the reported values for MCD and NCD for these

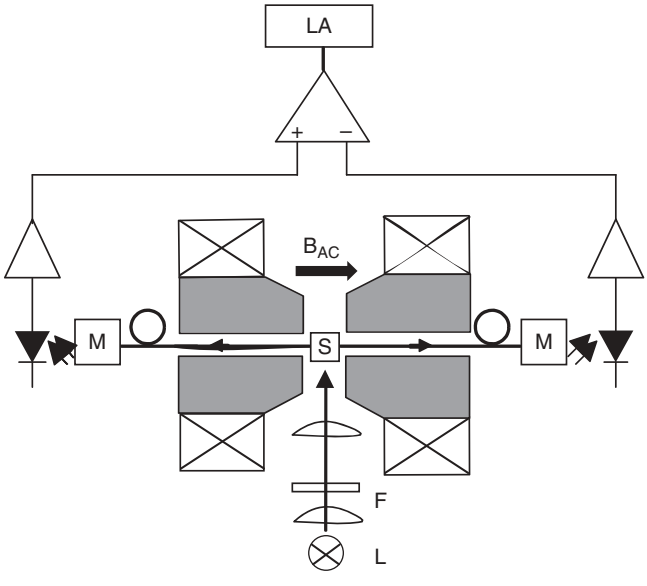

Figure 16.1. Schematic setup for detecting magnetochiral luminescence anisotropy. Sample (S) is excited around 350 nm with filtered (F), unpolarized light from a mercury-discharge lamp (L). Luminescence is collected in the directions parallel and antiparallel to the magnetic field by optical fibers (numerical aperture 0.47), specific emission wavelengths are selected by a grating monochromator (M, spectral resolution 2 nm), and detected by silicon photodiodes. The intensity difference between the two directions is phase-sensitively detected by a lock-in amplifier (LA) at the frequency of 0.9 Hz at which the magnetic field is alternated. (Redrawn from reference 17.)

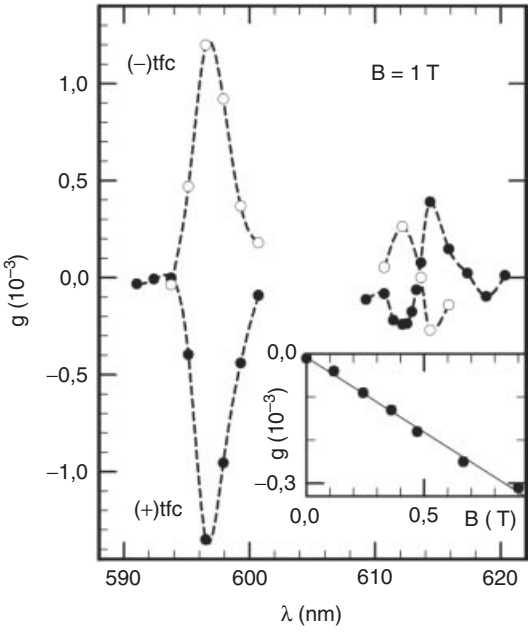

Figure 16.2. Magnetochiral luminescence anisotropy of Eu((±)tfc)$_3$ complexes, dissolved in deuterated dimethyl sulfoxide (5% wt/wt), as a function of luminescence wavelength, with excitation around 350 nm. The (alternating) magnetic field strength was 0.9 T. Filled symbols represent the Eu((+)tfc)$_3$ complex; open symbols represent its enantiomer, the Eu((−)tfc)$_3$ complex. Dashed lines are only meant to guide the eye. The inset shows the magnetochiral anisotropy of the Eu((−)tfc)$_3$ complex as a function of magnetic field strength, excitation around 350 nm, luminescence detected at 615.8 nm. Solid line is a linear fit. (Redrawn from reference 17.)

transitions, predicts the anisotropy factor to be $g_{MChA}/B \approx 5.10^{-3}T^{-1}$ for the $^5D_0 \rightarrow {}^7F_1$ transition and $g_{MChA}/B \approx 4.10^{-4}T^{-1}$ for the $^5D_0 \rightarrow {}^7F_2$ transition, in reasonable agreement with our observations. This simple model therefore seems to be useful to find order of magnitude estimates of MChA.

The results above represent the first unequivocal evidence for the existence of MChA in luminescence. More recently, MChA has also been observed in refraction [19, 20] and in absorption [21, 22], as discussed below.

16.3. MChD IN OPTICAL ABSORPTION

The absorption of unpolarized light by a chiral medium with a dielectric constant as given by Eq. (16.2) is most readily calculated by considering linearly polarized light, which can be decomposed into two circularly polarized waves of the same amplitude and opposite handedness. If $\varepsilon'_{\pm} \gg \varepsilon''_{\pm}, |\alpha k|, |\beta B|, |\gamma kB|$ and neglecting reflection, the intensity transmission coefficient T for linearly polarized light incident on such a medium with thickness L is found to be

$$T(\omega, k, B) = \exp\left\{-kL\left(2n'' + \frac{\gamma'' k \cdot B}{n'}\right)\right\} \cosh\left\{\frac{kL}{n'}(\alpha'' k + \beta'' B)\right\} \tag{16.9}$$

where $n' + in'' \equiv \sqrt{\varepsilon}$. This result holds for an arbitrary linear polarization, and therefore also for unpolarized light, and takes into account the change of the polarization state of the light on its path through the sample. The weak character of MChD suggests that the best method for its detection would be using an alternating magnetic field and phase-sensitive detection of the modulation of the transmitted intensity. When alternating the magnetic field at a frequency Ω and using Eq. (16.9), one finds the following for the

ratio between the modulated transmitted intensity I_Ω and the static transmitted intensity I_0, for $I_\Omega \ll I_0$:

$$\frac{I_\Omega}{I_0} = -\frac{kBL}{\sqrt{2}n'}\left(\gamma'' k - \beta'' \tanh\frac{\alpha'' k^2 L}{n'}\right). \tag{16.10}$$

The first term on the right-hand side represents the pure magnetochiral anisotropy in absorption. The second term stems from a cascading of natural and magnetic circular dichroism. Cascading occurs because NCD creates an excess of one circularly polarized component in the initially unpolarized light. Because of this excess, the MCD then leads to a transmitted intensity modulation at Ω. This cascaded MChD shows all the essential features of MChD given above, but can be discriminated from the pure effect by its dependence on the sample thickness and on the concentration of the active species. The cascaded effect would, for instance, occur in a binary mixture of molecules, one of which shows strong NCD while the other has strong MCD. Because both materials with $g_{NCD} > 0.1$ and materials with $g_{MCD} > 0.1T^{-1}$ are known, it is possible that a quite strong cascaded MChA could be observed in mixtures of such materials.

We have studied the chiral uniaxial crystal $\alpha - NiSO_4 \cdot 6H_2O$, because of its very large g_{NCD} and its reasonably large g_{MCD} [21]. Because of the weakly allowed character of the visible and near-infrared optical transitions of the $[Ni(OH_2)_6]^{2+}$ complex, $\alpha' k, \beta' B, \gamma' kB \ll \varepsilon'$, and the analysis outlined above should apply quantitatively. The handedness of each crystal was determined by measuring its NCD, and the MCD was found to be the same for the two crystal enantiomers. The transmission of the crystals, with their optical axes and the propagation direction of the light parallel to B, is measured with unpolarized light, with the magnetic field alternating and the transmitted intensity modulation being phase-sensitively detected. The ratio between the modulated intensity and the static intensity is equal to $\Delta A_{MChA} \cdot L \cdot B$, where

$$\Delta A_{MChA} = (\gamma'' k^2 - \beta'' k \tanh\tfrac{\alpha'' k^2 L}{n'})/\sqrt{2}n'. \tag{16.11}$$

Figure 16.3a shows the experimental spectra for ΔA_{MChA} for two crystals of opposite handedness, proving the essential characteristic of MChD that ΔA_{MChA} should be of opposite sign for the two enantiomers. Also shown is the cascaded MChD, calculated from the second term in Eqs. (16.10) and (16.11), using the observed NCD and MCD. From both the magnitude and lineshape of this calculated cascaded contribution to the MChD, it is clear that $\alpha - NiSO_4 \cdot 6H_2O$ shows predominantly the pure effect. The prediction for MChD on the basis of the Baranova model is also shown in Figure 16.3a, although the MCD of $\alpha - NiSO_4 \cdot 6H_2O$ does strictly speaking not fulfill the validity requirements for this model. The lineshape is evidently not correct, but the predicted magnitude agrees well with the experimental results, again confirming the usefulness of this simple model and the validity of its underlying assumptions.

We have also studied the MChD in absorption for the Cr(III)tris-oxalato complex in solution [22]. Both the NCD and the MCD spectrum of this complex are known. In particular, the spin-forbidden transition from the ground state $^4A_{2g}$ to the excited ^2E_g state shows fairly large values for both g_{NCD} and g_{MCD}, so we can expect a substantial g_{MChA} at this transition. The samples consisted of solutions of the pure enantiomers, resolved according to a literature method [23], in dimethylsulfoxide (DMSO). This solvent was used because in DMSO we have found the thermal racemization rate of the tris(oxalato)Cr(III) ion to be very low. No measurable decay of NCD occurred in such solutions over periods of days at room temperature, whereas in aqueous solution the

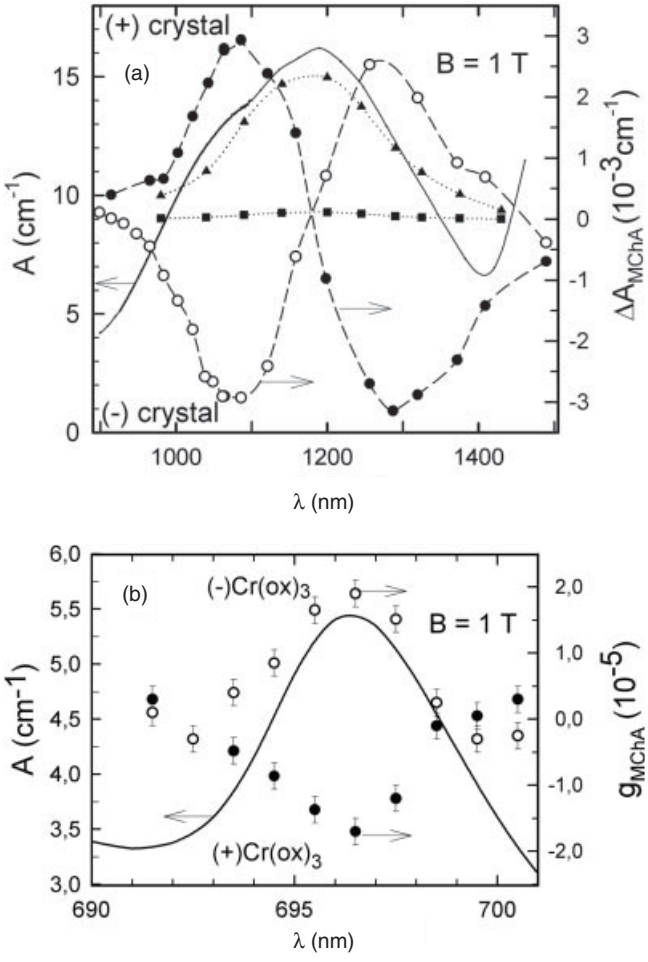

Figure 16.3. (a) Absorption (solid line) and magnetochiral absorption anisotropy of left (L)- and right (D)-handed α-$NiSO_4 \cdot 6H_2O$ crystals (circles). Dashed lines are only meant to guide the eye. Also shown are the calculated cascaded MChA effect (squares) and the prediction for MChA on the basis of the Baranova model (triangles). (b) Absorption (solid line) and magnetochiral absorption anisotropy (circles) of left (L)- and right (D)-handed tris(oxalato) Cr(III) complexes in DMSO.

NCD disappears on the timescale of hours. Concentrations were varied up to 0.3 molar. Figure 16.3b shows our result for the MChD spectrum of the two enantiomers. These spectra are clearly of opposite sign. It was verified that g_{MChA} varies linearly in B, again proving the existence of MChD in absorption. The dispersive-type lineshape is indicative of so-called A-terms [14], implying that the magnetic field influence on the optical properties is through the Zeeman effect. As discussed above, an order of magnitude estimate of the MChD, using the Baranova model, is approximately $g_{NCD} \cdot g_{MCD}/2$. At $\lambda = 701$ nm we have found $g_{MCD}/B = 2\ 10^{-3}\ \mathrm{T}^{-1}$ and $g_{NCD} = 2.2\ 10^{-3}$ which yields an estimate of $g_{MChA} = 2\ 10^{-6} T^{-1}$, close to the observed value. Because this value is quite low, and near the detection limits of our setup, one may wonder if this result is not strongly influenced by a cascaded contribution. In order to answer this question, we have studied the concentration dependence of the MChD. Figure 16.4 shows the MChD of this complex at a given wavelength as a function of the concentration of the complex, expressed as optical extinction for the given sample length. No significant concentration dependence of the experimental MChD is observed. This is to be expected for the true MChD, because it is a purely molecular property. The cascaded effect, however, should

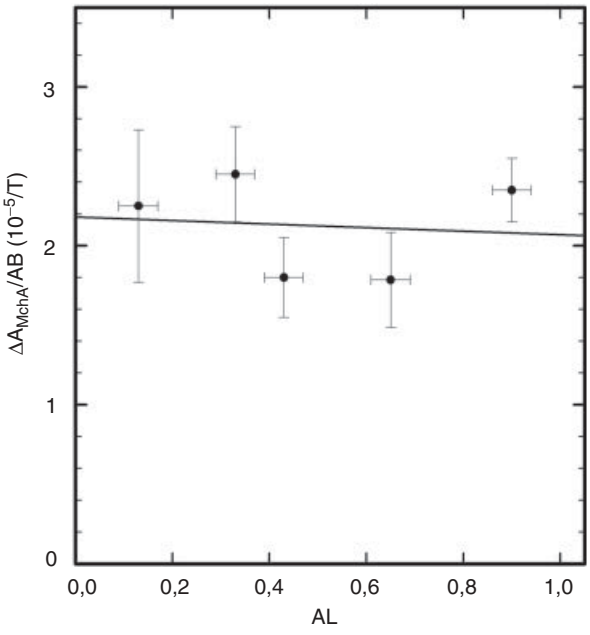

Figure 16.4. Magnetochiral anisotropy as a function of concentration of the l-tris(oxalato) Cr(III) ion in DMSO, expressed as optical density, at a wavelength of 696 nm (AL = 0.7 corresponds to a concentration of 0.2 M).

change with concentration, because both MCD and NCD are proportional to the concentration, and the cascaded effect is the mathematical product of both [Eq. (16.10)]. Figure 16.4 therefore shows that under these conditions, the true MChD dominates the cascaded effect. Using Eq. (16.10), we estimate that the cascaded effect contributes less than 10% to the observed MChD.

Our experimental limits of observation of MChD with our current setup are instead determined by the relative strength of MChD with respect to the normal absorption. For reasonable integration times, this limit is actually around $g_{MChA} \geq 5\ 10^{-7}\mathrm{T}^{-1}$. To go beyond this value, we would require larger magnetic fields and, in particular, higher modulation frequencies, since these would allow much lower noise in sources, detectors, and electronics.

It should be noted that MChD is by no means limited to the optical wavelength range. In fact, the equations above show that the effect becomes larger at large wavevectors (i.e., at short wavelengths), as confirmed by the observation of MChD for the absorption of X rays in Cr_2O_3 crystals [24]. However, interesting studies of MChD can also be envisaged at small wavevectors (e.g., in the infrared), in the form of vibrational transitions, or even at radiofrequencies, where MChD could allow for enantioselective nuclear magnetic resonance spectroscopy.

16.4. ENANTIOSELECTIVE MChD PHOTOCHEMISTRY

Asymmetric photochemistry with circularly polarized light (CPL), based on NCD, is well established and has been extensively reviewed [25, 26]. It is essentially based on the fact that somewhere in the reaction chain, a rate constant is proportional to the rate of absorbed photons, which is different for the two enantiomers. The Cr(III)tris-oxalato complex discussed above also has been extensively studied in this context, in a process called photoresolution [27]. This complex is unstable in aqueous solution and

spontaneously dissociates and reassociates. In equilibrium, one has a racemic mixture (equal concentrations of right- and left-handed complex). The dissociation is accelerated by the absorption of light, so under CPL irradiation, the more absorbing enantiomer will dissociate more often, whereas the subsequent random reassociation has the same rate for both enantiomers. This leads to an excess of the less absorbing enantiomer, the handedness of which depends on the handedness of the CPL. If this photoresolution is much faster than the thermal racemization, the size of the enantiomeric excess *ee* in dynamic equilibrium can be shown to be given by $ee_{CPL} = g_{NCD}/2$ [27]. As soon as the irradiation stops, the system will return to the racemic state due to thermal dissociation and random reassociation of the complexes.

Following the same reasoning, one should expect to obtain an enantiomeric excess through MChD when unidirectionally irradiating a racemic solution of this complex with unpolarized light in a magnetic field parallel to the irradiation direction. The handedness of the excess will be determined by the relative orientation of the light and the magnetic field. By a calculation similar to that used for photoresolution with CPL, detailed below, we find that to first order the magnitude of the excess in dynamic equilibrium is given by $ee_{MChA} = g_{MChA}/2$, where g_{MChA} is the magnetochiral anisotropy asymmetry factor defined in Eq. (16.6). In view of the smallness of g_{MChA}, the observation of such an excess represents a serious experimental challenge. Our setup for this experiment is shown in Figure 16.5 [28]. It consists of (a) a tunable optically pumped 0.5-W Ti-sapphire laser (680–750 nm) to drive the photoresolution and (b) a small green helium–neon laser (543.7 nm) with a photoelastic modulator to detect phase sensitively the resulting *ee* through its NCD ($g_{NCD} = 4.4 \times 10^{-2}$). The sample consists of a 50 μL of an initially racemic aqueous solution of potassium Cr(III)tris-oxalate, kept at 10°C to slow down thermal racemization.

We have first studied the dynamics of the photoresolution process of this complex under these conditions using circularly polarized light, without a magnetic field. The time to reach an equilibrium *ee* was found to be 6 min, whereas the thermal racemization time was around 70 min (Figure 16.6).

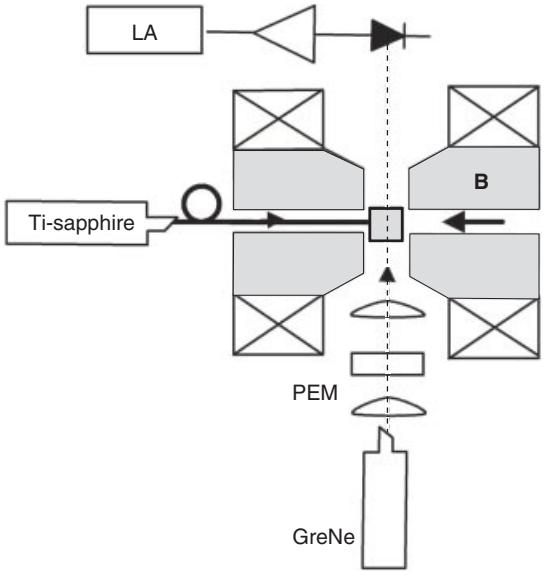

Figure 16.5. Experimental setup for determining photoresolution of the Cr(III)tris-oxalato complex. Monochromatic irradiation is performed with a Ti:sapphire laser around 696 nm, with a polarization state that can be selected between linear, circular, and unpolarized. The latter was obtained after passing the light through 10 m of 1-mm-diameter optical fiber. We have carefully checked that the light leaving the fiber has no net circular component exceeding 10^{-4}. Typical irradiation powers are 100 mW, which are absorbed in 50 μL of 0.2 M aqueous solution of $K_3Cr(ox)_3$, with a sample length of 7 mm, kept at 10°C. Enantiomeric excess (e.e.) is detected by measuring the NCD at 543.7 nm (green He–Ne laser, GreNe) using a photoelastic modulator (PEM) and a lock-in amplifier (LA). Measurements of *ee* are performed within 1 min after the magnetic field and the irradiation were switched off. (Redrawn from reference 28.)

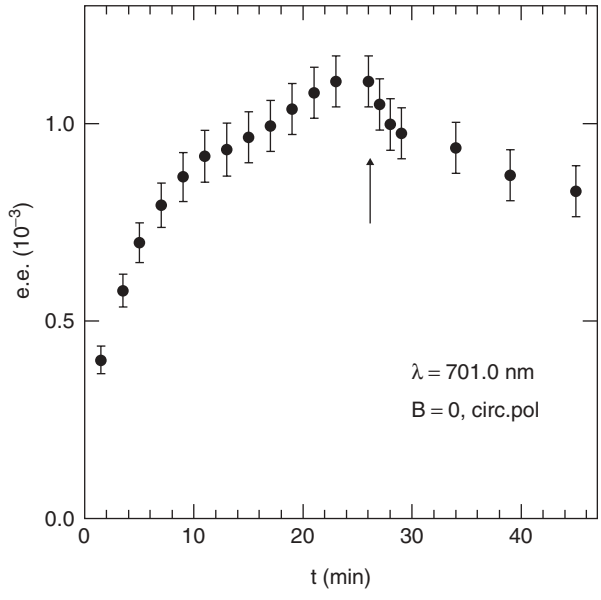

Figure 16.6. Photoresolution enantiomeric excess as a function of time. Photoresolution was performed by irradiating with 100-mW circularly polarized light at $\lambda = 701$ nm in zero magnetic field. The arrow indicates when the irradiation is stopped, and the system starts to relax to a racemic state. The photoresolution time constant is 6 min, and the thermal racemization time constant is 70 min. (Redrawn from reference 28.)

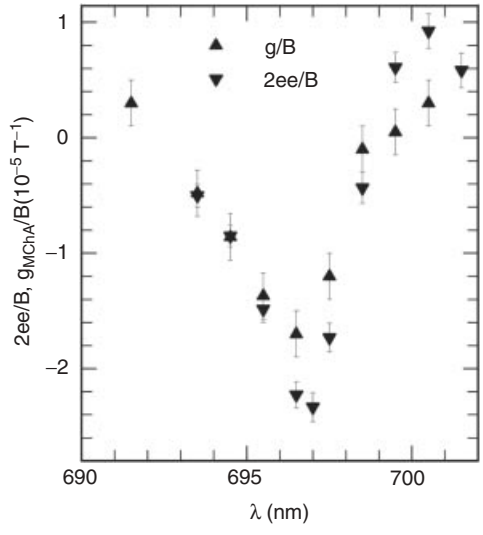

Figure 16.7. Comparison of the photochemical enantiomeric excess spectrum, obtained after 25 min of photoresolution of aqueous tris(oxalato)Cr(III) complexes with unpolarized light in 7.5 T (down triangles), with the MChA spectrum of the (+)-tris(oxalato)Cr(III) ion in DMSO (up triangles). The water spectrum is corrected for a 1-nm blueshift.

The result of the same experiment, using unpolarized light and applying a parallel magnetic field of 7.5 T, is shown in Figure 16.7, as a function of the excitation wavelength. Figure 16.8 shows for a given wavelength the dependence of the *ee* on the magnetic field strength, for fields parallel to the light and perpendicular to the light. In the first case, the *ee* is strictly linear in the field, including the sign, whereas in the second case, no significant *ee* can be detected. Both observations are as to be expected for MChA-driven photoresolution.

At $\lambda = 701$ nm we have found $g_{MCD}/B = 2 \times 10^{-3}$ T^{-1} and $g_{NCD} = 2.2 \times 10^{-3}$ for this complex (see Section 16.3) which yields an estimate for the $g_{MChA} = g_{NCD}\, g_{MCD}/2 = 2.2 \times 10^{-6}$ T^{-1} and for the $ee_{MChA} = g_{MChA}/2 = 1.1 \times 10^{-6}$ T^{-1}, close to the observed value of 1.7 $10^{-6} \times T^{-1}$, again confirming that we are dealing with true MChA. Still,

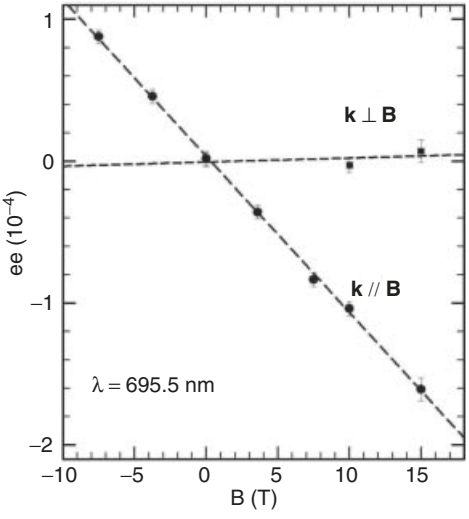

Figure 16.8. Enantiomeric excess obtained after irradiation with unpolarized light for 25 min at $\lambda = 695.5$ nm, as a function of magnetic field, with an irradiation direction **k** either parallel or perpendicular to the magnetic field **B**. Each point was obtained with a fresh, racemic starting solution. (Redrawn from reference 28.)

the smallness of the effect means that one should seriously consider the possibility of a cascading contribution, as discussed below.

Modeling the MChD photoresolution in detail is more complex than the photoresolution by CPL, because, similar to the absorption case discussed above, unpolarized incident light may become partially circularly polarized by MCD or NCD. This CPL component will then, through the classical photoresolution process, also give rise to an enantiomeric excess. We have developed a detailed model to obtain a quantitative description of enantioselectivity through MChD in photoresolution, taking into account all possible causes for an enantiomeric excess. This model also provides all the elements necessary to quantitatively model the MChD equivalents of other asymmetric photochemical processes with CPL that are well established and understood, like photodecomposition and direct photosynthesis [25, 26]. Here we will give only a short version; more details can be found in reference 22.

We assume a racemic mixture of equal concentrations of dextro- (N_D) and levo-enantiomers (N_L) of the complex, together with partly dissociated, achiral complexes (N_X). The incident, unpolarized light beam is described as having equal intensities of left- and right-circularly polarized light, I_l and I_r respectively, propagating along the z direction. Because of optical absorption and chemical reactions, I_l, I_r, N_D, and N_L will depend on the spatial coordinate z and time t. This can be expressed by the following differential equations:

$$\begin{aligned}
\frac{\partial N_D(z,t)}{\partial t} &= -D\frac{\partial^2 N_D(z,t)}{\partial z^2} - YN_D(z,t)(I_r(z,t)\alpha_{D,r} \\
&\quad + I_l(z,t)\alpha_{D,l}) + KN_X(z,t) - pN_D(z,t), \\
\frac{\partial N_L(z,t)}{\partial t} &= -D\frac{\partial^2 N_L(z,t)}{\partial z^2} - YN_L(z,t)(I_r(z,t)\alpha_{L,r} \\
&\quad + I_l(z,t)\alpha_{L,l}) + KN_X(z,t) - pN_L(z,t),
\end{aligned} \tag{16.12}$$

$$\frac{\partial I_r}{\partial z}(z,t) = -I_r(z,t)(N_D(z,t)\alpha_{D,r} + N_L(z,t)\alpha_{L,r} + N_X(z,t)\alpha_{X,r}),$$
$$\frac{\partial I_l}{\partial z}(z,t) = -I_l(z,t)(N_D(z,t)\alpha_{D,l} + N_L(z,t)\alpha_{L,l} + N_X(z,t)\alpha_{X,l}). \tag{16.13}$$

where D describes the diffusion of complexes, Y the photodissociation process, K the random reassociation into chiral complexes, and p the thermal dissociation of chiral complexes. The different molar absorption coefficients for levo- and dextro-complexes and left- and right-circularly polarized light are given by (see reference 22)

$$\alpha_{D,r} = \frac{k}{n'}(\tilde{\varepsilon}'' + \alpha''k + \beta''B + \gamma''\vec{B}\vec{k}),$$
$$\alpha_{D,l} = \frac{k}{n'}(\tilde{\varepsilon}'' - \alpha''k - \beta''B + \gamma''\vec{B}\vec{k}),$$
$$\alpha_{L,r} = \frac{k}{n'}(\tilde{\varepsilon}'' - \alpha''k + \beta''B - \gamma''\vec{B}\vec{k}), \tag{16.14}$$
$$\alpha_{L,l} = \frac{k}{n'}(\tilde{\varepsilon}'' + \alpha''k - \beta''B - \gamma''\vec{B}\vec{k}),$$

where, as before, α'' describes NCD, β'' describes MCD, and γ'' describes MChD. Equations (16.12) and (16.13) have to be solved self-consistently, with the following boundary conditions:

1. Racemic mixture before irradiation:

$$N_D(z, t = 0) = N_L(z, t = 0) = \text{const} \equiv \frac{N}{2}. \tag{16.15}$$

2. Total Cr(III) concentration independent of z and t:

$$N_D(z,t) + N_L(z,t) + N_X(z,t) = \text{const} \equiv N_{\text{total}}. \tag{16.16}$$

3. Irradiation with unpolarized light:

$$I_r(z = 0, t) = I_l(z = 0, t) = \text{const} \equiv \frac{I_0}{2}. \tag{16.17}$$

For the moment, we neglect diffusion; that is, we put $D = 0$ in Eq. (16.12). It can be shown that even infinitely rapid diffusion does not affect the dominant terms in the results for the enantiomeric excess [22]. The essential features of the model can already be obtained from Eq. (16.12) in the photostationary state. This yields, upon rearrangement,

$$\frac{\Delta N(z)}{N(z)} \equiv \frac{N_D(z) - N_L(z)}{N_D(z) + N_L(z)} = \frac{I_r(z)(\alpha_{L,r} - \alpha_{D,r}) + I_l(z)(\alpha_{L,l} - \alpha_{D,l})}{I_r(z)(\alpha_{L,r} + \alpha_{D,r}) + I_l(z)(\alpha_{L,l} + \alpha_{D,l}) + \frac{2p}{Y}}. \tag{16.18}$$

By insertion of Eqs. (16.13) and (16.14) into Eq. (16.18) and defining $\Delta I \equiv I_l - I_r$ and $I \equiv I_l + I_r$, we get

$$\frac{\Delta N(z)}{N(z)} = \frac{\alpha''k\Delta I(z)}{\beta''B\Delta I(z) + \varepsilon''I(z) + \frac{n'p}{kY}} + \frac{\gamma''\vec{B}\vec{k}I(z)}{\beta''B\Delta I(z) + \varepsilon''I(z) + \frac{n'p}{kY}}. \tag{16.19}$$

We see that there are two terms that can lead to an enantiomeric excess ($\Delta N \neq 0$). The first term on the right-hand side is proportional to α'' (i.e., NCD) and to ΔI (i.e., a net circularly polarized component in the light). This is the classical photoresolution mechanism studied by Stevenson and Verdieck [27]. It will be clear that if a net circular component is generated upon propagation of an initially unpolarized light beam, this term will also lead to an enantiomeric excess. This is exactly what MCD does, as will be shown below. The second term on the right-hand side of Eq. (16.19), proportional to the magnetochiral parameter γ'', describes the true magnetochiral enantioselective photochemistry, which only depends on the total intensity I, independent of the state of polarization. Equation (16.19) can be simplified because for all cases $\beta'' B(I_r(z) - I_l(z)) \ll \varepsilon''(I_r(z) + I_l(z))$ and for our experimental conditions, thermal dissociation is negligible ($p = 0$). This yields

$$\frac{\Delta N(z)}{N(z)} \approx \frac{\alpha'' k \Delta I(z)}{\varepsilon'' I(z)} + \frac{\gamma'' \vec{B}\vec{k}}{\varepsilon''} = \frac{g_{NCD}}{2}\frac{\Delta I(z)}{I(z)} + \frac{g_{MChA}}{2}. \tag{16.20}$$

The first term is the Stevenson and Verdieck result [27] (for circularly polarized light, $\Delta I/I = 1$). The second term describes the enantiomeric excess due to the true magnetochiral anisotropy.

From the equations above, it will be clear that as far as the light is concerned, the only important quantity is $\Delta I/I$. It can be easily shown that in the photostationary state, Eqs. (16.13) and (16.14) lead to

$$\frac{\Delta I(z)}{I(z)} = -\tanh\left(\frac{k}{n'}\int_0^z \alpha'' k(N_D - N_L)(z') + \beta'' B(N_D + N_L)(z')\, dz'\right), \tag{16.21}$$

where we have used $\alpha_{X,r} = \alpha_{X,l}$ as the (partly) dissociated ion is no longer chiral. Equation (16.21) only contains the parameters α'' and β'', combined with ΔN and N respectively, indicating that the appearing circular polarization is exclusively due to MCD and NCD in accordance with our understanding of MChD as a polarization-independent phenomenon. Equation (16.21) can be simplified by inserting the extinction coefficient $A \approx N\frac{k\varepsilon''}{\sqrt{\varepsilon'}}$ and refractive index $n' \approx \sqrt{\varepsilon'}$, which yields

$$\frac{\Delta I(z)}{I(z)} = -\tanh\left(\frac{A}{2}\int_0^z \left(g_{NCD}\left(\frac{\Delta N(z')}{N(z')}\right) + g_{MCD}\right) dz'\right) \tag{16.22}$$

The sets of differential equations (16.12) and (16.13) have now been reduced to the two coupled equations (16.20) and (16.22), which can be solved iteratively. The details can be found in reference 22. Here we give the result up to third order in the anisotropy factors:

$$\begin{aligned}\left(\frac{\Delta I(z)}{I(z)}\right) &= -\tanh\left(\frac{g_{MCD}}{2}Az - \frac{g_{NCD}^2 g_{MCD}}{16}A^2z^2 + \frac{g_{NCD}g_{MChA}}{4}Az + O(g^4)\right)\\ &\approx -\frac{g_{MCD}}{2}Az + \frac{g_{NCD}^2 g_{MCD}}{16}A^2z^2 + \frac{g_{MCD}^3}{24}A^3z^3 - \frac{g_{NCD}g_{MChA}}{4}Az + O(g^4)\end{aligned} \tag{16.23}$$

and

$$\left(\frac{\Delta N(z)}{N(z)}\right) \approx \frac{g_{MChA}}{2} - \frac{g_{NCD}g_{MCD}}{4}Az + \frac{g_{MCD}^3 g_{NCD}}{48}A^3z^3 + \frac{g_{NCD}^3 g_{MCD}}{32}A^2z^2 - \frac{g_{NCD}^2 g_{MChA}}{8}Az + O(g^5), \tag{16.24}$$

leading to

$$ee = \frac{g_{MChA}}{2} - \frac{g_{NCD}g_{MCD}AL}{8} - \frac{g_{NCD}^2 g_{MChA}AL}{8} + \frac{g_{MCD}^3 g_{NCD}(AL)^3}{192} + \frac{g_{NCD}^3 g_{MCD}(AL)^2}{96} + O(g^5). \tag{16.25}$$

In each higher iteration order n, additional terms of the order g^{2n} are obtained. Because such terms are very small, Eq. (16.25) should already be a good estimate of the enantiomeric excess. The first term on the right-hand side of Eq. (16.25) describes the true enantioselective magnetochiral photochemistry. All other subsequent terms are due to cascading. For our experiment on Cr(III)tris-oxalato complexes, we have $AL \approx 1$, $g_{\mathrm{MCD}} \approx 10^{-2}$, and $g_{\mathrm{NCD}} \approx 10^{-3}$, so we can conclude that amongst the cascading terms, the term $g_{\mathrm{MCD}}g_{\mathrm{NCD}}\mathrm{AL}/8$, is dominant. This term describes the first cascading step—that is, the enhancement of one enantiomer over the other due to the effect of a net circularly polarized light component that results from MCD. Because MCD only depends on $N_D + N_L$, the diffusion of the enantiomers of the complex does not in first order affect the cascading mechanism. This justifies its neglect.

In Figure 16.7 we compare our results for the photochemical enantiomeric excess spectrum with our MChD spectrum of the resolved ion, described earlier. The MChD spectrum was obtained at a concentration that is a factor 2 lower than the photochemical excess spectrum, and with a sample length that is also a factor 2 smaller. Therefore AL is a factor of 4 smaller in the MChD spectrum than in the photochemical spectrum. The good agreement between the two spectra confirms that the cascading term [the second term on the right-hand side of Eq. (16.25)] does not contribute significantly and that the true magnetochiral effect dominates the cascaded one in our photochemistry results.

We conclude from our experimental results and their good agreement with detailed modeling that indeed the MChA can lead to *ee* in a photochemical reaction in magnetic field. Our results can only suggest that magnetochiral anisotropy merits consideration in the discussion on the origins of the homochirality of life [29]. Issues of spectral, spatial, and temporal averaging have to be addressed, similar to the case of photochemistry with CPL, and a study of MChA in diamagnetic molecules of biological relevance is clearly needed. Because much smaller MChA effects are expected in such systems, this remains a significant experimental challenge.

16.5. MAGNETOCHIRAL DICHROISM IN A FERROMAGNET

So far all examples of molecules showing MChA were paramagnetic or diamagnetic, and the observed effects are strictly linear in the external magnetic field. Testing the MChA of a chiral ferromagnet has two fundamental interests compared to the measurements performed on such systems: (i) The effect being proportional to the magnetization must

be enhanced in the ferromagnetic state and (ii) the bistability inherent to the existence of a magnetically ordered state can be exploited for data storage with a detection based on MChA rather than magnetic circular dichroism. In order to incorporate structural chirality at the molecular level, the magnetism in such systems must be based on organic or metal–organic molecules, rather than inorganic materials. Significant progress has been made in the science of these so-called "molecular magnets" since they were first discovered in the early 1990s. Much less progress has been made in the even more demanding task of producing molecular materials exhibiting both long-range magnetic order and chirality through the concomitant control of both the magnetic properties via electron spin interactions and chirality via the absolute configuration of the structural elements. An important design strategy for achieving a large boost in the MChD is expected to be that the same structural centers must support both the chirality and the magnetism. Alternatively, one might aim for a strong cascaded MChD by having very strong MCD and NCD on two different centers.

In order to observe ferromagnetic MChD, Train et al. [30] have designed and synthesized the two enantiomers of an inorganic coordination compound that crystallizes as a chiral ferromagnet with magnetic and optical properties tailored to support a large MChD. They have constructed a chiral bimetallic $[Mn^{II}Cr^{III}\ (ox)_3]^-$ anionic network by introducing a configurationally stable chiral alkyl chain on a tetra-alkyl ammonium cation. The pairs of Mn^{II} and Cr^{III} ions are bridged by oxalate ligands $C_2O_4{}^{2-}$, with each metal ion being tris-chelated and thereby exhibiting a propeller-like chiral structure of D_3 symmetry. A subtle supramolecular enantioselective interaction of the enantiopure chiral cation with a racemic mixture of the metallic components permitted the construction of two-dimensional heterometallic layers with opposite absolute configurations at the two metal centers, resulting in mirror-image single crystals of $[N(CH_3)(n-C_3H_7)_2((S)sec\text{-}C_4H_9)]^+[(\Lambda)\text{-}Mn^{II}(\Delta)\text{-}Cr^{III}(ox)_3]^-$ or $[N(CH_3)(n\text{-}C_3H_7)_2((R)sec\text{-}C_4H_9)]^+[(\Delta)\text{-}Mn^{II}(\Lambda)\text{-}Cr^{III}(ox)_3]^-$, where R and S denote the absolute configurations of the chiral alkyl chains and Δ and Λ represent the absolute configurations of the propeller-like chiral metal centers, which crystallize in the chiral space group $P6_3$. The magnetic properties of the two enantiomers of $[N(i\text{-}Bu)MePr_2][MnCr(ox)_3]$ in the paramagnetic region indicate that the exchange interaction between the manganese(II) and the chromium(III) ions is ferromagnetic with a Curie–Weiss temperature of 9.3 K. The compounds undergo an abrupt paramagnetic to ferromagnetic phase transition at $T_C = 7$ K.

We have performed MChD absorption measurements on plate-like single crystals with the c axis aligned along the light propagation direction. Unpolarized incident light was guided onto the sample by means of optical fibers, as was the transmitted light, which was detected by a photomultiplier. The wavelength-dependence of the optical transmission of the crystals was measured in an alternating field superconducting magnet ($B_{max} = 1.2$ T, frequency 4.3 Hz), in which the sample temperature could be varied between 70 K and 2.5 K. A commercially available mercury short arc lamp in combination with a monochromator has been used as a light source. The use of an ac magnet allows for the direct phase-sensitive measurement of the MChA in the optical transmission (see Section 16.3).

In Figure 16.9, the MChD is plotted as a function of wavelength for the two enantiomers being in the ferromagnetic phase. Clearly, the enantiomers show a strong and opposite anisotropy in their optical response, thus proving the existence of MChA in the chiral ferromagnetic state. The MChA is significant in magnitude in the range between 570 nm and 640 nm, whereas the NCD peaks around 550 nm, like most chiral Cr^{3+}

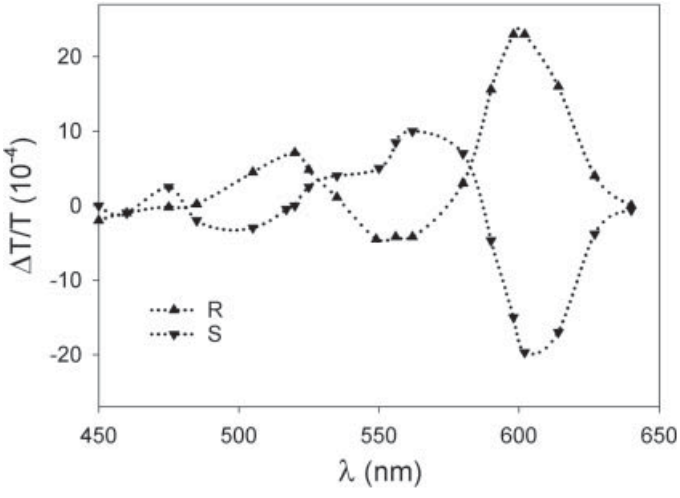

Figure 16.9. Magnetochiral dichroism measured at 4.0 K for $[N(CH_3)(n\text{-}C_3H_7)_2((S)sec\text{-}C_4H_9)]^+$ $[(\Lambda)\text{-}Mn^{II}(\Delta)\text{-}Cr^{III}(ox)_3]^-$ (up triangles) and $[N(CH_3)(n\text{-}C_3H_7)_2((R)sec\text{-}C_4H_9)]^+$ $[(\Delta)\text{-}Mn^{II}(\Lambda)\text{-}Cr^{III}(ox)_3]^-$ (down triangles). (Redrawn from reference 30.)

systems. This behavior is not yet understood and complicates a comparison with the results on paramagnetic Cr^{3+} shown above. However, it is safe to say that the effect is at least two orders of magnitude larger in the ferromagnetic state than in the paramagnetic state at 1 T.

In order to study the relation between the ferromagnetism and MChD, the temperature dependence of the MChD is measured for [N((*S*)-*sec*-Bu)MePr$_2$][(Δ)-Mn(Λ)-Cr] at a fixed wavelength, chosen at the maximum MChD signal at 615 nm (Figure 16.10). In the paramagnetic phase a relatively weak anisotropy is observed. The MChA increases gradually when approaching the Curie temperature and gains an order of magnitude around the transition into the ferromagnetic phase. This behavior follows the thermal variation of the magnetization, also shown in Figure 16.10.

Our results confirm the expected enhancement of MChA in the ferromagnetic state. Practical applications of such an effect have to await the discovery of room-temperature chiral ferromagnets.

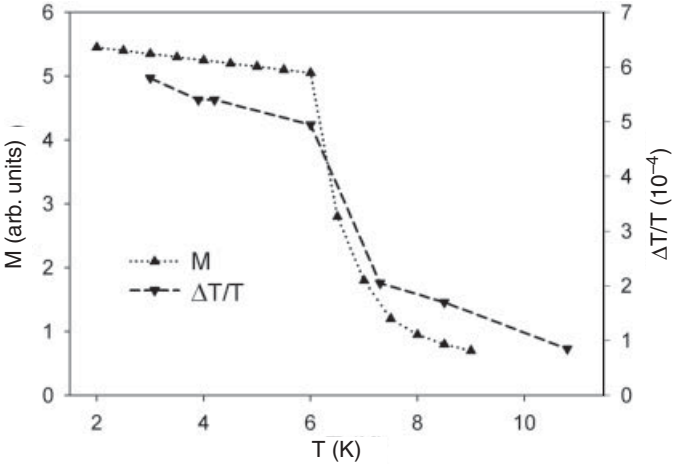

Figure 16.10. Temperature dependence of the MChD effect (down triangles) measured at 615 nm and field-cooled (up triangles) magnetization of $[N(CH_3)(n\text{-}C_3H_7)_2((S)sec\text{-}C_4H_9)]^+$ $[(\Lambda)\text{-}Mn^{II}(\Delta)\text{-}Cr^{III}(ox)_3]^-$ (arbitrary units). (Redrawn from reference 30.)

16.6. MAGNETOCHIRAL BIREFRINGENCE

So far only MChA in absorption and emission have been described. Their experimental observations prove that the imaginary part of the corresponding complex material parameter in Eq. (16.2) is unequal to zero; and through the Kramers–Kronig relations, we can infer that therefore the real part of this parameter cannot be zero either; that is, magnetochiral anisotropy must also exist as a difference in refractive index for unpolarized light propagating in chiral media, parallel or antiparallel to the magnetic field. This effect was baptized magnetochiral birefringence (MChB). The first experimental observation of such an effect was reported by Kleindienst and Wagnière [19], using a dedicated interferometer designed to cancel all contributions from MCB and NCB. A few years later, the existence of MChB was confirmed by Vallet et al. [20], using a ring laser interferometer. Although both experiments convincingly showed the existence of MChB, the values they reported for the same substance are different by a factor of 20, which so far remains unexplained. Detailed calculations [6, 15] seem to favor the lower values of the experimental observations, but have not yet been proven to be reliable in this domain.

The MChA luminescence and absorption experiments measure γ'' [Eq. (16.2)] and are intrinsically resonant with electronic transitions in the medium. In the previous sections, we have reported fairly large effects, with relative anisotropies up to 10^{-3} T^{-1}. In contrast, in the two MChB experiments mentioned above, which were performed far away from electronic resonances and which measure γ', only refractive index anisotropies up to 10^{-8} T^{-1} were reported. For both cases, the observed orders of magnitude agree with those predicted by the simple Baranova model [10]. One may wonder whether under resonant conditions the refractive MChA effect could be much larger. Such a situation was considered theoretically by Eritsyan, who calculated the transmission through a nonabsorbing cholesteric liquid crystal in a magnetic field parallel to the helix axis, for wavelengths close to the cholesteric Bragg resonance [31]. In this work, only the α' and β' terms of Eq. (16.2), corresponding to NCB and MCB, were taken into account, but nevertheless a strongly resonant transmission anisotropy of the order of 10^{-4} T^{-1} was predicted. We have already pointed out in Sections 16.3 and 16.4 that in absorption and photochemistry, these two terms together can lead to a cascaded form of MChA, proportional to $\alpha \cdot \beta$, that has (phenomenologically speaking) the same properties as the genuine MChA, proportional to γ. Eritsyan's prediction therefore corresponds to a cascaded resonant MChB. Note that the existence of such an enhancement is not trivial, because the Bragg resonance involves forward and backward traveling waves in the medium, and the MChA has opposite signs for these two propagation directions, which might lead to the conclusion that MChA is largely canceled out under such conditions, instead of being enhanced.

Cholesteric liquid crystals (ChLC) show a helical structure in their collective molecular orientation with a pitch that can be in the visible wavelength region. By a proper choice of ChLC mixtures, both left- and right-handed helices—and consequently, both signs of α' and γ'—can be realized. Around wavelengths resonant with the cholesteric pitch, $\alpha' k$ can reach values up to 0.5. In the isotropic phase, these materials have typically $\alpha' k \simeq 10^{-5} T^{-1}$, implying an enhancement of five orders of magnitude of the optical activity by means of the Bragg resonance. The NCB parameter β' will be 10^{-6} T^{-1} for these diamagnetic systems, but it has been experimentally established that the Faraday effect is enhanced near a Bragg resonance [32]. Intuitively, one could therefore expect a strong enhancement of the MChA on the Bragg resonance and we have specifically

designed an experiment to observe such enhancement [33]. The ChLC sample cells used consisted of two glass plates separated by a spacer with a thickness that can be chosen between 10 μm and 1 mm. The cells were filled with the LC mixture in the isotropic phase and alignment of the helix axis perpendicular to the plates was obtained by gently shearing the plates. The good crystalline quality could be easily verified by visual inspection. Two different mixtures of cholesteryl chloride and cholesteryl oleyl carbonate were used, one with a left-handed helix (1:3 ChCl/ChOC) and one with a right-handed helix (4:1 ChCl/ChOC), at temperatures of 300 K and 343 K respectively. Note that the two types of samples are not (strictly speaking) enantiomers and, therefore, that MChA strength, line width, and so on, need not be identical. However, the chiroptical properties of the two types of samples are of similar magnitude but of opposite sign and the magneto-optical properties should be similar on the basis of the close chemical similarity of their components. Similar magnitudes and opposite signs should be therefore expected for the MChA of the two types of samples.

Figure 16.11 shows a typical transmission spectrum, with a clear Bragg resonance, and the transmission difference between left- and right circularly polarized light, for a left- and a right-handed sample. The maxima in the circular differential spectra coincide with the Bragg resonances of the respective ChLCs. The magnetochiral anisotropy of such ChLCs was measured by applying a 0.5-T alternating magnetic field parallel to the helix axis. Unpolarized, incoherent light from a lamp, filtered by interference filters with a typical transmission bandwidth of 10 nm, was guided to the cell by means of an optical fiber (diameter 1 mm, numerical aperture 0.45). The light transmitted through the ChLC, parallel to the magnetic field direction, was collected by a similar fiber, which guided it to a photodiode detector. The magnetic field-induced transmission changes were phase-sensitively detected by a lock-in amplifier. We define the relative magnetochiral transmission anisotropy η as

$$\eta \equiv \frac{1}{B}\frac{T(B \uparrow\uparrow k) - T(B \uparrow\downarrow k)}{T(B \uparrow\uparrow k) + T(B \uparrow\downarrow k)}. \tag{16.26}$$

The inset of Figure 16.12 shows the observed ΔT for a left-handed sample as a function of magnetic field. A clear linear relation is observed, of opposite slopes for the two handednesses (not shown). The observed order of magnitude agrees reasonably well with

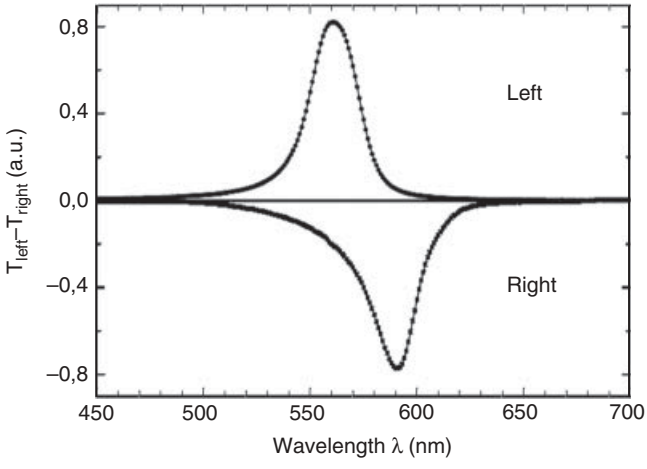

Figure 16.11. Transmission difference between left- and right-circularly polarized light for two different ChLC mixtures (both ChCl:ChOC, in different weight ratios, sample thickness: 50 μm). Top: Left-handed ChLC (weight ratio 1:3) at room temperature. Bottom: Right-handed ChLC (weight ratio 4:1) at 343 K. (Redrawn from reference 33.)

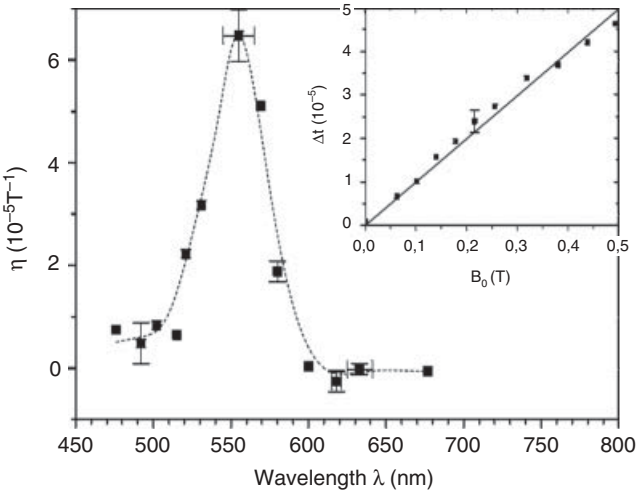

Figure 16.12. Inset: Relative transmission anisotropy $\Delta t = \eta B$ versus magnetic field for a left-handed sample consisting of 1:5 ChCl:ChOC at room temperature, layer thickness $d = 500$ μm, $\lambda = 481$ nm $\sim \lambda_{Bragg}$. Main figure shows the wavelength dependence of the normalized relative transmission anisotropy η for a left-handed sample consisting of 1:3 ChCl:ChOC at room temperature, $d = 500$ μm, $B = 0.38$ T (line is guide to the eye). The maximum observed corresponds approximately to the Bragg resonance of the sample. (Redrawn from reference 33.)

the predictions by Eritsyan and illustrates that under resonant conditions, refractive MChA can be quite strong. By rapid cooling to liquid nitrogen temperatures, we could freeze in the cholesteric structure and we observed the same MChA as at room temperature, thereby excluding magnetic realignment of the molecules as cause for the observed MChA.

Figures 16.12 and 16.13 show the wavelength dependence of MChA for a left- and a right-handed ChLC. A clear resonance is observed that is close to the Bragg resonance. This is completely different from the spectrum predicted by Eritsyan, which has a derivative-type lineshape, with a zero-crossing at the Bragg resonance, and large and opposite values in the two opposite wings of the Bragg band [31]. This large discrepancy suggests that the theoretical treatment by Eritsyan is incomplete, and that the γ term of Eq. (16.2) plays a dominant role in the observed MChA. Clearly, the development of a theory involving the γ term is called for. Figure 16.14 shows the observed temperature dependence of η. The observed η clearly vanishes upon approaching the

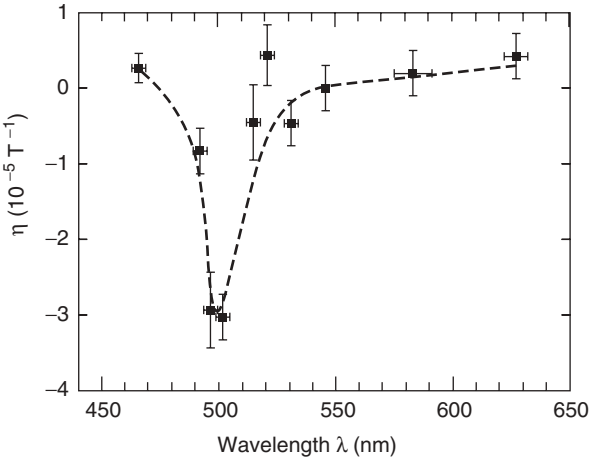

Figure 16.13. Wavelength dependence of η for a right-handed sample consisting of 4:1 ChCl:ChOC at 343 K, $B = 0.37$ T, $d = 50$ μm (line is guide to the eye). The maximum in negative sense observed corresponds approximately to the Bragg resonance of the sample. The order of magnitude is similar to that in Figure 16.12, whereas the sign has changed. (Redrawn from reference 33.)

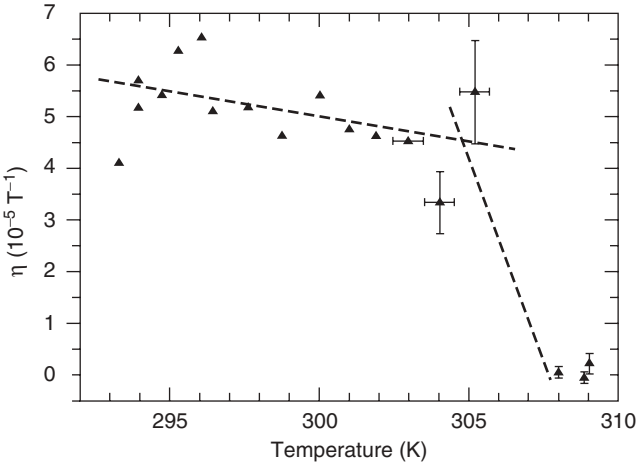

Figure 16.14. Temperature dependence of η. The anisotropy vanishes at the cholesteric–isotropic phase transition temperature that was at 306 K for this sample, consisting of 1:5 ChCl:ChOC, $d = 500$ μm, $\lambda = 481$ nm $\sim \lambda_{Bragg}$. (Redrawn from reference 33.)

cholesteric–isotropic phase transition temperature, which was at 306 K for this sample. This behavior confirms that the strong MChA results from the collective cholesteric molecular alignment and the Bragg resonance that accompanies it.

Our results show that resonant enhancement of MChB around the Bragg scattering condition exists. This suggests that it should be possible to observe MChB in Bragg scattering of unpolarized or linearly polarized X rays by chiral crystals in magnetic fields. Thereby one could obtain specific chiral information of crystal structures, as an alternative to X-ray natural circular dichroism measurements by use of polarization modulation of synchrotron radiation [24]. Our results also suggest that MChB of molecules could be measured by incorporating them into a photonic crystal matrix.

16.7. OTHER MANIFESTATIONS OF MChA

Many analogies between electronic transport and light propagation are known. Such analogies are founded on the wave-particle duality of both electrons and photons. However, an important aspect of photons, namely their polarization, is not so easily experimentally accessible for electrons. Only in recent years, the subject of spin-polarized electronic transport has made significant progress and has attracted much attention for applications in future electronics systems ("spintronics"). At the same time a new polarization-independent optical effect was discovered, the magnetochiral anisotropy, as described in the previous sections of this chapter. The existence of this effect and its properties have been deduced from elementary symmetry arguments. These symmetry arguments may also be applied to the case of electrical transport, and the question naturally comes to mind if MChA exists for electronic magnetotransport in chiral conductors. As we already pointed out in the introduction of this chapter, a spinning particle moving parallel to a magnetic field is chiral, so it seems plausible that such chirality will interact enantioselectively with any chirality of the environment of the particle.

This question has been studied in detail by us [34, 35]. Time- and parity-reversal symmetry arguments require that up to the second-order magnetic contributions, the electrical two-terminal resistance R of any chiral conductor is given by

$$R(\mathbf{B}, \mathbf{I})^{D/L} = R_0(1 + \beta B^2 + \Omega^{D/L}\mathbf{B} \cdot \mathbf{I}), \tag{16.27}$$

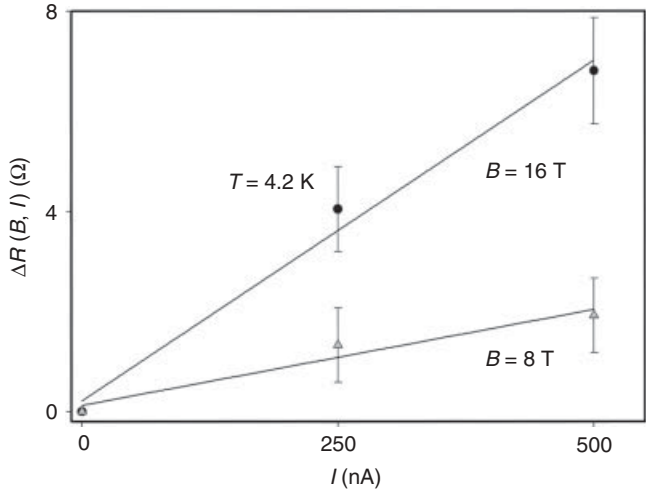

Figure 16.15. Current dependence of the electrical MChA of a metallic, chiral carbon nanotube. $\Delta R(\mathrm{B}, \mathrm{I}) \equiv R(\mathrm{B} \uparrow\uparrow \mathrm{I}) - R(\mathrm{B} \uparrow\downarrow \mathrm{I})$ is shown as a function of I for two different magnetic field strengths at liquid helium temperature (dotted lines are guides to the eye). Room-temperature two-terminal resistance of this tube was 8kΩ. (Redrawn from reference 35.)

where I is the current traversing the conductor, β describes the normal quadratic magnetoresistance present in all conductors, and $\Omega^L = -\Omega^D$. The third term on the right-hand side represents magnetochiral anisotropy, similar to the optical case. Experimental verification of the validity of Eq. (16.27) has been obtained for metallic helices, twisted wires [34], and carbon nanotubes [35] (Figure 16.15) [36], and the microscopic mechanisms underlying these forms of electrical MChA were elucidated. These results open the possibility to do enantioselective measurements in magnetic fields using techniques that so far are insensitive to chirality, like scanning tunneling probe spectroscopy, electron loss spectroscopy, and neutron scattering. Similar to the case of enantioselective photochemistry using unpolarized light in a magnetic field, the existence of MChA in electrical transport enables enantioselective electrochemistry in a magnetic field. Indeed, electro-deposition in magnetic fields parallel to the deposition current was shown to result in chiral films [37], the handedness of which will depend on the relative orientation of current and field.

Now that the existence of MChA in electron transport in firmly established, one may wonder if the effect can exist for general particle or momentum transport—that is, is there a mechanical MChA? There are several well-known mechanical effects due to a magnetic field. Anisotropic objects or objects having an anisotropic magnetic susceptibility can be aligned by a magnetic field, proportional to H^2. Also proportional to H^2 is the magnetostrictive effect. All objects experience a force in a magnetic field gradient, proportional to $M \cdot \nabla H, M$ being the magnetization, which can be used for magnetic levitation. The Einstein–deHaas effect is the only known linear magnetomechanical effect, and it corresponds to an angular momentum that any object acquires if a magnetic field is applied. The semiclassical explanation of this effect is that applying a magnetic field causes Larmor precession of the electrons of the object and that angular momentum conservation requires the body to rotate in the opposite sense in order to compensate for the angular momentum of the electrons. The inverse of the Einstein–deHaas effect is called the Barnett effect, and it describes the magnetization induced in an object that is set into rotation. Classically speaking, the object's electrons lag behind when the object is set in rotation, and this corresponds to a circular current and, therefore, to an axial magnetization. For a detailed discussion of these two so-called gyromagnetic effects, see reference 38. When considering magnetomechanical effects for the case of a chiral

object, imposing time reversal and parity invariance, one readily finds that any chiral object subject to a magnetic field B will acquire a linear momentum p:

$$\vec{p} = \zeta^{D/L}\vec{B}, \tag{16.28}$$

where $\zeta^D = -\zeta^L$ and ζ can be called a magnetochirodynamical coupling parameter. The inverse effect corresponds to

$$\vec{M} = \zeta'^{D/L}\vec{p}; \tag{16.29}$$

that is, any chiral object imparted with momentum p will acquire a magnetic moment. Calculations have confirmed the general case described in Eq. (16.28) for chiral carbon nanotubes [39] and for chiral molecules in an isotropic radiation field [40], but so far no experimental verification of these effects has been reported. Because such a magnetochirodynamical effect would allow separating spatially the two enantiomers in a magnetic field, it could be of considerable interest.

16.8. CONCLUSION

In this chapter we have described our current understanding of magnetochiral anisotropy. The optical implementations of MChA are well established, albeit that only a limited number of data exist and that some of are them are disputed. The existence of MChA in electrical transport is solidly proven, but there still remains a large unexplored potential. The existence of MChA in the mechanical properties of chiral systems has been suggested, but so far no experimental confirmation exists. We firmly believe that the combination of chirality and magnetic field may still hold some other surprises.

ACKNOWLEDGMENTS

We gratefully acknowledge the contributions of G. Duchs, J. Folling, C. Koerdt, V. Krstic, E. Raupach, C. Train, and G. Wagnière to this work, as well as the inspiring discussions with L. Barron, E.W. Meier, B. van Tiggelen, and P. Wyder.

REFERENCES

1. S. F. Mason, From Pasteur to parity non-conservation: Theories of the origin of molecular chirality, in *Circular Dichroism*, 2nd ed., N. Berova, K. Nakanishi, R. W. Woody, eds., Wiley-VCH, New York, **1994**.
2. D. B. Cline, ed., *Physical Origin of Homochirality in Life*, American Institute of Physics, New York, **1996**.
3. M. Avalos, R. Babiano, P. Cintas, J. L. Jimenez, J. C. Palacios, L. D. Barron, *Chem. Rev*. **1998**, *9*, 2391–2404.
4. W. A. Bonner, *Orig. Life Evol. Biosph*. **1995**, *25*, 175–190.
5. L. D. Barron, *J. Am. Chem. Soc*. **1986**, *108*, 5539–5542.
6. L. D. Barron, *Science* **1994**, *266*, 1491–1492.
7. M. P. Groenewege, *Mol. Phys*. **1962**, *5*, 541–553.

8. D. L. Portigal, E. Burstein, *J. Phys. Chem. Solids* **1971**, *32*, 603–608.
9. N. B. Baranova, Y. Bogdanov, B. Y. Zeldovich, *Opt. Commun*. **1977**, *22*, 243–247.
10. N. B. Baranova, B. Y. Zeldovich, *Mol. Phys*. **1979**, *38*, 1085–1098.
11. G. Wagnière, A. Meier, *Chem. Phys. Lett*. **1982**, *93*, 78–82.
12. G. Wagnière, *Chem. Phys. Lett*. **1984**, *110*, 546–549.
13. L. D. Landau, E. M. Lifshitz, L. P. Pitaevski, *Electrodynamics of Continuous Media*, Pergamon, Oxford, **1984**.
14. L. D. Barron, J. Vrbancich, *Mol. Phys*. **1984**, *51*, 715–730.
15. S. Coriani, M. Pecul, A Rizzo, P. Jorgensen, M. Jaszunski, *J. Chem. Phys* **2002**, *117*, 6417–6428.
16. B. Jansik, A. Rizzo, L. Frediani, K. Ruud, S. Coriani, *J. Chem. Phys*. **2006**, *125*, 234105.
17. G. L. J. A. Rikken, E. Raupach, *Nature* **1997**, *390*, 493–494.
18. E. Raupach, *The Magneto-chiral Anisotropy*, Ph. D. thesis, University of Konstanz, ISBN 3-89649-769-3, Hartung Gorre Verlag, Konstanz, **2002**.
19. P. Kleindienst, G. Wagnière, *Chem. Phys. Lett*. **1998**, *288*, 89–97.
20. M. Vallet, R. Ghosh, A. Le Floch, T. Ruchon, F. Bretenaker, J. Y. Thépot, *Phys. Rev. Lett*. **2001**, *87*, 183003.
21. G. L. J. A. Rikken, E. Raupach, *Phys. Rev. E* **1998**, *58*, 5081–5084.
22. E. Raupach, G. L. J. A. Rikken, C. Train, B. Malézieux, *Chem. Phys*. **2000**, *261*, 373–380.
23. G. B. Kaufmann, L. T. Takahashi, N. Sugisaka, *Inorg. Synth*. **1966**, *8*, 207–209.
24. J. Goulon, A. Rogalev, F. Wilhelm, C. Goulon-Ginet, P. Carra, D. Cabaret, C. Brouder, *Phys. Rev. Lett*. **2002**, *88*, 237401.
25. H. Rau, *Chem. Rev*. **1983**, *83*, 535–547.
26. Y. Inoue, *Chem. Rev*. **1992**, *92*, 741–770.
27. K. L. Stevenson,. J. F. Verdieck, *Mol. Photochem*. **1969**, *1*, 271–288.
28. G. L. J. A. Rikken, E. Raupach, *Nature* **2000**, *405*, 932–935.
29. G. Wagnière, A. Meier, *Experientia* **1983**, *39*, 1090–1091.
30. C. Train, R. Gheorghe, V. Krstic, L. M. Chamoreau, N. S. Ovanessyan, G. L. J. A. Rikken, M. Gruselle, M. Verdaguer, *Nature Mater*. **2008**, *7*, 729–734.
31. O. S. Eritsyan, *J. Exp. Theor. Phys*. **2000**, *90*, 102–108.
32. C. Koerdt, G. L. J. A. Rikken, E. Petrov, *Appl. Phys. Lett*. **2003**, *82*, 1538–1540.
33. G. Düchs, C. Koerdt, G. L. J. A. Rikken, *Phys. Rev. Lett*. **2003**, *91*, 073902.
34. G. L. J. A. Rikken, J. Fölling, P. Wyder, *Phys. Rev. Lett*. **2001**, *87*, 236602.
35. V. Krstić, S. Roth, M. Burghard, K. Kern, G. L. J. A. Rikken, *J. Chem. Phys*. **2002**, *117*, 11315–11319.
36. J. Wei, M. Shimogawa, Z. H. Wang, I. Radu, R. Dormaier, D. H. Cobden, *Phys. Rev. Lett*. **2005**, *95*, 256601.
37. I. Mogi, K. Watanabe, *Sci. Technol. Adv. Mater*. **2006**, *7*, 342–345, *ibid* **2008**, *9*, 024210.
38. S. V. Vonsovskii, *Magnetism*, Wiley, New York, **1976**.
39. V. Krstić, G. Wagnière, G. L. J. A. Rikken, *Chem. Phys. Lett*. **2004**, *390*, 25–29.
40. G. L. J. A. Rikken, B. A. van Tiggelen, V. Krstić, G. Wagnière, *Chem. Phys. Lett*. **2005**, *403*, 298–302.

17

X-RAY DETECTED OPTICAL ACTIVITY

Jose Goulon, Andrei Rogalev, and Christian Brouder

17.1. PHENOMENOLOGICAL BASES

17.1.1. X-Ray Dichroisms

Optical activity (OA) describes a peculiar interaction of matter with a polarized radiation field: it does exist only in systems with no inversion (I) symmetry, even though its measurement always *conserves* parity [1]. In this chapter, we review the information content of OA in the X-ray range. In particular, we shall concentrate on X-ray dichroism experiments in which one measures at a given photon energy $E(eV) = \hbar\omega$ the variations of the X-ray absorption cross sections $\sigma(E)$ on inverting a given Stokes–Poincaré polarization component S_j ($j = 1, 2, 3$):

$$\Delta\sigma_j(E) = \sigma(E, S_j = -1) - \sigma(E, S_j = +1).$$

The Stokes–Poincaré parameters are most conveniently defined in terms of the unit, complex polarization vectors **e**. For a transverse electric wave propagating along the z axis [1]:

$$\begin{aligned} S_0 &= +(e_x e_x^* + e_y e_y^*), \\ S_1 &= +(e_x e_x^* - e_y e_y^*), \\ S_2 &= -(e_x e_y^* + e_y e_x^*), \\ S_3 &= -i(e_x e_y^* - e_y e_x^*), \end{aligned}$$

Comprehensive Chiroptical Spectroscopy, Volume 1: Instrumentation, Methodologies, and Theoretical Simulations, First Edition. Edited by N. Berova, P. L. Polavarapu, K. Nakanishi, and R. W. Woody.
© 2012 John Wiley & Sons, Inc. Published 2012 by John Wiley & Sons, Inc.

with $S_0 = 1.S_1$ and S_2 are linear polarization rates relative to azimuthal angles $(0, \pi/2)$ and $(\pi/4, 3\pi/4)$, whereas S_3 is the (left, right) circular polarization rate. X-ray dichroisms $\Delta\sigma_j$ are most often measured over the typical energy range of the X-ray absorption near edge structure (XANES) [2], which are also called near edge X-ray absorption fine structure (NEXAFS) in soft X-ray spectroscopy [3]. Recall that the absorption edges are characteristic of a given element and result from the photoexcitation of electrons in a given core state—for example, the $1s$ state at a K-edge, or $2s$, $2p_{1/2}, 2p_{3/2}$ states at spin–orbit split L-edges.

Regarding terminology, *natural* dichroisms refer to measurements conserving time-reversal symmetry (Θ). Natural circular dichroism (NCD) has long been identified as a major chiroptical tool to study optical activity at optical wavelengths, whereas magnetic circular dichroism (MCD) probes the magneto-optical properties of matter [1].

As recently as 1998–1999 the reality of X-ray natural circular dichroism (XNCD) was definitively established by a series of joint experiments carried out at the European Synchrotron Radiation Facility (ESRF) on a variety of gyrotropic single crystals [4–8]. One may wonder why it took such a long time to detect OA in the X-ray spectral range, given that X rays were discovered by Röntgen in 1895 [9], whereas, precisely the same year, Cotton reported his first measurement of circular dichroism at optical wavelengths [10]. One reason is that, for a very long time, there was no suitable source of circularly polarized X rays to carry out such delicate experiments. As emphasized in Section 17.2, X-ray absorption spectroscopy (XAS) greatly benefitted from the development of third-generation synchrotron radiation sources: The recent availabilty of intense circularly polarized X-ray beams delivered by powerful helical undulators [12, 13] offering the capability to flip rapidly the circular polarization rate considerably enhanced the sensitivity of both X-ray natural or magnetic circular dichroism measurements [14]. On the other hand, one should not forget that the existence of natural OA in deep core level spectroscopies has long been a questionable issue [15].

17.1.2. Spatial Dispersion

Spatial dispersion [11] manifests itself when the transverse plane wave is approximated as

$$\mathbf{e}_q e^{i\mathbf{k}\cdot\mathbf{r}} \simeq \mathbf{e}_q (1 + i\mathbf{k}\cdot\mathbf{r}), \tag{17.1}$$

where $\mathbf{e}_q = [e_x + iqe_y]/\sqrt{2}$ denotes the circular polarization vector of a photon of helicity $q = \pm 1$ and wavevector $\mathbf{k} \parallel \mathbf{z}$. OA arises from the existence of interference terms mixing multipoles of opposite parity—for example, electric and magnetic dipoles ($E1M1$) or electric dipole and quadrupole ($E1E2$) in the interaction Hamiltonian. The Curie symmetry principle, however, states that this is possible only in systems with broken inversion (I) symmetry.

At optical wavelengths, OA is strongly dominated by $E1M1$ terms. In deep inner-shell spectroscopies, the transition probabilities $E1M1$ and $M1M1$ are forbidden by selection rules in the monoelectronic approximation and vanish [16], at least in nonrelativistic theories. Thus, it was the challenge of the first XNCD experiments to prove that OA could still be measured in the X-ray spectral range due to the contribution of the $E1E2$ interference terms which, in contrast, are fairly small at optical wavelengths [17]. There is, however, a dramatic restriction which is that the $E1E2$ interference terms also vanish in systems that lack orientational order. This stems from the orthogonality of the spherical harmonics $Y_\ell^m(\theta, \phi)$ associated with the electric dipole ($\ell = 1$) and quadrupole

($\ell = 2$), respectively. The immediate consequence is that no XNCD signal should survive in isotropic samples (e.g., liquid solutions); this explains why most XNCD spectra were recorded so far on single crystals.

Recently, high-quality data collected at the ESRF with a uniaxial crystal rotated at the magic angle made it possible to detect a very weak XNCD signal assigned to nonvanishing $E1M1$ terms. The relative intensity of such terms may well increase in the *soft* X-ray regime (e.g., below 1 keV); this is supported by recent observations of weak XNCD signatures measured at the K-edges of light elements (C,N,O...) [18, 19]. One would expect even more intense (soft) XNCD signatures at the $L_{2,3}$-edges of first row transition metals owing to the existence of larger magnetic dipoles at spin–orbit split edges [20].

Recall that, in single crystals, OA is a tensor property resulting from the spatial dispersion of the dielectric response. For nonmagnetic materials, it is defined through the constitutive equation [11, 21]:

$$\mathcal{D}_i = [\varepsilon_d]_{ij} E_j + \eta_{ijk} \nabla_j E_k \tag{17.2}$$

where $[\epsilon_d]_{ij}$ stands for the rank 2 permittivity tensor whereas the third-rank OA tensor η_{ijk} should be antisymmetric in the exchange of the first and third indices. Thus, in Cartesian coordinates, at most 9 components out of 27 could be independent. This makes it often preferable to substitute η_{ijk} with its dual, rank 2, *gyrotropy* tensor defined as

$$g_{\ell j} = \frac{1}{2} \epsilon_{i\ell k} \eta_{ijk}, \tag{17.3}$$

where $\epsilon_{i\ell k}$ is the Levi–Civita unit tensor. The decomposition of η into irreducible representations invariant under the operations of the rotation group $\mathcal{O}_3$ was shown to yield three parity-odd spherical tensors of rank 0, 1, 2, that is, (i) a pseudoscalar; (ii) a polar vector; and (iii) a traceless, rank 2 pseudodeviator. It has long been recognized that enantiomorphism does exist only for crystal classes that exhibit a nonzero pseudoscalar part. Jerphagnon and Chemla pointed out that the polar vector part of OA existed in pyroelectric materials [21]. However, it cannot cause any dichroism in absorption or reflection at normal incidence [22]. It will be shown below that it can be detected in the X-ray resonant scattering regimes [23]. There cannot be any contribution of the $E1E2$ interference terms to the pseudoscalar part of the OA tensor: one may thus expect a nonvanishing XNCD signal only when the pseudodeviator part is nonzero. Table 17.1, derived from reference 21, clarifies which ones among the 21 classes of noncentrosymmetric crystals may exhibit XNCD.

17.1.3. Complex Gyration Tensor

Let us assume that all X-ray modes propagating inside a crystal are nearly parallel to the incident wavevector **k**. This is quite realistic for X rays, given that their refractive index $n = 1 - \delta$ is very close to unity ($\delta \leq 10^{-5}$). Then, the complex forward scattering amplitude can be expanded as [25]

$$a^*_{\alpha\beta} = \alpha^*_{\alpha\beta} + \zeta^*_{\alpha\beta\gamma} k_\gamma + \cdots. \tag{17.4}$$

The first term ($\alpha^*_{\alpha\beta} \propto [E1E1]_{\alpha\beta}$) is the rank 2 electric dipole polarizability tensor; the second one ($\zeta^*_{\alpha\beta\gamma} \propto [E1E2]_{\alpha\beta\gamma}$) is the rank 3 complex gyration tensor that contains all

TABLE 17.1. Irreducible Parts in $O(3)$ of the OA Tensor for Odd Parity Crystal Classes [21]

Crystal Classes	Point Groups	Pseudo Scalar: Enantiomorphism	Polar Vector: Pyroelectricity	Pseudo Deviator: **XNCD**
$\bar{4}3m\,\bar{6}m2\bar{6}$	$T_d D_{3h} C_{3h}$	−	−	−
432 23	$O\ T$	+	−	−
622 32 422	$D_6 D_3 D_4$	+	−	+
$6mm\ 3m\ 4mm$	$C_{6v} C_{3v} C_{4v}$	−	+	−
6 3 4	$C_6 C_3 C_4$	+	+	+
$\bar{4}2m$	D_{2d}	−	−	+
$\bar{4}$	S_4	−	−	+
$mm2$	C_{2v}	−	+	+
222	D_2	+	−	+
2	C_2	+	+	+
m	C_s	−	+	+
1	C_1	+	+	+

information about OA. In Eq. (17.4), we deliberately omitted the higher-order contributions from the electric quadrupole polarizability tensor and the electric dipole–electric octupole interference terms that mix multipole moments of the same parity and, thus, *do not* contribute to OA. As shown by Buckingham and his colleagues [26, 27], one may check that $\mathrm{Re}\{\alpha^*_{\alpha\beta}\}$ is time-reversal even: These terms are mainly responsible for X-ray natural linear dichroisms and for the angular dependence of the XANES spectra of oriented single crystals [28]. In contrast, $\mathrm{Im}\{\alpha^*_{\alpha\beta}\}$—which is time-reversal odd—is primarily responsible for X-ray magnetic circular dichroism (XMCD) signatures first observed by Schütz et al. [29] with firm X rays, or by Chen et al. [30] using soft X rays. Indeed, the pioneering X-ray Faraday rotation experiment reported by Siddons et al. [31] also referred to time-reversal odd terms, but involved the energy dispersive part (f) rather than the absorbing part (g) of the spectra [25].

Let us focus next on the physical content of the complex gyration tensor:

$$\begin{aligned}
\mathrm{Im}\{\zeta^*_{\alpha\beta\gamma}\} &= -\frac{1}{3}\mathrm{Re}\{[\mathrm{E1E2}]_{\alpha\beta\gamma} - [\mathrm{E1E2}]_{\beta\alpha\gamma}\} \\
&\quad + \frac{1}{\omega}\mathrm{Im}\{\epsilon_{\delta\gamma\alpha}[\mathrm{E1M1}]_{\beta\delta} - \epsilon_{\delta\gamma\beta}[\mathrm{E1M1}]_{\alpha\delta}\}, \\
\mathrm{Re}\{\zeta^*_{\alpha\beta\gamma}\} &= +\frac{1}{3}\mathrm{Im}\{[\mathrm{E1E2}]_{\alpha\beta\gamma} + [\mathrm{E1E2}]_{\beta\alpha\gamma}\} \\
&\quad + \frac{1}{\omega}\mathrm{Re}\{\epsilon_{\delta\gamma\alpha}[\mathrm{E1M1}]_{\beta\delta} + \epsilon_{\delta\gamma\beta}[\mathrm{E1M1}]_{\alpha\delta}\}.
\end{aligned}$$

As shown by Barron [1], the imaginary part is anti-hermitean ($\mathrm{Im}\zeta^*_{\alpha\beta\gamma} = -\mathrm{Im}\zeta^*_{\beta\alpha\gamma}$) and time-reversal *even*; it is indeed the term responsible for natural OA. On the other hand, $\mathrm{Re}\zeta^*_{\alpha\beta\gamma}$ is hermitean and time-reversal *odd*: this term is responsible for a so-called *nonreciprocal* OA observed only in magnetoelectric (ME) systems. Concentrating onto the absorptive terms (g) in the formulation of the gyration tensor, one may now predict the existence of a specific dichroism related to OA for every Stokes component:

(i) X-ray ME linear dichroism:

$$\Delta\sigma_1 \propto \mathrm{Re}[\zeta^*_{\beta\beta\gamma}(g) - \zeta^*_{\alpha\alpha\gamma}(g)].$$

(ii) X-ray ME Jones dichroism:

$$\Delta\sigma_2 \propto 2\mathrm{Re}\{\zeta^*_{\alpha\beta\gamma}(g)\}.$$

(iii) X-ray natural circular dichoism:

$$\Delta\sigma_3 \propto 2\mathrm{Im}\{\zeta^*_{\alpha\beta\gamma}(g)\}.$$

(iv) X-ray magnetochiral dichroism:

$$\sigma_0(+H) - \sigma_0(-H) \propto \mathrm{Re}[\zeta^*_{\beta\beta\gamma}(g) + \zeta^*_{\alpha\alpha\gamma}(g)].$$

Note that the X-ray ME linear dichroism (XMELD), the ME Jones dichroism, and the magnetochiral dichroism (XMχD) are all nonreciprocal effects. Recall that the magnetochiral dichroism could be observed with unpolarized light [32–35]; this is why this effect is also called *directional* dichroism in ME materials. It is quite remarkable that the ME Jones dichroism and the XNCD both stem from the same components of the Cartesian gyration tensor, one should pay attention, however, to the key difference that the nonreciprocal Jones dichroism—which is to be measured with a *linearly* polarized light—refers to the *real part* of the latter tensor components, whereas the imaginary parts are responsible for XNCD.

17.1.4. Biaxial Crystals and Bigyrotropy

For biaxial crystals that are anisotropic in a plane perpendicular to the direction [0, 0, k] of the wavevector, it is preferable to use the linear combinations

$$\begin{aligned}
t^* &= [\alpha^*_{xx} + \alpha^*_{yy}] + [\zeta^*_{xxz} + \zeta^*_{yyz}],\\
u^* &= [\alpha^*_{xx} - \alpha^*_{yy}] + [\zeta^*_{xxz} - \zeta^*_{yyz}],\\
v^* &= [\alpha^*_{xy} + \alpha^*_{yx}] + [\zeta^*_{xyz} + \zeta^*_{yxz}],\\
w^* &= [\alpha^*_{xy} - \alpha^*_{yx}] + [\zeta^*_{xyz} - \zeta^*_{yxz}]
\end{aligned}$$

or the relevant real parts (t,u,v,w) and imaginary parts (t',u',v',w'). As pointed out by Barron [1], the Stokes vector inside the sample is a function of the X-ray penetration depth d and satisfies the linear differential equation:

$$\frac{\partial}{\partial z}|\mathbf{S}(z)\rangle = a\mathbf{M}\cdot|\mathbf{S}(z)\rangle \tag{17.5}$$

where $a = \frac{1}{2}\omega N c\mu_0$, μ_0 being the free space permeability and N the number density of absorbing centers. The differential Müller matrix $\mathbf{M}$ is to be identified with

$$\mathbf{M} = \begin{bmatrix} t' & u' & -v' & w \\ u' & t' & -w' & v \\ -v' & w' & t' & u \\ w & -v & -u & t' \end{bmatrix}. \tag{17.6}$$

The integration of Eq. (17.5) has been detailed elsewhere [25]. We shall restrict ourselves here to the analysis of XNCD experiments performed with a fully polarized incident X-ray beam ($S_1 = S_2 = 0$; $S_3 = \pm 1$). Up to the second order, one obtains

$$\Delta\sigma_3 \simeq 2(a.w.d) - (ad)^2[uv' - vu'] - \cdots. \tag{17.7}$$

The first term on the right-hand side characterizes the crystal gyrotropy. However, even in the absence of spurious natural linear dichroism, there is a second-order term proportional to $[uv'-vu']$ which can generate an additional XNCD signal that may exist even for nongyrotropic crystals. This was first anticipated by Born and Huang in 1954 [36]. This second-order term is at the origin of the X-ray *crystal optics effect* predicted by Machavariani using a different formalism [37].

17.1.5. X-Ray Circular Intensity Differentials

Graham and Raab noted that a practical way to access the vector part of OA at optical wavelengths was to carry out reflectivity measurements in a suitable geometry—that is, with the optic axis **c** perpendicular to the scattering plane ($\mathbf{c} \perp [\mathbf{k}, \mathbf{k_s}]$). Then, the quantity of interest is the normalized circular intensity differential (CID) defined as

$$CID^{(\sigma,\pi)} = \frac{I_S^{L(\sigma,\pi)} - I_S^{R(\sigma,\pi)}}{I_S^{L(\sigma,\pi)} + I_S^{R(\sigma,\pi)}}, \tag{17.8}$$

where the (σ, π) superscripts need to be specified only when a given polarization component of the scattered light (perpendicular or parallel to the scattering plane) is analyzed. For scattering at 90°, $CID^{(\sigma)}$ and $CID^{(\pi)}$ refer to *polarized* or *depolarized* circular intensity normalized differences, respectively. Notice that $CID^{(\sigma)}$ is equivalent to a measurement of the degree of circularity of the light scattered at 90° since, according to Barron [1], $CID^{(\sigma)} = -S_3^{sc}$. As pointed out by Graham and Raab [22], the vector part of OA contributes to a CID ratio that reaches its maximum for scattering at $\theta_S = 45°$ but vanishes at either normal or grazing incidences. Unfortunately, it is well known that specular reflection of X rays is only possible at grazing angles—that is, far from $\theta_S = 45°$.

As detailed elsewhere [23], we found it possible to transpose this approach using *resonant* elastic or inelastic X-ray scattering (REXS, RIXS) [24]. Key issues in X-ray diffraction are related to the anisotropy of the anomalous dispersion (AAD) or the anisotropic tensor susceptibility (ATS). Actually, the understanding of these questions has much progressed over the past 20 years thanks to a detailed analysis of the nonzero components of the $E1E2$ interference terms.

Neglecting magnetic terms, one may derive the total elastic scattering amplitude from the main Kramers–Heisenberg formula:

$$F = \mathbf{e_s^*} \cdot \mathbf{e_i} \langle J | e^{i(\mathbf{k}-\mathbf{k}_s)\cdot\mathbf{r}} | J \rangle + \frac{1}{m} \sum_N \frac{\langle J | \mathbf{e_s^*} \cdot \mathbf{P} e^{-i\mathbf{k}_s\cdot\mathbf{r}} | N \rangle \langle N | \mathbf{e_i} \cdot \mathbf{P} e^{i\mathbf{k}\cdot\mathbf{r}} | J \rangle}{E_J - E_N + \hbar\omega + i\gamma} \tag{17.9}$$

where $\mathbf{k}$ and $\mathbf{e_i}$ denote the wavevector and polarization vector of the incident X-ray beam, $\mathbf{k}_s$, with $\mathbf{e_s}$ being similarly the wavevector and polarization vector of the scattered X-ray beam. In Eq. (17.9), $\hbar\omega$ is the photon energy, $\mathbf{P} = -i\hbar\nabla$, whereas m denotes the electron mass. The "electrodynamics" convention for the phase of time evolution ($e^{-i\omega t}$)

was preferred to the "crystallographers" convention in which all scattering factors should be replaced by their complex conjugates. In a crystal, each point $\mathbf{G}$ of the Bravais lattice will add its own contribution $F(\mathbf{G})$. The term $F(0)$ should be expanded into a sum over all sites n of the unit cell: $F(0) = \sum_n e^{i\mathbf{q}\cdot\mathbf{r}_n} f_n$, where $\mathbf{r}_n$ is the position of site n, $\mathbf{q} = \mathbf{k} - \mathbf{k}_s$ is the scattering vector, and f_n is the scattering factor for site n. Recall that f_n is the sum of multipole terms:

$$f_n = f_{nT} + f_{ndd} + f_{ndq} + f_{nqq} + \cdots. \tag{17.10}$$

Here f_{nT} denotes the Thomson scattering contribution: $f_{nT} = (\mathbf{e}_\mathbf{s}^* \cdot \mathbf{e}_\mathbf{i}) f_0$ where $f_0 = \langle I | e^{i\mathbf{q}\cdot\mathbf{r}} | I \rangle$ is real; f_{ndd} is the dipole–dipole contribution, f_{ndq} is the dipole–quadrupole contribution and f_{nqq} is the quadrupole–quadrupole contribution. To simplify notation, we shall drop hereafter the site index n.

We introduce next the scattering factors $f^{\sigma\sigma}$,$f^{\sigma\pi}$,$f^{\pi\sigma}$, and $f^{\pi\pi}$, where the two superscripts refer to the linear polarization states of the incident and scattered beams, respectively. Left/right-circular polarization states of the incident beam will be described using the complex polarization vectors: $\mathbf{e}_\mathbf{i} = (e_\pi \pm i e_\sigma)/\sqrt{2}$, so that

$$f^{L/R\sigma} = (1/\sqrt{2})(f^{\pi\sigma} \pm i f^{\sigma\sigma}),$$
$$f^{L/R\pi} = (1/\sqrt{2})(f^{\pi\pi} \pm i f^{\sigma\pi}).$$

The total scattered intensity corresponding to a right/left incident light—that is, $I^{L/R} = I^{L/R,\sigma} + I^{L/R,\pi}$—then becomes

$$I^{L/R} = \frac{|f^{\pi\sigma} \pm i f^{\sigma\sigma}|^2 + |f^{\pi\pi} \pm i f^{\sigma\pi}|^2}{2}, \tag{17.11}$$

whereas the unormalized CID—that is, $\Delta I = I_S^L - I_S^R$—is given by

$$\Delta I = -2\mathrm{Im}[f^{\sigma\sigma}(f^{\pi\sigma})^* + f^{\sigma\pi}(f^{\pi\pi})^*]. \tag{17.12}$$

One would easily check that

$$f^{\sigma\sigma} = f_0 + f_{dd}^{\sigma\sigma} + f_{dq}^{\sigma\sigma} + f_{qq}^{\sigma\sigma},$$
$$f^{\pi\pi} = \cos 2\theta_s f_0 + f_{dd}^{\pi\pi} + f_{dq}^{\pi\pi} + f_{qq}^{\pi\pi},$$

where θ_s is the Bragg angle. We also have

$$f^{\pi\sigma} = f_{dd}^{\pi\sigma} + f_{dq}^{\pi\sigma} + f_{qq}^{\pi\sigma},$$
$$f^{\sigma\pi} = f_{dd}^{\sigma\pi} + f_{dq}^{\sigma\pi} + f_{qq}^{\sigma\pi}.$$

Let us keep in mind that the dominant terms are the Thomson and dipole–dipole contributions. Neglecting again the quadrupole–quadrupole contributions, we finally obtain

$$\begin{aligned}\Delta I \simeq\ & -2f_0\mathrm{Im}(f_{dd}^{\pi\sigma} + f_{dq}^{\pi\sigma}) + 2\cos 2\theta_s f_0 \mathrm{Im}(f_{dd}^{\sigma\pi} + f_{dq}^{\sigma\pi}) \\ & + 2\mathrm{Im}[f_{dd}^{\sigma\sigma}(f_{dd}^{\pi\sigma})^* + f_{dd}^{\sigma\sigma}(f_{dq}^{\pi\sigma})^* + f_{dq}^{\sigma\sigma}(f_{dd}^{\pi\sigma})^* \\ & + f_{dd}^{\sigma\pi}(f_{dd}^{\pi\pi})^* + f_{dq}^{\sigma\pi}(f_{dd}^{\pi\pi})^* + f_{dd}^{\sigma\pi}(f_{dq}^{\pi\pi})^*].\end{aligned}$$

Let us write explicitly the dipole–dipole and dipole–quadrupole contributions:

$$f_{dd} = \sum_N \frac{m\omega_{JN}^2}{E_J - E_N + \hbar\omega + i\gamma} \sum_{\alpha\beta} e^*_{s\alpha} e_{i\beta} d_{\alpha\beta}, \tag{17.13}$$

$$f_{dq} = (i/2) \sum_N \frac{m\omega_{JN}^2}{E_J - E_N + \hbar\omega + i\gamma} \sum_{\alpha\beta\gamma} e^*_{s\alpha} e_{i\beta} (t_{\alpha\beta\gamma} k_\gamma - t^*_{\beta\alpha\gamma} k_{s\gamma}), \tag{17.14}$$

where $d_{\alpha\beta} = \langle J|r_\alpha|N\rangle\langle N|r_\beta|J\rangle$; $t_{\alpha\beta\gamma} = \langle J|r_\alpha|N\rangle\langle N|r_\beta r_\gamma|J\rangle$, whereas $\omega_{JN} = (E_J - E_N)/\hbar$. Recall that, in a nonmagnetic crystal, the wavefunctions $|J\rangle$ and $|N\rangle$ are time-reversal even, so that $d_{\alpha\beta}$ and $t_{\alpha\beta\gamma}$ are real as well. This results in the usual permutation symmetries: $d_{\beta\alpha} = d_{\alpha\beta}$ and $t_{\alpha\gamma\beta} = t_{\alpha\beta\gamma} \propto \mathrm{Re}[E1E2]_{\alpha\beta\gamma}$.

17.2. INSTRUMENTATION AND METHODS

17.2.1. X-Ray Source and Optics

Let us insist that the amplitude of the dichroic signal which we want to measure can be as small as 10^{-4} of the total X-ray absorption cross section. This sets very high the level of sophistication of a beamline designed to measure such tiny dichroisms free of artifacts. Most of the experiments discussed in the next section were carried out at the ESRF beamline ID12 which is dedicated to polarization-dependent XAS over the energy range 2–15 keV, which corresponds to rather "firm" X rays [38]. Since the performances of this beamline were already discussed elsewhere, we shall highlight only a few points that, in our opinion, are crucial for X-ray-detected OA (XDOA) experiments.

Three helical undulators (HU) are available in the user operating mode: the first one (HU-52) is of the HELIOS-II type [12]; the second one (HU-38) is of the APPLE-II type [13, 39]; the last one is a so-called "electromagnet-permanent magnet hybrid undulator" (EMPHU) [40]. All of them can generate either circularly or linearly polarized X rays and complement one to each other. The EMPHU is restricted to energies below 4 keV and is flux-limited, but it offers the major advantage that one can flip the circular polarization from left to right in typically 160 ms. The Helios-II or Apple-II undulators still offer—at a much slower rate—a perfect control of the polarization with the advantage of much higher photon fluxes, especially at high energy. A helical undulator of the APPLE-II type was also used at SPring-8 (Japan) to detect XNCD spectra at the K-edge of oxygen and nitrogen in the soft X-ray range. There is still some interest in using two coaxial helical undulator segments emitting X-ray beams with opposite helicities [41]: A kicker magnet installed in the storage ring could then be used to periodically deflect the electron beam at low frequency ($\sim$1 Hz) and switch on/off alternatively the radiation of each segment. Such a complicated concept was first developed at the ESRF for the soft X-ray beamline branch ID12B [38], but it was finally abandonned.

The monochromator is the most critical component of the XAS spectrometer because the quality of the spectra can suffer from a poor energy resolution, from the transmission of unwanted harmonics or from instabilities of the exit beam during energy scans. The ESRF beamline ID12 is equipped with a UHV-compatible, fixed-exit, double-crystal monochromator manufactured by KoHzu Seiki Co. according to very strict ESRF specifications. The high quality of the mechanics allows one to obtain a fixed-exit beam (within ± 5 μm) over the whole Bragg angular range (6°–80°). The monochromator is

currently equipped with a pair of Si (111) crystals. The temperature of each individual crystal is kept near -140°C ($\pm 0.2^{\circ}$) by a cryogenic cooling system developed in-house and which proved to be completely vibration-free. The stability of the maximum of the rocking curve was found to be better than 0.1 arcsec over periods of several hours. For two consecutive energy scans, a reproducibility of 1 meV or even better is currently achieved.

At this stage, let us emphasize that the high degree of polarization of the undulator beam, unfortunately, is not fully preserved downstream from the double crystal monochromator, except for completely σ or π polarized beams. This is well illustrated by numerical simulations of the polarization transfer in a Si (111) double-crystal monochromator. Assuming that the undulator beam is 100% circularly polarized, we have plotted in Figure 17.1a the Stokes–Poincaré polarization rates (S_1', S_2', S_3') of the monochromatic X-ray beam over the whole energy range of interest (2–10 keV). Arrows were added which point to the K-edge photoionization energy of several elements that are relevant in the context of the results discussed in Section 17.3.

One immediately notices that the values of S_3' get dramatically low at $\sim$2.8 keV; this makes XNCD or XMCD measurements nearly impossible at that energy because the Bragg angle coincides with the Brewster angle ($\Theta_B = 45^{\circ}$) at which the monochromator acts as a perfect linear polarizer ($S_1' = 1$). There is another severe difficulty: Due to differences in the diffracted intensities of the σ and π components of the electric field, the Stokes–Poincaré component S_2' of the monochromatic beam is never zero, except at $\Theta_B = 45^{\circ}$. Note that the intensity of the unwanted S_2' component can be as large as 20% at 2.2 keV. Even worse: Whenever the helicity of the undulator beam is reverted, not only the circular polarization of the monochromatic X-ray beam is altered, but there is also a systematic inversion of S_2', whereas S_1' remains unchanged. This may dramatically affect XNCD experiments on *biaxial* crystals because the weak gyrotropic XNCD signal can be totally masked by a much stronger linear dichroism signal [8, 43]. One may face some similar problem with uniaxial crystals whenever the optic axis is not set parallel to the X-ray wavevector **k**.

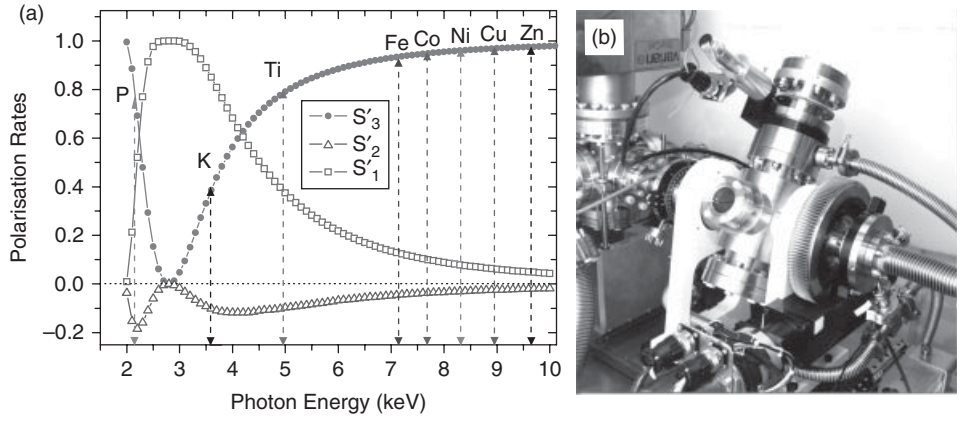

Figure 17.1. (a) Calculated polarization rates of the monochromatic X-ray beam transmitted by a Si (111) double-crystal monochromator under the assumption that the incident X-ray beam was 100% circularly polarized. Arrows point to the energies of the absorption K-edges of selected elements ranging from phosphorous (P) to zinc (Zn). (b) UHV-compatible diamond QWP chambers; highly accurate rotations or the diamond plate are possible along two orthogonal axes.

This problem is not so crucial in the soft X-ray range where grating monochromators operated at grazing incidence are most often used due to the lack of suitable crystals for experiments below 2 keV. Unfortunately, grating monochromators have a rather poor efficiency; this is the price to be paid for their excellent polarization transfer.

A full characterization of the polarization state of the monochromatic beam is needed. This is why beamline ID12 was equipped with a pair of UHV-compatible quarter-waveplate (QWP) devices operated with diamond single crystals [42]. A picture of such a device is shown in Figure 17.1b. Regarding X-ray linear dichroism (XLD) experiments, the QWP device can convert a monochromatic, circularly polarized X-ray beam into a linearly polarized beam with a freely adjustable azimuthal angle of the polarization vector [38]; a fast piezoactuator makes it easy to switch from one linear polarization to the orthogonal one by inverting the sign of the angular offset $\Delta\theta_{QWP}$ which is of the order of only 100 arcsec. Flipping the polarization vector several times for each data point of a spectral scan is quite helpful because the dichroism measurements get less sensitive to low-frequency instabilities of the source.

17.2.2. Detection Modes

XNCD spectra of thick single crystals cannot be recorded in the transmission mode owing to their excessive absorption; in practice, it is much more convenient to measure the *total* X-ray fluorescence yield. As illustrated with Figure 17.2a, the XNCD cube chamber is equipped with eight Si-photodiodes collecting the fluorescence photons over a large solid angle [44]. A backscattering geometry proved to be most convenient since it makes it possible to (i) set the optical axis of the crystal perfectly collinear with the wavevector **k** of the incident X rays and (ii) rotate the crystal around the direction of **k**. The latter rotation $R(\chi)$ was found crucial for OA experiments on biaxial systems. Regarding nonreciprocal dichroisms on ME systems, the sample was inserted inside the bore of a superconducting electromagnet so that a magnetic field **H** and an electric field **E** both parallel to the wavevector **k** could be applied simultaneously for ME annealing or poling.

Recall that raw experimental data should be carefully corrected for fluorescence reabsorption [45, 46], as well as for amplitude distortions caused by multiple fluorescence lines or scattering within the sample. Unfortunately, the detection sensitivity, tends to deteriorate at low excitation energy (i.e., below 3 keV) due to poor fluorescence yields: this is why other detection schemes based on total or partial electron yields are most often preferred in the soft X-ray regime. Such detection modes, however, become *surface* sensitive due to the small escape depth of photoelectrons; this may complicate the interpretation of XNCD experiments. For measurements in the gas phase or with nanometric thin films, transmission measurements remain the best choice in the soft X-ray range.

Note that beamline ID12 is equipped with an UHV compatible, high resolution Bragg-type analyzer operated in the Johann geometry [44]. Resonant inelastic X-ray scattering (RIXS) or X-ray fluorescence photons emitted along the vertical (Z) axis are analyzed using an Si crystal (100 mm in diameter) spherically bent to a fixed curvature radius ($R = 1$ m) defining the Rowland circle on which the sample source point as well as the detector have to be both located. For Bragg angles near 45°, the analyzer works again as a linear polarimeter selecting the polarization component normal to the diffraction plane; as illustrated in Figure 17.2a, the rotation R_Z around the vertical axis makes it possible to explore a possible anisotropy of the emission channel around this

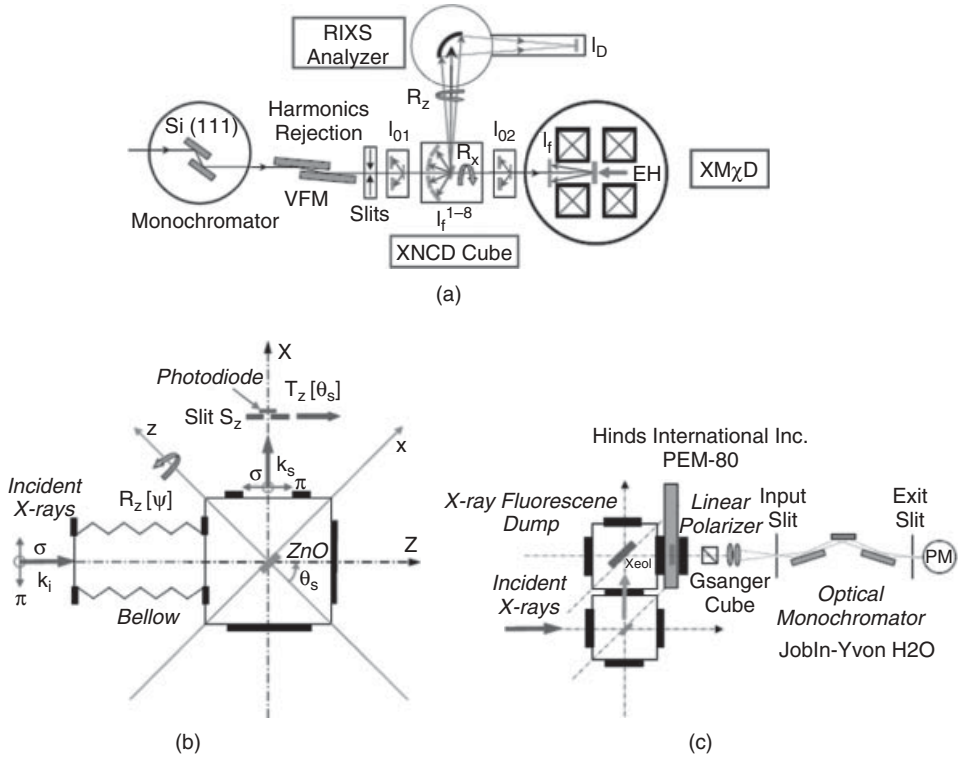

Figure 17.2. (a) Configuration in use for XNCD or XMχD experiments. In XNCD experiments, gyrotropic crystals can be freely rotated around the direction of the incident X-ray beam (rotation R_χ). Beamline ID12 is equipped with a UHV-compatible RIXS analyzer that can be rotated around the vertical axis (Z) to select a given linear polarization. (b) Reflectometer adapted to measure the vector part of OA in zincite. (c) CP-XEOL detection; the combination of a photoelastic modulator (PEM) and a Gsänger linear polarizer made it possible to resolve the right/left-handed polarizations of the luminescence. (*See insert for color representation of the figure.*)

axis. RIXS can be turned into a very rich source of additional information, although it suffers from dramatically low count rates and poor signal-to-noise ratios in comparison with the total fluorescence yield detection mode.

Actually, the relaxation mechanisms for the deep core hole created by the absorption of an X-ray photon are quite complex and involve both radiative and nonradiative processes. We like to draw attention onto the strong optical luminescence that may be excited by X rays in some systems (e.g., rare earth organometallic complexes). Actually, we produced the first experimental evidence of the circular polarization of the X-ray excited optical luminescence (XEOL) of a solution of the Eu(III)(ℓ-FACAM)$_3$ complex (**1**) in which ℓ-FACAM is a 3-trifluoroacetyl-ℓ-camphorato] leavogyre chiral ligand [47]. The experimental setup used for these experiments is shown in Figure 17.2c. Note that the same experimental configuration could possibly be used to detect a magnetochiral dichroism in XEOL emission, as predicted by Wagnière [50] and first observed by Rikken and Raupach in 1997 [49]. Unfortunately, much of the element selectivity expected from XEOL-detected X-ray excited spectra very often gets lost due to the strong excitation of luminescence by secondary photoelectrons [48].

Finally, we have reproduced in Figure 17.2b a schematic view of the X-ray reflectometer which was used to measure the vector part of OA in hexagonal ZnO (zincite) [23]. The whole reflectometer chamber can be rotated around the horizontal axis (Y) perpendicular to the diffraction plane [X, Z] defined with respect to the fixed laboratory frame {X,Y,Z}, whereas {x,y,z} is a reference frame attached to the crystal. For the (300) reflection of zincite, the Bragg angle (θ_S) decreases from 43.19° to 42.75° when the photon energy is scanned over the Zn K-edge XANES range (9654.6–9434.7 eV). For such small angular changes, there is no need for an expensive 2θ goniometer: One may simply use a trivial translation (T_Z) of a narrow slit ($\delta S_z \simeq 0.5$ mm) in front of a large size ($70 \times 12\text{mm}^2$) Si photodiode. An azimuthal rotation ($\Delta\psi$) around the sample axis was also implemented using a compact vacuum stepper motor attached to the sample holder.

17.3. XDOA: ILLUSTRATIVE EXAMPLES

17.3.1. XNCD Experiments

17.3.1.1. Uniaxial Crystals. The existence of XNCD was unambiguously confirmed by careful measurements performed at the ESRF [4] on a levorotatory crystal of α-$LiIO_3$ belonging to the enantiomorphous crystal class 6. A fairly large XNCD signal (up to 6% when normalized to the edge jump) was observed at the iodine L_1 absorption edge. At the L_2 and L_3 absorption edges, the XNCD signatures were less intense and exhibited similar spectral shapes with the same sign; this is at variance with the commonly inverted sign of the XMCD spectra recorded at spin–orbit split edges. Whereas spin–orbit and exchange splitting are the driving concepts in XMCD, this is obviously not the case for the $E1E2$ interference terms contributing to XNCD. This interpretation was fully supported by a comparison of the experimental spectra with *ab initio* simulations carried out in the framework of the multiple scattering theory [51].

There is often a well-resolved pre-edge feature in the K-edge XANES spectra of transition metals. This is a favorable energy range to detect XNCD because such pre-edge signatures are currently assigned to $1s \rightarrow 3d$ quadrupolar transitions [28]. As a typical example [52], we have reproduced in Figure 17.3a the Ni K-edge XAS and XNCD spectra of enantiomorphous single crystals of an α-$NiSO_4 \cdot 6H_2O$. These uniaxial crystals (with four formula units per unit cell) should belong to the enantiomorphpous tetragonal space groups $P4_12_12$ or $P4_32_12$ [53]. Hexahydrate nickel sulfate has long been known to show natural OA only in the crystalline state, due to the chiral arrangement of the water molecules; there are typically four $Ni^{2+}(H_2O)_6$ octahedrons located along a screw axis parallel to the tetragonal **c** axis which is the optic axis. Enantiomorphous crystals of hexahydrate nickel sulfate were also used by Hou and Bloembergen to demonstrate the existence the para-magnetoelectric (pME) effect [54], and, more recently, by Rikken and Raupach to prove the existence of the magnetochiral dichroism in absorption [55].

As illustrated with Figure 17.3a, the maximum amplitude of the Ni K-edge XNCD signal normalized to the edge jump is ~1%. Curiously, this maximum is not found in the pre-edge region but at somewhat higher energy, whereas the XNCD spectrum extends well above the absorption edge. This is differing from all XNCD spectra recorded so far on chiral transition metal complexes. In order to make sure that this XNCD spectrum had to be assigned to the $E1E2$ interference term, XNCD spectra were recorded for several orientations of the crystal—for example, on setting the optic axis either parallel or perpendicular to the X-ray wavevector. From symmetry considerations [51], it can

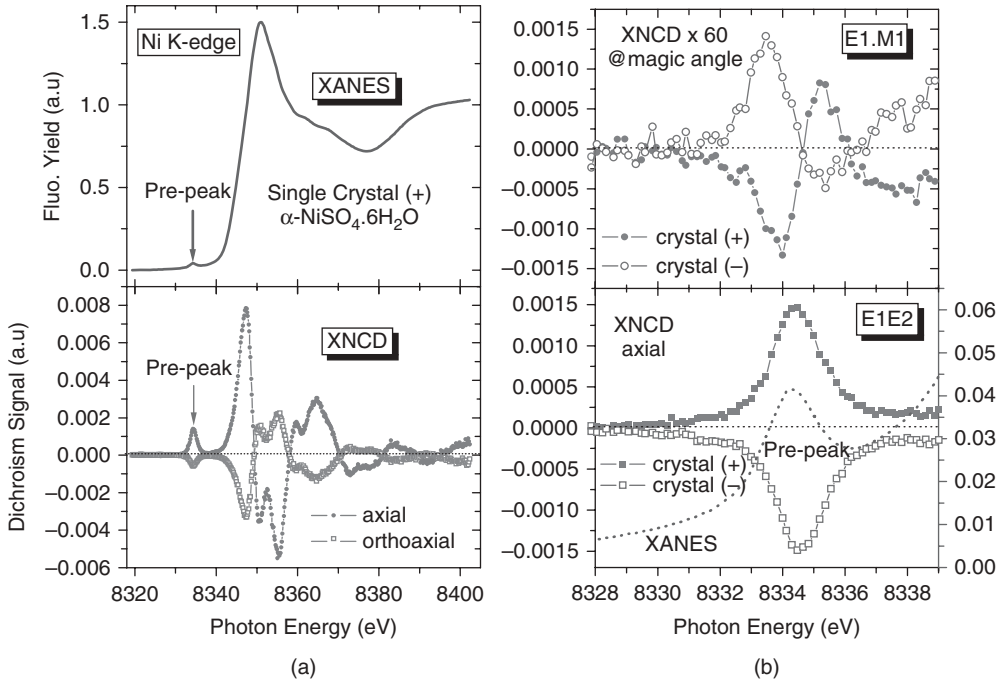

Figure 17.3. (a) Axial and orthoaxial XNCD spectra of a dextrogyre single crystal of $\alpha-NiSO_4 \cdot 6H_2O$ recorded at the Ni K-edge. A polarization averaged XANES spectrum was included for reference. Note that the XNCD signatures have opposite signs. (b) XNCD spectra recorded in the pre-peak range for two enantiomorph crystals. XNCD spectra measured at the magic angle exhibit weak stuctures assigned to the *E*1*M*1 interference term; Note that the *E*1*M*1 dichroism was multiplied by a factor of 60 in order to make it comparable with the *E*1*E*2 signal that largely dominates the axial XNCD spectra of each enantiomorph crystal.

be anticipated that, for point group D_4, the angular dependence of the XNCD signal should vary as $3\cos^2\theta - 1$, where θ denotes the angle between the X-ray wavevector $\mathbf{k}$ and the optic axis of the crystal. This is confirmed with Figure 17.3a: The orthoaxial XNCD spectrum recorded with the X-ray wavevector perpendicular to the optic axis ($\theta = \pi/2$) is not only twice weaker but, interestingly, it has the opposite sign with respect to the XNCD spectrum recorded in the parallel configuration. A similar result had previously been reported by Peacock et al. [56], who measured at the ESRF the angular dependence of the XNCD spectra of the "propeller"-like cobalt complex $\mathbf{2} = \text{CoPPL} = \{\Lambda, \Delta[\text{Co(en)}_3\text{Cl}_3]\}_2 \cdot \text{NaCl} \cdot 6\text{H}_2\text{O}$ [57].

Since the sign of the XNCD signal can change for different orientations of the optic axis, then one should be able to identify one peculiar orientation of the optic axis for which the contribution of the $E1E2$ interference terms should vanish; this precisely happens when the optic axis is set at the magic angle (54.73°) from the X-ray wavevector. Clearly, the only chance to detect a hypothetical $E1M1$ contribution was to record XNCD spectra in this geometry. This stimulated us to perform a whole series of angle-dependent XNCD measurements with enantiomorphous crystals. The results are illustrated in Figure 17.3b, where we focus on the Ni pre-edge range. We found a very weak XNCD signal that may reasonably be assigned to the $E1M1$ interference term, the corresponding signals have the opposite sign for enantiomorphous crystals, but their amplitudes are as small as 3×10^{-5} with respect to the edge jump. By comparison, the

XNCD signatures recorded in the same energy range with the X-ray wavevector parallel to the optic axis are ~60 times larger; this made it possible for the first time to scale properly the respective contributions of $E1M1$ and $E1E2$ interference terms in the firm X-ray range. Note that, for a given enantiomer, the $E1M1$ and $E1E2$ signatures do not peak at the same energy and have the opposite sign.

Interestingly, the $E1M1$ signatures were observed essentially in the pre-edge range in which the final states may be described by localized atomic states. This may perhaps indicate that $E1M1$ transitions become allowed in multielectron processes involving valence electrons (e.g., shake up/down) and which are not subject to standard selection rules. Also supporting such a tentative interpretation was the independent observation of a very weak XNCD signal measured at the Co K-edge with a powdered sample of CoPPL. This is illustrated with Figure 17.4a (bottom), where we compare the XNCD spectra of the Δ-CoPPL complex recorded either with a single crystal or a powdered pellet; for the sake of comparison, we also reproduced (Figure 17.4a, top) the XNCD spectra of single crystals of both enantiomers. Recall that the $E1E2$ interference terms should vanish in a powdered sample that had no preferred orientational order; we nevertheless measured a weak residual XNCD signal in the pre-edge range, and this signal had the opposite sign when compared to the XNCD spectrum of the single crystal of the same enantiomer.

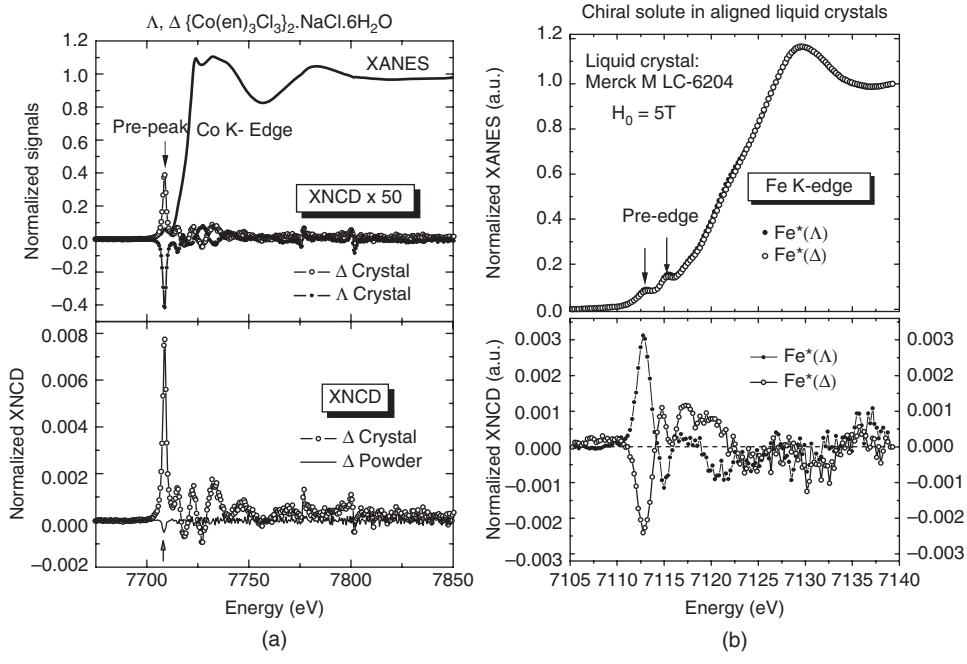

Figure 17.4. (a, top): Enantioselective, Co K-edge XNCD spectra of single crystals of Δ, Λ CoPPL complexes [6]. The XNCD signatures are mostly due to $E1E2$ interference terms. (a, bottom): XNCD spectra of Δ CoPPL recorded either with a single crystal or a powder pellet. In the powder spectrum, note the very weak, inverted signal (marked with an arrow) that could be assigned to the $E1.M1$ interference terms in the pre-edge. (b) Fe K-edge XNCD spectra of the two resolved enantiomers (Δ, Λ) of a chiral iron complex magnetically aligned in a liquid crystal phase (T_c = 66°C).

To fully exploit the enantioselectivity of the XNCD spectra, one would like to benefit from the higher intensity of the $E1E2$ interference terms that unfortunately vanish in powdered samples or solutions. We tried to break artificially the orientational isotropy of space—for example, on dissolving a chiral compound in a liquid crystal aligned in a high magnetic field [58]. For this pioneering test experiment, we used a complex of iron (II)—that is, **3** = (Cp)(I)Fe*(CO)[−PPh_2R], where the absorbing atom (Fe*) was in the asymmetric environment of four different ligands: (i) a cyclopentadienyl moiety η^5-C_6H_5, (ii) an iodine atom (I), (iii) a carbonyl group (CO), and (iv) a chiral tertiary phosphine (−PPh_2R) with R = −NMeC*HMePh. The stereoselective synthesis of the corresponding diastereoisomers, first described in reference 59, was reproduced for us at the university of Burgundy (Dijon, France). Both enantiomers were dissolved in a commercially available liquid crystal selected for its high diamagnetic susceptibility (Merck: MLC-6204). We have reproduced in Figure 17.4b the Fe* K-edge XANES spectra of the two chiral solutions magnetically aligned in a 5T magnetic field oriented along the direction of the X-ray wavector **k**. In the pre-edge range, we observed XNCD signatures featuring the opposite sign for the two enantiomers. This experiment turned out to be very delicate due to the poor solubility of the complex in the liquid crystal phase, whereas long data acquisitions caused strong radiation damages in the intense ESRF X-ray beam.

17.3.1.2. Biaxial Crystals. So far, the only successful attempt to extract a gyrotropic dichroism in a biaxial crystal was performed at the ESRF using single crystals of potassium titanyl phosphate ($KTiOPO_4$ = KTP) [8, 43]. The origin of gyrotropy in KTP (crystal class: $mm2$) is rather ambiguous [60]: It could originate from acentric distortions of the Ti sites featuring one short (1.75 Å) and five long (2.05 Å) Ti···O bonds; alternatively, it may be caused by a pseudohelical distribution of the K^+ cations with a coordination index alternating between 8 and 9. In general, the phosphate groups are not regarded as contributing to gyrotropic OA. As noted by Thomas et al. [61], it is a property of crystal class $mm2$ that no gyrotropic effect should be observed along the optic axis [001]; one may expect, however, quite significant CD signatures of opposite sign along the conjugate directions [120] and [$1\bar{2}0$] of KTP.

Experimentally, we faced a problem evocated in Section 17.2.1: The true gyrotropic XNCD signal was overlaid by a strong, linear dichroism caused by the simultaneous inversion of the spurious Stokes component S_2' of the monochromatic beam when the helicity (S_3) of the undulator radiation was inverted. From Figure 17.1a, one may expect this effect to be particularly strong at the potassium K-edge. Recall, however, that the gyrotropic XNCD signal should be invariant in a rotation $R(\chi)$ of the crystal around the direction of the X-ray wavevector—that is, the conjugate directions [120] and [$1\bar{2}0$] for crystals cut parallel to the (120) and ($1\bar{2}0$) planes, respectively. In contrast, the unwanted linear dichroisms measured for rotation angles satisfying the condition $\Delta\chi = 90^\circ$ should cancel out. Thus, it turned out to be possible to recover the gyrotropic signal on simply averaging all together the dichroism spectra recorded for $\chi_0, \chi_0 + 45^\circ, \chi_0 + 90^\circ, \chi_0 + 135^\circ$. The results are displayed in Figures 17.5a and 17.5b, which confirm the opposite sign of the gyrotropic XNCD signatures measured with KTP crystals cut parallel to the (120) and ($1\bar{2}0$) planes, respectively. The gyrotropic XNCD signal measured in the titanium pre-edge range (∼0.4%) was found much stronger than the signal (∼0.1%) measured in the potassium rising edge.

Since the gyrotropic XNCD signal was expected to be even weaker at the phosphorous K-edge, more sophisticated measurements were needed. Taking full advantage of a

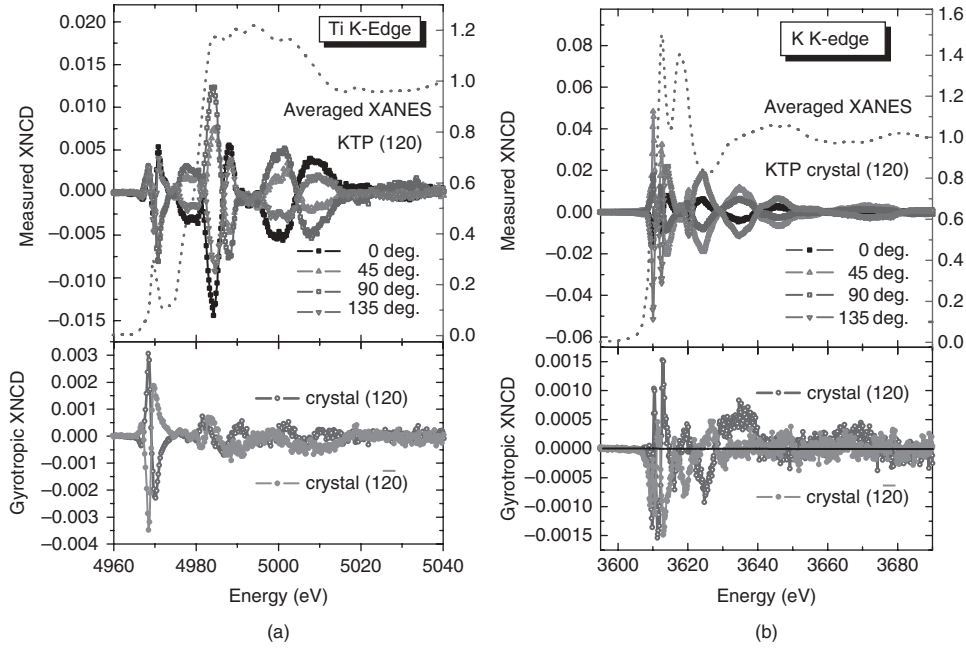

Figure 17.5. Gyrotropic part of XNCD in (120) or (1$\bar{2}$0) KTP single crystals. (a) At the titanium K-edge. (b) At the potassium K-edge. Note the inverted sign of the gyrotropic XNCD signals measured along the conjugated directions [120] and [1$\bar{2}$0], especially in the pre-edge range. The weak gyrotropic signals were burried in much stronger linear dichroisms that were led to cancel out in averaging spectra recorded on rotating the crystal by 90° around the direction of the wavevector **k**.

motorization of rotation R(χ), the X-ray fluorescence yield was recorded over a whole χ-scan for each energy of the monochromator and both helicities of the undulator beam. As illustrated in Figure 17.6A(a), the periodic plots $I_F^{(\pm)}(\chi)$ obtained for the two helicities of the undulator beam did exhibit a constant phase shift, which was the signature of a spurious linear dichroism. On Fourier filtering the CID signal [Figure 17.6A(b)], it became possible to extract the Re and Im parts of the linear dichroism [Figure 17.6B(a)] or resolve even weaker components—for example, due to quadrupolar anisotropies. We identified two Fourier-filtered components that were rotation-invariant: The first one was perfectly anticorrelated for measurements carried out with KTP crystals cut parallel to the (120) and (1$\bar{2}$0) planes, whereas the second one did not change its sign [see Figure 17.6B(b)]. The first component, which had a maximum amplitude of ~0.08%, was assigned to a true gyrotropic XNCD signal. The second one, which is slightly weaker (0.05%), was tentatively assigned to a nonvanishing contribution of the second-order term $uv'-vu'$ [8, 43].

In summary, we established that in KTP the crystal asymmetry was strong enough to induce a mixing of either p and d, or s and p atomic-like, quasi-bound final states not only at the titanium or potassium coordination sites, but at the phosphorus sites as well. Fourier filtering methods applied to extended χ scans also revealed an interesting potentiality that stimulated further applications in refined linear dichroims studies [62]. This review would be incomplete if we did not mention that Tanaka et al. [19] failed to detect any gyrotropic signal at the oxygen K-edge in the soft X-ray range using KTP crystals cut parallel to the (120) and (1$\bar{2}$0) planes.

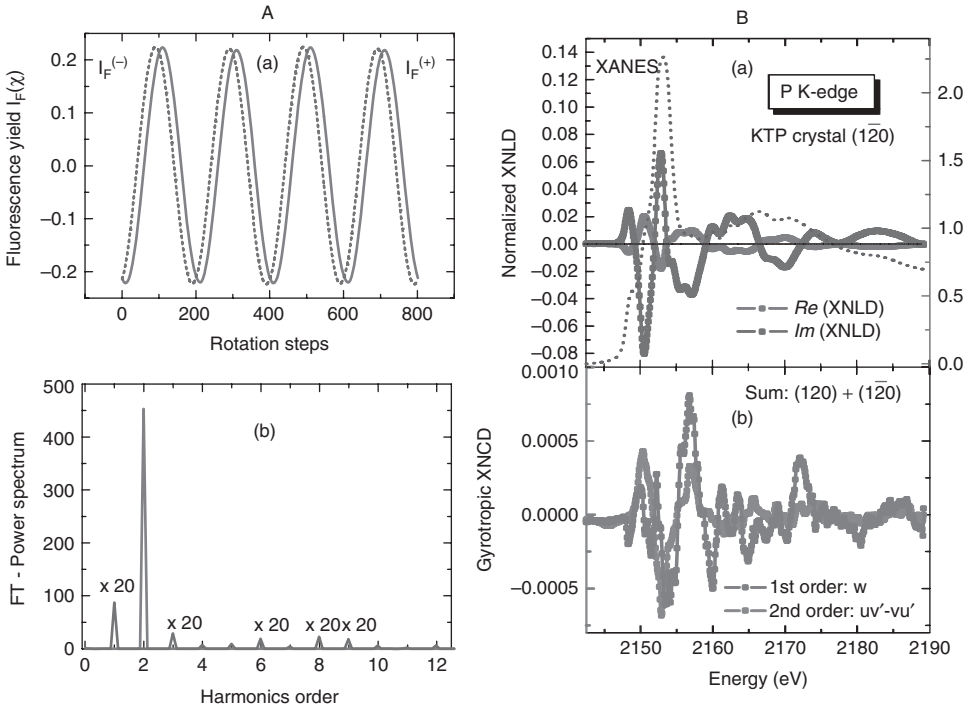

Figure 17.6. [A (a)] Angular dependence of the fluorescence yield $I_F(\chi)$ at the photon energy: 2150.47 eV. The two traces refer to opposite helicities of the undulator beam; their phase shift is the signature of the unwanted linear dichroism due to the monochromator. [A (b)] FT power spectrum of the difference is dominated by the second harmonics due to XLD. [B (a)] Extracted linear dichroisms at the phosphorous K-edge. [B (b)] Rotational invariant XNCD components; only the gyrotropic XNCD component changes its sign for the two conjugate directions [120] and [1$\bar{2}$0], respectively.

17.3.1.3. Soft XNCD. The first experiment that demonstrated a clear possibility to measure the contribution of the $E1M1$ interference terms at the carbon K-edge was performed by Turchini et al. at the ELLETRA synchrotron radiation source [18]. Since this experiment on methyloxirane was carried out in the gas phase using the transmission data acquisition mode, there was no ambiguity left regarding any contamination by the $E1E2$ mechanism or a possible confusion with another mechanism causing circular asymmetry in photoemission. As discussed by Alberti et al., photoabsorption and photoemission processes do not probe the molecular asymmetry in the same way [63]: Whereas in photoemission the photoelectrons feel essentially the asymmetry of the molecular potential in final states, CD in photoabsorption raises the open question of a molecular orbital structure for deep core electrons with its corollary that core electrons may not be fully localized at a given atomic site. Whereas the molecular picture does not look very convincing to describe inner-shell electrons with binding energies in excess of 2 keV, neither is a pure atomic picture fully satisfactory to describe the wavefunctions of electrons with binding energies below 500 eV. What makes the investigation of the $E1M1$ interference terms exciting is that the corresponding transition probabilities become allowed in a molecular picture. Interest in this subject was stimulated by *ab initio* calculations performed initially by two groups [64, 65]. In this context, the observation

of a nonvanishing $E1M1$ signal even at the K-edge of nickel shed a new light on this open question in reinforcing the role of relativistic effects and/or multielectron processes in the description of the final states.

The interest in soft XNCD was stimulated by the discovery of some enantiomeric excess (ee) of L-type amino acids in the Murchinson meteorite [66] and the concurrent idea that homochirality was possibly triggered by VUV or soft X-ray irradiation in space [67]. The first successful experiment carried out on so-called biomolecules was done at SPring-8 (Japan) by Nakagawa and his colleagues [19, 68]: They measured the drain current generated by soft X-rays in D- and L-serine thin films (~300 nm thick) evaporated in vacuum on a gold-coated BeCu substrate. This early experiment called for a few question marks—for example, regarding a possible enantioselective interaction with the metal surface as observed for cystine and glutathion on gold [69], or L-alanine on copper [70]. One might also worry about the surface sensitivity of the total electron yield detection mode. As in the experiment of Turchini et al. on methyloxirane, there was finally a need to remove from the spectra a polarization-dependent background, the origin of which was unclear. In more recent work by the same group [71, 72], thin films of amino acids were evaporated on SiN or SiC membranes whereas the data acquisition was performed in a safe transmission mode. We have reproduced in Figure 17.7 the oxygen K-edge XANES and XNCD spectra of D- and L-serine [71]. Given that there is no apparent orientational order of the adsorbed chiral molecules, it seems highly probable that the soft XNCD signatures have to be assigned to scalar $E1{\cdot}M1$ interference terms. This interpretation was supported by recent *ab initio* simulations [73, 74].

17.3.2. Gyrotropic Dichroisms in REXS and RIXS

17.3.2.1. Vector Part of OA in Zincite. Crystal classes $4mm$, $3m$, and $6mm$ have long been regarded as optically inactive; this is contradicted by Table 17.1, which

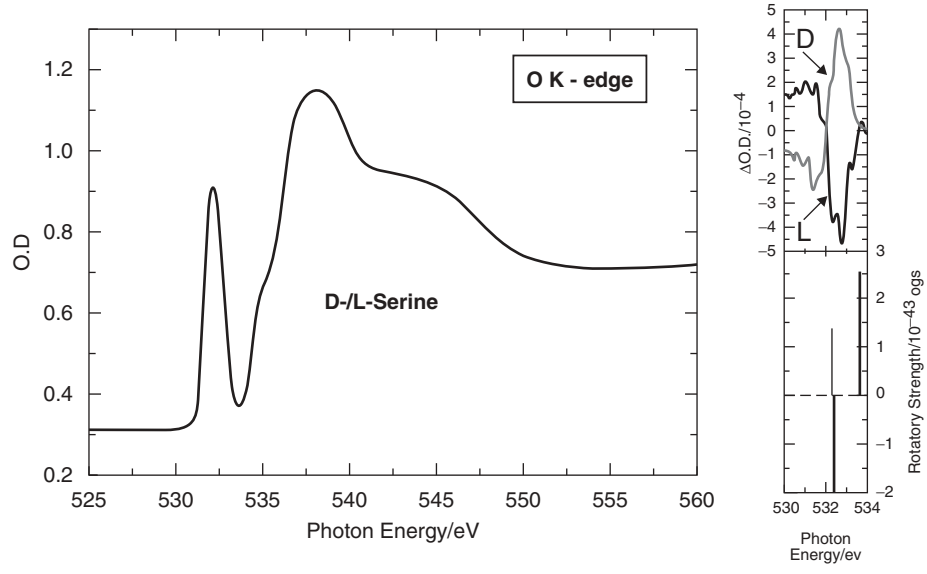

Figure 17.7. Oxygen K-edge XANES and soft XNCD spectra of D and L-serine. (Reproduced from reference 71.)

indicates that their OA tensor should have an irreducible part transforming as a polar vector in $\mathcal{O}_3$. Such a puzzling OA already stimulated the curiosity of Voigt in 1905 [75] and that of Fedorov 50 years later [76]. However, as recently as 1978, Ivchenko et al. measured the OA of an hexagonal crystal of cadmium sulfide (CdS) in the exciton resonance region where OA effects are enhanced [77, 78]. More recently, Graham and Raab pointed out that the vector part of OA should affect reflectivity measurements at optical wavelengths, especially at incidences angles close to 45° [22]. We suggested in Section 17.1.5 that this effect could be detected in the coherent resonant elastic X-ray scattering regime at Bragg angles near 45°.

The first experiment of this type was performed at the ESRF using a high-quality single crystal of zincite (ZnO) featuring the hexagonal structure of wurtzite [23]. Recall that ZnO has long been known to be pyroelectric [79]. We decided to look at the strong reflection on the (300) crystal planes because the Zn atoms contribute for 80% of the structure factor of this reflection characterized by a Bragg angle varying from 43.13° to 42.69° over the whole energy range of the Zn K-edge XANES spectrum. Hereafter, one will prefer the now commonly accepted acronym DANES for diffraction anomalous near edge structure. A brief description of the reflectometer used to record the DANES spectra was already given in Section 17.2.2. The crystal **c** axis was kept strictly perpendicular to the scattering plane. Under such conditions, the angular width of the (300) reflection was only 5.4 arcsec.

The CID spectra reproduced in Figire 17.8A(a) were obtained from DANES spectra recorded with (left, right) circularly polarized incident photons. As pointed out by Graham and Raab [22], the sign of the CID spectra should be inverted if the angle between the **c** axis of the crystal and the reflection plane is rotated from $+90°$ to $-90°$. This is nicely confirmed by Figure 17.8a. In contrast, such a 180° rotation should leave any spurious linear dichroism unchanged. In Figure 17.8A(b), we show that the noninverted part of the CID spectra matches fairly well a rescaled XLD spectrum which was simultaneously obtained in monitoring the fluorescence yield detected by an Si photodiode operated in the backscattering geometry [23]. This is consistent with the fact that the monochromatic X-ray beam should be contaminated with a weak S_2' component, the amplitude of which was found to be $\sim$2% at 9.7 keV.

17.3.2.2. CID in the RIXS Regime. In a subsequent project, we tried to reproduce the same experiment, but on measuring *inelastic* scattering rather than elastic scattering of X rays. Our goal was to get rid of the constraint to find a suitable reflection with a Bragg angle near 45°: since RIXS photons are emitted in the whole solid angle, the direction of the analysis could be kept fixed—for example, at 90° from the wavevector of the incident X-ray wavevector. For this experiment, we used the high-resolution fluorescence analyzer sketched in Figure 17.2a. The geometrical arrangement of the zincite crystal was basically the same as in the previous experiment: the **c** axis was set perpendicular to the plane of incidence whereas the angle of incidence was now strictly 45°. Emission along the vertical axis could now be analyzed both in energy and polarization using a spherically bent Si(440) crystal analyzer since the Bragg angles were respectively 48.37° and 48.55° for the $K\alpha_1$ and $K\alpha_2$ fluorescence lines of zinc.

High-resolution XANES spectra that were recorded at the Zn K-edge with the analyzer tuned to the energy of the Zn $K\alpha_1$ line are reproduced in Figure 17.8b. In contrast, the sensitivity of the XCID experiment was rather frustrating: We found a weak signal peaking at strictly the same energies (marked with arrows) as in the previous experiment and that could be assigned to the expected polar OA, but the signal-to-noise ratio was

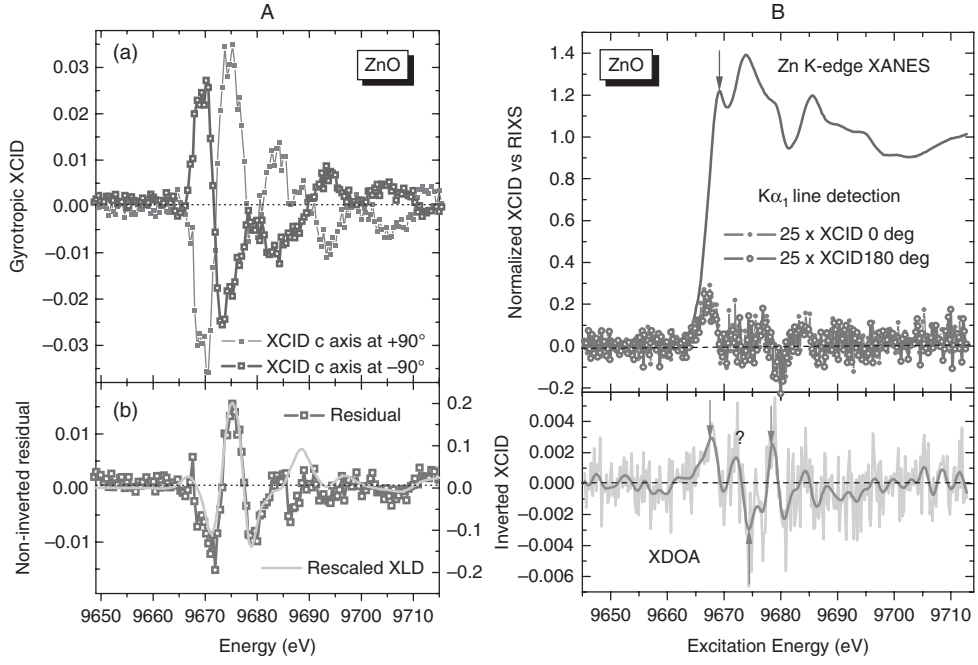

Figure 17.8. [A (a)] Anticorrelated parts of the XCID factor of the DANES spectra of zincite measured with the (300) reflection when $\mathbf{c} \perp [\mathbf{k}, \mathbf{k}_s]$ and $\psi = \pm\pi/2$. [A (b)] Noninverted part of the XCID spectra compared to a rescaled XLD spectrum [23]. (b) Zn K-edge XANES and XCID spectra of zincite measured with the crystal analyzer tuned to the Kα_1 fluorescence line of zinc; the XDOA signature (marked with arrows) does correspond to the anticorrelated part of the XCID spectra recorded for $\psi = \pm\pi/2$, but it is unfortunately burried in a large statistical noise.

dramatically poor. This failure could have been anticipated: Whereas the intensity of the Zn Kα_1 fluorescence line nicely reproduces the XANES, it cannot reproduce the vector part of OA which does not contribute to any absorption. The weak signal that reproduces the vector part of OA should be due to a resonant Raman scattering (RRS) process that is very weak at the energy of the Kα_1 line. In this energy range, we are essentially analyzing fluorescence photons that do not carry any signal but contribute to the huge statistical noise seen by the detector. It is our guess that the result would have been more convincing if the analyzer had been operated in the energy range of the Kβ lines of zinc.

On the other hand, fluorescence emissions and RIXS processes are both sensitive to the pseudo-deviator part of OA. This is illustrated in Figure 17.9 with an early experiment performed with the single crystal of α-lithium iodate which we used to reveal the existence of a strong XNCD signal at the L_1-edge of iodine [4]. The emission spectra were analyzed near the Lβ_3 fluorescence line of iodine peaking at 4313.4 eV: In the corresponding process, electrons from the M shell are filling the core hole created by the photoionization process in the L shell. We used a Si (620) crystal analyzer to catch the Si(311) asymmetric reflection with a large Bragg angle of 61.36°. To maximize the solid angle covered by the analyzer, the optic axis of the crystal was tilted by ~20° with respect to the wavevector of the incident, circularly polarized, X-ray beam. As illustrated with Figure 17.9a, only a three-dimensional plot can give a full picture of the RIXS intensity as a function of both the excitation and emission energies of the X-ray photons [80]. The excitation energy was scanned over the whole range of the iodine L_1 XANES spectrum which exhibits a strong *white line* assigned to $2s \rightarrow 5p$ transitions. On the high-energy

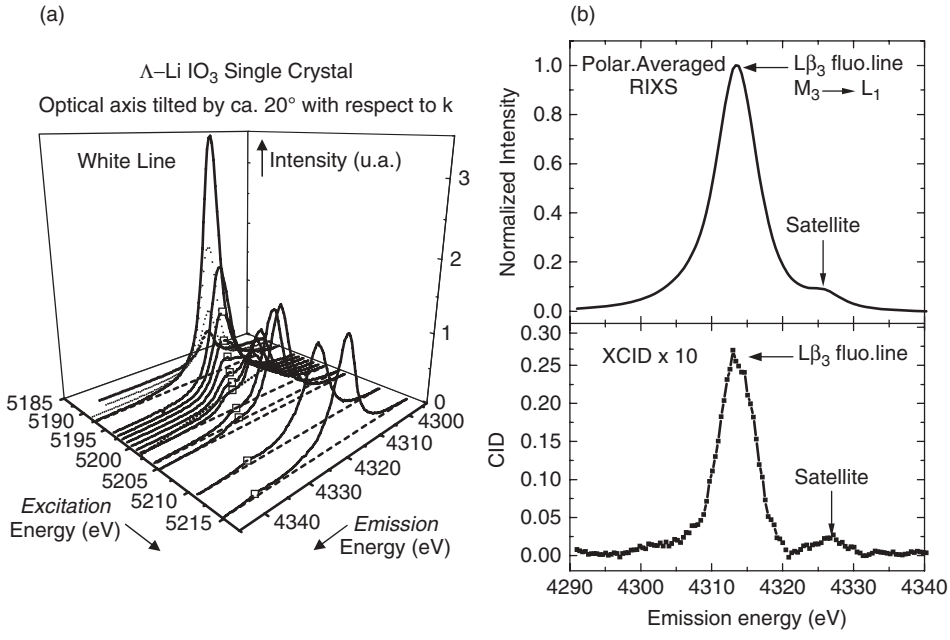

Figure 17.9. (a) 3D map of the emission intensity at excitation energies near the iodine L_I-edge. Note the presence of a dispersive emission satellite marked with square symbols. (b) RIXS and X-ray CID spectra measured at the excitation energy $E = 5207$ eV corresponding to the maximum of the XNCD signal [81].

side of the Lβ_3 fluorescence line, there is clearly an energy dispersive satellite which looks typical of a RIXS process.

The emission spectum reproduced in Figure 17.9b was recorded at a discrete excitation energy (5207 eV) that did correspond to the maximum of the XNCD signal as measured in absorption process [4]. The XCID emission spectrum reproduced in Figure 17.9b exhibits a strong gyrotropic signal not only at the emission energy of the Lβ_3 fluorescence line, but over the whole range of the RIXS satellite as well. To the best of our knowledge, this is the first example of a gyrotropic effect measured in X-ray emission spectra [81]. Since the dispersive satellite is usually regarded as a typical signature of multielectron excitation processes, this experiment suggests that multielectron processes could enhance both $E1M1$ and $E1E2$ transition probabilities.

Unfortunately, with a Bragg angle of 61.36°, the crystal analyzer could not be used as a perfect linear polarimeter, and a reliable polarization analysis of the X-ray emission would have been difficult in this configuration. Nevertheless, we pointed out elsewhere [25] that a careful analysis of the linear polarization of emission spectra combined with the inversion of the Stokes component S_2' would give us access to the dispersive terms of the gyration and OA tensors that cause optical rotation. Even more important, RRS spectra could open a new way to measure the OA properties of light elements (C,N,O) without the UHV constraints and surface sensitivity of soft X rays.

17.3.3. X-Ray Magnetochiral Dichroism

In this section, we are concerned with systems in which parity (I) and time-reversal (Θ) symmetries are broken while the structure remains invariant in the combined action of

the product $I\Theta$. This condition is implicitly satisfied in molecular magnets made of fully resolved chiral building blocks [82]. More generally, it was recognized by Dzyaloshinski that this condition precisely characterized linear ME systems [83]. This stimulated us to try to detect the X-ray magnetochiral dichroism (XMχD) of a single crystal of chromium sesquioxide (Cr_2O_3) cooled down to its antiferromagnetic (AFM) phase [84–86]: this is the generic example used by Dzyaloshinski to predict the existence of a ME susceptibility that was sucessfully measured by Astrov [87]. It was recognized by several authors that such a ME susceptibility was another consequence of spatial dispersion and should give rise to OA effects explicitly related to $E1E2$ interference terms [88–91].

A prerequisite to the detection of an XMχD signal in Cr_2O_3 was the creation of ME *single* domains within the crystal: this turned out to be possible after a proper ME annealing or *poling* procedure [92] which consisted of cooling slowly the crystal below the Néel temperature ($T_N = 307$ K) while applying parallel or antiparallel electric and magnetic fields oriented along the crystal **c** axis set itself parallel to the X-ray wavevector ($\mathbf{E} \parallel \mathbf{H} \parallel \mathbf{k}$). Keeping in mind that the magnetochiral dichroism is a property of unpolarized light, we tried to generate artificially an unpolarized X-ray beam by the incoherent superposition of fluorescence detected spectra recorded consecutively with right- and left-circularly polarized incident photons: $F_0 = F(I_0^{RCP}) + F(I_0^{LCP})$.

The Cr K-edge XMχD spectra displayed in Figure 17.10a were obtained from the difference of such polarization averaged XANES spectra recorded for 180° domains

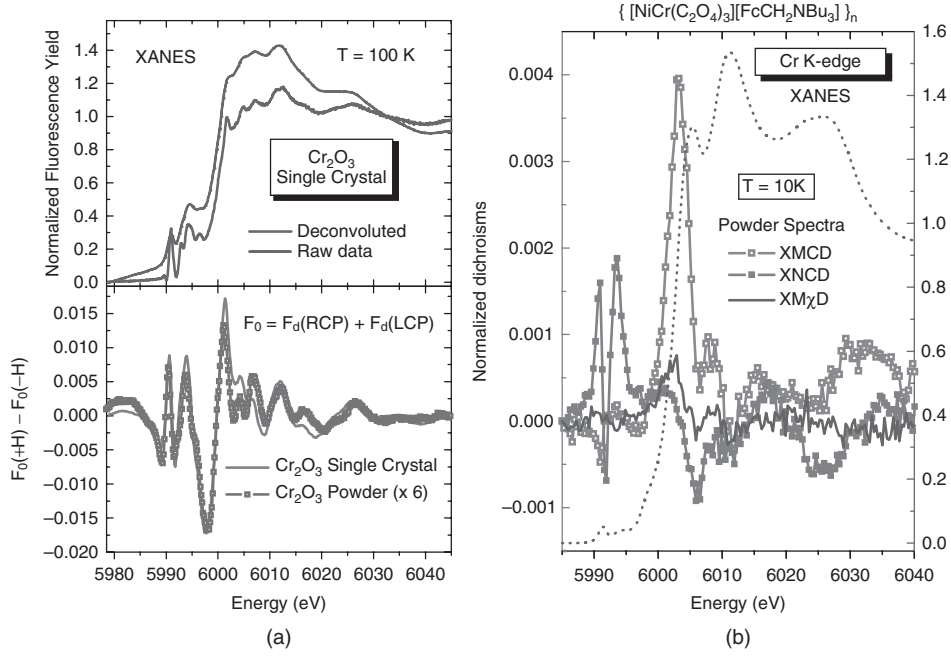

Figure 17.10. (a) Cr K-edge XMχD spectra of Cr_2O_3 recorded with a single crystal ($\mathbf{c} \parallel \mathbf{k}$) or a powdered pellet. The measured dichroisms refer to 180° domains grown under the conditions of time-reversality after ME annealing. The upper traces reproduce the Cr K-edge XANES spectra obtained with or without numerical deconvolution. (a) Cr K-edge XMCD and XNCD spectra of the chemically resolved Δ and Λ enantiomers of the molecular magnet **4**. All spectra were measured with powdered samples cooled down below the Curie temperature ($T_c = 16$ K).

grown under the condition of time-reversality after proper ME poling. All spectra were measured at 50 K. For the sake of comparison, in Figure 17.10a we included XANES spectra recorded at the same temperature for an equidomain crystal: Whereas the first trace corresponds to the raw experimental data, we also show on the same plot a numerically deconvoluted XANES spectrum that has an artificially enhanced energy resolution because the broadening effects due to the core–hole lifetime were partly compensated. Given that rotational isotropy of space is broken when single domains are grown under the conditions of time-reversality after ME poling, we suspected that XMχD spectra could be recorded with powdered samples. This is confirmed by Figure 17.10a: The XMχD spectrum of a powdered pellet of Cr_2O_3 looks very similar to the XMχD spectrum of the single crystal, except that the dichroism intensity was reduced by a factor close to 6 in the powder, in perfect agreement with theoretical predictions [58].

It is well documented that there are 58 magnetic groups for which ME effects are allowed. However, only 31 out them are compatible with the existence of a magnetochiral dichroism [58]: they all have in common the specific property that the ME susceptibility tensor should have nonzero off-diagonal terms [92, 93]. Much of our difficulties started when we realized that the magnetic group $\bar{3}'m'$ quoted in texbooks for the ME phase of Cr_2O_3 was *not* such a group compatible with XMχD. Having carefully checked the full reliability of our XMχD spectra, which turned out to be perfectly reproducible under various experimental conditions, we found that the only magnetic group that would reconcile all experimental observations would be $\bar{3}'$. Its lower symmetry would reflect the existence at the chromium sites of unquenched *orbital* angular moments—for example, due to a weak magnetic polarization of the oxygen atoms. Such a small magnetic perturbation would be too small to be seen by neutron scattering; in contrast, it can easily be detected by Cr K-edge X-ray dichroism measurements that do not probe the spin magnetization but only the *orbital* magnetization. This may not be an isolated example of discrepancy between neutron scattering and other methods regarding the assignment of the true ME group [94]. Within our interpretation, the ME susceptibility tensor of Cr_2O_3 would keep unchanged diagonal terms reflecting the antiferromagnetic arrangement of the spin postulated by Dzyaloshinski, plus weak off-diagonal terms characterizing spin–orbit interactions and a second-order *orbital* ME susceptibility.

XMχD spectra were also measured at the Photon Factory on $GaFeO_3$ by Tokura and his colleagues [95–97], who introduced a different terminology (X-ray directional dichroism) for their measurements at the Fe K-edge. Since this system is weakly ferrimagnetic, there was no need for ME annealing. Interestingly, the magnetic group of $GaFeO_3$ ($m'2'm$ below $T_c \simeq 205$ K) belongs to the 31 ME groups that are compatible with XMχD but also with the existence of ferrotoroidic spin order.

Recently, we revisited a series of prospective test experiments performed in 2002 on chiral molecular magnets—that is, molecular systems in which, according to Barron [98], "*chirality and magnetism shake hands*." We concentrated our efforts on the 2-D bimetallic oxalate polymeric networks **4** = $\{[Ni^{II}Cr^{III}(C_2O_4)_3][Fc\ CH_2NBu_3]\}_n$ with chemically resolved (Δ) or (Λ) absolute configurations of the chiral $[Cr(C_2O_4)_3]^{3-}$ anions. Let us emphasize that all experiments reported below were carried out on powdered samples. Below the Curie temperature ($T_c \simeq 16$ K), three dichroisms were tentatively extracted at the chromium K-edge:

$$\Delta F_{XMCD} = [F(I_0^{LCP}, H\uparrow) - F(I_0^{RCP}, H\uparrow)]/2 + [F(I_0^{RCP}, H\downarrow) - F(I_0^{LCP}, H\downarrow)]/2,$$

$$\Delta F_{XNCD} = [F(I_0^{LCP}, H\uparrow) - F(I_0^{RCP}, H\uparrow)] + [F(I_0^{LCP}, H\downarrow) - F(I_0^{RCP}, H\downarrow)],$$

$$\Delta F_{XM\chi D} = [F(I_0^{LCP}, H\uparrow) + F(I_0^{RCP}, H\uparrow)] - [F(I_0^{LCP}, H\downarrow) + F(I_0^{RCP}, H\downarrow)].$$

We have reproduced in Figure 17.10b these dichroisms properly normalized with respect to the edge jump [99]. We easily measured a rather weak XMCD signal (0.4%) that shows up mainly in the edge; as expected, this dichroism did remain strictly identical for both enantiomers. Although the sample was a powdered pellet, we observed a well-structured, enantioselective XNCD signal (0.2%) in the pre-edge; this was not totally unexpected since the magnetization of the sample breaks down the isotropy of space and makes it now possible to detect $E1E2$ interference terms. We finally succeeded in extracting a very weak, enantioselective magnetochiral dichroism (0.075%) that again did show up in the edge as the XMCD signal. Strong baseline distortions, most probably caused by severe radiation damages over long data acquisition times, did hamper the preliminary data analyses [99]. The intensity of the XMχD signal measured in a powdered sample does not look considerably less intense than the "strong" magnetochiral signal measured at optical wavelengths with single crystals [100].

17.4. UNIFYING THEORIES, FIRST PRINCIPLES SIMULATIONS

17.4.1. General Remarks

At the microscopic level, the X-ray absorption cross section including electric dipole and quadrupole transitions is [28]

$$\sigma(\hbar\omega) = 4\pi^2\alpha_0\hbar\omega \sum_f \left| \langle f|\mathbf{e}\cdot\mathbf{r} + \frac{i}{2}(\mathbf{e}\cdot\mathbf{r})(\mathbf{k}\cdot\mathbf{r})|g\rangle \right|^2 \times \delta(E_f - E_g - \hbar\omega) \tag{17.15}$$

where α_0 is the fine structure constant, $|g\rangle$ the ground state, $|f\rangle$ the final states, E_g and E_f their energies, and $\hbar\omega$ the photon energy. The electric dipole–quadrupole crossed term is

$$\sigma_{E1E2} = 2\pi^2\alpha_0\hbar\omega i \sum_f [\langle f|\mathbf{e}\cdot\mathbf{r}|g\rangle^* \langle f|\mathbf{e}\cdot\mathbf{r}\mathbf{k}\cdot\mathbf{r}|g\rangle - c.c.] \times \delta(E_f - E_g - \hbar\omega),$$

where $c.c.$ stands for complex conjugate. The time-reversal operator Θ satisfies $\langle\Theta\phi|\Theta\psi\rangle = \langle\phi|\psi\rangle^*$. Therefore,

$$\langle f|\mathbf{e}\cdot\mathbf{r}|g\rangle^* = \langle\Theta f|\Theta\mathbf{e}\cdot\mathbf{r}|g\rangle = \langle\Theta f|\mathbf{e}^*\cdot\mathbf{r}|\Theta g\rangle,$$

where we used $\Theta\mathbf{e}\cdot\mathbf{r} = \mathbf{e}^*\cdot\mathbf{r}\Theta$. Magnetic energies are negligible with respect to the experimental resolution of X-ray spectra. Therefore, we can consider that $|f\rangle$ is time-reversal invariant and we only have to consider the time-reversal symmetry of the ground

state. We write $|g\rangle = |g^+\rangle + |g^-\rangle$, where $|g^\pm\rangle$ is even and odd with respect to time-reversal. Thus,

$$T = i[\langle f|\mathbf{e}^* \cdot \mathbf{r}|\Theta g\rangle\langle f|\mathbf{e} \cdot \mathbf{rk} \cdot \mathbf{r}|g\rangle - c.c.]$$

becomes the sum of three terms $T = T^{++} + T^{+-} + T^{--}$, where

$$T^{++} = i[\langle f|\mathbf{e}^* \cdot \mathbf{r}|g^+\rangle\langle f|\mathbf{e} \cdot \mathbf{rk} \cdot \mathbf{r}|g^+\rangle - c.c.],$$

which is time-reversal invariant, corresponds to XNCD.

$$\begin{aligned} T^{+-} = i[&\langle f|\mathbf{e}^* \cdot \mathbf{r}|g^+\rangle\langle f|\mathbf{e} \cdot \mathbf{rk} \cdot \mathbf{r}|g^-\rangle \\ &- \langle f|\mathbf{e}^* \cdot \mathbf{r}|g^-\rangle\langle f|\mathbf{e} \cdot \mathbf{rk} \cdot \mathbf{r}|g^+\rangle + (\mathbf{e} \leftrightarrow \mathbf{e}^*)], \end{aligned}$$

which is time-reversal odd, gives rise to nonreciprocal linear dichroism and magnetochiral dichroism. The term T^{--} is also time-reversal even, but it is generally much smaller than T^{++}. A similar analysis was carried out by van der Laan [101]. The term describing XNCD can be written as the scalar product of $Y_2(\mathbf{k})$ with a second-rank spherical tensor obtained by coupling $\langle g|Y_1(\mathbf{r})|f\rangle$ and $\langle f|Y_2(\mathbf{r})|g\rangle$ [51]. This rank-2 tensor is parity-odd because it is the product of an odd electric dipole transition with an even electric quadrupole transition. This is in full agreement with Table 17.1. A similar discussion could be extended to $E1M1$ terms.

17.4.2. Sum-Rules and Effective XDOA Operators

There may be a chance to get a deeper insight into the physical origin of XDOA if one succeeds in relating the transition probability $\propto E1E2$ to some ground state ($|g\rangle$) observable—that is, to some *effective* operator. This is precisely the aim of the edge-selective spectroscopic sum rules. In 1998, Natoli et al. were the first to question about the physical content of the XNCD integral [51, 102] :

$$\Sigma_{E1E2} = \int_{\Delta E} \frac{\sigma_{E1E2}(E)}{E^2}\, dE \propto \langle g|\mathcal{N}^{(2)}(\ell, \ell')|g\rangle, \tag{17.16}$$

where σ_{E1E2} denotes the X-ray absorption cross section of the $E1E2$ interference terms in a finite energy range ΔE that should include, whenever this is relevant, the two partners (j_+, j_-) of a spin–orbit split edge. On the right-hand side, ℓ refers to the final angular momentum of the electric dipole ($E1$) transition, whereas ℓ' refers to that of the quadrupole transition ($E2$). The monoelectronic selection rules imply that ℓ and ℓ' have opposite parities so that the rank-2 operator $\mathcal{N}^{(2)}(\ell\ \ell')$ probes the mixing of orbitals of different parity in final states. Indeed, there is the perennial problem of XAS that, due to the core hole perturbation, $|g\rangle$ cannot be a true ground state [58, 103]: for brevity, we shall forget about this problem here and we shall concentrate on the physical nature of the operator $\mathcal{N}$. Actually, it can be shown that Eq. (17.16) includes all dichroisms introduced in Section 17.1.3 if one rewrites the right-hand side in a tensor form [58]:

$$\Sigma_{E1E2} = \sum_{b=1}^{3} \sum_{\beta=-b}^{b} \sum_{\theta=\pm 1} (-1)^\beta \mathcal{T}_\beta^{(b,\beta)} \mathcal{N}_{-\beta}^{(b,\theta)}. \tag{17.17}$$

Here $\mathcal{N}_{-\beta}^{(b,\theta)}$ are rank-b spherical tensors that describe OA in parity nonconserving systems, whereas $\mathcal{T}_{\beta}^{(b,\theta)}$ are spherical tensors of same rank that characterize the polarization states of the incident X-ray photons. All spherical tensors were systematically split into their time-reversal even ($\theta = 1$) and time-reversal odd ($\theta = -1$) parts.

Carra et al. [104, 105] were the first to realize and prove that all operators $\mathcal{N}_{-\beta}^{(b,\theta)}$ could be built from a triad of mutually orthogonal vector operators that had a clear physical meaning:

1. $\mathbf{n} = \mathbf{r}/r$ is a time-reversal *even*, polar vector associated with an electric dipole moment.
2. $\mathbf{L}$ is the time-reversal *odd* axial vector of the orbital angular momentum.
3. $\Omega = [(\mathbf{n} \times \mathbf{L}) - (\mathbf{L} \times \mathbf{n})]/2$ is a *toroidal* vector that is *odd* with respect to both inversion I and time-reversal Θ.

Interestingly, Ω was identified with the *orbital* anapole moment [106–108]. Recall that the concept of anapole was introduced in 1958 by Zel'dovich [109] to describe parity-violating interactions.

The next step concerned the identification of the effective operators of natural OA. This turned out to be possible simply on looking at the irreducible spherical tensors of rank n contributing to $\mathcal{N}$:

- At order $n = 0$, $\mathcal{N}^{(0,1)} = \mathbf{L} \cdot \Omega \equiv 0$. The scalar term thus vanishes as anticipated for $E1E2$ cross sections.
- At order $n = 1$, $\mathcal{N}^{(1,1)} = \mathbf{L} \times \Omega \propto \mathbf{r}$. The polar vector part of natural OA is associated with an *electric dipole*, a result that is fully consistent with the existence of pyroelectic or even ferroelectric ordering.
- At order $n = 2$, $\mathcal{N}^{(2,1)} = \mathbf{L} \otimes \Omega = [\mathbf{L}, \Omega]$. This term, written as either a dyad product or a commutator, defines a spherical tensor that looks like a charge quadrupole with odd parity with respect to inversion.

It becomes immediately transparent that, at K-edges, the effective operator of XNCD is the dyad product of two vectors that are time-reversal *odd* and are both related to orbital magnetism. Indeed, a similar exercise makes it possible to identify which are the effective operators of the X-ray ME dichroisms:

- At order $n = 1$, $\mathcal{N}^{(1,-1)} = \Omega$. At a K-edge, the magnetochiral (directional) dichroisms are proportional to the projection of the orbital anapole moment along the direction of the X-ray wavevector.
- At order $n = 2$, $\mathcal{N}^{(2,-1)} = \mathbf{L} \otimes \mathbf{r} = [\mathbf{L}, \mathbf{r}]$. This dyad product which is odd with respect to inversion and time reversal is the effective operator for all nonreciprocal *linear* ME dichroisms [110].
- At order $n = 3$, $\mathcal{N}^{(3,-1)} = [[\mathbf{L}, \mathbf{L}], \Omega]$. This rank-3 tensor could be seen as a small charge octupole with odd parity with respect to I and Θ; it merely adds a second-order correction to all nonreciprocal dichroisms.

Another presentation of the sum rules and many details on the multiplet approach can be found in van der Laan's review paper [111]. We have developed elsewhere a detailed discussion of the practical conditions under which such effective operators could contribute to X-ray dichroism [58]. Clearly, the XMχD sum rule provided us with a unique opportunity to quantify the expectation value of the *orbital* anapole moment

TABLE 17.2. Expectation Values of the Effective XNCD Operators [58]

Compound:	[Δ]-CoPPL	[Λ]-CoPPL	KTP [120]	KTP [1$\bar{2}$0]	$LiIO_3$	TeO_2
Absorption edge:	Co K-edge	Co K-edge	Ti K-edge	Ti K-edge	I L_1-edge	Te L_1-edge
⟨**Effective operator**⟩:	$\langle \mathbf{L} \otimes \Omega \rangle$	$\langle \mathbf{L} \otimes \Omega \rangle$	$\langle \mathbf{L} \otimes \Omega \rangle$	$\langle \mathbf{L} \otimes \Omega \rangle$	$\langle \mathbf{L} \otimes \Omega \rangle$	$\langle \mathbf{L} \otimes \Omega \rangle$
Atomic units:	**+0.424**	**-0.409**	**+0.016**	**-0.011**	**+0.50**	**+0.77**

in Cr_2O_3 : $\langle \Omega_z \rangle \approx 0.03$ a.u. This is a fairly small value in comparison with the values currently retained for spin anapoles [58]. This result fully supports our remark that it would be very difficult—if not simply impossible—to access the orbital (off-diagonal) components of the ME tensor using conventional ME susceptibility measurements. We summarized as well in Table 17.2 the expectation values of the effective XNCD operators deduced from selected experiments carried out at the ESRF.

At this stage, one may still ask whether the sum-rules could be extended to the $E1M1$ interference terms. This exercise was ultimately conducted by Marri and Carra with the prospect of eventual applications at optical wavelengths [112]. It revealed that the effective operators were basically the same as for the $E1E2$ interference terms, but with the major difference that one had to deal with two-electron operators. This was a key requirement to obtain a nonvanishing pseudoscalar term for natural OA.

17.4.3. Ab Initio Calculations

17.4.3.1. **E1E2 *Interference Terms.*** First principle simulations of XNCD spectra were essential to give credit to our speculation that natural XDOA was dominated by the $E1E2$ interference terms, at least in the firm X-ray regime [4, 51, 102]. So far, most calculations were performed in the framework of the theory of multiple scattered waves (MSW) as adapted by Natoli et al. to simulate XANES and extended X-ray absorption fine structure (EXAFS) spectra [113–115]. Starting from an arbitrary partition of space into local (muffin-tin) atomic potentials immersed in a constant interstitial potential of spherical symmetry, one is interested in calculating the wavefunction of an excited photoelectron scattered by the potentials of the atoms surrounding the absorbing element, as well as by the own potential of the absorber. This approach was found to suit remarkably well the needs of X-ray absorption spectroscopy even though it suffers from serious limitations to describe covalent chemical bonding in such a cluster of atoms. An extended formulation of the *optical theorem* led us to rewrite the XNCD cross section at a K- or L_1-edge as

$$\sigma_{E1E2} \propto D_1 Q_2 \mathrm{Re}[\sum_{\nu} Y_2^{\nu *}(\hat{\mathbf{k}}) \tau^{00}(\ell, \ell'; 2\nu)], \tag{17.18}$$

where D_ℓ and $Q_{\ell'}$ are the dipole ($E1$) and quadrupole ($E2$) radial integrals in the photoionization process of the $1s$ or $2s$ core level with the selection rules $\ell = 1$ and $\ell' = 2$, respectively. In Eq. (17.18), $Y_\ell^m(\hat{\mathbf{u}})$ are spherical harmonics (with the Condon–Shortley phase convention) evaluated at the angles of the unit vector $\hat{\mathbf{u}}$. This reminds us that the angular dependence of the XNCD signal is to be described by rank-2 spherical tensors.

On the other hand, the *scattering path* operator τ^{ij} is a kind of symbolic supermatrix describing the scattering process of a photoelectron starting from atom i and ending at atom j, whereas κ is the photoelectron wavevector. What makes the specificity of the

EXAFS regime is the possibility to replace τ^{00} with the first few terms of a truncated Born series expansion:

$$\tau^{00} = \kappa[H^{00}] + \sum_{i\neq 0} \kappa^2 [H^{0i}][T^i][H^{i0}] + \sum_{j\neq i\neq 0} \kappa^3 [H_{0i}][T^i][H^{ij}][T^j][H^{j0}] + \cdots \tag{17.19}$$

where $[T^i]$ refers to the scattering matrix of the atomic potential i, whereas the propagator $[H^{ij}]$ contains all the information on the stereogeometry of the cluster required to describe the scattering process from atom $i \rightarrow$ atom j. The scattering *order* is to be identified with the relevant exponent of the wavevector κ. The series expansion (19) was typically used to analyze the XNCD spectrum of tellurium oxide (TeO_2), which was found to extend into the chiral-EXAFS regime at the Te L_1 edge [43]. As emphasized by Natoli et al. [51, 102], it is the remarkable peculiarity of the chiral-EXAFS regime in XNCD that the first nonvanishing terms in Eq. (17.19) starts with the scattering order $n = 3$. One should also pay attention to the restriction that any path compensated by its mirror image does not contribute to the XNCD signal.

Several FORTRAN codes now include the calculation of σ_{E1E2} as an option: (i) *Continuum* is the original code of Natoli and co-workers; (ii) FEFF8.10 was developed by Ankudinov and Rehr [116] and proved to be most convenient to calculate the phase shifts of high-order scattering paths; (iii) FDMNES is a new code written by Joly and which gained many adepts [117] since it offers useful new options such as the capability to vary the local charge or the possibility to integrate numerically the Schrödinger equation over arbitrary (non-muffin-tin) potentials [118]; and (iv) *Dich* was developed by Brouder to simulate a variety of linear and circular X-ray dichroisms in solids; its starting point is the construction of a self-consistent potential using well-established methods of band structure calculation—for example, the TB-LMTO-ASA code of Andersen and Jepsen [119] which delivers densities and cross densities of states (DOS) in a crystal [102]. The iodine L_1-edge XNCD spectrum of α-$LiIO_3$ was used as a testing bench for these codes; all of them reproduced correctly the rather strong XNCD signal of this crystal. The respective advantages and limitations of each code became more perceptible when Benayoun [120] tried to reproduce the much weaker XNCD signatures observed at the potassium or titanium edges of KTP. Whereas the weak potassium K-edge signatures could be reproduced astonishingly well, the results were much less convincing at the titanium K-edge: The covalent nature of the Ti$\cdots$O bonds certainly added some difficulty, but the main problem was identified as arising from destructive interferences of XNCD signatures associated with nonequivalent titanium sites [120].

We have reproduced in Figure 17.11a the experimental XNCD spectrum recorded at the iodine L_1-edge with the α-$LiIO_3$ single crystal; we included in the same graph two simulations performed with *Dich*. It immediately appears that there is a fair agreement with the full multiple scattering calculation carried out with a modest cluster of 35 atoms; the agreement was nearly as good with a direct calculation of the p, d cross densities of states [102]. Similarly, we have reproduced in Figure 17.11b the XNCD spectrum of a para-tellurite single crystal recorded at the tellurium L_1-edge. This spectrum clearly exhibits oscillations that extend into the EXAFS regime. Interestingly, the largest dichroism was now found in the strong $2s \rightarrow 5p$ white line. From simulations carried out with *Dich* on small clusters, we concluded that the main source of the chiral-EXAFS signal was to be assigned to the stereogeometry of the first few shells of oxygen and tellurium neighbors; we did not observe any further improvement on increasing the size of the

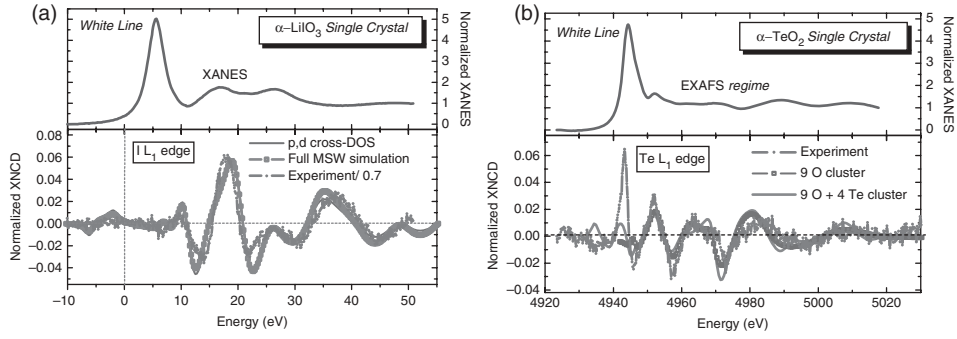

Figure 17.11. (a) The iodine L_1-edge XNCD spectrum of an $\alpha-LiIO_3$ single crystal could be reproduced reasonably well either from direct *p, d* cross-DOS calculations or using a full MSW simulation. To make comparisons easier, the experimental XNCD data were divided by the factor 0.7. Note that the maximum of the XNCD signal was not found in the strong white line of the XANES spectrum. (b) In contrast, the maximum of Te L_1-edge XNCD spectrum of the α-TeO_2 crystal coincides with the white line of the XANES spectrum, whereas oscillations extend into the chiral-EXAFS regime. Chiral-EXAFS oscillations could be reproduced with small clusters restricted to either 9 oxygen atoms or 9 oxygen +4 tellurium atoms.

cluster up to 89 atoms. This finding seems to be at odd with the recommendations made by Ankudinov and Rehr [116], who supported the systematic use of large size clusters (over 100 atoms). We have to admit that none of the various codes reproduced the intense XNCD signal in the white line; this, most probably, reflects a covalent participation of Te 4*d* wavefunctions in the very short Te $\cdots$ O bonds (1.879 Å).

We are not aware of any code satisfactorily reproducing the nonreciprocal ME dichroisms.

17.4.3.2.* E*1*M*1 *Rotatory Strengths. Sophisticated methods have developed in molecular quantum chemistry to describe excited states; such tools look more suitable to analyze gas-phase experiments at the K-edge of the first row elements. Technical aspects regarding specifically the calculations of the $E1 \cdot M1$ pseudoscalar rotatory strengths were reviewed by Kimberg and Kosugi (K&K) [73], who compared three approaches: (i) The STEX method (static-exchange approximation) initiated by Hunt and Goddard was developed and intensively used by Ågren et al. [65, 122, 123] in the context of the building block picture commonly retained to interpret NEXAFS spectra [3]; (ii) the second approach, called "HF excited state," was mostly developed by Kosugi [124, 125] and implemented in his code GSCF3; and (iii) the RPA approach (random phase approximation) of Altick and Glassgold [126] used by Alagna et al. is most easily accessible through the DALTON package [127].

One major difficulty is to describe properly how the core hole is screened by the excited photoelectron. In this respect, Ågren and co-workers recently formulated a new concept of complex polarization propagator (CPP) including the imaginary part of the molecular polarizability and combined this approach with self-interaction correction (SIC) [128]. This concept was experimented by Jiemchooroj and Norman to simulate the carbon K-edge XNCD spectra of chiral fullerenes [129]. In their review, K&K also compared various models for screening ranging from unrelaxed to fully relaxed core states and investigated the dependence of the calculated rotatory strength on the corresponding basis set. It was found that the RPA approach provided the most consistent and less

time-consuming results in a context where, for the time being, neither experimental nor theoretical methods for soft XNCD were yet accurate and robust enough to really discriminate different models. At this stage, it remains far from obvious to us whether or not these methods would allow one to reproduce the $E1M1$ spectra recorded in the firm X-ray range (e.g., at the Ni K-edge) where relativistic effects get more important for high-Z elements. Further work in this direction is clearly desirable.

We regard as very exciting the simulated carbon K-edge XNCD spectra reported by Villaume and Norman for neurotransmitter biomolecules such as noradrenaline and *L*-DOPA, in which the XNCD response of the chiral center was found to be much stronger than for the carbon atoms of the dihydroxyphenyl ring referred to as the chromophore unit [130]. The next step would be to check how far this prediction can be confirmed experimentally; this looks like a formidable challenge, given that such XNCD measurements would simultaneously require a high spectral resolution and a fairly high sensitivity without radiation damage.

17.5. CONCLUDING REMARKS

XDOA encompasses a whole variety of polarization-dependent measurements in X-ray absorption, excitation, or resonant scattering modes over a broad energy range extending from soft to firm X rays. XDOA was shown to offer an unique opportunity to disentangle the respective contributions of the $E1E2$ and $E1M1$ interference terms. All methods considered in this chapter benefit from the common advantage to be *element*- and *edge*-selective. This was nicely illustrated in the case of KTP where the effects of crystal asymmetry could be probed at several K-edges (e.g., K, Ti, P, etc.). Element selectivity also makes XDOA methods considerably less sensitive to impurities which may spoil other chiroptical methods, especially at optical wavelengths. Unfortunately, XDOA also suffers from major handicaps, such as (a) the need to access to synchrotron radiation sources, (b) long data acquisition times enhancing the risks of severe radiation damages especially for organometallic complexes, and (c) the burden of UHV environment in the soft X-ray range. There is also a lack for *site* selectivity with, perhaps, a few exceptions including DANES or, possibly, XEOL experiments.

It seems premature to predict as yet what will be the true impact (in the long term) of soft XNCD measurements on biomelecules. Anyhow, one may reasonably expect growing applications of XDOA in advanced material sciences: XMχD could develop as a unique tool to probe the existence of a (still poorly known) *ferrotoroidal* order in selected ME systems; in the related field of multiferroics, new information could also be gained from a combination of natural and nonreciprocal dichroism measurements. In semiconductor physics, systematic measurements of the polar (vector) part of OA could be helpful in refining the electronic and magnetic properties of III–V semiconductors (e.g., GaAs, GaN) which are of major technological importance.

Even more important, edge-selective sum rules make it now possible to access to the effective operators responsible for OA. An important implication of the K-edge sum rules is that natural OA results from the scalar, vector, or direct product of two vector operators that are time-reversal *odd* and refer to *orbital* magnetism—that is, the orbital angular momentum and the orbital anapole. This bridges the gap between chirality and orbital magnetism in a way that Pasteur could not anticipate while he tried hard (for many years) to unravel the link existing between these two fields of physical chemistry [131, 132].

ACKNOWLEDGMENTS

Illuminating discussions with Profs. L. D. Barron, A. D. Buckingham, I. E. Dzyaloshinski, E. Katz, and C. R. Natoli had a stimulating influence on this work. We like to mention here a long-standing, fruitful collaboration with our ESRF colleague Paolo Carra, who passed away in 2006. Chemically resolved syntheses of diastereoisomers **3** were performed by Professor C. Moise in Dijon, and those of molecular magnets **4** were done by Dr. C. Train in Paris, whereas large-size crystals of nickel sulfate hexahydrate were grown at the ESRF by Dr. A. Bossak. We are indeed grateful to Dr. F. Wilhelm for his assistance at the ESRF beamline ID12, to Professor C. Goulon-Ginet, and Dr. D. Cabaret for their help in data analyses.

REFERENCES

1. L. D. Barron, *Molecular Light Scattering and Optical Activity*, Cambridge University Press, Cambridge, **1982**.
2. P. J. Durham, *Theory of XANES*, in *X-Ray Absorption, Chemical Analysis*, Vol. 92, D. C. Koningsberger and R. Prins, eds., Wiley-Interscience, New York, **1988**, Chapter 2.
3. J. Stoehr, *NEXAFS Spectroscopy, Springer Series in Surface Science*, Vol. 25, R. Gomer, ed., Springer-Verlag, Berlin, **1996**, Chapter 6.3.
4. J. Goulon, C. Goulon-Ginet, A. Rogalev, V. Gotte, C. Brouder, C. R. Natoli, *J. Chem. Phys*. **1998**, *108*, 6394–6403.
5. L. Alagna, T. Prosperi, S. Turchini, J. Goulon, A. Rogalev, C. Goulon-Ginet, C. R. Natoli, B. Stewart, R. Peacock, *Phys. Rev. Lett*. **1998**, *80*, 4799–4802.
6. B. Stewart, R. D. Peacock, L. Alagna, T. Prosperi, S. Turchini, J. Goulon, A. Rogalev, C. Goulon-Ginet, *J. Am. Chem. Soc*. **1999**, *121*, 10233–10234.
7. J. Goulon, C. Goulon-Ginet, A. Rogalev, G. Benayoun, C. Brouder, C. R. Natoli, *J. Synchrotron Rad*. **1999**, *6*, 673–675.
8. J. Goulon, C. Goulon-Ginet, A. Rogalev, G. Benayoun, C. Malgrange, C. Brouder, *Proc. SPIE* **1999**, *3773*, 316–325.
9. W. C. Röntgen, *Communication to the Würtzburg Physical and Medical Society*, Würtzburg, **1895**.
10. A. Cotton, *C. R. Acad. Sci. Paris* **1895**, *120*, 989–1044.
11. L. D. Landau, E. M. Lifshitz, *Electrodynamics of Continuous Media*, Pergamon Press, New York, **1960**.
12. P. Elleaume, *J. Synchrotron Rad*. **1994**, *1*, 19–26.
13. S. Sasaki, *Nucl. Instrum. Methods Phys. Res*. **1994**, *A347*, 83–86.
14. A. Rogalev, F. Wilhelm, N. Jaouen, J. Goulon, J. P. Kappler, *X-ray magnetic circular dichroism: Historical perspective and recent highlights*, in *Magnetism: A Synchrotron Radiation Approach*, E. Beaurepaire, H. Bulou, F. Scheurer, and J.-P. Kappler, eds., *Springer Lecture Notes in Physics*, Vol. 697, Springer, Berlin, **2006**, pp. 71–93.
15. J. Goulon, in *Polarized Synchrotron Radiation, Polarized Electrons and Magnetism*, E. Beaurepaire, B. Carrière, and J. P. Kappler, eds., IPCMS, **1989**, Chapter VI, pp. 333–386.
16. J. W. Cooper, *Phys. Rev*. **1993**, *A47*, 1841–1851.
17. L. D. Barron, *Mol. Phys*. **1971**, *21*, 241–246.
18. S. Turchini, N. Zema, S. Zennaro, L. Alagna, B. Stewart, R. D. Peacock, T. Prosperi, *J. Am. Chem. Soc*. **2004**, *126*, 4532–4533.
19. M. Tanaka, K. Nakagawa, A. Agui, K. Fuji, A. Yokoya, *Phys. Scr*. **2005**, *T115*, 873–876.

20. J. Goulon, F. Sette, C. Moise, A. Fontaine, D. Perey, P. Rudolf, F. Baudelet, *Jpn. J. Appl. Phys*. **1993**, *Suppl. 32-2*, 284–289.
21. J. Jerphagnon, D. Chemla, *J. Chem. Phys*. **1976**, *65*, 1522–1529.
22. E. B. Graham, R. E. Raab, *J. Opt. Soc. Am*. **1996**, *A13*, 1239–1248.
23. J. Goulon, N. Jaouen, A. Rogalev, F. Wilhelm, C. Goulon-Ginet, C. Brouder, Y. Joly, E. N. Ovchinnikova, V. E. Dmitrienko, *J. Phys.: Condens. Matter* **2007**, *18*, 156201(18pp).
24. M. Altarelli, *Resonant X-Ray Scattering*, in: *Magnetism: A Synchrotron Radiation Approach*, E. Beaurepaire, H. Bulou, F. Scheurer, and J.-P. Kappler, eds., *Springer Lecture Notes in Physics*, Vol. 698, Springer, Berlin, **2006**, pp. 201–242.
25. J. Goulon, C. Goulon-Ginet, A. Rogalev, V. Gotte, C. Brouder, C. Malgrange, *Eur. Phys. J*. **1999**, *B12*, 373–385.
26. A. D. Buckingham, *Adv. Chem. Phys*. **1968**, *12*, 107–142.
27. A. D. Buckingham, M. B. Dunn, *J. Chem. Soc. A* **1971**, 1988–1991.
28. C. Brouder, *J. Phys.: Condens. Matter* **1990**, *2*, 701–738.
29. G. Schütz, W. Wagner,, W. Wilhelm, P. Kienle, R. Zeller, R. Frahm, G. Materlick, *Phys. Rev. Lett*. **1987**, *58*, 737–740.
30. C. T. Chen, F. Sette, Y. Ma, S. Modesti, *Phys. Rev*. **1990**, *B42*, 7262–7265.
31. D. P. Siddons, M. Hart, Y. Amemiya, J. B. Hastings, *Phys. Rev. Lett*. **1990**, *64*, 1967–1970.
32. G. H. Wagnière, A. Meier, *Chem. Phys. Lett*. **1982**, *93*, 78–81.
33. L. D. Barron, J. Vrbanovich, *Mol. Phys.* **1984**, *51*, 715–730.
34. N. B. Baranova, B. Ya. Zeldovich, *Mol. Phys*. **1979**, *38*, 1085–1098.
35. G. H. Wagnière, *Chem. Phys*. **1999**, *245*, 165–173.
36. M. Born, K. Huang, *Dynamical Theory of Crystal Lattices*, Clarendon, Oxford, **1954**, pp. 336–338.
37. V. S. Machavariani, *J. Phys. C: Cond. Matter* **1995**, *7*, 5151–5154.
38. J. Goulon, A. Rogalev, C. Gauthier, C. Goulon-Ginet, S. Pasté, R. Signorato, C. Neumann, L. Varga, C. Malgrange, *J. Synchrotron Rad*. **1998**, *5*, 232–238.
39. J. Chavanne, C. Penel, P. Van Vaerenbergh, *Proc. Part. Accel. Conf*. **2001**, 2459–2461.
40. A. Rogalev, J. Goulon, G. Benayoun, P. Elleaume, J. Chavanne, C. Penel, P. Van Vaerenbergh *Proc. SPIE* **1999**, *3773*, 275–283.
41. T. Muro, T. Nakamura, T. Matsushita, T. Wakita, K. Fukumoto, H. Kimura, T. Hirono, T. Kinoshita, T. Hara, K. Shirasawa, M. Takeuchi, H. Kitamura, *A.I.P. Conf. Proc*. **2007**, *879*, 571–574.
42. C. Malgrange, L. Varga, C. Gilès, A. Rogalev, J. Goulon, *Proc. SPIE* **1999**, *3773*, 326–339.
43. J. Goulon, C. Goulon-Ginet, A. Rogalev, G. Benayoun, C. Brouder, C. R. Natoli, *J. Synchrotron Rad*. **2000**, *7*, 182–188.
44. J. Goulon, A. Rogalev, G. Goujon, C. Gauthier, E. Moguiline, A. Solé, S. Feite, F. Wilhelm, N. Jaouen, C. Goulon-Ginet, P. Dressler, P. Rohr, M.-O. Lampert, R. Henck, *J. Synchrotron Rad*. **2005**, *12*, 57–69.
45. J. Goulon, C. Goulon-Ginet, R. Cortès, J.-M. Dubois, *J. Phys. (France)* **1982**, *43*, 539–548.
46. M. Loos, I. Ascone, C. Goulon-Ginet, J. Goulon, C. Guillard, M. Lacroix, M. Breysse, D. Faure, T. Descourières, *Physica* **1989**, *B 158* 145–148.
47. C. Gauthier, I. Ascone, J. Goulon, R. Cortès, J. M. Barbe, R. Guilard, *Chem. Phys*. **1990**, *147*, 165–172.
48. A. Rogalev, J. Goulon, X-ray excited optical luminescence spectroscopies, in *Chemical Applications of Synchrotron Radiation*, T.-K. Sham, ed., *Advanced Series in Physical Chemistry*, Vol. 12B, World Scientific, Hachensack, NJ, **2002**, Chapter 15.
49. G. L. J. A. Rikken, E. Raupach, *Nature* **1997**, *390*, 493–494.

50. G. Wagnière, *Chem. Phys. Lett*. **1984**, *110*, 546–551.
51. C. R. Natoli, C. Brouder, P. Sainctavit, J. Goulon, C. Goulon-Ginet, A. Rogalev, *Eur. Phys. J*. **1998**, *B4*, 1–11.
52. A. Rogalev, J. Goulon, F. Wilhelm, A. Bosak *X-Ray Detected Optical Activity, Springer Proceedings in Physics* Vol. 133, Springer, Berlin, **2010**, pp. 169–190.
53. K. Stadnicka, A. M. Glazer, M. Koralewski, *Acta Crystallogr*. **1987**, *B43*, 319–325.
54. S. L. Hou, N. Bloembergen, *Phys. Rev*. **1965**, *138*, A1218–A1226.
55. G. L. J. A. Rikken, E. Raupach, *Phys. Rev*. **1998**, *E58*, 5081–5084.
56. R. D. Peacok, T. Prosperi, B. Stewart, *Chem. Phys. Lett*. **2007**, *444*, 375–378.
57. K. Nakatsu, M. Shiro, Y. Saito, H. Kuroya, *Bull. Chem. Soc. Jpn*. **1957**, *30*, 158–164.
58. J. Goulon, A. Rogalev, F. Wilhelm, C. Goulon-Ginet, P. Carra, I. Marri, C. Brouder, *J. Exp. Theor. Phys*. **2003**, *92*, 402–431.
59. H. Brünner, J. Doppelberger, *Bull. Soc. Chim. Belg*. **1975**, *84*, 923–931.
60. P. A. Thomas, A. M. Glazer, B. E. Watts, *Acta Cryst*. **1990**, *B46*, 333–343.
61. P. A. Thomas, J. Tebbutt, A. M. Glazer, *J. Appl. Crystallogr*. **1991**, *24*, 963–967.
62. D. Cabaret, C. Brouder, M.-A. Arrio, P. Sainctavit, Y. Joly, A. Rogalev, J. Goulon, *J. Synchrotron Rad*. **2001**, *8*, 460–462.
63. G. Alberti, S. Turchini, G. Contini, N. Zema, T. Prosperi, S. Stranges, V. Feyer, P. Bolognesi, L. Avaldi, *Phys. Scr*. **2008**, *78*, 058120(6pp).
64. L. Alagna, S. Di Fonzo, T. Prosperi, S. Turchini, P. Lazzaretti, P. Malagoli, R. Zanasi, C. R. Natoli, P. J. Stephens, *Chem. Phys. Lett*. **1994**, *223*, 402–410.
65. V. Caravetta, O. Plachkevytch, O. Vahtras, H. Ågren, *Chem. Phys. Lett*. **1997**, *275*, 70–78.
66. J. R. Cronin, S. Pizzarello, *Science* **1997**, *275*, 951–955.
67. F. Raulin, P. Coll, N. Smith, M.-C. Gazeau, Radiation induced prebiotic syntheses on Titan, pp. 73–85 in *The Role of Radiation in the Origin and Evolution of Life*, M. Akaboshi, N. Fujii, and N. Navarro-Gonzalèz, eds., Kyoto University Press, Kyoto, Japan, **2000**.
68. K. Nakagawa, F. Kaneko, Y. Ohta, M. Tanaka, T. Kikada, A. Agui, F. Fuji, A. Yokoya, K. Yagi-Watanabe, Y. Yamada, *J. Electr. Spectrosc. Relat. Phenom*. **2005**, *144–47*, 271–273.
69. A. Kúhnle, T. R. Linderoth, B. Hammer, F. Besenbacher, *Nature, Lett*. **2002**, *415*, 891–893.
70. I. Stensgard, *Surf. Sci. Lett*. **2003**, *545*, L747–L752.
71. K. Nakagawa, T. Matsui, Y. Izumi, A. Agui, M. Tanaka, T. Muro, *Radiat. Phys. Chem*. **2009**, *78*, 1198–1201.
72. Y. Izumi, A. Imazu, A. Mimoto, M. Tanaka, K. Nakagawa, M. Tanaka, A. Agui, T. Muro, *J. Phys. Conf. Series* **2009**, *190*, 012209(4pp).
73. V. Kimberg, N. Kosugi, *J. Chem. Phys*. **2007**, *126*, 245101(10p).
74. A. Jiemchooroj, U. Ekström, P. Norman, *J. Chem. Phys*. **2007**, *127*, 165104(8p).
75. W. Voigt, *Ann. Phys. Leipzig* **1905**, *18*, 645–694.
76. F. I. Fedorov, *Opt. Spectrosc. (USSR)* **1959**, *6*, 237–240.
77. E. L. Ivchenko, S. A. Permogorov, A. V. Selkin, *Sol. St. Comm*. **1978**, *28*, 345–348.
78. E. L. Ivchenko, Spatial dispersion effects in the exciton resonance region, in *Excitons*, I. E. Rashba and M. D. Sturge, eds., North-Holland, Amsterdam, **1987**.
79. J. Albertsson, S. C. Abrahams, Å. Kvick, *Acta Crystallogr*. **1989**, *B 45*, 34–40.
80. P. Carra, M. Fabrizio, T. Thole, *Phys. Rev. Lett*., **1995**, *74*, 3700–3704.
81. C. Dallera, M. Krisch, F. Sette, J. Goulon, A. Rogalev, C. Goulon-Ginet, *ESRF Expt. Report*, **1998**, *Proposal HE 217*, 2–pp.
82. R. Andrès, M. Brissard, M. Gruselle, C. Train, J. Vaissermann, B. Malézieux, J.-P. Jamet, M. Verdaguer, *Inorg. Chem*. **2001**, *40*, 4633–4640.
83. I. E. Dzyaloshinskii, *Sov. Phys. JETP Lett*. (English translation), **1960**, *10*, 628–629.

84. J. Goulon, A. Rogalev, F. Wilhelm, C. Goulon-Ginet, P. Carra, D. Cabaret, C. Brouder, *Phys. Rev. Lett*. **2002**, *88*, 237401(4pp).
85. J. Goulon, A. Rogalev, F. Wilhelm, N. Jaouen, C. Goulon-Ginet, P. Carra, I. Marri, C. Brouder, *Phys. Scr*. **2005**, *T115*, 54–58.
86. A. Rogalev, J. Goulon, F. Wilhelm, *C. R. Physique* **2008**, *9*, 642–656.
87. D. N. Astrov, *Sov. Phys. JETP* (English translation) **1960**, *11*, 708–709; *13*, 729–733.
88. R. R. Birss, R. G. Shrubsall, *Philos. Mag*. **1967**, *15*, 687–700.
89. R. M. Hornreich, S. Shtrikman, *Phys. Rev*. **1968**, *171*, 1065–1074.
90. E. B. Graham, R. E. Raab, *J. Phys.: Condens. Matter* **1994**, *6*, 6725–6732.
91. B. B. Kritchevtsov, V. V. Pavlov, R. V. Pisarev, V. N. Gridnev, *J. Phys.: Condens. Matter* **1993**, *5*, 8233–8244.
92. H. Schmid, *J. Phys.: Condens. Matter* **2008**, *20*, 434201(24pp).
93. J.-P. Rivera, *Eur. Phys. J*. **2009**, *B71*, 299–313.
94. H. Schmid, Magnetoelectric effects in insulating materials, in *Introduction to Complex Medium for Optics and Electromagnetiscs*, W. S. Weigelhofer and A. Lakhtakia, eds., SPIE Press, Bellingham, WA, **2004**, pp. 167–194.
95. M. Kubota, T. Arima, Y. Kaneko, J. P. He, X. Z. Yu, Y. Tokura, *Phys. Rev. Lett*. **2004**, *92*, 137401(4pp).
96. T. Arima, *J. Phys.: Condens. Matter*, **2008**, *20*, 434211(9pp).
97. J-i. Igarashi, T. Nagao, *J. Phys. Soc. Jpn*, **2010**, *79*, 014705(7p).
98. L. D. Barron, *Nature materials*, **2008**, *7*, 691–692.
99. J. Goulon, A. Rogalev, F. Wilhelm, N. Jaouen, C. Goulon-Ginet, C. Train, G. Champion, C. Cartier, M. Gruselle, M. Verdaguer, *ESRF Expt. Report*, **2003**, *Proposal HE 1246*, 2–pp.
100. C. Train, R. Gheorghe, V. Krstic, L.-M. Chamoreau, N. S. Ovanesyan, G. L. J. A. Rikken, M. Gruselle, M. Verdaguer, *Nature materials*, **2008**, *7*, 729–734.
101. G. van der Laan, *J. Synchrotron Rad*., **2001**, *8*, 1059–60.
102. C. Brouder, C. R. Natoli, P. Sainctavit, J. Goulon, C. Goulon-Ginet, A. Rogalev, *J. Synchrotron Rad*., **1999**, *6*, 261–263.
103. S. Di Matteo, C. R. Natoli, *J. Synchrotron Rad*. **2002**, *9*, 9–16.
104. P. Carra, R. Benoist, *Phys. Rev*. **2000**, *B62*, R7703–R7706.
105. P. Carra, A. Jerez, I. Marri, *Phys. Rev*. **2003**, *B67*, 045111 7pp.
106. I. B. Khriplovich, M. E. Prospelov, *Z. Phys. D: Atoms, Mol. Clusters*, **1990**, *17*, 81–84.
107. I. B. Khriplovich, *Parity Nonconservation in Atomic Phenomena*, Gordon and Breach Science Publishers, OPA Amsterdam, **1991**.
108. R. R. Lewis, *Phys. Rev*. **1994**, *A49*, 3376–3380.
109. I. B. Zel'dovich, *Sov. Phys. JETP Lett*. (Engl. translation), **1958**, *6*, 1184–1186.
110. J. Goulon, A. Rogalev, C. Goulon-Ginet, G. Benayoun, L. Paolasini, C. Brouder, C. Malgrange, P. A. Metcalf, *Phys. Rev. Lett*. **2000**, *85*, 4385–4388.
111. G. van der Laan, in *Magnetism: A Synchrotron Radiation Approach, Lecture Notes in Physics*, Vol. 697, E. Beaurepaire, H. Bulou, F. Scheurer, and J.-P. Kappler, eds., Springer, Berlin, **2006**, pp. 143–200.
112. I. Marri, P. Carra, C. M. Bertoni, *J. Phys. A: Math. Gen*. **2006**, *39*, 1969–1978.
113. C. R. Natoli, D. K. Misemer, S. Doniach, *Phys. Rev*., **1980**, *A22*, 1104–1108.
114. F. W. Kutzler, C. R. Natoli, D. K. Misemer, S. Doniach, *J. Chem. Phys*., **1980**, *73*, 3274–3288.
115. C. R. Natoli, M. Benfatto, S. Doniach, *Phys. Rev*., **1986**, *A34*, 4682–4694.
116. A. L. Ankudinov, J. Rehr, *Phys. Rev*. **2000**, *B62*, 2437–2445.

117. A. Rogalev, J. Goulon, F. Wilhelm, K. A. Kozlovskaya, E. N. Ovchinnikova, L. V. Soboleva, A. F. Konstantinova, V. E. Dmitrienko, *Crystallogr. Rep*. **2008**, *53*, 416–422 (in Russian).
118. Y. Joly, *Phys. Rev*., **2001**, *B63*, 125120(10p).
119. O. Jepsen, O. K. Andersen, *Z. Phys*. **1995**, *B97*, 35–47.
120. G. Benayoun, Ph.D. thesis, **2001**, Université Joseph Fourier, Grenoble (France), 176–pp.
121. W. J. Hunt, W. A. Goddard III, *Chem. Phys. Lett*., **1969**, *3*, 414–418.
122. H. Ågren, V. Caravetta, O. Vahtras, L. G. M. Pettersson, *Chem. Phys. lett*. **1994**, *222*, 75–81.
123. K. Kaznacheyev, A. Osanna, C. Jacobsen, O. Plashkevych, O. Vahtras, H. Ågren, V. Caravetta, A. P. Hitchcok, *J. Phys. Chem*. **2002**, *A 106*, 3153–3168.
124. N. Kosugi, H. Kuroda, *Chem. Phys. Lett*. **1980**, *74*, 490–493.
125. N. Kosugi, *Theor. Chim. Acta* **1987**, *72*, 149–173.
126. P. L. Altick, A. E. Glassgold, *Phys. Rev*. **1964**, *133*, 632–646.
127. DALTON Release 2.0, *a molecular electronic structure program*, **2010**.
128. G. Tu, Z. Rinkevicius, O. Vahtras, H. Ågren, U. Ekström, P. Norman, V. Caravetta, *Phys. Rev*. **2007**, *A76*, 022506(7p).
129. A. Jiemchooroj, P. Norman, *J. Chem. Phys*. **2008**, *128*, 234304(4p).
130. S. Villaume, P. Norman, *Chirality* **2009**, *21*, E13–E19.
131. L. Pasteur, *Rev. Sci*. **1884**, *7*, 2–6.
132. H. D. Flack, *Acta Cryst*. **2009**, *A65*, 371–389.

18

LINEAR DICHROISM

Alison Rodger

18.1. INTRODUCTION

Linear dichroism (LD) is the difference in absorption of light linearly polarized parallel and perpendicular to an orientation axis:

$$LD = A_{//} - A_{\perp}. \tag{18.1}$$

LD is related to the main subject of this book, namely circular dichroism (CD), in that both require the difference between the absorbances of different polarized light beams to be measured and CD spectropolarimeters can be adapted to produce the required alternating beams of polarized light for LD. The main practical differences between CD and LD (apart from the polarizations of light used) are that LD signals tend to be orders of magnitude larger than CD signals, so the data are easier to collect, and LD measurements are performed on systems that are either intrinsically oriented or are oriented during the experiment, so the samples are harder to prepare. Since oriented molecular systems are intrinsic features of the world in which we live, being key components of biological cells as well as leading to macroscopic effects such as crystals, liquid crystals, membranes, and muscles, LD is a useful structural probe. It is particularly useful for determining relative orientations of components of molecular systems. A selection of general references may be found in references 1–10.

In this chapter we shall first outline the principles of LD and then illustrate its application by covering a range of examples, first under steady-state conditions (Section

Comprehensive Chiroptical Spectroscopy, Volume 1: Instrumentation, Methodologies, and Theoretical Simulations, First Edition. Edited by N. Berova, P. L. Polavarapu, K. Nakanishi, and R. W. Woody.
© 2012 John Wiley & Sons, Inc. Published 2012 by John Wiley & Sons, Inc.

18.2), then for kinetic processes (Section 18.3), and finally to probe bending, stiffening, and relaxation of polymers (Section 18.4). Issues relating to the collection of data are covered in Sections 18.5 and 18.6. The chapter concludes with derivations of the two key LD equations. The particular focus is on electronic spectroscopy of biomacromolecules, including DNAs, fibrous proteins, and membrane proteins, because it is for such samples that LD provides data not available from other techniques. Our emphasis will also be on samples that can be flow-oriented since, again, LD provides structural data on solution phase systems not obtainable from other techniques. However, applications are not limited to these.

18.1.1. A Small-Molecule Stretched-Film Example of LD Spectroscopy

A simple example of an oriented sample is a stretched sheet of polyethylene into which some substance, such as the linear molecule tetracene (Figure 18.1), has been allowed to solubilize. Let us assume that the tetracene molecules are perfectly oriented with their long axis along the stretch direction of the film. If we take "parallel" to be the direction of stretch of the film, then transitions whose polarization (direction of transient electron displacement) is along the stretch direction will have a positive LD signal since their $A_{\perp}$ is zero (we are assuming perfect orientation) and their $A_{//}$ is nonzero. Conversely, transitions polarized perpendicular to the stretch direction will have a negative LD. Inspection of Figure 18.1 would thus lead us to conclude (correctly) that the 278-nm band of tetracene is long-axis polarized and the 475-nm region is short-axis polarized. The positive LD signal near 400 nm reflects the significant extent of mixing of long-axis character from the intense 278-nm band into the short-wavelength region of the 450 nm short-axis polarized transition.

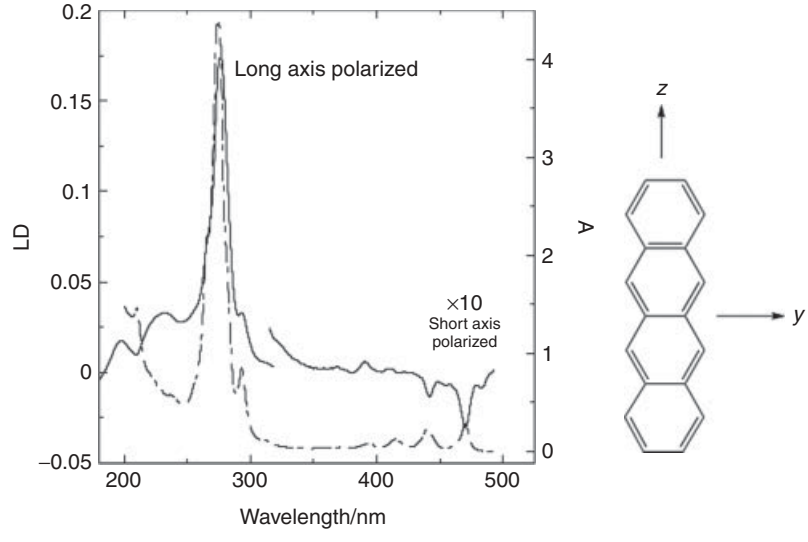

Figure 18.1. LD (solid lines) for the approximately uniaxial rodlike molecule tetracene oriented in a stretched polyethylene film (10 × stretched pipette tip bag, solvent 5% CH_2Cl_2 in methylhexane) with absorbance (dashed lines) in methyl cyclohexane:diethyl ether (20:1). (Redrawn from reference 1.)

The tetracene film LD data of Figure 18.1 are comparatively easy to interpret since the molecule shows a high degree of orientation and its transitions must be either along its long axis or perpendicular to this. More commonly, particularly when we orient biomacromolecules using shear flow (see below), the degree of orientation is low and the transitions can be at any angle with respect to the orientation axis. In such cases it is convenient to express the reduced LD, namely LD^r, in terms of the equation

$$LD^r = \frac{LD}{A_{iso}} = \frac{3}{2} S (3\cos^2 \alpha - 1), \tag{18.2}$$

where S is referred to as the orientation parameter ($S = 1$ for a perfectly oriented sample and $S = 0$ for an unoriented one) and α is the angle between the molecular orientation axis and the transition moment polarization (Figure 18.2). The molecular orientation axis, z, is the most oriented direction of the molecule. $z = Z$, the parallel direction, when $S = 1$. Strictly, Eq. (18.2) holds only for uniaxial orientation, but in practice most molecules and orientation methods approximate to this case. $\alpha = 0^\circ$ for a transition oriented parallel to the orientation direction, so LD>0 for such a transition as observed for tetracene; $\alpha = 90^\circ$ for a transition oriented perpendicular to the orientation direction, so LD<0 for such a transition; and LD = 0 when $\alpha = 54.7^\circ$, the so-called magic angle. Equation (18.2) is derived in Section 18.5.

In some situations it is relatively straightforward to determine S. In others it is the biggest challenge to extracting the information we want from the LD spectrum. In the case of tetracene (Figure 18.1), let us first assume that the strong positive peak at 278 nm is of pure z polarization, where z is the long axis of the molecule. Thus $\alpha = 0$. From Eq. (18.2), since the film absorbance at 278 nm is 0.13 and the LD is 0.174, we deduce

$$S = \frac{LD}{A_{iso} 3} \approx \frac{0.174}{3 \times 0.13} = 0.45. \tag{18.3}$$

Thus the orientation process for this long molecule is very efficient.

Equation (18.2) is only valid for samples where the long axis of the molecule is the molecular orientation axis. A number of samples have the molecular orientation axis perpendicular to the long axis of the sample. These include carbon nanotubes, flow distorted liposomes (Figure 18.3), and peptidoglycan sacculi. In these cases [8, 11]

$$LD^r = \frac{LD}{A_{iso}} = \frac{3S}{4} (1 - 3\cos^2 \beta), \tag{18.4}$$

where β is the angle between the normal to the surface of the liposome (or other structure) and the transition moment polarization as illustrated in Figure 18.3. The derivation of Eq. (18.4) is given in Section 18.5.

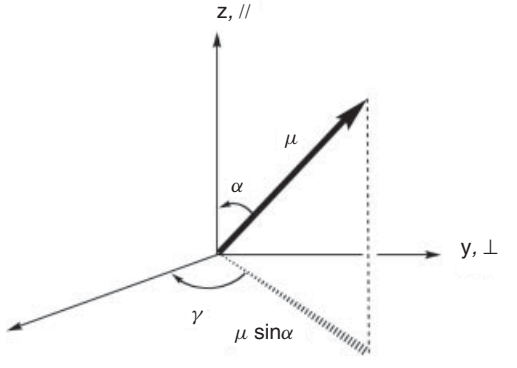

Figure 18.2. The orientation of an electric dipole transition moment, μ, (whose length/magnitude is μ). The magnitude of the projection of μ onto the z axis is $\mu \cos\alpha$ and onto the x/y plane is $\mu \sin\alpha$. The y component of this projection is $\mu \sin\alpha \sin\gamma$. For a perfectly oriented molecular system, $Z = z$ and $S = 1$.

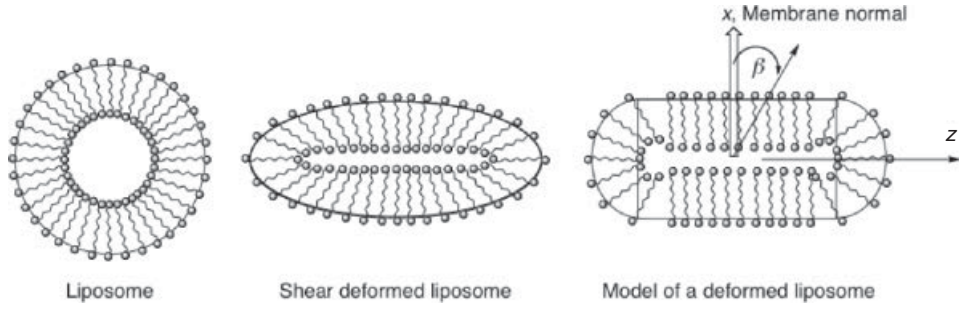

Figure 18.3. Schematic diagram of the geometric parameters relevant for liposomes distorted in shear flow.

18.2. FLOW LINEAR DICHROISM FOR STRUCTURE ANALYSIS

18.2.1. LD of DNA

Double-helical DNA (or RNA) can be viewed as a more or less vertical spiral staircase whose steps are made of pairs of purine and pyrimidine nitrogenous bases that are hydrogen bonded together. The support is the backbone of alternating phosphate groups and ribose sugars that adopt a helical structure. The UV spectroscopy of DNA that is accessible to bench-top CD instruments (i.e., down to ~180 nm) is due almost exclusively to transitions polarized in the plane of the DNA bases. An indication of the transition polarizations is given in Figure 18.4 along with the net absorbance spectra of the four bases that make up DNA.

When DNA is flow-oriented (see Section 18.6.2 for how to do this), the helix axis is the orientation axis. This means that the base transitions are all polarized approximately perpendicular to the orientation axis in accord with the negative LD spectra of Figure 18.5. The shortest piece of DNA that can be flow-oriented is about 250 base pairs. DNAs of this length, however, give very weak LD signals. To use LD quantitatively, lengths should be 800 or more base pairs. Naturally occurring DNA samples such as calf thymus DNA usually end up being tens to hundreds of thousands of base pairs in length, which proves to be ideal.

Figure 18.5a shows the LD of the same DNA measured down to 180 nm on three different instruments [12]. Presumably the synchrotron one is the best. The unoptimized bench-top instrument spectrum provides a warning: at low wavelengths it is particularly important to check that the signals are proportional to concentration and pathlength, in accordance with the Beer–Lambert law (cf. Chapter 2) so that the measured signal is true. In this case there was sufficient stray light hitting the photomultiplier tube that the high-tension voltage trace provided no warning of a problem.

Figure 18.5b shows the absorbance, LD, and LD^r spectra of calf thymus DNA in a Couette flow cell. The transitions are all in the plane of the DNA bases, so they are approximately perpendicular to the helix axis. The LD is therefore approximately a negative version of the absorbance spectrum. The fact that the B-DNA LD spectrum is similar to, but not the same as, the negative of the absorbance results in the LD^r spectrum being fairly constant across the 260-nm band, but not completely so. This tells us that, in solution, the bases are not rigidly perpendicular to the helix axis. From a careful analysis

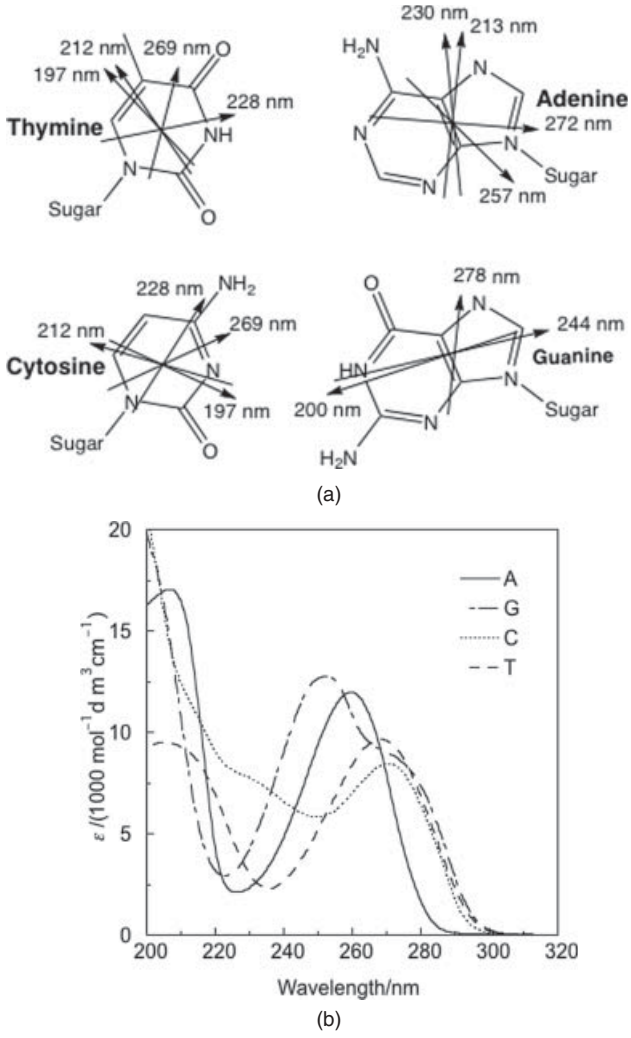

Figure 18.4. (a) Probable transition polarizations for UV transitions of adenine, guanine, cytosine, and thymine from crystal data [64–68] and LD measurements on monomeric nucleobases in stretched films [53]. (b) UV spectra of the DNA nucleotides deoxyadenosine 5′-monophosphate (A), deoxyguanosine 5′-monophosphate (G), deoxycytidine 5′-monophosphate (C), and thymidine 5′-monophosphate (T) (that of uracil is very similar). (Redrawn from reference 1.)

of solution LD studies, it has become apparent that the bases of B-DNA in solution lie at an average angle of $\sim 80^\circ$ (or even less) from the helix axis [13] (though by convention we assume 86° in a calculation [14]). By way of contrast, almost perfectly perpendicular orientation seems to apply to DNA in stretched films [15]. The data in Figure 18.5b show $LD^r \sim -0.15$. Using this value and $\alpha = 86^\circ$ in Eq. (18.2) leads to $S \sim 0.10$, which is a typical value for DNA experiments.

The theoretical limiting value of LD^r for a transition polarized perpendicular to an orientation axis is -1.5 [Eq. (18.2)]. This value is never reached with DNA in solution. In principle, at least, S may be calculated from first principles [14]. In practice, for macromolecular systems, S is usually determined more or less reliably by empirical means either by using known maximum LD^r values (perhaps from a parallel experiment assuming the DNA orientation does not change) or by calibrating with a probe dye whose

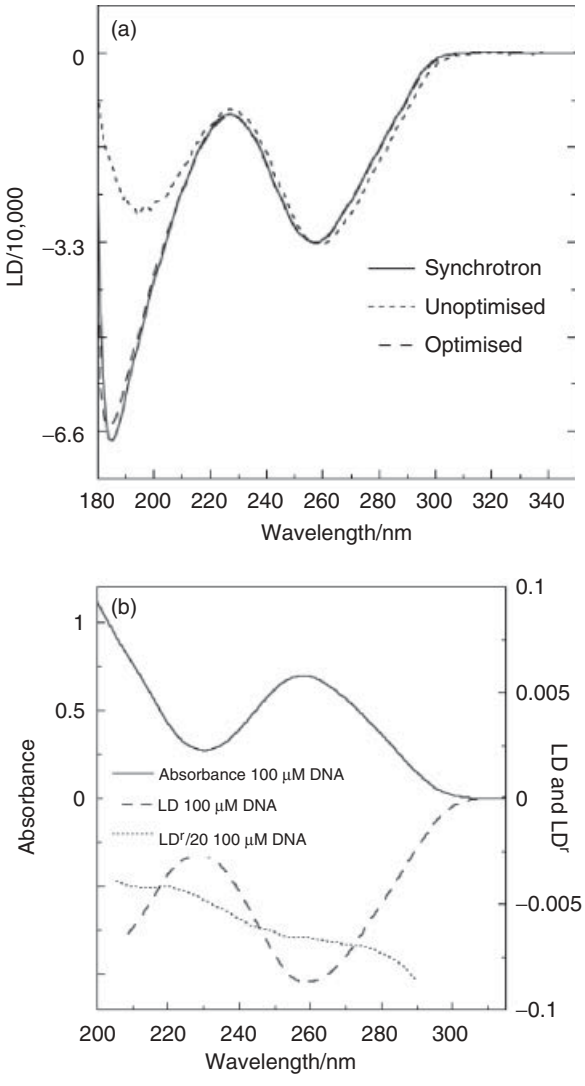

Figure 18.5. (a) LD of DNA from *M. luteus* (200 μM base) in water measured on three spectrometers: a nonoptimized bench-top instrument; an optimized bench-top instrument; and the ASTRID UV1 synchrotron beamline [12]. (b) Absorbance, LD, and reduced LD, $LD^r = LD/A$, spectra of calf thymus DNA (100 μM). Absorbance was measured in a 1-cm-pathlength cuvette, LD measured in a 1-mm-pathlength Couette flow cell. The pathlength difference has been accounted for in determining LD^r. (Redrawn from reference 1.)

binding geometry is known and whose spectroscopy is in a different place from that of the DNA and any other ligand of interest [16, 17].

18.2.2. LD of DNA-Bound Ligands

Once the orientation of DNA itself is understood, a next step is to use LD to probe the binding and orientation on DNA of small (or large) ligand molecules. A key feature of such LD studies is that if there is no specific binding, then there will be no LD of the ligand transitions. Conversely, the presence of an LD signal from an absorption band of the putative ligand immediately indicates that it is bound. It should be noted that the same is not true of absorbance: in most situations some ligands are bound and some free, so the isotropic absorbance will be a mixture of that due to bound and free ligands. Thus care must be taken in calculating LD^r to use only the absorbance of bound ligands.

Although LD *cannot* tell us *where* a ligand binds to DNA, it can be used to determine the *orientation* of the ligand (if the ligand's transition moments have been assigned). This may provide enough information to enable the binding mode to be deduced. Broadly speaking, a ligand may bind to DNA:

1. **Externally** bound to the phosphate backbone: this is usually orientationally fairly nonspecific and the induced LD is correspondingly small.
2. **Intercalated** between DNA bases: this mode requires planar aromatic molecules (or parts of molecules; see, e.g., Figure 18.6a) that insert between DNA base pairs, causing the DNA to unwind and open up a slot between adjacent base pairs so the ligand may be sandwiched between them. The LD of the intercalated part is then negative, because the transitions we probe are in-plane polarized $\pi \rightarrow \pi^*$ transitions. The LD^r of a typical intercalator is shown in Figure 18.7a. The intercalator signal (at ~500 nm) is slightly more negative than that of DNA because the intercalator locally stiffens the DNA, giving it a slightly larger LD intensity. The wavelength of an intercalated ligand's absorbance is usually red-shifted relative to that of unbound ligand.
3. In the **minor groove**: this mode is frequently adopted by aromatic molecules containing inter-ring bonds with some rotational freedom. For example, long crescent-shaped molecules, such as Hoechst 33258 illustrated in Figure 18.6b, fit

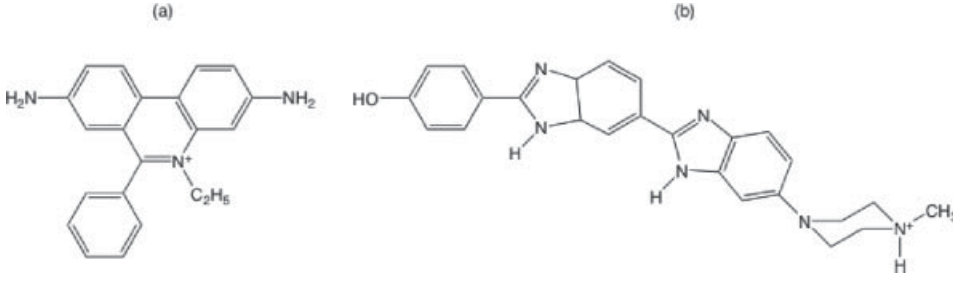

Figure 18.6. DNA binding ligands: (a) ethidium and (b) Hoechst 33258.

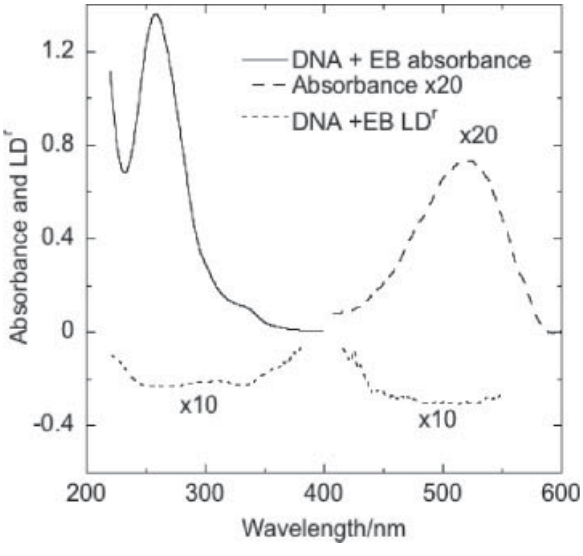

Figure 18.7. (a) Absorbance and LD^r spectra of the intercalator ethidium bromide in 5 mM phosphate buffer, pH = 6.9, bound to calf thymus DNA (200 μM). DNA base:ligand ratio is 20:1 [69]. (Redrawn from reference 1.)

neatly into the minor groove with the molecule following the curvature of the groove. The long axis of such molecules is oriented at about 45° to the helix axis making the LD of the long-axis polarized transition positive. The short-axis polarized transition of minor groove binding molecules are perpendicular to the helix axis, so approximately parallel to the base transitions resulting in negative LD signals [18]. Minor groove binders tend to be selective for A–T–rich sequences that have a deeper electrostatic potential than G–C–rich sequences. Also, G sterically hinders minor groove binding as it has an amine group in the groove.

4. In the **major groove**: this type of binding is found for several regulatory proteins and there is enough space to accommodate most smaller ligands, including fairly bulky metal complexes, in a variety of orientations.

The absorption spectra and LD of $[Ru(tpyanth)_2]^{2+}$ (Figure 18.8) in the absence and presence of DNA illustrates both intercalative and groove binding behavior. First, note

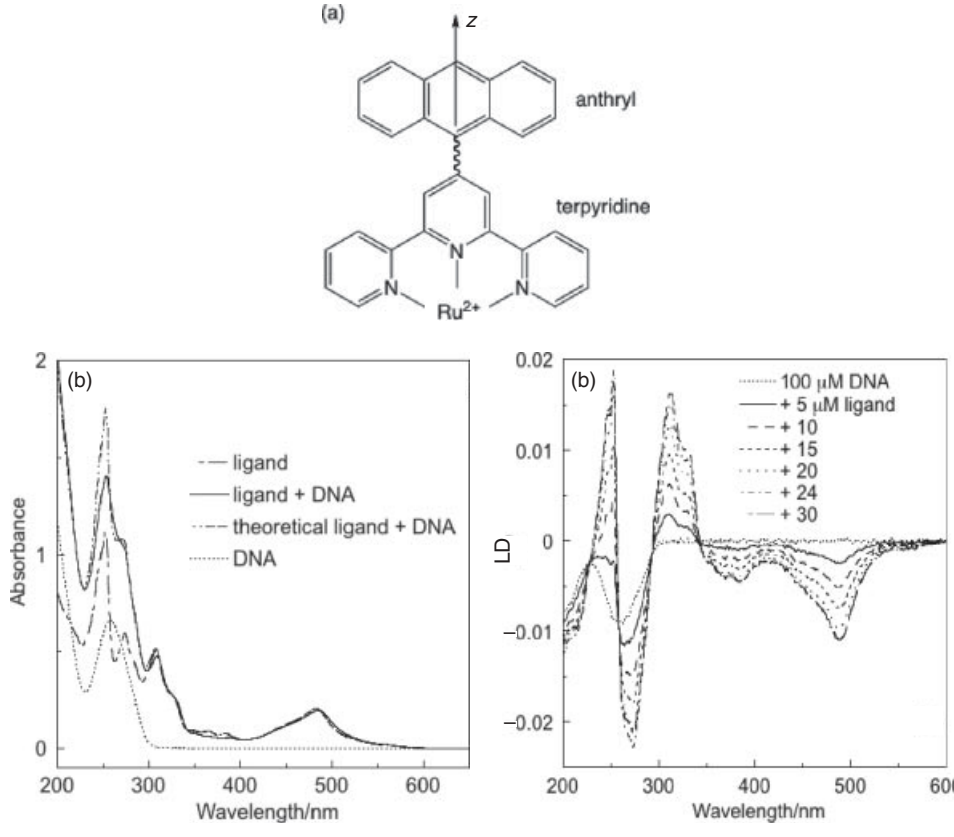

Figure 18.8. (a) $[Ru(tpyanth)_2]Cl_2$, *z* indicates the approximate orientation of the metal complex long axis; a second anthrylterpyridine ligand is oriented perpendicular to the one illustrated making an approximately octahedral coordination geometry. (b) UV–visible absorption spectrum in water of $[Ru(tpyanth)_2]^{2+}$ (10 μM); $[Ru(tpyanth)_2]^{2+}$ (10 μM) plus calf thymus DNA (100 μM); and calf thymus DNA (100 μM) together with the ''theoretical'' sum spectrum. (c) LD spectra from a titration series of $[Ru(tpyanth)_2]^{2+}$ with ct-DNA (100 μM). Metal complex concentrations are indicated in the figure. (Redrawn from reference 17.)

that the absorption maxima shift to longer wavelengths and the intensity is lower than the spectrum made from the sum of the component parts. This is consistent with enhanced π-stacking upon addition of the DNA which could arise from either (a) intercalation of part of the ligand—probably the anthryl group—between DNA base pairs or (b) metal complex stacking mediated by the DNA template. The spectra are consistent with the anthracene group intercalating: negative LD^r for the anthracene short-axis transition from 350 to 400 nm and the two terpyridine groups lying perpendicular to one another and to the z axis (Figure 18.6), fitting into a groove, with a positive terpy LD signal at 320 nm.

18.2.3. LD of Cytoskeletal Proteins

The cytoskeleton in both prokaryotic and eukaryotic cells is dependent on the rapid and controlled assembly and disassembly of polymers (fibers) whose monomeric units are themselves folded proteins which change little, if at all, when they form the fibers. In some cases a single linear polymer forms, in other cases further assembly into bundles (thicker fibers) of some kind occurs. Some protein fibers, such as tubulin, assemble to form more complicated structures directly. Monomeric proteins before polymerization have no flow LD signal, thus they provide no background signal to interfere with attempts to follow kinetics of fiber assembly, disassembly and reorganization. The possibilities of LD spectroscopy can be illustrated by looking at the bacterial homologue of tubulin, FtsZ, and tubulin itself [10].

FtsZ is a bacterial protein that polymerizes to form the so-called Z-ring which then contracts and pulls in the cell membrane, eventually forming two daughter cells. *In vitro* (and presumably *in vivo*), FtsZ polymerizes to form linear polymers or protofilaments on the seconds timescale when GTP (guanine triphosphate) and Mg^{2+} are present. The protofilament LD spectrum for *E. coli* FtsZ is the 0 mM Ca^{2+} spectrum of Figure 18.9. Upon addition of Ca^{2+}, the FtsZ protofilaments bundle together [19], tilting the guanines from horizontal, causing the 260 nm LD to become positive. The protein YgfE performs the same role as the calcium ions but at more biologically realistic concentrations [19]. LD

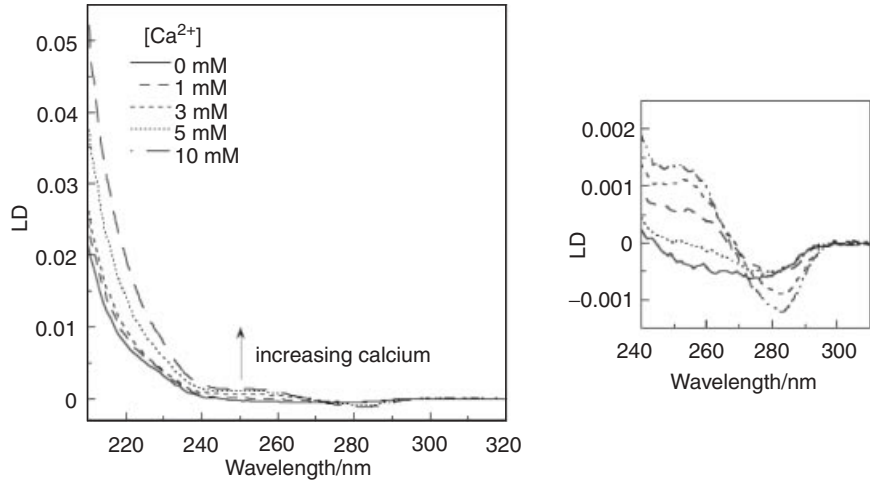

Figure 18.9. FstZ (11 μM) polymerization in the presence of $MgCl_2$ (10 mM) and varying amounts of Ca^{2+} (50 mM MES buffer pH 6.5, 50 mM KCl, 0.1 mM EDTA, and GTP (0.2 mM)). The GTP region is expanded on the right. (Redrawn from reference 19.)

is currently the only technique that can follow such a reorganization of the components of this complicated molecular system in real time.

18.2.4. LD of Membrane Peptides and Liposomes

Membrane proteins make up to 30% of all proteins coded for by most genomes [20], and they facilitate a wide range of cellular functions and are a means by which the cell communicates with its environment. There is also an increasing family of antimicrobial peptides that bind to lipid membranes [21]. The mechanism by which such antimicrobial peptides act has become a complex issue. It is widely accepted that it is important to understand how the peptides act in order to exploit fully the use of peptides as antimicrobial agents [22]. However, the techniques that have been so successfully applied to understand structural questions for globular proteins, including crystallography and NMR, are not as readily applied for the study of membrane proteins. Membrane proteins and peptides are not easy to crystallize, and they usually require lipid or detergent environments to remain soluble and folded. Although progress is being made with solution and solid-state NMR, the size of the membrane protein-detergent complexes usually results in slow tumbling rates and poor resolution spectra with broad peaks.

LD, although not an atomic-level resolution technique, has been found to be ideally suited to membrane environments following the discovery by Ardhammar et al. [11] that liposomes (model membranes, Figure 18.3) become sufficiently distorted in shear flow to become aligned. Rodger et al. showed that membrane peptides and proteins were also flow-aligned when bound to liposomes [23, 24] and their orientation could thus be determined. The expected LD band signs for an α-helical peptide on and in a liposome membrane are illustrated in Figure 18.10. One can also follow insertion in real time to give insight into peptide folding and insertion in membranes (see Section 18.3.4) [25–29]. In solution, LD has the advantage over other biophysical techniques of being insensitive to off-membrane events: unbound ligands or peptides are invisible because they do not orient.

LD is the ideal technique for probing insertion/binding (or not) into/onto membranes in real time: the signal is zero unless the analyte (for example a peptide) binds to the membrane. Furthermore, an α-helical peptide on the surface has opposite signed LD signals from when it is inserted, as summarized in Figure 18.10. β-sheet LD spectra are simpler than α-helical ones because the $n-\pi^*$ region ($\sim$220 nm) of the β-sheet spectrum has canceling contributions of opposite polarization and β strands have no 208-nm band. Thus the LD of liposome-bound β structures is a single positive signal at 200 nm if the sheet is lying on the surface and is a negative signal if it is inserted. Examples are given in Figure 18.11.

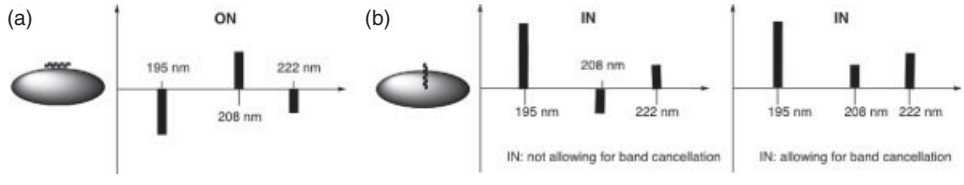

Figure 18.10. Schematic illustration of expected LD signals for an α-helix (a) on the surface of or (b) inserted in a membrane. The right-hand part of (b) is what is expected in a spectrum, given the reality of overlap between bands and net cancellation. Similarly, the 208-nm positive band for (a) may not be apparent.

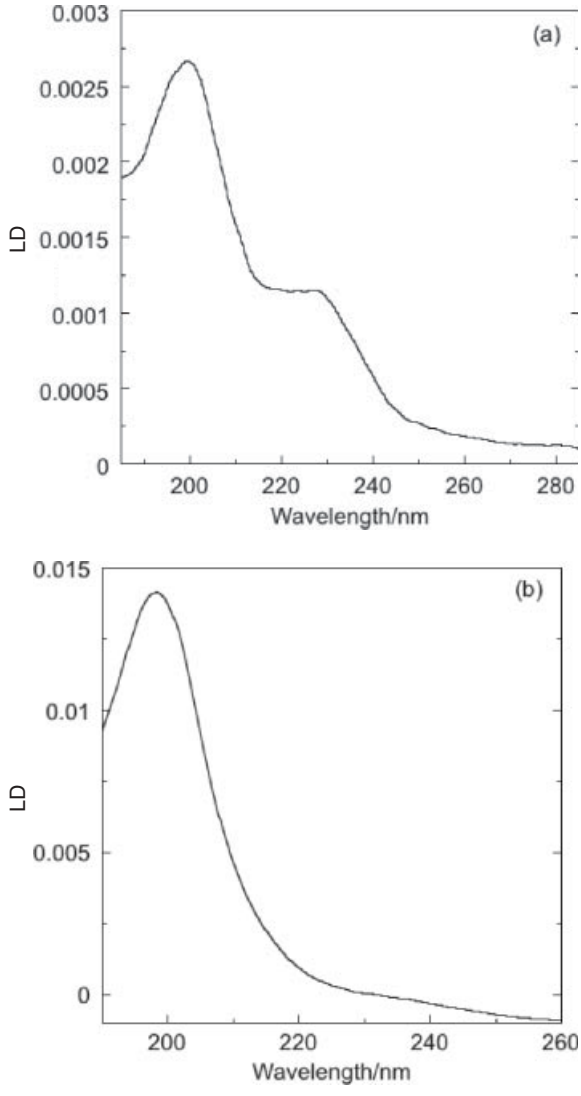

Figure 18.11. (a) LD of the α-helical frog peptide aurein 2.5 with sequence: GLFDIVKKVVGAFGSL-NH_2 inserted into a lipid bilayer liposome composed of 50:50 DPPC (dipalmitoylphosphatidylcholine) and DPPG (dipalmitoylphosphatidylglycerol) at 50°C (i.e., in the liquid phase). (Redrawn from reference 70.) (b) LD of the β-sheet fragment GLRILLLKV (derived from the T-cell antigen receptor) with liposomes made from phosphatidyl choline extracted from soya beans, showing that it sits on the membrane surface. (Redrawn from reference 71.)

18.2.5. Peptidoglycan Layer of Bacterial Cells

The peptidoglycan layer forms a "net" around a bacterial cell and helps maintain the structure and shape of the cell [30]. The inhibition of synthesis of this layer is a common *modus operandi* of current antibiotics since in the absence of the peptidoglycan layer the cell autolyzes and dies due to its internal osmotic pressure. As the name implies, the peptidoglycan layer is a mixed peptide-sugar complex. The peptidoglycan sacculi from the MC6R41 strain of *E. coli* (which has a defective FtsI gene that causes it to divide less often at higher temperatures) are rod-shaped, making them easily oriented and thus excellent subjects for linear dichroism as illustrated in Figure 18.12. The structure of the peptidoglycan layer is debated: do the glycan strands run along the long axis of the cylinder, or along the short axis, or perpendicular to the surface [30]? The LD of Figure 18.12 is only consistent with the first of these, [Eq. (18.4)], meaning that LD resolves this long running debate [31].

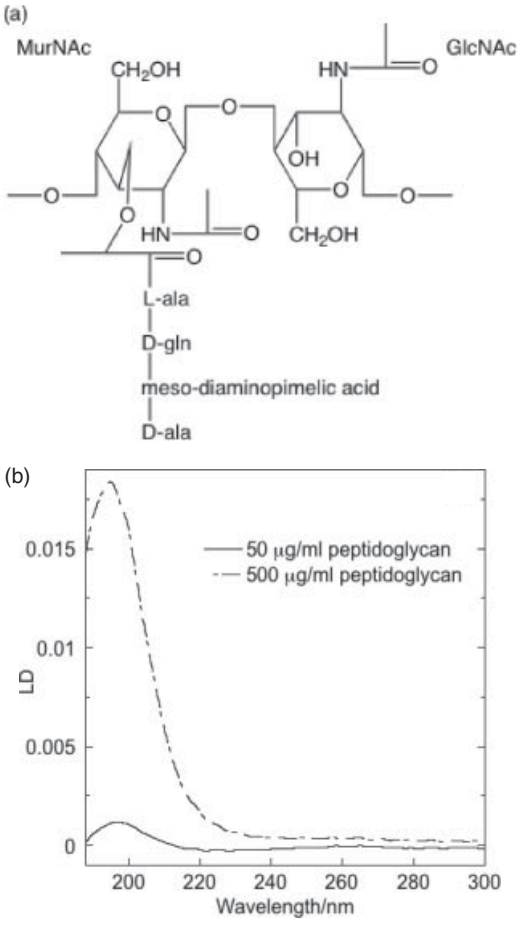

Figure 18.12. (a) A primary structure of peptidoglycan, with both types of sugar and a tetrapeptide chain extending from the MurNAc component. The ε-amino group on the meso-diaminopimelic acid is replaced when the peptide is cross-linked. GlcNAc denotes *N*-acetylglucosamine; MurNAc denotes *N*-acetylmuramic acid. (b) The LD spectra of two concentrations of peptidoglycan as indicated in the figure. Pathlength was 0.5 mm. (Redrawn from reference 1.)

18.2.6. Site-Specific LD Spectroscopy: DNA Binding of Recombination Enzymes

A class of proteins that has been extensively studied due to their important biological roles are recombination enzymes, such as RecA (in *E. coli*) [32, 33] and Rad51 (in eukaryotes including human) [34]. While crystals of the pure proteins have been obtained and studied using X-ray diffraction, their mechanistically more interesting DNA complexes have largely escaped structural examination because their filamentous characters make them impossible to crystallize. Such filamentous structures, however, may be easily aligned in shear flow, providing excellent targets for LD spectroscopy. The technique of site-specific LD (SSLD) combined with the available protein crystal structures has enabled structures of some DNA–protein complexes to be determined. SSLD can be implemented by replacing one of the aromatic residues (say a tryptophan) of a protein with an optically "invisible" residue and thereafter comparing the LD of this mutant with that of the wild-type protein. Provided that the orientations and structures of the DNA complexes are not significantly changed by the residue replacement, the difference LD spectrum will be that of the replaced residue and may thus provide specific information about its orientation in the protein. In this way, SSLD can give orientation data for a large number

of chromophores. It could in principle be used to solve three-dimensional structures in systems that for some reason are not amenable to X-ray crystallography or NMR study.

Nordén and co-workers used a SSLD approach combined with molecular modeling to determine the three-dimensional structure of a fibrous protein complex: Rad51 bound to DNA [34]. In eukaryotes, from yeast to human, Rad51 is involved in homologous recombination. Rad51 is functional when it assembles into long fibrous structures around DNA. Thus the "active" form of Rad51 is too large for NMR and too flexible to form crystals for X-ray diffraction. To assemble the whole structure of the Rad51 filament, one must know how the monomers are oriented in space in the protein fibril; this is the key role of the SSLD data. In order to define precisely an object's orientation in space, three angles are needed. Two of three angles were determined from minimization of the misfit functional between experimentally measured angles (SSLD data) and angles of trial filament structures. The resulting model was then refined to determine the third angle and the radius of a filament (based on the fact that two monomers have to be connected to each other). The net result was the three-dimensional structure of human Rad51 in its active filamentous form.

In this work an indirect SSLD method was used to avoid needing to determine S. At certain wavelengths (around 200, 215, and 250 nm for Rad51) in the far-UV region, a tyrosine and (parallel) phenylalanine transition have coinciding absorption coefficients. Thus if a tyrosine is replaced by a phenylalanine, we expect the LD intensity (after normalization with respect to the orientation factors S) of wild-type and modified nucleoprotein filaments to be the same at the "magic wavelengths." So they proceeded by normalizing the wild-type and modified LD spectra to have the same LD intensity at a "magic wavelength."

18.3. LD TO FOLLOW KINETIC PROCESSES

18.3.1. Tubulin Polymerization and Depolymerization

LD is the ideal technique to follow kinetic processes that involve reorientation of chromophores. The eukaryotic protein tubulin is, like FtsZ, a polymer of protein monomers with a GTP between each monomer unit. As its name implies, tubulin forms tubules: hollow cylindrical filaments assembled from dimers of α-tubulin and β-tubulin. Tubulin polymers radiate from the centrosome of a cell to attachment sites just under the cell membrane during cell division. Microtubules also play a role in moving cells and organelles and interact with motor proteins. They are thus very attractive dynamic drug targets. LD is the ideal (and perhaps only) technique to follow the kinetics of processes such as the fiber assembly and disassembly as illustrated in Figure 18.13 [35]. The high concentrations of tubulin needed to initiate polymerization mean that the data are only reliable down to about 235 nm because the sample absorbance is too high below this point. This is just sufficient to probe the assembly of both the backbone (235 nm) and the aromatic spectral regions (280 nm) and to show the effect of various drugs on tubulin. Taxol stabilizes the polymers (Figure 18.13a), whereas colchicine (which is used in the treatment of gout) results in tubulin depolymerizing (Figure 18.13b) by preventing the monomers from polymerizing.

18.3.2. Self-Assembly of Sup35 Yeast Prion Fragment, GNNQQNY

Amyloid-like fibrils, similar in structure to fibrils that are deposited in a number of protein misfolding diseases, including Alzheimer's disease and the transmissible spongiform

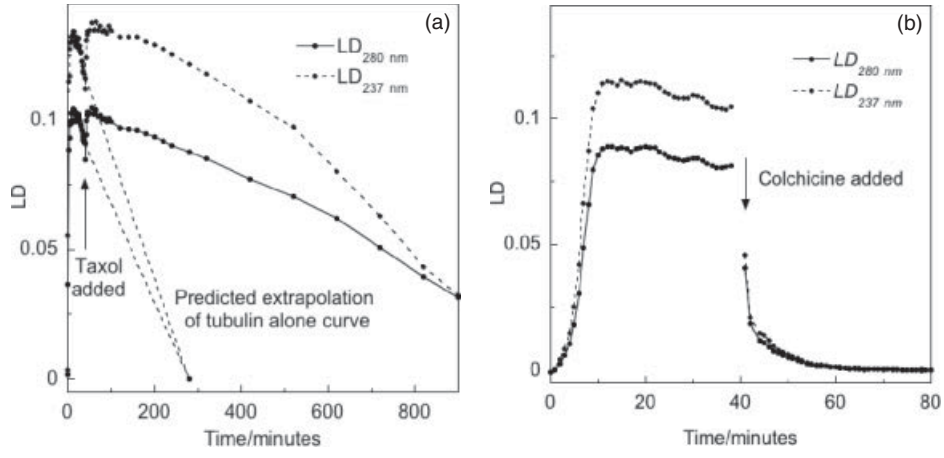

Figure 18.13. Capillary LD at two absorbance wavelengths of tubulin polymers (28 μM monomer) at 37°C. (a) Tubulin before and after addition of taxol (final concentrations 25.5 μM and 18.2 μM, respectively). Dotted lines indicate the rate of depolymerization in the absence of taxol. (b) Tubulin before and after addition of colchicine (final concentrations 25.5 μM and 18.2 μM, respectively). (Redrawn from reference 35.)

encephalopathies, can be formed by many different proteins and peptides. LD spectra of the fibrils formed from a fragment of the yeast prion, Sup35 with sequence GNNQQNY, have contributed to knowledge regarding side-chain packing of amyloid-forming peptides. Two crystal structures have been published: both structures have a cross-β steric zipper arrangement but different packing of the peptide, particularly the tyrosine residue. The positive strong π-to-π^* transition at 195 nm (Figure 18.14a) is consistent with the cross-β structure [10]. The LD spectra measured as a function of time (Figure 18.14b) show a

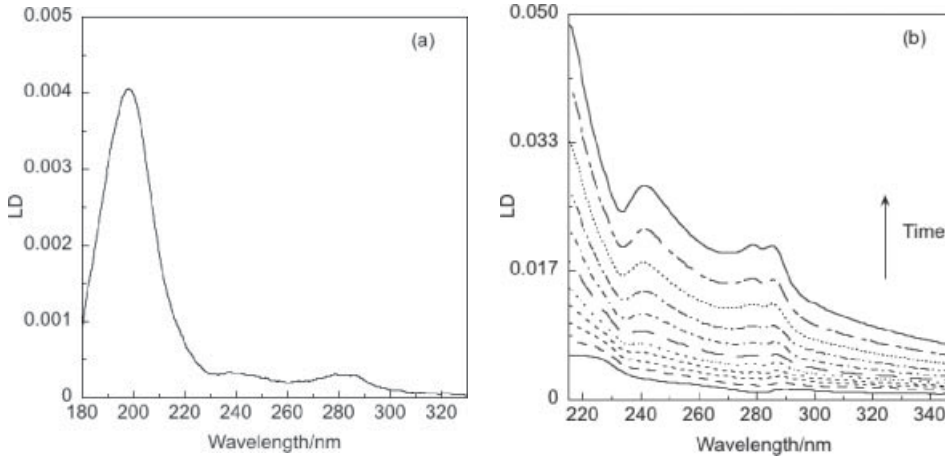

Figure 18.14. (a) LD spectrum of mature GNNQQNY fiber sample at 0.2 mg/mL. (b) Kinetics of fiber/crystal formation by GNNQQNY at 2 mg/mL. Spectra were measured at 8-min intervals. The aromatic region changes sign from negative to positive at early time points. Units are in millivolts, because the data were collected at the Astrid Synchrotron [27, 72]. (Redrawn from reference 36.)

reorientation of the tyrosine chromophore (280 nm), suggesting a structural rearrangement occurs as the crystals form [36].

18.3.3. Kinetics: Dipeptide Hydrogels

Hydrogels are networks of water-insoluble polymers dispersed in water to result in a flexible highly aqueous (typically over 99%) material. Hydrogels made from self-assembling oligopeptides are being developed. The attraction of these hydrogels is that their formation is reversible since they are held together by noncovalent interactions. Potential applications include as scaffolds for tissue engineering and for drug release, since the aim is that the assembly/disassembly process can be controlled by changing a variable such as temperature or pH. A particularly nice application has been developed by Adams and co-workers [37], where the assembly is controlled by the controlled increase in pH that follows from the *in situ* hydrolysis of glucono-δ-lactone to gluconic acid. Figure 18.15 shows the flow LD of a naphthalene–alanylvaline in aqueous solution as it forms the fibers that make up the network of the hydrogel. LD is currently the only way to determine the orientations of the naphthalene chromophores within the fibers. From the CD band signs [37], we know that the 236-nm LD signal results from the out-of-phase coupling (thus perpendicular to the line between the long axes of the naphthalenes) of the transition moments [1, 2] and the 218-nm signal from in-phase coupling. If the naphthalenes were stacked vertically like steps on a ladder, then both transitions would be expected to have a negative LD. This is in contrast to what is observed in Figure 18.15. From Eq. (18.2) we therefore deduce that this means that the naphthalene long axes are tilted by (significantly) more than 35° ($= (90^\circ - 55^\circ)$) from the perpendicular.

18.3.4. Kinetics of Membrane Peptide Insertion into Liposomes

Melittin is a 26-residue amphiphilic cationic peptide with a proline residue at position 14 that allows it to form kinked helices in nonpolar environments [38]. Its secondary

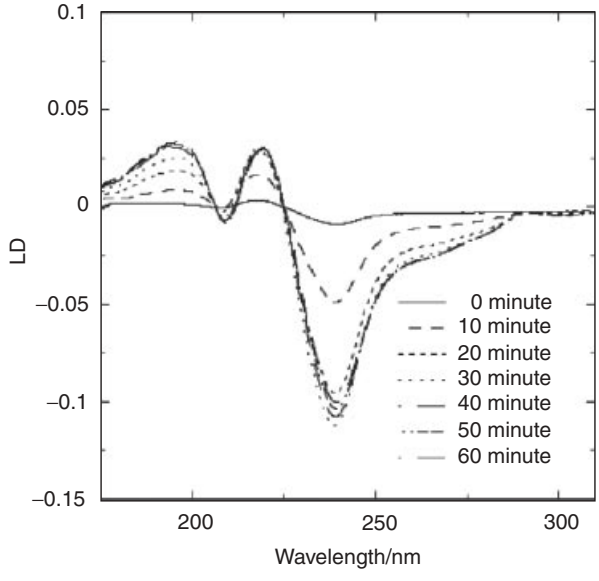

Figure 18.15. Evolution of LD with time on addition of a solution of naphthalene–alanylvaline dipeptide (0.5 wt%) to glucono-δ-lactone (14.42 mg/mL). Data are shown for 0 min and then subsequently every 10 min. Signals increase with time until 50 min, when the magnitude decreases once again. (Redrawn from reference 37.)

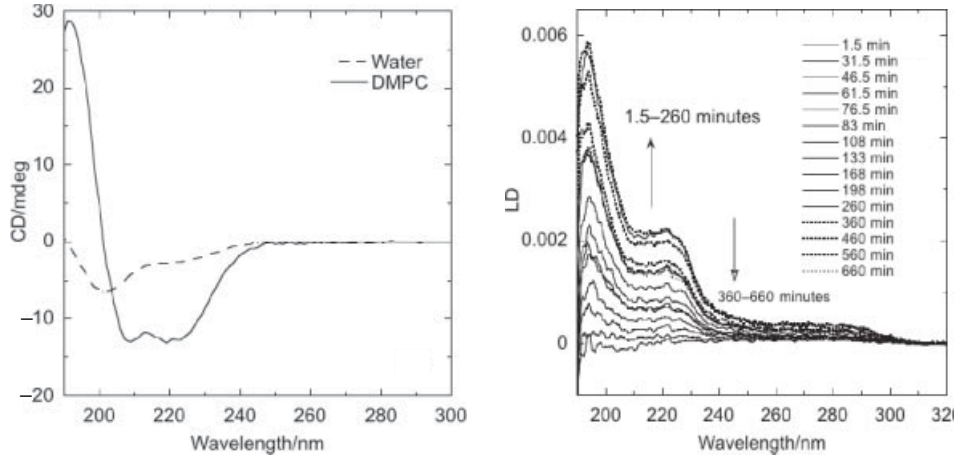

Figure 18.16. (a) CD spectra of melittin (0.1 mg/mL) as a function of environment (lipid:melitin molecular ratio 100:1) Pathlength = 2 mm. (b) LD of melittin (0.1 mg/mL) when added to DMPC liposomes (at molar ratio of lipid:peptide of 100:1) at (37°C) as a function of time. (Redrawn from reference 40.)

structure changes from random coil in aqueous solutions to helical in membranes, as shown in Figure 18.16a [39]. As shown in Figure 18.16b [40], at time zero (when the melittin is already helical as shown by the CD) we have LD ~ 0. After a few minutes a positive LD signal is apparent in the regions of 224 nm and 192 nm. The minimum at 210 nm is in fact the negative signal from the long-wavelength component of the $\pi - \pi^*$ transition (Figure 18.16). Given that the α-helical CD signature of melittin tells us that it is membrane-associated from the beginning of the LD experiment, it is intriguing that the initial LD is approximately zero. If the melittin α-helix is lying flat on the surface, then its LD sign pattern should simply be approximately opposite from that observed at later time as illustrated in Figure 18.16. The only other option for having LD $= 0$ but the peptide membrane-associated (which it is, otherwise it would not be folded) is that the dominant 222-nm and 192-nm bands are oriented with transition moments having average orientation close to the magic angle of $\beta = 54.7^\circ$ [Eq. (18.4)]. Since melittin is known to kink at its central proline, the LD therefore suggests that the kink angle is $\sim 110^\circ$ as illustrated in Figure 18.17. The peptide then tilts and inserts to give the later time spectra. After ~ 5 h the LD decreases as the melittin disrupts the membranes so they cannot be flow-oriented.

18.4. LD TO DETERMINE DNA BENDING, STIFFENING, AND RELAXATION

With LD we usually focus on the information it provides about relative orientations of chromophores. In addition, hidden in the orientation parameter, S, is a wealth of information about the length, flexibility, and introduction of, for example, kinks into the structure being oriented. Extracting that information is, however, non-trivial. Here we limit consideration to illustrating the potential with two examples.

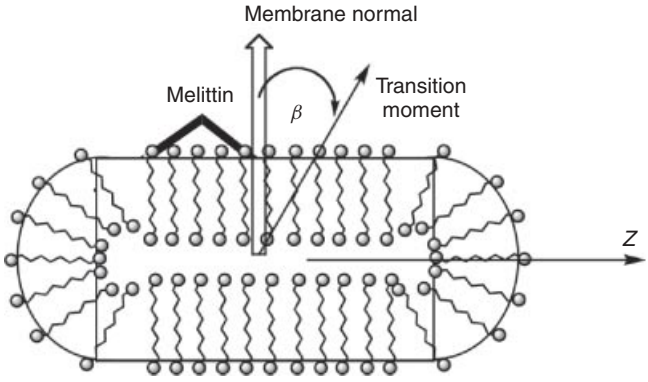

Figure 18.17. Schematic illustration of melittin (bold lines) bound on the surface of the liposome with the backbone lying at the magic angle to the membrane normal. (Redrawn from reference 40.)

18.4.1. DNA Bending Upon Ligand Binding

Examples of DNA conformational changes easily detected by LD are those induced by spermine, $[NH_3(CH_2)_3\ NH_2(CH_2)_4\ NH_2(CH_2)_3\ NH_3]^{4+}$, or $[Co(NH_3)_6]^{3+}$, which, when added to DNA, decrease the LD because the DNA is first bent and then condensed [41, 42]. Similarly the tetra-cationic di-iron triple helicate of Figure 18.18 bends the DNA and intramolecularly coils it [43, 44].

18.4.2. Flow Orientation of Brain Microtubules

Tubulin protein monomers assemble into microtubule fibers that are key components of eukaryotic cytoskeletons and are involved in many cellular processes, including mitosis, cytokinesis, and vesicular transport. The resulting fibers are very stiff and can be modeled as a rigid rod. The LD signal outside the absorbance region is due to the anisotropic turbidity, LD^{τ}, of the sample. If LD^{τ} is measured in a Couette flow cell as a function of time after the cell stops rotating, it is possible to study the orientational relaxation of the microtubules. The relaxation becomes slower with increasing concentrations of tubulin; and at concentrations above 1 mg/mL, some orientation remains at "infinite" time. Data such as those illustrated in Figure 18.19 may be fitted to a tri-exponential decay with a rapid time constant of 4 s, an intermediate one of 40 s, a slow one of 400 s, and a fraction of microtubules that remain oriented [45]. The different rates reflect different reorientation processes in what is an inherently complex system. Conversely, Couette flow LD can be used to follow the development of orientation when shear flow is applied [1].

18.5. PRACTICALITIES OF LD SPECTROSCOPY

There are two aspects to measuring LD spectra: the instrument and the orientation of the sample. There are many ways to orient samples. In this chapter we shall focus on the commonly used ones of stretched films, flow orientation, and orientation by evaporation or assembly.

18.5.1. Spectrometers for LD Spectroscopy

The instrument used to collect LD data can be a normal absorbance spectrometer with polarizers, where either the polarizer or sample is rotated, or it can be a circular dichroism

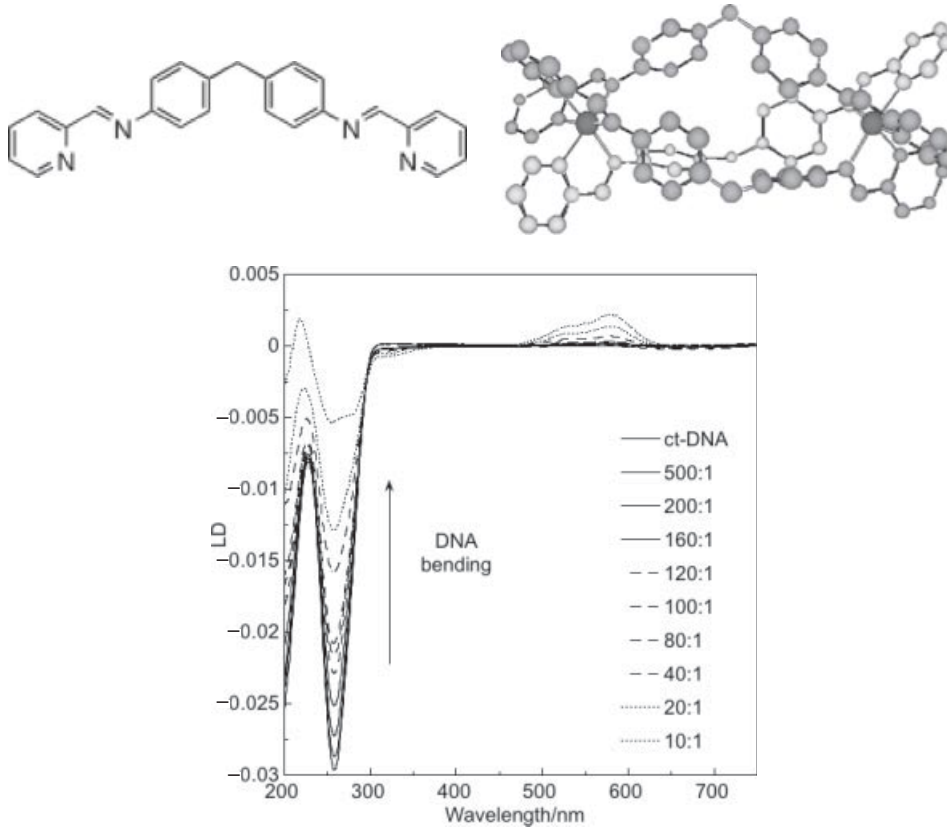

Figure 18.18. The LD of a tetracationic di-iron triple helicate $[Fe(LL)_3]^{4+}$(LL = $C_{25}H_{20}N_4$) binding to calf thymus DNA showing the effect on the DNA LD as the ligand bends the DNA. ct-DNA (500 μM, 20 mM NaCl, 1 mM sodium cacodylate buffer pH = 7); DNA: ligand ratios are shown on the figure. (Redrawn from reference 43.)

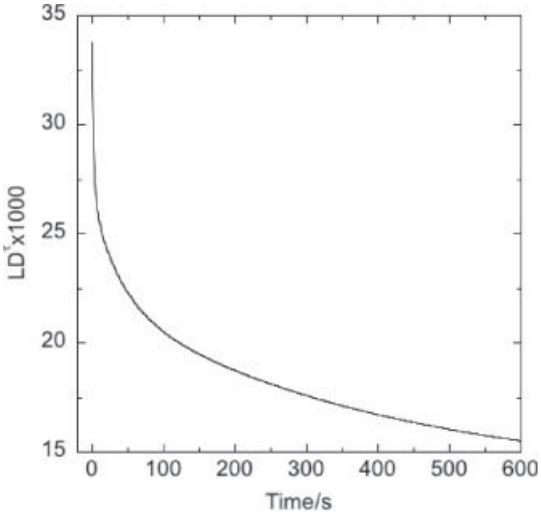

Figure 18.19. Decay of microtubule LD (0.37 mg/mL, 33°C) as a function of time after the shear rate has been reduced from $G = 100s^{-1}$ to 0. (Redrawn from reference 45.)

spectropolarimeter (cf. Chapter 2) with the alternating beams of circularly polarized light converted to alternating beams of linearly polarized light by doubling the voltage across the photoelastic modulator (cf. Chapter 2). The latter option is now the way most LD spectra are collected, and most modern instruments can be converted from CD to LD using the instrument software (if the option has been installed by the manufacturer or instrument builder). Alternatively, one may add a quarter-waveplate into the CD machine light beam to achieve the same effect.

18.5.2. Calibration of LD Spectrometers

Calibration of CD machines is well-established, typically using a chemical (chiral) substance with established molar ellipticity (cf. Chapter 2). Once an instrument is calibrated for CD, it is reasonable to assume that it is also calibrated for LD, but this should be checked in some way, at least to ensure that the LD of a sample rotated by 90° changes sign and retains the same magnitude. Most instruments adapted for LD are provided with a physical device, such as a polarizer or a slab of (isotropic) fused silica tilted 10-45° from normal incidence for this purpose. Unfortunately, clear instructions on using such devices are usually not provided. From knowledge of the refractive index of silica, the reflection of the tilted plate of silica may be calculated accurately for two orthogonal light beam polarizations, including the effects of multiple reflections, as described in reference 46. As computed in reference 46, the LD of a fused silica plate tilted at 45° should be as summarized in Table 18.1.

Calibration achieves two things:

1. At low LD amplitudes, calibration provides the accurate numerical correlation between instrument signal (photomultiplier current ratio <AC>/<DC>) and the true LD of the sample.
2. At high LD amplitudes (LD > 0.1), calibration provides the correction that needs to be applied to LD signals when the deflection of <AC>/<DC> as a function of LD no longer follows a linear relationship (cf. Chapter 2). For a strongly oriented sample with moderate absorption, LD (in contrast to CD) easily exceeds the 0.1 limit, so for accurate quantitative analysis an appropriate careful calibration is required.

18.5.3. Instrument Parameters for LD

CD spectropolarimeters give the operator considerable control over the time constant, τ (time over which the machine averages data or, equivalently, response time, $\rho = 2\tau$); scan speed, s; and bandwidth, b (the wavelength range of incident light). The choice of parameters is usually determined by deciding what quality of data is required. The issues for CD data collection and LD data collection are essentially the same, though LD is usually easier as signals are larger. If the perfect spectrum for a database is being collected, then operator and instrument time is not a consideration. However, if, for

TABLE 18.1. LD of a Fused Silica Plate Tilted at 45° [46]

λ (nm):	200	250	300	350	400	500	550	600	650	700
LD:	0.0812	0.0740	0.0708	0.0689	0.0678	0.0664	0.0659	0.0656	0.0653	0.0650

example, a series of 50 spectra is required, then minimizing runtime is attractive. Some issues are as follows.

1. Signal-to-noise ratio increases approximately as the square root of the number of scans, the time constant, and the intensity of the light beam.
2. The high-tension voltage must not get too high, which means that concentration and/or pathlength must be considered as discussed below. A rule of thumb is to keep it below 600 V on most instruments, though this should be confirmed by checking that data follow the Beer–Lambert Law (cf. Chapter 2). Unfortunately stray light can give a false sense of security as the photomultiplier tube does not distinguish light of the correct wavelength passing through the sample from any other source of light.
3. τ should be as large as possible subject to $\tau \times s \leq b/2$. If τ is too long for the chosen s and b, then the maxima of peaks (both positive and negative) will be cut off and their wavelengths shifted. A control scan using $\tau' = \tau/2$ (or $s' = s/2$) should be used to check that spectra are not being distorted by the chosen parameters.
4. The data interval determines how often a data point is collected. If the instrument works in a stopped-scan mode (it stops at each point to collect data), then this parameter determines the scan speed. Some instruments let one deal with scan speed and data collection time more or less independently, in which case one needs to ensure that the spectrum is not distorted by scanning too quickly.

18.5.4. Light Beams and Cells

All of the light beam incident upon the cell must pass through the sample and not be clipped or reflected by the walls or base of the cell or the meniscus of the solution. This is particularly an issue for micro-volume cells (see below). Sometimes careful masking and/or focusing are required to avoid this issue. In doing this, one should note that

1. Beam width is dependent on the instrument slit width, which in turn may be designed to depend on the lamp energy, so may be (much) larger in the UV region of the spectrum than in the visible region.
2. Chromatic aberration results in focal points from lenses being a function of wavelength.

18.5.5. Baselines, Wavelength Ranges

The baseline in an LD experiment is rarely flat, because it depends on the intrinsic birefringence of the spectropolarimeter optics and that of the sample holder. The options for baselines with LD are more complicated than those for CD (cf. Chapter 2). With flow LD, if a flow-through system is used, then simply stopping the flow should unorient the sample so a baseline can be measured. With a Couette flow cell (Section 18.6.2), this is only an option if the LD signal at all orientations of the rotating quartz components is the same. Our experience is that this is the case with our microvolume cells but not always with larger cells. A baseline of the same cell rotating slowly, causing no measurable orientation of the sample, may be used if the motor is stable at low rotation speeds, and the scan speed is slow compared with the rotation speed. Alternatively, a spectrum of only the solvent/buffer with higher rotation speed may be measured as the baseline. However, if the sample scatters light significantly, then the contribution of scattering to the spectrum needs to be taken into account.

With films (Section 18.6.1), the best baselines are either an identical matching film without analyte or the same film before the analyte has been added (though make sure solvent has been applied in the same way as the sample will be, since the polymer of the film often swells upon addition of solvent).

LD spectra often also need to be zeroed, so it is essential that data at least 20 nm beyond the normal absorption envelope are available. When the baseline spectrum is subtracted from the sample spectrum, the region outside the absorption envelope should be flat. If it is not, then light scattering is probably contributing to the spectrum (cf. Section 18.5.6).

18.5.6. Light Scattering

Many of the molecules for which we wish to measure LD are of comparable size to the wavelength of light. As a result, they often scatter light significantly. This has two effects: (i) It contributes LD intensity to the signal as in Figure 18.20a because as well as differentially absorbing the two incident polarizations of light (the basis of the LD and CD), the samples may also differentially scatter the light, and (ii) it may cause false maxima in the spectra as illustrated in Figure 18.20b. The origins of light scattering are complicated, depending not only on size regime of the particles but also on their shape. Thus, if at all possible, one should avoid it occurring rather than try to correct for it. In general, scattering can be reduced either by reducing the size of the particles or by collecting a high percentage of the scattered photons. However, these options may either be insufficient or unavailable. Nordh et al. [47] showed that a simple empirical correction can often be subtracted from the observed LD spectrum to remove the sloping baseline [48], as illustrated in Figure 18.20a.

$$\mathrm{LD}^{\mathrm{Scattering}} = a\lambda^{-k}. \tag{18.5}$$

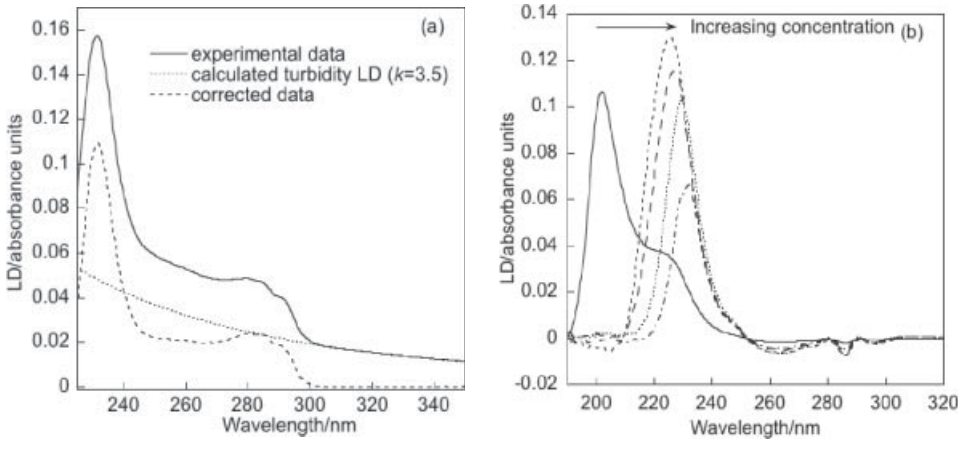

Figure 18.20. (a) Light scattering and a method of correction [47] applied to an LD spectrum of polymerized tubulin: the experimental data (—); the calculated turbidity (or scattering) LD [Eq. (18.5)], using a k value of 3.5, with a determined by rescaling the curve at 320 nm where there is no intrinsic absorbance (---); and the corrected data (– – –) [35]. (b) Far-UV LD spectra showing false maxima in the spectra of strongly light scattering F-actin fibers. F-actin concentrations 93, 74, 62, 53, and 12 μM. The true spectrum is the 12 μM solid line. The high-tension voltage of the instrument remained below 600 V (usually considered acceptable) throughout the experiment. (Redrawn from reference 7.)

TABLE 18.2. Absorbance Flattening Effects for Samples Where the Light Passes Through a Sample of Which Half Has No Absorbance and Half Has the Indicated Absorbance [1]

A of Clear Part of the Solution	A of Dense Part of Solution	$A_{apparent}$ of Inhomogeneous Solution	A for the Analogous Homogeneous Solution	Error (%)
0	3	0.30	1.5	80
0	2	0.29	1.0	71
0	1	0.26	0.5	48
0	0.5	0.19	0.25	24

18.5.7. Absorbance Flattening

The phenomenon of absorption flattening is a suppression of the absorbance signal in regions of high absorbance in nonhomogeneous samples, causing the Beer–Lambert law to break down [49, 50]. Unfortunately, most LD samples are not homogeneous, being membranes or fibers suspended in aqueous solution. Table 18.2 illustrates the seriousness of the problem [1]. For membrane and fiber systems, one somehow has to remove the local high concentrations. Mao and Wallace have outlined how this may be done by reducing membrane particle size [51]. Unfortunately, the problem cannot always be avoided, in which case methods such as those of reference 49 can be used to correct measured data. In practice it must be confessed that the ostrich approach is usually taken and the issue is ignored.

18.6. ORIENTATION METHODS OF SAMPLES FOR LD SPECTROSCOPY

LD can be used to give relative orientations of subunits of a system, often in a situation where no other technique can be used. However, this is only possible if the sample can be macroscopically oriented in a manner that does not perturb the molecules of interest. Which orientation method one should use depends on the sample and the question being asked. Long and relatively rigid polymers, such as double-stranded DNA or RNA, or molecular assemblies of micrometer dimension, may be oriented in a fluid by shear flow whereas small molecules require a stronger orienting force. Some molecules, which cannot themselves be oriented, may be oriented when they bind to another molecule that is oriented. The sensitivity of bench-top instruments based on CD spectropolarimeters is of the order of one part in a million, so the orientation method does not have to be particularly efficient to give a good LD signal. The most widely used orientation methods are described below.

18.6.1. Stretched Polymers as Matrices in Which to Orientate Small Molecules

Small molecules can often be absorbed into polymer films. When the film is mechanically stretched, either before or after the small molecules are added, the included molecules align their long axes preferentially along the stretch direction. In 1934 A. Jablonski was the first to propose a method for orienting molecules by adsorption in anisotropic matrices [52]. In practice, one of two types of films enable one to prepare aligned samples of most molecules: polyethylene for nonpolar molecules and polyvinyl alcohol

Figure 18.21. A mechanical film stretcher with oppositely threaded screws to ensure even stretching of the film. (*See insert for color representation of the figure.*)

for polar molecules. Polyvinyl chloride is also valuable in some applications. A typical film stretcher that gives a uniform stretching force is illustrated in Figure 18.21.

Polyethylene (PE) is microcrystalline; and when it is mechanically stretched along the manufacturer's stretch direction, a molecular orienting environment is produced. PE films for LD are the simplest to prepare, because almost any reasonable quality PE may be used (e.g., sandwich bags) and the analyte added onto the film dropwise either before or after stretching. By convention the parallel direction of the polarized light is usually taken to be horizontal (i.e., parallel to the floor), so the stretch direction of the film should be aligned horizontally. It is advisable not to stretch too close to the breaking point of the polymer, since the film has a tendency to become opaque and to rip suddenly. With a film stretcher (Figure 18.21), a stretch factor of 5–10 is fairly straightforward. One should always endeavor to collect the sample spectrum on the same part of the film as the baseline.

Polyvinylalcohol (PVA) is a near-universal host for polar molecules; the film is transparent in the UV (above 200 nm) and in the visible region of the spectrum, though it has a strong absorption over large regions of the infrared [53]. Small molecules inserted in a dry (less than a few percent water) PVA film may be oriented by stretching under low heat. PVA films are more difficult to prepare than PE films, but the quality of the resulting data is often better. To prepare a PVA film, one mixes well-hydrolyzed low-molecular-weight commercial PVA powder in cold water (10% w/v) to make a slurry which is then heated to near boiling to form a viscous solution. The sample solution (typically the sample is prepared at a concentration of ~5 mM in water, but the aim is to have the final film with a maximum absorbance of between 0.1 and 1) is then added to half of the PVA solution, and the mixture is cast onto a glass plate and left to dry. The same volume of water is added to the remainder of the solution which is also cast

onto a glass plate and left to dry to make a baseline film. Finally the films are stretched by the same factor (typically 2–5) at an elevated temperature (~80°C) by holding the films in the hot air from a hair dryer as they are being stretched. It is also advisable to stretch the films a little and then measure the spectra before trying a larger stretch on a precious sample, because the films are quite brittle.

18.6.2. Flow Orientation of Macromolecules

If a rigid or semiflexible polymer, such as DNA or a protein fiber, is dissolved in a solvent and then flowed past a stationary surface at 0.1-3 m s^{-1}, then the molecules experience sufficient shear forces to give a net orientation of the long axis of the polymer along the flow direction. If light is incident on the sample perpendicular to the flow direction, then the absorbance parallel to the flow, $A_{//}$, and the absorbance perpendicular to the flow direction, $A_{\perp}$, are different so an LD signal may be measured. If the cell components are quartz, then data in the visible and UV regions may be collected.

The obvious method for producing the required flow rate is to use a linear flow-through system such as provided by an HPLC pump or a pair of syringes. However, such an open system has an inherently large sample requirement and tends not to be completely stable. Another problem is that any air bubble in the system will multiply as the sample circulates through the tubing. In 1964, Wada [54, 55] solved these problems with the invention of a Couette flow cell for LD where the sample is endlessly flowed between two cylinders, one of which rotates and one of which is stationary. This is schematically illustrated in Figure 18.22.

Some Couette flow cells are illustrated in Figure 18.23. The most recent developments include microvolume Couette flow cells, which require 25–60 μL of sample rather than the milliliters of the previous Couette cells, and Peltier temperature control [56, 57]. These developments have increased both the range of samples and types of experiments that can be undertaken.

18.6.3. The Effect of Shear Rate, Sample Viscosity and Particle Length on Flow LD Signals

One of the key experimental parameters for flow LD is how fast the Couette cell spins. This is directly related to shear rate by

$$G/s^{-1} = \frac{dv_z}{dx} = \frac{2\pi R_o \Omega}{60(R_o - R_i)}, \tag{18.6}$$

where the rate of rotation Ω is revolutions per minute (rpm) for an outer rotating Couette cell with outer cylinder radius R_o and inner cylinder radius R_i. The dependence of LD on shear rate for some DNAs is illustrated in Figure 18.24 (note the plots are −LD versus G^2 or G). To a first approximation, most DNAs with which one works have a linear dependence on G. Stiffer polymers reach saturation at lower G than the semiflexible DNA. Others (often including DNA) do not reach saturation before the flow becomes turbulent.

Flow LD magnitudes are also dependent on solution viscosity, η, as illustrated in Figure 18.25. Viscosity itself is a function of both temperature and shear rate: the viscosity of water at 60° is half that at 20° and the viscosity of water at G = 1000 s^{-1} is one-third that at 0 s^{-1} [58]. Thus temperature, G and η dependence of LD cannot be considered

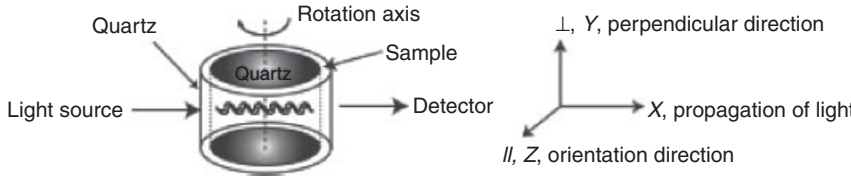

Figure 18.22. Schematic diagram of a Couette flow cell showing flow orientation in a coaxial flow cell with radial incident light. {*X,Y,Z*} denotes the laboratory-fixed axis system. (Redrawn from reference 1.)

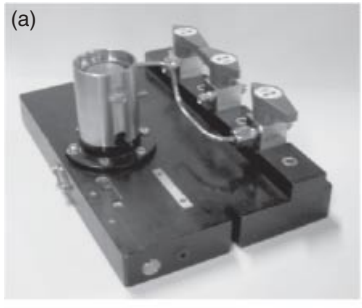

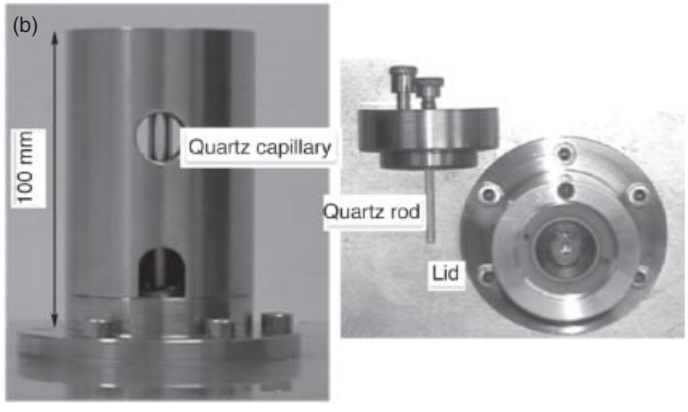

Figure 18.23. (a) Large-volume (2–3 mL) inner rotating cylinder Couette flow cell with 500-μm annular gap [6]. (b) Microvolume (25–60 μL) outer rotating [56, 57] Couette flow cell showing the outer quartz capillary (3-mm inner diameter) and inner quartz rod (2.5-mm outer diameter) which, when assembled, results in an annular gap of 250 μm. (*See insert for color representation of the figure.*)

in isolation. Small LD signals can be enhanced by adding, for example, glycerol to the solution to increase its viscosity [16, 59].

18.6.4. Orientation by Evaporation or Assembly

Many molecules may be oriented simply by evaporating them onto a surface that is transparent to the radiation. This method works particularly well for planar aromatic molecules. However, the plate may need to be tilted for LD measurements since the molecules usually orient preferentially parallel to the surface of the quartz, resulting in the unique axis being perpendicular to the plate and all in-plane directions having the same distribution of molecular orientations. Orientation by evaporation has probably been most extensively used for infrared studies of lipid bilayers and molecules bound to the bilayers

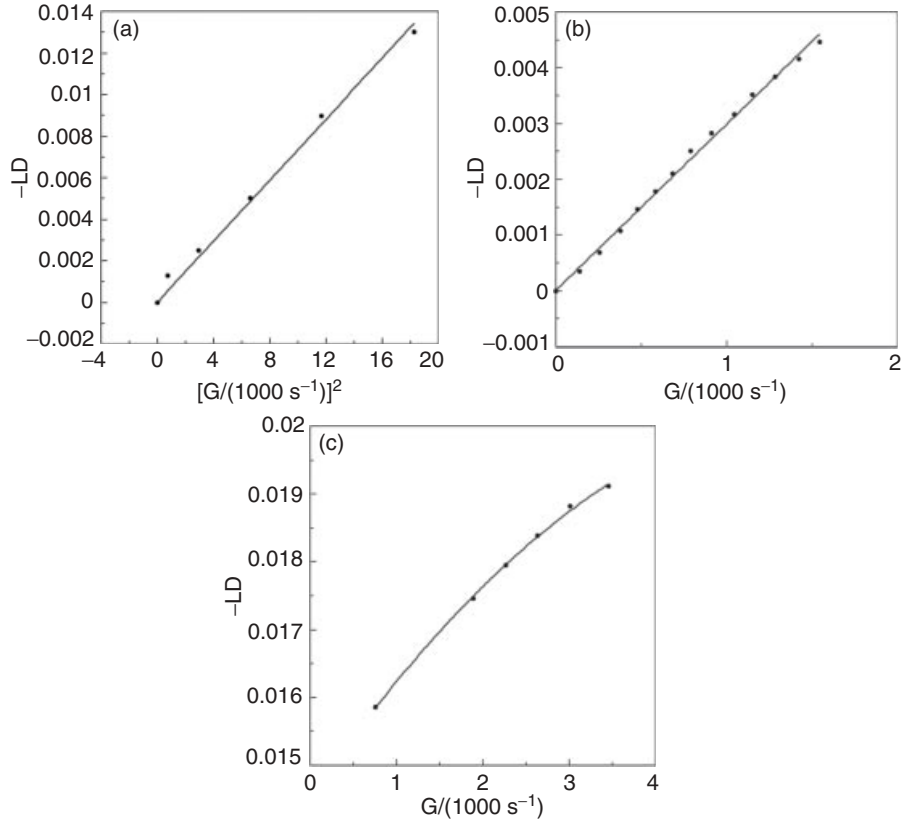

Figure 18.24. (a) −LD (at 260 nm) versus G^2 (G = shear rate) for a 450-base-pair DNA (130 μM, 10 mM NaCl, 23°C). (b) −LD (at 260 nm) versus G for a linearized plasmid DNA (pC3.1 variant, 6882 base pairs) (100 μM, 0.1 M NaCl, 30°C) and (c) −LD (at 260 nm) versus G for calf thymus DNA (200 μM base, 10 mM salt, 23°C). LD cell has $R_o = 3.00$ mm and $R_i = 2.75$. (Redrawn from reference 58.)

[60]. It is also used for oriented CD studies of membrane proteins. Monomolecular layers of surface-assembled dye molecules have been studied in this way [4].

The extent to which the solvent needs to be removed depends on the sample. Most work with lipids usually proceeds by drying the sample then adding a salt solution, chosen to give the required humidity, to the atmosphere [61]. The lipids spontaneously orient as the humidity is reduced, resulting in bilayers of lipid with thin water interstitia separating the bilayers. Some molecules such as Alzheimer's fibers are sufficiently large and rigid that simply pipetting them onto a surface from solution may produce a significant degree of orientation [36].

18.7. SOME DERIVATIONS

18.7.1. Equation (18.2)

The main equation used in this chapter to interpret LD spectra is Eq. (18.2). Its derivation proceeds as follows. Let Z be the macroscopic orientation direction (denoted // above) and let Y be the perpendicular direction. Assume first that the molecule of interest is

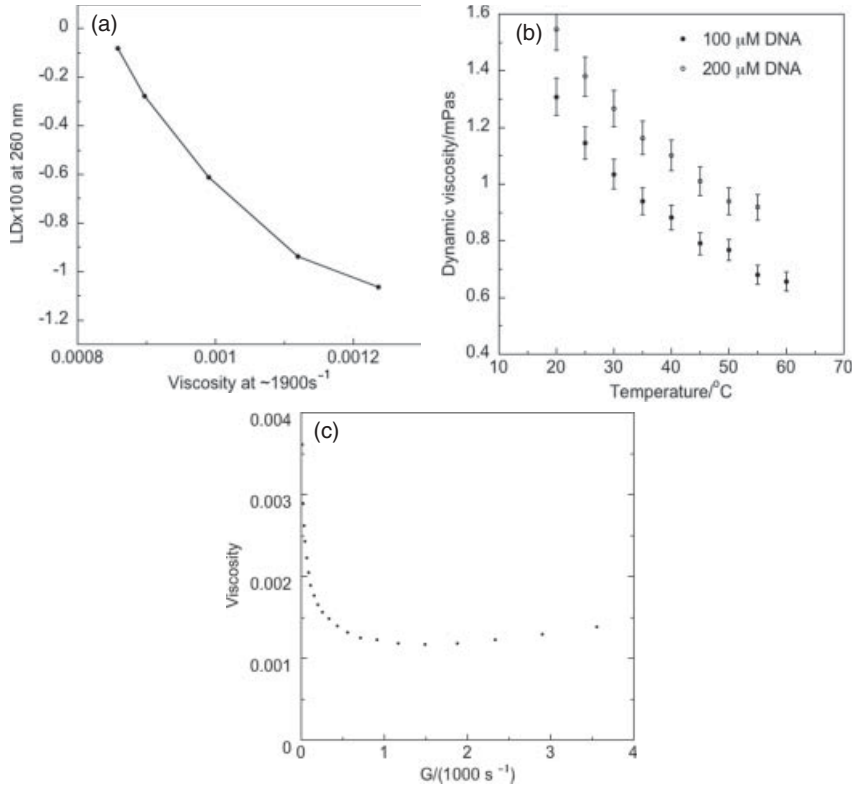

Figure 18.25. (a) Viscosity dependence of Couette flow LD (measured on a Jasco J-815 spectropolarimeter) at 260 nm for a solution of DNA (200 μM calf thymus DNA in water). The viscosity was determined on the same solution as the LD using an Advanced Rheometer AR100. The viscosity was varied by changing the temperature from 20–60°C. The shear rate was 1900 s^{-1}. (b) Temperature dependence of the dynamic viscosity of DNA (200 μM calf thymus DNA in water). (c) Shear-rate dependence of the dynamic viscosity of DNA (200 μM calf thymus DNA in water). Viscosities for (b) and (c) were determined using a Cannon–Manning 25 E50 semi-micro viscometer. (Redrawn from reference 73.)

perfectly oriented so that the molecular orientation axis, z, lies along the macroscopic parallel direction—that is, $z = Z$, $S = 1$. Since absorbance is proportional to the square of the component of the electric dipole transition moment, μ, which lies along the direction of the electric field of the light, we may write (using the definitions of α and γ in Figure 18.2)

$$\begin{aligned} A_Z &= k\mu^2 \cos^2 \alpha, \\ A_Y &= k\mu^2 \sin^2 \alpha \sin^2 \gamma, \end{aligned} \tag{18.7}$$

where k is a constant. Thus

$$\begin{aligned} LD &= A_{//} - A_{\perp} = A_Z - A_Y \\ &= k\mu^2(\cos^2 \alpha - \sin^2 \alpha \sin^2 \gamma). \end{aligned} \tag{18.8}$$

Similarly, the isotropic absorbance is the average of the absorbance in the *X, Y*, and *Z* directions, so

$$\begin{aligned} A_{iso} &= \frac{1}{3}(A_Z + A_Y + A_X) = \frac{1}{3}(A_Z + 2A_Y) \\ &= \frac{1}{3}k\mu^2(\cos^2\alpha + 2\sin^2\alpha\sin^2\gamma). \end{aligned} \tag{18.9}$$

Since the experiment does not restrict the value of γ, we average over $\sin^2\gamma$ to give

$$\begin{aligned} LD &= k\mu^2\left(\cos^2\alpha - \frac{1}{2}\sin^2\alpha\right) \\ &= \frac{k\mu^2}{2}(2\cos^2\alpha - \sin^2\alpha) \\ &= \frac{k\mu^2}{2}(3\cos^2\alpha - 1) \end{aligned} \tag{18.10}$$

and

$$A_{iso} = \frac{k\mu^2}{3}(\cos^2\alpha + \sin^2\alpha) = \frac{k\mu^2}{3}. \tag{18.11}$$

Equation (18.2) follows upon acknowledging that actually the orientation is not perfect so, including S, we get

$$LD = \frac{3}{2}A_{iso}S(3\cos^2\alpha - 1). \tag{18.12}$$

18.7.2. Equation (18.4)

Shear-deformed liposomes, peptidoglycan sacculi, and carbon nanotubes are cylindrical systems where the analytes are oriented uniformly about the normal to the surface of the cylinder. The LD under such circumstances is described by Eq. (18.4) because there is an additional element of rotational averaging required. Let z be along the long axis of the cylinder and let x be the normal to the surface of the cylinder that goes through the chromophore whose LD we are measuring. Let β be the angle between x and μ. The analyte orientation will not be affected by the shear flow (the forces are too small), so on average any analyte transition moment, μ, will be uniformly distributed about the x axis. Let ψ be the angle between the projection of μ onto the y/z plane and z. Thus in the local cylinder coordinate system

$$\mu = \mu(\cos\beta, \sin\beta\sin\psi, \sin\beta\cos\psi)_{\{x,y,z\}}, \tag{18.13}$$

where μ is the magnitude of μ. The reduced linear dichroism is by definition

$$LD^r = S\frac{A_Z - A_Y}{A_{iso}} = 3S\frac{(\mu_Z^2 - \mu_Y^2)}{\mu^2}. \tag{18.14}$$

Now, $\mu_z = \mu_Z$ and μ_Y may be written as the dot product of the transition moment vector and the vector for the Y axis in the $\{x,y,z\}$ coordinate system. Thus

$$\begin{aligned}\mu_y &= \mu \cdot y \\ &= \mu(\cos\beta, \sin\beta\sin\psi, \sin\beta\cos\psi)_{\{x,y,z\}} \cdot (\sin\gamma, \cos\gamma, 0)_{\{x,y,z\}} \\ &= \mu(\cos\beta\sin\gamma + \sin\beta\sin\psi\cos\gamma),\end{aligned} \tag{18.15}$$

where γ take values from 0 to 2π. Thus,

$$\mathrm{LD}^{\mathrm{r}} = 3S\begin{pmatrix}\sin^2\beta\cos^2\psi - \cos^2\beta\sin^2\gamma - \sin^2\beta\sin^2\psi\cos^2\gamma \\ -2\cos\beta\sin\gamma\sin\beta\sin\psi\cos\gamma\end{pmatrix}. \tag{18.16}$$

Both ψ and γ take values from 0 to 2π, so upon averaging over them:

$$\begin{aligned}\mathrm{LD}^{\mathrm{r}} &= 3S\frac{2\sin^2\beta - 2\cos^2\beta - \sin^2\beta}{4} \\ &= \frac{3}{4}S(1 - 3\cos^2\beta),\end{aligned} \tag{18.17}$$

which is Eq. (18.4).

18.8. INTERPLAY OF THEORY AND EXPERIMENT

Interpretation of the LD of isolated transitions is straightforward as long as S is known. Some examples were given above. However, typically with molecules large enough to give LD spectra, transitions of different polarization are overlaid. The matrix method that has been developed to calculate CD spectra has also been applied to LD spectra of fibrous proteins, and work is in progress to use it on membrane-bound peptides [62, 63]. Coupling this approach with molecular dynamics has the potential to enable LD to be used to determine atomic-resolution structures.

REFERENCES

1. B. Nordén, A. Rodger, T. R. Dafforn, *Linear Dichroism and Circular Dichroism: A Textbook on Polarized Spectroscopy*, Royal Society of Chemistry, Cambridge, **2010**.
2. A. Rodger, B. Nordén, *Circular Dichroism and Linear Dichroism*, Oxford University Press, Oxford, **1997**.
3. M. R. Hicks, J. Kowalski, A. Rodger, *Chem. Soc. Rev*. **2010**, 39, 3380–3393.
4. B. Nordén, *Appl. Spectroscopy Rev*. **1978**, *14*, 157–248.
5. B. Nordén, C. Elvingson, M. Jonsson, B. Åkerman, *Q. Rev. Biophys*. **1991**, *24*, 103–164.
6. A. Rodger, *Meth. Enzymol*. **1993**, *226*, 232–258.
7. A. Rodger, R. Marrington, M. A. Geeves, M. Hicks, L. de Alwis, D. J. Halsall, T. R. Dafforn, *Phys. Chem. Chem. Phys*. **2006**, *8*, 3131–3171.
8. A. Rodger, J. Rajendra, R. Marrington, M. Ardhammar, B. Nordén, J. D. Hirst, A. T. B. Gilbert, T. R. Dafforn, D. J. Halsall, C. A. Woolhead, C. Robinson, T. J. Pinheiro, J. Kazlauskaite, M. Seymour, N. Perez, M. J. Hannon, *Phys. Chem. Chem. Phys*. **2002**, *4*, 4051–4057.

9. J. Michl, E. W. Thulstrup, *Spectroscopy with Polarized Light*, VCH, New York, **1986**.
10. T. R. Dafforn, J. Rajendra, D. J. Halsall, L. C. Serpell, A. Rodger, *Biophys. J*. **2004**, *86*, 404–410.
11. M. Ardhammar, N. Mikati, B. Nordén, *J. Am. Chem. Soc*. **1998**, *120*, 9957–9958.
12. M. Rittman, S. Vrønning Hoffmann, E. Gilroy, M. Hicks, A. Rodger, *Phys. Chem. Chem. Phys*. **2011**, *In press*,
13. P. J. Chou, J. W. C. Johnson, *J. Am. Chem. Soc*. **1993**, *115*, 1205–1214.
14. Y. Matsuoka, B. Nordén, *Biopolymers* **1982**, *21*, 2433–2452.
15. Y. Matsuoka, B. Nordén, *Biopolymers* **1982**, *22*, 1731–1746.
16. C. Hiort, B. Nordén, A. Rodger, *J. Am. Chem. Soc*. **1990**, *112*, 1971–1982.
17. K. K. Patel, E. A. Plummer, M. Darwish, A. Rodger, M. J. Hannon, *J. Inorg. Biochem*. **2002**, *91*, 220–229.
18. B. Nordén, M. Kubista, T. Kurucsev, *Q. Rev. Biophys*. **1992**, *25*, 51–170.
19. R. Marrington, E. Small, A. Rodger, T. R. Dafforn, S. Addinall, *J. Biol. Chem*. **2004**, *279*, 48821–48829.
20. E. Wallin, G. von Heijne, *Protein Sci*. **1998**, *7*, 1029–1038.
21. M. Vaara, *Curr. Opin. Pharmacol*., **2009**, *9*, 571–576.
22. R. E. W. Hancock, D. S. Chappel, *Peptide Antibiotics*, **1999**, *43*, 1317–1323.
23. J. Rajendra, M. Baxendale, L. G. Dit Rap, A. Rodger, *J. Am. Chem. Soc*. **2004**, *126*, 11182–11188.
24. J. Rajendra, A. Damianoglou, M. Hicks, P. Booth, P. M. Rodger, A. Rodger, *Chem. Phys*. **2006**, *326*, 210–220.
25. E. K. Esbjorner, C. E. B. Caesar, B. Albinsson, P. Lincoln, B. Nordén, *Biochem. Biophys. Res. Commun*. **2007**, *361*, 645–650.
26. E. K. Esbjörner, K. Oglecka, P. Lincoln, A. Gräslund, B. Nordén, *Biochemistry* **2007**, *46*, 13490–13504.
27. M. R. Hicks, T. Dafforn, A. Damianoglou, P. Wormell, A. Rodger, S. V. Hoffmann, *Analyst* **2009**, *134*, 1623–1628.
28. M. R. Hicks, A. Damianoglou, A. Rodger, T. R. Dafforn, *J. Mol. Biol*. **2008**, *383*, 358–366.
29. S. M. Ennaceur, M. R. Hicks, C. J. Pridmore, T. R. Dafforn, A. Rodger, J. M. Sanderson, *Biophys. J*. **2009**, *96*, 1399–1407.
30. W. Vollmer, J.-V. Höltje, *J. Bacteriol*. **2009**, *186*, 5978–5987.
31. R. Snowdon, Private communication, **2009**.
32. P. Hagmar, B. Nordén, D. Baty, M. Chartier, M. Takahashi, *J. Mol. Biol*. **1992**, *226*, 1193–1205.
33. B. Nordén, C. Elvingson, M. Kubista, B. Sjöberg, H. Ryberg, M. Ryberg, K. Mortensen, M. Takahashi, *J. Mol. Biol*. **1992**, *226*, 1175–1192.
34. A. Reymer, K. Frykholm, K. Morimatsu, M. Takahashi, B. Nordén, *Proc. Natl. Acad. Sci. USA* **2009**, *106*, 13248–13253.
35. R. Marrington, M. Seymour, A. Rodger, *Chirality* **2006**, *18*, 680–690.
36. K. E. Marshall, M. R. Hicks, T. L. Williams, S. V. Hoffmann, A. Rodger, T. R. Dafforn, L. C. Serpell, *Biophys. J*. **2010**, *98*, 330–338.
37. L. Chen, K. Morris, A. Laybourn, D. Elias, M. R. Hicks, A. Rodger, L. Serpell, D. Adams, *Langmuir* **2010**, *26*, 5232–5242.
38. H. Raghuraman, A. Chattopadhyay, *Biosci Rep*. **2007**, *27*, 189–223.
39. J. C. Talbot, *FEBS Lett*. **1979**, *102*, 191–193.
40. A. Damianoglou, A. Rodger, C. Pridmore, T. R. Dafforn, J. A. Mosely, J. M. Sanderson, M. R. Hicks, *Protein Peptide Lett*. **2010**, *17*, 1351–1362.

41. A. Rodger, A. Parkinson, S. Best, *Eur. J. Inorg. Chem*. **2001**, *9*, 2311–2316.
42. A. Rodger, K. J. Sanders, M. J. Hannon, I. Meistermann, A. Parkinson, D. S. Vidler, I. S. Haworth, *Chirality* **2000**, *12*, 221–236.
43. M. J. Hannon, V. Moreno, M. J. Prieto, E. Molderheim, E. Sletten, I. Meistermann, C. J. Isaac, K. J. Sanders, A. Rodger, *Angew. Chem. Int. Ed*. **2001**, *40*, 879–884.
44. I. Meistermann, V. Moreno, M. J. Prieto, E. Molderheim, E. Sletten, S. Khalid, P. M. Rodger, J. Peberdy, C. J. Isaac, A. Rodger, M. J. Hannon, *Proc. Natl. Acad. Sci*. **2002**, *99*, 5069–5074.
45. J. Nordh, J. Deinum, B. Nordén, *Eur. Biophys. J*. **1986**, *14*, 113–122.
46. B. Nordén, S. Seth, *Appl. Spectrosc*. **1985**, *39*, 647–455.
47. J. Nordh, J. Deinum, B. Nordén, *Eur. Biophys. J*, **1986**, *14*, 113–122.
48. A. Rodger, R. Marrington, M. A. Geeves, M. Hicks, L. de Alwis, D. J. Halsall, T. R. Dafforn, *Phys. Chem. Chem. Phys*. **2006**, *8*, 3161–3171.
49. D. J. Gordon, G. Holzwarth, *Arch. Biochem. Biophys*. **1971**, *142*, 481–488.
50. B. Nordén, *Spectrosc. Lett*. **1977**, *10*, 483–488.
51. D. Mao, B. A. Wallace, *Biochemistry* **1984**, *23*, 2667–2673.
52. A. Jablonski, *Nature* **1934**, *133*, 140–140.
53. Y. Matsuoka, B. Nordén, *J. Phys. Chem*. **1982**, *86*, 1378–1386.
54. A. Wada, *Biopolymers* **1964**, *2*, 361–380.
55. A. Wada, *Appl. Spectrosc. Rev*. **1972**, *6*, 1–30.
56. R. Marrington, T. R. Dafforn, D. J. Halsall, M. Hicks, A. Rodger, *Analyst* **2005**, *130*, 1608–1616.
57. R. Marrington, T. R. Dafforn, D. J. Halsall, A. Rodger, *Biophys. J*. **2004**, *87*, 2002–2012.
58. M. Rittman, E. Gilroy, H. Koohy, A. Rodger, A. Richards, *Sci. Prog*. **2009**, *92*, 163–204.
59. T. R. Dafforn, D. J. Halsall, A. Rodger, *Chem. Commun*. **2001**, 2410–2411.
60. D. Marsh, M. Muller, F. J. Schmitt, *Biophys. J*. **2000**, *78*, 2499–2510.
61. F. E. M. O'Brien, *J. Sci. Instrum*. **1948**, *25*, 73–76.
62. B. Bulheller, A. Rodger, J. D. Hirst, *Phys. Chem. Chem. Phys*. **2007**, *9*, 2020–2035.
63. B. M. Bulheller, A. Rodger, M. R. Hicks, T. R. Dafforn, L. C. Serpell, K. Marshall, E. H. C. Bromley, P. J. S. King, K. J. Channon, D. N. Woolfson, J. D. Hirst, *J. Am. Chem. Soc*. **2009**, *131*, 13305–13314.
64. A. Holmén, A. Broo, B. Albinsson, B. Nordén, *J. Am. Chem. Soc*. **1997**, *119*, 12240–12250.
65. L. B. Clark, *J. Phys. Chem*. **1990**, *94*, 2973–2879.
66. L. B. Clark, *J. Am. Chem. Soc*. **1977**, *99*, 3934–3938.
67. F. Zaloudek, J. S. Novros, L. B. Clark, *J. Am. Chem. Soc*. **1985**, *107*, 7344–7351.
68. J. A. L. Williams, C. Cheong, J. I. Tinoco, L. B. Clark, *Nucl. Acids Res*. **1986**, *14*, 6649–6659.
69. E. Tuite, B. Nordén, *Biorg. Med. Chem*. **1995**, *3*, 701–711.
70. F. Probert, Private communication, **2009**.
71. D. Turner, Private communication, **2009**.
72. C. Dicko, M. R. Hicks, T. R. Dafforn, F. Vollrath, A. Rodger, S. V. Hoffmann, *Biophys. J*. **2008**, *95*, 5974–5977.
73. E. L. Gilroy, M. R. Hicks, D. J. Smith, A. Rodger, Viscosity of aqueous DNA solutions determined using dynamic light scattering, *Analyst*, **2011**, DOI: 10.1039/C1AN15475C.

19

ELECTRO-OPTICAL ABSORPTION SPECTROSCOPY

Hans-Georg Kuball and Matthias Stolte

19.1. INTRODUCTION

Chiroptical analysis by chirality measurements like CD and ORD is, aside from X-ray diffraction, the best-established method for the determination of the absolute configuration of chiral compounds. For that purpose, sector and helicity rules or methods for quantum mechanical numerical calculations for correlating the sign of the chirality measurements [e.g., the *Cotton* effect (CE) of one or more absorption bands] with the absolute configuration of a molecule, or at least for the absolute configuration of a chromophore[1] and its surrounding within a molecule, are required [1, 2]. The "exciton chirality method" [1] is one of the most important helicity rules, which is based on the quantum mechanical theory of a coupled oscillator [3]. Originally developed as the "dibenzoate chirality method" [4], the exciton chirality method can be applied to molecules possessing at least two allowed electric dipole transitions in neighboring spectral regions, located in different parts of the molecule. In Figure 19.1, the effect of coupling electronic transitions of two chromophores in a molecule of C_2 symmetry is depicted with its two exciton transitions, $|N\rangle \rightarrow |K_1\rangle$ and $|N\rangle \rightarrow |K_2\rangle$. The CD of the $\alpha(A \rightarrow B)$ transition is negative, and for the $\beta(A \rightarrow A)$ transition it is positive for a dihedral angle ω between about 0 and -90° to -110°, by which a negative (left-hand side of Figure 19.1) couplet is obtained. The

[1] There are many different definitions in use for the notion "chromophore." In this chapter, "chromophore" means a part of a molecule which is changed by excitation with light of a selected wavelength, leading to an excited state possessing different properties.

Comprehensive Chiroptical Spectroscopy, Volume 1: Instrumentation, Methodologies, and Theoretical Simulations, First Edition. Edited by N. Berova, P. L. Polavarapu, K. Nakanishi, and R. W. Woody.
© 2012 John Wiley & Sons, Inc. Published 2012 by John Wiley & Sons, Inc.

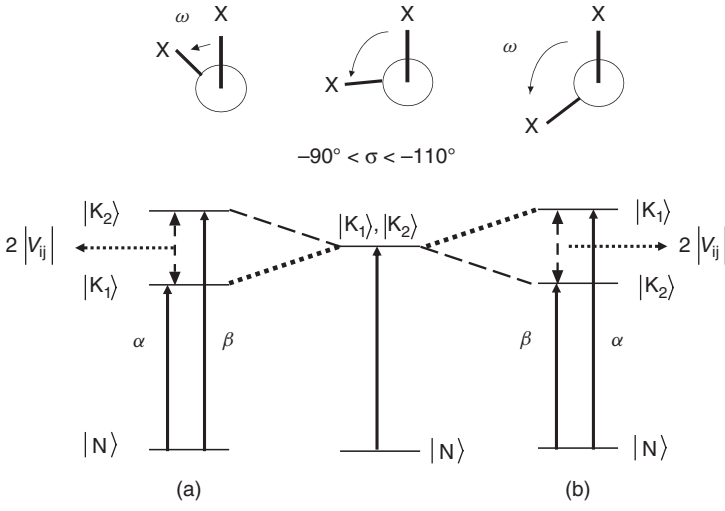

Figure 19.1. Variation of a schematic term scheme of a chromophore of C_2 symmetry with *negative chirality*, possessing dihedral angles between (a) zero and $-\sigma$ and (b) $-\sigma$ and $(-\sigma + 90^\circ)$. (Redrawn from reference 7.)

sign of the CD and, thus, the sign of the couplet will be reversed for ω between -90° and -110° and between -180° and -200° in spite of the fact that the absolute configuration is maintained. Here, the sign change originates at the crossing of the energy levels of the excited states $|K_1\rangle$ and $|K_2\rangle$ as a function of the dihedral angle between -90° and -110°. The amplitude A of the couplet is zero if the excited states $|K_1\rangle$ and $|K_2\rangle$ are accidentally degenerate ($V_{ij} = 0$).

The shape, amplitude, and sign of the couplet are determined by the shape and intensity of the CD bands (Figure 19.2) belonging to the transitions $|N\rangle \rightarrow |K_1\rangle$ and $|N\rangle \rightarrow |K_2\rangle$ of the coupled chromophores, their transition moment directions, and their energies $E^{\alpha/\beta}$ [1]. Often the *Davydov* splitting ($2V_{ij}$) of the exciton chromophore leads only to a broadening of the absorption band or to the creation of a band with a small shoulder. Even then, the CD spectra possess the shape of a couplet (Figure 19.2) because the CD bands belonging to the transitions $|N\rangle \rightarrow |K_1\rangle$ and $|N\rangle \rightarrow |K_2\rangle$ are large and of opposite signs. This characteristic bandshape is a prerequisite for the broad applicability of the exciton chirality method [1].

But there is often a hidden presupposition, namely, the spectroscopic assignment either to the α or β transition of the exciton bands (Figure 19.1). For many rigid molecules, this assignment is often made unequivocally due to their molecular geometry or to an approximate calculation of localized transitions. But there are examples—flexible

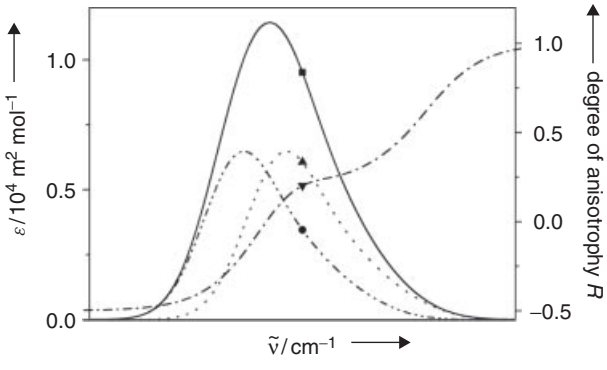

Figure 19.2. Exciton absorption band (■,—) and the degree of anisotropy $R(\tilde{\nu}) = [\varepsilon_{\parallel}(\tilde{\nu}) - \varepsilon_{\perp}(\tilde{\nu})]/3\varepsilon(\tilde{\nu})$ (▼,-·-·) as a result of a superposition of the absorption bands ((●,-·-·), (▲,·····)) of a molecule of C_2 symmetry belonging to the α(A → B) and β (A → A) exciton transitions. (Redrawn from reference 7.)

molecules in solutions—where an unequivocal assignment is impossible. A conformational change caused by increasing the dihedral angle about one axis, as shown in Figure 19.1, can lead to a crossing of the energy states accompanied by a sign change of the couplet without a change of the absolute configuration (Figure 19.1). In all these cases, linear dichroism in any of its possible application techniques allows the determination of the transition moment direction for a safe assignment of the α and β transitions. So-called polarized spectroscopy is a well-proven technique for determining transition moment directions [5, 6]. For a few examples, such measurements were undertaken in order to prove the applicability of the exciton chirality method [4]. But often the sensitivity of the polarized spectroscopy is not sufficient for an assignment of differently polarized exciton transitions. The same problem arises with the anisotropy of circular dichroism (ACD) of anisotropic phases, which is related to the CD as polarized spectroscopy is to absorption spectroscopy [7, 8]. In this chapter the highly sensitive electro-optical absorption (EOA) spectroscopy (electrochromism) will be applied in an analysis of exciton transitions. In addition to the information obtained from the polarized spectroscopy [5, 6], dielectric properties like the dipole moment of the ground state, the dipole moment change during the excitation, and some coordinates of the (hyper)polarizability tensor—important for nonlinear optical behavior—can be evaluated. For some steroids and mesobilirubin, the technique of the method will be demonstrated.

19.2. WORKING EQUATIONS FOR POLARIZED SPECTROSCOPY AND ELECTRO-OPTICAL ABSORPTION SPECTROSCOPY

Polarized spectroscopy [5] as well as EOA spectroscopy (electrodichroism [9–12]) are based on measurements of the absorbance $E(\tilde{\nu}, \varphi)$ with linearly polarized light propagating perpendicular to the optical axis of, for example, a uniaxial phase. φ is the azimuth of the linearly polarized light with respect to the applied external electric field $\mathbf{F}$. With EOA spectroscopy, the very small difference in absorbance $E^{\mathbf{F}}(\tilde{\nu}, \varphi) - E(\tilde{\nu})$ of a dilute solution, in the presence ($E^{\mathbf{F}}(\tilde{\nu})$) and in the absence ($E(\tilde{\nu})$) of an externally applied electric field $\mathbf{F}$, is directly measured as a function of the wavenumber $\tilde{\nu}$ [eq. (19.1)].

$$L(\tilde{\nu}, \varphi)E(\tilde{\nu}) = [E^{\mathbf{F}}(\tilde{\nu}, \varphi) - E(\tilde{\nu})]\frac{1}{\mathbf{F}^2}. \tag{19.1}$$

Measurements with two different azimuth angles, $\varphi = 0^\circ$ and $\varphi = 90^\circ$, are sufficient for a complete description of the absorption anisotropy of a uniaxial sample. Whereas $E(\tilde{\nu})$ is the absorbance of a solution with isotropically distributed molecules in the absence of an electric field, $E^{\mathbf{F}}(\tilde{\nu})$ is the hypothetical absorbance of a solution with isotropically distributed molecules in the presence of an electric field calculable from the relation

$$E^{\mathbf{F}}(\tilde{\nu}) = \frac{1}{3}[E^{\mathbf{F}}(\tilde{\nu}, 0^\circ) + 2\, E^{\mathbf{F}}(\tilde{\nu}, 90)], \tag{19.2}$$

valid for uniaxial phases, which are different for different experimental conditions. For $\mathbf{F} \neq \mathbf{0}$ or for any other interaction for ordering molecules (stretched polymers, liquid crystals), one can expect the internal field to be different from the situation of $\mathbf{F} = \mathbf{0}$.

$L(\tilde{\nu},\varphi)E(\tilde{\nu})$ is the sum of all contributions to the anisotropy of absorption of all compounds, conformers, or aggregates j in the solution, or for compounds with overlapping absorption bands (k = 1, 2, ...) when the absorbance is given by

$$E(\tilde{\nu}) = \sum_{\mathrm{j}} \varepsilon_{\mathrm{j}} c_{\mathrm{j}} d = \sum_{\mathrm{j}} \sum_{\mathrm{k}} \varepsilon_{\mathrm{j}}^{\mathrm{k}} c_{\mathrm{j}} d. \tag{19.3}$$

Taking into account the electric field dependence of phase properties like density, volume, chemical equilibria, and so on, the following equation holds:

$$L(\tilde{\nu},\varphi)\frac{E(\tilde{\nu})}{\tilde{\nu}} = \sum_{\mathrm{i}} \sum_{\mathrm{k}} \left(L_{\mathrm{i}}^{\mathrm{k}}(\tilde{\nu},\varphi) c_{\mathrm{i}} + \frac{\partial^2 c_{\mathrm{i}}}{\partial F^2} \right) \frac{\varepsilon_{\mathrm{i}}^{\mathrm{k}}(\tilde{\nu})}{\tilde{\nu}} d. \tag{19.4}$$

The contribution of the kth absorption band of a compound/conformer j to the electrochromism of the solution is given by

$$L_{\mathrm{j}}^{\mathrm{k}}(\tilde{\nu},\varphi) = A_{\mathrm{j}}^{\mathrm{k}}(\tilde{\nu},\varphi) + \frac{1}{15} B_{\mathrm{j}}^{\mathrm{k}}(\tilde{\nu},\varphi) t_{\mathrm{j}}^{\mathrm{k}}(\tilde{\nu}) + \frac{1}{15} C_{\mathrm{j}}^{\mathrm{k}}(\tilde{\nu},\varphi) u_{\mathrm{j}}^{\mathrm{k}}(\tilde{\nu}). \tag{19.5}$$

$A_{\mathrm{j}}^{\mathrm{k}}(\varphi), B_{\mathrm{j}}^{\mathrm{k}}(\varphi)$, and $C_{\mathrm{j}}^{\mathrm{k}}(\varphi)$ are the electro-optical coefficients of the kth transition of the species j. They depend on the orientational distribution of the molecules in solution due to their ground-state dipole moment $\boldsymbol{\mu}_{\mathrm{g}}$, their polarizability and hyperpolarizability, the shift of the kth absorption band proportional to the difference $\Delta\boldsymbol{\mu} = \boldsymbol{\mu}_{\mathrm{e}}^{\mathrm{k}} - \boldsymbol{\mu}_{\mathrm{g}}$ between the ground-state dipole moment and the corresponding excited-state dipole moment $\boldsymbol{\mu}_{\mathrm{e}}^{\mathrm{k}}$, and the electric field dependence of the electric transition dipole moment $\boldsymbol{\mu}_{\mathrm{eg}}^{\mathrm{k}}$ of the kth transition. The functions $t_{\mathrm{j}}^{\mathrm{k}}(\tilde{\nu})$ and $u_{\mathrm{j}}^{\mathrm{k}}(\tilde{\nu})$ are proportional to the first und second derivatives of the bandshape function $\varepsilon_{\mathrm{j}}^{\mathrm{k}}(\tilde{\nu})$ (see Appendix). Via the second term of Eq. (19.4), the electrostriction and also the electric field dependence of conformational equilibria (for example), can be taken into account.

For solutions built up by different species, only the derivatives of $E(\tilde{\nu})$ [Eq. (19.3)] and not those of the absorption bands of the different compounds/conformers $\varepsilon_{\mathrm{j}}^{\mathrm{k}}$ are available:

$$t(\tilde{\nu}) = \frac{1}{hc} \left(\frac{E(\tilde{\nu})}{\tilde{\nu}} \right)^{-1} \frac{\partial}{\partial \tilde{\nu}} \left(\frac{E(\tilde{\nu})}{\tilde{\nu}} \right), \qquad u(\tilde{\nu}) = \frac{1}{2h^2c^2} \left(\frac{E(\tilde{\nu})}{\tilde{\nu}} \right)^{-1} \frac{\partial^2}{\partial \tilde{\nu}^2} \left(\frac{E(\tilde{\nu})}{\tilde{\nu}} \right). \tag{19.6}$$

Thus, the multilinear fit with $E(\tilde{\nu})/\tilde{\nu}\, c_0\, d$ as a weighting factor as a function of $t(\tilde{\nu})$ and $u(\tilde{\nu})$ yields

$$L(\tilde{\nu},\varphi)\frac{E(\tilde{\nu})}{\tilde{\nu}\, c_0\, d} = T_1(\tilde{\nu},\varphi)\frac{E(\tilde{\nu})}{\tilde{\nu}\, c_0\, d} + T_2(\tilde{\nu},\varphi)\frac{E(\tilde{\nu})}{\tilde{\nu}\, c_0\, d} t(\tilde{\nu}) + T_3(\tilde{\nu},\varphi)\frac{E(\tilde{\nu})}{\tilde{\nu}\, c_0\, d} u(\tilde{\nu}), \tag{19.7}$$

which leads from measurements with $\varphi = 0^\circ$ and $\varphi = 90^\circ$ to six modified electro-optical coefficients $T_{\mathrm{i}}(\tilde{\nu},\varphi), \mathrm{i} = 1, 2$, and 3 [see Appendix, Eqs. (19.A8) and (19.A9)].

For solutions of aggregates in supramolecular chemistry, or solutions with different conformers, and so on, the $T_{\mathrm{i}}(\tilde{\nu},\varphi), \mathrm{i} = 1$ to 3, are, in principle, wavelength-dependent. To increase the quantity of independent experimental information, the EOA spectrum $L(\tilde{\nu},\varphi)$ as a function of wavenumbers can be measured. But, in general, experimental information cannot be increased simply by enlarging the frequency region. The problem

is that, as with all spectroscopic methods, then the number of unknowns for the description of the molecular basis of the spectra also increases. Neither the variation of the spectra nor the accuracy of the measured spectra is sufficient to calculate all the molecular parameters that determine the spectra. Truly independent experimental data and independent quantifiable molecular information are only available in special situations. This complexity is one of the reasons why EOA spectroscopy has never been applied in analyzing complex phases with success up to now.

Until now, suitable information could only be obtained from spectral regions in which a uniformly polarized absorption band contributed to the spectrum or in cases where only a few differently polarized absorption bands determine the spectra in the spectral region under consideration. For these conditions to exist, either the coefficients $T_{\mathrm{i}}(\tilde{\nu}, \varphi), \mathrm{i} = 1$ to 3, have to be wavelength-independent, or only weakly wavelength-dependent. To find suitable spectral regions for highly polar compounds with $\mathrm{j} = 1$ and $\mathrm{k} \neq 1$, Wortmann [12] analyzed linear combinations of $L(\tilde{\nu}, \varphi)$ like

$$L_{\mathrm{p}} = 6[L(\tilde{\nu}, 0^{\circ}) - 3L(\tilde{\nu}, 90^{\circ})] \tag{19.8}$$

for parallel and

$$L_{\mathrm{s}} = 6[L(\tilde{\nu}, 90^{\circ}) - 2L(\tilde{\nu}, 0^{\circ})] \tag{19.9}$$

for perpendicular transitions in which, according to Eq. (19.5), wavelength dependence based on superposition of different transitions remains in the corresponding spectral regions. For less polar complex systems, a more sophisticated technique is needed. There are two possibilities: The spectral regions are determined either where L_{p}^{tu}, a linear combination of the type

$$\begin{aligned} L_{\mathrm{p}}^{tu} &= xL(\tilde{\nu}, 0^{\circ}) - yL(\tilde{\nu}, 90^{\circ}) \\ &\quad - (xT_2(\tilde{\nu}, 0^{\circ}) - yT_2(\tilde{\nu}, 90^{\circ}))t(\tilde{\nu}) - (xT_3(\tilde{\nu}, 0^{\circ}) - yT_3(\tilde{\nu}, 90^{\circ}))u(\tilde{\nu}), \end{aligned} \tag{19.10}$$

is independent of the wavelength or where L^{u} is a linear function of $L(\tilde{\nu}, 90^{\circ})$:

$$L^{u} = L(\tilde{\nu}, 0^{\circ}) - Uu(\tilde{\nu}) = VL(\tilde{\nu}, 90^{\circ}) + W \tag{19.11}$$

with

$$U = \frac{T_3(\tilde{\nu}, 0^{\circ})T_2(\tilde{\nu}, 90^{\circ}) - T_2(\tilde{\nu}, 0^{\circ})T_3(\tilde{\nu}, 90^{\circ})}{T_2(\tilde{\nu}, 90^{\circ})}, \tag{19.12}$$

$$V = \frac{T_2(\tilde{\nu}, 0^{\circ})}{T_2(\tilde{\nu}, 90^{\circ})}, \tag{19.13}$$

and

$$W = \frac{T_1(\tilde{\nu}, 0^{\circ})T_2(\tilde{\nu}, 90^{\circ}) - T_2(\tilde{\nu}, 0^{\circ})T_1(\tilde{\nu}, 90^{\circ})}{T_2(\tilde{\nu}, 90^{\circ})}. \tag{19.14}$$

For suitably chosen coefficients (x, y), the correction terms as a function of $t(\tilde{\nu})$ and $u(\tilde{\nu})$ can be made negligible. With $(x, y) = (6,12)$ or $(-12,-6)$ the correction term is zero for transitions polarized parallelly or perpendicularly to the static dipole moment of the

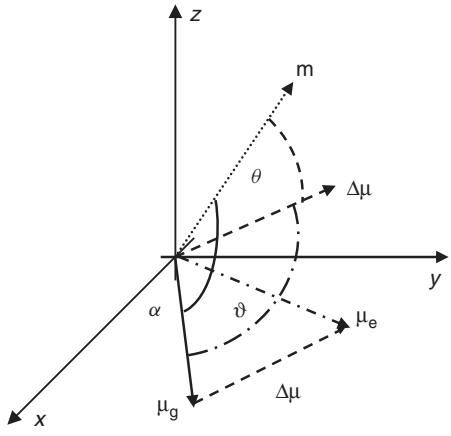

Figure 19.3. The transition dipole moment unit vector **m** (···) and the ground-state dipole moment vector $\boldsymbol{\mu}_g$ (—) enclose the angle α. θ is the angle between **m** and the vector difference $\Delta\boldsymbol{\mu} = \boldsymbol{\mu}_e - \boldsymbol{\mu}_g$ (·····), where $\boldsymbol{\mu}_e$ (-·-·-) is the dipole moment of the Franck–Condon excited state. $\boldsymbol{\mu}_g$ and $\Delta\boldsymbol{\mu}$ include the angle ϑ.

electronic ground state. For absorption bands based on a uniformly polarized transition or on superposed uniformly polarized transitions possessing absorption bands with the same spectral functions, it follows that

$$V = \frac{F + 2G}{2F - G} = \frac{1 + 2Q}{2 - Q} = \frac{Q^{-1} + 2}{2Q^{-1} - 1}. \tag{19.15}$$

Neglecting the effects of the anisotropy of polarizability (see Appendix) results in (see Figure 19.3)

$$Q = \frac{G}{F} = \frac{\cos\alpha \cos\theta}{\cos\vartheta}. \tag{19.16}$$

Again, we have to point out the conclusion that wavelength independence proves that an absorption band determined by only one uniformly polarized transition is not unequivocal. Two borderline cases should be discussed, namely whether (a) overlapping absorption bands possessing the same or approximately the same spectral functions or (b) molecules possessing spectral regions in which each exciton band can be seen separately are responsible for the wavelength independence. Examples of the first case are compounds with very small exciton splitting or simply compounds possessing different conformers with only weakly coupled chromophores.

19.3. EXPERIMENTALS

19.3.1. The Electro-Optical Absorption Spectrometer and EOA Measurements

In principle, the EOA spectrometer (Figure 19.4) is a classical spectrometer for polarized spectroscopy, with a few special features. Light is needed that is polarized parallel and perpendicular with respect to the applied electric field. In order to obtain two polarized light beams of approximately the same intensity, a depolarizer (DP) and a polarizer (PO) unit is positioned before the sample cell. The cell possesses two flat electrodes at a distance of about 3 mm. Any reflection from the surface of these electrodes must be carefully avoided. The superposition of a DC and an AC high voltage does, however,

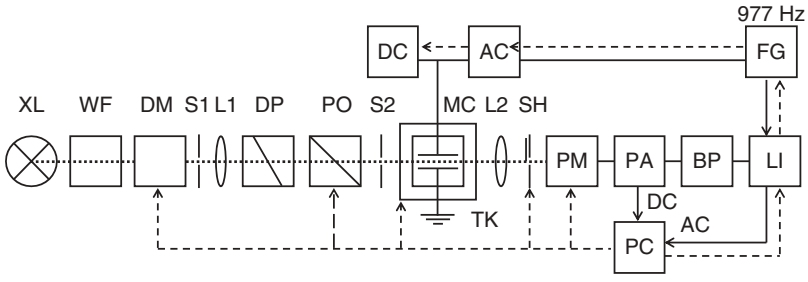

Figure 19.4. Electro-optical absorption spectrometer (data control = —; data transfer = ·····; light beam = · · ·; XL = Osram 450-W Xenon lamp; WF = water filter; DM = double monochromator; S1, S2 = slits; L1, L2 = lenses; DP = Hanle depolarizer; PO = Glan polarizer; MC = measuring cell (distance between the electrodes is about 3 mm); TK = PT100, unit for temperature control; SH = shutter; PM = photomultiplier; PA = pre-amplifier; BP = band pass; LI = lock-in amplifier; PC = measuring and control equipment; AC and DC = high-voltage supply for AC and DC voltage each up to 10 kV) [9, 11].

provide us with two phenomena: an ordering of the molecules (orientational distribution function different from 1) and modulation of the absorption signal because of the variation of the distribution function and, thus, the alteration of the ordering of the molecules with the frequency of the electric field. The application of the high DC and AC electric field creates an important difference as compared to polarized spectroscopy, where molecules are oriented in stretched sheets or in liquid crystals. Here the Stark effect influences the energy of the molecules via their dipole moments and their anisotropy of polarizability.

The absorption of the solution is modulated proportional to the square of the applied electric field **F**. The superposition of the AC and DC electric field then leads to the signal

$$\mathbf{M}(\mathbf{F}_{\mathrm{DC}} + \mathbf{F}_{\mathrm{AC}} \cos \omega t)^2 = \mathbf{M}_0 + \mathbf{M}_1 \cos \omega t + \mathbf{M}_2 \cos 2\omega t + \cdots . \tag{19.17}$$

Either the ω- or 2ω-modulated signal can be measured. In general, the ω-modulated signal is more sensitive [11, 13]. For $L(\tilde{\nu}, \varphi)$, for $\varphi = 0^\circ$ and $\varphi = 90^\circ$, together with the UV-vis spectrum and its derivations $t(\tilde{\nu})$ and $u(\tilde{\nu})$, six modified electro-optic coefficients $T_{\mathrm{i}}(\tilde{\nu}, \varphi), \mathrm{i} = 1, 2$, and 3, can be obtained in a multilinear fit as a function of $\tilde{\nu}$ according to Eq. (19.7).

19.3.2. UV-vis and EOA Spectra

Three examples have been chosen to demonstrate the applicability and the borderline cases of the EOA spectroscopy for analyzing exciton transitions in connection with the assignment for the "Exciton Chirality Method." All three chiral compounds **2**, **4** and **5** possess dipole moments of the ground state of medium or even small size. For each achiral basis chromophore [i.e., dipyrrinone (**1**) and ethyl *p*-dimethylaminobenzoate (**3**); see Chart 19.1] the EOA spectra should also be analyzed. All five compounds possess a structureless long-wavelength absorption band (Figures 19.5 to 19.8). The interaction between the two monomeric units "**1**" leads in **2** to a red shift of about 36 nm, whereas for **4** and **5** almost no shift was observed. The absorption coefficients ($\varepsilon(\tilde{\nu})$) of **2, 4** and **5** are approximately twice those of the monomers **1** and **3**, respectively (Table 19.1). Therefore,

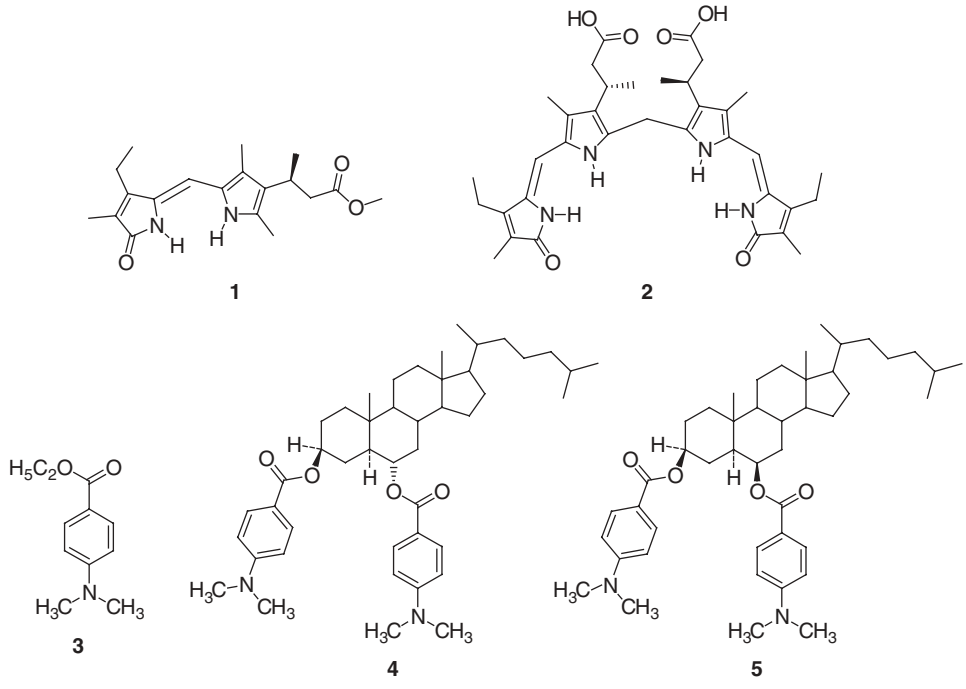

Chart 19.1. Dipyrrinone (**1**), β,β'-dimethyl-mesobilirubin-XIII*a* (**2**), ethyl *p*-dimethylaminobenzoate (**3**), 5α-cholestane-3β,6α-diol-bis(*p*-dimethylaminobenzoate) (**4**), and 5α-cholestan-3β,6β-diol-bis(*p*-dimethylaminobenzoate) (**5**).

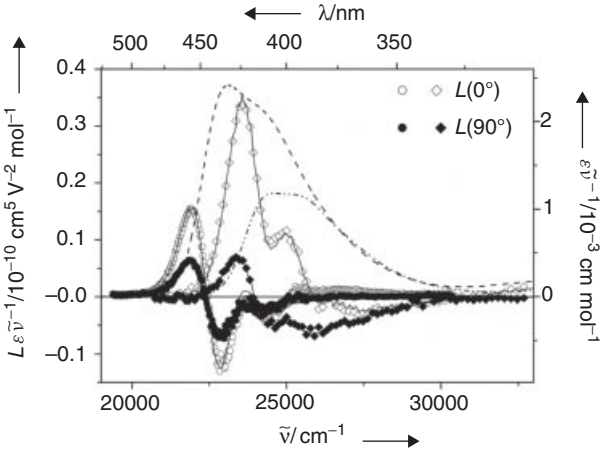

Figure 19.5. UV–vis spectra (**1**: ·····, **2**: ---), the experimental EOA spectra ($\varphi = 0°$: open symbols; $\varphi = 90°$: filled symbols), and the multilinear fit (solid line) of the EOA spectra of **1** (◊, ♦) and 2(o, •), measured in 1,4-dioxane at $T = 298$ K.

the factor $\sqrt{2}$ holds true for the transition moments, μ_{eg}. In order to attain properties of the two exciton transitions of **2**, **4**, and **5**, spectral regions have to be found in which $L(\tilde{\nu}, \varphi)$ is determined by only one or at most by two transitions. In these spectral regions, according to the standard technique introduced by Wortmann [12], the linear combination L_p for parallel- and L_s for perpendicular-polarized light must be wavelength-independent [Eqs. (19.8) and (19.9)]. An improvement of this technique is the application of Eq.

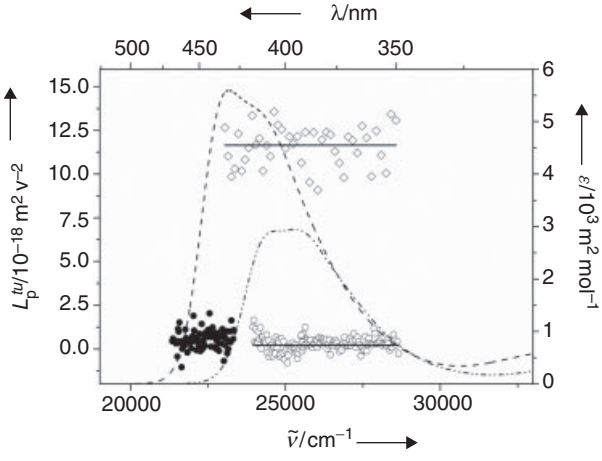

Figure 19.6. UV–vis spectra (**1**: ·····, **2**: –·–·), the linear combination L_p^{tu} according to Eq. (19.10) (♦), and *E*-6*D* (—) of **1** (◇) and **2** (long-wavelength band: o; short-wavelength band: •), measured in 1,4-dioxane at $T = 298$ K.

TABLE 19.1. Characteristic Data of the Long-Wavelength Absorption Bands in 1,4-Dioxane at $T = 298$ K

Parameter		1	2	3	4	5
λ_{eg}	(nm)	395.4	431.2	306.7	306.2	305.9
$\tilde{\nu}$	(cm^{-1})	25291	23191	32605	32658	32690
ε	(m^2mol^{-1})	2946.1	5604.5	2581.9	5769.4	5160.3
μ_{eg}	(10^{-30}Cm)	22.2	31.3	18.0	27.3	26.1

(19.10), which has been shown to be superior. Whereas for **2**, two different spectral regions exist in which L_p^{tu} is wavelength-independent but different in size, for **4** and **5**, again, L_p^{tu} is constant throughout the spectral region of their absorption (Figures 19.6 and 19.8).

According to this result, L^u for **4** and **5** is a linear function of $L(\tilde{\nu}, 90^\circ)$ through the long-wavelength absorption band (Figure 19.9). Here again, the situation is different

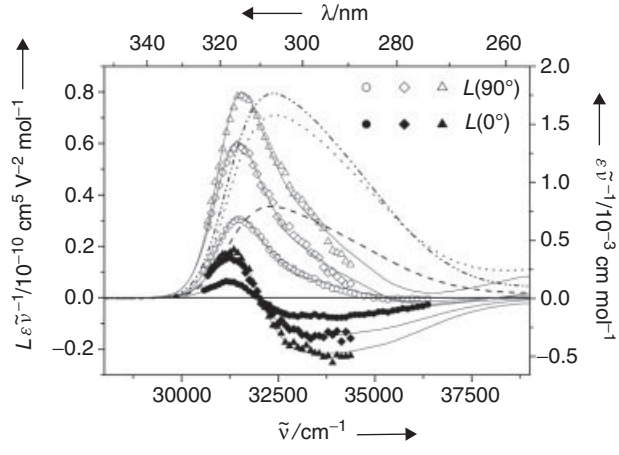

Figure 19.7. UV–vis spectra (3: –·–·, 4: ·····, 5: ·····), the experimental EOA spectra ($\varphi = 0^\circ$: open symbols; $\varphi = 90^\circ$: filled symbols) and the multilinear fit (—) of the EOA spectra of **3** (o, •), **4** (◇, ♦) and **5** (△,▲), measured in 1,4-dioxane at $T = 298$ K.

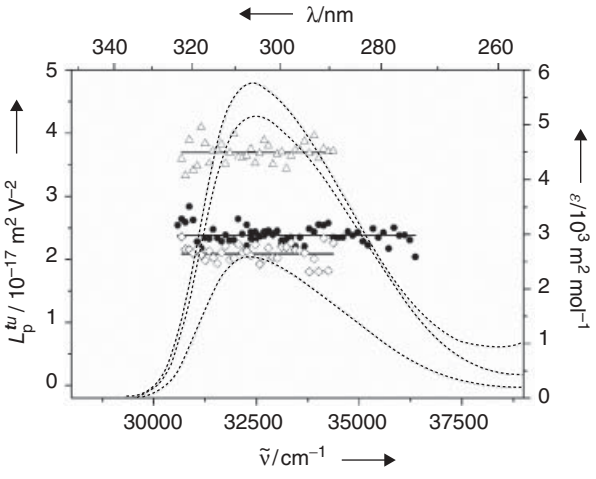

Figure 19.8. UV–vis spectra (**3**: –·–·, **4**: – – –, **5**: ·····), the linear combination L_p^{tu} according to Eq. (19.10), and *E*-6*D* (—) of **3** (•), **4** (◊) and **5** (△), measured in 1,4-dioxane at $T = 298$ K.

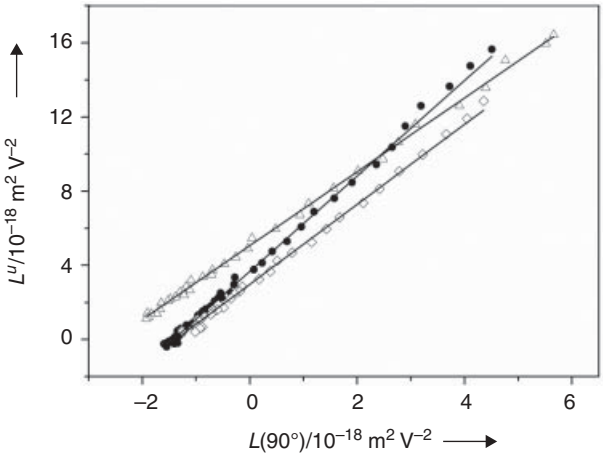

Figure 19.9. L^u as a function of $L(90^\circ)$ of **3** (•), **4** (◊) and **5** (△), measured in 1,4-dioxane at $T = 298$ K.

for **2** where in two regions linear functions $L^u(L(\tilde{\nu}, 90^\circ))$ with different slopes exist (Figure 19.10). Thus, whereas for **2**, two exciton transitions can be proven which do not have parallel polarization, for **4** and **5** an exciton splitting cannot be identified. This finding can be correlated to the fact that neither the positions nor the spectral functions of the absorption bands of the three benzoate chromophores **3**, **4**, and **5** are influenced by the intermolecular interaction between the benzoate groups (Table 19.1).

Finally, we should point out that the shoulder of the UV–vis band of **2** (Figures 19.5 and 19.6) is not based on the exciton splitting. On the one hand, this shoulder does not coincide with the spectral regions in which the functions Eqs 19.10 and 19.11 are linear and possess different slopes; on the other hand, this shoulder exists in the long-wavelength absorption band of the "monomeric" unit **1**.

19.4. QUANTITATIVE ANALYSIS

The long-wavelength absorption bands of **1** and **3** are, as discussed earlier, uniformly polarized, and the dipole moments of the ground state are large enough to demonstrate

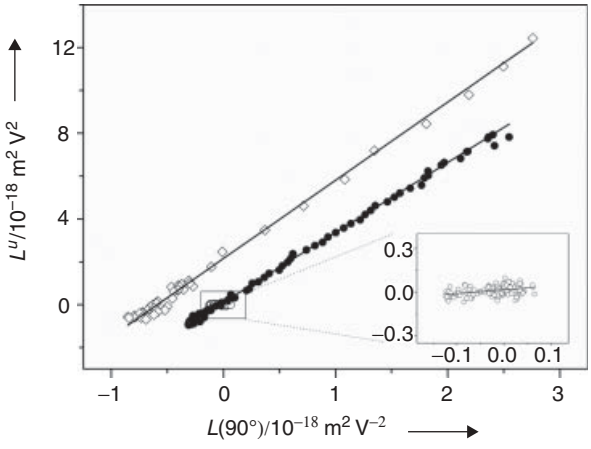

Figure 19.10. L^u as a function of $L(90^\circ)$ of **1** (◊) and **2** (long-wavelength band: o; short-wavelength band: •), measured in 1,4-dioxane at $T = 298$ K (Insert resembles an enhancement of the long-wavelength band of **2** from 416 to 348 nm).

TABLE 19.2. Dielectric Properties of **1** and **3** to **5** in 1,4-Dioxane at $T = 298$ K

Parameter		**1**	**3**	**4**	**5**
$\mu_g^{\parallel a}$	(10^{-30} Cm)	6.5±0.2	9.4±0.2	8.8±0.3	11.7±0.4
μ_g	(10^{-30} Cm)	14±2	29±3	22±2	37±4
$\Delta\mu^{\parallel a}$	(10^{-30} Cm)	22.5±0.7	23.7±0.7	22.8±0.9	24.0±1.1
V	(1)	3.60±0.04	2.63±0.02	2.19±0.02	2.00±0.01
Q	(1)	1.11±0.01	0.92±0.01	0.81±0.01	0.75±0.01
W	(10^{-20} V^{-2} m^2)	214.2±3.5	371.2±2.4	298.5±3.1	506.5±3.2
α	(°)	46	51[b]	48	51
ϑ	(°)	53	35	14	[c]
θ	(°)	16	0	0	[c]

[a]The abbreviations $\mu_g^{\parallel} = \mu_g\sqrt{\frac{(3\cos^2\alpha-1)}{2}}$ and $\Delta\mu^{\parallel} = \frac{1}{2}\Delta\mu(\cos\vartheta + \cos\alpha\cos\theta)$ present the quantities obtained directly from the electro-optical coefficients; $\Delta\mu$ itself cannot be calculated. The estimates of the angles are not sufficiently good.
[b]α is 29° by using the dipole moment $\mu_g = 37 \times 10^{-30}$ Cm ($\mu_g = 11.1D$) determined with Hedestrand's method [14] in cyclohexane (1 Debye $= 3.33562 \times 10^{-30}$ Cm).
[c]The accuracy of the experimental data is not sufficient to calculate these quantities.

the standard technique of the analysis of the EOA spectra [9–13]. From the multilinear fit of the EOA spectra, six electro-optical constants $T_i(\tilde{\nu}, \varphi)$ (i = 1,2, and 3; $\varphi = 0^\circ$ and 90°) are obtained from which dielectric properties (Table 19.2) can be calculated if polarizability effects are neglected. The angles given in Table 19.2 are rough estimates. For α of **3**, an angle between 30 and 50° should be considered realistic. The large errors of 10% to 20% in the dipole moment μ_g are a consequence of the assumptions needed for their evaluation. Thus, the difference between the solvent-corrected moments $\mu_g = 37 \times 10^{-30}$ Cm of the classical Hedestrand method [14] and $\mu_g = 29 \times 10^{-30}$ Cm of the EOA spectrum is acceptable—also because the values are measured in very different solvents, namely cyclohexane and 1,4-dioxane. The dipole moments for **4** and **5**, given in Table 19.2, are lower bounds because they are evaluated under the assumption that only one of the exciton transition contributes to $L(\tilde{\nu}, \varphi)$.

Taking both contributions of the exciton bands into account, it follows that [Eqs. (19.A8) and (19.A9)]

$$\mu_g(corrected) \simeq \mu_g \left(\frac{2(3\cos^2\alpha - 1)}{3\cos^2\alpha_1(1+\cos\rho) + 3\cos^2\alpha_2(1-\cos\rho) - 2} \right)^{\frac{1}{2}}, \quad (19.18)$$

where α_1 and α_2 are the angles between the dipole moment and the transition moments of the α and β transitions possessing the intensity ratio $\{(1+\cos\rho)/(1-\cos\rho)\}$. In Eq. (19.18), α is an average value over correction terms. Thus, it follows that $\mu_g(corrected) \geq \mu_g$ (Table 19.2) for **4** or **5**.

The EOA spectrum of **2** is smaller than that of **1** (Figure 19.5). A rough estimate yields 1×10^{-30} Cm or less for the static or induced dipole moment. According to the theory developed by Liptay et al. [9, 10], the ordering of **2** is either due to the interaction of its static dipole moment or due to the dipole moment induced by the interaction of the anisotropy of its polarizability with the external field. Because of the smallness of the EOA spectrum of **2**, data like those given in Table 19.2 for **1**, **3**, **4**, and **5** cannot be evaluated.

19.5. DISCUSSION

In addition to the determination of the transition moment directions, information about the polarity and the variation of charge distribution can be obtained from the EOA spectra. For the 4-dimethyl-aminobenzoate steroids, the shift of charge induced by the excitation is, on average, parallel to the direction of the transition moment and approximately parallel to the dipole moment change $\Delta\boldsymbol{\mu} = \boldsymbol{\mu}_e^k - \boldsymbol{\mu}_g(\theta \simeq 0)$. For the application to **3** of the exciton chirality method, it is also important to know that the dipole moment of the ground state and the transition moment enclose an angle of about 40° (Table 19.2). The exciton splitting for **4** and **5** cannot be proven by establishing the different polarization directions of the two transitions. This fact can only be understood by assuming either that the angle between the two transition moments is small or that the bandshape and the position of both exciton bands are approximately the same. The large EOA spectrum (Figure 19.7) allows the conclusion that the positive contribution of the β band dominates the spectrum. In spite of that, there is no means of deciding whether the α or β band lies on the long- or short-wavelength side of the long-wavelength band of the spectrum.

The dielectric molecular quantities such as $\boldsymbol{\mu}_g, \Delta\boldsymbol{\mu}$, and so on, for mesobilirubin **2** could not be calculated because the experimentally measured EOA spectrum was too small. Nevertheless, an assignment of the exciton transitions is possible. The electrochromism is positive for the long-wavelength transition (band I) and negative for band II, as depicted in Figure 19.11. The difference $L(\tilde{\nu}, 0^\circ) - L(\tilde{\nu}, 90^\circ)$ for the first peak of the EOA spectrum of band I is positive, whereas in the first peak of band II the difference $L(\tilde{\nu}, 0^\circ) - L(\tilde{\nu}, 90^\circ)$ is negative. Thus, the long-wavelength side of the spectrum (band I) is polarized parallel to the orientation axis x_3^* and polarized perpendicular to the C_2 axis. The orientation axis is approximately the long axis of the molecule [7, 8]. Therefore, it follows that the α transition determines the long-wavelength side of the absorption band. Band II belongs to the β transition at higher energy. This assignment confirms the results obtained for mesobilirubin **2** from polarized spectroscopy in a liquid crystal phase [15, 16].

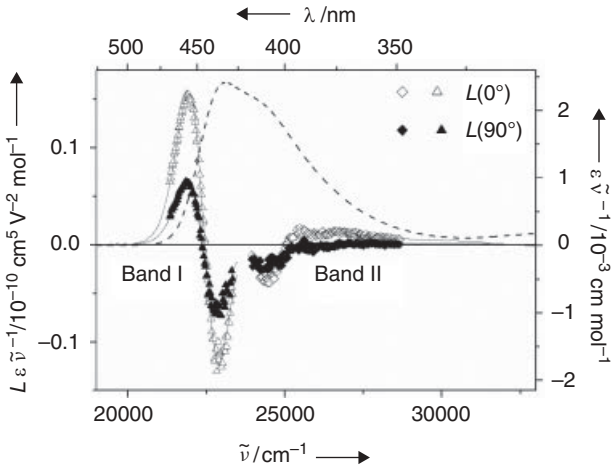

Figure 19.11. UV–vis spectra (---), the experimental EOA spectra ($\varphi = 0°$: open symbols; $\varphi = 90°$: filled symbols), and the multilinear fit (—) of the EOA spectra of **2** measured in 1,4-dioxane at $T = 298$ K and evaluated for band I (△, ▲), and II (◇, ◆), separately.

19.6. SUMMARY

EOA spectroscopy allows the determination and characterization of exciton transitions in order to confirm a symmetric or antisymmetric exciton coupling, as shown for mesobilirubin **2**. Even when the exciton splitting is not large enough to be identified by the EOA spectrum, as happens with the steroids **4** and **5**, the determination of dielectric properties such as the dipole moment of the ground state yields additional structural information. For this, the dipole moment of the monomeric form should be measured as shown in the example of *p*-dimethylaminobenzoate **3**. Important pieces of information other than those obtained by polarized spectroscopy can then be analyzed. Therefore, the additional information about dielectric properties obtained via the Stark effect is an advantage of EOA spectroscopy as compared to polarized spectroscopy. Another experimental advantage is the fact that all measurements can be done in solution—preferably in solvent 1,4-dioxane—with concentrations similar to those used in UV–vis and CD spectroscopy. That only sufficiently polar compounds can be analyzed is a disadvantage. A large anisotropy of polarizability, like in the case of the analyzed mesobilirubin **2**, allows an analysis only when the exciton splitting is sufficiently large.

ACKNOWLEDGMENTS

Thanks are owed to Professor Dr. Nina Berova, Columbia University New York, and Professor Dr. David Lightner, University of Nevada, for providing us with the steroids **4** and **5** and dipyrrinone **1** and mesobilirubin **2**, respectively. Financial support for this work by the Volkswagen Foundation within the priority program "Complex Materials: Cooperative Projects of the Natural, Engineering and Biosciences" is gratefully acknowledged.

APPENDIX

Basic equations for EOA spectroscopy (electrochromism), according to Liptay et al. [9, 10, 12], for a compound j possessing an isolated absorption band k. In this section the standard symbols for the six electro-optical constants of a molecule *D, E, F, G, H*, and

I are maintained. $E(\nu)$ is the absorbance and $\mathbf{F}$ is the electric field vector. Equations (A1) and (A2) are only correct if the absorption anisotropy is measured with the linear polarized eigenstates of light for the solution in an electric field (polarized parallel and perpendicular to the applied electric field):

$$L(\tilde{\nu},\varphi) = Dr(\varphi) + \frac{1}{6}E\ s(\varphi) + [F\ r(\varphi) + G\ s(\varphi)]t(\tilde{\nu}) + [H\ r(\varphi) + Is(\varphi)]\ u(\tilde{\nu}), \tag{A1}$$

$$r(\varphi) = \frac{1}{5}(2 - \cos^2\varphi), \qquad s(\varphi) = \frac{1}{5}(3\cos^2\varphi - 1), \tag{A2}$$

$$t(\tilde{\nu}) = \frac{1}{hc}\left(\frac{\varepsilon}{\tilde{\nu}}\right)^{-1}\frac{\partial}{\partial\tilde{\nu}}\left(\frac{\varepsilon}{\tilde{\nu}}\right), \tag{A3}$$

$$u(\tilde{\nu}) = \frac{1}{2h^2c^2}\left(\frac{\varepsilon}{\tilde{\nu}}\right)^{-1}\frac{\partial^2}{\partial\tilde{\nu}^2}\left(\frac{\varepsilon}{\tilde{\nu}}\right),$$

$$u(\tilde{\nu}) = \frac{1}{2h^2c^2}\left[\left(\frac{\partial}{\partial\tilde{\nu}}\ln\left(\frac{\varepsilon}{\tilde{\nu}}\right)\right)^2 + \frac{\partial^2}{\partial\tilde{\nu}^2}\ln\left(\frac{\varepsilon}{\tilde{\nu}}\right)\right], \tag{A4}$$

$$L(\tilde{\nu},0^\circ) = \frac{1}{5}\left\{D + \frac{1}{3}E + [F + 2G]t(\tilde{\nu}) + [H + 2I]u(\tilde{\nu})\right\}, \tag{A5}$$

$$L(\tilde{\nu},90^\circ) = \frac{1}{5}\left\{2D - \frac{1}{6}E + [2F - G]t(\tilde{\nu}) + [2H - I]u(\tilde{\nu})\right\}. \tag{A6}$$

The electro-optical coefficients according to Liptay et al. [9–12] for a solution of a compound j and an isolated absorption band k are (the tilde indicates a transposed vector (bold symbol) or tensor (underlined bold symbol))

$$E = \left(\frac{f}{k_BT}\right)^2[3(\tilde{\mathbf{m}}\boldsymbol{\mu}_g)^2 - \tilde{\boldsymbol{\mu}}_g\boldsymbol{\mu}_g] + \left(\frac{f^2}{k_BT}\right)[3(\tilde{\mathbf{m}}\underline{\boldsymbol{\alpha}}\mathbf{m}) - \mathrm{Tr}(\underline{\boldsymbol{\alpha}})] + \left(\frac{3f^2}{k_BT}\right)[\tilde{\mathbf{R}}^{(2)}\boldsymbol{\mu}_g], \tag{A7a}$$

$$D = \frac{f^2}{k_BT}\tilde{\mathbf{R}}^{(1)}\boldsymbol{\mu}_g, \tag{A7b}$$

$$G = \left(\frac{f^2}{k_BT}\right)[(\tilde{\mathbf{m}}\boldsymbol{\mu}_g)(\tilde{\mathbf{m}}\Delta\boldsymbol{\mu})] + \frac{1}{2}f^2\tilde{\mathbf{m}}\Delta\underline{\boldsymbol{\alpha}}\mathbf{m} + \frac{1}{2}f^2\tilde{\mathbf{R}}^{(2)}\Delta\boldsymbol{\mu}, \tag{A7c}$$

$$F = \left(\frac{f^2}{k_BT}\right)\tilde{\boldsymbol{\mu}}_g\Delta\boldsymbol{\mu} + \frac{1}{2}f^2\mathrm{Tr}(\underline{\boldsymbol{\alpha}}) + f^2\tilde{\mathbf{R}}^{(1)}\Delta\boldsymbol{\mu}, \tag{A7d}$$

$$\Delta\boldsymbol{\mu} = \boldsymbol{\mu}_e - \boldsymbol{\mu}_g,$$

$$I = f^2(\tilde{\mathbf{m}}\Delta\boldsymbol{\mu})^2, \tag{A7e}$$

$$H = f^2\Delta\tilde{\boldsymbol{\mu}}\Delta\boldsymbol{\mu}, \tag{A7f}$$

$$\mathbf{R}^{(1)} = 2|\boldsymbol{\mu}_{eg}|^{-2}\underline{\boldsymbol{\alpha}}_{eg}\boldsymbol{\mu}_{eg}, \qquad \mathbf{R}^{(2)} = 2|\boldsymbol{\mu}_{eg}|^{-2}[\underline{\boldsymbol{\alpha}}_{eg}\boldsymbol{\mu}_{eg} + \mathrm{Tr}(\underline{\boldsymbol{\alpha}}_{eg})\boldsymbol{\mu}_{eg}], \tag{A7g}$$

$$2\mathbf{R}^{(1)} \simeq \mathbf{R}^{(2)}.$$

The electro-optical coefficients for a solution with j compounds and k supposed absorption bands are

$$T_1(\tilde{\nu},0^\circ) = \sum_{\mathrm{j}}\sum_{\mathrm{k}} \left\{ \frac{1}{5}\left(D_{\mathrm{j}}^{\mathrm{k}} + \frac{1}{3}E_{\mathrm{j}}^{\mathrm{k}}\right) \frac{\varepsilon_{\mathrm{j}}^{\mathrm{k}}(\tilde{\nu}) c_{\mathrm{j}} d}{E(\tilde{\nu})} \right\}, \tag{A8a}$$

$$T_2(\tilde{\nu},0^\circ) = \sum_{\mathrm{j}}\sum_{\mathrm{k}} \left\{ \frac{1}{5}(F_{\mathrm{j}}^{\mathrm{k}} + 2G_{\mathrm{j}}^{\mathrm{k}}) \frac{\varepsilon_{\mathrm{j}}^{\mathrm{k}}(\tilde{\nu}) c_{\mathrm{j}} d}{E(\tilde{\nu})} \frac{t_{\mathrm{j}}^{\mathrm{k}}(\tilde{\nu})}{t(\tilde{\nu})} \right\}, \tag{A8b}$$

$$T_3(\tilde{\nu},0^\circ) = \sum_{\mathrm{j}}\sum_{\mathrm{k}} \left\{ \frac{1}{5}(H_{\mathrm{j}}^{\mathrm{k}} + 2I_{\mathrm{j}}^{\mathrm{k}}) \frac{\varepsilon_{\mathrm{j}}^{\mathrm{k}}(\tilde{\nu}) c_{\mathrm{j}} d}{E(\tilde{\nu})} \frac{u_{\mathrm{j}}^{\mathrm{k}}(\tilde{\nu})}{u(\tilde{\nu})} \right\}, \tag{A8c}$$

and

$$T_1(\tilde{\nu},90^\circ) = \sum_{\mathrm{j}}\sum_{\mathrm{k}} \left\{ \frac{1}{5}\left(2D_{\mathrm{j}}^{\mathrm{k}} - \frac{1}{6}E_{\mathrm{j}}^{\mathrm{k}}\right) \frac{\varepsilon_{\mathrm{j}}^{\mathrm{k}}(\tilde{\nu}) c_{\mathrm{j}} d}{E(\tilde{\nu})} \right\}, \tag{A9a}$$

$$T_2(\tilde{\nu},90^\circ) = \sum_{\mathrm{j}}\sum_{\mathrm{k}} \left\{ \frac{1}{5}(2F_{\mathrm{j}}^{\mathrm{k}} - G_{\mathrm{j}}^{\mathrm{k}}) \frac{\varepsilon_{\mathrm{j}}^{\mathrm{k}}(\tilde{\nu}) c_{\mathrm{j}} d}{E(\tilde{\nu})} \frac{t_{\mathrm{j}}^{\mathrm{k}}(\tilde{\nu})}{t(\tilde{\nu})} \right\}, \tag{A9b}$$

$$T_3(\tilde{\nu},90^\circ) = \sum_{\mathrm{j}}\sum_{\mathrm{k}} \left\{ \frac{1}{5}(2H_{\mathrm{j}}^{\mathrm{k}} - I_{\mathrm{j}}^{\mathrm{k}}) \frac{\varepsilon_{\mathrm{j}}^{\mathrm{k}}(\tilde{\nu}) c_{\mathrm{j}} d}{E(\tilde{\nu})} \frac{u_{\mathrm{j}}^{\mathrm{k}}(\tilde{\nu})}{u(\tilde{\nu})} \right\}. \tag{A9c}$$

T is the temperature in K, k_{B} is Boltzmann's constant, $\underline{\boldsymbol{\alpha}}$ is the static polarizability tensor, and $\underline{\boldsymbol{\alpha}}_{\mathrm{eg}}$ the transition polarizability tensors of second rank. Higher order contributions of the direct field dependence of the electric transition dipole moments and the electric field fluctuation in solution are neglected here. The factor f stands for the solvent correction within the Onsager continuum theory. In most cases for nonpolar or only weakly polar solvents—for example, for 1,4-dioxane—the following approximations

$$f = \frac{\varepsilon(2\varepsilon_{\mathrm{m}} + 1)(n^2 + 2)}{(2\varepsilon_{\mathrm{m}} + n^2)(2\varepsilon + 1)} \tag{A10}$$

can be taken. ε_{m} and ε are the microscopic and the relative permittivity, respectively.

REFERENCES

1. N. Harada, K. Nakanishi, *Circular Dichroic Spectroscopy—Exciton Coupling in Organic Stereochemistry*, University Science Books, Mill Valley, **1983**; N. Berova, K. Nakanishi, R. W. Woody, eds., *Circular Dichroism, Principles and Applications*, WILEY-VCH, John Wiley & Sons, New York, **2000**; D. A. Lightner, J. E. Gurst, *Organic Conformational Analysis and Stereochemistry from Circular Dichroism Spectroscopy*, Wiley-VCH, John Wiley & Sons, New York, **2000**.
2. H.-G. Kuball, Chiroptical analysis, in *Encyclopedia of Analytical Science*, Vol. 1, 2nd edi., Paul J. Worsfeld, Alan Townshend, and Colin F. Poole, eds., Elsevier, Amsterdam, **2004**, pp. 60–119.
3. S. F. Mason, R. H. Seal, R. D. Roberts, *Tetrahedron* **1974**, *30*, 1671–1682.

4. N. Harada, K. Nakanishi, *J. Am. Chem. Soc*. **1969**, *91*, 3989–3991.
5. J. Michl, E. W. Thulstrup, Spectroscopy with Polarized Light—Solute Alignment by photoselection, in *Liquid Crystal, Polymers, and Membranes*, VCH Publishers, New York, **1986**.
6. A. Rodger, B. Nordén, *Circular Dichroism and Linear Dichroism*, Oxford University Press, Oxford, **1997**.
7. H.-G. Kuball, E. Dorr, T. Höfer; O. Türk, *Monatsh. Chem*. **2005**, *136*, 289–324.
8. H.-G. Kuball, H. Friesenhan, A. Schönhofer, Optical activity of oriented molecules, in *Polarized Spectroscopy of Ordered Systems, NATO ASI Series, Series C: Mathematical and Physical Sciences*, Vol. 242, B. Samori and E. W. Thulstrup, eds., Kluwer Academic Publishers, Dordrecht, **1988**, pp. 391–420.
9. W. Liptay, *Angew. Chem*. **1969**, *81*, 195–232.
10. W. Liptay, D. Wehning, J. Becker, T. Rehm, *Z. Naturforsch*. **1982**, *37A*, 1369–1395; W. Liptay, J. Becker, D. Wehning, W. Lang, O. Burkhard, *Z. Naturforsch*. **1982**, *37A*, 1396–1408; W. Liptay, J. Becker, *Z. Naturforsch*. **1982**, *37A*, 1409–1415; W. Liptay, D. Wehning, J. Becker, T. Rehm, *Z. Naturforsch*. **1982**, *37A*, 1416–1426; W. Liptay, T. Rehm, D. Wehning, L. Schanne, W. Baumann, W. Lang, *Z. Naturforsch*. **1982**, *37A*, 1427–1448.
11. W. Baumann, Determination of dipole moments in ground and excited States, in *Physical Methods of Chemistry*, Vol. 3B, B. W. Rossiter and J. F. Hamilton, eds., John Wiley & Sons, New York, **1989**, pp. 45–131.
12. R. Wortmann, *Habilitationsschrift*, Universität Mainz, **1993**.
13. M. Stolte, *Dissertation*, Universität Kaiserslautern, **2008**.
14. P. C. M. Weisenborn, A. H. Huizer, C. A. G. O. Varma, *J. Chem. Soc. Faraday Trans*. **1989**, *85*(12), 1895–1912.
15. C. L. Killet, *Dissertation*, Universität Kaiserslautern, **1995**.
16. D. Bauman, C. Killet, S. E. Boiadjiev, D. A. Lightner, A. Schönhofer, H.-G. Kuball, *J. Phys. Chem*. **1996**, *100*, 11546–11558.

PART III

THEORETICAL SIMULATIONS

20

INDEPENDENT SYSTEMS THEORY FOR PREDICTING ELECTRONIC CIRCULAR DICHROISM

Gerhard Raabe, Joerg Fleischhauer, and Robert W. Woody

20.1. INTRODUCTION

The use of *ab initio* methods to predict the electronic circular dichroism of molecules has made great advances in recent years, as described in Chapters 21–23 of this volume. However, such high-level methods are limited to relatively small molecules, and biological macromolecules are beyond their reach. For such systems, an approach that focuses upon the individual chromophores and their interactions is the method of choice. The *independent systems theory* was introduced by Kirkwood [1] and was elaborated by Tinoco [2] and by Schellman and co-workers [3]. As described in the next section, the macromolecule is divided into groups that are independent in the sense that they are assumed to not exchange electrons, but they are coupled through Coulombic interactions. A classical version of this approach was developed by DeVoe [4, 5], framed in terms of polarizabilities and linear oscillators. This model has been developed further by Applequist [6], providing the *atom dipole interaction* model. These methods have been reviewed previously [7–11]. Although the independent systems theory is most commonly applied to macromolecules, it also has been used for small molecules (reviewed by Sandstrom [12]), for which its lower accuracy vis-á-vis *ab initio* methods may be offset by greater transparency of interpretation.

Our aim is to calculate the rotational strength for the electronic transition of a macromolecule (polypeptide, protein, or nucleic acid) from the ground state 0 to the excited state A:

$$R_{0A} = \mathrm{Im}\langle 0|\hat{\boldsymbol{\mu}}|A\rangle \bullet \langle A|\hat{\mathbf{m}}|0\rangle. \tag{20.1}$$

Comprehensive Chiroptical Spectroscopy, Volume 1: Instrumentation, Methodologies, and Theoretical Simulations, First Edition. Edited by N. Berova, P. L. Polavarapu, K. Nakanishi, and R. W. Woody.
© 2012 John Wiley & Sons, Inc. Published 2012 by John Wiley & Sons, Inc.

In this expression, which is also called the *dipole length formula*, $\hat{\boldsymbol{\mu}}$ is the electric dipole moment operator,

$$\hat{\boldsymbol{\mu}} = -e \sum_{i=1}^{n_{\mathrm{el}}} \hat{\mathbf{r}}_i, \tag{20.2}$$

and $\hat{\mathbf{m}}$ is the magnetic dipole moment operator,

$$\hat{\mathbf{m}} = -\frac{e}{2mc} \sum_{i=1}^{n_{\mathrm{el}}} (\hat{\mathbf{r}}_i \times \hat{\mathbf{p}}_i) = \gamma \sum_{i=1}^{n_{\mathrm{el}}} (\hat{\mathbf{r}}_i \times \hat{\mathbf{p}}_i). \tag{20.3}$$

$\hat{\mathbf{r}}_i$ and $\hat{\mathbf{p}}_i = \frac{h}{2\pi i} \hat{\nabla}_i$ are the position and the linear momentum operator of electron i, respectively. m and $-e$ are the mass and the charge of an electron, and c is the velocity of light *in vacuo*.

To our knowledge, the most appropriate quantum mechanical methods to get at least qualitatively the electric and magnetic transition moments of these macromolecules is the theory of Tinoco [2] and the so-called matrix method [3, 13], which is based on Tinoco's method.

20.2. THE TINOCO THEORY

Within the framework of Tinoco's theory [2] and also in the matrix method [3, 13], the molecule is divided into n groups for which the Schrödinger equation can be solved, at least approximately. The groups, or chromophores, are usually π-electron systems that are bonded to α carbons in a polypeptide chain or to glycosidic carbons in a polynucleotide chain. Conceptually, these bonds can be broken, and the bonds to carbon or nitrogen can be replaced by bonds to hydrogen atoms. For polynucleotides, the chromophores are separated by many single bonds, so there is no problem with overlapping of the charge densities of the chromophores. For polypeptides, if one breaks all bonds of the CONH group to the α carbons, the model chromophore is formamide, which is not a good model for the peptide group. Alternatively, one could leave the bond between the CONH group and one C_α intact, converting that C_α to a methyl group. If the C_α–C' bond is retained, the model chromophore is acetamide, whereas retention of the C_α–N bond gives *N*-methylformamide as the model. These are both better models for the peptide than formamide, but the best and most widely used model is *N*-methyl acetamide. This involves converting both the C_α atoms flanking the CONH to methyl groups, leading to overlap of the chromophores at each C_α. In practice, the potential difficulty posed by this overlap is avoided because the transition densities for the transitions of interest and the monopoles (*vide infra*) that describe them are centered on the CONH atoms.

The Hamiltonian for the total system consisting of these n groups is

$$\hat{\boldsymbol{H}} = \sum_{i=1}^{n} \hat{\boldsymbol{H}}_{0i} + \sum_{i=1}^{n-1} \sum_{j>i}^{n} \hat{\boldsymbol{V}}_{ij}, \tag{20.4}$$

where $\hat{\boldsymbol{V}}_{ij}$ is the classical electric potential energy of the charges belonging to groups i and j. For the ground state of group i we have the Schrödinger equation,

$$\hat{\boldsymbol{H}}_{0i} \varphi_{i0} = E_{i0} \varphi_{i0}, \tag{20.5}$$

while we have the following for an excited state a of the same group:

$$\hat{\boldsymbol{H}}_{0i}\varphi_{i\mathrm{a}} = E_{i\mathrm{a}}\varphi_{i\mathrm{a}}. \tag{20.6}$$

To solve the equation

$$\hat{\boldsymbol{H}}\,\Psi_K = E_K\,\Psi_K, \tag{20.7}$$

Tinoco applied perturbation theory up to the first order. Besides the unperturbed ground-state function

$$\psi_0 = \prod_{k=1}^{n}\varphi_{k0}, \tag{20.8}$$

he used functions for singly excited states[1]

$$\psi_{ia} = \varphi_{ia}\prod_{k\neq i}^{n}\varphi_{k0} \tag{20.9}$$

and doubly excited states

$$\psi_{ia,jb} = \varphi_{ia}\varphi_{jb}\prod_{k\neq i,j}^{n}\varphi_{k0}, \tag{20.10}$$

which are eigenfunctions of the unperturbed Hamiltonian $\hat{\boldsymbol{H}}_0 = \sum_{i=1}^{n}\hat{\boldsymbol{H}}_{0i}$.

One obtains the following for the first-order perturbed ground state:

$$\Psi_0^1 = \psi_0 - \sum_{i=1}^{n}\sum_{a}\frac{V_{ia,0}}{h\nu_a}\psi_{ia} - \sum_{i=1}^{n-1}\sum_{a}\sum_{j>i}^{n}\sum_{b}\frac{V_{ia,jb;0}}{h(\nu_a+\nu_b)}\psi_{ia,jb}. \tag{20.11}$$

If N groups are identical—and this is normally the case for macromolecules—one has N-fold degeneracy and, therefore, the correct zeroth-order perturbed excited-state wavefunctions have to be determined first:

$$\Psi_{\mathrm{AK}}^0 = \sum_{i=1}^{N} C_{ia\mathrm{K}}\psi_{ia}. \tag{20.12}$$

To get these functions one has to form the $N\times N$ Hamiltonian matrix between the N functions $\psi_{ia}(i=1,\ldots,N)$ and to diagonalize it. With the N eigenfunctions $(\Psi_{\mathrm{AK}}^0, K = 1,\ldots,N)$ thus obtained, the function ψ_0, and the other singly excited functions ψ_{jb} $(b\neq a)$, one finally obtains the following for the first-order perturbed excited state:

$$\begin{aligned}
\Psi_{AK}^1 &= \Psi_{AK}^0 + \frac{\int(\psi_0)^*\hat{\boldsymbol{V}}\,\Psi_{\mathrm{AK}}^0\,d\tau}{h\nu_a}\psi_0 + \sum_{j=1}^{n}\sum_{b\neq a}\frac{\int(\psi_{jb})^*\hat{\boldsymbol{V}}\,\Psi_{AK}^0\,d\tau}{h(\nu_a-\nu_b)}\psi_{jb}\\
&= \sum_{i=1}^{N}\mathrm{C}_{iaK}\left\{\psi_{ia} + \frac{\int(\psi_0)^*\hat{\boldsymbol{V}}\,\psi_{ia}\,d\tau}{h\nu_a}\psi_0 + \sum_{j=1}^{n}\sum_{b\neq a}\frac{\int(\psi_{jb})^*\hat{\boldsymbol{V}}\,\psi_{ia}\,d\tau}{h(\nu_a-\nu_b)}\psi_{jb}\right\}\\
&= \sum_{i=1}^{N}\mathrm{C}_{iaK}\left\{\psi_{ia} + \sum_{j\neq i}^{n}\frac{V_{i0a,j00}}{h\nu_a}\psi_0 + \sum_{j\neq i}^{n}\sum_{b\neq a}\frac{V_{j0b,i0a}}{h(\nu_a-\nu_b)}\psi_{jb}\right.\\
&\quad\left. + \sum_{j\neq i}^{n}\sum_{b\neq a}\frac{V_{iab,j00}}{h(\nu_a-\nu_b)}\psi_{ib}\right\}.
\end{aligned} \tag{20.13}$$

[1] To calculate the excited states, Tinoco only considered singly excited states of the chromophores.

The denominators in the above equations are, according to perturbation theory, the differences of the zeroth-order energies of the interacting states. The meaning of the matrix elements of the perturbation operator, for example $V_{i0a,j0b}$, can be found in Appendix A. With these functions we can now calculate the electric dipole transition moment:

$$\boldsymbol{\mu}_{0\mathrm{AK}} = \int (\Psi_0^1)^* \hat{\boldsymbol{\mu}} \Psi_{AK}^1 \, d\tau. \tag{20.14a}$$

Taking into account that $\boldsymbol{\mu}_{iab} = \boldsymbol{\mu}_{iba}$ for real functions, we get

$$\begin{aligned}\boldsymbol{\mu}_{0\mathrm{AK}} &= \sum_{i=1}^{N} \mathrm{C}_{ia\mathrm{K}} \left\{ \begin{array}{l} \boldsymbol{\mu}_{i0a} + \dfrac{\boldsymbol{\mu}_{i00} - \boldsymbol{\mu}_{iaa}}{h\nu_a} V_{ia,0} - \displaystyle\sum_{j\neq i}^{n} \sum_{b\neq a} \frac{V_{i0a,j0b}}{h(\nu_b^2 - \nu_a^2)} 2\nu_b \boldsymbol{\mu}_{j0b} \\ \\ - \displaystyle\sum_{b\neq a} \frac{V_{iab,0}}{h(\nu_b - \nu_a)} \boldsymbol{\mu}_{i0b} - \sum_{b\neq a} \frac{V_{i0b,0}}{h\nu_b} \boldsymbol{\mu}_{iba} - \sum_{j\neq i}^{N} \frac{V_{i0a,j0a}}{2h\nu_a} \boldsymbol{\mu}_{ja0} \end{array} \right\} \\ &\equiv \sum_{i=1}^{N} \mathrm{C}_{ia\mathrm{K}} (\boldsymbol{\mu}_{ia}) \end{aligned} \tag{20.14b}$$

for an excitation of the molecule from the ground state Ψ_0^1 to the excited state Ψ_{AK}^1. With $\mathbf{m}_{iab} = -\mathbf{m}_{iba}$ for real functions, we get for the magnetic dipole transition moment

$$\mathbf{m}_{\mathrm{AK0}} = \int (\Psi_{\mathrm{AK}}^1)^* \hat{\boldsymbol{m}} \Psi_0^1 \, d\tau, \tag{20.15a}$$

$$\begin{aligned}\mathbf{m}_{\mathrm{AK0}} &= \sum_{i=1}^{N} \mathrm{C}_{ia\mathrm{K}}^* \left\{ \begin{array}{l} \left[\mathbf{m}_{ia0} + \dfrac{i\pi}{c} \mathbf{R}_i \times \boldsymbol{\mu}_{i0a} \nu_a \right] \\ \\ - \displaystyle\sum_{j\neq i}^{n} \sum_{b\neq a} \frac{V_{i0a,j0b} 2\nu_a}{h(\nu_b^2 - \nu_a^2)} \left[\mathbf{m}_{jb0} + \frac{i\pi}{c} \mathbf{R}_j \times \boldsymbol{\mu}_{j0b} \nu_b \right] \\ \\ - \displaystyle\sum_{b\neq a} \frac{V_{iab,0}}{h(\nu_b - \nu_a)} \left[\mathbf{m}_{ib0} + \frac{i\pi}{c} \mathbf{R}_i \times \boldsymbol{\mu}_{i0b} \nu_b \right] \\ \\ - \displaystyle\sum_{b\neq a} \frac{V_{i0b,0}}{h\nu_b} \left[\mathbf{m}_{iab} - \frac{i\pi}{c} \mathbf{R}_i \times \boldsymbol{\mu}_{iba} (\nu_b - \nu_a) \right] \\ \\ - \displaystyle\sum_{j\neq i}^{N} \frac{V_{i0a,j0a}}{2h\nu_a} \left[\mathbf{m}_{j0a} - \frac{i\pi}{c} \mathbf{R}_j \times \boldsymbol{\mu}_{ja0} \nu_a \right] \end{array} \right\} \\ &\equiv \sum_{i=1}^{N} \mathrm{C}_{ia\mathrm{K}}^* [\mathbf{m}_{ia}]. \end{aligned} \tag{20.15b}$$

Employing Eq. (20.1), we then obtain the following for the rotational strength in the *dipole length form*:

$$\begin{aligned} R_{0A} &= \sum_{K=1}^{N} R_{0AK} = \mathrm{Im} \sum_{K=1}^{N} \boldsymbol{\mu}_{0aK} \bullet \mathbf{m}_{aK0} = \sum_{K=1}^{N} \sum_{i=1}^{N} C_{iaK}(\boldsymbol{\mu}_{ia}) \bullet \sum_{l=1}^{N} C^{*}_{laK}[\mathbf{m}_{la}] \\ &= \sum_{i=1}^{N} \sum_{l=1}^{N} \delta_{il}(\boldsymbol{\mu}_{ia}) \bullet [\mathbf{m}_{la}] \\ &= \sum_{i=1}^{N} (\boldsymbol{\mu}_{ia}) \bullet [\mathbf{m}_{ia}] \end{aligned} \tag{20.16a}$$

or, in more detail:

$$R_{0A} = \mathrm{Im} \sum_{i=1}^{N} \left\{ \begin{aligned} &\boldsymbol{\mu}_{i0a} \bullet \mathbf{m}_{ia0} && (20.16b_1) \\ &- 2 \sum_{j \neq i}^{n} \sum_{b \neq a} \frac{V_{i0a,j0b}}{h(\nu_b^2 - \nu_a^2)} (\boldsymbol{\mu}_{ia0} \bullet \mathbf{m}_{jb0} \nu_a + \boldsymbol{\mu}_{jb0} \bullet \mathbf{m}_{ia0} \nu_b) && (20.16b_2) \\ &- \sum_{b \neq a} \frac{V_{iab,0}}{h(\nu_b - \nu_a)} (\boldsymbol{\mu}_{i0a} \bullet \mathbf{m}_{ib0} + \boldsymbol{\mu}_{i0b} \bullet \mathbf{m}_{ia0}) && (20.16b_3) \\ &- \sum_{b \neq a} \frac{V_{i0b,0}}{h \nu_b} (\boldsymbol{\mu}_{i0a} \bullet \mathbf{m}_{iab} + \boldsymbol{\mu}_{iba} \bullet \mathbf{m}_{ia0}) && (20.16b_4) \\ &- \sum_{j \neq i}^{N} \frac{V_{i0a,j0a}}{2h \nu_a} (\boldsymbol{\mu}_{i0a} \bullet \mathbf{m}_{j0a} + \boldsymbol{\mu}_{ja0} \bullet \mathbf{m}_{ia0}) && (20.16b_5) \\ &+ \frac{\sum_{j \neq i}^{N} V_{i0a,j00}}{h \nu_a} (\boldsymbol{\mu}_{i00} - \boldsymbol{\mu}_{iaa}) \cdot \mathbf{m}_{ia0} && (20.16b_6) \\ &- \frac{2i\pi}{c} \sum_{j \neq i}^{n} \sum_{b \neq a} \frac{V_{i0a,j0b}}{h(\nu_b^2 - \nu_a^2)} \nu_a \nu_b (\mathbf{R}_j - \mathbf{R}_\mathbf{i}) \bullet \boldsymbol{\mu}_{j0b} \times \boldsymbol{\mu}_{i0a} && (20.16b_7) \\ &+ \frac{i\pi \sum_{j \neq i}^{N} V_{i0a,j00}}{ch} (\boldsymbol{\mu}_{i00} - \boldsymbol{\mu}_{iaa}) \cdot \mathbf{R}_i \times \boldsymbol{\mu}_{i0a} && (20.16b_8) \\ &+ \frac{i\pi}{c} \sum_{b \neq a} \frac{V_{iab,0}}{h} \mathbf{R}_i \bullet \boldsymbol{\mu}_{i0a} \times \boldsymbol{\mu}_{i0b} && (20.16b_9) \\ &+ \frac{i\pi}{c} \sum_{b \neq a} \frac{V_{i0b,0}}{h} \mathbf{R}_i \bullet \boldsymbol{\mu}_{iba} \times \boldsymbol{\mu}_{i0a} && (20.16b_{10}) \\ &- \frac{i\pi}{c} \sum_{j \neq i}^{N} \frac{V_{i0a,j0a}}{2h} (\mathbf{R}_j + \mathbf{R}_i) \bullet \boldsymbol{\mu}_{i0a} \times \boldsymbol{\mu}_{ja0} && (20.16b_{11}) \end{aligned} \right\}$$

The contributions ($20.16b_1$) to ($20.16b_{11}$) obtained here are identical with those of Eqs. 20.44a–20.44i of Sears and Beychok [8], only the analogues of ($20.16b_{11}$) and ($20.16b_5$) are missing in their paper since they did not take degeneracy into account. Our results are also identical with those of Tinoco [2], except that all the origin-dependent terms [($20.16b_8$) to ($20.16b_{11}$)] and also $16b_5$, which stems from degeneracy, are missing in Tinoco's Eq. (IIIb-22). Terms ($20.16b_6$) and ($20.16b_8$), sometimes called charge-transfer terms, were erroneously omitted in two previous reviews [9, 10] through a spurious analogy with the dipole-velocity approximation (*vide infra*).

Another expression for the rotational strength, the so-called *dipole velocity form*, can be obtained by replacing the electric dipole transition moment in (20.1) by its relation to the so-called *nabla* integral [14] $\langle 0|\hat{\boldsymbol{\nabla}}|A\rangle$:

$$\langle 0|\hat{\boldsymbol{\mu}}|A\rangle = \frac{eh^2}{4\pi^2 m[E_{\mathrm{A}} - E_0]}\langle 0|\hat{\boldsymbol{\nabla}}|A\rangle, \tag{20.17}$$

which is valid only for exact wavefunctions. The resulting expression for the rotational strength

$$R_{0A} = \frac{eh^2}{4\pi^2 m}\mathrm{Im}\frac{\langle 0|\hat{\boldsymbol{\nabla}}|A\rangle\bullet\langle A|\hat{\mathbf{m}}|0\rangle}{E_A - E_0} \tag{20.18}$$

is origin-independent also for approximate wavefunctions, whereas (20.1), which is called the dipole length formula, is not origin-independent for approximate wave functions. For exact wave functions and energies, both expressions give the same result. For the rotational strengths in the *dipole velocity form*, one obtains the following from (20.18) by introducing the functions Ψ_0^1 and Ψ_{AK}^1:

$$R_{0A} = -\frac{e^2\hbar^2}{4\pi m^2 c\nu_a}\sum_{i=1}^{N}\left\{\begin{array}{l}
\boldsymbol{\nabla}_{i0\mathrm{a}}\bullet(\mathbf{r}\times\boldsymbol{\nabla})_{ia0} \\
-2\sum_{j\neq i}^{n}\sum_{b\neq a}\frac{V_{i0a,j0b}}{h(\nu_b^2-\nu_a^2)}\nu_a(\boldsymbol{\nabla}_{i0a}\bullet(\mathbf{r}\times\boldsymbol{\nabla})_{jb0}+\boldsymbol{\nabla}_{j0b}\bullet(\mathbf{r}\times\boldsymbol{\nabla})_{ia0}) \\
-\sum_{b\neq a}\frac{V_{iab,0}}{h(\nu_b-\nu_a)}(\boldsymbol{\nabla}_{i0a}\bullet(\mathbf{r}\times\boldsymbol{\nabla})_{ib0}+\boldsymbol{\nabla}_{i0b}\bullet(\mathbf{r}\times\boldsymbol{\nabla})_{ia0}) \\
-\sum_{b\neq a}\frac{V_{i0b,0}}{h\nu_b}(\boldsymbol{\nabla}_{iba}\bullet(\mathbf{r}\times\boldsymbol{\nabla})_{ia0}+\boldsymbol{\nabla}_{i0a}\bullet(\mathbf{r}\times\boldsymbol{\nabla})_{iab}) \\
-2\sum_{j\neq i}^{n}\sum_{b\neq a}\frac{V_{i0a,j0b}}{h(\nu_b^2-\nu_a^2)}\nu_a(\mathbf{R}_j-\mathbf{R}_i)\bullet\boldsymbol{\nabla}_{jb0}\times\boldsymbol{\nabla}_{i0a} \\
-\sum_{j\neq i}^{N}\frac{V_{i0a,j0a}}{2h\nu_a}(\boldsymbol{\nabla}_{i0a}\bullet(\mathbf{r}\times\boldsymbol{\nabla})_{j0a}+\boldsymbol{\nabla}_{ja0}\bullet(\mathbf{r}\times\boldsymbol{\nabla})_{ia0}) \\
-\sum_{j\neq i}^{N}\frac{V_{i0a,j0a}}{2h\nu_a}(\mathbf{R}_j-\mathbf{R}_i)\bullet\boldsymbol{\nabla}_{i0a}\times\boldsymbol{\nabla}_{j0a}
\end{array}\right\}. \tag{20.19}$$

A detailed derivation of this formula for the nondegenerate case can be found in the supplement at the end of this chapter, following the reference section. The matrix elements of the nabla operator required in this expression can be calculated from the electric dipole transition moments using Eq. (20.17) or from the wavefunctions.

The theory of Tinoco has been used to predict the CD of many biopolymers, as shown in Table 20.1 and in greater detail in Table S1 of the supplement at the end of this chapter.

TABLE 20.1. Applications of Tinoco Theory

System	References
α helix	18, 39, 77, 78
3_{10} helix	18
poly(Pro) helices	38
Unordered polypeptides	79–81
β sheet	36, 39
Heme proteins	82–89
Flavoproteins	86
Rhodopsin	90
Ribonuclease	21, 91
Insulin	92, 93
Avian pancreatic polypeptide	94
Mononucleos(t)ides	95–98
Dinucleotides	37, 99

20.3. THE MATRIX METHOD

The matrix method was introduced by Bayley, Nielsen, and Schellman [3, 13] and is an all-order version of Tinoco's perturbation theory [2]. In the matrix method as generally applied, one considers only mixing of singly excited states—that is, the basis set in Eq. (20.9), which are solutions of the unperturbed first term of the Hamiltonian in Eq. (20.4). The off-diagonal matrix elements of the perturbation term in Eq. (20.4) are calculated by methods described below. The diagonal elements are the excitation energies, corrected for the change in electrostatic energy upon excitation: $\langle ia|\hat{\boldsymbol{H}}|ia\rangle = (E_{ia} - E_0) + \sum_{j\neq i}^{n}(V_{iaa;j00} - V_{i00;j00})$. In many cases, this correction is neglected, but it can be significant, particularly with polar chromophores. After solving the eigenvalue problem $\mathbf{HC} = \mathbf{CE}$, one obtains the eigenvectors (columns of $\mathbf{C}$) and energies (diagonal elements of $\mathbf{E}$). The excited states will then be

$$\Psi_K = \sum_{i=1}^{n}\sum_{a=1}^{n_i} C_{iaK}\,\psi_{ia}, \tag{20.20}$$

where C_{iaK} is the component of eigenvector K corresponding to excited state a in residue i and ψ_{ia} is the wavefunction corresponding to this chromophoric excited state, as in Eq. (20.9). The second summation is over all n_i excited states of group i. Mixing of singly excited configurations with the ground configuration is generally neglected for two reasons. First, inclusion of such mixing without including doubly excited configurations would lead to blue shifts in the absorption and CD spectra. Second, consideration of such mixing would necessitate inclusion of electric and magnetic dipole transition moments connecting excited states. A perturbation calculation has shown that mixing with the doubly excited configurations makes a negligible contribution to the CD for polypeptides [15]. Thus, the ground state is unaffected by mixing in the usual matrix method and is therefore

$$\Psi_0 = \prod_{i=1}^{n}\varphi_{i0} \tag{20.21}$$

as in Eq. (20.8). The electric dipole transition moment for the transition $0 \rightarrow K$ is given by

$$\langle 0|\hat{\boldsymbol{\mu}}|K\rangle = \sum_{i=1}^{n}\sum_{a=1}^{n_i} \mathrm{C}_{iaK}\boldsymbol{\mu}_{i0a} = (\boldsymbol{C}^{-1}\boldsymbol{\mu}^0)_K, \tag{20.22}$$

where $\mathbf{C}^{-1}$ is the inverse of $\mathbf{C}$ and contains the eigenvectors as rows; $\boldsymbol{\mu}^0$ is an $N_e \times 3$ matrix in which the rows contain the three components of the transition moments for the individual chromophores; $N_e = \sum_{i=1}^{n} n_i$ is the number of excited states; and the subscript K on the matrix denotes the Kth row of the matrix. We can write the magnetic dipole transition moment in the same way:

$$\langle 0|\hat{\mathbf{m}}|K\rangle = \sum_{i=1}^{n}\sum_{a=1}^{n_i} \mathrm{C}_{\mathrm{ia K}}[\mathbf{m}_{i0a} + (i\pi\,\nu_{i0a}/c)(\mathbf{R}_i \times \boldsymbol{\mu}_{i0a})] = (\mathrm{C}^{-1}\mathbf{m}^0)_K. \tag{20.23}$$

The rotational strength is then given by

$$R_{0K} = \mathrm{Im}\{\boldsymbol{\mu}_{0K}\bullet\mathbf{m}_{K0}\} = \mathrm{Im}\{(\mathrm{C}^{-1}\boldsymbol{\mu}^0)_K\bullet(\mathbf{C}^{-1}\mathbf{m}^0)_K^+\} = \mathrm{Im}\{(\mathrm{C}^{-1}\boldsymbol{\mu}^0)_K\bullet(\mathbf{m}^{0+}\mathrm{C})_K\}, \tag{20.24}$$

where the superscript + denotes transposition. We have used the unitary properties of the eigenvector matrix and have assumed that the eigenvectors are real.

Because the original matrix method [3] used the dipole length formulation, the results show an origin dependence. This problem was not significant for the small molecules that were initially studied, but becomes serious for large molecules (e.g., proteins). Goux and Hooker [16] introduced an origin-independent formulation using the dipole velocity form in their calculations on ribonuclease. They defined a chiral strength, the chiroptical analogue of the oscillator strength in absorption:

$$c_{0K} = (\alpha/3)\mathrm{Re}\{\mathbf{p}_{0K}\bullet\mathbf{L}_{K0}\}, \tag{20.25}$$

where $\alpha = 2\pi e^2/hc$ is the fine-structure constant and $\mathbf{p}_{0K}$ and $\mathbf{L}_{K0}$ are, respectively, the linear and angular momentum matrix elements between the ground state and excited state K. The chiral strength is related to the rotational strength by

$$\mathrm{c}_{0K} = (8\pi^2 mc/3he^2\lambda_{0K})R_{0K}, \tag{20.26}$$

where $\lambda_{0\mathrm{K}}$ is the wavelength of the $0 \rightarrow K$ transition. Alternatively, one can use the rotational strength in the dipole velocity form [Eq. (20.18)]. By analogy to Eqs. 20.22–20.24, the dipole velocity form of the rotational strength is given by

$$R_{0K} = -[eh^2/4\pi^2(E_K - E_0)](\mathbf{C}^{-1}\boldsymbol{\nabla}^0)_K\bullet(\mathbf{m}^{0+}\mathbf{C})_K,$$

where $\boldsymbol{\nabla}^0$ is an $N_e \times 3$ matrix, the rows of which contain the three components of the nabla matrix elements for the individual chromophores, which can be obtained from the electric dipole transition moments by Eq. (20.17) or calculated from the wavefunctions. All recent calculations of protein CD have used one of these origin-independent formulations.

The most important problem—which is also the case when using the Tinoco method—is to calculate the matrix elements of the perturbation operator (see Appendix A). The simplest method, which can be applied if the distance between the two interacting groups is sufficiently large, uses the transition dipole moments $\boldsymbol{\mu}_{i0b}$ and the ground-state dipole moments $\boldsymbol{\mu}_{i00}$ of all groups and calculates the energy of interaction using the point–dipole interaction. For distances that are not large compared to the size of the interacting groups, it is important to use the monopole or distributed dipole approximation [2]. The interaction of the transition charge densities for transition $0 \rightarrow a$ in group i and that for $0 \rightarrow b$ in group j, for example, is approximated by

$$V_{i0a,j0b} = \sum_s \sum_t q_{is0a} q_{jt0b} / |\mathbf{R}_{jt0b} - \mathbf{R}_{is0a}|, \tag{20.27}$$

where q_{is0a} is the charge of monopole s for the transition $0 \rightarrow a$ in group i and $\mathbf{R}_{is0a}$ is its position, and correspondingly for monopole t of transition $0 \rightarrow b$ in group j. The monopole charges and positions are chosen so that they reproduce the electric dipole transition moment or the permanent dipole moment of the charge density:

$$\boldsymbol{\mu}_{i0a} = \sum_s q_{is0a} \mathbf{R}_{is0a}. \tag{20.28}$$

If the chromophore is di- or triatomic or has high symmetry, monopole charges positioned at the atomic centers can be calculated to fit the observed electric dipole transition moment, as Moffitt [17] did for the amide $\pi\pi^*$ transition. Monopoles can also be calculated from wavefunctions by the method of Tinoco [2], as described in several studies [18, 19]. A very clear method to calculate the charges and the positions of the monopoles was given by Kramer [20] and is also described in the appendix of reference 21. Besley and Hirst [22] performed high-level *ab initio* calculations to obtain wavefunctions for different groups and generated from these the potential for static and transition charge densities. They then fit monopole charges to these potentials, using fixed positions near the atomic centers. Rogers and Hirst [23] used the same approach to generate monopoles for aromatic side-chain transitions.

Recently, several more exact methods have been developed for calculating the coupling of transitions densities, which is a critical parameter for Förster resonance energy transfer (FRET) as well as for CD theory. The gold standard is provided by numerical integration of Eq. (A6) using *ab initio* wavefunctions, as described by Krueger et al. [24]. Their method is called the transition density cube (TDC) method because the (nonoverlapping) volume of each transition density is divided into a large number of small cubes. (Krueger et al. used cubes of ~0.3 Å on a side and found that decreasing the cube size had no significant effect on the results.) The charge on each cube is proportional to the product of the ground- and excited-state wavefunctions for the group evaluated at the center of the cube. Thus, this method makes the monopole approximation essentially exact by placing monopoles at a grid of closely spaced points in each of the two groups, rather than at or near atomic centers only.

The TDC method is very demanding computationally. A less demanding algorithm, the transition-density-fragment interaction (TDFI) method, has been developed by Fujimoto and Hayashi [25] for FRET and by Fujimoto [26] for matrix method calculations of CD. In TDFI, the coupling energy is calculated using single-electron density matrices for the excited states in the two groups and the two-electron repulsion integrals

over the molecular orbitals in the two groups. For further details, the original papers [24, 25] should be consulted. For a specific example of the exciton interaction between two all-*trans* polyene aldehyde Schiff base chromophores [26], the TDC method gave 741 cm^{-1} for the coupling matrix element, whereas TDFI gave 703 $cm^{-1}$and atom-centered monopoles with charges fit to the electrostatic potential of the transition charge density gave 646 cm^{-1}. By contrast, the point-dipole approximation gave 1332 cm^{-1}. Thus, the TDFI method gave an appreciably better approximation to the integral than potential-fitted monopoles, and the point-dipole value deviated by about a factor of two.

Extension of CD measurements into the vacuum ultraviolet, especially with synchrotron light sources, has revealed transitions in polypeptides that are believed to result from inter-amide charge-transfer (CT) transitions—for example, the 175- and 160-nm CD bands of the α-helix [27–29]. Two methods for extending the matrix method to include CT transitions have been reported. Woody [19] adopted the approach of Longuett-Higgins and Murrell [30], retaining the Hamiltonian of Eq. (20.4), but allowing the locally excited configurations treated in the original matrix method to mix with CT configurations, such as $n_i \rightarrow \pi^*_{i\pm1}$, in which an electron from the nonbonding orbital of group i is excited to the antibonding π^* orbital of group $i+1$ or $i-1$. He considered only CT across the hydrogen bonds and found a negligible CD contribution, but CT along the chain promises to be more significant [31, 32]. Hirst and co-workers [33–35] have adopted a different approach. Without specifying a Hamiltonian, they have expanded the matrix to include CT configurations. They treat locally excited configurations using wave functions for a monoamide and CT configurations using wave functions for a diamide [35].

Calculations of polypeptide and nucleic acid CD using Tinoco's method initially [18, 36–39] included mixing of discrete transitions at low energies with the large number of transitions deep in the ultraviolet, approximated by polarizability tensors [1, 2]. However, data on bond polarizability anisotropies were sparse and of questionable quality. In addition, the CD spectra of the α helix and β sheet (Chapters 14 and 15 in volume 2) showed little net rotational strength down to ~180 nm; that is, the spectra were *conservative* [37], indicating that there is little net mixing of the $n\pi^*$ and $NV_1\pi\pi^*$ transitions with high-energy transitions. This led later workers to neglect the effects of high-energy transitions, despite the distinctly nonconservative CD spectrum of the poly(Pro) II (P_{II}) conformation (Chapters 14 and 15 in volume 2) and of the 260-nm region of A-form polynucleotides (Chapter 17 in Volume 2).

Johnson and Tinoco [40] first incorporated high-energy transitions in the matrix method. They considered the mixing of each polymer transition with the high-energy transitions, described by polarizability tensors. The rotational strength of each polymer transition was multiplied by a bandshape function, and the sum over all polymer levels of the resulting CD contributions was expanded in a Taylor's series about $\bar{\nu}$, the average frequency. Only the first two terms were retained: The first had a shape determined by the bandshape function, and the shape of the second was that of the first derivative of the function. These two terms represented the nonconservative and the conservative CD spectra, respectively. The method is attractive because summation over all polymer levels makes it unnecessary to explicitly diagonalize the Hamiltonian matrix. However, because of the truncation of the Taylor's series, the transitions considered must be pseudodegenerate. The method is suitable for the 260-nm region of nucleic acids to which it was applied in calculations on DNA and RNA [40] and dinucleotides [41, 42]. The $n\pi^*$ and NV_1 transitions of polypeptides are also pseudodegenerate, but the method neglects electrostatic mixing of excited states and is therefore unsuitable for polypeptide systems.

To provide a satisfactory treatment of the CD of the P_{II} polypeptide conformation, Woody [15] extended the matrix method to include the effects of mixing of each polymer transition $0 \rightarrow K$ with the high-energy transitions, modeled by polarizability tensors, $\boldsymbol{\alpha}_l$. Zubkov and Vol'kenshtein [39] had previously applied a similar approach to calculations on the α helix and β sheet. Utilizing Woody's more compact formulation, the electric-dipole-allowed components have a rotational strength contribution from this mixing given by the matrix equation:

$$\boldsymbol{R}_\mu = \gamma_\mu \sum_l \mathbf{C}^+ \mathbf{G} \boldsymbol{\alpha}_\ell \mathbf{F} \mathbf{C}. \tag{20.29}$$

The matrix $\boldsymbol{R}_\mu$ has dimensions $N_e \times N_e$, where N_e is the number of discrete transitions included in the matrix method. The diagonal element $(R_\mu)_{KK}$ is the contribution of the polarizable groups to the rotational strength of polymer transition $0 \rightarrow K$ through mixing with the electric dipole transition moments of the discrete transitions. The parameter $\gamma_\mu = \pi \nu_0^2 / [\lambda_K (\nu_0^2 - \nu_K^2)]$, where ν_0 is the average frequency of the high-energy transitions, usually taken to be 10^5 cm^{-1}, ν_K is the frequency of the polymer transition $0 \rightarrow K$, and λ_K is its wavelength. $\mathbf{C}$ and $\mathbf{C}^+$ are the eigenvector matrices from the diagonalization of the Hamiltonian matrix. $\mathbf{G}$ is a matrix with the general element

$$G_{j\ell} = \sum_t \frac{q_{jbt} \mathbf{R}_{jbt,l}}{|\mathbf{R}_{jbt,l}|^3}, \tag{20.30}$$

where q_{jbt} is the charge of monopole t for the transition $0 \rightarrow b$ in group j and $\mathbf{R}_{jbt,l} = \mathbf{R}_l - \mathbf{R}_{jbt}$. The polarizability matrix, $\boldsymbol{\alpha}_l$, is a $3N_\alpha \times 3N_\alpha$ matrix, where N_α is the number of polarizable groups of type l, and the nonzero elements of the matrix are 3×3 submatrices along the diagonal, one for each of the groups of type l. $\mathbf{F}$ is a matrix with the general element:

$$\mathbf{F}_{ia\ell} = \boldsymbol{\mu}_{i0a} \times \mathbf{R}_{i\ell}, \tag{20.31}$$

where $\mathbf{R}_{il} = \mathbf{R}_l - \mathbf{R}_i$ is the vector from the center of transition i to the polarizable group l.

The contributions to the rotational strength of the polymer transition $0 \rightarrow K$ from magnetically allowed transitions mixing with the high-energy transitions are given by the matrix equation:

$$\boldsymbol{R}_m = \gamma_m \sum_l \mathbf{C}^+ \mathbf{G} \boldsymbol{\alpha}_l \mathbf{m}^+ \mathbf{C}, \tag{20.32}$$

where $\boldsymbol{R}_m$ is an $N_e \times N_e$ matrix, of which the diagonal elements, $(R_m)_{KK}$, are the contributions of the polarizable groups to the rotational strength for the polymer transition $0 \rightarrow K$ through mixing with magnetically allowed discrete transitions. The parameter γ_m equals $\nu_0{}^2/(\nu_0{}^2 - \nu_K{}^2)$; and $\mathbf{m}^+$ is a $3N_\alpha \times N_e$ matrix, the ith column of which consists of N_α repetitions of the components of $\mathbf{m}_i{}^*$, the complex conjugate of the magnetic dipole transition moment vector for transition $0 \rightarrow a$ in group i.

Woody [15] utilized polarizability tensors for individual bonds and lone pairs that were calculated for *N*-methylacetamide using the method of Garmer and Stevens [43]. These tensors are obtained by applying finite-field perturbations to localized *ab initio* wave functions. The use of bond and lone-pair polarizabilities is much to be preferred

TABLE 20.2. Applications of the Matrix Method

System	References
Linear dipeptides	3, 100–102
Cyclic dipeptides	103–106
Linear oligopeptides	107, 108
α helix	13, 109–116
3_{10} helix	113
Poly(Pro) helices	13, 15, 109, 113, 117
β sheet	13, 109, 118–121
β turns	122
Ribonuclease	16, 21, 72, 123
Lysozyme	124
Adenylate kinase	125
Pancreatic trypsin inhibitor	126, 127
Gene 5 protein	71, 128
β-lactamase	62
Villin headpiece	129
Calmodulin fragment	130
Palmitoyl transferase (PagP)	131
Ubiquitin	132
p62 UBA domain	133
Multiple proteins	22, 23, 33, 35, 61, 63–65, 134–136
Dinucleotides	40, 42
Polynucleotides	40, 138–149
Retinal Schiff base dimer	26

relative to using the polarizability of the whole amide group. It is not possible to obtain a unique decomposition of the experimental molecular polarizabilities into individual bond contributions [44].

Woody [15] showed that this method satisfactorily reproduces the strongly nonconservative CD spectrum of polypeptides such as poly(Glu) and poly(Lys) in the P_{II} conformation. Poly(Pro)II itself, however, still presents theoretical challenges. This method does not reproduce the poly(Pro)II CD spectrum, perhaps because of conformational heterogeneity or because the polarizability parameters are not suitable for the pyrrolidine ring of the Pro side chain. Woody also found that although the net contributions of high-energy transitions to α-helix CD are small, there are significant contributions to individual polymer transitions of opposing sign that modify the shape of the CD spectrum.

The matrix method has been applied to the prediction of the CD spectrum of many polypeptide and polynucleotide systems, as shown in Table 20.2 and in greater detail in Table S2 of the supplement at the end of this chapter, following the reference section.

20.4. CLASSICAL POLARIZABILITY (DeVoe) THEORY

Optical activity is not an inherently quantum mechanical phenomenon and thus can be described by classical theory. DeVoe [4, 5] developed such a theory, in which linear oscillators play the role of electric dipole transition moments and their moments about an arbitrary origin correspond to magnetic dipole transition moments. Each electronic

transition within a group is represented by a polarizability tensor, $\boldsymbol{\alpha}_i$, which is frequency-dependent and is represented in dyadic form by

$$\boldsymbol{\alpha}_i(\nu) = \alpha_i(\nu)\mathbf{e}_i\mathbf{e}_i, \tag{20.33}$$

where α_i is the scalar polarizability and $\mathbf{e}_i$ is a unit vector in the direction of polarization of the oscillator. The molecule is considered to consist of a collection of N_e such oscillators. The electric field of an incident light wave induces an electric dipole moment, $\boldsymbol{\mu}_i^{ind} = \mu_i^{ind}\mathbf{e}_i$, in each oscillator:

$$\boldsymbol{\mu}_i^{ind} = \boldsymbol{\alpha}_i \bullet \mathbf{E}_i^{eff}, \tag{20.34}$$

where $\boldsymbol{\alpha}_i$ is the polarizability tensor of oscillator i and $\mathbf{E}_i^{eff}$ is the electric field at oscillator i. This field consists of the applied field at the oscillator, $\mathbf{E}_i^{ext}$, and the field generated by all of the other induced moments:

$$\boldsymbol{\mu}_i^{ind} = \mu_i^{ind}\mathbf{e}_i = \alpha_i\mathbf{e}_i\mathbf{e}_i \bullet (\mathbf{E}_i^{ext} - \sum_{j\neq i}\mathbf{T}_{ij} \bullet \boldsymbol{\mu}_j^{ind}) = \alpha_i(\mathbf{e}_i \bullet \mathbf{E}_i^{ext} - \sum_{j\neq i} G_{ij}\mu_j^{ind})\mathbf{e}_i, \tag{20.35}$$

where $G_{ij} = \mathbf{e}_i \bullet \mathbf{T}_{ij} \bullet \mathbf{e}_j$ is the point dipole interaction energy between dipoles $\boldsymbol{\mu}_i^{ind}$ and $\boldsymbol{\mu}_j^{ind}$. Thus the scalar-induced moments are given by a set of N_e equations of the form

$$\alpha_i^{-1}\mu_i^{ind} + \sum_{j\neq i} G_{ij}\mu_j^{ind} = \mathbf{e}_i \bullet \mathbf{E}_i^{ext} \tag{20.36}$$

that can be written in matrix form:

$$\mathbf{B}\boldsymbol{\mu} = \mathbf{E}^{ext}, \tag{20.37}$$

where a representative element of the $\mathbf{B}$ matrix is given by

$$B_{ij} = (\delta_{ij}/\alpha_i) + G_{ij}. \tag{20.38}$$

Here, δ_{ij} is the Kronecker delta and G_{ij} is zero if oscillators i and j are on the same group. The induced dipole moments are obtained by inverting the $\mathbf{B}$ matrix, giving

$$\boldsymbol{\mu} = \mathbf{B}^{-1}\mathbf{E}^{ext} = \mathbf{A}\mathbf{E}^{ext}. \tag{20.39}$$

Thus the matrix $\mathbf{A} = \mathbf{B}^{-1}$ is the polarizability tensor for the collection of oscillators. This matrix provides the information required to calculate the absorption and CD spectra of the molecule.

$$\varepsilon(\nu) = -(8\pi^2 N_0/6909\lambda)\sum_i\sum_j \mathrm{Im}(A_{ij})\mathbf{e}_i \bullet \mathbf{e}_i, \tag{20.40}$$

$$\Delta\varepsilon(\nu) = (16\pi^3 N_0/6909\lambda^2)\sum_i\sum_j \mathrm{Im}(A_{ij})[\mathbf{R}_{ij} \bullet \mathbf{e}_i \times \mathbf{e}_j - 4b_j\mathbf{e}_i \bullet \mathbf{e}_j']. \tag{20.41}$$

The second term in Eq. (20.41) arises from coupling of the magnetic dipole transition moment j and the electric dipole transition moment i. Here, $\mathrm{b}_j = c\ \mathrm{Im}|\mathbf{m}_j|/(2\pi\nu_j|\boldsymbol{\mu}_j|)$,

where c is the velocity of light *in vacuo*, ν_j is the frequency of oscillator j, and $|\mathbf{m}_j|$ and $|\boldsymbol{\mu}_j|$ are, respectively, the magnitudes of the magnetic and electric dipole transition moments of oscillator j. The vector $\mathbf{e}'_j$ is the unit vector in the direction of the magnetic dipole transition moment. This term has rarely been used, limiting the DeVoe method to $\pi\pi^*$ transitions.

The **A** matrix is complex because the oscillator polarizabilities are generally complex. We obtain these polarizabilities from the absorption spectrum of the individual isolated groups—for example, the peptide group and aromatic amino acids for proteins, and the pyrimidines and purines for nucleic acids. The scalar polarizability of oscillator i is given by

$$\alpha_i(\nu) = \alpha'_i(\nu) + i\alpha''_i(\nu). \tag{20.42}$$

The imaginary part of the polarizability, $\alpha''_i(\nu)$, is proportional to the molar extinction coefficient:

$$\alpha''_i(\nu) = -(6909c/8\pi^2\nu \mathrm{N}_0)\varepsilon_i(\nu). \tag{20.43}$$

The real part of the polarizability is obtained from the imaginary part by the Kronig–Kramers [45, 46] transform:

$$\alpha'(\nu) = -(2/\pi)\wp \int_0^\infty \frac{\nu'\alpha''_i(\nu')d\nu'}{(\nu'^2 - \nu^2)}, \tag{20.44}$$

where $\wp$ denotes the Cauchy principal value of the integral—that is, integration that avoids the singularity.

The dipole–dipole interaction, G_{ij}, has been defined in the point-dipole approximation, but this approximation is unsatisfactory at short distances, when the separation is comparable to or less than the extent of the dipoles. It is therefore preferable to define G_{ij} as

$$G_{ij} = V_{ij}/|\boldsymbol{\mu}_i||\boldsymbol{\mu}_j|, \tag{20.45}$$

where V_{ij} is the interaction between transition charge densities calculated in the monopole approximation [2] [Eq. (20.27)] and $|\boldsymbol{\mu}_i|, |\boldsymbol{\mu}_j|$ are the magnitudes of transition moments i and j, respectively.

Levin and Tinoco [47] extended the DeVoe theory to the case of infinite helical polymers, using periodic boundary conditions. The use of helical symmetry permits calculation of the CD and absorption by inversion of three matrices (one for the axial direction and two for the directions perpendicular to the axis) of dimension $\eta \times \eta$ for each electronic transition, where η is the number of transitions in the repeating unit.

In contrast to the matrix method [3], the bandshape of the transition enters the DeVoe calculation from the beginning in defining the frequency dependence of the group polarizabilities, rather than being introduced at the end of the calculation as an arbitrary bandshape function associated with each transition. This is an advantage of the DeVoe method.

Another advantage of the DeVoe method is that it is a weak-coupling [48] method, meaning that it assumes that the electronic coupling among chromophores is small compared to the vibronic band widths. The matrix method [3] implicitly assumes the opposite

case—that is, strong coupling. In proteins and nucleic acids as well as in most small molecule systems, the coupling is at best intermediate, with the electronic coupling comparable to the vibronic band widths. Therefore, weak coupling is a better approximation than strong coupling. In practice, however, the predictions of the DeVoe method are quite similar to those of the matrix method, consistent with the demonstration by Tinoco [2] that the perturbation theory expressions for predicting dipole and rotational strengths are equivalent for strong and weak coupling.

The CD and absorption spectra are calculated at each wavelength of interest, requiring the inversion of the **B** matrix at each wavelength. This is a disadvantage computationally relative to the matrix method, which requires a single matrix diagonalization. In addition to the substantially greater number of matrix operations in the DeVoe method, matrix inversion is more computer intensive than matrix diagonalization.

Another drawback of the DeVoe method is that it is limited to electrically allowed transitions and is not suited to treating the peptide $n\pi^*$ transition, for example. Inclusion of the magnetic moments in the DeVoe method permits treatment of the coupling between electric and magnetic dipole transition moments in different groups (Schellman's μ–m term [49]), but does not include the important one-electron contribution [2, 50] of static-field mixing within individual groups.

The DeVoe method has been used extensively in stereochemical studies of organic molecules. These applications have been reviewed [51, 52], and references to selected systems are given in Table 20.3. The DeVoe method is a useful adjunct to the exciton chirality method (Chapter 4 in Volume 2) in systems with two coupled transitions, and it is indispensable when more than two transitions are involved. A valuable feature of the recent review of Superchi et al. [52] is the illustration of the application of the DeVoe model to 1,1′-binaphthyl. Applications of the DeVoe method to biologically important molecules are also referenced in Table 20.3.

Applequist et al. have developed a method that is closely related to the DeVoe model, called the Atom Dipole Interaction model [53]. The method was first applied to the prediction of molecular polarizabilities. Atoms were assigned isotropic polarizabilities, and the moments induced in the atoms by an applied field were allowed to interact via

TABLE 20.3. Applications of DeVoe Theory

System	Model[a]	References
Biaryls	D	150–152
Paracyclophanes	D	153, 154
Aryl sulfoxides	D	155, 156
Pseudoisocyanine	I	157
Porphyrins	D	158–160
Nucleosides	D	147, 161, 162
DNA and RNA	D,I	148, 163–169
α helix	A,I	56, 58, 76
Poly(Pro) I and II	A	68, 170
Collagen	A	171
β sheet	A,I	56, 58, 172
β turns	A,I	58, 173, 174
Cyclic peptides	A,I	174–178
Poly(β-amino acids)	A	179–181
Proteins	A	60, 182

[a] D, DeVoe; A, Applequist; I, Ito.

the point dipole interaction, giving rise to the molecular polarizability as in Eq. (20.39). It was found that a small set of parameters (e.g., three polarizabilities for carbon in aliphatic, carbonyl, and nitrile environments) could account satisfactorily for the average polarizability of a wide range of molecules and, less well, for the anisotropy. The model was also applied to prediction of optical rotation, depolarization factors, Kerr constants, and Raman mean polarizabilities and anisotropies [6] with generally satisfactory results.

Applequist [54] extended his model to treat the amide group as a single unit with a frequency-dependent polarizability tensor (dispersive) and all other atoms as frequency-independent, isotropic polarizabilities (nondispersive). The parameters for the amide polarizability were optimized [54, 55] to give the best fit to mean polarizability, anisotropy, and Kerr constant data for eight primary, secondary, and tertiary amides.

Ito et al. [56–58] have developed a formalism based upon the DeVoe method and have applied it to various systems. Ito [57] has summarized this work and related it to other theoretical methods.

The classical models of DeVoe, Applequist, and Ito have been applied to many systems, as shown in Table 20.3 and in greater detail in Table S3 of the supplement at the end of this chapter, following the reference section.

20.5. APPLICATIONS

Independent systems theory has been applied to many systems for predicting CD and absorption spectra. The range of systems studied can be judged from the entries in Tables 20.1–20.3, which list applications of Tinoco's theory, the matrix method, and DeVoe theory, respectively, together with references. More complete annotated tables may be found at the end of this chapter. In this chapter, we will limit the discussion of applications of these methods to the prediction of CD spectra for proteins, an area in which there has been much recent activity. Appendix B is a compilation of data and references for the principal chromophoric groups in both proteins and nucleic acids.

The prediction of protein CD spectra from X-ray or NMR structures has been reviewed previously [11, 59]. Three different models have been used: the atom dipole interaction model [60]; the matrix method using semiempirical parameters [21, 61, 62]; and the matrix method using *ab initio* parameters [22, 63–65].

Hirst et al. [64] compared the performances of these methods, measured by the Spearman rank correlation coefficient for three characteristic wavelengths: 190, 208, and 220 nm. This comparison is reproduced in part in Table 20.4. Overall, the *ab initio*-based matrix method gives the best results, although the semiempirical matrix method performs equally well at 220 nm, and the dipole interaction model performs slightly better at 190 nm, although the sample of proteins was smaller. The *ab initio* model works better because it represents the static and transition charge densities by a set of point charges that best fits the *ab initio* electrostatic potentials. An earlier *ab initio* model [63] used point charges to fit only the *ab initio* dipole and quadrupole moments, and this did not perform as well as the semiempirical model [61]. The slightly superior performance of the dipole interaction model at 190 nm may reflect the value of including mixing of the $\pi\pi^*$ transition with very-high-energy transitions, which are missing in the standard matrix method, but have been incorporated in an extended version of the matrix method [15]. The dipole interaction model is not expected to work well at 220 nm because it does not include the $n\pi^*$ transition.

All three methods work best for α-helix-rich proteins and give poorer results for β-rich proteins. The two matrix methods do very poorly with β-II proteins [66], such as the serine proteases, predicting a positive $\pi\pi^*$ couplet in contrast to the observed

TABLE 20.4. Comparison of Performance of Three Models for Predicting Protein Far-UV CD[a]

Model	Proteins	Correlation Coefficient[b]		
		190 nm	208 nm	220 nm
Dipole interaction[c]	15	0.89	0.75	0.74
Matrix, semiempirical[d]	47	0.68	0.67	0.93
Matrix, *ab initio*[e]	47	0.86	0.80	0.94

[a] Based upon Hirst et al. [64]
[b] Spearman rank correlation coefficient, comparing calculated and experimental CD at three wavelengths.
[c] Hirst et al. [64] calculated correlation coefficients from data of Bode and Applequist [60].
[d] Calculated by Hirst et al. [64], using parameters of Woody and Sreerama [61], but considering only the $n\pi^*$ and $NV_1\pi\pi^*$ transitions.
[e] Calculated using the parameters of Besley and Hirst [22].

negative band near 200 nm. This is probably related to the poor performance [15] of the matrix method for the P_{II} conformation, which dominates the CD spectrum of β-II proteins [67]. (Bode and Applequist [60] did not include any β-II proteins in their set of proteins. This would have been interesting because the dipole interaction model handles the poly(Pro)II helix well [68], in contrast to the matrix method.)

Although the correlation coefficients for the *ab initio* model are superior to those for the semiempirical model, the latter generally gives better band shapes, especially for α-helix-rich proteins. The *ab initio* model uses a fixed band width of 15 nm for all transitions, and this does not permit the resolution of the 222- and 208-nm bands of the α helix. Hirst et al. [64] explored various combinations of constant band widths, effective dielectric constants, and inclusion of two higher-energy transitions. They found combinations that gave resolution of the long-wavelength α-helix bands, but at the expense of increased mean absolute error. By contrast, the semiempirical model uses different band widths for different transitions, using an empirical relationship between band width and absorption maximum [69]. With this model, the 222- and 208-nm band of the α helix are resolved.

Near-UV CD spectra of proteins have been calculated by the matrix method using both semiempirical [61, 70–72] and *ab initio* [23] parameters. Rogers and Hirst [23] compared results from their *ab initio* model with those from a hybrid using their *ab initio* peptide backbone parameters with the Woody and Sreerama [61] side-chain parameters, applying these two models to 30 proteins and to 20 mutant proteins. Quantitative comparisons used mean absolute errors, presumably using $[\theta]_{max}$ and $\Delta[\theta]_{max}$, respectively. The mean absolute errors in the far and near UV are shown in Table 20.5. In the far UV, inclusion of side-chain contributions increases the mean absolute error, as was noted by Hirst [63] and by Woody and Sreerama [61]. The *ab initio* parameters produce only a minor increment, however. In the near UV, the *ab initio* parameters lead to significantly better predictions for wild-type and mutant CD spectra.

Bulheller and Hirst [73] have created a website called DichroCalc that uses *ab initio* parameters and the matrix method to calculate the CD and linear dichroism (see Chapter 18 of this volume) spectra of a protein. The user submits a Protein Data Bank (PDB) [74] file for the protein of interest, or a series of files if multiple conformers (e.g., from an NMR structure or molecular dynamics trajectory) are to be considered. The output spectrum is returned by email.

Hirst and co-workers [34, 35] have extended the matrix method to include charge-transfer transitions between neighboring amide groups—for example, an $n_i \rightarrow \pi^*_{i\pm1}$ transition in which a nonbonded electron on peptide group i is excited to the π_* orbital of peptide group $i \pm 1$. Parameters for including these transitions, which are believed

TABLE 20.5. Comparison of Mean Absolute Error[a] for Side-Chain Models for Predicting Protein CD[b]

Model	Far-UV	Near UV		
	30 Proteins	30 Proteins	20 Mutants	20 Diff. Spectra
Ab initio backbone	6100			
Ab initio backbone+*ab initio* side chain	6300	110	170	54
Ab initio backbone+semiempirical side chain	7300	240	200	98

[a] Mean residue ellipticity in deg cm^2 $dmol^{-1}$.
[b] Data of Rogers and Hirst [23].

to be responsible for the bands at ~175 and 160 nm in the α-helix CD spectrum (see reference 29 for a review), were generated by *ab initio* calculations on a dipeptide in various conformations. In a survey of 71 proteins, inclusion of CT transitions had little effect on the Spearman rank correlation coefficients at 190 or 222 nm, but markedly improved the correlation coefficient at 175 nm, from 0.46 to 0.79.

Jiang et al. [65] have recently reported combined molecular dynamics/*ab initio* matrix method simulations of the CD spectra of three α-helix-rich and two β-rich proteins. For each sampled structure along the MD trajectory, the transition energies (the diagonal elements of the Hamiltonian matrix) were calculated from the *in vacuo* energy corrected by the difference in energy between the excited- and ground-state charge densities in the electrostatic field generated by the remainder of the molecule and the solvent. The dispersion in transition energies thus generated, combined with the structural variations along the trajectory, led to a broad distribution of transition energies, especially for the $\pi\pi^*$ transition, with energy shifts from -8000 to $+6000$ cm^{-1}, relative to the unperturbed transition. The matrix method was applied to each sampled structure along the trajectory, and the resulting CD and absorption spectra were averaged over the trajectory. In generating the CD spectrum for a given conformer, a relatively small band width (7.5 nm) was used, but the spread of transition energies, exciton splitting, and conformational fluctuations led to realistic bandshapes, and reasonable agreement with experiment was obtained for both hemoglobin (α-helix-rich) and a lectin (β-rich). Agreement was poorer for leptin, another α-helix-rich protein, in the long-wavelength region, and for monellin, a β-rich protein, in the 190-nm region, but was still semiquantitatively satisfactory.

In another recent development, Abramavicius et al. [75] have used the methods described by Jiang et al. [65] to simulate two-dimensional absorption and CD spectra in the far UV. Experimental measurements of such 2D spectra have yet to be reported but should significantly augment conventional 1D spectra.

20.6. SOFTWARE AVAILABLE

One of the authors of this chapter (JF) developed software to perform calculations for proteins employing either Tinoco's theory or the matrix method, and another author (RWW) has written software to perform matrix method calculations for proteins. Fortran source codes of the programs MATMAC (JF) and PROTEIN (RWW), including sample input and output files, are available from the authors. Bulheller and Hirst [73] have established a website (DichroCalc, `http://comp.chem.nottingham.ac.uk/dichrocalc/`) to

which investigators can submit protein structures in the form of Protein Data Bank (PDB) [74] files for calculation of CD and linear dichroism spectra using the matrix method and the *ab initio* parameters of Hirst and co-workers [22, 23]. A program package for calculating peptide and protein CD by the method of Applequist [55, 60, 76] may be downloaded from the website `http://www.public.iastate.edu/~jba/homepage.html` by clicking on the entry "CaPPS program package."

APPENDIX A

$$H^0_{0,0} = \int (\psi^0_0)^* \sum_{l=1}^{n} \hat{H}_{0l}\,\psi_0\, d\tau = \sum_{l=1}^{n} E^0_{l0} \equiv E^0, \tag{A1}$$

$$H^0_{ia,ia} = \int (\psi_{ia})^* \sum_{l=1}^{n} \hat{H}_{0l}\,\psi_{ia}\, d\tau = E^0 + E^0_{ia} - E^0_{i0}, \tag{A2}$$

and

$$H^0_{ka,lb;ka,lb} = \int (\psi_{ka,lb})^* \sum_{i=1}^{n} \hat{H}_{0i}\,\psi_{ka,lb}\, d\tau = E^0 + E^0_{ka} - E^0_{k0} + E^0_{lb} - E^0_{l0}. \tag{A3}$$

The matrix elements of $\hat{V}$ are

$$V_{00} = \int (\psi_0)^* \hat{V}\,\psi_0\, d\tau = \sum_{i=1}^{n-1}\sum_{j>i}^{n} \int\int \varphi^*_{i0}\varphi^*_{j0}\hat{V}_{ij}\varphi_{i0}\varphi_{j0}\, d\tau_i\,\tau_j = \sum_{i=1}^{n-1}\sum_{j>i}^{n} V_{i00,j00}, \tag{A4}$$

$$V_{0,ia} = \int (\psi_0) * \hat{V}\,\psi_{ia}\, d\tau = \sum_{j\neq i} \int\int \varphi^*_{i0}\varphi^*_{j0}\hat{V}_{ij}\varphi_{ia}\varphi_{j0}\, d\tau_i\,\tau_j = \sum_{j\neq i} V_{i0a,j00} \tag{A5}$$

$$V_{0;ia,jb} = \int\int \varphi^*_{i0}\varphi^*_{j0}\hat{V}_{ij}\varphi_{ia}\varphi_{jb}\, d\tau_i\, d\tau_j = V_{i0a,j0b} \tag{A6}$$

$$V_{ia,jb} = \int\int \varphi^*_{ia}\varphi^*_{j0}\hat{V}_{ij}\varphi_{i0}\varphi_{jb}\, d\tau_i\, d\tau_j = V_{ia0,j0b} \tag{A7}$$

$$V_{ia,ib} = \sum_{j\neq i}^{n} \int\int \varphi^*_{ia}\varphi^*_{j0}\hat{V}_{ij}\varphi_{ib}\varphi_{j0}\, d\tau_i\, d\tau_j = \sum_{j\neq i} V_{iab,j00} \tag{A8}$$

APPENDIX B

TABLE B1. Model Chromophores

Chromophore	Model	Transition	λ_{max} (nm)	$\lvert\mu\rvert$ (D)	Polarization
Peptide [183]	*N*-AcGly	$n\pi^*$	213	0	$\perp^a$
		NV_1	187	3.0	$-55(5)^\circ$
		NV_2	139	1.7	$+10$ or $+61(10)^\circ$

(*continued*)

TABLE B1. (*Continued*)

Chromophore	Model	Transition	λ_{max} (nm)	$\|\mu\|$ (D)	Polarization
Phe [184]	Toluene	L_b	260	0.3	$\perp^b$
		L_a	205	2.1	||
		B_b	185	4.3	$\perp$
		B_a	185	4.3	||
Tyr [110]	Phenol	L_b	277	1.1	$\perp^b$
		L_a	227	2.5	||
		B_b	192.5	4.7	$\perp$
		B_a	192.5	4.7	||
Trp [185, 186]	Indole	L_b	287	1.7	$42(5)^{\circ c}$
		L_a	265	2.6	$-46(5)^{\circ}$
		B_b	220	5.3	$0(15)^{\circ}$
		B_a	~200	4.6	$> \pm 30$
Asn, Gln[183]	Propanamide	$n\pi*$	208	0	$\perp^a$
		NV_1	181	2.6	$-35(3)^{\circ}$
		NV_2	127	1.6	$+46(8)^{\circ}$
Asp, Glu[187]	Ala	$n_1\pi*$	196	0	$\perp^d$
		$n_2\pi*$	196	0	$\perp$
		$\pi\pi*$	166	3.2	O-O
His [188]	Imidazolium	$\pi\pi*_1$	207	3.0	$\|\|^e$
		$\pi\pi*_2$	178	1.6^f	$\perp$
Arg	Guanidinium	$\pi\pi*_1$	180^g	3.4^g	$\|\|^h$
		$\pi\pi*_2$	180^g	3.4^g	$\perp$
Disulfide	H_2S_2	$n_1\sigma*$	220–370	0.4–0.7	$\|\|^{i,j}$
		$n_2\sigma*$	250–325	0.0–0.7	$\perp$
Adenosine [189]	Adenine[k]	$\pi\pi*_1$	275	2.4	$83(8)^{\circ l}$
		$\pi\pi*_2$	270	3.4	$25(5)^{\circ}$
		$\pi\pi*_3$	213	3.4	$-45(5)^{\circ}$
		$\pi\pi*_4$	204	2.2	$15(5)^{\circ}$
Guanosine [190]	9-Ethylguanine	$n\pi*$(?)	300	weak	$\perp$
		$\pi\pi*_1$	278	3.1	$-4(3)^{\circ l}$
		$\pi\pi*_2$	254	3.7	$-75(3)^{\circ}$
		M	227	~1.0	
		$\pi\pi*_3$	204	4.2	$-75(5)^{\circ}$
		$\pi\pi*_4$	189	4.4	$-9(4)^{\circ}$
Thymidine [191]	Thymine	$\pi\pi*_1$	278	3.4	-12 or $70^{\circ m}$
		$\pi\pi*_2$	213	3.5	-31 or 91°
Cytidine [192]	Cytosine	$\pi\pi*_1$	267	2.8	$6(2)^{\circ m}$
		$\pi\pi*_2$	233	1.2	$-35(30)^{\circ}$
		$\pi\pi*_3$	221	2.5	$76(3)^{\circ}$
		$\pi\pi*_4$	200	3.9	-26 or $86(3)^{\circ}$
		$\pi\pi*_5$	161	2.3	~0 or $\sim 60^{\circ}$
		$\pi\pi*_6$	154	2.6	~0 or $\sim 60^{\circ}$

[a] $\perp$ relative to the amide plane. Numerical values refer to in-plane polarization, measured relative to the carbonyl bond (C → O) with the positive sense toward the N atom of the amide group. Experimental values are (-55°, $+10^{\circ}$ or 61°) for NV_1, NV_2 of secondary amide (peptide), and (-35°, $+46^{\circ}$) for primary amide (Asn, Gln).
[b] Relative to the C_γ-C_η direction, i.e., to "long axis".
[c] Relative to the long axis which is directed from the midpoint of the C_5–C_6 bond through C_2 (see below).
[d] $\perp$ relative to the carboxylate plane. O–O is the line connecting the carboxylate oxygens. Two $n\pi^*$ transitions result from in-phase and out-of-phase combinations of lone-pair orbitals on the two oxygens. CNDO/S gives a splitting of less than 1 nm for the two $n\pi^*$ excited states.

TABLE B1. (*Continued*)

[e] Relative to the twofold axis of imidazolium cation.
[f] Theoretical value from CASPT2 [193]. Grebow and Hooker [188] did not report the intensity of the second $\pi\pi^*$ transition.
[g] Estimated from data of Sussman and Gratzer, quoted as a private communication by Wetlaufer [194].
[h] Relative to one of the three equivalent C–N bonds.
[i] Wavelengths and intensities depend on dihedral angle. Wavelength ranges quoted here are derived from experiment, whereas the intensities are obtained from CNDO/UV.
[j] Relative to the twofold axis that is perpendicular to the disulfide bond and bisects it.
[k] Model spectrum derived from the polarized absorption spectra of 9-methyladenine and 6-(methylamino)purine.
[l] The angle is positive going toward C_6 from the C_4–C_5 bond (see below).
[m] The angle is positive going toward N_3 from the N_1–C_4 axis (see structures below).

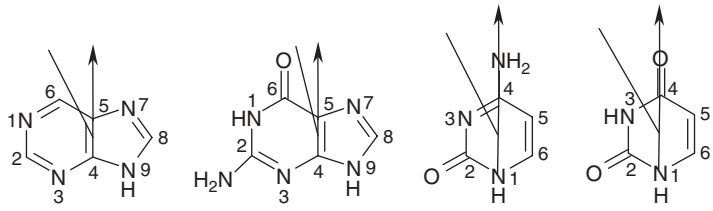

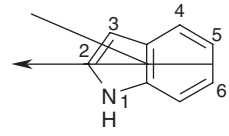

REFERENCES

1. J. G. Kirkwood, *J. Chem. Phys*. **1937**, *5*, 479–491.
2. I. Tinoco, Jr., *Adv. Chem. Phys*. **1962**, *4*, 113–160.
3. P. M. Bayley, E. B. Nielsen, J. A. Schellman, *J. Phys. Chem*. **1969**, *73*, 228–243.
4. H. DeVoe, *J. Chem. Phys*. **1964**, *41*, 393–400.
5. H. DeVoe, *J. Chem. Phys*. **1965**, *43*, 3199–3208.
6. J. Applequist, *Acc. Chem. Res*., **1977**, *10*, 79–85.
7. P. M. Bayley, *Prog. Biophys. Mol. Biol*., **1973**, *27*, 1–76.
8. D. W. Sears, S. Beychok, Circular dichroism, in *Physical Principles and Techniques of Protein Chemistry*, S. J. Leach, ed., Academic, New York, **1973**, pp. 445–593.
9. R. W. Woody, Theory of circular dichroism of proteins, in *Circular Dichroism and Conformational Analysis of Biomolecules*, G. D. Fasman, ed., Plenum, New York, **1996**, pp. 109–157.
10. A. Koslowski, N. Sreerama, R. W. Woody, Theoretical approach to electronic optical activity, in *Circular Dichroism—Principles and Applications*, N. Berova, K. Nakanishi, and R. W. Woody, eds., Wiley-VCH, New York, **2000**, pp. 55–95.
11. N. Sreerama, R. W. Woody, *Meth. Enzymol*. **2004**, *383*, 318–351.

12. J. Sandstrom, Determination of absolute configurations and conformations by semiempirical calculation of CD spectra, in *Circular Dichroism—Principles and Applications*, N. Berova, K. Nakanishi, and R. W. Woody, eds., Wiley-VCH, New York, **2000**, pp. 459–490.
13. V. Madison, J. Schellman, *Biopolymers* **1972**, *11*, 1041–1076.
14. D. Bohm, *Quantum Theory*, Dover Publications, New York, **1989**, p. 427.
15. R. W. Woody, *J. Am. Chem. Soc*., **2009**, *131*, 8234–8245.
16. W. J. Goux, T. M. Hooker, Jr., *J. Am. Chem. Soc*. **1980**, *102*, 7080–7087.
17. W. Moffitt, *Proc. Natl. Acad. Sci. USA*, **1956**, *42*, 736–746.
18. R. W. Woody, I. Tinoco, Jr., *J. Chem. Phys*., **1967**, *46*, 4927–4945.
19. R. W. Woody, *J. Chem. Phys*. **1968**, *49*, 4797–4806.
20. B. Kramer, Verknuepfung von Molekueldynamik mit verschiedenen theoretische Methoden zur Berechnung von CD-Spektren, und Berechnung der MCD-Spektren von organischen Radikalen und Arylsulfiden im Vergleich mit experimentellen Daten. Ph.D. thesis, **1991**.
21. G. Kurapkat, P. Krüger, A. Wollmer, J. Fleischhauer, B. Kramer, E. Zobel, A. Koslowski, H. Botterweck, R. W. Woody, *Biopolymers* **1997**, *41*, 267–287.
22. N. A. Besley, J. D. Hirst, *J. Am. Chem. Soc*. **1999**, *121*, 9636–9644.
23. D. M. Rogers, J. D. Hirst, *Biochemistry* **2004**, *43*, 11092–11102.
24. B. P. Krueger, G. D. Scholes, G. R. Fleming, *J. Phys. Chem. B* **1998**, *102*, 5378–5386.
25. K. J. Fujimoto, S. Hayashi, *J. Am. Chem. Soc*. **2009**, *131*, 14152–14153.
26. K. J. Fujimoto, *J. Chem. Phys*. **2010**, *133*, 124101-1–124101-9.
27. L. Serrano-Andres, M. P. Fülscher, *J. Am. Chem. Soc*. **1998**, *120*, 10912–10920.
28. L. Serrano-Andres, M. P. Fülscher, *J. Phys. Chem. B* **2001**, *105*, 9323–9330.
29. R. W. Woody, A. Koslowski, *Biophys. Chem*. **2002**, *101*, 535–551.
30. H. C. Longuet-Higgins, J. N. Murrell, *Proc. Phys. Soc. London A* **1955**, *68*, 601–611.
31. G. J. Bartlett, A. Choudhary, R. T. Raines, D. N. Woolfson, *Nature Chem. Biol*. **2010**, *6*, 615–620.
32. C. Fufezan, *Proteins Struct. Funct. Bioinform*. **2010**, *78*, 2831–2838.
33. A. T. B. Gilbert, J. D. Hirst, *J. Mol. Struct. (Theochem)* **2004**, *675*, 53–60.
34. M. T. Oakley, J. D. Hirst, *J. Am. Chem. Soc*. **2006**, *128*, 12414–12415.
35. B. M. Bulheller, A. J. Miles, B. A. Wallace, J. D. Hirst, *J. Phys. Chem. B* **2008**, *112*, 1866–1874.
36. E. S. Pysh, *Proc. Natl. Acad. Sci. USA*, **1966**, *56*, 825–832.
37. C. A. Bush, J. Brahms, *J. Chem. Phys*. **1967**, *46*, 79–88.
38. E. S. Pysh, *J. Mol. Biol*. **1967**, *23*, 587–599.
39. V. A. Zubkov, M. V. Vol'kenshtein, *Mol. Biol. (Engl. transl. of Molekul. Biologiya)* **1970**, *4*, 483–490.
40. W. C. Johnson, Jr., I. Tinoco, Jr., *Biopolymers* **1969**, *7*, 727–749.
41. W. C. Johnson, Jr., I. Tinoco, Jr., *Biopolymers*, **1969**, *8*, 715–731.
42. W. C. Johnson, Jr., M. S. Itzkowitz, I. Tinoco, Jr., *Biopolymers*, **1972**, *11*, 225–234.
43. D. R. Garmer, W. J. Stevens, *J. Phys. Chem*. **1989**, *93*, 8263–8270.
44. C. G. LeFevre, R. J. W. LeFevre, *Rev. Pure Appl. Chem*. **1955**, *5*, 261–318.
45. H. A. Kramers, *Atti Congr. Intern. Fisici, Como* **1927**, *2*, 545–557.
46. R. d. L. Kronig, *J. Opt. Soc. Am*. **1926**, *12*, 547–557.
47. A. I. Levin, I. Tinoco, Jr., *J. Chem. Phys*. **1977**, *66*, 3491–3497.
48. W. T. Simpson, D. L. Peterson, *J. Chem. Phys*. **1957**, *26*, 588–593.
49. J. A. Schellman, *Acc. Chem. Res*. **1968**, *1*, 144–151.
50. E. U. Condon, W. Altar, H. Eyring, *J. Chem. Phys*. **1937**, *5*, 753–775.

51. C. Rosini, M. Zandomeneghi, P. Salvadori, *Tetrahedron: Asymmetry* **1993**, *4*, 545–554.
52. S. Superchi, E. Giorgio, C. Rosini, *Chirality* **2004**, *16*, 422–451.
53. J. Applequist, J. R. Carl, K. K. Fung, *J. Am. Chem. Soc*. **1972**, *94*, 2952–2960.
54. J. Applequist, *J. Chem. Phys*. **1979**, *71*, 4324–4331.
55. K. A. Bode, J. Applequist, *J. Phys. Chem. A* **1996**, *100*, 17825–17834.
56. H. Ito, Y. Arakawa, Y. J. I'Haya, *J. Chem. Phys*. **1993**, *98*, 8835–8842.
57. H. Ito, *Trends Chem. Phys*. **2000**, *8*, 75–130.
58. H. Ito, *Bull. Chem. Soc. Jpn*. **2003**, *76*, 59–71.
59. M. T. Oakley, B. M. Bulheller, J. D. Hirst, *Chirality* **2006**, *18*, 340–347.
60. K. A. Bode, J. Applequist, *J. Am. Chem. Soc*. **1998**, *120*, 10938–10946.
61. R. W. Woody, N. Sreerama, *J. Chem. Phys*. **1999**, *111*, 2844–2845.
62. C. Christov, S. Gabriel, B. Atanasov, J. Fleischhauer, *Z. Naturforsch*. **2001**, *56a*, 757–760.
63. J. D. Hirst, *J. Chem. Phys*. **1998**, *109*, 782–788.
64. J. D. Hirst, K. Colella, A. T. B. Gilbert, *J. Phys. Chem. B* **2003**, *107*, 11813–11819.
65. J. Jiang, D. Abramavicius, B. M. Bulheller, J. D. Hirst, S. Mukamel, *J. Phys. Chem. B* **2010**, *114*, 8270–8277.
66. J. Wu, J. T. Yang, C. S. C. Wu, *Anal. Biochem*. **1992**, *200*, 359–364.
67. N. Sreerama, R. W. Woody, *Protein Sci*. **2003**, *12*, 384–388.
68. J. Applequist, *Biopolymers* **1981**, *20*, 2311–2322.
69. A. Brown, C. M. Kemp, S. F. Mason, *J. Chem. Soc. A* **1971**, *751–755*.
70. I. B. Grishina, R. W. Woody, *Faraday Discuss*. **1994**, *99*, 245–262.
71. T. M. Thompson, B. L. Mark, C. W. Gray, T. C. Terwilliger, N. Sreerama, R. W. Woody, D. M. Gray, *Biochemistry* **1998**, *37*, 7463–7477.
72. A. Y. M. Woody, R. W. Woody, *Biopolymers* **2003**, *72*, 500–513.
73. B. M. Bulheller, J. D. Hirst, *Bioinformatics* **2009**, *25*, 539–540.
74. H. M. Berman, J. Westbrook, Z. Feng, G. Gilliland, T. N. Bhat, H. Weissig, I. Shindyalov, P. E. Bourne, *Nucl. Acids Res*. **2000**, *28*, 235–242.
75. D. Abramavicius, J. Jiang, B. M. Bulheller, J. D. Hirst, S. Mukamel, *J. Am. Chem. Soc*. **2010**, *132*, 7769–7775.
76. J. Applequist, *J. Chem. Phys*. **1979**, *71*, 4332–4338.
77. J. A. Schellmann, P. Oriel, *J. Chem. Phys*. **1962**, *37*, 2114–2124.
78. J. N. Vournakis, J. F. Yan, H. A. Scheraga, *Biopolymers* **1968**, *6*, 1531–1550.
79. A. E. Tonelli, *Macromolecules*, **1969**, *2*, 635–637.
80. D. Aebersold, E. S. Pysh, *J. Chem. Phys*. **1970**, *53*, 2156–2163.
81. V. A. Zubkov, T. M. Birshtein, I. S. Milevskaya, *Biopolymers* **1971**, *10*, 2051–2061.
82. M.-C. Hsu, R. W. Woody, *J. Am. Chem. Soc*. **1969**, *91*, 3679–3681.
83. M.-C. Hsu, R. W. Woody, *J. Am. Chem. Soc*. **1971**, *93*, 3515–3525.
84. J. Fleischhauer, A. Wollmer, *Z. Naturforsch*. **1972**, *27 b*, 530–532.
85. R. Woody, Circular dichroism probes of hemoglobin structure, in *Biochemical and Clinical Aspects of Hemoglobin Abnormalities*, W. S. Caughey, ed., Academic, New York, **1978**, pp. 279–298.
86. R. W. Woody, Contributions of aromatic amino acid residues to the optical activity of protein–ligand complexes, in *Protein–Ligand Interactions*, H. Sund and G. Blauer, eds., Walter de Gruyter, Berlin, **1975**, pp. 60–77.
87. W. Strassburger, A. Wollmer, H. Thiele, J. Fleischhauer, W. Steigemann, E. Weber, *Z. Naturforsch*. **1978**, *33 c*, 908–911.
88. G. Blauer, N. Sreerama, R. W. Woody, *Biochemistry* **1993**, *32*, 6674–6679.

89. C. Kiefl, N. Sreerama, R. Haddad, L. Sun, W. Jentzen, Y. Qiu, J. A. Shelnutt, R. W. Woody, *J. Am. Chem. Soc*. **2002**, *124*, 3385–3394.
90. G. Pescitelli, N. Sreerama, P. Salvadori, K. Nakanishi, N. Berova, R. W. Woody, *J. Am. Chem. Soc*. **2008**, *130*, 6170–6181.
91. E. H. Strickland, *Biochemistry* **1972**, *11*, 3465–3474.
92. E. H. Strickland, D. Mercola, *Biochemistry* **1976**, *15*, 3875–3884.
93. A. Wollmer, J. Fleischhauer, W. Strassburger, H. Thiele, D. Brandenburg, G. Dodson, D. Mercola, *Biophys. J*. **1977**, *20*, 233–243.
94. W. Strassburger, U. Glatter, A. Wollmer, J. Fleischhauer, D. A. Mercola, T. L. Blundell, I. Glover, J. E. Pitts, I. J. Tickle, S. P. Wood, *FEBS Lett*. **1982**, *139*, 295–299.
95. D. W. Miles, W. H. Inskeep, M. J. Robins, M. W. Winkley, R. K. Robins, H. Eyring, *J. Am. Chem. Soc*. **1970**, *92*, 3872–3881.
96. D. W. Miles, L. B. Townsend, M. J. Robins, R. K. Robins, W. H. Inskeep, H. Eyring, *J. Am. Chem. Soc*. **1971**, *93*, 1600–1608.
97. W. H. Inskeep, D. W. Miles, H. Eyring, *J. Am. Chem. Soc*. **1970**, *92*, 3866–3872.
98. N. N. H. Teng, M. S. Itzkowitz, I. Tinoco, Jr., *J. Am. Chem. Soc*. **1971**, *93*, 6257–6264.
99. M. Warshaw, C. A. Bush, I. Tinoco, Jr., *Biochem. Biophys. Res. Commun*. **1965**, *18*, 633–638.
100. R. W. Woody, *Biopolymers* **1978**, *17*, 1451–1467.
101. R. W. Woody, *Eur. Biophys. J*. **1994**, *23*, 253–262.
102. J. M. Dungan III, T. M. Hooker, Jr., *Macromolecules* **1981**, *14*, 1812–1822.
103. R. Nagarajan, R. W. Woody, *J. Am. Chem. Soc*. **1973**, *95*, 7212–7222.
104. T. M. Hooker, Jr., P. M. Bayley, W. Radding, J. A. Schellman, *Biopolymers* **1974**, *13*, 549–566.
105. P. E. Grebow, T. M. Hooker, *Biopolymers* **1975**, *14*, 1863–1883.
106. J. Fleischhauer, J. Grötzinger, B. Kramer, P. Krüger, A. Wollmer, R. W. Woody, E. Zobel, *Biophys. Chem*. **1994**, *49*, 141–152.
107. Z. G. Liu, K. Chen, A. Ng, Z. S. Shi, R. W. Woody, N. R. Kallenbach, *J. Am. Chem. Soc*. **2004**, *126*, 15141–15150.
108. S. Abbate, S. Barlati, M. Colombi, S. L. Fornili, P. Francescato, F. Gangemi, F. Lebon, G. Longhi, P. Manitto, T. Recca, G. Speranza, N. Zoppi, *Phys. Chem. Chem. Phys*. **2006**, *8*, 4668–4677.
109. E. S. Pysh, *J. Chem. Phys*. **1970**, *52*, 4723–4733.
110. A. K. Chen, R. W. Woody, *J. Am. Chem. Soc*. **1971**, *93*, 29–37.
111. R. W. Woody, *Biopolymers* **1972**, *11*, 1149–1171.
112. T. M. Cooper, R. W. Woody, *Biopolymers* **1990**, *30*, 657–676.
113. M. C. Manning, R. W. Woody, *Biopolymers* **1991**, *31*, 569–586.
114. D.-H. Chin, R. W. Woody, C. A. Rohl, R. L. Baldwin, *Proc. Natl. Acad. Sci. USA* **2002**, *99*, 15416–15421.
115. C. D. Andrew, S. Bhattacharjee, N. Kokkoni, J. D. Hirst, G. R. Jones, A. J. Doig, *J. Am. Chem. Soc*. **2002**, *124*, 12706–12714.
116. S. Bhattacharjee, G. Tóth, S. Lovas, J. D. Hirst, *J. Phys. Chem. B* **2003**, *107*, 8682–8688.
117. L. Tterlikkis, F. M. Loxsom, W. Rhodes, *Biopolymers* **1973**, *12*, 675–684.
118. R. W. Woody, *Biopolymers* **1969**, *8*, 669–683.
119. M. C. Manning, R. W. Woody, *Biopolymers* **1987**, *26*, 1731–1752.
120. M. C. Manning, M. Illangasekare, R. W. Woody, *Biophys. Chem.* **1988**, *31*, 77–86.
121. R. W. Woody, *Tetrahedron: Asymmetry* **1993**, *4*, 529–544.

122. R. W. Woody, Studies of theoretical circular dichroism of polypeptides: Contributions of ß turns, in *Peptides, Polypeptides, and Proteins*, E. R. Blout, F. A. Bovey, M. Goodman, and N. Lotan, eds., John Wiley & Sons, New York, **1974**, pp. 338–350.
123. W. J. Goux, T. M. Hooker, Jr., *J. Am. Chem. Soc*. **1975**, *97*, 1605–1606.
124. W. J. Goux, T. M. Hooker, Jr., *Biopolymers* **1980**, *19*, 2191–2208.
125. R. W. Snyder, T. M. Hooker, Jr., *Biopolymers* **1982**, *21*, 547–563.
126. M. C. Manning, R. W. Woody, *Biochemistry* **1989**, *28*, 8609–8613.
127. N. Sreerama, M. C. Manning, M. E. Powers, J.-X. Zhang, D. P. Goldenberg, R. W. Woody, *Biochemistry* **1999**, *38*, 10814–10822.
128. T. C. Mou, N. Sreerama, T. C. Terwilliger, R. W. Woody, D. M. Gray, *Protein Sci*. **2002**, *11*, 601–613.
129. S. Jang, N. Sreerama, V. H. C. Liao, S. H. F. Lu, F. Y. Li, S. Shin, R. W. Woody, S. H. Lin, *Protein Sci*. **2006**, *15*, 2290–2299.
130. L. Settimo, S. Donnini, A. H. Juffer, R. W. Woody, O. Marin, *Peptide Science* **2006**, *88*, 373–385.
131. M. A. Khan, C. Neale, C. Michaux, R. Pomès, G. Privé, R. W. Woody, R. E. Bishop, *Biochemistry* **2007**, *46*, 4565–4579.
132. J. H. Choi, H. Lee, K. K. Lee, S. Hahn, M. Cho, *J. Chem. Phys*. **2007**, *126*, 045102-1–045102-14.
133. C. L. Evans, J. E. Long, T. R. A. Gallagher, J. D. Hirst, M. S. Searle, *Proteins Struct. Funct. Bioinform*. **2008**, *71*, 227–240.
134. J. D. Hirst, *Enantiomer* **1998**, *3*, 215–220.
135. J. D. Hirst, N. A. Besley, *J. Chem. Phys*. **1999**, *111*, 2846–2847.
136. D. M. Rogers, J. D. Hirst, *Chirality* **2004**, *16*, 234–243.
137. W. C. Johnson, Jr., I. Tinoco, Jr., *J. Am. Chem. Soc*. **1972**, *94*, 4389–4390.
138. D. S. Moore, T. E. Wagner, *Biopolymers* **1973**, *12*, 201–221.
139. D. S. Moore, T. E. Wagner, *Biopolymers* **1974**, *13*, 977–986.
140. D. S. Studdert, R. C. Davis, *Biopolymers* **1974**, *13*, 1377–1389.
141. D. S. Studdert, R. C. Davis, *Biopolymers* **1974**, *13*, 1391–1403.
142. D. S. Studdert, R. C. Davis, *Biopolymers* **1974**, *13*, 1405–1416.
143. S. Y. Chung, G. Holzwarth, *Biopolymers* **1975**, *14*, 1531–1545.
144. B. Johnson, K. S. Dahl, I. Tinoco, Jr., V. I. Ivanov, V. B. Zhurkin, *Biochemistry* **1981**, *20*, 73–78.
145. V. Rizzo, J. A. Schellman, *Biopolymers* **1984**, *23*, 435–470.
146. A. L. Williams, C. Cheong, I. Tinoco, Jr., L. B. Clark, *Nucl. Acids Res*. **1986**, *14*, 6649–6659.
147. D. S. Moore, A. L. Williams, *Biopolymers* **1986**, *25*, 1461–1491.
148. P. Richterich, F. M. Pohl, *Biopolymers* **1987**, *26*, 231–250.
149. D. E. Callahan, T. M. Hooker, Jr., *Biopolymers* **1987**, *26*, 457–461.
150. G. Gottarelli, G. Proni, G. P. Spada, D. Fabbri, S. Gladiali, C. Rosini, *J. Org. Chem*. **1996**, *61*, 2013–2019.
151. C. Rosini, S. Superchi, H. W. I. Peerlings, E. W. Meijer, *Eur. J. Org. Chem*. **2000**, *61–71*.
152. L. Di Bari, M. Lelli, G. Pintacuda, G. Pescitelli, F. Marchetti, P. Salvadori, *J. Am. Chem. Soc*. **2003**, *125*, 5549–5558.
153. C. Rosini, R. Ruzziconi, S. Superchi, F. Fringuelli, O. Piermatti, *Tetrahedron: Asymmetry* **1998**, *9*, 55–62.
154. L. Minuti, A. Taticchi, C. Rosini, D. Lanari, A. Marrocchi, S. Superchi, *Tetrahedron Asymmetry* **2002**, *13*, 1257–1263.
155. C. Rosini, M. I. Donnoli, S. Superchi, *Chem. Eur. J*. **2001**, *7*, 72–79.

156. M. I. Donnoli, E. Giorgio, S. Superchi, C. Rosini, *Org. Biomol. Chem*. **2003**, *1*, 3444–3449.
157. H. Ito, M. Agatsuma, Y. J. I'Haya, *Bull. Chem. Soc. Jpn*. **1991**, *64*, 3700–3706.
158. R. W. Woody, Circular dichroism contributions of heme–heme and chlorophyll–chlorophyll interactions, in *Optical Properties and Structure of Tetrapyrroles*, G. Blauer and H. Sund, eds., Walter de Gruyter & Co., Berlin, **1985**, pp. 239–259.
159. R. W. Woody, *Chirality* **2005**, *17*, 450–455.
160. G. Pescitelli, S. Gabriel, Y. Wang, J. Fleischhauer, R. W. Woody, N. Berova, *J. Am. Chem. Soc*. **2003**, *125*, 7613–7628.
161. D. S. Moore, *Biopolymers* **1980**, *19*, 1017–1038.
162. A. L. Williams, D. S. Moore, *Biopolymers* **1983**, *22*, 755–786.
163. C. L. Cech, W. Hug, I. Tinoco, Jr., *Biopolymers* **1976**, *15*, 131–152.
164. C. L. Cech, I. Tinoco, Jr., *Nucl. Acids Res*. **1976**, *3*, 399–404.
165. C. L. Cech, I. Tinoco, Jr., *Biopolymers* **1977**, *16*, 43–65.
166. H. Ito, T. Eri, Y. J. I'Haya, *Chem. Phys. Lett*. **1976**, *39*, 150–156.
167. H. Ito, Y. J. I'Haya, *J. Chem. Phys*. **1982**, *77*, 6270–6286.
168. H. Ito, Y. J. I'Haya, *Chem. Phys. Lett*. **1987**, *142*, 25–32.
169. H. Ito, S. Tanaka, M. Miyasaka, *Biopolymers* **2002**, *65*, 61–80.
170. K. A. Thomasson, J. Applequist, *Biopolymers* **1991**, *31*, 529–535.
171. J. W. Caldwell, J. Applequist, *Biopolymers* **1984**, *23*, 1891–1904.
172. J. Applequist, *Biopolymers* **1982**, *21*, 779–795.
173. B. K. Sathyanarayana, J. Applequist, *Int. J. Pept. Protein Res*. **1986**, *27*, 86–94.
174. H. Ito, *J. Chem. Phys*. **1998**, *108*, 93–108.
175. B. K. Sathyanarayana, J. Applequist, *Int. J. Pept. Protein Res*. **1985**, *26*, 518–527.
176. S. L. Lowe, R. R. Pandey, J. Czlapinski, G. Kie-Adams, M. R. Hoffmann, K. A. Thomasson, K. S. Pierce, *J. Pept. Res*. **2003**, *61*, 189–201.
177. K. L. Carlson, S. L. Lowe, M. R. Hoffmann, K. A. Thomasson, *J. Phys. Chem. A* **2005**, *109*, 5463–5470.
178. K. L. Carlson, S. L. Lowe, M. R. Hoffmann, K. A. Thomasson, *J. Phys. Chem. A* **2006**, *110*, 1925–1933.
179. K. A. Bode, J. Applequist, *Macromolecules* **1997**, *30*, 2144–2150.
180. J. Applequist, K. A. Bode, *J. Phys. Chem. A* **2000**, *104*, 7129–7132.
181. J. Applequist, K. A. Bode, D. H. Appella, L. A. Christianson, S. H. Gellman, *J. Am. Chem. Soc*. **1998**, *120*, 4891–4892.
182. K. A. Bode, J. Applequist, *Biopolymers* **1997**, *42*, 855–860.
183. L. B. Clark, *J. Am. Chem. Soc*. **1995**, *117*, 7974–7986.
184. J. Petruska, *J. Chem. Phys*. **1961**, *34*, 1120–1136.
185. B. Albinsson, B. Nordén, *J. Phys. Chem*. **1992**, *96*, 6204–6212.
186. L. Serrano-Andres, B. O. Roos, *J. Am. Chem. Soc*. **1996**, *118*, 185–195.
187. P. A. Snyder, P. M. Vipond, W. C. Johnson, Jr., *Biopolymers* **1973**, *12*, 975–992.
188. P. E. Grebow, T. M. Hooker, Jr., *Biopolymers* **1975**, *14*, 871–881.
189. L. B. Clark, *J. Phys. Chem*. **1990**, *94*, 2873–2879.
190. L. B. Clark, *J. Am. Chem. Soc*. **1977**, *99*, 3934–3938.
191. J. S. Novros, L. B. Clark, *J. Phys. Chem*. **1986**, *90*, 5666–5668.
192. F. Zaloudek, J. S. Novros, L. B. Clark, *J. Am. Chem. Soc*. **1985**, *107*, 7344–7351.
193. L. Serrano-Andres, M. P. Fülscher, B. O. Roos, M. Merchan, *J. Phys. Chem*. **1996**, *100*, 6484–6491.
194. D. B. Wetlaufer, *Adv. Protein Chem*. **1962**, *17*, 303–390.

SUPPLEMENT TO CHAPTER 20: DERIVATION OF TINOCO'S EQUATION IN DIPOLE VELOCITY FORM

We consider the case of nondegenerate excited states. Degenerate and pseudodegenerate cases are best treated by the matrix method. To first order in the perturbation, our wavefunctions are [see Eqs. (20.11) and (20.13)]

$$\Psi_0^1 = \psi_0 - \sum_k \sum_{l\neq k} \sum_c \frac{V_{k0c;l00}}{h\nu_c}\psi_{kc} - \sum_k \sum_{l\neq k} \sum_c \sum_d \frac{V_{k0c;l0d}}{2h(\nu_c+\nu_d)}\psi_{kc,ld}, \tag{S1}$$

$$\Psi_A^1 = \psi_{ia} + \sum_{j\neq i} \frac{V_{i0a;j00}}{h\nu_a}\psi_0 - \sum_{j\neq i}\sum_{b\neq a} \frac{V_{i0a;j0b}}{h(\nu_b-\nu_a)}\psi_{jb} - \sum_{j\neq i}\sum_{b\neq a} \frac{V_{iab;j00}}{h(\nu_b-\nu_a)}\psi_{ib}. \tag{S2}$$

The gradient matrix element is

$$\begin{aligned}(\Psi_0^1|\hat{\boldsymbol{\nabla}}|\Psi_A^1) &= \boldsymbol{\nabla}_{0A} \\ &= \left(\psi_0 - \sum_k \sum_{l\neq k} \sum_c \frac{V_{k0c;l00}}{h\nu_c}\psi_{kc} - \sum_k \sum_{l\neq k} \sum_c \sum_d \frac{V_{k0c;l0d}}{2h(\nu_c+\nu_d)}\psi_{kc,ld}|\hat{\boldsymbol{\nabla}}|\psi_{ia}\right. \\ &\quad \left. + \sum_{j\neq i} \frac{V_{i0a;j00}}{h\nu_a}\psi_0 - \sum_{j\neq i}\sum_{b\neq a} \frac{V_{i0a;j0b}}{h(\nu_b-\nu_a)}\psi_{jb} - \sum_{j\neq i}\sum_{b\neq a} \frac{V_{iab;j00}}{h(\nu_b-\nu_a)}\psi_{ib}\right).\end{aligned} \tag{S3}$$

Retaining only first-order terms, we obtain

$$\begin{aligned}\boldsymbol{\nabla}_{0A} = \boldsymbol{\nabla}_{i0a} &+ \sum_{j\neq i} \frac{V_{i0a;j00}}{h\nu_a}\boldsymbol{\nabla}_{i00} - \sum_{j\neq i}\sum_{b\neq a} \frac{V_{i0a;j0b}}{h(\nu_b-\nu_a)}\boldsymbol{\nabla}_{j0b} - \sum_{j\neq i}\sum_{b\neq a} \frac{V_{iab;j00}}{h(\nu_b-\nu_a)}\boldsymbol{\nabla}_{i0b} \\ &- \sum_k \sum_{l\neq k} \sum_c \frac{V_{k0c;l00}}{h\nu_c}\boldsymbol{\nabla}_{kc;ia} - \sum_k \sum_{l\neq k} \sum_c \sum_d \frac{V_{k0c;l0d}}{2h(\nu_c+\nu_d)}\boldsymbol{\nabla}_{kc,ld;ia}.\end{aligned} \tag{S4}$$

The second term on the right-hand side (rhs) of Eq. (S4) is zero because of the anti-Hermitian character of the gradient operator. The fifth term on the rhs vanishes unless $i = k$. If $c = a$, then the gradient matrix element becomes $\boldsymbol{\nabla}_{iaa}$, which is zero because it is a diagonal element of an anti-Hermitian operator. If $c \neq a$, the fifth term reduces to

$$\sum_{l\neq i}\sum_{c\neq a} \frac{V_{i0c;l00}}{h\nu_c}\boldsymbol{\nabla}_{ica} = \sum_{j\neq i}\sum_{b\neq a} \frac{V_{i0b;j00}}{h\nu_b}\boldsymbol{\nabla}_{iba}, \tag{S5}$$

where we have changed the summation indices to our conventional j and b.

The sixth term on the rhs of Eq. (S4) vanishes unless $k = i$ or $l = i$. In the former case, the term vanishes unless $c = a$ and the gradient matrix element becomes $\boldsymbol{\nabla}_{ld0}$. In the latter case, the term vanishes unless $d = a$ and the gradient matrix element becomes $\boldsymbol{\nabla}_{kc0}$. These two cases give equivalent results and occur with equal frequency, so we can

consider only one of them if we delete the factor of two in the denominator.

$$-\sum_{k}\sum_{l\neq k}\sum_{c}\sum_{d}\frac{V_{k0c;l0d}}{2h(\nu_c+\nu_d)}\nabla_{kc,ld;ia}=-\sum_{l\neq i}\sum_{d\neq a}\frac{V_{i0a;l0d}}{h(\nu_a+\nu_d)}\nabla_{ld0}$$
$$=-\sum_{j\neq i}\sum_{b\neq a}\frac{V_{i0a;j0b}}{h(\nu_a+\nu_b)}\nabla_{jb0}, \qquad \text{(S6)}$$

where we have again changed the indexing in the last step. Thus the gradient matrix element becomes

$$\nabla_{0A}=\nabla_{i0a}-\sum_{j\neq i}\sum_{b\neq a}\frac{V_{i0a;j0b}}{h(\nu_b-\nu_a)}\nabla_{j0b}-\sum_{j\neq i}\sum_{b\neq a}\frac{V_{iab;j00}}{h(\nu_b-\nu_a)}\nabla_{i0b}$$
$$-\sum_{j\neq i}\sum_{b\neq a}\frac{V_{i0b;j00}}{h\nu_b}\nabla_{iba}-\sum_{j\neq i}\sum_{b\neq a}\frac{V_{i0a;j0b}}{h(\nu_a+\nu_b)}\nabla_{jb0}. \qquad \text{(S7)}$$

The second and fifth terms in Eq. (S7) can be combined as follows:

$$-\sum_{j\neq i}\sum_{b\neq a}\frac{V_{i0a;j0b}}{h(\nu_b-\nu_a)}\nabla_{j0b}-\sum_{j\neq i}\sum_{b\neq a}\frac{V_{i0a;j0b}}{h(\nu_a+\nu_b)}\nabla_{jb0}$$
$$=-\sum_{j\neq i}\sum_{b\neq a}\frac{V_{i0a;j0b}}{h(\nu_b-\nu_a)}\nabla_{j0b}+\sum_{j\neq i}\sum_{b\neq a}\frac{V_{i0a;j0b}}{h(\nu_a+\nu_b)}\nabla_{j0b}$$
$$=-2\sum_{\mathrm{j}\neq\mathrm{i}}\sum_{\mathrm{b}\neq\mathrm{a}}\frac{\nu_{\mathrm{a}}V_{\mathrm{i0a;j0b}}}{h(\nu_{\mathrm{b}}^2-\nu_a^2)}\nabla_{j0b}. \qquad \text{(S8)}$$

Thus, the gradient matrix element is

$$\nabla_{0A}=\nabla_{i0a}-2\sum_{j\neq i}\sum_{b\neq a}\frac{\nu_a V_{i0a;j0b}}{h(\nu_b^2-\nu_a^2)}\nabla_{j0b}-\sum_{j\neq i}\sum_{b\neq a}\frac{V_{iab;j00}}{h(\nu_b-\nu_a)}\nabla_{i0b}$$
$$-\sum_{j\neq i}\sum_{b\neq a}\frac{V_{i0b;j00}}{h\nu_b}\nabla_{iba}. \qquad \text{(S9)}$$

Compare Eq. (S9) with Tinoco's Eq. (IIIB-18) for the electric dipole transition moment. The last two terms in (IIIB-18) have no counterpart. Term (IIIB-18e) is the "charge transfer" term and is missing because the factors corresponding to $\boldsymbol{\mu}_{\mathrm{iaa}}$ and $\boldsymbol{\mu}_{\mathrm{i00}}$ are zero in the dipole velocity approximation. Term (IIIB-18f) is missing because we are treating the nondegenerate case so there is no excited state a on groups other than i. The remaining terms agree except for two discrepancies. The last term in Eq. (S9) is ∇_{iba}, whereas ∇_{iab} would be expected by analogy to Tinoco's Eq. (IIIB-18d). However, if one carries through the derivation for the $\boldsymbol{\mu}$ operator, the correct order of subscripts is *iba*. It appears that Tinoco reversed the order for appearance's sake; and, of course, for the $\boldsymbol{\mu}$ operator such a reversal is immaterial. In the second term, the numerator contains a factor of ν_a, whereas Tinoco's term (IIIB-18b) has a factor of ν_b. Recall that this term arises from the combination of two terms, one with a denominator of $(\nu_b-\nu_a)$ and the other with a denominator of $(\nu_b+\nu_a)$. These terms also contain factors of ∇_{j0b} and ∇_{jb0}, respectively, in the case of the gradient matrix element, and contain factors of $\boldsymbol{\mu}_{j0b}$

and $\boldsymbol{\mu}_{jb0}$, respectively, in the case of the electric dipole transition moment. The effect of reversing the order of the subscript is different in the two cases: For the gradient operator, reversal leads to opposite signs for the two terms, whereas for the electric dipole moment, the two terms are of the same sign. When they are combined, the numerators contain factors of ν_a in the first case and of ν_b in the second case. Note that Tinoco's Eqs. (IIIB-20b) and (IIIB-20g) are analogous to the second term of Eq. (S9), involving a matrix element of an anti-Hermitian operator. They have the factor of ν_a in the numerator, as we obtain for the gradient matrix element.

We also need the $(\mathbf{r} \times \boldsymbol{\nabla})$ matrix element. We can readily obtain this by replacing the gradient operator in Eq. (S9) with the magnetic moment operator, $(\mathbf{r} \times \hat{\boldsymbol{\nabla}}) + \mathbf{R} \times \hat{\boldsymbol{\nabla}}$, where $\mathbf{r}$ is the position vector relative to the group origin and $\mathbf{R}$ is the position of the group origin relative to the molecular origin. Note that the order of states in the subscripts must be reversed in each term because the order of states in the matrix element is reversed. Thus we have

$$
\begin{aligned}
(\mathbf{r} \times \boldsymbol{\nabla})_{A0} &= (\Psi_A^1 | \mathbf{r} \times \hat{\boldsymbol{\nabla}} | \Psi_0^1) \\
&= (\mathbf{r} \times \boldsymbol{\nabla})_{ia0} - 2 \sum_{j \neq i} \sum_{b \neq a} \frac{\nu_a V_{i0a;j0b}}{h(\nu_b^2 - \nu_a^2)} (\mathbf{r} \times \boldsymbol{\nabla})_{jb0} \\
&\quad - \sum_{j \neq i} \sum_{b \neq a} \frac{V_{iab;j00}}{h(\nu_b - \nu_a)} (\mathbf{r} \times \boldsymbol{\nabla})_{ib0} - \sum_{j \neq i} \sum_{b \neq a} \frac{V_{i0b;j00}}{h \nu_b} (\mathbf{r} \times \boldsymbol{\nabla})_{iab} \\
&\quad + \mathbf{R}_i \times \boldsymbol{\nabla}_{ia0} - 2 \sum_{j \neq i} \sum_{b \neq a} \frac{\nu_a V_{i0a;j0b}}{h(\nu_b^2 - \nu_a^2)} \mathbf{R}_j \times \boldsymbol{\nabla}_{jb0} \\
&\quad - \sum_{j \neq i} \sum_{b \neq a} \frac{V_{iab;j00}}{h(\nu_b - \nu_a)} \mathbf{R}_i \times \boldsymbol{\nabla}_{ib0} - \sum_{j \neq i} \sum_{b \neq a} \frac{V_{i0b;j00}}{h \nu_b} \mathbf{R}_i \times \boldsymbol{\nabla}_{iab}. \qquad \text{(S10)}
\end{aligned}
$$

Comparing this expression with Tinoco's Eq. (IIIB-20), we find that the first four terms of Eq. S10 agree in form with (IIIB-20f) through (III B-20i), except for what is clearly a misprint in Tinoco's review in (IIIB-20f): $\mathbf{m}_{i0a}$ should be $\mathbf{m}_{ia0}$. There is a difference in sign between the fourth term on the rhs of Eq. (S10) and (IIIB-20i) of Tinoco, but this is accompanied by a reversal in the order of the subscripts. Substitution of $\boldsymbol{\mu}$ for $\boldsymbol{\nabla}$ demonstrates that the last four terms of Eq. (S10) are equivalent to Tinoco's terms (IIIB-20a)–(IIIB-20d), with the proviso that he disregarded the order of the subscripts in the electric dipole transition moments because they are immaterial.

We are now ready to develop the expression for the rotational strength in the dipole velocity formalism:

$$
\begin{aligned}
R_A = -\frac{e^2 \hbar^2}{4\pi m^2 c \nu_A} \boldsymbol{\nabla}_{0A} \bullet (\mathbf{r} \times \boldsymbol{\nabla})_{A0} = -\frac{e^2 \hbar^2}{4\pi m^2 c \nu_A} \Bigg\{ \boldsymbol{\nabla}_{i0a} - 2 \sum_{j \neq i} \sum_{b \neq a} \frac{\nu_a V_{i0a;j0b}}{h(\nu_b^2 - \nu_a^2)} \boldsymbol{\nabla}_{j0b} \\
- \sum_{j \neq i} \sum_{b \neq a} \frac{V_{iab;j00}}{h(\nu_b - \nu_a)} \boldsymbol{\nabla}_{i0b} - \sum_{j \neq i} \sum_{b \neq a} \frac{V_{i0b;j00}}{h \nu_b} \boldsymbol{\nabla}_{iba} \Bigg\}
\end{aligned}
$$

$$\bullet \left\{ (\mathbf{r}\times\boldsymbol{\nabla})_{ia0} - 2\sum_{j\neq i}\sum_{b\neq a}\frac{\nu_a V_{i0a;j0b}}{h(\nu_b^2-\nu_a^2)}(\mathbf{r}\times\boldsymbol{\nabla})_{jb0} \right.$$

$$- \sum_{j\neq i}\sum_{b\neq a}\frac{V_{iab;j00}}{h(\nu_b-\nu_a)}(\mathbf{r}\times\boldsymbol{\nabla})_{ib0} - \sum_{j\neq i}\sum_{b\neq a}\frac{V_{i0b;j00}}{h\nu_b}(\mathbf{r}\times\boldsymbol{\nabla})_{iab}$$

$$+ \mathbf{R}_i\times\boldsymbol{\nabla}_{ia0} - 2\sum_{j\neq i}\sum_{b\neq a}\frac{\nu_a V_{i0a;j0b}}{h(\nu_b^2-\nu_a^2)}\mathbf{R}_j\times\boldsymbol{\nabla}_{jb0}$$

$$\left. - \sum_{j\neq i}\sum_{b\neq a}\frac{V_{iab;j00}}{h(\nu_b-\nu_a)}\mathbf{R}_i\times\boldsymbol{\nabla}_{ib0} - \sum_{j\neq i}\sum_{b\neq a}\frac{V_{i0b;j00}}{h\nu_b}\mathbf{R}_i\times\boldsymbol{\nabla}_{iab}\right\}. \tag{S11}$$

Retaining only the first-order terms, this reduces to

$$R_A = -\frac{e^2\hbar^2}{4\pi m^2 c\nu_A}\{\boldsymbol{\nabla}_{i0a}\bullet(\mathbf{r}\times\boldsymbol{\nabla})_{ia0} \tag{S12a}$$

$$- 2\sum_{j\neq i}\sum_{b\neq a}\frac{\nu_a V_{i0a;j0b}}{h(\nu_b^2-\nu_a^2)}\boldsymbol{\nabla}_{\mathrm{i0a}}\bullet(\mathbf{r}\times\boldsymbol{\nabla})_{jb0} \tag{S12b}$$

$$- \sum_{j\neq i}\sum_{b\neq a}\frac{V_{iab;j00}}{h(\nu_b-\nu_a)}\boldsymbol{\nabla}_{\mathrm{i0a}}\bullet(\mathbf{r}\times\boldsymbol{\nabla})_{ib0} \tag{S12c}$$

$$- \sum_{j\neq i}\sum_{b\neq a}\frac{V_{i0b;j00}}{h\nu_b}\boldsymbol{\nabla}_{i0a}\bullet(\mathbf{r}\times\boldsymbol{\nabla})_{iab} \tag{S12d}$$

$$- 2\sum_{j\neq i}\sum_{b\neq a}\frac{\nu_a V_{i0a;j0b}}{h(\nu_b^2-\nu_a^2)}\boldsymbol{\nabla}_{j0b}\bullet(\mathbf{r}\times\boldsymbol{\nabla})_{ia0} \tag{S12e}$$

$$- \sum_{j\neq i}\sum_{b\neq a}\frac{V_{iab;j00}}{h(\nu_b-\nu_a)}\boldsymbol{\nabla}_{i0b}\bullet(\mathbf{r}\times\boldsymbol{\nabla})_{ia0} \tag{S12f}$$

$$- \sum_{j\neq i}\sum_{b\neq a}\frac{V_{i0b;j00}}{h\nu_b}\boldsymbol{\nabla}_{iba}\bullet(\mathbf{r}\times\boldsymbol{\nabla})_{ia0} \tag{S12g}$$

$$+ \boldsymbol{\nabla}_{i0a}\bullet\mathbf{R}_i\times\boldsymbol{\nabla}_{ia0} \tag{S12h}$$

$$- 2\sum_{j\neq i}\sum_{b\neq a}\frac{\nu_a V_{i0a;j0b}}{h(\nu_b^2-\nu_a^2)}\boldsymbol{\nabla}_{i0a}\bullet\mathbf{R}_j\times\boldsymbol{\nabla}_{jb0} \tag{S12i}$$

$$- \sum_{j\neq i}\sum_{b\neq a}\frac{V_{iab;j00}}{h(\nu_b-\nu_a)}\boldsymbol{\nabla}_{i0a}\bullet\mathbf{R}_i\times\boldsymbol{\nabla}_{ib0} \tag{S12j}$$

$$- \sum_{j\neq i}\sum_{b\neq a}\frac{V_{i0b;j00}}{h\nu_b}\boldsymbol{\nabla}_{i0a}\bullet\mathbf{R}_i\times\boldsymbol{\nabla}_{iab} \tag{S12k}$$

$$- 2\sum_{j\neq i}\sum_{b\neq a}\frac{\nu_a V_{i0a;j0b}}{h(\nu_b^2-\nu_a^2)}\boldsymbol{\nabla}_{j0b}\bullet\mathbf{R}_i\times\boldsymbol{\nabla}_{ia0} \tag{S12l}$$

$$- \sum_{j\neq i}\sum_{b\neq a} \frac{V_{iab;j00}}{h(\nu_b - \nu_a)} \nabla_{i0b} \bullet \mathbf{R}_i \times \nabla_{ia0}. \tag{S12m}$$

$$\left. - \sum_{j\neq i}\sum_{b\neq a} \frac{V_{i0b;j00}}{h\nu_b} \nabla_{iba} \bullet \mathbf{R}_i \times \nabla_{ia0} \right\} \tag{S12n}$$

Term (S12a) is the zeroth-order term. Term (S12b) is combined with term 12*e*:

$$-2\sum_{j\neq i}\sum_{b\neq a} \tfrac{\nu_a V_{i0a;j0b}}{h(\nu_b^2-\nu_a^2)} \nabla_{\mathrm{i0a}} \bullet (\mathbf{r}\times\nabla)_{jb0} - 2\sum_{j\neq i}\sum_{b\neq a} \tfrac{\nu_a V_{i0a;j0b}}{h(\nu_b^2-\nu_a^2)} \nabla_{j0b} \bullet (\mathbf{r}\times\nabla)_{ia0}$$

$$= -2\sum_{j\neq i}\sum_{b\neq a} \tfrac{\nu_a V_{i0a;j0b}}{h(\nu_b^2-\nu_a^2)} \{\nabla_{\mathrm{i0a}} \bullet (\mathbf{r}\times\nabla)_{jb0} + \nabla_{j0b} \bullet (\mathbf{r}\times\nabla)_{ia0}\}. \tag{S13}$$

Term (S12c) is combined with term (S12f):

$$-\sum_{j\neq i}\sum_{b\neq a} \tfrac{V_{iab;j00}}{h(\nu_b-\nu_a)} \nabla_{i0a} \bullet (\mathbf{r}\times\nabla)_{ib0} - \sum_{j\neq i}\sum_{b\neq a} \tfrac{V_{iab;j00}}{h(\nu_b-\nu_a)} \nabla_{i0b} \bullet (\mathbf{r}\times\nabla)_{ia0}$$

$$= -\sum_{j\neq i}\sum_{b\neq a} \tfrac{V_{iab;j00}}{h(\nu_b-\nu_a)} \{\nabla_{i0a} \bullet (\mathbf{r}\times\nabla)_{ib0} + \nabla_{i0b} \bullet (\mathbf{r}\times\nabla)_{ia0}\} \tag{S14}$$

Term (S12d) is combined with term (S12g):

$$-\sum_{j\neq i}\sum_{b\neq a} \frac{V_{i0b;j00}}{h\nu_b} \nabla_{i0a} \bullet (\mathbf{r}\times\nabla)_{iab} - \sum_{j\neq i}\sum_{b\neq a} \frac{V_{i0b;j00}}{h\nu_b} \nabla_{iba} \bullet (\mathbf{r}\times\nabla)_{ia0}$$

$$= -\sum_{j\neq i}\sum_{b\neq a} \frac{V_{i0b;j00}}{h\nu_b} \{\nabla_{i0a} \bullet (\mathbf{r}\times\nabla)_{iab} + \nabla_{iba} \bullet (\mathbf{r}\times\nabla)_{ia0}\}. \tag{S15}$$

Term (S12h) is zero because two factors in the scalar triple product are antiparallel. Term (S12i) is combined with term (S12l):

$$-2\sum_{j\neq i}\sum_{b\neq a} \frac{\nu_a V_{i0a;j0b}}{h(\nu_b^2-\nu_a^2)} \nabla_{i0a} \bullet \mathbf{R}_j \times \nabla_{jb0} - 2\sum_{j\neq i}\sum_{b\neq a} \frac{\nu_a V_{i0a;j0b}}{h(\nu_b^2-\nu_a^2)} \nabla_{j0b} \bullet \mathbf{R}_i \times \nabla_{ia0}$$

$$= -2\sum_{j\neq i}\sum_{b\neq a} \frac{\nu_a V_{i0a;j0b}}{h(\nu_b^2-\nu_a^2)} \nabla_{j0b} \bullet (\mathbf{R}_j - \mathbf{R}_i) \times \nabla_{ia0}$$

$$= -2\sum_{j\neq i}\sum_{b\neq a} \frac{\nu_a V_{i0a;j0b}}{h(\nu_b^2-\nu_a^2)} \mathbf{R}_{ij} \bullet \nabla_{jb0} \times \nabla_{i0a}. \tag{S16}$$

Term (S12j) is combined with term (S12m):

$$-\sum_{j\neq i}\sum_{b\neq a} \frac{V_{iab;j00}}{h(\nu_b-\nu_a)} \nabla_{i0a} \bullet \mathbf{R}_i \times \nabla_{ib0} - \sum_{j\neq i}\sum_{b\neq a} \frac{V_{iab;j00}}{h(\nu_b-\nu_a)} \nabla_{i0b} \bullet \mathbf{R}_i \times \nabla_{ia0}$$

$$= -\sum_{j\neq i}\sum_{b\neq a} \frac{V_{iab;j00}}{h(\nu_b-\nu_a)} \{\nabla_{i0a} \bullet \mathbf{R}_i \times \nabla_{ib0} + \nabla_{i0b} \bullet \mathbf{R}_i \times \nabla_{ia0}\}$$

$$= -\sum_{j\neq i}\sum_{b\neq a} \frac{V_{iab;j00}}{h(\nu_b-\nu_a)} \{\nabla_{i0a} \bullet \mathbf{R}_i \times \nabla_{ib0} - \nabla_{i0a} \bullet \mathbf{R}_i \times \nabla_{ib0}\} = 0. \tag{S17}$$

Term (S12k) is combined with term (S12n):

$$-\sum_{j\neq i}\sum_{b\neq a}\frac{V_{i0b;j00}}{h\nu_b}\nabla_{i0a}\bullet\mathbf{R}_i\times\nabla_{iab}-\sum_{j\neq i}\sum_{b\neq a}\frac{V_{i0b;j00}}{h\nu_b}\nabla_{iba}\bullet\mathbf{R}_i\times\nabla_{ia0}$$

$$=-\sum_{j\neq i}\sum_{b\neq a}\frac{V_{i0b;j00}}{h\nu_b}\{\nabla_{i0a}\bullet\mathbf{R}_i\times\nabla_{iab}+\nabla_{iba}\bullet\mathbf{R}_i\times\nabla_{ia0}\}$$

$$=-\sum_{j\neq i}\sum_{b\neq a}\frac{V_{i0b;j00}}{h\nu_b}\{\nabla_{i0a}\bullet\mathbf{R}_i\times\nabla_{iab}-\nabla_{i0a}\bullet\mathbf{R}_i\times\nabla_{iab}\}=0. \tag{S18}$$

Thus, the rotational strength is

$$R_A=-\frac{e^2\hbar^2}{4\pi m^2 c\nu_A}\{\nabla_{i0a}\bullet(\mathbf{r}\times\nabla)_{ia0} \tag{S19a}$$

$$-2\sum_{j\neq i}\sum_{b\neq a}\frac{\nu_a V_{i0a;j0b}}{h(\nu_b^2-\nu_a^2)}\{\nabla_{i0a}\bullet(\mathbf{r}\times\nabla)_{jb0}+\nabla_{j0b}\bullet(\mathbf{r}\times\nabla)_{ia0}\} \tag{S19b}$$

$$-\sum_{j\neq i}\sum_{b\neq a}\frac{V_{iab;j00}}{h(\nu_b-\nu_a)}\{\nabla_{i0a}\bullet(\mathbf{r}\times\nabla)_{ib0}+\nabla_{i0b}\bullet(\mathbf{r}\times\nabla)_{ia0}\} \tag{S19c}$$

$$-\sum_{j\neq i}\sum_{b\neq a}\frac{V_{i0b;j00}}{h\nu_b}\{\nabla_{i0a}\bullet(\mathbf{r}\times\nabla)_{iab}+\nabla_{iba}\bullet(\mathbf{r}\times\nabla)_{ia0}\} \tag{S19d}$$

$$\left.-2\sum_{j\neq i}\sum_{b\neq a}\frac{\nu_a V_{i0a;j0b}}{h(\nu_b^2-\nu_a^2)}\mathbf{R}_{ij}\bullet\nabla_{jb0}\times\nabla_{i0a}\right\}. \tag{S19e}$$

Note that Eq. (S19) agrees in form with that of Tinoco's (IIIB-22) with two exceptions. The analog of (IIIB-22e), the "charge-transfer" term, is absent. Term (S19e) has the factor ∇_{jb0} in contrast to $\boldsymbol{\mu}_{j0b}$ in Tinoco's Eq. (IIIB-22f), but use of the relationship between $\boldsymbol{\mu}$ and ∇ demonstrates that the two expressions are equivalent. Unlike the dipole-length form [Eq. (20.16)], this form is origin-independent, as should be the case.

TABLE S1. Calculations with the Tinoco Method

Year	Reference	Subject Studied	States Included[a]	Comments
1962	1	Cotton effect of α helix at 225 nm	$n\pi^*$, NV_1, NV_2	Cotton effect at 225 nm is the result of mixing of $n\pi^*$ and $\pi\pi^*$ states.
1966	2	$n\pi^*$ and $\pi\pi^*$ rotational strengths of parallel and antiparallel β-pleated sheets of poly-L-lysine	$n\pi^*$, $\pi\pi^*$	Contributions of exciton interactions are small for β structure in contrast to α helix.
1967	3	Non conservative character of the CD spectra of dinucleoside phosphates	$\pi\pi^*$ of near UV, polarizability approximation for far UV	Far-UV transitions cause spectra similar to those observed.
1967	4	α helix and 3_{10} helix of poly-L-alanine	$n\pi^*$, $n'\pi^*$, $n\sigma^*$, NV_1, NV_2; polarizability approximation for higher states	Three CD bands predicted above 190 nm.
1967	5	Poly-L-proline I and II, collagen triple helix	$n\pi^*$, $n'\pi^*$, $n\sigma^*$, NV_1; polarizability approximation for higher states	Exciton contributions dominate for PPI; for PPII, these are weaker and non-exciton contributions to high-energy exciton band are dominant.
1968	6	Charge transfer between two hydrogen-bonded peptide groups	L$n\pi^*$, L$\pi\pi^*$, CT$n\pi^*$, CT$\pi\pi^*$[a]	Mixing of the $n\pi^*$state with intergroup charge transfer does not contribute significantly to the $n\pi^*$ rotational strength of an α helix.
1969	7	Random coil poly-L-alanine	$n\pi^*$ $n'\pi^*$, NV_1, NV_2; polarizability approximation for higher states	Parameters either from reference 4 or from an *ab initio* study [8].
1969	9	Heme rotational strengths of myoglobin	Heme $\pi\pi^*$ transitions; Phe, Tyr, Trp, His $\pi\pi^*$ transitions; peptide $n\pi^*$, $\pi\pi^*$; $\sigma\sigma^*$ of alkyl side chains,	Coupling of heme with aromatic side chains is largely responsible for heme CD bands.
1970	10	ApA, poly(rA),poly(dA)	four $n\pi^*$, two $\pi\pi^*$	$n\pi^*$ transition will give rise to small CD bands.
1971	11	Heme rotational strength of sperm whale myoglobin and horse oxyhemoglobin	Heme $\pi\pi^*$ transitions; $n\pi^*$, $\pi\pi^*$ of peptide; E_{1u} of phenyl; B_2,A_1,B_2',A_1' of phenol; I–IV of imidazole and indole; $\sigma\sigma^*$of alkyl side chains	Coupling of heme transitions with $\pi\pi^*$ transitions in aromatics accounts for CD of all four heme transitions in both myoglobin and hemoglobin.
1972	12	Hemoglobin from *Chironomus thummi thummi*	Soret state, $\pi\pi^*$ of aromatics and His	Coupling of the Soret state with the $\pi\pi^*$ states of the aromatics reproduces the negative sign of the Soret Cotton effect.
1972	13	Near-UV CD of ribonuclease S and A	NV_1, NV_2 of peptides; NV_1 of Gln, Asn, Glu, Asp; L_b,L_a,B_b,B_a of phenol; B_b, B_a of phenyl; 4 states of imidazolyl; 2 states of guanidino of Arg	About 70% of the CD at 275 nm is due to coupling of the ^1L_b tyrosyl band with $\pi\pi^*$ transitions of other groups.

(*continued*)

TABLE S1. (*Continued*)

Year	Reference	Subject Studied	States Included[a]	Comments
1973	14	Vacuum UV CD of alkyl amino acids	See original paper for details	Signs of $n\pi^*$ and $\pi\pi^*$ reproduced by calculations but magnitudes uncertain; can define conformation of carboxylate group.
1976	15	Tyrosyl CD of monomers, dimers, and hexamers of pig insulin	See entry for reference 13	CD at 275 nm strongly increases upon formation of dimers and hexamers, about 40% of the tyrosyl CD of the hexamer comes from the interaction of A14-tyrosine and B1-phenylalanine.
1977	16	Tyrosyl CD of monomers, dimers, and hexamers of des-B1-Phe-insulin	See entry for reference 13	Probably due to the dynamics of side chains, B1-phenylalanine does not contribute significantly to the A14-tyrosine CD.
1978	17	Hemoglobin from *Chironomus thummi thummi*	Soret, $\pi\pi^*$ of aromatics, states of the peptide backbone; see also reference 11 and 13	Calculated rotational strength in reasonable agreement with experimental value, role of aromatic side-chain probably overestimated in reference 12.
1983	18	CD of cyclic dimers of amino acids	$n\pi^*$, NV_1, NV_2, $n\sigma^*$, $\pi\sigma^*$, $\sigma\sigma^*$, polarizability approximation for higher states	Intense bands below 180 nm are probably due to $\sigma\sigma^*$ transitions of the backbone.
1993	19	Optical activity of hemoproteins in the Soret region	Soret; $n\pi^*$, $\pi\pi^*$ for peptides; $\pi\pi^*$ for imidazole; higher states of peptides and thioethers by the polarizability approximation.	Intrinsic chirality due to deviations of the heme from planarity contributes significantly to the Soret CD; as to possible origins of such distortions see references 20 and 21.
2002	22	Intrinsic optical activity of hemoproteins in the Soret region	Soret; $n\pi^*$, $\pi\pi^*$ for peptides; $\pi\pi^*$ for aromatics; high-energy states of peptide and Met sulfur	MD simulations performed; intrinsic rotational strength contributes significantly, correlating with heme ruffling.
2008	23	Schiff base retPSB chromophore of rhodopsin	$n\pi^*$, $\pi\pi^*$ for peptides; $\pi\pi^*$ for aromatics; states of retPSB calculated by TDDFT and ZINDO	CD bands in the Vis and near UV are largely determined by the intrinsic chirality of the retinal.

[1]J. A. Schellmann, P. Oriel, *J. Chem. Phys*. **1962**, *37*, 2114–2124.
[2]E. S. Pysh, *Proc. Natl. Acad. Sci. USA*, **1966**, *56*, 825–32.
[3]C. A. Bush, J. Brahms, *J. Chem. Phys*. **1967**, *46*, 79–88.
[4]R. W. Woody, I. Tinoco Jr., *J. Chem. Phys*. **1967**, *46*, 4927–4945.
[5]E. S. Pysh, *J.Mol.Biol*. **1967**, *23*, 587–599.
[6]R. W. Woody, *J. Chem. Phys*. **1968**, *49*, 4797–4806.
[7]A. E. Tonelli, *Macromolecules* **1969**, *2*, 635–637.

[8]H. Basch, M. B. Robin, N. A. Kuebler, *J. Chem. Phys*. **1968**, *49*, 5007–5018.
[9]M.-C. Hsu, R. W. Woody, *J. Am. Chem. Soc*. **1969**, *91*, 3679–3681.
[10]C. A. Bush, *J. Chem. Phys*. **1970**, *53*, 3522–3530.
[11]M.-C. Hsu, R. W. Woody, *J. Am. Chem. Soc*. **1971**, *93*, 3515–3525.
[12]J. Fleischhauer, A. Wollmer, *Z. Naturforsch*. **1972**, 27*b*, 530–532.
[13]E. H. Strickland, *Biochemistry* **1972**, *11*, 3465–3474.
[14]P. A. Snyder, P. M. Vipond, W. C. Johnson, Jr., *Biopolymers* **1973**, *12*, 975–992.
[15]E. H. Strickland, D. Mercola, *Biochemistry* **1976**, *15*, 3875–3884.
[16]A. Wollmer, J. Fleischhauer, W. Strassburger, H. Thiele, D. Brandenburg, G. Dodson, D. Mercola, *Biophys. J*. **1977**, *20*, 233–243.
[17]W. Strassburger, A. Wollmer, H. Thiele, J. Fleischhauer, W. Steigemann, E. Weber, *Z. Naturforsch*, **1978**, 33*c*, 908–911.
[18]R. L. Bowman, M. Kellerman, W. C. Johnson, Jr., *Biopolymers* **1983**, *22*, 1045–1070.
[19]G. Blauer, N. Sreerama, R. W. Woody, *Biochemistry* **1993**, *32*, 6674–6679.
[20]W. Jentzen, J.-G. Ma, J. A. Shelnutt, *Biophys. J*. **1998**, *74*, 753–763.
[21]W. Jentzen, X.-Z. Song, J. A. Shelnutt, *J. Phys. Chem. B* **1997**, *101*, 1684–1699.
[22]C. Kiefl, N. Sreerama, R. Haddad, L. Sun, W. Jentzen, Y. Qiu, J. A. Shelnutt, R. W. Woody, *J. Am. Chem. Soc*. **2002**, *124*, 3385–3394.
[23]G. Pescitelli, N. Sreerama, P. Salvadori, K. Nakanishi, N. Berova, R. W. Woody, *J. Am. Chem. Soc*. **2008**, *130*, 6170–6181.
[a]L, Local; CT, charge transfer.

TABLE S2. Calculations with the Matrix Method

Year	Reference	Subject Studied	States Included[b]	Comments
1969	1	Model compound with two peptide groups connected by an α carbon	$n\pi^*$, NV_1	Introduction of the matrix method.
1969	2	$n\pi^*$ and $\pi\pi^*$ bands of parallel and antiparallel β-sheets of poly-L-lysine and poly-L-serine	$n\pi^*$, $\pi\pi^*$	Model β sheets probably exist in the antiparallel β structure.
1970	3	α helix, β sheet, poly(Pro) helices	$n\pi^*$, $\pi\pi^*$, $n'\pi^*$	Good agreement, except for poly(Pro)II helix.
1971	4	Poly-L-tyrosine	$n\pi^*$, lowest $\pi\pi^*$ for peptide, 4 lowest states of phenol	Compound probably forms a right-handed helix in solution; see also references 5 and 6
1972	7	α helix, β structures, polyproline I, polyproline II, collagen, poly-*N*-methyl alanine, α, β, and nonperiodic regions of of myoglobin, lysozyme, ribonuclease S, α-chymotrypsin	$n\pi^*$, NV_1	Applied methods adequately describe the optical activity of the ordered polypeptides except polyproline II and collagen.
1972	8	Poly-L-phenylalanine and *p*-substituted derivatives	See original paper for details[a]	These aromatic polypeptides probably form right handed helices.
1973	9	CD of gliotoxin and related compounds	Peptide $n\pi^*$, $\pi\pi^*$ disulfide $n\sigma^*$, $n_S \rightarrow$ peptide π^* CT	CT transitions from sulfur nonbonding to amide π^* orbitals account for bands observed at 260 and 310 nm.
1975	10	Contribution of Tyr to optical activity of ribonuclease S	See original paper for details	Positive ellipticity at 240 nm entirely due to ^1L_a state of Tyr.
1974	11	CD contributions of base interactions with sugar and phosphate in DNA and RNA	$\pi\pi^*$ in bases, high-energy transitions in sugars and P	Negligible effects.
1974	12	Ala and Pro diketopiperazines	Peptide $n\pi^*$, NV_1	Rule relating sign of $\pi\pi^*$ couplet to folding of DKP ring; DKP ring in cyclo(Ala-Ala) in solution is folded in opposite sense to crystal
1974	13	DNA and RNA	$\pi\pi^*$ in bases	Tilting of base pair planes and distance from helix axis are important; either theory or geometry are inaccurate.
1974	14	DNA and RNA	$n\pi^*$ and $\pi\pi^*$ in bases	R ~0.1 DBM for $n\pi^*$ in guanine, others small.
1974	15	DNA and RNA—effects of choice of wavefunctions	$n\pi^*$ and $\pi\pi^*$ in bases	Large variation, none of the tested wave functions gave uniquely satisfactory results.
1974	16	β turns	Peptide $n\pi^*$, NV_1	CD spectra varied but dominant pattern is like that of β sheet, but red-shifted ~10 nm.
1975	17	cyclo(Ala-His), cyclo(His-His)	peptide $n\pi^*$, NV_1; first $\pi\pi^*$ trans. of imidazole	His side-chain conformation in cyclo(Ala-His) depends on protonation state.

1978	18	Contributions of aromatic side chains in di- and tripeptides	$n\pi^*$, NV_1, NV_2 for amide; L_a,L_b,B_a,B_b for aromatics; further details in references 4 and 8	L_a rotational strength has a positive sign in the preferred conformations.
1980	19	Near-UV CD of ribonuclease S	$n_1\sigma^*$, $n_4\sigma^*$ for disulfide; ^1L_b, ^1L_a, ^1B_b, ^1B_a for Tyr; $\pi\pi^*_1$, $\pi\pi^*_2$ for His	Introduced origin-independent version of matrix method; near-UV CD contains significant contributions of disulfides and Tyr.
1980	20	Near-UV CD of lysozyme	For details see original paper	Near-UV CD of lysozyme can be explained in terms of negative rot. strength due to Trp ^1L_a and S_2 $n\sigma^*$ and of positive rotational strength due to Trp and Tyr ^1L_b bands.
1981	21	AcAlaNHMe and AcSerNHMe	Peptide $n\pi^*$, NV_1	Conformational energy calculations give reasonable results for these dipeptides in nonpolar solvents, but not in polar solvents.
1981	22	Conformational dependence of DNA CD	$\pi\pi^*$ in bases	275-nm positive band correlates linearly with helix winding angle and base-pair twist; correlation with other geometric parameters is weaker.
1982	23	Adenylate kinase	$n\pi^*$, NV_1 for peptide; B_b, B_a for Phe; L_b, L_a, B_a, B_b for Tyr	Computational results in reasonable agreement with experiment.
1984	24	DNA and RNA	$\pi\pi^*$ in bases	Mixed sequence DNA in B and A form and RNA in A form reproduced well, but simple-sequence DNA and RNA are not, including $(dG\text{-}dC)_n$ in Z-form.
1986	25	DNA, RNA	$\pi\pi^*$ in bases	Sign of couplet below 200 nm is correlated with helix sense of DNA
1987	27	Proteins with closely packed antiparallel β sheets	lowest $n\pi^*$, NV_1	First theoretical study of the effects of the interaction of two secondary structures on the CD of proteins.
1987	28	DNA	$\pi\pi^*$ in bases	Distance-dependent dielectric constant and oligonucleotide crystal structures gave good agreement for B-DNA but not for Z-DNA.
1988	29	α helices, twisted β sheets, and β turns	$n\pi^*$, NV_1	The minimum number of turns to give the characteristic spectrum on an α helix is two or three; twist strongly affects CD of β sheets.

(*continued*)

TABLE S2. (*Continued*)

Year	Reference	Subject Studied	States Included[b]	Comments
1989	30	Bovine pancreatic trypsin inhibitor	$n\pi^*$, $n'\pi^*$, NV_1, NV_2 for peptides; L_a, L_b, B_a, B_b for aromatics	Both Tyr and Phe side chains must be included to get good agreement with experimental data; almost all rotational strength at 275 nm comes from the L_b state of Tyr.
1990	31	Tropomyosin, effect of conformation on the CD of interacting helices	$n\pi^*$, NV_1, for peptides, L_a, L_b, B_a, B_b for aromatics	See original paper for details.
1990	32	G quartets	$\pi\pi^*$ transitions at 280, 250, and 202 nm in G	Experimental spectrum reproduced with geometry from fiber diffraction.
1991	33	Right-handed α, $\alpha_{II}, \omega, \pi, 3_{10}$ helices; poly(Pro) helices; effect of hybridization	Peptide $n\pi^*$, $n'\pi^*$, NV_1, NV_2	Inclusion of NV_2 significantly improves the calculated CD between 180 and 250 nm.
1993	34	CD tensor elements of parallel and antiparallel β sheets	Peptide $n\pi^*$, NV_1	CD in all three principal directions are different; calculated CD sensitive to choice of position for NV_1 transition.
1994	35	Cyclo(Tyr-Tyr)	Peptide $n\pi^*$, NV_1; Tyr L_b, L_a, B_a, B_b, $\sigma\pi^*$, $\pi\sigma^*$	Calculated CD averaged over an MD trajectory; solvent has little effect on calculated CD of a given conformer but must be included in MD to promote conformational transitions.
1994	36	Contributions of Trp to far UV CD of proteins	The six lowest states of indole; $n\pi^*$, NV_1 for peptide	Trp B_b state can contribute significantly to the CD around 225 nm.
1997	37	CD of ribonuclease A and S	$n\pi^*$, NV_1, NV_2 in peptides; Tyr and Phe L_b, L_a, B_a, B_b; $n_1\sigma^*$ and $n_4\sigma^*$ for disulfide; for other side-chain transitions, see original paper	Near-UV CD largely due to Tyr 73 and 115; disulfide largely responsible for 240-nm band; far-UV CD not reproduced well.
1998	38	CD of four Tyr → Phe mutants of the F1 gene 5 single-stranded DNA binding protein (g5p)	$n\pi^*$, $n'\pi^*$, NV_1, NV_2, for peptide; L_a, L_b, B_a, B_b for aromatics	Structure of g5p in solution probably differs from that stabilized in the crystal.
1998	39	Comparison of *ab initio*-derived and semiempirically derived electronic parameters	$n\pi^*$, NV_1 for peptide	CD of 20 proteins calculated, correlation between calculated and measured intensities at 220 nm tested.
1998	40	Comparison of *ab initio* and semiempirically derived electronic parameters	$n\pi^*$, NV_1 for peptide	CD of 23 proteins calculated, correlation between calculated and measured intensities at 190 and 220 nm tested.
1999	41	Comparison of semiempirically- and *ab initio*-derived electronic parameters	$n\pi^*$, NV_1, NV_2 for peptide	Used new INDO/S parameters and Clark's transition moment direction [42] for NV_1 of *N*-acetylglycine; improvement over the results in references 39 and 40

1999	43	Comparison of *ab initio*-and semiempirically derived electronic parameters	$n\pi^*$, NV_1 for peptide	See original paper for comments on reference 41
1999	44	Performance of solution phase *ab initio* parameters for CD calculations	$n\pi^*$, NV_1 for peptide	CD of 29 proteins calculated, correlation at 190, 208, and 220 nm tested.
1999	45	Pancreatic trypsin inhibitor	$n\pi^*$, NV_1, $n'\pi^*$, NV_2 for peptide; L_b, L_a, B_b, B_a for aromatics; two lowest $n\sigma^*$ in disulfides	Far-UV CD difference spectra of four mutants in which aromatic side chains are replaced by Leu are reproduced reasonably well, two are not.
2000	46	Influence of hydrogen bonding on electronic parameters for CD calculations on proteins	$n\pi^*$, $n'\pi^*$, NV_1, NV_2 for peptide	No improvement over the results obtained with a parameter set obtained with a continuum solvent model, CD of 29 proteins calculated.
2001	47	Class A β-lactamase from *Escherichia coli* (TEM-1)	$n\pi^*$, NV_1, NV_2, for peptide; L_a, L_b, B_a, B_b for indole; for rest see reference 37	Omission of Trp results in a reversal of the sign of the Cotton effect at 280 nm.
2002	48	Interaction of Phe and Tyr side chains with Lys and Arg side chains and helicity of α-helices	$n\pi^*$, NV_1 for peptide; L_a, L_b, B_a, B_b for aromatics	Tyr-Lys and Phe-Lys interactions are similar and strongly depend on the side-chain conformation.
2002	49	Short α helices	$n\pi^*$, NV_1, NV_2 for peptide	NV_1 transition moment direction has large effect on calculated CD; Clark's [42] value gives best result; helices as short as one turn have qualitatively same pattern as long helices.
2003	50	Individual Tyr side-chain contributions to the CD of ribonuclease	$n\pi^*$, NV_1, NV_2 for peptide; L_a, L'_a, B_a, B_b for Phe; L_b, L_a, B_a, B_b for Tyr; $n\sigma^*$ for disulfides	Sign and approximate magnitude of L_b CD for each of six Tyr correctly predicted.
2003	51	Influence of Tyr on the CD of helical peptides	$n\pi^*$, NV_1 for peptide, L_a, L_b, B_a, B_b for Tyr	Tyr can contribute as much as $\pm$5000 deg cm^2 dmol^{-1} to mean residue ellipticity at 220 nm.
2003	52	Performance of solution phase *ab initio* parameters for CD calculations	$n\pi^*$, NV_1 for peptide	CD of 47 proteins in the far UV calculated, correlation at 190, 208, and 220 nm tested, best results for proteins with high α-helical content.
2004	53	β-lactamase, barnase, human carbonic anhydrase II	$n\pi^*$, NV_1 for peptide, ^1L_a, ^1L_b, ^1B_a, ^1B_b for Tyr, Phe, Trp	Side chains have a marked influence on the near and far UV CD, parameters from *ab initio* calculations.
2004	54	Influence of aromatic side-chains on the CD of proteins	$n\pi^*$, NV_1 for peptide ^1L_a, ^1L_b, ^1B_a, ^1B_b for aromatics	Parameters from *ab initio* calculations reproduce near-UV CD spectra better than previously used semiempirical parameters.
2004	55	Influence of charge transfer states on the CD of proteins	$Ln\pi^*$, $L\pi\pi^*$, $CTn\pi^*$, $CT\pi\pi^{*b}$	Electronic parameters derived from *ab initio* calculations on model compounds with two peptide groups for the states including CT between the two groups.

(*continued*)

TABLE S2. (*Continued*)

Year	Reference	Subject Studied	States Included[b]	Comments
2007	56	CD of palmitoyltransferase PagP	$n\pi^*$, NV_1, NV_2 for peptide; ^1L_a, L_b, B_a, B_b for Tyr, Trp; L_a, B_a, B_b for Phe	Exciton coupling between Tyr 26 and Trp 66 produces positive band at 233 nm and provides a sensitive conformational probe.
2008	57	G quartets	$\pi\pi^*$ in bases	Calculations reproduce empirical correlation between CD spectra of G quartets and the relative polarity of stacked quartets.
2008	58	s^6G in DNA	$\pi\pi^*$ in bases	Calculations reproduce the observed long-wavelength band in 6-thioG probes introduced at various positions.
2008	59	Influence of charge transfer states on the CD of proteins	$Ln\pi^*$, $L\pi\pi^*$, $CTn\pi^*$, $CT\pi\pi^*$[b]	Vacuum-UV CD of 71 proteins calculated. Agreement with experiment significantly improved.
2009	60	Poly(Pro)II helix of poly(Ala) and poly(Pro)	$n\pi^*$, NV_1, NV_2 for peptide; high-energy transitions in backbone and side chain	Modified exciton model reproduces CD of poly(Ala) in poly(Pro)II conformation well, but not that of poly(Pro).
2010	61	α-rich proteins (hemoglobin, leptin, tropomyosin), β-rich proteins (lectin, monellin, Ftsz)	$n\pi^*$ and NV_1 for peptides	Combined MD simulation with CD calculations for structures along trajectory, taking into account spread in transition energies due to structural variation and electrostatic energies.
2010	62	Retinal Schiff base dimer	Lowest energy $\pi\pi^*$ transition	Introduced transition density fragment interaction method for calculating coupling between the retinal chromophores; good agreement with *ab initio* splitting.

[1]P. M. Bayley, E. B. Nielsen, J. A. Schellman, *J. Phys. Chem.* **1969**, *73*, 228–243.
[2]R. W. Woody, *Biopolymers* **1969**, *8*, 669–683.
[3]E. S. Pysh, *J. Chem. Phys*. **1970**, *52*, 4723–4733.
[4]A. K. Chen, R. W. Woody, *J. Am. Chem. Soc*. **1971**, *93*, 29–37.
[5]T. Ooi, R. A. Scott, G. Vanderkooi, H. A. Scheraga, *J.Chem.Phys*. **1967**, *46*, 4410–4426.
[6]J. F. Yan, G. Vanderkooi, H. A. Scheraga, *J. Chem. Phys*. **1968**, *49*, 2713–2726.
[7]V. Madison, J. Schellman, *Biopolymers* **1972**, *11*, 1041–1076.
[8]R. W. Woody, *Biopolymers* **1972**, *11*, 1149–1171.
[9]R. Nagarajan, R. W. Woody, *J. Am. Chem. Soc*., **1973**, *95*, 7212–7222.
[10]W. J. Goux, T. M. Hooker, Jr., *J. Am. Chem. Soc*. **1975**, *97*, 1605–1606.
[11]D. S. Moore, T. E. Wagner, *Biopolymers*, **1974**, *13*, 977–986.
[12]T. M. Hooker, Jr., P. M. Bayley, W. Radding, J. A. Schellman, *Biopolymers*, **1974**, *13*, 549–566.
[13]D. S. Studdert, R. C. Davis, *Biopolymers* **1974**, *13*, 1377–1389.

[14]D. S. Studdert, R. C. Davis, *Biopolymers* **1974**, *13*, 1391–1403.
[15]D. S. Studdert, R. C. Davis, *Biopolymers* **1974**, *13*, 1405–1416.
[16]R. W. Woody, Studies of theoretical circular dichroism of polypeptides: Contributions of ß turns, in *Peptides Polypeptides and Proteins*, E. R. Blout, F. A. Bovey, M. Goodman, and N. Lotan, Eds., John Wiley & Sons, New York, **1974**, pp. 338–350.
[17]P. E. Grebow, T. M. Hooker, *Biopolymers* **1975**, *14*, 1863–1883.
[18]R. W. Woody, *Biopolymers* **1978**, *17*, 1451–1467.
[19]W. J. Goux, T. M. Hooker, Jr., *J. Am. Chem. Soc*. **1980**, *102*, 7080–7087.
[20]W. J. Goux, T. M. Hooker, Jr., *Biopolymers* **1980**, *19*, 2191–2208.
[21]J. M. Dungan, III, T. M. Hooker, Jr., *Macromolecules* **1981**, *14*, 1812–1822.
[22]B. B. Johnson, K. S. Dahl, I. Tinoco, Jr., V. I. Ivanov, V. B. Zhurkin, *Biochemistry* **1981**, *20*, 73–78.
[23]R. W. Snyder, T. M. Hooker, Jr., *Biopolymers* **1982**, *21*, 547–563.
[24]V. Rizzo, J. A. Schellman, *Biopolymers* **1984**, *23*, 435–470.
[25]A. L. Williams, C. Cheong, I. Tinoco, Jr., L. B. Clark, *Nucl. Acids Res*. **1986**, *14*, 6649–6659.
[26]D. S. Moore, A. L. Williams, *Biopolymers* **1986**, *25*, 1461–1491.
[27]M. C. Manning, R. W. Woody, *Biopolymers* **1987**, *26*, 1731–1752.
[28]D. E. Callahan, T. M. Hooker, Jr., *Biopolymers* **1987**, *26*, 457–461.
[29]M. C. Manning, M. Illangasekare, R. W. Woody, *Biophys. Chem*. **1988**, *31*, 77–86.
[30]M. C. Manning, R. W. Woody, *Biochemistry* **1989**, *28*, 8609–8613.
[31]T. M. Cooper, R. W. Woody, *Biopolymers* **1990**, *30*, 657–676.
[32]G. Gottarelli, P. Palmieri, G. P. Spada, *Gazz. Chim. Ital*. **1990**, *120*, 101–107.
[33]M. C. Manning, R. W. Woody, *Biopolymers* **1991**, *31*, 569–586.
[34]R. W. Woody, *Tetrahedron: Asymmetry* **1993**, *4*, 529–544.
[35]J. Fleischhauer, J. Grötzinger, B. Kramer, P. Krüger, A. Wollmer, R. W. Woody, E. Zobel, *Biophys. Chem*. **1994**, *49*, 141–152.
[36]R. W. Woody, *Eur. Biophys. J*. **1994**, *23*, 253–262.
[37]G. Kurapkat, P. Krüger, A. Wollmer, J. Fleischhauer, B. Kramer, E. Zobel, A. Koslowski, H. Botterweck, R. W. Woody, *Biopolymers* **1997**, *41*, 267–287.
[38]T. M. Thompson, B. L. Mark, C. W. Gray, T. C. Terwilliger, N. Sreerama, R. W. Woody, D. M. Gray, *Biochemistry* **1998**, *37*, 7463–7477.
[39]J. D. Hirst, *Enantiomer* **1998**, *3*, 215–220.
[40]J. D. Hirst, *J. Chem. Phys*. **1998**, *109*, 782–788.
[41]R. W. Woody, N. Sreerama, *J. Chem. Phys*. **1999**, *111*, 2844–2845.
[42]L. B. Clark, *J. Am. Chem. Soc*. **1995**, *117*, 7974–7986.
[43]J. D. Hirst, N. A. Besley, *J. Chem. Phys*. **1999**, *111*, 2846–2847.
[44]N. A. Besley, J. D. Hirst, *J. Am. Chem. Soc*. **1999**, *121*, 9636–9644.
[45]N. Sreerama, M. C. Manning, M. E. Powers, J.-X. Zhang, D. P. Goldenberg, R. W. Woody, *Biochemistry* **1999**, *38*, 10814–10822.
[46]N. A. Besley, J. D. Hirst, *J. Mol. Struct. (Theochem)* **2000**, *506*, 161–167.
[47]C. Christov, S. Gabriel, B. Atanasov, J. Fleischhauer, *Z. Naturforsch*. **2001**, *56a*, 757–760.
[48]C. D. Andrew, S. Bhattacharjee, N. Kokkoni, J. D. Hirst, G. R. Jones, A. J. Doig, *J. Am. Chem. Soc*. **2002**, *124*, 12706–12714.
[49]D.-H. Chin, R. W. Woody, C. A. Rohl, R. L. Baldwin, *Proc. Natl. Acad. Sci. USA*, **2002**, *99*, 15416–15421.
[50]A-Y. M. Woody, R. W. Woody, *Biopolymers* **2003**, *72*, 500–513.
[51]S. Bhattacharjee, G. Tóth, S. Lovas, J. D. Hirst, *J. Phys. Chem. B* **2003**, *107*, 8682–8688.

TABLE S2. (*Continued*)

[52]J. D. Hirst, K. Colella, A. T. B. Gilbert, *J. Phys. Chem. B* **2003**, *107*, 11813–11819.
[53]D. M. Rogers, J. D. Hirst, *Chirality* **2004**, *16*, 234–243.
[54]D. M. Rogers, J. D. Hirst, *Biochemistry* **2004**, *43*, 11092–11102.
[55]A. T. B. Gilbert, J. D. Hirst, *J. Mol. Struct. (Theochem)* **2004**, *675*, 53–60.
[56]M. A. Khan, C. Neale, C. Michaux, R. Pomès, G. Privé, R. W. Woody, R. E. Bishop, *Biochemistry* **2007**, *46*, 4565–4579.
[57]D. M. Gray, J.-D. Wen, C. W. Gray, R. Repges, C. Repges, G. Raabe, J. Fleischhauer, *Chirality* **2008**, *20*, 431–440.
[58]R. Repges, C. Beuck, E. Weinhold, G. Raabe, J. Fleischhauer, *Chirality* **2008**, *20*, 978–984.
[59]B. M. Bulheller, A. J. Miles, B. A. Wallace, J. D. Hirst, *J. Phys. Chem. B* **2008**, *112*, 1866–1874.
[60]R. W. Woody, *J. Am. Chem. Soc*. **2009**, *131*, 8234–8245.
[61]J. Jiang, D. Abramavicius, B. M. Bulheller, J. D. Hirst, S. Mukamel, *J. Phys. Chem. B* **2010**, *114*, 8270–8277.
[62]K. J. Fujimoto, *J. Chem. Phys*. **2010**, *133*, 124101-1–124101-9.
[a]Choice of states in the calculations critically depends on the substituents.
[b]CT: charge transfer; L, local.

TABLE S3. Calculations Employing the DeVoe Theory and Its Derivatives

Year	Reference	Type[a]	Subject Studied	States Included	Comments
1964	1	D	Classical theory of absorption and refraction for molecular aggregates, molecular crystals, and polymers	General theory	Introduction of the polarizability or DeVoe theory.
1965	2	D	Classical theory of refraction, absorption, optical rotation, and circular dichroism of molecular aggregates, crystals and polymers	General theory	Results agree with those from quantum mechanical theories to the same order; sum rules show conservation of oscillator and rotational strength.
1971	3	D	Optical properties of 1-MeU crystal	Three lowest $\pi\pi^*$ transitions	Spectral shapes and intensities agree well with experiment for the first crystal band, less well for the second band.
1976	4	D	CD of Ado, ApA, and oligo(A)	Two $\pi\pi^*$ transitions at $\lambda > 220$ nm, two at 187.5 and 207 nm; three background bands at 119 nm	First application of DeVoe theory to poly nucleotides; good agreement obtained with an effective dielectric constant of 2.
1976	5	D	CD of poly(I) in multistranded geometries	Two $\pi\pi^*$ transitions at 246.5 and 266 nm for inosine	A negative CD at long wavelengths does not necessarily indicate a left-handed polynucleotide helix; supports a four-stranded helix with tilted bases.
1977	6	D	CD of double-stranded poly nucleotides with repeating sequence	Four $\pi\pi^*$ transitions between 186 and 281 nm for G and A, three between 175 and 270 nm for U and C; three background bands for each base at 119 nm	Non-nearest neighbor interactions might be important when three or more base pairs of the same kind appear in a sequence; agreement with experiment good for poly(A•U), poly(G•C), and poly(dG-dC); less satisfactory for other sequences and geometries.
1980	7	D	CD of Ado and 2′-dAdo	Four $\pi\pi^*$ transitions between 185 and 300 nm; three background bands at 119 nm for A	DeVoe theory in combination with the Kirkwood theory provides a basis for the calculation of CD spectra of nucleos(t)ides.
1983	8	D	CD of G- and C-containing nucleic acids	Four $\pi\pi^*$ transitions for G and C	Derivation of $\pi\pi^*$ transition parameters for G and C by comparison of calculated and measured CD spectra of cyclic GMP and cyclic CMP.

(*continued*)

TABLE S3. (*Continued*)

Year	Reference	Type[a]	Subject Studied	States Included	Comments
1986	9	D	CD of RNAs	The four lowest $\pi\pi^*$ states for each base	New parameters for A and U derived by optimizing transition moment parameters for calculating cyclic nucleotide CD; these, combined with those for G and C (see reference 8), resulted in better agreement between calculated and measured spectra for RNAs.
1987	10	D	CD of oligo(dG-dC) in the A, B, and Z form of DNA	The four lowest $\pi\pi^*$ states, three background transitions	The point dipole approximation leads to results comparable to those from the point monopole approximation; good results required modification of transition moment direction of second transition in G.
1993	11	D	Study of the importance of many-body effects for optical activity of aromatic compounds, allenes, acetylenes, dienes	See original paper	Perturbative approach to DeVoe theory.
1996	12	D	CD of 4,4'-biphenanthryl derivatives and related helicenes	^1B_b	The correct location of the interacting transition dipole moments is essential to reproduce the experimental spectra.
1998	13	D	CD of 4-substituted [2.2]-paracyclophanes	^1L_a, $^1B_{a,b}$	The L_a couplet is reproduced well; in the $B_{a,b}$ region, the sign of the couplet is given correctly but the intensity is underestimated.
2000	14	D	^1B couplet of dendrimers derived from the 1,1′-binaphthyl moiety	^1B	Careful quantitative analysis of CD data provides information regarding the conformation of the binaphthyl moiety.
2001	15	D	CD of aryl alkyl sulfoxides	^1B_b at 220 nm, $\sigma\sigma^*$ at 210 nm for the S═O chromophore	The coupled oscillator mechanism appears to be the major source of CD between 200 and 250 nm
2002	16	D	CD of a [2.2]paracyclophane-based diene	^1L_a for 1,4-dimethylbenzene at 225 nm and for 1-phenylbutadiene at 300 nm	An observed Cotton effect at 320 nm is reproduced in sign and intensity.
2003	17	D	CD of Yb heterobimetallic catalysts	^1B_b	Couplet sign is correct but intensity is overestimated.

2003	18	D	CD of aryl methyl sulfoxides	Two long-axis naphthyl transitions in the ^1B_b region (220 and 215 nm); three oscillators for the allowed transitions of a phenanthrene chromophore (250, 240, and 205 nm); $\sigma\sigma^*$ for the S═O chromophore	Agreement with experiment supports assignment of absolute configuration.
2003	19	D	Porphyrin-porphyrin interaction in dimeric tetraarylporphyrins	B transition (Soret band) of the porphyrins	Quantitative prediction of the CD spectra requires application of the hybrid or the circular oscillator model.
2004	20	D	Review article		The DeVoe model is useful in solving a wide range of stereochemical problems.
2005	21	D	Heme-heme interactions in tetramers and dimers of hemoglobin subunits	B transition (Soret band) of the hemes	Heme–heme interactions contribute significantly to the CD of hemoglobin, and therefore it is likely that they also contribute significantly to the CD of other multiheme proteins.
Modification of the DeVoe method by Applequist					
1972	22	A	Application of an atom dipole interaction model for molecular polarizabilities of polyatomic molecules	High-energy transitions	A model using isotropic atomic polarizabilities can reproduce mean polarizabilities and (less accurately) polarizability anisotropies
1979	23	A	CD of α-helical polypeptides	$\pi\pi^*$ transition of the peptide unit (NC'O); high-energy transitions	Polarizability and $\pi\pi^*$ transition parameters for the NC′O group together with isotropic polarizabilities of other atoms result in good agreement with experimental data.
1981	24	A	CD of helical poly(L-proline) forms I and II	Peptide $\pi\pi^*$ transition; high-energy transitions	The calculated spectra of $(Pro)_n$ were found to be sensitive to side-chain structure; reasonable agreement with experiment.
1982	25	A	CD of polypeptide β_A and β_P structures	Peptide $\pi\pi^*$ transition; high-energy transitions	Calculated CD spectra are very sensitive to variations of the side chain structure and conformation, better agreement between calculated and measured spectra for the β_A form.
1984	26	A	Absorption, CD, and LD spectra of collagen triple helices	Peptide $\pi\pi^*$ transition; high-energy transitions	Calculated spectra of $(Gly\text{-}Pro\text{-}Ala)_3$ and $(Gly\text{-}Ala\text{-}Pro)_3$ are in fairly good agreement with experiment.

(*continued*)

TABLE S3. (*Continued*)

Year	Reference	Type[a]	Subject Studied	States Included	Comments
1985	27	A	CD of cyclic dipeptides	$\pi\pi^*$ for the peptide chromophore; high-energy transitions	Calculated CD spectra are in reasonable qualitative agreement with their experimental counterparts, although the calculations exaggerate the magnitudes of the splitting of the normal modes for non-Pro-containing peptides.
1986	28	A	CD of β-turn model peptides	$\pi\pi^*$ for the peptide chromophore; high-energy transitions	Predicted CD spectra for cyclic tripeptides agree qualitatively with experiment, whereas matrix method calculations do not.
1991	29	A	CD of helical poly(L-proline) forms I and II	$\pi\pi^*$ for the peptide chromophores; high-energy transitions	While the calculated spectra were sufficiently sensitive to side chain torsion angles to suggest a preferred ring conformation in the case of poly(Pro) II this was not the case for poly(Pro) I.
1996	30	A	Polarizabilies, anisotropies, and Kerr constants of halomethanes aldehydes, ketones, and amides	High-energy transitions	Newly optimized atomic polarizabilities give an improved fit for anisotropies and Kerr constants but a slightly poorer fit for mean polarizabilities.
1996	31	A	New polarizability tensor for amide $\pi\pi^*$ transition; CD of α helix, β sheets, poly(Pro) helices	$\pi\pi^*$ for the peptide chromophore; high-energy transitions	New polarizability parameters [30] give improved agreement with experiment for β sheets and poly(Pro) II helix, small improvements for α helix and poly(Pro) I helix.
1997	32	A	CD of poly(β-amino acid) helices	$\pi\pi^*$ for the peptide chromophore; high-energy transitions	Available spectra agree qualitatively with the predictions for four helical forms; the sensitivity of the calculated spectra to the choice of the optical parameters emphasizes that care has to be exerted when they are used to interpret experimental data by means of calculations.
1997	33	A	CD of helix bundles and coiled coils in α-spectrin and tropomyosin	$\pi\pi^*$ for the peptide chromophore; high-energy transitions	It appears that CD is governed by the average backbone conformation and is not a sensitive tool for distinguishing between single straight helices and twisted helices or aggregates thereof.
1998	34	A	CD of globular proteins	$\pi\pi^*$ for the peptide chromophore; high-energy transitions	The success of the applied model probably has its origin in the inclusion of non-chromophoric backbone and side chain atoms.
1998	35	A	CD of the helical foldamer poly[(1*R*, 2*R*)-*trans*-2-amino-cyclopentanecarboxylic acid]	$\pi\pi^*$ for the peptide chromophore; high-energy transitions	CD spectrum calculated for L_{-3} helix, indicated by NMR, agrees well with experiment.

2000	36	A	CD of fully extended poly(β-amino acid) chains	$\pi\pi^*$ for the peptide chromophore; high-energy transitions	The CD spectra are highly nonconservative in that the achiral arrays of chromophores obtain their rotational strength from their interaction with the nondispersive atoms.
2003	37	A	CD of cyclo(Pro)$_3$	$\pi\pi^*$ for the peptide chromophore; high-energy transitions	Although no single low-energy conformation gave good agreement with experimental CD spectrum, the Boltzmann-weighted average spectrum did.
2005	38	A	CD of aliphatic cyclic dipeptides	$\pi\pi^*$ for the peptide chromophore; high-energy transitions	Combination of MP2- or DFT-optimized geometries with the dipole interaction model significantly improved the calculated spectra compared with those obtained from molecular mechanics calculations.
2006	39	A	CD of cyclo(L-proline-L-proline)	$\pi\pi^*$ for the peptide chromophore; high-energy transitions	Agreement between measured and calculated CD spectra close to quantitative for the 185-nm band.
			Modification of the DeVoe method by Ito		
1976	40	I	CD and ORD of single-stranded poly(rA)	Two transitions at 260.5 and 207 nm for A	Extension of Applequist's theory in terms of a linear response function of the complex frequency-dependent polarizability for a helical polymer.
1982	41	I	CD of satellite DNAs	Four $\pi\pi^*$ transitions between 186 and 281 nm for G and A; three between 175 and 270 nm for T and C	Inclusion of the polarizability tensors of the sugar-phosphate residues into the total polarizability tensor of double-stranded DNA.
1987	42	I	CD for the B/Z transition of poly[dG•dC]	See reference 41	Inversion of long-wavelength band for Z-DNA is reproduced.
1991	43	I	Splitting of the J-aggregate band in pseudoisocyanine	Lowest $\pi\pi^*$	The splitting originates from excitonic interaction between at least two polymer chains.
1993	44	I	CD of α-helical and β-sheet polypeptides	$n\pi^*$ at 222 nm and $\pi\pi^*$ at 193 nm for the peptide	The one-electron mixing of the $n\pi^*$ and $\pi\pi^*$ transitions, absent in the DeVoe method, was included by using the matrix method to calculate the $n\pi^*$ electric dipole transition moment.
1998	45	I	CD of cyclo(Gly-Pro-Gly-D-Ala-Pro) with β- and γ-turns	$n\pi^*$ and $\pi\pi^*$ transitions at 222 and 193 nm for chiral amide chromophores	Polarizability tensor theory employing Green's function matrix; the results seem to support the solid-state structure rather than the NMR structure for the molecule in solution.
2000	46	I	Review article		Applications of linear response polarizability tensor theory to calculation of CD spectra of DNA, polypeptides, and molecular aggregates.

(*continued*)

TABLE S3. (*Continued*)

Year	Reference	Type[a]	Subject Studied	States Included	Comments
2002	47	I	CD of DNA quadruplexes	See reference 41	The linear response polarizability tensor theory qualitatively reproduces the observed CD and UV spectra.
2003	48	I	CD of polypeptides having α-helix, β-sheet, and β-turn structures	Amide $n\pi^*$ and $\pi\pi^*$ transitions at 210 and 185 nm for achiral formamide, at 210 and 185 nm for achiral and chiral myristamide	Extended Fano–DeVoe theory similar to the matrix method.

[1]H. DeVoe, *J. Chem. Phys*. **1964**, *41*, 393–400.
[2]H. DeVoe, *J. Chem. Phys*. **1965**, *43*, 3199–3208.
[3]H. DeVoe, *J. Phys. Chem*. **1971**, *75*, 1509–1515.
[4]C. L. Cech, W. Hug, I. Tinoco, Jr., *Biopolymers* **1976**, *15*, 131–152.
[5]C. L. Cech, I. Tinoco, Jr., *Nucl. Acids Res*. **1976**, *3*, 399–404.
[6]C. L. Cech, I. Tinoco, Jr., *Biopolymers* **1977**, *16*, 43–65.
[7]D. S. Moore, *Biopolymers* **1980**, *19*, 1017–1038.
[8]A. L. Williams, D. S. Moore, *Biopolymers* **1983**, *22*, 755–786.
[9]D. S. Moore, A. L. Williams, *Biopolymers* **1986**, *25*, 1461–1491.
[10]P. Richterich, F. M. Pohl, *Biopolymers* **1987**, *26*, 231–250.
[11]C. Rosini, M. Zandomeneghi, P. Salvadori, *Tetrahedron: Asymmetry* **1993**, *4*, 545–554.
[12]G. Gottarelli, G. Proni, G. P. Spada, D. Fabbri, S. Gladiali, C. Rosini, *J. Org. Chem*. **1996**, *61*, 2013–2019.
[13]C. Rosini, R. Ruzziconi, S. Superchi, F. Fringuelli, O. Piermatti, *Tetrahedron: Asymmetry* **1998**, *9*, 55–62.
[14]C. Rosini, S. Superchi, H. W. I. Peerlings, E. W. Meijer, *Eur. J. Org. Chem*. **2000**, 61–71.
[15]C. Rosini, M. I. Donnoli, S. Superchi, *Chem. Eur. J*. **2001**, *7*, 72–79.
[16]L. Minuti, A. Taticchi, C. Rosini, D. Lanari, A. Marrocchi, S. Superchi, *Tetrahedron-Asymmetry* **2002**, *13*, 1257–1263.
[17]L. Di Bari, M. Lelli, G. Pintacuda, G. Pescitelli, F. Marchetti, P. Salvadori, *J. Am. Chem. Soc*. **2003**, *125*, 5549–5558.
[18]M. I. Donnoli, E. Giorgio, S. Superchi, C. Rosini, *Org. Biomol. Chem*. **2003**, *1*, 3444–3449.
[19]G. Pescitelli, S. Gabriel, Y. Wang, J. Fleischhauer, R. W. Woody, N. Berova, *J. Am. Chem. Soc*. **2003**, *125*, 7613–7628.
[20]S. Superchi, E. Giorgio, C. Rosini, *Chirality* **2004**, *16*, 422–451.
[21]R. W. Woody, *Chirality*, **2005** *17*, 450–455.
[22]J. Applequist, J. R. Carl, K.-K. Fung, *J. Am. Chem. Soc*. **1972**, *94*, 2952–2960.
[23]J. Applequist, *J. Chem. Phys*. **1979**, *71*, 4332–4338.
[24]J. Applequist, *Biopolymers* **1981**, *20*, 2311–2322.

[25]J. Applequist, *Biopolymers*, **1982**, *21*, 779–795.
[26]J. W. Caldwell, J. Applequist, *Biopolymers* **1984**, *23*, 1891–1904.
[27]B. K. Sathyanarayana, J. Applequist, *Int. J. Pept. Protein Res*. **1985**, *26*, 518–527.
[28]B. K. Sathyanarayana, J. Applequist, *Int. J. Pept. Protein Res*. **1986**, *27*, 86–94.
[29]K. A. Thomasson, J. Applequist, *Biopolymers* **1991**, *31*, 529–535.
[30]K. A. Bode, J. Applequist, *J. Phys. Chem*. **1996**, *100*, 17820–17824.
[31]K. A. Bode, J. Applequist, *J. Phys. Chem*. **1996**, *100*, 17825–17834.
[32]K. A. Bode, J. Applequist, *Macromolecules* **1997**, *30*, 2144–2150.
[33]K. A. Bode, J. Applequist, *Biopolymers* **1997**, *42*, 855–860.
[34]K. A. Bode, J. Applequist, *J. Am. Chem. Soc*. **1998**, *120*, 10938–10946.
[35]J. Applequist, K. A. Bode, D. H. Appella, L. A. Christianson, S. H. Gellman, *J. Am. Chem. Soc*. **1998**, *120*, 4891–4892.
[36]J. Applequist, K. A. Bode, *J. Phys. Chem. A* **2000**, *104*, 7129–7132.
[37]S. L. Lowe, R. R. Pandey, J. Czlapinski, G. Kie-Adams, M. R. Hoffmann, K. A. Thomasson, K. S. Pierce, *J. Pept. Res*. **2003**, *61*, 189–201.
[38]K. L. Carlson, S. L. Lowe, M. R. Hoffmann, K. A. Thomasson, *J. Phys. Chem. A* **2005**, *109*, 5463–5470.
[39]K. L. Carlson, S. L. Lowe, M. R. Hoffmann, K. A. Thomasson, *J. Phys. Chem. A* **2006**, *110*, 1925–1933.
[40]H. Ito, T. Eri, Y. J. I'Haya, *Chem. Phys. Lett*. **1976**, *39*, 150–156.
[41]H. Ito, Y. J. I'Haya, *J. Chem. Phys*. **1982**, *77*, 6270–6280.
[42]H. Ito, Y. J. I'Haya, *Chem. Phys. Lett*. **1987**, *142*, 25–32.
[43]H. Ito, M. Agatsuma, Y. J. I'Haya, *Bull. Chem. Soc. Jpn*. **1991**, *64*, 3700–3706.
[44]H. Ito, Y. Arakawa, Y. J. I'Haya, *J. Chem. Phys*. **1993**, *98*, 8835–8842.
[45]H. Ito, *J. Chem. Phys*. **1998**, *108*, 93–108.
[46]H. Ito, *Trends Chem. Phys*. **2000**, *8*, 75–130.
[47]H. Ito, S. Tanaka, M. Miyasaka, *Biopolymers* **2002**, *65*, 61–80.
[48]H. Ito, *Bull. Chem. Soc. Jpn*. **2003**, *76*, 59–71.
[a]D, original DeVoe; A, Applequist; I, Ito.

21

AB INITIO ELECTRONIC CIRCULAR DICHROISM AND OPTICAL ROTATORY DISPERSION: FROM ORGANIC MOLECULES TO TRANSITION METAL COMPLEXES

Jochen Autschbach

21.1. INTRODUCTION

The electronic and vibrational chiroptical properties of molecules and molecular aggregates are of fundamental and of applied interest in chemistry, biochemistry, physics, and other scientific disciplines [1–7]. In particular during the past decade, a large number of research studies have demonstrated that molecular chiroptical properties can be computed reliably, starting from first principles quantum theory. A number of review articles, for instance references 8–18, document the progress made in the computational chiroptics field in recent years.

Theoretical work dating back almost as far as the first rigorous formulation of modern quantum theory has allowed researchers to gain a deeper understanding of the electronic and structural origins of optical activity [19–25]. However, these pioneering theoretical works had to rely on formal derivations along with calculations for simple models, on calculations using semiempirical wavefunctions, or—in the case of transition metal complexes—on crystal field and ligand field theories. During the 1980s and 1990s the development of Hartree–Fock (HF) methods for calculations of natural electronic optical activity [26–28] paved the way for subsequent developments of methods that incorporate electron correlation, either based on wavefunctions or within density functional theory (DFT). In particular during the first decade of the new millennium, a "renaissance" in chiroptical methods [11] has been made possible by the availability of efficient first-principles theory-based electron correlation methods that can be used to predict, confirm, and assign experimental data. Predominantly, these are linear response theory approaches

Comprehensive Chiroptical Spectroscopy, Volume 1: Instrumentation, Methodologies, and Theoretical Simulations, First Edition. Edited by N. Berova, P. L. Polavarapu, K. Nakanishi, and R. W. Woody.
© 2012 John Wiley & Sons, Inc. Published 2012 by John Wiley & Sons, Inc.

rooted in time-dependent density functional theory (TDDFT [18]) and methods using coupled cluster wavefunctions [10]. It is now possible to perform first-principles computations of electronic optical activity for relatively large organic molecules, transition metal complexes, and metal clusters. A combination of such electronic structure calculations with classical or *ab initio* molecular dynamics can be used to investigate how dynamics, temperature, or solvent effects influence the chiroptical response of a molecule and molecular aggregates.

This chapter is concerned with computations of electronic circular dichroism (ECD) as well as optical rotation (OR) and optical rotatory dispersion (ORD). A brief introduction to the theoretical and computational aspects of electronic optical activity (ECD and ORD) is provided, and in the remainder of the chapter the author hopes to demonstrate the wide range of applicability of modern theoretical methods. Much of the material has been compiled, updated, and revised from three recent review articles [8, 18, 29] where the reader can find additional information on the subject. Separate sections in this chapter highlight applications to organic molecules and to transition metal complexes (with some citations to recent work on metal clusters). Right after this Introduction, a section on theoretical aspects introduces equations for the rotatory strengths and the optical rotation parameter in terms of exact wavefunctions. Subsequently, it is sketched how one might approach calculations of ECD and ORD using approximate electronic structure methods, followed by a more detailed description of TDDFT. Sections 21.2.3 and 21.2.4, focus on more technical details of the theoretical formalism and might be of interest mainly to theoreticians. At the end of Section 21.2 the reader can find a brief discussion of some more general computational considerations pertaining to the *ab initio* modeling of ECD and ORD. The discussion of organic molecules (Section 21.3) and metal complexes (Section 21.4) occasionally refers to the material presented in the theory section, but the author has tried to render each part reasonably self-contained such as to allow a reader who is interested in a particular topic to skip other sections. Additional information and a tutorial on computations of chiroptical properties can be found in reference 8.

21.2. CALCULATING ECD AND ORD STARTING FROM FIRST PRINCIPLES

In this section some of the theoretical background for electronic chiroptical properties is reviewed and related to electronic structure methods that can be used to compute these properties. Particular attention is given to time-dependent density functional theory (TDDFT). General references for this section are the textbook by Kauzmann [21], a seminal article by Condon [20], and references 1, 8, and 30.

21.2.1. Exact Wavefunctions, Sum-over-States (SOS) Equations

The calculation of ECD spectra requires excitation energies and transition moments. Conceptually, there are different ways to approach this problem. Suppose it were possible to solve the time-independent electronic Schrödinger equation (SE)

$$\hat{\mathcal{H}}\Psi_i = \Psi_i E_i \tag{21.1}$$

exactly.[1] In this case, a conceptually straightforward approach would be to calculate the N-electron ground-state wavefunction and energy, Ψ_0 and E_0, along with the desired number of excited states Ψ_j and E_j. The excitation frequencies are $\omega_j = (E_j - E_0)/\hbar$. The transition moments for each excitation from the ground state are

$$T_j = \langle \Psi_0 | \hat{T} | \Psi_j \rangle, \tag{21.2}$$

where $\hat{T}$ is an operator for one of the transition moments. For instance, with $\hat{T} = \hat{D}_u = -e \sum_{i=1}^{N} r_{u,i}$ one obtains the u component, $u = x$, y, or z, of the electric transition dipole vector, and with $\hat{T} = \hat{M}_u = -e/(2m_e c) \sum_{i=1}^{N} (\mathbf{r}_i \times \hat{\mathbf{p}}_i)_u$ one obtains the u component of the magnetic transition dipole vector for the excitation from the ground state[2] to state no. j. In the previous equations, the summations run over the electrons with positions $\mathbf{r}_i$ and momentum operators $\hat{\mathbf{p}}_i = -\imath\hbar(\partial/\partial \mathbf{r}_i)$. The theory contains a few empirically determined fundamental parameters such as the unit charge e, the electron mass m_e, Planck's constant $\hbar = h/(2\pi)$, and the speed of light c, and it is nonrelativistic. A relativistic version can be worked out, for instance by starting with the Dirac–Coulomb–Breit equation, but for the purpose of this chapter it is sufficient to consider the electronic SE as the basis for a description of chemical and spectroscopic phenomena.[3]

Suppose, furthermore, that it were possible to solve the SE not only for a few states, but for the complete set of wavefunctions. In that case, the real isotropic *optical rotation parameter* β as a function of the frequency ω of the incident light can be calculated from the set of excitation frequencies and transition moments as

$$\beta(\omega) = \frac{2c}{3\hbar} \sum_{j \neq 0} \frac{R_j}{\omega_j^2 - \omega^2}, \tag{21.3}$$

where

$$R_j = \mathrm{Im}\left[\sum_u \langle \Psi_0 | \hat{D}_u | \Psi_j \rangle \langle \Psi_j | \hat{M}_u | \Psi_0 \rangle \right] = \mathrm{Im}[\mathbf{D}_j \cdot \mathbf{M}_j^*] \tag{21.4}$$

is the isotropic *rotatory strength* for excitation number j of the molecule, and $\mathbf{D}_j$ and $\mathbf{M}_j$ are the electric and magnetic transition dipole moment vectors, respectively. Further details on how this equation is derived are given below. The rotatory strength of each transition as well as the OR parameter have opposite signs for a pair of enantiomers of a chiral molecule. The *sum-over-states* (SOS) expression for the optical rotation in Eq. (21.3) assumes an infinite lifetime of the excited states but is otherwise exact. The OR parameter β is the real part of a complex function $\tilde{\beta} = \beta + \imath\beta'$ and accompanied by an imaginary part $\beta'(\omega)$. At an excitation frequency, the OR parameter of Eq. (21.3)

[1] Unfortunately, one cannot solve the SE analytically for many-electron systems. Furthermore, it is impractical to solve for *all* excited states even with a suitable approximation of the SE unless the molecule and the basis set are small.

[2] The excitation is assumed to take place from the ground state. Therefore, it is not necessary to write T_{0j}, ω_{0j}, and so on. If the reference state is not the ground state, the expressions can be easily modified, for instance by replacing subscripts j with nj to indicate transitions between Ψ_n and Ψ_j.

[3] The electronic SE does not consider nuclear motion, and therefore the description is far from exact. For instance, see Section 21.3.4 regarding vibrational effects.

diverges while the imaginary part becomes nonzero, as indicated by the presence of δ functions in the imaginary part:

$$\beta'(\omega) = \frac{\pi c}{3\hbar\omega} \sum_{j\neq 0} R_j \left[\delta(\omega_j - \omega) + \delta(\omega_j + \omega)\right]. \tag{21.5}$$

A quantity closely related to β is the mixed electric–magnetic polarizability of the molecule, G'. The real part of G' is given as

$$G' = -\omega\beta = -\frac{2c}{3\hbar} \sum_{j\neq 0} \frac{\omega R_j}{\omega_j^2 - \omega^2}. \tag{21.6}$$

Depending on the theoretical formalism used, it can be more convenient to consider G' instead of β. Note that G' vanishes for zero frequency (i.e., infinite wavelength), of the incident light (static limit), whereas β might have a nonzero static limit. Both β and G' are the isotropic averages of rank-2 tensors, the OR tensor with Cartesian components β_{uv}, and the G' tensor with Cartesian elements G'_{uv}, where $u, v, \in \{x, y, z\}$. The isotropic averages are given by 1/3 of the sum of the diagonal tensor elements, that is, $\beta = (1/3)(\beta_{xx} + \beta_{yy} + \beta_{zz})$ and similarly for G'. This chapter only considers isotropic media—for instance, solutions of freely rotating chiral molecules, or gas-phase measurements. For chiroptical properties of samples with oriented molecules, see Chapter 12 and references [31–38].

If one includes in the derivation of the SOS equation of the optical rotation parameter dephasing constants Γ_j for the excited states, the equation for the real part of the OR parameter reads[4]

$$\beta_{uv}(\omega) = \frac{c}{3\hbar\omega} \sum_{j\neq 0} R_j \left[\frac{(\omega_j - \omega)}{(\omega_j - \omega)^2 + \Gamma_j^2} - \frac{(\omega_j + \omega)}{(\omega_j + \omega)^2 + \Gamma_j^2}\right] \tag{21.7}$$

and the imaginary part is given by

$$\beta'_{uv}(\omega) = \frac{c}{3\hbar\omega} \sum_{j\neq 0} R_j \left[\frac{\Gamma_j}{(\omega_j - \omega)^2 + \Gamma_j^2} + \frac{\Gamma_j}{(\omega_j + \omega)^2 + \Gamma_j^2}\right]. \tag{21.8}$$

In the limit where all Γ_j are zero, Eqs. (21.3) and (21.5) are obtained again.

For an ensemble of noninteracting molecules, the molecular parameter β, given here in cgs units of cm^4, can be converted to an isotropic optical rotation (OR) angle in terms of specific rotation $[\alpha]$ or molar rotation $[\phi]$ as detailed elsewhere in this book. The rotatory strength is the chiroptical equivalent of the line strength of absorption spectra [39]. To simulate ECD spectra the excitations are typically broadened with an empirical broadening function (often Gaussian) to obtain a CD intensity in terms of $\Delta\varepsilon$ or the ellipticity $[\theta]$.

[4] Please note that the corresponding expression in reference 8 has an incorrect sign.

21.2.2. Response Methods in Approximate Wavefunction Theories and Time-Dependent DFT in a Nutshell

If approximate Schrödinger equations for ground and excited states can be solved in a practical way, approximate absorption and ECD spectra can be obtained from the calculated energies of the states along with the transition moments calculated explicitly from Eq. (21.2) using the approximate wavefunctions. If all excited states are calculated, then a value of the OR parameter that is correct within the approximations of the computational model can be obtained from the SOS formula in Eq. (21.3). Typically, however, even with approximate wavefunction methods, only a rather limited number of excited states can be calculated and therefore the SOS equation for β is of limited practical value. Moreover, for the currently most widely applied electronic structure method, density functional theory (DFT), excitation spectra, and optical rotations cannot be accessed in this manner because DFT has been formulated rigorously for ground states only, not for excited states.

Consider a conceptually different approach: Suppose an efficient approximate method were available to calculate the OR parameter $\beta(\omega)$ for a given input frequency ω directly. According to Eq. (21.3), determining the corresponding ECD spectrum is then "simply" a matter of finding for which frequencies ω the real part of the OR parameter diverges, as indicated in Figure 21.1. Whenever ω coincides with one of the excitation frequencies ω_j, the expression for β becomes singular in the absence of excited states damping. It would be tedious to scan point by point through a frequency range of interest (although this can be a practical way to compute an ECD spectrum). Alternatively, it can be possible to derive from the equation for $\beta(\omega)$ an equation system that mathematically represents such a scan in the following sense: The solution of the equation system yields the excitation energies and the desired transition moments but bypasses the explicit calculation of excited-state wavefunctions. Since the OR parameter β is calculated for the electronic ground state, such an approach is also possible in DFT. However, since β is related to oscillating time-dependent perturbations of the molecule, time-dependent DFT (TDDFT) and time-dependent wavefunction-based response methods are required.

As a starting point for the approach sketched in the previous paragraph, one needs an equation for the OR parameter or for G' derived for the approximate electronic structure method of choice. This is accomplished by considering a perturbation of the electric dipole moment **d** with Cartesian components d_u of a chiral molecule by a magnetic field (components B_v), or alternatively the magnetic dipole moment **m** of a molecule being perturbed by an electric field (component $\mathcal{E}_v$). The physical origin of optical rotation is a

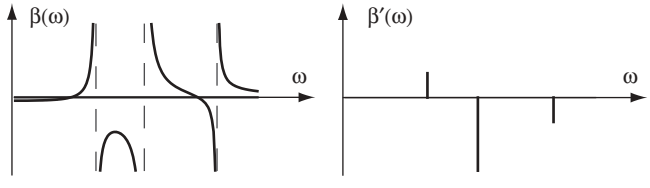

Figure 21.1. Behavior of the real and the imaginary part of the OR parameter [Eqs. (21.3) and (21.5)] in the vicinity of excitation frequencies (dashed lines in left panel, ''line spectrum'' in the right panel). The line spectrum indicates the δ-function shape of β', while the length of the lines is proportional to the rotatory strengths used to generate the plot in the left panel. For broadened versions, see Figure 21.2.

difference in the refractive indices of the medium for left- and right-hand circular polarized light, n_L, n_R. The refractive index for electromagnetic waves at optical frequencies is, in turn, related to dynamic electronic polarizations in the medium, governed at the molecular level by electric and magnetic dipole and higher-order multipole polarizability tensors. An expansion in the electromagnetic field amplitudes around the coordinate origin yields [1, 20, 21]

$$d'_u = \alpha_{u,v}\mathcal{E}_v - c^{-1}\beta_{u,v}(\partial\mathcal{B}_v/\partial t) + \cdots, \tag{21.9a}$$

$$m'_u = \chi_{u,v}\mathcal{B}_v + c^{-1}\beta_{u,v}(\partial\mathcal{E}_v/\partial t) + \cdots, \tag{21.9b}$$

for each component of the molecular dipole moment perturbations, where in addition to the OR tensor elements the elements of the polarizability tensor (α) and the magnetizability tensor (χ) appear in lowest order. Terms of higher order in the field amplitudes or in the multipole expansion are indicated by "$\cdots$". The terms involving β are the lowest-order terms that lead to a difference between n_L and n_R. The fact that time derivatives of the fields are involved with the mixed electric–magnetic perturbations highlights the fact that the observable optical activity vanishes as $\omega \to 0$. In a nutshell, the SOS equation for the OR parameter as given in Eq. (21.3) is obtained from Eqs. (21.9a, 21.9b) as follows [21, 40]:

(i) Assume perturbing fields of frequency ω (alternatively, one can start with a general time dependent field and then do a Fourier transformation afterwards).

(ii) Expand the dipole moment expectation values as perturbation series in $\mathcal{E}_v, \mathcal{B}_v$ and collect the terms linear in the field amplitudes. Each term in the SE, Eq. (21.1), is also expanded as a perturbation series of zeroth, first, and higher orders in the field amplitudes.

(iii) Step (ii) involves the unperturbed ground-state wavefunction, along with its dynamic electric or magnetic field perturbation to first order. The first-order wavefunction is then expressed on the basis of unperturbed excited-states wavefunctions, with a set of unknown coefficients. This is the origin of the sum-over-states, where the excited-states wavefunctions are supposed to be known explicitly.

(iv) Equations for the expansion coefficients for the first–order wavefunction in terms of unperturbed excited states Ψ_j of step (iii) are obtained from the terms in the SE that are linear in the field amplitudes. Putting it all together and taking the isotropic average of the tensor components yields Eq. (21.3) for the OR parameter, with a similar equation for G'.

Instead of assuming exact wavefunctions as a starting point for a calculation, one can define the expectation value for the electronic electric and magnetic dipole moments within whatever approximate first-principles electronic structure method is chosen, consider a time-dependent perturbing field of frequency ω, and derive the equations for the mixed electric–magnetic perturbations directly within the approximate method. Since one is concerned here with dynamic perturbations of the dipole moments linear in the field strengths, the task is accomplished by resorting to dynamic *linear response* methods—that is, first-order time-dependent variational or nonvariational perturbation theory. For example, within the DFT framework, one uses variational dynamic linear response TDDFT methods. Within the coupled cluster (CC) wavefunction methods, nonvariational dynamic linear response methods are employed, as detailed in the chapter

by Crawford (Chapter 23, this volume). Semiempirical methods employ parameterized approximate versions of time-dependent Hartree–Fock linear variational perturbation theory [41–44], and so on. The final form of the equations depends on the chosen electronic structure method, as well as on other factors such as whether variational or nonvariational parameters are determined with respect to the AO basis functions, or (as typical, for instance, in TDDFT) in a basis of molecular orbitals (MOs). For the interested reader, an account of the TDDFT linear response approach to calculations of ORD and CD is given further below.

To gain a rough idea of how one proceeds from an equation for the OR parameter to arrive at equations for ECD spectra, without the explicit use of excited states wavefunctions, consider the following generic example: In the absence of excited states dephasing, the calculation of the linear magnetic dipole moment perturbation of Eq. (21.9b) of a chiral molecule might require the solution of an equation system

$$[\mathbb{M} - \omega^2]\mathbf{x} = \mathbf{b}, \tag{21.10}$$

where a set of parameters $\mathbf{x}$ such as perturbed MO coefficients or wavefunction parameters is determined and subsequently used in conjunction with magnetic dipole integrals (e.g. over the AO or MO basis) to calculate β. The actual equations for the quantities in (21.10) and the dimension of the matrix problem depend on specific details of the chosen approximate electronic structure method. Furthermore, in nonvariational methods it can be necessary to solve additional equations. In the example, $\mathbf{b}$ is supposed to be a constant right-hand-side (rhs) vector that depends on the nature of the perturbing field, that is, the electric field. The matrix $\mathbb{M}$ may or may not be Hermitian. The formal solution of Eq. (21.10) is obtained by multiplying from the left with the inverse of $[\mathbb{M} - \omega^2]$ to yield

$$\mathbf{x} = [\mathbb{M} - \omega^2]^{-1}\mathbf{b}. \tag{21.11}$$

One can write the inverse matrix in Eq. (21.11) in form of its spectral resolution. For simplicity, assume that $\mathbb{M}$ is Hermitian. Given the complete set $\{\mathbf{F}_j\}$ of eigenvectors of $\mathbb{M}$, with eigenvalues ω_j^2, the inverse is

$$[\mathbb{M} - \omega^2]^{-1} = \sum_j \frac{\mathbf{F}_j \mathbf{F}_j^\dagger}{\omega_j^2 - \omega^2}. \tag{21.12}$$

Compare Eq. (21.12) with the SOS equation for the OR parameter: Both expressions appear in a very similar form. That is, the eigenvalues of the matrix $\mathbb{M}$ yield the (squares of) the excitation energies, and the eigenvectors can be used to calculate the transition moments and the rotatory strengths. If one is interested in the ECD spectrum, it is usually sufficient to determine a set of lowest eigenvalues along with the associated eigenvectors. For calculations of β, one solves Eq. (21.10) directly in an efficient way, without taking the spectral resolution detour.

As the reader can imagine, many details were glossed over in the previous paragraph, but as a general idea it emerges that: (i) The OR parameter, or G', can be calculated in first-principles quantum chemical methods by solving a set of linear response equations for a given input frequency ω. (ii) The formal solutions of these equations can be written in a spectral form that resembles a SOS equation, typically involving a generalized eigenvalue-type problem. The excitation energies are obtained from the eigenvalues, and expressions for the transition moments can be obtained in

terms of the eigenvectors. In exact wavefunction theory, the result leads back to the original SOS equations for β and G'.

21.2.3. TDDFT and Molecular Orbital Linear Response Theory for Electronic Chiroptical Properties

For the interested reader the formalism is sketched in this section in more detail for the case of molecular-orbital-based Kohn–Sham TDDFT, because of its widespread application in the chiroptics area of research. Some definitions are going to be helpful before proceeding to the details of the calculation of chiroptical properties.[5] For the unperturbed system, using a standard AO basis set $\{\chi_\mu\}$ to expand the singly occupied Kohn–Sham molecular spin orbitals φ_i as $\varphi_i = \sum_\mu \chi_\mu C_{\mu i}$, the electron density is given as

$$\rho(\mathbf{r}) = \sum_i n_i \varphi_i^* \varphi_i = \sum_{\mu,\nu,i} n_i C_{\mu i}^* C_{\nu i} \chi_\mu^*(\mathbf{r}) \chi_\nu(\mathbf{r}), \tag{21.13}$$

where the n_i are the MO occupation numbers and assumed here to be 0 or 1. The MO coefficients and the occupation numbers are conveniently collected in matrices $\mathbb{C}$ and $\mathbb{n}$ (with $\mathbb{n}$ being diagonal).[6] The electronic Coulomb potential is given as

$$V_C(\mathbf{r}) = \int d^3r' \cdot \frac{\rho(\mathbf{r}')}{|\mathbf{r} - \mathbf{r}'|} \tag{21.14}$$

and in DFT it is accompanied by $V_{XC} = \delta E_{XC}/\delta\rho$, the exchange–correlation (XC) potential which is obtained from the XC energy as its functional derivative with respect to the electron (spin) density. The canonical Kohn–Sham equations used to determine the time-independent MOs read in matrix form

$$\mathbb{F}\mathbb{C} = \mathbb{S}\mathbb{C}\mathbb{E}. \tag{21.15}$$

Here, $\mathbb{F} = \mathbb{h} + \mathbb{V}_C + \mathbb{V}_{XC}$ is the AO matrix of the Kohn–Sham Fock operator, where $\mathbb{h}$ collects the one-electron operator matrix elements for kinetic energy and electron–nuclear attraction. The matrix $\mathbb{E} = \mathbb{C}^\dagger \mathbb{F} \mathbb{C}$ is a diagonal matrix[7] with elements ε_i, the so-called orbital energies, and $S_{\mu,\nu} = \langle \chi_\mu | \chi_\nu \rangle$ is an element of the AO overlap matrix $\mathbb{S}$.

In wavefunction theory, in the presence of time-periodic perturbations the time-dependent wavefunction $\Psi(t)$ can be written as a product of a time-dependent phase factor times a time-periodic phase-free function Φ such that

$$\left(\hat{H} - \imath \frac{\partial}{\partial t}\right) \Phi = \Phi Q(t) \tag{21.16}$$

has the formal structure of the Schrödinger equation; here the operator in parentheses replaces the Hamiltonian, and the quasi energy

$$Q(t) = \left\langle \Phi \left| \hat{H} - \imath \frac{\partial}{\partial t} \right| \Phi \right\rangle \tag{21.17}$$

[5] Hartree atomic units are used in this section.

[6] Notation $\mathbb{A}, \mathbb{B}, \ldots$ indicates matrices.

[7] There is the assumption here and in the remainder of this section that the unperturbed orbitals are canonical.

takes the role of the energy. In the presence of time-dependent external fields the quasi energy can be used as a starting point for analytic derivative perturbation methods [45–47]. The symbol $\imath$ is used in this chapter to denote $\sqrt{-1}$ in order to avoid confusion with orbital indices.

In the *adiabatic approximation* of TDDFT, where the XC potential is not explicitly time-dependent, a quasi-energy functional that is suitable for TDDFT response methods can be written in matrix form as [48]

$$\begin{aligned}\tilde{Q}(t) &= Q(t) - \mathrm{tr}_{\mathbb{n}}\mathbb{\Lambda}\left[\mathbb{C}^{\dagger}\mathbb{S}\mathbb{C} - \mathbb{1}\right] \\ &= \mathrm{tr}_{\mathbb{n}}\left\{\mathbb{C}^{\dagger}\mathbb{h}\mathbb{C} + \frac{1}{2}\mathbb{C}^{\dagger}\mathbb{V}_{\mathrm{C}}\mathbb{C} - \imath\left[\mathbb{C}^{\dagger}\dot{\mathbb{S}}\mathbb{C} + \mathbb{C}^{\dagger}\mathbb{S}\dot{\mathbb{C}}\right] - \mathbb{\Lambda}\left[\mathbb{C}^{\dagger}\mathbb{S}\mathbb{C} - \mathbb{1}\right]\right\} + E_{\mathrm{XC}}[\rho(t)],\end{aligned} \tag{21.18}$$

where $\mathrm{tr}_{\mathbb{n}}$ indicates that the diagonal elements of the resulting matrices should be multiplied with the MO occupation numbers and added. The basis set can be time-periodic and dependent on one or more perturbation parameters. The basis functions are denoted as ξ_μ in order to distinguish them from their static AO counterparts χ_μ which do not depend on the magnetic or electric field. The matrix $\dot{\mathbb{S}}$ has elements $\left\langle \xi_\mu \middle| \frac{\partial}{\partial t}\xi_\nu \right\rangle$, and $\dot{\mathbb{C}} = (\partial/\partial t)\mathbb{C}(t)$. The matrix $\mathbb{h}$ may now include matrix elements of the operators for perturbing time-dependent external fields, and the electron density, the MO coefficients, and potentially also the overlap matrix $\mathbb{S}$ are now time-dependent. The functional includes variational constraints with Lagrangian multipliers $\lambda_{ij}(t)$ collected in the matrix $\mathbb{\Lambda}$. These terms ensure that the MOs remain orthonormal when the MO coefficients are varied. In the absence of time-dependent external fields, the static limit of Q (time derivatives vanish) is the energy functional used to derive Eq. (21.15), with the set of Lagrange multipliers for the unperturbed system being the set of orbital energies ε_i.

One can define an element of the G' tensor in the frequency domain as a time-averaged quasi-energy derivative:

$$G'_{u,v}(\omega) = \mathrm{Im}\ \frac{d^2\tilde{Q}}{d\mathcal{B}_u(-\omega)d\mathcal{E}_v(\omega)}, \tag{21.19}$$

where the frequencies of the two fields need to have opposite sign in order to yield a nonvanishing time average of the response. The order of differentiation in Eq. (21.19) can be chosen based on convenience. For the second derivative in Eq. (21.19), one needs the perturbed MO coefficients to first order in the amplitudes of one of the fields.[8] The perturbed MO coefficients to first order can be obtained from a perturbation expansion of the time-dependent Kohn–Sham equations which read in matrix form (AO basis)

$$\mathbb{F}\mathbb{C} - \imath[\dot{\mathbb{S}}\mathbb{C} + \mathbb{S}\dot{\mathbb{C}}] = \mathbb{S}\mathbb{C}\mathbb{\Lambda}. \tag{21.20}$$

As an example, consider an electric field perturbing the orbitals, and assume that the basis set does not depend on the electric field amplitudes. This simplifies the procedure since no perturbation expansion of $\mathbb{S}$ and $\dot{\mathbb{S}}$ needs to be considered in this part of the calculation. The MO coefficients can be expanded into Fourier components as

[8] This is after elimination of redundant terms involving the second derivative of $\mathbb{C}$ and its first derivative with respect to the amplitudes of the other field.

$\mathbb{C}(t) = \mathbb{C}^{(0)} + \mathbb{C}^{(+)} e^{i\omega t} \mathcal{E}_u(+\omega) + \mathbb{C}^{(-)} e^{-i\omega t} \mathcal{E}_u(-\omega) + \cdots$, and similarly for $\mathbb{F}(t)$ and other time-dependent quantities. One usually parameterizes $\mathbb{C}^{(\pm)} = \mathbb{C}^{(0)} \mathbb{A}^{(\pm)}$ where the matrices $\mathbb{A}^{(+)}, \mathbb{A}^{(-)}$ mix unoccupied with occupied MOs to describe the first-order perturbations [in a sense much like excited states wavefunctions enter the SOS expression for $\beta(\omega)$]. Collecting from Eq. (21.20) terms linear in the electric field amplitude and neglecting any dependence of the basis set on the perturbation yields, after multiplication from the left with $\mathbb{C}^{(0)\dagger}$,

$$\mathbb{F}^{(\pm)} + \mathbb{E}^{(0)} \mathbb{A}^{(\pm)} - \mathbb{A}^{(\pm)} \mathbb{E}^{(0)} \pm \omega \mathbb{A}^{(\pm)} = \mathbb{N}^{(\pm)}, \tag{21.21}$$

where $\mathbb{C}^{(0)\dagger} \mathbb{S}^{(0)} \mathbb{C}^{(0)} = \mathbb{1}$ (MO orthonormalization) was used to simplify a number of terms. To first order, only the matrix elements between occupied and unoccupied orbitals are needed to obtain the response function.[9] Once the matrices $\mathbb{A}^{(\pm)}$ are determined, one can calculate G' or the OR parameter β. It is beneficial at this point to introduce spin indices σ, τ for the MOs to keep track of their spins. Indices a, b refer to unoccupied MOs, and indices i, j refer to occupied MOs. In Eq. (21.21), $\mathbb{F}^{(\pm)}$ is the perturbed Kohn–Sham Fock operator in the basis of unperturbed MOs (not AOs), with matrix elements

$$F^{(\pm)}_{ai\sigma} = h^{(\mathcal{E}_v)}_{ai\sigma} + \sum_{b,j,\tau} [K_{ai\sigma,jb\tau} A^{(\pm)}_{bj\tau} + K_{ai\sigma,bj\tau} A^{*(\mp)}_{bj\tau}], \tag{21.22}$$

where the superscript $(\mathcal{E}_v)$ indicates the electric field perturbation explicitly. The quantities

$$K_{ai\sigma,bj\tau} = \int d^3 r_1 d^3 r_2 \varphi^*_{a\sigma}(\mathbf{r}_1) \varphi_{i\sigma}(\mathbf{r}_1) \left[r_{12}^{-1} + f^{\sigma\tau}_{XC}(\mathbf{r}_1, \mathbf{r}_2, \omega) \right] \varphi^*_{b\tau}(\mathbf{r}_2) \varphi_{j\tau}(\mathbf{r}_2) \tag{21.23}$$

are elements of a "supermatrix" $\overline{\mathbb{K}}$ (a matrix of matrices, indicated by the bar) which is sometimes called the TDDFT coupling matrix.[10] The r_{12}^{-1} terms in $\overline{\mathbb{K}}$ are related to the perturbation of the Coulomb potential by the external field, while the linear exchange-correlation (XC) response kernel $f^{\sigma\tau}_{XC}$ yields the first-order perturbation of the XC potential. It is in principle a function of frequency. In the adiabatic approximation of TDDFT, it is taken to be a frequency-independent object that can be obtained, for instance, as the functional derivative of a static DFT XC potential. A large variety of functionals is available for this purpose, including hybrid and range-separated hybrid functionals. For brevity, the notation in (21.23) refers to the 'pure' TDDFT terms only.

The perturbed Kohn–Sham Fock operator depends on the first-order perturbation of the MO coefficients; that is, $\mathbb{F}^{(\pm)}$ depends on $\mathbb{A}^{(\pm)}$ [Eq. (21.22)] and $\mathbb{A}^{(\pm)}$ is the solution of (21.21) which depends on $\mathbb{F}^{(\pm)}$. One can solve the so–called coupled perturbed time-dependent Kohn–Sham equations (21.21) self–consistently for $\mathbb{F}^{(\pm)}$. Initially unknown are the coupling terms involving elements of $\mathbb{A}^{(\pm)}$ in Eq. (21.22). With an initial guess of $\mathbb{h}^{(\mathcal{E}_v)}$ for the perturbed Fock operator, a converged solution is usually quickly found. Substituting (21.22) in Eq. (21.21) in order to resolve the dependence of $\mathbb{F}^{(\pm)}$ on the coefficients in $\mathbb{A}^{(\pm)}$ yields a system of uncoupled linear equations for the unknown

[9] The matrix $\mathbb{N}^{(\pm)}$ in Eq. (21.21) can be chosen as zero in the occupied–unoccupied blocks.

[10] Definitions in the literature may vary as to the ordering of indices.

elements of the matrices $\mathbb{A}^{(\pm)}$. Using a shorthand notation where matrix indices a, i and b, j and spin indices σ, τ are combined to single composite vector / (super)matrix indices $(a\,i\,\sigma)$ and $(b\,j\,\tau)$, the equation system obtained from (21.21) upon substitution of (21.22) can be written in compact form[11] as

$$\left[\begin{pmatrix} \overline{\mathbb{G}} & \overline{\mathbb{K}} \\ \overline{\mathbb{K}}^* & \overline{\mathbb{G}}^* \end{pmatrix} - \omega \begin{pmatrix} -\bar{\mathbb{1}} & \bar{\mathbb{0}} \\ \bar{\mathbb{0}} & \bar{\mathbb{1}} \end{pmatrix}\right] \begin{pmatrix} \mathbb{A}^{(+)} \\ \mathbb{A}^{*(-)} \end{pmatrix} = - \begin{pmatrix} \mathbb{h}^{(\mathcal{E}_v)} \\ \mathbb{h}^{*(\mathcal{E}_v)} \end{pmatrix}. \tag{21.24}$$

Here, $\overline{\mathbb{G}}$ has elements

$$G_{ai\sigma,bj\tau} = \delta_{\sigma\tau}\delta_{ab}\delta_{ij}(\varepsilon_{a\sigma} - \varepsilon_{i\sigma}) + K_{ai\sigma,jb\tau}, \tag{21.25}$$

$\mathbb{h}^{(\mathcal{E}_v)}$ collects the $(a\,i\,\sigma)$ matrix elements for the external field perturbation (here: the electric field). Quantities without a perturbation superscript index are of zeroth order in the field amplitude. The matrices in the uncoupled equation system have o^2v^2 elements, where o is the number of occupied and v the number of unoccupied ('virtual') orbitals—in contrast to the coupled equations (21.21) where the matrices have $o \cdot v$ elements. The dimension of the equation system usually makes it necessary to solve it iteratively in a way such that the full matrices are never stored, with an initial guess for the solution vectors $\mathbb{A}^{(+)}$ and $\mathbb{A}^{*(-)}$. Equations (21.21) and (21.24) are different representations of the same computational problem.

Once the coefficient sets $\mathbb{A}^{(+)}$ and $\mathbb{A}^{*(-)}$ for the electric field perturbation have been determined, the response function in Eq. (21.19) can be calculated. In the simplest scenario, when taking the quasi-energy derivatives, one assumes a basis set in Eq. (21.18) that does not depend on the magnetic field perturbation. After elimination of all redundant terms, the mixed electric–magnetic response function has the following, rather simple, expression in the MO basis:

$$\frac{d^2\tilde{Q}}{d\mathcal{B}_u(-\omega)d\mathcal{E}_v(\omega)} = \sum_{ai\sigma} n_i \left\{ h_{ia\sigma}^{(\mathcal{B}_u)} A_{ai\sigma}^{(\mathcal{E}_v,+)} + A_{ai\sigma}^{*(\mathcal{E}_v,-)} h_{ai\sigma}^{(\mathcal{B}_u)} \right\}, \tag{21.26}$$

where $h_{ai}^{(\mathcal{B}_u)} = -(1/2c)\langle\varphi_a|(\mathbf{r}\times\hat{\mathbf{p}})_u|\varphi_i\rangle$ is a matrix element of the external magnetic field perturbation operator (the orbital Zeeman term).

The advantage of having an explicit linear equation system such as (21.24) for the linear response coefficients instead of a set of coupled perturbed SCF equations such as (21.21) is the following: The solutions of Eq. (21.24) become singular where the matrix in square brackets on the left has vanishing eigenvalues. For simplicity, assume real unperturbed orbitals, in which case all quantities in Eq. (21.24) are real for an electric field perturbation. Adding and subtracting the two equations obtained from the 2×2 matrix–vector product in (21.24), solving one of them for $(\mathbb{A}^{(+)} - \mathbb{A}^{(-)})$, and substituting the result in the other equation yields

$$[(\overline{\mathbb{G}} - \overline{\mathbb{K}})(\overline{\mathbb{G}} + \overline{\mathbb{K}}) - \omega^2](\mathbb{A}^{(+)} + \mathbb{A}^{(-)}) = -2\mathbb{h}^{(\mathcal{E}_v)}. \tag{21.27}$$

[11] To avoid confusion: For the matrices $\mathbb{A}^{(\pm)}$ in Eq. (21.24) and $^{(\mathcal{E}_v)}$ one now considers only one of their occupied–unoccupied blocks such that the dimension of the equation system is the number of occupied times the number of unoccupied MOs.

Equation (21.27) has the same structure as the linear equation system (21.10) discussed above. Therefore, an equation resembling the SOS expression for the OR parameter can be derived formally within TDDFT. From such an equation, the excitation energies and transition moments can be calculated directly from a non-Hermitean eigenvalue problem involving the matrix $[(\overline{\mathcal{G}}-\overline{\mathcal{K}})(\overline{\mathcal{G}}+\overline{\mathcal{K}})]$ from (21.27) or from a modified version with a Hermitean matrix [49–51]. The excitation energies and transition moments are calculated without the need to compute excited states densities or wavefunctions, by considering time-dependent perturbations of the ground states.

21.2.4. Origin Dependence and GIAOs

For optical rotation and ECD calculations a complication arises: Molecular properties related to magnetic field perturbations are generally dependent on the choice of the coordinate origin when the basis set is incomplete. Such an origin dependence is a manifestation of a more general violation of invariance of calculated observables with respect to the gauge chosen for the magnetic vector potential [40] with incomplete basis sets or certain types of approximate wavefunctions. In TDDFT and various other classes of variational electronic structure methods, the origin dependence can be eliminated for some properties by introducing 'gauge including atomic orbital' (GIAO) basis functions. GIAOs and other distributed gauge origin methods are also in widespread use for computations of NMR chemical shifts where the magnetic field is static [52]. For dynamic response, one may define time-periodic GIAOs in reference to an oscillating magnetic field as [48]

$$\xi_\nu(t)=\exp\left[-\frac{\imath}{2c}\left(\mathbf{B}^{+}e^{\imath\omega t}+\mathbf{B}^{-}e^{-\imath\omega t}\right)\times\mathbf{R}_\nu\cdot\mathbf{r}\right]\chi_\nu, \tag{21.28}$$

where $\mathbf{R}_\nu$ is the center of a regular field-independent real AO basis function χ_ν. As far as TDDFT is concerned, with the magnetic-field-dependent GIAO basis set, practically all terms in the quasi-energy functional, Eq. (21.18), contribute to the magnetic field derivative when the mixed electric–magnetic response function is calculated. After elimination of redundant terms, and of terms that sum to zero because they involve products of symmetric with antisymmetric matrices, the the mixed electric–magnetic response can be calculated from

$$\begin{aligned}\frac{d^2\tilde{Q}}{d\mathcal{B}_u(-\omega)d\mathcal{E}_\nu(\omega)}=\sum_{\mu\nu}\Bigg\{&\sum_{ai\sigma}n_{i\sigma}h_{\mu\nu}^{(\mathcal{B}_u)}\left[C_{\mu i\sigma}^{*}C_{\nu a\sigma}A_{ai\sigma}^{(\mathcal{E}_\nu,+)}+C_{\mu a\sigma}^{*}C_{\nu i\sigma}A_{ai\sigma}^{*(\mathcal{E}_\nu,-)}\right]\\&-\sum_{ai\sigma}n_{i\sigma}\varepsilon_{i\sigma}S_{\mu\nu}^{(\mathcal{B}_u)}\left[C_{\mu i\sigma}^{*}C_{\nu a\sigma}A_{ai\sigma}^{(\mathcal{E}_\nu,+)}+C_{\mu a\sigma}^{*}C_{\nu i\sigma}A_{ai\sigma}^{*(\mathcal{E}_\nu,-)}\right]\\&+\sum_{ai\sigma}n_{i\sigma}\dot{S}_{\nu\mu}^{*(\mathcal{B}_u,+)}C_{\mu i\sigma}^{*}C_{\nu a\sigma}A_{ai\sigma}^{(\mathcal{E}_\nu,+)}+\dot{S}_{\mu\nu}^{(\mathcal{B}_u,-)}C_{\mu a\sigma}^{*}C_{\nu i\sigma}A_{ai\sigma}^{*(\mathcal{E}_\nu,-)}\Bigg\}\end{aligned} \tag{21.29}$$

with

$$h_{\mu\nu}^{(\mathcal{B}_u)}=-\frac{1}{2c}\langle\chi_\mu|(\mathbf{r}_\nu\times\hat{\mathbf{p}})_u|\chi_\nu\rangle+\frac{\imath}{2c}\langle\chi_\mu|\left[\mathbf{r}\times(\mathbf{R}_\nu-\mathbf{R}_\mu)\right]_u\hat{F}^{(0)}|\chi_\nu\rangle, \tag{21.30a}$$

$$S_{\mu\nu}^{({}^{B_u})} = \frac{\iota}{2c}\langle\chi_\mu|\big[\mathbf{r}\times(\mathbf{R}_\nu-\mathbf{R}_\mu)\big]_u|\chi_\nu\rangle, \tag{21.30b}$$

$$\dot{S}_{\mu\nu}^{({}^{B_u},\pm)} = \pm\frac{\iota\omega}{2c}\langle\chi_\mu|\big[\mathbf{r}\times\mathbf{R}_\nu\big]_u|\chi_\nu\rangle. \tag{21.30c}$$

The first sum on the rhs of (21.29) is equivalent to (21.26). One can show that the combined additional terms in Eq. (21.29) vanish in the complete basis set limit [53]. In addition to the GIAO overlap and perturbation operator matrix elements which are well known from GIAO methods for NMR parameters [52], for example, the terms involving the matrix $\dot{\mathcal{S}}^{(\pm)}$ are specific to dynamic response methods with time-periodic basis functions and originate from the 'operator' $\iota\partial/(\partial t)$ in the quasienergy expression acting on a time-dependent basis set. See also reference 54.

There are other ways to define origin independent magnetic properties. For optical rotation and ECD calculations, one of the popular choices is to employ what is sometimes called the *velocity gauge* for the dipole operator. The electric transition dipole moment in the rotatory strength, Eq. (21.4), can be replaced by its velocity (momentum) form by considering that in exact theory

$$\langle\Psi_0|\hat{\mathbf{D}}|\Psi_j\rangle = \iota\omega_j^{-1}\langle\Psi_0|\hat{\mathbf{P}}|\Psi_j\rangle. \tag{21.31}$$

In the last equation, $\hat{\mathbf{P}} = \sum_i \hat{\mathbf{p}}_i$ is the one-electron momentum operator. With incomplete basis sets, Eq. (21.31) and its analog in the MO basis are not exactly satisfied, but ORs calculated based on the velocity expression are origin-independent. Pedersen at al. [55] have shown that in velocity gauge G' may afford a sizable static limit, while in exact theory G' has to vanish for zero frequency. The nonvanishing velocity gauge $G'(0)$ is an artifact of basis set incompleteness. A modified velocity gauge for the optical rotation tensor [55] involves the subtraction of $G'(0)$ from $G'(\omega)$, with both tensors computed in velocity gauge at the same level of theory. There is some added computational cost because of the additional response calculation at zero frequency. An advantage of the velocity gauge is that it is generally applicable to variational and nonvariational electronic structure methods and easy to implement for OR and various other response properties [56].

21.2.5. Lineshapes, ORD patterns, Kramers–Kronig Transforms

Equations (21.7) and (21.8) show that both the real and the imaginary part of the complex OR parameter are determined by the rotatory strengths R_j. The real part β describes a refractive process, while the imaginary part β' describes a chiroptical absorption process. If the only broadening mechanism were a finite-lifetime dephasing of the excited states, the lineshapes would correspond to the Lorentzian function pairs of Eqs. (21.7) and (21.8). There are many other mechanisms that lead to ECD band broadening. Generally, the real and the imaginary part of the broadened OR parameter are related to each other in form of a Kramers–Kronig (KK) transform pair, such that [22, 57, 58][12]

$$\beta(\omega) = \frac{2}{\pi}\mathrm{PV}\int_0^\infty \frac{\mu\beta'(\mu)}{\mu^2-\omega^2}\,d\mu, \tag{21.32a}$$

$$\beta'(\mu) = -\frac{2\omega}{\pi}\mathrm{PV}\int_0^\infty \frac{\beta(\mu)}{\mu^2-\omega^2}\,d\mu. \tag{21.32b}$$

[12] The real and imaginary part are assumed to vanish as $\omega \to \pm\infty$.

At each frequency point ω the integration over μ includes the singularity where $\mu = \omega$. To properly take into account these singularities, "PV" indicates that the principal value of the integral should be taken. The lineshape functions in Eqs. (21.7) and (21.8) represent KK transform pairs, and so do the SOS equations (21.3) and (21.5) for infinite excited state lifetimes. Often, in spectral simulations the calculated ECD "line" spectra, corresponding to the δ functions of Eq. (21.5), are broadened with Gaussian functions. A normalized lineshape function pair for Gaussian broadening is [59]

$$g^R(\omega;\omega_j) = \imath \frac{1}{\sigma\sqrt{2\pi}} \exp\left(-\frac{(\omega-\omega_0)^2}{2\sigma^2}\right) \mathrm{erf}\left(\imath \frac{(\omega-\omega_0)}{\sigma\sqrt{2}}\right), \tag{21.33a}$$

$$g^I(\omega;\omega_j) = \frac{1}{\sigma\sqrt{2\pi}} \exp\left(-\frac{(\omega-\omega_j)^2}{2\sigma^2}\right), \tag{21.33b}$$

where R and I indicate the real (refractive) and the imaginary (absorptive) part, respectively. For a parameter σ equal to $\Gamma_j/\sqrt{\ln 4}$, the Gaussian absorption line has the same width at half peak height as a normalized Lorentzian curve. The error function along the imaginary axis in (21.33a) can be calculated by using numerical routines for the so–called Dawson integral (see reference 59 for further details).

The qualitative behavior of the real and imaginary part of the OR parameter, or alternatively of the real and imaginary part of the molar rotation $[\phi]$ and the molar ellipticity $[\theta]$ which also constitute a KK transform pair, is shown in Figure 21.2. The sign of the peak/trough pattern in the "anomalous" dispersion region of the ORD around an excitation is dictated by the sign of the rotatory strengths for the transition. As shown in the figure, the ORD in the low-frequency (long-wavelength) domain might in some cases exhibit a sign change that is not indicative of an excitation frequency, but rather of competing influences of excitations with different signs of their rotatory strengths on the low-frequency ORD. In the example, the negative sign of the low-frequency ORD is dominated by the intense second transition. As ω approaches the first excitation from below, the influence of the first transition (in the example with positive rotatory strength) eventually becomes dominant and the ORD changes sign well before ω passes through the first excitation frequency.

21.2.6. General Computational Considerations

As so often in computational chemistry, a study of ECD and ORD of a chiral molecule begins with a determination of the molecular structure. The most common choices here

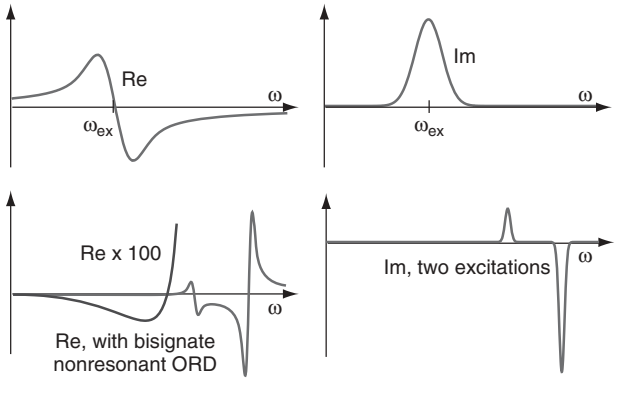

Figure 21.2. Qualitative behavior of the electronic linear chiroptical response in the vicinity of an excitation frequency ω_{ex}. Re = real part (e.g., molar rotation $[\phi]$, OR parameter β), Im = imaginary part (e.g., molar ellipticity $[\theta]$, OR parameter β'). A Gaussian broadening was used for this figure [59]. In the lower panel, competition between the first and the intense second transition causes a bisignate nonresonant ORD.

are to determine optimized local minimum structures, usually from a conformational search, or to take structures from molecular dynamics (MD) or Monte Carlo (MC) simulations. Chiroptical properties can then be computed from first principles and subsequently averaged if more than one structure is employed. See Figure 21.3 for a simple flow chart. Semiempirical methods are available for some types of computations (e.g., to simulate the CD of polypeptides [39, 60], and for other applications [13]). More generally applicable first-principles methods are nowadays fast enough to treat relatively large systems. Among the currently popular methods are TDDFT, Hartree–Fock (HF, to some extent), and correlated post-HF wavefunction-based theories such as coupled cluster (CC).

In general, electronic chiroptical properties are sensitive to the approximations made in the electronic structure calculation, and it is therefore advisable to use the most accurate method that one can afford for a given molecule. Beyond the usual method/basis set considerations that are ubiquitous in computational chemistry, if comparisons with experiment are the main interest it is important to check how well the computational model represents experimental conditions. Among the important influences are solvent and concentration effects, as well as finite temperature. Molecular vibrations, even at 0 K, can have a profound impact on optical rotations and should be considered whenever

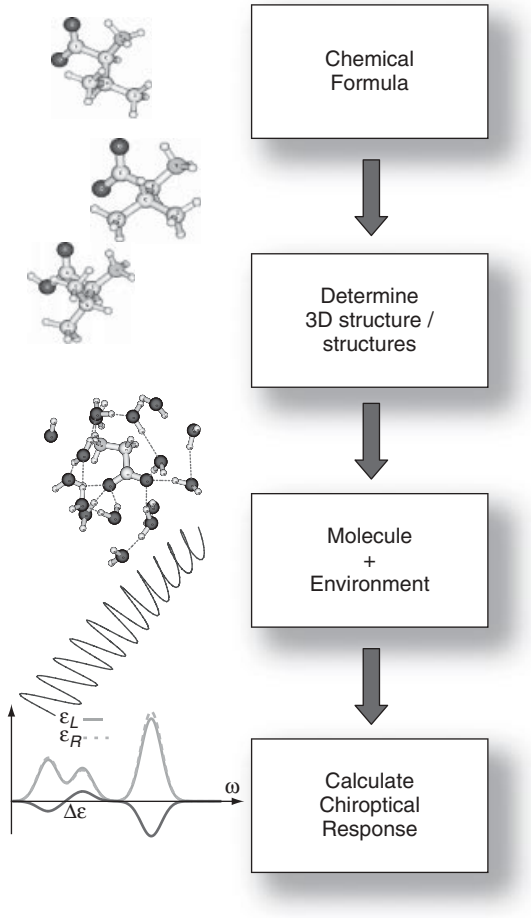

Figure 21.3. Simple flow chart for computations of chiroptical properties of a molecule. The calculations may involve some or all of the following tasks: (1) Optimizing structures, conformer search, molecular dynamics (MD), or Monte Carlo (MC) simulations. (2) Modeling the environment (e.g., solvent). (3) Computing electronic CD, ORD for a selected set of molecules. (4) Averaging over conformer distributions or MD /MC run(s). (5) Calculating vibrational corrections (ORD) or vibronic coupling (CD).

possible [61–64]. In calculations of ECD spectra, bandshapes are often modeled with an empirical broadening when comparisons are made with experiment. However, it can be feasible to calculate vibronic transitions explicitly from first principles, to some degree of approximation [65–71], which takes some empiricism out of ECD spectra simulations.

HF theory is deprecated for computing electronic chiroptical properties because electron correlation is important for their accurate theoretical description. One may argue that a well-parameterized semiempirical method can be preferable over HF. The latter has the *ab initio* label but tends to yield spectra of poor quality. Correlated *ab initio* wavefunction methods can achieve excellent agreement with experiment. For smaller molecules it is possible to perform correlated wavefunction-based ECD and ORD computations routinely, for instance with efficient variants of coupled cluster (CC) methods such as CC2 [72, 73] (an approximate CC singles-doubles) or CC with localized orbitals [74, 75]. Going beyond doubles in the cluster expansion appears to be too demanding at present for routine applications, but might be required in selected cases [73]. Unfortunately, post-HF wavefunction methods tend to scale rather unfavorably with the size of the system. The scaling problem is exacerbated when trying to converge calculations with respect to electron correlation effects—for example, in coupled-cluster SD–SDT–SDTQ, and so on, hierarchies, because increasingly large one-particle basis sets or basis functions that depend on the interelectronic distances are needed to describe the electron cusps accurately.

Currently, most theoretical studies of chiroptical properties employ TDDFT, which has a manageable scaling with system size and typically also has somewhat lower demands on the basis set. TDDFT is an umbrella acronym for a large variety of different levels of approximation. For a description of some of the approximations in TDDFT and their potential detrimental impact on calculated ECD spectra and on optical rotation, the reader is referred to reference 8. Among the more common problems are the asymptotic behavior of the XC potential and self–interaction errors. Hybrid functionals with a large fraction of HF exchange (50%) are often employed for calculations of electronic chiroptical properties, in part to balance these issues. In recent years, so-called range-separated or long-range-corrected or Coulomb-attenuated functionals [76–78] have become popular. It appears that these functionals have fewer difficulties to treat charge-transfer (CT) excitations than more commonly used functionals [79–81]. "Double–hybrid" functionals that include a perturbative electron correlation term were introduced recently and have also been shown to yield better CD band positions than standard nonhybrid and hybrid functionals [82]. Regarding the adiabatic approximation introduced in Section 2.2, one of its better known consequences is an inability of adiabatic XC kernels to describe simultaneous excitations of more than one electron. Because of the sometimes pronounced effects from other approximations in the XC potential and kernel, along with basis set truncation effects, it is somewhat unclear how strongly the adiabatic approximation in comparison limits the ability to accurately predict ECD and ORD in the UV–vis range of frequencies.

21.3. ECD AND ORD CALCULATIONS FOR ORGANIC MOLECULES

The literature on *ab initio* calculations of ECD and ORD of organic molecules is vast and has been reviewed a number of times in recent years [8–11, 13, 18]. This section is intended as a brief overview of the capabilities of contemporary theoretical methods to solve a wide array of problems with calculations of ECD and ORD. Regarding

computational benchmark data, the emphasis is on TDDFT since correlated *ab initio* and semiempirical wavefunction methods are discussed in other chapters. Solvent effects are discussed in detail in other chapters as well. The reader is referred to these chapters and references 18 and 8 for details and a review of recent literature.

21.3.1. ECD Spectra: Selected Examples

Among the first TDDFT calculations of electronic CD reported in the literature are those for [n]–helicenes [83]. These molecules have fascinated researchers for a long time and have also drawn significant efforts from theoreticians [84–86]. The spectra are in some sense[13] representative for the range and limitations of available first-principles theory-based computational methods suitable for ECD spectra calculations of general organic and inorganic molecules ranging in size from small to large. Good agreement with experiment was obtained in Reference 83 with the BP86 nonhybrid functional and the SV(P) Gaussian-type basis augmented with a set of diffuse functions at the ring centers. The way the spectra were simulated is very typical for molecules of this size: The vertical excitations were calculated, blue–shifted by 0.45 eV, and subsequently broadened with Gaussian functions to mimic the experimental bandshapes. Figure 21.4 shows a calculated CD spectrum of (M)-hexahelicene obtained by the author. A similar spectrum was published in reference 87. These and other computed spectra from references 83 and 87 demonstrate the aforementioned good agreement between calculations and experiment that can be obtained from first-principles computations as long as electron correlation is considered to some degree. "Good" agreement with experiment has the following

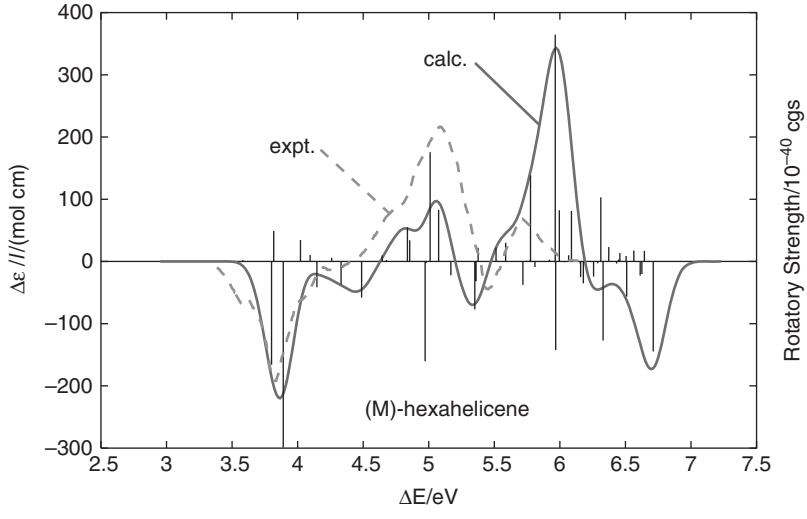

Figure 21.4. CD spectrum of (M)-hexahelicene. TDDFT calculations with the BP86 functional and a double-ζ polarized Slater-type basis, using the code described in reference 87. Gaussian broadening ($\sigma = 0.15$ eV) of the vertical excitations. Calculated excitation energies shifted by +0.45 eV. Experimental data for the CD spectrum taken from reference 83.

[13] The helicene chromophore is inherently chiral and the ECD is intense. Calculations on molecules where an achiral chromophore is weakly perturbed by a nearby chiral center can be more challenging.

meaning in this context: The main spectral features are correctly reproduced, and overall the broadened vertical CD spectra simulated from the calculations match the experimental spectra quite well after a global shift of the excitations which is often necessary, for instance because of a tendency of TDDFT to underestimate excitation energies [49]. As a general rule, intensities are difficult to reproduce correctly, and in the simulated spectra they depend on the chosen broadening. Although the broadening parameters are 'fudge factors' in these types of calculations there are physically reasonable limits for them, and within these limits they usually cannot arbitrarily change the spectra. As a rule of thumb, intensities tend to agree to within a factor of 2–5 between theory and experiment.

Charge-transfer excitations that often plague TDDFT computations are not a strong concern for the spectrum of hexahelicene, and even the performance of a long established gradient functional such as BP86 is very agreeable. For molecules with different types of chromophores, it can be necessary to resort to shape corrected XC potentials, hybrids without or with range separation in the exchange component, or to correlated wavefunction methods (if computationally affordable for the molecule of interest). Regarding the performance of range-separated hybrid functionals, Shcherbin and Ruud [88] explored the robustness of several parameterizations of the Coulomb-attenuated B3LYP functional (CAM–B3LYP) [77] for chiroptical response calculations, with rotatory strengths as the main focus. The test set comprised 14 molecules that had previously been benchmarked for optical activity by a number of groups using TDDFT and CC [87, 89–92]. The calculations showed that it is difficult to parameterize the CAM-B3LYP functional to yield correct excitation energies and have the correct asymptotic behavior across a diverse set of molecules, while simultaneously producing uniformly accurate results for the rotatory strengths. See also a recent optical rotation benchmark where range-separated hybrids did on average not give better agreement with experiment than standard hybrids [192]. In general there is no "one size fits all" type of functional to compute sensitive response properties, and therefore researchers need to ascertain that the chosen functional and basis set are capable of getting the important physics right.

For large molecules, locating and considering all thermally accessible conformers in the calculations can become cumbersome. Missing a conformer can be an important source of error when attempting to compare calculations with experiment. If different conformers afford ECD bands of opposite signs and/or very different magnitude, this can also lead to a deterioration of the computed results even if the electronic structure method is, in principle, able to deliver an agreement with experiment such as shown in Figure 21.4 or better. In the context of conformer averaging, the accuracy of the relative energies of the conformers is of vital importance. For nonrigid molecules, depending on the degree of cancellation of ECD strength, errors in the calculated mole fractions can be just as influential as those in the calculated CD. Such issues have been discussed in more detail in many applications of computational methods to calculate ECD and OR of flexible molecules; for a selection see references 17 and 93–100.

An ECD example from natural product chemistry is shown in Figure 21.5. One way of bypassing the problem of conformer distributions in solution is to record a spectrum in a solid-state matrix. In this case, computations may focus on a single structure [13, 102–104]. Figure 21.5 shows the computed, solid-state, and solution-phase CD of (5S,6S,10aR) Blennolide A. The agreement of the computed CD spectrum with experiment is seen to be reasonable both for the solid-state (KCl disc) and the solution-phase (dichloromethane) spectrum. Among other cases where a combination of solid-state CD and computations was used to assign an absolute configurations are globosuxanthone A [105], papyracillic acids [106], ascochin and ascodiketone [107], massarilactones

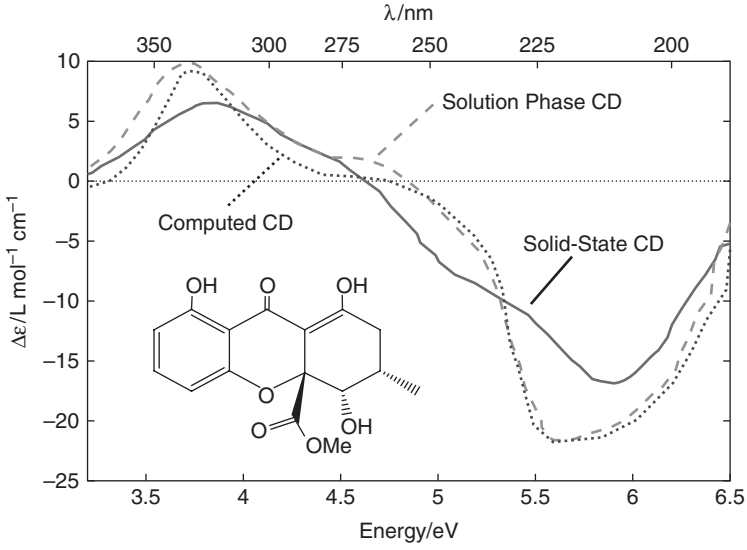

Figure 21.5. Comparison of solid-phase (KCl), solution-phase (dichloromethane) and computed (B3LYP/TZVP) CD spectrum for (5S,6S,10aR) Blennolide A. Spectral data used to prepare the figure were published by Zhang et al. [101].

[108], 2,3-dihydropyrenophorolic acid and 2,3,10,11-tetrahydropyrenophorol [109], oxepino[2,3-*b*]chromones, 20-acetylsinularolide B [110], fusidilactone D [111], blennolide G [110], tetracyanobutadienes [112], and macropodumines [113].

21.3.2. Single-Wavelength Optical Rotation Calculations

Single-wavelength calculations of OR have demonstrated great utility for routine assignments of absolute configurations (ACs) of organic molecules [12, 15, 16, 18]. However, since all calculations have inherent systematic errors, and because the computational model typically strongly oversimplifies the conditions under which experimental data are obtained, AC assignments need to take the computational error bars into consideration. Stephens et al. [16] pointed out that for a reasonably safe AC assignment within the 95% confidence interval the computed specific rotation of the correct enantiomer should be within $\pm 2\sigma$ from the experimentally measured value and simultaneously the calculated OR for the other enantiomer has to be outside of the $\pm 2\sigma$ interval. Here, σ is the RMS deviation of the calculated OR from experiment for a given level of theory. If the molecule has multiple conformers, or more than one stereocenter, the criteria should be even more strict.

The simplest and most commonly used computational model is to ignore solvent effects and to neglect vibrational corrections. Stephens et al. determined for B3LYP/aug-cc−pVDZ//B3LYP/6-31G(d) gas-phase GIAO TDDFT computations a value for 2σ of about 58 deg/[dm (g/cm^{-3})], meaning that reasonably safe AC assignments can be made with this computational model if $[\alpha]_D$ has roughly this magnitude or higher [16, 89]. The value for σ was determined with a benchmark set of 65 chiral rigid molecules with relatively small specific rotations not exceeding 100 deg/[dm (g/cm^{-3})]. The selection of molecules included 17 alkanes, 16 alkenes, 19 ketones, and 13 heterocycles. The calculated and experimental ORs did not agree in sign for eight of the 65 molecules. Subsequently, McCann and Stephens [114] computed ORs and ECD spectra of 26 conformationally rigid alkenes with $[\alpha]_D$ up to ± 500 deg/[dm (g/cm^3)], along with two conformationally flexible alkenes. The RMS deviation between the calculations and experiment was found to be 29 deg/[dm (g/cm^{-3})] ($2\sigma = 58$), consistent with the RMS

error from reference 16. The calculated ECD spectra were considered to be of "modestly good to poor" quality.

Although B3LYP remains a popular functional, it is likely that currently accepted (and expected) error bars of single-wavelength OR calculations will be refined in the near future, based on calculations with better performing functionals or reasonably fast correlated wavefunction methods. In order to yield significantly smaller RMS deviations, the computational model is likely going to require solvent effects and temperature-dependent vibrational corrections [61, 63, 115], although errors in the gas-phase static equilibrium value might remain a dominant source of error [116]. For small-cage bicyclic structures that are abundant in commonly used benchmark sets the basis set, convergence is perhaps slower than previously suspected [117].

As a consequence of the SOS nature of OR, Eq. (21.3), the accuracy of OR calculations is indirectly influenced by the accuracy of the rotatory strengths and the associated electronic transition energies in the ECD spectrum. A way to reduce errors from shifts in the computed excitation energies can be to apply wavelength corrections and to calculate the optical rotation from a SOS [118]. Wavelength corrections have also been discussed in reference 119 in a concerted OR & ECD study of $[3_2]$(1,4)barrelenophanedicarbonitrile. It might be possible to include a wavelength correction in the linear response equations for β, to be supplied as an empirical parameter in the computations. If the OR is calculated from a sum over states one needs to keep in mind that the SOS equation for OR converges extremely slowly as a function of how many excitations are included [98, 120, 121].

Optical rotations have been computed for helicenes [90, 91]. The transitions in the UV–vis range calculated from TDDFT are too low in energy compared to experiment, as pointed out in Section 21.3.1. Given that the energy denominators in the SOS of the optical rotation parameter decrease if the spectrum is red-shifted, and given that the available computed spectra agree reasonably well with experiment for the CD intensities, one may expect an overestimation of the OR magnitude in TDDFT computations, which is indeed what has been found. As an example, for (M)-hexahelicene a BP86 value from reference 91 is -5259 deg/[dm (g/cm^{-3})], compared to an experimental specific rotation of -3640. A hybrid functional (B3LYP) result of -4887 deg/[dm (g/cm^{-3})] obtained by Grimme agrees somewhat better with experiment, although it is still too large in magnitude [90]. Similar trends have been reported for other [n]-helicenes as well [90, 91]. We recently obtained excellent agreement with the experimental OR of hexahelicene [122] using the BHLYP functional, which has a larger (50%) fraction of HF exchange than B3LYP (20%). However, the trend of TDDFT to underestimate the energies of certain types of excitations that are typically present in organic molecules does not lead to a uniform tendency to overestimate OR magnitudes, as evidenced by the more or less statistical errors reported in several benchmark studies where diverse test sets of molecules were considered [16, 89–91, 114]. For response property calculations, it appears that functionals such as BHLYP with an elevated fraction of HF exchange tend to perform better than B3LYP or nonhybrid functionals, but not to a degree that would allow to make a recommendation for their "black box" use. Likewise, range-separated hybrids do not cure all TDDFT problems, as already mentioned above in the context of ECD spectra.

Norbornenone has gained some notoriety for its large optical rotation that seems to be particularly sensitive to approximations in the computational model. The specific rotation in solution (hexane) is -1146 deg/[dm (g/cm^{-3})] [123]. Moscowitz [124] considered the twisted arrangement of the C═O and C═C bonds an inherently chiral chromophore. The electronic coupling between the two double-bond moieties is very important; the related

molecules norbornanone and α-pinene with *either* a C═O *or* a C═C chromophore have small specific rotations (within ±50 deg). The OR depends particularly sensitively on the O═C-C═C dihedral angle, as was shown by computations [120]. Hybrid DFT calculations (B3LYP/aug-cc-pVDZ) using an optimized geometry yield a specific rotation that is very close to experiment [89, 94]. However, CC theory gives a much smaller magnitude of the optical rotation [94]. Nonhybrid DFT strongly overestimates the OR magnitude [91].

21.3.3. Optical Rotatory Dispersion

Instead of considering the optical rotation at a single frequency, configurational assignments can be bolstered by considering the ORD over a larger frequency range. One may conceptually separate the "normal" dispersion of the OR in the off-resonance (transparent frequency) regime from the "anomalous" dispersion around electronic transitions. See Figure 21.2 for a qualitative illustration.

An example for a successful calculation of ORD in the transparent frequency range is the case of (P)-(+)-[4]triangulane [75, 125]. Experimentally, the specific rotation in the neat state ranges from around 200 deg/[dm (g/cm^{-3})] at 589.3 nm to over 600 deg/[dm (g/cm^{-3})] at 365 nm. Coupled-cluster (CC) and TDDFT methods were compared in reference 75. Both methods yielded ORs that agreed well with experiment, with CC performing being somewhat better (assuming negligible vibrational corrections and medium effects). It was noted, however, that the CC calculations required a large amount of computer time.

As an example for a concerted computational and experimental study of flexible molecules, Wiberg et al. [126] have considered the ORD of 2,3-hexadiene and 2,3-pentadiene. The ORD of 2,3-hexadiene was experimentally measured in gas phase, in neat liquid, and in a number of different solvents, demonstrating sizable differences between the gas-phase and condensed-phase optical activity. The rotation of the ethyl group as shown in Figure 21.6 gave rise to three conformers of 2,3-hexadiene labeled *cis*, gauche(+), and gauche(−).

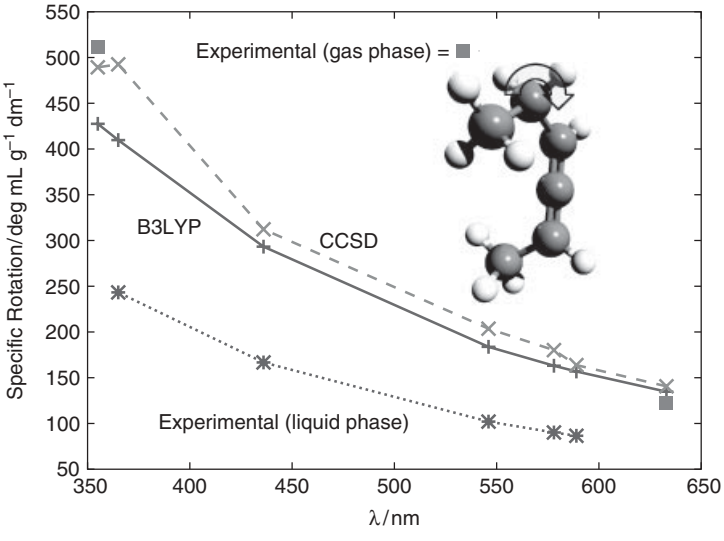

Figure 21.6. Calculated rotamer averaged and experimental ORD of 2,3-hexadiene. Data to prepare the figure were taken from Wiberg et al. [126].

Figure 21.6 shows the calculated Boltzmann-averaged nonresonant ORD of 2,3-hexadiene along with experimentally measured optical rotations for selected wavelengths for liquid and gas phase, as reported by Wiberg et al. [126]. The computations agree well with the gas-phase measurements, in particular for the CCSD level of theory. The computations also highlight the potential importance of solvent effects, which contribute to the RMS deviations between theory and experiment discussed in the previous section.

Some molecules exhibit a bisignate nonresonant ORD, which can be caused by different influences; among those are vibrational effects. A bisignate ORD can also be caused by the intrinsic electronic optical activity of the molecule, as illustrated in Figure 21.2, via a competition of low-frequency and higher-frequency transitions with rotatory strengths of different signs and magnitudes. A selection of small molecules with bisignate nonresonant ORD for which computations have been performed is β−pinene [118, 127], spiroselenurane [118, 128], methyloxirane [118], dimethyloxirane [8] and *trans*-dimethylcyclopropane [91, 129].

For absolute configuration assignments based on resonant ORD, it can be sufficient if the calculations reproduce the ORD sign pattern as a function of wavelength [48, 118, 130]. As an example, Giorgio et al. [130] have measured and computed the ORD of nine rigid organic molecules [(−)-verbenone, (−)-4-methylverbenene, (−)-fenchone, (−)-methylenefenchone, (+)-camphor, (−)-methylenecamphor, (+)-nopinone, (−)-β-pinene, and (−)-Tröger's base]. The computations employed Hartree–Fock and DFT (B3LYP), along with the rather small 6-31G(d) Gaussian-type basis set. The sign patterns of the calculated ORDs matched the experimental ones, prompting the authors to conclude that such calculations are suitable for AC assignments as long as the ORD includes resonant frequencies. Since the OR is generally sensitive to the quality of the basis set, it is presently unclear if such a "small basis but more data points" approach can be applied more routinely.

One of the drawbacks of the calculations of reference 130 has been that no excited states damping was considered in the calculations. The divergent ORD (see Figure 21.1) makes a direct comparison with experiment difficult. It was later shown that computations employing damping in the linear response calculations allow for a direct comparison with experimental resonant ORD [129]. For the study reported in reference 129, five organic molecules were selected from reference 130 (verbenone, fenchone, camphor, nopinone, Tröger's base), another was selected from reference 91 (dimethyl-cyclopropane [131]), and as an example for a transition metal complex the tris-bidentate $[Co(en)_3]^{3+}$ complex ion was chosen [see the section on metal complexes (Section 21.4) regarding the latter]. Some authors refer to the damping method as the complex polarization propagator, or as complex linear response, since the calculations yield bot the real and the imaginary part of the OR parameter at a given frequency. Employing a global empirical damping factor γ yields OR parameters that conceptually correspond to letting each $\Gamma_j = \gamma$ in Eqs. (21.7) and (21.8). The ORD calculated in this way with damping corresponds to the Kramers–Kronig transformation of the ECD broadened with Lorentzian functions, which was explicitly demonstrated in reference 121. The dampened ORD curves reported in reference 129 matched the experimental trends and the magnitudes of the peaks and troughs of the ORD quite well in the 200- to 600-nm range—except for Tröger's base, for which agreement was somewhat worse. As an example for these calculations, the calculated ORD of fenchone is compared to experimental data in Figure 21.7.

Two drawbacks of the method to calculate damped resonant ORD were subsequently addressed in reference 59. One drawback is that one needs to compute the ORD at a

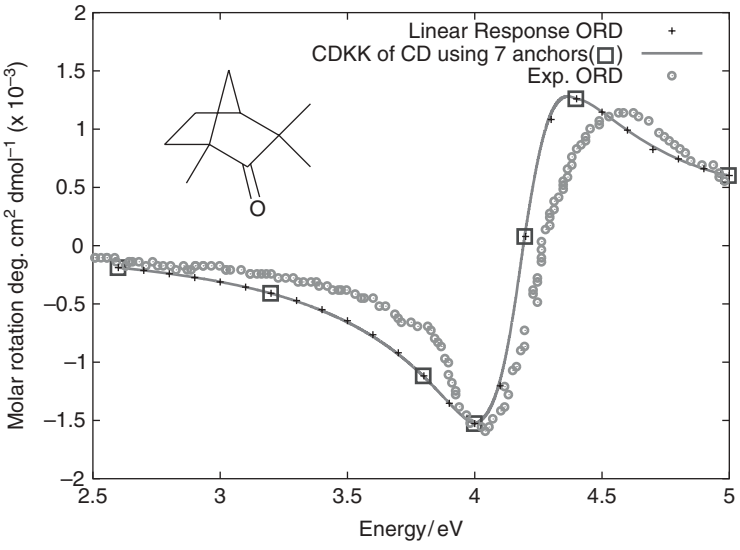

Figure 21.7. Comparison of experimental ORD of fenchone in the carbonyl *n*-to-π^* transition region with TDDFT calculations of the OR on a fine frequency grid using a damping parameter, as well as with the ORD calculated from a 7–anchor point chained KK transformation [59]. TDDFT calculations using an asymptotically corrected XC potential (SAOP) and a diffuse triple-ζ doubly polarized Slater-type basis set.

relatively large number of frequency points in the resonance region in order to obtain a well-resolved rotatory dispersion curve. The other drawback is that the damping technique causes an intrinsic Lorentzian lineshape, although typically a Gaussian lineshape would be more realistic [132]. Both issues can be addressed by realizing that rapid oscillations of the ORD are caused by transitions nearby in frequency and that these oscillations are well described by simply performing a KK transformation of the ECD bands corresponding to these nearby transitions. However, the complete ORD includes contributions from all other excitations as well, creating a kind of "baseline" on which the anomalous dispersion is superimposed. One can combine calculations of the ORD at a few 'anchor' frequency points with calculations of the ECD spectrum over the frequency region of interest in form of so–called subtractive KK transformations [59, 133]. With such transformations, the rapid oscillations in the UV–vis range ORD are obtained from the KK transformation of the UV–vis range ECD spectrum while the calculated anchor points $\beta(\omega_i)$ eliminate errors from not including the complete spectrum. If the ECD is broadened with Lorentzian functions first, one can use the subtractive transformations in a two-step forward–backward fashion to create ORD curves related to Gaussian or other lineshapes [59].

In reference 59 it was found that $N-1$ KK transformations with two anchor points, chained together over a set of N anchors like a splines fit, performed better than a straightforward application of a single N anchor point transformation. We have dubbed this technique a "chained doubly subtractive Kramers–Kronig" (CDKK) transformation. Figure 21.7 shows a 7-point CDKK (line) that agrees almost perfectly with the ORD calculated on 25 frequency points. The computational time savings were about a factor of 3 in this case since the calculation of a few excitation frequencies is comparable to calculating the ORD for one frequency. The computing effort for the KK transformations is negligible. The subtractive KK technique was also applied with just two anchor points to the [4] triangulane system of reference 75 discussed above, indicating that it can significantly save computational resources for larger systems and in combination with computationally expensive correlated wavefunction-based linear response methods.

21.3.4. Effects from Molecular Vibrations on Optical Rotation and ECD Spectra

Vibrational effects can play an important role in the chiroptical response of a molecule [61, 118, 134]. On the extreme end, if a molecule becomes chiral by isotopic substitution, vibrational corrections would be essential. In less extreme cases, the OR might exhibit pronounced zero-point vibraional corrections (ZPVCs) and temperature effects that are not simply explained by changes in mole fractions (if the molecule has multiple conformers) or by temperature-dependent solvent effects.

Vibrational corrections to calculated ORs have been investigated for a number of small molecules at various levels of theory [73, 116, 134–136]. Regarding the overall expected magnitude of zero-point vibrational corrections (ZPVCs) for optical rotations, Mort and Autschbach [61] have considered a set of 22 rigid organic molecules (B3LYP/aug-cc-pVDZ). The individual ZPVCs varied between 2% and 155%, with a median of about 20% relative to the calculated equilibrium optical rotation. The *average* agreement of computed and experimental data did not improve when including vibrational corrections. One reason might be that solvent effects need to be considered simultaneously. Another reason might be the performance of B3LYP for the equilibrium ORs. Pedersen et al. [116] recently proposed to combine TDDFT vibrational corrections with CC equilibrium optical rotations in order to obtain more accurate results. Another issue is the basis set convergence, which was already pointed out.

The data set needed to generate ZPVCs of optical rotations can also be used to predict temperature effects as far as the temperature-dependent population of vibrational excited states is concerned [62, 63, 73]. Following an initial report for fenchone [62], in reference 63 the temperature-dependent ORs of α-pinene, β-pinene, *cis*-pinane, camphene, camphor, and fenchone were calculated with TDDFT (B3LYP/aug-cc-pVDZ). The study was motivated by the availability of experimental data for these molecules and previous speculation that the observed T-dependence originated in vibrational effects [137].

For four out of the six compounds the temperature dependence seen experimentally was reproduced. A selection of the results at one of the wavelengths considered is shown in Figure 21.8. The experimental trends are reproduced by the calculations excellently to moderately well, demonstrating that the observed T-dependence for these molecules might indeed be dominated by vibrational effects. The temperature trends calculated for β-pinene and *cis*-pinane were opposite to the experimental trends. These cases were analyzed further by considering low-lying excitations in their ECD spectra, but the analysis was inconclusive. It is presently unclear if the disagreement between theory and experiment for these molecules is caused by basis set incompleteness or by deficiencies in the functionals or whether the temperature-dependence of the OR for these molecules is not dominated purely by vibrational effects.

A recurring problem in calculations of vibrational averages is the treatment of hindered rotations, in particular of methyl rotations. In reference 64 a computational protocol for treatment of such hindered rotations has been suggested. In a nutshell, in this approach a quasi-free rotation of a functional group is treated separately from the vibrational average, using numerically calculated hindered-rotor wavefunctions. When there is strong coupling between the modes, the rotation cannot be cleanly separated. The validity of the rotational separation can be tested by comparing rotational averages calculated with relaxed and unrelaxed potentials. Large differences indicate strong coupling. To calculate the relaxed potentials, the molecular coordinates are optimized for each rotational angle, except along the rotational coordinate.

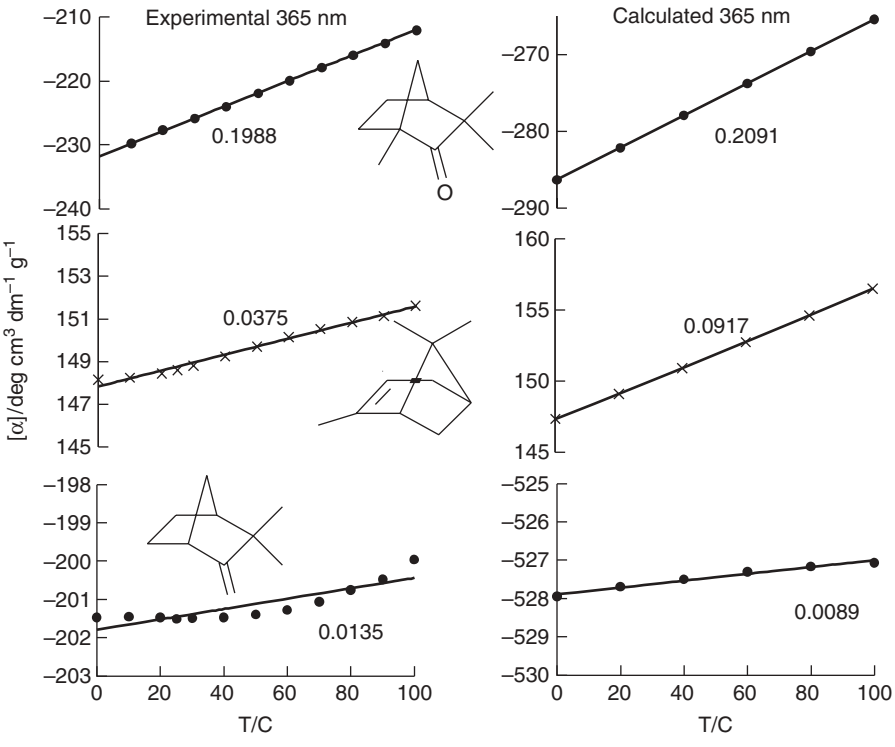

Figure 21.8. Temperature dependence of the optical rotation at 365 nm. Top to Bottom: Fenchone, α-pinene, Camphene. Calculated data to prepare the graphs were taken from reference 63, experimental data from reference 137. Additional data for 546 and 589 nm were also reported in these references. The slopes of linear fits are given in the figures in units of deg/[dm (g/cm^{-3}] per K.

Vibrational effects are also encountered when considering the lineshapes and vibrational fine structure of ECD spectra. Typically, when ECD spectra are simulated, the computed "stick spectra" corresponding to vertical electronic transitions are broadened with Gaussian or sometimes with Lorentzian functions. Bandshapes and widths in electronic spectra resulting from vibronic fine structure can also be computed directly [65, 68–71, 138–140]. In these approaches, an empirical broadening is still applied, but to the individual vibronic transitions. The shape and width of the complete electronic CD band is then determined nonempirically by the computed distribution and the computed intensities of the vibronic transitions. One should keep in mind that there are other broadening mechanisms and that the presence of solvent, for instance, may need particular consideration.

Several studies have considered vibronic effects in ECD spectra at a first-principles level. Promising results were obtained for *trans*-(2,3)-dimethyloxirane [68] by computing Franck–Condon (FC) factors within TDDFT. The ECD spectrum for this molecule is shown in Figure 21.9 in comparison with experiment. The experimental gas-phase spectrum displays well-resolved vibronic fine structure, which is for the most part reproduced in the simulated spectrum. An empirically broadened vertical spectrum has negative CD intensity between 7.5 and 8 eV, which does not agree with experiment [87], unlike the spectrum of Figure 21.9. A follow–up study by Nooijen [138] has focused on the

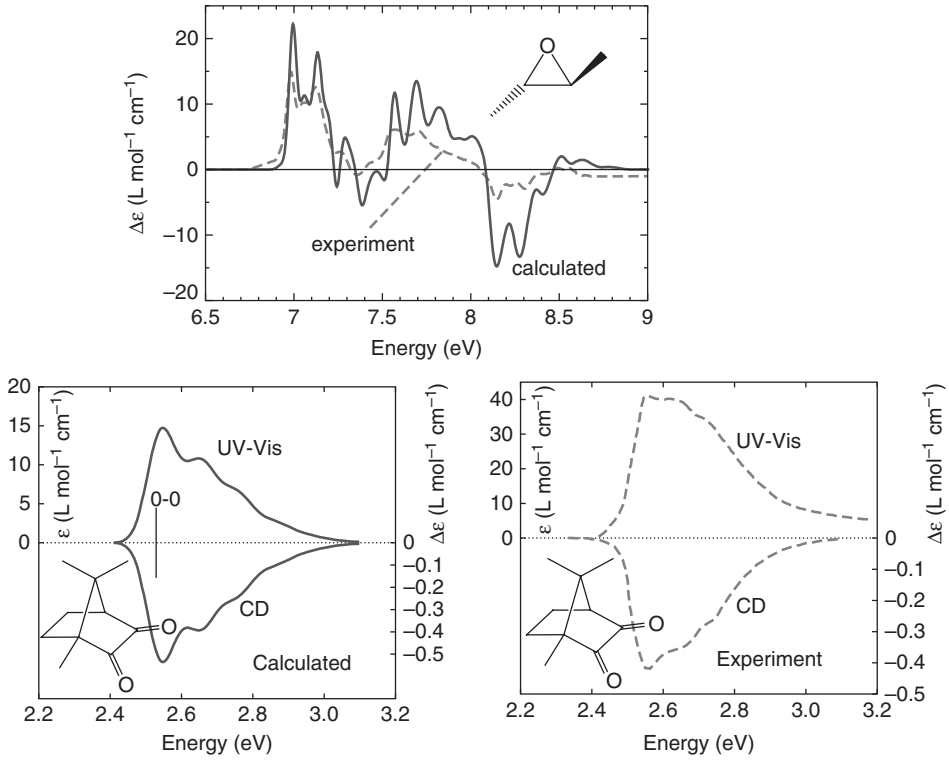

Figure 21.9. Experimental spectra, as well as simulated gas-phase spectra based on computed DFT/TDDFT electronic and vibrational transitions, for (−)-(2*S*,3*S*)-*trans*-dimethyloxirane (DMO, top, SAOP potential) and *d*-camphorquinone (bottom, CAM-B3LYP). Data to prepare the graphs were taken from references 68 and 69. Experimental gas-phase data for DMO originally reported in reference 141. Solution data for camphorquinone were published in reference 142.

intensity differences in the computed and experimental spectrum at higher energy. Lin et al. [70] have applied a methodology reported by Santoro et al. [139] to calculate the vibronic fine structure in the CD spectrum of (*R*)-(+)-3-methylcyclopentanone and obtained a convincing agreement between simulation and experiment. Figure 21.9 shows another example applying the method of Santoro et al.: the absorption and ECD spectrum for the lowest energy excitation of *d*-camphorquinone. The example has been taken from a recent TDDFT study of this molecule and (*S*, *S*)-*trans*-β-hydrindanone which had the aim of modeling their circular polarized *emission* (CPL) spectra [69]. As can be seen, the predicted absorption and ECD bandshapes and band widths agree well with experiment. The calculated absorption intensity appears to lack some intensity, but the deviation from experiment is within typical boundaries. For the carbonyl centered valence transition underlying the spectra of Figure 21.9, basis set effects and the functional dependence were demonstrated to be relatively modest. The CPL and emission spectra (not shown) agreed similarly well with experiment as the ECD and absorption spectra.

21.3.5. Chiral Sectors in Molecules from an *Ab Initio* Perspective

Chiral-response "sector maps" computed from first principles were recently used to describe ECD and OR induced by small perturbations in nonchiral chromophores

[98, 143, 144]. The computation of such sector maps has been inspired by the sector rules for ketones that are well known to chemists [44, 124, 145–147]. The first-principles theory-derived maps can be constructed by creating a grid around the chromophore of interest and by scanning the chiroptical response induced in the chromophore by a point charge or another perturbing entity on each grid point. The ECD and OR computations are based on first-principles methods. However, one needs to keep in mind that the maps are simplified models for the corresponding chromophores in chiral molecules because the nature of the perturbation is highly idealized. An example is the OR induced by a perturbing charge around a carboxylate functional group, which is a common chromophore in chiral organic molecules. In Figure 21.10 both a three–dimensional scan of the chiral sectors and a contour map are shown.

The sign pattern around the C—O bonds resembles those of the ketone sectors, with the carboxylate map resembling somewhat of an overlay of two C═O sector maps at a 120° angle. A model for such a chromophore has been considered by Jorgensen in 1971 [148] to rationalize the pH dependence of the optical rotation of amino acids (see below for further details). Sector rules for other chromophores of interest can easily be constructed from such computed maps.

An example for an application of computed sector maps is the OR of phenylalanine [143]. Sector maps for the phenyl chromophore (benzene) were computed for the molar rotation and for the ECD of selected transitions. The findings of reference 143 were in agreement with a revision of the benzene sector rule by Pescitelli et al., who investigated a set of chiral molecules with phenyl substituents (PhCH(Me)R, with R = Et, ^{n}Pr, ^{i}Pr, and ^{t}Bu) [149].

Sector maps have recently helped to uncover the reasons why the optical rotation of natural amino acids in aqueous solution becomes more positive upon adding a strong acid. This interesting effect has been described quite some time ago by Clough, Lutz, and Jirgensons [150–152] (CLJ). TDDFT computations [98] (BHLYP and B3LYP, aug-cc-pVDZ basis set) have been carried out for a number of amino acids which demonstrated that the molecular origin of the CLJ effect can be traced back to a sign change of the CD of the lowest-lying excitation in the carboxylic acid functional group upon protonation. Sector maps computed for an achiral glycine model were used to rationalize this trend. The glycine optical rotation sectors are shown in Figure 21.11. They are seen to be

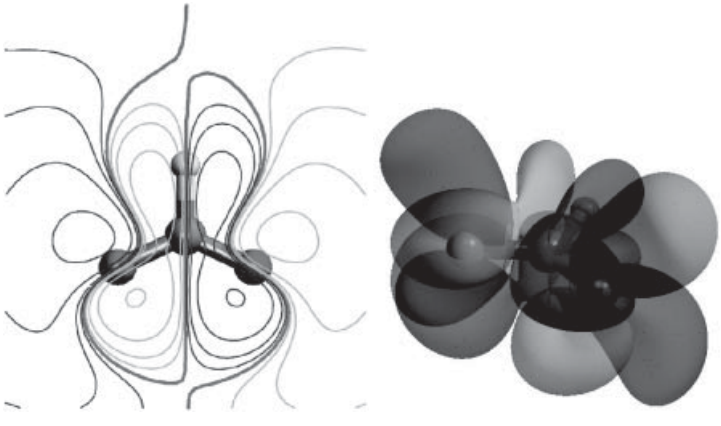

Figure 21.10. Optical rotation induced in the $-COO^{-}$ chromophore by a point charge (B3LYP/aug-cc-pVDZ, formate model, arbitrary units). Left: Contour map 1.3 Å above the molecular plane. Right: 3D Isosurfaces. Arbitrary units. Darker shaded isosurfaces and contours indicate negative induced optical rotation.

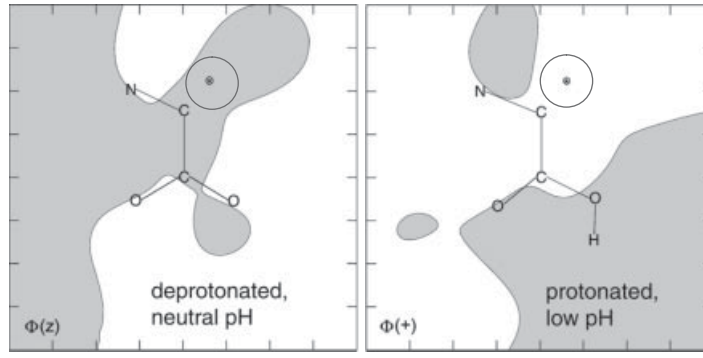

Figure 21.11. Molar rotation sectors for glycine, obtained with perturbing point charges of −0.1 and +0.3 for the deprotonated and protonated carboxylic acid groups, respectively (BHLYP/aug-cc-pvDZ). The scan was performed 1.3 Å above the chromophore plane. White areas indicate an induced positive optical rotation, gray areas indicate negative optical rotation. The circles indicate the approximate position of the link atom for the amino acid side chain. See reference 98 for further details.

strongly distorted compared to that of a carboxylate group in the absence of the α-amino substituent (Figure 21.10) which renders the application of an overlapping carbonyl model invalid. Moreover, the calculations showed that the sector model is only applicable if the perturbing charge changes sign from negative to positive upon protonation at the carboxylate group. In reference 98 this "antioctant" behavior was rationalized by the overall positive charge of the protonated species, causing the side chain to compete for electronic charge with the amino acid chromophore.

The CLJ effect can be generalized to other α-substituted chiral carboxylic acids [144]. A combination of computed OR, ECD, and sector maps (BHLYP/aug-cc-pVDZ) for hydroxo and fluoro acids indicated that the physical origin of the generalized CLJ effect is the same as for amino acids. This links the absolute configuration directly to the sign of the generalized CLJ effect. For conformationally flexible molecules with small optical rotations, the presence of a CLJ-type effect can potentially improve the reliability of computation-aided assignments of absolute configurations, at the cost of additional computations needed to compare protonated and deprotonated species.

21.4. METAL COMPLEXES AND METAL CLUSTERS

Chiral metal complexes have for a long time resisted a theoretical treatment by first-principles methods, mainly because of the relatively large number of electrons present in even the smallest members of this class of compounds. Semiempirical computational studies of ECD in metal complexes dating back up to several decades have been reviewed by Kuroda and Saito [25]; see also references 153–155. This section focuses on more recent theoretical work carried out with TDDFT.

A number of studies have aimed at developing a better understanding of the origin of optical activity in the various types of transitions that may take place in a transition metal complex, such as ligand-field (LF) transitions involving mainly *d* orbitals, ligand-to-metal and metal-to-ligand charge transfer (LMCT, MLCT), and predominantly ligand-based transitions such as π-to-π^* in complexes with phen, bipy, and other unsaturated ligands,

which may afford intense exciton coupling CD bands. Other theoretical works have focused more closely on the performance of TDDFT, in particular how some of the better known issues such as self-interaction errors and the difficulties of standard functionals to treat CT excitations affect calculated CD spectra. At the time of writing this chapter, there has been only a small body of data available for OR/ORD for metal complexes calculated from first principles. Much of the discussion in this section therefore focuses on ECD spectra.

21.4.1. Representative Examples and Benchmark Computations

Figure 21.12 shows three representative cases where simulated CD spectra (Gaussian broadened vertical excitations) of transition metal complexes are compared to experiment. The complexes have D_3 symmetry, with electrically and magnetically allowed transitions between the A_1 ground state and excited states of A_2 and E symmetry. As it is the case for two of the spectra in Figure 21.12, global shifts of calculated excitation energies are often applied to align band peaks with experiment, both for organic molecules and for metal complexes. For the Co ethylene diamine complex, only part of the spectrum is shifted.

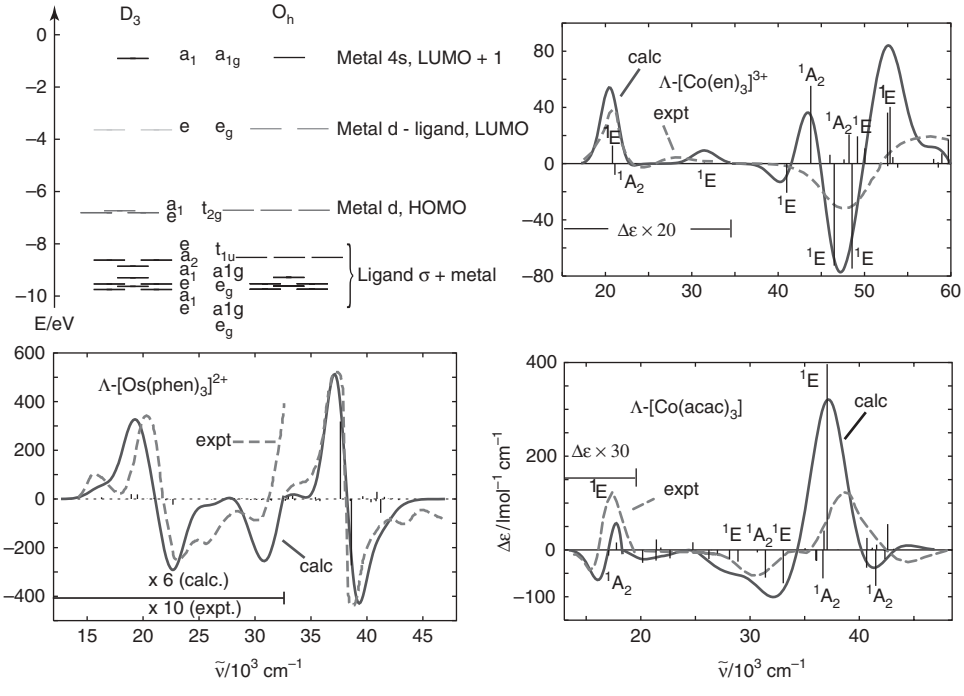

Figure 21.12. Representative examples of calculated CD spectra of Λ tris–bidentate metal complexes, in comparison with experiment. Data to prepare the figures were taken from references 25 and 156–159. Also shown is a calculated orbital diagram for $[Co(en)_3]^{3+}$ in D_3 symmetry, along with the orbital levels of a hypothetical octahedral complex. The first pair of calculated *d*-to-*d* transitions for $[Co(en)_3]^{3+}$ was shifted by -6×10^3 cm^{-1}. All calculated transitions for $[Co(acac)_3]$ was shifted by -4×10^3 cm^{-1}, and for $[Os(phen)_3]^{2+}$ by $+2 \times 10^3$ cm^{-1}. Parts of the spectra are magnified.

The spectrum of the tris(ethylenediamine)–cobalt(III) complex ion, $[Co(en)_3]^{3+}$, is comparatively simple. There is a range of weakly intense LF transitions (T_{1g} in O_h parent symmetry, split into A_1 and E components under D_3 symmetry) below $35 \times 10^3 cm^{-1}$, followed by a set of more intense LMCT excitations. The TDDFT-based assignment is in agreement with the assignment based on experimental observations [25, 156]. The sign and ordering of the A_1/E pairs of excitations for a given absolute configuration depend on the geometric distortion of the ligand atoms relative to an idealized octahedral system [160], which is discussed in detail in Section 4.2. The LF excitations are relatively pure HOMO to LUMO transitions when calculated with TDDFT. The orbital diagram for $[Co(en)_3]^{3+}$ shows that the energy splitting between A_1 and E has a corresponding splitting of the t_{2g} HOMO levels into a_1 and e components of different energy upon distortion of the ligand field from achiral O_h to chiral D_3. The experimental spectrum of $[Co(en)_3]^{3+}$ [25] affords two additional very weak bands around 13 to 18×10^3 cm^{-1} assigned to triplet states that were not modeled. Reference 156 reported the lowest calculated triplet state of $[Co(en)_3]^{3+}$ to be $4 \times 10^3 cm^{-1}$ below the S_1 state, in decent agreement with the experimental spectral data. Apart from the excitation energies, the intensities and of course in particular the signs of the rotatory strengths are of critical importance and are seen to be reasonably well predicted by the computations. Other Co(III) complexes studied in reference 156 and follow-up work [161, 162] showed similar agreement with experiment as $[Co(en)_3]^{3+}$.

For tris(acetylacetonato)-cobalt(III), $[Co(acac)_3]$, the agreement with experiment is overall better than that for $[Co(en)_3]^{3+}$. The spectrum of the acac complex is more complex since the experimentally accessible part of the spectrum also includes ligand-based transitions, and the metal and ligand atoms have π interactions that contribute to the spectrum [163]. The first two CD bands have weak intensity and are pure LF transitions. The remainder of the spectrum cannot be cleanly separated into LMCT and ligand π-to-π^*. However, the analysis of the calculated spectra showed that the range from 20 to 34×10^3 cm^{-1} is dominated by LMCT excitations with additional contributions from MLCT, and the range above 40×10^3 cm^{-1} is dominated by ligand π-to-π^* transitions (yielding the intense exciton coupling CD) with additional contributions from MLCT and LMCT [156, 163].

The spectrum of tris(phenantroline)-osmium(II), $[Os(phen)_3]^{2+}$, has been assigned with the help of TDDFT calculations in reference 157. Figure 21.12 shows that the agreement with experiment is remarkably good. The intense CD bands around 35 to 40×10^3 cm^{-1} originate from a "helical" coupling of the long axis polarized π-to-π^* transitions of the phen ligands (see Section 21.4.2 for details). In the lower-energy portion of the spectrum, the most intense transition are of MLCT character, including the lowest-energy HOMO–LUMO metal-d to ligand π^* transition. The LF transitions have weak intensity and do not contribute significantly to the CD intensity.

An issue that has been noted occasionally is the sometimes too covalent metal–ligand bonding obtained in DFT calculations [164] that, along with self-interaction errors in the XC potential and kernel [157], may lead to overestimated frequencies for LF transitions and underestimated LMCT frequencies in TDDFT calculations. The 3d shell in first row transition metals appears to be notoriously difficult to treat with DFT/TDDFT, a fact that has also been pointed out in theoretical work on NMR parameters and electric field gradients of 3d metals [165, 166]. As an example, the LF transitions of $[Co(en)_3]^{3+}$ in Figure 21.12 had to be red-shifted by 6×10^3 cm^{-1} or 0.7 eV in order to match the experimental band peaks. This is a large error and is outside of what is typically expected for valence excitations calculated with TDDFT (unless charge-transfer excitations are of

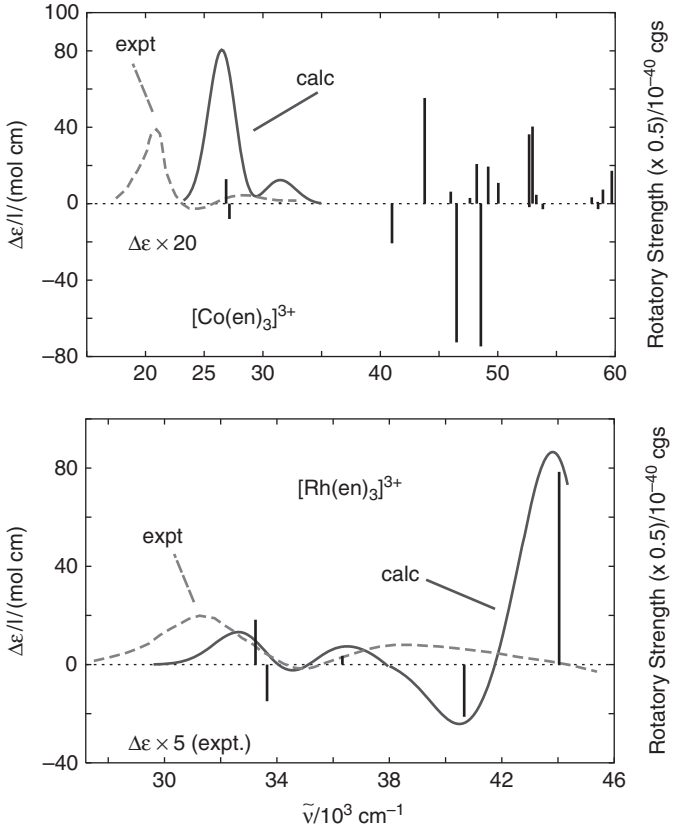

Figure 21.13. CD spectra of Λ-$[Co(en)_3]^{3+}$ and Λ-$[Rh(en)_3]^{3+}$ (*ob*$_3$-conformers) calculated with nonhybrid TDDFT. Excitations not shifted. Data to prepare the figures were taken from reference 156. See also Figure 21.12.

concern, depending on the functional). Other Co^{III} complexes for which calculated spectra were reported in reference 156 afforded similar overestimations for the LF excitation frequencies, ranging from 2 to 8×10^{-3} cm^{-1}.

Heavier metals appear to be somewhat less prone to cause problems in calculations, as far as approximations in the functional are concerned. This point is highlighted by Figure 21.13 where unshifted CD spectra for the LF transitions of Λ-$[Co(en)_3]^{3+}$ and its rhodium analog, Λ-$[Rh(en)_3]^{3+}$, are compared to experiment. The results are representative for other Co(III) and Rh(III) complexes [156, 161, 162, 167]. The LF transition frequencies are more strongly overestimated in the Co complex.

Another illustrative case is the CD spectrum of tris(phenantroline)-iron(II), $[Fe(phen)_3]^{2+}$ [157], as illustrated in Figure 21.14. TDDFT computations with different functionals have no difficulties with reproducing the intense exciton CD bands around 35 to 40×10^{-3} cm^{-1}—although the calculated intensities vary by about a factor of two, depending on whether a nonhybrid or a hybrid functional is used. Similar results were reported for $[Ru(phen)_3]^{2+}$ and $[Os(phen)_3]^{2+}$. Calculations on a $(phen)_3$ ligand system with a ghost atom in place of the metal showed that the metal orbitals do not play an important role in the exciton CD bands [157]. The main source for the intense CD in the ligand π-to-π^* energy range is a through-space electrostatic coupling of the ligand π-to-π^* excitons. The lower energy range of the CD spectra, dominated by CT and ligand-field excitations involving the metal *d* orbitals, is modeled well by TDDFT for the Os and Ru complex. The situation is somewhat different for the low-energy

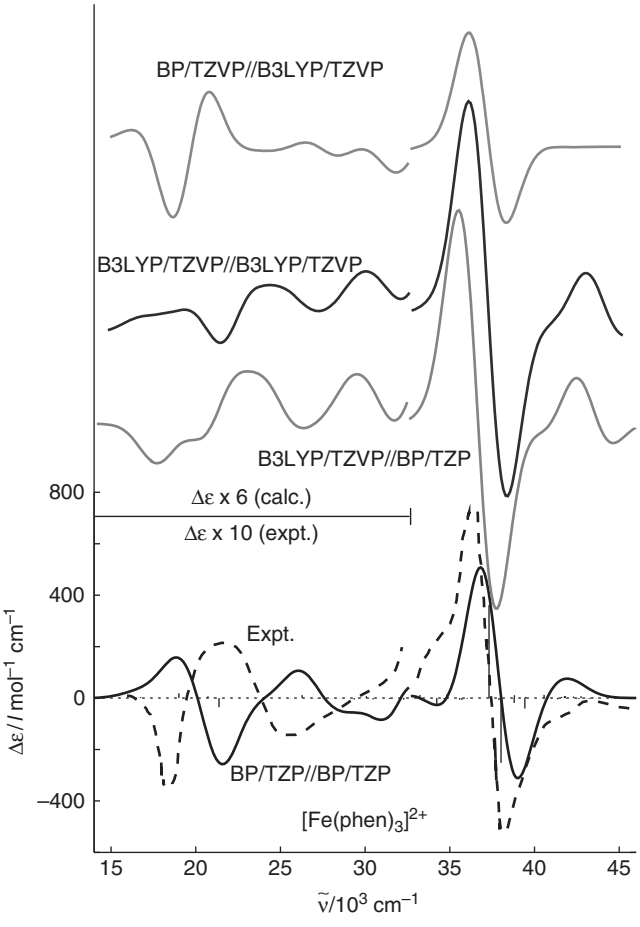

Figure 21.14. Calculated and experimental CD spectra of Λ-$[Fe(phen)_3]^{2+}$. Data to prepare the figure were taken from references 157 and 158. Gaussian broadening with $\sigma = 0.13$ eV. The notation indicates the theory level used to calculate the spectrum // theory level used to optimize the geometry. The calculated transitions were shifted by $+1$, -2, -2, $+2 \times 10^3$ cm^{-1}, respectively (top to bottom) as explained in reference 157. Note that the spectra are magnified below 33×10^3 cm^{-1}.

region of the $[Fe(phen)_3]^{2+}$ spectrum [157]. Figure 21.14 demonstrates that both the B3LYP//BP and BP//B3LYP combinations for spectrum//geometry yield an acceptable sign pattern whereas the BP//BP and B3LYP//B3LYP combinations do not.[14] In such calculations, it is always advisable to compare different classes of functionals (e.g., nonhybrid versus hybrid versus range separated hybrid) in order to ensure that the calculated spectra are not very sensitive to approximations in the electronic structure calculations or to small changes in the geometry. For the Fe complex, additional calculations performed with local HF potentials and other functional combinations indicated that DFT self-interaction errors might be causing problems with calculating the frequencies of transitions involving *d* orbitals accurately [157].

Many of the currently most popular functionals (example: B3LYP) were developed before the year 2000. Thus, an extensive review from 2004 by Rosa et al. [168] dealing with the performance of TDDFT for excitation spectra of metal complexes remains a valuable guidance on the subject. For more recent reviews see also references 29, 169, and 170. Rosa et al. were not able to identify a single functional or class of functionals

[14] The calculations were performed with two different TDDFT programs. Some of the differences in the spectra, deemed to be minor, are due to differences in the types of basis sets that were employed.

that was clearly superior in a broader range of applications to metal complexes, although it appeared that asymptotically corrected XC potentials offered clear improvements over standard nonhybrid functionals. It is likely that similar improvements will be found for range-separated functionals versus standard hybrids. Rosa et al. further pointed out that TDDFT often does not have problems with describing transitions that are formally classified as MLCT or LMCT because not much charge is actually transferred and the metal *d*-shell populations remain fairly constant [168]. Diagnostic tools are available to identify cases where charge transfer might be a problem [81].

Solvent effects on the ECD spectra of metal complexes can be noticeable. For group 8 $(phen)_3$ complexes 157 they were found to be much less pronounced than some of the solvent effects on LMCT band calculated for some Co(III) complexes with +3 overall charge such as $[Co(en)_3]^{3+}$ and $[Co(tn)_3]^{3+}$ [156]. The solvent effects in references 156 and 157 were modeled by a continuum model (COSMO). Jensen et al. revisited solvent effects on the CD spectrum of $[Co(en)_3]^{3+}$ [171], using a combination of force-field molecular-dynamics simulations with discrete solvent molecules treated by a discrete reaction field (DRF) model and TDDFT calculations coupled with DRF. The solvent effects were overall very similar to those obtained from the COSMO continuum model in static computations. Some degree of solvent broadening of the LMCT bands was obtained in the DRF computations due to the underlying molecular dynamics, but the excitations had to be further broadened empirically in order to match the experimental band widths, indicating that solvent broadening is not the main mechanism that determines the CD band widths for this system.

Most of the available benchmarks and assignments of CD spectra of metal complexes are concerned with closed-shell systems. A smaller number of computational studies on metal complexes with unpaired electrons are also available. For TDDFT applications, a complication is that in the Kohn–Sham approach the noninteracting reference system is assumed to have a single determinant wavefunction. This creates issues with spatially degenerate ground states. Fan et al. [172] have investigated the CD of high-spin trigonal dihedral Cr(III) complexes. Two examples are shown in Figure 21.15. A spin-unrestricted TDDFT method to compute the CD spectra was implemented. The spectra were compared to structurally related closed-shell Co(III) complexes (see Figure 21.12). Similar shifts of the excitation energies for Co(III) and Cr(III) had to be applied to match the spectra with experiment. The *d* orbitals of Cr(III) are spatially more extended than those of Co(III). A consequence of this is a larger ligand field splitting in the Cr complexes, resulting in a blue shift of the LF and LMCT transitions for Cr relative to Co. For some of the ligands the spectral trends were similar between Co and Cr, for instance with $[M(thiox)_3]^{3-}$, but not so similar for the acac and oxalate complexes. TDDFT computations of CD spectra of metal complexes with unpaired electrons have, for example, also been reported in reference 173 ($[Co^{II}(bipy)_3]^{2+}$) and in reference 174 (bis(biuretato) spin triplet cobalt complexes).

Applications of first-principles quantum chemical methods to calculate ECD spectra of quite large and structurally complex metal systems shows that these methods are mature and demonstrate their usefulness in a wide range of scientific areas. For example, Coughlin et al. [175] have synthesized neutral iridium(III) luminophores and characterized them by CPL and ECD. TDDFT calculations of ECD were performed for $(MeOmppy)_2Ir(acac)$ at the B3LYP/LANL2DZ level of theory. The comparison of simulated and experimental spectra was favorable, predicting the structure to be a Δ configuration. To support the assignment, calculations were also performed on fac-Δ-$Ir(pppy)_3$ with a known structure (pppy = phenylpinenopyridine). In another study [176], Coughlin et al. considered

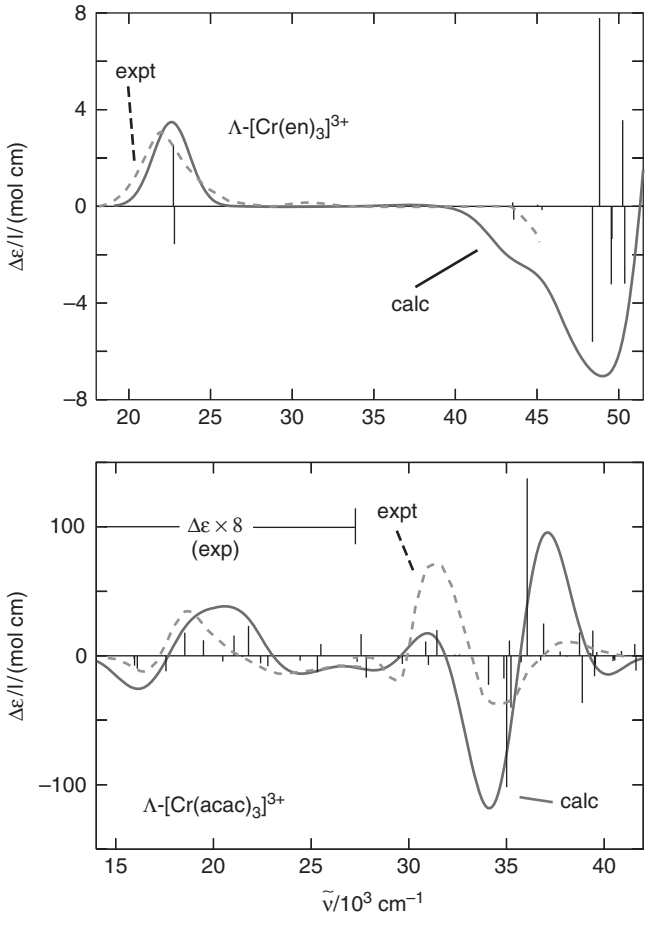

Figure 21.15. Calculated and experimental CD spectra for two high spin Cr(III) complexes. Data to prepare the figures were taken from reference 172. Excitations below/above 40×10^3 cm^{-1} shifted by $\mp 6 \times 10^3$ cm^{-1} for $[Cr(en)_3]^{3+}$. Exp. spectrum magnified by a factor of 2. Global shift of -5×10^3 cm^{-1} for $[Cr(acac)_3]$. Spectra for the analogous Co(III) complexes are shown in Figure 21.12.

UV–vis and CD spectra of Fe, Ru, and Zn complexed with a large enantiopure hemicage ligand. The TDDFT computed excitation energies and intensities agreed well with experimental data, allowing us to assign the configuration around the metal center. An example related to the development of molecular wires is the absolute configuration of the nickel metal complex $Ni_3[(C_5H_5N_2)]_4Cl_2$ [177]. The absolute configuration was determined by comparing experimental and calculated ORD and ECD (BHLYP/LANL2DZ) as well as vibrational circular dichroism spectra. Each method indicated the same (P)-helical structure for the enantiomer with a negative specific rotation at 589.3 nm. Kobyashi et al. investigated the CD spectra of a chiral oxovanadium(IV) phthalocyanine complexes [178]. The most intense bands of a simulated CD spectrum for a model complex, based on TDDFT calculations, were in agreement with experiment, yielding a configurational assignment as right-handed. An analogous silicon phthalocyanine was studied as well. The calculations indicated that a lack of Q bands for the Si system is caused by a cancellation of rotatory strengths of opposite signs in low-energy conformers.

Tunable chiroptical properties of helicene derivatives containing metal centers have been investigated by Crassous, Autschbach, Reau et al. [122, 179, 180]. For instance, organometallic helicene structures incorporating metals such as Pt and Ir have been prepared in enantiopure form, and their crystal structures have been determined [179]. For

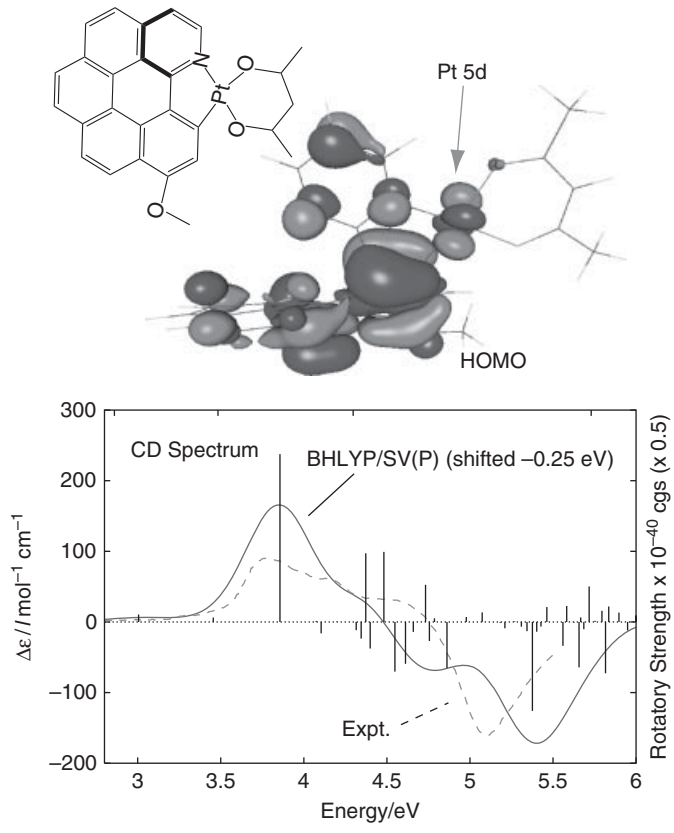

Figure 21.16. Structure, ECD spectrum, and HOMO of a (P)-platina–helicene. For details see Norel et al.[179].

the Pt-helicenes TDDFT (BHLYP), computations of ECD spectra and molar rotations were carried out with the intent to quantify the involvement of the metal orbitals in the optical activity of the helicene backbone. The computed UV–vis absorption as well as the ECD spectrum matched well with experiment after a modest red shift of 0.25 eV, as shown in Figure 21.16. The agreement between calculation and experiment is comparable to that obtained for pristine helicenes themselves (see references 93 and 87 and Section 21.3.1). Regarding the optical rotation at 589.3 nm, the experimental molar rotation is $[\phi] = 8.2 \times 10^3$ deg cm^{-2} dmol^{-1} (dichloromethane). The computed gas-phase molar rotation was 10.3×10^3 deg cm^2 dmol^{-1}. For comparison, the molar rotation of pristine hexahelicene has been measured to be 12.0×10^3 and calculated to have the same value (BHLYP/SV(P)) [90]. The calculations for the platinahelicenes revealed significant participation of the metal (in particular from Pt $5d_\pi$ orbitals) in the excitations in the UV–vis spectral range, rationalizing why the metallahelicenes displayed an intense phosphorescence. The involvement of a Pt $5d$ orbital in the HOMO of the platina-helicene, for instance, is clearly visible in Figure 21.16.

A communication by Graule et al. [180] reported preliminary data on metal–bis(helicene) complexes. The structure for a Pd complex is shown in Figure 21.17), along with the calculated and experimental CD spectrum. The agreement between the simulated and the experimental CD spectrum for the Pd complex is seen to be quite good. A red-shift of 0.25 eV was applied to match the positions of the first intense CD bands. An analysis of the computed spectrum showed that the intense bands can be assigned to π-to-π^* transitions within the extended π framework of the

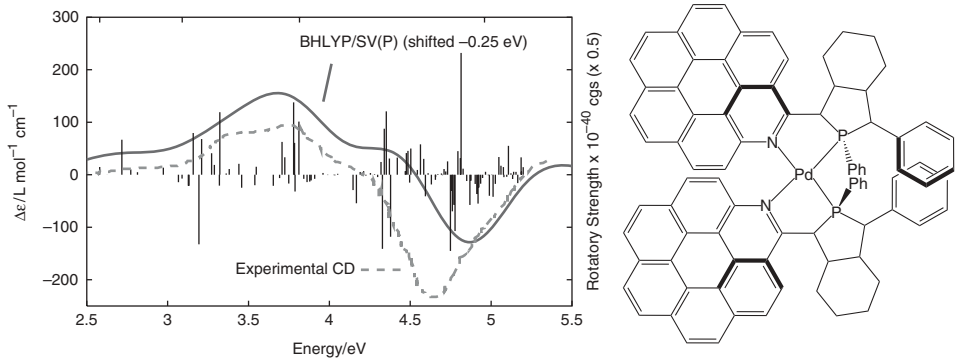

Figure 21.17. Structure of a Pd-bis(phosphole–helicene) complex and a comparison of the computed (BHLYP/SV(P)) and experimental CD spectrum. Data to prepare the figure were taken from reference 180.

phosphole–helicene ligands. Contrary to what was initially expected, the CD bands cannot be assigned separately to excitations centered in the helicene and phosphole moieties, respectively.

In reference 122, Graule et al. investigated the reasons for the drastic difference in magnitude for the optical rotation (and ECD intensities) between analogous bis(phosphole–helicene) Pd and Cu complexes. The experimentally measured molar rotation of the Pd complex was 23.1×10^3 deg cm^2 dmol$^{-1}\pm$ 2% in dichloromethane. For an analogous Cu complex it was $13.1 \times 10^3\pm$ 2%. The calculations yielded a similar difference of the molar rotations. A detailed analysis uncovered that the nature of the metal (preferring square planar versus tetrahedral coordination) dictates (a) the conformation of the ligand adopted in the complexes and (b) the relative orientations of various chromophore moieties with respect to each other. The different ligand conformations adopted in the Pd and Cu complex are the main reason for the very different CD intensities as well as for the large difference in the optical rotations of the two systems, whereas metal orbitals hardly participate in the excitations.

Although metal clusters pose their own challenges to first-principles theoretical calculations and have very different spectral properties than metal complexes, it is appropriate here to cite some recent computational work related to the optical activity of gold clusters. Garzón et al. recently employed calculations of ECD spectra to investigate the origin of the optical activity for Au_{25} clusters protected by 18 cysteine or glutathione ligands [181]. The computations were performed for the cysteine system and agreed reasonably well with an experimental ECD spectrum for the glutathione protected cluster. TDDFT computations of ECD spectra of Au_{14}(R-methylthiirane) suggested that chiral signatures might be observable in the IR/NIR spectral region for an ensemble of gold clusters passivated with chiral adsorbates [182]. Provorse and Aikens [183] used TDDFT computations to study gold complexes of the type $[Au_{11}L_4X_2]^+$ with X=Cl, Br, and L representing coordination of the gold cluster by chiral mono and bidentate phosphine ligands. The authors pointed out that their study was the first to demonstrate how the optical activity of the metal core depends sensitively on the presence and chiral arrangement of surrounding ligands. Given the tremendous interest in gold and other metal clusters one can expect many more studies of this type to appear in the near future. The required careful benchmarking of potential shortcomings, in particular of TDDFT,

for these types of applications is also likely going to benefit computational studies in coordination chemistry.

As far as the OR and ORD of transition metal complexes is concerned, the author is aware of only a few calculations at the *ab initio* level. Some of the calculations on metal organic helicene systems and a tri-Ni complex were already discussed above. The prototypical system representing a chelate complex with saturated ligands is $[Co(en)_3]^{3+}$ [25]. The ORD in the visible range was already reported in the 1930s separately for the Λ and the Δ enantiomer (Mathieu 1934, Jaeger 1937, in reference 184). The anomalous OR dispersion in the visible wavelength range is caused by the LF transitions. Figure 21.18 shows the experimental ORD along with nonhybrid and hybrid TDDFT data [185]. The ORD curves reflect the TDDFT errors in the d-to-d excitation energies, which are seen to be somewhat less pronounced for the hybrid functional. Overall, however, apart from a wavelength shift the computed dispersion curves reproduce the experimental ORD. The calculated PBE0 specific rotation at 589.3 nm is $[\alpha]_D = 105$ deg/[dm (g/cm^{-3})], which is in reasonable agreement with an experimental rotation of 123 deg/[dm (g/cm^{-3})] that was reported for a solution of the tris-bromide monohydrate salt [184].

21.4.2. Spectral Assignments and Analyses

Much of the recent computational work on metal complexes has been directed at uncovering the origin of the optical activity in the excitations. A series of papers by Ziegler et al. has focused on tris–bidentate complexes with local D_3 symmetry [161–163, 167, 172, 187]. If one considers the six metal-coordinating ligand atoms in such a pseudo-octahedral complex, as shown in Figure 21.19, a lowering of the symmetry from O_h to D_3 can be considered as a sequence of a polar elongation or compression along the threefold symmetry axis ($O_h \rightarrow$ achiral D_{3d}) followed by an azimuthal distortion. Deviations of the polar ratio s/h and azimuthal angle ϕ from their values for an ideal octahedron ($s/h = 1.22, \phi = 60^\circ$) quantify the structural chirality around the metal center [188]. More recently, Fan and Ziegler employed the angle ω shown in Figure 21.19 for additional analyses. For an ideal octahedron, $\omega = \pm 35.3^\circ$. It is convenient to define the distortions $\Delta(s/h)$, $\Delta\phi$, and $\Delta\omega$ which adopt values of zero for an idealized octahedral ligand arrangement.

Jorge, Ziegler, et al. have investigated the origin of the CD of LF and LMCT transitions in Co^{III} and Rh^{III} complexes with saturated σ bonding ligands. An analysis of the

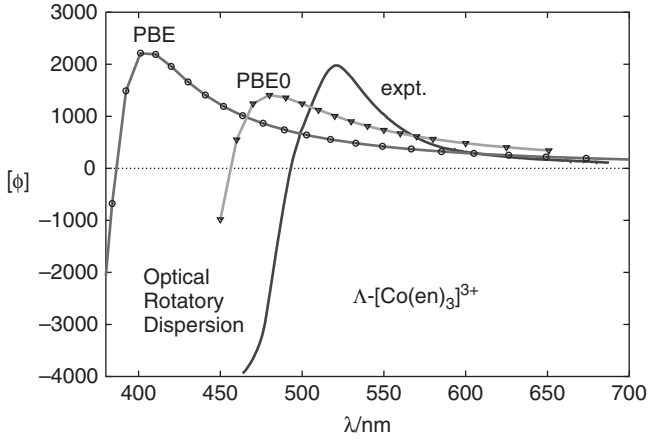

Figure 21.18. Molar rotation of Λ-$[Co(en)_3]^{3+}$. Straight line: Experimental data for a solution of Λ-$[Co(en)_3]^{3+}$ (bromide salt) as reported in reference 184. Nonhybrid (revised PBE) and hybrid (PBE0) TDDFT data from reference 185 (calculated for the Δ configuration and inverted)). A global damping constant of 0.007 au was applied to obtain a nonsingular resonant ORD (see Section 21.3.3).

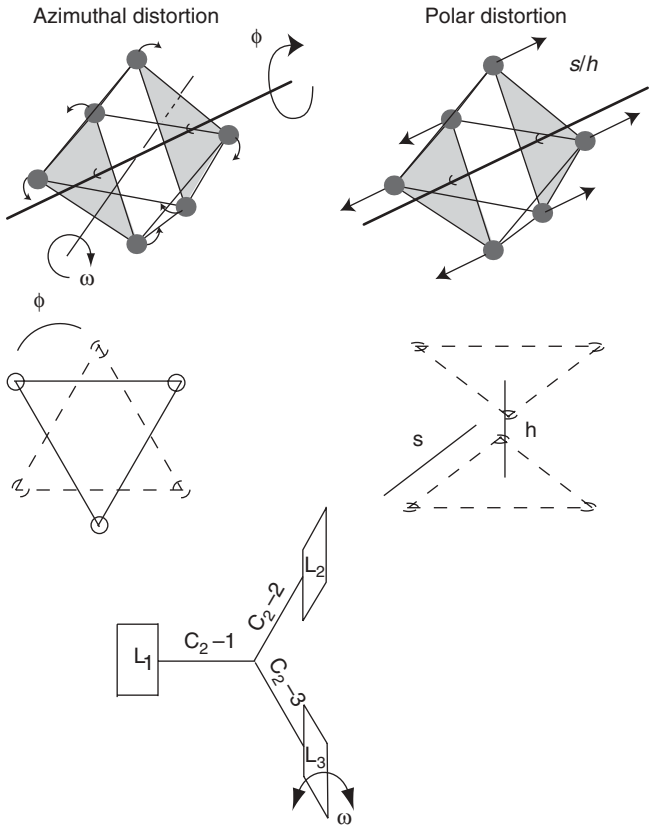

Figure 21.19. Distortion of an octahedral ligand environment in a trigonal–dihedral environment. For D_3 symmetric tris–bidentate complexes, ω is the angle between the threefold symmetry axis and the line connecting the two coordinating atoms of the bidentate ligands.

transition dipole moments in terms of contributions from individual orbitals (canonical and localized) allowed to relate the TDDFT results to semiempirical models developed several decades ago. Reference 161 focused on the LF transitions. Formally, these transitions derive from the parity-forbidden crystal-field transitions between the t_{2g} and e_g d-orbital levels of an octahedral environment. The $^1T_{1g}$ HOMO–LUMO d-to-d transition splits into an A_2/E pair upon lowering the symmetry from O_h to D_3 [25]. The energetic ordering is determined mainly by the sign of $\Delta(s/h)$, with the energy splitting between A_2 and E being correlated to the magnitude of $\Delta(s/h)$. The question then arises whether the circular dichroism of the LF transition is predominantly caused by a small geometry distortion of the nitrogen ligands away from perfect octahedral symmetry, or by a weak electronic coupling of the metal and ligand backbone orbitals, or by a combination of these and perhaps other factors. In order to understand better what happens to the transitions upon these distortions, a model based on first-order perturbation theory can be set up [161]. Instead of O_h parent symmetry, consider the D_{3d} subgroup, initially at a $\Delta(s/h) = 0$ geometry. The T_{1g} transition splits into a A_{2g}/E_g pair under D_{3d}, for which the rotatory strengths are (upon taking the imaginary parts of the expressions)

$$R(A_2) = \langle A_{1g}|\hat{\mathbf{D}}|A_{2g}\rangle\langle A_{2g}|\hat{\mathbf{M}}|A_{1g}\rangle, \tag{21.34a}$$

$$R(E) = \sum_{d}^{a,b}\langle A_{1g}|\hat{\mathbf{D}}|E_g^d\rangle\langle E_g^d|\hat{\mathbf{M}}|A_{1g}\rangle, \tag{21.34b}$$

where *a,b* are the components of the twofold degenerate E state. For notational brevity, the 'Im' of equation (21.4) is omitted in this section, and it is understood that the scalar product of the transition moment vectors is taken. The electric and magnetic moment operators have been defined in Section 21.2.1. Under D_{3d} symmetry, the electric dipole operator matrix elements vanish because the operator is *ungerade* (u, odd) and the wavefunctions involved in the ligand field transitions are *gerade* (g, even). The magnetic moment matrix elements can be nonzero because the components of $\hat{\mathbf{M}}$ belong to the even symmetry species (irreducible representations). Thus, the leading order effects that cause the circular dichroism in the LF transitions can be considered as those that create nonvanishing electric transition dipoles. The $\Delta\phi$ azimuthal distortion lowers the symmetry to D_3 and mixes g with u species. For small distortions, a perturbation Hamiltonian $\partial\hat{H}/\partial\phi$ is associated with a vibrational normal mode of a_{1u} symmetry. The azimuthal distortion mixes some odd symmetry (u) LMCT character in the ligand field transitions, with the sign of the perturbation depending whether $\Delta\phi > 0$ or $\Delta\phi < 0$. This behavior is supported by experimental data (see below for further details).

It is convenient at this point to switch to a one-electron orbital picture instead of using many-determinant excited-state wavefunctions for the perturbations. The following discussion is based on the analysis in reference 161. The rotatory strengths can be analyzed conveniently in terms of MOs within a TDDFT approach, for example [18]. The metal-centered symmetry orbitals of d character under D_{3d} symmetry are shown in Figure 21.20. In D_{3d} symmetry, the LF transitions (formally HOMO to LUMO) rotatory strengths have orbital contributions such as

$$R(A_2) \propto \langle \pi(e_{ga})|\hat{\mathbf{D}}|\sigma^*(e_{gb})\rangle\langle\sigma^*(e_{gb})|\hat{\mathbf{M}}|\pi(e_{ga})\rangle, \tag{21.35a}$$

$$R(E) \propto \langle \pi(e_{ga})|\hat{\mathbf{D}}|\sigma^*(e_{ga})\rangle\langle\sigma^*(e_{ga})|\hat{\mathbf{M}}|\pi(e_{ga})\rangle, \tag{21.35b}$$

where, as pointed out in the caption of Figure 21.20, the LUMO $\sigma^*(e_{gb})$ represent antibonding combinations of the metal d_σ orbitals and ligand σ combinations. The electric dipole integrals in Eqs. (21.35a) and (21.35b) vanish because the electric dipole operator is of odd symmetry. For the model, it is sufficient to (a) consider the mixing of the $\pi(e_g)$ HOMOs with odd ligand combinations $L_\sigma(e_u)$ upon azimuthal distortion and (b) focus on the electric dipole integrals. In the distorted system of lower D_3 symmetry, the HOMO levels of e symmetry are to first order

$$\pi(e_d) = \pi(e_{gd}) + \Delta\phi \cdot C \cdot L_\sigma(e_{ud}) \qquad (d = a, b). \tag{21.36}$$

The mixing coefficient C is given by first-order perturbation theory as

$$C = \frac{\langle L_\sigma(e_{ud})|\partial\hat{F}/\partial\phi|\pi(e_{gd})\rangle}{\varepsilon[\pi(e_{gd})] - \varepsilon[L_\sigma(e_{ud})]}, \qquad (d = a, b) \tag{21.37}$$

where a complete AO basis is assumed for brevity. In Eq. (21.37), $\hat{F}$ is an effective one-electron operator such as the DFT Fock operator introduced in Section 21.2.3, and the ε are orbital energies. Considering these perturbations, the rotatory strengths of the azimuthal distorted system are dominated by orbital contributions such as

$$R(A_2) \propto \Delta\phi \cdot C \cdot \langle L_\sigma(e_{ua})|\hat{\mathbf{D}}|\sigma^*(e_{gb})\rangle\langle\sigma^*(e_{gb})|\hat{\mathbf{M}}|\pi(e_{ga})\rangle, \tag{21.38a}$$

$$R(E) \propto \Delta\phi \cdot C \cdot \langle L_\sigma(e_{ua})|\hat{\mathbf{D}}|\sigma^*(e_{ga})\rangle\langle\sigma^*(e_{ga})|\hat{\mathbf{M}}|\pi(e_{ga})\rangle \tag{21.38b}$$

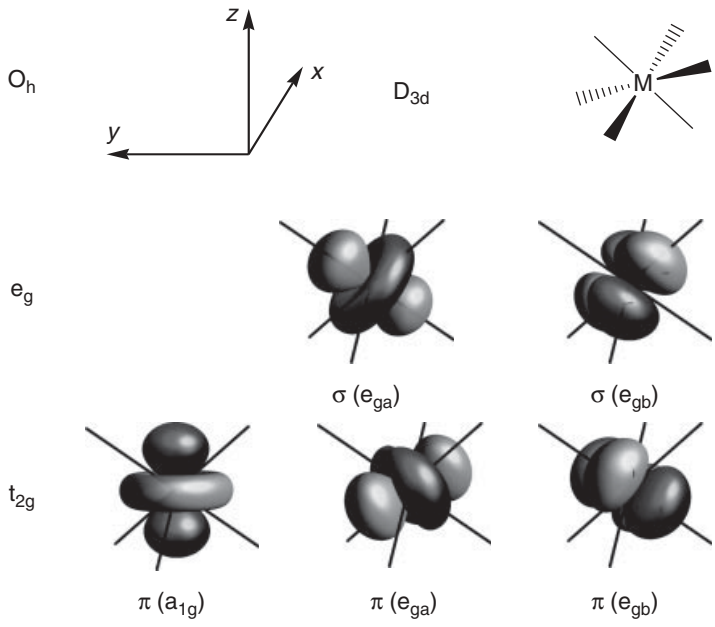

Figure 21.20. Metal-centered symmetry adapted *d* orbitals in D_{3d} symmetry in relation to octahedral parent symmetry. The occupied levels of $t_{2g}(O_h)$ parentage have local π symmetry with respect to the metal–ligand bonds. The unoccupied e_g orbitals have local σ symmetry. In the LUMO they form antibonding combinations with ligand σ orbital combinations of the same symmetry. The orthonormal *d* set depicted here is given by [161, 162] $\pi(a_{1g}) = d_{z2}, \pi(e_{ga}) = \sqrt{\frac{2}{3}}d_{x2-y2} + \sqrt{\frac{1}{3}}d_{yz}, \pi(e_{gb}) = \sqrt{\frac{1}{3}}d_{xz} + \sqrt{\frac{2}{3}}d_{xy}, \sigma(e_{ga}) = \sqrt{\frac{1}{3}}d_{x2-y2} - \sqrt{\frac{2}{3}}d_{yz}, \pi(e_{gb}) = \sqrt{\frac{2}{3}}d_{xz} - \sqrt{\frac{1}{3}}d_{xy}$.

with the coefficient C given in Eq. (21.37). In this orbital-based perturbation theory ansatz the sign and magnitude of $\Delta\phi$ determines the relative sign and magnitude of the rotatory strengths $R(A_2)$ and $R(E)$ for these transitions for a given absolute configuration of the complex.

A survey of structural data [161] for Co^{III} and Rh^{III} complexes with the ligands en, pn, tn, acac, and ox showed that for these systems the angle ϕ is usually lower than 60° and that for these systems in the Λ configuration we have $R(E) > 0, R(A) < 0$. An exception is the complex $[Co(tn)_3]^{3+}$, for which—depending on the conformations of the chelate rings—ϕ can be slightly above or below 60°, with a concomitant change in the signs of the rotatory strengths of the LF transitions. Another factor that determines the CD spectra in the low-frequency range is, as already pointed out, the sign and magnitude of $\Delta(s/h)$. The deviation from the octahedron value of 1.22 determines which of the excited states, A_2 or E, is lower in energy. Most of the complexes surveyed in reference 161 exhibit $s/h > 1.22$, along with $\omega_E - \omega_{A_2} < 0$. The authors noted that the sign of the frequency difference is not easy to predict from qualitative considerations.

An MO analysis of the TDDFT-derived electric transition dipole moments for the excitations was reported in reference 161 to test the relevance of various semiempirical theories. For example, in a crystal field model the only source of optical activity of the LF transitions can be a mixing of even with odd metal-centered orbitals, mainly *nd* with $(n + 1)p$, under the azimuthal distortion. The TDDFT analysis of model complexes indicated that this mechanism contributes less than five percent to the optical activity. A dynamic theory by Mason and Seal [159] attributed the optical activity of the LF transitions to matrix elements between occupied and unoccupied ligand orbitals. The TDDFT analysis found that this mechanism is also of minor importance (<5%) for complexes with saturated ligands. However, for Co^{III} complexes with the ligands acac and ox, such contributions were found to be significant. Already in a perfect octahedral arrangement of the coordinating ligand atoms, there can be a participation of even and odd ligand π orbitals in the HOMO and LUMO levels of the complex, which significantly

complicates the spectral analysis. As a consequence, in the presence of such ligands, the simple model for the sign pattern of the rotatory strengths depending on the azimuthal distortion may break down.

In a follow-up study [162], Jorge et al. extended the orbital-mixing model of reference 161 to the LMCT excitations of complexes with saturated σ binding ligands. For pairs of LF and LMCT transitions that are of the same symmetry, the signs are coupled and alternating. The excitations originate in occupied ligand σ orbitals that are of t_{1u} parentage in O_h symmetry. In analogy to the rotatory strengths of Eqs. (21.35a), (21.35b), for the LMCT excitations one finds orbital contributions such as

$$R(A_2) \propto \langle L_\sigma(e_{ua})|\hat{\mathbf{D}}|\sigma^*(e_{gb})\rangle\langle\sigma^*(e_{gb})|\hat{\mathbf{M}}|L_\sigma(e_{ua})\rangle, \tag{21.39a}$$

$$R(E) \propto \langle L_\sigma(e_{ua})|\hat{\mathbf{D}}|\sigma^*(e_{ga})\rangle\langle\sigma^*(e_{ga})|\hat{\mathbf{M}}|L_\sigma(e_{ua})\rangle. \tag{21.39b}$$

In O_h and D_{3d} parent symmetry, the LMCT excitations are electric dipole allowed, but magnetic dipole forbidden since the magnetic dipole operator is of even symmetry. The leading terms in the rotatory strengths upon azimuthal distortion are now obtained from a mixing of the ligand orbitals $L_\sigma(e_u)$ with even occupied $\pi(e_{gd})$ metal orbitals such that the mixing causes nonzero magnetic transition dipoles. The perturbed occupied orbitals to consider are

$$L_\sigma(e_{ud}) = L_\sigma(e_{ud}) + \Delta\phi \cdot C' \cdot \pi(e_{gd}) \qquad (d = a, b), \tag{21.40}$$

where the mixing coefficient C' is the *negative* of the mixing coefficient C of Eq. (21.37) as long as the orbitals are real. The reason is that the same orbitals are involved in the equation for the mixing coefficient, but they must be interchanged because now the perturbation of the ligand based orbitals are of concern. The sign change stems from the orbital energy denominator in Eq. (21.37). From substituting (21.40) in the magnetic moment integrals of (21.39a) and (21.39b) and using $C' = -C$, the rotatory strengths of the LMCT excitations in the perturbation model are seen to afford orbital contributions such as

$$R(A_2) \propto -\Delta\phi \cdot C \cdot \langle L_\sigma(e_{ua})|\hat{\mathbf{D}}|\sigma^*(e_{gb})\rangle\langle\sigma^*(e_{gb})|\hat{\mathbf{M}}|\pi(e_{ga})\rangle, \tag{21.41a}$$

$$R(E) \propto -\Delta\phi \cdot C \cdot \langle L_\sigma(e_{ua})|\hat{\mathbf{D}}|\sigma^*(e_{ga})\rangle\langle\sigma^*(e_{ga})|\hat{\mathbf{M}}|\pi(e_{ga})\rangle. \tag{21.41b}$$

These are the same expressions as those for the LF transitions, but with the opposite signs. The model predicts similar intensities for the CD of the LF and LMCT excitations, although typically the circular dichroism of the LMCT transitions is far more intense. However, in agreement with experiment and first-principles theory the perturbation model predicts that (a) the circular dichroism of the LF and LMCT excitations in σ bonded trigonal dihedral metal complexes exhibits alternating sign patterns and (b) their the coupled signs of the CD bands depend on the sign of the polar distortion of the complex relative to an idealized octahedral ligand arrangement. The model indicates that the origin of the optical activity is the mixing of odd and even metal and ligand orbital combinations due to a slightly distorted arrangement of the σ coordinating ligand atoms. The analysis of the TDDFT excitation vectors of a number of complexes and model systems in terms of orbital contributions (cf. Section 21.2.2) has supported this model in favor of other possible mechanisms [161, 162].

The authors of reference 162 further investigated the influence of conformational changes on the ECD of various Co^{III} and Rh^{III} complexes with aliphatic bidentate amine ligands. Of concern here is the orientation of the chelate rings with respect to the threefold symmetry axis [25]. The two possible configurations are termed *ob* and *lel*, depending on whether the C—C bonds of the amine backbone are oblique or approximately parallel to the threefold axis. An alternative way of labeling the geometries derives from the rotational sense δ or λ of the helical configuration of the ligand chelate ring. In the case of $[Co(en)_3]^{3+}$ the differences in the CD for the ob_3 and lel_3 conformers were shown to be rather minor, but somewhat more noticeable for $[Co(tn)_3]^{3+}$ [156]. The systems studied by Jorge et al. in reference 162 also included S- and R-pn (pn = 1,2-propyldiamine). In this ligand, the methyl group has a strong preference for an equatorial orientation with respect to the chelate ring. By comparing a large set of experimental data with computed data, it was shown that the TDDFT computations correctly reproduced changes in the CD spectra due to changes in the chelate ring conformations. The signs and intensities of the CD transitions as a function of *ob* versus *lel* conformation are a direct consequence of the sign and size of the chelate bite angle, which is in turn dictated by the preferred configuration of the rings. Thus, the configurations of the chelate rings determine the geometry of the six nitrogens around the metal center. As the perturbation theory models clearly illustrate, the geometry arrangement of the nitrogen sextet is mainly responsible for the sign, energetic ordering, and CD intensity of the d-to-d and LMCD transitions.

Fan and Ziegler recently extended the model to be numerically more predictive, by explicitly deriving expressions of the rotatory strengths in terms of orbital overlap integrals and matrix elements of the dipole operators. A proof of concept was provided for $[Co(en)_3]^{3+}$ in reference 187. Subsequently, the model was applied to trigonal dihedral Co^{III} complexes with the ligands acac, ox, mal, and thiox, with a focus on the transitions involving π orbitals [163]. A third paper of the series investigated group 8 tris-bidentate phen and bipy complexes [167].

As pointed out above, π-to-π^* transitions that take place within the ligands can couple electronically and may exhibit very strong circular dichroism. Examples are the $[Fe(phen)_3]^{2+}$ complex for which CD spectra are shown in Figure 21.14, $[Os(phen)_3]^{2+}$ and $[Co(acac)_3]$ (both Figure 21.12). The CD spectra of the group 8 $(phen)_3$ complexes have been analyzed in detail in references 157 and 172 based on TDDFT calculations. For detailed analyses of the acac complexes, and related systems with ox, thiox, and mal, ligands, see references 156 and 163. Much insight into the nature of the exciton coupling CD in these systems was obtained decades ago by Mason and co-workers; see, for instance, references [158, 189–191] regarding phen and bipy complexes. Consider the phen ligand as an example. In a D_3 propeller arrangement, the intense long-axis (ℓ) polarized π-to-π^* excitons of the three ligands can couple as shown in Figure 21.21 and create the strong exciton CD seen in the $[Fe(phen)_3]^{2+}$ spectrum. Because of the helical arrangement of the ligands, the rotatory strengths of the coupled excitations are nonzero and arise from the linear combinations of the *electronic* dipole moments in the couplet [189]. Assume an octahedral parent geometry such that the angles between each transition dipole vector $\mathbf{D}_\ell$ of the long-axis polarized transition and the C_3 of the complex is $\omega = 35.3^\circ$ (Figure 21.19), with the centers of the phen ligands at a distance r from each other (r is the distance between the origins of the transition dipole vectors in Figure 21.21). Mason [189] derived for a degenerate point dipole coupling model an

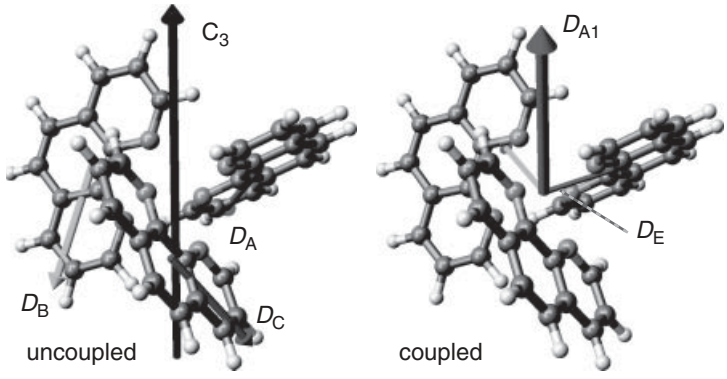

Figure 21.21. D_3-symmetric arrangement of three phen ligands as adopted in complexes such as $[Fe(phen)_3]^{2+}$, $[Os(phen)_3]^{2+}$. Shown here is a Λ configuration. Left: The arrows centered in the phen ligands represent the electric transition dipoles D_A, D_B, D_C for the long-axis polarized π-to-π^* transition in the phen ligands A, B, C. Right: The arrows represent electric transition dipoles for the A_2 and E components of the coupled set of excitations.

exciton splitting energy of

$$V = \frac{\hbar}{3}[\omega_{A_2} - \omega_E] = \frac{\mathbf{D}_\ell \cdot \mathbf{D}_\ell}{4r^3} \tag{21.42}$$

along with rotatory strengths of

$$R(E) = -R(A_2) = \sqrt{\frac{2}{3}}\pi\tilde{\nu}_\ell r(\mathbf{D}_\ell \cdot \mathbf{D}_\ell) \tag{21.43}$$

for a Λ configuration (cgs units). Here, $R(E)$ is the rotatory strength for the two E components combined. TDDFT computations for the Λ configurations of a number of $(phen)_3$ and $(bipy)_3$ complexes indeed yielded positive rotatory strengths for the E transitions assigned to coupled ligand π-to-π^*, which appeared at lower frequency in the spectra than the A_2 components of the exciton couplets, in agreement with experiment and the dipole coupling model [157, 167]. Irrespective of the low-energy part of the spectra, the π-to-π^* frequency range is therefore a reliable indicator of the absolute configuration of these complexes. Regarding the geometry dependence of the rotatory strengths, Fan et al. [167] derived a common $\sin\omega \cdot \cos\omega$ behavior, where ω is the tilt angle shown in Figure 21.19. Since ω changes sign when going from a Λ to a Δ arrangement of the ligands around the metal, the $\sin\omega\cos\omega$ term determines the sign change of the exciton CD when comparing Λ to Δ configurations.

21.5. CONCLUDING REMARKS

Chemists have a variety of computational tools available to investigate electronic optical activity. Theoretical methods that were derived from first principles can be applied to general types of molecules, transition metal complexes, metal clusters, fullerenes, nanotubes, and many other systems. The quality of the computational model is of critical

importance. There is always the important decision about which basis set and electronic structure method to select, but the computational model should ideally also consider the environment of a molecule (solvent, solid-state matrix, counterions, and so on), and it is important to check whether it is necessary to explicitly consider vibrational effects. Computing vibrational fine structure and bandshapes for ECD spectra is not yet routinely carried out, but the available studies show good promise. The majority of computations are presently performed with some type of density functional method. The continuing development of functionals for DFT and TDDFT remains as important as ever. Established computational error bars and performance expectations derived from numerous benchmarks with the B3LYP functional and a variety of gradient corrected nonhybrid functionals from static-structure gas-phase computations are likely going to be revised in the foreseeable future.

ACKNOWLEDGMENTS

The author would like to acknowledge support of his research by the National Science Foundation and the US Department of Energy. Special thanks to Jing Fan for providing material for one of the figures, and to Lucia Nitsch-Velasquez and Mark Rudolph for help with preparing some of the graphical material.

REFERENCES

1. L. D. Barron, *Molecular Light Scattering and Optical Activity*, 2nd ed., Cambridge University Press, New York, **2004**.
2. N. Berova, K. Nakanishi, R. W. Woody, eds., *Circular Dichroism. Principles and Applications*, 2nd ed., VCH, New York, **2000**.
3. M. Quack, *Angew. Chem. Int. Edit*. **2002**, *41*, 4618–4630.
4. E. Zavattini, G. Zavattini, G. Ruoso, E. Polacco, E. Milotti, M. Karuza, U. Gastaldi, G. Di Domenico, F. Della Valle, R. Cimino, S. Carusotto, G. Cantatore, M. Bregant, *Phys. Rev. Lett*. **2006**, *96*, 110406–5.
5. G. Pályi, C. Zucchi, L. Caglioti, eds., *Progress in Biological Chirality*, Elsevier, Oxford, **2004**.
6. P. H. Vaccaro, *Nature* **2009**, *458*, 289–290.
7. R. K. Kondru, P. Wipf, D. N. Beratan, *Science* **1998**, *282*, 2247–2250.
8. J. Autschbach, *Chirality* **2010**, *21*, E116–E152.
9. M. Pecul, K. Ruud, The *ab initio* calculation of optical rotation and electronic circular dichroism, in *Advances in Quantum Chemistry*, Vol. *50*, Elsevier, San Diego, **2005**, pp. 185–212.
10. T. D. Crawford, *Theor. Chem. Acc*. **2006**, *115*, 227–245.
11. P. L. Polavarapu, *Chem. Rec*. **2007**, *7*, 125–136.
12. P. L. Polavarapu, *Chirality* **2002**, *14*, 768–781.
13. G. Bringmann, T. Bruhn, K. Maksimenka, Y. Hemberger, *Eur. J. Org. Chem*. **2009**, 2717–2727.
14. N. Berova, L. Di Bari, G. Pescitelli, *Chem. Soc. Rev*. **2007**, *36*, 914–931.
15. P. J. Stephens, F. J. Devlin, J. R. Cheeseman, M. J. Frisch, O. Bortolini, P. Besse, *Chirality* **2003**, *15*, S57–S64.
16. P. J. Stephens, D. M. McCann, J. R. Cheeseman, M. J. Frisch, *Chirality* **2005**, *17*, S52–S64.

17. P. Mukhopadhyay, P. Wipf, D. N. Beratan, *Acc. Chem. Res*. **2009**, *42*, 809–819.
18. J. Autschbach, L. Nitsch-Velasquez, M. Rudolph, *Top. Curr. Chem*. **2011**, *298*, 1–98.
19. L. Rosenfeld, *Z. Phys*. **1928**, *52*, 161–168.
20. E. U. Condon, *Rev. Mod. Phys*. **1937**, *9*, 432–457.
21. W. Kauzmann, *Quantum Chemistry*, Academic Press, New York, **1957**.
22. A. Moscowitz, *Adv. Chem. Phys*. **1962**, *4*, 67–112.
23. C. Djerassi, *Optical Rotatory Dispersion*, McGraw-Hill, New York, **1960**.
24. D. J. Caldwell, H. Eyring, *The Theory of Optical Activity*, Wiley-Interscience, New York, **1971**.
25. R. Kuroda, Y. Saito, circular dichroism of inorganic complexes: Interpretation and applications, in *Circular Dichroism: Principles and Applications*, 2nd ed. N. Berova, K. Nakanishi, and R. W. Woody, eds., VCH, New York, **2000**, pp. 563–599.
26. A. E. Hansen, T. D. Bouman, *Adv. Chem. Phys*. **1980**, *44*, 545–644.
27. T. Helgaker, K. Ruud, K. L. Bak, P. Jørgensen, J. Olsen, *Faraday Discuss*. **1994**, *99*, 165–180.
28. K. D. Bak, A. E. Hansen, K. Ruud, T. Helgaker, J. Olsen, P. Jørgensen, *Theor. Chim. Acta* **1995**, *90*, 441–458.
29. J. Autschbach, *Coord. Chem. Rev*. **2007**, *251*, 1796–1821.
30. R. G. Parr, W. Yang, *Density Functional Theory of Atoms and Molecules*, Oxford University Press, New York, **1989**.
31. H.-G. Kuball, M. Acimis, J. Altschuh, *J. Am. Chem. Soc*. **1979**, *101*, 20–27.
32. H.-G. Kuball, T. Höfer, Cirlcular dichroism of oriented molecules, in *Circular Dichroism. Principles and Applications*, N. Berova, K. Nakanishi, and R. W. Woody, eds., VCH, **2000**, Chapter 5, pp. 133–158.
33. H.-G. Kuball, *Enantiomer* **2002**, *7*, 197–205.
34. J. R. L. Moxon, A. R. Renshaw, *J. Phys. Condens. Matter* **1990**, *2*, 6807–6836.
35. J. R. L. Moxon, A. R. Renshaw, I. J. Tebbutt, *J. Phys. D. Appl. Phys*. **1991**, *24*, 1187–1192.
36. W. Kaminsky, A. M. Glazer, *Ferroelectrics* **1996**, *183*, 133–141.
37. K. Claborn, J. Herreros Cedres, C. Isborn, A. Zozulya, E. Weckert, W. Kaminsky, B. Kahr, *J. Am. Chem. Soc*. **2006**, *128*, 14746–14747.
38. K. Claborn, C. Isborn, W. Kaminsky, B. Kahr, *Angew. Chem. Int. Edit*. **2008**, *47*, 5706–5717.
39. J. A. Schellman, *Chem. Rev*. **1975**, *75*, 323–331.
40. R. McWeeny, *Methods of Molecular Quantum Mechanics*, 2nd ed., Academic Press, London, **1992**.
41. S. F. O'Shea, D. P. Santry, *Theor. Chim. Acta* **1975**, *37*, 1–16.
42. D. P. Santry, *Chem. Phys. Lett*. **1979**, *61*, 417–420.
43. D. P. Santry, T. E. Raidy, *Chem. Phys. Lett*. **1979**, *61*, 413–416.
44. J.-H. Pao, D. P. Santry, *J. Am. Chem. Soc*. **1966**, *88*, 4157–4163.
45. K. Sasagane, F. Aiga, R. Itoh, *J. Chem. Phys*. **1993**, *99*, 3738–3778.
46. O. Christiansen, C. Hättig, J. Gauss, *J. Chem. Phys*. **1998**, *109*, 4745–4757.
47. F. Aiga, T. Tada, R. Yoshimura, *J. Chem. Phys*. **1999**, *111*, 2878–2888.
48. M. Krykunov, J. Autschbach, *J. Chem. Phys*. **2005**, *123*, 114103–114110.
49. R. Bauernschmitt, R. Ahlrichs, *Chem. Phys. Lett*. **1996**, *256*, 454–464.
50. R. E. Stratmann, G. E. Scuseria, M. J. Frisch, *J. Chem. Phys*. **1998**, *109*, 8218–8224.
51. S. Hirata, M. Head-Gordon, R. J. Bartlett, *J. Chem. Phys*. **1999**, *111*, 10774–10786.
52. R. Ditchfield, *Mol. Phys*. **1974**, *27*, 789–807.
53. M. Krykunov, J. Autschbach, *J. Chem. Phys*. **2006**, *125*, 034102–034110.

54. A. J. Thorvaldsen, K. Ruud, A. Rizzo, S. Coriani, *J Chem Phys* **2008**, *129*, 164110.
55. T. B. Pedersen, H. Koch, L. Boman, A. M. J. Sánchez de Merás, *Chem. Phys. Lett*. **2004**, *393*, 319–326.
56. M. Krykunov, J. Autschbach, *J. Chem. Phys*. **2007**, *126*, 024101–024112.
57. F. W. Byron, R. W. Fuller, *The Mathematics of Classical and Quantum Physics*, Addison-Wesley, Reading, MA, **1969**.
58. P. Polavarapu, *J. Phys. Chem. A* **2005**, *109*, 7013–7023.
59. M. Rudolph, J. Autschbach, *Chirality* **2008**, *20*, 995–1008.
60. P. M. Bayley, E. B. Nielsen, J. A. Schellmann, *J. Phys. Chem*. **1969**, *73*, 228–243.
61. B. C. Mort, J. Autschbach, *J. Phys. Chem. A* **2005**, *109*, 8617–8623.
62. B. C. Mort, J. Autschbach, *J. Phys. Chem. A* **2006**, *110*, 11381–11383.
63. B. C. Mort, J. Autschbach, *Chem. Phys. Chem*. **2007**, *8*, 605–616.
64. B. C. Mort, J. Autschbach, *Chem. Phys. Chem*. **2008**, *9*, 159–170.
65. S. Grimme, Calculation of the electronic spectra of large molecules, in *Reviews in Computational Chemistry*, Vol. 20, K. B. Lipkowitz, R. Larter, and T. R. Cundari, eds., John Wiley & Sons, Hoboken, NJ, **2004**, pp. 153–218.
66. M. Dierksen, S. Grimme, *J. Chem. Phys*. **2004**, *120*, 3544–3554.
67. M. Dierksen, S. Grimme, *J. Chem. Phys*. **2005**, *122*, 244101–244109.
68. J. Neugebauer, E. J. Baerends, M. Nooijen, J. Autschbach, *J. Chem. Phys*. **2005**, *122*, 234305–234307.
69. B. Pritchard, J. Autschbach, *Chem. Phys. Chem*. **2010**, *11*, 2409–2415.
70. N. Lin, F. Santoro, X. Zhao, A. Rizzo, V. Barone, *J. Phys. Chem. A* **2008**, *112*, 12401–12411.
71. N. Lin, Y. Luo, F. Santoro, X. Zhao, A. Rizzo, *Chem. Phys. Lett*. **2008**, *464*, 144–149.
72. C. Hättig, F. Weigend, *J. Chem. Phys*. **2000**, *113*, 5154–5161.
73. J. Kongsted, T. B. Pedersen, M. Strange, A. Osted, A. E. Hansen, K. V. Mikkelsen, F. Pawlowski, P. Jorgensen, C. Hattig, *Chem. Phys. Lett*. **2005**, *401*, 385–392.
74. T. D. Crawford, R. A. King, *Chem. Phys. Lett*. **2002**, *366*, 611–622.
75. T. D. Crawford, L. S. Owens, M. C. Tam, P. R. Schreiner, H. Koch, *J. Am. Chem. Soc*. **2005**, *127*, 1368–1369.
76. Y. Tawada, T. Tsuneda, S. Yanagisawa, T. Yanai, K. Hirao, *J. Chem. Phys*. **2004**, *120*, 8425–8433.
77. T. Yanai, D. P. Tew, N. C. Handy, *Chem. Phys. Lett*. **2004**, *393*, 51–57.
78. E. Livshits, R. Baer, *Phys. Chem. Chem. Phys*. **2007**, *9*, 2932–2941.
79. M. J. G. Peach, P. Benfield, T. Helgaker, D. J. Tozer, *J. Chem. Phys*. **2008**, *128*, 044118.
80. T. Stein, L. Kronik, R. Baer, *J. Am. Chem. Soc*. **2009**, *131*, 2818–2820.
81. J. Autschbach, *Chem. Phys. Chem*. **2009**, *10*, 1–5.
82. L. Goerigk, S. Grimme, *J. Phys. Chem. A* **2009**, *113*, 767–776.
83. F. Furche, R. Ahlrichs, C. Wachsmann, E. Weber, A. Sobanski, F. Vögtle, S. Grimme, *J. Am. Chem. Soc*. **2000**, *122*, 1717–1724.
84. I. J. Tinoco, R. W. Woody, *J. Chem. Phys*. **1964**, *40*, 160–165.
85. D. A. Lightner, D. T. Hefelfinger, T. W. Powers, G. W. Frank, K. N. Trueblood, *J. Am. Chem. Soc*. **1972**, *94*, 3492–3497.
86. W. S. Brickell, A. Brown, C. M. Kemp, S. F. Mason, *J. Chem. Soc. (A)* **1971**, 756–760.
87. J. Autschbach, T. Ziegler, S. J. A. van Gisbergen, E. J. Baerends, *J. Chem. Phys*. **2002**, *116*, 6930–6940.
88. D. Shcherbin, K. Ruud, *Chem. Phys*. **2008**, *349*, 234.

89. P. J. Stephens, F. J. Devlin, J. R. Cheeseman, M. J. Frisch, *J. Phys. Chem. A* **2001**, *105*, 5356–5371.
90. S. Grimme, *Chem. Phys. Lett*. **2001**, *339*, 380–388.
91. J. Autschbach, T. Ziegler, S. Patchkovskii, S. J. A. van Gisbergen, E. J. Baerends, *J. Chem. Phys*. **2002**, *117*, 581–592.
92. K. Ruud, P. J. Stephens, F. J. Devlin, P. R. Taylor, J. R. Cheeseman, M. J. Frisch, *Chem. Phys. Lett*. **2003**, *373*, 606–614.
93. M. C. Tam, T. D. Crawford, *J. Phys. Chem. A* **2006**, *110*, 2290–2298.
94. T. D. Crawford, M. C. Tam, M. L. Abrams, *J. Phys. Chem. A* **2007**, *111*, 12057–12068.
95. S. M. Wilson, K. B. Wiberg, J. R. Cheeseman, M. J. Frisch, P. H. Vaccaro, *J. Phys. Chem. A* **2005**, *109*, 11752–11764.
96. M. D. Kundrat, J. Autschbach, *J. Phys. Chem. A* **2006**, *110*, 4115–4123.
97. M. D. Kundrat, J. Autschbach, *J. Phys. Chem. A* **2006**, *110*, 12908–12917.
98. M. D. Kundrat, J. Autschbach, *J. Am. Chem. Soc*. **2008**, *130*, 4404–4414.
99. M. Pecul, K. Ruud, A. Rizzo, T. Helgaker, *J. Phys. Chem. A* **2004**, *108*, 4269–4276.
100. S. Grimme, C. Mück-Lichtenfeld, *Chirality* **2008**, *20*, 1009–1015.
101. W. Zhang, K. Krohn, U. Flörke, G. Pescitelli, L. Di Bari, S. Antus, T. Kurtán, J. Rheinheimer, S. Draeger, B. Schulz, *Chem. Eur. J*. **2008**, *14*, 4913–4923.
102. G. Bringmann, K. Maksimenka, T. Bruhn, M. Reichert, T. Harada, R. Kuroda, *Tetrahedron* **2009**, *65*, 5720.
103. H. Hussain, K. Krohn, U. Floerke, B. Schulz, S. Draeger, G. Pescitelli, S. Antus, T. Kurtán, *Eur. J. Org. Chem*. **2007**, *2007*, 292.
104. Z. Hassan, H. Hussain, V. U. Ahmad, S. Anjum, G. Pescitelli, T. Kurtán, K. Krohn, *Tetrah. Asym*. **2007**, *18*, 2905.
105. H. Hussain, K. Krohn, U. Flörke, B. Schulz, S. Draeger, G. Pescitelli, P. Salvadori, S. Antus, T. Kurtán, *Tetrah. Asym*. **2007**, *18*, 925.
106. J. Dai, K. Krohn, B. Elsässer, U. Flörke, S. Draeger, B. Schulz, G. Pescitelli, P. Salvadori, S. Antus, T. Kurtán, *Eur. J. Org. Chem*. **2007**, *2007*, 4845.
107. K. Krohn, I. Kock, B. Elsässer, U. Flörke, B. Schulz, S. Draeger, G. Pescitelli, S. Antus, T. Kurtán, *Eur. J. Org. Chem*. **2007**, *2007*, 1123.
108. K. Krohn, U. Farooq, U. Flörke, B. Schulz, S. Draeger, G. Pescitelli, P. Salvadori, S. Antus, T. Kurtán, *Eur. J. Org. Chem*. **2007**, *2007*, 3206.
109. K. Krohn, H. Hussain, U. Flörke, B. Schulz, S. Draeger, G. Pescitelli, P. Salvadori, S. Antus, T. Kurtán, *Chirality* **2007**, *19*, 464–470.
110. W. Zhang, K. Krohn, J. Ding, Z.-H. Miao, X.-H. Zhou, S.-H. Chen, G. Pescitelli, P. Salvadori, T. Kurtan, Y.-W. Guo, *J. Nat. Prod*. **2008**, *71*, 961–966.
111. S. Qin, K. Krohn, U. Flörke, B. Schulz, S. Draeger, G. Pescitelli, P. Salvadori, S. Antus, T. Kurtán, *Eur. J. Org. Chem*. **2009**, *2009*, 3279.
112. J. L. Alonso-Gómez, A. G. Petrovic, N. Harada, P. Rivera-Fuentes, N. Berova, F. Diederich, *Chem. Eur. J*. **2009**, *15*, 8396–8400.
113. Y.-W. Guo, T. Kurtán, K. Krohn, G. Pescitelli, W. Zhang, *Chirality* **2009**, *21*, 561–568.
114. D. M. McCann, P. J. Stephens, *J. Org. Chem*. **2006**, *71*, 6074–6098.
115. B. Mennucci, J. Tomasi, R. Cammi, J. R. Cheeseman, M. J. Frisch, F. J. Devlin, S. Gabriel, P. J. Stephens, *J. Phys. Chem. A* **2002**, *106*, 6102–6113.
116. T. B. Pedersen, J. Kongsted, T. D. Crawford, *Chirality* **2009**, *21*, E68–E75.
117. A. Baranowska, A. Sadlej, *J. Comput. Chem*. **2010**, *31*, 552–560.
118. P. L. Polavarapu, *Chirality* **2006**, *18*, 348–356.

119. P. J. Stephens, D. M. McCann, F. J. Devlin, J. R. Cheeseman, M. J. Frisch, *J. Am. Chem. Soc*. **2004**, *126*, 7514–7521.
120. K. B. Wiberg, Y. G. Wang, S. M. Wilson, P. H. Vaccaro, J. R. Cheeseman, *J. Phys. Chem. A* **2006**, *110*, 13995–14002.
121. M. Krykunov, M. D. Kundrat, J. Autschbach, *J. Chem. Phys*. **2006**, *125*, 194110–194113.
122. S. Graule, M. Rudolph, W. Shen, J. A. G. Williams, C. Lescop, J. Autschbach, J. Crassous, R. Reau, *Chem. Eur. J*. **2010**, *16*, 5976–6005.
123. K. B. Wiberg, P. H. Vaccaro, J. R. Cheeseman, *J. Am. Chem. Soc*. **2003**, *125*, 1888–1896.
124. A. Moscowitz, Theory and analysis of rotatory dispersion curves, in C. Djerassi, *Optical Rotatory Dispersion*, McGraw-Hill, New York, **1960**, pp. 150–177.
125. A. de Meijere, A. F. Khlebnikov, S. I. Kozhushkov, R. R. Kostikov, P. R. Schreiner, A. Wittkopp, C. Rinderspacher, H. Menzel, D. S. Yufit, J. A. K. Howard, *Chem. Eur. J*. **2002**, *8*, 828–842.
126. K. B. Wiberg, Y. G. Wang, S. M. Wilson, P. H. Vaccaro, W. L. Jorgensen, T. D. Crawford, M. L. Abrams, J. R. Cheeseman, M. Luderer, *J. Phys. Chem. A* **2008**, *112*, 2415–2422.
127. K. B. Wiberg, Y. Gui Wang, P. H. Vaccaro, J. R. Cheeseman, G. Trucks, M. J. Frisch, *J. Phys. Chem. A* **2004**, *108*, 32–38.
128. A. G. Petrovic, J. He, P. L. Polavarapu, L. S. Xiao, D. W. Armstrong, *Org. Biomol. Chem*. **2005**, *3*, 1977–1891.
129. J. Autschbach, L. Jensen, G. C. Schatz, Y. C. E. Tse, M. Krykunov, *J. Phys. Chem. A* **2006**, *110*, 2461–2473.
130. E. Giorgio, R. G. Viglione, R. Zanasi, C. Rosini, *J. Am. Chem. Soc*. **2004**, *126*, 12968–12976.
131. W. R. Moore, H. W. Anderson, S. D. Clark, T. M. Ozretich, *J. Am. Chem. Soc*. **1971**, *93*, 4932–4934.
132. P. J. Stephens, N. Harada, *Chirality* **2010**, *22*, 229–233.
133. R. K. Ahrenkiel, *J. Opt. Soc. Am*. **1971**, *61*, 1651–1655.
134. K. Ruud, R. Zanasi, *Angew. Chem. Int. Edit*. **2005**, *44*, 3594–3596.
135. J. Kongsted, T. B. Pedersen, L. Jensen, A. E. Hansen, K. V. Mikkelsen, *J. Am. Chem. Soc*. **2006**, *128*, 976–982.
136. J. Kongsted, K. Ruud, *Chem. Phys. Lett*. **2008**, *451*, 226.
137. K. B. Wiberg, Y. Wang, M. J. Murphy, P. H. Vaccaro, *J. Phys. Chem. A* **2004**, *108*, 5559–5563.
138. M. Nooijen, *Int. J. Quantum Chem*. **2006**, *106*, 2489–2510.
139. F. Santoro, R. Improta, A. Lami, J. Bloino, V. Barone, *J. Chem. Phys*. **2007**, *126*, 084509–084513.
140. F. Santoro, A. Lami, R. Improta, J. Bloino, V. Barone, *J. Chem. Phys*. **2008**, *128*, 224311–224317.
141. A. Breest, P. Ochmann, F. Pulm, K. H. Goedderz, M. Carnell, J. Hormes, *Mol. Phys*. **1994**, *82*, 539–551.
142. C. K. Luk, F. S. Richardson, *J. Am. Chem. Soc*. **1974**, *96*, 2006–2009.
143. M. D. Kundrat, J. Autschbach, *J. Chem. Theor. Comput*. **2009**, *5*, 1051–1060.
144. L. Nitsch-Velasquez, J. Autschbach, *Chirality*, **2010**, *22*, E81–E95.
145. W. Moffitt, R. B. Woodward, A. Moscowitz, W. Klyne, C. Djerassi, *J. Am. Chem. Soc*. **1961**, *83*, 4013–4018.
146. R. R. Gould, R. Hoffmann, *J. Am. Chem. Soc*. **1970**, *92*, 1813–1818.
147. D. A. Lightner, The octant rule, in *Circular Dichroism: Principles and Applications*, 2nd ed., N. Berova, K. Nakanishi, and R. Woody, eds., John Wiley & Sons, New York, **2000**, pp. 261–304.
148. E. C. Jorgensen, *Tetrahedron Lett*. **1971**, *12*, 863–866.

149. G. Pescitelli, N. Sreerama, P. Salvadori, K. Nakanishi, N. Berova, R. W. Woody, *J. Am. Chem. Soc*. **2008**, *130*, 6170–6181.
150. G. Clough, *J. Chem. Soc., Trans*. **1918**, *113*, 526–554.
151. O. Lutz, B. Jirgensons, *Ber. Dtsch. Chem. Ges. B* **1930**, 448–460.
152. O. Lutz, B. Jirgensons, *Ber. Dtsch. Chem. Ges. B* **1931**, *64*, 1221–1232.
153. C. J. Ballhausen, *Molecular Electronic Structures of Transition M et al Complexes*, McGraw-Hill, London, **1979**.
154. B. E. Douglas, Y. Saito, eds., *Stereochemistry of Optically Active Transition M et al Compounds*, Vol. 119 of *ACS Symposium Series*, Americal Chemical Society, Washington, D.C., **1980**.
155. M. Ziegler, A. von Zelewsky, *Coord. Chem. Rev*. **1998**, *177*, 257–300.
156. J. Autschbach, F. E. Jorge, T. Ziegler, *Inorg. Chem*. **2003**, *42*, 2867–2877.
157. B. Le Guennic, W. Hieringer, A. Görling, J. Autschbach, *J. Phys. Chem. A* **2005**, *109*, 4836–4846.
158. A. J. McCaffery, S. F. Mason, B. J. Norman, *J. Chem. Soc. A* **1969**, 1428–1441.
159. S. F. Mason, R. H. Seal, *Mol. Phys*. **1976**, *31*, 755–775.
160. R. R. Judkins, D. J. Royer, *Inorg. Chem*. **1974**, *13*, 945–950.
161. F. E. Jorge, J. Autschbach, T. Ziegler, *Inorg. Chem*. **2003**, *42*, 8902–8910.
162. F. E. Jorge, J. Autschbach, T. Ziegler, *J. Am. Chem. Soc*. **2005**, *127*, 975–985.
163. J. Fan, T. Ziegler, *Inorg. Chem*. **2008**, *47*, 4762–4773.
164. R. K. Szilagyi, M. Metz, E. Solomon, *J. Phys. Chem. A* **2002**, *106*, 2994–3007.
165. M. Bühl, *Ann. Rep. NMR Spectrosc*. **2008**, *64*, 77–125.
166. R. Bast, P. Schwerdtfeger, *J. Chem. Phys*. **2003**, *119*, 5988–5994.
167. J. Fan, J. Autschbach, T. Ziegler, *Inorg. Chem*. **2010**, *49*, 1355–1362.
168. A. Rosa, G. Ricciardi, O. Gritsenko, E. J. Baerends, Excitation energies of metal complexes with time-dependent density functional theory, in *Principles and Applications of Density Functional Theory in Inorganic Chemistry I*, eds. N. Kaltsoyannis, J. E. McGrady, Vol. *112* of *Structure and Bonding*, Springer, Heidelberg, **2004**, pp. 49–115.
169. D. Rappoport, F. Furche, Excited states and photochemistry, in *Time-Dependent Density Functional Theory*, M. A. L. Marques, C. A. Ullrich, F. Nogueira, A. Rubio, K. Burke, and E. K. U. Gross, eds., Vol. 706 of *Lecture Notes in Physics*, Springer, Berlin, **2006**.
170. J. Autschbach, Spectroscopic properties obtained from time–dependent density functional theory (TD–DFT), in *Encyclopedia of Inorganic Chemistry*, Wiley-VCH, **2009**.
171. L. Jensen, M. Swart, P. T. van Duijnen, J. Autschbach, *Int. J. Quantum Chem*. **2006**, *106*, 2479–2488.
172. J. Fan, M. Seth, J. Autschbach, T. Ziegler, *Inorg. Chem*. **2008**, *47*, 11656–11668.
173. A. Vargas, M. Zerara, E. Krausz, A. Hauser, L. M. Lawson Daku, *J. Chem. Theor. Comput*. **2006**, *2*, 1342–1359.
174. P. W. Thulstrup, E. Larsen, *Dalton Trans*. **2006**, 1784–1789.
175. J. Coughlin, M. Westrol, K. Oyler, N. Byrne, E. Kraml, C. Zysman-Colman, M. Lowry, S. Bernhard, *Inorg. Chem*. **2008**, *47*, 2039–2048.
176. F. J. Coughlin, K. D. Oyler, J. Pascal, Robert A., S. Bernhard, *Inorg. Chem*. **2008**, *47*, 974–979.
177. D. W. Armstrong, F. A. Cotton, A. G. Petrovic, P. L. Polavarapu, M. M. Warnke, *Inorg. Chem*. **2007**, *46*, 1535–1537.
178. N. Kobayashi, F. Narita, K. Ishii, A. Muranaka, *Chemistry* **2009**, *15*, 10173–10181.
179. L. Norel, M. Rudolph, N. Vanthuyne, J. G. Williams, C. Lescop, C. Roussel, J. Autschbach, J. Crassous, R. Reau, *Angew. Chem. Int. Edit*. **2010**, *49*, 99–102.

180. S. Graule, M. Rudolph, N. Vanthuyne, J. Autschbach, C. Roussel, J. Crassous, R. Reau, *J. Am. Chem. Soc*. **2009**, *131*, 3183–3185.
181. A. Sanchez-Castillo, C. Noguez, I. Garzon, *J. Am. Chem. Soc*. **2010**, *132*, 1504–1505.
182. M.-R. Goldsmith, C. B. George, G. Zuber, R. Naaman, D. H. Waldeck, P. Wipf, D. N. Beratan, *Phys. Chem. Chem. Phys*. **2006**, *8*, 63–67.
183. M. R. Provorse, C. M. Aikens, *J. Am. Chem. Soc*. **2010**, *132*, 1302–1310.
184. H. Lehl, K.-C. Buschbeck, R. Gagarin, Kobalt B/2, in *Gmelins Handbuch der Anorganischen Chemie*, Verlag Chemie, Weinheim, **1964**, pp. 357–358.
185. J. Autschbach, *Comp. Lett*. **2007**, *3*, 131–150.
186. L. Jensen, J. Autschbach, G. C. Schatz, *J. Chem. Phys*. **2005**, *122*, 224115.
187. J. Fan, T. Ziegler, *Chirality* **2008**, *20*, 938–950.
188. E. J. Stiefel, G. F. Brown, *Inorg. Chem* **1972**, *11*, 434–436.
189. S. F. Mason, *Inorg. Chim. Acta Rev*. **1968**, *2*, 89–109.
190. S. F. Mason, B. J. Peart, *J. Chem. Soc. Dalton Trans*. **1973**, *9*, 949–954.
191. S. F. Mason, B. J. Peart, *J. Chem. Soc. Dalton Trans*. **1973**, *9*, 944–949.
192. M. Srebro, N. Govind, W.A. de Jong, J. Autschbach, *J. Phys. Chem*. A **2011**, DOI 10.1021/jp 2055409.

22

THEORETICAL ELECTRONIC CIRCULAR DICHROISM SPECTROSCOPY OF LARGE ORGANIC AND SUPRAMOLECULAR SYSTEMS

Lars Goerigk, Holger Kruse, and Stefan Grimme

22.1. INTRODUCTION

Electronic circular dichroism (ECD) spectroscopy plays an important role in chemistry, biology, pharmaceutics, and medicine. Particularly, the comparison between experimentally and theoretically obtained spectra has become a strong tool for the determination of absolute configurations of unknown compounds and helps reveal their structure-chiroptic properties. Compared to UV–vis spectroscopy, the fact that ECD bands can have positive or negative signs adds an additional useful dimension, as the spectra then become sensitive to geometric and electronic properties of the analyzed molecule. This, however, requires more sophisticated methods in concomitant theoretical treatments that simultaneously must yield accurate excitation energies, band intensities, and signs. For detailed general discussions on theoretical ECD spectroscopy, see references 1–4. While small systems can be accurately treated with sophisticated *ab initio* techniques, the application of theoretical methods to larger systems of actual chemical interest is a challenging task. Herein, we try to give useful hints on how to tackle this challenge. First, we summarize important facts about theoretical ECD and will give an overview of *ab initio*, semiempirical and DFT methods. We will also give useful advice for carrying out calculations of ECD properties. We will then apply some of the presented methods to large systems covering different aspects that might also occur in the analysis of unknown compounds. These include exciton coupling, charge-transfer excitations, and noncovalent interactions in aggregates, inclusion compounds, and conformationally flexible molecules. Particularly the latter problem will be discussed in detail in some kind of general "tutorial".

Comprehensive Chiroptical Spectroscopy, Volume 1: Instrumentation, Methodologies, and Theoretical Simulations, First Edition. Edited by N. Berova, P. L. Polavarapu, K. Nakanishi, and R. W. Woody.
© 2012 John Wiley & Sons, Inc. Published 2012 by John Wiley & Sons, Inc.

Usually we will employ methods that have already been applied to chiroptical properties, but we will also test—to the best of our knowledge for the first time—the performance of range-separated density functionals and the SCS-CC2 approach for ECD spectroscopy.

22.2. THEORY

22.2.1. Theoretical Circular Dichroism Spectroscopy

In ECD spectroscopy, one of the main quantities of interest is the rotational strength R, which determines the sign and the intensity of an ECD band [5]. Experimentally, it is obtained by integrating the area under the corresponding band. In cgs units, R reads

$$R_{exp} = 2.297 \times 10^{-39} \int_{\lambda_1}^{\lambda_2} \frac{\Delta\epsilon\,(\lambda)}{\lambda}\, d\lambda, \tag{22.1}$$

where λ is the radiation wavelength and $\Delta\epsilon$ is the difference in the extinction coefficients of left-and right-circularly polarized light.

Theoretically, R_{0i} (for the transition between the electronic ground state to the ith excited state) can be obtained according to Rosenfeld as the imaginary part of the dot product between the electric ($\vec{\mu}_{0i}$) and magnetic ($\vec{m}_{0i}$) transition dipole moments:

$$\begin{aligned} R_{0i} &= \mathrm{Im}\left(\langle\psi_0 \mid \hat{\mu} \mid \psi_i\rangle\langle\psi_0 \mid \hat{m} \mid \psi_i\rangle\right) \\ &= \mid \vec{\mu}_{0i} \mid\mid \vec{m}_{0i} \mid \cdot \cos\left(\vec{\mu}_{i0}, \vec{m}_{0i}\right), \end{aligned} \tag{22.2}$$

where ψ is the wavefunction of the respective state and $\hat{\mu}$ and $\hat{m}$ are the electric and magnetic dipole moment operators. Thus, the sign and absolute value of R depend on the absolute values of both transition moments and their relative orientation to each other. There are two common ways of calculating rotational strengths. The first one is the so-called dipole length formalism

$$R_{0i}^{r} = \frac{1}{2c}\langle\psi_0 \mid \hat{r} \mid \psi_i\rangle\langle\psi_i \mid \hat{r} \times \hat{\nabla} \mid \psi_0\rangle, \tag{22.3}$$

while the so-called the dipole velocity formula reads

$$R_{0i}^{\nabla} = \frac{1}{2c\omega_{0i}}\langle\psi_0 \mid \hat{\nabla} \mid \psi_i\rangle\langle\psi_i \mid \hat{r} \times \hat{\nabla} \mid \psi_0\rangle. \tag{22.4}$$

Compared to the length form, the velocity form has the advantage of being gauge-invariant; that is, it does not depend on the specific choice of the coordinate system used in the calculation. However, it is less sensitive toward the quality of the wavefunction ψ. For theoretical ECD spectroscopy and the related calculation of optical rotatory dispersion (ORD) it was shown that, particularly for time-dependent density functional theory (TD-DFT), the length form is more robust; for example, it shows a quicker convergence to the basis set limit [6]. In Figure 22.1, TD-BHLYP spectra of (*M*)-hexahelicene are presented, which show that there is almost no difference between rotational strengths in length and velocity form. A similar example was also discussed in reference 7. Herein, only the length form will be used.

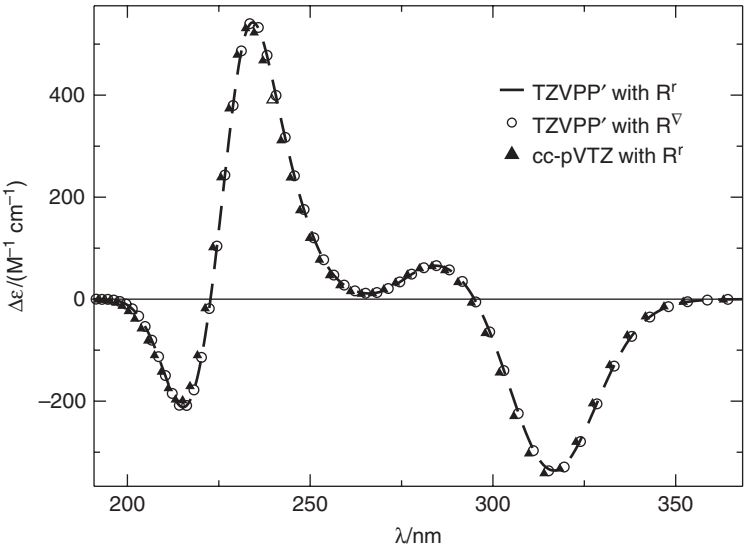

Figure 22.1. Comparison of the influence of technical parameters for the theoretical ECD spectra of (*M*)-hexahelicene. The spectra were obtained with the TD-BHLYP method and the basis sets TZVPP′ and cc-pVTZ. In the case of the TZVPP′ basis, two spectra were simulated by using the rotational strengths obtained with the dipole length (R^r) and velocity (R^∇) formalism, respectively. The cc-pVTZ spectrum was simulated by using R^r values.

Often, theoretical spectra are directly compared with experimental ones. For that purpose, it is not sufficient to just compare the experimental band positions with the excitation energies and intensities of theoretical transitions. It is possible that several transitions lie within the range of a certain band, or that transitions with opposite signs lie close to each other. Therefore, it is strongly recommended to actually simulate an ECD spectrum. This is usually done by overlapping Gaussian functions for each transition:

$$\Delta\epsilon(E) = \frac{1}{2.297 \times 10^{-39}} \frac{1}{\sqrt{2\pi\sigma}} \sum_{i}^{A} \Delta E_i R_i e^{\left[-(E-\Delta E_i/2\sigma)\right]^2}, \tag{22.5}$$

where σ is the width of an absorption band at a height of $\frac{1}{e}$, A is the number of excited states, and ΔE_i and R_i are the excitation energy and the rotational strength of the ith transition. Usually a value of $\sigma = 0.2$ eV is chosen for the bandwidth.

22.2.2. Theoretical Methods

22.2.2.1. Wavefunction-Based Methods. Herein, we will only give an overview of single reference methods [8]. Multireference methods (e.g., CAS-SCF, CAS-PT2, or MR-CI) are useful in electronically complicated cases and are often used for the calculation of excited-state potential energy hypersurfaces and conical intersections. Furthermore, only methods for excited states with dominant single excitation character are considered. For a more detailed review on the calculation of electronic excited states, see also reference 9.

The basis for treating single reference cases with wavefunction-based methods is Hartree–Fock theory, in which the expectation value of one Slater determinant (or one configuration) is minimized variationally. The electron–electron interaction is treated within a mean-field approach; that is, each electron experiences just an averaged field of the others. For many-electron systems, this approximation leads to a higher total energy compared to the exact solution. This difference defines the electron correlation energy. Electron correlated methods, like configuration interaction, coupled cluster, or

many-body perturbation theory, use an HF determinant as starting point for a further treatment of the electron–electron interaction. The computational effort for Hartree–Fock formally only scales with $\mathcal{O}(N^4)$, with N being the number of basis functions; electron correlated methods scale at least with $\mathcal{O}(N^5)$. For the calculation of electronic excited-state properties, one can also rely on uncorrelated or correlated methods. An overview of different methods is given in Figure 22.2; methods marked with an asterisk will be used in the following examples.

In principle, the most simple uncorrelated approach to excited-state properties is the configuration interaction singles model (CIS). The CIS wavefunction $|\,\psi^{CIS}\rangle$ is described as a sum of the HF reference $|\,\psi^{HF}\rangle$ and all singly excited configurations $|\,\psi_i^a\rangle$ (which consist of two determinants for a singlet wavefunction) with respect to that reference, that is,

$$|\,\psi^{CIS}\rangle = c_0\,|\,\psi^{HF}\rangle + \sum_{ia} c_i^a\,|\,\psi_i^a\rangle. \tag{22.6}$$

In a pictorial way, one electron is taken out of an occupied orbital i and "excited" into a virtual orbital a to create a singly excited configuration. The coefficients c are determined variationally. Usually, the CIS method systematically overestimates excitation energies by up to 1 eV or more and the calculated states can be in the wrong order. The transition moments and, thus, the rotational strengths are of only moderate accuracy. Improvements can be achieved by including electron correlation in a perturbative treatment (PT). There are different flavors of this approach (not every one is size-extensive). In the present context, we will make use of the SCS-CIS(D) method [10]. CIS(D) stands for *configuration interaction singles with perturbative doubles correction* [11]; the acronym SCS for *spin component scaling*, which means that electron pair energies of same and opposite spin are scaled differently [12]. SCS-CIS(D) can yield excitation energies with an average error of about 0.2 eV for large organic chromophores [13]. However, it is just a correction to the CIS excitation energies and not to the rotational strengths.

The second uncorrelated approach based on a HF determinant is linear response theory, which is in this context also known as time-dependent Hartree–Fock (TD-HF) or as random-phase approximation (RPA) [14]. TD-HF can be written as an eigenvalue

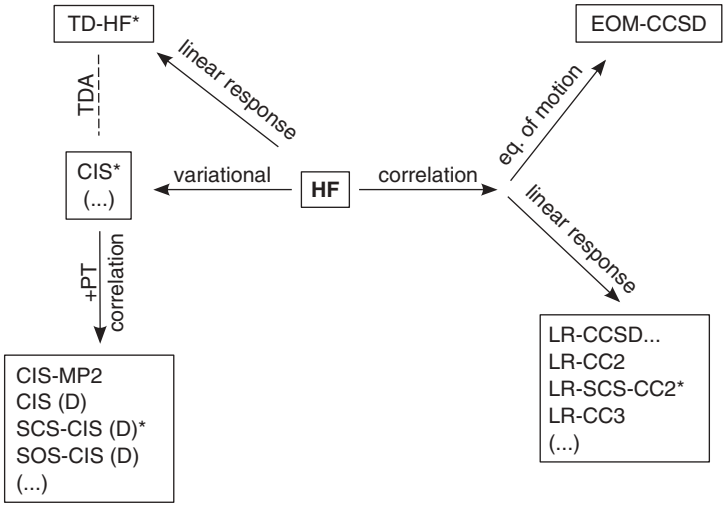

Figure 22.2. Overview of wavefunction-based single-reference methods for the calculation of electronic excited states. Methods marked with an asterisk are applied in the present work.

problem according to

$$\begin{pmatrix} \mathbf{A} & \mathbf{B} \\ \mathbf{B} & \mathbf{A} \end{pmatrix} \begin{pmatrix} \mathbf{X} \\ \mathbf{Y} \end{pmatrix} = \Delta E \begin{pmatrix} \mathbf{1} & \mathbf{0} \\ \mathbf{0} & -\mathbf{1} \end{pmatrix} \begin{pmatrix} \mathbf{X} \\ \mathbf{Y} \end{pmatrix}, \tag{22.7}$$

where ΔE is the excitation energy, $\mathbf{X}$ and $\mathbf{Y}$ are solution vectors describing single excitations and de-excitations, and $\mathbf{A}$ and $\mathbf{B}$ are related to the corresponding Hamiltonian matrices between these (de-)excitations. The CIS method can be derived from TD-HF, by setting the matrix $\mathbf{B}$ to zero [Tamm–Dancoff approximation (TDA)] [15]. TD-HF yields excitation energies of CIS quality but usually yields better rotational strengths.

A route to a more sophisticated treatment of excited states is based on an electron correlated ground-state description. In principal, the CIS model can be extended by including higher excited determinants (CISD, CISDT,...), but because these truncated CI models are not size-extensive, they are in practice of no use. The truncated coupled cluster model, however, includes higher excitations and is still size-extensive. One way of describing excited states is the equation-of-motion coupled cluster model (EOM-CC) [16]. Another way is linear response coupled cluster (LR-CC), which yields the same excitation energies as the EOM model. CC is iterative, though, and each iteration scales (depending on the model) with $\mathcal{O}(N^6)$ (for CCSD), $\mathcal{O}(N^8)$ (for CCSDT), and more. Alternatives are approximated coupled cluster models, like CC2 [17] and CC3 [18], which are approximations to CCSD and CCSDT and scale with $\mathcal{O}(N^5)$ and $\mathcal{O}(N^7)$, respectively. Particularly the CC2 model has become the "gold-standard" single-reference method for excitation energies of large molecules. In this work, we will apply the corresponding spin-component scaled approach SCS-CC2 [19]. For large chromophores, CC2 and SCS-CC2 have an average error of about 0.17–0.20 eV [13]. ECD spectra, calculated with SCS-CC2, are reported for the first time herein.

One final comment has to be made on wavefunction-based methods in general. In contrast to DFT methods (*vide infra*), the exchange and correlation potentials decay with the correct asymptotic behavior. As a result, Rydberg states and charge-transfer states are described correctly (apart from errors due to finite basis sets and approximations to the exact correlation energy).

22.2.2.2. Semiempirical Methods. The time-consuming part in wavefunction-based methods is the calculation of the two-electron integrals. Semiempirical methods make approximations to these integrals. Based on different levels of approximation, integral contributions are completely or partially neglected. The remaining integrals are parameterized to either experimental or theoretical data, and furthermore often calculated within a minimal atomic orbital basis. Typically, excited-state properties are calculated with either a linear response or a CIS approach. There is a huge variety of different semiempirical methods. Herein, we will consider the Pariser–Pople–Parr (PPP) [20] and the Zerner's Intermediate Neglect of Differential Overlap method [21] for electronic spectra (ZINDO/S). The PPP approach only considers π-electrons Thus, it is only applicable to conjugated planar or slightly bent systems. In this work, we will consider PPP within a linear response scheme (TD-PPP). The ZINDO/S method considers all valence electrons. It is specially parameterized to spectroscopic properties in the framework of CIS.

22.2.2.3. Density Functional Theory. The basis of density functional theory (DFT) is the first Hohenberg–Kohn theorem, which states that there is a direct correlation between a system's electron density $\rho(r)$ and its electronic energy E [22]. Both

properties are connected by a functional, which depends on the electron density and for which an adequate mathematical description has to be found. For chemical applications, the acronym DFT usually stands for the so-called Kohn–Sham (KS) approach, in which the kinetic energy is based on a reference system of noninteracting electrons, which still yields the electron density of the real system (KS-DFT) [23]. This kinetic energy contribution is computed by introducing orbitals (KS orbitals). The Kohn–Sham functional $F[\rho(r)]^{KS}$ can be divided into functionals of the kinetic electronic energy $T_e[\rho(r)]$, the interaction energy between electrons and nuclei $V_{en}[\rho(r)]$, the electronic Coulomb energy $J[\rho(r)]$, the exchange energy $E_x[\rho(r)]$ of the indistinguishable electrons, and the electron correlation energy $E_c[\rho(r)]$. The functionals of the exchange and correlation energies are combined to the so-called exchange-correlation functional $E_{xc}[\rho(r)]$ (Eq. 22.8). [24]:

$$\begin{aligned} F[\rho]^{KS} &= T_e[\rho] + V_{eK}[\rho] + J[\rho] + E_{xc}[\rho], \\ E_{xc}[\rho] &= E_x[\rho] + E_c[\rho]. \end{aligned} \tag{22.8}$$

The only remaining unknown part of the Kohn–Sham functional is $E_{xc}[\rho(r)]$. KS-DFT is an exact theory, meaning that the exact total energy could be calculated, if the true functional $E_{xc}[\rho(r)]$ were known, which is practically impossible. It is still a topic in actual research to find adequate approximations to this functional.

Technically, the Kohn–Sham equations are solved iteratively, like it is done for the wave mechanical Hartree–Fock theory. But in contrast to the latter one, DFT already incorporates electron correlation effects and thereby can yield better results than Hartree–Fock at the same or even less computational cost.

Therefore, DFT is usually applied for obtaining both good ground state geometries and electronic excited-state properties. The latter are obtained with the help of linear response theory. The resulting TD-DFT equation is similar to that of TD-HF [Eq. (22.7)]. Within the adiabatic approximation, standard time-independent ground-state functionals serve as the basis for the exchange-correlation (xc) kernel in current TD-DFT [25]. For a recent basic criticism of fundamental aspects of TD-DFT see references [26] and [27].

According to Perdew, a classification of density functionals is possible within a metaphorical "Jacob's Ladder" scheme [28]. Each class of functionals is ascribed to a rung on this ladder (Figure 22.3). With reaching a higher rung, an improved accuracy of the results is expected. On the other hand, higher rung functionals are mathematically more involved and are characterized by an increase in computational cost.

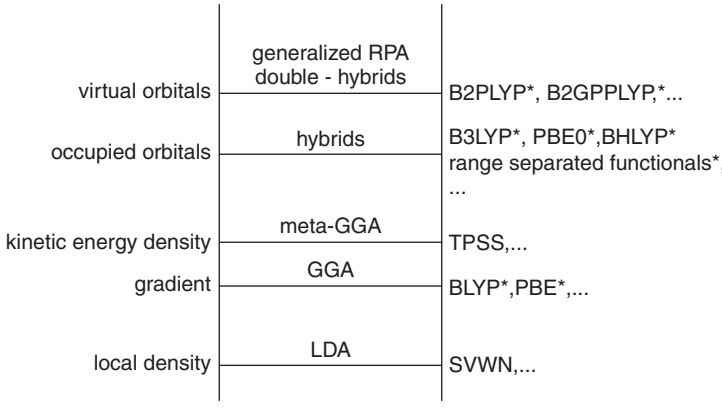

Figure 22.3. The "Jacob's Ladder" hierarchy of density functionals. Methods marked with an asterisk are applied in the present work.

The lowest rung on Jacob's Ladder just takes into account the information on the local electron density. That is why these functionals are ascribed to the local density approximation (LDA). Because the electron density strongly varies in molecules, LDA functionals are insufficient for describing these. The next two rungs take additionally into account the gradient [general gradient approximation (GGA)] and the kinetic energy density (meta-GGA). In fourth place are the so-called hybrid functionals for which some part of the DFT exchange is substituted by wave mechanical Fock exchange. So-called global hybrids (e.g., B3LYP [29, 30] and PBE0 [31]) include a constant amount of Fock exchange, whereas range-separated functionals (RSFs, e.g., CAM-B3LYP [32] and LCωPBE [33]) differ between short-and long-range regions and they mix in different amounts of Fock exchange in these regions. Fifth-rung functionals additionally take into account the information of virtual KS orbitals. To this rung belong the so-called double-hybrid functionals, which were developed by Grimme [34, 35]. Besides Fock exchange, double-hybrids also include an orbital-dependent, perturbative contribution to the correlation energy. Herein, we will make use of the B2PLYP [34] and B2GPPLYP [36] functionals. Table 22.1 shows the amounts of Fock exchange of the various functionals used in this work, which is important for classification in excited-state TD-DFT treatments.

Problems in current density functional formulations are the so-called self-interaction error (SIE)—unphysical Coulomb interaction of an electron with itself—a wrong decay of the electron density for large distances between electrons and nuclei and the inability of describing nonlocal correlation effects, like, for example, London dispersion. The latter problem can be easily accounted for by adding an empirical dispersion correction (DFT-D [43]/DFT-D3 [40]). Later, we will show that this can be of utter importance for obtaining good geometries and relative energies of conformers. When calculating excited-state properties, the self-interaction error can lead to artificial low-lying excited states that have no experimental counterpart ("ghost states"). This effect is most prominent for GGA functionals, and it can be counterbalanced by mixing in high amounts of Fock exchange (BHLYP and double-hybrids are practically free of ghost states). High amounts of Fock exchange are also helpful for a correct description of states with ionic character,

TABLE 22.1. Overview of the Amount of Fock Exchange (a_X) in Density Functionals Used in This Work

Functional	a_X
BLYP [37, 38]	0.00
PBE [39]	0.00
B3LYP [29, 30]	0.20
PBE0 [31]	0.25
PBE38 [40]	0.375
BHLYP [41]	0.50
CAM-B3LYP [32]	$0.19^a/0.65^b$
LCωPBE [33]	$0.00^a/1.00^b$
ωB97X [42]	$0.158^a/1.00^b$
B2PLYP [34]	0.53^c
B2GPPLYP [36]	0.65^c

[a] Short-range part.
[b] Long-range part.
[c] Double-hybrids also mix in a portion of perturbative correlation (0.27 for B2PLYP; 0.36 for B2GPPLYP).

as demonstrated for large aromatic chromophores [44, 45]. This problem should not be neglected, because these ghost states can have a strong influence on the shape of the ECD spectra, as shown later on. The wrong decay of the exchange-correlation potential leads to an underestimation of Rydberg and particularly charge-transfer states. RSFs were designed to counterbalance this problem, because they include high amounts of Fock exchange in the important long-range region.

Benchmark studies have shown that GGA and meta-GGA functionals lead to red-shifted excitation energies (underestimation; average error of 0.5 eV for large chromophores [13, 46]), whereas too high amounts of Fock exchange in hybrid functionals can lead to a blue shift. However, at least 40% of Fock exchange is required for the correct treatment of large, organic chromophores [13, 44–47]. Double-hybrid functionals are the most accurate functionals at the moment and are comparable to or more accurate than (SCS-)CC2 (with an average absolute error of about 0.16 eV for large, organic chromophores) [13, 46]. Rotational strengths are adequate on all these levels. Experience shows that they improve for hybrid functionals. Due to their construction [35], double-hybrids yield better excitation energies but similar rotational strengths as hybrids. In 2009, we also showed that TD-B2PLYP is a useful and accurate method for the calculation of ECD spectra [7].

22.2.3. General Recommendations for the Calculation of ECD Spectra

The simulation of ECD spectra has stronger requirements with regard to the methods applied than does the simulation of pure UV–vis spectra. Our experience from published literature and peer-review appointments made us also note that in many applications the TD-B3LYP/6-31G* level of theory is used as a standard, "black box"-like approach without checking whether or not it is appropriate for the particular problem. Therefore, we will mention in the following some important points that should be considered, particularly for the treatment of larger systems.

1. The shape of an ECD spectrum depends strongly on the molecular structures. Particularly in larger systems, noncovalent interactions can play a decisive role and should be adequately considered by the chosen method. The application of electron correlated methods to structure optimizations of chemically relevant systems is limited due to their high computational cost, however. An economically way is to make use of dispersion corrected DFT. Excitation energies have to be predicted with high accuracy, otherwise, bands of opposite signs could cancel each other out and cannot be observed in the theoretical spectrum. On the other hand, it is also possible to calculate artificial bands that are not observed in experiment. TD-DFT is usually the method of choice for the calculation of spectra. However, one should not trust the result of merely one functional. It is wise to apply at least two different functionals with different amounts of Fock exchange, to make sure that no artifacts influence the outcome of a certain study.
2. Usually, basis sets of triple-ζ quality should be applied. When Rydberg states are considered, it is crucial to include diffuse functions. To save computing time, it is worthwhile to use Ahlrichs-type basis sets instead of the Dunning-type sets, because the first one includes less primitive atomic basis functions. For larger systems, compromises can be made and certain functions neglected. Herein, we will sometimes make use of a truncated TZVPP basis dubbed TZVPP′. This is a normal Ahlrichs-type TZVPP [48] basis, but with discarded f functions;

f functions play no dominant role in excitations of organic molecules, but their evaluation is very time-consuming. Furthermore, a TZVP [48] basis—that is, with just one set of polarization functions—is applied to hydrogen atoms, which further decreases the total number of basis functions. To demonstrate the usefulness of this approach, an example is given in Figure 22.1. The ECD spectrum of (*M*)-hexahelicene was calculated with cc-pVTZ [49] and TZVPP′. Both basis sets give almost identical results. The total computation time is increased by a factor of 2.5 for cc-pVTZ compared to TZVPP′. In a recent study, we also found factors of up to five, when diffuse functions are added [7]. Another possible way of saving computational time, without any loss of accuracy, is applying smaller basis sets on substituents that are not part of the chromophore. Sometimes it is also possible to substitute larger moieties by smaller ones if their influence on the total spectrum is expected to be negligible. If for the complete molecule a double-ζ basis (like SV(P) [50]) has to be applied, it is advisable to do this after a study of the basis set effect (maybe on a model system or something comparable).

3. ECD spectra are usually shown on an electron-volt or nanometer scale. For analyzing theoretical spectra, usually differences in band maxima and absorption energies are considered. When doing such an analysis, it is important to consider the type of energy scale that is chosen for the ECD spectra. If, for example, an error of 10 nm is found in a region between 330 and 340 nm, this error is 0.1 eV. A difference of 10 nm in an energetically higher-lying region (e.g., from 190 to 200 nm) corresponds to a much higher value of 0.3 eV. When a theoretical method suffers from systematic errors, it is common practice to apply a constant shift to the spectrum. However, this should be done carefully and under consideration of the above-mentioned point.
4. If the theoretical results are compared with experimental ECD spectra, one should always carefully consider the experimental setup. Solvent effects can usually lead to a red shift of the absorption bands, which is important when theoretical gas-phase spectra are used for the analysis. In principle, it is possible to do such a comparison, but one has to bear in mind that solvent effects can reach up to 0.1 eV. The less polar the solvent is, the less prominent these uncertainties become. It is also possible to simulate solvent effects with, for example, continuum solvation models [like PCM [51] or COSMO [52] models (see Section 22.3.1)]. However, this approach is not advisable when, for example, hydrogen bonds between the solvent and the solute are expected, because these cannot be described by continuum solvation models. Moreover, one has to check enantiomeric purity in the measurement because this influences the ECD intensities, of course. In general, it is acceptable if the theoretical and experimental intensities differ by a factor between one and two. More important than the absolute intensities is the question whether the relative intensities between two absorption bands can be reproduced by theory. However, large deviations of more than a factor of two may be a hint that the theoretical treatment is not adequate or that, for example, the experiment was not carried out properly (e.g., impurities etc.).
5. Various quantum chemical codes implemented either all or just some of the methods, described in the theoretical section. The programs usually differ in efficiency. We will not comment on these differences, but will just state which codes we used for the presented calculations. Usually, all HF, CIS, SCS-CC2, and (TD)-DFT calculations were performed with the TURBOMOLE 6.0 suite of programs [53–57]. We strongly suggest the use of the resolution of the identity (density

fitting) approximation, when possible, which is very efficiently implemented in TURBOMOLE and was applied whenever possible [55, 57, 58]. Calculations with RSFs were performed with GAUSSIAN09 [59]. ZINDO/S computations were done with ORCA 2.7 [60]. The perturbative SCS-CIS(D) correction and the TD-PPP treatments were carried out with two different programs, which were developed in our group [61, 62].

22.3. EXAMPLES

22.3.1. Determining the Absolute Configuration of a Pharmaceutically Relevant Molecule

A recent study of the Waldmann group identified an indolin-2-on-3-spirothiazolidinone compound as a promising starting point for the development of antibiotics directed against *Mycobacterium tuberculosis*. A TD-B2PLYP simulated ECD spectrum helped to assign the absolute configuration of one of these compounds [63]. We will first discuss the result of this investigation because it presents a straightforward example in actual research, and additionally a first application of the TD-B2PLYP procedure.

In the calculations of the ECD spectra, a model compound with (*R*)-configuration, where two of the phenyl rings have been replaced by methyl groups, has been used. The main reason for this simplification was the reduction of the conformational freedom, making a conformational analysis unnecessary. At ambient temperatures, the contributions of the neglected phenyl rings is expected to be averaged out in the experiment but would lead to a huge number of different conformations that have to be computed (and averaged) in the theoretical treatment. The spectrum was computed with TD-B2PLYP [34, 35] in combination with the COSMO model [52] to account for bulk solvation effects in acetonitrile, based on a COSMO-PBE0/TZVP′ structure. Here, the TZVP′ basis set denotes a triple-ζ polarized basis set TZVP on all atoms except sulfur, where a (larger) set of (2d1f) polarization functions has been employed (TZVPP). Since a fully consistent COSMO/TD-DFT treatment of electronically excited states was technically not possible while preparing this chapter, we applied the COSMO model to the calculation of the ground state and solely used the COSMO modified orbitals and eigenvalues in a subsequent standard gas-phase TD-DFT treatment. A similar situation holds true for the perturbative correction needed for TD-B2PLYP. Different from the other examples in this work, a σ value of 0.35 eV for the width of the absorption band at a height of $1/e$ is used in this case, because of the broadness of the experimentally measured bands.

In order to check how sensitive the results are with respect to this choice, the PBE0 [31] hybrid functional additionally has been applied. The computed ECD spectra shown in Figure 22.4 result from 15 individual electronic transitions. The comparison with the experimental ECD spectrum (enantiomerically pure) shows good agreement for both computed spectra. The errors for band positions are below 0.3 eV with TD-B2PLYP for all four ECD bands, and the signs of all Cotton effects are computed correctly. Also, since the two different density functionals give qualitatively the same answer, the assignment of the absolute configuration is quite definite and revealed the (*R*)-configuration of the model compound.

22.3.2. Treatment of a Large Alleno-Acetylenic Macrocycle

In 2009, Alonso-Gómez et al. published the synthesis, the ECD spectrum, and a theoretical analysis (based on the ZINDO method) of an enantiomerically pure alleno-acetylenic

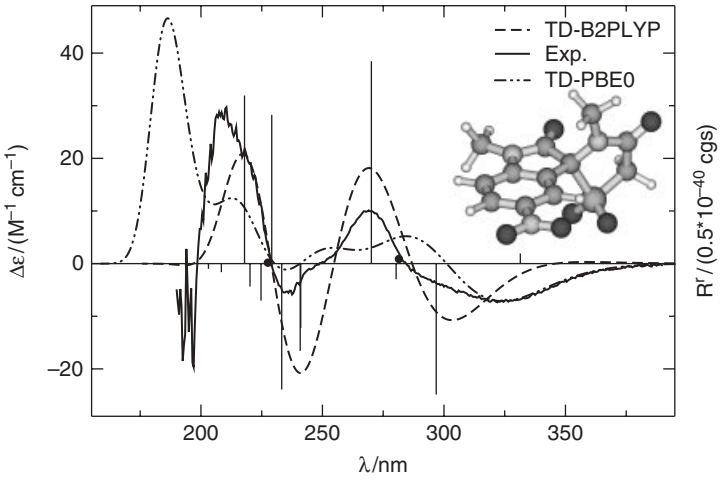

Figure 22.4. Comparison of theoretical and experimental ECD spectra of the investigated spirothiazolidinone model compound (COSMO-PBE0/TZVP′ structure shown above. Oxygen: dark gray, carbon: gray, nitrogen: light gray, hydrogen: white, sulfur: gray and larger). The theoretical spectra were obtained with TD-B2PLYP and TD-PBE0 using the def2-TZVPP [64] basis set. In each case, the first 15 transitions were computed. Bars indicate the positions and rotational strengths of electronic transitions calculated with TD-B2PLYP. Dots mark transitions with small rotational strengths. The experimental spectrum was recorded in acetonitrile. To account for solvent effects, the COSMO continuum model with a dielectric constant of $\epsilon = 35.9$ was applied.

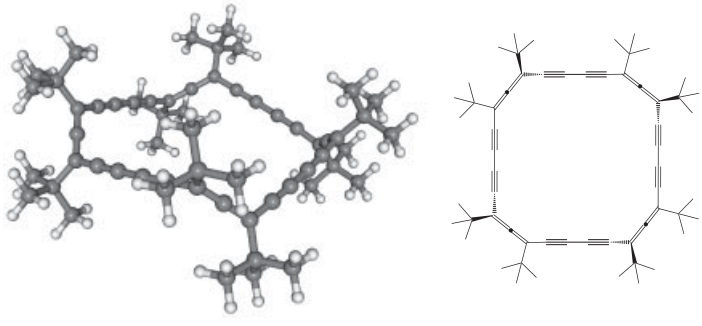

Figure 22.5. Structure of the investigated alleno-acetylenic macrocycle in (*P,P,P,P*)-configuration [65].

macrocycle, which shows extraordinarily high ECD intensities [65]. The optimized structure (taken from reference 65) is shown in Figure 22.5. The system is D_4 symmetric, contains 132 atoms, and has a (*P,P,P,P*)-configuration. The ECD spectrum was recorded in *n*-hexane and is shown in Figure 22.6. It exhibits two main absorption bands of opposite signs at around 300 and 250 nm. The first band shows three shoulders, which could be caused either by vibronic effects or by overlapping transitions. This system serves as a good example of how to treat large chromophores. In D_4 symmetry, only transitions into states of $^1A_2$ and ^1E are ECD active. If the programs can handle such non-abelian point groups, significant reduction of the computational effort can be gained. For example in D_4, only 12 transitions had to be calculated for B2GPPLYP, whereas in C_2 symmetry the number increased to 29, because many forbidden transitions had to be additionally calculated.

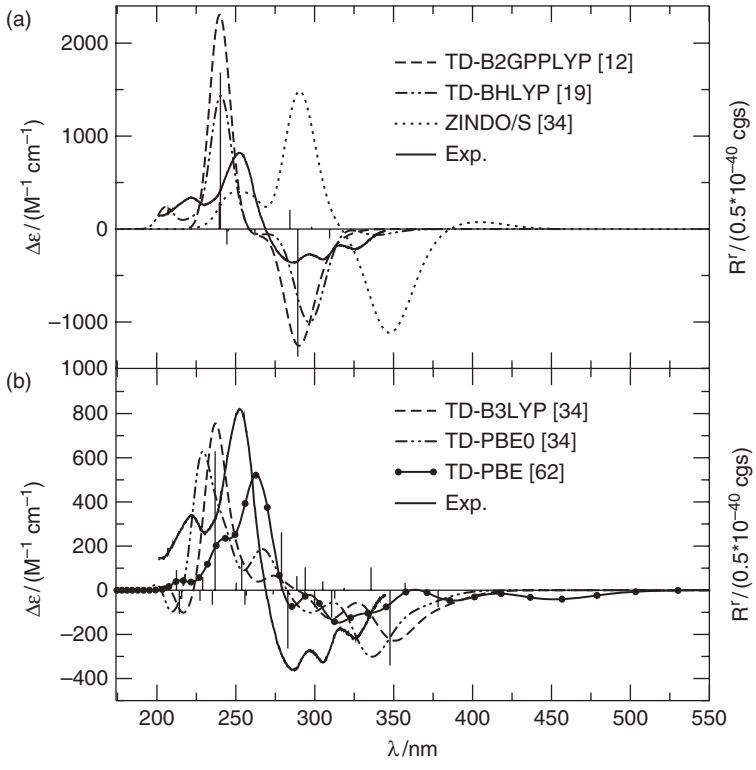

Figure 22.6. Electronic circular dichroism spectra of the investigated alleno-acetylenic macrocycle in (*P,P,P,P*)-configuration. The theoretical spectra were obtained with the TD-B2GPPLYP, TD-BHLYP, and ZINDO/S methods (a), as well as with the TD-B3LYP, TD-PBE0, and TD-PBE (b) approaches. A TZVPP′ basis was used for the chromophore, and an SV(P) set was used for the *tert*-butyl substituents. The numbers in brackets show how many transitions were necessary to calculate each spectrum. Positions and rotational strengths of the transitions are marked with vertical lines for TD-B2GPPLYP and TD-B3LYP. The experimental spectrum was recorded in *n*-hexane.

We start the discussion of the theoretical spectra with the ZINDO/S method (Figure 22.6). Computation of 32 transitions was necessary to cover the experimental energy range. The ZINDO/S method seems to be adequate for the determination of the absolute configuration of the molecule, as two large bands with the correct signs are obtained. However, qualitatively the spectrum is incorrect due to a small band of positive sign at around 425 nm. Moreover, the spectrum is red-shifted compared to experiment.

We continue the discussion with the results for various TD-DFT methods. Due to the system's size, different basis sets were used for different parts of the molecule. The important chromophore (i.e., the carbon backbone) was treated with the TZVPP′ basis. The *tert*-butyl substituents, which are not part of the chromophore, were treated with the smaller SV(P) basis. Alternatively, it would have also been possible to substitute the large *tert*-butyl moieties by methyl groups and to treat the entire molecule with the TZVPP′ basis. If no severe conformational problems suggest an exchange to smaller substituents, keeping the original ones is in general favored, since they can indirectly influence the chromophore (sterically or electronically). However, test calculations with the BHLYP functional showed that the resulting spectrum is almost identical to the one obtained with the first approach, on which we will concentrate in the following discussion.

Due to the relating low computational costs, it seems tempting to use a GGA functional for the calculations. However, functionals with no or low amounts of Fock exchange suffer from low-lying, artificial ("ghost") states. This is also observed in this case for the PBE functional (Figure 22.6b) because it was necessary to calculate 60 transitions for the spectrum. Most of the ghost states are found at large wavelengths.

Therefore, three bands of negative sign are found between 475 and 280 nm, which do not bear resemblance with the experiment. When going to the PBE0 and B3LYP hybrids, the numbers of ghost states are reduced. Thirty-two transitions were needed for covering the whole energetic range of the spectrum. Both spectra are very similar to each other. Two bands with correct signs are obtained. The first bands are red-shifted compared to experiment, while the second ones are blue-shifted. Furthermore, the first band, also exhibits shoulders, which could be evidence for the claim that several transitions overlap. However, when reducing the number of ghost states even more—that is, when performing BHLYP and B2GPPLYP calculations (19 and 12 transitions, respectively, needed)—the shoulders vanish. B2GPPLYP yields two bands of correct signs and of excellent position at 289 and 240 nm. Because only one transition is dominant for the band intensity, we deduce that the fine structure observed experimentally is caused by vibronic effects, which are not covered by our theoretical treatment. Theoretical methods for treating vibronic effects in ECD spectra have been developed, but are currently not applicable to systems of this size [66, 47]. The intensities of the B2GPPLYP spectrum are, like for most of the other methods, overestimated by a factor of roughly two. The relative intensities between the two bands are reproduced quite well, though.

Summarizing, we have seen that making use of symmetry is crucial, when treating large systems. The basis set size can be reduced by using less basis functions for moieties, which are not part of the chromophore. It is also necessary to compare different density functionals with each other in order to avoid interpretation of artifacts.

22.3.3. Exciton Coupling in a Merocyanine-Dimer Aggregate

An important feature of large molecules and supramolecular aggregates can be the occurrence of intra- or intermolecular exciton coupling. Exciton coupling is caused by the through space interaction between the electric transition dipole moments in different chromophores. This phenomenon is particularly well observed in ECD spectra, which are then characterized by two consecutive absorption bands of similar intensities but opposite signs. A supermolecular, theoretical treatment of this phenomenon is a nontrivial task, because the correct description of such long-range interactions is very dependent on the theoretical model chosen. In particular, it is a difficult case for TD-DFT methods, for which the exchange-correlation potentials decay too rapidly with intermolecular distance. To show the differences between various theoretical approaches, we discuss a large merocyanine dimer-aggregate, for which an experimentally measured ECD spectrum is available (the monomer is shown in Figure 22.7 with $R = OC_{12}H_{25}$) [67]. In 2008, we performed the first supermolecular quantum chemical calculation for an exciton coupled ECD spectrum based on this system [68]. Due to its large size, though, the long dodecoxy moieties were replaced by methoxy groups ($R = OCH_3$ in Figure 22.7). The theoretically treated system contains 150 atoms, which is computationally demanding for sophisticated quantum chemical approaches.

For the present context, we will review our theoretical investigation, i.e., CIS, SCS-CIS(D), TD-PPP, TD-PBE, and TD-PBE0 methods, and will extend it with the semiempirical ZINDO/S method and various other TD-DFT approaches, including a double-hybrid and range-separated functionals (RSFs).

The first important step in treating this aggregate is obtaining a good geometry with a method that adequately accounts for noncovalent London dispersion effects. This represents a crucial point in the entire procedure because it determines the alignment of the chromophores with respect to each other and eventually the coupling of the transition moments. Unfortunately, wavefunction-based methods are far out of reach for the

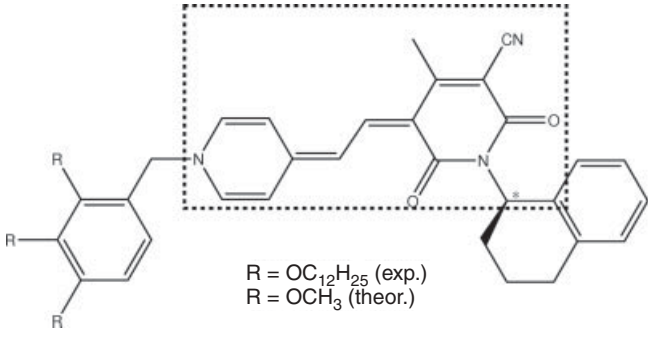

Figure 22.7. Structures of the merocyanine dye monomers used in experiment[67] and in the present theoretical investigation. The stereoisomer with (*R*)-configuration of the marked carbon atom is considered. The basic chromophore is highlighted by the dashed box.

optimization of such a large system. DFT, on the other hand, cannot correctly account for London dispersion effects. However, a good way to bypass this deficiency is dispersion corrected DFT. For the current system we chose the B97-D [43] GGA-functional in combination with a triple-ζ basis set with one set of polarization functions (TZVP). During this unconstrained geometry optimization, we scanned for different conformers. The energetically most stable conformer found is shown in Figure 22.8 and turned out to be the only relevant one. Because of the flatness of the corresponding potential energy surfaces and the many degrees of freedom, this structure is not necessarily the real most stable conformer in solution. However, as will be seen below, it can lead to a very good agreement with experimental ECD spectra and it is therefore likely that it reasonably represents the thermal average that is observed experimentally. The structure is also in accordance with related experimental observations [69].

For obtaining quantitatively correct excitation energies and transition moments, in general a basis set of at least triple-ζ quality is necessary. However, the large system size restricts the choice of basis set. The ECD spectra shown in Figure 22.9 were, thus, calculated with the double-ζ basis set SV(P). This choice had been validated by a check of the basis set completeness in TD-DFT calculations for one monomer. We found differences between SV(P) and an extended TZVPP set of only 0.08 eV for the relevant bright state and, thus, the SV(P) results can be considered as being semiquantitatively correct.

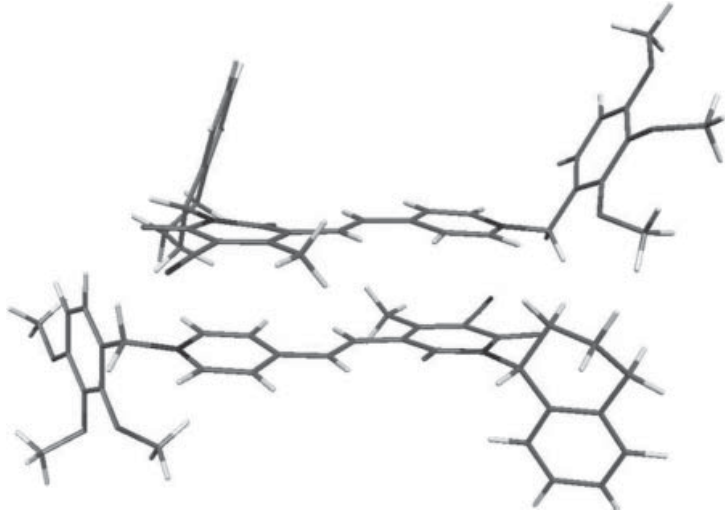

Figure 22.8. B97-D/TZVP optimized structure of the theoretically investigated merocyanine dimer [68].

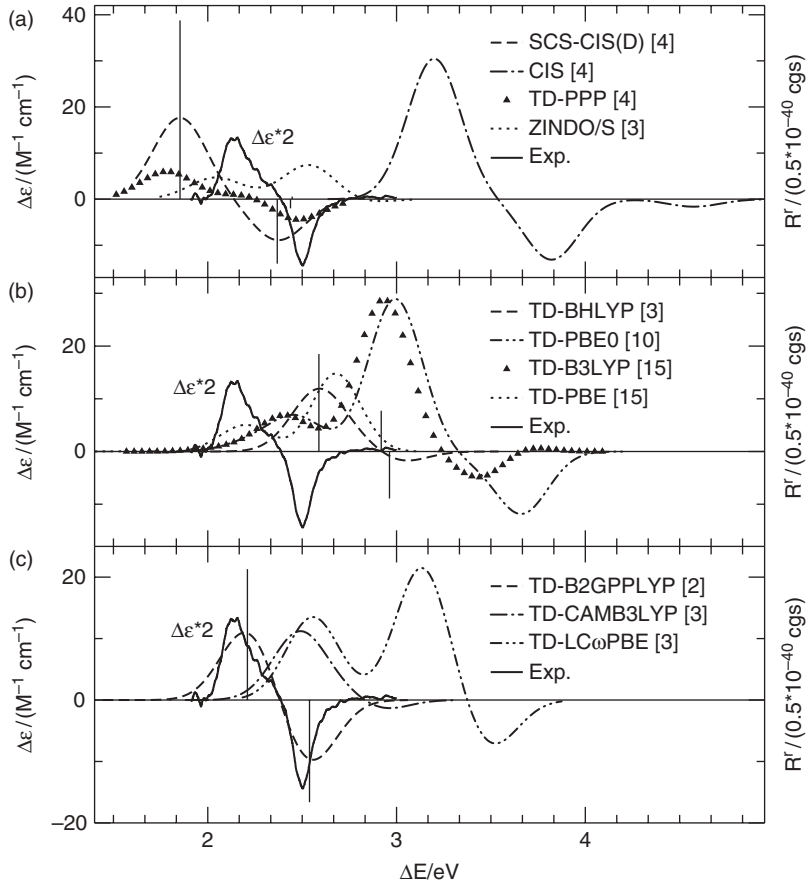

Figure 22.9. Electronic circular dichroism spectra of the investigated merocyanine dimer. The theoretical spectra were obtained with the SCS-CIS(D), CIS, TD-PPP, and ZINDO/S methods (a), as well as with the TD-PBE, TD-B3LYP, TD-PBE0, and TD-BHLYP (b), and the TD-CAM-B3LYP, TD-LCωPBE, and TD-B2GPPLYP approaches (c). An SV(P) basis was applied in the all-electron treatments. The numbers in brackets show how many transitions were necessary to calculate each spectrum. Positions and rotational strengths of the transitions are marked with vertical lines for SCS-CIS(D), TD-BHLYP and TD-B2GPPLYP. The experimental spectrum (scaled by a factor of two) was recorded in 1,4-dioxane [67]. The theoretical spectra are partially taken from reference 68.

Having obtained a good structure and having checked the basis set dependence, calculations were carried out for both the monomer and the dimer, with various methods. The experimental ECD spectrum of the dimer was recorded in 1,4-dioxane [67] and is shown in all three parts of Figure 22.9. It clearly features the typical characteristic of an exciton coupled ECD spectrum with two absorption bands of opposite signs at 2.14 and 2.50 eV and similar absolute intensities. Theoretical results for the first two excited states of the monomer and the two exciton coupled states of the dimer (that result from coupling of the lowest state of each monomer) are given in Table 22.2.

The ECD spectrum obtained by the CIS calculation is shown in Figure 22.9a. We calculated the first four electronic transitions, though it turned out that only the first two were necessary to yield the desired absorption bands. Most importantly, their signs are the

TABLE 22.2. Theoretical Results for the First Two Excited States of the Merocyanine Monomer and the Two Exciton Coupled States of the Dimer (Values Are Partially Taken from Reference 68.)

	Monomer		Dimer		
	ΔE^a	f^{rb}	ΔE^a	f^{rb}	R^{rc}
SCS-CIS(D)	2.16	1.290	1.85	0.001	77.6
	3.78	0.024	2.37	2.230	−28.0
TD-PPP	2.29	1.418	1.78[d]	0.001	27.3
	3.21	0.002	2.46[d]	2.525	−16.2
ZINDO/S	2.27	1.167	2.54[e]	1.521	24.3
	3.51	0.002	2.2.80[e]	0.057	−2.7
TD-BHLYP	2.83	1.531	2.59[f]	0.001	37.0
	3.74	0.018	2.96[f]	0.005	−17.8
TD-PBE0	2.78	1.418	2.99[g]	2.345	78.7
	3.08	0.001	3.64[g]	0.009	−42.3
TD-B3LYP	2.64	1.286	2.93[h]	2.218	80.7
	2.89	0.001	3.47[h]	0.006	−34.2
TD-PBE	2.11	0.002			
	2.28	8×10^{-5}		[i]	
TD-B2GPPLYP	2.51	1.604	2.21	0.0.001	42.6
	3.37	0.018	2.54	0.043	−33.3
TD-CAM-B3LYP	2.74	1.472	2.49[f]	0.001	36.2
	3.62	0.017	2.86[f]	0.005	−18.4
TD-LCωPBE	2.74	1.533	3.14[e]	2.604	56.5
	4.15	0.017	3.50[e]	0.031	−17.9

[a] In eV.
[b] Oscillator strength in the length form.
[c] Rotational strength in the length form in 10^{-40} cgs units.
[d] The exciton coupled states are here the first and fourth excited states.
[e] The exciton coupled states are here the second and third excited states.
[f] The exciton coupled states are here the first and third excited states.
[g] The exciton coupled states are here the fourth and ninth excited states.
[h] The exciton coupled states are here the fourth and eleventh excited states.
[i] No exciton coupled states found.

same as in the experiment, which supports the reliability of the optimized structure. The band positions are blue-shifted by more than 1 eV, which is the typical error for vertical CIS excitation energies for valence states. The band intensities are severely overestimated by factors of about five and two, respectively. The SCS-CIS(D) correction leads to a large red shift for the excitation energies of about 1.4 eV compared to CIS and to a theoretical spectrum, which is in very good agreement with experiment (errors of about 0.3 and 0.1 eV). The first two electronic transitions in the SCS-CIS(D) spectrum are closer to each other than in the CIS one. Nevertheless, the intensities are still overestimated (e.g., by a factor of two in the case of the first band). The spectrum obtained by the semiempirical TD-PPP treatment is also shown in the same figure. It is also in good agreement with experiment with excitation energies of 1.78 and 2.50 eV, respectively. The band intensities are lower than observed experimentally. In contrast to the CIS and SCS-CIS(D) methods, where the two bands are formed by two transitions, two additional excited states can be found in the energy range of the TD-PPP absorption bands at 2.11

and 2.23 eV. However, due to their small rotational strengths (-3.0 and 7.1×10^{-40} cgs), they do not influence appearance of the spectrum. The semiempirical ZINDO/S does not correctly reproduce the shape of the spectrum. Exciton coupling is observed, but only for the second and third excited states. The third transition has, moreover, only a very small intensity. Furthermore, an artificial band with positive sign is observed, which is energetically lower then the exciton coupled states.

Figure 22.9b contains the ECD spectra obtained with common TD-DFT methods. This example clearly shows a breakdown of current density functionals when trying to describe long-range exciton coupling. Instead of the desired two transitions leading to an exciton coupled ECD spectrum, a lot of ghost states are calculated. The TD-PBE spectrum was calculated with 15 transitions, and it still does not feature the typical exciton couplet. Results for the monomer already indicate that PBE is inadequate for the description of this dye. The first two transitions lie with 2.11 and 2.28 eV too close to each other when compared to SCS-CIS(D) with 2.16 and 3.78 eV (Table 22.2). Moreover, both transitions feature very low oscillator strengths. Admixture of Fock exchange as in TD-B3LYP and TD-PBE0 improves the description. The excitation energies of the monomer increase and the large oscillator strengths of the first transition indicate that the right state is lowest in energy. Nevertheless, also B3LYP and PBE0 do not provide correct ECD spectra (Figure 22.9b). They are qualitatively similar to the CIS spectrum in the high-energy region with the exciton coupled states and also show severe overestimations of the band intensities by factors of five and two. Moreover, the exciton coupled states are not the lowest-lying ones. Many artificial states influence the shape of the spectrum in the region where the experimental ECD signals are observed. In addition to the intense, artificial absorption bands around 2.4 eV, several ghost states lie between the two exciton coupled ones. Mixing in 50% Fock exchange as in TD-BHLYP reduces the number of ghost states dramatically. Only three states were necessary with BHLYP. Exciton coupling is observed, but the second band is much too low in intensity. Range-separated functionals are expected to correct the erroneous decay of the exchange potential. Although less artificial states are observed, no overall improvement can be seen (Figure 22.9c). The LCωPBE functional yields a spectrum similar to B3LYP and PBE0 and CAM-B3LYP performs similarly to BHLYP.

The double-hybrid functional B2GPPLYP is the only density functional that correctly predicts the spectrum. The excitation energies are with 2.21 and 2.54 eV in very good agreement with experiment. Only two excited states were computed, and the band intensities are even lower than for SCS-CIS(D) and, thus, closer to experiment.

In conclusion, we have seen that treating exciton coupling adequately is very difficult. Wavefunction-based methods like SCS-CIS(D) give accurate results, but are time-consuming. Semiempirical methods show an ambiguous behavior. TD-PPP gave very good results for this system, ZINDO/S did not. TD-DFT methods—in particular, GGAs—are inadequate for treating long-range exciton coupling. Global and range-separated hybrid functionals are also not satisfying. The double-hybrid B2GPPLYP is the only functional in this study that yields excellent agreement with experiment.

22.3.4. Approaching a Supramolecular Organic Capsule with TD-DFT

In general, only successful TD-DFT applications are discussed in the literature. Herein, we like to discuss instead a very problematic case for TD-DFT. The system under scrutiny is the calix[4]resorcinearene dimer by Rebek and co-workers [70] encapsulating

a chiral alcohol [(*R*)-2-tetradecanol] [71]. This supramolecular aggregate offers, apart from the encapsulated chromophore of the alcohol, eight benzene rings and eight fused imide–pyrazine moieties, providing potentially complicated exciton coupled and charge-transfer absorption bands. This system presents two major hurdles. One is of course the pure size of the system with 269 atoms. The structure itself can be obtained from DFT-D calculations with a GGA-type functional within reasonable time and effort [72]. The DFT-D methodology for the treatment of London dispersion is crucial for this complex. The common approach to use the B3LYP/6-31G* level of theory is overrepulsive and does not predict encapsulation of the guest molecule [73]. We employed B97-D/TZVP optimized structures (Figure 22.10). Unfortunately, ECD calculations with TD-DFT and GGA functionals suffer from the self-interaction error and too-fast-decaying xc-potentials as mentioned in previous sections. This second hurdle can be partially solved by using global hybrids or RSFs, which, however, constitute a major effort in computing time with a reasonable triple-ζ basis set, since the scaling is linear with respect to the number of states [roots in the linear equations; see Eq. (22.7)] and each state involves repeated calculations of expensive exchange integrals. We therefore have to restrict ourselves to the double-ζ basis set SV(P) and consider only eight excited states for this system.

Figure 22.11a shows rotational strengths (R^r) for the supramolecular complex calculated with functionals based on Perdew's PBE potential with different amounts of Fock exchange and from TD-HF.

The TD-PBE method exhibits very small, barely visible, R^r values. These very small values indicate that all these states are ghost states. Also the calculation of additional states (up to a total of 20) combined with a larger basis set (TZVP) did not show any improvement in the intensities. This clear failure of the xc-kernel shows that it is dangerous to rely on GGA functionals for TD-DFT even if they might constitute the only computationally feasible functional type. The TD-PBE result represents one extreme, the other extreme is TD-HF. TD-HF, as well as CIS, suffers from a missing description of electron correlation.

As mentioned in the theory section, the errors of excitation energies for TD-HF/CIS are usually too high (usually overestimation and errors above 1 eV) and often wrong ordering for states of different electronic character can be observed. The strong advantage over TD-DFT, on the other hand, is the correct asymptotic behavior of the potential. If this becomes crucial, TD-HF might become an option. In our case, TD-HF is used as an upper bound to the exact Fock exchange included in global and RSFs. In that sense, TD-PBE can be seen as the corresponding 'lower bound' with no Fock exchange. The intermediate methods with a variable amount of Fock exchange show the expected behavior. The

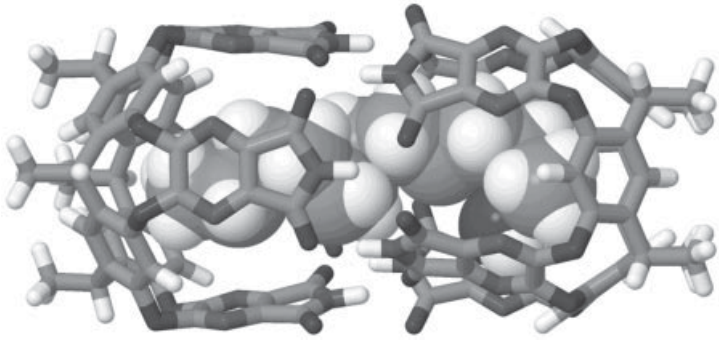

Figure 22.10. B97-D/TZVP optimized structure of the calix[4]resorcinarene dimer with a (*R*)-2-tetradecanol guest.

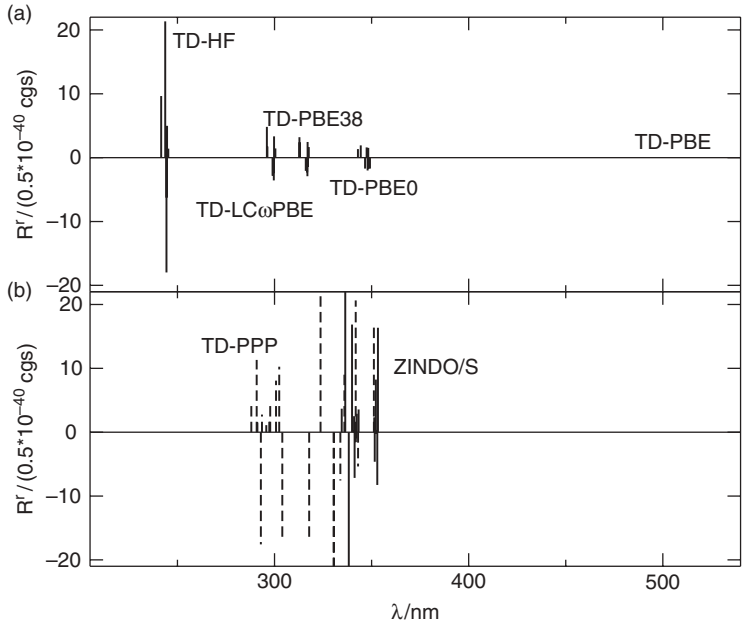

Figure 22.11. Positions and rotational strengths of the calculated transitions in the calix[4]resorcinearene aggregate from TD-DFT (a) and semiempirical schemes (b). These are marked by vertical lines (dashed lines for TD-PPP). Eight transitions were calculated with TD-DFT in the SV(P) basis sets, and 20 transitions were calculated with the semiempirical methods.

increase of Fock exchange from TD-PBE0 (25%) or TD-PBE38 (37.5%) leads to an increase of the rotational strengths and to a blue shift of the excitation energies. The long-range corrected functional LCωPBE has the advantage of the correct asymptotic behavior of the exchange potential (100% Fock exchange in long-range region) and performs similar to the global TD-PBE38 hybrid.

We are not able to quantify the errors for the excitation energies. The experimental ECD band occurs at 344 nm, which is in between the PBE0 and PBE38 result. It is common to shift the simulated ECD spectrum if the method inherits a systematical error. If we estimate the peaks of the simulated bands (PBE0: 345 nm, PBE38: 315 nm, LCωPBE: 289 nm), we get shifts of PBE0 = 0.0 eV, PBE38 = 0.3 eV, and LCωPBE = 0.7 eV that would have to be applied. TD-HF is in this respect far off (about 1.5 eV).

There is little chance of tackling this large system with wavefunction-based methods like CC2, CIS(D), or its SCS variants due to their computational demands. We are basically left with semiempirical methods. Figure 22.11b shows rotational strength from TD-PPP (dashed lines) and from ZINDO/S (bold lines) calculations. TD-PPP has been successfully applied to this systems with an averaged spectrum based on semiempirical molecular dynamics simulations [71]. As mentioned, the experiment exhibits one (weak) ECD band at 344 nm, for which a reasonable, qualitative agreement could be achieved. For 20 calculated states we see that strong rotational strengths from both semiempirical approaches and the low-lying excitations occur roughly in the correct energy range. In contrast to TD-DFT, we can easily obtain an (at least qualitatively correct) simulated ECD spectrum. However, as always when working with semiempirical methods, careful inspection of the results is mandatory.

22.3.5. How to Treat Conformationally Flexible Systems

In the previous examples, only one (the most stable) conformer of each system was relevant. Treating such cases is straightforward. A qualitatively good structure

has to be obtained and the spectra can then be calculated with different theoretical methods and compared to experiment. Usually, though, systems of chemical interest are conformationally flexible. Each conformer can yield a completely different spectrum, and therefore these spectra have to be combined to a total spectrum if a meaningful comparison to experiment is to be made. Herein, we discuss the *(S)*-2-(3-fluoro-(*p*-tolyl)propyl)naphthalene molecule (Figure 22.12) as an example for a conformationally flexible organic molecule. It is a challenging system, because it contains two aromatic chromophores. Thus, stacked (due to London dispersion effects) and nonstacked conformers are possible, whose spectra can exhibit locally excited, CT, and exciton coupled states. In this example, we show how to obtain a total ECD spectrum based on the accurate SCS-CC2 method.

The applied procedure is depicted schematically in Figure 22.13. It can be generalized also to other systems and other methods. After having created a reasonable start structure, a very fast screening for different conformers can be easily done with a standard force field, like, for example, AMBER [74]. In the present case, this yielded 44 different conformers. These were then further investigated. Due to the size of the system and the huge number of conformers, we decided to use a GGA-functional. Because stacked conformers were found, it was crucial, though, to make use of the empirical dispersion correction (DFT-D3) [40]. This, in combination with the BLYP functional, had previously been proven to be the best GGA methods for the correct energetic ordering of such conformers [40]. At the beginning of the optimization procedure, it is useful to employ a small basis set, like SV(P). This preoptimization reduced the number of conformers to 22. Many of the force-field conformers resulted to belong to the same local minimum on the BLYP-D3/SV(P) hypersurface. The remaining 22 structures were then further optimized with the TZVP basis. To decide which conformers are important for the total ECD spectrum, their relative energies have to be determined. Therefore, we chose one of the most accurate DFT methods, which is the B2GPPLYP functional in combination with the DFT-D3 correction [75]. Usually, relative energies converge slower with basis set size than geometries. Therefore, a larger basis set was used, that is, def2-TZVPP.

Having obtained good structures and relative energies for the 22 different conformers, one has to decide which conformers are necessary for the calculation of the total ECD spectrum. At room temperature, relative energies of up to 1.5 kcal/mol should be considered. In the present case, 10 of the 22 conformers are within this 1.5 kcal/mol range. Their relative energies and thermal populations are given in Table 22.3. The structures are shown in Figure 22.14.

The relative energy between the two most stable structures is 0.16 kcal/mol. The other structures lie at least 0.90 kcal/mol higher in energy than the most stable one. Eight structures are characterized by stacked alignments of the aromatic moieties. The two structures **6** and **10** are the only nonstacked ones that lie within the considered 1.5 kcal/mol range.

For each relevant conformer, a single ECD spectrum had to be calculated. This was done at the SCS-CC2/TZVPP′ level of theory including 10 transitions (see Figure 22.14). The spectra are a good example that the structure has a decisive influence on their shape

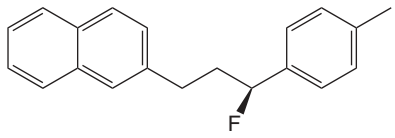

Figure 22.12. Structure of (*S*)-2-(3-fluoro-(*p*-tolyl)propyl)napthalene used as a flexible model compound.

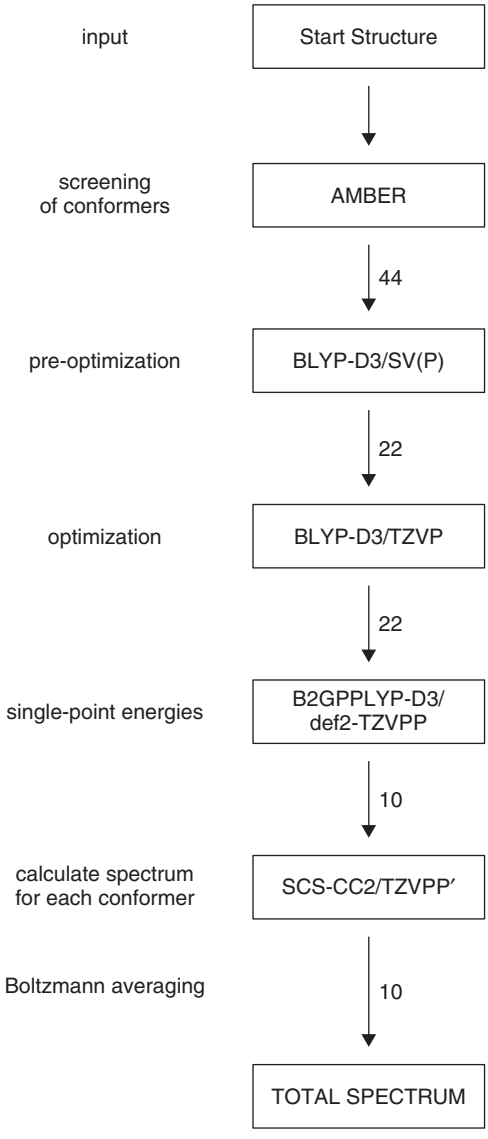

Figure 22.13. A schematic representation of how a total ECD spectrum can be obtained for the present model compound. The numbers indicate how many conformers were considered in each step.

and appearance. All spectra show transitions in the region of about 4.5 eV. The intensities and signs of the band, though, vary significantly. The nature of these bands is in all cases a local valence transition within the naphthyl moiety. Additional bands are predicted in a range of 5.5 to about 6.5 eV. Again, their intensities and signs differ significantly. The stacked conformers exhibit CT and valence transitions in these regions, whereas the nonstacked ones show local valence transitions, particularly on the tolyl unit. In the case of conformer **10**, a band at about 7 eV is observed. Although this conformer is energetically high-lying, it can still have an important influence on the total spectrum, because the other conformers do not exhibit transitions in this region. A very important observation is made for the two most stable conformers. Their spectra exhibit bands with similar positions but usually of opposite signs. This has a dramatic influence on the total spectrum, because these bands may almost completely cancel each other out. This is, in

TABLE 22.3. Relative Energies and Boltzmann Weights for 10 Conformers of (*S*)-2-(3-Fluoro-(*p*-tolyl)propyl)naphthalene, Based on B2GPPLYP-D3 and B3LYP Calculations

	B2GPPLYP-D3		B3LYP	
No.	ΔE^a	Weight[b]	ΔE^a	Weight[b]
1	0.00	35.7	4.43	—
2	0.16	27.3	4.53	—
3	0.90	7.8	5.09	—
4	1.09	5.7	5.44	—
5	1.10	5.6	4.62	—
6	1.29	4.0	1.23	11.1
7	1.30	4.0	4.91	—
8	1.37	3.5	4.82	—
9	1.40	3.4	5.12	—
10	1.47	3.0	0.00	88.9

[a]Energy difference in kcal/mol with respect to the most stable conformer (**1** for B2GPPLYP-D3/def2-TZVPP and **10** for B3LYP/TZVPP′).
[b]Boltzmann weights in % at 298.15 K. Only conformers within an relative energy range of 1.5 kcal/mol are considered.

fact, a "worst case" scenario in an investigation of a conformationally flexible system and, thus, our analysis should be considered as a tough test for the theoretical approaches applied.

To obtain the final spectrum, each individual spectrum has to be scaled by a certain factor, which reflects the relative population N at a certain temperature. For the ith conformer, the Boltzmann population is given by

$$N_i = \frac{\exp\left(\frac{-\Delta E_i}{R_{\text{gas}}T}\right)}{\sum_i^{all} \exp\left(\frac{-\Delta E_i}{R_{\text{gas}}T}\right)}, \tag{22.9}$$

where ΔE_i is the energy difference of the ith conformer with respect to the most stable one, R_{gas} is the universal gas constant, and T is the temperature (here $T = 298.15$ K was chosen). For each individual conformer, the rotational strengths are scaled by these

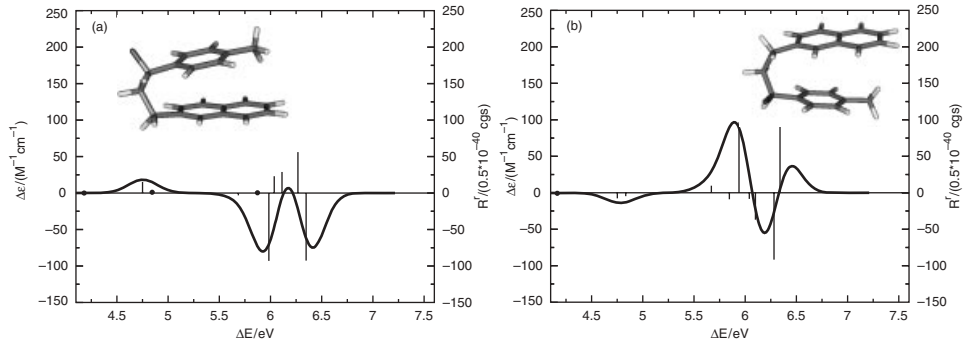

Figure 22.14. Structures and SCS-CC2/TZVPP′ ECD spectra for the 10 most stable conformers of (*S*)-2-(3-fluoro-(*p*-tolyl)propyl)naphthalene. For each conformer the 10 lowest electronic transitions were calculated.

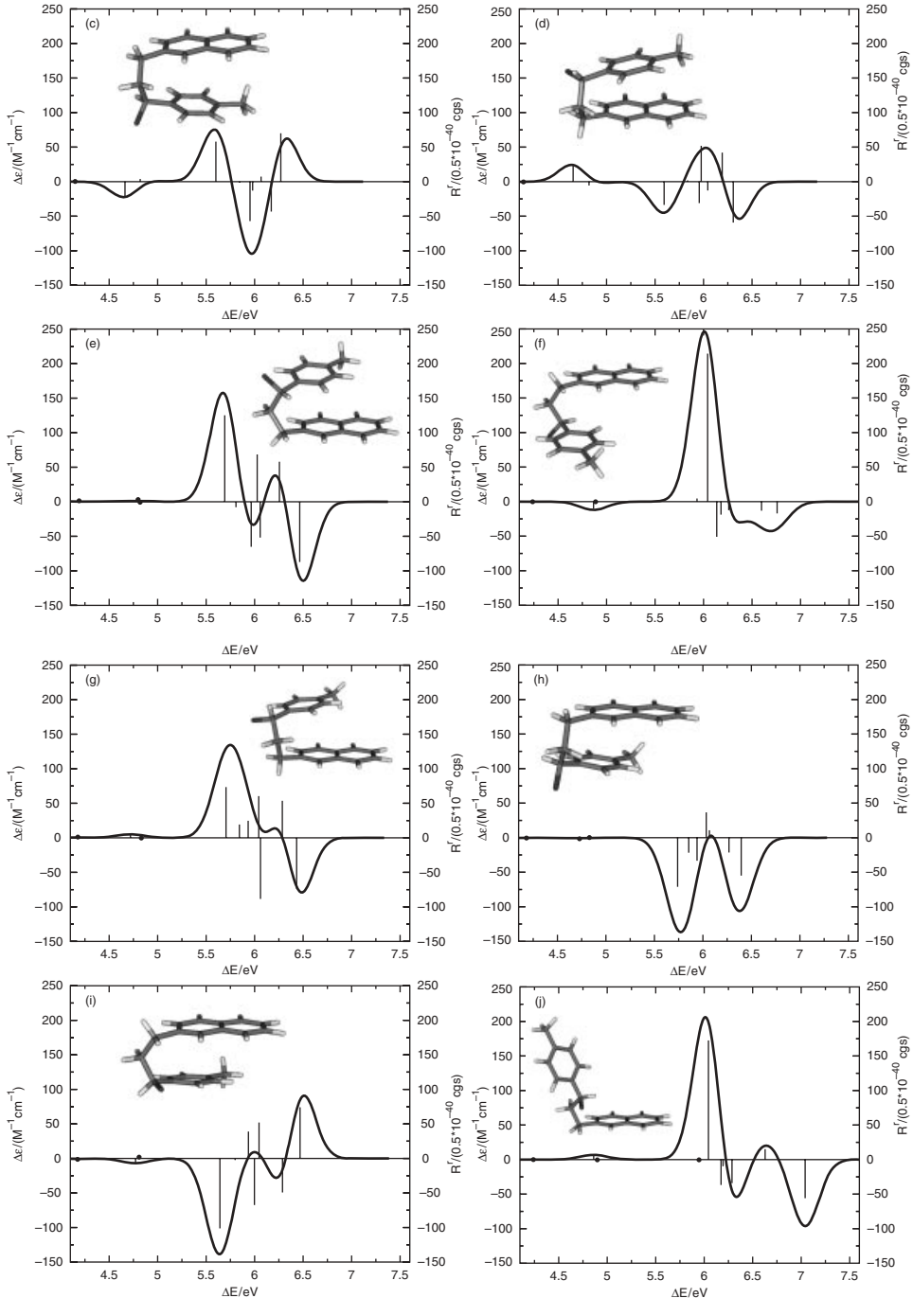

Figure 22.14. (*Continued*)

weights and a final spectrum of all combined transition energies and rotational strengths is simulated. The resulting SCS-CC2 spectrum is shown in Figure 22.15a. The spectrum shows three major bands. The first one at around 4.6 eV has a positive sign and is caused by the local valence transitions within the naphthyl moiety, as explained for the individual conformers. The second band of positive signs and the third band of negative signs have shoulders, indicating several overlapping transitions. Mainly, these are caused by the mixed local and CT transitions of the conformers. The shoulder at around 7.2 eV is caused by the valence transition of conformer **10**, thus showing the importance of also including conformers with a low Boltzmann weight (3%).

For performing the Boltzmann averaging, it is crucial that the conformational energies are accurate. To demonstrate this, we repeated the investigation using energies from the popular B3LYP functional without any dispersion corrections. The relative energies are shown in Table 22.3. The most stable conformer at the B3LYP level is conformer **10**, which is nonstacked. The only conformer within a 1.5-kcal/mol range is the second nonstacked conformer **6**. All relative energies between the stacked and the most stable conformers are 4.4 kcal/mol or higher. The reason is that B3LYP does not correctly describe London dispersion effects. Thus, these conformers do not play any role in the Boltzmann averaging. Consequently, only two conformers are necessary to compute the total spectrum, which is shown in Figure 22.15b and is completely different from the one based on B2GPPLYP-D3 relative energies.

Finally, it is possible to use the total spectrum in Figure 22.15a as reference for other methods. SCS-CC2 is assumed to describe local and CT transitions quite accurately. We consider only states up to 6 eV (the first two bands) and compare the SCS-CC2 spectrum to various TD-DFT methods. For each method, the single spectra were averaged using the same B2GPPLYP-D3 Boltzmann weights. Figure 22.16 shows these spectra obtained with the BLYP, B3LYP, CAM-B3LYP, BHLYP, and B2GPPLYP functionals and the TZVPP′ basis. Spectra were also calculated with PBE, and PBE0, but they were very similar to BLYP and B3LYP, respectively, and, therefore, not shown. Again, it is observed that small amounts of Fock exchange lead to a higher number of excited states to be calculated (e.g., 25 for each conformer for BLYP). Furthermore, these excited states are more red-shifted than for other functionals. Particularly, for BLYP, many artificial bands are observed between 3.5 and 5 eV. The model compound is a difficult case for TD-DFT methods in general, because also CT excitations play an important role. This is why also the BHLYP and B2GPPLYP functionals do not perform very well, although the excitation energies are better than for BLYP and B3LYP and less artificial bands are observed. The intensities of BHLYP and B2GPPLYP, though, are very low, and higher in the case of B3LYP. CAM-B3LYP performs similar to the BHLYP functional.

In summary, it was shown how an ECD spectrum can be calculated for conformationally flexible systems. The important steps are the screening for possible conformers, the determination of their geometries, and accurate relative energies. These treatments should be carried out with methods that can correctly describe London dispersion effects. A straightforward Boltzmann averaging then gives weights for the individual conformer spectra and finally leads to a total spectrum that can be compared with experiment. As a rule of thumb, conformers that are in an energy range of 1.5 kcal/mol with respect to the most stable one should be considered when the averaging is done for room temperature. Note that this procedure does not account for quantum mechanical averaging effects that may result from large amplitude nuclear motions. These could be modeled by performing molecular dynamics simulations and an averaging over the resulting trajectories.

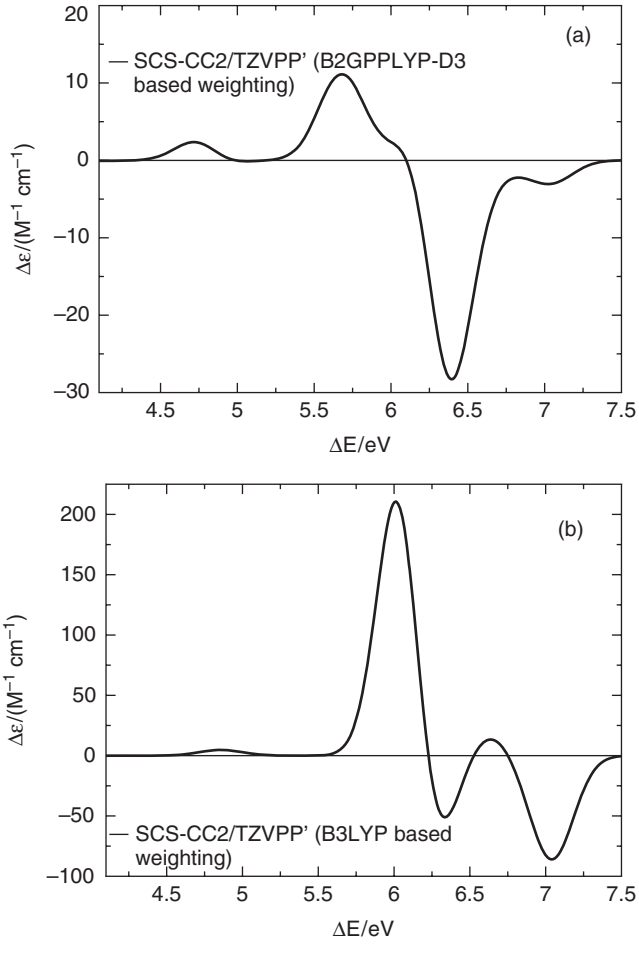

Figure 22.15. Computed SCS-CC2/TZVPP′ ECD spectra of *(S)*-2-(3-fluoro-(*p*-tolyl)propyl)napthalene based on a Boltzmann averaging with B2GPPLYP-D3 (a) and B3LYP (b) relative energies.

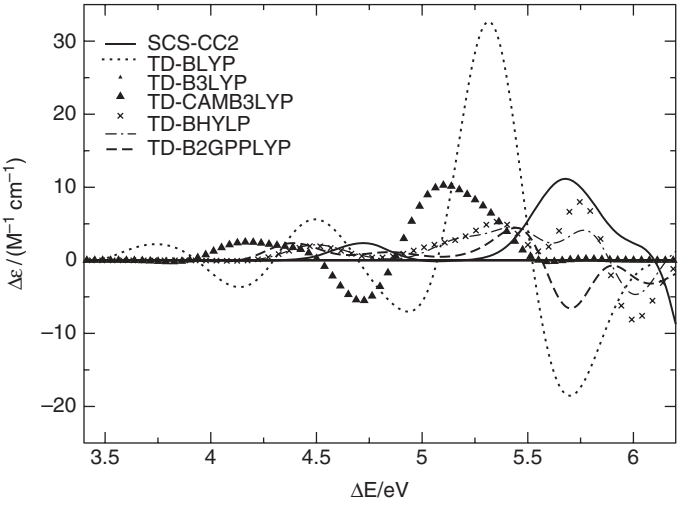

Figure 22.16. Computed ECD spectra of *(S)*-2-(3-fluoro-(*p*-tolyl)propyl)naphthalene obtained with the TD-BLYP, TD-B3LYP, TD-BHLYP, and TD-B2GPPLYP methods. An SCS-CC2 spectrum is shown as reference. The TZVPP′ basis was used in all cases.

22.3.6. Theoretical Treatment of Experimentally Investigated Cyclophane Derivatives

In this example, we make use of the work of Mori et al.[76], who investigated conformationally flexible, donor–acceptor substituted *para*-cyclophanes with charge-transfer and exciton-coupled transitions. Three structures and their respective conformational analyses are taken from their work. The authors' approach differs slightly from the one suggested in Section 22.3.5. BLYP-D/TZV2P optimized conformers underwent SCS-MP2/TZVPP single-point calculations that were used to calculate each conformer's Boltzmann weights. The SCS-MP2 level of theory is competitive to B2GPPLYP-D3 for these systems. For each conformer the eight lowest states were taken into account.

We picked a charge-transfer-dominated cyclophane (**1**), an exciton-coupling-dominated cyclophane (**2**), and a "mixed" cyclophane (**3**) that shows both charge-transfer transitions and exciton coupling (see Figure 22.17). We tested a number of long-range corrected functionals (LCωPBE, ωB97X, CAM-B3LYP) for their performance and applied the double-hybrid B2GPPYLP and the global hybrid BHLYP. For a detailed discussion of ECD in cyclophanes see reference 77.

Figure 22.18 depicts the results for the charge-transfer-dominated cyclophane **1**. All functionals predict the correct sign for each band and therefore would lead to a correct assignment of the absolute configuration. However, the excitation energies are quite different for the methods. A constant shift of the spectra could resolve much of this often observed, systematic deficiency. Particularly the first state, a pure charge-transfer one, is very sensitive to the method employed. Among the selection, TD-B2GPPLYP gives the best excitation energies, while TD-LCωPBE yields the worst. For the excitation energies TD-CAM-B3LYP improves only slightly over TD-BHLYP, and TD-ωB97X is similar to TD-LCωPBE. Additionally, the simulation of the charge-transfer-dominated bands, like the very first, suffer from too high intensities.

The exciton-coupled spectrum of cyclophane **2** is shown in Figure 22.19. The experimental spectrum features for the first two bands a shoulder, indicating overlapping transitions or vibronic effects. Regarding the total shape of the spectrum, the RSFs perform better than TD-BHLYP or TD-B2GPPLYP. However, the band positions of TD-B2GPPLYP are remarkably accurate, ignoring the fact that the functional is unable to recover the experimentally observed shoulders, but instead forms a separate band. The RSFs show these shoulders. Notice that TD-CAM-B3LYP yields the best excitation energies and intensities. Interestingly, the quality of the intensities computed by TD-LCωPBE and TD-ωB97X decrease with higher excitations.

The cyclophane **3** (ECD spectrum in Figure 22.20) constitutes the most difficult case. This is seen already for the first two bands ($\Delta\epsilon$ increased by a factor of 10). Only one of

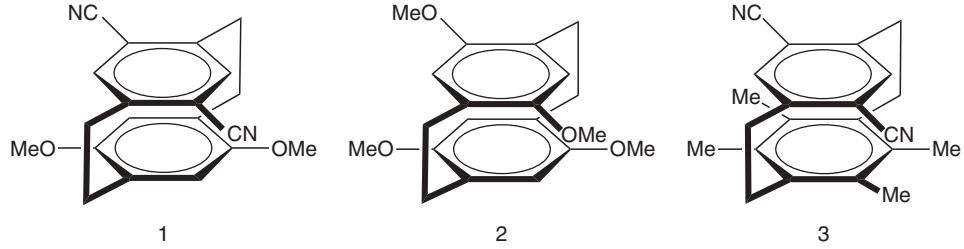

Figure 22.17. Chiral *para*-cyclophanes investigated in this study.

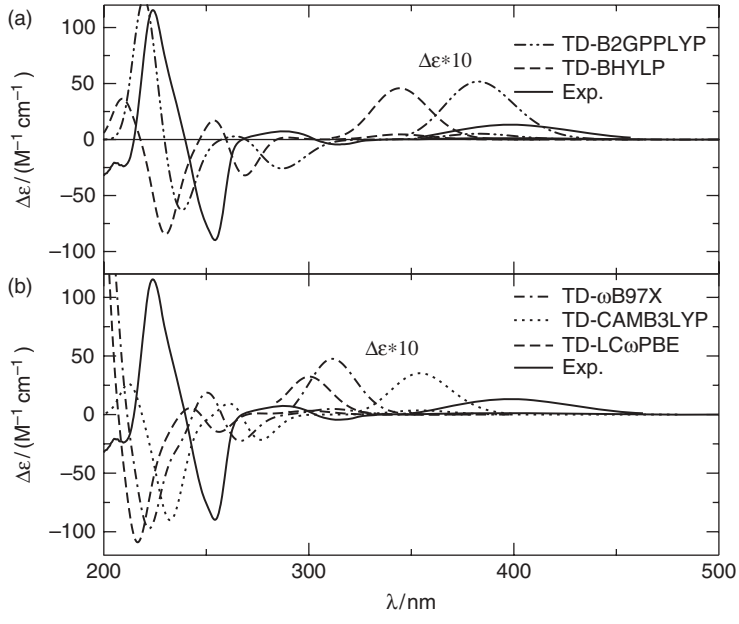

Figure 22.18. Electronic circular dichroism spectra of the investigated charge-transfer cyclophane **1**. The theoretical spectra were obtained with TD-BHLYP and TD-B2GPPYLP (a), as well as with TD-LCωPBE, TD-ωB97X and TD-CAM-B3LYP (b). In each case, the first eight transitions were computed. The def2-TZVPP basis set has been applied. For a better visualization, the first band of each spectrum was scaled by a factor of 10. The experimental spectrum is taken from reference 76.

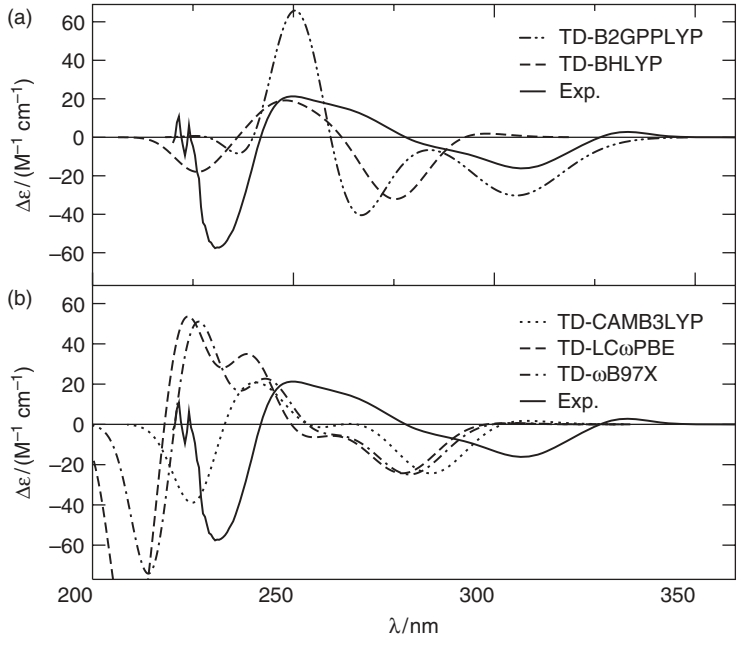

Figure 22.19. Electronic circular dichroism spectra of the investigated exciton coupled cyclophane **2**. The theoretical spectra were obtained with TD-BHLYP and TD-B2GPPYLP (a), as well as with TD-LCωPBE, TD-ωB97X and TD-CAM-B3LYP (b). In each case, the first eight transitions were computed. The def2-TZVPP basis set has been applied. The experimental spectrum is taken from reference 76.

the bands is reproduced and its intensity is largely overestimated by all functionals. TD-B2GPPLYP is unable to reproduce the last band. TD-BHLYP and RSFs improve slightly and reproduce at least the general shape. Note that the band at 260 nm has a very weak shoulder below 300 nm. All functionals produce a band near this region, indicating that close-lying transitions partly cancel out in the experiment but not in the calculation. Taking this into account, all functionals can be used to assign the absolute configuration with TD-B2GPPLYP not being able to reproduce the high-lying transitions (the last band)

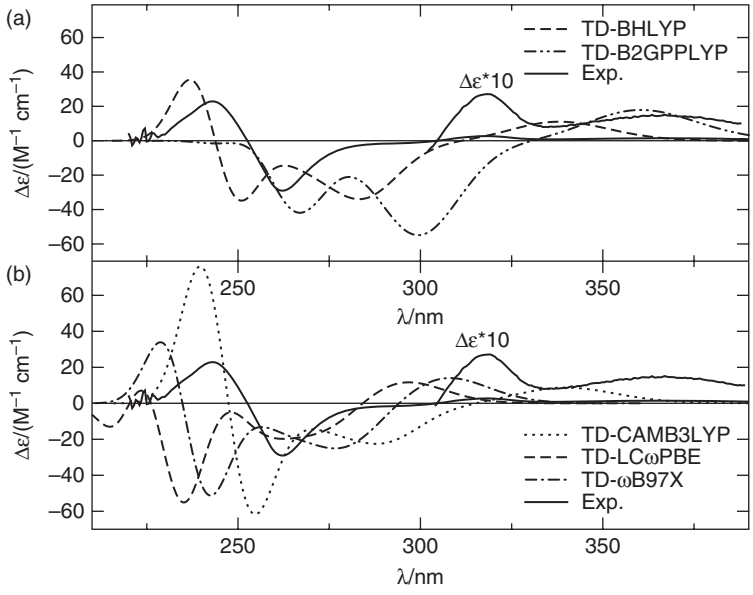

Figure 22.20. Electronic circular dichroism spectra of the investigated cyclophane **3**. The theoretical spectra were obtained with TD-BHLYP and TD-B2GPPYLP (a), as well as with TD-LCωPBE, TD-ωB97X, and TD-CAM-B3LYP (b). In each case, the first eight transitions were computed. The def2-TZVPP basis set has been applied. For a better visualization, the first two bands of the experimental spectrum was scaled by a factor of 10. The experimental spectrum is taken from reference 76.

correctly. Note that in this region the perturbative correction becomes already problematic [7]. The RSFs yield the best relative intensities with TD-CAM-B3LYP showing the best excitation energies among them.

For the investigated cyclophanes, the assignment of the absolute configuration is possible with all applied functionals. Among the tested methods, TD-B2GPPYLP and TD-CAM-B3LYP seem to perform best. However, the differences are small and often only a systematic error in the excitation energies is found.

22.4. SUMMARY

Electronic circular dichroism (ECD) spectroscopy is a strong experimental tool for the analysis of large organic and supramolecular compounds. A corresponding theoretical treatment, however, is still a challenging task. We have tried to give useful advice for practical calculations and mentioned important aspects that should, in our opinion, be considered in any calculation of ECD spectra. This has been underlined and demonstrated with six examples, covering exciton coupling, charge-transfer excitations and noncovalent interactions in aggregates, inclusion compounds, and conformationally flexible molecules. Particularly, an accurate treatment of conformationally flexible systems is nontrivial and has to be carried out carefully. London dispersion corrections are essential in DFT for an accurate description of ground-state properties that indirectly influence the shape of an ECD spectrum.

Our examples showed that correlated *ab initio* methods are, in general, recommended for the simulation of ECD spectra, but are rarely applicable for technical reasons. The "cheaper" semiempirical methods are not equally well applicable, and their performance strongly depends on the case under study. TD-DFT is the economically best approach, but the functionals used have to be chosen carefully and cannot be applied in a "black box" fashion. GGA functionals turned out to be not reliable, not even for qualitative considerations. Global hybrid functionals should include 40% to 50% of Fock exchange,

so that (for example) the B3LYP and PBE0 standard functionals cannot be recommended in general. Range-separated hybrid functionals were applied for the first time in calculations of ECD spectra. They are, in general, better than global hybrids and yield good excitation energies and rotational strengths. In the worst cases, though, they are comparable to global hybrids. For not too high-lying energy states, double-hybrid functionals are usually the best methods and can be recommended in general for ECD, which confirms previous conclusions [7].

ACKNOWLEDGMENTS

This work was carried out in the framework of the SFB 858, DFG "Synergetische Effekte in der Chemie—Von der Additivität zur Kooperativität." L. G. was supported with a scholarship by the "Fonds der Chemischen Industrie." H. K. was supported by a scholarship by the IRTG 1444, DFG "Generation of Supramolecular Functional Cavities—Container Molecules, Macrocycles and Related Compounds." The authors want to thank C. Mück-Lichtenfeld for his technical assistance.

REFERENCES

1. C. Diedrich, S. Grimme, *J. Phys. Chem. A* **2003**, *107*, 2524–2539.
2. T. D. Crawford, *Theor. Chem. Acc*. **2006**, *115*, 227–245.
3. T. D. Crawford, M. C. Tam, M. L. Abrams, *J. Phys. Chem. A* **2007**, *111*, 12057–12068.
4. G. Bringmann, T. Bruhn, K. Maksimenka, Y. Hemberger, *Eur. J. Org. Chem*. **2009**, 2717–2727.
5. L. Barron *Molecular Light Scattering and Optical Activity*, Oxford University Press, New York, **2004**.
6. S. Grimme, F. Furche, R. Ahlrichs, *Chem. Phys. Lett*. **2002**, *361*, 321–328.
7. L. Goerigk, S. Grimme, *J. Phys. Chem. A* **2009**, *113*, 767–776.
8. T. Helgaker, P. Jørgensen, J. Olsen, *Molecular Electronic-Structure Theory*, John Wiley &Sons, New York, **2000**.
9. S. Grimme Calculation of the electronic spectra of large molecules, in *Reviews in Computational Chemistry*, Vol. 20, K. B. Lipkowitz and D. B. Boyd, eds., Wiley-VCH, New York, **2004**. pp. 153–218.
10. Y. M. Rhee, M. Head-Gordon, *J. Phys. Chem. A* **2007**, *111*, 5314–5326.
11. M. Head-Gordon, R. J. Rico, M. Oumi, T. J. Lee, *Chem. Phys. Lett*. **1994**, *219*, 21–29.
12. S. Grimme, *J. Chem. Phys*. **2003**, *118*, 9095–9102.
13. L. Goerigk, S. Grimme, *J. Chem. Phys*. **2010**, *132*, 184103.
14. A. D. McLachlan, M. A. Ball, *Rev. Mod. Phys*. **1964**, *127*, 844–855.
15. A. Fetter, J. Walecka *Quantum Theory of Many-Particle Systems*, McGraw-Hill, New York, **1971**.
16. J. F. Stanton, R. J. Bartlett, *J. Chem. Phys*. **1993**, *98*, 7029–7039.
17. O. Christiansen, H. Koch, P. Jørgensen, *Chem. Phys. Lett*. **1995**, *243*, 409–418.
18. H. Koch, O. Christiansen, P. Jørgensen, A. M. S. de Merás, T. Helgaker, *J. Chem. Phys*. **1997**, *106*, 1808–1818.
19. A. Hellweg, S. A. Grün, C. Hättig, *Phys. Chem. Chem. Phys*. **2008**, *10*, 4119–4127.

20. M. Scholz, H.-J. Köhler, Quantenchemische Näherungsverfahren und ihre Anwendung in der organischen Chemie, Vol. 3, Quantenchemie–Ein Lehrgang; Deutscher Verlag der Wissenschaften: Berlin, **1981**.
21. J. Ridley, M. Zerner, *Theoret. Chem. Acta (Berl.)* **1973**, *32*, 111–134.
22. P. Hohenberg, W. Kohn, *Phys. Rev. B* **1964**, *136*, 864–871.
23. W. Kohn, L. J. Sham, *Phys. Rev*. **1965**, *140*, A1133–A1138.
24. W. Koch, M. C. Holthausen, *A Chemist's Guide to Density Functional Theory*, Wiley-VCH, New York, **2001**.
25. R. Bauernschmitt, R. Ahlrichs, *Chem. Phys. Lett* **1996**, *256*, 454–464.
26. J. Schirmer, A. Dreuw, *Phys. Rev. A* **2007**, *75*, 022513.
27. A. Dreuw, J. Schirmer, *Phys. Rev. A* **2008**, *78*, 056502.
28. J. P. Perdew, A. Ruzsinszky, J. Tao, V. N. Staroverov, G. E. Scuseria, G. Csonka, *J. Chem. Phys*. **2005**, *123*, 62201.
29. A. D. Becke, *J. Chem. Phys*. **1993**, *98*, 5648–5652.
30. P. J. Stephens, F. J. Devlin, C. F. Chabalowski, M. J. Frisch, *J. Phys. Chem*. **1994**, *98*, 11623–11627.
31. C. Adamo, V. Barone, *J. Chem. Phys*. **1999**, *110*, 6158–6170.
32. T. Yanai, D. P. Tew, N. C. Handy, *Chem. Phys. Lett*. **2004**, *393*, 51–57.
33. O. A. Vydrov, G. E. Scuseria, *J. Chem. Phys*. **2006**, *125*, 234109.
34. S. Grimme, *J. Chem. Phys*. **2006**, *124*, 034108.
35. S. Grimme, F. Neese, *J. Chem. Phys*. **2007**, *127*, 154116.
36. A. Karton, A. Tarnopolsky, J. F. Lamère, G. C. Schatz, J. M. L. Martin, *J. Phys. Chem. A* **2008**, *112*, 12868–12886.
37. A. D. Becke, *Phys. Rev. A* **1988**, *38*, 3098–3100.
38. C. Lee, W. Yang, R. G. Parr, *Phys. Rev. B* **1988**, *37*, 785–789.
39. J. P. Perdew, K. Burke, M. Ernzerhof, *Phys. Rev. Lett*. **1996**, *77*, 3865–3868.
40. S. Grimme, J. Antony, S. Ehrlich, H. Krieg, *J. Chem. Phys*. **2010**, *132*, 154104.
41. A. D. Becke, *J. Chem. Phys*. **1993**, *98*, 1372–1377.
42. J.-D. Chai, M. Head-Gordon, *J. Chem. Phys*. **2008**, *128*, 084106.
43. S. Grimme, *J. Comput. Chem*. **2006**, *27*, 1787–1799.
44. S. Grimme, M. Parac, *Chem. Phys. Chem*. **2003**, *4*, 292–295.
45. M. Parac, S. Grimme, *Chem. Phys*. **2003**, *292*, 11–21.
46. L. Goerigk, J. Moellmann, S. Grimme, *Phys. Chem. Chem. Phys*. **2009**, *11*, 4611–4620.
47. M. Dierksen, S. Grimme, *J. Phys. Chem. A* **2004**, *108*, 10225–10237.
48. A. Schäfer, C. Huber, R. Ahlrichs, *J. Chem. Phys*. **1994**, *100*, 5829–5835.
49. T. H. Dunning, Jr., *J. Chem. Phys*. **1989**, *90*, 1007–1023.
50. A. Schäfer, H. Horn, R. Ahlrichs, *J. Chem. Phys*. **1992**, *97*, 2571–2577.
51. M. Cossi, V. Barone, *J. Chem. Phys*. **2001**, *115*, 4708.
52. A. Klamt, G. Schürmann, *J. Chem. Soc. Perkin Trans. 2* **1993**, 799–805.
53. TURBOMOLE, version 6.0: R. Ahlrichs et al., Universität Karlsruhe **2009**. See `http://www.turbomole.com`.
54. R. Ahlrichs, M. Bär, M. Häser, H. Horn, C. Kölmel, *Chem. Phys. Lett*. **1989**, *162*, 165–169.
55. K. Eichkorn, O. Treutler, H. Öhm, M. Häser, R. Ahlrichs, *Chem. Phys. Lett*. **1995**, *240*, 283–289.
56. F. Furche, D. Rappoport, Density functional methods for excited states: Equilibrium structure and electronic spectra, in *Theoretical and Computational Chemistry*, Vol. 16, M. Olivucci, ed., Elsevier, Amsterdam, **2005**, pp. 93–128.

57. C. Hättig, F. Weigend, *J. Chem. Phys*. **2000**, *113*, 5154–5161.
58. F. Weigend, M. Häser, H. Patzelt, R. Ahlrichs, *Chem. Phys. Lett*. **1998**, *294*, 143–152.
59. Gaussian 09, Revision A.02, M. J. Frisch, G. W. Trucks, H. B. Schlegel, G. E. Scuseria, M. A. Robb, J. R. Cheeseman, G. Scalmani, V. Barone, B. Mennucci, G. A. Petersson, H. Nakatsuji, M. Caricato, X. Li, H. P. Hratchian, A. F. Izmaylov, J. Bloino, G. Zheng, J. L. Sonnenberg, M. Hada, M. Ehara, K. Toyota, R. Fukuda, J. Hasegawa, M. Ishida, T. Nakajima, Y. Honda, O. Kitao, H. Nakai, T. Vreven, J. A. Montgomery, Jr., J. E. Peralta, F. Ogliaro, M. Bearpark, J. J. Heyd, E. Brothers, K. N. Kudin, V. N. Staroverov, R. Kobayashi, J. Normand, K. Raghavachari, A. Rendell, J. C. Burant, S. S. Iyengar, J. Tomasi, M. Cossi, N. Rega, J. M. Millam, M. Klene, J. E. Knox, J. B. Cross, V. Bakken, C. Adamo, J. Jaramillo, R. Gomperts, R. E. Stratmann, O. Yazyev, A. J. Austin, R. Cammi, C. Pomelli, J. W. Ochterski, R. L. Martin, K. Morokuma, V. G. Zakrzewski, G. A. Voth, P. Salvador, J. J. Dannenberg, S. Dapprich, A. D. Daniels, O. Farkas, J. B. Foresman, J. V. Ortiz, J. Cioslowski, D. J. Fox, Gaussian, Inc., Wallingford CT, **2009**.
60. F. Neese, ORCA V.2.7—an *ab initio*, density functional and semiempirical program package, University of Bonn, Germany, **2009**. See `http://www.thch.uni-bonn.de/tc/orca/`.
61. RICC: A coupled-cluster program using the RI approximation. S. Grimme, University of Münster, **2007**.
62. PPP 1.1. A TD-PPP and SCI-PPP program. S. Grimme, University of Münster, **2006**.
63. V. Vintonyak, K. Warburg, H. Kruse, S. Grimme, K. Huebel, D. Rauh, H. Waldmann, *Angew. Chem. Int. Ed*. **2010**, *49*, 5902–5905.
64. F. Weigend, R. Ahlrichs, *Phys. Chem. Chem. Phys*. **2005**, *7*, 3297–3305.
65. J. L. Alonso-Gómez, P. Rivera-Fuentes, N. Harada, N. Berova, F. Diederich, *Angew. Chem. Int. Ed*. **2009**, *48*, 5545–5548.
66. M. Dierksen, S. Grimme, *J. Chem. Phys*. **2004**, *120*, 3544–3554.
67. J. Seibt, A. Lohr, F. Würthner, V. Engel, *Phys. Chem. Chem. Phys*. **2007**, *9*, 6214–6218.
68. L. Goerigk, S. Grimme, *Chem. Phys. Chem*. **2008**, *9*, 2467–2470.
69. F. Würthner, S. Yao, T. Debaerdemaeker, R. Wortmann, *J. Am. Chem. Soc*. **2002**, *124*, 9431–9447.
70. T. Heinz, D. Rudkevich, J. Rebek, *Nature 394*, 764–766.
71. C. Siering, J. Torang, H. Kruse, S. Grimme, S. Waldvogel, *Chem.l Comm*. **2010**, *46*, 1625–1627.
72. H. Kruse, Quantenchemische Berechnungen von organischen Einschlussverbindungen, Diploma Thesis,University of Muenster; **2008**.
73. M. P. Waller, H. Kruse, C. Mück-Lichtenfeld, S. Grimme, *Chem. Soc. Rev*. submitted.
74. *PCmodel 9.1*; Serena Software: Bloomington, **2005**.
75. L. Goerigk, S. Grimme, *J. Chem. Theory Comput*. **2011**, *7*, 291–309.
76. T. Mori, Y. Inoue, S. Grimme, *J. Phys. Chem. A* **2007**, *111*, 7995–8006.
77. S. Grimme, A. Bahlmann, in *Modern Cyclophane Chemistry*, R. Gleiter and H. Hopf, eds., Wiley-VCH, Weinheim, **2004**, pp 311–336.

23

HIGH-ACCURACY QUANTUM CHEMISTRY AND CHIROPTICAL PROPERTIES

T. Daniel Crawford

23.1. INTRODUCTION

In 1973, Pople devised the concept of a "theoretical model chemistry"—defined as a method for computing an approximate electronic wavefunction with only the number of electrons (and spin multiplicity), as well as the charges and coordinates of the nuclei as input [1]. The resulting wavefunction can then be used to compute a range of chemically relevant properties, including reaction energies, potential energy surfaces, vibrational and electronic spectra, and more. A complete model, Pople said, was one that can be applied to any configuration of nuclei. His idea sparked the development of a wide array of generally applicable quantum chemical methods and ultimately the great triumph of modern theoretical chemistry: first principles, *predictive* models of molecular properties.

Key to the success of quantum chemistry is the concept of a convergent *ab initio* model—that is, one that is formally exact and thus may be systematically improved in its mathematical completeness towards the limit of the solution to the electronic Schrödinger equation. This allows the precise calibration of theoretical data even in the absence of experiment and, in many cases, has provided simulations of molecular properties of such high accuracy that they have overturned and even superseded empirical results [2].

Comprehensive Chiroptical Spectroscopy, Volume 1: Instrumentation, Methodologies, and Theoretical Simulations, First Edition. Edited by N. Berova, P. L. Polavarapu, K. Nakanishi, and R. W. Woody.
© 2012 John Wiley & Sons, Inc. Published 2012 by John Wiley & Sons, Inc.

In the last two decades, a variety of quantum chemical models have focused on chiroptical properties [3], including optical rotation [4–15], electronic circular dichroism [12, 14, 16–23], vibrational circular dichroism [5, 24–30], and Raman optical activity [31–42]. One of the primary goals of this work has been the construction of computational tools to assist synthetic chemists in the elucidation of absolute stereochemical configurations of chiral compounds. Although the experimental determination of these properties is now well established, such measurements can only be used to establish the three-dimensional structure of the compound if the circular dichroism, birefringence, or scattering intensity differences are known *a priori*. Such analyses are vital to modern synthetic organic chemistry, for example, where the laboratory synthesis of chiral species such as natural products requires careful control over the absolute and relative configurations of stereogenic centers [43]. Thus, if theory can provide accurate, reliable, and computationally efficient predictions of chiroptical properties as references for corresponding spectral measurements, the sythesis of new chiral compounds—including new chiral drugs—could be sped by years or even decades.

The purpose of this chapter is to provide an overview of the most accurate and reliable quantum chemical method currently in use: coupled cluster theory [44–46]. The power of this approach is in the accuracy of its predictions for a wide array of molecular properties, an accuracy that can be systematically controlled through improvements in the level of electron correlation employed and the completeness of the basis set. Lee and Scuseria [47] provided a detailed analysis of the performance of coupled cluster methods with large basis sets including up to g-type angular momentum functions for equilibrium geometries, vibrational frequencies (both harmonic and fundamental), dissociation energies, enthalpies of formation, dipole moments, static polarizabilities, and excitation energies for a large number of small molecules. As compared to the best available experimental data, average errors for bond distances (including multiply bonded species) did not exceed 0.003 Å, while experimental fundamental vibrational frequencies were reproduced to within 8.0 cm^{-1} on average. They reported binding energies to be accurate to 1.0 kcal/mol for single bonds and 2.0 kcal/mol for multiple bonds, and similarly impressive results for other properties.

More recently, Helgaker et al.[48] reported statistical analyses of coupled cluster methods with even larger basis sets (in many cases including extrapolations to the complete basis set limit), and they found that the errors relative to experiment for many properties exhibit normal distributions. They demonstrated that both the center and spread of the error distribution can be controlled by systematic improvements in the correlation treatment and the basis set, and the proposed protocols involving sequences of coupled cluster computations can methodically approach the exact answer to the electronic Schrödinger equation. In many cases, significant discrepancies between theory and experiment can thus be attributed to errors in the latter [2], making the coupled cluster method the "gold standard" of quantum chemistry. On this basis, there is much reason for optimism as to the potential usefulness of coupled cluster theory for predicting the optical properties of chiral molecules.

We will begin with an overview of the history of coupled cluster theory, followed by a brief primer on the fundamental aspects of the ground-state theory. After a discussion of its extension to properties such as optical rotation and electronic circular dichroism through the so-called linear response and equation-of-motion variants, we will review a number of specific applications, including both its successes and failures. We will conclude with a prospectus on the future of the method and its potential to reach the goal of a computational tool for the determination of absolute configurations.

23.2. COUPLED CLUSTER THEORY

23.2.1. History

The origins of the coupled cluster method lie in the theory of nuclear matter, starting with the pioneering work of Coester and Kümmel in the early 1960s [49]. They were the first to recognize the usefulness of an exponential form of the wavefunction, and thus they dubbed it exp(S) theory. A few years later, Čížek and Paldus adapted the idea for electronic wavefunctions [50–52], and they were the first to develop convenient mathematical and diagrammatic schemes for deriving the working equations [53]. Based on a suggestion by Sinanoğlu, they adopted the name *coupled pair many-electron theory* (CPMET)—which we now know as the coupled cluster doubles (CCD) method—since their model focused on only pairs of electrons. In the early 1970s, however, it became clear that this moniker was inadequate for the more generalized form of the theory, and Harris soon produced the now-popular neologism *coupled cluster theory* [54].

There have many been contributors to the field of coupled cluster since the earliest efforts by Čížek and Paldus. The Bartlett group at the University of Florida's Quantum Theory Project has been among the most prolific and influential [44, 45, 55–59], starting with their report of the first implementation of (CCD) in 1978 [60] (published simultaneously as an implementation by Pople et al. [61]). Bartlett and co-workers have been responsible for many "firsts" in coupled cluster theory, including the first implementations of coupled cluster singles and doubles (CCSD) [62], triples (CCSDT) [63], quadruples (CCSDTQ) [64], and pentuples (CCSDTQPH) [65], as well as a variety of approximate schemes to balance accuracy and computational cost [66, 67]. The most reliable and popular coupled cluster method is undoubtedly CCSD(T)—CCSD augmented with a perturbational estimate of triple substitutions—which was first reported by Raghavachari et al. in 1989 [68]. An alternative approximate hierarchy has been introduced by the Scandinavian groups, starting from CC2 [69], which provides an intermediate between second-order perturbation theory and CCSD, and including CC3 [70, 71], which incorporates the effects of connected triples but, unlike CCSD(T), is applicable to frequency-dependent properties such as optical rotation.

The computation of molecular properties within coupled cluster theory began with the work of Monkhorst in 1977 [72], who developed response equations for first- and second-order properties. Soon thereafter, Mukherjee and co-workers reported an approach for computing excitation energies and dynamic polarizabilities [73, 74] using related formalisms. In the 1980s, Sekino and Bartlett further developed coupled cluster response formalisms, particular for excitation energies and transition properties [75], and in 1993 Stanton and Bartlett reported the development of the equation-of-motion coupled cluster (EOM-CC) method for excitation energies, transition strengths, and polarizabilities [76, 77]. In 1990, Koch and Jørgensen reported on a new formulation of coupled cluster computing response properties [78] with applications to excitation energies [79], and their approach has been used and extended many times since [9, 10, 13, 69–71 80–92].

23.2.2. Fundamentals

All many-body electronic structure methods, including perturbation theory, configuration interaction, and coupled cluster, are based on expansion of the wavefunction in a set of Slater determinants—antisymmetrized products of orthonormal one-electron molecular orbitals (MOs) [93]. The MOs themselves are typically (but not always) obtained from a Hartree–Fock self-consistent-field (SCF) computation, which produces both a set

of *occupied* orbitals, $\{\phi_i\}$, and a set of *unoccupied* orbitals, $\{\phi_a\}$.[1] The set of Slater determinants that can be constructed from the MOs are grouped based on the number of orbitals they have in common with a *reference* determinant, $|\Phi_0\rangle$ (e.g., the Hartree–Fock wavefunction): Those that differ from $|\Phi_0\rangle$ by substitution of one occupied orbital, ϕ_i, by an unoccupied orbital, ϕ_a, are called *singles* and are denoted $|\Phi_i^a\rangle$, and those that differ by substitution of two orbitals, ϕ_i and ϕ_j, by ϕ_a and ϕ_b, are called *doubles* and are denoted $|\Phi_{ij}^{ab}\rangle$, and so on.

In models such as configuration interaction (CI) [94], the total wavefunction is written as a linear combination of Slater determinants, for example,

$$|\Phi_{\mathrm{CI}}\rangle = |\Phi_0\rangle + \sum_{ia} t_i^a |\Phi_i^a\rangle + \frac{1}{4}\sum_{ijab} t_{ij}^{ab} |\Phi_{ij}^{ab}\rangle + \cdots, \tag{23.1}$$

where the t_i^a, t_{ij}^{ab}, and so on, are the expansion coefficients (amplitudes) and the prefactor of 1/4 corrects for double counting of determinants. If all possible determinants are included in the expansion, then the wavefunction represents the exact solution to the electronic Schrödinger equation within the space spanned by the set of MOs—that is, the full CI wavefunction. Unfortunately, the number of determinants grows factorially with the number of electrons and MOs, thus limiting the practical construction of full CI wavefunctions for molecules containing around 10 electrons at most. As a result, the expansion must be truncated to low substitution levels to keep the computational requirements manageable (e.g., singles and doubles to form CISD) up to triples for CISDT, and so on.

The coupled cluster method differs from CI and perturbation theory in that it uses an *exponential* rather than linear form for the wavefunction [44–46],

$$|\Phi_{\mathrm{CC}}\rangle = e^{\hat{T}} |\Phi_0\rangle, \tag{23.2}$$

where the *cluster operator*, $\hat{T} = \hat{T}_1 + \hat{T}_2 + \cdots$ generates the required sets of Slater determinants from the reference, $|\Phi_0\rangle$; that is, the singles cluster operator gives

$$\hat{T}_1 |\Phi_0\rangle = \sum_{ia} t_i^a |\Phi_i^a\rangle, \tag{23.3}$$

and the doubles cluster operator gives

$$\hat{T}_2 |\Phi_0\rangle = \frac{1}{4}\sum_{ijab} t_{ij}^{ab} |\Phi_{ij}^{ab}\rangle, \tag{23.4}$$

and so on. The advantage of the exponential form can be seen from its power-series expansion:

$$e^{\hat{T}} = 1 + \hat{T} + \frac{1}{2}\hat{T}^2 + \frac{1}{6}\hat{T}^3 + \cdots. \tag{23.5}$$

[1] We will adopt a common convention that occupied MOs are labeled with indices i, j, k, etc., and unoccupied MOs by a, b, c, etc.

Thus, if we choose to truncate the $\hat{T}$ operator at only singles and doubles (yielding the CCSD method [62]), then the exponential produces products of $\hat{T}_1$ and $\hat{T}_2$ operators,

$$e^{\hat{T}_1+\hat{T}_2} = 1 + \hat{T}_1 + \hat{T}_2 + \frac{1}{2}\hat{T}_1^2 + \hat{T}_1\hat{T}_2 + \frac{1}{2}\hat{T}_2^2 + \frac{1}{6}\hat{T}_1^3 + \frac{1}{2}\hat{T}_1^2\hat{T}_2 + \frac{1}{2}\hat{T}_2^2\hat{T}_1 + \frac{1}{6}\hat{T}_2^3 + \cdots, \tag{23.6}$$

where, for example, the action of a product of $\hat{T}_1$ and $\hat{T}_2$ on the reference determinant is a triple,

$$\hat{T}_1\hat{T}_2|\Phi_0\rangle = \frac{1}{4}\sum_{ijkabc} t_i^a t_{jk}^{cd} |\Phi_{ijk}^{abc}\rangle. \tag{23.7}$$

Therein lies one of the principal advantages of coupled cluster theory: Even when the cluster operator is truncated (e.g., singles and doubles), the exponential wavefunction implicitly incorporates higher substitution levels—triples, quadruples, and so on. As a result, the coupled cluster expansion converges toward the full configuration interaction limit much more quickly than the linear expansion of CI, making it a much more accurate and reliable approach. Furthermore, the method is systematically improvable; that is, greater and greater accuracy can be obtained by increasing the substitution level included in $\hat{T}$, with the proviso, of course, that each new level incurs greater computational cost.

At first blush, the exponential expansion of Eq. (23.5) may appear to involve an infinite number of terms (or at least as many terms as the number of electrons). However, the mathematical structure of the equations leads to a natural and convenient trunction. If we insert the exponential wavefunction into the Schrödinger equation and then multiply on the left by the inverse of the exponential, we obtain

$$e^{-\hat{T}}\hat{H}e^{\hat{T}}|\Phi_0\rangle = E_{\mathrm{CC}}|\Phi_0\rangle. \tag{23.8}$$

The similarity-transformed Hamiltonian on the left-hand side of the equation acts as an effective Hamiltonian, which may be written as an expansion of commutators, namely,

$$\begin{aligned}\overline{H} \equiv e^{-\hat{T}}\hat{H}e^{\hat{T}} = \hat{H} + \left[\hat{H},\hat{T}\right] + \frac{1}{2}\left[\left[\hat{H},\hat{T}\right],\hat{T}\right] + \frac{1}{6}\left[\left[\left[\hat{H},\hat{T}\right],\hat{T}\right],\hat{T}\right] \\ + \frac{1}{24}\left[\left[\left[\left[\hat{H},\hat{T}\right],\hat{T}\right],\hat{T}\right],\hat{T}\right] + \cdots.\end{aligned} \tag{23.9}$$

It may be shown [46] that this expression exactly truncates at the fourth-order commutator because the electronic Hamiltonian, $\hat{H}$, contains at most two-electron (Coulombic) potentials. If we project the Schrödinger equation on the left by the reference determinant, we obtain an equation for the energy,

$$E_{\mathrm{CC}} = \langle\Phi_0|\overline{H}|\Phi_0\rangle, \tag{23.10}$$

whereas left-projection by the determinants corresponding to the substitution level of $\hat{T}$ yields sets of equations that may be solved for the amplitudes—for example,

$$0 = \langle\Phi_i^a|\overline{H}|\Phi_0\rangle \tag{23.11}$$

for the singles,

$$0 = \langle \Phi_{ij}^{ab} | \overline{H} | \Phi_0 \rangle \tag{23.12}$$

for the doubles, and so on. These formal equations must, of course, be converted into forms that can be subsequently programmed and solved on the computer, and the literature is replete with algebraic and diagrammatic techniques for carrying out this task [44–46, 95, 96].

It should be noted that, because of the exponential wavefunction, the final expressions are nonlinear in the cluster amplitudes (unlike the linear equations of CI) and the equations for the singles, doubles, etc., are coupled and thus must be solved simultaneously (hence the origin of the name "coupled cluster" theory). Furthermore, in contrast to CI, the energy, E_{CC} is not variational and hence not an upper bound to the exact energy. However, in practice, this shortcoming rarely has any drawbacks. On the other hand, the coupled cluster energy (and other properties discussed later) does have two other important physical characteristics: It scales linearly with the number of electrons, a feature commonly referred to as *size extensivity*, and the total energy of isolated fragments is exactly the sum of their individual energies, which is known as *size consistency* [56]. The former is essential for a method to be applicable to large molecules, clusters, or condensed phases, and the latter is necessary for reliable simulations of many chemical reactions. (And neither is possible for truncated CI methods.)

An alternative formulation of the coupled cluster equations is based on the minimization of a Lagrangian function [97, 98],

$$\mathcal{L}_{CC} \equiv \langle \Phi_0 | \left(1 + \hat{\Lambda}\right) \overline{H} | \Phi_0 \rangle, \tag{23.13}$$

where the $\hat{\Lambda} = \hat{\Lambda}_1 + \hat{\Lambda}_2 + \cdots$ operator generates substituted Slater determinants in the bra on the left in a manner analogous to $\hat{T}$, for example,

$$\langle \Phi_0 | \hat{\Lambda}_2 = \frac{1}{4} \sum_{ijab} \lambda_{ab}^{ij} \langle \Phi_{ij}^{ab} |, \tag{23.14}$$

and the λ_{ab}^{ij} amplitudes act a set of Lagrange multipliers. Minimization of $\mathcal{L}_{CC}$ with respect to $\hat{\Lambda}$ yields the $\hat{T}$ amplitude equations above, while minimization with respect to $\hat{T}$ yields equations for the $\hat{\Lambda}$ amplitudes, for example,

$$\langle \Phi_0 | \left(1 + \hat{\Lambda}\right) \left(\overline{H} - E_{CC}\right) | \Phi_{ij}^{ab} \rangle = 0. \tag{23.15}$$

While this formulation is not strictly necessary to obtain either the energy or the $\hat{T}$ amplitudes, it is extraordinarily useful for computation of analytic derivatives of the energy [99–101] and, as we will see below, properties such as optical rotation and circular dichroism spectra. In addition, the Lagrangian formulation reveals that the coupled cluster wavefunction can be viewed as having two distinct forms: (a) the right-hand form given in Eq. (23.2) and (b) a left-hand form [102],

$$\langle \tilde{\Phi}_{CC} | = \langle \Phi_0 | \left(1 + \hat{\Lambda}\right) e^{-\hat{T}}. \tag{23.16}$$

In this sense, the author is fond of thinking of coupled cluster theory as a "chiral" quantum chemical method.

23.3. RESPONSE THEORY FOR CHIROPTICAL PROPERTIES

The semiclassical derivation of expressions for molecular properties such as optical rotation or circular dichroism often makes use of time-dependent perturbation theory, where the Hamiltonian is partitioned into a zeroth-order time-independent term and a time-dependent field [3, 103, 104],

$$\hat{H} = \hat{H}_0 + \hat{V}(t). \tag{23.17}$$

It is assumed that we have available as zeroth-order wavefunctions the exact solutions to the time-independent electronic Schrödinger equation, $|\psi_n\rangle$, which are eigenfunctions of $\hat{H}_0$. These stationary states are inserted into the time-dependent Schrödinger equations to obtain perturbed wavefunctions, which are then used in an expansion of the expectation value of a one-electron operator, such as the electric or magnetic dipole moments, in orders of the external time-dependent multipole field. The desired properties are finally obtained from tensors that modulate the contributions of each component of the field, and the tensors themselves are written as sums over excited states (i.e., the zeroth-order wave functions). For optical rotation and circular dichroism, the relevant tensor is [3]

$$\mathbf{G}'(\omega) = -2\omega \sum_{n\neq 0} \frac{\mathrm{Im}[\langle\psi_0|\vec{\mu}|\psi_n\rangle\langle\psi_n|\vec{m}|\psi_0\rangle]}{\omega_{n0}^2 - \omega^2}, \tag{23.18}$$

where $\vec{\mu} = -\vec{r}$ and $\vec{m} = -\frac{1}{2}\vec{L} = -\frac{1}{2}\vec{r}\times\vec{p}$ are the electric- and magnetic-dipole vector operators, respectively, and ω denotes the frequency of the incident polarized radiation field. The trace of $\mathbf{G}'$ is related to the *specific rotation* [i.e., the total rotation, normalized for path length (dm) and concentration (g/mL)], which is commonly denoted as $[\alpha]_\omega$. In addition, the *rotational strengths* of electronic circular dichroism (ECD) spectra are directly related to the residues of $\mathbf{G}'$, namely,

$$R_{n0} = \mathrm{Im}\left\{\langle\psi_0|\vec{\mu}|\psi_n\rangle \cdot \langle\psi_n|\vec{m}|\psi_0\rangle\right\}. \tag{23.19}$$

A disadvantage of time-dependent perturbation theory lies in its generalization to approximate wavefunctions, such as coupled cluster or configuration interaction. An equivalent but more convenient approach is that of response theory [78, 86, 105–108], where the time-dependent expectation value described above is written as an expansion in the frequency-dependent perturbation operator, $\hat{V}(\omega)$ [which is the Fourier transform of $\hat{V}(t)$],

$$\begin{aligned}\langle\hat{A}\rangle =& \langle\psi_0|\hat{A}|\psi_0\rangle + \int_{-\infty}^{\infty} d\omega \langle\langle\hat{A};\hat{V}(\omega)\rangle\rangle_\omega e^{-i\omega t} \\ &+ \frac{1}{2}\int_{-\infty}^{\infty} d\omega \int_{-\infty}^{\infty} d\omega' \langle\langle\hat{A};\hat{V}(\omega),\hat{V}(\omega')\rangle\rangle_{\omega,\omega'} e^{-i(\omega+\omega')t} + \cdots,\end{aligned} \tag{23.20}$$

where the Fourier coefficients, $\langle\langle\hat{A};\hat{V}(\omega)\rangle\rangle_\omega$, $\langle\langle\hat{A};\hat{V}(\omega),\hat{V}(\omega')\rangle\rangle_{\omega,\omega'}$, and so on, are referred to as linear, quadratic, and so on, response functions, respectively. These functions play the same role as the property tensors arising from time-dependent perturbation theory, and indeed the two become identical for exact states, as elegantly demonstrated

by Olsen and Jørgensen [105, 106]. In particular, the $\mathbf{G}'(\omega)$ optical activity tensor above is related to the mixed electric-dipole/magnetic-dipole linear response function,

$$\mathbf{G}'(\omega) = \mathrm{Im}\langle\langle \vec{\mu}; \vec{m} \rangle\rangle_{\omega}. \tag{23.21}$$

In Olsen and Jørgensen's subsequent application of response theory to multiconfigurational SCF wavefunctions, they demonstrated another advantage over time-dependent perturbation theory, namely that the response of the wavefunction need not be formulated as an expansion of excited states, but may instead be computed for each perturbation operator in any complete yet convenient set of functions. This approach requires only the solution of systems of linear equations for each $\hat{V}(\omega)$, and thus is far less expensive than the computation of the complete set of excited states. In this sense, response theory may be thought of as a noncanonical form of time-dependent perturbation theory.

23.3.1. Coupled Cluster Linear Response Theory

The extension of response theory to coupled cluster is problematic because of the asymmetric nature of the wavefunction, where the distinct left- and right-hand forms [cf. Equations (23.2) and (23.16)] complicate the formulation of an "expectation value." Indeed, there is no guarantee that the time-dependent left- and right-hand coupled cluster wavefunctions will even yield a real expectation value of Hermitian operators as required in the exact theory, leading to an often-used coupled cluster expression that naturally extracts only the real component [86],

$$\langle \hat{A} \rangle_{\mathrm{CC}} = \frac{1}{2} \left(\langle \tilde{\Phi}_{\mathrm{CC}} | \hat{A} | \Phi_{\mathrm{CC}} \rangle + \langle \tilde{\Phi}_{\mathrm{CC}} | \hat{A} | \Phi_{\mathrm{CC}} \rangle^{*} \right), \tag{23.22}$$

where $\langle \tilde{\Phi}_{\mathrm{CC}}|$ and $|\Phi_{\mathrm{CC}}\rangle$ are now time-dependent forms of Eqs. (23.16) and (23.2), respectively. In addition, distinct left- and right-hand wavefunctions require solution of two different time-dependent Schrödinger equations, namely,

$$\hat{H} e^{i\epsilon} e^{\hat{T}} |\Phi_0\rangle = i \frac{\partial}{\partial t} e^{i\epsilon} e^{\hat{T}} |\Phi_0\rangle \tag{23.23}$$

and

$$\langle \Phi_0 | \left(1 + \hat{\Lambda}\right) e^{-\hat{T}} e^{-i\epsilon} \hat{H} = -i \frac{\partial}{\partial t} \langle \Phi_0 | \left(1 + \hat{\Lambda}\right) e^{-\hat{T}} e^{-i\epsilon}, \tag{23.24}$$

where $\exp(i\epsilon)$ is a complex phase factor, and both $\hat{T}$ and $\hat{\Lambda}$ are implicitly time-dependent. (Although the reference determinant is also time-dependent, conventional coupled cluster response theory neglects this, in part because it adds significantly to the complexity of the equations and because $\hat{T}_1$ typically accounts for most of the orbital relaxation effects.) In spite of these difficulties, Koch and Jørgensen reported the first application of coupled cluster response theory in 1990 [78], and several reformulations have been reported since [86, 88, 107], including extension to higher levels of electron correlation beyond CCSD [70, 71].

If the time-dependent Schrödinger equation for the right-hand wavefunction is projected onto the set of substituted determinants, $|\Phi_{ij\ldots}^{ab\cdots}\rangle$, the time evolution of the cluster amplitudes may be obtained, namely [78],

$$-i \langle \Phi_{ij\ldots}^{ab\cdots} | \overline{H} | \Phi_0 \rangle = \dot{t}_{ij\ldots}^{ab\cdots}. \tag{23.25}$$

If the cluster operator is then expanded in orders of the time-dependent pertubation, $\hat{V}(t)$, the commutator expansion of the similarity-transformed Hamiltonian becomes

$$\begin{aligned}\overline{H} &= e^{-\hat{T}^{(0)}-\hat{T}^{(1)}-\hat{T}^{(2)}-\cdots}\left(\hat{H}_0+\hat{V}(t)\right)e^{\hat{T}^{(0)}+\hat{T}^{(1)}+\hat{T}^{(2)}+\cdots} \\ &= \overline{H}_0+\overline{V}+\left[(\overline{H}_0+\overline{V}),\hat{T}^{(1)}\right]+\left[(\overline{H}_0+\overline{V}),\hat{T}^{(2)}\right] \\ &\quad+\frac{1}{2}\left[\left[(\overline{H}_0+\overline{V}),\hat{T}^{(1)}\right],\hat{T}^{(1)}\right]+\cdots.\end{aligned} \tag{23.26}$$

In this equation, $\overline{H}_0$ and $\overline{V}$ are similarity transformed using only $\hat{T}^{(0)}$, which are the same as $\hat{T}$ for the time-independent/unperturbed wavefunction. If this expansion is inserted into the time-evolution equation above, we obtain, for example in first order,

$$\dot{t}^{ab\cdots(1)}_{ij\cdots} = -i\langle\Phi^{ab\cdots}_{ij\cdots}|\left(\overline{V}+\left[\overline{H}_0,\hat{T}^{(1)}\right]\right)|\Phi_0\rangle. \tag{23.27}$$

The Fourier transform of this expression may then be used to obtain a frequency-domain system of linear equations that may be solved for the perturbed wavefunction amplitudes,

$$\langle\Phi^{ab\cdots}_{ij\cdots}|(\omega-\overline{H}_0)\hat{T}^{\omega}_V|\Phi_0\rangle = \langle\Phi^{ab\cdots}_{ij\cdots}|\overline{V}(\omega)|\Phi_0\rangle. \tag{23.28}$$

Finally, the first-order perturbed $\hat{T}^{(1)}$ operator (as well as its left-hand counterpart, $\hat{\Lambda}^{(1)}$) may be inserted into the expansion of the expectation value of the operator $\hat{A}$ in Eq. (23.22), which is then subjected to yet another Fourier transform to identify the linear response function. For the specific case of the optical activity tensor, the corresponding expression becomes

$$\begin{aligned}\mathbf{G}(\omega) = \mathrm{Im}\Bigg\{\hat{C}^{\pm\omega}\hat{P}\left(\vec{\mu}(-\omega),\vec{m}(\omega)\right)\Bigg[&\langle\Phi_0|(1+\hat{\Lambda})\left[\overline{\mu},\hat{T}^{\omega}_m\right]|\Phi_0\rangle \\ &+\frac{1}{2}\langle\Phi_0|(1+\hat{\Lambda})\left[\left[\overline{H}_0,\hat{T}^{\omega}_{\mu}\right],\hat{T}^{-\omega}_m\right]|\Phi_0\rangle\Bigg]\Bigg\},\end{aligned} \tag{23.29}$$

where the overbar denotes the similarity transformation of the given operator analogous to $\overline{H}$ using the unperturbed $\hat{T}$ operator. The permutation operator $\hat{C}^{\pm\omega}$ simultaneously changes the signs on the chosen field frequency and takes the complex conjugate of the expression, and $\hat{P}$ symmetrizes the expression with respect to the perturbations $\vec{\mu}$ and $\vec{m}$.

Equation (23.28) also gives some insight into the computation of excited states. If the identity, expressed as a projector over all Slater determinants, is inserted between $\overline{H}_0$ and $\hat{T}^{\omega}_V$, we obtain

$$\sum_{kl\ldots cd\ldots}\langle\Phi^{ab\cdots}_{ij\cdots}|\left(\omega-\overline{H}_0\right)|\Phi^{cd\cdots}_{kl\cdots}\rangle\langle\Phi^{cd\cdots}_{kl\cdots}|\hat{T}^{\omega}_V|\Phi_0\rangle = \langle\Phi^{ab\cdots}_{ij\cdots}|\overline{V}|\Phi_0\rangle. \tag{23.30}$$

The matrix on the left-hand side will become singular as the external field frequency, ω, approaches an eigenvalue of $\overline{H}_0$, that is, as ω approaches resonance. As a result, the perturbed wavefunctions become infinite, leading to first-order poles in the response function at the excitation frequencies of the molecule—which is the correct behavior according to time-dependent perturbation theory for exact wavefunctions. (Note that if

we were to allow the MOs to respond to the external field, the pole structure would become second-order, which is unphysical.) Thus, we may obtain excited-state energies, E_n, and wavefunctions, $\mathcal{R}_n$, by diagonalization of the $\overline{H}_0$ matrix [76, 78],

$$\overline{H}_0 \mathcal{R}_n = E_n \mathcal{R}_n. \tag{23.31}$$

However, the similarity-transformed Hamiltonian is no longer Hermitian, which implies that the right-hand eigenvalue problem above has a distinct left-hand counterpart, namely,

$$\mathcal{L}_n \overline{H}_0 = \mathcal{L}_n E_n, \tag{23.32}$$

where the two sets of wavefunctions are biorthonormal, that is, $\langle \mathcal{L}_n | \mathcal{R}_m \rangle = \delta_{mn}$. Once the excited-state wavefunctions are known, then the rotational strengths of Eq. (23.19) may be computed for simulation of the electronic circular dichroism spectrum through the residues of the linear response function:

$$R_{n0} = -\mathrm{Tr}\left[\lim_{\omega \to \omega_{n0}} (\omega - \omega_{n0}) \mathbf{G}'(\omega) \right], \tag{23.33}$$

where ω_{n0} is the excitation energy for the nth excited state.

23.3.2. Equation-of-Motion Coupled Cluster

An alternative approach for computing response properties is the equation-of-motion coupled cluster (EOM-CC) method, originally discussed by Stanton and Bartlett [76]. The central difference between the coupled cluster response theory described above and EOM-CC is in their respective definitions of the perturbed wavefunctions: The former uses an exponentiated perturbation operator [cd. Eq. (23.26)], while the latter uses a linear expansion,

$$\hat{T}(t) = \hat{T}^{(0)} + \hat{T}^{(1)} + \hat{T}^{(2)} + \cdots, \tag{23.34}$$

and uses the perturbational partitioning of the similarity transformed Hamiltonian rather than the bare Hamiltonian. This leads to different choices of the zeroth-order wavefunctions for the right-hand side,

$$|\Phi^{(0)\rangle} = |\Phi_0\rangle, \tag{23.35}$$

and for the left-hand side,

$$\langle \tilde{\Phi}^{(0)}| = \langle \Phi_0| \left(1 + \hat{\Lambda}\right), \tag{23.36}$$

which may be contrasted with Eqs. (23.2) and (23.16), respectively. This leads to the following final expression for the linear response function in the EOM-CC formalism:

$$\mathbf{G}'(\omega) = -\mathrm{Im}\left\{ \hat{C}^{\pm\omega} \hat{P} \left(\vec{\mu}(-\omega), \vec{m}(\omega) \right) \langle \Phi_0 | (1 + \hat{\Lambda}) \left[\overline{\mu}, \hat{T}_m^{\omega} \right] | \Phi_0 \rangle \right\}, \tag{23.37}$$

which differs from Eq. (23.29) only in the elimination of the terms that are quadratic in $\hat{T}_V^{\omega}$. While this makes the response function somewhat less expensive to evaluate [109],

it also results in a lack of size extensivity of $\mathbf{G}'(\omega)$ (or, equivalently, a lack of size intensivity in the final specific rotation, $[\alpha]_\omega$, meaning that the property does not change with the size of the system).

On the other hand, the use of a linear perturbed wavefunction expansion does not alter the expression for the perturbed wavefunctions themselves given in Eq. (23.28). Thus, the identification of the eigenvalues and eigenfunctions of $\overline{H}_0$ with excited states described in the previous section still holds for EOM-CC. Indeed, the resulting excitation energies and wavefunctions are identical between EOM-CC and linear response methods. However, since transition properties are determined as the residues of the response function, the resulting rotational strengths obtained from $\mathbf{G}'(\omega)$ will differ somewhat between the two formulations, and the EOM-CC rotational strength will not be size-intensive as in the exact theory. Crawford and Sekino [110] recently investigated a modified approach that corrects the lack of size extensivity of the EOM-CC $\mathbf{G}'(\omega)$ tensor but still avoids the expensive quadratic terms. This method, which is based on an earlier idea of Sekino and Bartlett [109], was termed EOM-CC_L (the subscript L stands for "linearized") and was found to reduce the computational cost relative to that of the full linear response function by up to 30% with no loss of accuracy.

23.3.3. Origin Invariance

A subtle but important problem that arises in computations of $\mathbf{G}'(\omega)$ is that of origin invariance. Specifically, a translation of the coordinate origin along an arbitrary vector, $\vec{a}$, alters the trace of $\mathbf{G}'(\omega)$, which thus leads to an unphysical change in the value of $[\alpha]_\omega$. This problem can be understood in terms of the linear response function by first noting that the origin shift changes the coordinate, linear momentum, and angular momentum vectors as $\vec{r}' = \vec{r} - \vec{a}, \vec{p}' = \vec{p}$, and $\vec{r}' \times \vec{p}' = \vec{r} \times \vec{p} - \vec{a} \times \vec{p}$, respectively. Using the expressions for $\vec{\mu}$ and $\vec{m}$ given above, the corresponding linear-response tensor at the new origin may then be written as

$$\langle\langle \vec{r}'; \vec{r}' \times \vec{p}' \rangle\rangle_\omega = \langle\langle \vec{r}; \vec{r} \times \vec{p} \rangle\rangle_\omega - \langle\langle \vec{r}; \vec{a} \times \vec{p} \rangle\rangle_\omega. \tag{23.38}$$

The provenance of the origin dependence is clearly the second term on the right-hand side of the equation, whose trace may be written in terms of its Cartesian components as

$$\begin{aligned} \mathrm{Tr}\langle\langle \vec{r}; \vec{a} \times \vec{p} \rangle\rangle_\omega = a_x \left[\langle\langle r_z; p_y \rangle\rangle_\omega - \langle\langle r_y; p_z \rangle\rangle_\omega \right] + a_y \left[\langle\langle r_x; p_z \rangle\rangle_\omega - \langle\langle r_z; p_x \rangle\rangle_\omega \right] \\ + a_z \left[\langle\langle r_y; p_x \rangle\rangle_\omega - \langle\langle r_x; p_y \rangle\rangle_\omega \right]. \end{aligned} \tag{23.39}$$

A lesson learned from computations of NMR chemical shieldings [111–113], which exhibit related origin-dependence problems, is that the use of gauge-including atomic orbitals (GIAOs) or London atomic orbitals (LAOs) [114, 115] can overcome the origin dependence of many magnetic-field-dependent properties. GIAOs may be defined as

$$\chi_\nu(\vec{B}; \vec{R}_\nu; \vec{r}) = \exp\left(-\frac{i}{2} (\vec{B} \times \vec{R}_\nu) \cdot \vec{r} \right) \chi(0; \vec{R}_\nu; \vec{r}), \tag{23.40}$$

where $\vec{R}_\nu$ is the coordinate of the nucleus on which the νth basis function resides and $\chi(0; \vec{R}_\nu; \vec{r})$ is the original (Gaussian) basis function. However, in order for GIAOs to

resolve the origin dependence issue in optical rotation computations, the electronic structure model used to compute $\langle\langle \vec{r}; \vec{p} \rangle\rangle_\omega$ must satisfy the corresponding equation-of-motion of the response function [116],

$$\omega\langle\langle \vec{r}; \vec{r} \rangle\rangle_\omega = \langle [\vec{r}, \vec{r}] \rangle_0 + \langle\langle \vec{r}; [\vec{r}, \hat{H}] \rangle\rangle_\omega. \tag{23.41}$$

In that case, when GIAOs are employed, the response function $\langle\langle \vec{r}; \vec{p} \rangle\rangle_\omega$ whose cartesian components appear in Eq. (23.39) is replaced naturally by $\langle\langle \vec{r}; [\vec{r}, H] \rangle\rangle_\omega$, which, by Eq. (23.41), is equal to $-i\omega\langle\langle \vec{r}; \vec{r} \rangle\rangle_\omega$ [31, 117].[2] As a result, the trace in Eq. (23.39) becomes zero because each response function on the right-hand side will involve only components of $\vec{r}$. Unfortunately, the above equation of motion is not generally satisfied by coupled cluster methods [86, 90], even in a complete basis set. Thus GIAOs, while effective for NMR properties, which may be formulated as simple analytic energy derivatives, do not solve the origin problem for coupled cluster theory.

An alternative approach advocated by Grimme et al. [118] and by Pedersen et al. [119] is to use the velocity representation of the electric dipole operator, namely,

$$\mathrm{Tr}\langle\langle \vec{r}; \vec{r} \times \vec{p} \rangle\rangle_\omega = \frac{1}{\omega}\mathrm{Tr}\langle\langle \vec{p}; \vec{r} \times \vec{p} \rangle\rangle_\omega. \tag{23.42}$$

In this case, the trace on the right-hand side of this equation is inherently origin-independent because of the resulting appearance of the symmetric response function $\langle\langle \vec{p}; \vec{p} \rangle\rangle_\omega$ in the analogy to Eq. (23.39), thus forcing the trace to zero. However, the resulting coupled cluster response function does not decay to zero in the static limit as it does in the length representation. Pedersen and co-workers recommended an approach to circumvent this problem by shifting $\langle\langle \vec{p}; \vec{r} \times \vec{p} \rangle\rangle_\omega$ by its static-limit value, $\langle\langle \vec{p}; \vec{r} \times \vec{p} \rangle\rangle_0$, to account for this error. While this approach adds somewhat to the computational cost because of the need to solve an additional set of six perturbed wavefunction equations, the result is a well-behaved, origin-invariant expression for the optical rotation. This method applies equally well to DFT and coupled cluster theory.

23.4. PERFORMANCE

At present, there are two publicly available quantum chemistry program packages capable of computing optical rotation and circular dichroism spectra using coupled cluster theory: DALTON [120] and PSI [121]. The first implementation of coupled cluster optical rotations was reported by Ruud and Helgaker [122] in DALTON in 2002 in an application to H_2O_2 and H_2S_2 as model systems. In 2003, Ruud et al. [9] carried out a larger study of 13 chiral organic molecules for comparison of CC2 and CCSD values of $[\alpha]_D$ to solution-phase experimental data. Our own entry into the field began in 2004 with an independent implementation of the coupled cluster linear response function within the PSI3 package and initial applications to (*S*)-methyloxirane [10] and (*P*)-[4]triangulane [13]. The first

[2] This relationship depends on the use of the commutator relationship

$$[\vec{r}, \hat{H}] = i\vec{p},$$

which holds in the limit of a complete basis set.

coupled cluster computations of circular dichroism spectra appeared earlier in 1999 with an application to the ethylene chromophore of (−)-*trans*-cyclooctene [89]. We have carried out our own efforts in this regard with applications to (*S*)-2-chloropropionitrile [21], (*S*)-methylthiirane [22], and others [123, 124].

Since these first steps, numerous computations of coupled cluster level optical rotation and circular dichroism have appeared in the literature. One of the most systematic studies to date was reported by Crawford and Stephens in 2008 [15], who examined 12 paradigmatic chiral molecules—including *cis*-pinane, α- and β-pinene, nopinone, 2-brendanone, and more. The molecules were chosen because their experimental sodium D-line specific rotations are well established, but also because Stephens et al. had observed that B3LYP [28, 125, 126] yields incorrect signs for half of the molecules in the set [127]. The coupled cluster computations for these relatively large molecules consumed roughly two years of CPU time and yielded a rather disappointing result: The average absolute errors between DFT and CCSD were nearly the same, and both were poor [28.4 and 25.4 deg $dm^{-1}(g/mL)^{-1}$, respectively]. While several sources of error were considered, including basis sets, electron correlation, and vibrational effects, the most significant missing ingredient in the quantum chemical models was the lack of solvent, which is well known to strongly perturb specific rotations and other chiroptical properties in many cases [128, 129].

Therefore, the most robust studies of optical rotation to date have compared coupled cluster predictions to new gas-phase data from ultrasensitive cavity ring-down polarimetry (CRDP) measurements pioneered by the Vaccaro group at Yale [130, 131]. In a 2006 study [21] of (*S*)-2-chloropropionitrile (Figure 23.1a), Kowalczyk et al. found that CCSD-level optical rotations (with the modified velocity gauge) with large basis sets compare superbly to newly published CRDP data across the entire range of wavelengths. B3LYP, on the other hand, gives rotations too large by approximately a factor of two due to its tendency both to underestimate the key excitation energies appearing in the the denominator of Eq. (23.18) and to overestimate the corresponding rotational strengths in the numerator, as made clear by the simulated circular dichroism spectra in Figure 23.1b.

A 2004 study of (*S*)-methyloxirane by Tam et al. revealed some additional pitfalls to accurate predictions of optical rotation in small molecules. As summarized in Figure 23.2, B3LYP and CCSD optical rotations were found to differ significantly, with the former exhibiting a much earlier zero-crossing than the latter as the wavelength of the incident light is decreased towards the lowest excited state. However, although the DFT value for the 355 nm rotation is positive and thus in qualitative agreement with the experimental value of +7.5 deg/[dm (g/mL)] [131], the good comparison occurs only because of the B3LYP model's concomitant *underestimation* of the lowest Rydberg excitation energy of methyloxirane, yielding too small of a numerator in Eq. (23.18) (just as for 2-chloropropionitrile). On the other hand, while the CCSD approach gives the correct excitation energy, the shape of the optical rotation pole is clearly underestimated, leading to an incorrect sign of the rotation at 355 nm. Subsequent studies by Ruud and Zanasi [132] and by Kongsted et al. [133] demonstrated that incorporation of both vibrational corrections and higher levels of electron correlation shift the coupled cluster rotation at 355 nm to within the experimental error bars, giving the one of first indications of the potential importance of molecular vibrations on optical rotation.

Conformational flexibility presents even greater challenges. The most common approach is to carry out a simple Boltzmann average over the property of interest computed at the equilibrium structure of each relevant conformer, using weighting factors obtained from theoretical or experimental estimates of the conformer populations

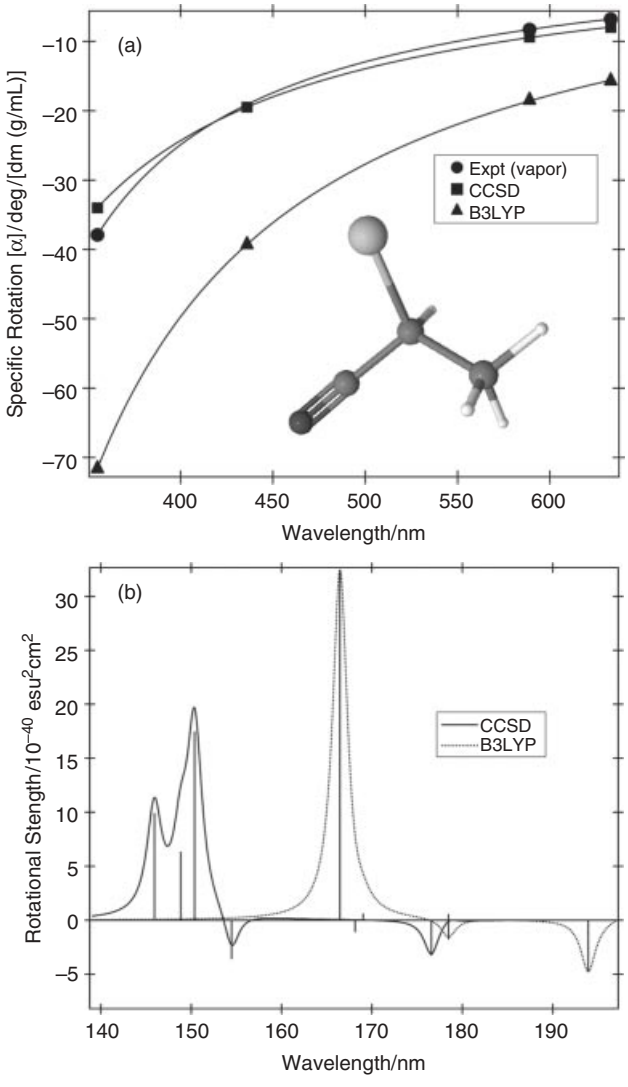

Figure 23.1. (a) Theoretical and experimental gas-phase optical rotatory dispersion spectra and (b) theoretical circular dichroism spectra of (*S*)-(−)-2-chloropropionitrile. Experimental data taken from ref. 131 and theoretical data taken from reference 21.

at the desired temperature. This method is often used for electronic absorption or vibrational spectra, where the transition energies and strengths do not typically vary substantially between conformers. However, this is not the case for circular dichroism spectra or specific rotation, for which numerous studies have demonstrated their high degree of sensitivity to even small changes in key torsional angles. Polavarapu and co-workers [134, 135] examined this sensitivity in their analysis of H_2O_2, H_2S_2, allene, and dichloroallene, while Wiberg et al. [136–138] and Crawford and co-workers [123, 139] have explored such dihedral-angle dependence of specific rotation in substituted butanes, butenes, and epichlohydrin in comparison to gas-phase CRDP data. All such studies report dramatic differences in chiroptical response between conformers, including differences of sign leading to cancellation in the Boltzmann averaging procedure.

For example, in a comparison of CCSD-specific rotations to new gas-phase data for 3-chloro-1-butene (see Figure 23.3), Crawford and co-workers [123] obtained

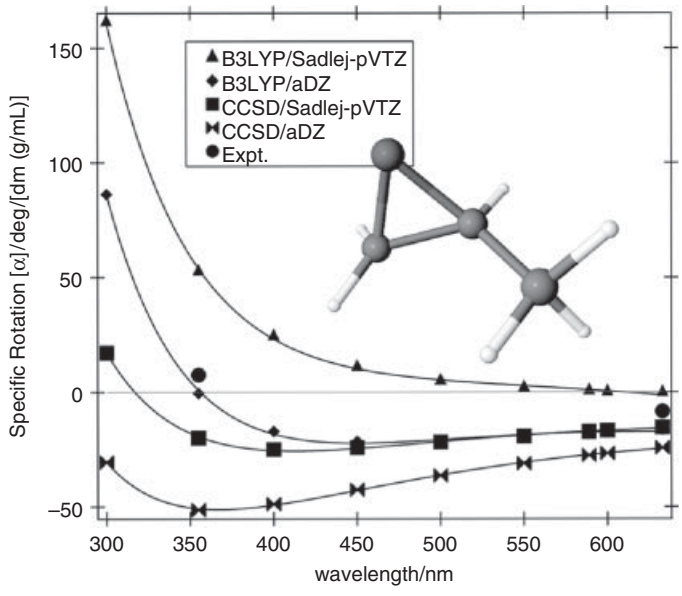

Figure 23.2. Theoretical optical rotatory dispersion curves of (*S*)-methyloxirane. Experimental data at 355 and 633 nm are indicated by closed, black circles. Experimental data were taken from reference 131 and theoretical data from reference 10.

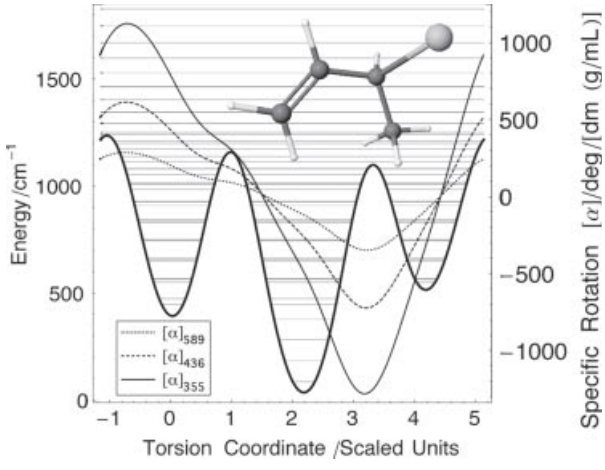

Figure 23.3. Carbon backbone torsional potential of and associated vibrational energy-level structure 3-chloro-1-butene (left-hand axis); CCSD/aug-cc-pVDZ optical rotation of the (*R*)-enantiomer as a function of the torsional coordinate (right-hand axis). The modified velocity gauge representation was used to compute the specific rotations. Data taken from reference 142.

theoretical estimates of the relative Gibbs free energies of its three competing conformers using the G3 composite method [140] and complete-basis-set extrapolations of CCSD(T) energies [141]. Wilson et al. [131] reported gas-phase specific rotations for (*S*)-3-chloro-1-butene of $[\alpha]_{633} = 53.3 \pm 1.0$ deg dm^{-1}(g/mL)$^{-1}$ and $[\alpha]_{355} = 259.4 \pm 1.0$ deg dm^{-1}(g/mL)$^{-1}$. CCSD computations with a triple-zeta basis set on the nonhydrogen atoms and the modified velocity gauge representation yield corresponding rotations of 51.0 and 248.1 deg dm^{-1}(g/mL)$^{-1}$, respectively, in excellent agreement with experiment. CCSD length gauge representation results are poorer at 72.5 and 336.1 deg dm^{-1}(g/mL)$^{-1}$, while B3LYP disagrees further at 86.5 and 469.9 deg dm^{-1}(g/mL)$^{-1}$.

However, the question as to the fundamental validity of the simple Boltzmann approach used above was considered by Crawford and Allen [142]. The Boltzmann averaging technique requires three principal assumptions: (1) The vibrational wavefunctions are localized within each conformer's potential well; (2) the specific rotation does

not vary with vibrational quantum number; and (3) the vibrational partition functions for the conformers are identical. Using (*R*)-3-chloro-1-butene as a model, Crawford and Allen constructed an analytic torsional potential for the carbon backbone using a Fourier series fit to the zero-point vibrationally corrected intrinsic reaction coordinate, and solved the corresponding one-dimensional vibrational Schrödinger equation (Figure 23.3). They then used the resulting vibrational wavefunctions to compute a more rigorous vibrational Boltzmann average. They found that, while the two approaches compared well over a fairly wide range of temperatures, the success of the simple Boltzmann approach is greatly aided by a favorable cancellation of errors between the three approximations. Only further studies will reveal if this cancellation is reliable.

A more systematic comparison to gas phase data was reported recently by Pedersen et al. [143], who examined the impact of basis sets, electron correlation, and molecular vibrations on optical rotation in both rigid and conformationally flexible molecules, including *cis*-pinane, α- and β-pinenes, fenchone, 2-chloropropionitrile, limonene, and 3-chloro-1-butene. In particular, they confirmed that coupled cluster linear-response methods provide the best available comparison to experimental gas-phase specific rotations with an average absolute error of 29% (standard deviation of 11%) versus an average absolute error of 111% for B3LYP (standard deviation of 30%), though the sample size of only seven molecules is likely too small to consider the results statistically significant. In addition, zero-point vibrational effects, while important for some compounds, are not as substantial a contributor to the total rotations as electron correlation. Furthermore, they reported that DFT methods can provide a reasonable estimate of vibrational corrections to coupled-cluster-level equilibrium specific rotations, thus yielding a more computationally efficient approach.

While coupled cluster predictions have been found to perform well relative to gas-phase chiroptical measurements in most cases, there are still mysteries to be considered. For example, Vaccaro and co-workers have obtained a CRDP measurements of $[\alpha]_{355} = 180.3$ deg dm^{-1}(g/mL)$^{-1}$ for the bicyclic ketone, (*1S,4R*)-fenchone. However, quantum chemical studies carried out by Pedersen et al. [143] differ substantially with experiment, yet agree with each other, with B3LYP, CC2, and CCSD yielding values of 452.7, 419.4, and 455.5 deg dm^{-1}(g/mL)$^{-1}$, respectively. The discrepancy does not appear to be related to basis set or vibrational effects, because B3LYP-based harmonic vibrational corrections using double- and triple-zeta basis sets are only 22.6 and 19.6 deg dm^{-1}(g/mL)$^{-1}$, respectively.

Another bicyclic ketone that challenges theory is (*1S,4S*)-norbornenone. As noted originally by Ruud et al. [9], DFT (specifically B3LYP) yields a specific rotation of $[\alpha]_D = -1216$ deg dm^{-1}(g/mL)$^{-1}$, rather close to the (liquid phase) experimental value of -1146 deg dm^{-1}(g/mL)$^{-1}$, but CCSD (using the origin-dependent length gauge) fails dramatically, giving $[\alpha]_D = -741$ deg dm^{-1}(g/mL)$^{-1}$. Our later studies have shown that use of the origin-independent modified velocity gauge with CCSD only worsens the discrepancy, giving -558 deg dm^{-1}(g/mL)$^{-1}$ [15]. Mort and Autschbach reported [144] that DFT-based vibrational corrections shift the computed values only by approximately -53 deg dm^{-1}(g/mL)$^{-1}$, and our own unpublished computations using larger basis sets (as well as incrementing the number and type of functions on the carbonyl and alkene moieties) have shown no significant changes. The remaining sources of the discrepancy include higher-level correlation effects (triples and higher), as well as the possibility of large differences between gas- and liquid-phase rotations. Additional theoretical and experimental studies currently underway may help to explain the disagreement and inform the development of improved computational methods.

23.5. FUTURE DIRECTIONS

While the above studies demonstrate that, apart from select problem cases such as fenchone, the coupled cluster linear response method is currently the most accurate and reliable approach for predicting electronic chiroptical properties in the gas-phase, clearly the missing piece of the puzzle is a correspondingly accurate and reliable model of such properties in liquids. A number of important analyses of solvent effects on optical rotation have been carried out using DFT, starting with the work by Mennucci et al. [145], who developed a combination of the polarizable continuum model (PCM) with B3LYP. They reported sodium D-line specific rotations in reasonable agreement with corresponding measurements in cyclohexane, acetone, methanol, and acetonitrile, but significant errors appeared for others, such as CCl_4, benzene, and $CHCl_3$. Given the inherent limitations in their model, they attributed the discrepancies to nonelectrostatic effects, and the role of the exchange-correlation functional in the errors they observed remains unknown. Pecul et al. [146] reported analogous DFT-based PCM studies of electronic circular dichroism in 2005 for methyloxirane, camphor, norbornenone, and fenchone. They found that the reliability of their predictions depended not only on the shortcomings of available exchange-correlation functionals, but also on the type of transition in question, with Rydberg-type excitations and the $n \rightarrow \pi^*$ transitions of norcamphor and norbornenone indicated as especially problematic, perhaps due to specific solute–solvent interactions.

Kongsted et al. [133, 147] published extensive coupled cluster analyses for the optical rotation of (*S*)-methyloxirane under solvated conditions, simulated using a continuum dielectric medium surrounding a spherical solute cavity [147]. Despite the inclusion of very high levels of electron correlation (including estimates of connected triple excitations [70, 71]), this approach failed to reproduce experimental trends, yielding specific rotations at 355 nm with the wrong sign as compared to measurements in cyclohexane. More recently, Kongsted and Ruud [148] carried out a DFT-PCM/B3LYP analysis of methyloxirane specific rotations that included both solvent and zero-point vibrational effects. They found reasonable agreement in solvent shifts for cyclohexane, but not for acetonitrile and water, which they again attributed to specific molecular interactions not described by continuum-based models.

In 2008, Wiberg et al. examined the remarkable difference between vapor- and liquid-phase optical rotation in 2,3-pentadiene and 2,3-hexadiene [124]. Vapor-phase cavity-ring-down polarimetry (CRDP) measurements yielded rotations a factor of two larger than those in the liquid-phase, which vary little with the choice of solvent (or even the neat state). While coupled cluster computations agree well with the vapor-phase data (Figure 23.4), Wiberg et al. speculated that torsional deformation of the solute in a condensed medium could lead to a shift in the specific rotation. However, Monte Carlo simulations of the neat liquid yielded no evidence of such a structural change. Existing theoretical models were not capable of assessing the direct impact of the medium on the chiroptical response of the solute, and thus no final conclusions were possible as to the detailed reason(s) for the divergence between the vapor- and condensed-phase results.

Dynamic effects were considered by Beratan and co-workers [149, 150], who carried out ground-breaking combined continuum and molecular dynamics (MD) simulations of methyloxirane in clusters of water [149] and of benzene [150], obtaining DFT specific rotations as averages over snapshots taken along the MD trajectories. They obtained very good qualitative agreement with experiment in both cases and found that, while the chiroptical response of the solute molecule was found to dominate in water, the solvent cavity contributed at least as much to the optical rotation in benzene. However, given

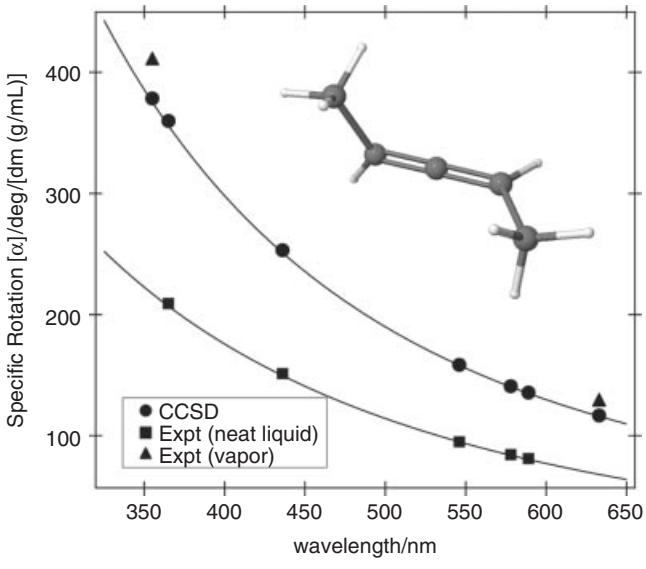

Figure 23.4. Experimental and theoretical optical rotatory dispersion spectra of (*P*)-(+)-2,3-pentadiene (dimethylallene). The specific rotation in the neat liquid (and numerous polar and nonpolar solvents) is roughly half that of the vapor-phase, and the latter is reproduced faithfully by coupled cluster theory. All data taken from reference 124.

that DFT has been shown to provide fortuitous agreement with gas-phase experimental data in the case of methyloxirane [10, 132, 147, 148], the reliability of this approach remains in doubt.

These studies suggest that the path forward requires systematic combination of coupled cluster treatments with both explicit and implicit solvent models. The QM/MM approach under development by Christiansen, Kongsted, Mikkelsen, and co-workers [151, 152] is certainly promising, and perhaps with additional coupling to the effective fragment potential approach of Gordon and co-workers [153, 154] will provide an improved description of the solvent. Clearly, much work remains before we can finally achieve the ultimate goal of a reliable computational tool for the prediction of optical rotation and circular dichroism spectra in condensed phases.

ACKNOWLEDGMENTS

This work was supported by grants from the U.S. National Science Foundation, including a CAREER award (CHE-0133174), two continuing grants (CHE-0715185 and CHE-1058420), and a multiuser chemistry research, instrumentation, and facilities award (CRIF:MU, CHE-0741927). Additional support was provided by a subcontract from Oak Ridge National Laboratory by the Scientific Discovery through Advanced Computing (SciDAC) program of the U.S. Department of Energy, the division of Basic Energy Science, Office of Science, under contract number DE-AC05-00OR22725.

REFERENCES

1. J. A. Pople, Theoretical models for chemistry, in DW. Smith and W. B. McRae, eds., *Energy, Structure, and Reactivity*, John Wiley & Sons, New York, **1973**, pp. 51–61.
2. H. F. Schaefer, *J. Mol. Struct. (Theochem)* **1997**, *398*, 199–209.

3. L. D. Barron, *Molecular Light Scattering and Optical Activity*, 2nd edition, Cambridge University Press, Cambridge, U.K., ed., **2004**.
4. P. L. Polavarapu, *Mol. Phys*. **1997**, *91*(3), 551–554.
5. J. R. Cheeseman, M. J. Frisch, F. J. Devlin, P. J. Stephens, *Chem. Phys. Lett*. **1996**, *252*, 211–220.
6. J. R. Cheeseman, M. J. Frisch, F. J. Devlin, P. J. Stephens, *J. Phys. Chem. A* **2000**, *104*, 1039–1046.
7. P. J. Stephens, F. J. Devlin, J. R. Cheeseman, M. J. Frisch, *J. Phys. Chem. A* **2001**, *105*(22), 5356–5371.
8. S. Grimme, *Chem. Phys. Lett*. **2001**, *339*, 380–388.
9. K. Ruud, P. J. Stephens, F. J. Devlin, P. R. Taylor, J. R. Cheeseman, M. J. Frisch, *Chem. Phys. Lett*. **2003**, *373*, 606–614.
10. M. C. Tam, N. J. Russ, T. D. Crawford, *J. Chem. Phys*. **2004**, *121*, 3550–3557.
11. C. Diedrich, S. Kausemann, S. Grimme, *J. Comp. Meth. Sci. Eng*. **2004**, *4*, 1–8.
12. M. Pecul, K. Ruud, *Adv. Quantum Chem*., **2005**, *50*, 185–212.
13. T. D. Crawford, L. S. Owens, M. C. Tam, P. R. Schreiner, H. Koch, *J. Am. Chem. Soc*., **2005**, *127*, 1368–1369.
14. T. D. Crawford, *Theor. Chem. Acc*. **2006**, *115*, 227–245.
15. T. D. Crawford, P. J. Stephens, *J. Phys. Chem. A* **2008**, *112*, 1339–1345.
16. S. Grimme, S. D. Peyerimhoff, S. Bartram, F. Vögtle, A. Breest, J. Hormes, *Chem. Phys. Lett*. **1993**, *213*(1–2), 32–40.
17. F. Pulm, J. Schramm, J. Hormes, S. Grimme, S. D. Peyerimhoff, *Chem. Phys*. **1997**, *224*, 143–155.
18. S. Grimme, *Chem. Phys. Lett*. **1996**, *259*, 128–137.
19. S. Grimme, J. Harren, A. Sobanski, F. Vögtle, *Eur. J. Org. Chem*. **1998**, pages 1491–1509.
20. M. Pecul, K. Ruud, T. Helgaker, *Chem. Phys. Lett*. **2004**, *388*, 110–119.
21. T. D. Kowalczyk, M. L. Abrams, T. D. Crawford, *J. Phys. Chem. A* **2006**, *110*, 7649–7654.
22. T. D. Crawford, M. C. Tam, M. L. Abrams, *Mol. Phys*. **2007**, *105*, 2607–2617.
23. T. D. Crawford, M. C. Tam, M. L. Abrams, *J. Phys. Chem. A* **2007**, *111*, 12057–12068.
24. P. J. Stephens, *J. Phys. Chem*. **1985**, *89*, 748–752.
25. P. J. Stephens, K. J. Jalkanene, F. J. Devlin, C. F. Chabalowski, *J. Phys. Chem*. **1993**, *97*, 6107–6110.
26. P. J. Stephens, F. J. Devlin, C. S. Ashvar, C. F. Chabalowski, M. J. Frisch, *Faraday Discuss*. **1994**, *99*, 103–119.
27. K. L. Bak, P. Jørgensen, T. Helgaker, K. Ruud, *Faraday Discuss*. **1994**, *99*, 121–129.
28. P. J. Stephens, F. J. Devlin, C. F. Chabalowski, M. J. Frisch, *J. Phys. Chem*. **1994**, *98*(45), 11623–11627.
29. P. J. Stephens and F. J. Devlin, *Chirality* **2000**, *12*, 172–179.
30. T. B. Freedman, X. Cao, R. K. Dukor, L. A. Nafie, *Chirality* **2003**, *15*, 743–758.
31. T. Helgaker, K. Ruud, K. L. Bak, P. Jørgensen, J. Olsen, *Faraday Discuss*. **1994**, *99*, 165–180.
32. L. A. Nafie, *Annu. Rev. Phys. Chem*. **1997**, *48*, 357–386.
33. P. Bouř, *Chem. Phys. Lett*. **1998**, *288*, 363–370.
34. P. Bouř, *J. Comp. Chem*. **2001**, *22*(4), 426–435.
35. W. Hug, *Chem. Phys*. **2001**, *264*, 53–69.
36. W. Hug, G. Zuber, A. de Meijere, A. E. Khlebnikov, H.-J. Hansen, *Helv. Chim. Acta* **2001**, *84*, 1–21.
37. K. Ruud, T. Helgaker, P. Bouř, *J. Phys. Chem. A* **2002**, *106*, 7448–7455.

38. M. Pecul, A. Rizzo, *Mol. Phys*. **2003**, *101* (13), 2073–2081.
39. L. D. Barron, L. Hecht, I. H. McColl, E. W. Blanch, *Mol. Phys*. **2004**, *102* (8), 731–744.
40. M. Pecul, K. Ruud, *Int. J. Quantum Chem*. **2005**, *104* (5), 816–829.
41. M. Pecul, E. Larnparska, C. Cappelli, L. Frediani, K. Ruud, *J. Phys. Chem. A* **2006**, *110* (8), 2807–2815.
42. M. Pecul, *Chirality* **2010**, *21*, 98–104.
43. E. L. Eliel, S. H. Wilen, *Stereochemistry of Organic Compounds*, John Wiley & Sons, New York, **1994**.
44. R. J. Bartlett, M. Musial, *Rev. Mod. Phys*. **2007**, *79*, 291–352.
45. I. Shavitt, R. J. Bartlett, *Many-Body Methods in Chemistry and Physics: MBPT and Coupled-Cluster Theory*, Cambridge University Press, Cambridge, **2009**.
46. T. D. Crawford, H. F. Schaefer, An introduction to coupled cluster theory for computational chemists, in K. B. Lipkowitz and D. B. Boyd, eds., *Reviews in Computational Chemistry*, Vol. 14, VCH Publishers, New York, **2000**, Chapter 2, pp. 33–136.
47. T. J. Lee, G. E. Scuseria; Achieving chemical accuracy with coupled-cluster theory, in *Quantum Mechanical Electronic Structure Calculations with Chemical Accuracy*, S. R. Langhoff, ed., Kluwer Academic Publishers, Dordrecht, **1995**, pp. 47–108.
48. T. Helgaker, T. A. Ruden, P. Jørgensen, J. Olsen, W. Klopper, *J. Phys. Org. Chem* **2004**, *17* (11), 913–933.
49. F. Coester, H. Kümmel, *Nucl. Phys*. **1960**, *17*, 477–485.
50. J. Čížek, *J. Chem. Phys*. **1966**, *45*, 4256–4266.
51. J. Čížek, *Adv. Chem. Phys*. **1969**, *14*, 35.
52. J. Čížek, J. Paldus, *Int. J. Quantum Chem. Symp*. **1971**, *5*, 359.
53. J. Paldus, J. Čížek, *Adv. Quantum Chem*. **1975**, *9*, 105–197.
54. The name "coupled cluster" was first used by Frank A. Harris of the University of Utah, according to H. Monkhorst, Quantum Theory Project, University of Florida.
55. R. J. Bartlett, *Annu. Rev. Phys. Chem*. **1981**, *32*, 359–401.
56. R. J. Bartlett, C. E. Dykstra, J. Paldus, Coupled-cluster methods for molecular calculations, in *Advanced Theories and Computational Approaches to the Electronic Structure of Molecules*, C. E. Dykstra, eds., D. Reidel, Dordrecht, **1984**, pp. 127–159.
57. R. J. Bartlett, *J. Phys. Chem*. **1989**, *93*, 1697–1708.
58. R. J. Bartlett, Coupled-cluster theory: An overview of recent developments, in *Modern Electronic Structure Theory*, D. R. Yarkony, eds., Vol. 2 of *Advanced Series in Physical Chemistry*, World Scientific, Singapore, **1995**, Chapter 16, pp. 1047–1131.
59. R. J. Bartlett, How and why coupled-cluster theory became the pre-eminent method in an *ab initio* quantum chemistry, in *Theory and Applications of Computational Chemistry: The First Forty Years*, C. Dykstra et al., eds., Elsevier, New York, **2005**, Chapter 42, pages 1191–1221.
60. R. J. Bartlett, G. D. Purvis, *Int. J. Quantum Chem. Symp*. **1978**, *14*, 561–581.
61. J. A. Pople, R. Krishnan, H. B. Schlegel, J. S. Binkley, *Int. J. Quantum Chem. Symp*. **1978**, *14*, 545–560.
62. G. D. Purvis, R. J. Bartlett, *J. Chem. Phys*. **1982**, *76*, 1910–1918.
63. J. Noga, R. J. Bartlett, *J. Chem. Phys*. **1987**, *86* (12), 7041–7050. Erratum: **1988**, *89*, 3401.
64. S. A. Kucharski, R. J. Bartlett, *J. Chem. Phys*. **1992**, *97* (6), 4282–4288.
65. M. Musial, S. A. Kucharski, R. J. Bartlett, *J. Chem. Phys*., **2002**, *116* (11), 4382–4388.
66. J. Noga, R. J. Bartlett, M. Urban, *Chem. Phys. Lett*. **1987**, *134* (2), 126–132.
67. R. J. Bartlett, J. D. Watts, S. A. Kucharski, J. Noga, *Chem. Phys. Lett*. **1990**, *165* (6), 513–522. Erratum: **1990**, *167*, 609.

68. K. Raghavachari, G. W. Trucks, J. A. Pople, M. Head-Gordon, *Chem. Phys. Lett*. **1989**, *157*, 479.
69. O. Christiansen, H. Koch, P. Jørgensen, *Chem. Phys. Lett*. **1995**, *243*, 409–418.
70. H. Koch, O. Christiansen, P. Jørgensen, A. M. S. de Merás, T. Helgaker, *J. Chem. Phys*. **1997**, *106*(5), 1808–1818.
71. O. Christiansen, H. Koch, P. Jørgensen, *J. Chem. Phys*. **1995**, *103*(17), 7429–7441.
72. H. J. Monkhorst, *Int. J. Quantum Chem. Symp*. **1977**, *11*, 421–432.
73. D. Mukherjee, P. K. Mukherjee, *Chem. Phys*., **1979**, *39*, 325–335.
74. S. Ghosh, D. Mukherjee, S. N. Bhattacharyya, *Chem. Phys*. **1982**, *72*, 161–176.
75. H. Sekino, R. J. Bartlett, *Int. J. Quantum Chem. Symp*. **1984**, *18*, 255.
76. J. F. Stanton, R. J. Bartlett, *J. Chem. Phys*. **1993**, *98*(9), 7029–7039.
77. J. F. Stanton, R. J. Bartlett, *J. Chem. Phys*. **1993**, *99*, 5178–5183.
78. H. Koch, P. Jørgensen, *J. Chem. Phys*. **1990**, *93*(5), 3333–3344.
79. H. Koch, H. J. Aa. Jensen, P. Jørgensen, T. Helgaker, *J. Chem. Phys*. **1990**, *93*(5), 3345–3350.
80. R. Kobayashi, H. Koch, P. Jørgensen, *Chem. Phys. Lett*. **1994**, *219*, 30–35.
81. H. Koch, R. Kobayashi, P. Jørgensen, *Int. J. Quantum Chem*. **1994**, *49*, 835.
82. H. Koch, O. Christiansen, P. Jørgensen, J. Olsen, *Chem. Phys. Lett*. **1995**, *244*, 75–82.
83. O. Christiansen, H. Koch, A. Halkier, P. Jørgensen, T. Helgaker, A. S. de Merás, *J. Chem. Phys*. **1996**, *105*(16), 6921–6931.
84. O. Christiansen, H. Koch, P. Jørgensen, *J. Chem. Phys*. **1996**, *105*(4), 1451–1459.
85. O. Christiansen, A. Halkier, H. Koch, P. Jørgensen, T. Helgaker, *J. Chem. Phys*. **1998**, *108*(7), 2801–2816.
86. T. B. Pedersen, H. Koch, *J. Chem. Phys*. **1997**, *106*(19), 8059–8072.
87. T. B. Pedersen, H. Koch, *Chem. Phys. Lett*. **1998**, *293*, 251–260.
88. T. B. Pedersen, H. Koch, *J. Chem. Phys*. **1998**, *108*(13), 5194–5204.
89. T. B. Pedersen, H. Koch, K. Ruud, *J. Chem. Phys*. **1999**, *110*(6), 2883–2892.
90. T. B. Pedersen, H. Koch, C. Hättig, *J. Chem. Phys*. **1999**, *110*(17), 8318–8327.
91. T. B. Pedersen, H. Koch, *J. Chem. Phys*. **2000**, *112*(5), 2139–2147.
92. T. B. Pedersen, B. Fernández, H. Koch, *J. Chem. Phys*. **2001**, *114*(16), 6983–6993.
93. A. Szabo, N. S. Ostlund, *Modern Quantum Chemistry: Introduction to Advanced Electronic Structure Theory*, 1st ed., McGraw-Hill, New York, **1989**.
94. C. D. Sherrill, H. F. Schaefer, *Adv. Quantum Chem*. **1999**, *34*, 143–269.
95. S. A. Kucharski, R. J. Bartlett, *Adv. Quauntum Chem*. **1986**, *18*, 281–344.
96. F. E. Harris, H. J. Monkhorst, D. L. Freeman, *Algebraic and Diagrammatic Methods in Many-Fermion Theory*, Oxford University Press, New York, **1992**.
97. T. Helgaker, P. Jørgensen, N. C. Handy, *Theor. Chim. Acta* **1989**, *76*, 227–245.
98. T. Helgaker, P. Jørgensen, J. Olsen, *Molecular Electronic Structure Theory*, John Wiley & Sons, New York, **2000**.
99. L. Adamowicz, W. D. Laidig, R. J. Bartlett, *Int. J. Quantum Chem. Symp*. **1984**, *18*, 245.
100. A. C. Scheiner, G. E. Scuseria, J. E. Rice, T. J. Lee, H. F. Schaefer, *J. Chem. Phys*. **1987**, *87*(9), 5361.
101. J. Gauss, W. J. Lauderdale, J. F. Stanton, J. D. Watts, R. J. Bartlett, *Chem. Phys. Lett*. **1991**, *182*(3,4), 207–215.
102. R. F. Bishop, H. G. Kümmel, *Physics Today* **1987**, *40*(3), 52–60.
103. D. J. Caldwell, H. Eyring, *The Theory of Optical Activity*, John Wiley & Sons, New York, **1971**.

104. J. Linderberg, Y. Öhrn, *Propagators in Quantum Chemistry*, 2nd ed., John Wiley & Sons, Hoboken, NJ, **2004**.
105. J. Olsen, P. Jørgensen, *J. Chem. Phys*. **1985**, *82*(7), 3235–3264.
106. J. Olsen, P. Jørgensen, Time-dependent response theory with applications to self-consistent field and multiconfigurational self-consistent field wave functions, in *Modern Electronic Structure Theory*, D. Yarkony, ed., Vol. 2 of *Advanced Series in Physical Chemistry*, World Scientific, Singapore, **1995**, Chapter 13, pp. 857–990.
107. O. Christiansen, P. Jørgensen, and C. Hättig, *Int. J. Quantum Chem*. **1998**, *68*, 1–52.
108. T. B. Pedersen, Introduction to Response Theory, in *Handbook of Computational Chemistry*, Vol. 1, A. J. Sadlej and J. Leszczynski (Eds.). Contribution accepted for publication by Springer, **2011**.
109. H. Sekino, R. J. Bartlett, *Adv. Quantum Chem*. **1999**, *35*, 149–173.
110. T. D. Crawford, H. Sekino, *Prog. Theor. Chem. Phys*. **2009**, *19*, 225–239.
111. R. Ditchfield, *Mol. Phys*. **1974**, *27*(4), 789–807.
112. K. Wolinski, J. F. Hinton, P. Pulay, *J. Am. Chem. Soc*. **1990**, *112*(23), 8251–8260.
113. J. Gauss, J. F. Stanton, *J. Chem. Phys*. **1995**, *103*(9), 3561–3577.
114. F. London, *J. Phys. Radium* **1937**, *8*, 397–409.
115. T. Helgaker, P. Jørgensen, *J. Chem. Phys*. **1991**, *95*(4), 2595–2601.
116. P. Jørgensen, J. Simons, *Second Quantization-Based Methods in Quantum Chemistry*, Academic Press, New York, **1981**.
117. K. L. Bak, A. E. Hansen, K. Ruud, T. Helgaker, J. Olsen, P. Jørgensen, *Theor. Chim. Acta* **1995**, *90*, 441–458.
118. S. Grimme, F. Furche, R. Ahlrichs, *Chem. Phys. Lett*. **2002**, *361*, 321–328.
119. T. B. Pedersen, H. Koch, L. Boman, A. M. J. S. de Meras, *Chem. Phys. Lett*. **2004**, *393*(4–6), 319–326.
120. Dalton, a molecular electronic structure program, Release 2.0 (**2005**), written by T. Helgaker, H. J. Aa. Jensen, P. Jørgensen, J. Olsen, K. Ruud, H. Å gren, A. A. Auer, K. L. Bak, V. Bakken, O. Christiansen, S. Coriani, P. Dahle, E. K. Dalskov, T. Enevoldsen, B. Fernandez, C. Hättig, K. Hald, A. Halkier, H. Heiberg, H. Hettema, D. Jonsson, S. Kirpekar, R. Kobayashi, H. Koch, K. V. Mikkelsen, P. Norman, M. J. Packer, T. B. Pedersen, T. A. Ruden, A. Sanchez, T. Saue, S. P. A. Sauer, B. Schimmelpfennig, K. O. Sylvester-Hvid, P. R. Taylor, and O. Vahtras.
121. T. D. Crawford, C. D. Sherrill, E. F. Valeev, J. T. Fermann, R. A. King, M. L. Leininger, S. T. Brown, C. L. Janssen, E. T. Seidl, J. P. Kenny, W. D. Allen, *J. Comp. Chem*. **2007**, *28*, 1610–1616.
122. K. Ruud, T. Helgaker, *Chem. Phys. Lett*. **2002**, *352*, 533–539.
123. M. C. Tam, M. L. Abrams, T. D. Crawford, *J. Phys. Chem. A*, **2007**, *111*(44), 11232–11241.
124. K. B. Wiberg, Y.-g. Wang, S. M. Wilson, P. H. Vaccaro, W. L. Jorgensen, T. D. Crawford, M. L. Abrams, J. R. Cheeseman, M. Luderer, *J. Phys. Chem. A* **2008**, *112*, 2415–2422.
125. C. Lee, W. Yang, R. G. Parr, *Phys. Rev. B*. **1988**, *37*, 785–789.
126. A. D. Becke, *J. Chem. Phys*. **1993**, *98*, 5648–5652.
127. P. J. Stephens, D. M. McCann, J. R. Cheeseman, M. J. Frisch, *Chirality* **2005**, *17*, S52–S64.
128. N. Berova, K. Nakanishi, R. W. Woody, eds., *Circular Dichroism: Principles and Applications*, 2nd ed., John Wiley & Sons, New York, **2000**.
129. Y. Kumata, J. Furukawa, T. Fueno, *Bull. Chem. Soc. Japan* **1970**, *43*(12), 3920–3921.
130. T. Müller, K. B. Wiberg, P. H. Vaccaro, *J. Phys. Chem. A* **2000**, *104*, 5959–5968.
131. S. M. Wilson, K. B. Wiberg, J. R. Cheeseman, M. J. Frisch, P. H. Vaccaro, *J. Phys. Chem. A* **2005**, *109*(51), 11752–11764.
132. K. Ruud, R. Zanasi, *Angew. Chem. Int. Ed. Engl*. **2005**, *44*(23), 3594–3596.

133. J. Kongsted, T. B. Pedersen, L. Jensen, Aa. E. Hansen, K. V. Mikkelsen, *J. Am. Chem. Soc*. **2006**, *128*(3), 976–982.
134. P. L. Polavarapu, D. K. Chakraborty, K. Ruud, *Chem. Phys. Lett*. **2000**, *319*, 595–600.
135. F. Wang, P. L. Polavarapu, *J. Phys. Chem. A* **2000**, *104*, 6189–6196.
136. K. B. Wiberg, P. H. Vaccaro, J. R. Cheeseman, *J. Am. Chem. Soc*. **2003**, *125*, 1888–1896.
137. K. B. Wiberg, Y. G. Wang, P. H. Vaccaro, J. R. Cheeseman, G. Trucks, M. J. Frisch, *J. Phys. Chem. A* **2004**, *108*(1), 32–38.
138. K. B. Wiberg, Y.-G. Wang, P. H. Vaccaro, J. R. Cheeseman, M. R. Luderer, *J. Phys. Chem. A* **2005**, *109*(15), 3405–3410.
139. M. C. Tam, T. D. Crawford, *J. Phys. Chem. A* **2006**, *110*, 2290–2298.
140. L. A. Curtiss, K. Raghavachari, *Theor. Chem. Acc*. **2002**, *108*, 61–70.
141. A. Halkier, T. Helgaker, P. Jørgensen, W. Klopper, H. Koch, J. Olsen, A. K. Wilson, *Chem. Phys. Lett*. **1998**, *286*(3–4), 243–252.
142. T. D. Crawford, W. D. Allen, *Mol. Phys*. **2009**, *107*, 1041–1057.
143. T. B. Pedersen, J. Kongsted, T. D. Crawford, *Chirality* **2009**, *21*, S68–S75.
144. B. C. Mort and J. Autschbach, *J. Phys. Chem. A* **2005**, *109*(38), 8617–8623.
145. B. Mennucci, J. Tomasi, R. Cammi, J. R. Cheeseman, M. J. Frisch, F. J. Devlin, S. Gabriel, P. J. Stephens, *J. Phys. Chem. A* **2002**, *106*(25), 6102–6113.
146. M. Pecul, D. Marchesan, K. Ruud, S. Coriani, *J. Chem. Phys*. **2005**, *122*(2), 024106.
147. J. Kongsted, T. B. Pedersen, M. Strange, A. Osted, Aa. E. Hansen, K. V. Mikkelsen, F. Pawlowski, P. Jørgensen, C. Hättig, *Chem. Phys. Lett*. **2005**, *401*, 385–392.
148. J. Kongsted, K. Ruud, *Chem. Phys. Lett*. **2008**, *451*, 226–232.
149. P. Mukhopadhyay, G. Zuber, M. R. Goldsmith, P. Wipf, D. N. Beratan, *Chem. Phys. Chem*. **2006**, *7*(12), 2483–2486.
150. P. Mukhopadhyay, G. Zuber, P. Wipf, D. N. Beratan, *Angew. Chem. Int. Ed*. **2007**, *46*(34), 6450–6452.
151. O. Christiansen, *Theor. Chem. Acc*. **2006**, *116*, 106–123.
152. J. Kongsted, A. Osted, K. V. Mikkelsen, O. Christiansen, *Mol. Phys*. **2002**, *100*(11), 1813–1828.
153. M. S. Gordon, M. A. Freitag, P. Bandyopadhyay, J. H. Jensen, V. Kairys, W. J. Stevens, *J. Phys. Chem. A* **2001**, *105*(2), 293–307.
154. M. S. Gordon, L. V. Slipchenko, H. Li, J. H. Jensen, V. Kairys, W. J. Stevens, *Annu. Rep. Comp. Chem*. **2007**, *3*, 177–193.

24

AB INITIO METHODS FOR VIBRATIONAL CIRCULAR DICHROISM AND RAMAN OPTICAL ACTIVITY

Kenneth Ruud

24.1. INTRODUCTION

Despite the fact that the first observations of vibrational chiroptical responses were made less than 40 years ago [1–5], vibrational chiroptical spectroscopies have matured to become an important method for the determination of absolute configurations of chiral molecules [6, 7], as well as a tool in the study of secondary and tertiary structures of biomolecules [8–13]. Indeed, vibrational circular dichroism (VCD) in combination with reliable *ab initio* calculations has been shown to be a reliable tool for determining the absolute configuration of chiral compounds, and in a few cases even leading to a reassignment of previous structure determinations done using circular dichroism (CD) [14] or X-ray spectroscopy [15]. This is an impressive achievement for an experimental technique that was first observed in 1974 [1–3] and for which the formal quantum mechanical theory was derived in 1985 [16] and for which a reliable computational protocol was only made available approximately 15 years ago [17, 18]. Today, commercial VCD instruments are available, and several computational chemistry programs [19–21] offer the possibility to calculate the atomic axial and polar tensors that determine the VCD rotational strengths [16].

As for other chiroptical spectroscopic techniques, such as electronic circular dichroism (CD) [22, 23] and optical rotation (OR) [24, 25], the vibrational chiroptical spectroscopies give information about the stereochemistry of the molecule, but in addition they also provide fingerprinting information from the molecular vibrations. Vibrational chiroptical spectroscopies thus provide the stereochemical information of CD and OR with the

Comprehensive Chiroptical Spectroscopy, Volume 1: Instrumentation, Methodologies, and Theoretical Simulations, First Edition. Edited by N. Berova, P. L. Polavarapu, K. Nakanishi, and R. W. Woody.
© 2012 John Wiley & Sons, Inc. Published 2012 by John Wiley & Sons, Inc.

detailed level of information provided by vibrational spectrocopies. However, the added information content of VCD and vibrational Raman optical activity (ROA) also makes it more difficult to analyze the observed spectra. Neither for VCD nor for ROA do there currently exist simple rules-of-thumb for relating observed rotatory strengths or circular intensity differences for specific vibrational bands to a specific stereochemical structure, comparable to for instance the octant rule used to analyze CD rotatory strengths [26, 27].

Although specific vibrational bands are used both in VCD and ROA for analyzing secondary structures of biomolecules [28–30], the improvements in the design of experimental VCD and ROA spectrometers have been accompanied by a corresponding rapid development in *ab initio* methodology for calculating the molecular property tensors that determine the VCD and ROA spectra, contributing to the development and use of these experimental techniques. It is today possible to perform calculations on systems containing more than 200 atoms [31–33], comparing the spectrum calculated using *ab initio* methods directly to the experimentally observed spectrum, and from this directly deduce the absolute configuration of a chiral species. However, there are a number of factors that need to be considered in such a procedure, such as conformational averaging [34–37], the treatment of specific interactions and solvent effects [38–43], and the level of theory used [44–48], and this is treated in different chapters of this book. However, the basic working equations for calculating vibrational chiroptical spectra are today well-developed and are expected to remain state of the art for some time to come.

In this chapter I will give a basic introduction to the working equations that define vibrational circular dichroism and Raman optical activity, highlighting the intrinsic molecular property tensors that define the observable rotatory strengths (VCD) or circular intensity differences (ROA). I will also give the basic strategy used in most programs that calculate these property tensors, illustrating that the cost of calculating the chiroptical properties are in general much less than the cost of determining the vibrational force field. Some emphasis will also be given to the problem of ensuring that the calculated results are independent of the choice of molecular gauge origin, an obstacle that for a long time prevented the routine application of *ab initio* theory to the calculation of vibrational chiroptical responses.

The remainder of this chapter is divided into three main parts. In Section 24.2, an outline of the principles behind energy derivative theory is given, with the purpose of giving a qualitative understanding of the methodology used when doing an *ab initio* VCD or ROA calculation. The main purpose of this section is to provide a fairly nontechnical introduction to the general principles of the methodologies, as well as introduce some of the concepts and challenges that are often discussed in the literature in relation to the calculation of vibrational chiroptical spectra. In Section 24.3, a brief summary of the theory of VCD and ROA is given, primarily with the aim of introducing the tensors that determine VCD and ROA spectra. Some comments on different methodologies introduced to calculate VCD and ROA spectra are also given in this section. In Section 24.4, I present the working equations for *ab initio* calculations of VCD and ROA spectra for the specific case of a Hartree–Fock wavefunction. This section is more technical, and it may be skipped by users of VCD and ROA calculations not interested in all details of an *ab initio* VCD or ROA calculation. Finally, in Section 24.5 I give some concluding remarks and give some comments on remaining challenges in the calculation of VCD and ROA spectra. Applications of the computational methodologies and different approximations to these equations are not considered in this chapter, and the reader is referred to other chapters for more information on these practical aspects of VCD and ROA calculations.

24.2. ENERGY DERIVATIVE THEORY AND PERTURBATION-DEPENDENT BASIS SETS

It is useful to outline in very general terms the principles behind energy derivative theory, in order to illustrate the salient features of the approach without being hampered by the complicated equations that appear once an explicit parameterization of the wavefunction is considered, and without considering the explicit form of the Hamiltonian. This will allow us to illustrate important features of calculations of VCD and ROA spectra without too complicated equations. The discussion of energy derivative theory will be restricted to variational wavefunctions—that is, wavefunctions that are fully optimized with respect to all the parameters λ that define the wavefunction

$$\left.\frac{\partial E\,(\lambda, x^*)}{\partial \lambda}\right|_{\lambda=\lambda^*} = 0 \qquad \forall x^*, \tag{24.1}$$

where E denotes the molecular energy, x^* denotes an external perturbation at some reference perturbational strength, and λ^* the optimized wave function parameters in the absence of the applied perturbation. We have here explicitly indicated that the molecular energy depends both on the wavefunction parameters λ and on the applied external perturbation x. Hartree–Fock (HF) theory and Kohn–Sham density-functional theory (KS-DFT) both fall into the class of variational wavefunctions, and in both these cases the wavefunctions are parameterized in terms of the molecular orbital coefficients. We note that any nonvariational wavefunction can be cast into a variational form through the use of Lagrangian multipliers [49, 50], allowing the (quasi)energy derivative methodology also to be used for nonvariational wavefunctions [51]. Let us now apply an external perturbation to our molecular system, and consider how the variational condition in Eq. (24.1) changes to first order. We will then get two contributions

$$\left.\frac{\partial^2 E\,(\lambda, x)}{\partial \lambda \partial x}\right|_{\lambda=\lambda^*, x=x^*} + \left.\frac{\partial^2 E\,(\lambda, x)}{\partial \lambda^2}\right|_{\lambda=\lambda^*, x=x^*} \left.\frac{\partial \lambda}{\partial x}\right|_{\lambda=\lambda^*, x=x^*} = 0, \tag{24.2}$$

where we have utilized the chain rule for differentiation since the wavefunction parameters λ will change in the presence of the applied perturbation. In this expression, $\partial^2 E/\partial \lambda^2$ is often referred to as the electronic Hessian, $\partial^2 E/\partial \lambda \partial x$ as the property gradient, and $\partial \lambda/\partial x$ the response vector containing the perturbed wavefunction parameters. In the case of conventional molecular orbital-based theories, $\partial \lambda/\partial x$ corresponds to the perturbed molecular orbital coefficients. The response vector is the key quantity when determining a molecular property, and it can in principle can be obtained from the equation

$$\frac{\partial \lambda}{\partial x} = -\left(\frac{\partial^2 E\,(\lambda, x)}{\partial \lambda^2}\right)^{-1} \frac{\partial^2 E\,(\lambda, x)}{\partial \lambda \partial x}, \tag{24.3}$$

where we have not explicitly indicated that the derivatives are to be evaluated at $\lambda = \lambda^*, x = x^*$ for ease of notation. The number of wavefunction parameters can in many cases grow to be very large, making it neither attractive nor feasible to explicitly construct and invert the electronic Hessian. For this reason, Eq. (24.3) is often reformulated in terms of a linear response equation [52, 53]

$$\left(\frac{\partial^2 E\,(\lambda, x)}{\partial \lambda^2}\right)\sigma = \frac{\partial^2 E\,(\lambda, x)}{\partial \lambda \partial x}, \tag{24.4}$$

which is solved iteratively [53, 54]. σ is referred to as the trial vector, and convergence is reached when the difference between the electronic Hessian multiplied with the trial vector equals the property gradient on the right-hand side to within a predefined convergence threshold. At convergence, the trial vector represents, to within the convergence threshold, the response vector $\partial\lambda/\partial x$ [see Eq. (24.2)]. In the context of static energy derivatives of Hartree–Fock theory or Kohn–Sham DFT, Eq. (24.4) is the conventional coupled-perturbed Hartree–Fock or coupled-perturbed Kohn–Sham equations, respectively [55, 56]. Equation (24.4) may give the impression that the electronic Hessian must be constructed explicitly, but it can be shown that one can construct directly the vector arising from multiplying the electronic Hessian with the trial vector [53]. Strategies for solving the linear response equation have been discussed for instance by Jørgensen and co-workers on both a molecular orbital basis [53, 57] and an atomic orbital basis [54, 58].

With an approach for obtaining perturbed wavefunction parameters at hand, we are now in a position to consider molecular properties that can be expressed as (quasi-)energy derivatives. Let us start by considering the first-order energy correction due to an applied perturbation x. Keeping in mind the implicit dependence of λ on the perturbation x, we have

$$\frac{dE\,(\lambda,x)}{dx} = \frac{\partial E\,(\lambda,x)}{\partial x} + \frac{\partial E\,(\lambda,x)}{\partial \lambda}\frac{\partial \lambda}{\partial x} = \frac{\partial E\,(\lambda,x)}{\partial x}, \tag{24.5}$$

where the last equality follows from the fact that we are only considering variational wavefunctions [see Eq. 1)]. The partial derivative with respect to the applied perturbation in Eq. (24.5), $\partial E/\partial x$, indicates that we only include the contributions that have an explicit dependence on the applied perturbation, either through our interaction Hamiltonian or through the basis set (*vide infra*), whereas the implicit dependence, the changes in the molecular orbitals due to the perturbation, is given by $\partial\lambda/\partial x$ and is determined by Eq. (24.2). Equation (24.5) embodies the Hellmann–Feynman theorem, which states that for variationally optimized wavefunctions, first-order molecular properties can be calculated as expectation values of the interaction Hamiltonian (since this is the only part of the Hamiltonian that will depend on the applied perturbation x), and first-order properties are thus determined by the unperturbed electron density only.

Second derivatives can now be obtained by differentiating Eq. (24.5), using Eq. (24.3), where we also for ease of notation do not indicate the explicit dependence of the energy on the perturbations x and y and the wavefunction parameters λ

$$\begin{aligned}\frac{d^2E}{dxdy} &= \frac{\partial^2 E}{\partial x\,\partial y} + \frac{\partial^2 E}{\partial x\,\partial \lambda}\frac{\partial \lambda}{\partial y} + \frac{\partial^2 E}{\partial y\,\partial \lambda}\frac{\partial \lambda}{\partial x} + \frac{\partial \lambda}{\partial x}\frac{\partial^2 E}{\partial \lambda^2}\frac{\partial \lambda}{\partial y} + \frac{\partial E}{\partial \lambda}\frac{\partial^2 \lambda}{\partial x\,\partial y} \\ &= \frac{\partial^2 E}{\partial x\,\partial y} - \left(\frac{\partial^2 E}{\partial x\,\partial \lambda}\right)\left(\frac{\partial^2 E}{\partial \lambda^2}\right)^{-1}\left(\frac{\partial^2 E}{\partial y\,\partial \lambda}\right).\end{aligned} \tag{24.6}$$

The contribution from the second-order perturbed wavefunction parameters $\partial^2\lambda/\partial x\,\partial y$ do not contribute due to the variational nature of the wavefunction [see Eq. (24.1).

Equation (24.6) allows us to comment on two general features of energy-derivative theory. The first of these is the so-called interchange theorem of Dalgarno and Stewart [59, 60]. We note from the linear equations in Eq. (24.4) that we can rewrite the second derivative of the molecular energy with respect to the two perturbations x and y in two

equivalent manners:

$$\frac{d^2E}{dxdy} = \frac{\partial^2 E}{\partial x \partial y} + \frac{\partial^2 E}{\partial x \partial \lambda}\frac{\partial \lambda}{\partial y} = \frac{\partial^2 E}{\partial x \partial y} + \frac{\partial^2 E}{\partial y \partial \lambda}\frac{\partial \lambda}{\partial x}. \tag{24.7}$$

We can thus choose whether we would like to obtain wavefunctions perturbed with respect to perturbation x or perturbation y. From a physical point of view, this corresponds to whether we choose to measure how a property x interacts with a density perturbed by the perturbation y, or vice versa, which of course are equivalent ways of obtaining the same physical response. In many cases, it does not matter which of these perturbed wavefunctions we determine. If, however, we consider a property such as the electric dipole gradient appearing in the calculation of vibrational circular dichroism (*vide infra*), which is the second derivative of the energy with respect to an external electric field and nuclear displacements, then the choice we make regarding which perturbed wavefunctions we determine becomes crucial. If we decide to determine the wavefunctions perturbed by the applied electric field, then we would have to determine three perturbed wavefunctions, corresponding to the three Cartesian components of the electric field. If we instead choose to determine the wavefunctions perturbed by the nuclear displacements, we instead need to determine $3N$ perturbed wavefunctions, corresponding to the displacements in the three Cartesian directions of all the N nuclei in the molecule. Clearly it is in this case advantageous to determine the wavefunction perturbed by the electric field, because we then only need to solve three linear response equations, independent of the size of the molecular system.

Secondly, we can also use Eq. (24.6) to introduce the so-called $n + 1$ and $2n + 1$ rules [57, 61], which state that an energy correction to order $n + 1$ or $2n + 1$, respectively, can be determined from the perturbed wavefunction to order n. For second-order properties, both these rules show that only the first-order perturbed wavefunction needs to be determined using the linear set of equations [Eq. (24.4).] However, for third-order molecular properties, which occur in the calculation of the property gradients that determine vibrational Raman optical activity, the $n + 1$ rule requires the determination of the second-order perturbed wavefunction, whereas the $2n + 1$ rule allows us to use only first-order perturbed wavefunctions. It may at first appear that the $2n + 1$ rule would be the method of choice. However, we recall from Eq. (24.7) that we do not need determine the perturbed wavefunction for one of the applied perturbations in the case of a straightforward differentiation of the molecular energy corresponding to the $n + 1$ rule. The $2n + 1$ rule, on the other hand, would eliminate the second-order perturbed wavefunction parameters by introducing an additional first-order perturbed equation [61, 62]. Thus, if we are for instance interested in the polarizability gradient contribution to Raman and ROA spectra (*vide infra*) $d\alpha/dR = d^3E/dF^2dR$, then the $n + 1$ rule would require us to determine nine perturbed equations independent of the molecular size (three first-order perturbed wavefunctions with respect to the electric field, and six second-order perturbed wavefunctions with respect to the square of the electric field), whereas the $2n + 1$ rule would require us to solve $3 + 3N$ equations (three first-order perturbed wavefunctions for the electric field and $3N$ first-order perturbed wavefunctions for the nuclear displacements), making in this case the $n + 1$ rule the method of choice.

It is instructive to relate the above very schematic description of energy derivative theory that forms the foundations for the modern implementations of VCD and ROA in quantum chemistry programs to the exact-state expression. This will illustrate the connection between energy derivative theory and the expressions we are used to seeing

for the relevant VCD and ROA tensors using sum-over-states expressions. For exact states, we can represent the property gradient and molecular Hessians as, respectively,

$$\frac{\partial^2 E}{\partial \lambda_n \partial x} = \left\langle 0 \left| \frac{\partial \hat{H}}{\partial x} \right| n \right\rangle |\, n \rangle\,, \tag{24.8}$$

$$\frac{\partial^2 E}{\partial \lambda_m \partial \lambda_n} = \left(E_n^0 - E_0^0\right) |n\rangle\langle n| \delta_{nm}, \tag{24.9}$$

where E_n^0 denotes the energy of the nth excited state of the unperturbed system. Here and in the remainder of the chapter, atomic units have been used. From Eq. (24.6), (24.8), and (24.9), we see that we can express the dipole gradient for exact states as

$$\frac{d^2 E}{dF_\alpha dR_{K,\beta}} = \left\langle 0 \left| \frac{\partial^2 \hat{H}}{\partial F_\alpha \partial R_\beta} \right| 0 \right\rangle - \sum_{n \neq 0} \frac{\left\langle 0 \left| \frac{\partial \hat{H}}{\partial F_\alpha} \right| n \right\rangle \left\langle n \left| \frac{\partial \hat{H}}{\partial R_{K,\beta}} \right| 0 \right\rangle}{E_n^0 - E_0^0}, \tag{24.10}$$

where F_α denotes the α component of the external electric field, and $R_{K,\beta}$ denotes a distortion of nucleus K in the β Cartesian direction. The molecular Hamiltonian in the presence of a static electric field F can be written as (using atomic units here and throughout the chapter)

$$\hat{H} = \sum_i \left(-\tfrac{1}{2}\nabla_i^2 - \textstyle\sum_K \frac{Z_K}{|R_K - r_i|} \right) + \tfrac{1}{2} \textstyle\sum_{i \neq j} \frac{1}{|r_i - r_j|} + \tfrac{1}{2} \textstyle\sum_{K \neq L} \frac{Z_K Z_L}{|R_K - R_L|} - \boldsymbol{\mu}\mathbf{F}, \tag{24.11}$$

where Z_K is the nuclear charge, summations of i and j run over all electrons and summations of K and L run over all nuclei. We have here also introduced the molecular dipole moment operator

$$\hat{\mu}_\alpha = \sum_K Z_K R_{K,\alpha} - \sum_i r_{i,\alpha}. \tag{24.12}$$

Inserting this Hamiltonian into the expression for the electric field gradient in Eq. (24.10), we get the final expression for the electric field gradient

$$\frac{d^2 E}{dF_\alpha dR_{K,\beta}} = Z_K - \sum_{n \neq 0} \frac{\left\langle 0 \left| \sum_i r_{i,\alpha} \right| n \right\rangle \left\langle n \left| \sum_i \frac{Z_K (R_{K,\beta} - r_{i,\beta})}{|R_K - r_i|^3} \right| 0 \right\rangle}{E_n^0 - E_0^0}. \tag{24.13}$$

As already noted, for exact wavefunctions, the sum-over-states expression for the molecular property is equivalent to the energy-derivative expression in Eq. (24.6). From a computational point of view, Eq. (24.6) is much more advantageous, because it does not require the determination of an explicit representation of all excited states in the molecule, as required by Eq. (24.10). The linear sets of equations in Eq. (24.6) can furthermore be a useful starting point for determining the perturbed wavefunction for any choice of wavefunction. The explicit expressions for the electronic Hessian and property gradients will differ depending on the exact parameterization of the wavefunction, but the general structure of the expressions for the second-order properties will remain the same.

In this general presentation of energy derivative theory, we have not considered frequency-dependent perturbations. However, using the quasi-energy formalism, we can

see that we can continue to utilize the framework of energy-derivative theory, but now instead considering derivatives of the quasi-energy [51, 62]. However, the overall structure of the formalism remains largely the same as that presented here, and we defer the discussion of the differences related to static molecular properties to Section 24.4, where we discuss the explicit expressions for the polarizability gradients appearing in the *ab initio* calculation of ROA spectra.

Before proceeding to a more detailed discussion of the expressions for VCD and ROA spectra, we must also consider the concept of *perturbation-dependent basis sets* (PDBS), and the complications they introduce in the calculation of vibrational chiroptical properties. In relation to VCD and ROA, there are two different sets of PDBS that may arise: One is related to the geometrical distortions of the nuclei occurring during the vibrational motion, and the other is related to the magnetic component of the applied electromagnetic fields in case London atomic orbitals are used [63].

Let us first consider the dependence on the molecular geometry. In a conventional molecular electronic structure calculation, the electronic structure of the molecules is represented in terms of molecular or Kohn–Sham orbitals ψ_i^{MO}, which in turn are represented as linear combinations of basis functions centered on the atomic nuclei

$$\psi_i^{\mathrm{MO}} = \sum_{\mu} C_{i\mu}\chi_{\mu}(\mathbf{R}_K); \tag{24.14}$$

here $\chi_{\mu}(\mathbf{R}_K)$ represents the atomic-centered basis functions, which are normally represented in terms of Cartesian or spherical Gaussian basis functions. A Cartesian Gaussian can be written as

$$\chi_{\mu}^{k}(R_K) = N_{\mu}\mathbf{r}_K^{\mathbf{k}}\exp(-aR_K^2), \tag{24.15}$$

where N_{μ} is a normalization constant, $\mathbf{k}$ is a vector containing the order of the polynomial in the different Cartesian directions, and a is the orbital exponent. We have explicitly indicated the dependence of the basis functions on the position of the nucleus K to which they are attached.

If the position of the nuclei change, the atom-centered basis functions will also change due to the explicit dependence on the nuclear positions. More specifically, we will represent changes in the molecular geometries as derivatives of the nuclear coordinates. Due to the explicit dependence of the atom-centered basis functions on the positions of the nuclei, a perturbation due to changes in the molecular geometry will have two consequences for our calculations of molecular properties: (1) We will get new, differentiated atomic integrals, where the new contributions arise from the explicit dependence of the basis functions on the nuclear positions, and (2) the molecular orbitals will no longer be orthonormal. Let us consider the consequences of these two additional contributions in some more detail.

A change in the nuclear geometry can be decribed by considering a Taylor expansion of the energy with respect to the nuclear displacements, and the changes can thus be described as derivatives with respect to nuclear displacements. For computational simplicity, these derivatives are calculated in the Cartesian basis. Considering the integral of a one-electron operator $\hat{O}(R_C)$, which may depend on one or more centers C as is the case for the nuclear attraction operator, the first-order geometric derivative of this

integral can be written as

$$\frac{d}{dR_K}\left\langle \chi_\mu\left(\mathbf{R}_A\right)\left|\hat{O}\left(\mathbf{R}_C\right)\right|\chi_\nu\left(\mathbf{R}_B\right)\right\rangle = \delta_{AK}\left\langle \frac{d\chi_\mu(\mathbf{R}_A)}{dR_K}\left|\hat{O}\left(\mathbf{R}_C\right)\right|\chi_\nu\left(\mathbf{R}_B\right)\right\rangle + \delta_{CK}\left\langle \chi_\mu\left(\mathbf{R}_A\right)\left|\frac{d\hat{O}(\mathbf{R}_C)}{dR_K}\right|\chi_\nu\left(\mathbf{R}_B\right)\right\rangle + \delta_{BK}\left\langle \chi_\mu\left(\mathbf{R}_A\right)\left|\hat{O}\left(\mathbf{R}_C\right)\right|\frac{d\chi_\nu(\mathbf{R}_B)}{dR_K}\right\rangle, \tag{24.16}$$

which has a more complicated structure than a regular one-electron interaction operator such as the dipole moment operator, which would only contain the middle term in Eq. (24.16). However, the evaluation of geometrical derivatives of one-electron integrals is fairly straightforward [64]. The largest complication in terms of integral evaluations arises from the fact that also the two-electron repulsion integrals are dependent on the nuclear positions, and we will therefore always have to evaluate differentiated two-electron integrals when perturbation-dependent basis sets are involved [65, 66], increasing both the computational complexity and the computational costs.

The second complication that arises when perturbation-dependent basis sets are involved is that the unperturbed reference orbitals will no longer remain orthonormal due to the dependence of the basis functions on the applied perturbation. These orbitals are thus no longer suited as reference orbitals when calculating the perturbed wavefunctions. To be more explicit, let us consider the optimized wavefunction of our system in the absence of the applied perturbation. The self-consistent optimization procedure is then normally designed such that the optimized molecular orbitals (MOs) constitute an orthonormal set that we can express as

$$\psi_i^{\mathrm{UMO}}\left(x = x^*\right) = \sum_\mu C_{i\mu}^{(0)}\chi_\mu\left(x = x^*\right), \tag{24.17}$$

where $\left\langle \psi_i^{\mathrm{UMO}}\left(x = x^*\right) \mid \psi_i^{\mathrm{UMO}}\left(x = x^*\right)\right\rangle = \delta_{ij}$. As we change the external perturbation ($x \neq x^*$), these *unmodified molecular orbitals (UMO)* will no longer be orthonormal since the molecular orbital coefficients remain unchanged while the atomic basis functions change:

$$\left\langle \psi_i^{\mathrm{UMO}}(x) \mid \psi_i^{\mathrm{UMO}}(x)\right\rangle \neq \delta_{ij}, \qquad \psi_i^{\mathrm{UMO}}(x) = \sum_\mu C_{i\mu}^{(0)}\chi_\mu(x). \tag{24.18}$$

In the literature, this problem has been solved in two different manners. The most common approach is that the equations that determine the perturbed MO coefficients are defined subject to the constraint that the reference molecular orbitals should remain orthonormal [18, 62, 67, 68]. In the first analytic implementation of VCD and ROA spectra using London atomic orbitals [17, 69], a slightly different approach was used. These implementations were derived using second quantization [70], and it was therefore important that the reference orbitals remained orthonormal at any perturbation strength, and a set of orthonormal MOs were therefore introduced such that $\left\langle \phi_i^{\mathrm{OMO}}(x) \mid \phi_i^{\mathrm{OMO}}(x)\right\rangle = \delta_{ij}$. The OMOs were related to the UMOs through a transformation with a unitary matrix [71]

$$\phi_i^{\mathrm{OMO}}(x) = \sum_j T_{ij}(x)\psi_j^{\mathrm{UMO}}(x). \tag{24.19}$$

$T_{ij}(x)$ is not uniquely defined, and care must be exercised in choosing a form for the connection matrix $T_{ij}(x)$ that allows for a meaningful definition of the orthonormal molecular orbitals [71, 72].

Let us finally note that in both VCD and ROA, we will be concerned with the magnetic component of the electromagnetic field applied to the sample. However, when representing an external magnetic field in our molecular Hamiltonian, this is normally done in terms of a magnetic vector potential $\mathbf{A}(\mathbf{r}_{iO})$ defined such that

$$\mathbf{B} = \nabla \times \mathbf{A}(r_{iO}) . \tag{24.20}$$

We note that the magnetic vector potential does not uniquely define the external magnetic field, because we can add the gradient of any scalar function to the magnetic vector potential and still obtain the same magnetic field:

$$\mathbf{B}' = \nabla \times (\mathbf{A} + \nabla f) = \nabla \times \mathbf{A} + \nabla \times \nabla f = \nabla \times \mathbf{A} = \mathbf{B}. \tag{24.21}$$

We thus have a gauge freedom in our definition of the magnetic vector potential. In quantum chemical calculations, it is customary to assume the Coulomb gauge ($\nabla \cdot \mathbf{A} = 0$), in which case we can represent the magnetic vector potential as

$$\mathbf{A} = \frac{1}{2}\mathbf{B} \times \mathbf{r}_{iO}, \tag{24.22}$$

and the gauge freedom is reduced to a freedom in the choice of gauge origin **O**. Although calculated quantities in principle should be independent of the choice of gauge origin, this is not the case in approximate calculations. For variational methods, gauge origin independence can be achieved in the limit of a complete basis set, whereas for methods such as truncated coupled cluster theory, gauge origin independence is not achieved even in the limit of a complete basis set [73, 74].

The problem of gauge origin dependence of calculated VCD and ROA parameters is a critical one, as the results in practice will depend on the location of the molecule in space, and several early attempts using distributed origins were introduced in the calculation of VCD spectra to overcome this problem [75–78]. In 1993, London atomic orbitals [63] were introduced in the calculation of VCD spectra by Helgaker, Jørgensen and co-workers [17], and in 1995 the same groups also introduced the use of London orbitals for the tensors that determine ROA spectra [69], providing a very efficient way of ensuring that the calculated results were origin-independent and at the same time also ensured fast basis set convergence. These works lay much of the foundation for the development of efficient *ab initio* methods for calculating VCD and ROA spectral parameters (*vide infra*). Today, all methods in use for the calculation of VCD spectra, and many calculations of ROA spectra, use London atomic orbitals.

London atomic orbitals [63], also commonly referred to as Gauge-Including Atomic Orbitals (GIAOs) [79], are defined by multiplying each individual atomic basis function by a magnetic-field-dependent phase factor

$$\omega_\mu(\mathbf{B}) = \exp(-i\,\mathbf{A}_{KO} \cdot \mathbf{r})\,\chi_\mu(\mathbf{R}_K) . \tag{24.23}$$

The effect of the magnetic vector potential appearing in the complex phase factor

$$\mathbf{A}_{KO} = \frac{1}{2}\mathbf{B} \times \mathbf{R}_{KO} \tag{24.24}$$

is to move the global gauge origin O to the "best" local gauge origin for each individual basis function, which is chosen to be the center to which the basis function is attached. It can be shown that this choice of local gauge origin is optimal in the sense that for a one-electron, one-center system, the London orbital is correct to first order in the external magnetic field, whereas the conventional Gaussian basis function is only correct to zeroth order [17].

24.3. THE THEORY OF VIBRATIONAL CIRCULAR DICHROISM AND RAMAN OPTICAL ACTIVITY

24.3.1. Vibrational Circular Dichroism

Vibrational circular dichroism is the vibrational analog of CD, corresponding to the differential absorption of left- and right-circularly polarized light in the infrared wavelength region, thus corresponding to excitations in the vibrational manifold rather than between different electronic states. Phenomenologically, we can therefore write the rotational strength for a transition between two different vibrational states i and j for normal mode k (v_i^k and v_j^k) as [16]

$$R_{\alpha\beta}^{k;ij} = \Im\left(\left\langle v_i^k \left|\mu_\alpha\right| v_j^k\right\rangle \left\langle v_i^k \left|m_\beta\right| v_j^k\right\rangle\right), \tag{24.25}$$

where we have introduced the operator for the molecular electric dipole moment in Eq. (24.12) and the magnetic dipole operator

$$\hat{m}_\alpha = -\sum_i \frac{1}{2} l_{i,\alpha} = -\frac{1}{2}\sum_{\beta\gamma} \varepsilon_{\alpha\beta\gamma} \sum_i r_{i,\beta} p_{i,\gamma}, \tag{24.26}$$

where we have introduced the linear momentum operator of each particle $\mathbf{p}_i = -\imath\hbar\nabla_i$ and the orbital angular momentum $\mathbf{l}_j = (\mathbf{r}_j \times \mathbf{p}_j)$ and where $\varepsilon_{\alpha\beta\gamma}$ is an element of the Levi–Civita antisymmetric tensor.

Using harmonic oscillator wavefunctions as basis functions for the vibrational wavefunctions v_i^k and doing a Taylor expansion of the dependence of the electric and magnetic dipole moments with respect to the nuclear distortions, truncating the Taylor expansion at linear order, the rotational strength can be shown to be given as [16]

$$\begin{aligned} R_{\alpha\beta}^k &= \Im\left(\left\langle \nu_0 \left| \left.\frac{\partial \mu_\alpha}{\partial \mathbf{Q}_k}\right|_{\mathbf{R}_e} \mathbf{Q}_k \right| \nu_k \right\rangle \left\langle \nu_k \left| \left.\frac{\partial m_\beta}{\partial \mathbf{Q}_k}\right|_{\mathbf{R}_e} \mathbf{Q}_k \right| \nu_0 \right\rangle\right) \\ &= \frac{1}{2} \left.\frac{\partial \mu_\alpha}{\partial \mathbf{Q}_k}\right|_{\mathbf{R}_e} \left.\frac{\partial m_\beta}{\partial \mathbf{Q}_k}\right|_{\mathbf{R}_e}, \end{aligned} \tag{24.27}$$

where Q_i denotes the ith mass-weighted vibrational normal mode of the molecule. All derivatives are evalued at the molecular equilibrium geometry, indicated by the subscript $\mathbf{R}_e$. We have assumed that only the vibrational ground state is sufficiently populated at normal experimental conditions. The use of harmonic oscillator vibrational wavefunctions and only the terms linear in the Taylor expansion with respect to nuclear displacements is often referred to as the double-harmonic approximation or the Placzek approximation [80]. Within this approximation, only transitions to the first vibrationally excited state is possible for each vibrational normal mode.

In the calculation of VCD spectra, the geometrical derivatives of the electric and magnetic dipole moments in Eq. (24.27) are usually calculated with respect to the Cartesian displacements of the nuclei, followed by a transformation of these geometrically differentiated tensors to the normal coordinate basis, defined in matrix form as

$$\mathbf{Q} = \mathbf{L}^{-1}\mathbf{X}, \tag{24.28}$$

where $\mathbf{X}$ is a vector collecting the mass-weighted Cartesian coordinates of all the nuclei, and $\mathbf{L}^{-1}$ is the transformation matrix from the mass-weighted Cartesian coordinates $\mathbf{X}$ to the normal coordinate basis $\mathbf{Q}$. $\mathbf{L}$ diagonalizes both the kinetic energy and harmonic electronic potential energy of the nuclei.

The first term in Eq. (24.27), the gradient of the electric dipole moment, is referred to as the atomic polar tensor due to the symmetry properties of the tensor [81], whereas the gradient of the magnetic dipole moment operator in a similar manner is referred to as the atomic axial tensor.

The rotatory strength is only nonzero when the molecule is *vibrationally* chiral. It is important to realize that this means that we may have instances in which a molecule is achiral with respect to the electron density, but may be vibrationally chiral. One of the most striking examples of a vibrationally chiral system that has been synthesized and stereochemically characterized is chirally deuterated neopentane [7].

We have already encounted the *atomic polar tensor* in Eq. (24.10) and noted that it can be expressed as the second derivative of the electronic energy, once with respect to the external electric field and once with respect to the nuclear distortions. The sum-over-states expression for the dipole gradient was given in Eq. (24.13); and for easier comparison with the atomic axial tensor, we note that we alternatively can write the exact sum-over-states expression for the dipole gradient as

$$P^{K}_{\alpha\beta} = Z_K - \left\langle \Psi^{\mathrm{el}}_0 \right| \hat{\mu}_\alpha \left| \frac{\partial \Psi^{\mathrm{el}}_0}{\partial R_{K,\beta}} \right\rangle \Bigg|_{\mathbf{R}_e,\mathbf{F}=\mathbf{0}}, \tag{24.29}$$

that is, as the transition moment between the ground electronic state and the first-order perturbed wavefunction due to the nuclear distortion. We note that the atomic polar tensor also determines the intensities of regular infrared spectroscopy.

In contrast to the electric dipole gradient, the gradient of the magnetic dipole moment is zero within the Born–Oppenheimer approximation. This is because the magnetic dipole moment for a closed-shell molecule is quenched (since it corresponds to an expectation value of an imaginary operator), making the rotational strength in Eq. (24.27) zero.

Stephens showed that by including also nonadiabatic effects, a vibrationally induced magnetic moment can arise that will lead to a nonvanishing rotational strength [16]. Vibrational circular dichroism is thus an example of a nonadiabatic effect in a similar manner as properties such as the nuclear spin-rotation constant or the rotational g tensor [82, 83].

Following Stephens [16], we can write the vibronic wavefunction as a combination of a pure Born–Oppenheimer zeroth-order wavefunction and the first-order perturbed wavefunction due to the nonadiabatic coupling matrix elements as

$$\Psi^{\mathrm{pert}}_{Ii} = \Psi^{(0)}_{Ii} + \sum_{(J,j)\neq(0,0)} \frac{\left\langle \Psi^{(0)}_{Ii} \left| \hat{H}^{\mathrm{el}} + \hat{T}_K \right| \Psi^{(0)}_{Jj} \right\rangle}{E_{Ii} - E_{Jj}} \left| \Psi^{(0)}_{Jj} \right\rangle \tag{24.30}$$

where $\Psi_{Ii}^{(0)}$ denotes a vibronic wavefunction corresponding to the ith vibrational level of the Ith electronic state, $\hat{H}^{\mathrm{el}}$ represents the electronic Hamiltonian [see Eq. (24.11)], and $\hat{T}_K$ is the operator for the kinetic energy of the nuclei [16]. We do not go into the details of the derivation here, referring the interested reader instead to the original work of Stephens [16], but note that the atomic axial tensors as evaluated using this nonadiabatic wavefunction can, to leading order in the geometry dependence, be expressed as the overlap of the magnetic field-perturbed and geometry-perturbed wavefunctions

$$M_{K,\alpha\beta} = I_{K,\alpha\beta} + J_{K,\alpha\beta}, \tag{24.31}$$

$$I_{K,\alpha\beta} = \left\langle \frac{\partial \Psi_0^{\mathrm{el}}}{\partial R_{K,\alpha}} \middle| \frac{\partial \Psi_0^{\mathrm{el}}}{\partial B_\beta} \right\rangle \Bigg|_{\mathbf{R}_e,\mathbf{B}=\mathbf{0}}, \tag{24.32}$$

$$J_{K,\alpha\beta} = \frac{i}{4}\varepsilon_{\alpha\beta\gamma} Z_K R_{K\gamma}. \tag{24.33}$$

The sum-over-states expression for the atomic axial tensor is given as [16]

$$I_{\alpha\beta}^K = -\sum_{n\neq 0} \frac{\left\langle 0 \left| \frac{\partial \hat{H}}{\partial R_{K,\alpha}} \right| n \right\rangle \left\langle n \left| \frac{\partial \hat{H}}{\partial B_\beta} \right| 0 \right\rangle}{\left(E_n^0 - E_0^0\right)^2}. \tag{24.34}$$

We note that the atomic axial tensor cannot be expressed directly as an energy derivative since it involves the overlap over two perturbed wavefunctions. However, comparing with the expression for the atomic polar tensor, we note that we could calculate the atomic axial tensors as the product of two perturbed wavefunctions, once perturbed with respect to the external magnetic field and once with respect to the nuclear distortions. This approach forms the basis for all the early implementations of the atomic axial tensors [17, 18, 67].

Recently, Coriani et al. made the observation that the linear response function (second-order frequency-dependent quasi-energy derivative) corresponding to a mixed perturbation due to geometrical distortions and magnetic perturbations at a frequency ω of the applied perturbations is given as [68]

$$\left\langle\left\langle \frac{\partial \hat{H}}{\partial R_{K,\alpha}}; \frac{\partial \hat{H}}{\partial B_\beta} \right\rangle\right\rangle_\omega = \sum_{n\neq 0} \frac{2\omega}{\left(E_n^0 - E_0^0\right)^2} \left\langle 0 \left| \frac{\partial \hat{H}}{\partial R_{K,\alpha}} \right| n \right\rangle \left\langle n \left| \frac{\partial \hat{H}}{\partial B_\beta} \right| 0 \right\rangle, \tag{24.35}$$

which means that we can define the AATs as the frequency derivative of the linear response equation in Eq. (24.35) evaluated at zero frequency, that is,

$$I_{\alpha\beta}^K = \tfrac{1}{2}\tfrac{d}{d\omega} \left\langle\left\langle \tfrac{\partial H}{\partial R_{K,\alpha}}; \tfrac{\partial H}{\partial B_\beta} \right\rangle\right\rangle_\omega \Big|_{\omega=0}. \tag{24.36}$$

The development of theoretical methods for the calculation of VCD spectra has been reviewed on several occasions [37, 84]. We here only note that two major breakthroughs were necessary for making the calculations reliable and routine: (1) the introduction of London atomic orbitals for ensuring that the results were independent of the choice of the global gauge origin and for ensuring fast basis set convergence [17]; and (2) the use of density functional theory for calculating the force field and rotational strengths [18]. Stephens et al. have in several studies demonstrated the powers of this computational

approach (see reference 37 and references therein) and how the combined use of experimental VCD spectra with *ab initio* calculations is a very efficient and reliable approach for determining the absolute configurations of chiral molecules [44–46]. It is particularly noteworthy that VCD has also been shown to lead to a reassessment of earlier determinations of the absolute configuration of chiral molecules based on CD [14] as well as X-ray crystallography [15]. Density-functional theory has been the dominating correlated approach for calculating VCD spectra, and the only other fully correlated approach we are aware of for calculating the atomic axial and polar tensors is the multiconfigurational self-consistent-field approach of Bak et al. [17].

In the original implementations [17, 18, 67], the cost of a VCD calculation is of the same order of magnitude as that of determining the force field itself, and indeed there is very little computational overhead relative to a force-field calculation (three response equations due to the external magnetic field induction need to be solved in addition to the $3N$ equations that need to be solved for the nuclear distortions). However, basis set requirements for the atomic axial and polar tensors may differ from that of the force field, potentially leading to a higher computational cost than the force field alone if the perturbed densities for the nuclear displacements need to be recalculated with a different basis set. However, Stephens et al. have demonstrated that basis sets of TZ2P or cc-pVTZ quality in combination with hybrid density functionals such as B3LYP and B3PW91 gives results of an accuracy sufficiently high to unambigously assign experimental spectra, both for the force field and the rotational strengths [37]. We note that in case a different computational level is desired for the force field and the APT and AAT tensors, the approach of Coriani et al. [68] is particularly well-suited for such calculations, because this reduces the number of perturbed densities that must be determined to six.

Extensions of the basic VCD calculations to also decribe solvent effects have been presented by Cappelli et al. [85], including also nonequilibrium effects in the solvent due to the vibrational excitations in the solute. Although solvent effects have been shown to be non-negligible, these methods have not been much utilized, largely because only very rarely does the solvent as modeled by a dielectric continuum model lead to a reversal of the sign of the VCD rotational strengths. The use of the continuum model is therefore in general not important in terms of determining the absolute configuration of chiral molecules in solution. An instance where more elaborate models may be required, is when specific interactions such as hydrogen bonding are important for the calculated spectra [38, 39] or when molecules aggregate in the solvent [40, 42].

24.3.2. Raman Optical Activity

In ROA, the key quantity is the differential scattering of right- and left-circularly polarized light. The general expression of scattered circular polarization experiments for a scattering angle ξ are given by the expression [81]

$$\begin{aligned} I^R_{\mathrm{SCP}}(\xi) - I^L_{\mathrm{SCP}}(\xi) = \frac{1}{90c}\left(\frac{\omega^2\mu_o}{4\pi}\right)^2 \frac{\hbar}{2\omega_i}\Big[&90aG'_i + 26\beta^2_{G_i} - 2\beta^2_{A_i} \\ &+ \cos(\xi)\left(180aG'_i - 20\beta^2_{G_i} - 12\beta^2_{A_i}\right) \\ &+ \cos^2(\xi)\left(90aG'_i + 2\beta^2_{G_i} + 6\beta^2_{A_p}\right)\Big]. \end{aligned} \tag{24.37}$$

The corresponding expressions for specific experimental setups, both for Raman and ROA experiments, can be found in references 86 and 87.

In Eq. (24.37), we have introduced a number of Raman and ROA invariants, defined respectively as

$$a_i^2 = \frac{1}{9}\left(\frac{\partial \alpha_{\alpha\alpha}}{\partial Q_i}\right)\Big|_{\mathbf{R}_e}\left(\frac{\partial \alpha_{\beta\beta}}{\partial Q_i}\right)\Big|_{\mathbf{R}_e}, \tag{24.38}$$

$$\beta_i^2 = \frac{1}{2}\left[3\left(\frac{\partial \alpha_{\alpha\beta}}{\partial Q_i}\right)\Big|_{\mathbf{R}_e}\left(\frac{\partial \alpha_{\alpha\beta}}{\partial Q_i}\right)\Big|_{\mathbf{R}_e} - \left(\frac{\partial \alpha_{\alpha\alpha}}{\partial Q_i}\right)\Big|_{\mathbf{R}_e}\left(\frac{\partial \alpha_{\beta\beta}}{\partial Q_i}\right)\Big|_{\mathbf{R}_e}\right], \tag{24.39}$$

$$aG_i' = \frac{1}{9}\left(\frac{\partial \alpha_{\alpha\alpha}}{\partial Q_i}\right)\Big|_{\mathbf{R}_e}\left(\frac{\partial G'_{\beta\beta}}{\partial Q_i}\right)\Big|_{\mathbf{R}_e}, \tag{24.40}$$

$$\beta_{G_i}^2 = \frac{1}{2}\left[3\left(\frac{\partial \alpha_{\alpha\beta}}{\partial Q_i}\right)\Big|_{\mathbf{R}_e}\left(\frac{\partial G'_{\alpha\beta}}{\partial Q_i}\right)\Big|_{\mathbf{R}_e} - \left(\frac{\partial \alpha_{\alpha\alpha}}{\partial Q_i}\right)\Big|_{\mathbf{R}_e}\left(\frac{\partial G'_{\beta\beta}}{\partial Q_i}\right)\Big|_{\mathbf{R}_e}\right], \tag{24.41}$$

$$\beta_{A_i}^2 = \frac{\omega}{2}\left[\left(\frac{\partial \alpha_{\alpha\beta}}{\partial Q_i}\right)\Big|_{\mathbf{R}_e}\left(\frac{\varepsilon_{\alpha\gamma\delta}\partial A_{\gamma,\delta\beta}}{\partial Q_i}\right)\Big|_{\mathbf{R}_e}\right] \tag{24.42}$$

where ω_i is the frequency corresponding to the vibrational excitation of the ith vibrational mode, and implicit summation over repeated Greek indices has been used in all equations above.

$\alpha_{\alpha\beta}$, $G'_{\alpha\beta}$, and $A_{\gamma,\delta\beta}$ are, respectively, the electric dipole–electric dipole, electric dipole–magnetic dipole, and electric dipole–electric quadrupole polarizabilities, defined in terms of sum-over-states expressions for exact wave functions as [81]

$$\alpha_{\alpha\beta} = 2\sum_{n\neq 0}\omega_{n0}\frac{\langle 0|\hat{\mu}_\alpha|n\rangle\langle n|\hat{\mu}_\beta|0\rangle}{\omega_{n0}^2-\omega^2}, \tag{24.43}$$

$$G'_{\alpha\beta} = -2\omega\sum_{n\neq 0}\mathrm{Im}\frac{\langle 0|\hat{\mu}_\alpha|n\rangle\langle n|\hat{m}_\beta|0\rangle}{\omega_{n0}^2-\omega^2}, \tag{24.44}$$

$$A_{\alpha,\beta\gamma} = 2\sum_{n\neq 0}\omega_{n0}\frac{\langle 0|\hat{\mu}_\alpha|n\rangle\langle n|\hat{\Theta}_{\beta\gamma}|0\rangle}{\omega_{n0}^2-\omega^2}, \tag{24.45}$$

The electric and magnetic dipole moment operators $\hat{\mu}$ and $\hat{m}$ were defined in Eqs. (24.12) and (24.26), respectively. $\hat{\Theta}$ is the traceless electric quadrupole operator defined as

$$\hat{\Theta}_{\alpha\beta} = \frac{1}{2}\sum_K Z_K\left[R_{K,\alpha}r_{K,\beta} - \frac{1}{3}\delta_{\alpha\beta}R_{K,\gamma}R_{K,\gamma}\right] - \frac{1}{2}\sum_i\left[r_{i,\alpha}r_{i,\beta} - \frac{1}{3}\delta_{\alpha\beta}r_{i,\gamma}r_{i,\gamma}\right].$$

We note that G' will vanish in the limit of a static field ($\omega = 0$), as can be easily seen from Eq. (24.44).

The first full *ab initio* ROA spectra presented in the literature were computed at the Hartree–Fock level of approximation by Polavarapu and co-workers in 1990 [88, 89]. These calculations utilized the observation and implementation by Amos [90] that even though the mixed electric dipole–magnetic dipole polarizability in Eq. (24.44) vanishes in the limit of a static field, $(1/\omega)G'(\omega)$ does have a static limit.

The decoupling of the calculation of the force field from the ROA CIDs opens for the obvious possibility of calculating the force field that determines the normal coordinates at a different, and in general a much higher, level of theory than the more computationally expensive polarizability gradients. This combination of different computational levels are the dominating mode of operation in ROA calculations, to a large extent motivated by the somewhat stronger importance of the quality of the force field in obtaining reliable ROA spectra compared to the quality of the polarizability gradients (although the number of thorough investigations of basis set requirements and correlation effects on the polarizability gradients are limited [47, 48, 69, 91, 92]). This hybrid computational approach was also used in early studies of vibrational circular dichroism (VCD); see, for example, reference 93.

In the calculation of the mixed electric dipole–magnetic dipole polarizability in the work of Polavarapu and co-workers [88, 89], conventional basis sets were used. In 1995, Helgaker et al. presented the first gauge-origin-independent calculations of ROA spectra at the Hartree–Fock and multiconfigurational self-consistent field (MCSCF) level of theory [69]. Gauge-origin independence was ensured through the use of London atomic orbitals [63].

Another extension introduced in the work of Helgaker et al. relative to that of Polavarapu and co-workers is that the static-limit approximation was lifted, the different mixed polarizabilities now being calculated from response functions [51, 52, 70, 94] solved at the frequency of the applied laser light. Interestingly, reference 69 also represents (to date) one out of only two studies [92] of ROA CIDs using correlated wavefunctions (excluding DFT).

An important step forward in terms of improving the quality of calculated ROA CIDs was made in 2001, when Ruud, Helgaker, and Bouř presented the first calculations of ROA CIDs at the DFT level of theory [91]. This is an extention of the approach presented in reference 69, building on the implementation of linear response theory at the DFT level [95, 96] and the corresponding extension of the calculation of optical rotations to the DFT level using London atomic orbitals [97, 98]. Within a Kohn–Sham formalism, the implementation of ROA CIDs at the DFT level represents a rather minor modification of an existing TDHF code, assuming that routines for numerical integration of the relevant exchange-correlation kernels are present.

Luber and Reiher implemented the mixed electric dipole–electric quadrupole polarizability into the Turbomole program [99] enabling faster calculations of ROA spectra by utilizing the efficiency of the Turbomole integral package. Hess, Reiher and co-workers have introduced a numerical approach in which only selected vibrational modes are targeted, or only vibrations in a specific frequency window [100]; and although applicable to both VCD and ROA calculations, it has largely been used for ROA calculations in the domain of vibrational chiroptical spectroscopy [31, 33]. The approach can start from trial modes and obtain the true normal modes using Davidson diagonalization techniques [101]. These normal modes can then be used to determine the polarizability derivatives numerically without ever having to construct the full quantum-mechanical force field. For very large molecules, this has obvious advantages, because characteristic vibrational frequencies can be targeted, or only the relevant vibrational frequencies within the frequency window accessible to the ROA spectrometer. The method has allowed for ROA calculations on very large systems, involving more than 400 atoms in the largest calculations [33]. The combination of a local-mode optimization with analytical calculations of the ROA CIDs may prove to be a computationally very efficient approach for the study

of ROA spectra of large molecules, as well as for VCD when used in conjunction with the recent developments of Coriani et al. [68].

Jensen et al. have utilized the complex polarization propagator approach [102, 103] to calculate resonance Raman optical activity spectra [104]. The necessary geometry derivatives of the different mixed polarizabilities were also in this approach obtained using numerical differentiation.

The first analytic implementations of ROA CIDs have started to appear very recently [86, 105, 106]. The first of these, and the only one published to date [105], used the $2n + 1$ rule to calculate ROA CIDs at the Hartree–Fock level of theory, thus requiring the solution $3N + 12$ response equations. In this implementation, London orbitals were furthermore not included. More recent implementations utilize the $n + 1$ rule, reducing the number of response equations to be determined to 45, independent of the size of the molecule [86, 106]. One of these implementations [106] include also contributions from the exchange-correlation functionals to allow for calculations at the DFT level of theory, as well as the use of London atomic orbitals, and is distributed as part of the Gaussian program [20].

A somewhat different set of developments are the description of the effects of a solvent on the calculation of ROA spectra. Whereas the polarizable continuum model (PCM) is routinely used to include solvent effects on the vibrational frequencies, the only study in which the PCM has been applied to all quantities determining the ROA spectrum is the study by Pecul et al., [107], in which a nonequilibrium scheme for the interaction between the solvent and the solute is included also in the calculation of the ROA CIDs. The study also takes into account local field effects on the interaction tensors [108, 109].

24.4. THE *AB INITIO* THEORY OF VIBRATIONAL CIRCULAR DICHROISM AND RAMAN OPTICAL ACTIVITY

We described in Section 24.2 the basic principles of energy-derivative theory in a rather general fashion, in order to illustrate the general principles behind these kinds of calculations without having to introduce a specific wave function parameterization and without having to introduce a complicated formalism that would distract from the essential features of the approach. In this section, in contrast, we will present the working equations for calculating the tensors that determine the intensities of VCD and ROA spectra. Although there exist several independent implementations of VCD and ROA in the literature, they all follow the same computational strategy and are thus covered by the presentation. We will, however, in the case of VCD, focus on a new formulation of the atomic axial tensors that was recently introduced by Coriani et al. [68], which not only provides a derivation of the atomic axial tensors that are much closer to the regular energy-derivative scheme, but also holds promise for reducing the computational cost of AAT calculations. The approaches used to calculate force fields can be found elsewhere and will not be discussed here [110–112]. Let us also note that some of the details presented here in the context of ROA has already been discussed in some detail in a recent mini-review [86].

Compared to many other molecular properties, the number of theoretical developments of *ab initio* methods for the calculation of VCD and ROA spectra, and corresponding implementations, is rather limited. The reason for this is in part due to the limited experimental activity using this spectroscopic tool, but also the computational complexity of the relevant molecular properties that are needed for determining the VCD and

ROA spectra. As described in the previous section, several different implementations of *ab initio* methods for VCD and ROA calculations have been published in recent years, and an increasing number of *ab initio* programs can calculate VCD and ROA spectra, most notably the Dalton [19], Gaussian [20], ADF [21] (VCD only), and Turbomole [99, 113] (ROA only, in combination with SNF [114]) programs, but also the CADPAC program [115], with which the first *ab initio* ROA calculations were done [88, 89].

We will first introduce the starting point for our formalism, before focussing on the specific equations for the tensors that determine the VCD and ROA intensities.

24.4.1. Quasi-energy Derivative Theory in the Atomic Orbital Basis

The formalism we will utilize here is based on the a framework derived for an atomic orbital-based response theory, in which the basis functions can be both time- and perturbation-dependent [62, 66]. The formulation uses the elements of the density matrix as the basic parameters. By working in the atomic-orbital basis without explicitly using molecular orbitals, the approach is designed with modern linear-scaling methods in mind [54, 116–118].

Our starting point is the molecular gradient of the quasi-energy Q^g defined for an atomic orbital basis which is time-dependent and which depends explicitly on the externally applied perturbation g (in this case corresponding to a change of the nuclear positions: $g = R - R_e$) [119]:

$$Q^g = \frac{dQ}{dg} = \left\{ \frac{\partial \tilde{E}(\mathbf{D})}{\partial g} - \mathrm{Tr}\,\mathbf{S}^g\mathbf{W} \right\}_t . \tag{24.46}$$

In this equation, $\{\ldots\}_t$ indicates that we have performed a time averaging over a full period of the applied electromagnetic field. We have also introduced the density matrix $\mathbf{D}$ in the atomic orbital basis, the generalized (time-dependent) self-consistent field (SCF) energy of the system, $\tilde{E}(\mathbf{D})$, defined as

$$\begin{aligned} \tilde{E}(\mathbf{D}) = {} & h_{\mathrm{nuc}} + v_{\mathrm{nuc}} \\ & + \mathrm{Tr}\,(\mathbf{h} - \tfrac{i}{2}\mathbf{T} + \mathbf{V})\mathbf{D} \\ & + \mathrm{Tr}\,\tfrac{1}{2}\mathbf{G}(\mathbf{D})\mathbf{D}. \end{aligned} \tag{24.47}$$

The expression for the quasi-energy gradient is then

$$\begin{aligned} Q^g = {} & \Big\{ h^g_{\mathrm{nuc}} + v^g_{\mathrm{nuc}} \\ & + \mathrm{Tr}\,(\mathbf{h}^g - \tfrac{i}{2}\mathbf{T}^g + \mathbf{V}^g)\mathbf{D} \\ & + \mathrm{Tr}\,\tfrac{1}{2}\mathbf{G}^g(\mathbf{D})\mathbf{D} - \mathrm{Tr}\,\mathbf{S}^g\mathbf{W} \Big\}_t , \end{aligned} \tag{24.48}$$

where we have defined an antisymmetric time-differentiated overlap matrix

$$T_{\mu\nu} = \langle \chi_\mu | \dot{\chi}_\nu \rangle - \langle \dot{\chi}_\mu | \chi_\nu \rangle, \qquad \dot{\chi}_\mu = \frac{d}{dt}\chi_\mu, \tag{24.49}$$

and the nuclear repulsion energy h_{nuc}. $\mathbf{h}$ is the conventional one-electron operator integral, containing the kinetic energy and nuclear attraction contributions [see also Eq. (24.11)]

$$h_{\mu\nu} = \left\langle \chi_\mu \left| -\tfrac{1}{2}\nabla^2 - \sum_K \frac{Z_K}{|R_K - r|} \right| \chi_\nu \right\rangle, \tag{24.50}$$

and $\mathbf{G}(\mathbf{D})$ is the two-electron interaction, which in the atomic orbital basis can be written as

$$G_{\mu\nu}(\mathbf{D}) = \sum_{\rho\sigma} D_{\sigma\rho}(g_{\mu\nu\rho\sigma} - g_{\mu\sigma\rho\nu}), \tag{24.51}$$

with the two-electron integrals being defined as

$$g_{\mu\nu\rho\sigma} = \int\int \chi_\mu^*(\mathrm{x}_1)\chi_\nu(\mathrm{x}_1)\frac{1}{r_{12}}\chi_\rho^*(\mathrm{x}_2)\chi_\sigma(\mathrm{x}_2)\, d\mathrm{x}_1 d\mathrm{x}_2, \tag{24.52}$$

where x_i comprises a spin coordinate and a spatial coordinate. v_{nuc} in Eq. (24.47) is the potential energy between the nuclei and the external fields, while $\mathbf{V}$ describes the interaction between the electrons and the external fields. In the specific case of ROA, using the electric quadrupole approximation, the field-molecule interation operator entering into our Hamiltonian is given by

$$\begin{aligned}\hat{V}(t) &= -F(t)\,\hat{\mu} - Q(t)\,\hat{\Theta} - B(t)\hat{m} \\ &= -\big(f\ \exp(-i\omega t) + f^*\exp(i\omega t)\big)\hat{\mu} \\ &\quad -\big(q\ \exp(-i\omega t) + q^*\exp(i\omega t)\big)\hat{\Theta} \\ &\quad -\big(-ib\ \exp(-i\omega t) + ib^*\exp(i\omega t)\big)\hat{m},\end{aligned} \tag{24.53}$$

in which the monochromatic electromagnetic wave is represented as an oscillating inhomogeneous electric field and an oscillating homogeneous magnetic field

$$F_\alpha(\mathbf{r},t) = F_\alpha(t) + Q_{\alpha\beta}(t)r_\beta, \qquad B_\alpha(\mathbf{r},t) = B_\alpha(t), \tag{24.54}$$

which in turn are expressed in terms of complex-valued frequency component vectors f, q, and b:

$$f = \{f_x, f_y, f_z\}, \tag{24.55}$$

$$q = \{q_{xx}, q_{xy}, q_{yy}, q_{xz}, q_{yz}, q_{zz}\}, \tag{24.56}$$

$$b = \{b_x, b_y, b_z\}, \tag{24.57}$$

which we treat as perturbations (perturbation strengths). These are determined by the direction, intensity, phase, and polarization of the applied radiation. Since the magnetic moment operator $\hat{m}$ carries an imaginary phase factor, $-i$ has been extracted from b to avoid imaginary perturbed integrals $\mathbf{V}^b = (d/db)\mathbf{V}$ and properties (quasi-energy derivatives).

In the expression for the quasi-energy gradient Eq. (24.46), we have also introduced the derivative of the overlap matrix

$$S^g_{\mu\nu} = \frac{\partial S_{\mu\nu}}{\partial g} = \frac{\partial}{\partial g}\langle\chi_\mu|\chi_\nu\rangle, \tag{24.58}$$

and the energy-frequency-weighted density matrix

$$\mathbf{W} = \mathbf{D}\tilde{\mathbf{F}}\mathbf{D} + \tfrac{i}{2}\dot{\mathbf{D}}\mathbf{S}\mathbf{D} - \tfrac{i}{2}\mathbf{D}\mathbf{S}\dot{\mathbf{D}}, \tag{24.59}$$

where we have introduced the generalized (time-dependent) Fock matrix in the AO basis $\tilde{\mathbf{F}}$ defined as the partial derivative of the generalized SCF energy in Eq. (24.47) with respect to the density matrix transposed:

$$\tilde{\mathbf{F}} = \frac{\partial \tilde{E}(\mathbf{D})}{\partial \mathbf{D}^T} = \mathbf{h} + \mathbf{V} - \tfrac{i}{2}\mathbf{T} + \mathbf{G}(\mathbf{D}). \tag{24.60}$$

The gradient defined in Eq. (24.46) can be considered as a generalization to time-dependent basis sets of the expression for the conventional geometrical gradient of a molecular system as introduced by Pulay [120].

As shown in references 62 and 119, we can obtain higher-order, static, and frequency-dependent molecular properties by term-by-term differentiation of Eq. (24.48), following the principles of energy-derivative theory as outlined in Section 24.2, and we will use this to formulate the working expressions for the tensors that determine the VCD and ROA intensities. We will consider these two spectroscopies separately in the next two subsections.

24.4.2. *Ab Initio* Calculation of Vibrational Circular Dichroism

The VCD spectrum is determined by the product of the (static) atomic polar tensor [the electric dipole gradient; see Eq. (24.29)], and the atomic axial tensor in Eq. (24.32). Starting with the dipole gradient, this can be obtained by differentiating the quasi-energy gradient for the geometrical energy gradient with respect to the external electric field. In doing so, we note that since the electric field f only appear in the operator $\hat{V}$ (which gives rise to v_{nuc} and $\mathbf{V}$), and not in the atomic orbitals, derivatives of h_{nuc}, $\mathbf{h}$, $\mathbf{G}$, and $\mathbf{S}$ involving these perturbations will vanish.

$$\begin{aligned} Q^{gf^*} = \frac{dQ^g}{df^*} = \Big\{ & v^{gf^*}_{\text{nuc}} + \operatorname{Tr}\mathbf{V}^{gf^*}\mathbf{D} \\ & + \operatorname{Tr}\left(\mathbf{h}^g + \mathbf{V}^g - \frac{i}{2}\mathbf{T}^g + \mathbf{G}^g(\mathbf{D})\right)\mathbf{D}^{f^*} - \operatorname{Tr}\mathbf{S}^g\mathbf{W}^{f^*}\Big\}_t, \end{aligned} \tag{24.61}$$

where we have used that $\operatorname{Tr}\mathbf{G}^g(\mathbf{D}^f)\mathbf{D}=\operatorname{Tr}\mathbf{G}^g(\mathbf{D})\mathbf{D}^f$. Note that we consider f and f^* as being independent perturbations when differentiating. When perturbing a time-independent system, this greatly simplifies the equations since all derivatives will be of the form

$$\mathbf{D}^{ab\ldots} = \exp\left(-i\left(\omega_a + \omega_b \ldots\right)t\right)\,\mathbf{M}, \tag{24.62}$$

with **M** being time-independent. However, the dipole gradient only involves a static external electric field, in which case the matrix **T** vanishes, reducing the expression for the dipole gradient in Eq. (24.61) to

$$Q^{gf} = \frac{dQ^g}{df} = v_{\text{nuc}}^{gf} + \text{Tr}\,\mathbf{V}^{gf}\mathbf{D} + \text{Tr}\left(\mathbf{h}^g + \mathbf{V}^g + \mathbf{G}^g(\mathbf{D})\right)\mathbf{D}^f - \text{Tr}\,\mathbf{S}^g\left(\mathbf{D}\tilde{\mathbf{F}}\mathbf{D}\right)^f. \tag{24.63}$$

We note that this equation only requires us to determine three perturbed densities, corresponding to the three Cartesian components of the electric field, independent of the size of the molecular system. We will not go into the details on how to determine the perturbed densities, because this will take us too far off our main focus on how to obtain suitable expressions for *ab initio* calculations of VCD and ROA spectra. Suffice it to note here that the determination of the perturbed densities constitutes a significant fraction of the computational time needed for calculating the properties that determine VCD and ROA intensities. The perturbed densities are determined by iteratively solving a set of linear equations as discussed in Section 24.2 and schematically illustrated in Eq. (24.4). More information on the determination of the perturbed densities by solving linear response equations can be found in the Appendix, as well as in the literature (see, e.g., references 53 and 54).

Let us now turn our attention to the atomic axial tensor. We note from Eq. (24.32) that this tensor is the dot product of two perturbed wavefunctions, and thus not directly expressible as an energy derivative. An alternative formulation as presented by Coriani et al. [68] is to express the AAT as the frequency derivative of the linear response function corresponding to perturbations due to an external magnetic field and nuclear discplacements, as illustrated in Eq. (24.35), and this is the approach we will also be considering here.

Instead of differentiating the quasi-energy gradient with respect to an electric field, let us differentiate it with respect to a frequency-dependent magnetic field, including also contributions from the London atomic orbitals

$$Q^{gb^*} = \frac{dQ^g}{db^*} = \left\{\text{Tr}\left(\mathbf{h}^{gb^*} + \mathbf{V}^{gb^*} - \frac{i}{2}\mathbf{T}^{gb^*} + \mathbf{G}^{gb^*}(\mathbf{D})\right)\mathbf{D} + \text{Tr}\left(\mathbf{h}^g + \mathbf{V}^g - \frac{i}{2}\mathbf{T}^g + \mathbf{G}^g(\mathbf{D})\right)\mathbf{D}^{b^*} - \text{Tr}\,\mathbf{S}^g\mathbf{W}^{b^*}\right\}_t. \tag{24.64}$$

Following Eq. (24.35), we differentiate the magnetic dipole gradient in Eq. (24.64) with respect to the frequency ω, setting the frequency to zero, which gives [68]

$$\left.\frac{d}{d\omega}Q^{gb}\right|_{\omega=0} = -\frac{i}{2}\text{Tr}\left[\mathbf{T}^{gb\omega} + \mathbf{D}\mathbf{T}^{g\omega}\mathbf{D}^b\right] + \text{Tr}\,\mathbf{S}^g\mathbf{W}^{b\omega} + \text{Tr}\left\{\left[\mathbf{h}^g + \mathbf{V}^g - \frac{i}{2}\mathbf{T}^g + \mathbf{G}^g(\mathbf{D})\right]\mathbf{D}^{b^*\omega}\right\}. \tag{24.65}$$

We thus note that we can calculate the AATs without determining the perturbed wavefunction parameters with respect to the geometrical distortions, as has normally been done in the implementations presented in the literature to date [17, 18, 67]. Indeed, this formulation only requires the determination of six perturbed densities, namely the

magnetic-field-perturbed densities evaluated at zero frequency, $\mathbf{D}^b$, and the second-order perturbed densities, $\mathbf{D}^{b\omega}$, of which there are also only three components. It is beyond the scope of this chapter to discuss in detail how these latter perturbed densities are determined, and we only note that they are determined using the regular linear response solver with a modified right-hand side. For more details, the interested reader is referred to the work of Coriani et al. [68].

24.4.3. *Ab Initio* Calculation of Raman Optical Activity

We recall that the quantities that determine the circular intensity difference in ROA are the isotropic and anisotropic invariants of gradients of the electric dipole polarizability, the mixed electric dipole–magnetic dipole polarizability, and the mixed electric dipole–electric quadrupole polarizability, see Eqs. (24.38–24.42). Focusing first on the electric dipole polarizability and the mixed electric dipole–electric quadrupole polarizability, we can obtain the working expressions for these polarizability gradients by differentiating the expression for the dipole gradient in Eq. (24.61) a second time, with respect to f or q, respectively,

$$\begin{aligned}\frac{d\alpha}{dg} = Q^{gf^*f} = \Big\{ &\operatorname{Tr}\mathbf{V}^{gf^*}\mathbf{D}^f + \operatorname{Tr}\mathbf{V}^{gf}\mathbf{D}^{f^*} \\ &+ \operatorname{Tr}\big(\mathbf{h}^g + \mathbf{G}^g(\mathbf{D})\big)\mathbf{D}^{f^*f} \\ &+ \operatorname{Tr}\mathbf{G}^g(\mathbf{D}^{f^*})\mathbf{D}^f - \operatorname{Tr}\mathbf{S}^g\mathbf{W}^{f^*f}\Big\}_t, \end{aligned} \tag{24.66}$$

$$\begin{aligned}\frac{dA}{dg} = Q^{gf^*q} = \Big\{ &\operatorname{Tr}\mathbf{V}^{gf^*}\mathbf{D}^q + \operatorname{Tr}\mathbf{V}^{gq}\mathbf{D}^{f^*} \\ &+ \operatorname{Tr}\big(\mathbf{h}^g + \mathbf{G}^g(\mathbf{D})\big)\mathbf{D}^{f^*q} \\ &+ \operatorname{Tr}\mathbf{G}^g(\mathbf{D}^q)\mathbf{D}^{f^*} - \operatorname{Tr}\mathbf{S}^g\mathbf{W}^{f^*q}\Big\}_t, \end{aligned} \tag{24.67}$$

where we have used that f and q only appear linearly in v_{nuc} and $\mathbf{V}$.

Similarly, the formula for the gradient of the G' tensor, $Q^{gf^*b} = -(d/dg)G'$, is obtained by differentiating Eq. (24.61) with respect to b:

$$\begin{aligned}Q^{gf^*b} = \Big\{ &\operatorname{Tr}\mathbf{V}^{gf^*}\mathbf{D}^b \\ &+\operatorname{Tr}\big(\mathbf{h}^{gb} + \mathbf{V}^{gb} - \tfrac{i}{2}\mathbf{T}^{gb} + \mathbf{G}^{gb}(\mathbf{D})\big)\mathbf{D}^{f^*} \\ &+\operatorname{Tr}\big(\mathbf{h}^g + \mathbf{G}^g(\mathbf{D})\big)\mathbf{D}^{f^*b} \\ &+\operatorname{Tr}\mathbf{G}^g(\mathbf{D}^b)\mathbf{D}^{f^*} \\ &-\operatorname{Tr}\mathbf{S}^{gb}\mathbf{W}^{f^*} - \operatorname{Tr}\mathbf{S}^g\mathbf{W}^{f^*b}\Big\}_t. \end{aligned} \tag{24.68}$$

Compared to Eqs. (24.66) and (24.67), this formula has six additional contributions, which are all due to the fact that the integrals depend on b through the London atomic orbitals. We do not discuss these equations in more detail here, noting only that these equations allow us to calculate ROA CIDs solving only 45 response equations; thus no perturbed densities due to the geometrical distortions are needed [86, 106].

24.5. CONCLUDING REMARKS AND OUTLOOK

In this chapter, an overview of the general principles that apply when calculating vibrational chiroptical properties have been given in terms of energy derivative theory. The complications that arise because the basis functions used in *ab initio* calculations of molecular properties depend explicitly on both the nuclear positions and the external magnetic field perturbation when London atomic orbitals are used have been given special attention. The working equations for the calculation of VCD and ROA spectra have been given for the specific case of a Hartree–Fock wavefunction, focusing on the most recent derivation of the working equations in which the elements of the density matrix in the atomic-orbital basis has been used as variational parameters [62]. We have, in particular, highlighted a recent derivation of the atomic axial tensors that enter into the calculation of VCD spectra by Coriani et al. [68] that allows the AATs to be determined by solving only six linear response equations, a significant improvement over the conventional $3N + 3$ response equations that normally have to be solved in convential implementations. VCD calculations are in this formulation comparable in cost to ROA calculations using the $n + 1$ rule [86].

As of today, Kohn–Sham density functional theory is the dominating method of choice for calculating VCD spectra [37]. In the case of ROA, DFT has until recently been more sparingly used, and often DFT force fields have been used in combination with Hartree–Fock calculations of ROA CIDs [47, 121]. However, with the introduction of analytic calculations of ROA CIDs with London orbitals at the Kohn–Sham DFT level of theory [86, 106], it is expected that there will be an increasing number of ROA studies all carried out at the DFT level of theory. In the case of VCD, Stephens and co-workers have done a number of studies to determine the level of theory required for the reliable calculation of VCD spectra [18, 44–46]. The number of benchmark studies for ROA CIDs are much more limited [47, 48, 69, 91, 92]. These benchmark studies have to a large extent been based on a qualitative comparison with experimental spectra, ignoring in most cases the effects of the solvent, even though solvent effects can be expected to be significant. As such, there is a need for accurate benchmark calculations, for instance at the coupled-cluster level of theory, in order to assess the reliability of the more approximate DFT calculations. Except for a few very early studies at the MCSCF level of theory [17, 69, 92], no correlated *ab initio* studies of VCD and ROA spectra have been presented to date if we here do not consider DFT as a correlated *ab initio* method. However, due to the low symmetry of chiral molecules and the general high computational costs of correlated *ab initio* calculations, these methods are not expected to become routine, and they will primarily serve as benchmarks for more approximate methods.

An important future development will be the inclusion of anharmonic effects in VCD and ROA spectra. An early study of anharmonic effects was presented by Bak and co-workers [122], and there is also some recent work by Danecek et al. [123] However, these methods are still hampered by the lack of analytic methods that would allow anharmonic effects to be included in a routine manner. The development of very general approaches for calculating molecular properties of arbitrary order for time- and perturbation-dependent basis sets may help rectify this situation in the future [62].

The majority of VCD and ROA studies have focused on organic molecules. A few studies have, however, also considered chiral complexes involving metal atoms [99, 124–126]. If VCD and ROA show promise as a structural tool also for such compounds,

there will in the future be a need for considering also relativistic effects on VCD and ROA spectra.

Although not directly a methodological concern, the development of suitable models for describing solvent effects are much needed. Both for ROA and VCD, there has been presented implementations of the polarizable continuum model for the inclusion of solvent effects in an approximate manner [85, 107]. Whereas such implicit solvent models may be suitable in many cases for VCD due to the nonpolar solvents that are normally employed, such implicit solvent models can be expected to be much less satisfactory for ROA, because water is often the solvent of choice. At the same time, water will lead to strong specific interactions with the solute through hydrogen bonding, and a reliable consideration of these effects will require the use of more sophisticated solvent models. The cost of ROA calculations have until recently prevented systematic studies of the accuracy and reliability of different implicit and explicit solvent effects on the calculated ROA spectra [43]. Related to these effects are also aggregation effects (dimerization), for instance, induced by the solvent [40–42].

The recent developments of analytic *ab initio* methods for the calculation VCD and ROA spectra have made a significant impact on the development of these spectrocopic techniques, and theoretical calculations are in many cases an integral part of vibrational chiroptical studies. Although further methodological developments are needed, in part to include anharmonicites, relativistic effects, and solvent effects, as well as to extend the methods to increasingly larger molecules [33], current *ab initio* theory provides results of an accuracy that in many cases are sufficient for a detailed analysis of experimental spectra. The major challenges are currently the development of reliable computational protocols, in particular in relation to conformationally flexible molecules. This remains a major challenge in which theory and experiment will have to continue to collaborate in order to further our understanding of the many computational parameters and models that affect a calculated VCD or ROA spectrum.

ACKNOWLEDGMENTS

This work has received support from the Norwegian Research Council through a Centre of Excellence Grant (Grant No 179568/V30) and Grant No 191251/V30. I am grateful to Sonia Coriani and Andreas Thorvaldsen for a preprint of reference 68.

APPENDIX: DETERMINATION OF THE PERTURBED DENSITY MATRICES

For completeness, we summarize here the determination of the perturbed densities from solving the linear response equation [Eq. (24.4)] in the atomic-orbital basis for a Hartree–Fock wavefunction. The presentation follows that already given in reference 86, and it is based on the derivation in reference 62.

The required first- and second-order perturbed densities $\mathbf{D}^f = (\mathbf{D}^{f^*})^T$, $\mathbf{D}^q$, $\mathbf{D}^b$, $\mathbf{D}^{f^*f}$, $\mathbf{D}^{f^*q}$, and $\mathbf{D}^{f^*b}$ can be determined by solving the corresponding derivatives of the time-dependent SCF equation and idempotency constraint [62]

$$\tilde{\mathbf{F}}\mathbf{D}\mathbf{S} - \tfrac{i}{2}\mathbf{S}(\mathbf{D}\mathbf{S})^\bullet = \mathbf{S}\mathbf{D}\tilde{\mathbf{F}} + \tfrac{i}{2}(\mathbf{S}\mathbf{D})^\bullet\mathbf{S}, \tag{24.69}$$

$$\mathbf{D}\mathbf{S}\mathbf{D} = \mathbf{D}, \tag{24.70}$$

where the time-dependent Fock matrix $\tilde{\mathbf{F}}$ is given by Eq. (24.60) and $(\mathbf{D}\mathbf{S})^\bullet = (d/dt)\mathbf{D}\mathbf{S}$.

Eqs. (24.69) and (24.70) have been derived previously [62], and this derivation will not be repeated here and we focus on determining derivatives of Eqs. (24.69) and (24.70).

In the first step of the procedure, all known (lower-order) terms are collected in a right-hand-side **N**, and from the perturbed idempotency constraint a set of equations are obtained for the higher-order perturbed densities, which can then be evaluated. For a second-order equation for $\mathbf{D}^{f^*b}$, this is

$$\mathbf{D}^{f^*b}\mathbf{SD} + \mathbf{DSD}^{f^*b} - \mathbf{D}^{f^*b} = \mathbf{N}, \tag{24.71}$$

$$\mathbf{N} = -\begin{pmatrix} \mathbf{D}^b\mathbf{S}^{f^*}\mathbf{D} + \mathbf{D}^b\mathbf{SD}^{f^*} + \mathbf{DS}^b\mathbf{D}^{f^*} \\ +\mathbf{DS}^{f^*}\mathbf{D}^b + \mathbf{D}^{f^*}\mathbf{SD}^b + \mathbf{D}^{f^*}\mathbf{S}^b\mathbf{D} \\ +\mathbf{DS}^{f^*b}\mathbf{D} \end{pmatrix}, \tag{24.72}$$

in which perturbed overlap matrices $\mathbf{S}^{f^*}$ and $\mathbf{S}^{f^*b}$ are zero since the basis set is independent of the electric field. An equation of the form of Eq. (24.71) has the general solution

$$\begin{aligned} \mathbf{D}^{f^*b} &= \mathbf{NSD} + \mathbf{DSN} - \mathbf{N} + \mathbf{D}^{f^*b}_{\text{hom}} \\ &= \mathbf{D}^{f^*b}_{\text{par}} + \mathbf{D}^{f^*b}_{\text{hom}}, \end{aligned} \tag{24.73}$$

where we call $\mathbf{D}^{f^*b}_{\text{par}}$ the "particular" component of the solution, and the "homogeneous" component $\mathbf{D}^{f^*b}_{\text{hom}}$ can be any solution of the corresponding homogeneous equation

$$\mathbf{D}^{f^*b}_{\text{hom}}\mathbf{SD} + \mathbf{DSD}^{f^*b}_{\text{hom}} - \mathbf{D}^{f^*b}_{\text{hom}} = \mathbf{0}, \tag{24.74}$$

which must be determined by the corresponding perturbed time-dependent self-consistent field (TDSCF) equation.

If transformed to a basis of Hartree–Fock molecular orbitals **C**, the particular component has occupied–occupied and virtual–virtual blocks only, whereas the homogeneous component only has virtual–occupied and occupied–virtual blocks.

In the second step of the procedure, all known terms (lower-order and $\mathbf{D}^{f^*b}_{\text{par}}$) in the perturbed TDSCF equation are collected on the right-hand side as **M**, which can be evaluated. For instance, the equation for $\mathbf{D}^{f^*b}_{\text{hom}}$ is given by

$$\mathbf{G}\big(\mathbf{D}^{f^*b}_{\text{hom}}\big)\mathbf{DS} - \mathbf{SDG}\big(\mathbf{D}^{f^*b}_{\text{hom}}\big) + \mathbf{FD}^{f^*b}_{\text{hom}}\mathbf{S} - \mathbf{SD}^{f^*b}_{\text{hom}}\mathbf{F} - (\omega_{f^*} + \omega_b)\mathbf{SD}^{f^*b}_{\text{hom}}\mathbf{S} = \mathbf{M}, \tag{24.75}$$

$$\mathbf{M} = -\begin{pmatrix} \tilde{\mathbf{F}}^{f^*b}_{\text{par}}\mathbf{DS} - \mathbf{SD}\tilde{\mathbf{F}}^{f^*b}_{\text{par}} \\ +\big(\tilde{\mathbf{F}}^b - \frac{\omega_{f^*}}{2}\mathbf{S}^b\big)(\mathbf{D}^{f^*}\mathbf{S} + \mathbf{DS}^{f^*}) \\ -(\mathbf{S}^{f^*}\mathbf{D} + \mathbf{SD}^{f^*})\big(\tilde{\mathbf{F}}^b + \frac{\omega_{f^*}}{2}\mathbf{S}^b\big) \\ +\big(\tilde{\mathbf{F}}^{f^*} - \frac{\omega_b}{2}\mathbf{S}^{f^*}\big)(\mathbf{D}^b\mathbf{S} + \mathbf{DS}^b) \\ -(\mathbf{S}^b\mathbf{D} + \mathbf{SD}^b)\big(\tilde{\mathbf{F}}^{f^*} + \frac{\omega_b}{2}\mathbf{S}^{f^*}\big) \\ +\big(\mathbf{F} - \frac{\omega_{f^*}+\omega_b}{2}\mathbf{S}\big)\big(\mathbf{D}^{f^*b}_{\text{par}}\mathbf{S} + \\ \quad \mathbf{D}^b\mathbf{S}^{f^*} + \mathbf{D}^{f^*}\mathbf{S}^b + \mathbf{DS}^{f^*b}\big) \\ -\big(\mathbf{S}^{f^*b}\mathbf{D} + \mathbf{S}^b\mathbf{D}^{f^*} + \mathbf{S}^{f^*}\mathbf{D}^b + \\ \quad \mathbf{SD}^{f^*b}_{\text{par}}\big)\big(\mathbf{F} + \frac{\omega_{f^*}+\omega_b}{2}\mathbf{S}\big) \end{pmatrix}, \tag{24.76}$$

$$\begin{aligned} \tilde{\mathbf{F}}^{f^*b}_{\text{par}} &= \mathbf{h}^{f^*b} - \tfrac{i}{2}\mathbf{T}^{f^*b} + \mathbf{V}^{f^*b} + \mathbf{G}^{f^*b}(\mathbf{D}) \\ &\quad + \mathbf{G}^b(\mathbf{D}^{f^*}) + \mathbf{G}^{f^*}(\mathbf{D}^b) + \mathbf{G}(\mathbf{D}^{f^*b}_{\text{par}}), \end{aligned} \tag{24.77}$$

where again, since the basis set is independent of f^*, the following are all zero: $\mathbf{S}^{f^*b}$, $\mathbf{S}^{f^*}$, $\mathbf{h}^{f^*b}$, $\mathbf{T}^{f^*b}$, $\mathbf{V}^{f^*b}$, $\mathbf{G}^{f^*b}$, and $\mathbf{G}^{f^*}$. In addition, in the case of ROA CIDs, $\omega_b = -\omega_{f^*} = \omega$, thus $\omega_{f^*}+\omega_b$ is also zero.

To bring Eq. (24.75) to the more familiar form of an SCF response equation in the AO basis [127, 54], $\mathbf{D}^{f^*b}_{\text{hom}}$ can be expressed in terms of another matrix $\mathbf{X}$ as an $\mathbf{S}$-commutator $[\mathbf{X},\mathbf{D}]_\mathbf{S}$

$$\mathbf{D}^{f^*b}_{\text{hom}} = \mathbf{XSD} - \mathbf{DSX} = [\mathbf{X},\mathbf{D}]_\mathbf{S}, \tag{24.78}$$

which brings Eq. (24.75) to the form

$$\left(\mathbf{E}^{[2]} - (\omega_{f^*} + \omega_b)\mathbf{S}^{[2]}\right)(\mathbf{X}) \;=\; \mathbf{M}, \tag{24.79}$$

$$\begin{aligned}\mathbf{E}^{[2]}(\mathbf{X}) = {}& \mathbf{G}\big([\mathbf{X},\mathbf{D}]_\mathbf{S}\big)\mathbf{DS} - \mathbf{SDG}\big([\mathbf{X},\mathbf{D}]_\mathbf{S}\big) \\ & + \mathbf{F}[\mathbf{X},\mathbf{D}]_\mathbf{S}\mathbf{S} - \mathbf{S}[\mathbf{X},\mathbf{D}]_\mathbf{S}\mathbf{F},\end{aligned} \tag{24.80}$$

$$\mathbf{S}^{[2]}(\mathbf{X}) = \mathbf{S}[\mathbf{X},\mathbf{D}]_\mathbf{S}\mathbf{S}, \tag{24.81}$$

where $\mathbf{E}^{[2]}$ and $\mathbf{S}^{[2]}$ are the generalized electronic Hessian and metric operators. Equation (24.79) is then solved iteratively, either in the AO basis [54] or after transformation to the MO basis [52, 53]:

$$\mathbf{X} = \mathbf{C}\begin{bmatrix}\mathbf{0} & \mathbf{Y}\\ \mathbf{Z} & \mathbf{0}\end{bmatrix}\mathbf{C}^T, \qquad \mathbf{C}^T\mathbf{MC} = \begin{bmatrix}\mathbf{0} & \mathbf{K}\\ \mathbf{L} & \mathbf{0}\end{bmatrix}. \tag{24.82}$$

We note that the structure of Eq. (24.79) corresponds to the general form of the linear response function given in Eq. (24.4).

REFERENCES

1. G. Holzwarth, E. C. Hsu, H. S. Mosher, T. R. Faulkner, A. Moscowitz, *J. Am. Chem. Soc*. **1974**, *96*, 251–252.
2. L. A. Nafie, J. Cheng, P. J. Stephens, *J. Am. Chem. Soc*. **1975**, *97*, 3842–3843.
3. L. A. Nafie, T. A. Keiderling, P. J. Stephens, *J. Am. Chem. Soc*. **1976**, *98*, 2715–2723.
4. L. D. Barron, M. P. Bogaard, A. D. Buckingham, *J. Am. Chem. Soc*. **1973**, *95*, 603–605.
5. W. Hug, S. Kint, G. F. Bailey, J. R. Scherer, *J. Am. Chem. Soc*. **1975**, *97*, 5589–5590.
6. P. L. Polavarapu, *Ang. Chemie Int. Ed*. **2002**, *41*, 4544–4546.
7. J. Haesler, I. Schindelholz, E. Riguet, C. G. Bochet, W. Hug, *Nature* **2007**, *446*, 526–529.
8. R. K. Dukor, T. A. Keiderling, *Biopolymers* **1991**, *31*, 1747–1761.
9. J. Kubelka, T. A. Keiderling, *J. Am. Chem. Soc*. **2001**, *123*, 12048–12058.
10. A. F. Bell, L. Hecht, L. D. Barron, *J. Am. Chem. Soc*. **1998**, *120*, 5820–5821.
11. L. D. Barron, L. Hecht, A. F. Bell, G. Wilson, *Appl. Spectrosc*. **1996**, *50*, 619–629.
12. P. L. Polavarapu, Z. Deng, *Faraday Discuss*. **1994**, *99*, 151–163.
13. P. Bour, J. Kubelka, T. A. Keiderling, *Biopolymers* **2002**, *65*, 45–59.
14. A. Aamouche, F. J. Devlin, P. J. Stephens, *Chem. Commun*. **1999**, 361–362.
15. F. J. Devlin, P. J. Stephens, P. Besse, *Tetrahedron-Asymm*. **2005**, *16*, 1557–1566.
16. P. J. Stephens, *J. Phys. Chem*. **1985**, *89*, 748–752.

17. K. L. Bak, P. Jørgensen, T. Helgaker, K. Ruud, H. J. Aa. Jensen, *J. Chem. Phys*. **1993**, *98*, 8873–8887.
18. J. R. Cheeseman, M. J. Frisch, F. J. Devlin, P. J. Stephens, *Chem. Phys. Lett*. **1996**, *252*, 211–220.
19. DALTON. **2005**; a molecular electronic structure program, Release 2.0 (2005), see `http://www.kjemi.uio.no/software/dalton/dalton.html`.
20. Gaussian 03, Revision C.02. M. J. Frisch, G. W. Trucks, H. B. Schlegel, G. E. Scuseria, M. A. Robb, J. R. Cheeseman, J. A. Montgomery, Jr., T. Vreven, K. N. Kudin, J. C. Burant, J. M. Millam, S. S. Iyengar, J. Tomasi, V. Barone, B. Mennucci, M. Cossi, G. Scalmani, N. Rega, G. A. Petersson, H. Nakatsuji, M. Hada, M. Ehara, K. Toyota, R. Fukuda, J. Hasegawa, M. Ishida, T. Nakajima, Y. Honda, O. Kitao, H. Nakai, M. Klene, X. Li, J. E. Knox, H. P. Hratchian, J. B. Cross, V. Bakken, C. Adamo, J. Jaramillo, R. Gomperts, R. E. Stratmann, O. Yazyev, A. J. Austin, R. Cammi, C. Pomelli, J. W. Ochterski, P. Y. Ayala, K. Morokuma, G. A. Voth, P. Salvador, J. J. Dannenberg, V. G. Zakrzewski, S. Dapprich, A. D. Daniels, M. C. Strain, O. Farkas, D. K. Malick, A. D. Rabuck, K. Raghavachari, J. B. Foresman, J. V. Ortiz, Q. Cui, A. G. Baboul, S. Clifford, J. Cioslowski, B. B. Stefanov, G. Liu, A. Liashenko, P. Piskorz, I. Komaromi, R. L. Martin, D. J. Fox, T. Keith, M. A. Al-Laham, C. Y. Peng, A. Nanayakkara, M. Challacombe, P. M. W. Gill, B. Johnson, W. Chen, M. W. Wong, C. Gonzalez, and J. A. Pople; Gaussian, Inc., Wallingford, CT, **2004**.
21. G. Velde, F. Bickelhaupt, E. Baerends, C. Guerra, S. V. Gisbergen, J. Snijders, T. Ziegler, *J. Comput. Chem*. **2001**, *22*, 931–967.
22. G. Snatzke, in *Circular Dichroism: Principles and Applications*; N. Berova, K. Nakanishi, and R. W. Woody, eds., Wiley-VCH, New York, **2000**, p. 1.
23. M. Pecul, K. Ruud, *Adv. Quantum Chem*. **2005**, *50*, 185–212.
24. P. L. Polavarapu, *Chirality* **2002**, *14*, 768–781.
25. T. D. Crawford, *Theor. Chem. Acc*. **2006**, *115*, 227–245.
26. W. Moffitt, R. Woodward, A. Moscowitz, W. Klyne, C. Djerassi, *J. Am. Chem. Soc*. **1961**, *83*, 4013–4018.
27. T. D. Bouman, D. Lightner, *J. Am. Chem. Soc*. **1976**, *98*, 3145–3154.
28. C. Zhao, P. L. Polavarapu, C. Das, P. Balaram, *J. Am. Chem. Soc*. **2000**, *122*, 8228–8231.
29. L. Barron, L. Hecht, E. Blanch, A. Bell, *Prog. Biophys. Mol. Bio*. **2000**, *73*, 1–49.
30. R. Silva, J. Kubelka, P. Bour, S. Decatur, T. Keiderling, *Proc. Natl. Acad. Sci. USA* **2000**, *97*, 8318–8323.
31. C. Herrmann, K. Ruud, M. Reiher, *ChemPhysChem* **2006**, *7*, 2189–2196.
32. C. R. Jacob, S. Luber, M. Reiher *J. Phys. Chem. B* **2009**, *113*, 6558–6573.
33. S. Luber, M. Reiher, *J Phys. Chem. B* **2010**, *114*, 1057–1063.
34. J. Kapitan, V. Baumruk, V. Kopecky, P. Bour, *J. Phys. Chem. A* **2006**, *110*, 4689–4696.
35. F. Wang, P. L. Polavarapu, *J. Phys. Chem. A* **2000**, *104*, 10683–10687.
36. T. Buffeteau, D. Cavagnat, A. Bouchet, T. Brotin, *J. Phys. Chem. A* **2007**, *111*, 1045–1051.
37. P. J. Stephens, F. J. Devlin, J.-J. Pan, *Chirality* **2008**, *20*, 643–663.
38. E. Tajkhorshid, K. Jalkanen, S. Suhai, *J. Phys. Chem. B* **1998**, *102*, 5899–5913.
39. W. Han, K. Jalkanen, M. Elstner, S. Suhai, *J. Phys. Chem. B* **1998**, *102*, 2587–2602.
40. J. He, P. L. Polavarapu, *J. Chem. Theory Comput*. **2005**, *1*, 506–514.
41. J. Sadlej, J. Dobrowolski, J. Rode, M. Jamroz, *Phys. Chem. Chem. Phys*. **2006**, *8*, 101–113.
42. M. Losada, H. Tran, Y. Xua *J. Chem. Phys*. **2008**, *128*, 014508.
43. K. H. Hopmann, K. Ruud, M. Pecul, A. Kudelski, M. Dračinský, P. Bouř, *J. Phys. Chem. B*., **2011**, *115*, 4128–4137.
44. F. J. Devlin, P. J. Stephens, J. R. Cheeseman, M. J. Frisch, *J. Am. Chem. Soc*. **1996**, *118*, 6327–6328.

45. F. J. Devlin, P. J. Stephens, J. R. Cheeseman, M. J. Frisch, *J. Phys. Chem. A* **1997**, *101*, 9912–9924.
46. F. J. Devlin, P. J. Stephens, J. R. Cheeseman, M. J. Frisch, *J. Phys. Chem. A* **1997**, *101*, 6322–6333.
47. G. Zuber, W. Hug, *J. Phys. Chem. A* **2004**, *108*, 2108–2118.
48. M. Reiher, V. Liegeois, K. Ruud *J. Phys. Chem. A* **2005**, *109*, 7567–7574.
49. T. Helgaker, P. Jørgensen, *Theor. Chim. Acta* **1989**, *75*, 111–127.
50. F. Aiga, K. Sasagane, R. Itoh, *J. Chem. Phys*. **1993**, *99*, 3779–3789.
51. O. Christiansen, P. Jørgensen, C. Hättig, *Int. J. Quantum Chem*. **1998**, *68*, 1–52.
52. J. Olsen, P. Jørgensen, *J. Chem. Phys*. **1985**, *82*, 3235–3264.
53. P. Jørgensen, H. J. Aa. Jensen, J. Olsen, *J. Chem. Phys*. **1988**, *89*, 3654–3661.
54. S. Coriani, S. Høst, B. Jansik, L. Thøgersen, J. Olsen, P. Jørgensen, S. Reine, F. Pawlowski, T. Helgaker, P. Salek, *J. Chem. Phys*. **2007**, *126*, 154108.
55. J. A. Pople, R. Krishnan, H. B. Schlegel, J. S. Binkley, *Int. J. Quantum Chem*. **1978**, *14*, 545–560.
56. A. Komornicki, G. B. Fitzgerald, *J. Chem. Phys*. **1993**, *98*, 1398–1421.
57. T. Helgaker, P. Jørgensen, in *Methods in Computational Molecular Physics*, S. Wilson and G. H. F. Diercksen, eds., Plenum, New York, **1992**, pp. 353–421.
58. T. Kjærgaard, P. Jørgensen, J. Olsen, S. Coriani, T. Helgaker, *J. Chem. Phys*. **2008**, *129*, 054106.
59. A. Dalgarno, A. Stewart, *Proc. R. Soc. Lon. Ser. A* **1958**, *247*, 245–259.
60. B. Kirtman, *J. Chem. Phys*. **1968**, *49*, 3895–2898.
61. K. Kristensen, P. Jørgensen, A. J. Thorvaldsen, T. Helgaker, *J. Chem. Phys*. **2008**, *129*, 214103.
62. A. J. Thorvaldsen, K. Ruud, K. Kristensen, P. Jørgensen, S. Coriani, *J. Chem. Phys*. **2008**, *129*, 214108.
63. F. London, *J. Phys.* (Paris) **1937**, *8*, 397–409.
64. B. Gao, A. J. Thorvaldsen, K. Ruud, *Int. J. Quantum Chem*. **2011**, *111*, 858–872.
65. S. Reine, E. Tellgren, T. Helgaker, *Phys. Chem. Chem. Phys*. **2007**, *9*, 4771–4779.
66. R. Bast, U. Ekström, B. Gao, T. Helgaker, K. Ruud, A. J. Thorvaldsen, *Phys. Chem. Chem. Phys*. **2011**, *13*, 4224–4229.
67. V. P. Nicu, J. Neugebauer, S. K. Wolff, E. J. Baerends, *Theor. Chem. Acc*. **2008**, *119*, 245–263.
68. S. Coriani, A. J. Thorvaldsen, K. Kristensen, P. Jørgensen, *Phys. Chem. Chem. Phys*. **2011**, *13*, 4224–4229.
69. T. Helgaker, K. Ruud, K. L. Bak, P. Jørgensen, J. Olsen, *Faraday Discuss*. **1994**, *99*, 165–180.
70. J. Linderberg Y. Öhrn, *Propagators in Quantum Chemistry*, 2nd ed., John Wiley & Sons, Hoboken, NJ, **2004**.
71. J. Olsen, K. L. Bak, K. Ruud, T. Helgaker, P. Jørgensen, *Theor. Chim. Acta* **1995**, *90*, 421–439.
72. K. L. Bak, Aa. E. Hansen, K. Ruud, T. Helgaker, J. Olsen, P. Jørgensen, *Theor. Chim. Acta* **1995**, *90*, 441–458.
73. T. B. Pedersen, H. Koch, C. Hättig, *J. Chem. Phys*. **1999**, *110*, 8318–8327.
74. T. B. Pedersen, H. Koch, L. Boman, A. S. de Meras, *Chem. Phys. Lett*. **2004**, *393*, 319–326.
75. P. J. Stephens, *J. Phys. Chem*. **1987**, *91*, 1712–1715.
76. P. J. Stephens, K. Jalkanen, R. D. Amos, P. Lazzeretti, R. Zanasi, *J. Phys. Chem*. **1990**, *94*, 1811–1830.

77. K. Jalkanen, R. Kawiecki, P. J. Stephens, R. D. Amos, *J. Phys. Chem*. **1990**, *94*, 7040–7055.
78. Aa. E. Hansen, P. J. Stephens, T. D. Bouman, *J. Phys. Chem*. **1991**, *95*, 4255–4262.
79. Aa. E. Hansen, T. D. Bouman, *J. Chem. Phys*. **1985**, *82*, 5035–5047.
80. G. Placzek, in *Handbuch der Radiologie*, Vol. *6*, E. Marx, ed., Akademische Verlagsgesellschaft, Leipzig, **1934**, p. 205.
81. L. D. Barron, *Molecular Light Scattering and Optical Activity*, 2nd ed., Cambridge University Press, Cambridge, **2004**.
82. W. H. Flygare, *Chem. Rev*. **1974**, *74*, 653–687.
83. J. Gauss, K. Ruud, T. Helgaker, *J. Chem. Phys*. **1996**, *105*, 2804–2812.
84. L. A. Nafie, T. Freedman, *Enantiomer* **1998**, *3*, 283–297.
85. C. Cappelli, S. Corni, B. Mennucci, R. Cammi, J. Tomasi, *J. Phys. Chem. A* **2002**, *106*, 12331–12339.
86. K. Ruud, A. J. Thorvaldsen, *Chirality* **2010**, *21*, E54–E67.
87. W. Hug, in *Handbook of Vibrational Spectroscopy*, Vol. *1*, J. M. Chalmers and P. Griffiths, eds., John Wiley & Sons, New York, **2002**, pp. 745–758.
88. P. L. Polavarapu, *J. Phys. Chem*. **1990**, *94*, 8106–8112.
89. P. Bose, P. L. Polavarapu, L. D. Barron, L. Hecht, *J. Phys. Chem*. **1990**, *94*, 1734–1740.
90. R. D. Amos, *Chem. Phys. Lett*. **1982**, *87*, 23–26.
91. K. Ruud, T. Helgaker, P. Bour, *J. Phys. Chem. A* **2002**, *106*, 7448–7455.
92. M. Pecul, A. Rizzo, *Mol. Phys*. **2003**, *101*, 2073–2081.
93. P. J. Stephens, K. Jalkanen, F. J. Devlin, C. F. Chabalowski, *J. Phys. Chem*. **1993**, *97*, 6107–6110.
94. K. Sasagane, F. Aiga, R. Itoh, *J. Chem. Phys*. **1993**, *99*, 3738–3778.
95. T. Helgaker, P. Wilson, R. D. Amos, N. C. Handy, *J. Chem. Phys*. **2000**, *113*, 2983–2989.
96. P. Salek, O. Vahtras, T. Helgaker, H. Ågren, *J. Chem. Phys*. **2002**, *117*, 9630–9645.
97. J. R. Cheeseman, M. J. Frisch, F. J. Devlin, P. J. Stephens, *J. Phys. Chem. A* **2000**, *104*, 1039–1046.
98. K. Ruud, T. Helgaker, *Chem. Phys. Lett*. **2002**, *352*, 533–539.
99. S. Luber, M. Reiher, *Chem. Phys*. **2008**, *346*, 212–223.
100. M. Reiher, J. Neugebauer, *J. Chem. Phys*. **2003**, *118*, 1634–1641.
101. E. R. Davidson, *J. Comput. Phys*. **1975**, *17*, 87–94.
102. P. Norman, D. M. Bishop, H. J. Aa. Jensen, J. Oddershede, *J. Chem. Phys*. **2001**, *115*, 10323–10334.
103. M. Krykunov, M. D. Kundrat, J. Autschbach, *J. Chem. Phys*. **2006**, *125*, 194110.
104. L. Jensen, J. Autschbach, M. Krykunov, G. C. Schatz, *J. Chem. Phys*. **2007**, *127*, 134101.
105. V. Liegeois, K. Ruud, B. Champagne, *J. Chem. Phys*. **2007**, *127*, 204105.
106. J. R. Cheeseman, G. S. Scalmani, M. J. Frisch, unpublished.
107. M. Pecul, E. Lamparska, C. Cappelli, L. Frediani, K. Ruud, *J. Phys. Chem. A* **2006**, *110*, 2807–2815.
108. R. Cammi, B. Mennucci, J. Tomasi, *J. Phys. Chem. A* **2000**, *104*, 4690–4698.
109. L. Ferrighi, L. Frediani, C. Cappelli, P. Salek, H. Ågren, T. Helgaker, K. Ruud, *Chem. Phys. Lett*. **2006**, *425*, 267–272.
110. T. U. Helgaker, in *Geometrical Derivatives of Energy Surfaces and Molecular Properties*, P. Jørgensen and J. Simons, eds., Reidel. Dordrecht, **1986**, pp. 1–6.
111. T. U. Helgaker, J. Almlöf, H. J. Aa. Jensen, P. Jørgensen, *J. Chem. Phys*. **1986**, *84*, 6266–6279.
112. J. F. Stanton, J. Gauss, *Int. Rev. Phys. Chem*. **2000**, *19*, 61–95.

113. R. Ahlrichs, M. Bär, M. Häser, H. Horn, C. Kölmel, *Chem. Phys. Lett*. **1989**, *162*, 165–169.
114. J. Neugebauer, M. Reiher, C. Kind, B. Hess, *J. Comput. Chem*. **2002**, *23*, 895–910.
115. CADPAC: The Cambridge Analytic Derivatives Package Issue 6, Cambridge. A suite of quantum chemistry programs developed by R. D. Amos, with contributions from I. L. Alberts, J. S. Andrews, S. M. Colwell, N. C. Handy, D. Jayatilaka, P. J. Knowles, R. Kobayashi, K. E. Laidig, G. Laming, A. M. Lee, P. E. Maslen, C. W. Murray, J. E. Rice, E. D. Simandiras, A. J. Stone, M.-D. Su, and D. J. Tozer, **1995**.
116. J. Kussmann, C. Ochsenfeld, *J. Chem. Phys*. **2007**, *127*, 204103.
117. A. M. N. Niklasson, M. Challacombe, *Phys. Rev. Lett*. **2004**, *92*, 193001.
118. V. Weber, A. M. N. Niklasson, M. Challacombe, *Phys. Rev. Lett*. **2004**, *92*, 193002.
119. A. J. Thorvaldsen, L. Ferrighi, K. Ruud, H. Ågren, S. Coriani, P. Jørgensen, *Phys. Chem. Chem. Phys*. **2009**, *11*, 2293–2304.
120. P. Pulay, *Mol. Phys*. **1969**, *17*, 197.
121. M. Pecul, K. Ruud, *Int. J. Quantum Chem*. **2005**, *104*, 816–829.
122. O. Bludsky, K. L. Bak, P. Jørgensen, V. Spirko, *J. Chem. Phys*. **1995**, *103*, 10110–10115.
123. P. Danecek, J. Kapitan, V. Baumruk, L. Bednarova, V. Kopecky, P. Bour, *J. Chem. Phys*. **2007**, *126*, 224513.
124. Y. He, X. Cao, L. Nafie, T. Freedman, *J. Am. Chem. Soc*. **2001**, *123*, 11320–11321.
125. H. Sato, T. Taniguchi, K. Monde, S. Nishimura, A. Yamagishi, *Chem. Lett*. **2006**, *35*, 364–365.
126. S. Luber, M. Reiher, *ChemPhysChem* **2010**, *11*, 1876–1887.
127. H. Larsen, P. Jørgensen, J. Olsen, T. Helgaker, *J. Chem. Phys*. **2000**, *113*, 8908–8917.

25

MODELING OF SOLVATION EFFECTS ON CHIROPTICAL SPECTRA

Magdalena Pecul

25.1. INTRODUCTION

One of the main reasons for calculations of chiroptical spectra is to establish the unknown absolute configuration of an optically active molecule by comparison of the calculated spectrum and the experimental one. The other leading motivation is to derive information about the conformations of a flexible molecule. However, the chiroptical spectra are notoriously very sensitive to solvent effects—for example, significant changes of a basic chiroptical observable, natural optical rotation (OR), with a change of a solvent are a common occurence, even to the extent of the optical rotation changing its sign [1, 2]. The same is true of the other chiroptical phenomena, such as electronic circular dichroism (which we will refer to as circular dichroism, CD), vibrational circular dichroism (VCD), and vibrational Raman optical activity (ROA). Therefore, modeling of the solvent influence is of paramount importance in the calculations of the chiroptical spectra.

This chapter is focused on the discussion of solvent models and their applications in computational chiroptical spectroscopy. First, a short overview of the solvent models applied in computational chemistry in general is presented. Next, we discuss their applications to modeling of (a) specific electronic chiroptical phenomena (electronic circular dichroism and optical rotation including optical rotatory dispersion) and (b) the vibrational optical activity (VOA) phenomena (vibrational circular dichroism and vibrational Raman optical activity). Discussion of simulation of solvent effects in each kind of chiroptical spectroscopy is preceded by a very brief description of the theory of a given chiroptical phenomenon. For a more extensive discussion we refer the reader to

Comprehensive Chiroptical Spectroscopy, Volume 1: Instrumentation, Methodologies, and Theoretical Simulations, First Edition. Edited by N. Berova, P. L. Polavarapu, K. Nakanishi, and R. W. Woody.
© 2012 John Wiley & Sons, Inc. Published 2012 by John Wiley & Sons, Inc.

the other chapters in this volume (Chapters 21–24). Theoretical studies of solvent effects on optical rotation and electronic circular dichroism completed before 2006 have been reviewed in reference [3], so we will focus now on the more recent developments.

25.2. SOLVENT MODELS

There are two main approaches used for evaluating the effects that a solvent surrounding an optically active molecule has on its chiroptical properties: (a) those where only the solute molecule is treated quantum mechanically and the solvent is treated as a source of potential and (b) those where both the solute molecule and the solvent molecules are treated at the same level. In the first approach, the solvent can be modeled as either (a) a macroscopic continuum dielectric medium (assumed homogeneous and isotropic) characterized by a scalar dielectric constant (the polarizable continuum models, PCM) or (b) an essembly of discrete charges, usually obtained from molecular dynamics simulations. Molecular dynamics can also be used in the second approach, where both the solute molecule and some neighboring molecules of the solvent are explicitly included in the quantum chemical calculations (supermolecular approach). The solute–solvent clusters can be also generated by geometry optimization. Below, we present a short description of both approaches.

25.2.1. Polarizable Continuum Models

All polarizable continuum models are based on a concept that the interactions between a solute molecule and a solvent can be approximated by assuming that a solvent is a uniform polarizable medium (dielectric or conductive) and a solute molecule is placed in a cavity cut in the medium. In contemporary computational applications of the polarizable continuum models the solute molecule is treated quantum mechanically, and the appropriate terms describing its interactions with uniform polarizable medium are added to the Hamiltonian. Computational techniques based on the polarizable continuum model have been developed independently by several groups. They differ mainly in the cavity shape and in the way the charge interaction with the medium is calculated. The cavity is defined as a sphere, an ellipsoid, or a more complicated shape following the surface of the molecule.

To compute the electrostatic component of the solvation free energy, this model requires the solution of a classical electrostatic Poisson problem. Nowadays, one of the most popular methods of solving this problem is a polarized continuum model developed primarily by the group of Tomasi and co-workers [4–6]. In this approach, the cavity is made from spheres centered on nuclei in the solute molecule, and the cavity surface is divided into a number of small surface elements, where the reaction field is modeled by distributing charges onto the surface elements—that is, by creating apparent surface charges [7–10]. The electrostatic part of the solvent–solute interaction represented by the charge density spread over the cavity surface (*apparent surface charges*, ASC) gives rise to an operator to be added to the Hamiltonian of the isolated system in order to obtain the final effective Hamiltonian and the related free energy functional.

ASC-PCM calculations [5, 6] can be carried out in different ways. The most widespread approach is the IEF-PCM method (*Integral Equation Formalism*) by Cancés, Mennucci, and Tomasi [9], which uses a molecule-shaped cavity to define the boundary between the solute and the solvent. Amovilli and Mennucci have also described an

approach where repulsion and dispersion terms are computed self-consistently as part of the reaction field operator [11]. A related implementation of PCM is the self-consistent isodensity polarizable continuum (SCI-PCM) model of Foresman et al. [12], in which the cavity is constructed on the basis of an isosurface of the total electron density of the solute (calculated at the same level of theory as used for further quantum chemical calculations). Scalmani and Frisch [13] have recently published a new variation of ASC-PCM model (based on IEF-PCM and the continous charge approach proposed by York and Karplus [14]), where the free energy in solution (and its first and second derivatives) is a continuous function of all the parameters involved in the definition of the model, including the position of the atoms of the solute and the presence of external perturbing electric and/or magnetic fields.

Another widespread approach is the COSMO method (*COnductorlike Screening MOdel*) by Klamt [15–17] in which the surrounding medium is modeled as a conductor instead of a dielectric (that is, it uses scaled conductor boundary condition instead of the dielectric boundary condition for the calculation of the polarization charges of a molecule in a continuum). A variation on the COSMO model is C-PCM [18], in which construction of a cavity and treatment of reaction field is based on the IEF-PCM approach. Other polarizable-continuum model-based methods, like the MPE (*multipole expansion method*) by Rivail and Rinaldi [19, 20] and by Mikkelsen et al. [21, 22] with a spherical cavity, are less widespread, but also applied to the calculations of molecular properties.

Various models based on the concept of polarizable continuum are available for calculations of chiroptical properties in Gaussian 09 [23], Dalton [24], and ADF [25, 26], and, for calculations of electronic CD spectra, in ORCA [27].

25.2.2. Supermolecular Approach

An altenative way to model solvent effects is to treat solvent molecules explicitly, at the same footing as the solute. The quantum chemical calculations are carried out for the cluster of the solute with a certain number of solvent molecules, and the solvent effects are estimated as a difference between the results obtained for such complex and for an isolated solute molecule. The number of solvent molecules to be taken into account is necessarily limited by available computational resources, and as a rule only the first solvation shell is treated in this fashion. Thus, the supermolecular approach takes into account only the short-range solvent effects. Long-range solvent effects can be accounted for by combining supermolecular approach and one of the PCM models by placing the solute–solvent cluster in the cavity in a dielectric medium.

The geometries of the solute–solvent cluster are usually generated either by means of geometry optimization or from single configuration (snapshots) of a classical MD simulation trajectory. The first approach does not require any additional programing, but is difficult to automatize and therefore is labor-intensive. It can also introduce unphysical bias by neglecting thermal motion and taking into account only stable structures. Both these shortcomings can be rectified by employing molecular dynamics (classical or quantum) or Monte Carlo simulations to generate the structures of the solute–solvent clusters.

25.2.3. Molecular Dynamics

Molecular dynamics simulations, in the form of either classical molecular dynamics or CPMD (Carr–Parrinello Molecular Dynamics), can be used to generate solute–solvent

clusters as MD "snapshots" to be transfered to a quantum mechanical program where the property in question is implemented. An alternative way of employing MD for modeling solvent effects is to use it to generate electric field surrounding the solute by putting charges in the positions of solvent atoms (an example of this approach for chiroptical properties in presented in reference 28). This leads to a solvent model similar to PCM, but with discrete charges. Yet another use of MD is possible in calculations of vibrational properties. In this case, one can employ MD directly and can simulate vibrational spectra from MD trajectories (as done, for example, in references 29 and 30). However, the majority of application of MD for modeling of chiroptical properties in solution employ MD to generate solute–solvent clusters for supermolecular calculations.

25.3. SOLVENT EFFECTS ON ELECTRONIC CIRCULAR DICHROISM AND NATURAL OPTICAL ROTATION

25.3.1. Theoretical Description of OR and CD

25.3.1.1. Optical Rotation. The specific optical rotation, characterizing natural optical rotation, is related to the trace of the mixed electric dipole–magnetic dipole polarizability $G'_{\alpha\beta}$ [31]:

$$[\alpha]_\omega = 288 \cdot 10^{-30} \frac{\pi^2 N_A a_0^4 \omega^2}{M} \frac{1}{3} \mathrm{Tr}(\omega^{-1} G'_{\alpha\beta}(\omega)), \tag{25.1}$$

In these equations, N_A is Avogadro's number, a_0 is the Bohr radius, M is the molar mass of the molecule in g·mol^{-1}, and ω the frequency of the light in atomic units. $G'_{\alpha\beta}$ is also expressed in atomic units. The units of $[\alpha]_\omega$ are deg cm^3 · g^{-1} · dm^{-1}.

Using response theory [32], the mixed electric dipole–magnetic dipole polarizability can be expressed as

$$G'_{\alpha\beta} = \mathrm{Im}\langle\langle \hat{\mu}_\alpha; \hat{m}_\beta \rangle\rangle_\omega, \tag{25.2}$$

The mixed electric dipole–electric quadrupole polarizability, which contributes to the optical rotation of oriented samples (and to ROA, see below) can be expressed as

$$A_{\alpha\beta\gamma} = -\mathrm{Re}\langle\langle \hat{\mu}_\alpha; \hat{Q}_{\beta\gamma} \rangle\rangle_\omega. \tag{25.3}$$

Expressions $\langle\langle A; B \rangle\rangle_\omega$ in the above equations denote linear response functions.

The dipole moment operator $\hat{\mu}_\alpha$ can be expressed either in the length gauge formalism (using the position operator $\hat{r}_\alpha$) or in the velocity gauge formalism (using the momentum operator $\hat{p}_\alpha$), although application of the latter to the calculations of OR require some additional manipulation of the formula (see reference 33). For more details see Chapter 21.

25.3.1.2. Circular Dichroism. Circular dichroism, the differential absorption of left-and right-circularly polarized light by a sample of one enantiomer, is usually expressed as the difference between the molar extinction coefficients for left- and right-circularly polarized light: $\varepsilon_L(\lambda) - \varepsilon_R(\lambda)$. This quantity is related to the rotatory strength ^nR of the transition between the ground state 0 and the nth excited state (electronic states for electronic CD, vibrational states for VCD). The rotatory strength

${}^nR$ was derived from quantum mechanical theory by Rosenfeld [31]; and it was shown for isotropic samples to be given as the product of the electric dipole and magnetic dipole transition moments, which in atomic units can be written as

$$ {}^nR = \langle 0|\boldsymbol{\mu}|n\rangle \cdot \langle n|\mathbf{m}|0\rangle. \tag{25.4} $$

For oriented samples, there is also a contribution from interactions with the electronic quadrupole moment [34]

$$ {}^nR^{Q}_{\alpha\beta} = \frac{3}{4}\omega_{n0}\epsilon_{\alpha\gamma\delta}\langle 0|\hat{\mu}_\gamma|n\rangle\langle n\left|\hat{Q}_{\delta\beta}\right|0\rangle. \tag{25.5} $$

This contribution is purely anisotropic, and thus it vanishes upon orientational averaging and does not contribute in the case of isotropic samples such as a liquid.

In linear response theory, the scalar rotatory strength is calculated as a residue of the linear response function [32, 35]. For a transition from the ground state $|0\rangle$ to an excited state $|n\rangle$, it is in the velocity and length gauges given by, respectively,

$$ {}^nR^{v} = \frac{1}{2\omega_n}\langle 0|\mathbf{p}|n\rangle \cdot \langle n|\mathbf{L}|0\rangle = \frac{1}{2\omega_n}\mathrm{Tr}\{\lim_{\omega\to\omega_n}(\omega-\omega_n)\langle\langle \mathbf{p};\mathbf{L}\rangle\rangle_\omega\}, \tag{25.6} $$

$$ {}^nR^{r} = -\frac{\mathrm{i}}{2}\langle 0|\mathbf{r}|n\rangle \cdot \langle n|\mathbf{L}|0\rangle = \mathrm{Tr}\{\lim_{\omega\to\omega_n}(\omega-\omega_n)\langle\langle \mathbf{r};\mathbf{L}\rangle\rangle_\omega\}. \tag{25.7} $$

In these expressions, $\mathbf{r}, \mathbf{p}$, and $\mathbf{L}$ are the electronic position, momentum, and orbital angular-momentum operators, respectively; $\hbar\omega_n$ is the excitation energy of the nth electronic transition.

The response theory was applied to the study of optical rotation in 1998 [36], building on the implementation for Raman optical activity presented in 1994 [37]. The first calculations of rotatory strengths based on this general linear response formalism appeared in 1994 [35]. Time-dependent density functional theory (TDDFT) implementations for OR and ECD have been presented by a number of groups [38–43], and those are methods that are usually applied nowadays in calculations of natural optical activity.

25.3.2. Modeling of Solvent Effects on OR and ECD: General Aspects

It is possible to carry out gas-phase measurements of CD and OR [1, 44], but this kind of experiment is limited to small molecules, and therefore most of the measurements are carried out in solutions. Moreover, a particularly important field of CD application is structural investigation of molecules of biological importance (mostly peptides) in aqueous environment. Thus, modeling of the solvent effects is an indispensable aspect of calculations of CD and ORD (optical rotatory dispersion) spectra.

OR and CD have for a long time been recognized as being very sensitive to the molecular environment, and very early there have been attempts to account for solvent effects. Solvent effects on the optical rotation are traditionally accounted for using the Lorentz effective field approximation [45], in which the optical rotation is multiplied by a local field factor

$$ \gamma_{\mathrm{LF}} = \frac{\epsilon_s(\omega)+2}{3}, \tag{25.8} $$

where $\epsilon_s(\omega)$ is the frequency-dependent dielectric constant of the solvent. This relation, which results in an increase of the optical rotation with increasing solvent polarity for all solvated molecules, has been shown many times not to describe properly the actual effects [46, 47], and more sophisticated models (PCM or explicit solvent) are required.

In the case of optical rotation the supermolecular calculations (both rigid models and molecular dynamics) present a certain problem: The G' tensor, and consequently the optical rotation, is an extensive property (similarly as, for example, electric dipole polarizability) and supermolecular calculations result in optical rotation of the cluster composed of the solute and solvent molecules, not in optical rotation of the solute. It is not certain to what extent this is physically grounded. On the one hand, one can argue that there is a contribution to the optical rotation from the chiral arrangement of solvent molecules induced by a chiral solute. On the other hand, the size of such cluster, which influences the final result, is chosen arbitrarily and can introduce unphysical effects. This problem is less important in the calculations of CD spectra: The contribution from the solvent can usually be extracted by analyzing the type of electron excitation and can be considered separately. The vibrational spectroscopies are not problematic in this respect, since vibrations are essentially localized and can be ascribed to the solute, solvent, or low-frequency solute–solvent intermolecular modes.

25.3.3. Modeling of Solvent Effects on OR and ECD: Specific Applications

25.3.3.1. Optical Activity of Peptides and Amino Acids. Most of the calculations of CD spectra for peptides or peptide models (such as *N*-methylacetamide, NMA) are carried out accounting for the presence of the aqueous environments. Šebek, Kejík, and Bouř [48] modeled the conformational dependence of NMA electronic CD spectra, simulating the presence of water by means of COSMO and molecular dynamics. NMA was also used as a model system by Jiang et al. [49], who used it to construct an effective electronic Hamiltonian, which they employed to reproduce CD spectra of proteins on the basis of MD simulation of protein folding in aqueous environment. A similar model system, *N*-methyl-acetamide, has been studied by Cappelli and Mennucci [50], with hydration effects of CD spectra and OR simulated by means of IEF-PCM. These publications were focused on simulations of electronic transitions in amide chromophore, but a similar methodology was employed also for modeling of CD of coupled tryptophane chromophores: They have been approximated by indole rings, and aqueous environment was modeled by means of IEF-PCM [51]. The CD spectrum (both one- and two-photon) of tryptophane monomer was calculated by Guillaume et al. [52], and the solvent effects were also simulated by means of the IEF-PCM model.

As already mentioned above, molecular dynamics can also be used to generate point charges used to mimic solvent influence on the solute. This method has been applied for modeling influence of aqueous environment on the optical rotation and rotatory strengths of alanine and glycine by Kundrat and Autschbach [28]. The authors found it superior to the continuum model (COSMO variety). In the follow-up work [53], the same authors used molecular dynamics (with explicit water molecules) to study optical rotation and rotatory strengths also of phenylalanine and proline. They interpreted the observed optical rotations (including solvent shifts) in terms of sector rules, rationalizing them by a presence (or lack) of a perturbing group in a given sector.

The publications focused on the solvent effects on the CD spectra of amino acids and peptides are, as discussed above, numerous. The building blocks of nucleic acids

also attracted some attention in this respect: The CD spectra have been computed for adenine–guanine stacked dimers, with the aqueous solution modeled by means of linear response DFT and the state-specific polarizable continuum model [54].

25.3.3.2. Optical Activity of Other Organic Molecules. One of the favorite molecules in the theoretical studies of optical rotation is propylene oxide (methyloxirane). The reason for this is twofold: small size of propylene oxide, allowing for the use of highly accurate models of electronic structure, and remarkable sensitivity of its OR to the presence of a solvent (it is one of the cases when solvation changes a sign of OR [1]). There have been many attempts to reproduce the solvent effects on OR of propylene oxide, first by Kongsted et al. [55], who found that the single-center multipole-based spherical cavity dielectric continuum model used in conjunction with coupled cluster solute electronic structure model [56] is inadequate for the purpose. IEF-PCM model at the DFT computational level, with accounting for vibrational corrections on OR, was found to be more succesful [57]. This was somewhat in contradiction to the works of Mukhopadhyay et al. [58, 59], who performed molecular dynamics simulations for propylene oxide dissolved in water [58] and in benzene [59] and compared the results for optical rotatory dispersion with those obtained using the continuum COSMO model of the solution. They have concluded that the use of explicit solvent model is essential to render the optical rotation in agreement with experiment, since the contribution to OR from a dissymmetric solvent around the chiral solute (solvent imprint) can exceed the OR contribution of the solute itself. The molecular dynamics simulation of the propylene oxide–water mixture were repeated by Losada, Nguien, and Xu [60], who also calculated optical rotation of the propylene oxide–water clusters with up to three water molecules.

Optical rotation and circular dichroism of molecules structurally related to propylene oxide have also been calculated with accounting for solvent effects (usually using continuum models). Wilson et al. [61] employed a self-consistent isodensity polarizable continuum model (SCI-PCM) [12] to calculate optical rotatory dispersion of epichlorohydrin and epifluorohydrin (propylene oxide with one of the methyl group hydrogen atoms substituted by a chlorine or fluorine atom, respectively). They have found that, although the sign of the optical rotation at a given optical frequency may be rendered wrong by DFT calculations with the SCI-PCM model, the shape of the ORD curve is rendered correctly. IEF-PCM calculations of vibrational corrections on the optical rotation on fluoro-oxirane (which may be treated as propylene oxide derivative with the methyl group replaced by the fluorine atom) were carried out by Pedersen et al. [62], as the continuation of the work of the same group on propylene oxide [57].

Supermolecular method is also the method of choice in calculations of self-aggregation effects. Yang and Xu [63] used glycidol as a model system to study self-aggregation effects on optical rotation by means of ORD measurements in glycidol/$CDCl_3$ solutions of different concentrations and DFT calculations for the glycidol monomer, dimer, and trimer. They concluded on the basis of VCD spectra (see below) that at high concentration (3.5 M) contributions from the dimer are dominant, but they had problems with reproducing the experimental ORD curves. Mori, Inoue, and Grimme [64] calculated the effects of dimer conformation on optical rotation and circular dichroism of a chiral donor–acceptor dyad (*N*-(((S)-1-methylpropyloxy)-2-naphthoxypropyl)-4-cyanopyridinium), also employing the COSMO model to account for solvent influence on the conformational equilibrium.

The concept of ”solvent inprint” [59]—that is, contribution to chiroptical response from a normally achiral solvent due to chirality induced by a chiral solute (chirality

transfer)—has been the subject of the paper by Wang and Cann [65], who performed molecular dynamics simulations for two solvents (ethanol and benzyl alcohol) and three chiral solutes (styrene oxide, acenaphthenol, and *n*-(1-(4-bromophenyl)ethyl) pivalamide). They have discussed the results in terms of chirality indexes.

Continuum models (mostly IEF-PCM and COSMO) have been used, with varying degree of success, in numerous density functional calculations of CD and OR for organic molecules [61, 62, 64, 66–74]. Capelli et al. [66] used IEF-PCM to simulate the effects of methanol solution on the CD spectrum of (2R,3S,4R)-(+)-3,3′,4,4′,7-flavanpentol, which improved somewhat the agreement of the calculated spectrum with experiment. The same work reports on the calculations (employing MD) of the CD spectrum of the flavonoid in the presence of explicit water molecules and peptide fragments. IEF-PCM was used to simulate solvent effects on other flexible molecules, including γ-methyl paraconic acid [67] and its derivatives [69], with good results. In the case of another paraconic acid derivative, 4,4-dimethyl-5-oxo-tetrahydrofuran-3-carboxylic acid [74], the use of IEF-PCM reversed the sign of the computed specific rotation, which led to assignment of the absolute configuration in agreement with that from the CD spectrum. Calculations of solvent effects on optical rotation by means of IEF-PCM led Mennucci et al. [70] to the conclusion that the absolute configuration of two out of six natural cyclohexene oxides they have studied is incorrectly assigned in the literature. Another group which used IEF-PCM model in quantum chemical calculations of optical rotation and CD spectra for the purpose of establishing the absolute configuration was Kwit et al. [73], who reassigned on this basis the absolute configuration of a *trans*-diastereomer of the natural cytokine modulator cytoxazone. The IEF-PCM calculations of solvent effects on the optical rotation were less sucessful in the case of α-*R*-methylbenzylamine studied by Fischer, Compton, and Pagni [68]. The authors attributed this fact to the forming of the hydrogen bonds by the solute, not accounted for by means of the PCM model. Poor performance of IEF-PCM for solvent effects on the CD spectrum was observed by Pedersen et al. [62] for 3-methyl-cyclopentanone, probably because of the same reason. It is worth noting that solvent effects also on two-photon circular dichroism of 3-methyl-cyclopentanone have been simulated by the authors.

25.3.3.3. Optical Activity of Metal Complexes. CD is used not only in the studies of organic molecules, but also in inorganic chemistry, and solvent effects play an important role also in this field. Jensen et al. [75] used a discrete reaction field (DRF) model (modeling solvent by means of with point charges in positions obtained from MD simulations) to study the circular dichroism spectrum of $[Co(ethylenediamine)_3]^{3+}$ complex in water, and they compared the results with COSMO simulations. They concluded that neither model leads to perfect agreement with experiment, since both tend to overestimate CD intensities. These studies were extended later to the chiral chelate complexes of chromium(III), with the aqueous environment modeled by means of COSMO [76]. Other examples of calculations of CD and OR for chiral inorganic complexes with accounting for solvent effects can be found in the review by Autschbach [77] and in Chapter 21.

25.4. SOLVENT EFFECTS ON VIBRATIONAL CIRCULAR DICHROISM AND RAMAN OPTICAL ACTIVITY

25.4.1. Theoretical Description of VCD and ROA

25.4.1.1. Vibrational Circular Dichroism. The intensity of vibrational circular dichroism (the difference between absorption coefficients for left- and right-polarized

light for a given vibrational transition) is determined, like its electronic counterpart, by a rotatory strength, the imaginary part of the scalar product of the electric and magnetic transition dipole moments [see Eq. (25.4)], the only difference being that the transition moments involve (in Born–Oppenheimer approximation) the vibrational wavefunctions instead of the electronic ones. However, the evaluation of the vibrational rotatory strength was found to be less straightforward than the electronic rotatory strength, since the electronic contribution to the magnetic dipole moment vanishes for a vibrational transition in Born–Oppenheimer approximation. The solution to this was proposed by Stephens [78], who, by considering the first-order correction to the BO wavefunction, obtained the leading nonvanishing contribution to the electronic part of the magnetic moment and presented a working formula for VCD intensities. This treatment relates the vibrational rotatory strength of the fundamental transition in the ith normal mode to atomic polar and atomic axial tensors:

$$R_i = \hbar^2 \mathrm{Im}[\boldsymbol{P}_i^{\lambda} \cdot \boldsymbol{M}_i^{\lambda}], \tag{25.9}$$

where

$$P_{i\beta}^{\lambda} = \sum_{\alpha} P_{\alpha\beta}^{\lambda} S_{\lambda\alpha,i}, \qquad M_{i\beta}^{\lambda} = \sum_{\alpha} M_{\alpha\beta}^{\lambda} S_{\lambda\alpha,i}. \tag{25.10}$$

$P_{i\beta}^{\lambda}$ and $M_{\alpha\beta}^{\lambda}$ are atomic polar tensors and atomic axial tensors, respectively, and $S_{\lambda\alpha,i}$ transforms normal coordinates into Cartesian coordinates. λ is the nucleus number, and α and β are Cartesian coordinates. This approach has been implemented by Cheeseman et al. [79] for density functional theory [79] and most of the contemporary calculations of VCD spectra employ it.

25.4.1.2. Raman Optical Activity. Raman optical activity is described by means of the absolute difference between intensities of the scattered light with the incident light circularly polarized left and right, $I_k^R - I_k^L$, where $I_k^{L,R}$ are the scattered intensities with linear k polarization for right- (R) and left- (L) circularly polarized incident light, and k denotes the Cartesian component (Incident Circular Polarization Raman Optical Activity, ICP-ROA). Alternatively, ROA can be measured as a small circularly polarized component in the scattered light using incident light of fixed polarization, including unpolarized light (Scattered Circular Polarization Raman Optical Activity, SCP-ROA). These two approaches are equivalent in the far-from resonance limit. The differential scattering intensity between right- and left-circularly polarized light for the backward scattering is given by [80, 81]

$$I^R - I^L(180) = 24\beta(G')^2 + 8\beta(A)^2, \tag{25.11}$$

where

$$\beta(G')^2 = \frac{3\alpha_{ki}^{v} G_{ki}'^{v} - \alpha_{kk}^{v} G_{ii}'^{v}}{2}, \tag{25.12}$$

$$\beta(A)^2 = \frac{1}{2}\omega_{rad}\alpha_{ki}^{v}\epsilon_{kjl}A_{jli}^{v}, \tag{25.13}$$

Here ω_{rad} is the radiation angular frequency, and ϵ_{kjl} is the unit third rank antisymmetric tensor.

Within the double harmonic approximation (employed in most calculations of the ROA spectra), the other quantities in Equations (25.12) and (25.13), defined as products

of vibrational transition moments, can be described by means of geometric derivatives of optical tensors.

$$\alpha^{v}_{ki} G'^{v}_{ki} = <0|\alpha_{ki}|1><1|G'_{ki}|0> \approx \frac{1}{2\omega}\left(\frac{\partial \alpha_{ki}}{\partial Q}\right)_0 \left(\frac{\partial G'_{ki}}{\partial Q}\right)_0, \qquad (25.14)$$

$$\alpha^{v}_{ki} \epsilon_{kjl} A^{v}_{jli} = <0|\alpha_{ki}|1><1|\epsilon_{kjl} A_{jli}|0> \approx \frac{1}{2\omega}\left(\frac{\partial \alpha_{ki}}{\partial Q}\right)_0 \epsilon_{kjl} \left(\frac{\partial A_{jli}}{\partial Q}\right)_0. \qquad (25.15)$$

The tensors in Eqs. (25.15) and (25.15) are the electric dipole–electric dipole polarizability $\boldsymbol{\alpha}$, the imaginary part of the electric dipole–magnetic dipole polarizability $\mathbf{G}'$ [see Eq. (25.2)], and the real part of the electric dipole–electric quadrupole polarizability $\mathbf{A}$ [see Eq. (25.3)] [81]. Q is the normal coordinate of the vibration under study. The subscript 0 indicates that the quantities are calculated at the equilibrium geometry.

25.4.2. Modeling of Solvent Effects on Vibrational Optical Activity: General Aspects

Matrix isolation (first reported in 1982 [82]) and gas-phase VCD measurements are becoming more and more popular nowadays, but the majority of VCD spectra are taken in solution. Thus, taking into account the influence of a solvent on VCD spectra is an important element of computational VCD spectroscopy. This aspect is even more essential in the case of ROA spectra, since the first gas-phase measurements have been reported only recently [83] and the possibility of matrix isolation measurements of ROA is at present rather limited on account of low sensitivity of this spectroscopic method. Most of the ROA measurements are carried out either in neat liquids or in aqueous solutions; thus for a meaningful comparison with experimental spectra, simulations of the solvent (or self-aggregation effects) are essential.

Solvent effects on VCD and ROA spectra are usually modeled using either MD or one of the variations of PCM. The MD simulations of the vibrational spectra (both VCD and ROA) employing the standard harmonic approximation encounter a certain problem not present for electronic properties: The transformation of geometric hessian to normal coordinates in the harmonic approximation is strictly correct only when the energy gradient with respect to geometric coordinates vanishes—that is, in the geometry minimum (or at least a stationary point). Therefore a MD "snaphot" should not be used directly for VOA calculations. Using directly the MD "snaphots" leads to a very large number of imaginary frequencies and unphysical artifacts in the simulated spectra. This is avoided when the solute–solvent structures obtained from MD simulations are subjected to geometry optimization. However, this procedure is not only time-consuming, but also contrary to the purpose of MD, which is to probe a range of structures the solute–solvent assembly assumes at a given temperature and pressure—geometry optimization brings it back to the situation when thermal effects are not accounted for. One possible solution to this dilemma is to use some scheme of partial optimization, separating low- and high-frequency modes and allowing for calculations of the intensities for vibrational transitions in the high-frequency spectral region (low-frequency modes are often inaccessible experimentally and thus of less interest). Such a scheme—that is, partial geometry optimization in normal coordinates—was proposed by Bouř and Keiderling [84].

Another mode of use of molecular dynamics (or more precisely MD combined with quantum chemical calculations) is to simulate VCD spectra from MD trajectories, as presented by Yang and Cho [29]. They propose to simulate directly the VCD spectra

by Fourier transforming the cross-correlation function of the time-dependent electric and magnetic dipole moments, which are evaluated using the atomic partial charges, the coordinates, and velocities of the constituent atoms of the solute molecule at each time step of the QM/MM MD simulation. This approach was used to simulate the VCD spectum of the aqueous solution of alanine dipeptide analogue (CH_3)CO-Ala-NH(CH_3), with the peptide analogue molecule treated at the Hartree–Fock level [29]. A similar idea has been presented before in the group of Bouř [30], although, as far as we know, not used for prediction of VCD (or ROA) spectra.

Most PCM calculations of solvent effects on VOA employ either IEF-PCM or COSMO. As already mentioned, Scalmani and Frisch [13] have recently published a new variation of ASC-PCM model, a continuous surface charge (CSC) approach, and demonstrated its numerical performance for the ROA spectrum of alanine decapeptide. It is likely to become another popular polarizable continuum model for the studies of vibrational chiroptical properties.

25.4.3. Modeling of Solvent Effects on VOA: Specific Applications

25.4.3.1. Solvent Effects on VOA of Amino Acids and Peptides. The main area of applications of VCD and ROA is structural investigation of amino acids, peptides, and proteins, and thus it is not suprising that most of the modeling of solvent effects (predominantly aqueous environment) has been carried out in this area. Extensive studies on hydration of the simplest amino acid, alanine, and *N*-acetyl L-alanine *N′*-methyl amide (alanine dipeptide) have been carried by Jalkanen et al. [85] by means of supermolecular calculations and the hybrid model (supermolecular calculations combined with PCM). The authors compare the results obtained by means of Born–Oppenheimer molecular dynamics simulations with 20 solvating water molecules and the rest of the solvent modeled by means of various polarizable continuum models, with the previous results obtained by the same group employing simpler aqueous environment models (four water molecules in reference 86). The authors conclude that the hybrid model is the best approach currently available, and they advocate its use for further studies of amino acids and peptides. Calculations of the ROA spectra for the same dipeptide have been presented by Mukhopadhyay, Zuber, and Beratan [87]. In this case, Monte Carlo simulations in a water environment have been used to obtain the structures. Molecular dynamics with two different force fields have been run by Lee et al. [88] for hydrated *N*-acetylproline amide, and the VCD spectra have been calculated by means of DFT from amide I local mode frequencies, vibrational coupling constant, dipole strength, and rotational strength obtained as functions of the two backbone dihedral angles ψ and ϕ.

The use of a hybrid model (explicit solvent molecules for the first solvation shell and polarizable continuum model for the remaining part of the solvent) seems to be the best approach to simulate the solvent effects on VOA spectrum of a peptide. However, it has been suggested, on the basis of the results obtained for several models of tight β-turns in peptides, that if for computational reasons it is not feasible, even the use of a continuum model (COSMO in this case) alone is advantageous [89]. Comparison of performance of nuclear magnetic resonance and ROA spectroscopy in conformational analysis for model proline-containing dipeptides (Pro-Gly, Gly-Pro, Pro-Ala, and Ala-Pro) has been carried out by Buděšínský et al. [90], with the COSMO model of the aqueous environment. They also have found that even in the case of hydrated hydrogen-bond forming molecules, the use of polarizable continuum model alone significantly improves the agreement of the calculated vibrational chiroptical spectra with experiment. This finding was confirmed

by the calculations carried out by Pecul et al. [91] for ROA spectra of hydroxyproline in zwitterion, anionic and cationic forms.

Explicit solvation of helical dipeptides (up to 21 amide groups) was modeled by Kubelka et al. [92] by peforming geometry optimization of peptide with two water molecules added to each amide CO group and one added to each amide NH group. They concluded that this approach performs quite well, reproducing for example the (−,+,−)-shaped amide I′ band for N-deuterated α-helical peptides. The subject was revisited later [93] and the VCD spectra of 15-amide alanine α-helices were simulated by means of DFT calculations combined with the property transfer method, again with explicit solvent molecules. The influence of degree of solvation was studied, and it was found to affect primarily the frequency shifts of the unsolvated amide group vibrations.

Substantial solvent effects have been found on the VCD bands of the β-hairpin structures by Bouř and Keiderling [94], who modeled them by performing moleular dynamics and then adding electrostatic field-based parameterization correction to the force field and intensity tensors to compensate for the solvent electrostatic field. The β-hairpin structure has been further studied by this group using a larger peptide model and MD solvent simulations [95], but only the IR spectrum was calculated. The VCD spectrum of a β-sheet hairpin has been calculated before by Hilario et al. [96], but only the most tightly bonded water molecules were used to model solvent effects.

Würtz, Jürgensen and Jalkanen [97] have simulated the VCD and ROA spectra of tri-L-serine in neutral, zwitterion, anionic, and cationic forms in aqueous solution and compared the results with experimental spectra taken at different pH values. They have accounted for the aqueous environment by using explicit water molecules, IEF-PCM model (also using a hybrid approach with both explicit water molecules and a dielectric continuum) and a simple Onsager model with a spherical cavity. In the conclusions, the authors stressed the necessity of having explicit water molecules present in the model when simulating chiroptical spectra of a peptide, suggesting that formation of hydrogen bonds between water molecules in the first solvation shell and polar parts of the peptide is of critical importance for the VOA response.

Šebek et al. [98] have studied the pH effects on the ROA spectrum of the L-alanyl-L-alanine dipeptide by means of MD calculations on the dipeptide–water clusters (for the zwitterion, anion, and cation forms of the dipeptide), followed by normal mode optimization and DFT calculations of the ROA spectra for the MD snapshots, with the bulk solvent effects simulated by means of C-PCM. They have used the calculated spectra to extract conformational ratios from the experimental spectra, obtaining results in agreement with nuclear magnetic resonance analysis. Both MD simulations and the COSMO model were also used to simulate the effects of aqueous environment on the VCD spectrum of a cyclic hexapeptide (Phe-^{D}Pro-Gly-Arg-Gly-Asp) [99].

25.4.3.2. Solvent Effects on VOA of Other Organic Molecules. Apart from the studies on peptides and amino acids, the solvent-induced changes on ROA and VCD have been studied in a number of organic molecules. Propylene oxide, one of the smallest stable chiral organic molecules, has been chosen as a model system by Losada, Nguyen, and Xu [60] to study solvent effects not only on optical rotation (as already mentioned), but also on VCD spectra. They have calculated VCD spectra of propylene oxide interacting with one, two, and three water molecules and compared them with the experimental spectrum, concluding that the binary PO–H_2O complex is the dominating species in aqueous solution at room temperature. They have also observed, in both experiment and theoretical calculations, the phenomenon of so-called chirality transfer in VCD

spectra: vibrational optical activity of a normally achiral molecule (here water) induced by the presence of a chiral partner (propylene oxide).

Similarly as in the case of electronic chiroptical spectra, modeling of VOA often requires accounting for self-aggregation effects, and recently there have been several papers describing such calculations. Yang and Xu [63], already mentioned, calculated dimerization effects also on the VCD spectrum of glycidol, and they compared the results with measurements for glycidol dissolved in $CDCl_3$. They found that in order to simulate the spectrum at high concentrations (1.1 M and higher) it is necessary to take into account contributions from the glycidol dimer, which completely dominate the spectrum at 3.5 M. A similar investigation has been carried out by Losada, Tran, and Xu [100] for lactic acid in $CDCl_3$, CH_3OH, and H_2O soluations. Binary and higher aggregates of lactic acid were found to dominate the spectrum in $CDCl_3$ at 1.0 M and higher concentrations, while in the hydrogen-bond-forming solvents the best agreement between theory and experiment was found for lactamide dimer with two (methanol) and six (water) molecules attached. Shin-ya et al. [101] analyzed the VCD spectrum of 1-phenylethanol in Ar matrix, diluted CS_2 solution, and neat liquid. They have found that the neat liquid 1-phenylethanol spectrum can be reproduced by calculations for 1-phenylethanol dimers, while for diluted (0.1 M) CS_2 solution the population-weighted linear combination of the VCD spectra for the monomer and the dimers is in agreement with experiment. Similar studies were also performed by Nicu et al. [102] for complexes of benzoyl-benzoic acid with ammonia and lactic acid and methyl lactate with water. Effects of explicit solvation by DMSO molecules and of forming a cyclodextrin complex have also been studied for three dialkyl tartrates—dimethyl tartrate, diethyl tartrate, and diisopropyl tartrate—by Zhang and Polavarapu [103].

An area very closely related to the computational studies of solvent effect on VCD spectra is modeling of so-called chirality transfer in VCD spectra: vibrational optical activity of a normally achiral molecule induced by the presence of a chiral environment. Certain aspects of this phenomenon were studied in some of the works quoted above [100, 102]; but since this has been discussed recently in the review paper by Sadlej, Dobrowolski, and Rode [104], we are not going to examine it here.

Taking into account explicit solvation seems to be necessary to predict VCD spectrum of a solute forming hydrogen bonds with a solvent (that is, usually in the case of an aqueous solvent and a polar solute). However, it has been shown that in the case of solute and solvent of low polarity, the use of continuum model also improves significantly the agreement of the calculated spectra with experiment [105]. This has been demonstrated by Debie et al. [105] for pulegone (naturally occuring enone) in carbon disulfhide and chloroform solutions. They have also shown that taking into account the presence of solvent by including explicitly only one solvent molecule leads to worse agreement with experiment than PCM calculations. On the other hand, there are cases where the popular IEF-PCM model (as available in Gaussian 03) fails to render correctly the solvent effects on the VCD spectra, as shown by Polavarapu et al. [106] for dibromo-1,1-binaphthol. The results for dibromo-1,1-binaphthol were improved by the use of continuous charge approach variation of PCM [13], as mentioned by Polavarapu et al. [107] in their work on the absolute configuration of garcinia acid, where they applied the new PCM implementation to calculate solvent effects on VCD, CD, and ORD spectra of garcinia acid dimethyl ester. It is also worth mentioning that calculations of CD without accounting for solvent effects yielded wrong absolute configuration of garcinia acid dimethyl ester, and the use of the continuous charge approach PCM rectified this.

25.5. CONCLUDING REMARKS

There are two main groups of methods used for calculating the solvent-induced changes on the chiroptical spectra: polarizable continuum models and supermolecular approach with the solute–solvent clusters generated either by means of quantum chemical geometry optimization or by molecular-dynamics-based methods. MD can also be used to create trajectories used for calculations of vibrational optical activity spectra or to construct discrete reaction field surrounding the solute molecule. The collected computational evidence allows us to conclude that when there are hydrogen bonds formed between the solute and the solvent (e.g., for peptides in aqueous environment), the best choice of the solvent model is the use of molecular dynamics coupled with quantum chemical calculations for the solute–solvent clusters. The influence of the bulk solvent outside the first solvation shell can be modeled by means of one of the polarizable continuum models. The use of an explicit solvent model is not always possible due to high computational cost of such procedure. In such cases the use of a polarizable contunuum model alone is advantageous, since it is computationally inexpensive (the cost is little more than that for an isolated solute molecule), and in most cases it reproduces correctly the solvent-induced changes on chiroptical properties, allowing for example for correct assignment of the absolute configuration. PCM models are particularly useful for solvents of low polarity and for highly polar solvents but not for hydrogen-bond-forming ones. In the case of hydrogen-bond-forming solvents, the performance of PCM is less predictable, but in some cases it has been found to bring the results closer to experiment. New polarizable continuum models are under developement, so it is likely to remain a popular method of accounting for solvent effects.

REFERENCES

1. T. Müller, K. B. Wiberg, P. H. Vaccaro, *J. Phys. Chem. **A*** **2000**, *104*, 5959–5968.
2. Y. Kumata, J. Furukawa, T. Fueno, *Bull. Chem. Soc. Jpn*. **1970**, *43*, 3920–3921.
3. M. Pecul, K. Ruud, in *Continuum Solvation Models in Chemical Physics: From Theory to Applications*, B. Mennucci and R. Cammi, eds., Wiley–VCH, Weinheim, **2007**, pp. 206–219.
4. J. Tomasi, M. Persico, *Chem. Rev*. **1994**, *94*, 2027–2094.
5. J. Tomasi, B. Mennucci, R. Cammi, *Chem. Rev*. **2005**, *105*, 2999–3094.
6. R. Cammi, B. Mennucci, J. Tomasi, in *Computational Chemistry, Review of Current Trends*, Vol. 8, J. Leszczynski, ed., World Scientific, Singapore, **2003**.
7. S. Miertus, E. Scrocco, J. Tomasi, *Chem. Phys*. **1981**, *55*, 117–129.
8. R. Cammi, J. Tomasi, *J. Comp.Chem*. **1985**, *16*, 1449–1458.
9. E. Cancés, B. Mennucci, J. Tomasi, *J. Chem. Phys*. **1997**, *107*, 3032–3041.
10. B. Mennucci, E. Cances, J. Tomasi, *J. Phys. Chem. **B*** **1997**, *101*, 10506–10517.
11. C. Amovilli, B. Mennucci, *J. Phys. Chem. **B*** **1997**, *101*, 1051–1057.
12. J. B. Foresman, T. A. Keith, K. B. Wiberg, J. Snoonian, M. J. Frisch, *J. Phys. Chem*. **1996**, *100*, 16098–16104.
13. G. Scalmani, M. J. Frisch, *J. Chem. Phys*. **2010**, *132*, 114110.
14. D. M. York, M. Karplus, *J. Phys. Chem. **A*** **1999**, *103*, 11060–11079.
15. A. Klamt, G. Schüürmann, *J. Chem. Soc., Perkin Trans. 2* **1993**, 799–805.
16. A. Klamt, *J. Phys. Chem*. **1995**, *99*, 2224–2235.
17. A. Klamt, V. Jonas, *J. Chem. Phys*. **1996**, *105*, 9972–9980.

18. V. Barone, M. Cossi, *J. Phys. Chem. A* **1998**, *102*, 1995–2001.
19. J. L. Rivail, D. Rinaldi, *Theor. Chim. Acta* **1973**, *32*, 57–70.
20. J. L. Rivail, D. Rinaldi, in *Computational Chemistry, Review of Current Trends*, Vol. 1, J. Leszczynski, ed., World Scientific, Singapore, **1996**.
21. K. V. Mikkelsen, E. Dalgaard, P. Swanstrøm, *J. Phys. Chem*. **1987**, *91*, 3081–3092.
22. K. V. Mikkelsen, P. Jørgensen, H. J. A. Jensen, *J. Chem. Phys*. **1994**, *100*, 6597–6607.
23. M. J. Frisch, G. W. Trucks, H. B. Schlegel, G. E. Scuseria, M. A. Robb, J. R. Cheeseman, G. Scalmani, V. Barone, B. Mennucci, G. A. Petersson, H. Nakatsuji, M. Caricato, X. Li, H. P. Hratchian, A. F. Izmaylov, J. Bloino, G. Zheng, J. L. Sonnenberg, M. Hada, M. Ehara, K. Toyota, R. Fukuda, J. Hasegawa, M. Ishida, T. Nakajima, Y. Honda, O. Kitao, H. Nakai, T. Vreven, J. A. Montgomery, Jr., J. E. Peralta, F. Ogliaro, M. Bearpark, J. J. Heyd, E. Brothers, K. N. Kudin, V. N. Staroverov, R. Kobayashi, J. Normand, K. Raghavachari, A. Rendell, J. C. Burant, S. S. Iyengar, J. Tomasi, M. Cossi, N. Rega, J. M. Millam, M. Klene, J. E. Knox, J. B. Cross, V. Bakken, C. Adamo, J. Jaramillo, R. Gomperts, R. E. Stratmann, O. Yazyev, A. J. Austin, R. Cammi, C. Pomelli, J. W. Ochterski, R. L. Martin, K. Morokuma, V. G. Zakrzewski, G. A. Voth, P. Salvador, J. J. Dannenberg, S. Dapprich, A. D. Daniels,. Farkas, J. B. Foresman, J. V. Ortiz, J. Cioslowski, D. J. Fox, J. A. Pople, *Gaussian 09 Revision A.02*, Gaussian Inc., Wallingford, CT, **2009**.
24. DALTON, *a molecular electronic structure program, Release 2.0 (2005), see* `http://www.kjemi.uio.no/software/dalton/dalton.html`, **2005**.
25. G. T. Velde, F. M. Bickelhaupt, E. J. Baerends, C. F. Guerra, S. J. A. van Gisbergen, J. G. Snijders, T. Ziegler, *J. Comp. Chem*. **2001**, *22*, 931–967.
26. *ADF2009.01, SCM, Theoretical Chemistry, Vrije Universiteit, Amsterdam, The Netherlands, see* `http://www.scm.com`, **2009**.
27. F. Neese, *ORCA—an ab initio, Density Functional and Semiempirical program package, Version 2.6. University of Bonn*, **2008**.
28. M. D. Kundrat, J. Autschbach, *J. Chem. Theory Comput*. **2008**, *4*, 1902–1914.
29. S. Yang, M. Cho, *J. Chem. Phys*. **2009**, *131*, 135102.
30. J. Horniek, P. Kapralova, P. Bouř, *J. Chem. Phys*. **2007**, *127*, 084502.
31. L. Rosenfeld, *Z. Phys*. **1928**, *52*, 161–174.
32. J. Olsen, P. Jørgensen, *J. Chem. Phys*. **1985**, *82*, 3235–3264.
33. T. B. Pedersen, H. Koch, L. Boman, A. M. J. S. de Meras, *Chem. Phys. Lett*. **2004**, *393*, 319–326.
34. T. B. Pedersen, A. E. Hansen, *Chem. Phys. Lett*. **1995**, *246*, 1–8.
35. K. L. Bak, A. E. Hansen, K. Ruud, T. Helgaker, J. Olsen, P. Jørgensen, *Theor. Chim. Acta* **1995**, *90*, 441–458.
36. P. L. Polavarapu, C. Zhao, *Chem. Phys. Lett*. **1998**, *296*, 105–110.
37. T. Helgaker, K. Ruud, K. L. Bak, P. Jørgensen, J. Olsen, *Faraday Discuss*. **1994**, *99*, 165–180.
38. K. Ruud, T. Helgaker, *Chem. Phys. Lett*. **2002**, *352*, 533–539.
39. J. R. Cheesemen, M. J. Frisch, F. J. Devlin, P. J. Stephens, *J. Phys. Chem. A* **2000**, *104*, 1039–1046.
40. S. Grimme, *Chem. Phys. Lett*. **1996**, *259*, 128–137.
41. S. Grimme, M. Waletzke, *J. Chem. Phys*. **1999**, *111*, 5645–5655.
42. J. Autschbach, T. Ziegler, *J. Chem. Phys*. **2002**, *116*, 891–896.
43. K. Yabana, G. F. Bertsch, *Phys. Rev. A* **1999**, *60*, 1271–1279.
44. S. M. Wilson, K. B. Wiberg, J. R. Cheeseman, M. J. Frisch, P. H. Vaccaro, *J. Phys. Chem. A* **2005**, *109*, 11752–11764.

45. H. A. Lorentz, *The Theory of Electrons*, Tuebner, Leipzig, Germany, 1916, pp. 305, reprinted by Dover, New York, **1951**.
46. B. Mennucci, J. Tomasi, R. Cammi, J. R. Cheeseman, M. J. Frisch, F. J. Devlin, P. J. Stephens, *J. Phys. Chem. **A*** **2002**, *106*, 6102–6113.
47. P. J. Stephens, F. J. Devlin, J. R. Cheeseman, M. J. Frisch, B. Mennucci, J. Tomasi, *Tetrahedron–Asymmetry* **2000**, *11*, 2443–2448.
48. J. Šebek, Z. Kejík, P. Bouř, *J. Chem. Phys*. **2006**, *110*, 4702–4711.
49. J. Jiang, D. Abramavicius, B. M. Bulheller, J. D. Hirst, S. Mukamel, *J. Phys. Chem. **B*** **2010**, *114*, 8270–8277.
50. C. Cappelli, B. Mennucci, *J. Phys. Chem. **B*** **2008**, *112*, 3441–3450.
51. A. Roy, P. Bouř, T. A. Keiderling, *Chirality* **2009**, *21*, E163–E171.
52. M. Guillaume, K. Ruud, A. Rizzo, S. Monti, Z. Lin, X. Xu, *J. Phys. Chem. **B*** **2010**, *114*, 6500–6512.
53. M. D. Kundrat, J. Autschbach, *J. Chem. Theory Comput*. **2009**, *5*, 1051–1060.
54. F. Santoro, V. Barone, A. Lami, R. Improta, *Phys. Chem. Chem. Phys*. **2010**, *12*, 4934–4948.
55. J. Kongsted, T. B. Pedersen, M. Strange, A. Osted, A. E. Hansen, K. V. Mikkelsen, F. Pawlowski, P. Jórgensen, C. Hättig, *Chem. Phys. Lett*. **2005**, *401*, 385–389.
56. O. Christiansen, K. V. Mikkelsen, *J. Chem. Phys*. **1999**, *110*, 8348–8361.
57. J. Kongsted, K. Ruud, *Chem. Phys. Lett*. **2008**, *451*, 226–232.
58. P. Mukhopadhyay, G. Zuber, M. Goldsmith, P. Wipf, D. N. Beratan, *ChemPhysChem* **2006**, *7*, 2483–2486.
59. P. Mukhopadhyay, G. Zuber, P. Wipf, D. N. Beratan, *Angew. Chem. Int. Ed*. **2007**, *46*, 6450–6452.
60. M. Losada, P. Nguyen, Y. Xu, *J. Phys. Chem. **A*** **2008**, *112*, 5621–5627.
61. S. M. Wilson, K. B. Wiberg, M. M. Murphy, P. H. Vaccaro, *Chirality* **2008**, *20*, 357–369.
62. T. B. Pedersen, J. Kongsted, D. Crawford, K. Ruud, *J. Chem. Phys*. **2009**, *130*, 034310.
63. G. Yang, Y. Xu, *Phys. Chem. Chem. Phys*. **2008**, *10*, 6787–6795.
64. T. Mori, Y. Inoue, S. Grimme, *J. Org. Chem*. **2006**, *71*, 9797–9806.
65. S. Wang, N. M. Cann, *J. Chem. Phys*. **2008**, *129*, 054507.
66. C. Capelli, S. Bronco, S. Monti, *Chirality* **2005**, *17*, 577–589.
67. D. Marchesan, S. Coriani, C. Forzato, P. Nitti, G. Pitacco, K. Ruud, *J. Phys. Chem. **A*** **2005**, *109*, 1449–1453.
68. A. T. Fischer, R. N. Compton, R. M. Pagni, *J. Phys. Chem. **A*** **2006**, *110*, 7067–7071.
69. S. Coriani, A. Baranowska, L. Ferrighi, C. Forzato, D. Marchesan, P. Nitti, G. Pitacco, A. Rizzo, K. Ruud, *Chirality* **2006**, *18*, 357–369.
70. B. Mennucci, M. Claps, A. Evidente, C. Rosini, *J. Org. Chem*. **2007**, *72*, 6680–6691.
71. W. Al-Basheer, R. M. Pagni, R. N. Compton, *J. Phys. Chem. **A*** **2007**, *111*, 2293–2298.
72. A. Rizzo, N. Lin, K. Ruud, *J. Chem. Phys*. **2008**, *128*, 164312.
73. M. Kwit, M. D. Rozwadowska, J. Gawroński, A. Grajewska, *J. Org. Chem*. **2009**, *74*, 8051–8063.
74. S. Coriani, C. Forzato, G. Furlan, P. Nitti, G. Pitacco, M. Ringholm, K. Ruud, *Tetrahedron: Asymmetry* **2009**, *20*, 1459–1467.
75. L. Jensen, M. Swart, P. T. van Duijnen, K. Autschbach, *Int. J. Quantum Chem*. **2006**, *106*, 2479–2488.
76. J. Fan, M. Seth, J. Autschbach, T. Ziegler, *Inorg. Chem*. **2008**, *47*, 11656–11668.
77. J. Autschbach, *Coord. Chem. Rev*. **2007**, *251*, 1796–1821.
78. P. J. Stephens, *J. Phys. Chem*. **1985**, *89*, 748–752.

79. J. R. Cheeseman, M. J. Frisch, F. J. Devlin, P. J. Stephens, *Chem. Phys. Lett*. **1996**, *252*, 211–220.
80. L. D. Barron, A. D. Buckingham, *Mol. Phys*. **1971**, *20*, 1111–1119.
81. L. D. Barron, *Molecular Light Scattering and Optical Activity*, Cambridge University Press, Cambridge, **1982**.
82. D. W. Schlosser, F. Devlin, K. Jalkanen, P. J. Stephens, *Chem. Phys. Lett*. **1982**, *88*, 286–291.
83. Šebestík and Bouř, J. Šebestík, P. Bouř, *J. Phys. Chem. Lett.* **2011**, *2*, 498–502.
84. P. Bouř, T. Keiderling, *J. Chem. Phys*. **2004**, *117*, 4126–4132.
85. K. J. Jalkanen, I. M. Degtyarenko, R. M. Nieminen, X. Cao, L. A. Nafie, F. Zhu, L. D. Barron, *Theor. Chim. Acta* **2008**, *119*, 191–210.
86. K. J. Jalkanen, R. M. Nieminen, K. Frimand, J. Bohr, H. Bohr, R. C. Wade, E. Tajkhorshid, S. Suhai, *Chem. Phys*. **2001**, *265*, 125–151.
87. P. Mukhopadhyay, G. Zuber, D. N. Beratan, *Biophys. Journ*. **2008**, *95*, 5574–5586.
88. K.-K. Lee, K.-I. Oh, H. Lee, C. Joo, H. Han, M. Cho, *ChemPhysChem* **2007**, *8*, 2218–2226.
89. J. Kim, J. Kapitaán, A. Lakhani, P. Bouř, T. A. Keiderling, *Theor. Chem. Acc*. **2008**, *119*, 81–97.
90. M. Buděšínský, P. Daněček, L. Bednárová, J. Kapitán, V. Baumruk, P. Bouř, *J. Phys. Chem.* ***A*** **2008**, *112*, 8633–8640.
91. M. Pecul, C. Deillon, A. J. Thorvaldsen, K. Ruud, *J. Raman Spectrosc*. **2010**, *41*, 1200–1210.
92. J. Kubelka, R. Huang, T. A. Keiderling, *J. Phys. Chem.* ***B*** **2005**, *109*, 8231–8243.
93. D. R. Turner, J. Kubelka, *J. Phys. Chem.* ***B*** **2007**, *111*, 1834–1845.
94. P. Bouř, T. Keiderling, *J. Phys. Chem.* ***B*** **2005**, *109*, 23687–23697.
95. J. Kim, R. Huang, J. Kubelka, P. Bouř, T. A. Keiderling, *J. Phys. Chem.* ***B*** **2006**, *110*, 23590–23602.
96. J. Hilario, J. Kubelka, T. A. Keiderling, *J. Am. Chem. Soc*. **2003**, *125*, 7562–7574.
97. V. Würtz Jürgensen, K. Jalkanen, *Phys. Biol*. **2006**, *3*, S63–S79.
98. J. Šebek, J. Kapitaán, J. Šebestík, V. Baumruk, P. Bouř, *J. Phys. Chem.* ***A*** **2009**, *113*, 7760–7768.
99. P. Bouř, J. Kim, J. Kapitaán, R. P. Hammer, R. Huang, L. Wu, T. A. Keiderling, *Chirality* **2008**, *20*, 1104–1119.
100. M. Losada, H. Tran, Y. Xu, *J. Chem. Phys*. **2008**, *128*, 014508.
101. K. Shin-ya, H. Sugeta, S. Shin, Y. Hamada, Y. Katsumoto, K. Ohno, *J. Phys. Chem.* ***A*** **2007**, *111*, 8598–8605.
102. V. P. Nicu, J. Neugebauer, E. J. Baerends, *J. Phys. Chem.* ***A*** **2008**, *112*, 6978–6991.
103. P. Zhang, P. L. Polavarapu, *J. Phys. Chem.* ***A*** **2009**, *113*, 7760–7768.
104. J. C. Dobrowolski, J. E. Rode, J. Sadlej, *J. Mol. Struct. (Theochem)* **2007**, *810*, 129–134.
105. E. Debie, P. Bultinck, W. Herrebout, B. van der Veken, *Phys. Chem. Chem. Phys*. **2008**, *10*, 3498–3508.
106. P. L. Polavarapu, N. Jeirath, S. Walia, *J. Phys. Chem.* ***A*** **2009**, *113*, 5423–5431.
107. P. L. Polavarapu, G. Scalmani, E. K. Hawkins, C. Rizzo, N. Jeirath, I. Ibnusaud, D. Habal, D. S. Nair, S. Haleema, *J. Nat. Prod*. **2011**, *74*, 321–328.

26

COMPLEXATION, SOLVATION, AND CHIRALITY TRANSFER IN VIBRATIONAL CIRCULAR DICHROISM

Valentin Paul Nicu and Evert Jan Baerends

26.1. INTRODUCTION

Accurate determination of the absolute configuration (AC) using VCD requires correct interpretations of the VCD spectra. This in turn requires careful consideration of two very important aspects:

1. *The accuracy of the calculated VCD spectra*. This is because on the one hand when using VCD spectroscopy the absolute configuration (AC) of chiral compounds is determined based on a comparison between experimental and calculated VCD spectra, whereas on the other hand the calculated VCD spectra depend sensitively on the choice of computational parameters used in calculations.
2. *The effects induced in VCD spectra by the solvent*. This is because most of the time we compare experimental spectra measured in solution with computed spectra obtained from calculations on a single molecule.

Both these aspects will be discussed in this chapter. First, in Section 26.2 we will introduce the concept of robustness of the normal modes in a VCD spectrum. We will show that this concept can be used to determine the stability of the calculated VCD signs and, therefore, to assess the reliability of a VCD prediction. Then, in Section 26.3 we will discuss the effects induced in VCD spectra by molecular complex formation—that is, one of the most important sources of perturbations in solutions. The chapter will be finalized with some concluding remarks and general guidelines for the interpretation of VCD spectra.

Comprehensive Chiroptical Spectroscopy, Volume 1: Instrumentation, Methodologies, and Theoretical Simulations, First Edition. Edited by N. Berova, P. L. Polavarapu, K. Nakanishi, and R. W. Woody.
© 2012 John Wiley & Sons, Inc. Published 2012 by John Wiley & Sons, Inc.

All calculated VCD spectra presented in this chapter have been computed using the VCD implementation [1] in the Amsterdam Density Functional (ADF) program package [2–4] using the BP86 and OLYP exchange-correlation functionals and the ADF TZP basis set. We note that the exchange-correlations functionals most often used for computing VCD spectra are the B3LYP and B3PW91 hybrid functionals. However, as shown in reference 1, the pure functionals BP86 and OLYP yield VCD spectra that reproduce the experimental one at least as good as the spectra obtained using the hybrid functionals mentioned above.

26.2. CONCEPT OF ROBUSTNESS IN VCD SPECTROSCOPY

26.2.1. Theory

As discussed in Chapter 24, the VCD intensity of the fundamental transition ($|0\rangle \rightarrow |1\rangle$) of the ith vibrational mode is given by the rotational strength $R(i)$:

$$R(i) = \vec{E}_{01}(i)\mathrm{Im}[\vec{M}_{10}(i)] = |\vec{E}_{01}(i)||\mathrm{Im}[\vec{M}_{10}(i)]|\cos[\xi(i)], \tag{26.1}$$

where $\vec{E}_{01}(i)$ and $\mathrm{Im}[\vec{M}_{10}(i)]$ are the electric (EDTM) and magnetic (MDTM) transition dipole moment vectors of the fundamental vibrational transition of the ith normal mode, $|\vec{E}_{01}(i)|$ and $|\mathrm{Im}[\vec{M}_{10}(i)]|$ are the length of the vectors $\vec{E}_{01}(i)$ and $\mathrm{Im}[\vec{M}_{10}(i)]$, respectively, and $\xi(i)$ is the angle between these two vectors. (Note that $\mathrm{Im}[\vec{M}_{10}(i)]$ is a real quantity because $\vec{M}_{10}(i)$ is purely imaginary.)

As can be seen in Eq. (26.1), the sign of $R(i)$ is determined by the cosine of the angle, $\xi(i)$, that is, $R(i)>0$ if $\xi(i) < 90^\circ$, whereas if $\xi(i) > 90^\circ$, we have $R(i)<0$. From Eq. (26.1) the cosine of the angle $\xi(i)$ can be written

$$\cos[\xi(i)] = \frac{\vec{E}_{01}(i)\mathrm{Im}[\vec{M}_{10}(i)]}{|\vec{E}_{01}(i)||\mathrm{Im}[\vec{M}_{10}(i)]|}. \tag{26.2}$$

Rotational strength has two important properties: (1) It is zero for achiral molecules, and (2) for enantiomeric pairs it has equal magnitude but opposite sign. These two properties can also be interpreted from the perspective of the ξ angles.

The first property implies that in achiral molecules the EDTM and MDTM associated with a given vibrational transition are perpendicular; that is, because in general these two vectors are not zero, they must be perpendicular in order to yield a zero rotational strength:

$$|\vec{E}_{01}(i)| \neq 0, \quad |\mathrm{Im}[\vec{M}_{10}(i)]| \neq 0, \quad R(i) = 0 \Rightarrow \cos[\xi(i)] = 0 \Leftrightarrow \xi(i) = 90^\circ. \tag{26.3}$$

The second property is equivalent to

$$R_R(i) = -R_S(i) \Rightarrow \cos[\xi_R(i)] = -\cos[\xi_S(i)] \Leftrightarrow \xi_R(i) = 180^\circ - \xi_S(i), \tag{26.4}$$

where the subscripts R and S label the two enantiomers of a chiral molecule.

From Eq. (26.4) it is clear that chiral molecules have, in general, angles ξ that are different from 90°. However, it should be noted that modes with angles ξ of 90° can be encountered in chiral molecules because $\xi_R(i) = \xi_S(i) = 90^\circ$ is also a solution of Eq. (26.4).

Finally, we note that symmetry constraints can impose restrictions on the orientation of the EDTM and MDTM of a given normal mode; that is, depending on the irreducible representation to which a given normal mode i belongs, only certain values are permitted for its associated angle $\xi(i)$ [5]. For example, in chiral molecules with C_2 symmetry, the EDTMs and MDTMs associated to the modes belonging to the A irreducible representation are required to be along the C_2 symmetry axis; that is, they are either parallel ($\xi = 0^\circ$) or antiparallel ($\xi = 180^\circ$).

26.2.2. Distribution of the ξ Angles in Chiral Molecules

In this section we will investigate the distributions of the values taken by the angles ξ in chiral molecules. The discussion is based on the results obtained in reference 5.

The distributions of the ξ angles of 28 chiral molecules calculated using the BP86 functional and the TZP basis set have been analyzed statistically by calculating for each molecule the average value, $\overline{\xi}$, and the standard deviation, $\sigma(\xi)$. Schematic representations of the 28 test molecules are shown in Figure 26.1. As can be seen, our test molecules consist of two chiral molecules with symmetry (i.e., molecules 1 and 2 in Figure 26.1), and 26 chiral molecules without symmetry (i.e., molecules 3 to 28 in Figure 26.1), ranging from very small (5 atoms) to relatively large molecules (48 atoms).

In the case of the nonsymmetric chiral molecules it was found [5] that the angles ξ have a Gaussian distribution that is roughly centered on the 90° value, that is, $\overline{\xi} \cong 90^\circ$. Depending on the molecule, the standard deviations, $\sigma(\xi)$, vary between 10° and 40°. On the other hand, the angle distributions of the chiral molecules with symmetry have peaks not only at 90° but also at 0° and 180°. As discussed in the previous section, some irreducible representations require the EDTM and MDTM to be along a certain symmetry axis—that is, either parallel ($\xi = 0^\circ$) or antiparallel ($\xi = 180^\circ$). The peaks at 0° and 180° of the angle distribution are attributed to modes belonging to those irreducible representations.

In the following, three suggestive molecules will be considered and their angle distributions will be analyzed. The angle distributions of these molecules are shown in Figure 26.2 as XY diagrams with the abscissa axis representing the angle interval from 0° to 180° (divided into 10° intervals) and the ordinate axis indicating the number of normal modes in a given 10° interval.

First, we consider Tröger's base—that is, molecule 1 in Figure 26.1. Tröger's base is a chiral molecule that has C_2 symmetry. The angle distribution of Tröger's base is shown in the upper panel of Figure 26.2. As can be seen, the distribution has peaks near 0°, 90°, and 180°. The peaks near 0° or 180° are due to the modes of A symmetry, which have EDTMs and MDTMs along the C_2 symmetry axis. The angles ξ of the modes of B symmetry have a Gaussian distribution centered on 90°; that is, there are no symmetry restrictions for the orientation of the EDTMs and MDTMs in these modes.

The angle distribution of Tröger's base has a standard deviation $\sigma(\Delta\xi)$ of 66.7°. This value is much larger then the typical values encountered for chiral molecules without symmetry, that is, $10^\circ < \sigma(\xi) < 40^\circ$. Clearly, because of the peaks near 0° or 180°, chiral molecules with symmetry have more modes with angles ξ far from the 90° value than chiral molecules without symmetry.

Next we will consider the Pulegone molecule—that is, molecule 14 in Figure 26.1. The angle distribution of Pulegone is shown in the middle panel of Figure 26.2. The distribution has a standard deviation $\sigma(\xi)$ of 32.6°. This means that approximately 35% of the modes of Pulegone have ξ angles that differ from 90° by at least 32.6°; that is,

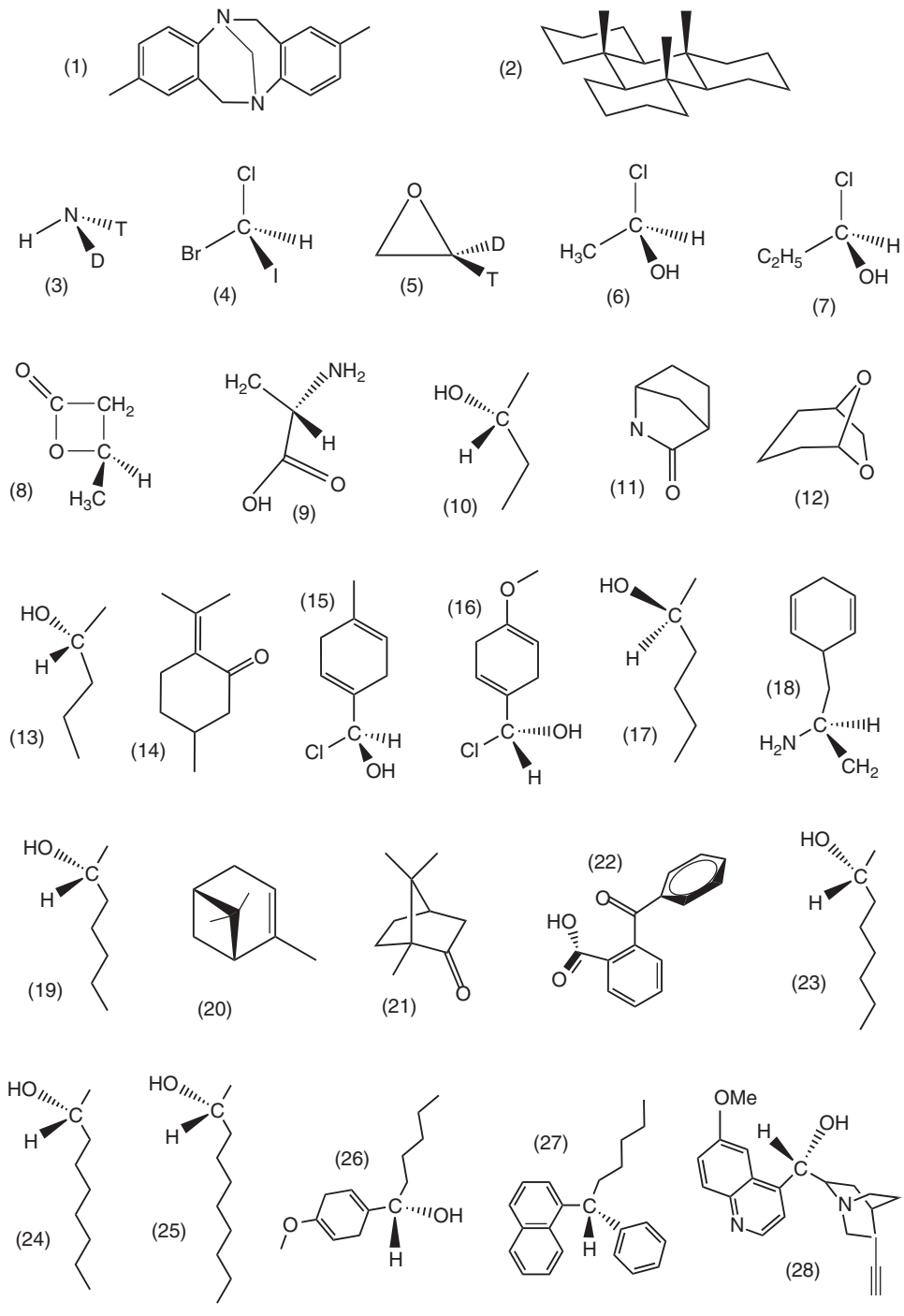

Figure 26.1. Schematic representation of the 28 chiral molecules analyzed.

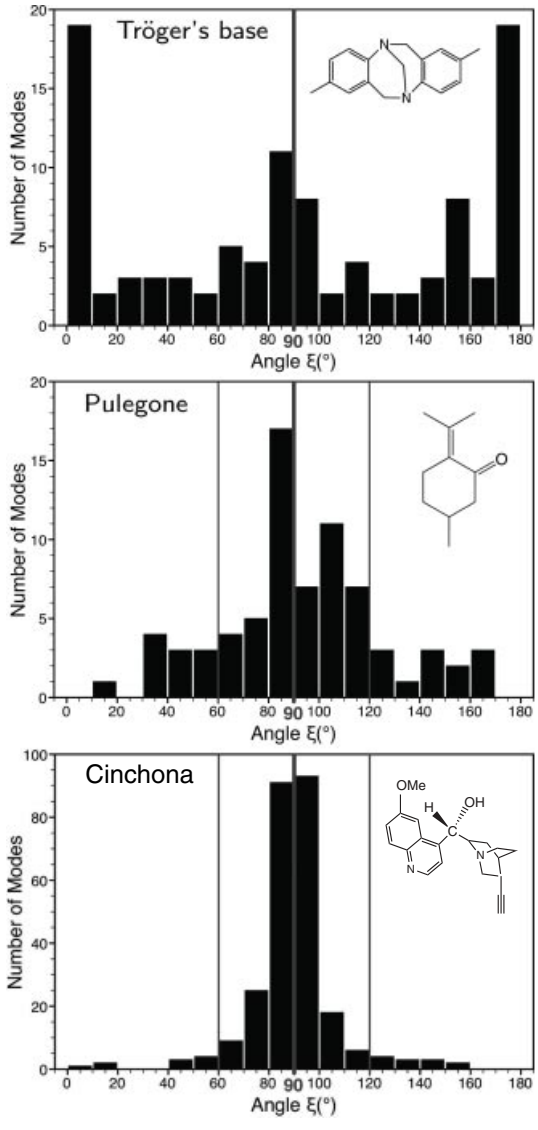

Figure 26.2. Distributions of the angles ξ of Tröger's base (upper panel), Pulegone (middle panel), and Cinchona (lower panel). The abscissa axis gives the angle interval from 0° to 180° divided into 10° intervals, whereas the ordinate axis gives the number of modes in a given angle interval.

approximately 65% of the members of a distribution are situated within the range of two standard deviations. As can be seen in Figure 26.2 (middle panel), the distribution of the angles ξ of Pulegone still has significant values outside the angle interval between 60° and 120°.

The last example we consider is cinchona—that is, molecule 28 in Figure 26.1. The angle distribution of Cinchona is shown in the lower panel of Figure 26.2. The distribution has a standard deviation $\sigma(\xi)$ of 12.5°; and as can be seen, it is squeezed around the 90° line. Only 12 out of the 132 modes of cinchona have values that differ from 90° by 30° or more.

As will be shown in Section 26.2.4, this large variation among the angle distributions of various molecules has very important implications in VCD spectroscopy. There is a direct correlation between the spreading of the angle distribution around the 90° value

and the agreement between calculation and experiment; that is, the larger the spread the better the agreement.

Finally, it is worth mentioning that the angle distributions presented in Figure 26.2 have been obtained using all normal modes of a molecule, that is, $3N-6$ (N being the number of atoms of the considered molecule). However, as shown in reference 5, very similar distributions are obtained also when considering only the normal modes in the fingerprint region—that is, the frequency interval between 800 and 1800 cm^{-1} that is usually considered in VCD spectroscopy. (Typically half of the normal modes of a molecule are in the fingerprint region).

26.2.3. Dependence of ξ on Computational Parameters

We continue by investigating the dependence of the computed ξ angles on the computational parameters used in calculations. For this purpose, we monitor the differences between the distributions of the angles ξ calculated with two different sets of computational parameters. Such an investigation is not only of intrinsic interest but also justified by the fact that a rather wide range of computational parameters (e.g., exchange-correlation functionals and/or basis sets) is currently used for VCD calculations.

For a consistent evaluation of the differences between the ξ distributions of the same molecule obtained from calculations with two different sets of computational parameters, a one-to-one correspondence between the normal modes in the two calculations has to be established first. Assuming that the relaxed structures obtained with the two sets of computational parameters have the same orientation and represent the same conformation, one can make a one-to-one correspondence between the modes of the two calculations by calculating normal mode overlaps—that is, by calculating inner products between mass-weighted Cartesian displacement vectors (i.e., the eigenvectors of the mass-weighted Hessian) obtained from the two calculations. For more details on the calculation of normal mode overlaps, the reader is referred to references 6 and 7. Here, we just note that (1) two identical modes will have an overlap of 1, and (2) an overlap of 0.9 indicates that the two modes are 81% similar, that is, $0.9^2 = 0.81$.

Because the restrictions imposed by symmetry on the orientation of the EDTMs and MDTMs are not affected by the choice of computational parameters, only the 26 non-symmetric chiral molecules in Figure 26.1 (i.e., molecules 3 to 28), have been considered for the present investigation. For each molecule the differences between the ξ angles of two calculations have been analyzed as follows. After establishing a one-to-one mapping between the modes of two calculations, only the pairs of modes whose modes have an overlap of at least 0.9 have been selected for the analysis—that is, approximately 90% of the modes of a molecule. Then, for each selected mode pair the difference $\Delta\xi$ between the angles ξ of the modes in the pair is calculated. Finally, the distributions of the $\Delta\xi$ values are analyzed separately for each molecule by calculating the mean value $\overline{\Delta\xi}$ and the standard deviations $\sigma(\Delta\xi)$.

First we will discuss the dependence of the ξ angles on the exchange-correlation functionals (the rest of the computational parameters being identical in the two calculations). Two pure (i.e., nonhybrid) exchange-correlation functionals have been considered for this purpose (i.e., BP86 versus OLYP).

Going from BP86 to OLYP represents the typical change of computational parameters that one tests in order to improve the agreement between the calculated and experimental VCD spectra. The two functionals yield similar VCD spectra that reproduce the experimental one quite well. However, based on the agreement between calculations

and experiment, neither functional can be considered as being superior; that is, neither yields VCD spectra that consistently reproduce the experiment better than the other one [1, 5, 7, 8].

The analysis of the differences $\Delta\xi$—that is, $\Delta\xi = \xi_{BP86} - \xi_{OLYP}$ calculated for the 26 nonsymmetric molecules in Figure 26.1,—has shown that for the modes with significant VCD intensities (see below for more details), the differences $\Delta\xi$ for the modes in a molecule have a Gaussian distribution. The $\Delta\xi$ distributions are centered roughly on the 0° value, indicating that one functional does not have a systematic bias toward larger or smaller ξ for all modes with respect to the other functional. Depending on the molecule, the $\Delta\xi$ distributions have standard deviations, $\sigma(\Delta\xi)$, between 6° and 10°. The maximum deviation, $\Delta\xi_{max}$, was found to be smaller than 30°—that is, slightly more than three $\sigma(\Delta\xi)$.

Similar variations of $\Delta\xi$ distributions (i.e., $\overline{\Delta\xi} \cong 0^\circ, 6^\circ < \sigma(\Delta\xi) < 10^\circ$ and $\Delta\xi_{max} < 30^\circ$) have been observed also when comparing (1) calculations with different basis sets (e.g., DZP versus TZP, TZP versus TZ2P) and (2) vacuum calculations to calculations where the effects of the solvent have been modeled using continuum solvation models (e.g., COSMO).

Regarding the modes with weak VCD intensities—that is, modes with very small EDTMs and/or MDTMs—it was found that these modes can exhibit very large variation of their angles (i.e., $\Delta\xi$ of 60°–70° are not uncommon), when going from one set of computational parameters to another. To substantiate this affirmation, in the following we consider the mode 52 of benzoyl-benzoic acid (BBA)—that is, molecule 22 in Figure 26.1.

Table 26.1 lists the frequencies, rotational strengths, angles ξ, and the Cartesian components of the EDTMs and MDTMs calculated with the BP86 and OLYP exchange-correlation functionals for mode 52 of BBA. The overlap between the BP86 and OLYP displacement vectors of mode 52 is also given in Table 26.1. As can be seen, the two functionals have predicted very similar frequencies and nuclear displacement vectors for the mode 52 of BBA; that is, the normal mode overlap is 0.99, but there are very different values for the angles ξ, namely 49.9° in the free molecule (FM) versus 111.7° in the molecular complex (MC).

TABLE 26.1. Comparison of the Frequencies (cm^{-1}), Rotational Strengths (10^{-44} esu · cm), ξ Angle, Electric Dipole Transition Moments (10^{-21} esu · cm), and Magnetic Dipole Transition Moments (10^{-25} esu · cm) of the Normal Mode 52 of Benzoyl Benzoic Acid (Molecule 22 in Figure 26.1) Calculated Using the BP86 and OLYP Functionals

Overlap: 0.99		$\Delta\xi = 61.8^\circ$	
	Frequency	R	ξ
BP86:	1151.5	+1.3	49.9°
OLYP:	1162.0	−1.0	111.7°
$\vec{E}_{01}(i)$	x	y	z
BP86:	−1.7	+0.7	−2.2
OLYP:	−3.1	+1.5	+1.3
$\mathrm{Im}[\vec{M}_{01}(i)]$	x	y	z
BP86:	−14.6	−35.3	−54.6
OLYP:	−12.3	−35.8	−61.1

The origin of this large variation of ξ can be understood by comparing the Cartesian components of the EDTMs and MDTMs calculated for this mode with the two functionals. A look at the EDTMs of mode 52 reveals that (1) the magnitude of the EDTM of this mode has a very small value (almost zero) in both BP86 and OLYP calculations and (2) the two functionals have predicted very different Cartesian EDTM components for this mode. On the other hand, when comparing the MDTMs of mode 52 we see that (1) mode 52 has a relatively large MDTM and (2) the two functionals have predicted very similar values for the Cartesian components of the MDTM of this mode.

The very large variation observed for the angle ξ of mode 52 when going from BP86 to OLYP is related to the different direction of the EDTM in the two calculations. This in turn is a consequence of the fact that EDTM associated to the mode 52 is almost zero—a value much smaller than the EDTMs of the rest of the modes of BBA. Since the two functionals have predicted very similar values for the frequency, nuclear displacement vectors, and MDTM of mode 52 (i.e., physical quantities with significant magnitudes), it should be clear that the very small values of the EDTM of mode 52 depends too sensitively on the exchange-correlation functional used in calculations (most likely on other computational parameters too) and cannot be predicted accurately.

26.2.4. Criteria for Robustness

The study in Section 26.2.2 has shown that the ξ associated to the normal modes of a chiral molecule have Gaussian distributions centered the 90° values. On the other hand, the study in Section 26.2.3 has shown that the variations $\Delta\xi$ induced in ξ by the use of different sets of computational parameters have a Gaussian distribution that is centered on the 0° value and have standard deviation between 6° and 10°.

These findings have two important consequences:

1. The use of different computational parameters can induce changes in the values of the ξ angles across the 90° line for modes with angles ξ close to 90°. That is, normal modes obtained from calculations with different computational parameters, which are otherwise almost identical, can have different VCD signs.
2. The use of different computational parameters is expected to induce no VCD sign changes in normal modes that have ξ angles that differ from 90° by more than 30°. The specified threshold value (i.e. 30°) represents a bit more than three standard deviations and therefore is a very conservative criterion; that is, 99.7% of the members of a distribution fall within the range of three standard deviations.

The two observations made above can be summed up by introducing the concept of robustness of the normal modes in a VCD spectrum. That is, the modes in a VCD spectrum can be classified as robust and nonrobust [5, 9]. The *robust* modes are characterized by angles ξ that are far from 90° (i.e., by at least 30°), and as a result their VCD sign is not sensitive to small perturbations of computational or experimental nature. Consequently, the VCD sign of the robust modes can be accurately predicted by calculations. The nonrobust modes, on the other hand, have angles ξ that are close to 90°. Because of this, even the smallest perturbation (e.g, the use of slightly different computational parameters; the use of different solvents) can affect the VCD sign of the nonrobust modes. As a result, the VCD sign of nonrobust modes cannot be accurately predicted from calculations and therefore should not be trusted.

Besides the modes that have angles ξ close to 90°, also the modes with weak VCD intensities (i.e., with very small EDTM or MDTM), should be assigned as nonrobust.

As shown in the previous section, these modes can exhibit very large variation of their ξ angles upon changing computational parameters, because the direction of the dipole transition moments with small magnitude cannot be computed accurately. We note that an absolute measure, valid for all molecules, to determine what should be considered small in this context cannot be given. The magnitudes of the total EDTM and MDTM of a normal mode depend on the type of mode and on the number of atoms involved in the normal mode motion—that is, on the molecule. In reference 5, an unstable sign has been found if for a given molecule, the EDTM/MDTM is less than 10% of the mean value of the EDTMs/MDTMs of all the modes of the respective molecule. As a conservative threshold, we recommend a magnitude of at least 30% of the mean value of the EDTM (or MDTM) values of the molecule. However, more studies are needed for determining an exact threshold.

26.2.5. Validation of the Concept of Robustness

26.2.5.1. Effects of Various Computational Parameters on VCD Spectra. In this section we will investigate the relevance of the similarities/discrepancies induced between experimental and calculated VCD spectra by the use of various computational parameters. A very good example in this regard, which illustrates both the principle and the usefulness of the robustness concept, is the combined computational–experimental study of Pulegone (i.e., molecule 14 in Figure 26.1), presented in reference 7. Here, we will summarize the most important conclusions of this study.

We start by comparing in Figure 26.3 (left panel) the experimental and calculated (BP86/TZP) VCD spectra of Pulegone. As can be seen, apart from a few small discrepancies (indicated by rectangles), there is a rather good agreement between calculation and experiment.

We continue by evaluating the robustness of the modes in the calculated VCD spectrum of Pulegone in Figure 26.3. A convenient way to do this is by plotting the computed values of the angles ξ as dots on top of the VCD spectra. This is illustrated in the right panel of Figure 26.3. The baseline of the calculated VCD spectrum is the 90° line; the y coordinate of each dot gives the magnitude of each ξ angle (see the vertical left axis), while the x coordinate gives the frequency of the mode.

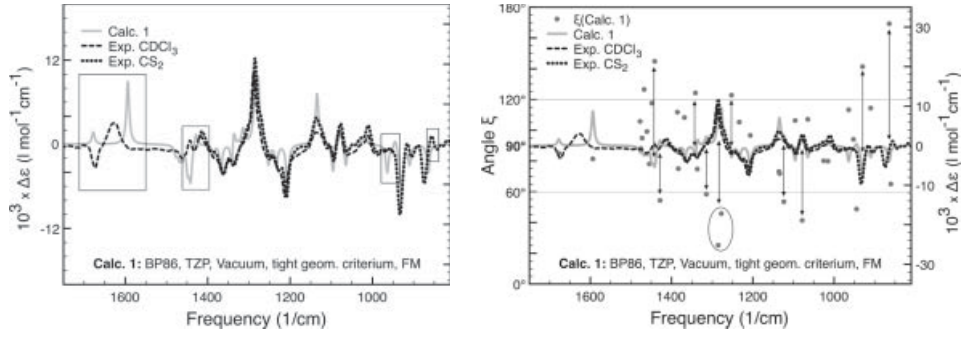

Figure 26.3. Comparison of the experimental and calculated (BP86/TZP) VCD spectra of Pulegone (left panel). The most important discrepancies between calculations and experiment are indicated by rectangles in the left panel. Right panel: Robust mode analysis for the calculated VCD spectrum of Pulegone. The dots indicate the values of the ξ angles, whereas the arrows indicate the robust modes. The experimental spectra were provided by Bultinck et al. [26].

In the interval between 800 and 1800 cm^{-1}, calculation **1** has predicted 38 modes for Pulegone. Out of these 38 modes, only 10 have been identified as robust. In Figure 26.3 (right panel) the robust modes have been indicated with arrows. As can be seen, most of the peaks that stand out in the experimental VCD spectrum of Pulegone correspond to robust modes. Furthermore, except for the robust mode at 1442 cm^{-1}, we have sign agreement between calculation and experiment for all robust modes.

The sign discrepancy observed for robust mode at 1442 cm^{-1}—that is, mode 56 of Pulegone—could be attributed to mode mixing. That is, because calculation **1** has predicted 9 modes within 50 cm^{-1} around mode 56 which can easily be mixed by small perturbations (e.g., solvent effects), it is possible that the modes predicted by calculation **1** are not good representation of modes in experiment but rather linear combinations of the real modes. Regarding the rest of the discrepancies, as can be seen, they are attributed to nonrobust modes.

Therefore, for the comparison between the calculated and experimental VCD spectra of Pulegone in Figure 26.3, we have on the one hand good sign agreement for 9 out of the 10 modes whose VCD sign we can calculate accurately—that is, the robust modes—and on the other hand sign discrepancies mostly for nonrobust modes—that is, modes whose VCD sign cannot be predicted accurately form calculations. Consequently, we can conclude that the agreement between calculations and experiment in Figure 26.3 is of sufficient quality to provide an accurate determination of the AC of Pulegone.

Having established that the AC of Pulegone can be determined accurately from a simple vacuum calculation performed for the isolated molecule, we continue by investigating the significance of the similarities/discrepancies obtained between the calculated and experimental VCD spectra of Pulegone when using various computational parameters. We will do this from the perspective of robustness by monitoring the dependence of the calculated ξ angles of Pulegone on (1) exchange-correlation functionals (i.e., BP86 versus OLYP), (2) solvation model (i.e., vacuum versus COSMO, (3) criteria for geometry optimization [i.e., tight (10^{-6} hartree for the energy and 10^{-4} hartree/angstrom for the gradients) versus the ADF default (10^{-4} hartree for the energy and 10^{-3} hartree/angstrom for the gradients], and (4) molecular complex formation [i.e., calculations for the isolated Pulegone molecule versus calculations performed for the molecular complex formed between one Pulegone molecule and one solvent molecule (i.e. $CDCl_3$)]. By combining all these computational parameters, 16 different calculations have been performed for Pulegone (labeled from **1** to **16**). A list with the computational parameters used in each of the 16 calculations is given in Table 26.2.

In Figure 26.4 (left panel) the values of the angles ξ predicted by the 16 calculations in Table 26.2 have been plotted as dots (each calculation in a different gray nuance) on top of the VCD spectrum (and angles) obtained from calculation **1** (i.e., our reference calculation). As can be seen, the dots often exhibit very large vertical variations that in a few situations cross the 90° line. This clearly indicates that the values calculated for the ξ angles depend sensitively on the choice of computational parameters and that the 16 calculations in Table 26.2 predict different VCD signs for some of the modes of Pulegone.

To highlight the difference between robust and nonrobust modes, it is useful to (a) plot the angles of the modes identified as nonrobust in the calculation **1** and their homologous modes in the rest of the calculations using the same symbols and (b) use a different symbol for the angles of the robust modes in calculation **1** and their homologous modes in the rest of the calculations. This has been done in the right panel of Figure 26.4 where black dots have been used for the non-robust modes and empty circles for the robust modes.

TABLE 26.2. Computational Parameters Used in the 16 Calculations Performed for Pulegone

Calculation	Computational Details
1	TZP, BP86, Vacuum, tight geometry, free molecule
2	TZP, BP86, Vacuum, tight geometry, molecular complex
3	TZP, BP86, Vacuum, default geometry, free molecule
4	TZP, BP86, Vacuum, default geometry, molecular complex
5	TZP, BP86, COSMO, tight geometry, free molecule
6	TZP, BP86, COSMO, tight geometry, molecular complex
7	TZP, BP86, COSMO, default geometry, free molecule
8	TZP, BP86, COSMO, default geometry, molecular complex
9	TZP, OLYP, Vacuum, tight geometry, free molecule
10	TZP, OLYP, Vacuum, tight geometry, molecular complex
11	TZP, OLYP, Vacuum, default geometry, free molecule
12	TZP, OLYP, Vacuum, default geometry, molecular complex
13	TZP, OLYP, COSMO, tight geometry, free molecule
14	TZP, OLYP, COSMO, tight geometry, molecular complex
15	TZP, OLYP, COSMO, default geometry, free molecule
16	TZP, OLYP, COSMO, default geometry, molecular complex

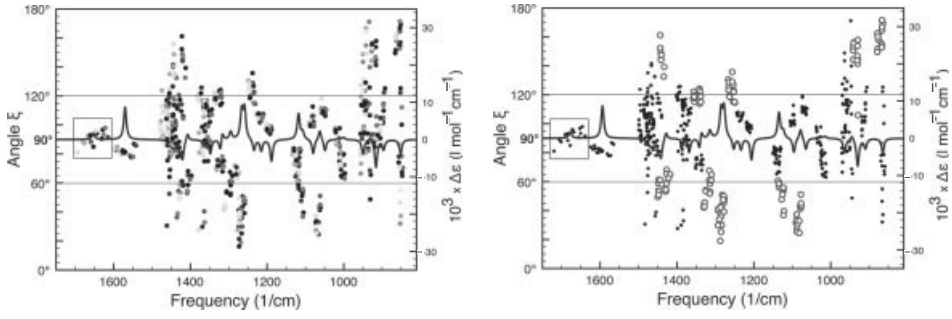

Figure 26.4. Dependence of the calculated ξ angles of Pulegone on the computational parameters. The left panel shows the angles ξ obtained from the 16 calculations in Table 26.2 (each calculation has a different gray nuance) plotted on top of the VCD spectrum obtained form calculation **1**. The right panel shows the variation of the values of the angles ξ of the robust modes (circles) and of the nonrobust modes (black dots) in the 16 calculations.

The robust modes will be discussed first. As can be seen, even though the angles of some of the robust modes exhibit rather large vertical variations, no VCD sign changes (i.e., crossing of the 90° line), are observed for the robust modes. Since most of the features that stand out in the VCD spectrum of Pulegone are associated to robust modes, and since most of the robust modes identified in calculation **1** are also robust in the rest of the calculations, it should be clear that all 16 calculations in Table 26.2 yield VCD spectra that reproduce fairly well the experiment. Thus, any of these calculations can be used to determine the AC of Pulegone.

Before discussing the nonrobust modes, we should also mention that mode 56—that is, the robust mode at 1442 cm^{-1} that in calculation **1** had a different VCD sign than in experiment—can be found in only 8 out of the 16 calculations (see the fewer number of points associated with this mode in the right panel of Figure 26.4). As we have expected,

this mode can indeed mix easily with its neighbors. Clearly, the fact that a mode is robust is not an absolute guarantee of sign agreement between calculations and experiment.

Next we consider the nonrobust modes. A look at the clusters of points associated with the nonrobust modes shows that, except for a few modes with very weak VCD intensities that exhibit very large variations of their angles (e.g., the weak mode at 847 cm^{-1}), the vertical variations of the dots are comparable to the ones observed for the robust modes. However, unlike in the case of the robust modes, here we have some modes that exhibit changes across the 90° line. That is, the use of different computational parameters induces VCD sign changes for some of the normal modes.

One such example is the C = O stretching mode of Pulegone—that is, the mode at 1675 cm^{-1}. Since for this mode we have sign discrepancies between calculations and experiment (see Figure 26.3), in the following, we will analyze it in more detail. Figure 26.5 shows a comparison of the values predicted by the 16 calculations in Table 26.2 for the angles ξ and rotational strengths of this mode. As can be seen, all 16 calculations predict for the angle ξ of this mode values that are very close to 90°. However, the calculated angles are both larger and smaller than 90°; that is, some of the calculations predict a positive VCD sign for this mode while others predict a negative VCD sign. This might falsely suggest that the sign discrepancy observed in Figure 26.3 for this mode can be corrected if one uses a different set of computational parameters. However, because this mode is nonrobust, one should recognize that the sign agreements/disagreements between calculations and experiment bear no relevance. For example, even the use of different convergence criteria for the geometry optimization (compare calculations **10** and **12** in Figure 26.5) has yielded rotational strengths of different signs for this mode. Clearly, the VCD sign calculated for this mode depends too sensitively on the choice of computational parameters and cannot be predicted accurately from calculations.

We can conclude that this study has not only demonstrated the usefulness of the robustness concept introduced in Section 26.2.4, but has also revealed a very important implication of this concept; that is, sign discrepancies between the calculated and experimental VCD spectra should be of no concern if they are encountered for modes that are non-robust.

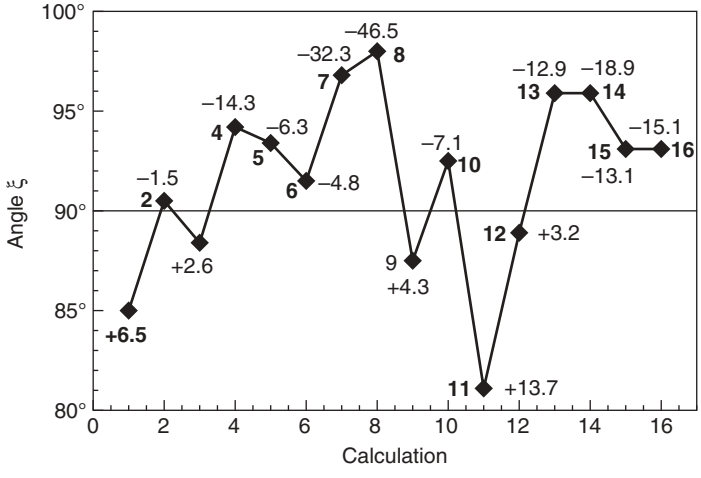

Figure 26.5. Comparison of the ξ angle and rotational strengths predicted by the 16 calculations in Table 26.2 for the C═O stretching mode of Pulegone.

26.2.5.2. Reliability of VCD Predictions. In this section we will extend further the ideas introduced in the previous section by showing that the robustness concept can also be used to assess the reliability of a VCD prediction.

The first molecule we consider is Tröger's base—that is, molecule 1 in Figure 26.1. As can be seen in the left panel of Figure 26.6, where the calculated (BP86/TZP) and "experimental" VCD spectra of Tröger's base are compared, we have an almost perfect agreement between the calculated and experimental VCD spectra of this molecule. There are two important facts that are responsible for this very good agreement between calculation and experiment. Firstly, approximately 60% of the modes of Tröger's base in the fingerprint region are robust. Furthermore, as can be seen in Figure 26.6, all intense signals in the VCD spectrum of Tröger's base are assigned to robust modes. Secondly, Tröger's base is a very rigid molecule that at room temperature has practically a single conformation populated in solution [10].

The next molecule we consider is α-pinene—that is, molecule 20 in Figure 26.1. As can be seen in the right panel of Figure 26.6, where a comparison of the calculated (BP86/TZP) and "experimental" VCD spectra of α-pinene is shown, there is a rather good agreement between calculation and experiment, but not as good as in the case of Tröger's base. We note that, like Tröger's base, α-pinene is a rigid molecule that has a single conformation populated at room temperature [11].

Compared to Tröger's base, α-pinene has much fewer robust modes in the fingerprint region—that is, only approximately 20% (8 out of 39). It should also be pointed out that (1) all robust modes stand out in the VCD spectrum of α-pinene and have the same signs in the calculated and the experimental spectra (see Figure 26.6), and (2) the few sign discrepancies between calculations and experiment in Figure 26.6 are observed for modes that are not robust.

The two examples considered in this section, and also in the study of Pulegone (which is in the same category as α-pinene) in the previous section, suggest that there is a direct correlation between the number of robust modes of a molecule and the agreement between its experimental and calculated VCD spectra; that is, the greater the number of robust modes, the better the agreement. As a result, the concept of robustness can also be used to assess how reliable a VCD prediction of the AC is: The more robust modes there are, the more likely that good agreement is not accidental.

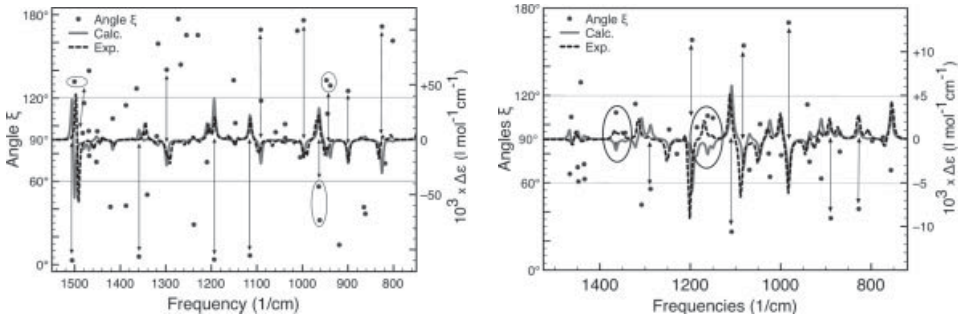

Figure 26.6. Comparison of the experimental and calculated (BP86/TZP) VCD spectra for Tröger's base (left panel) and α-Pinene (right panel). The dots indicate the values of the ξ angles, whereas the arrows indicate the robust modes. The ''experimental'' spectra were obtained by Lorentzian broadening (with a half-width of 8 cm^{-1}) of the experimental VCD intensities reported by Stephens and co-workers [10, 11].

Finally, we note that in the case of flexible molecules that have very few robust modes one should not over interpret the superficial agreement between calculations and experiment. Such situations are at the limit of applicability of VCD spectroscopy. This is because not only we cannot trust the calculated VCD signs, but we are also unable to calculate accurately the Boltzmann weights of the various conformations. The reason is twofold. On one hand the accuracy of the calculated relative energies is, depending on the level of theory, on the order of 2-3 kcal/mol, and on the other hand a relative energy of 1 kcal/mol between two conformers will yield Boltzmann weights of approximately 84% and 16% for the two conformers. If VCD "predictions" of the AC are being made in cases like this one, than they must be verified against predictions made with other spectroscopic techniques, e.g. ROA, ECD, OR.

26.3. EFFECTS OF MOLECULAR COMPLEX FORMATION IN VCD SPECTRA

Correct interpretation of VCD spectra required a good knowledge/understanding of the effects induced by the solvent in VCD spectra. The reason is twofold. On one hand, the measured VCD spectrum can depend sensitively on the solvent used, while on the other hand most often one compares VCD spectra measured in solution to VCD spectra obtained form calculations performed on isolated molecules.

For this reason, the number of studies investigating the solvent effects on VCD spectra has increased rapidly in recent years [13–20]. These studies have shown that long-range dielectric effects, as given by a polarizable continuum model for the solvent, while sometime useful, are not sufficient to model the solvation effect on the spectra; that is, explicit hydrogen bonding has to be taken into account. Since the formation of a molecular complex between a solute molecule and a solvent molecule is indeed the most important interaction causing perturbation of the VCD signals compared to the gas phase, in this section we will investigate in detail the effects of complexation on the VCD signals.

There are four main types of perturbations induced by molecular complex formation that can affect the shape of the measured VCD spectra:

1. Perturbation of the conformational populations of the solute.
2. Perturbation of the normal modes of the solute.
3. Perturbation of the electronic structure of the solute.
4. Transfer of chirality.

In the following, each of these cases will be discussed in detail using a suggestive example molecule. The effects induced in VCD spectra by these four perturbations will also be analyzed from the perspective of robustness. This investigation will not only provide a better understanding of the effects induced by complex formation on VCD spectra, but will also help us better define the concept of robustness introduced in the previous section. That is, according to the definition of robustness in Section 26.2.4, the VCD sign of robust modes is not sensitive to small perturbations. As it will be shown, the findings in the current study will shed some more light on what can be considered a small/large perturbation.

26.3.1. Perturbation of the Conformational Populations of the Solute

In the case of flexible chiral molecules that have more than one conformation populated at room temperature, molecular complex formation between solute and solvent molecules can result in changes of the Boltzmann populations of the various conformations of the solute; that is, some conformations of the solute will be stabilized/destabilized by the association of the solvent. This can significantly affect the shape of the measured/calculated VCD spectra as the various conformers of a chiral molecule have different VCD spectra.

As an example, we consider the binaphthol molecule—that is, a chiral molecule with C2 symmetry that has three conformations [21]. The three conformers of binaphthol are shown in Figure 26.7. As can be seen, they differ in the orientation of the two O—H bonds.

The O and H atoms of the two O—H bonds can form intermolecular hydrogen bonds with solvent molecules; that is, two solvent molecules can associate to one binaphthol molecule (one at each O—H bond; see Figure 26.8).

To investigate the effects of molecular complex formation on the relative energies of the three conformers of binaphthol, in the following we will consider molecular complexes formed between the three conformations of binaphthol with two different solvents, namely CH_2Cl_2 and DMSO.

Table 26.3 shows a comparison between the relative energies of the three conformers in Figure 26.7 obtained from BP86/TZP calculations performed for the isolated conformers (calculation A in Table 26.3) and for molecular complexes form with CH_2Cl_2 and DMSO (calculations B and C, respectively, in Table 26.3). As can be seen, the calculations performed for the isolated molecule (A) and for the molecular complexes formed with CH_2Cl_2 (B) predict conformation 1 as the most stable (thus dominant) conformation of binaphthol, whereas the calculations performed for the molecular complexes formed with DMSO (C) predicts conformations 2 and 3 as the most stable (thus dominant) conformations.

Indeed, as can be seen in the left panel of Figure 26.9, the VCD spectra measured in the CH_2Cl_2 and DMSO solvents are quite different. Moreover, the VCD spectrum measured in CH_2Cl_2 is very well reproduced by the spectra obtained from calculations performed for conformation 1 with or without associated CH_2Cl_2 molecules (see middle

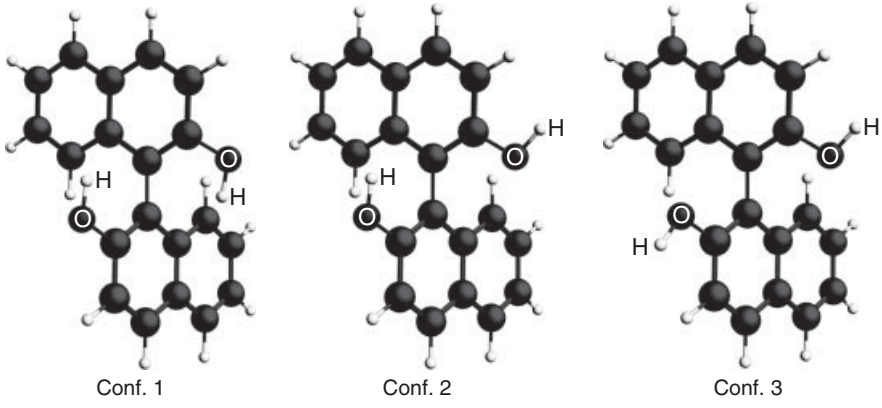

Figure 26.7. The three conformations of binaphthol.

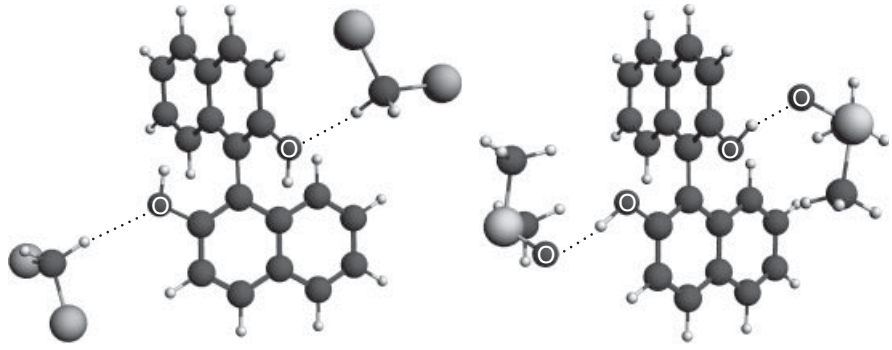

Figure 26.8. The most stable molecular complexes form between one binaphthol molecule and two solvent molecules. Left panel shows the molecular complex formed using the conformer 1 of binaphthol and two CH_2Cl_2 solvent molecules (one at each OH bond). Right panel shows the molecular complex formed using the conformer 3 of binaphthol and two DMSO solvent molecules (one at each OH bond).

TABLE 26.3. Comparison of the Relative Energies (kcal/mol) of the Three Conformations Calculated at BP86/TZP Level for the Isolated Binaphthol (A), the Molecular Complex Made Between One Binaphthol Molecule and Two CH_2Cl_2 Molecules (B), and the Molecular Complex Made Between One Binaphthol Molecule and Two DMSO Molecules (C)

Calculation	A	B	C
Conformation 1	0.00	0.00	2.34
Conformation 2	3.90	2.49	0.08
Conformation 3	7.25	8.10	0.00

panel of Figure 26.9), whereas the spectrum measured in DMSO is rather well reproduced by the spectrum obtained from calculations performed for conformation 3 with associated DMSO molecules (see lower panel of Figure 26.9). We note that according to the relative energies given in Table 26.3, in order to reproduce the VCD spectrum measured in DMSO, one should consider not only the VCD spectra of the molecular complex formed between conformation 3 of binaphthol and two DMSO molecules, but also the spectrum calculated for the molecular complex formed with conformation 2 of binaphthol. However, because all the peaks in the VCD spectrum of the MC formed with conformation 2 had very weak intensities, this spectrum was neglected.

Finally, it should be clear that a change in the relative populations of the various conformations—that is, the contributions of the various conformation to the final spectrum—will most likely result in a change of the number of robust modes in the frequency interval of interest; that is, each conformations has a different number of robust modes. The physical meaning of robustness will, of course, be unchanged.

26.3.2. Perturbation of the Normal Modes

The perturbation induced in the molecular systems forming a molecular complex can cause some of the normal modes to mix. Mode mixing is not restricted to modes of the same molecular system but can happen also between solute and solvent modes.

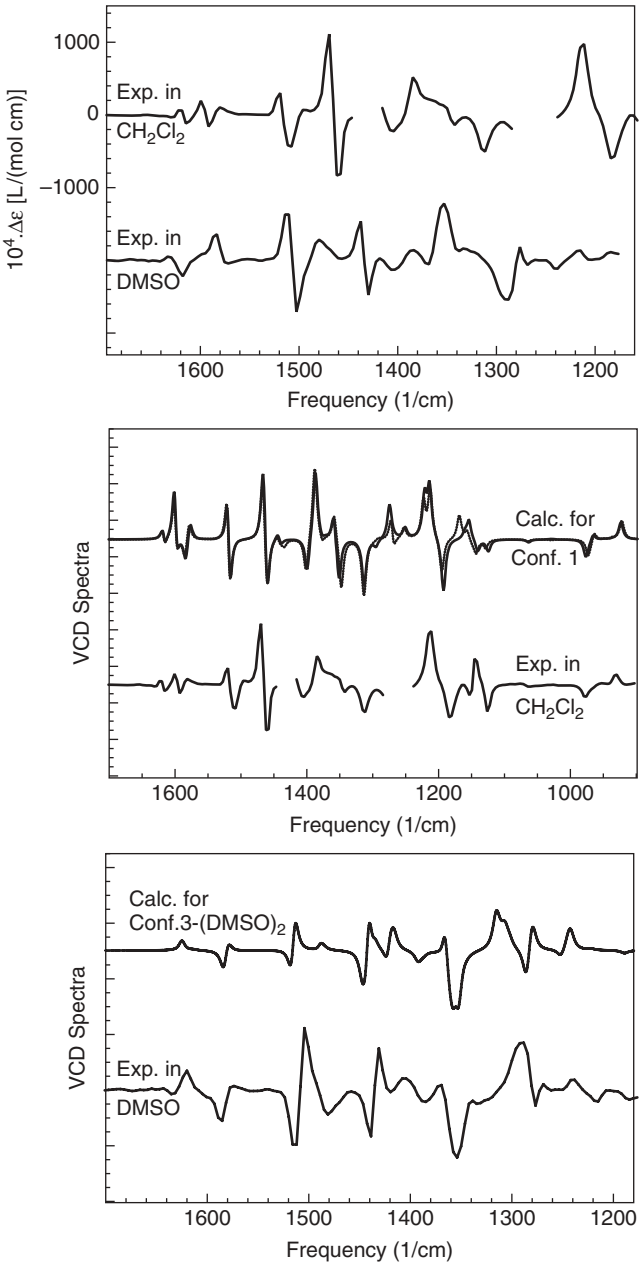

Figure 26.9. VCD spectra of binaphthol. Upper panel: Comparison between the experimental VCD spectra measured in CH_2Cl_2 and DMSO solvents. Middle panel: Comparison between experimental VCD spectrum measured in CH_2Cl_2 and calculated (BP86/TZP) spectra for conformation 1 of binaphthol (free molecule continuos line, molecular complex dotted line). Lower panel: Comparison between experimental VCD spectrum measured in DMSO and calculated (BP86/TZP) spectra for conformation 3 of binaphthol (molecular complex). Experimental spectra were provided by Professor Polavarapu.

In this section we will consider only the modes of the solute. In particular, two very general cases will be considered in this section: (1) the case of normal modes that are unaffected by the molecular complex formation and (2) the case of the modes that are (strongly) mixed by the molecular complex formation. The more particular case of the modes that are not affected by the molecular complex formation even though they are localized almost exclusively on the solute atoms involved in the intermolecular bonds will be discussed in the next section. The case of the solvent modes (induced chirality) will be discussed in Section 26.3.4.

The percentage of the solute modes that mix, as well as the strength of the mixing, depends sensitively on the shape, size, and relative orientation of the solute and solvent molecules, as well as on the strength of the intermolecular bond. For example, the association of a $CDCl_3$ solvent molecule to the Pulegone molecule (the case studied in Section 26.2.5.1) has caused approximately 20% of the fingerprint modes of Pulegone to mix strongly. In the binaphthol molecule, on the other hand, the association of the two CH_2Cl_2 solvent molecules to conformer 1 caused approximately 15% of the fingerprint modes of this conformer to mix strongly, while the association of two DMSO molecules to conformer 3 has caused approximately 45% of the fingerprint modes of this conformer to mix strongly. (By strong mixing we mean that upon complex formation a mode of the FM exhibits a change of more than 19%; that is, it has an overlap with a MC mode smaller than 0.9.)

As an example, we will consider the molecular complex (MC) formed between one 1-amino–1-phenyl–pentanol molecule and one $NCCH_3$ solvent molecule (see Fig. 26.10). A normal mode analysis has shown that approximately 20% of the modes of 1-amino–1-phenyl–pentanol mix upon the association of the $NCCH_3$ molecule.

First we consider the case of the modes that are unaffected (or very little affected) by molecular complex formation. Although not a rule, most often this is the case of the modes localized far away from the intermolecular bonds. As an example we consider mode 31 of FM. The mode is localized on the phenyl ring (i.e., far from the intermolecular bond) and consists of (the phenyl) in plane movements of the H atoms. As can be seen in Figure 26.10, the association of the $NCCH_3$ solvent molecule leaves this mode practically unchanged. Indeed, mode 31 of FM has an overlap of 0.99 with mode 39 of the MC. Furthermore, as can be seen in Table 26.4, the two modes also have very similar frequencies, EDTMs, MDTMs, dipole and rotational strengths, and ξ angles. It should therefore be clear that the robustness of the modes that do not mix and are not localized on the intermolecular bonds is not affected by molecular complex formation.

Next we discuss the case of mode mixing. Although not a rule, mode mixing is most likely to occur among (1) modes that have similar frequencies and involve movements

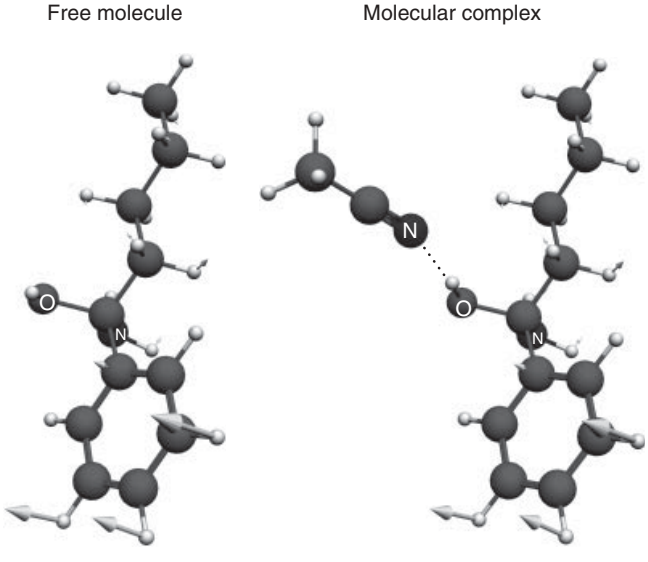

Figure 26.10. Example of a normal mode of 1-amino–1-phenyl–penthanol that is not affected by complex formation with $NCCH_3$: Comparison of the mode 31 of FM with the mode 39 of MC. The two modes have an overlap of 0.99.

TABLE 26.4. Mode Unaffected by Molecular Complex Formation.[a]

Overlap: 0.99		$\Delta\xi = 1.8^\circ$	
Molecule	Frequency	R	ξ
FM:	750.8	−71.5	115.6°
MC:	749.1	−65.4	117.3°
$\vec{E}_{01}(i)$	x	y	z
FM:	+13.4	−0.60	+86.8
MC:	+17.9	−2.80	+93.2
$\mathrm{Im}[\vec{M}_{01}(i)]$	x	y	z
FM:	−36.8	+142.5	−68.6
MC:	−38.1	+157.7	−65.0

[a]Comparisons of the frequencies (Frequency), rotational strengths (R), angles ξ, and Cartesian components of the electric ($\vec{E}_{01}$) and magnetic ($\mathrm{Im}[\vec{M}_{01}]$) dipole transition moments of modes 31 of FM (1-amino−1-phenyl−penthanol) and 39 of MC (1-amino−1-phenyl−penthanol$\cdots$NCCH$_3$). Units: Frequency (cm^{-1}), R (10^{-44} esu$^2\cdot$cm^2), $\vec{E}_{01}$(10^{-21} esu$\cdot$cm), $\mathrm{Im}[\vec{M}_{01}]$($10^{-25}$ esu$\cdot$cm).

of atoms or groups of atoms of the same type and (2) modes partially localized on the intermolecular bonds.

As an example, we consider mode 70 of the MC. This mode does not have a corresponding mode in the FM. As shown in Figure 26.11, this mode is a linear combination of three modes of FM, namely modes 59, 60, and 61. As can be seen in Figure 26.11, mode 70 of MC is very different from the modes of FM that mix to form it. That is, mode 70 of MC is localized only on the pentanol moiety and consists of CH rocking movements, whereas the modes 59, 60, and 61 of FM are localized also on the phenyl and OH moieties. Consequently, the electric and magnetic dipole transition moments of mode 70 of MC should be significantly different from those of the modes 59, 60, and 61 of FM. Indeed, as can be seen in Table 26.5, except for the mode frequencies, which are very similar, the four modes have very different dipole strengths, rotational strengths, and ξ angles—that is, very different EDTMs and MDTMs.

Regarding the robustness of the mixed modes, it should be clear that as a result of mode mixing, new robust/nonrobust modes will be created; and at the same time, some

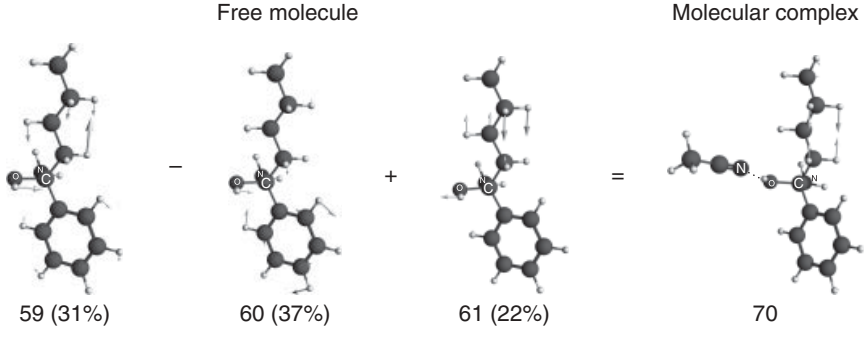

Figure 26.11. Normal modes of 1-amino−1-phenyl−penthanol that are mixed by molecular complex formation.

TABLE 26.5. Mode Mixing Cause by Molecular Complexation[a]

Molecule	NM	Overlap	Frequency	D	R	ξ
MC	70	—	1325.2	88.5	18.3	80.6
FM	59	−0.56	1315.6	33.8	+58.6	37.8°
FM	60	+0.61	1330.8	25.1	−1.7	91.8°
FM	61	−0.51	1335.2	115.3	−50.7	136.5°

[a]Comparison of the frequencies (Frequency), dipole (D) and rotational (R) strengths, and ξ angles of mode 70 of MC (1-amino−1-phenyl−penthanol$\cdots$NCCH$_3$) and of modes 59, 60, and 61 of FM (1-amino−1-phenyl−penthanol). Units: Frequency (cm^{-1}), D (10^{-40} esu$^2\cdot$cm^2), R(10^{-44} esu$^2\cdot$cm^2).

of the robust/nonrobust modes of the solute will disappear. This will result in a change (proportional to the percentage of modes that mix) in the number of robust/nonrobust modes in the frequency interval of interest. As before, the physical meaning of robustness is unchanged. It should also be clear that, because mode mixing can significantly change the sign and magnitude of rotational strengths, VCD sign discrepancies can be encountered between calculation and experiment for mixed modes assigned as robust, if the mixed modes are not a good representation of the experimental mode (see discussion of the mode 56 of Pulegone in Section 26.2.5.1).

There are two important conclusions. Firstly, the VCD spectra can be significantly affected by the mode mixing mechanism (triggered by molecular complex formation)—especially in situations when a large percentage (e.g., 45%) of the modes of the FM mix upon solvent association (see discussion in the previous section on the effects induced by the DMSO and CH_2Cl_2 association on the modes of binaphthol). Secondly, when molecular complex formation occurs, performing a normal mode analysis (i.e., mapping of the FM and MC modes) is essential not only to provide a good estimate for how significant the VCD spectra are affected by complexation, but also for interpreting the results of a robust mode analysis.

26.3.3. Perturbation of the Electronic Structure

Molecular complex formation gives rise to donor−acceptor interactions between occupied and virtual MOs localized on the solvent and solute moieties involved in the intermolecular hydrogen bonds [8]. As will be shown in this section, the charge transfer resulting from this interaction perturbs strongly the EDTMs and MDTMs of the modes localized on the moieties involved in intermolecular bonds. This in turn will affect significantly the IR and VCD intensities of these modes.

To illustrate the type of changes that can be induced in VCD spectra by charge transfer, in the following we will consider the tris(ethylenediaminato)cobalt(III) complex, $[Co(en)_3]^{3+}$, and we will investigate the changes induced in its VCD spectrum by chloride association.

The $[Co(en)_3]^{3+}$ molecule is a chiral transition metal consisting of three ethylenediaminato (en) bidentate ligands coordinated to the Co metal center. The $[Co(en)_3]^{3+}$ molecule has four different conformations [22, 23]. However, after the association of the Cl^- ions, only one of these conformers is predominantly populated at room temperature; that is, the conformer labeled as $\Lambda-\delta\delta\delta$ [23]. Therefore, in the following we will consider only this conformation.

The $\Lambda-\delta\delta\delta$ conformer of $[Co(en)_3]^{3+}$ has C_3 symmetry, and it is depicted in the upper panel of Figure 26.12. (In the left picture $\Lambda-\delta\delta\delta$ is viewed along the C_3 symmetry axis, whereas in the right picture $\Lambda-\delta\delta\delta$ is viewed along the C_2 symmetry axis.)

The middle panel of Figure 26.12 shows a schematic representation of the N—H bonds at each N atom of an ethylenediaminato ring. As can be seen, we can distinguish between (a) N—H axial bonds that are almost parallel to the C_3 axis and (b) N—H equatorial bonds that are almost perpendicular to the C_3 axis (the Z axis). The N—H axial bonds form two triads, one at the positive Z axis (hydrogens 26, 30, and 34 in Figure 26.12) and one at the negative Z axis (hydrogens 28, 32, and 36 in Fig. 26.12), whereas the equatorial N—H bonds form three dyads, namely, one at each C_2 symmetry axis.

In solution with excess Cl^- ions, the Cl^- ions can associate to $\Lambda-\delta\delta\delta$ by forming intermolecular hydrogen bonds with the N—H bonds. As shown in the lower panel of Figure 26.12, five Cl^- ions can associate to a single $\Lambda-\delta\delta\delta$: two Cl^- ions situated

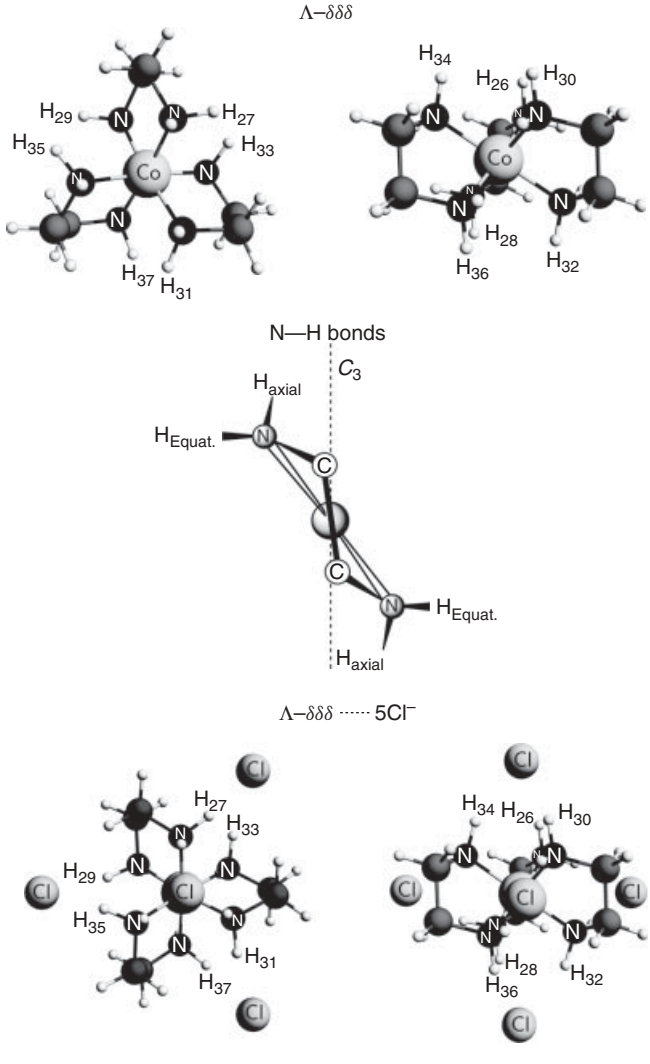

Figure 26.12. Optimized (BP86/TZP) structures of the $\Lambda-\delta\delta\delta$ and $\Lambda-\delta\delta\delta\cdots 5Cl^-$. Upper panel: Isolated $\Lambda-\delta\delta\delta$ viewed along the C_3 (left) and C_2 (right) symmetry axis. Middle panel: Schematic representation of the N–H axial and equatorial bonds. Lower panel: Isolated $\Lambda-\delta\delta\delta$ viewed along the C_3 (left) and C_2 (right) symmetry axes.

along the C_3 symmetry axis (one at each triad), and three Cl^- ions situated along the C_2 symmetry axes (one at each dyad).

26.3.3.1. Effects of Cl^- Association on VCD Spectra. Figure 26.13 shows comparisons between the VCD spectra calculated (BP86/TZP) for $\Lambda\text{–}\delta\delta\delta$ (FM) and $\Lambda\text{–}\delta\delta\delta\cdots 5Cl^-$ (MC) for the frequency intervals between 1000 and 1800 cm^{-1} (left panel) and between 2800 and 3600 cm^{-1} (right panel). The arrows in Figure 26.13 indicate the modes of the FM and of the MCs that are similar—that is, have an overlap of at least 0.90.

First we look at the fingerprint spectra—that is, the left panel of Figure 26.13. As indicated on the plot, six (i.e. half) of the peaks in the VCD spectrum of the FM are associated with the modes that are practically unaffected by the association of the Cl^- ions; that is, the overlaps between the FM and MC modes are at least 0.96. However, it is important to note that although the FM and MC modes are very similar, we have VCD sign discrepancies between FM and MC for four of the six peaks.

The comparisons of the VCD spectra for the frequency interval between 2800 and 3600 cm^{-1} (see right panel of Figure 26.13) reveals an equally interesting phenomenon. That is, the peaks in the VCD spectrum of $\Lambda\text{–}\delta\delta\delta\cdots 5Cl^-$ are approximately two orders of magnitude more intense than the peaks in the $\Lambda\text{–}\delta\delta\delta$ spectrum. Clearly, the association of the Cl^- ions affects significantly the VCD spectrum of $\Lambda\text{–}\delta\delta\delta$.

Visualization of the displacement vectors of the normal modes exhibiting VCD sign changes and giant enhancements has revealed that without exception these modes are localized predominantly on the atoms that are involved in intermolecular hydrogen bonding with the associated Cl^- ions. VCD sign changes are observed in the fingerprint region for bending modes—namely, N—H wagging, twisting, and scissoring modes (these modes are not always pure)—whereas giant enhancements are observed for N—H stretching modes.

Clearly, this is a first indication that the induced changes are related to the charge transfer resulting from the donor–acceptor interactions between the Cl^- ions as donors and the N—H bonds as acceptors. However, to elucidate the mechanisms inducing the VCD sign changes and giant enhancements, in the following sections we will investigate in detail (1) the dependence of the charge transfer on the movements of the H atoms (involved in hydrogen bonding) during stretching and bending modes and (2) the various

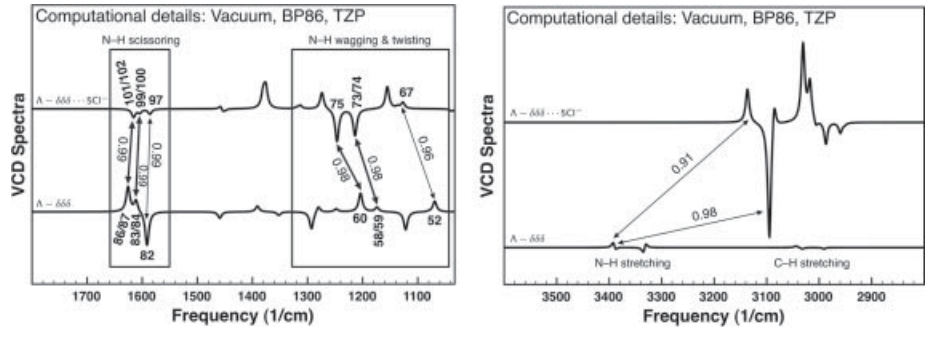

Figure 26.13. Comparison of the calculated (BP86/TZP) VCD spectra of $\Lambda\text{–}\delta\delta\delta$ and $\Lambda\text{–}\delta\delta\delta\cdots 5Cl^-$. Left panel: Frequency interval between 1000 and 1800 cm^{-1} that is, i.e. fingerprint region. Right panel: Frequency interval between 2800 and 3600 cm^{-1}, that is, the CH/NH stretching region.

contributions to the electric and magnetic dipole transition moments (DTM) of the modes exhibiting VCD sign changes and giant enhancements.

26.3.3.2. Theory. In this section we will introduce a few theoretical concepts that are required for understanding the VCD sign-change and giant-enhancement mechanisms.

The total electric and magnetic dipole transition moments can be decomposed into atomic contributions [24]:

$$\vec{\mu}(i) = \sum_{\lambda=1}^{N} \vec{\mu}^{\lambda}(i). \tag{26.5}$$

In Eq. (26.5), $\vec{\mu}(i)$ is either $\vec{E}_{01}(i)$ or $\mathrm{Im}[\vec{M}_{10}(i)]$, $\vec{\mu}^{\lambda}(i)$ is the atomic contribution to $\vec{\mu}(i)$ due to atom λ, and N is the total number of atoms of the molecule.

The atomic contributions, $\vec{\mu}^{\lambda}(i)$, can be further decomposed into nuclear (nuc) and electronic (el) components [24]:

$$\vec{\mu}^{\lambda}(i) = \vec{\mu}^{\lambda,nuc}(i) + \vec{\mu}^{\lambda,el}(i) \tag{26.6}$$

The nuclear component, $\vec{\mu}^{\lambda,nuc}(i)$, is determined by the movements of the λ nucleus during the normal mode motion, whereas the electronic component, $\vec{\mu}^{\lambda,el}(i)$, should be attributed to the electrons dragged along by the λ nucleus. It is important to note here that under normal circumstances (e.g., in isolated molecule) $\vec{\mu}^{\lambda,nuc}(i)$ and $\vec{\mu}^{\lambda,el}(i)$ have opposite signs; that is, even though the nucleus and the dragged electrons move in the same direction, they have opposite electric charges.

Finally, we note that in the molecular complex, because of the charge transfer, the electronic contributions, $\vec{\mu}^{\lambda,el}(i)$, can be decomposed into a contribution from the dragged electrons, $\vec{\mu}^{\lambda,el}_{drag}(i)$, and a charge transfer contribution, $\vec{\mu}^{\lambda,el}_{CT}(i)$:

$$\vec{\mu}^{\lambda,el}(i) = \vec{\mu}^{\lambda,el}_{drag}(i) + \vec{\mu}^{\lambda,el}_{CT}(i). \tag{26.7}$$

As will be shown in Section 26.3.3.5, the sign-change and giant-enhancement mechanisms can be explained by determining the relative orientation of the three components of the DTMs, that is, $\vec{\mu}^{\lambda,nuc}(i)$, $\vec{\mu}^{\lambda,el}_{drag}(i)$, and $\vec{\mu}^{\lambda,el}_{CT}(i)$.

26.3.3.3. Charge Displacements Determined by Nuclear Motion. The association of the Cl^- ions gives rise to donor–acceptor interactions between the $3p$ occupied orbitals of the Cl^- ions as donors and σ^* virtual orbitals of Λ–$\delta\delta\delta$ localized on the N—H bonds as acceptors [8]. The amount of charge transfer and the direction of the charge flow are determined mostly by the energy of the acceptor orbitals, which in turn is determined by the distances between the H atoms and the Cl^- ions—that is, on the normal mode.

To determine the direction of the charge flow caused by the atomic movements in a given normal mode, one should displace the atoms along the nuclear displacement vectors of the respective normal mode and perform a single-point calculation for the displaced (unrelaxed) geometry. Then, the direction of the transfer of charge can be estimated by comparing the Mulliken charges of the Cl^- ions in the equilibrium and displaced geometries.

The calculations performed for all the modes of interest have shown that irrespective of the type of normal mode (i.e., stretching, wagging, twisting, and scissoring), charge flows from a Cl^- into a N—H bond whenever the proton of the bond moves during

the normal mode motion closer to a Cl^- ion. When the proton moves away from the Cl^- ion, the opposite happens; that is, charge flows from the N—H bond onto the Cl^- ion. However, there are two significant differences between the stretching and bending modes. Firstly, and most importantly, in stretching modes the charge-flow and the nuclear displacement vector of the proton have opposite directions, whereas in a bending mode the two have the same direction. These two situations are illustrated schematically in Figure 26.14. Secondly, because during the stretching motion the proton moves much closer (farther away) from the Cl^- ions than in the bending modes, the amount of charge flowing in (out of) the N—H bonds is much larger (i.e. typical by a factor of 10) in the stretching mode than in the bending modes.

26.3.3.4. General Mechanism. Using the conclusions drawn in the previous two sections, in this section we will elucidate the general mechanism responsible for inducing sign changes and giant enhancement of the VCD intensities.

According to the discussion in Section 26.3.3.3, in stretching modes the charge transfer and the proton move in opposite directions (see Figure 26.14). This means that the dragged electrons and the charge transfer move in opposite directions. As a result, the $\vec{\mu}^{\lambda,el}_{drag}(i)$ and $\vec{\mu}^{\lambda,el}_{CT}(i)$ components have opposite signs. This means that in the molecular complex, because of charge transfer, the magnitude of the total electronic contributions

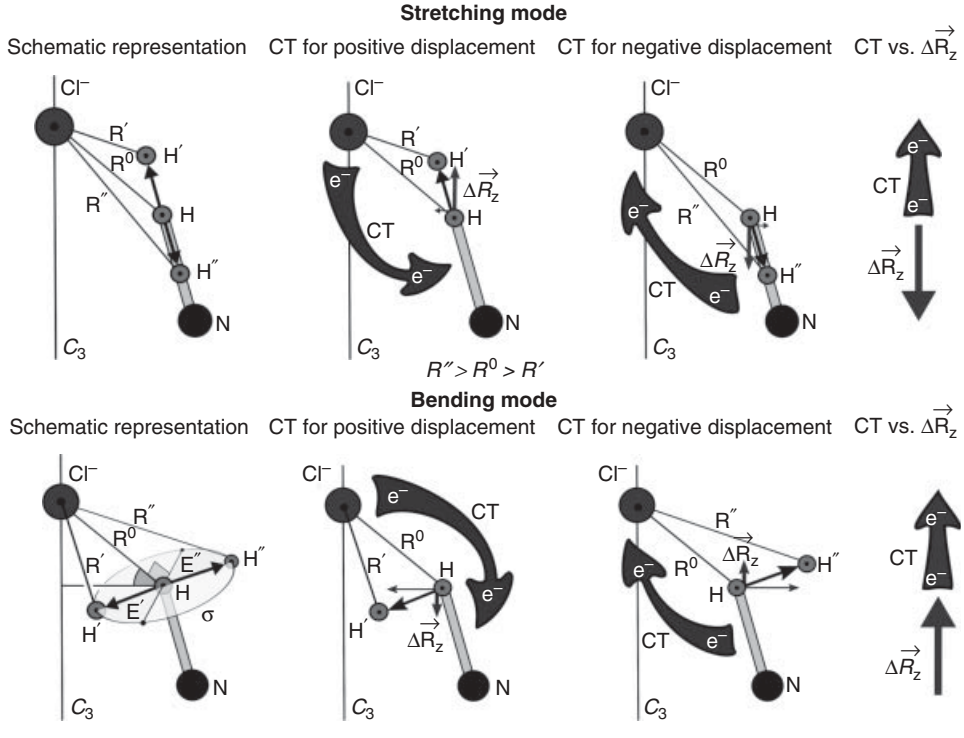

Figure 26.14. Schematic representation of stretching and bending modes of an N–H bond involved in intermolecular bond with a Cl^- ions. The relative directions of the displacement vector of the proton ($\Delta\vec{R}_z$) and of the charge transfer (CT) are also indicated. *Note*: Whenever the proton moves closer to the Cl^- ions, charge flows from the Cl^- ion into the N–H bond, whereas when the proton moves away from the Cl^- the opposite happens.

to the DTMs of the stretching modes is, in general, decreased:

$$|\vec{\mu}^{\lambda,el}(i)| = |\vec{\mu}^{\lambda,el}_{drag}(i)| - |\vec{\mu}^{\lambda,el}_{CT}(i)|. \tag{26.8}$$

Depending on the amount of charge transferred, the magnitude of the electronic contribution $\vec{\mu}^{\lambda,el}(i)$ either (a) becomes very small and therefore will be unable to counteract the nuclear contribution $\vec{\mu}^{\lambda,nuc}(i)$ anymore or (b) will change sign and therefore will reinforce $\vec{\mu}^{\lambda,nuc}(i)$. In both cases, charge transfer is expected to increase significantly the magnitudes of the atomic EDTMs and MDTMs in the molecular complex compared to the free molecule. This clearly explains the origin of the giant enhancement of the VCD intensities observed in the stretching modes. It should also be noted that since IR intensities are determined by the EDTMs, the giant enhancement of the intensities occurs also in the IR spectra [8]. A quantitative estimate, which confirms that the charge transfer effects for typical nuclear displacements in the vibration explain the magnitude of the effects, has been made in reference 9.

Next we consider the bending modes. Because in this case the charge transfer and the displaced proton move in the same direction (see Figure 26.14), the $\vec{\mu}^{\lambda,el}_{drag}(i)$ and $\vec{\mu}^{\lambda,el}_{CT}(i)$ components have the same sign. Thus, in bending modes, charge transfer is expected to increase the magnitude of the electronic components, $\vec{\mu}^{\lambda,el}(i)$:

$$|\vec{\mu}^{\lambda,el}(i)| = |\vec{\mu}^{\lambda,el}_{drag}(i)| + |\vec{\mu}^{\lambda,el}_{CT}(i)|. \tag{26.9}$$

We note that because, as discussed in Section 26.3.3.3, bending modes induce a much smaller flow of charge compared to a stretching mode, the increase of the $\vec{\mu}^{\lambda,el}(i)$ component will not eclipse the nuclear component. Therefore, the intensities of the bending modes will not exhibit the giant enhancements observed in the stretching modes.

To understand how the charge transfer affects the sign of the VCD intensities, it is necessary to analyze the relative magnitudes of the nuclear $\vec{\mu}^{\lambda,nuc}(i)$ and electronic $\vec{\mu}^{\lambda,el}(i)$ components in the FM. There are four cases (two for each type of mode):

(A) *Bending Modes of the FM with* $|\vec{\mu}^{\lambda,nuc}(i)| > |\vec{\mu}^{\lambda,el}(i)|$. Because charge transfer increases the magnitudes of the $|\vec{\mu}^{\lambda,el}(i)|$ components, it is possible that in the molecular complex, $|\vec{\mu}^{\lambda,el}(i)|$ will overcome $|\vec{\mu}^{\lambda,nuc}(i)|$; that is, in MC, $|\vec{\mu}^{\lambda,nuc}(i)| < |\vec{\mu}^{\lambda,el}(i)|$. If this happens, the total atomic EDTMs and MDTMs will exhibit a sign change. Furthermore, because as shown in reference 8, a charge flow along the Z axis will induce large EDTMs in the Z direction, as well as large MDTMs in the perpendicular plane (i.e., the XY plane), the sign change will occur for different Cartesian components of the EDTM and of the MDTM. This means that a charge flow along the Z axis will change the sign of the Z component of the EDTM and of the X and Y components of MDTM. Thus, in this situation, the charge transfer will induce a sign change of the rotational strengths.

(B) *Bending Modes of the FM with* $|\vec{\mu}^{\lambda,nuc}(i)| < |\vec{\mu}^{\lambda,el}(i)|$. No sign changes will occur in this case. In the FM the directions of the total atomic DTMs are determined by the $\vec{\mu}^{\lambda,el}(i)$ components. In the MC the magnitudes of the $\vec{\mu}^{\lambda,el}(i)$ components increase because of charge transfer, while the magnitudes of the $\vec{\mu}^{\lambda,nuc}(i)$ components change very little compared to their values in the FM; that is, $\vec{\mu}^{\lambda,nuc}(i)$ is mostly determined by the nuclear displacement vectors (which are very similar in the FM and MC). The net result will be an increase of the

VCD (also IR) intensity. However, as already mentioned, the increase of the IR and VCD intensities is nowhere near as spectacular as in the stretching modes.

(C) *Stretching Modes of the FM with* $|\vec{\mu}^{\lambda,nuc}(i)| > |\vec{\mu}^{\lambda,el}(i)|$. As already discussed, in stretching modes the magnitudes of the $|\vec{\mu}^{\lambda,el}(i)|$ components decrease significantly, which will result in a giant enhancement of the IR and VCD intensities. No sign changes are expected in this situation.

(D) *Stretching Modes of the FM with* $|\vec{\mu}^{\lambda,nuc}(i)| < |\vec{\mu}^{\lambda,el}(i)|$. In the FM the directions of the total atomic DTMs are determined by the $\vec{\mu}^{\lambda,el}(i)$ components. However, because in stretching modes the magnitudes of the $\vec{\mu}^{\lambda,el}(i)$ components decrease significantly (or can even change sign), it is very likely that in the molecular complex the directions of the total atomic DTMs are determined by the $\vec{\mu}^{\lambda,nuc}(i)$ components. Thus, in this case, besides a giant enhancement we will also have a VCD sign change.

Finally, we note that the conclusions obtained so far by analyzing the electronic and nuclear components of the DTMs of a single atom hold true also when considering the total DTMs. This is because the hydrogen atoms involved in the intermolecular bonds have atomic DTMs that, on one hand, are very similar—a consequence of symmetry—and, on the other hand, are much larger than the atomic DTMs of the rest of the atoms; that is, in the modes of interest the H atoms in the intermolecular bonds move during the normal mode motion with much larger amplitude than the rest of the atoms.

26.3.3.5. Validation. In this section we will validate the two mechanisms introduced in the previous section by comparing the electronic and nuclear contributions of the total EDTM and MDTM in the FM and in the MC for two suggestive normal modes: (a) a bending mode whose VCD intensity was affected by the sign-change mechanism and (b) a stretching mode whose VCD intensity was affected by the giant-enhancement mechanism.

For clarity, the total DTMs will be decomposed in three contributions: (1) one from all H atoms involved in intermolecular bonds (i.e., the axial and equatorial H atoms), (2) one from all N atoms, and (3) one from the remaining atoms. Furthermore, when comparing values taken by various physical quantities in FM and MC, we will omit the units for convenience (the units can be found in the tables showing the respective data).

The Sign-Change Mechanism. To illustrate the sign-change mechanism, we have chosen as an example the modes 60 of $\lambda{-}\delta\delta\delta$ and 75 of $\lambda{-}\delta\delta\delta\cdots 5Cl^{-}$. The two modes have A_2 symmetry and are depicted in Figure 26.15. As can be seen, the two modes are very similar and can be characterized as N—H waggings (though the axial H atoms move with much larger amplitudes than the equatorial H atoms).

The frequencies, dipole, and rotational strengths and the various contributions to the DTMs of these two modes are compared in Table 26.6. As can be seen, the association of the Cl^{-} ions has induced (1) a shift in the mode frequency from 1203.8 in FM to 1246.5 in MC, (2) an increase in the dipole strength (D) from 76.9 in FM to 123.9 in MC, (3) a VCD sign change from +194.4 in FM to −170.9 in MC, and (4) a very large variation of the angle ξ—that is, from 1.2° in FM to 179.1° in MC ($\Delta\xi = -177.9°$). Only the nuclear displacement vectors have been left unaffected by the association of the Cl^{-} ions; that is, two modes have an overlap of 0.98.

To understand these changes, we look at the electric and nuclear components of the DTMs of these two modes. We note that since the modes have A_2 symmetry, only

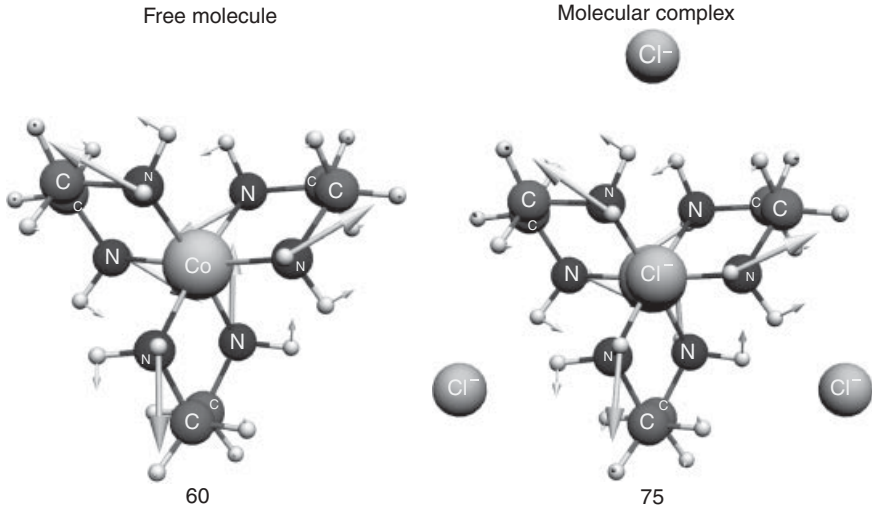

Figure 26.15. Comparison of the modes 60 of $\Lambda\text{-}\delta\delta\delta$ and 75 of $\Lambda\text{-}\delta\delta\delta\cdots 5Cl^-$. The two modes have an overlap of 0.98. The association of the Cl^- induces a VCD sign change.

TABLE 26.6. Sign-Change Mechanism Illustrated Using the Mode 60 of $\Lambda\text{-}\delta\delta\delta$ (FM) and Mode 75 of $\Lambda\text{-}\delta\delta\delta\cdots Cl_5$(MC)[a]

A Symmetry		Overlap: 0.98		$\Delta\xi = -177.9^\circ$	
Molecule	NM.	Frequency	D	R	ξ
FM:	60	1203.8	76.9	+194.4	1.2°
MC:	75	1246.5	123.9	−170.9	179.1°

	$(\vec{E}_{01})_z$			$(\vec{M}_{01})_z$		
FM	nuc	el	nuc+el	nuc	el	nuc + el
Hs in N–H:	+343.7	−277.4	+66.3	+526.6	−371.6	+155.0
All Ns:	−471.7	+482.0	+10.4	−178.1	+221.4	+43.3
REST:	+464.6	−453.6	+11.0	−98.4	+121.7	+23.4
TOTAL:	+336.7	−249.0	+87.7	+250.1	−-28.5	+221.6

	$(\vec{E}_{01})_z$			$(\vec{M}_{01})_z$		
MC	nuc	el	nuc + el	nuc	el	nuc+el
Hs in N–H:	+539.2	−675.2	−136.0	+469.4	−357.5	+111.9
All Ns:	−366.8	+382.3	+15.5	−176.3	+201.0	+24.7
REST:	+324.4	−315.2	+9.3	−104.6	+121.4	+16.9
TOTAL:	+496.8	−608.1	−111.3	+188.6	−35.1	+153.5

[a] Comparisons of the frequencies (Frequency), dipole (D) and rotational (R) strengths, angles ξ and *Z* Cartesian components of the electric ($\vec{E}_{01}$) and magnetic (Im[$\vec{M}_{01}$]) dipole transition moments. Units: Frequency (cm^{-1}), D ($10^{-40}esu^2 \cdot cm^2$), *R* ($10^{-44}esu^2 \cdot cm^2$), $\vec{E}_{01}$(10^{-21}esu · cm), Im[$\vec{M}_{01}$](10^{-25}esu · cm).

the Z Cartesian components should be considered (the other two components are zero by symmetry). It is also important to note that, as mentioned in Section 26.3.3.4, the contributions to the total DTMs from the H atoms involved in intermolecular bonds are much larger than the contributions from the rest of the atoms (compare the numbers in the "nuc+el" columns in Table 26.6 for FM and MC).

A comparison of the nuclear (nuc) and electronic (el) contributions to the total EDTMs shows that in the FM molecule the nuclear component is larger than the electronic one (+336.7 versus −249.0), whereas in the MC the reverse happens; that is, the nuclear contribution is smaller than the electronic one (+496.8 versus −608.1). Consequently, the total EDTM has changed sign when going from $\lambda{-}\delta\delta\delta$ to $\lambda{-}\delta\delta\delta\cdots 5Cl^{-}$ (+87.7 versus −111.3).

The increase in magnitude of the electronic component of the EDTM in the MC is brought about by the contribution from the H atoms involved in the intermolecular bonds—that is, the "Hs in N–H" contribution in Table 26.6. In fact, the phenomenon can be traced to the atomic EDTMs of the axial H atoms which exhibit exactly the same behavior; that is, in FM the nuclear contributions to the Z Cartesian component of the atomic EDTM of an axial H atom is larger than the electronic one, whereas in the MC the opposite happens.

We continue by investigating the components of the MDTMs. As can be seen, the Z Cartesian component of total MDTM does not change sign in MC with respect to the FM (+221.6 versus +153.5). The nuclear components of the total MDTMs are larger than the electronic ones in both FM and MC. Since the EDTM does change sign, this clearly explains the observed VCD sign change.

The observed VCD sign change in mode 75 of MC with respect to mode 60 of FM was caused by the mechanism described in Section 26.3.3.4 in case A. We note that because in the two modes the displacement vectors of the axial hydrogens are much larger than those of the equatorial hydrogens (see Figure 26.15), the transfer of charge induced during the normal mode motion happens mostly along the C_3—that is, the Z axis. As explained in Section 26.3.3.4 (see case A), this will change the sign of the Z component of the EDTM (as seen) and of the X and Y components of MDTM. This is why the Z Cartesian component of the MDTM did not change sign.

As mentioned, the sign-change (also giant-enhancement) mechanism can be traced back to the atomic contributions. Thus, even though symmetry dictates that the X and Y components of the total MDTMs of the two modes considered here are zero, one can still verify that the transfer of charge induces a sign change in the MDTMs—that is, by looking at the atomic MDTMs of the axial H atoms (which are not zero). As an example we will consider the Y Cartesian component of the MDTM of one of the axial H atoms. In the FM the nuclear and electronic contributions to the Y Cartesian component of the atomic MDTM of an axial hydrogen are +20.9 and—13.5, respectively, whereas in the MC the two components are +37.6 and—62.43, respectively. Thus, in the FM, the nuclear component is larger than the electronic one, whereas in the MC we have the opposite situation. Clearly, the Y Cartesian component of the atomic MDTM of an axial H_{28} atom has changed sign in MC compared to FM. It should also be noted here that the symmetry requirements (i.e., that the total DTMs have zero X and Y Cartesian components) are fulfilled even though the X and Y Cartesian components of the atomic DTMs are not zero—that is, via cancellation among the atomic DTMs of the symmetry-related atoms.

Finally, we note that the mode 60 of the FM is a robust mode. However, as shown here, this is not enough to preserve its VCD sign. Clearly, charge transfer is a very strong perturbation that can easily change the VCD sign of robust modes.

The Giant-Enhancement Mechanism. The IR/VCD giant-enhancement mechanism has been discussed in detail in reference 8. As an example, here we have considered the modes 107 of $\Lambda-\delta\delta\delta$ and 124 of $\Lambda-\delta\delta\delta\cdots 5Cl^-$. The two modes are depicted in Figure 26.16. As can be seen, the modes have E symmetry and consist of stretchings of the N–H axial and equatorial bonds. The frequencies, dipole and rotational strengths and the various contributions to the DTMs of these two modes are compared in Table 26.7. For brevity, only the Y Cartesian components of the electronic and nuclear components of the DTMs are shown in Table 26.7. We note that because the considered modes have E symmetry, the Z Cartesian components are zero, whereas the X and Y Cartesian components behave very similarly.

As can be seen in Table 26.7, the association of the Cl^- ions has induced a giant enhancement of both IR (18.9 in FM versus 1157.8 in MC) and VCD (−69.0 in FM versus −2062.1 in MC) intensities. On the other hand, the angles ξ and nuclear displacement vectors have been affected only slightly; that is, the FM and MC modes have an overlap of 0.93 while $\Delta\xi$ is 13.4°.

This giant enhancement of the intensities is brought about by the mechanism described in Section 26.3.3.4 in case C. Looking in Table 26.7 at the contributions from the axial and equatorial atoms (i.e., "Hs in N–H" rows in Table 26.7), we see that in the FM the nuclear and electronic contributions of both DTMs counteract each other as they have opposite signs (EDTM: −384.5 versus +339.3; MDTM: +518.7 versus −402.5). In the MC, however, the electronic component of the EDTMs of the hydrogens

TABLE 26.7. Giant-Enhancement Mechanism Illustrated Using the Mode 107 of $\Lambda-\delta\delta\delta$ (FM) and Mode 124 of $\Lambda-\delta\delta\delta\cdots Cl_5$ (MC)[a]

E symmetry		Overlap: 0.93		$\Delta\xi = -13.4°$	
Molecule	NM.	Frequency	D	R	ξ
FM:	107	3388.8	18.9	−69.0	165.5°
MC:	124	3094.9	1157.8	−2062.1	178.9 °

	$(\vec{E}_{01})_y$			$(\vec{M}_{01})_y$		
FM	nuc	el	nuc+el	nuc	el	nuc+el
Hs in N-H:	−384.5	+339.3	−45.2	+518.7	−402.5	+116.2
All Ns:	+194.5	−192.3	+2.2	−263.1	+301.3	+38.1
REST:	−6.0	+5.8	−0.2	+7.1	−7.0	+0.0
TOTAL:	−196.0	+152.8	−43.2	+262.7	−108.3	+154.4

	$(\vec{E}_{01})_y$			$(\vec{M}_{01})_y$		
MC	nuc	el	nuc + el	nuc	el	nuc+el
Hs in N–H:	−378.7	+55.5	−323.2	+315.1	+244.6	+559.7
All Ns:	+202.2	−219.6	−17.4	−177.7	+227.0	+49.2
REST:	−17.8	+18.2	+0.4	+23.6	−26.6	−3.0
TOTAL:	−194.2	−145.9	−340.1	+161.0	+445.0	+606.0

[a]Comparisons of the frequencies (Frequency), dipole (D) and rotational (R) strengths, angles ξ, and X and Y Cartesian components of the electric ($\vec{E}_{01}$) and magnetic (Im[$\vec{M}_{01}$]) dipole transition moments. Units: Frequency (cm^{-1}), $D(10^{-40}esu^2\cdot cm^2)$, $R(10^{-44}esu^2\cdot cm^2)$, $\vec{E}_{01}(10^{-21}esu\cdot cm)$, Im[$\vec{M}_{01}$]$(10^{-25}esu\cdot cm)$.

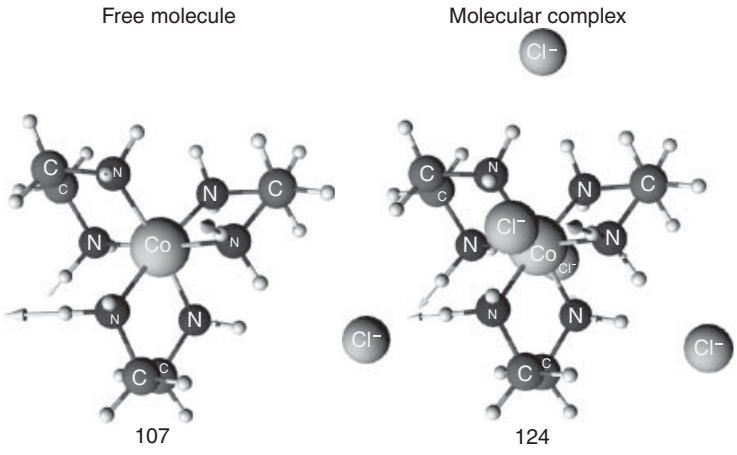

Figure 26.16. Comparison of the modes 107 of $\Lambda\text{-}\delta\delta\delta$ and 124 of $\Lambda\text{-}\delta\delta\delta\cdots 5Cl^-$. The two modes have an overlap of 0.93. The association of the Cl^- induces a giant enhancement of the IR and VCD intensities.

becomes much smaller (as expected), resulting in a much stronger dominance of the nuclear contributions (−378.7 versus +55.5). For the MDTM the electronic component reverses sign, thus reinforcing the nuclear component (+315.1 versus +244.6). Since the contributions from the rest of the atoms are rather small (see Table 26.7), the net effect is a large increase in magnitude for both EDTM and MDTM in the MC with respect to the FM (e.g., EDTM: −43.2 in FM versus −340.1 in MC; MDTM: +154.4 in FM versus +606.0 in MC). This, in turn, results in a huge enhancement of the IR and VCD intensities in the MC with respect to the FM (see Table 26.7). As in the case of the sign-change mechanism, the phenomenon can be traced back to the atomic DTMs [8].

26.3.3.6. Comparison with Experiment. In this section we will compare the calculated (BP86/TZP) VCD spectrum calculated for $\Lambda\text{-}\delta\delta\delta\cdots 5Cl^-$ to an experimental spectrum measured in solution with 10-fold excess Cl^- ions (see Figure 26.17). The calculated spectra have been obtained by broadening the calculated rotational strengths with Lorentzian bands with half-widths of 8 cm^{-1} (for the fingerprint modes) and 15 cm^{-1} (for the stretching modes). The experimental spectra are not real experimental spectra; that is, they have been obtained by broadening the experimental intensities reported by Nafie et. al [23] with Lorentzian bands with half-widths of 8 cm^{-1} (for the fingerprint modes) and 15 cm^{-1} (for the stretching modes). The calculated normal mode frequencies have not been scaled. As can be seen in Figure 26.17, the calculated VCD spectrum reproduces very well the "experimental" spectra. Almost all bands in the experimental spectra can be unambiguously assigned. The calculated normal mode frequencies are also very good—there is no need to scale the frequency. This validates further the VCD sign-change and giant-enhancement mechanisms introduced in Section 26.3.3.4.

26.3.4. Transfer of Chirality

The transfer of chirality phenomenon occurs when an achiral molecule, which normally is optically inactive, becomes optically active upon interacting with a chiral molecule. The phenomenon is most often encountered when considering the interaction between a chiral solute molecule and an achiral solvent molecule—for example, solute–solvent molecular complex formation (via intermolecular hydrogen bonding).

The number of studies investigating the chirality transfer phenomenon using VCD spectroscopy has increased very rapidly in recent years [9, 19, 20, 25–27].

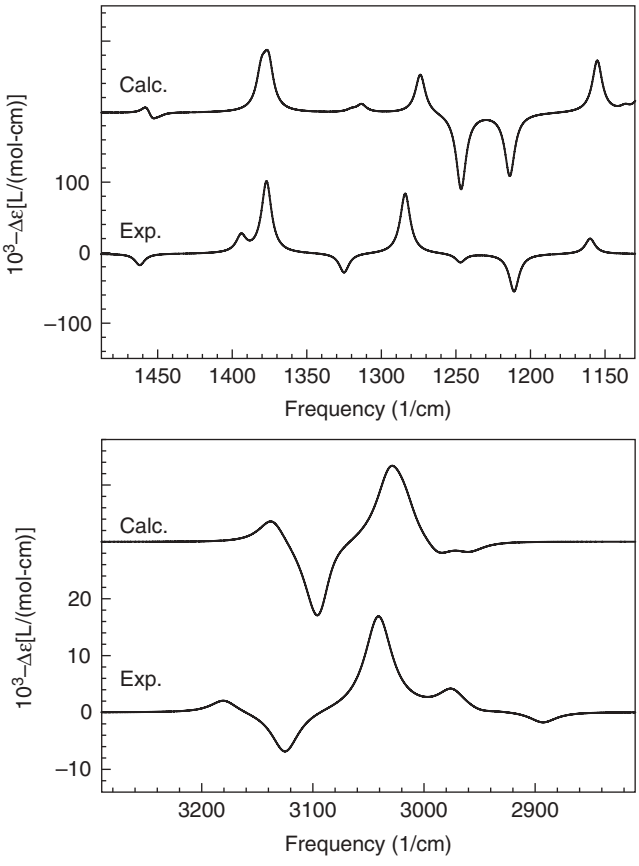

Figure 26.17. Comparison between the experimental and calculated VCD spectra of $[Co(en)_3]^{3+}$. The computed spectrum was obtained from BP86/TZP calculations for $\Lambda-\delta\delta\delta\cdots 5Cl^-$. The ''experimental'' spectrum was obtained by Lorentzian broadening of the experimental VCD intensities reported by Nafie and co-workers [23]. The experiments in reference 23 were performed in solution with 10-fold excess Cl^- ions.

From a physical point of view, the chirality transfer phenomenon is just another consequence of the mode mixing and charge transfer perturbations induced by molecular complex formation—that is, the cases discussed in Sections 26.3.2 and 26.3.3.

Due to symmetry constraints, the ETDM and MTDM associated to the fundamental transitions of all normal modes are perpendicular in isolated achiral molecules. As a result, the rotational strengths (i.e., the inner product between the ETDM and MTDM vectors) of all normal modes of an isolated achiral molecules are zero. That is, the achiral molecules are optically inactive. However, when involved in a molecular complex with a chiral solute molecule, the achiral solvent molecule can become optically active. This is because its EDTMs and MDTMs are affected by the mode mixing and charge transfer perturbations discussed in Sections 26.3.2 and 26.3.3, respectively, and as a result are no longer perpendicular.

To substantiate the above discussion, in the following we will compare (see Table 26.8) the C–D stretching mode of the isolated $CDCl_3$ molecule (FM) and of the $CDCl_3$ associated to a Pulegone molecule (MC)—that is, the molecular complex studied in Section 26.2.5.1. As can be seen, the C–D stretching is minimally affected by the molecular complex formations; that is, we have an overlap of 0.99 between the FM and MC modes and the two modes also have a very similar frequencies. Furthermore, as expected, the EDTM and MDTM of the FM are perpendicular (i.e., $\xi = 90.0^\circ$), whereas in the MC the two vectors are no longer perpendicular (i.e., $\xi = 91.8^\circ$). It is

TABLE 26.8. Transfer of Chirality in the 1:1 Pulegone–$CDCl_3$ Molecular Complex[a]

Overlap: 0.99		$\Delta\xi = -1.9^\circ$		
C–D Stretching	Frequency		R	ξ
FM	2309.0		0.0	90.0°
MC	2308.2		−1.2	91.9°
	$\vec{E}_{01}$			
Molecule	x	y	z	$\lvert\vec{E}_{01}\rvert$
FM	−1.01	+0.2	0.0	1.1
MC	+59.5	−4.6	−3.5	59.8
	$\vec{M}_{01}$			
Molecule	x	y	z	$\lvert\vec{M}_{01}\rvert$
FM	−0.1	−0.4	−1.2	1.2
MC	+2.8	+18.1	+57.5	60.3

[a]Comparison of the Frequencies (Freq.), Rotational Strengths (R), angles ξ, Cartesian components of the total electric (EDTM), and magnetic (MDTM) transition dipole moments of the C–D stretching mode in the free $CDCl_3$ (FM) and in the 1:1 Pulegone–$CDCl_3$ molecular complex (MC). Units: Frequency (cm^{-1}), D ($10^{-40}esu^2 \cdot cm^2$), R ($10^{-44}esu^2 \cdot cm^2$).

also important to note that the magnitudes of the EDTM and MDTM have increased significantly (i.e., almost a factor of 60), in the MC compared to the FM. As shown in reference 7, the perturbation responsible for the enhancement of the EDTM and MDTM of this mode, and therefore also for chirality transfer, is the charge transfer mechanism discussed in Section 26.3.3.3. Finally, we note that Bultinck et al. were indeed able to measure a weak VCD signal for the C–D stretching mode of the $CDCl_3$ [26].

Regarding the robustness of the C–D stretching mode of the $CDCl_3$, it should be clear that this mode is nonrobust: Not only its ξ angle is very close to 90.0°, but also its magnitude is very small. We note that this is in complete agreement with the conclusion obtained in reference [9] when studying the chirality transfer observed in the VCD spectra of the BBA–NH_3, water–methyl lactate, and water–D-lactic acid complexes. We can therefore conclude that since chirality transfer does not seem to lead to robust modes, its ability in providing useful information regarding the relative orientations of the solute and solvent molecule is very limited.

26.4. CONCLUSIONS

In this section, we will sum up the discussions presented in this chapter by giving a few general guidelines for interpreting the similarities/discrepancies between calculated and experimental VCD spectra.

First, according to the discussion in Section 26.2 and also in the Sections 26.3.1 and 26.3.3, it should be clear that the concept of robustness introduced in Section 26.2.4 is a very useful tool for (1) evaluating the reliability of VCD predictions and (2) assessing the significance of the similarities/discrepancies observed between experimental and calculated VCD spectra.

As the studies of the VCD spectra of Pulegone and binaphthol (measured in CH_2Cl_2 solvent) have shown, the absolute configuration (AC) of the solute can be determined accurately from calculations performed for single isolated solute molecules if the experimental VCD spectra have been measured in nonpolar solvents. That is, both the computed VCD spectra and the results of robust-mode analyses can be trusted in this situation. If, however, the VCD experiments have been performed in polar solvents and intermolecular hydrogen bonding (between solute and solvent molecules) exists in the experimental sample, the agreement between computed VCD spectra (obtained from calculations performed for single isolated solute molecules) and experiments can often be suboptimal. Moreover, since solute–solvent molecular complex formation can easily mix the solute modes (see Section 26.3.3.2) or trigger the VCD sign-change mechanism (see Section 26.3.3.3), VCD sign discrepancies between calculations and experiment can be expected even for peaks associated to modes assigned as robust in the VCD spectrum computed for the isolated solute molecule. Therefore, when intermolecular hydrogen bonding exists in the experimental sample, it is desirable to determine the AC of the solute by comparing the experiment VCD spectrum to computed spectra obtained from VCD calculations for the MC. As in the case of spectra computed for the FM, the reliability of the VCD prediction can be determined by performing a robust modes analysis for the spectrum calculated for the MC.

Second, it is important to realize that because the donor–acceptor interactions triggering the VCD sign-change and giant-enhancement mechanisms are typical interactions that are commonly encountered in both organic and inorganic compounds, these two mechanisms are very general and should affect the VCD intensities whenever intermolecular hydrogen bonding is present in the experimental sample. In fact, the sign-change and giant-enhancement mechanisms affect also the ROA spectra.

Third, since, as shown in Section 26.3.3, upon molecular complex formation, VCD sign changes can easily be induced even in robust modes, it is very important to determine whether or not molecular complex formation occurs in the experimental sample. This information can easily be obtained by performing an IR measurement in the C—H/N—H/O—H stretching region. In IR spectroscopy, the giant enhancement of the intensities of stretching modes also accompanied by large frequency shifts is a well-documented phenomenon that has been associated with the presence of hydrogen bonding in the experimental sample for a long time now [28].

Fourth, if intermolecular bonds between solute and solvent molecules are formed in the experimental sample, then by performing a normal modes analysis by mapping the calculated modes of the free molecule and of the molecular complex, one can get very good estimations (1) on how large are the effects induced in the VCD spectra by complexation and (2) regarding the frequency intervals where the VCD spectra are most affected by complexation. As shown in Section 26.3.3.5, additional information regarding possible VCD sign discrepancies between calculations and experiment can be obtained by analyzing the relative magnitudes of the nuclear and electronic components to the DTMs of normal modes of the FM.

Finally, the VCD sign-change and giant-enhancement mechanisms discussed in Section 26.3.3 should provide much more reliable information regarding the actual sites involved in the intermolecular complex and the bonding mechanism of complexation between solute and solvent molecules than the chirality transfer mechanism discussed in Section 26.3.4. As shown in Section 26.3.3, the VCD sign-change and giant-enhancement mechanisms induced changes in the VCD spectra that are (a) comparable to or larger than the typical VCD signals in the fingerprint region and (b) at least an order of

magnitude larger than the typical VCD signals in the N—H/O—H stretching region. Furthermore, the analysis of the VCD spectra in the frequency intervals below 1800 cm^{-1} and above 3000 cm^{-1} could in principle provide complementary information about the solute–solvent interactions. On the other hand, the VCD signals associated with chirality transfer are typically very weak—that is, approximately one order of magnitude smaller than the average VCD signals of a chiral molecule. Moreover, as discussed in Section 26.3.4, these signals are almost always associated with nonrobust modes.

26.5. ACKNOWLEDGMENT

EJB acknowledges support from the Korea Science and Engineering Foundation through the WCU program, grant no. R32-2008-000-10180-0.

REFERENCES

1. V. P. Nicu, J. Neugebauer, S. K. Wolff, E. J. Baerends, *Theor. Chem. Account*. **2008**, *119*, 245–263.
2. G. T. Velde, F. M. Bickelhaupt, E. J. Baerends, C. F. Guerra, S. J. A. Van Gisbergen, J. G. Snijders, T. Ziegler, *J. Comp. Chem*. **2001**, *22*, 931–967.
3. C. Fonseca Guerra, J. G. Snijders, G. Te Velde, E. J. Baerends, *Theor. Chem. Account*. **1998**, *99*, 391–403.
4. Amsterdam Density Functional Program. Theoretical Chemistry. Vrije Universiteit, Amsterdam, `http://www.scm.com`.
5. V. P. Nicu, E. J. Baerends, *PCCP* **2009**, *11*, 6107–6118.
6. W. Hug, M Fredorovsky, *Theor. Chem. Account*. **2008**, *119*, 113–131.
7. V. P. Nicu, E. Debie, W. Herrebout, B. Van der Veken, P. Bultinck, E. J. Baerends, *Chirality* **2010**, *21*, E287–E297.
8. V. P. Nicu, J. Autschbach, E. J. Baerends, *PCCP* **2009**, *11*, 1526–1538.
9. V. P. Nicu, J. Neugebauer, E. J. Baerends, *J. Phys. Chem. A* **2008**, *112*, 6978–6991.
10. A. Aamouche, F. J. Devlin, P. J. Stephens, *JACS* **2000**, *112*, 2346–2354.
11. F. J. Devlin, P. J. Stephens, J. R. Cheeseman, M. J. Frisch, *J. Phys. Chem. A* **1997**, *101*, 9912–9924.
12. A. Urakawa, D. M. Meier, H. Rugger, A. Baiker, *J. Phys. Chem. A* **2008**, *112*, 7250–7255.
13. F. Wang, P. L. Polavarapu, *J. Phys. Chem. A* **2000**, *104*, 1822–1826.
14. T. Burgi, A. Vargas, A. Baiker, *J. Chem. Soc.,Perkin Trans. 2* **2002**, 1596–1601.
15. T. B. Freedman, X. Cao, R. K. Dukor, L. A. Nafie, *Chirality* **2003**, *15*, 734–758.
16. V. W. Jurgensen, K. Jalkanen, *Phys. Biol*. **2006**, *3*, S63–S79.
17. T. B. Freedman, X. L. Cao, L. M. Phillips, P. T. W. Cheng, R. Dalterio, Y. Z. Shu, H. Zhang, N. Zhao, R. B. Shukla, A. Tymiak, S. K. Gozo, L. A. Nafie, J. Z. Gougoutas, *Chirality* **2006**, *18*, 746–753.
18. T. Kuppens, W. Herrebout, B. Van der Veken, P. Bultinck, *J. Phys. Chem. A* **2006**, *110*, 10191–10200.
19. M. Losada, Y. J. Xu, *PCCP* **2007**, *9*, 3127–3135.
20. M. Losada, H. Tran, Y. J. Xua, *J. Chem. Phys*. **2008**, *128*, 014508.
21. P. Polavarapu. N. Jeirath, S. Walia, *J. Phys. Chem. A* **2009**, *113*, 5423–5431.
22. E. J. Corey, J. C. Bailar, *JACS* **1959**, *81*, 2620–2629.

23. T. B. Freedman, X. L. Cao, D. A. Young, L. A. Nafie, *J. Phys. Chem. A* **2002**, *106*, 3560–3565.
24. P. J. Stephens, *J. Phys. Chem*. **1985**, *89*, 748–752.
25. E. Debie, L. Jaspers, P. Bultinck, W. Herrebout, B. Van der Veken, *Chem. Phys. Lett*. **2008**, *450*, 426–430.
26. E. Debie, P. Bultinck, W. Herrebout, B. Van der Veken, *PCCP* **2008**, *10*, 3498–3508.
27. G. C. Yang, Y. J. Xua, *J. Chem. Phys*. **2009**, *130*, 164–506.
28. G. C. Pimetel, A. L. McClellan, *The Hydrogen Bond*, W. H. Freeman and Company, San Francisco, **1960**.

INDEX

Comprehensive Chiroptical Spectroscopy, Volume 1: Instrumentation, Methodologies, and Theoretical Simulations, First Edition. Edited by N. Berova, P. L. Polavarapu, K. Nakanishi, and R. W. Woody.

© 2012 John Wiley & Sons, Inc. Published 2012 by John Wiley & Sons, Inc.